

Medical Radiology

Diagnostic Imaging

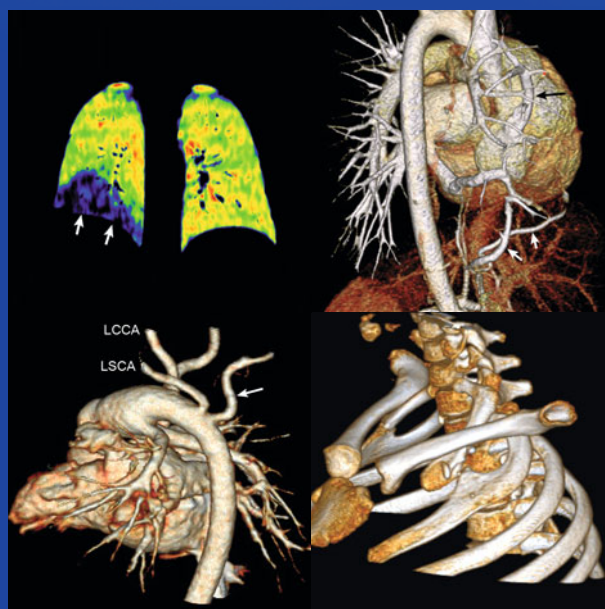
M.F. Reiser  
H.-U. Kauczor  
H. Hricak  
M. Knauth

Pilar Garcia-Peña  
R. Paul Guillerman  
*Editors*

# Pediatric Chest Imaging

*Third Edition*

 Springer



---

# Medical Radiology

## Diagnostic Imaging

### *Series editors*

Maximilian F. Reiser  
Hans-Ulrich Kauczor  
Hedvig Hricak  
Michael Knauth

### *Editorial Board*

Andy Adam, London  
Fred Avni, Brussels  
Richard L. Baron, Chicago  
Carlo Bartolozzi, Pisa  
George S. Bisset, Durham  
A. Mark Davies, Birmingham  
William P. Dillon, San Francisco  
D. David Dershaw, New York  
Sam Sanjiv Gambhir, Stanford  
Nicolas Grenier, Bordeaux  
Gertraud Heinz-Peer, Vienna  
Robert Hermans, Leuven  
Hans-Ulrich Kauczor, Heidelberg  
Theresa McLoud, Boston  
Konstantin Nikolaou, Munich  
Caroline Reinhold, Montreal  
Donald Resnick, San Diego  
Rüdiger Schulz-Wendtland, Erlangen  
Stephen Solomon, New York  
Richard D. White, Columbus

For further volumes:  
<http://www.springer.com/series/4354>



---

Pilar García-Peña • R. Paul Guillerman  
Editors

# Pediatric Chest Imaging

Third Edition

 Springer

*Editors*

Pilar García-Peña  
Departament of Pediatric Radiology  
Vall d'Hebron Children's University Hospital  
Barcelona  
Spain

R. Paul Guillerma  
Department of Pediatric Radiology  
Baylor College of Medicine  
Houston, TX  
USA

ISSN 0942-5373 ISSN 2197-4187 (electronic)  
ISBN 978-3-642-37336-7 ISBN 978-3-642-37337-4 (eBook)  
DOI 10.1007/978-3-642-37337-4  
Springer Heidelberg New York Dordrecht London

Library of Congress Control Number: 2014943247

© Springer-Verlag Berlin Heidelberg 2014

This work is subject to copyright. All rights are reserved by the Publisher, whether the whole or part of the material is concerned, specifically the rights of translation, reprinting, reuse of illustrations, recitation, broadcasting, reproduction on microfilms or in any other physical way, and transmission or information storage and retrieval, electronic adaptation, computer software, or by similar or dissimilar methodology now known or hereafter developed. Exempted from this legal reservation are brief excerpts in connection with reviews or scholarly analysis or material supplied specifically for the purpose of being entered and executed on a computer system, for exclusive use by the purchaser of the work. Duplication of this publication or parts thereof is permitted only under the provisions of the Copyright Law of the Publisher's location, in its current version, and permission for use must always be obtained from Springer. Permissions for use may be obtained through RightsLink at the Copyright Clearance Center. Violations are liable to prosecution under the respective Copyright Law.

The use of general descriptive names, registered names, trademarks, service marks, etc. in this publication does not imply, even in the absence of a specific statement, that such names are exempt from the relevant protective laws and regulations and therefore free for general use.

While the advice and information in this book are believed to be true and accurate at the date of publication, neither the authors nor the editors nor the publisher can accept any legal responsibility for any errors or omissions that may be made. The publisher makes no warranty, express or implied, with respect to the material contained herein.

Printed on acid-free paper

Springer is part of Springer Science+Business Media ([www.springer.com](http://www.springer.com))

---

## Contents

<b>Advances in Chest Radiography Techniques: CR, DR, Tomosynthesis, and Radiation Dose Optimization. . . . .</b>	<b>1</b>
Charles E. Willis and Steven Don	
<b>Classic Chest Radiology Findings, Pearls and Pitfalls . . . . .</b>	<b>13</b>
Gloria Soto and Karla Moënné	
<b>Ultrasound Study of the Pediatric Chest . . . . .</b>	<b>31</b>
Goya Enriquez, Celestino Aso, Xavier Serres, and Veronica del Prete	
<b>The Contribution of Nuclear Medicine to Pulmonary Imaging . . . . .</b>	<b>65</b>
Michael J. Gelfand and David L. Gilday	
<b>Helical Multidetector Chest CT . . . . .</b>	<b>75</b>
Pilar García-Peña, Tom A. Watson, and Catherine M. Owens	
<b>High-Resolution CT of the Lung in Children: Technique, Indications, Anatomy, and Features of Lung Disease. . . . .</b>	<b>111</b>
Javier Lucaya and Ana Coma	
<b>High-Resolution CT of the Lung in Children: Clinical Applications . . . . .</b>	<b>135</b>
Hubert Ducou Le Pointe	
<b>Fetal MR Imaging of the Chest . . . . .</b>	<b>157</b>
Pedro Daltro, Heron Werner, and Taísa Davaus Gasparetto	
<b>Neonatal Chest Imaging . . . . .</b>	<b>173</b>
Eric J. Crotty	
<b>Pulmonary Malformations Beyond the Neonatal Period . . . . .</b>	<b>197</b>
Josep M. Mata and Amparo Castellote	
<b>Congenital and Acquired Large Airway Disorders in Pediatric Patients . . . . .</b>	<b>219</b>
Evan J. Zucker, Monica Epelman, Ricardo Restrepo, and Edward Y. Lee	
<b>Congenital and Acquired Mediastinal Vascular Disorders in Children . . . . .</b>	<b>241</b>
Monica Epelman, Oleksandr Kondrachuk, Ricardo Restrepo, and Edward Y. Lee	
<b>Acute Chest Diseases: Infection and Trauma . . . . .</b>	<b>267</b>
José Fonseca Santos	

<b>Pediatric Tuberculosis</b> . . . . .	285
Pedro Daltro, Eloá Nunez-Santos, and Bernard F. Laya	
<b>Foreign Body Aspiration: Imaging Aspects</b> . . . . .	305
Benjamin Z. Koplewitz and Jacob Bar-Ziv	
<b>Imaging of the Pediatric Thymus and Thymic Disorders</b> . . . . .	327
Cassandra M. Sams and Stephan D. Voss	
<b>Pulmonary and Extrathymic Mediastinal Tumors</b> . . . . .	349
Karen Lyons, R. Paul Guillerman, and Kieran McHugh	
<b>Diffuse Lung Disease</b> . . . . .	373
R. Paul Guillerman	
<b>Thoracic Manifestations of Systemic Diseases</b> . . . . .	395
David V. Holland, R. Paul Guillerman, and Alan S. Brody	
<b>Radiology of the Chest Wall</b> . . . . .	431
Georg F. Eich, Christian J. Kellenberger, and Ulrich V. Willi	
<b>Pediatric Cardiac CT</b> . . . . .	459
Laureen Sena and Hyun Woo Goo	
<b>Pediatric Cardiac MRI</b> . . . . .	483
Rajesh Krishnamurthy and Taylor Chung	
<b>MRI of Lung Morphology and Perfusion</b> . . . . .	505
Sebastian Ley and Julia Ley-Zaporozhan	
<b>Hyperpolarized Gas MRI in Pediatric Lung Disease</b> . . . . .	513
Peter Komlosi, Jennifer L. Benjamin, and Talissa A. Altes	
<b>Interventional Radiology Management of Pediatric Chest Disorders</b> . . . . .	523
William E. Shiels II	
<b>Index</b> . . . . .	539

---

## Contributors

**Talissa A. Altes** Department of Radiology and Medical Imaging, University of Virginia, Charlottesville, VA, USA

**Celestino Aso** Department of Pediatric Radiology, Vall d'Hebron Hospitals, Barcelona, Spain

**Jacob Bar-Ziv** Department of Medical Imaging, Hadassah-Hebrew University Medical Centre, Jerusalem, Israel

**Jennifer L. Benjamin** Department of Radiology and Medical Imaging, University of Virginia, Charlottesville, VA, USA

**Alan S. Brody** Department of Radiology, Children's Hospital Medical Center, Cincinnati, OH, USA

**Amparo Castellote** Servei de Radiologia Pediàtrica, Hospital Vall d'Hebron, Barcelona, Spain

**Taylor Chung** Body and Cardiovascular Imaging, Department of Diagnostic Imaging, Children's Hospital and Research Center Oakland, Oakland, CA, USA

**Ana Coma** Department of Pediatric Radiology, Vall d'Hebrón Hospitals, Barcelona, Spain

**Eric J. Crotty** Department of Radiology, Cincinnati Children's Hospital Medical Center, University of Cincinnati College of Medicine, Cincinnati, OH, USA

**Pedro Augusto Daltro** Clínica de Diagnóstico por Imagem-CDPI, Rio de Janeiro, Brazil; Hospital dos Servidores do Estado-H.S.E., Rio de Janeiro, Brazil

**Veronica del Prete** Department of Pediatric Radiology, Vall d'Hebron Hospitals, Barcelona, Spain

**Steven Don** Mallinckrodt Institute of Radiology, Washington University School of Medicine, St. Louis, MO, USA

**Hubert Ducou Le Pointe** Service de Radiologie Pédiatrique, Hôpital d'Enfants Armand-Trousseau, Paris, France

**Georg F. Eich** Division of Pediatric Radiology, Kantonsspital, Aarau, Switzerland

**Goya Enriquez** Department of Pediatric Radiology, Vall d'Hebron Hospitals, Barcelona, Spain

**Monica Epelman** Department of Radiology, Nemours Children's Hospital, Orlando, FL, USA

**Pilar García-Peña** Professor Emeritus in Paediatric Radiology, Department of Paediatric Radiology, Vall d'Hebron Hospitals, Barcelona, Spain

**Taísa Davaus Gasparetto** Clínica de Diagnóstico por Imagem-CDPI, Rio de Janeiro, Brazil

**Michael J. Gelfand** Department of Radiology, Cincinnati Children's Hospital Medical Center, University of Cincinnati College of Medicine, Cincinnati, OH, USA

**David L. Gilday** Medical Imaging, Toronto Nuclear Medical Services, Toronto, ON, Canada

**Hyun Woo Goo** Department of Radiology and Research Institute of Radiology, University of Ulsan College of Medicine, Asan Medical Center, Seoul, Korea

**R. Paul Guillerman** Department of Pediatric Radiology, Texas Children's Hospital, Baylor College of Medicine, Houston, TX, USA

**David V. Holland** Mallinckrodt Institute of Radiology, Washington University School of Medicine, St. Louis, MO, USA

**Christian J. Kellenberger** Department of Diagnostic Imaging, The University Children's Hospital, Zurich, Switzerland

**Peter Komlosi** Department of Radiology and Medical Imaging, University of Virginia, Charlottesville, VA, USA

**Oleksandr Kondrachuk** Department of Radiology, Ukrainian Children's Cardiac Center, Kyiv, Ukraine

**Benjamin Z. Koplewitz** Department of Medical Imaging, Hadassah-Hebrew University Medical Centre, Jerusalem, Israel

**Rajesh Krishnamurthy** Department of Pediatric Radiology, Texas Children's Hospital, Associate Professor of Radiology and Pediatrics, Baylor College of Medicine, Houston, TX, USA

**Bernard F. Laya** St. Luke's Medical Center-Global City, Institute of Radiology, Taguig, Philippines

**Edward Y. Lee** Department of Radiology, Boston Children's Hospital and Harvard Medical School, Boston, MA, USA

**Sebastian Ley** Department of Diagnostic and Interventional Radiology, Chirurgische Klinik Dr. Rinecker, Munich, Germany; Division of Pediatric Radiology, Diagnostic and Interventional Radiology, Heidelberg, Germany

**Julia Ley-Zaporozhan** Division of Pediatric Radiology, Diagnostic and Interventional Radiology, Heidelberg, Germany; Division of Pediatric Radiology, Institute of Clinical Radiology, University Hospital Munich, Munich, Germany

**Javier Lucaya** Department of Pediatric Radiology and Institute of Diagnostic Imaging, Vall d'Hebrón Hospitals, Barcelona, Spain

**Karen Lyons** Department of Pediatric Radiology, Texas Children's Hospital, Baylor College of Medicine, Houston, TX, USA

**Josep M. Mata** UDIAT, Servei de Diagnòstic per la Imatge, Corporació Parc Taulí, Sabadell, Spain

**Kieran McHugh** Department of Radiology, Great Ormond Street Hospital for Children NHS Trust, London, UK

**Karla Moënné** Departamento de Diagnóstico por Imágenes, Clínica Las Condes, Santiago, Chile

**Eloá Nunez-Santos** Instituto Fernandes Figueira-Fiocruz, Rio de Janeiro, Rj-Brasil, Brazil



**Catherine M. Owens** Department of Cardiorespiratory Radiology, Great Ormond Street Hospital for Children, London, UK

**Ricardo Restrepo** Department of Radiology, Miami Children's Hospital, Miami, FL, USA

**Cassandra M. Sams** Department of Radiology, Boston Children's Hospital, Boston, MA, USA

**José Fonseca Santos** Hospital de Santa Maria, Lisbon, Portugal

**Laureen Sena** Department of Radiology, Boston Children's Hospital, Boston, MA, USA

**Xavier Serres** Department of Radiology, Vall d'Hebron Hospitals, Barcelona, Spain

**William E. Shiels II** Department of Radiology, Children's Hospital, Children's Radiological Institute, Columbus, OH, USA

**Gloria Soto** Departamento de Diagnóstico por Imágenes, Clínica Alemana de Santiago de Chile, Santiago, Chile

**Stephan D. Voss** Department of Radiology, Boston Children's Hospital, Boston, MA, USA

**Tom A. Watson** Department of Paediatric Radiology, Great Ormond Street Hospital for Children, London, UK

**Heron Werner** Clínica de Diagnóstico por Imagem-CDPI, Rio de Janeiro, Brazil

**Ulrich V. Willi** Emeritus, Department of Diagnostic Imaging, The University Children's Hospital, Zurich, Switzerland

**Charles E. Willis** Department of Imaging Physics, University of Texas M. D. Anderson Cancer Center, Houston, TX, USA

**Evan J. Zucker** Department of Radiology, Floating Hospital for Children, Tufts Medical Center, Boston, MA, USA

# Advances in Chest Radiography Techniques: CR, DR, Tomosynthesis, and Radiation Dose Optimization

Charles E. Willis and Steven Don

## Contents

<b>1</b>	<b>Introduction.....</b>	<b>1</b>
<b>2</b>	<b>Conventional Screen-Film Radiography.....</b>	<b>2</b>
<b>3</b>	<b>Digital Radiography .....</b>	<b>3</b>
3.1	Computed Radiography.....	4
3.2	Digital Flat-Panel Radiography.....	5
<b>4</b>	<b>Advanced Detector Technologies.....</b>	<b>5</b>
4.1	Structured Phosphor .....	5
4.2	Slot Scanner.....	5
4.3	Dual-Sided CR.....	6
4.4	Irradiation Side Sampling Digital Flat Panel.....	6
4.5	Gaseous/Avalanche Detectors .....	6
<b>5</b>	<b>Digital Image Processing .....</b>	<b>6</b>
5.1	Preprocessing .....	6
5.2	Latitude Reduction .....	7
<b>6</b>	<b>Dose Reporting.....</b>	<b>8</b>
6.1	Exposure Indicators .....	8
6.2	Dose Area Product .....	9
6.3	Informatics Initiatives for Dose Reporting.....	9
<b>7</b>	<b>Advanced Imaging Technologies with Potential Application to Pediatric Thoracic Radiography .....</b>	<b>10</b>
7.1	Dual Energy Subtraction .....	10
7.2	Tomosynthesis .....	10
<b>8</b>	<b>Radiation Dose Optimization in Pediatric Chest Radiography .....</b>	<b>10</b>
	<b>References.....</b>	<b>11</b>

## Abstract

A revolution in radiography has occurred in the last three decades; digital radiography has replaced screen-film radiography. To understand digital radiography, one must begin with the fundamental principles, which have not changed since Roentgen's time. The conversion of X-rays into a visible image, however, has changed from screen-film to digital radiography. A discussion on the characteristics of digital radiography and its most common forms, computed radiography (CR) and digital flat-panel radiography follows. The fundamentals of digital image processing are discussed, including pre-processing, latitude reduction, and contrast modification. Advanced technologies are also described, including structured phosphors, slot scanners, dual-sided CR, irradiation side sampling flat panels, and gaseous avalanche detectors. The potential application of dual energy subtraction radiography and tomosynthesis to pediatric thoracic radiography is also considered. The chapter concludes with a discussion on radiation dose optimization in pediatric chest radiography including the newest standards for exposure indicators, dose area product, dose reporting, and informatics initiatives to support dose reporting.

## 1 Introduction

The fundamental principles in creating a radiographic projection image remain unchanged from the time of Roentgen. That is, a polyenergetic beam of X-rays is produced by high voltage acceleration of electrons into a high-Z target such as tungsten where their kinetic energy is transformed into radiant energy. This X-ray beam, shaped by collimation, is directed toward a patient. The beam is differentially attenuated by portions of the patient's anatomy that differ in density, thickness, or composition, creating a shadow when

C. E. Willis (✉)  
Department of Imaging Physics, University of Texas  
M D Anderson Cancer Center, Houston, TX, USA  
e-mail: Chwillis@mdanderson.org

S. Don  
Mallinckrodt Institute of Radiology, Washington University  
School of Medicine, St. Louis, MO, USA

projected on a flat surface. Because the X-rays are too high in energy to be detected by the human eye, a process of conversion into a visible image must be employed in order for the shadow to be appreciated by a human observer. It is the process of conversion that has undergone a revolution during the last three decades, replacing screen-film radiography with digital radiography.

The design and terminology of the digital radiography is rooted in screen-film radiography. Many radiologists and technologists were trained in screen-film radiography. Much of the technical literature reflects the perspective of screen-film radiography. Many of our misconceptions about the new technology are caused by our attempt to apply familiar concepts from screen-film radiography. There are still hospitals using screen-film radiography today. To fully understand this new technology, a review of conventional screen-film radiography is worthwhile.

## 2 Conventional Screen-Film Radiography

Conventional screen-film radiography relies on conversion of X-rays into light through photoelectric interactions with an intensification screen. The fluorescent light from the screen creates a latent image by activating silver halide grains in the film so they are able to be reduced to elemental silver by a chemical developer. This developed image is then fixed by removing all remaining silver halide using acetic acid. The negative image is then viewed by transillumination. Dark areas, such as the lungs, show low attenuation and light areas, such as bones, show high attenuation of the original X-ray beam. The contrast that is visible in the conventional radiograph is governed by a number of well-known factors such as the X-ray beam quality, i.e., the effective energy, the patient anatomy in the beam, the ratio of scattered radiation to primary X-rays at the image receptor, the inherent properties of the screen-film combination manifested in the characteristic Hurter and Driffield curve, the specifics of the chemical development, and the manner of transillumination. All these variables were fine-tuned over more than a century of research and development and clinical practice. The result was a single rendering of the X-ray shadow that could be appreciated by a human observer and served as a permanent record of the radiographic examination.

The screen-film combination produced a diagnostic quality image under relatively limited conditions of exposure, so that exposure techniques needed to be tightly controlled. Radiographic technique guides were designed to accommodate different anatomical views and patient sizes while still delivering the necessary X-ray exposure to the image receptor. The wide variation in patient sizes from neonate to adult made it necessary to design specialized

technique guides for pediatric radiographic imaging. Automatic exposure control (AEC), the primary mechanism for controlling exposure factor technique for routine adult thoracic radiography, was unsuitable for most pediatric chest examinations because the physical dimensions of the AEC ion chambers did not correspond to appropriate pediatric anatomical regions, and even with smaller “pediatric chambers” the task of assuring proper registration of the anatomy of a small, non-compliant patient with a small AEC chamber was impractical. Mis-registration can result in either over- or under-exposure, and either can produce non-diagnostic screen-film radiographs. For this reason, manual or fixed technique is preferred in most pediatric radiographic imaging at most centers, although there is no universal agreement.

The optical density in the developed film depended on exposure in a unique manner specific to the screen-film combination, so a variety of screen-film cassettes were designed for different radiographic examinations. Selections included general purpose, extremity, and chest cassettes. Screen-film combinations for chest imaging were designed to produce a long enough latitude to capture the low attenuation regions of the lungs, as well as the higher attenuation regions of the mediastinum and bony structures of the thorax. The pinnacle of screen-film technology for the chest was the asymmetric screen-film combination where the front and rear intensification screens were not only of different thicknesses, but also composed of different materials.

The speed of a screen-film combination was the inverse of the amount of x-ray exposure necessary to produce one optical density unit (above base-plus-fog) in the film when developed according to the manufacturer’s specifications. Speed classes were created to categorize screen-film combinations for comparison to the speed of traditional calcium tungstate screens, so-called par speed screens, which were assigned a speed class of 100. These screens were termed “slow,” 200 speed class was also known as “medium,” and 400 speed class was called “fast.” Screen-film combinations of 800 and 1600 speed class were also manufactured and often used in bedside radiography.

It is possible to use the same material to produce screen-film combinations of different speed classes. The thicker the layer of screen material, the more light is produced by the same amount of X-ray exposure, and hence a faster screen-film system. The drawback of this approach is that the thicker the intensification screen, the more light is produced at different depths in the screen and consequently the more unsharpness or blur by the time the light reaches the film. The speed class is inversely related to the spatial resolution in the resulting radiograph. Slow speed screen-film systems, used in extremity cassettes, are also called “detail” cassettes because of their higher resolution.

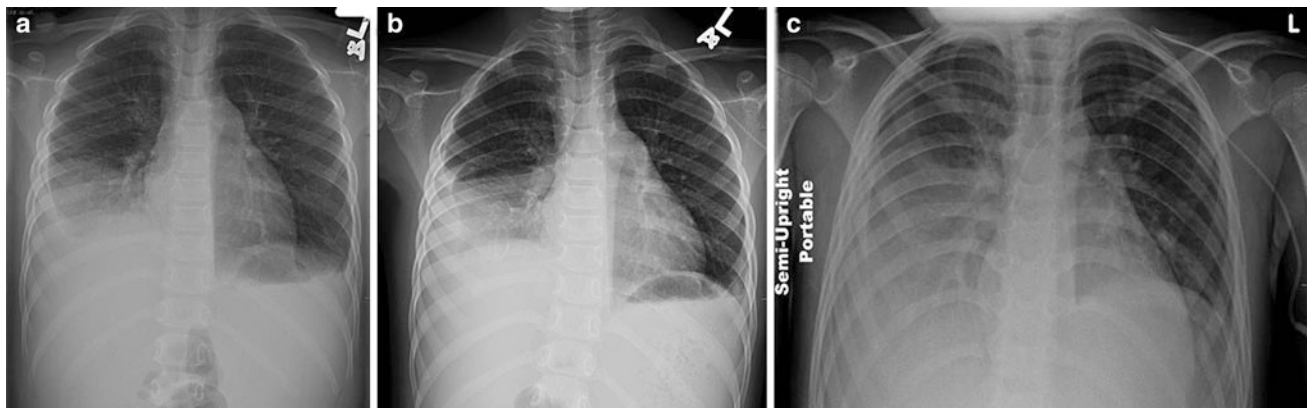


**Fig. 1** Three projection images of the same 8-year-old child. **a** Upright PA view at 180 cm SID with fixed grid using DR; **b** Upright AP view 4 days prior at 180 cm SID with fixed grid using DR; and **c** Semierect, portable AP view at 100 cm SID without grid using CR

In order to produce even more light, screen-film cassettes typically had two screens with the film sandwiched between. The photographic emulsion was usually coated on both sides of the polyester base resulting in a double-emulsion film. However, a single emulsion film could be used in conjunction with one or two screens in order to improve the resulting detail. Single emulsion film was typically used with small parts imaging such as mid to distal extremities.

The slower (lower) the speed class, the more the X-ray exposure needed to produce a diagnostic image and the higher the X-ray exposure to the patient. In order to reduce radiation exposure to pediatric patients, many hospitals adopted fast and ultra fast screen-film systems (600 speed or greater), sacrificing the spatial resolution in the radiographic image. Other hospitals that appreciated the visualization of small clinical features in the pediatric thorax deliberately chose medium speed class systems for pediatric radiography. It should be understood that patient radiation doses are small in projection radiography, and even with repeated examinations, the total dose does not approach the magnitude of a single fluoroscopic examination or that from a computed tomographic examination (Willis 2002).

Projection radiography of the pediatric chest is complicated by the variation in size and compliance among children. The same child may be imaged in a posterior–anterior (PA) orientation at an upright exposure station using a long source-to-image distance (SID), an anterior–posterior (AP) orientation at the same upright exposure station, in AP orientation atop a table using a short SID, and in AP orientation either bedside or in an ICU setting (Fig. 1). The variation in acquisition geometry causes variation in the distortion of clinical features projected on the same flat image receptor. This in turn complicates the determination of interval change by the radiologist.

The lack of compliance in children has led to the development of specialized accommodations for immobilization during the examination. Immobilization devices are

not completely radiolucent and cast shadows on the projected image (Fig. 2). Because some of the X-rays exiting the patient are attenuated by the device before reaching the image receptor, more X-rays must be used resulting in a small penalty in radiation dose to the patient.

Because there was only one copy of the image, competition arose between physicians who wanted to use the information contained in the radiograph. For example, radiologists needed the image for primary interpretation while intensivists needed the image to monitor the condition of the patient and to provide immediate feedback on therapeutic procedures such as central venous line placement. This competition was resolved by two methods: copy film and double-loading. Upon developing the radiograph, the darkroom technician could immediately produce a copy film which was supplied to the intensivist. In this case, the radiologist would interpret the original radiograph, and the intensivist would have an image of compromised quality. An alternative method was double-loading of cassettes, that is, placing two sheets of film between the two fluorescent intensification screens to produce two radiographs from a single exposure. This practice led to two radiographs of compromised image quality, but satisfied the needs of two geographically dispersed observers. Neither method was optimal for both physicians. Both methods required additional materials and technologist time.

### 3 Digital Radiography

With the advent of computers and improvement in image distribution using networks, screen-film radiography has been largely supplanted by digital radiography. Digital images are available at multiple locations within a hospital network at the same time. Both the radiologist and the patient care provider can view the same study simultaneously at disparate locations. An extensive review of the

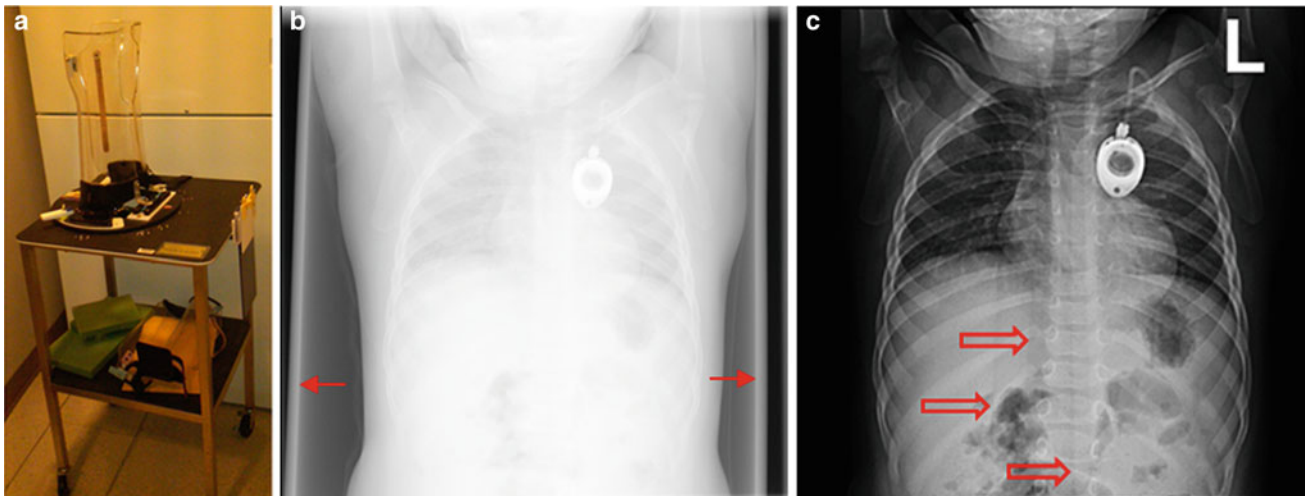


**Fig. 2** Patient immobilization devices affect image quality and impose a dose penalty. **a** Pigg-O-Stat<sup>TM</sup> **b** unprocessed DR image showing edges of the holder (*arrows*) **c** for presentation image showing vertical artifacts (*open arrows*)

technology and its application to chest radiography was published by Schaefer-Prokop et al. (2008).

Historically, digital radiography can be divided into two broad subtypes, computed radiography which requires a separate laser readout step and digital flat panel radiography which integrates the readout step into the imaging detector. These distinctions are blurred with the newer technologies. An alternative categorization divides digital radiography into “cassette-based” and “cassetteless” depending on the form-factor of the image receptor, irrespective of the image acquisition technology (Seibert 2007; Romlein 2007; Willis 2008).

### 3.1 Computed Radiography

Computed radiography (CR), also known as photo-stimulable phosphor (PSP) radiography, is based on the principle of photo-stimulable luminescence (PSL). A number of crystalline materials having some impurities that cause crystal defects, such as europium-doped barium fluorohalide, are able to store energy for an indeterminate period, and subsequently release that energy when exposed to light. The phenomenon has been known for centuries, but was only recently applied to imaging (Luckey 1975). An excellent review of CR has been published by Rowlands (2002). Coincident with the introduction of CR into clinical practice in the United States, the first reports of its use for radiographic imaging of the pediatric thorax are found (Kogutt et al. 1988; Cohen et al. 1989, 1991; Tarver et al. 1990; Merlo et al. 1991).

Three major film manufacturers competed to field CR products for clinical radiography. Oddly enough the original

motivation was simply the manufacture of film. Suppose that a radiographic image could be captured on a single media, and the output to a single type of film. Since the image was digitized as an intermediate step in the process, it could be modified so that the resulting film image mimicked the image that would have been produced by any one of a dozen screen-film combinations. Multiple identical copies of the image could be printed, resolving the competition between the radiologist and patient caregiver for a single unique radiograph. It is important to understand that digital imaging was not originally intended to replace film, rather to make the manufacture of film more efficient and was likely to produce and sell more film!

The physical mechanism of PSL is not completely understood. The interaction of X-rays with the PSP material excites electrons, which can de-excite by prompt emission of light (fluorescence). Some of the excited electrons do not immediately give up their energy; instead they are trapped at a higher than normal energy state in local potential energy “wells” associated with defects in the crystal lattice (also known as “color centers”). The trapped electrons constitute the latent image. Over time the trapped electrons can escape on their own, but the fading of the stored signal is very gradual. When the PSP is exposed to light of a particular wavelength using a laser reader, the trapped electrons absorb enough energy to escape their traps and de-excite with the emission of visible light. The amount of emitted light is proportional to the original amount of X-ray exposure, so that it faithfully represents the projected X-ray shadow. The light can be collected and amplified by a photomultiplier tube and converted by an analog-to-digital converter into a digital value that is representative of the original X-ray exposure to the PSP. The original design of the laser readers



was 90 s intended to compete with automatic film processor cycle time. The current generation of laser readers requires about 30–40 s to process the latent image.

### 3.2 Digital Flat-Panel Radiography

Digital radiography without the intermediate latent image and physical processing required by PSP-based radiography was first reported in the early 1980s. Scanned projection radiography was accomplished by means of a flying spot scanner that involved mechanical motion of a specially collimated X-ray generator and detector. The detector was a sodium iodide (NaI) scintillation crystal attached to a photomultiplier tube. Like CR, early application to pediatric chest radiography was reported almost simultaneously (Heller et al. 1982; Kushner 1983). Early reports also considered scanned linear arrays, such as the scout view of a Computed Tomography system as a means to generate a DR image of the chest.

Early DR systems relied on video cameras, and later charge-coupled device (CCD) arrays. Video cameras had very limited spatial resolution. CCD arrays have very small dimensions, therefore, a large field of view (FOV) must be minified somehow to conform to the small CCD array. This can be accomplished either by optical lenses or by tapered fiber optic bundles. Both of these methods have large losses in efficiency.

The amorphous silicon (a-Si) thin film transistor (TFT) array is the technology that made DR practical for medical imaging. The TFT array is bonded to the X-ray detector, eliminating the need for a separate reader step. Typical processing time is 10 s or less, much faster than CR. DR systems require some sort of X-ray conversion material. These flat-panel detectors are divided into indirect DR systems and direct DR systems based on the method of conversion. Indirect DR systems use an X-ray conversion layer, or *scintillator*, that converts X-rays into visible light by means of fluorescence. This is functionally similar to the intensification screen of the screen-film system, or to the input phosphor of an imaging intensifier for a fluoroscopy system. Gadolinium oxysulfide ( $\text{Gd}_2\text{O}_2\text{S}$ ) and cesium iodide (CsI) are used in commercial indirect DR systems. Both of these materials convert X-rays into visible light. Visible light is easier to convert into an electronic signal (charge).

Direct DR systems use a thick amorphous selenium (a-Se) layer which converts X-rays directly into charge without the intermediate fluorescence step. High voltage across the amorphous selenium causes the charges (electron/hole pairs) that are created to migrate directly to the TFT elements where they are collected without lateral diffusion. This gives direct DR exceptional sharpness (spatial resolution). Direct DR systems are most often found in mammography applications.

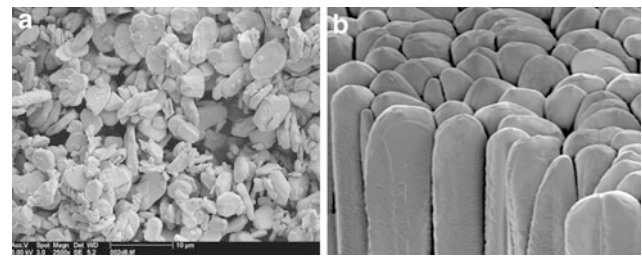


**Fig. 3** Photomicrographs of unstructured and structured phosphors. **a** unstructured or powder phosphor. Gadolinium oxysulfide ( $\text{GOS}$ ;  $\text{Gd}_2\text{O}_2\text{S}$ ) is used in DR and barium fluorobromide ( $\text{BaFBr}$ ) is used in CR. **b** structured or needle phosphor. Cesium iodide (CsI) is used in DR and cesium bromide ( $\text{CsBr}$ ) is used in CR. Courtesy of AGFA Healthcare

## 4 Advanced Detector Technologies

### 4.1 Structured Phosphor

X-ray conversion layers differ in a fundamental way.  $\text{Gd}_2\text{O}_2\text{S}$  crystals are contained in a binder medium without any particular structure. On the other hand, CsI crystals are needles arranged parallel to each other (Fig. 3). This structure channels the fluorescence within each crystal toward the TFT array and discourages lateral diffusion of the light. For this reason, indirect DR systems that use CsI are expected to have better sharpness than those that use  $\text{Gd}_2\text{O}_2\text{S}$ . Alternatively, CsI conversion layers can be designed to provide better efficiency than  $\text{Gd}_2\text{O}_2\text{S}$  with the same sharpness, simply by making them thicker.

The same principle can be applied to CR. Photo-stimulable phosphor materials are typically crystals contained in a binder without any organized structure. However, cesium bromide (CsBr) crystals can be made into an organized structure like CsI, and can also be doped to produce photo-stimulated luminescence (Leblans et al. 2000). The CsBr structured phosphor has the same advantages as CsI for restricted lateral diffusion of light over unstructured phosphors.

### 4.2 Slot Scanner

Scattered radiation degrades contrast in projection radiography. The anti-scatter grid is a well-known countermeasure, but has a penalty in requiring more X-ray exposure to get the same signal at the image receptor, with a corresponding increase in patient radiation dose. The amount of scattered radiation depends on the volume of tissue in the X-ray field—even for small patients this volume can be substantial when the entire image receptor is exposed at once. The mechanical slot-scanner moves a fan-shaped beam of X-rays across the FOV. In this way, a smaller volume of tissue is irradiated at one time, and the amount of



scattered radiation is much less. This reduction in scatter is achieved without any dose penalty to the patient.

Slot scanners have shown significantly reduced scatter fraction compared with anti-scatter grids (Samei et al. 2004; Liu et al. 2008) and have shown some improved detection of simulated nodules and interstitial lung pathology in phantom testing (Kroft et al. 2004, 2005) but there is no information on use in clinical pediatric chest imaging.

### 4.3 Dual-Sided CR

The light from PSL is emitted in all directions. Conventional CR scanner designs collect light from the same side of the imaging plate that is stimulated by the laser, collecting at best only one-half of the PSL that is emitted. If the phosphor material is coated onto a translucent base, then it is possible to collect PSL from the back side of the imaging plate as well. Combining the signal collected from the back with the signal from the front improves the efficiency of detection with a small penalty in sharpness. Uffmann et al. (2005) reported improvement in the detection of simulated nodules using dual-sided CR compared to single-sided CR.

### 4.4 Irradiation Side Sampling Digital Flat Panel

This flat panel detector is designed so that the X-ray beam exiting the patient passes through the TFT array before reaching the CsI X-ray conversion layer. The TFT array is relatively radio-transparent, so there is little loss of signal. The majority of X-ray interactions generate fluorescence closer to the TFT array, so that there is less unsharpness from spreading of the light. In addition, the CsI crystals are grown on a substrate and then reversed and optically coupled to the TFT array. In this way, the fluorescence exits the top of the crystals, instead of the base of the crystals so that there is less diffusion of light from needle-to-needle. This detector is intended to produce better spatial resolution than conventional indirect DR designs.

### 4.5 Gaseous/Avalanche Detectors

A novel xenon (Xe) high-pressure (6 atm) gas-filled detector has been incorporated into a commercial imaging product primarily intended for orthopedic imaging. The detector has a high voltage electrode and an antenna array that amplifies photoelectrons produced from interactions with the X-ray beam into an avalanche that is collected by printed microstrips. The imaging system incorporates two of these detectors each paired with an X-ray tube collimated

into a fan beam. The two fan beam/detector pairs are oriented orthogonally to each other. The subject stands upright in the imaging system and the fan beam/detector pairs descend from their highest extent to scan the patient simultaneously in the PA/AP and lateral orientation. The images are created line-by-line.

Commercial gas/avalanche slot scanners have been used for scoliosis examinations with a reduction in skin dose by a factor of 6–9 over CR systems with improved subjective image quality ratings (Deschenes et al. 2010; Despres et al. 2005). The time required to scan the thorax is 4–5 s, which may limit its utility for pediatric chest radiography, considering the potential for body motion, breathing, and multiple cardiac cycles during acquisition.

## 5 Digital Image Processing

The principal advantage of the digital image compared to the conventional radiograph is the ability for multiple caregivers simultaneously to view the study in disparate locations. In addition to the advantage of availability, the digital image can be modified from its original state creating an infinite variety of possible presentations. In fact, modification of the original digital image is not just a cosmetic enhancement; this is absolutely required in order to render it usable for clinical diagnosis. By changing processing, one can enhance the image to identify abnormalities such as pneumothorax or highlight catheter placement.

A plethora of schemes and brand names exist for digital image processing. These are often cited by sales personnel as basis for differentiation among products. Irrespective of the specific method of acquisition, functional categories of image processing can be identified.

### 5.1 Preprocessing

Preprocessing (sometimes called “pre-acquisition processing”) involves corrections that are applied to the raw digital data. These include, in the case of CR and linear scan systems, corrections for nonuniform light collection efficiency in one dimension across the image receptor, and in the case of DR and other two-dimensional fixed array systems, corrections for gain, and offset nonuniformity among individual detector elements and amplifiers as well as correction of nonfunctional (“dead”) detector elements (Fig. 4).

Preprocessing may also include rescaling of the numerical values of the digital data so that they bear a particular mathematical relationship to the X-ray exposure that produced them. For example, the raw data may have a linear relationship to the X-ray exposure and preprocessing may transform them so that they are linear with respect to the

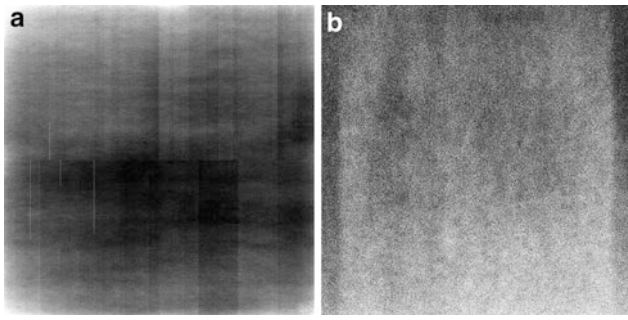


**Fig. 4** Flat field DR images. **a** uncorrected and **b** corrected for gain and offset. Proper calibration corrects for unequal gain among detector elements (dels) and for nonfunctional dels

logarithm of exposure. Preprocessing is applied automatically according to data gathered during calibration protocols. Preprocessing is generally transparent to the radiologist, unless there is an error in the calibration. The digital image that results from preprocessing is called the “original data” in IEC terminology, “for-processing data” in DICOM terminology, and may be called “raw, ranged data” for some systems that incorporate auto-ranging in their preprocessing (Fig. 5).

## 5.2 Latitude Reduction

DR systems have an extremely wide latitude compared to conventional screen-film systems, that is, they are able to capture X-ray exposures over a range of ten-thousand versus a range of one-hundred for screen-film radiography. DR systems are much more tolerant of underexposure and overexposure, reducing the need to retake images for these reasons. The range of exposures present in the X-ray shadow of any particular anatomic projection is only about a range of one-hundred. This means that the original DR image has extremely low contrast compared to a screen-film image. The primary purpose of digital image processing is therefore to determine the digital “values of interest” (VOI) that correspond to clinical features in the image and to remap those values to increase contrast, while sacrificing contrast elsewhere. Contrast is increased for clinical features by selectively reducing the overall latitude.

### 5.2.1 Exposure Recognition. Detection of Collimator Boundaries or Anatomy

The first task in determining the VOI is to locate the area within the field of view (FOV) that has received substantial X-ray exposure. The common method for accomplishing this is to locate the boundaries of collimation, which is fairly easy considering that the exposure outside the collimators is much less than inside the collimators, even if patient anatomy is in the beam. A more sophisticated method used by one manufacturer is to locate the edges of

the projected anatomy within the FOV. Both these methods are subject to interferences from shielding and high density materials such as orthopedic implants that overlie edges of the X-ray field. Collimation is notoriously variable in pediatric chest radiography, causing one manufacturer to develop special pediatric examinations that rely on a neural network to identify the VOI.

### 5.2.2 Window-Width and Window-Level Adjustment According to Grayscale Histogram

Most DR systems perform an analysis of a *grayscale histogram* which is a bar-graph of the number of picture elements (pixels) within the VOI versus their signal value (Fig. 5). The histogram analysis may involve some expectations about the shape of the histogram for the specific anatomic view, and results in a window-width (WW) and window-level (WL) for the default presentation of the digital image. The histogram analysis may also report a value indicative of the X-ray exposure that the image receptor received.

There are three important consequences of adjustment of the WW and WL by this automated method. First, over and underexposure are compensated by shifting the WL. Second, the latitude of images from patients of different sizes or acquired using different kVps are matched by changing the WW. Third, contrast of features within the VOI is maximized by displaying the digital image with the WW and WL.

### 5.2.3 Contrast Modification

The digital image can be subjected to any number of exotic processes to modify the contrast of specific features for specific purposes. All of these processes involve sacrificing contrast of some details in order to increase contrast of others. The simplest process is remapping of the digital values according to a nonlinear look-up-table (LUT) to achieve a screen-film-like appearance. A more complex process often used is called an *unsharp-mask*, where a blurred version of the images is subtracted from the original image to create a mask, which is added back to the original image to enhance the contrast of high frequency features, i.e., edge enhancement (Fig. 6). Even more complex methods decompose the digital image into frequency bands and apply filters or amplification (boost) in order to improve sharpness, reduce noise, or generate different contrast according to the size of objects in the image.

These automated processes are controlled by the specification of numerous adjustable parameters, some of which are under operator control and some of which may only be known to manufacturer personnel. The appropriate amount of image processing depends on the anatomic view and thickness. For example, the processing for a bedside neonatal chest image will differ greatly from the processing for an upright adult chest image. There are no standards for digital image

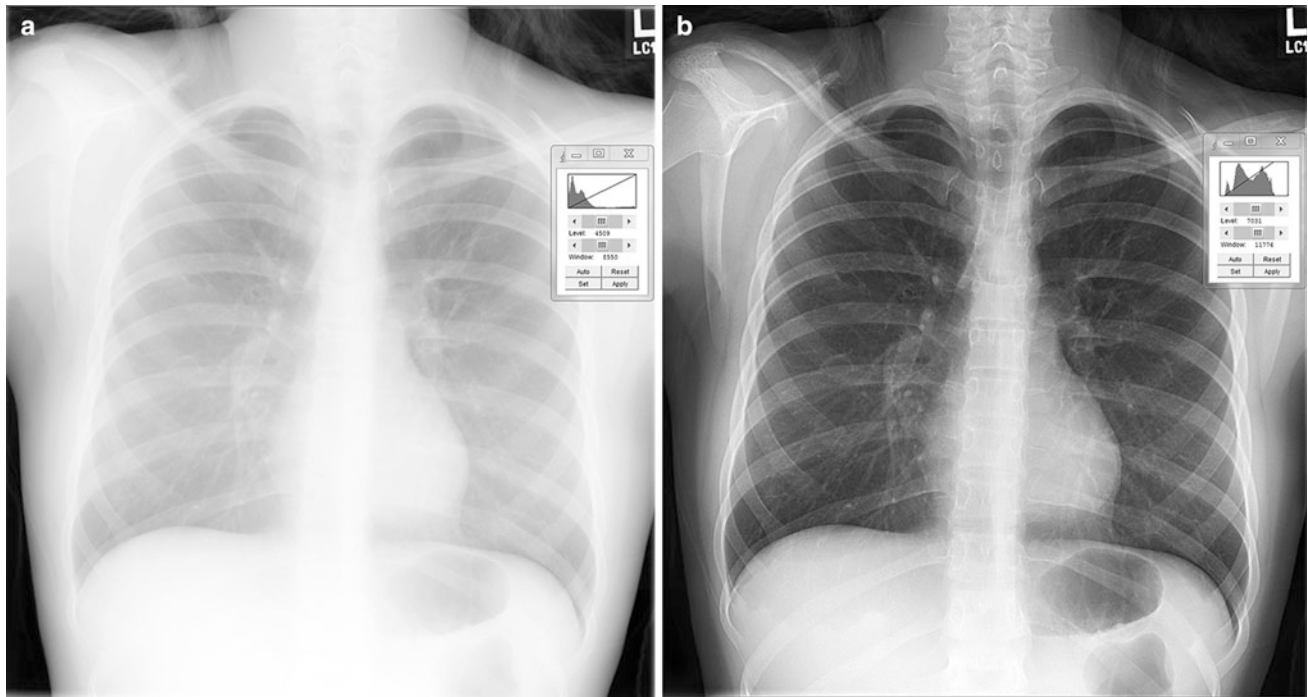


**Fig. 5** PA chest image of a 12-year-old female. **a** “for processing” image and grayscale histogram. Note the lack of contrast between soft tissue and bone in the “for processing” image. The wide histogram ranges from 234 through 8784 but the relevant image is centered at 1785. In the “for processing” image, grayscale values increase linearly with exposure. This DR system rescales the grayscale values during

processing so that their numerical values increase with the negative logarithm of exposure. **b** “for presentation” image and grayscale histogram. The “values of interest” (VOI) have been determined, the window-width and window-level adjusted so that contrast is appropriate for the final, displayed image

processing, so the nomenclature and parameter settings are unique from manufacturer to manufacturer. Obtaining the same look from two different manufacturers is possible, but complicated. Customization of image processing parameters for every possible radiographic view and patient size is extremely labor intensive, and is not adequately facilitated for the user in current DR systems.

## 6 Dose Reporting

### 6.1 Exposure Indicators

As mentioned in Sect. 5.2.2 above, histogram analysis of the digital image provides an indication of the radiation exposure to the image receptor. Until recently, there was no standardization of the mathematical form, calibration conditions, or units of exposure for exposure indicators. Each manufacturer had its own proprietary exposure indicator. The diversity in the relationship of these indicators to the receptor exposure, e.g., linear versus logarithmic, direct or inverse, confused technologists and radiologists. A parallel effort by the American Association of Physicists in Medicine (AAPM; Shepard et al. 2009) and the International Electrotechnical Commission (IEC; IEC 62494-1:2008) has

created a standard for exposure indicators that is linearly and directly related to the plate exposure (Seibert and Morin 2011) and is being implemented in many new digital radiography products. From a radiologist’s perspective, the standards are very similar and functionally equivalent. The Medical Imaging & Technology Alliance (MITA), representing many digital radiographic equipment manufacturers, has agreed to use the IEC standard (Vastagh 2011).

There are three terms that a radiologist should learn in order to understand the new standard (Don et al. 2012). The *Exposure Index (EI)* is a measure of the entrance air KERMA at the image receptor,  $K_{cal}$ . Its value is compared to a target air KERMA, *Exposure Index Target ( $EI_T$ )*, is the “optimized” reference exposure index that is specific for the particular anatomic view and image receptor. A *Deviation Index (DI)* is then reported to provide feedback on how far the actual exposure was from the target value. According to the IEC standard,

$$EI = K_{cal} \times 100 \mu\text{Gy}^{-1} (\text{unitless}) \quad (1)$$

$$DI = 10 \times \log_{10} (EI/EI_T) \quad (2)$$

Table 1 illustrates the relationship between the deviation index value and the fraction of the intended exposure to the image receptor.



**Fig. 6** Effect of edge enhancement. magnified portion of DR image from Fig. 5 processed with **a** less enhancement and **b** stronger enhancement of small features (identical to Fig. 5b). Note that the borders of the ribs and vertebral body edges are easier to discern

A deviation index of  $\pm 1$  corresponds to approximately one mAs station on a well-calibrated X-ray system. These mAs stations follow a geometric sequence known as a “Renard series” (also known as ISO R’10) where each step corresponds to a change of approximately 25 %. A deviation index of  $\pm 3$  corresponds to a doubling or halving of exposure from the target value.

Traditional exposure indicators and those that follow the new standard are both subject to interferences and require proper calibration to yield meaningful data. In the best case, they represent the exposure to the image receptor. The exposure indicators are not measures of patient dose. With some assumptions about patient thickness, X-ray field size, and technique factors such as kVp, source-to-image distance (SID), and presence of a grid, patient dose can be estimated from the value of the exposure indicator.

## 6.2 Dose Area Product

Dose Area Product (DAP), or more appropriately KERMA Area Product (KAP), is a quantity that represents the air KERMA at any point along the central axis of the X-ray beam times the field dimensions at that same point. The “dose” in

**Table 1** Deviation index versus Target exposure

Deviation index ( <i>DI</i> )	Fraction of intended exposure (%)
−3	50
−2	63
−1	79
0	100
1	126
2	158
3	200

DAP is actually the *dose to air*, so that DAP and KAP are fundamentally equivalent.<sup>1</sup> The value of DAP (in units of air KERMA times distance squared) is constant at any distance along the central axis, because the reduction in air KERMA from the inverse square law is counteracted by the divergence of the beam, as illustrated in Fig. 7. If the FOV is known at the entrance surface of the patient, the dose to the patient can be calculated from the entrance air KERMA.

DAP may be measured using an ion chamber attached to the collimator assembly, or it may be calculated from knowledge of the X-ray output and FOV. In the case of DAP, integrated DR systems have a distinct advantage over cassette-based systems and incompletely integrated “add-ons”; integrated systems have knowledge of the radiographic technique and collimation and can therefore estimate DAP. The radiographic technique and FOV can also be reported in the header of the digital image for retrospective analysis. It is important to note that the International Electrotechnical Commission (IEC) requires only  $\pm 35$  % accuracy in dosimetric indications such as DAP, so radiologists should not regard reported values as absolute.

## 6.3 Informatics Initiatives for Dose Reporting

In the development of connectivity to support electronic imaging, dose reporting was an afterthought. Early attempts to monitor dose relied on interpreting irradiation events reported via the DICOM Modality Performed Procedure Step (MPPS) or on inspection of DICOM header elements from individual images. These methods are still in use. Recent efforts have begun to define and standardize dose reporting within the existing framework of the Digital Imaging and Communications in Medicine (DICOM) standard and the Integrating the Healthcare Enterprise (IHE®) initiative.

<sup>1</sup> Some older systems report “EAP”, or “Exposure Area Product” in traditional units of Roentgen times distance squared.



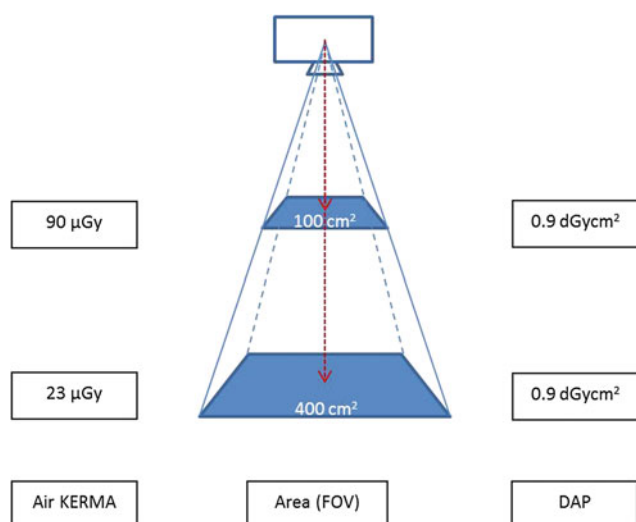


**Fig. 7** DAP is independent of distance from the X-ray tube. DAP is the product of Air KERMA and field size. Although Air KERMA decreases by the square of the distance from the X-ray tube, the field size increases at the same rate, therefore, DAP remains constant

The DICOM Radiation Dose Structured Report (SR) is the information object now intended to contain specific data about the dose delivered during an irradiation event, including projection radiography. The IHE Radiation Exposure Monitoring (REM) profile depends on the DICOM SR templates to retrieve and archive dose information. The emphasis of development of these standards was dose monitoring for Computed Tomography, so their current implementations are imperfect for projection radiography; however, there are active efforts to improve their functionality. When these features are fully standardized, they should facilitate the collection of dose information within a large healthcare enterprise, as well as multi-institutional data collection, such as the American College of Radiology's Dose Index Registry. These collections will enable the establishment of dose reference levels for comparing local practice patterns with national standards of practice.

## 7 Advanced Imaging Technologies with Potential Application to Pediatric Thoracic Radiography

### 7.1 Dual Energy Subtraction

The bony structures in the thorax can interfere with the inspection of soft tissue features in a radiographic projection. The attenuation of bone relative to soft tissue decreases as kVp increases. In fact, high kVp chest imaging is routinely performed to reduce the contrast of bone relative to soft tissue. Because of the differences in attenuation, a low

kVp image and a high kVp image can be combined using digital image processing to produce a bone-only and a soft tissue only image. Instead of making two exposures, it is possible to expose two image receptors simultaneously, one behind the other with a copper filter sandwiched in between, to produce a low energy image (front) and a hardened, high energy image (back). Dual energy subtraction is used extensively at some hospitals for adult chest radiography especially for pulmonary nodule detection, but there is only anecdotal incidental use for pediatric chest examinations.

There are other digital image processing methods for removing the bony structures from a single standard digital chest radiograph without a second exposure or second receptor. One method uses a neural network that is trained to detect bones and remove them. Another method detects the edges of bones and then reduces the contrast of the edges so that the bones are less visible to an observer.

### 7.2 Tomosynthesis

A limitation of projection radiography is that overlying anatomic structures sometimes interfere with the visibility of important clinical features. The lateral view is a practical method for visualizing underlying structures, as are other views such as obliques. Conventional tomography was a method of making an image of a single slice in the patient by moving the X-ray tube and image receptor to blur out details in other planes. With digital radiography, it is possible to acquire many projections from different aspects by tilting the X-ray tube. These images can be combined to reconstruct slices in multiple planes. The reconstruction can be repeated from the original digital images without making any additional exposures. The overall dose to the patient from digital tomosynthesis is much less than Computed Tomography (CT), and the spatial resolution within each slice is superior to CT.

Digital tomosynthesis is not yet widely used in chest radiography and has only been recently introduced into mammography. Digital tomosynthesis has been used in the evaluation of cystic fibrosis in children (Vult von Styern et al. 2012). Reductions in patient dose from CT, such as iterative reconstruction, and breathholding requirements for digital tomosynthesis may limit the application of digital tomosynthesis in pediatrics.

## 8 Radiation Dose Optimization in Pediatric Chest Radiography

Currently there is considerable enthusiasm for reducing the amount of ionizing radiation used in medical imaging of children. The Image Gently® campaign is an international

effort to optimize dose, including their recent “Back-to-Basics” campaign and a review article suggesting ten steps to manage radiation dose (Don et al. 2013). There are many ways to reduce patient dose (Willis 2009), however, optimization cannot be achieved without simultaneous consideration of image quality and the clinical purpose of the examination. The balance of these competing factors is discussed by Uffmann and Schaefer-Prokop (2009). It makes little sense to reduce the radiation dose if the resulting image is so noisy that important clinical features are no longer discernible. Different image receptor technologies also have different efficiencies reflected in the dose that is necessary to detect disease (Kroft et al. 2005). Better diagnostic quality at the same patient dose may be preferable to a lower dose that yields the same image quality.

Consider that the radiation dose to the patient in pediatric chest radiography is already very low, that the potential consequence of exposure to ionizing radiation, e.g., cancer, is displaced far in time from the exposure, and that our best estimates of risk of radiogenic cancer at these exposure levels are speculative and miniscule.

*“The American Association of Physicists in Medicine (AAPM) acknowledges that medical imaging procedures should be appropriate and conducted at the lowest radiation dose consistent with acquisition of the desired information. Discussion of risks related to radiation dose from medical imaging procedures should be accompanied by acknowledgement of the benefits of the procedures. Risks of medical imaging at effective doses below 50 mSv for single procedures or 100 mSv for multiple procedures over short time periods are too low to be detectable and may be nonexistent.”* (AAPM Position Statement 2011).

For thoracic radiography, as long as there is a valid reason for obtaining the radiograph, the benefits greatly outweigh any long-term, theoretical risk. The consequence of misinterpreting the patient’s condition is real and may be immediate. Heroic efforts to reduce radiation dose in pediatric chest radiography are therefore unwarranted in comparison to the urgency of the examination.

An argument can be made that small improvements in radiation dose have more impact for patients that undergo serial imaging, such as those in the NICU or PICU, rather than those who have routine examinations. While this is true, the urgency of the examination and the potential consequences of misinterpretation are also greater and more immediate, these patients generally have more important medical concerns than the possible risk of cancer later in life.

Nevertheless, we have extensive evidence of deleterious effects of ionizing radiation, and should make judicious use of radiation in our practice of pediatric radiology. Reduction of radiation dose in pediatric chest radiology should be a team effort among the pediatric radiologist, technologist,

and the diagnostic medical physicist. It should consider the image quality demanded by the diagnostic task, as well as modifications of digital image processing to accommodate the lower dose to the image receptor. Advances in dose reporting should facilitate oversight of technologist practice by the pediatric radiologist.

## References

- AAPM position statement on radiation risks from medical imaging. PP-25. 12/13/2011 <http://www.aapm.org/org/policies/details.asp?id=318&type=PP&current=true> Accessed 29 April 2013
- Cohen MD, Long B, Cory DA, Broderick NJ, Smith JA (1989) Digital imaging of the newborn chest. *Clin Radiol* 40:365–368
- Cohen MD, Katz BP, Kalasinski LA, White SJ, Smith JA, Long B (1991) Digital imaging with a photostimulable phosphor in the chest of newborns. *Radiology* 181(3):829–832
- Deschênes S, Charron G, Beaudoin G, Labelle H, Dubois J, Miron MC, Parent S (2010) Diagnostic imaging of spinal deformities: reducing patients radiation dose with a new slot-scanning X-ray imager. *Spine* 35:989–994
- Després P, Beaudoin G, Gravel P, de Guise JA (2005) Physical characteristics of a low-dose gas microstrip detector for orthopedic x-ray imaging. *Med Phys* 32(4):1193–1204
- Don S, Whiting BR, Rutz LJ, Apgar BK (2012) New exposure indicators for digital radiography simplified for radiologists and technologists. *Am J Roentgenol* 199(6):1337–1341. doi:10.2214/AJR.12.8678
- Don S, Macdougall R, Strauss K, Moore QT, Goske MJ, Cohen M, Herrmann T, John SD, Noble L, Morrison G, Lehman L, Whiting BR (2013) Image gently campaign back to basics initiative: ten steps to help manage radiation dose in pediatric digital radiography. *Am J Roentgenol* 200(5):W431–W436. doi:10.2214/AJR.12.9895
- Heller RM, Erickson JJ, Price RR (1982) Pediatric non-angiographic applications of digital radiography. In: Price RR, Rollo FD, Mo-nahan WG, James AE Jr (eds) *Digital radiography: a focus on clinical utility*. Grune & Stratton, New York, pp 267–277
- Kogutt MS, Jones JP, Perkins DD (1988) Low-dose digital computed radiography in pediatric chest imaging. *Am J Roentgenol* 151:775–779
- Kroft LJM, Geleijns J, Mertens BJA, Veldkamp WJH, Zonderland HM (2004) Digital slot-scan charge-coupled device radiography versus AMBER and bucky screen-film radiography for detection of simulated nodules and interstitial disease in a chest phantom. *Radiol* 231(1):156–163
- Kroft LJM, Veldkamp WJH, Mertens BJA, Boot MV, Geleijns J (2005) Comparison of eight different digital chest radiography systems: variation in detection of simulated chest disease. *Am J Roentgenol* 185:339–346
- Kushner DC (1983) Scanning beam low dose digital radiography: initial clinical trials relevant to pediatric radiology [abstr]. *Am J Roentgenol* 141:847
- Leblans P, Struye L, Willems P (2000) A new needle-crystalline computed radiography detector. *J Digit Imaging* 13(2)Suppl 0031:117–120
- Liu X, Shaw CC, Lai CJ, Altunbasa MC, Chen L, Han T, Wang T (2008) Scatter rejection and low-contrast performance of a slot-scan digital chest radiography system with electronic aft-collimation: a chest phantom study. *Med Phys* 35(6):2391–2402
- Luckey GW (1975) Apparatus and method for producing images corresponding to patterns of high-energy radiation. US Patent 3,859,527, 01 Jan 1975



- Medical electrical equipment—Exposure index of digital X-ray imaging systems—Part 1: Definitions and requirements for general radiography, International Electrotechnical Commission (IEC), international standard 62494-1-08 Geneva, Switzerland, 2008
- Merlo L, Bigli S, Cervi PM, Lupi L (1991) Computed radiography in neonatal intensive care. *Pediatr Radiol* 21:94–96
- Rowlands JA (2002) The physics of computed radiography. *Phys Med Biol* 47:R123–R166
- Romlein J (2007) CR versus DR? Blurred lines of distinction. *Applied Radiol December Suppl*:8–10
- Samei E, Saunders RS, Lo JY, Dobbins JT III, Jesneck JL, Floyd CE, Ravin CE (2004) Fundamental imaging characteristics of a slot-scan digital chest radiographic system. *Med Phys* 31(9):2687–2698
- Schaefer-Prokop C, Neitzel U, Venema HW, Uffmann M, Prokop M (2008) Digital chest radiography: an update on modern technology, dose containment and control of image quality. *Eur Radiol* 18:1818–1830
- Seibert JA (2007) Digital radiography: CR versus DR? Time to reconsider the options, the definitions, and the current capabilities. *Applied Radiol December Suppl*:4–7
- Seibert JA, Morin RL (2011) The standardized exposure index for digital radiography: an opportunity for optimization of radiation dose to the pediatric population. *Pediatr Radiol* 41:573–581
- Shepard SJ, Wang J, Flynn M, Gingold E, Goldman L, Krugh K, Leong DL, Mah E, Ogden K, Peck D, Samei E, Wang J, Willis CE (2009) An exposure indicator for digital radiography: AAPM Task Group 116 (Executive Summary). *Med Phys* 36(7):2898–2914
- Tarver RD, Cohen M, Broderick NJ, Conces DJ Jr (1990) Pediatric digital chest imaging. *J Thorac Imaging* 5(1):31–35
- Uffmann M, Prokop M, Eisenhuber E, Fuchsjaeger M, Weber M, Schaefer-Prokop C (2005) Computed radiography and direct radiography: influence of acquisition dose on the detection of simulated lesions. *Invest Radiol* 40(5):249–256
- Uffmann M, Schaefer-Prokop C (2009) Digital radiography: the balance between image quality and required radiation dose. *Eur J Radiol* 72(2):202–208
- Vastagh S (2011) Statement by MITA on behalf of the MITA CR-DR group of the X-ray section. *Pediatr Radiol* 41:566. doi: [10.1007/s00247-010-1961-7](https://doi.org/10.1007/s00247-010-1961-7)
- Vult von Steyern K, Björkman-Burtscher IM, Bozovic G, Wiklund M, Geijer M (2012) Description and validation of a scoring system for tomosynthesis in pulmonary cystic fibrosis. *Eur Radiol* 22:2718–2728
- Willis CE (2002) Computed radiography: a higher dose? *Pediatr Radiol* 32:745–750
- Willis CE (2008) Digital radiography: CR versus DR? Sometimes recognizing the distinction in technologies makes a difference. *Applied Radiol January*:25–28
- Willis CE (2009) Optimizing digital radiography of children. *Eur J Radiol* 72(2):266–273

---

# Classic Chest Radiology Findings, Pearls and Pitfalls

Gloria Soto and Karla Moënné

## Contents

<b>1</b>	<b>Introduction</b> .....	13
<b>2</b>	<b>Mediastinum</b> .....	14
2.1	Size and Shape .....	14
2.2	Pitfalls and Abnormalities.....	15
<b>3</b>	<b>Abnormal Radiological Density</b> .....	19
3.1	Technical Pitfalls.....	19
3.2	Chest Wall, Lung, and Pleural Findings .....	21
<b>4</b>	<b>Conclusion</b> .....	29
	<b>References</b> .....	29

---

## Abstract

Chest radiography is the most frequent examination performed in the majority of pediatric radiology departments. It remains the initial imaging study to evaluate most thoracic diseases in children. A systematic approach to the interpretation of children's chest radiographs, knowledge of basic radiological findings, and consideration of clinical information, are the key for a correct radiological diagnosis. Obtaining a technically adequate chest radiograph in small children is particularly challenging due to their lack of cooperation. Potential pitfalls related to suboptimal images have to be considered. Throughout this chapter we will discuss radiological findings of the normal and pathological pediatric chest, including pathologic conditions concerning the chest wall, pleura and lungs, and also some potential technical pitfalls.

---

## 1 Introduction

Chest radiography is the most frequent examination performed in most pediatric radiology departments (Frush et al. 2000), representing up to 30–50 % of the total workload (Khun and Effmann 2004). It is the initial imaging study to evaluate the vast majority of thoracic diseases in children (Enríquez et al. 2009).

Correct interpretation of chest radiographs requires trained radiologists and technically adequate images, a special challenge in uncooperative children.

A systematic approach in the interpretation of children's chest radiographs, knowledge of basic radiological findings, and consideration of clinical information, are key factors for a correct radiological diagnosis. On the other hand, failure in adequate interpretation can lead to wrong diagnosis and consequently to inappropriate therapeutic management (Enríquez et al. 2009).

---

G. Soto (✉)  
Departamento de Diagnóstico por Imágenes,  
Clínica Alemana de Santiago de Chile,  
Vitacura 5951, 8510080, Santiago, Chile  
e-mail: gloria.soto@gmail.com

K. Moënné  
Departamento de Diagnóstico por Imágenes,  
Clínica Las Condes, Lo Fontecilla 441,  
7591046, Santiago, Chile

Throughout this chapter we will discuss radiological findings related to:

- Mediastinum
  - Size and shape
  - Pitfalls and pathological conditions
- Abnormalities of radiological density
  - Technical pitfalls
  - Chest wall, lung, and pleural origin.

## 2 Mediastinum

### 2.1 Size and Shape

The variable size and shape of the normal mediastinum in children, and even in the same child, constitutes a special challenge in the interpretation of chest radiographs. (Nasseri and Eftekhari 2010).

Different divisions of the mediastinum, for both descriptive and diagnostic purposes, have been proposed in the literature. A simple method that applies to chest radiograph interpretation considers three mediastinal compartments: anterior, middle, and posterior (Fig. 1) (Fraser 1996).

#### 2.1.1 Thymus

Normal mediastinum is particularly prominent in small children due to the characteristic prominent thymus at this age.

The thymus is usually visible in chest radiographs of children under 3 years of age, and occasionally beyond that age. Size and growth pattern of the thymus has been matter of many studies. Classically, it has been considered that the thymus increases in size until puberty, and then involutes progressively. It has also been postulated that its prominence in small children is more related to the smaller body mass of children, rather than to a real absolute large volume. According to a study performed by Steinmann the thymus attains its maximum size during the first few months of life and does not grow any larger beyond that age (Nasseri and Eftekhari 2010).

Normal thymus has soft contours and does not compress adjacent structures. In chest radiographs it has a similar density to the adjacent heart and vascular structures. As a result, delineation of the borders of these structures is difficult and diagnostic errors can occur if the radiologic characteristics of the thymus are not considered.

Three classical radiological signs have been described regarding the radiologic representation of the thymus: (Enríquez et al. 2009; Nasseri and Eftekhari 2010).

- *Wave sign*: wavy contour of the thymus caused by indentation of its soft tissue by the anterior costal arches (Fig. 2).
- *Sail sign*: triangular and usually slightly convex appearance of the right lobe of the thymus delineated inferiorly

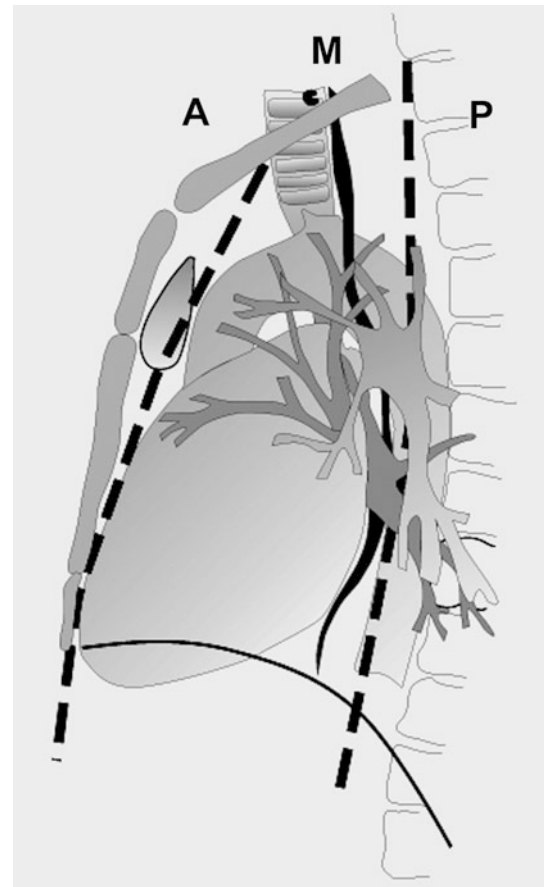


**Fig. 1** Diagram of a lateral view of the chest showing the three mediastinal compartments and the anatomic structures they contain. A Anterior compartment, M Medium compartment, and P Posterior compartment (Reprinted with permission from Moënné and Ortega 2012)

by the minor fissure of the right lung (Fig. 3). It is present in approximately 5 % of children and is seen both in frontal and lateral views (Nasseri and Eftekhari 2010).

- *Cardiothymic incisure*: small indentation seen in frontal views in one or both sides of the mediastinum (Fig. 4).

In patients under stress (acute respiratory illness, surgery, steroid therapy, radiotherapy and others), significant decrease in the size of the thymus can be seen, as well as changes in its configuration. Once stress is over, the thymus can grow up to 50 % more of its original size. This “thymic rebound” occurs mainly in children, though it can also be seen in adults (Nasseri and Eftekhari 2010).

It is important to remember the role of ultrasound (US) in characterizing normal thymus parenchyma. In cases of uncertain radiological images, US, using the anterior chest wall as acoustic window, is extremely helpful to identify the thymus and define its participation in mediastinal size and shape (Han et al. 2001).

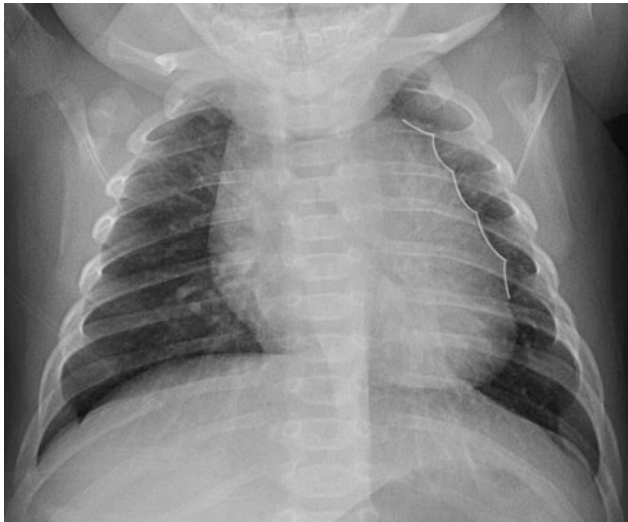


**Fig. 2** The wave sign: note the wavy contour of the thymus on the left side, caused by indentation of its soft tissue by the anterior costal arches

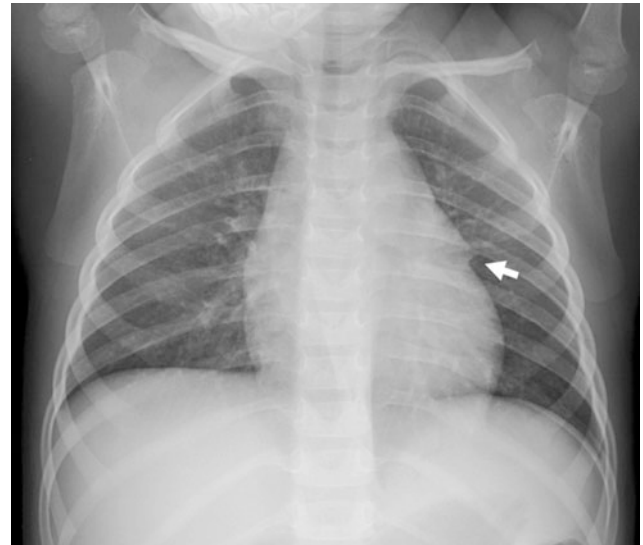


**Fig. 4** The cardiothymic incisure: the *arrow* shows a small indentation where the thymus contacts the cardiac border

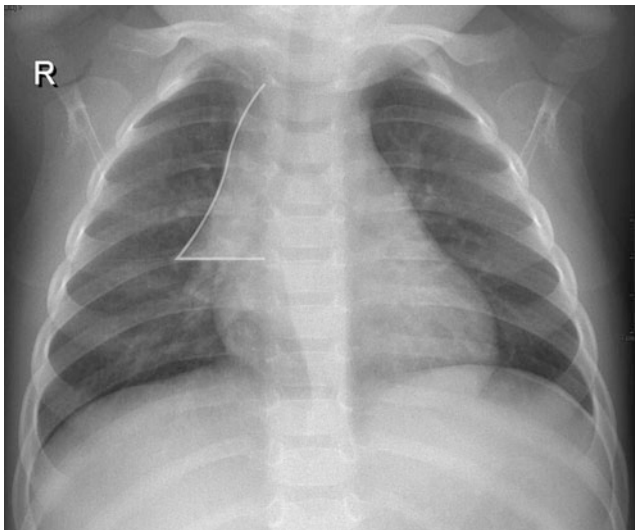


**Fig. 3** The sail sign: the right lobe of the thymus has a triangular shape with its inferior border limited by the horizontal fissure of the right lung

### 2.1.2 Heart

Changes in the size and configuration of the heart can also affect the radiological representation of the mediastinum. When analyzing the heart the position in which the child was examined must be considered. In supine position the heart appears more prominent than in standing position. It is important to remember that a supine frontal view is routinely used in infants, whereas toddlers and older children are generally examined in standing position (Enríquez et al. 2009). Lateral views are useful to evaluate posterior cardiac enlargement and, in absence of a large thymus, right ventricular size by noting the area of contact of the heart with the sternum (Fig. 5a, b).

Frontal views obtained in expiratory phase are a frequent cause of wrong diagnosis of mediastinum widening and heart enlargement (Fig. 6) (Enríquez et al. 2009)

### 2.1.3 Trachea

The trachea is represented in chest radiographs throughout all its extension, especially when digital technique is used. A careful analysis of the tracheal air column has to be done, both in frontal and lateral views. If a tracheal tube is present, proper position must be confirmed.

In the frontal view the proximal subglottic trachea shows bilateral symmetric convexities, a finding described as “shouldering” of the air column (Fig. 7). Distal to this the diameter of the trachea remains constant and its walls are parallel, except where the aortic arch causes a localized indentation. Occasionally in asymptomatic children an anomalous innominate artery or, less frequently, the common carotid artery can produce an anterior indentation of the trachea at the level of the sternal manubrium. This finding is only seen in small children, in whom there is proportionately less space in the upper mediastinum and therefore a greater possibility that these arteries indent the trachea. A frequent associated finding in these cases is tracheomalacia, believed to be the cause of symptoms, such as stridor and respiratory distress, present in some of these children (Swischuk 1971).

## 2.2 Pitfalls and Abnormalities

Due to the greater flexibility and relatively larger size of the trachea it is frequent to see in children less than 5 years of age lateral tracheal deviations and even angulations. This finding is more pronounced with cervical flexion and in

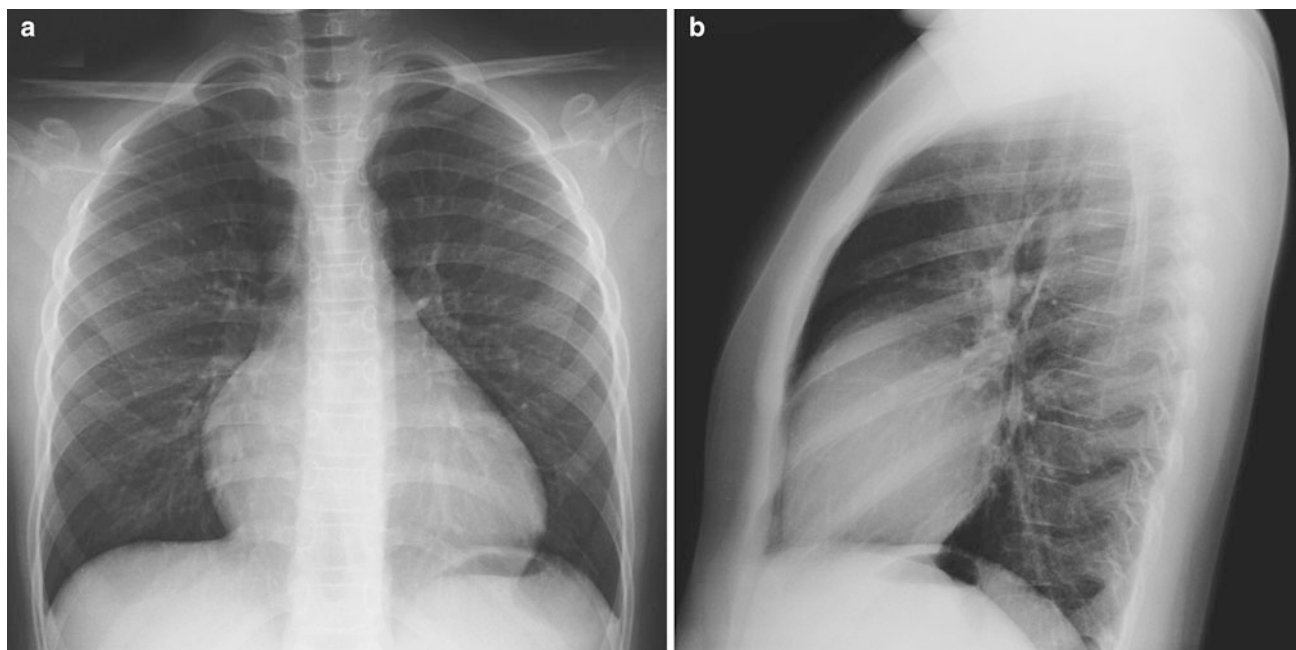


**Fig. 5** Frontal chest radiograph of a prominent heart (a). Lateral view shows wide contact of the anterior border of the heart with the sternum, indicating right ventricular enlargement (b)



**Fig. 6** Frontal under-inspired chest radiograph of a normal child. Note the apparent widening of the mediastinum and enlargement of the heart. The radiograph was repeated with adequate degree of inspiration and both the mediastinum and the heart showed a normal appearance

under-inspired images (Fig. 8) (Moëne and Ortega 2012). This physiologic tracheal deviation is usually toward the right, opposite direction to the aortic arch, which “anchors” the trachea avoiding lateral deviation toward its side.

Any anterior displacement of the intrathoracic trachea must be considered abnormal (Fig. 9), as well as any lateral deviation in children over 5 years of age (Chang et al. 1970).

*Recognizing “physiological” tracheal deviations is important to prevent performing unnecessary studies in healthy children.*



**Fig. 7** Frontal view of the proximal trachea. Note the bilateral symmetric convexities of the normal subglottic trachea, known as “tracheal shouldering”

When tracheal inflammation is present, underlying edema causes narrowing of the subglottic trachea with loss of the normal tracheal “shouldering” (Fig. 10). The inverted V configuration of the trachea under these circumstances is



**Fig. 8** Under-inspired (a) and well-inspired frontal chest radiographs (b) of a 2-year-old boy. Note the right-sided lateral deviation of the trachea that is completely straight in the well-inspired radiograph

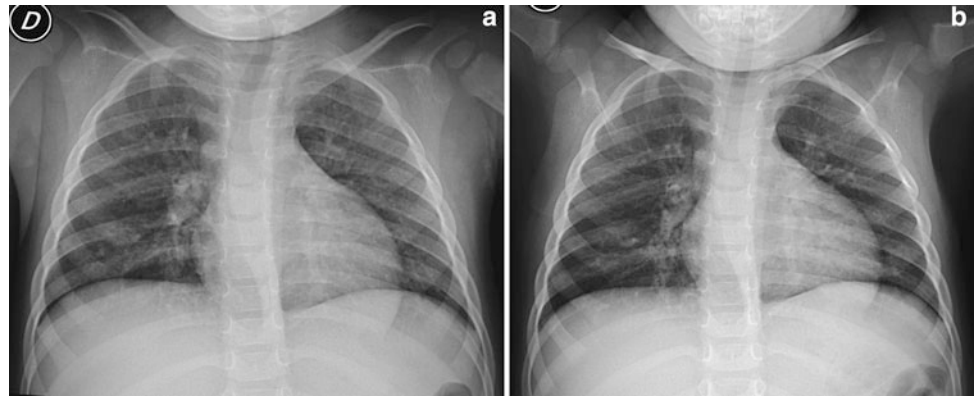


**Fig. 9** Lateral chest radiography showing anterior deviation of the trachea (a) secondary to a bronchogenic cyst, demonstrated on CT (b)

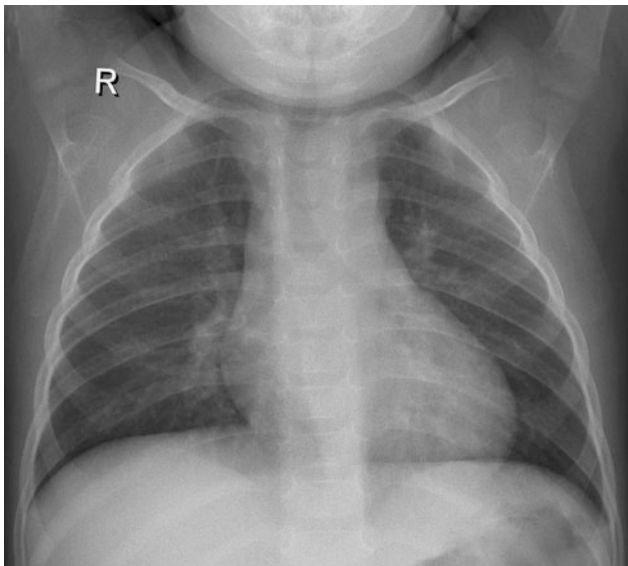
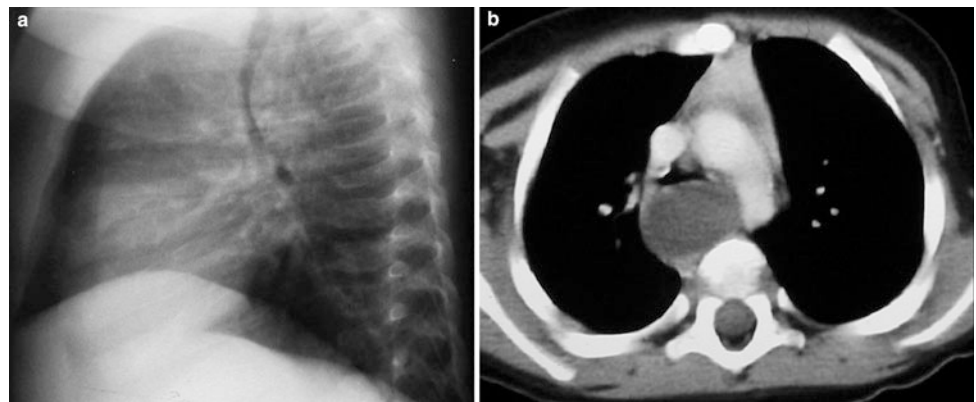


**Fig. 10** The steeple sign. Note the inverted V shape of the subglottic trachea representing underlying inflammation and edema in a child with croup. The normal “shouldering” of the trachea at this level is lost

called the *steeple sign*. It is a non-specific sign most frequently caused by croup or laryngotracheobronchitis. Even if the diagnosis of croup is clinical, radiographs may be requested to exclude other causes of stridor, such as foreign

body aspiration, an esophageal foreign body, congenital subglottic stenosis, epiglottitis or a subglottic hemangioma. In these cases the *steeple sign* helps to define croup as the cause of the symptoms (Salour 2000).

Any tracheal indentation or narrowing, other than those previously mentioned, has to be considered abnormal. Diffuse narrowing is usually congenital, due to complete cartilaginous tracheal rings (Fig. 11a, b). Focal narrowing is more frequently a complication of tracheal intubation. Tracheal compressions caused by vascular structures can be detected in radiographs, however CT or magnetic resonance (MR) imaging is mandatory to define the exact vascular anatomy and its relation to the airway. Tracheomalacia, defined as the dynamic collapse of the trachea during the expiratory phase, can be isolated or associated to vascular rings or tracheoesophageal fistula. Stridor and occasionally dyspnea are the clinical manifestations.

Masses, either congenital or tumoral, can originate in any mediastinal compartment. Chest radiographs can show compression or displacement of adjacent structures (Fig. 12), however, their characterization requires imaging with CT or MRI (Zylak et al. 2000).

*If a chest radiograph shows signs of mass effect over mediastinal structures, CT or MR studies are mandatory to complete imaging investigation.*



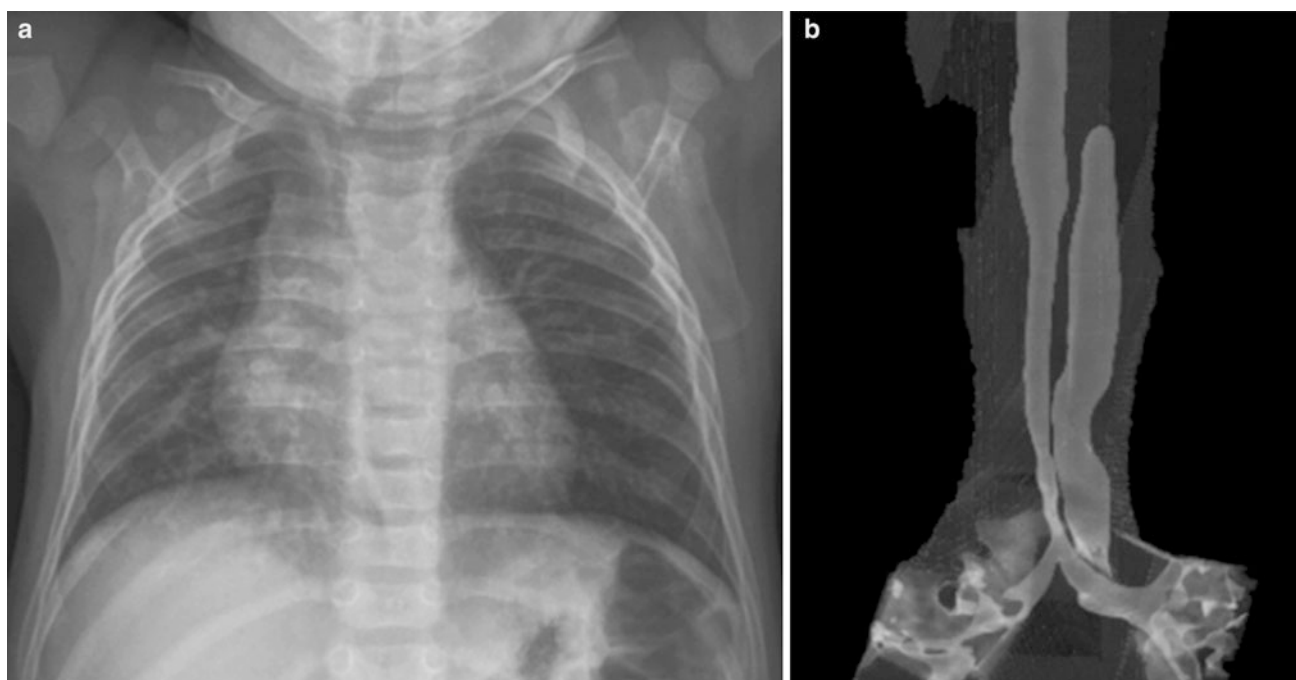


**Fig. 11** Frontal chest radiograph (a) and CT coronal volume rendering image of the trachea (b) in a child with type II pulmonary sling. Note the low T-shaped carina and the long segment narrowing of the intrathoracic trachea



**Fig. 12** A huge anterior mediastinal mass produces lateral deviation of the heart and trachea. CT showed a mediastinal teratoma

Pneumomediastinum can result from a variety of causes that may be either intra or extrathoracic, and that vary with age (Zylak et al. 2000). While occasionally it can be secondary to intrathoracic spread of air from the cervical region or from the abdomen, most cases are secondary to alveolar over distension and rupture due to high intra-alveolar pressure. (Chalumeau et al. 2001). A variety of conditions have been described in relation to pneumomediastinum in

children, including trauma, medical illnesses, and iatrogenic. Although in some children it may occur spontaneously, a trigger can be found in up to 70–90 % of cases; the most frequent are asthma, vomiting of any cause, situations involving repetitive Valsalva maneuver, and intense sport activities. In newborns respiratory effort can be the sole cause of pneumomediastinum.

Radiographic signs of pneumomediastinum reflect the free air dissecting different anatomic mediastinal structures (Zylak et al. 2000). The main radiological signs in children are:

- *Retrosternal and precardiac hyperlucency*: collection of air in the anterior mediastinum compartment (Fig. 13).
- *Periaortic and peritracheal lucent streaks*: dissection of air into the mediastinum or the mediastinal recesses (Fig. 14).
- *Angel-wing sign, or spinnaker sail sign*: elevation and lateralization of the lobes of the thymus by air in the mediastinum (Fig. 15).
- *Ring around the artery sign*: radiolucent line surrounding the right pulmonary artery, seen on the lateral view (Fig. 16).
- *Continuous diaphragm sign*: interposition of air between pericardium and diaphragm making visible the central part of the diaphragm in continuity with the diaphragmatic domes (Fig. 17).

Indirect signs of pneumomediastinum are *subcutaneous emphysema*, usually present in infants and older children but not in newborns, and *pneumopericardium*.



**Fig. 13** Pneumomediastinum: a large collection of air is seen in the retrosternal and pre cardiac region of the anterior mediastinum, in frontal (a) and lateral (b) chest views. Note elevation of the thymus lobes

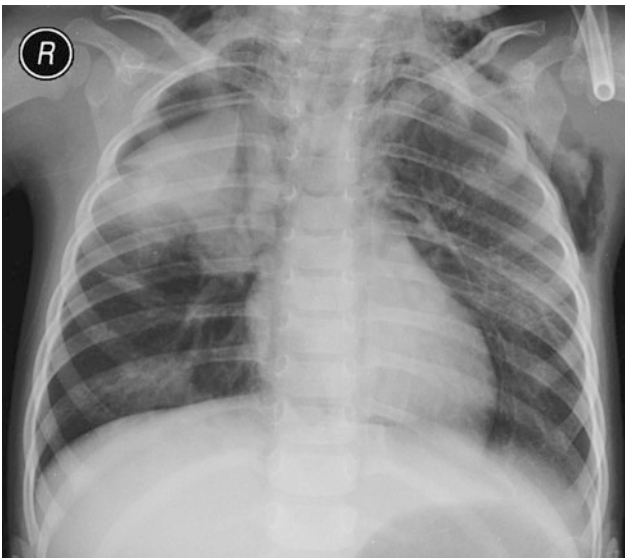


**Fig. 14** Frontal chest radiograph in a child with pneumomediastinum and right pneumothorax. Note streaks of air dissecting the upper mediastinal structures. The medial pleural line is also seen as well as subcutaneous emphysema

Pneumomediastinum may be difficult to differentiate from medial pneumothorax; lateral views are useful to differentiate both conditions. In addition, pneumomediastinum may be simulated by the Mach band effect, which corresponds to a lucent band adjacent to convex borders such as the cardiac contour. Identification of a pleural line, which is characteristic of pneumomediastinum, aids in differentiation.

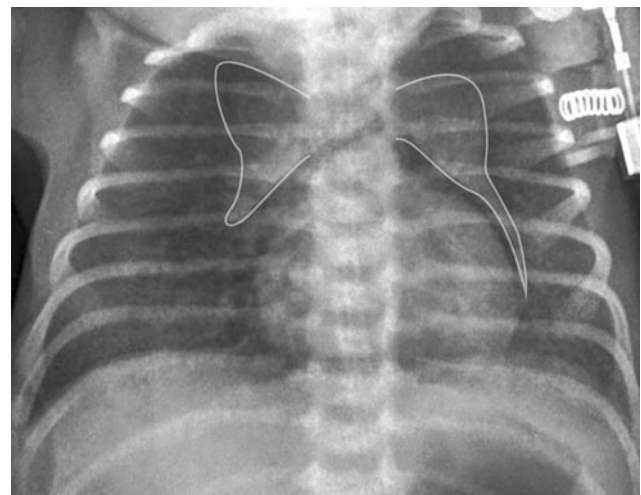


**Fig. 15** The “angel sign” elevation and lateralization of both thymic lobes that are separated by air from the adjacent mediastinal structures

### 3 Abnormal Radiological Density

#### 3.1 Technical Pitfalls

Rotation of the chest is the most frequent cause of an apparent hyperlucent lung. The posterior-most hemithorax looks larger and more lucent than the contra lateral. The best way to assess rotation is measuring the distance between the medial aspect of the anterior costal arches and



**Fig. 16** Lateral chest radiograph showing the “ring around the artery sign” in a 15-year-old girl with spontaneous pneumomediastinum. Note the radiolucent line surrounding the right pulmonary artery (arrow)



**Fig. 17** Frontal chest radiograph of an infant with pneumomediastinum showing the “continuous diaphragm sign”

the spine, which is symmetrical in the properly positioned child (Fig. 18). Evaluation of clavicular symmetry, a method widely used in adults, is less reliable in children, who can be symmetric in the upper part of the thorax and rotated inferiorly (Fig. 19). Another frequent cause of

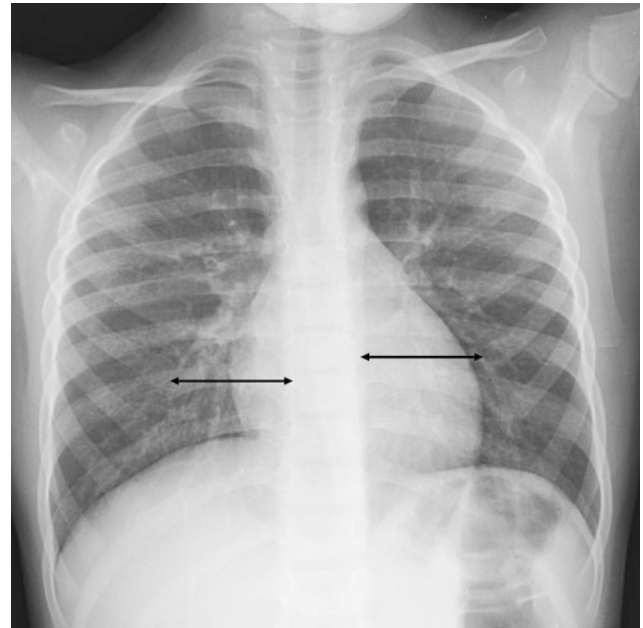


**Fig. 18** In a non-rotated frontal chest radiograph the distance between the medial aspect of the anterior costal arches and the spine is symmetric (arrows)

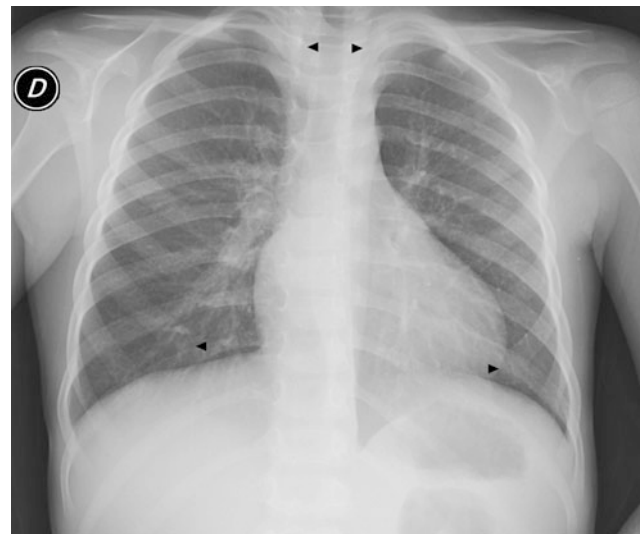


**Fig. 19** Frontal chest radiograph showing symmetry at the level of the clavicles (upper arrowheads). Note however the asymmetry in the length of the anterior costal arches in both hemithoraces (lower arrowheads) due to rotation of the inferior thorax

apparent unilateral lung hyperlucency is related to X-ray beam misalignment. Comparative evaluation of the chest wall soft tissues density on both hemithoraces is very useful to identify this technical pitfall since they will display the same asymmetry of transparency as the lungs (Fig. 20).

A poorly inspired film, very frequent in infants and uncooperative children, is another source of diagnostic



**Fig. 20** Apparent unilateral lung hyperlucency of the right hemithorax due to X-ray beam misalignment. Note similar asymmetry of the chest wall soft tissues density on both hemithoraces, the right side more lucent than the left

errors. An apparent increase in lung density, poor definition of vessels, and widening of the mediastinum are usual findings in this situation, and can easily be misinterpreted as abnormalities by the inexperienced radiologist. Regarding this topic, Leonard Swischuk, says: “*While many aspects of medicine are scientific, judging the degree of inspiration on a chest film is not in this category and probably never will be*” (Swischuk 1997). Experience, gained with practice, is the key to correctly determine if a radiograph has been obtained with an adequate degree of inspiration. Evaluation by counting the costal arches, or the intercostal spaces, is not always reliable, and, if used as the only parameter can be misleading, especially in infants (Fig. 21a, b). A useful clue is to evaluate the definition of the lung vessels, which are well-defined in adequately inspired films. The configuration of the thoracic cage also helps since in expiratory radiographs usually the transverse diameter predominates over the longitudinal diameter, as opposed to what happens in well-inspired images (Moënné and Ortega 2012).

## 3.2 Chest Wall, Lung, and Pleural Findings

### 3.2.1 Chest Wall

Poland syndrome, a rare congenital malformation of the chest wall consisting of hypoplasia or aplasia of the pectoralis major muscle and adjacent cartilaginous, osseous,

and soft tissue structures, causes increased transparency of the affected hemithorax (Fefferman and Pinkney 2005). The clue to establish the diagnosis is comparative analyses of the soft tissues of the chest wall, which are less dense and prominent in the affected side (Fig. 22a, b). Physical examination confirms the diagnosis.

### 3.2.2 Lung

#### 3.2.2.1 Decreased Lung Density

For a correct diagnostic approach of decreased density (or increase transparency) of one or both lungs, it is important to evaluate lung volume and vascularity.

Three scenarios must be considered when there is diffuse bilateral lung hyperlucency:

- Increased lung volume with normal vascularity
- Normal lung volume with decreased vascularity
- Increased lung volume with decreased vascularity.

#### 3.2.2.2 Increased Lung Volume with Normal Vascularity

Bilateral increase of lung volume with normal vascularity can be physiologic or secondary to diffuse mild obstruction of the small airway. To differentiate both situations, the position and configuration of the hemidiaphragms, and the mediastinal position have to be considered.

As already mentioned it is difficult, if not impossible, to control the respiratory phase in which radiographs are obtained in infants and uncooperative children. If the patient cries during the examination it is possible to obtain images during deep inspiration, showing large hyper lucent lungs. A clue to suspect that a deep inspiration is the cause is the presence of discrepancy of the lung volume in frontal versus lateral views (Fig. 23a, b).

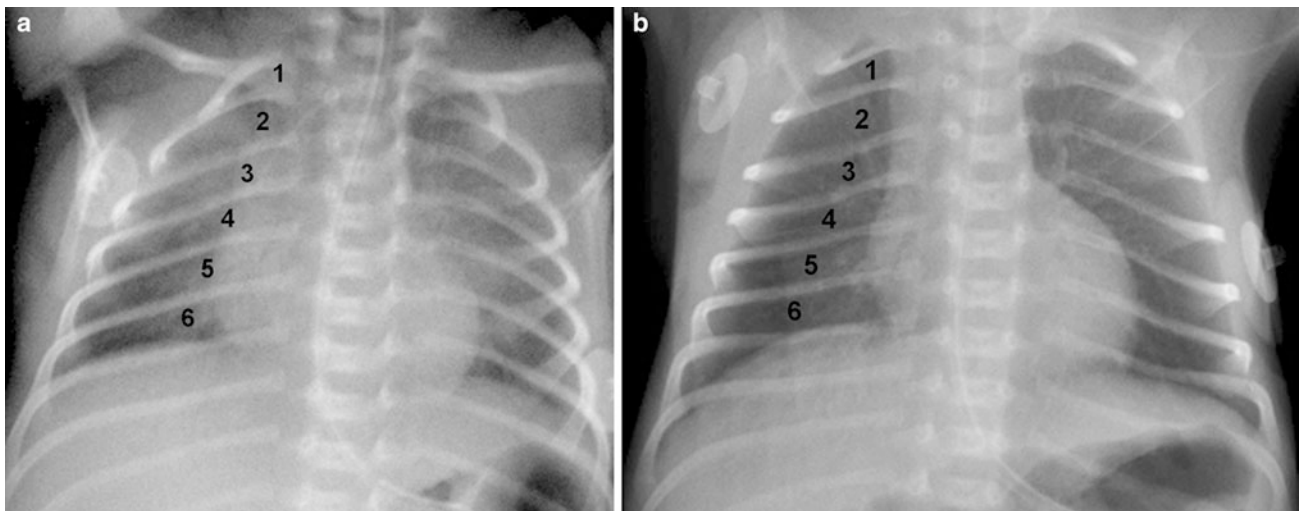
Air trapping due to airway obstruction, as seen in bronchiolitis and asthma, is constant throughout the respiratory cycle, hence diaphragmatic flattening is present in both frontal and lateral views (Bramson 2005) (Fig. 24a, b). In these cases an increase of retrosternal air is usually seen in the lateral view. Decreased lung vascularity could be found in severe cases.

*To diagnose air trapping, the diaphragm needs to be flattened on both frontal and lateral views.*

#### 3.2.2.3 Normal Lung Volume with Decreased Vascularity

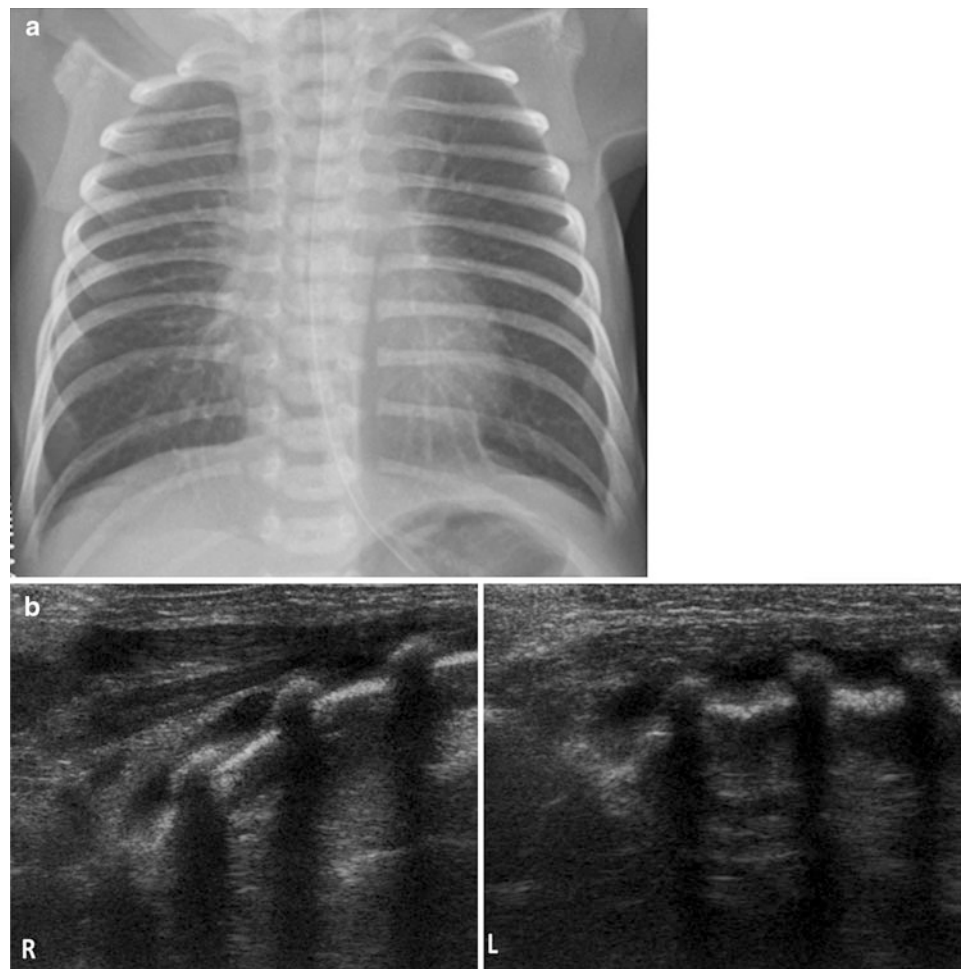
When a child has normal-sized hyperlucent lungs with decreased vascularity, a cardiovascular disease, such as





**Fig. 21** Chest radiographs of an infant obtained during expiration (a) and inspiration (b). In both cases six intercostal spaces can be counted over the diaphragmatic dome. This method is unreliable to decide the phase in which the radiograph was obtained

**Fig. 22** Poland Syndrome: apparent left lung hyperlucency due to hypoplasia of the left pectoralis major muscle. Note how the soft tissues of the left side of the chest wall are less dense and thinner than on the right side (a). Comparative US images of the chest wall show a very hypoplastic left pectoralis major muscle (b)



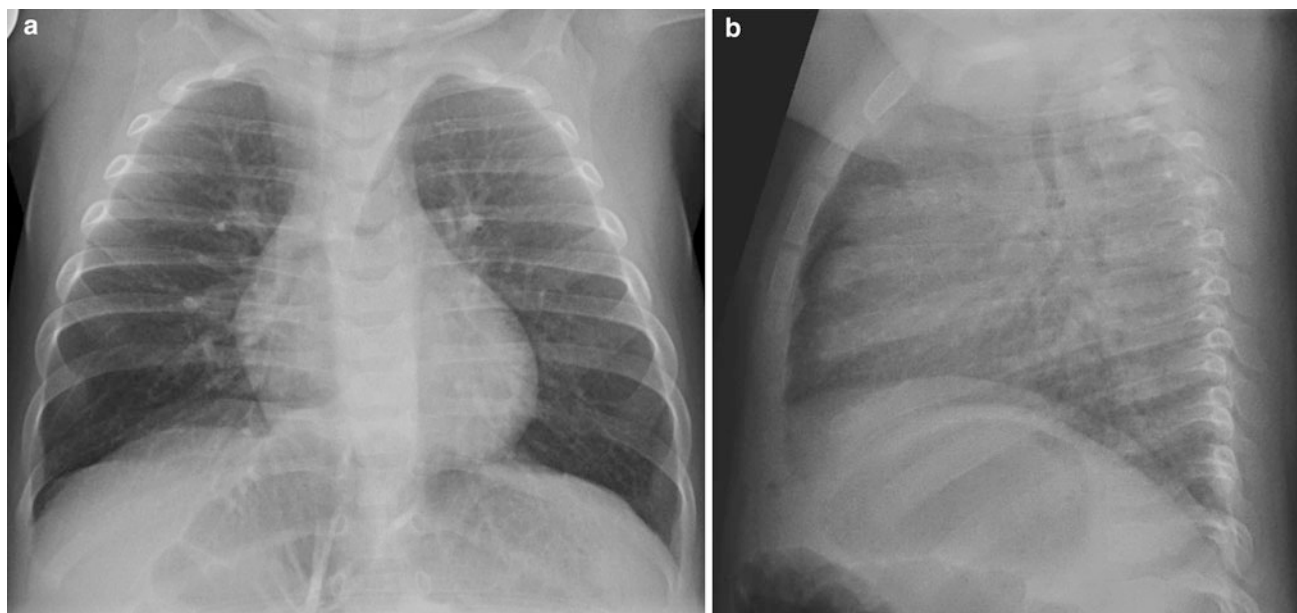


**Fig. 23** Frontal (a) and lateral (b) chest radiographs of the same child obtained within minutes. The frontal view shows flattened hemidiaphragms but in the lateral view the diaphragms are in normal high position, which rules out air trapping

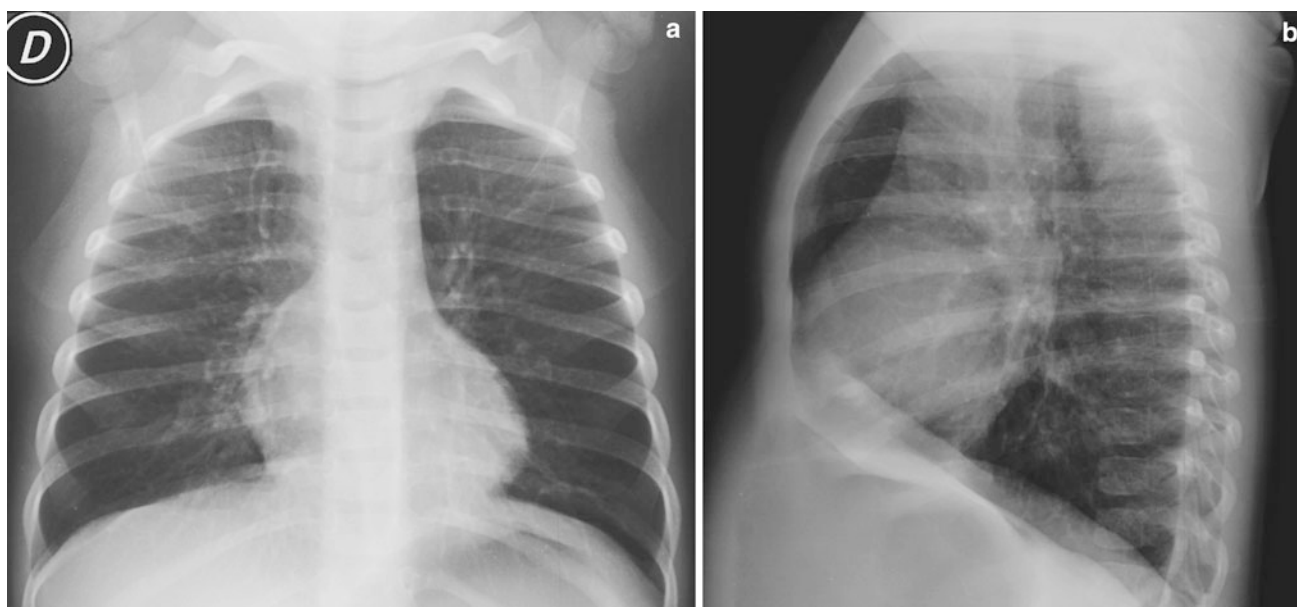


**Fig. 24** Frontal (a) and lateral (b) chest radiographs of a child with bronchiolitis. Note also flattening of the diaphragm and a retrosternal lucency in the lateral view

Tetralogy of Fallot or isolated pulmonary artery stenosis, is the most frequent cause. Evaluation of the cardiovascular silhouette may be useful to suspect the underlying anomaly, but advanced cardiac imaging is needed to establish the final diagnosis.

#### 3.2.2.4 Increased Lung Volume with Decreased Vascularity

Hyperlucent large lungs with decreased vascularity are characteristic finding of bronchiolitis obliterans, especially in advanced phases of the disease. Even if radiological



**Fig. 25** Frontal chest radiograph of a child with foreign body aspiration. The left lung is large and hyperlucent with less vessels due to air trapping caused by partial obstruction of the left main bronchus. Note the mediastinal shift to the right

findings are subtle, severe obstructive involvement of pulmonary function may be present. CT is the modality of choice to establish the final diagnosis.

### 3.2.2.5 Unilateral Hyperlucent Lung

Unilateral hyperlucent lung is seen in a variety of pathologic conditions and careful analysis of the radiographic findings is necessary to make the correct diagnosis (Alford et al. 1993). Once technical pitfalls and extrapulmonary causes are excluded, the main challenge is to define if the

hyperlucent lung corresponds to the normal or the abnormal lung. Comparative evaluation of lung vascularity is the clue: in general terms the abnormal lung is the one that displays less vascularity. It is important to mention that the evaluation of number and size of lung vessels is subjective, and that expertise is important to correctly assess lung vascularity.

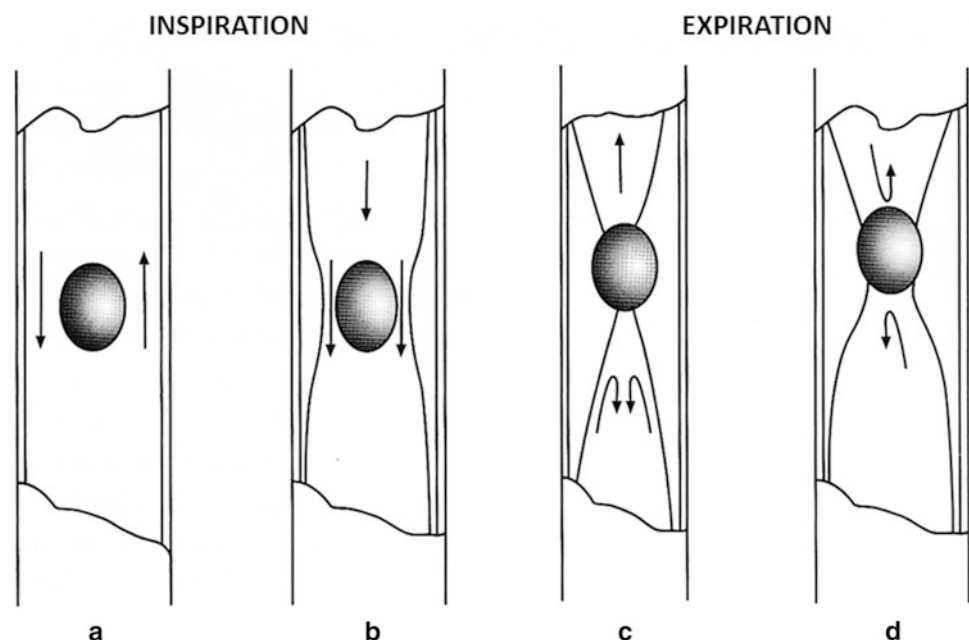
Aspiration of a foreign body is the more frequent pathologic cause of unilateral air trapping in children (Fig. 25). A two-way valve mechanism caused by partial bronchial obstruction causes air trapping during expiration (Fig. 26) (Kosucu et al. 2004; Alford et al. 1993). If radiologic findings are uncertain, expiratory images are of great help, as well as dynamic assessment of air trapping with fluoroscopy that will show mediastinal shift toward the contralateral side during expiration. It is important to mention that the history of choking, very useful for diagnosis, is not always present.

*In a child with asymmetric lung transparency, usually the lung with less vascularity is the abnormal one.*

Less frequently unilateral air trapping can be caused by extrinsic bronchial compressions, either vascular (e.g., pulmonary sling) or non-vascular (e.g., duplications cysts) (Alford et al. 1993). Similar findings can be seen with partially obstructive endobronchial tumors, which are extremely unusual in the pediatric age, being carcinoid the most frequent.

In Swyer James McLeod Syndrome, a predominantly unilateral bronchiolitis obliterans, the affected lung is hyperlucent and usually small (Fig. 27a, b). Lung hyperlucency is caused by air trapping due to small airway obstruction, and to the paucity of vascular structures in the affected parenchyma,

**Fig. 26** Foreign body aspiration: Diagram of two-way valve mechanism and air trapping during expiration (Modified with permission from Moëgne and Ortega 2012)





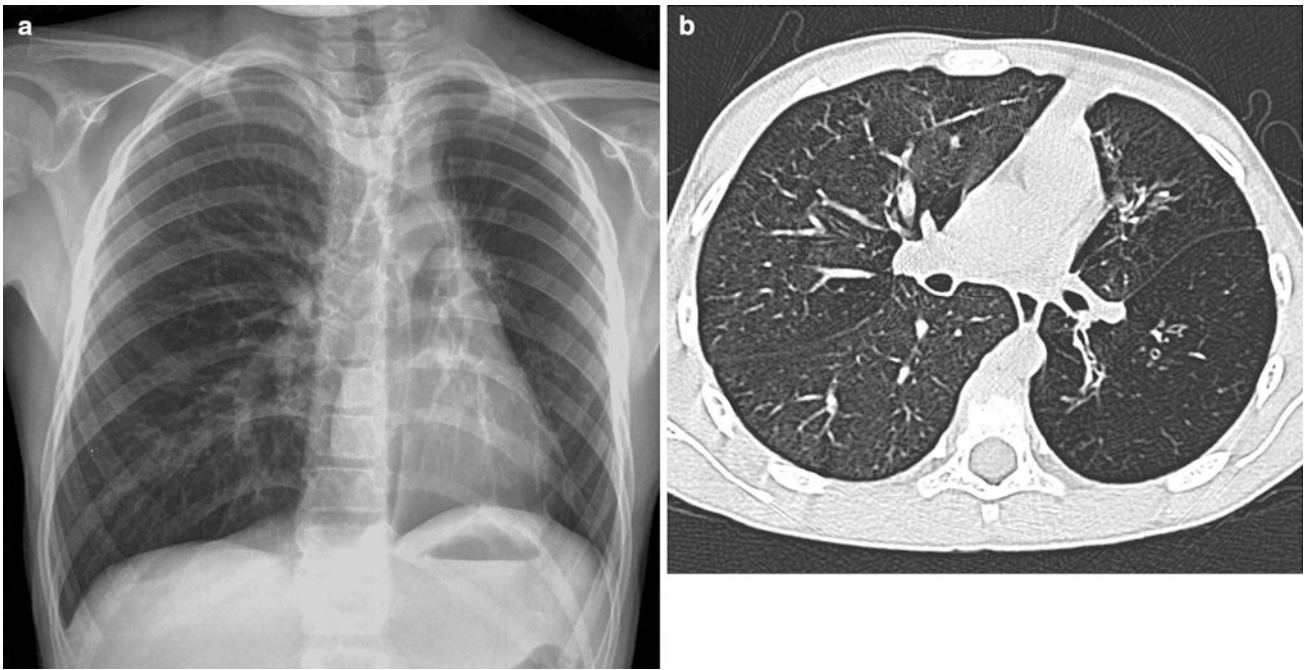


**Fig. 27** Frontal chest X-ray (a) of a 3-year-old boy with a Swyer James Syndrome. Note small hyperlucent left lung and large compensatory right lung. High resolution CT (b) shows characteristic

findings of bronchiolitis obliterans in the left lung. In other images of this study small areas of mosaic pattern were seen in the right lung indicating bilateral, though very asymmetric, lung involvement

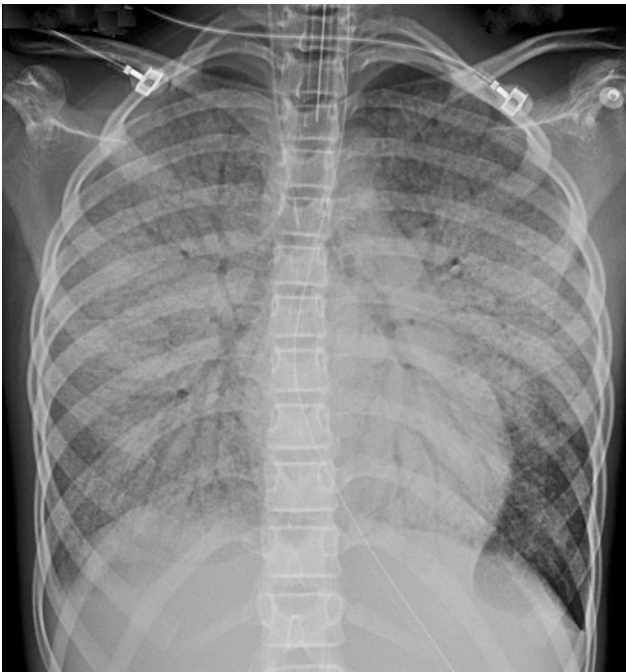


**Fig. 28** Air bronchogram. Note the air within the bronchi surrounded by high-density alveolar spaces in this child with acute pulmonary distress syndrome

with redistribution of blood flow to less affected lung. The diagnosis is strongly suggested by radiological findings and has to be confirmed with CT (Kuhn and Brody 2002).

### 3.2.2.6 Increased Lung Density

Conditions that produce increased lung density are usually grouped according to the pulmonary space involved (Fraser 1996):

- Mainly air space involvement
- Mainly interstitial space involvement
- Involvement of both alveolar and interstitial spaces.

*Air bronchogram* is the classical radiological sign of alveolar space involvement. It represents air in patent airways surrounded by high-density alveolar spaces. This sign is frequent in consolidations and in atelectasis (Fig. 28). When air space involvement is less confluent, not well-defined nodular opacities, representing acinar involvement, are noted.

The silhouette sign occurs when the density of lung parenchyma is the same or greater than the density of adjacent mediastinum or diaphragm, resulting in loss of delineation of their contours (Fig. 29a, b). This is a useful sign to localize abnormalities, especially when a lateral view is not available, and it facilitates detection of subtle alterations that otherwise could be unrecognized.

Atelectasis is frequent in children because collateral air circulation through Kohn pores and Lambert channels is less efficient than in adults (Effmann and Kuhn 2004). Radiological signs of atelectasis are described in Table 1. The most reliable sign is displacement of inter-lobar fissures. Since the anterior and medium compartments of the mediastinum are



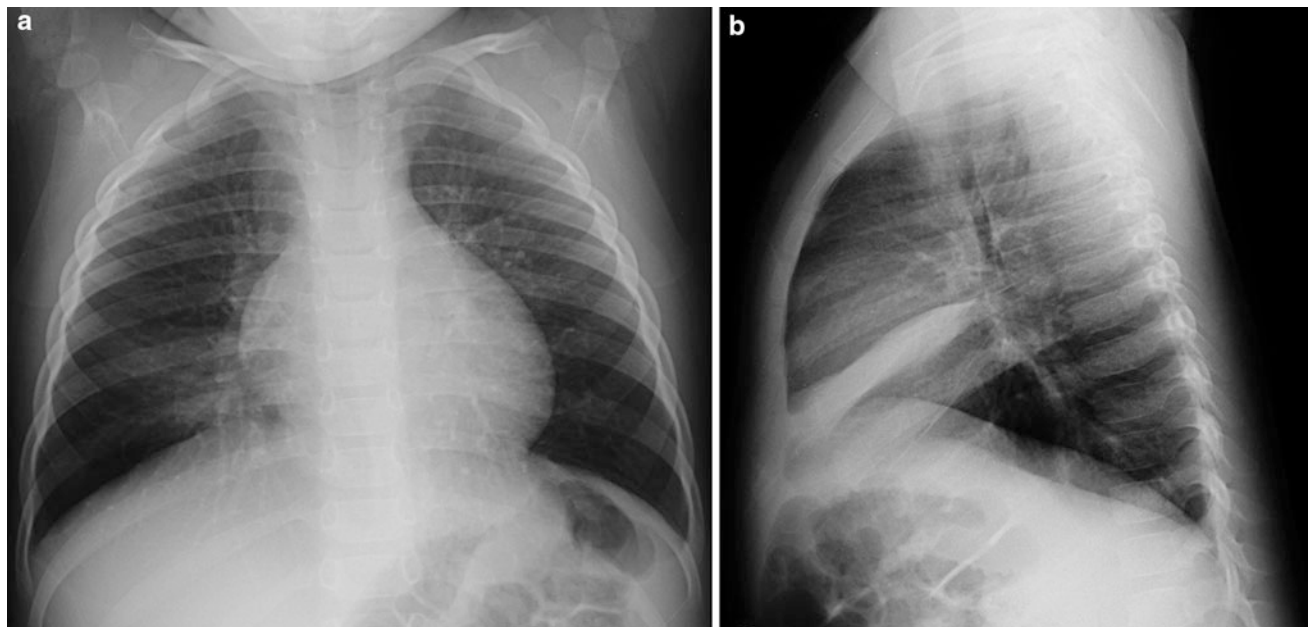


**Fig. 29** Silhouette sign. In frontal view, an increased lung density in the right causes subtle loss of delineation of the cardiac border (a). Lateral view demonstrates atelectasis of the middle lobe (b)

**Table 1** Radiological Signs of Atelectasis

Direct	Fissure displacement
Indirect	Increase of density
	Elevation of ipsilateral hemidiaphragm
	Ipsilateral mediastinal shift
	Smaller intercostal spaces
	Compensatory hyperinflation

less stable than the posterior compartment, and therefore displace more easily, it is frequent in atelectasis to note heart and thymus displacement, while the trachea remains in its normal position (Moënné and Ortega 2012).

### 3.2.3 Pleural Anomalies

Pleural effusion and pneumothorax are the main pleural abnormalities seen in children.

#### 3.2.3.1 Pleural Effusion

When the equilibrium between the rate of entry and exit of pleural fluid and protein is lost, the result is pleural effusion (McLoud 1998). An increase of pleural fluid can be seen in infectious, inflammatory, traumatic, renal, cardiovascular, and tumoral conditions, and it can be either a transudate or an exudate, as shown in Table 2.

Even if chest radiographs have limited sensibility in detecting small effusions, it is the method by which pleural effusions are usually detected in children. Sensibility is even lower if the patient is imaged in supine position, especially in bilateral effusions (Fraser 1996).

**Table 2** Types of effusions

Transudates	
Exudates	Empyema
	Hemothorax
	Chylothorax

US is the method of choice to characterize pleural effusions (Calder and Owens 2009) and helps to define the degree of therapeutic aggressiveness required for treatment (Donnelly 2005). Even if CT is highly sensitive in detecting small amounts of pleural fluid, it has a limited role in the evaluation of pleural effusions in children since it is less sensitive than US in demonstrating septums and loculi within the effusion (Donnelly 2005).

Gravity is the main force that determines fluid location within the pleural space. In standing position it initially locates between the diaphragm and the lung base from where it spills first to the posterior costophrenic sulcus, and then to the lateral costophrenic sulcus. Lateral views are important to detect small effusions since they show the posterior costophrenic sulcus, not seen on frontal views (Fig. 30). From the lateral costophrenic sulcus fluid ascends by capillarity through the pleural space, displaying a *Damoiseau curve* configuration (Fig. 31). Large pleural effusions can cause diffuse opacity of the hemithorax, with shift of the mediastinum to the contra lateral side. US is the method of choice to study the cause of an opaque hemithorax, showing the nature of the underlying disease.

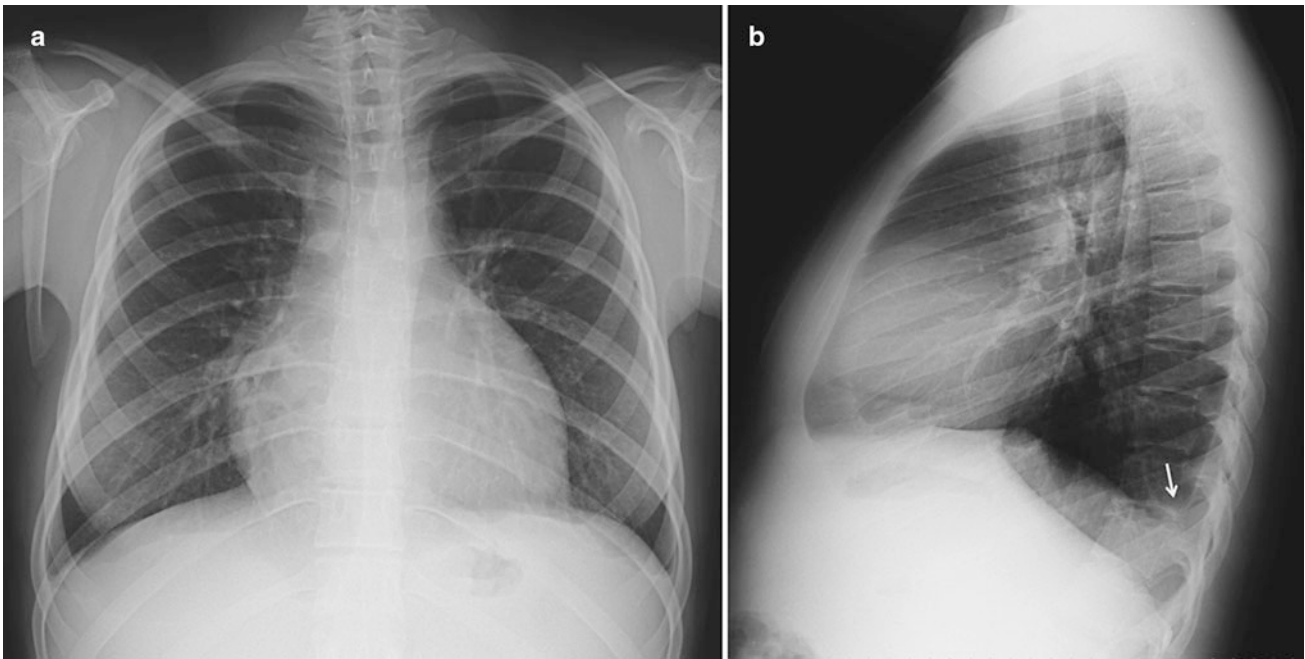


**Fig. 30** Frontal (a) and lateral (b) chest radiographs in a child with a small left pleural effusion shown on the lateral view by demonstrating blurring of the posterior costophrenic sulcus (arrow)



**Fig. 31** Left pneumonia with a large pleural effusion shows the characteristic Damoiseau curve configuration

Pleural effusions that collect in the subpulmonary space can be difficult to diagnose since in these cases the normal diaphragmatic shape is not lost, giving origin to the so-called “pseudo diaphragm” (Fig. 32). Table 3 shows the main radiological findings of subpulmonary pleural effusion.

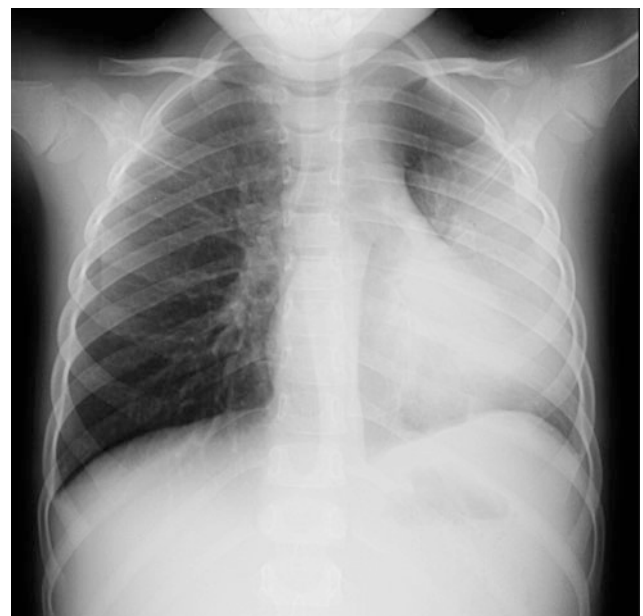


**Fig. 32** Left pneumonia with a predominantly subpulmonary pleural effusion showing the characteristic findings described on Table 3

In supine position, fluid layers beneath the lung producing a homogeneous increase of radiological density. Small effusions may be difficult to recognize, especially if bilateral. When the amount of pleural fluid increases it extends to the lateral aspect of the pleural space causing a progressive pleural opacity adjacent to the lateral chest wall

**Table 3** Radiological Signs of Subpulmonary Pleural Effusion

High position of the hemidiaphragm (“pseudo diaphragm”)
Lateralized dome of the “pseudo diaphragm” with a steep descent to the lateral costophrenic sulcus
Increase of the space between the “pseudo diaphragm” and the gastric fundus (left side effusions)
Lack of visualization of lung vessels through the diaphragm in frontal radiographs

(Fig. 33); eventually, the hemithorax will become diffusely opaque.

### 3.2.3.2 Pneumothorax

Air in the pleural space is always abnormal. It is caused by alveolar rupture secondary to trauma, lung air trapping, broncho-pulmonary fistula, pulmonary blebs, or barotrauma.

Identification of the “*free lung edge*,” which represents the visceral pleura delineated by air in the pleural cavity, is the classical sign of pneumothorax (Fig. 34). Variable degrees of adjacent lung atelectasis are usually present and in cases of tension pneumothorax mediastinum shift toward the contra lateral side will be present.

In standing position air initially surrounds the lung apex where the *free lung edge sign* will be first noted. In supine position free pleural air locates in the anterior-most part of the thoracic cavity, between the lung and the thoracic cage. If the amount of air is small it will not extend to the lateral aspect of the pleural cavity, and the *free lung edge sign* will



**Fig. 34** Right pneumothorax with visualization of the visceral pleura delineated by the air within the pleural cavity (“*free lung edge*” sign). Ipsilateral atelectasis flattening of the hemidiaphragm and mediastinal shift are also present

not be present, making the diagnosis more challenging. Several subtle radiological findings are useful to diagnose an anterior pneumothorax (Fig. 35):

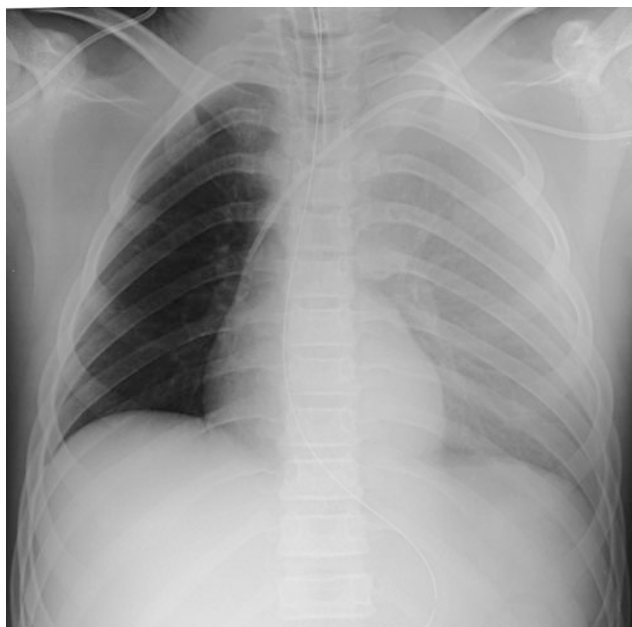


**Fig. 33** Frontal chest radiograph obtained in supine showing increase in density of the left hemithorax caused by pleural fluid layered under the lung



**Fig. 35** Predominantly anterior right pneumothorax. The right hemithorax is hyperlucent and shows the “*deep lateral costophrenic sulcus*” sign

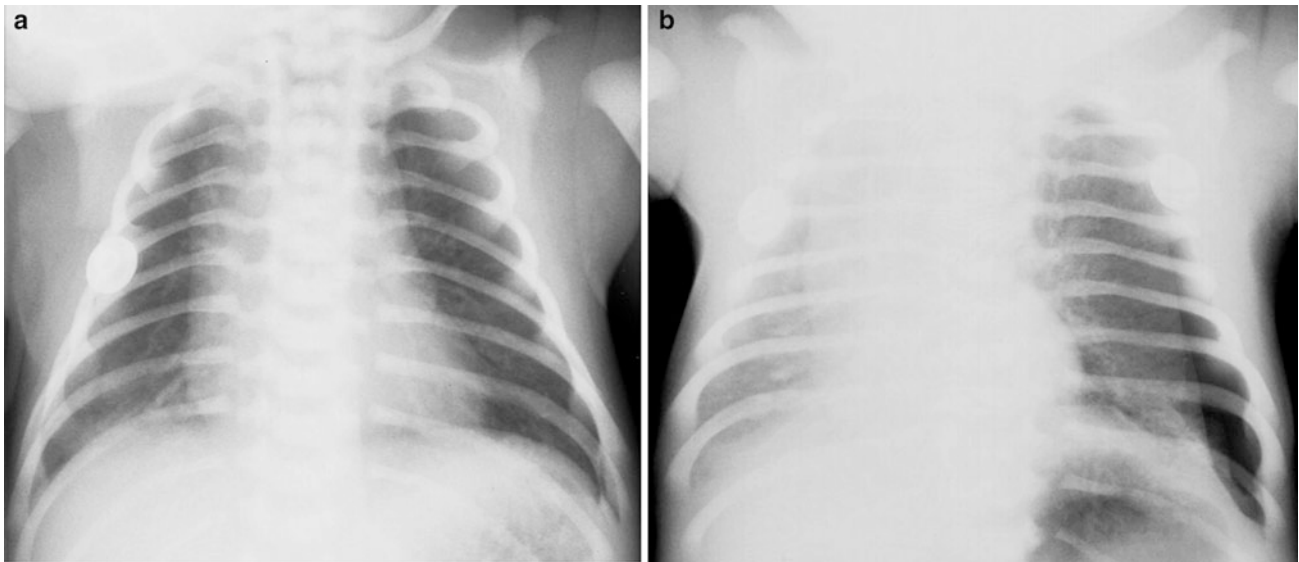


**Fig. 36** Frontal chest radiograph. (a) shows subtle left hemithorax hyperlucency and mediastinal shift, in a newborn. An expiratory view. (b) shows air in the pleural space and the “free lung edge” sign

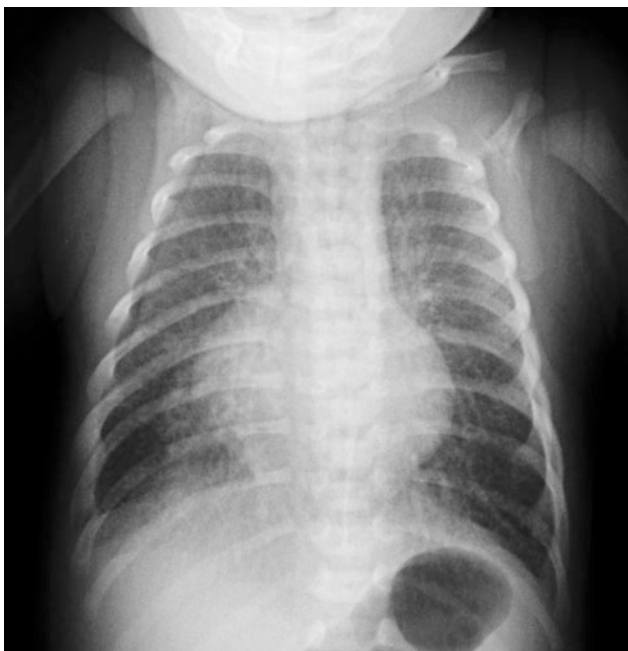


**Fig. 37** At the right side, a skin fold may be misinterpreted as a pneumothorax. Note that the line extends outside of the chest wall

- Hyperlucent hemithorax
- Increased definition of the mediastinum border
- Deep lateral costophrenic sulcus (Gordon 1980).

In children with uncertain findings, a cross-table lateral image or an expiratory radiograph can be useful to demonstrate the free pleural air (Fig. 36a, b).

A frequent pitfall, especially in newborns and small infants, is the interpretation of a skin fold as the *free lung edge sign*. The clues to properly recognize skin folds are to look for lung vessels between it and the thoracic wall, and to search for its extension to the soft tissues, beyond the border of the lung (Fig. 37).

## 4 Conclusion

Knowledge of the classical radiological findings as well as of the most frequent technical pitfalls is mandatory to interpret correctly chest radiographs in children and make correct diagnoses.

## References

- Alford B, McIlhenny J, Silen M et al (1993) Asymmetric radiographic findings in the pediatric chest: approach to early diagnosis. *Radiographics* 13:77–93
- Bramson RT, Griscom NT (2005) Interpretation of Chest Radiographs in Infants with Cough and Fever 236(1):22–29
- Calder A, Owens C (2009) Imaging of parapneumonic pleural effusions and empyema in children. *Pediatr Radiol* 39:527–537
- Chalumeau M, Le Clainche L, Sayeg N et al (2001) Spontaneous pneumomediastinum in children. *Pediatr Pulmonol* 31:67–75
- Chang L, Lee F, Gwinn J (1970) Normal lateral deviation of the trachea in infants and children. *AJR* 109:247–251
- Donnelly L (2005) Imaging in immunocompetent children who have pneumonia. *Radiol Clin N Am* 43:253–265
- Effmann E, Kuhn J (2004) Lung and airways chap I part II in Caffey’s pediatric diagnostic imaging. Mosby, Philadelphia, pp 891–898



- Enríquez G, García-Peña P, Lucaya J (2009) Pitfalls in chest imaging. *Pediatr Radiol* 38(Suppl 3):S356–S368
- Fefferman N, Pinkney L (2005) Imaging evaluation of chest wall disorders in children. *Radiol Clin N Am* 43:355–370
- Fraser R (1996) El tórax normal: sinopsis de las enfermedades del tórax. Marban, Madrid, Cap 1, pp 79–88
- Frush D, Donnelly L, Chotas H (2000) Contemporary pediatric thoracic imaging. *AJR* 175:841–851
- Gordon R (1980) The deep sulcus sign. *Radiology* 136:25–27
- Han B, Yoon H, Suh Y (2001) Thymic ultrasound I. Intrathymic anatomy in infants. *Pediatr Radiol* 31:474–479
- Kosucu P, Ahmetoglu A, Koramaz I et al (2004) Low-dose MDCT and virtual bronchoscopy in pediatric patients with foreign body aspiration. *AJR* 183:1771–1777
- Kuhn J, Brody A (2002) High-resolution CT of pediatric lung disease. *Radiol Clin N Am* 40(1):89–102
- Kuhn J, Effmann E (2004) Overview of imaging procedures in the pediatric neck and thorax. In: Caffey's pediatric diagnostic imaging, Mosby, Pensilvania, Sección IV, part I, 767–776
- McLoud T (1998) The pleura in thoracic radiology: The requisites, Mosby, Missouri, Chap 18, 483–513
- Moëne K, Ortega X (2012) Diagnóstico por imágenes del tórax pediátrico. Segunda edición. Buenos Aires, Ediciones Journal
- Nasseri F, Eftekhari F (2010) Clinical and radiologic review of the normal and abnormal thymus: pearls and pitfalls. *Radiographics* 30:413–428. Published on line doi:[10.1148/rg.302095131](https://doi.org/10.1148/rg.302095131)
- Salour M (2000) The steeple sign. *Radiology* 216:2 428–429
- Swischuk L (1997) Respiratory system, chap 1 in imaging of the newborn, infant and young child. Williams and Wilkins, Maryland, pp 1–158
- Swischuk L (1971) Anterior tracheal indentation in infancy and early childhood: normal or abnormal? *AJR* 112:12–17
- Zylak C, Standen J, Barnes G et al (2000) Pneumomediastinum revisited. *Radiographics* 20:1043–1057

# Ultrasound Study of the Pediatric Chest

Goya Enriquez, Celestino Aso, Xavier Serres, and Veronica del Prete

## Contents

<b>1</b>	<b>Introduction</b> .....	31
<b>2</b>	<b>Examination Technique</b> .....	32
<b>3</b>	<b>Lung Parenchyma</b> .....	32
3.1	Normal US Appearance and Artifacts.....	32
3.2	Congenital Malformations.....	32
3.3	Management of Congenital Malformations.....	36
3.4	Lung Consolidation .....	37
3.5	Interstitial Disease .....	40
3.6	Lung Tumors .....	42
<b>4</b>	<b>Pleural Space</b> .....	42
4.1	Normal Appearance and Artifacts .....	42
4.2	Pleural Effusions.....	42
4.3	Opaque Hemithorax.....	45
4.4	Pleural Tumors .....	45
4.5	Pneumothorax .....	46
<b>5</b>	<b>Chest Wall</b> .....	46
<b>6</b>	<b>Diaphragm</b> .....	47
6.1	Diaphragm Paralysis.....	47
6.2	Diaphragmatic Hernia .....	48
<b>7</b>	<b>Mediastinum</b> .....	49
7.1	Examination Technique.....	49
7.2	Normal US Appearance, Artifacts and Pitfalls .....	51
7.3	Indications for Mediastinal US .....	53
7.4	Mediastinal Abnormalities .....	55
<b>8</b>	<b>Conclusion</b> .....	60

## Abstract

The clinical applications of chest ultrasound (US) have been expanded in recent years. The chest is routinely studied prenatally by US which plays an important role in the detection of congenital lung malformations and congenital diaphragmatic hernias (CDH); severe cases of the latter could be treated in utero. US has several beneficial advantages such as portability and lack of ionising radiation and should be performed after careful chest X-ray assessment. Color, power, and pulsed Doppler capabilities permit the visualization of vessels without the need for venous contrast administration. Postnatal study of lung malformations detected in utero, consolidation, presence and characterization of pleural fluid, opaque hemithorax, palpable chest wall masses, abnormal mediastinal contours, and misleading chest X-ray findings constitute the main indications for chest US.

## 1 Introduction

Chest plain films continue to be the cornerstone of pediatric chest imaging, although some lesions may require further radiologic studies. Computed tomography (CT) and magnetic resonance (MR) provide excellent images of chest conditions that are easily understood by clinicians; however, these techniques are not universally available, particularly MR imaging. Ultrasonography (US) has also become a well-established tool to supplement plain film findings (Durand et al. 2001; Lobo 2006; Riccabonna 2008). US has several characteristics that are advantageous in children, such as lack of ionizing radiation, no sedation requirements, real-time visualization, wide availability, and portability (the examination can be performed at the bedside). The color and power Doppler capability of US enables visualization of vascular structures and perfusion of normal organs, tumors, or inflammatory lesions without the need for intravenous contrast administration, and M-mode

G. Enriquez (✉) · C. Aso · V. del Prete  
Department of Pediatric Radiology, Vall d'Hebron Hospitals,  
Ps Vall d'Hebron 119-129, 08035 Barcelona, Spain  
e-mail: genriquez@vhebron.net

X. Serres  
Department of Radiology, Vall d'Hebron Hospitals,  
Ps Vall d'Hebron 119-129, 08035 Barcelona, Spain



imaging has proved helpful for evaluating pneumothorax and lung and diaphragmatic motion.

US is the imaging modality of choice to examine the fetal chest, and routine use of this technique in pregnant women has considerably increased the detection of numerous congenital malformations. The information provided by US has widened our knowledge of the natural history of these conditions, and is extremely valuable for counseling and decision-making regarding prenatal management and delivery. (Bush et al. 2008; Cavoretto et al. 2008; Lecompte et al. 2009; Pariente et al. 2009; Witlox et al. 2009; Bulas and Egloff 2011).

Postnatal chest US examination of the lung parenchyma and mediastinum is performed using anatomic accesses between bones, known as acoustic windows. The low mineral content in neonates and small infants also enable transosseous (trans-sternal and transcostal) scanning. Furthermore, the presence of a large thymus in this age group provides an excellent acoustic window to examine the mediastinum. Since acoustic windows between more ossified bones have to be used to study the area of interest in older children, it is difficult to obtain a panoramic view of the chest, which constitutes one of the main limitations of chest US.

Although US has mainly been used to investigate pleural fluid, its clinical applications have been greatly expanded. (Kim et al. 2000; Koh et al. 2002; Coley 2011). In current clinical practice, chest US is used to study congenital lung malformations detected prenatally, assess lung consolidations and opaque hemithorax or abnormal mediastinal contours seen on plain films, determine the solid or cystic nature of a focal mass, image palpable wall lesions and, in general, clarify inconclusive plain film findings. In this chapter, we will discuss and illustrate the use of US for these purposes.

## 2 Examination Technique

Ultrasound of the chest should always be performed following careful evaluation of chest X-rays. Depending on the location of the lesion, the patient is placed in the supine, prone, or lateral decubitus position, and the appropriate transducer and acoustic window are selected. Smaller sector or convex transducers should be used for inter-rib studies and for transdiaphragmatic or suprasternal approaches. Linear probes are recommended for wall lesions and to better identify the pleuro-pulmonary interface. As usual, transducer frequency varies with age of the patient and depth of the lesion. High-frequency transducers (5–10 MHz) are best for imaging neonates and infants, and for very superficial lesions.

An array of acoustic windows, including supraclavicular, suprasternal, parasternal, intercostal, subxyphoid, transdiaphragmatic, and paravertebral approaches can be applied, and longitudinal, transverse, or axial views obtained as required.

As a complement to gray-scale images, color, power and pulsed Doppler are useful to identify the vascular supply in pulmonary congenital malformations, assess vascularity of lung consolidations, and study flow patterns within masses.

Sedation is seldom required for US exams. It is helpful to warm the gel and show the children toys or cartoons to hold their attention and facilitate the study. Furthermore, it is always advisable to avoid examining a hungry infant.

## 3 Lung Parenchyma

### 3.1 Normal US Appearance and Artifacts

The normal aerated lung is not seen as a well-delineated organ on US. Instead, it is inferred by a few scattered echogenic images with characteristic posterior comet-tail reverberations caused by interaction of the sound beam with interlobular septa. When using a subcostal approach, the comet-tail reverberations related to the aerated lung bases are observed adjacent to the diaphragm (Fig. 1). In real time during respiration, the normal lung exhibits a characteristic to-and-fro movement against the visceral pleura known as the “gliding sign” (Ben-Ami et al. 1993; Shankar et al. 2000). M mode, shows a pattern known as the “seashore sign” owing to its similarity to a sandy beach produced by lung motion (Fig. 2) (Coley 2011).

The main artifacts seen on US study of the aerated lung base are the so-called mirror image artifacts, caused by sound wave reflection when the ultrasound beam strikes the diaphragm. Depending on the angle at which the US beam is directed during transdiaphragmatic scanning of the lung base, a dual image of the liver or spleen can be observed above the diaphragm, simulating a parenchymal consolidation. This artifact, known as pseudo-consolidation (Ben-Ami et al. 1993), is indicative of normal air-filled lung. Mirroring of the image can also occur when using color Doppler, and results in duplication of vascular structures (Fig. 3).

### 3.2 Congenital Malformations

In countries where obstetric sonography is routinely performed, the detection rate of congenital lung malformations has risen considerably (Davenport et al. 2004). The fetal lung can be easily identified on prenatal US studies using a transverse four-chamber view of the fetal chest, a routine

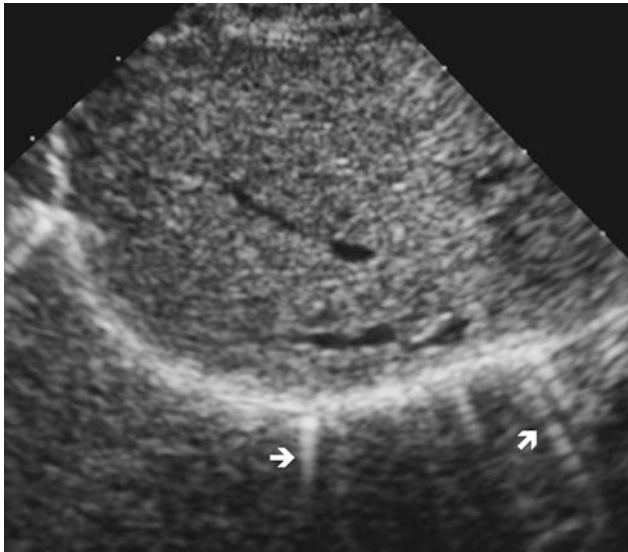


**Fig. 1** Transverse US scan of the right side shows several comet tails adjacent to the diaphragm (*arrows*), indicative of normal aerated lung

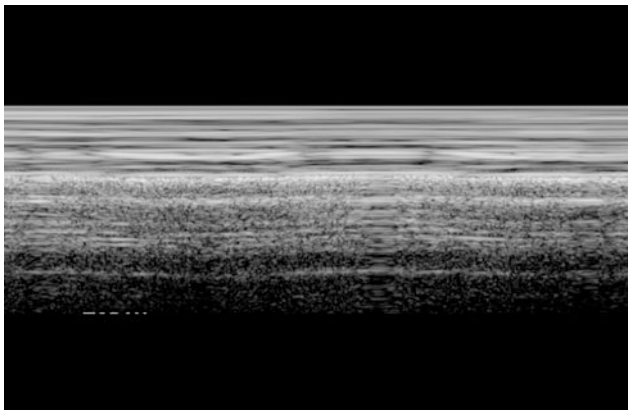


**Fig. 2** “Seashore sign” produced by lung motion, seen on transverse intercostal M-mode US scan

component of obstetric ultrasound protocols. It is seen as a solid structure of medium-level echogenicity that varies slightly throughout gestation. This US appearance is produced by the combination of the lung water content and parenchymal network of bronchial, vascular, and mesenchymal elements. Furthermore, lung vascularization can be readily assessed by pulsed, color, or power Doppler (Fig. 4).

Fetal congenital lung malformations present as areas of abnormal echogenicity exerting a mass effect on adjacent structures. They are hyperechoic with respect to normal lung parenchyma and may be either homogenous or with coexisting cysts. The size of the lesion may be overestimated since the compressed, unaffected lung can acquire echogenicity similar to that of the lesion and be considered a part of it. US is a sensitive technique for detecting

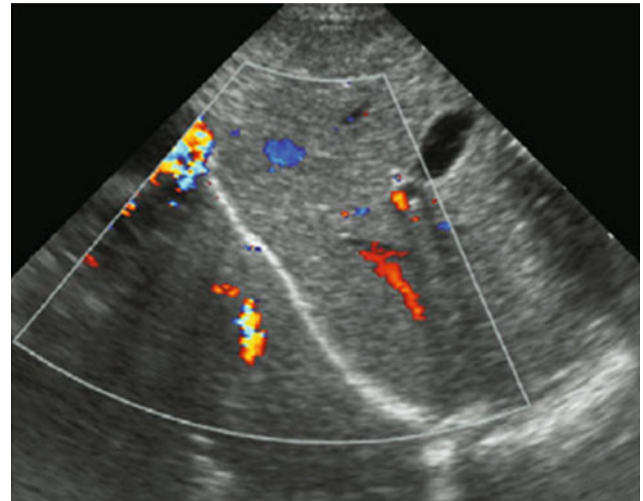


**Fig. 3** Mirror image artifact. Transdiaphragmatic longitudinal US scan in a 2-month-old boy shows “duplication” of the liver and its Doppler signals, projecting over the right lung base

congenital lung malformations, but is less reliable for establishing a specific diagnosis, since a similar echo pattern can be seen in many of these conditions.

Several classifications and terms are in use to describe bronchopulmonary malformations, which are now believed to represent a spectrum of anomalies that result from intrauterine airway obstruction (Langston et al. 2003; Correia-Pinto et al. 2010). These malformations include congenital pulmonary airway malformation (CPAM), pulmonary sequestration (PS), bronchogenic cyst (BC), bronchial atresia (BA), and congenital lobar overinflation (CLO). Additional anomalies such as pulmonary agenesis, tracheal bronchus, esophageal and tracheal atresia, and tracheoesophageal fistula are recognized as a part of the spectrum by some authors (Newman et al. 2006). The type of malformation and its sonographic appearance depend on the level and timing of the obstruction, with the vascular abnormality being an associated feature.

### 3.2.1 Congenital Pulmonary Airway Malformation

Congenital pulmonary airway malformation, previously known as congenital cystic adenomatoid malformation, accounts for 30–47 % of all fetal lung masses detected by US. CPAM is a hamartomatous malformation of the lung with abnormal branching of immature bronchioles that communicate with the tracheobronchial tree (Epelman et al. 2010; Correia-Pinto et al. 2010). Sonographic findings vary depending on the type of malformation (May et al. 1993). Stocker et al. initially classified CPAM into three histologic types (Stocker et al. 1977), which were later expanded into five types (Stocker 1994). The first three types are the forms most often recognized on US. Type 1, the most common, appears on US as single or multiple large cysts, often

**Fig. 4** US scan of normal fetal lung at 23 weeks' gestational age  
**a** Four-chamber view shows the lung as a solid medium-level echogenic structure (L)  
**b** Pulmonary vessels and their ramifications are very well seen on Power Doppler. Courtesy of Dr. Edgar Hernández, Ph. D. Clinic Hospital Barcelona

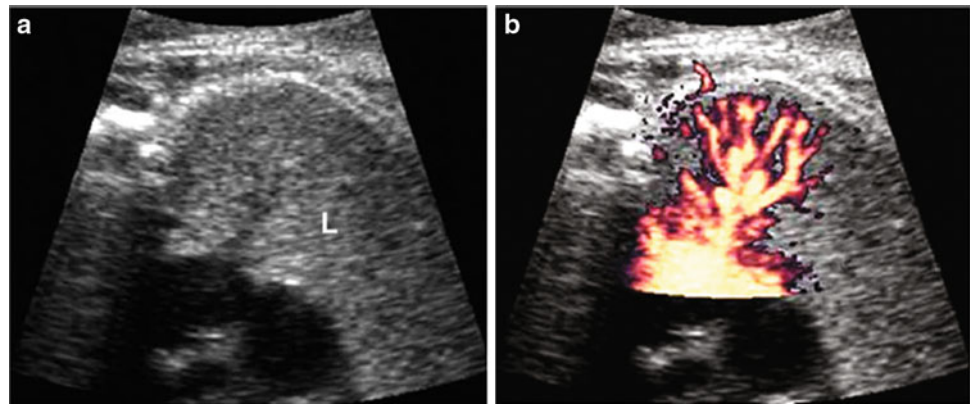
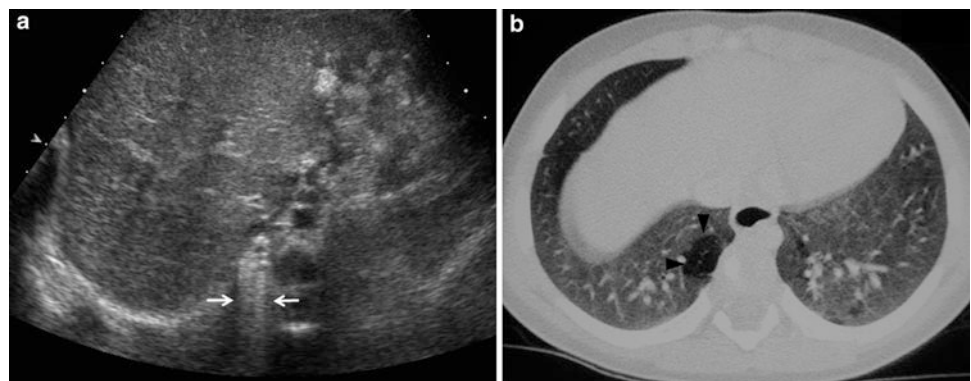


**Fig. 5** Postnatal studies in a newborn with prenatal diagnosis of congenital right lung malformation.  
**a** Transverse US scan shows a hyperechogenic area with evident B lines in the right hemithorax (arrows).  
**b** High-resolution, contrast-enhanced CT in the same patient confirmed the presence of a hyperlucent lesion (arrowhead) corresponding to CPAM



affecting the entire pulmonary lobe. Type 2 is seen as an echogenic mass with numerous small cysts. Type 3 malformations appear as homogenous echogenic masses without cysts.

Sonographic differentiation between CPAM and pulmonary sequestration may not always be possible. A systemic vessel arising from the aorta has also been described in patients with pulmonary airway malformation (Winters et al. 1997). Furthermore, hybrid lesions are often seen, consisting of CPAM associated with pulmonary sequestration in the same malformation; these represented around 50 % of cases in a pathologic series (Conran and Stocker 1999). Postnatal US study of CPAM is challenging. Since the abnormal lung communicates with the airways, the cysts, which contain fluid during fetal life, fill with air at birth, making their identification difficult on US. The air-filled cluster of cysts is seen as an area of increased echogenicity with a banded appearance (Fig. 5). This US finding, which is known as the “aurora sign,” has also been reported in several acquired interstitial lung diseases (Kohzaki et al. 2003). Therefore, CT and MRI are more suitable for postnatal study of the internal components of this malformation. Postnatal radiography, CT or MRI can be performed immediately if the patient is symptomatic or months later if asymptomatic to determine whether surgery is required.

### 3.2.2 Bronchopulmonary Sequestration

Bronchopulmonary sequestration is a congenital malformation consisting of nonfunctioning lung tissue, which lacks a normal connection to the tracheobronchial tree and is usually supplied by a systemic artery that arises from the thoracic or abdominal aorta. It is the second most common cause of a fetal chest mass, and two different types are classically recognized: intralobar and extralobar. Intralobar sequestration has been found to occur in older infants and some authors have considered it an acquired lesion (Frazier et al. 1997). Extralobar sequestration has its own pleural covering, and venous drainage is into the systemic circulation (azygos-hemiazygos system, portal vein, or inferior vena cava). It has been considered a congenital condition. (May et al. 1993; Ko et al. 2000). Currently, this categorical classification is not universally accepted since mixed systemic and pulmonary venous drainage has been observed in several cases of extralobar sequestration. (Pumberger et al. 2003). Moreover, the intralobar type is also found in neonates and is now considered a congenital rather than an acquired lesion (Newman 2006).

On US study, sequestration is seen as a homogenous or heterogenous echogenic mass usually located in the lower pulmonary lobes, but sometimes occurring at or below the diaphragm. We recommend a subxiphoid approach to study the mass, search for an anomalous feeding vessel arising



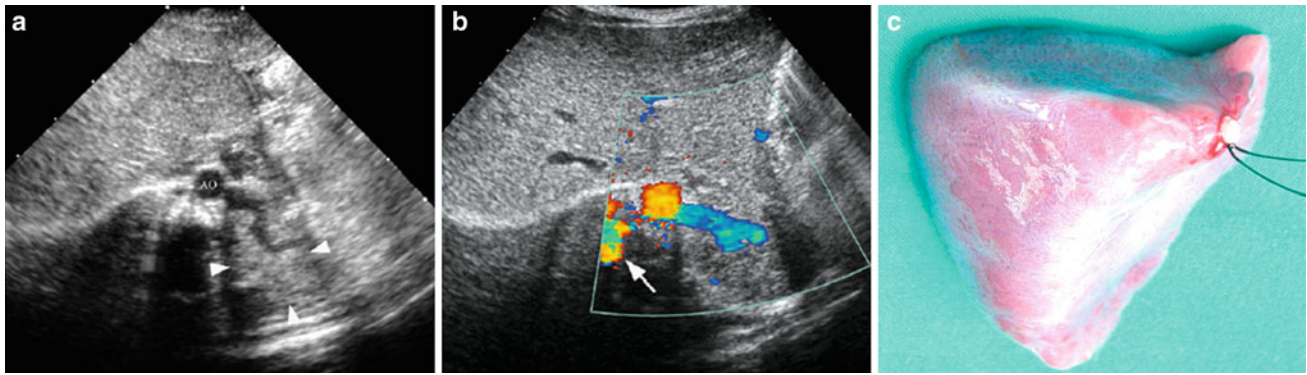


**Fig. 6** Extralobar solid sequestration in a 2-month-old boy **a** In this subxiphoid transverse scan, an echogenic mass (*arrowheads*) can be seen behind the left lobe of the liver. A tortuous vessel, likely to be a persistent primitive post-brachial artery, is seen arising from the aorta (AO) **b** Color Doppler shows the abnormal vessel originating at the

aorta and supplying the mass. Venous drainage is inferred to be through the enlarged azygos (*arrow*) **c** Photo of the surgical specimen of another patient with extralobar sequestration showing its triangular shape and the hilar vascular nutrition

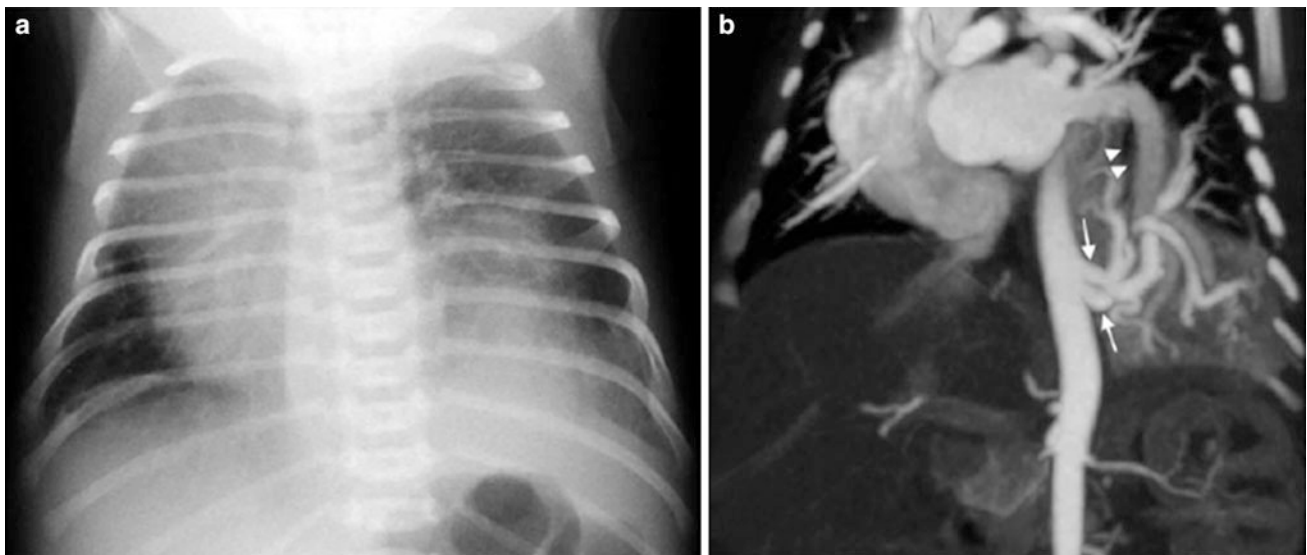


**Fig. 7** Intralobar sequestration in a newborn boy **a** Chest X-ray shows opacification of the left lung base **b** CT angiography demonstrates several systemic vessels arising from the aorta supplying the sequestration (*arrows*). A large vein is seen draining into the left atrium (*arrowheads*)

from the aorta, and investigate the systemic or pulmonary venous drainage (Fig. 6). The azygos may be enlarged in cases of systemic drainage to the azygos-hemiazygos system (Ko et al. 2000). Pulmonary venous drainage is better delineated by CT or MRI than by US (Fig. 7).

Solid pulmonary sequestrations, particularly those in infradiaphragmatic locations, should be differentiated from congenital neuroblastoma and adrenal hematomas (Manson and Daneman 2001; Langston et al. 2003; Vijayaraghavan et al. 2003). The presence of calcifications (common in neuroblastoma and exceedingly rare in neonatal

sequestration) as well as the obstetric history (sequestration is detected in the second trimester and neuroblastoma in the third trimester) are the main distinguishing factors (Fig. 8).

### 3.2.3 Lobar Overinflation

Lobar overinflation is characterized by hyperinflation of one part of the lung (usually the apical and posterior segments of the left upper lobe) and is seen on US as an area of homogenous hyperechogenicity with normal pulmonary supply and an absence of cysts (Daltro et al. 2010). The increased echogenicity is believed to be secondary to fluid accumulation in

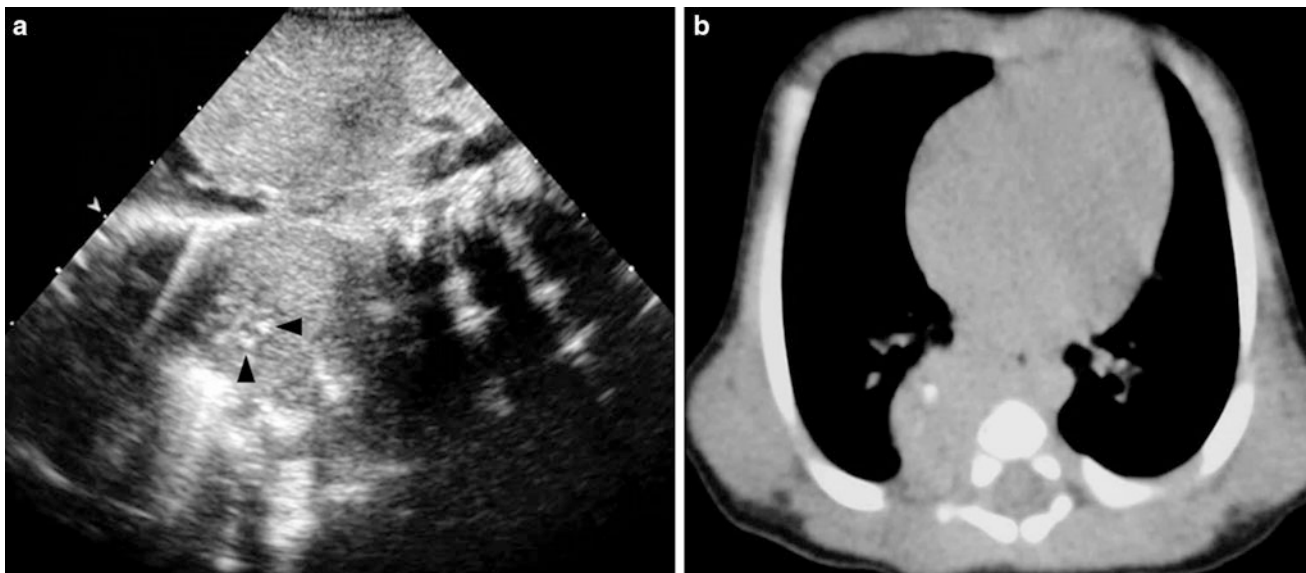


**Fig. 8** Postnatal US and CT of congenital neuroblastoma. **a** Longitudinal US scan shows a solid mass in the right paravertebral space with several echogenic foci (arrowheads) representing calcifications.

**b** Unenhanced high-resolution CT confirms the presence of calcifications within the mass. The lesion was detected prenatally in the third trimester of gestation

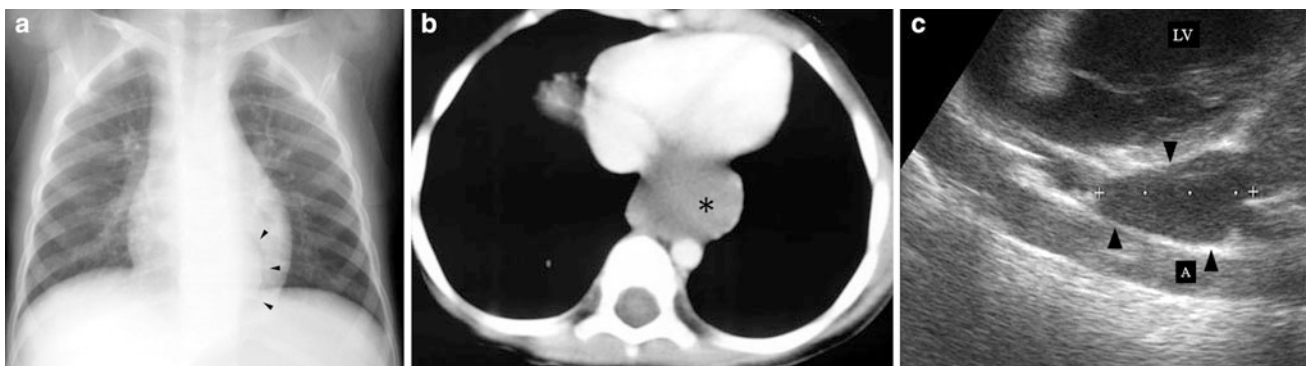


**Fig. 9** Bronchogenic cyst in a 4-year-old boy. **a** Chest plain film shows a curved *left paravertebral mass* (arrowheads). **b** On enhanced high resolution CT, a mass of uncertain nature is seen on the *left side*

(asterisk) **c** Sagittal US scan reveals the cystic characteristics of the lesion (arrowhead). LV left ventricle; A aorta

the affected lung (Pariante et al. 2009). Differentiation between CLO and a microcystic form of CPAM or PS may be very difficult before birth. Diagnosis can be confirmed postnatally by chest X-ray and CT imaging (Seo et al. 2006).

### 3.2.4 Bronchogenic Cyst

Bronchogenic cysts are usually located in the subcarinal region, but they may also be found within the pulmonary parenchyma. Depending on their content, intrapulmonary cysts are seen as unilocular anechoic or weakly echogenic lesions. US is particularly helpful in cases where CT is inconclusive regarding the solid or cystic nature of the lesion (Fig. 9).

## 3.3 Management of Congenital Malformations

Some congenital lung malformations completely or partially involute in the third trimester of gestation. When a huge mass displaces the mediastinum, prenatal interventions such as drainage of the largest cysts in cystic CAPM can be performed. The postnatal management of antenatally diagnosed lung malformations is highly controversial since most newborns are asymptomatic. (Aziz et al. 2004; Laberge et al. 2004). Reports in the literature tend toward conservative management of solid pulmonary sequestration since this malformation may regress spontaneously (García-Peña et al. 1998) (Fig. 10). Nonetheless, resection of cystic



**Fig. 10** Involution of prenatally diagnosed pulmonary sequestration **a** Neonatal MRI coronal view demonstrates a homogeneous solid mass in the left juxtaphrenic region (\*) **b** MRI performed 2 years later shows a small remnant of the lesion (arrow)

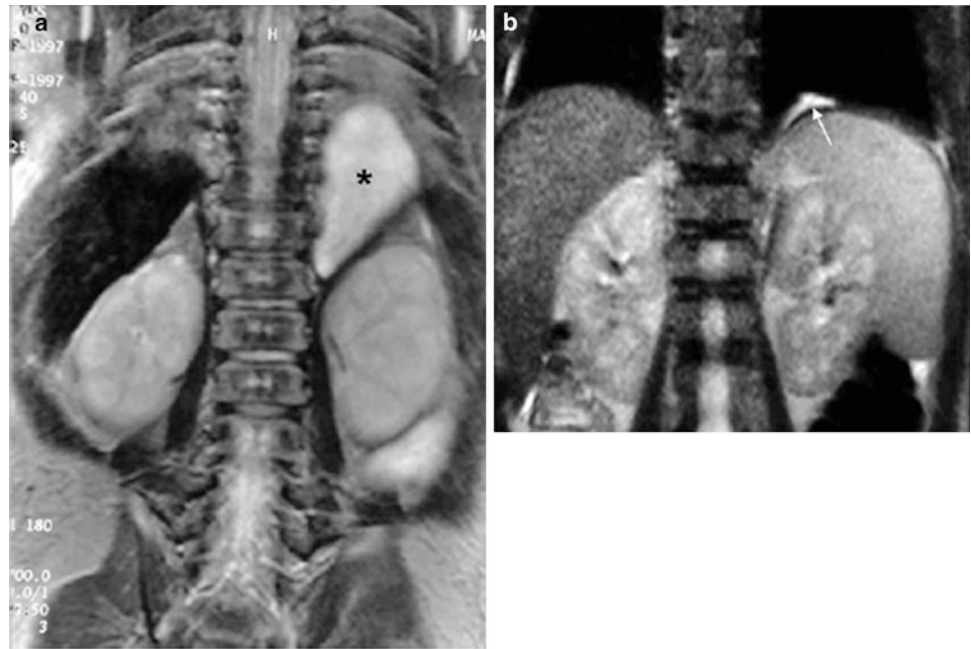
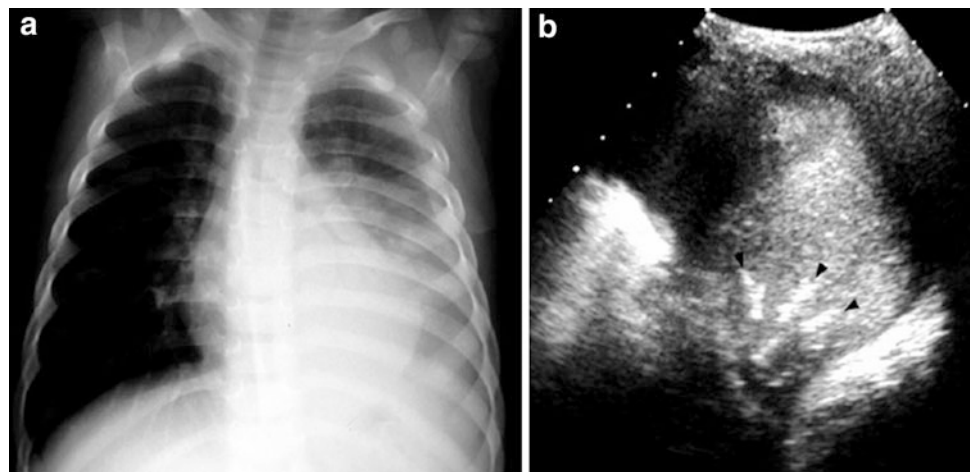


**Fig. 11** A 6-year-old girl with left-sided pneumonia and pleural effusion **a** Increased opacity of the left lung base associated with pleural fluid is visible on the chest radiograph **b** Intercostal axial US scan with the patient in a right decubitus position shows multiple bright, linear, branching structures (arrowheads), corresponding to air sonobronchograms



or solid/cystic malformations is still advocated owing to the risk of infection and potential malignant transformation to rhabdomyosarcoma or pulmonary blastoma (Papagiannopoulos et al. 2001; Hasiotou et al. 2004); however, the precise timing of surgery remains to be established. Further prospective studies with sufficient follow-up are required for the pros and cons of conservative versus surgical management to be assessed.

### 3.4 Lung Consolidation

Lung consolidation is the term applied to a lung parenchyma pattern in which pulmonary air is decreased or absent, as occurs in pneumonic consolidation and atelectasis. Pneumonic consolidation refers to filling of the normal air spaces

with fluid and inflammatory cells, thereby converting the reflective lung into a solid structure with echogenicity similar to liver (lung hepatization). The air-filled bronchi in the consolidated lung are seen as echogenic branching linear structures converging toward the lung root. This feature is known as the sonographic air bronchogram (Weinberg et al. 1986; Acunas et al. 1989; Yang et al. 1992; Seibert et al. 1998; Kim et al. 2000; Lichtenstein et al. 2009) and is equivalent to the air bronchogram observed on chest X-rays (Fig. 11). The loss of lung volume in atelectasis produces characteristic crowding of the air-filled bronchi and pulmonary vessels (Fig. 12) (Weinberg et al. 1986). In our experience, sonobronchograms are often visualized in patients in whom air bronchograms were not seen on X-rays, a fact that makes US a useful technique for clarifying inconclusive plain film findings (Fig. 13).

**Fig. 12** A 10-year-old boy with pleural effusion and secondary atelectasis of the ipsilateral lung  
**a** Transverse US scan of the right hemithorax shows profuse pleural fluid and atelectatic lung  
**b** Crowded pulmonary vessels, characteristic of pulmonary collapse, are demonstrated by power Doppler. This US finding explains why atelectasis is seen as a hyperintense lesion on CT

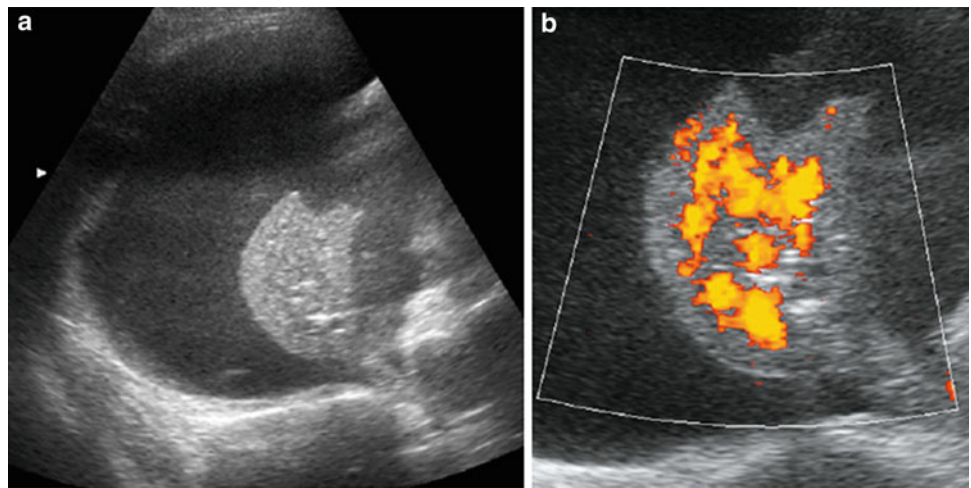


**Fig. 13** Numerous sonobronchograms not visualized on the chest plain film  
**a** Chest radiograph of a 4-year-old boy shows almost complete opacification of the right hemithorax. No airbronchograms are identified, hence differentiation between consolidation and pleural fluid is not possible  
**b** Subcostal US view shows that the opacification corresponds to a pulmonary consolidation with a huge sonobronchograms

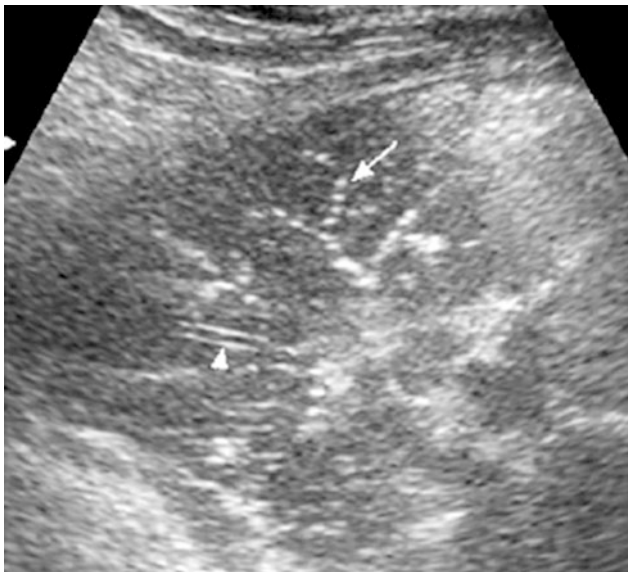
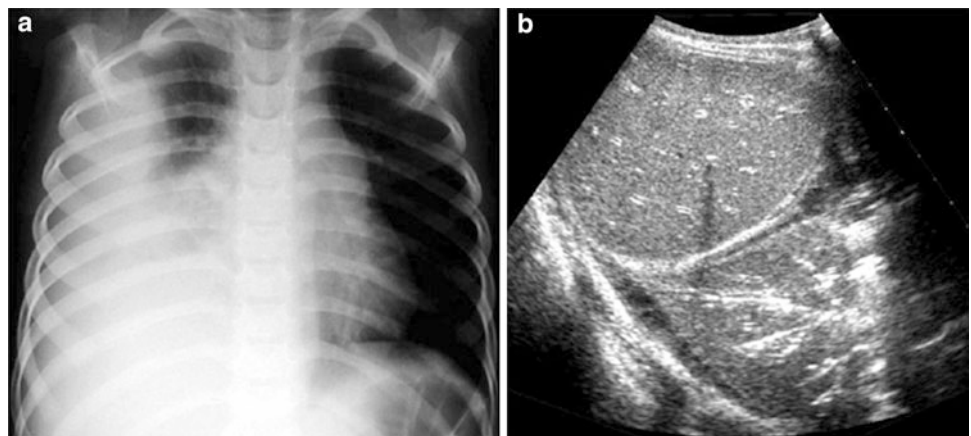


**Fig. 14** Sonographic fluid bronchogram in a 6-year-old boy with asthma. Transverse intercostal scan shows bright dots that moved in real time over a hypoechoic background (arrows). The well-defined walls of the pulmonary vessel are clearly seen (arrowhead) while the bronchus wall is imperceptible

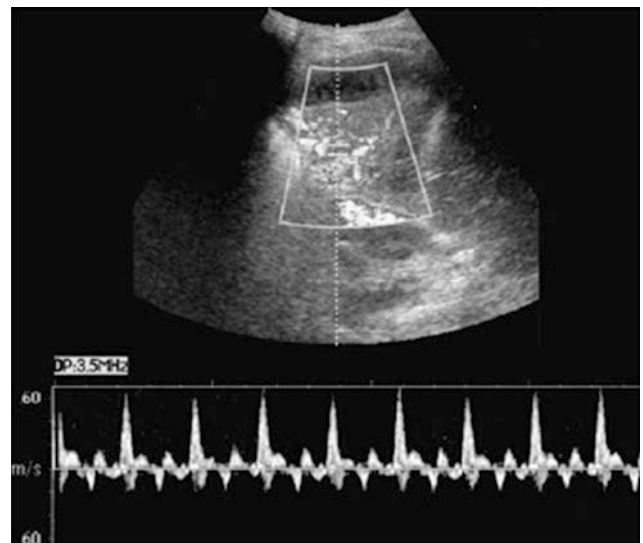


**Fig. 15** Characteristic spectral Doppler in pulmonary consolidation. Color Doppler US in a patient with pulmonary consolidation shows the characteristic quadriphasic pattern of the pulmonary arteries

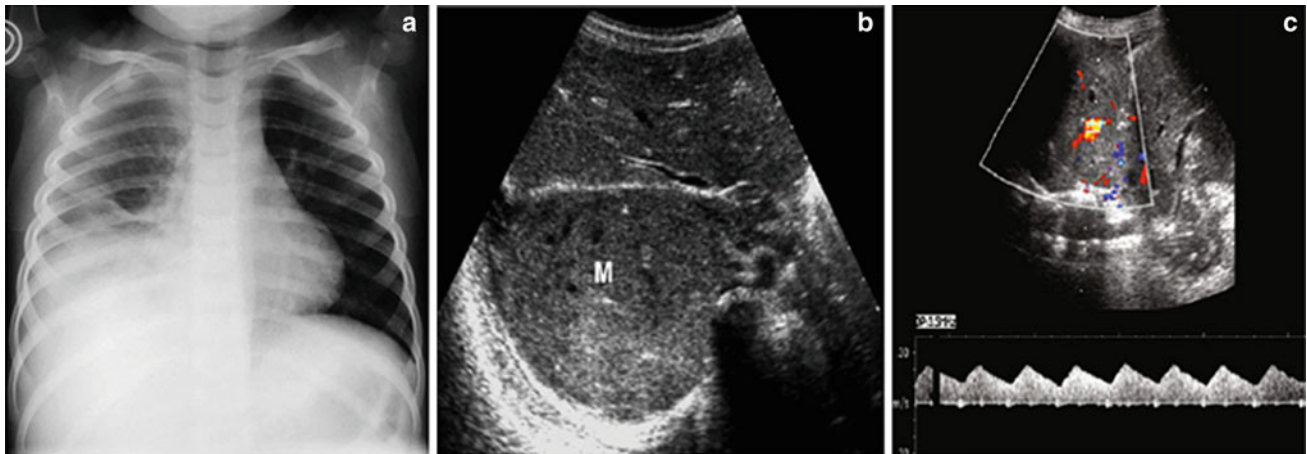


**Fig. 16** Extrapleural mass simulating pulmonary consolidation on the chest radiograph **a** Chest plain film of a 6-year-old boy presenting with fever who has been treated with antibiotics for a week shows opacification of the right lung base compatible with pleuro-pneumonia **b** Subcostal

transverse US view shows a heterogeneous solid lesion (M). No sonobronchograms were identified **c** The lesions have numerous internal vessels with a systemic wave pattern, a finding that rules out the diagnosis of pulmonary consolidation. The final diagnosis was Yolk sac tumor

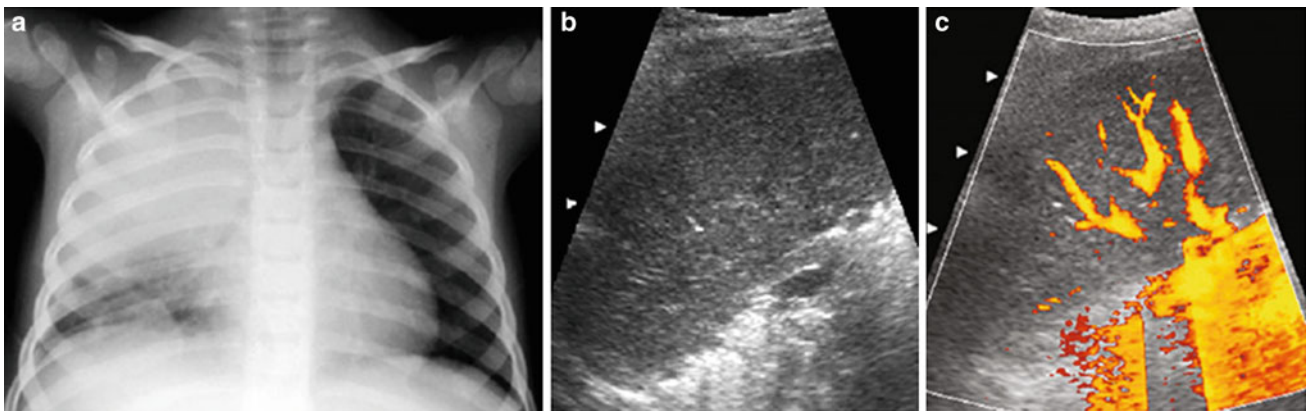


**Fig. 17** An 8-year-old boy with well-vascularized lobar pneumonia **a** Chest radiograph shows opacification of the right upper lobe **b** The consolidated lung has a homogeneous echogenicity (similar to that of

the liver) in this intercostal oblique US scan obtained with the patient in a prone position **c** Numerous pulmonary vessels are seen on power Doppler

In patients with asthma, cystic fibrosis, or severe inflammatory conditions, the bronchi contain mucus or secretions. In these cases, US demonstrates anechoic tubular branching structures known as the sonographic fluid bronchogram. (Yang et al. 1992; Kim et al. 2000). The fluid-filled bronchi have imperceptible walls and may contain air bubbles. These features may differentiate fluid bronchograms from pulmonary vessels on conventional US (Fig. 14), but definitive differentiation is made by color Doppler. The vessels seen within the consolidation on color or power Doppler can be identified as normal pulmonary vessels by their characteristic polyphasic (mainly quadriphasic) pattern depicted with pulsed Doppler (Fig. 15).

Sonographic air bronchograms, fluid bronchograms, air alveolograms, and pulmonary vessels within the lesion are characteristic features of lung consolidation and are never seen in pleural effusion or tumors. Hence, these findings are

essential for differentiating between these entities and should be actively investigated (Fig. 16). In peripheral lung consolidation, visualization of pulmonary vessels may be the only sonographic clue to the diagnosis.

According to the degree of vascularization, lobar pneumonia can be classified into three types:

- (1) Well-vascularized pneumonia. In these cases, the consolidation presents a homogenous appearance (similar to the echogenicity of the liver parenchyma) with multiple vascular structures (Fig. 17).
- (2) Poorly vascularized pneumonia without necrotic areas. In contrast to the first type, the number of vessels in the consolidated lung is scant, but the lesion remains homogenous (Fig. 18).
- (3) Poorly-vascularized pneumonia with necrotic areas. Very few vessels are visible on color Doppler. Consolidation is usually heterogenous with peripheral areas



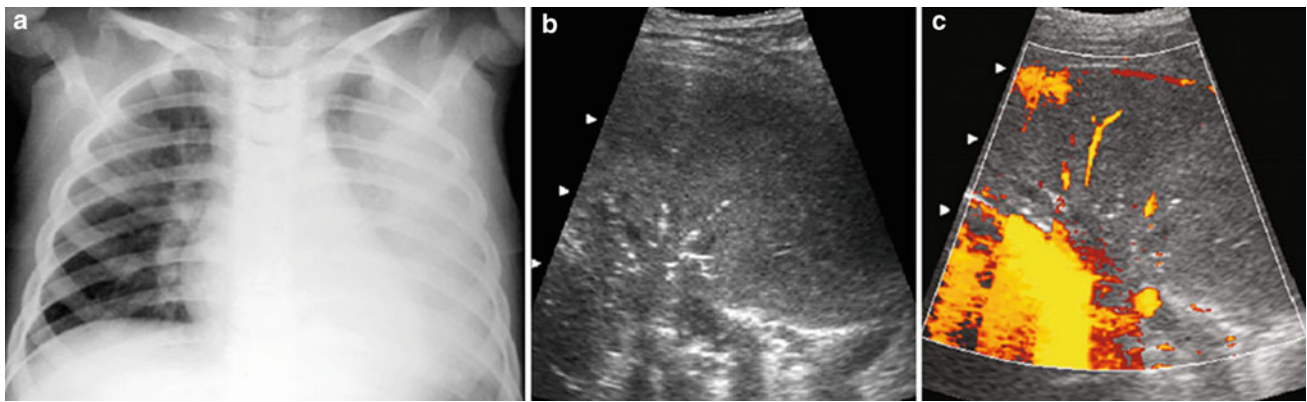
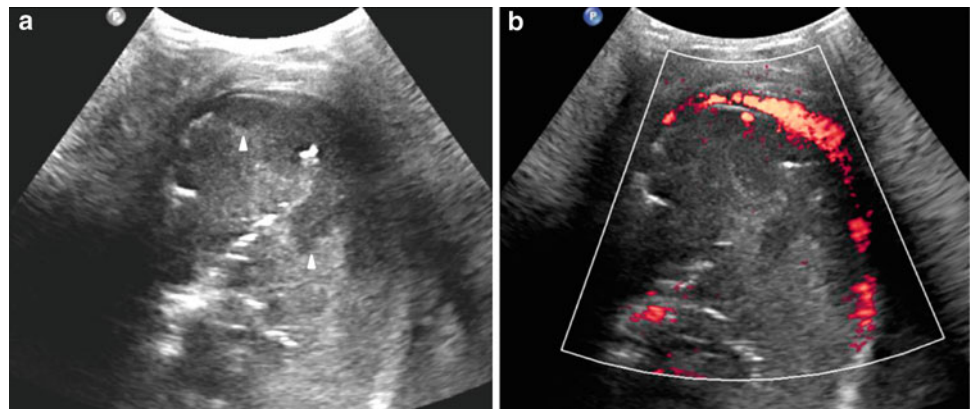


**Fig. 18** A 6-year-old girl with poorly-vascularized pneumonia **a** The chest radiograph discloses evidence of left lung opacification **b** Inter-costal oblique US scan with the patient in a prone position shows

homogeneous appearance of the affected lung base with central air sonobronchograms **c** Very few vessels are seen within the consolidation

**Fig. 19** Pneumonia with necrotic areas in a 5-year-old boy. **a** Gray-scale US scan shows several hypoechoic images corresponding to necrotic areas within the consolidation (arrowheads). **b** On power Doppler, no vessel signals are seen in the consolidation, although the pleural hypervascularization is clearly depicted



of cavitation seen as hypoechoic areas, sometimes containing internal echogenic debris (Fig. 19). The absence of vascularization can be localized or involve the whole area of consolidation. (Fig. 20).

The third type, known as necrotizing pneumonia, results from necrosis of the lung parenchyma due to occlusion of alveolar capillaries following severe lung infection. *Streptococcus pneumoniae* is one of the most common micro-organisms causing this complication in children (Kerem et al. 1994; Hedlund et al. 1999). In adults, the outcome of necrotizing pneumonia is generally poor and early surgical excision of the gangrenous lung is indicated. However, children can recover completely with medical treatment, although their clinical evolution is long and may require extended hospitalization (Ben-Ami et al. 1993). Thus, in our experience, US provides diagnostic and prognostic information that may influence therapy in children with lobar pneumonia. Contrast-enhanced chest CT in this group of children can provide information similar to that obtained with chest US (Donnelly and Klosterman 1997).

Follow-up studies with US are recommended in children with associated pleural fluid, those with lobar pneumonia

and severe clinical symptoms, and those who fail to respond to antibiotic therapy.

When studying consolidation, the radiologist should be aware of the inability of US to determine the extent of a deeply affected area. Acoustic reverberation artifacts, caused by areas of aerated lung interposed between the transducer and the deep area of interest, can hinder visualization of the entire consolidation.

### 3.5 Interstitial Disease

Several authors have described the value of US for assessing interstitial lung lesions (Agricola et al. 2005; Lichtenstein et al. 2009; Coley 2011). The findings obtained are based on the interaction of the sound beam with thickened subpleural interlobular septa, which produces the so-called *B lines* (vertically oriented echogenic lines). Some researchers have classified B lines as: B7 lines (7 mm apart), which indicate thickened interlobular septa, and B3 lines (3 mm apart), considered the equivalent of the ground-glass appearance on CT (Stefanidis et al. 2011).

**Fig. 20** Pneumonia with central area of necrosis **a** The chest radiograph shows a round pneumonia in the anterior segment of the upper right lobe bulging the minor fissure **b** US study shows a central hypoechoic area corresponding to necrosis (\*). The bulged minor fissure is well seen (arrowheads) **c** Power Doppler shows absence of vascularization in the necrotic area **d** The necrotic area within the consolidation was confirmed by CT

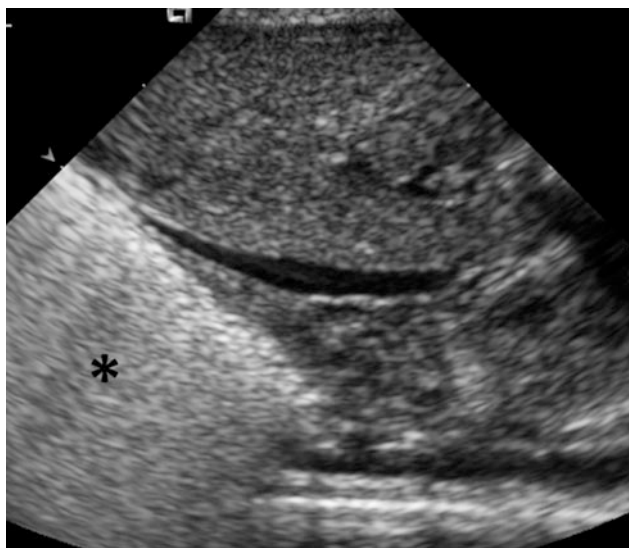
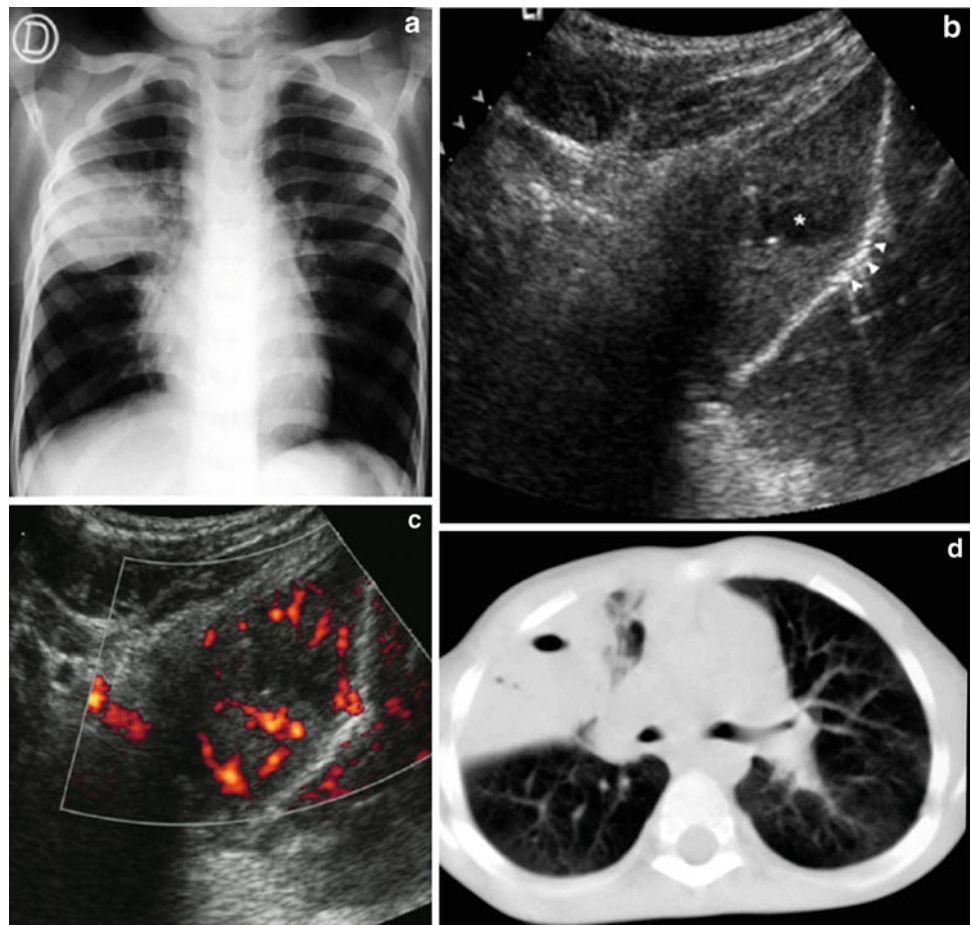


**Fig. 21** Characteristic US appearance of hyaline membrane disease. Longitudinal scan shows uniform hyperechogenicity of the right lung base. Compare with normal aerated lung in (Fig. 1)

The US patterns seen in several lung diseases affecting premature and newborn infants have been reported (Copetti and Cattarossi 2007; Lovrenski 2012). In premature infants, respiratory distress syndrome (RDS), the clinical expression

of surfactant deficiency and generalized alveolar-interstitial syndrome, shows a characteristic US pattern of bilateral, diffuse, compact B lines (Avni et al. 1990, 1996) (Fig. 21). Patients with this condition are treated with surfactant administration, and US is of value for following up the response to therapy (Cattarossi et al. 2010). It is known that surfactant administration rapidly improves pulmonary aeration, but the initial US appearance of the lung can persist even several days after treatment, indicating that lung fluid does not resolve as fast as pulmonary aeration (Copetti et al. 2008).

Numerous B lines, somewhat less compact than in RDS, can be seen in bronchopulmonary dysplasia, a chronic lung disease occurring in premature infants undergoing oxygen therapy (Pieper et al. 2004) (Fig. 22).

Transient tachypnea of the newborn (TNN) usually presents characteristic findings on chest X-ray. Nonetheless, severe cases may show features similar to those seen in pneumonia and sepsis. In patients with TNN, a typical US sign known as the “double lung point” has been reported (Copetti and Cattarossi 2007; Volpicelli 2011b) and provides a clue for the diagnosis. This feature refers to a clear difference between the US pattern seen in the upper and lower lung fields. More compact B lines are seen at the lung bases due to their greater volume.



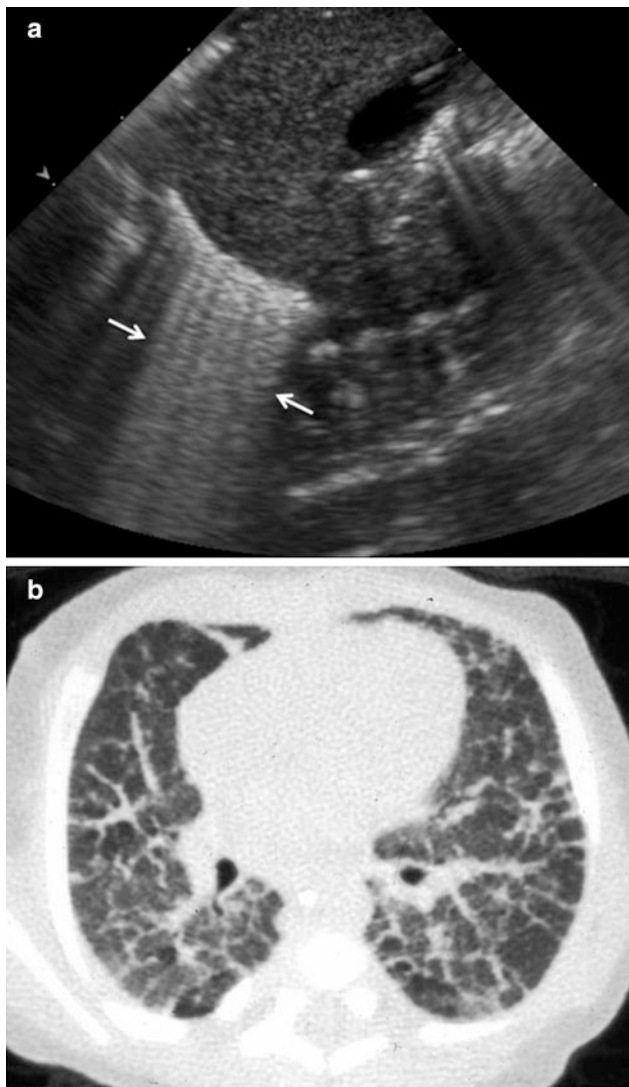


**Fig. 22** Premature infant with bronchopulmonary dysplasia. **a** Longitudinal US scan shows abundant B lines adjacent to the diaphragm. **b** Corresponding CT scan clearly shows thickening of the interlobular septa, the cause of the B lines on US

Knowledge of these US patterns may help neonatologists clarify certain clinical situations without the need for additional plain films and radiation exposure.

### 3.6 Lung Tumors

Primary lung tumors, including blastoma, mucoepidermoid carcinoma, hemangiopericytoma and rhabdomyosarcoma, are rare in children. The most common of these is pulmonary blastoma. It usually has a complex echogenic appearance and is located in the periphery of the lung. Due to the peripheral location of this lesion, sonography can be used to guide percutaneous biopsy of the mass.

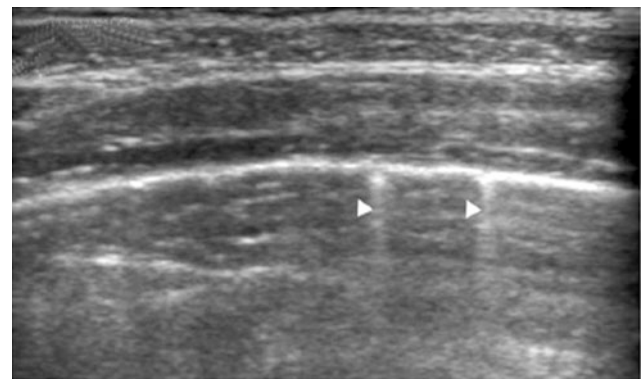


**Fig. 23** Intercostal transverse view of the normal pleura. The curving pleuralung interface is well visualized. The small echogenic dots superimposed on the linear interface (arrowheads) represent air in the alveoli as they glide against the pleura with respiratory motion

## 4 Pleural Space

### 4.1 Normal Appearance and Artifacts

The pleura is a very superficial structure that is well visualized by US. It is composed of two membranes, the visceral and parietal pleurae, separated by a potential space seen as a thin hypoechoic band during respiration in real time. On intercostal longitudinal scans, the pleura is visualized as a highly echogenic linear structure that acquires a curving configuration in the transverse view (Fig. 23). The sonographer should be aware of certain features related to the pleura that are of great diagnostic value. In real-time sonography, the visceral pleura moves with the respiratory excursions, and recognition of this movement provides clues to the diagnosis of several conditions, such as pneumothorax and pleural infiltration by pulmonary or extra-pleural tumors. The absence of visceral pleura movement is indicative of pneumothorax. Similarly, the absence of pulmonary tumor movement during respiration indicates that the pleura is infiltrated (Wernecke 2000).

The pleural surface is a strongly reflective structure, and when the US beam strikes it at certain angles, mirror artifacts (apparent duplication of adjacent structures) can occur. For example, intercostal muscles of the chest wall can reflect off the pleura and be projected over the lung, simulating pulmonary disease.

### 4.2 Pleural Effusions

Sonography is considered highly sensitive for confirming suspected pleural effusion on AP chest plain films and is often used for this purpose (Eibenberger et al. 1991; Kocijancic et al. 2003). We believe sonography should

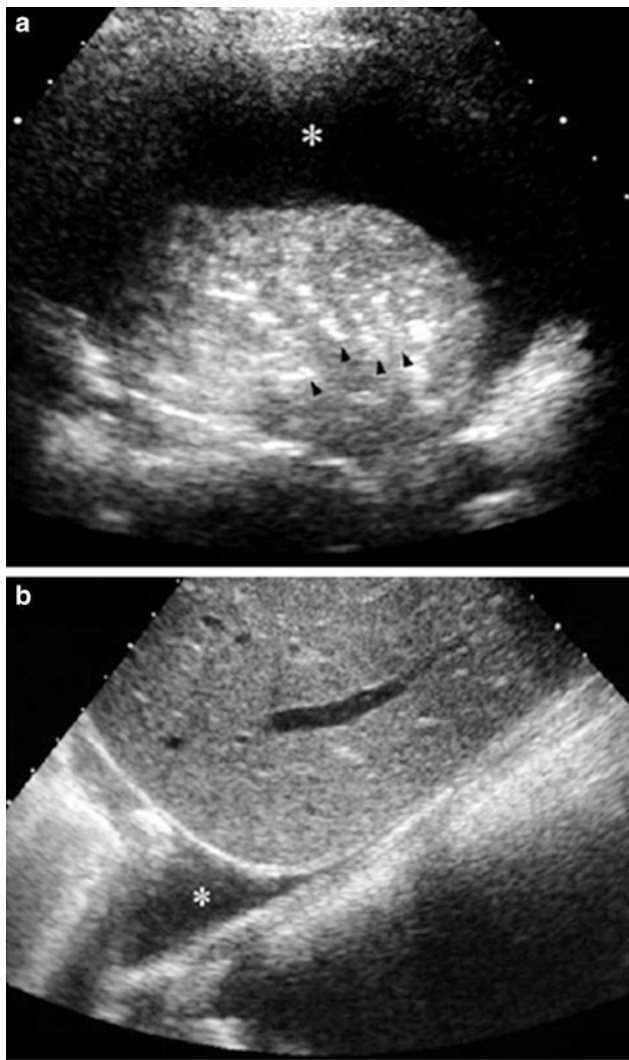


**Fig. 24** Sonographic appearance of pleural effusion **a** The pleural fluid (\*) is seen as an anechoic band between the parietal and visceral pleurae in this intercostal, transverse US scan. Note air-bronchograms (arrowheads) in the consolidated lung **b** Longitudinal sector scan through the liver shows the pleural fluid (\*) blurring the costophrenic angle

replace the routine practice of lateral decubitus plain film confirmation in these patients.

On US imaging through an intercostal approach, pleural fluid is identified as a band-like collection separating the parietal and visceral pleura surfaces. When scanning through the abdomen, the collection is seen just above the diaphragm, blurring the costophrenic angle (Fig. 24). Several sonographic signs typical of pleural fluid help to distinguish pleural effusion from ascites. The three most important are the presence of septa within the collection that move with respiration, the “crus sign,” and the “bare area sign” (Seibert et al. 1998). The crus sign, which is pathognomonic of pleural collection, results from displacement of the diaphragmatic crus away from the spine due to

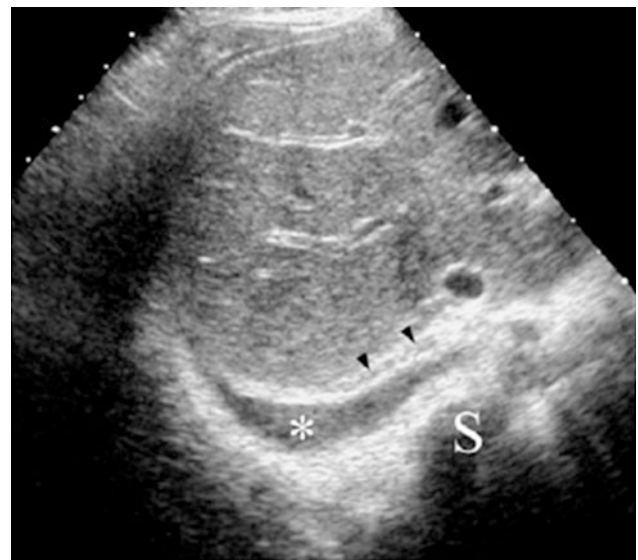


**Fig. 25** Sector transverse US scan through the liver shows useful sonographic findings that differentiate pleural effusion from ascites. Pleural effusion (\*) displaces the right diaphragmatic crus (arrowheads) away from the spine (S) and extends behind the right posterior portion of the liver (bare area)

interposition of fluid between this structure and the vertebral column (Fig. 25). The “bare area” refers to the posterior part of the right lobe of the liver, which is directly attached to the diaphragm without the covering layer of peritoneum. Peritoneal fluid cannot extend behind the right lobe at this point; thus, all fluid collections visualized behind the bare area are necessarily located in the pleural space.

One valuable advantage of sonographic study of pleural effusion is that it enables characterization of the nature of the fluid (Yang et al. 1992; Calder and Owens 2009). Simple effusions are anechoic, whereas complicated effusions present one or more of the following features: weakly echogenic debris with a swirling movement in real time (Fig. 26), mobile fibrin strands, septations (Fig. 27), and a honeycomb appearance (Fig. 28). Recognition of the septated nature of the pleural collection, information that influences patient management, is not usually provided by chest CT scans (Fig. 29) (Kurian et al. 2009).

The sonographic appearance of pleural effusion can be related to the classical division of pleural fluid into exudate or transudate, which depends on its protein content, pleural: serum LDH ratio, and other biochemical parameters. On sonography, both transudates and exudates can be anechoic, but collections presenting some of the complicated features mentioned above are always exudates.

Most exudative pleural effusions in pediatric patients are of infectious origin (Alkirinawi and Chernick 1996). These collections are known as parapneumonic effusion or empyema. The diagnosis of empyema is established when

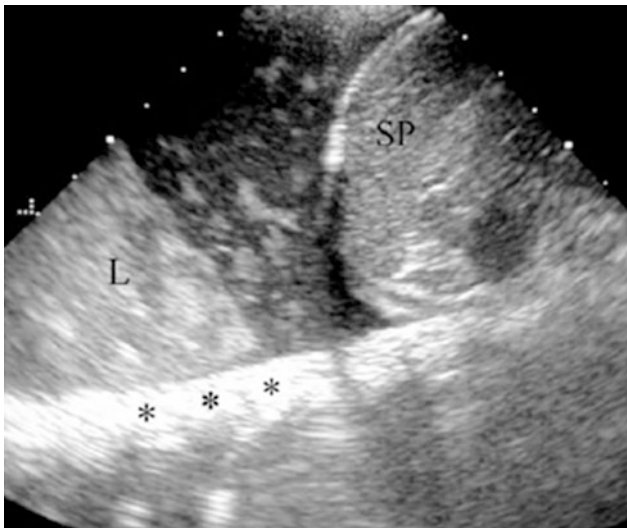


**Fig. 26** Pleural effusion with floating debris. Longitudinal transdiaphragmatic US demonstrates pleural effusion containing echogenic particles (evidencing its exudative nature) located between the spleen (SP) and the consolidated left lower lobe (L). The high echogenicity of the ribs (\*) results from good transmission of the sound beam through the consolidated lung and pleural fluid



**Fig. 27** Right sector intercostal longitudinal view demonstrates a collapsed right lower lobe (\*) surrounded by pleural effusion with multiple fibrin bands (arrows)

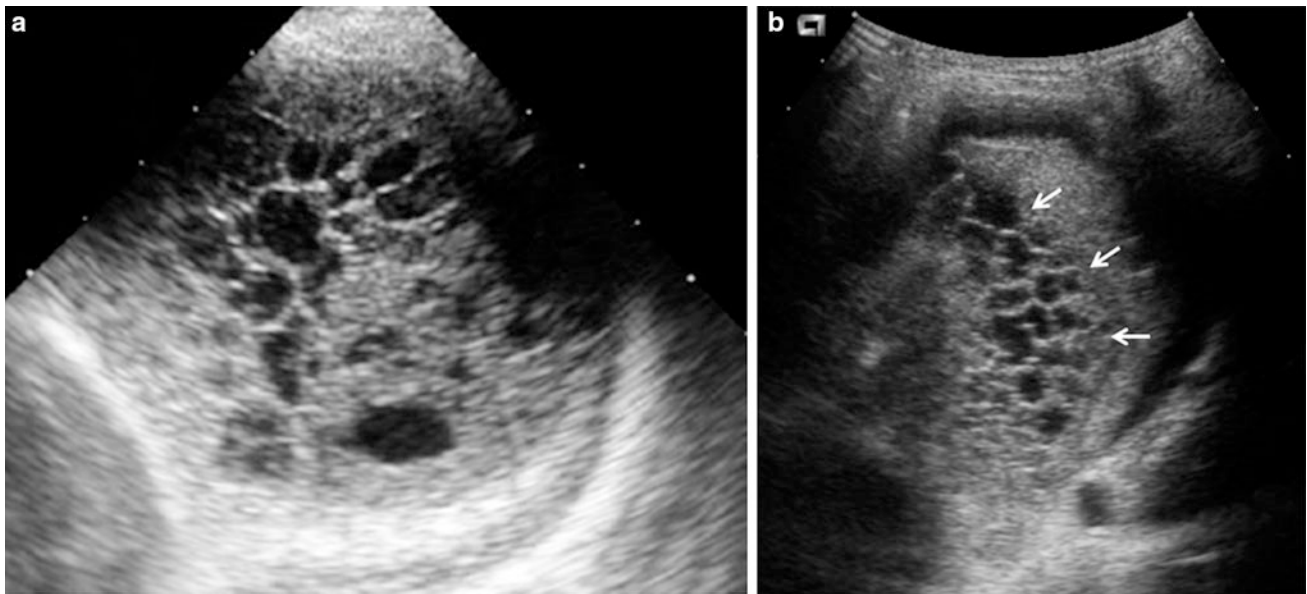


**Fig. 28** 8-year-old boy with streptococcal pneumonia. **a** In this *left* transverse intercostal scan, the pleural space is filled with profuse septations producing a honeycomb appearance. **b** Transverse US scan

in a different patient shows a similar honeycomb pattern in the pleural space along the *left* lung fissure (arrows)

pleural fluid is grossly purulent, organisms are identified on gram stain or culture, pleural fluid white blood cell count is greater than  $5 \times 10^9$  cells/L, pH is below 7.0, or glucose level is less than 40 mg/dL.

There is still a great deal of controversy around the clinical management of parapneumonic effusion and empyema. (Feola et al. 2003; Wells and Havens 2003; Hogan and Coley

2008; Calder and Owens 2009). Two main treatment approaches are used: nonoperative, in which patients are treated with antibiotics alone or combined with chest drainage and fibrinolytic instillation, and operative, consisting of pleural debridement or decortication. The goal of both these treatment methods is to evacuate infected debris and re-expand the lung, and to reduce hospital stay and morbidity.



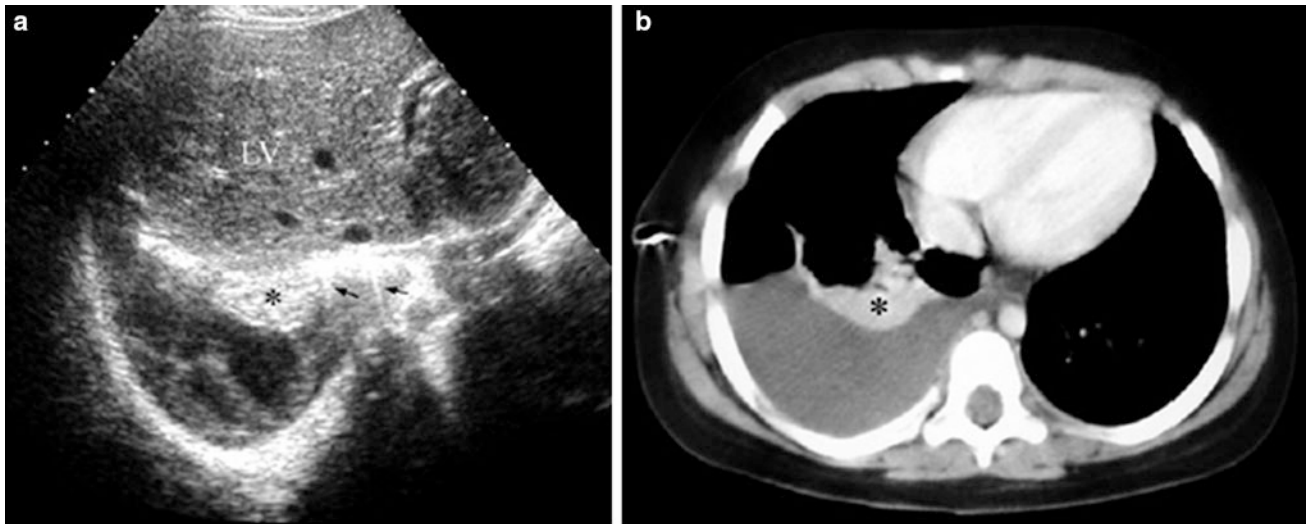


**Fig. 29** Transverse US scan (a) through the liver (LV) and enhanced CT scan (b) of a 5-year-old girl with pleural pneumonia. The compressed, atelectatic lung (\*) is clearly seen in both studies, but the

septated nature of the pleural collection is only evident on the US scan. Note comet tail artifacts in the normal aerated lung adjacent to the collapse (arrows)

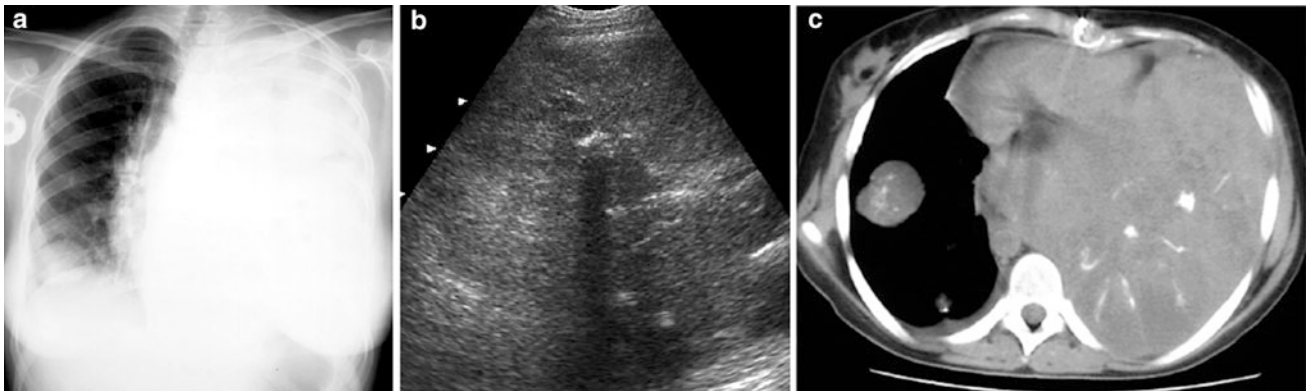


**Fig. 30** Opaque left hemithorax in a 17-year-old boy with osteogenic sarcoma of the left femur a The chest radiograph shows opaque hemithorax with increased volume, suggesting massive pleural effusion, as well as a nodule in the right lower lobe b Intercostal transverse US scan rules out pleural fluid and demonstrates that the left

hemithorax is occupied by a huge solid mass with echogenic areas and acoustic shadowing, suggestive of calcifications c Unenhanced CT demonstrates a huge partially ossified metastasis on the left and the right pulmonary nodule

The presence of a honeycomb pattern on US is not a contraindication for pleural drainage and fibrinolytic therapy (Wells and Havens 2003). Surgery should be used only in patients who do not respond to this therapy.

In our experience, small exudates can rapidly (within 24 h) increase in volume and change their sonographic appearance, despite antibiotic therapy. Thus, close sonographic monitoring of children with empyema is recommended. In addition, US is a valuable tool for localizing loculations for thoracocentesis or thoracostomy tube placement (Coley 2002). The incidence of pneumothorax is considerably reduced when pleural taps are sonographically guided, particularly in the case of small or loculated collections (Raptopoulos et al. 1991; Shankar et al. 2000).

### 4.3 Opaque Hemithorax

Opaque hemithorax on chest films is one of the main indications for chest US. In most cases, opaque hemithorax is caused by massive pleural effusion, but before pleural puncture is considered, US should be performed to confirm that the opacity is actually caused by fluid accumulation and not by a solid lesion or a mixture of both components (Fig. 30).

### 4.4 Pleural Tumors

Primary tumors originating in the pleura, such as mesothelioma, are very rare in children, and neoplastic involvement of this structure is most often due to metastasis. Metastatic



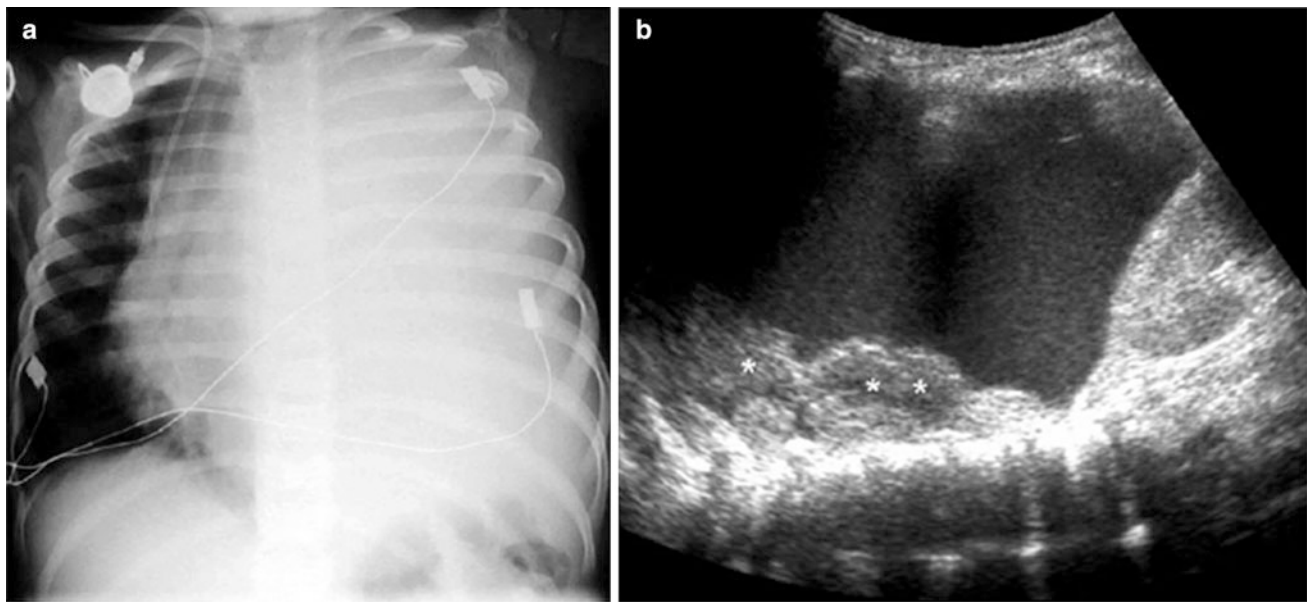


**Fig. 31** Massive pleural effusion in a patient with lymphoma **a** Chest radiograph shows opaque left hemithorax with mediastinal displacement to the right **b** Several pleural-based lymphomatous nodules (\*) are identified through the pleural fluid on US examination

disease to the pleura often causes large pleural effusions that are probably due to impaired lymphatic drainage. This secondary pleural fluid, which can be profuse in some patients, may mask the tumor mass on chest X-rays, and in these cases, ultrasound is particularly helpful (Fig. 31). Metastatic involvement of the pleura can be caused by various intrathoracic or extrathoracic tumors, such as Wilms tumor, lymphoma, neuroblastoma, and rhabdomyosarcoma (Fig. 32).

#### 4.5 Pneumothorax

Chest X-ray remains the method of choice for the diagnosis of pneumothorax, but several projections may be required to reveal its presence. In severely ill patients or trauma patients who cannot be easily moved, pneumothorax can be confirmed or ruled out by US without changing the patient's position (Barillari and Kiuru 2010; Volpicelli 2011a).

Small pockets of air in the pleural space appear as bright, echogenic lines or points. In contrast to what is seen in the normal aerated lung, the image of air in the pleural space does not show comet tail artifacts (Fig. 33). A large pneumothorax can impede visualization of visceral pleura movement, an important indirect sign of air in the pleural space. The presence of air and fluid in the pleural space (hydropneumothorax) results in an air-fluid level on US that can produce a particular movement in real time known as the “curtain sign” (Ben-Ami et al. 1993; Lichtenstein et al. 2000).

### 5 Chest Wall

The chest wall provides a structural framework that protects the intrathoracic organs. It is composed of nerve, bone, muscle, and vasculature, which can be affected by congenital malformations, infections, tumors, and metabolic diseases. Ultrasound is often the first test requested by clinicians to investigate chest wall abnormalities and disease; hence, the radiologist should be familiar with the characteristic US findings of these conditions.

Normal variants of the anterior chest wall related to the sternum, ribs, and costal cartilage may produce an asymptomatic palpable lump. These anomalies have been well described on CT studies (Donnelly and Frush 1999), but some of them, particularly those related to asymmetrical costal cartilage, can be easily recognized on US (Fig. 34).

Lymphatic and vascular malformations, and hemangiomas are common soft tissue masses occurring in the chest wall. Lymphatic malformations are usually visualized as single or multiple cystic images that may increase in size due to internal hemorrhage. In addition to establishing the diagnosis, US can be used to guide percutaneous sclerosing therapy for this condition. Vascular malformations are suspected clinically by skin discoloration (reddish or bluish, depending on the depth of the lesion), and the US findings vary according to the type (arterial, venous, or capillary) (Dubois et al. 2002). Hemangioma is seen as a well-circumscribed mass, superficial to the intercostal musculature (Fig. 35). Doppler study reveals a pattern of high systolic and



**Fig. 32** Thoracic neuroblastoma with pleural implants in a 2-year-old boy. **a** Chest X-ray shows pleural effusion, mediastinal displacement, and increased intercostal spaces and inconclusive calcifications on the right side. **b** Longitudinal US scan shows a huge mass with abundant

microcalcifications that were not conclusively identified on chest X-ray. **c** US scan at a different level depicts multiple masses of different sizes, corresponding to pleural metastasis (arrows)

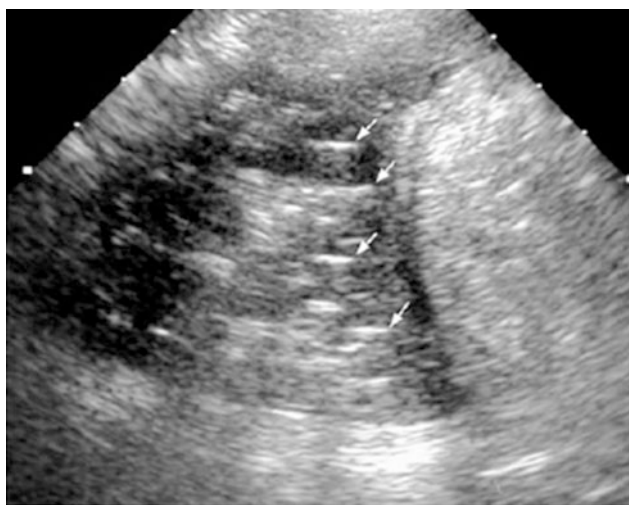


**Fig. 33** Longitudinal transdiaphragmatic US scan of the lung base in a 7-year-old girl. Air bubbles within the pleural effusion are seen as linear echogenic images without comet tail artifacts (arrows)

diastolic shifts. Lipomas and neurofibromas are other benign soft tissue masses encountered in children (Siegel 2002; Smeets et al. 1990).

Malignant chest wall lesions often arise from a rib or soft tissue, and plain films show features of an extrapleural lesion, such as widening of the intercostal space or irregularities of the rib contour. On US, the lesion is seen as an echogenic mass that may be accompanied by pleural fluid. The abnormal cortical surface of the rib or periosteal reaction may also be identified (Fig. 36). US- or CT-guided biopsy will provide the diagnosis.

## 6 Diaphragm

### 6.1 Diaphragm Paralysis

A common US study requested in clinical practice is assessment of diaphragmatic motility, which before the development of US, was performed with fluoroscopy.

Diaphragmatic paralysis is not uncommon after cardiac surgery or liver transplantation, and US evaluation of this condition can be performed at bedside in the intensive care unit. Since the paralysis is usually unilateral, the movement of the affected diaphragm can be compared to the normal contralateral one by real-time observation in the coronal plane. Use of M-mode allows spectral representation of the impaired and normal diaphragmatic movement (Epelman et al. 2005; Sanchez de Toledo et al. 2010).

## 6.2 Diaphragmatic Hernia

Congenital diaphragmatic hernia (CDH) is a developmental defect in the posterolateral region of the diaphragm that is currently detected by obstetric US. In CDH, the abdominal content herniates into the chest, which leads to varying degrees of hypoplasia of the ipsilateral lung and the contralateral lung, depending on the severity of mediastinal displacement. Morbidity and mortality are associated with the degree of pulmonary hypoplasia and pulmonary hypertension (Ruano et al. 2004, 2008; Wedegaertner et al. 2004; Büsing et al. 2008).

Prenatal assessment of the degree of pulmonary hypoplasia occurring in this condition can be performed by two-dimensional ultrasound (2-D US) using the lung-to-head ratio (LHR), an indirect measurement (Jani et al. 2007a, b), or by 3-D US with volumetry or magnetic resonance imaging (MRI) with planimetry for a direct estimation (Coakley et al. 2000; Paek et al. 2001; Rypens et al. 2001; Tanigaki et al. 2004; Williams et al. 2004; Osada et al. 2004; Ward et al. 2006; Peralta et al. 2006; Cannie et al. 2006, 2008a, b, c; Büsing et al. 2008; Jani et al. 2007a, b; Mong et al. 2008; Killian et al. 2009).

A major advantage of MRI is its capability to identify the ipsilateral lung remnant (apical cap), which is difficult to identify on US, even 3D US. Consequently, the apical cap is not included in the LHR calculation (Peralta et al. 2006).

A practical method for identifying the ipsilateral apical cap by 2D-US with color and power Doppler in fetuses with unilateral diaphragmatic hernia has been reported (Castellote et al. 2011) (Fig. 37), but further investigation is needed before the apical cap determined by this method can be included in the LHR calculation.

Fetuses with severe pulmonary hypoplasia (LHR 0.6–1.0) can benefit from fetal endoscopic tracheal occlusion (FETO). In this procedure, a balloon is inserted into the fetal trachea to prevent egression of lung fluid, thereby allowing the lungs to expand and mature (Fig. 38). The development of this treatment was based on the observation that increased bilateral lung size occurs in fetuses with congenital high airway obstruction syndrome (CHAOS) (Fig. 39). Postnatal tracheal (Mchugh et al. 2010) and

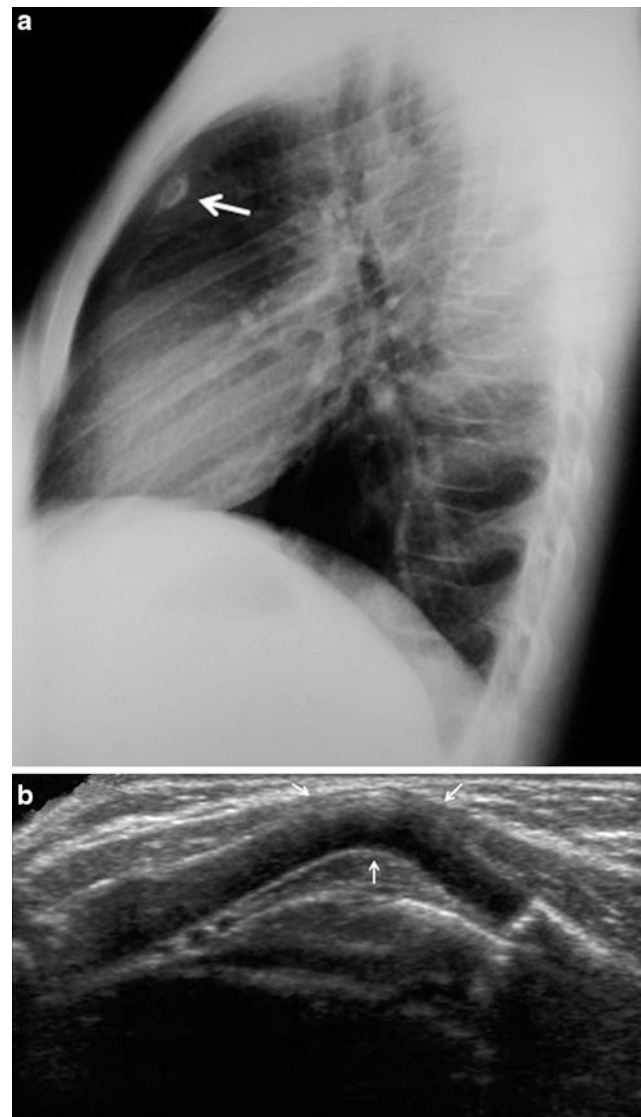


**Fig. 34** Fourteen-year-old girl with a palpable lump in the left upper quadrant of the chest. **a** Lateral plain film shows a small nodular image with a dense peripheral ring (*arrow*) behind the sternum. **b** Transverse US view confirms sharp angulation of a rib cartilage as the cause of the lump

bronchial (Enriquez et al. 2012) dilatation following FETO have been reported, but no related clinical repercussions have been described to date (Fig. 40).

Diaphragmatic hernia can also occur following trauma. In these cases, the hernia can present a misleading aspect on plain films and simulate a pulmonary consolidation. This is particularly common when the hernia is located on the right side, and the liver is the main herniated component. The echogenicity of the intrathoracic liver may be different from that of the intra-abdominal liver due to edema affecting the intrathoracic portion, which is constricted by the (usually small) orifice of the ruptured diaphragm, giving rise to the US “collar sign” (Fig. 41). (Aoki et al. 1998).



**Fig. 35** Chest wall hemangioma in a 1-month-old infant. **a** Gray-scale US demonstrates a solid elliptical mass superficial to the intercostal musculature (*arrow*). **b** On color Doppler, the mass is seen to have prominent vascularization

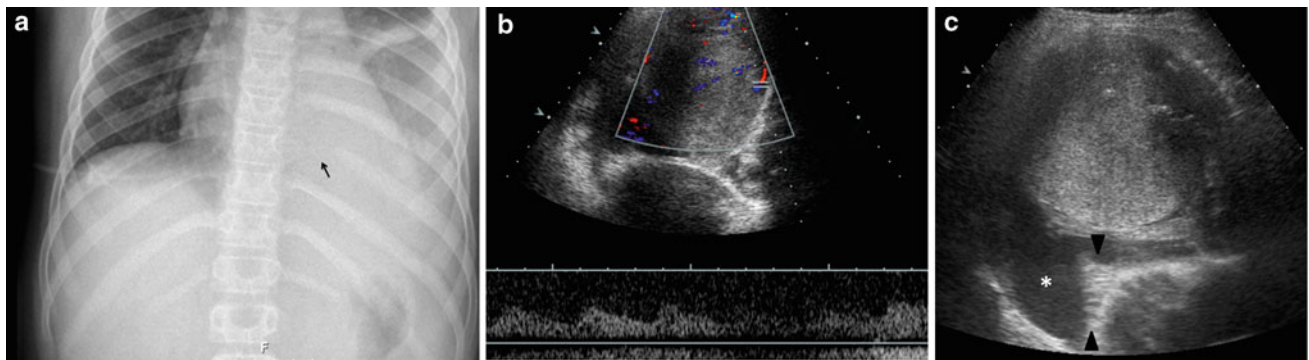
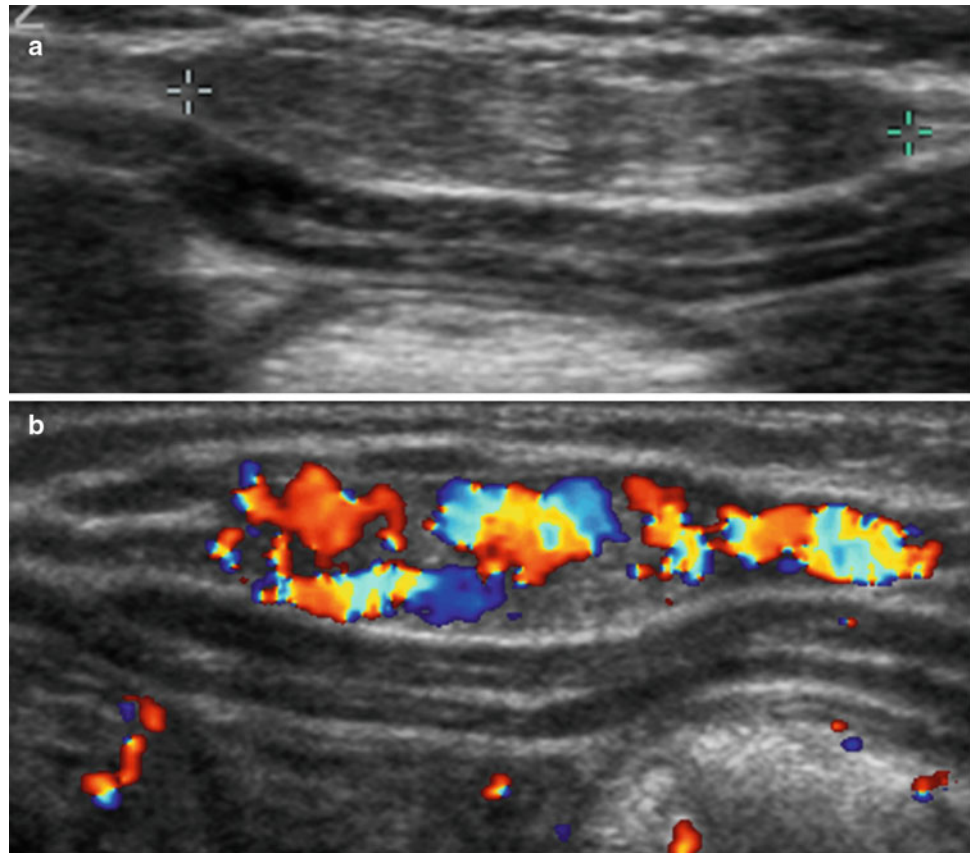


**Fig. 36** Fourteen-year-old girl with Ewing's sarcoma. **a** Chest X-ray shows opacity of the base of the *left hemithorax* and a lytic lesion of the posterior arch of the 9th *left rib* (*arrow*), a plain film finding indicative of an extrapleural mass. **b** Transverse US scan confirms the presence of a solid mass with a biphasic vascularization pattern

characteristic of systemic supply. **c** Transverse US view at a different level shows accompanying pleural fluid (*asterisk*) and parallel echogenic lines (*arrowheads*) adjacent to the rib indicating a sunbeam periosteal reaction

## 7 Mediastinum

### 7.1 Examination Technique

Sonographic study of the mediastinum requires a meticulous technique and extensive knowledge of the mediastinal anatomy. We recommend small sector or convex multifrequency probes. High-frequency linear transducers are

particularly useful in newborns and for studying superficially located lesions. It is advisable to adjust the depth to the region of interest, and reduce the number of foci and lateral field of vision to increase the frame rate. It is useful to include a large vessel or cardiac chamber in the field of study to establish anatomic relationships and analyze the echogenicity of the lesion to determine whether it is cystic or solid.



**Fig. 37** 23-week gestational age fetus with *left* diaphragmatic hernia. **a** On the T2-weighted coronal image, the ipsilateral lung cap (*asterisk*) and corresponding bronchus (*arrowhead*) are well depicted. L = liver, S = stomach **b** The ipsilateral cap was identified by following the course of the *left* pulmonary artery with power Doppler

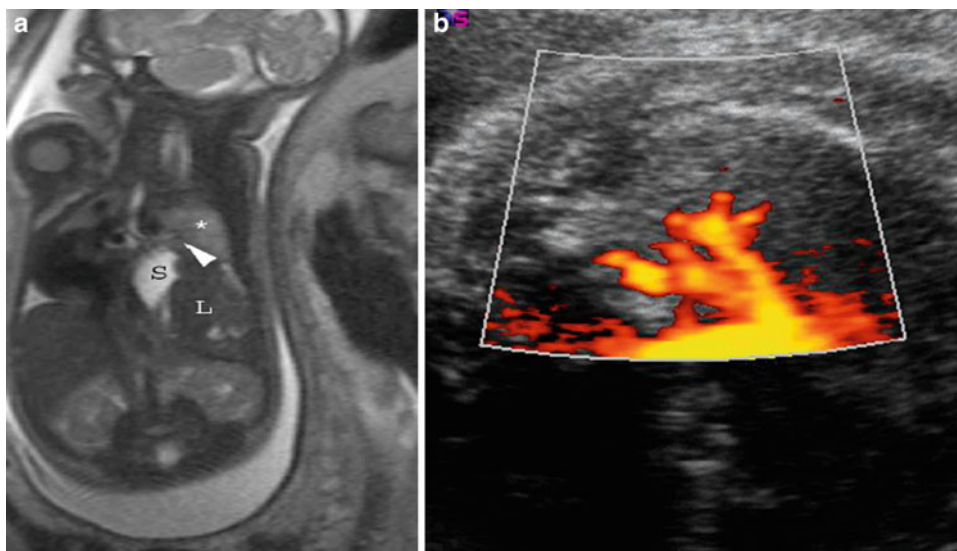


**Fig. 38** *Left* diaphragmatic hernia treated prenatally. **a** Prenatal US shows a cystic image “b” corresponding to the intratracheal balloon. Left L = *left lung*. Right L = *right lung*. **b** Prenatal MRI before balloon placement shows the *right lung* and no apical cap on the *left* side. **c** Prenatal MRI following balloon insertion clearly shows a significant increased size of the *right lung* as well as the *left* apical cap (*arrow*)

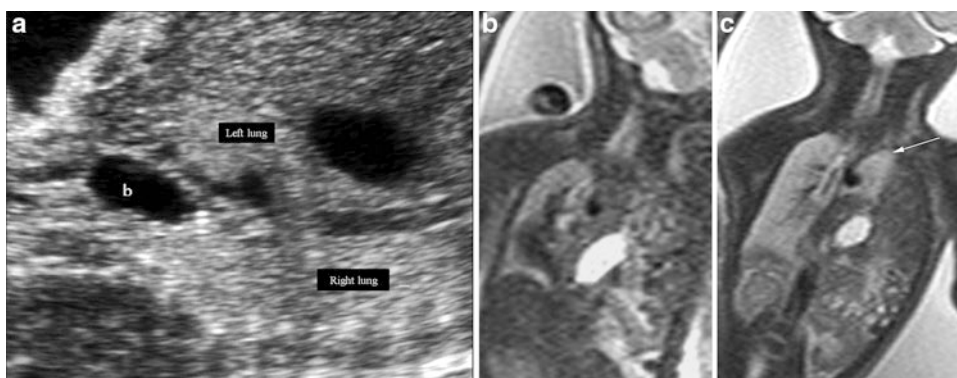


**Fig. 39** Laryngeal atresia in a 21-week gestational age fetus. **a** Coronal view of the fetal chest shows bilateral pulmonary overdistention with inversion of the diaphragms and increased echogenicity. Secretion-filled trachea (\*) and main bronchi (*arrows*) can be seen **b** Longitudinal view of the upper airway showing an echogenic area (*arrows*) corresponding to intrinsic laryngeal atresia (CHAOS syndrome). Courtesy of Dr. Elena Carreras, Ph. D. Autonomus University of Barcelona

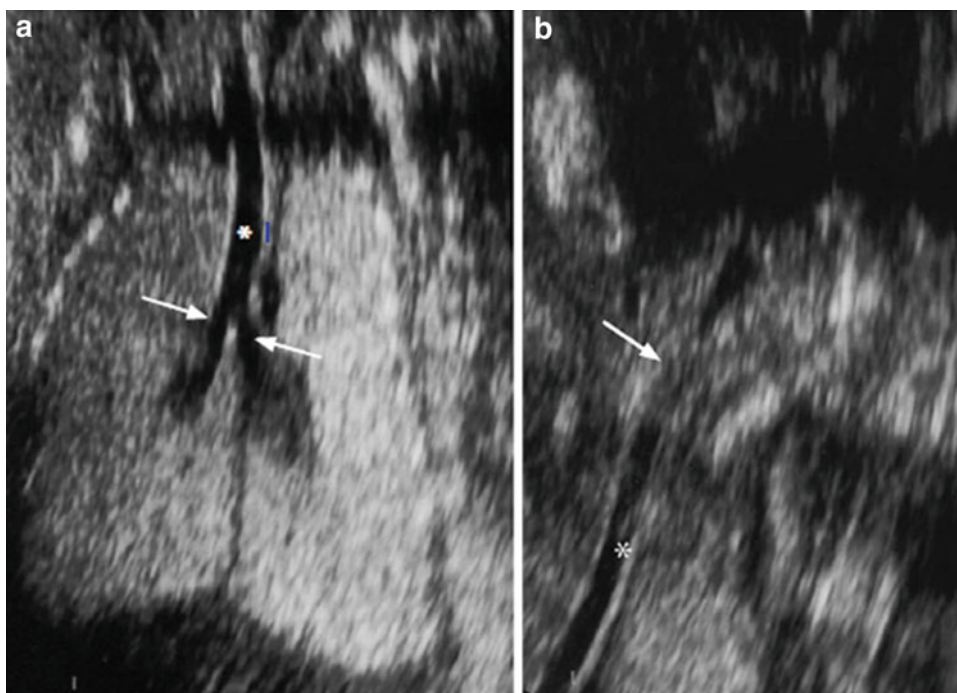


**Fig. 40** **a** Chest X-ray of a 5-year-old boy with CDH treated by prenatal tracheal occlusion shows marked dilatation of the distal two-thirds of the trachea. **b** Coronal MinIP CT imaging confirming tracheal and bilateral main bronchus dilatation

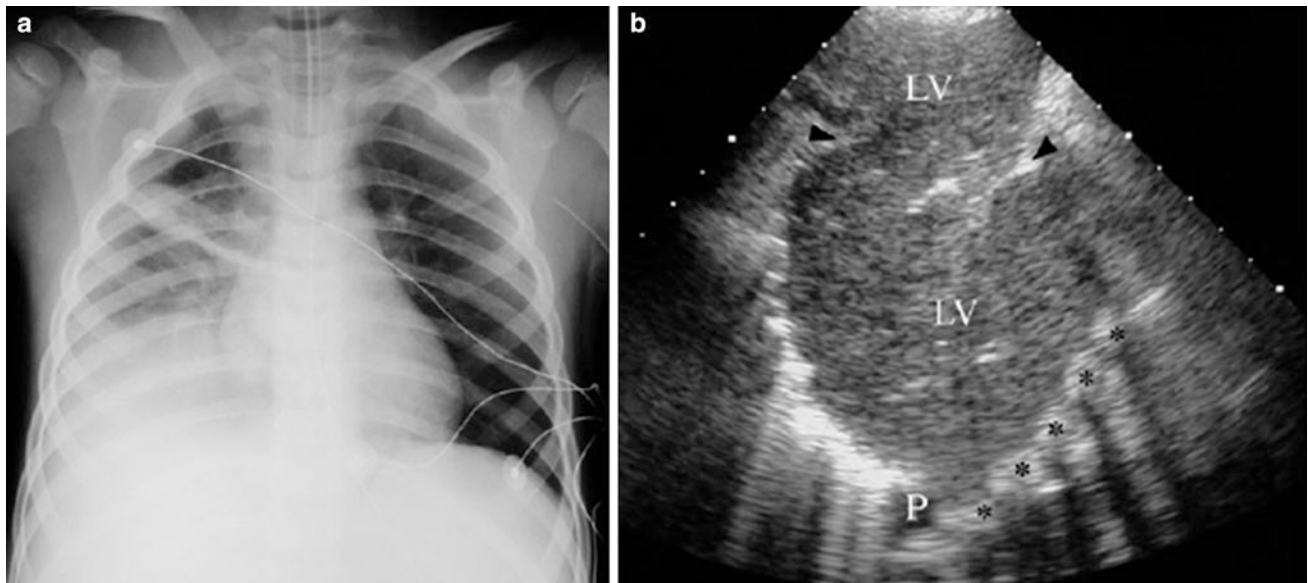
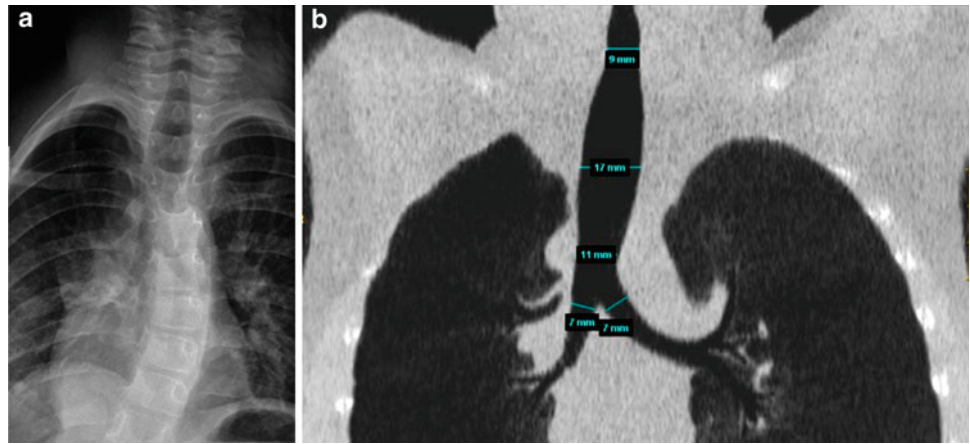


**Fig. 41** Diaphragmatic hernia in a 5-year-old girl with a motor vehicle injury **a** Chest Radiograph shows opacification of the right lung base and linear atelectasis in the right upper lobe **b** Longitudinal view of the right hemithorax reveals that the opacity corresponds to

herniation of the liver (LV) through a diaphragmatic rupture (arrow-head) (P pleural effusion). The chest wall is delineated by the ribs (\*)

Several acoustic windows are employed, such as the suprasternal, supraclavicular, parasternal, subxiphoid, and subcostal approaches; the most frequently used are the suprasternal and left parasternal. When examining through the suprasternal approach, the patient is placed in supine decubitus position with a cushion under the back and the neck slightly extended. The transducer is placed above the sternal manubrium and tilted caudally to obtain the coronal view, and is displaced laterally to encounter the space between the trachea and sternocleidomastoid muscle to obtain the sagittal view. For the parasternal approaches, a right or left lateral decubitus position (examined side down) is recommended to displace the mediastinum downwards and increase the acoustic window (Fig. 42).

In young children, the thymus can be used as an acoustic window to study the subcarinal area, whereas in older children, access is through the cardiac chambers. A paravertebral approach is recommended to study the posterior mediastinum.

The standard US slices differ from those obtained with CT. The majority are acquired in oblique, coronal, or sagittal planes and therefore, the same slice may show structures corresponding to more than one anatomic region.

## 7.2 Normal US Appearance, Artifacts and Pitfalls

Sonographic study of the mediastinum requires a meticulous technique and extensive knowledge of the mediastinal anatomy. We recommend the use of five standard sonographic

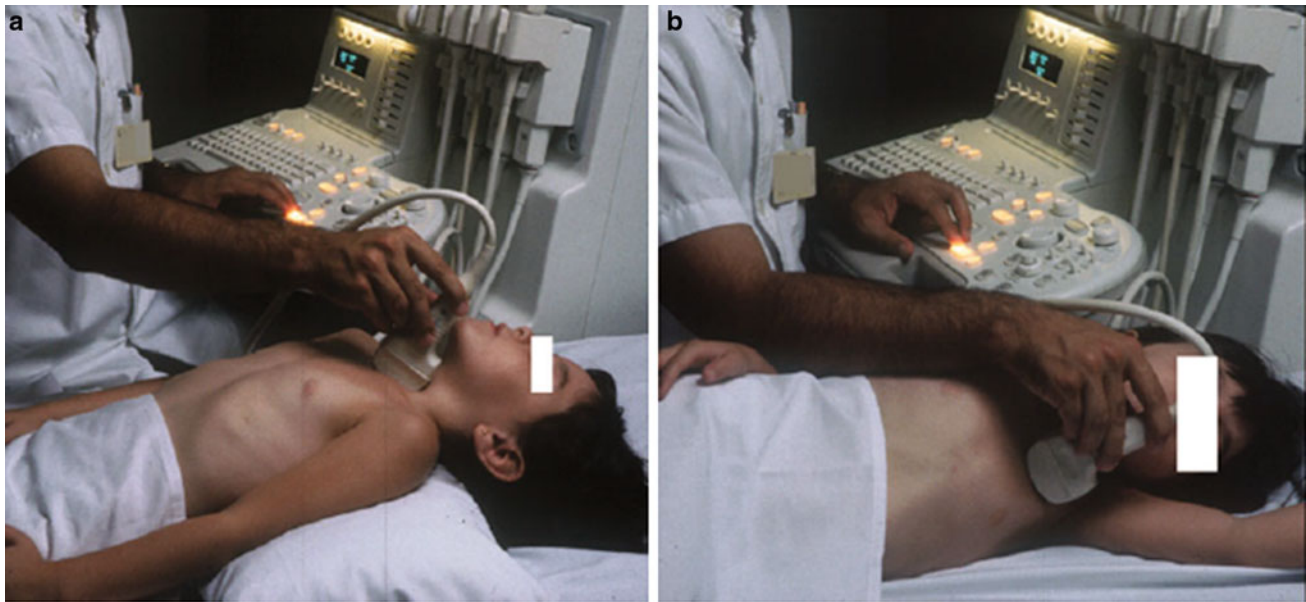


**Fig. 42** Patient positioning for US access to the mediastinum using the suprasternal (a) and left parasternal (b) approaches

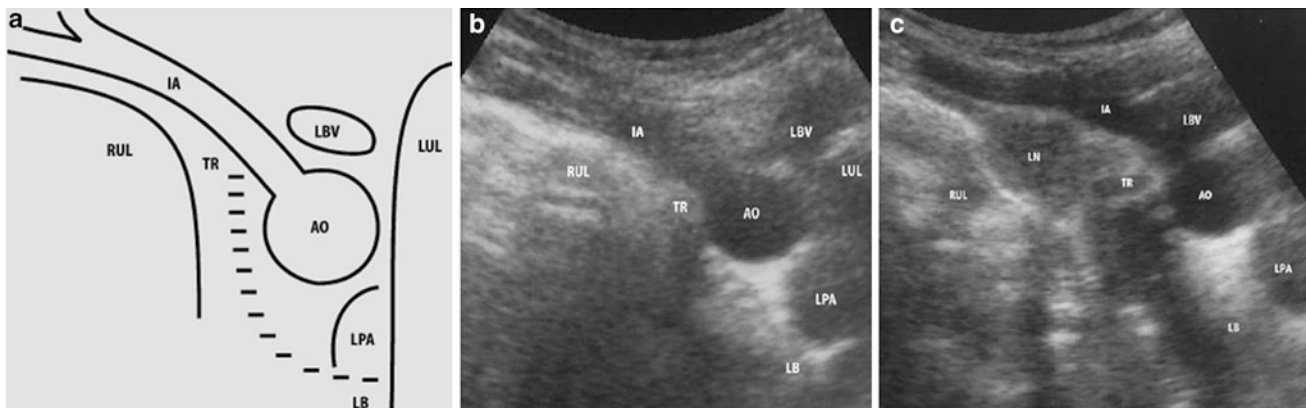


**Fig. 43** Suprasternal, oblique coronal section **a** Diagram **b** Normal US scan. Note echogenic line of the pleuralung interface where the right upper lobe abuts the trachea **c** In a patient with lymphadenopathy, the echogenic line is bowed and displaced by the mass (IA innominate

artery; *LBV* left brachiocephalic vein; *AO* aorta; *TR* trachea; *LB* left bronchus; *RUL* right upper lobe; *LUL* left upper lobe; *LPA* left pulmonary artery; *LN* lymph node)

slices (three obtained with the suprasternal approach and two with the left parasternal) to visualize the complete anterior and middle regions of the mediastinum. We stress that these standard US slices differ from those obtained with CT. The majority is obtained in oblique, coronal or sagittal planes and therefore, the same slice may show structures corresponding to more than one anatomic region.

- Oblique coronal view through the suprasternal approach. This section is used to visualize the paratracheal region, located between the right upper pulmonary lobe and the trachea. It is also useful for studying the aortopulmonary region, which is seen in this view as an echogenic triangular image. The probe is placed almost perpendicular to, and

slightly compressing, the right sternocleidomastoid muscle. The anatomic reference for this region is the innominate artery and the scan should include the pleural surface of the right upper lobe, the trachea and the upper margin of the left bronchus. The paratracheal region is a virtual space and is considered normal when the pleural surface of the upper lobe abuts the trachea. Pathology in this region is recognized by a separation of these two structures (Fig. 43).

- Coronal view through the suprasternal approach. This scan is not used to study a specific mediastinal region, but is very useful for visualizing the vessels, particularly the superior vena cava. The view should include the right pulmonary artery and its bifurcation, located within the



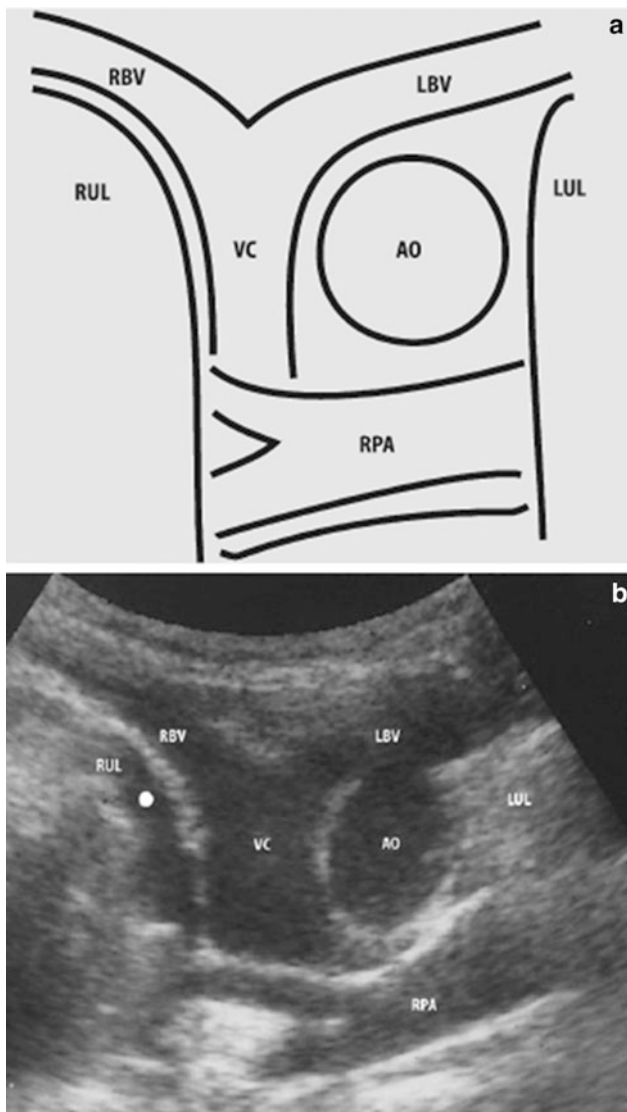


**Fig. 44** Suprasternal coronal section **a** Diagram **b** Normal US scan. (RBV right brachiocephalic vein; LBV left brachiocephalic vein; AO aorta; RUL right upper lobe; LUL left upper lobe; RPA right pulmonary artery; VC vena cava). The dot indicates a mirror artifact of the vessels adjacent to the pleura, mimicking pleural effusion

mediastinum (Fig. 44). It is particularly helpful to confirm or rule out superior vena cava thrombosis in patients with a central venous catheter.

- Oblique parasagittal view through the suprasternal approach. This view is used to visualize the aortopulmonary region, which has a characteristic ultrasound appearance and should be identified in all patients submitted to mediastinal exams. The probe is placed above the sternal manubrium between the trachea and left sternocleidomastoid muscle. Due to the presence of mediastinal fat at this level, the aortopulmonary region is seen as a highly echogenic, half-moon-shaped image. The anatomic reference for this region is the aortic arch and

the section should also include the origins of the left carotid and subclavian arteries (Fig. 45).

- Axial view through the left parasternal approach. This section is used to study the subcarinal and prevascular regions and is similar to the CT slices obtained for this area. The transducer is placed at the second intercostal space. The anatomic reference for this view is the pulmonary artery bifurcation (Fig. 46).
- Parasagittal view through the left parasternal approach. Also used to study the subcarinal and prevascular regions, the references for this section are the ascending aorta, the trachea, and the esophagus (Fig. 47). It is important to identify the esophagus by making the patient swallow saliva or water. For the two parasternal approaches, the patients should be placed in a left decubitus position to increase the size of the anatomic acoustic window.
- A number of artifacts are generated during mediastinal sonography. The most common are “mirror artifacts” consisting in duplicated images of vessels or normal and abnormal structures adjacent to the mediastinal pleura. Vascular “duplication” in this location can simulate a pleural fluid collection. The tracheal and bronchial cartilage can interrupt the air column in these structures and produce multiple parallel echogenic images with a step-ladder appearance that we refer to as “stair artifact” (Fig. 48).
- Some normal anatomic structures, such as the pericardial recesses and the esophagus can have a misleading sonographic appearance and simulate pathology. For example, the superior pericardial recess can mimic adenopathy in the aortopulmonary region (Fig. 49). The location, triangular shape, changes in size with the heartbeat, and anechoic appearance are the clues that differentiate the pericardial recess from lymph nodes.
- The normal esophagus may simulate a subcarinal solid mass, but can be properly identified by asking the patient to swallow saliva or fluid during the examination. The saliva is seen as an echogenic image passing through the apparently solid structure, thereby ruling out a mediastinal mass (Fig. 50). In patients with gastro-esophageal reflux, the passage of gastric content to the esophagus can be visualized in real time.

### 7.3 Indications for Mediastinal US

Scanning of children with mediastinal widening, evaluation of vascular anomalies and the search for lymph nodes are the main indications for mediastinal US in children. It can also be used to evaluate oesophageal atresia and tracheo-oesophageal fistula (Gassner and Geley 2005), to assess possible complications in patients with indwelling catheters (Maruyama and Koizumi 2006) and to perform mediastinal biopsies (Annessi et al. 2003; Gorguner et al. 2003).



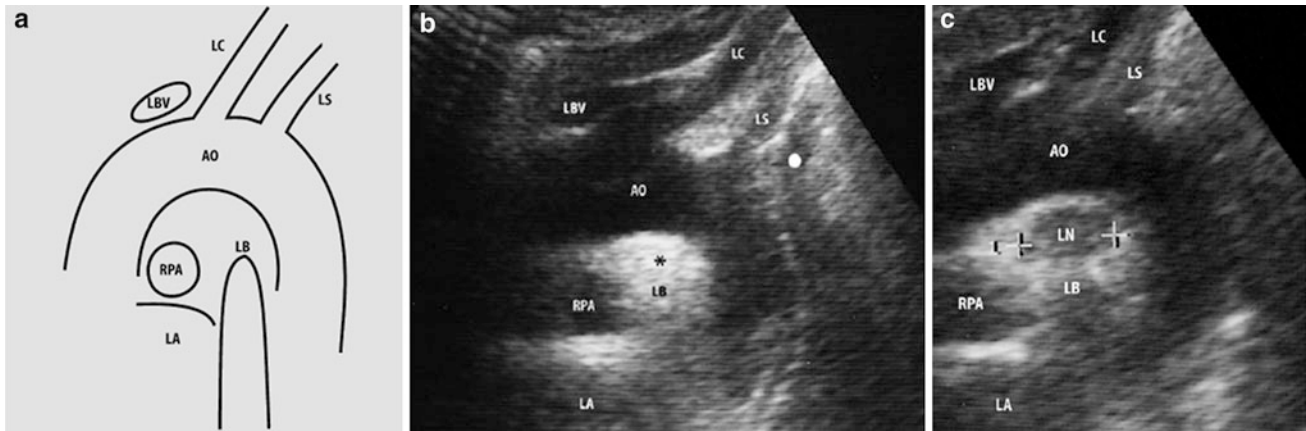


**Fig. 45** Suprasternal oblique parasagittal section **a** Diagram **b** Normal US scan. Note the normal hyperechoic appearance of the aortopulmonary region (\*) **c** US scan in a patient with lymphadenopathy in this region. (LBV left brachiocephalic vein; AO aorta; RPA right

pulmonary artery; LC left carotid artery; LS left subclavian artery; LA left atrium; LB left bronchus; LN lymph node. The dot indicates a mirror artifact of the vessel

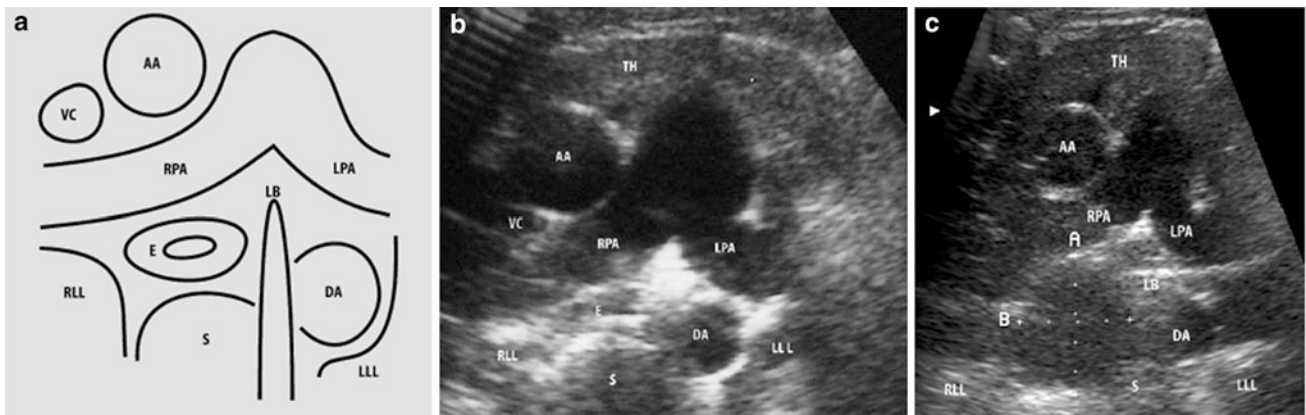


**Fig. 46** Left parasternal axial section **a** Diagram **b** Normal US scan **c** US scan in a patient with lymphadenopathy (AB calipers) in the subcarinal space. (TH thymus; AA ascending aorta; DA descending

aorta; E esophagus; RPA right pulmonary artery; LPA left pulmonary artery; VC vena cava; LB left bronchus; RLL right lower lobe; LLL left lower lobe; S spine)

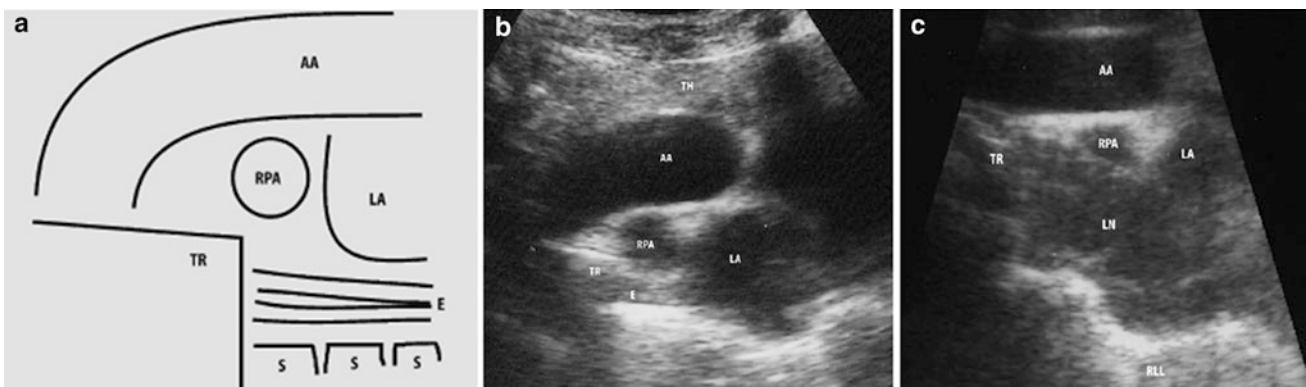


**Fig. 47** Left parasternal parasagittal section **a** Diagram **b** Normal US scan **c** US scan in a patient with lymphadenopathy in the subcarinal space compressing the right pulmonary artery (AA ascending aorta;

RPA right pulmonary artery; LA left atrium; S spine; TR trachea; TH thymus; E esophagus; LN lymph node)



**Fig. 48** Suprasternal oblique coronal view shows a staircase artifact caused by tracheal (*TR*) and left bronchial (*LB*) cartilage. *Arrow head* shows superior sinus of the pericardium (*RUL* right upper lobe; *LBV* left brachiocephalic vein; *LPA* left pulmonary artery)

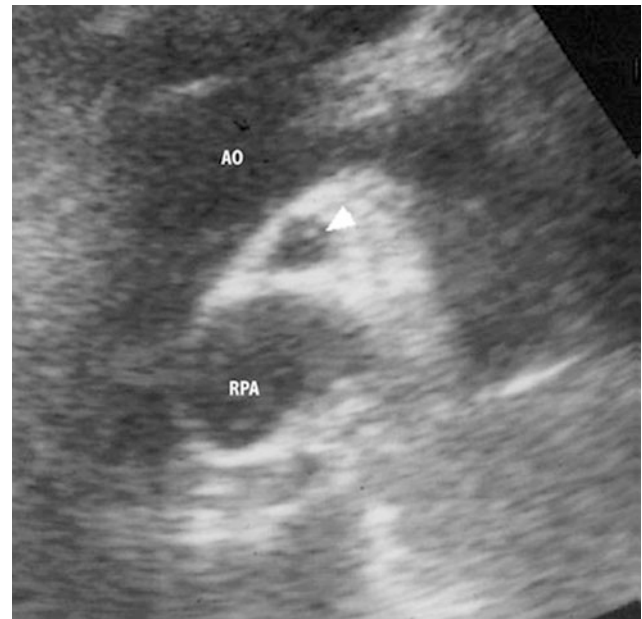


**Fig. 49** Suprasternal oblique parasagittal section shows the superior pericardial recess (*arrowhead*) simulating adenopathy in the aortopulmonary region. Its typical triangular shape and anechoic echotexture permit proper identification. Compare with Fig. 25c (*AO* aorta; *RPA* right pulmonary artery; *LA* left atrium)

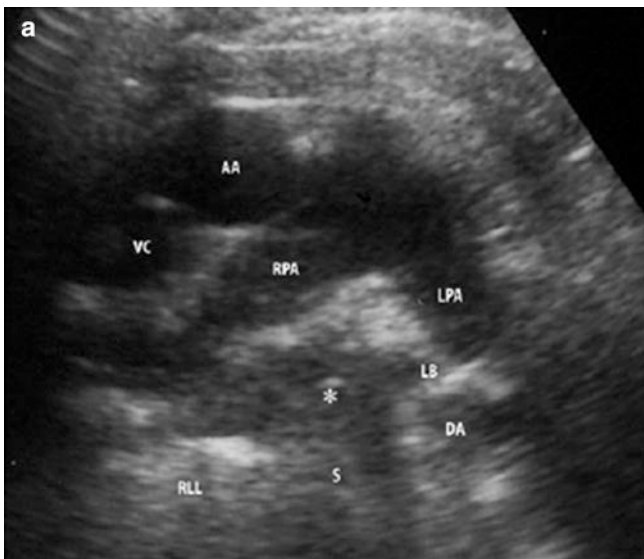
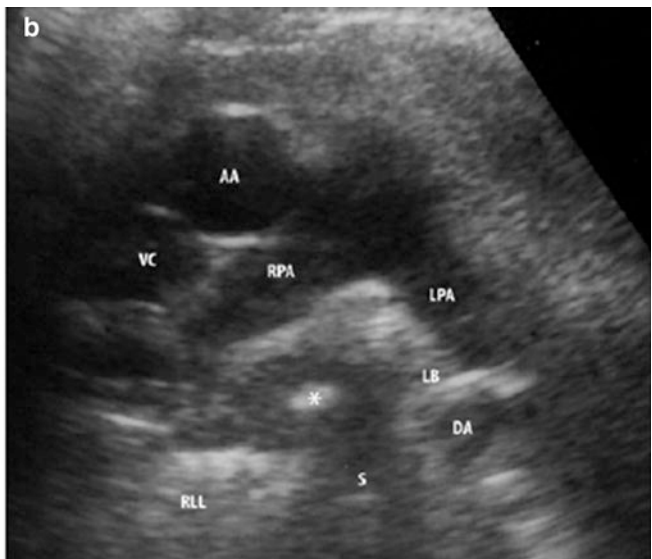


**Fig. 50 a** Esophagus (\*) simulates a mass in the subcarinal region in this axial view through the left parasternal approach **b** After the patient swallows, an echogenic image (\*) corresponding to saliva identifies



the esophagus. (*AA* ascending aorta; *DA* descending aorta; *RPA* right pulmonary artery; *LPA* left pulmonary artery; *LB* left bronchus; *RLL* right lower lobe; *S* spine; *VC* vena cava)

## 7.4 Mediastinal Abnormalities

For illustrative purposes, we have organized mediastinal pathologies according to the region (anterior, middle, and posterior) where they most frequently occur (Fig. 51) (Table 1).

### 7.4.1 Anterior Mediastinum

Anterior mediastinum pathology in children is commonly related to the thymus; thus, knowledge of the normal US appearance of this organ is essential to recognize lesions in this compartment. On chest X-rays, the thymus is identified by characteristic radiological signs, such as the “sail” and “thymic wave” signs. However, it often has a misleading

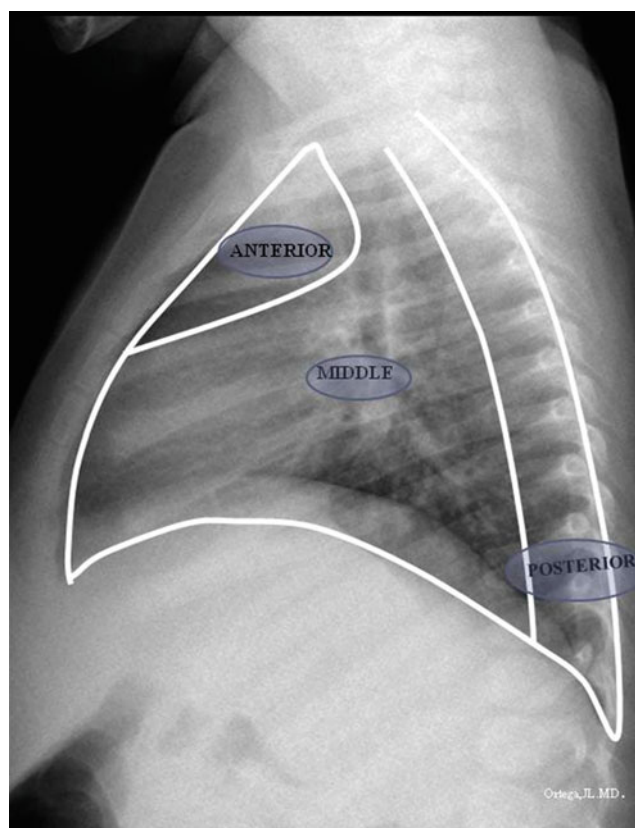


**Fig. 51** Lateral chest X-ray shows the three mediastinal compartments. *Anterior* from the sternum to the pericardium. *Middle* from the anterior margin of the pericardium up to 1 cm posterior to the anterior border of the vertebral bodies. *Posterior* from 1 cm posterior to the anterior border of the vertebral bodies to the paravertebral gutters

**Table 1** Most Common Mediastinal Lesions in Children

Anterior	Middle	Posterior
Teratoma	Bronchogenic Cyst	Neuroblastoma
Thymic Cyst	Esophageal Duplication Cyst	Ganglioneuroblastoma
Thymoma	Neuroenteric Cyst	Ganglioneuroma
Thymolipoma	Vascular Lesions:	Neurofibroma
Lipoma	Double Aortic Arch	Hydatid Cyst
Lymphatic Malformation	Pulmonary Artery Sling	
	Duplicated Superior Vena Cava	

appearance on plain films and simulates a mediastinal mass. In this situation, US can clarify the doubtful findings and avoid the practice of more invasive explorations.

On US, the normal thymus has a bilobulated appearance and a homogenous echotexture with some echogenic strands (Kim et al. 2000). It is hypoechoic relative to the thyroid gland and has a smooth, well-defined margin due to its fibrous capsule. It is a soft organ that does not compress

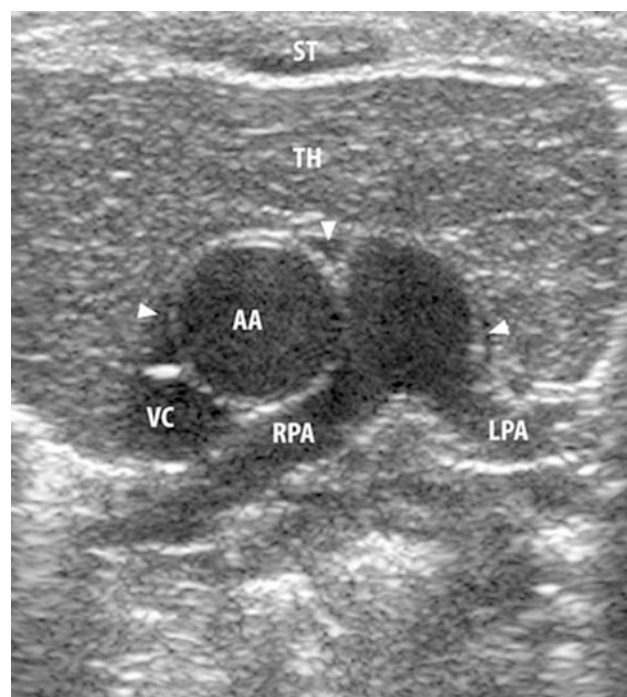


**Fig. 52** Transverse view of normal thymus (TH) in a 4-year-old boy. Vascular structures are not compressed by the gland, which has a rounded configuration (AA ascending aorta; VC vena cava; RPA right pulmonary artery; LPA left pulmonary artery; ST sternum; arrowheads, superior pericardial recesses)

neighboring vascular structures, a characteristic that can help the radiologist to differentiate it from mediastinal masses (Fig. 52). The normal thymus can vary considerably in position, extension, size, and configuration. In small children, the organ can extend from the cervical region to the diaphragm (Swischuk and John 1996; Fitoz et al. 2001). During respiration and particularly when the child is crying, the thymus can displace to above the sternal manubrium and simulate a cervical mass (Fig. 53).

One important characteristic of the thymus is its tendency to vary in size in response to acute stress. Rapid and severe involution of the gland, a process mediated by endogenous corticosteroid production, occurs in numerous clinical situations (e.g., burns, chemotherapy, or severe disease). Weeks to months after cessation of the stress, the thymus can regenerate and even enlarge by “rebound growth” (Fig. 54). This enlargement of the thymus affects both the cortex and medulla and must be differentiated from thymic growth associated with autoimmune diseases. Thymic growth in these cases is known as lymphoid follicular hyperplasia and affects only the medulla. It is a frequent finding in children with HIV infection.

Thymic aplasia and hypoplasia are two congenital anomalies generally associated with immunologic deficiency syndromes, such as DiGeorge’s syndrome, Nezelof’s



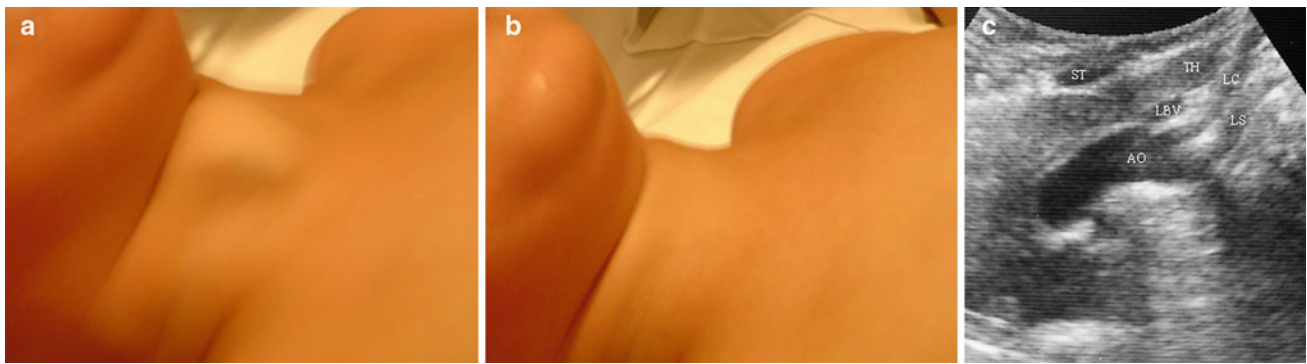


**Fig. 53** Clinical photo of a 2-month-old boy showing a mass extending above the sternal manubrium when the patient was crying (a). The mass disappeared when the child was at rest (b). (c) Suprasternal sagittal US

view shows cervical extension of the thymus (TH) which is seen anterior to the left carotid (LC) and left subclavian (LS) arteries (AO aorta; ST sternum; LBV left brachiocephalic vein)

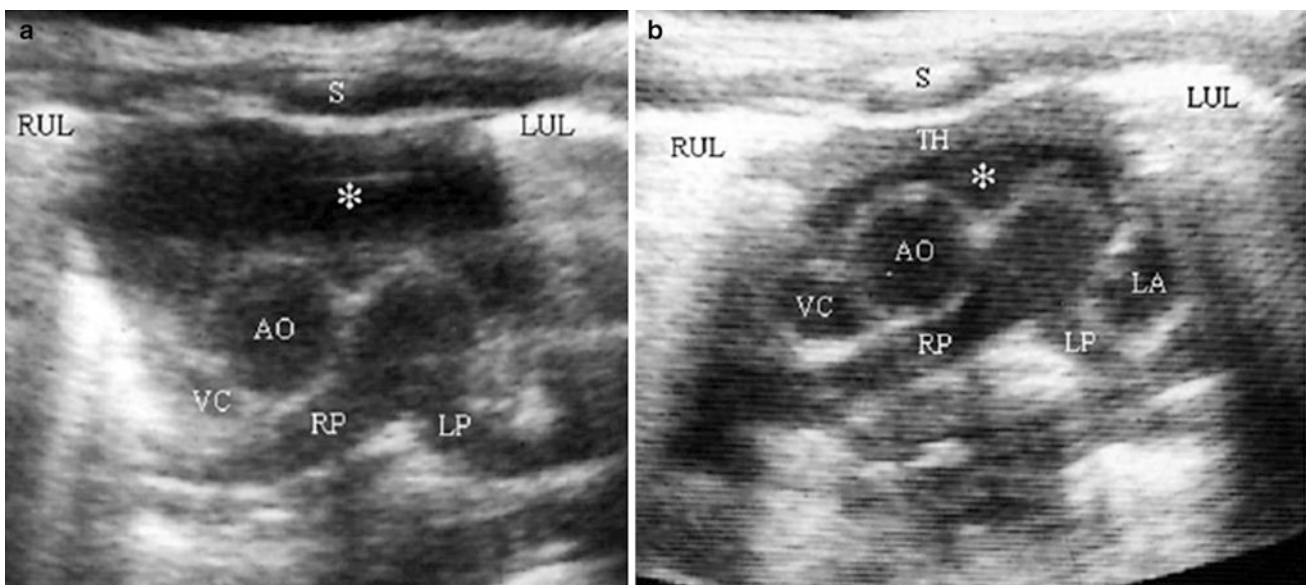


**Fig. 54** Premature newborn boy with severe respiratory distress a On suprasternal axial US, the thymus is not visualized and the anterior space is filled with pericardial fluid (thymic involution) b After 12 days the boy had improved clinically and the thymus is clearly seen on

US (thymic rebound) (TH thymus; AO ascending aorta; RP right pulmonary artery; LA left atrium; VC vena cava; asterisk, pericardial fluid; LUL left upper lobe; RUL right upper lobe; S sternum; LP left pulmonary artery)

disease, and ataxia telangiectasia. Other congenital alterations of the thymus include position anomalies, which are classified as ectopic or aberrant (Koumanidou et al. 1998). Ectopic thymus refers to thymic tissue located in any position except the normal pathway of embryologic descent of the gland (Fitoz et al. 2001). It is occasionally a life-threatening condition due to airway compression. US can detect this anomaly, but is not helpful in patients with ectopic tissue located behind the trachea or in the posterior mediastinum. Aberrant thymus refers to thymic tissue located anywhere along the normal pathway of embryologic descent of the gland. This condition is predominantly asymptomatic and presents as a cervical or suprasternal mass, which can be easily characterized by US. Aberrant thymus should be

suspected when the mass presents the same echogenicity as normal thymus (Song et al. 2011) (Fig. 55).

With the use of sonography, thymic cysts are now increasingly detected. They are seen as well-defined uni- or multilocular anechoic lesions, which can have peripheral calcifications (Rudick and Wood 1980). Multilocular thymic cysts are seen in approximately 1 % of pediatric patients with HIV infection (Avila et al. 1996) and, since this entity does not require specific treatment, US is recommended for serial follow-up (Fig. 56).

Primary tumors of the thymus (thymolipoma and thymoma) are exceedingly rare in children. Most thymic tumors in the pediatric age group are secondary to lymphoma or leukemia. The affected gland enlarges and appears as a



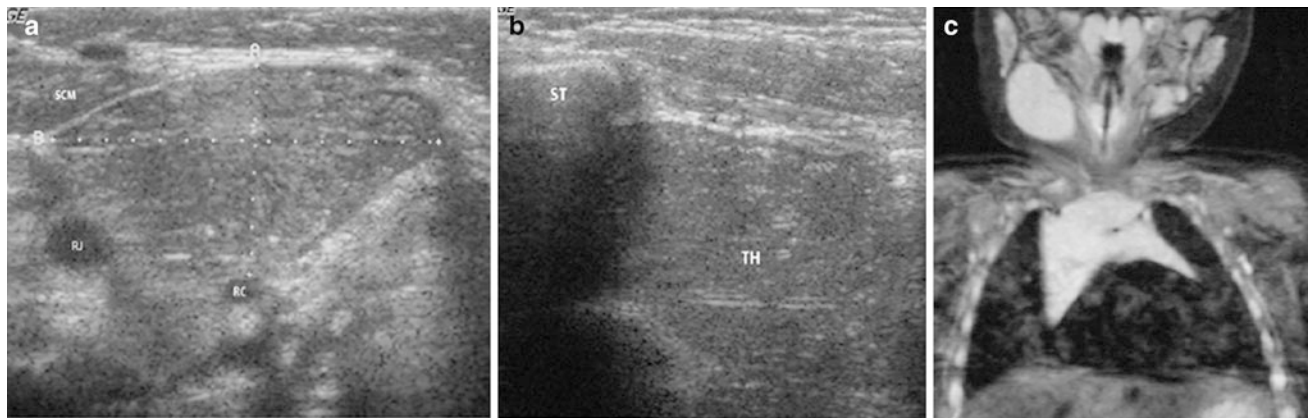


**Fig. 55** Aberrant thymus in a 1-month-old boy with right cervical mass **a** US axial view shows the mass (between calipers AB) located front of the right jugular vein (RJ) and right carotid artery (RC) and medial to the right sternocleidomastoid muscle (SCM) **b** The mass

presents the same echogenicity as the normal retrosternal thymus (TH) (ST, sternum) **c** On coronal FAT SAT MRI, T2- weighted image the cervical mass presents a signal intensity identical to normal thymus

**Fig. 56** Thymic cyst in a 1-year-old immunodeficient patient **a** Left parasternal US view shows a simple thymic cyst (calipers) **b** After 3 years the cyst has considerably decreased in size (TH thymus; AA ascending aorta; RP right pulmonary artery)

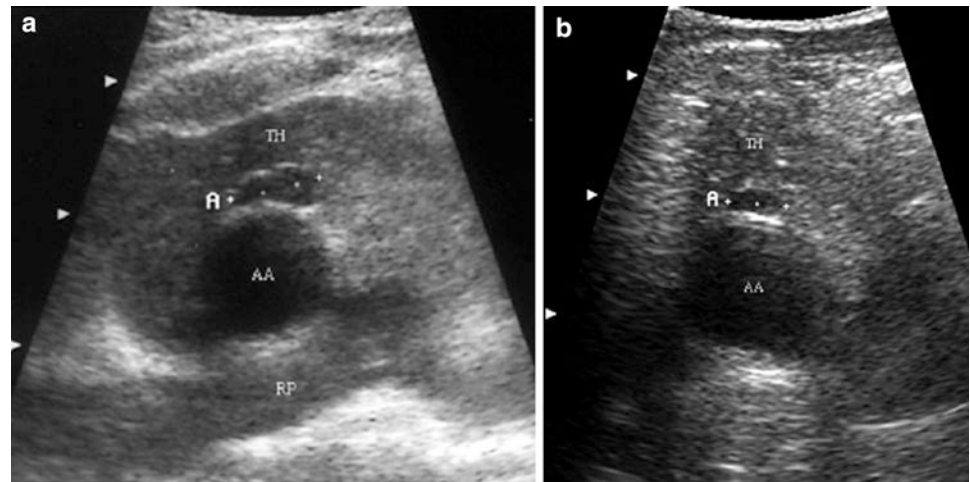
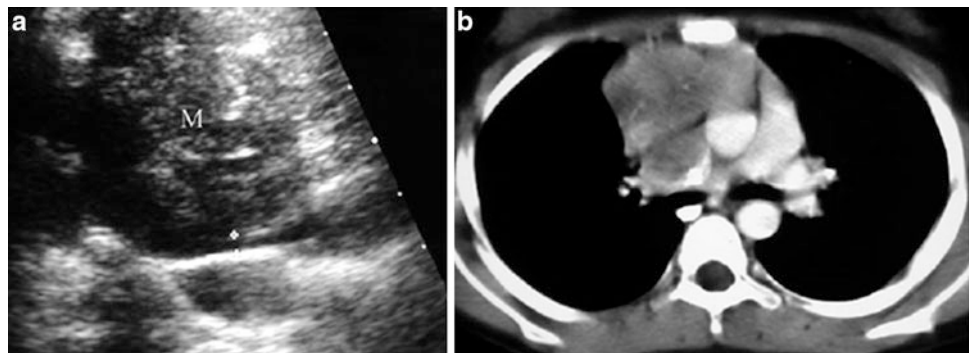


**Fig. 57** Germ cell tumor of the anterior mediastinum in a 4-year-old girl **a** Transverse US scan obtained with a parasternal approach shows a mass (M) with heterogeneous echotexture compressing the superior vena cava (between calipers) **b** Enhanced CT scan reveals the same findings as US. Note compression of the superior vena cava



hypoechoic, hyperechogenic, or heterogenous, fixed mass compressing the adjacent anatomic structures (Lemaitre et al. 1987; Hamrick-Turner et al. 1994; Kim et al. 2000; De Pascale et al. 2006). All thymic masses that are heterogenous on US should be further examined by CT or MRI.

Germ cell tumors include a wide spectrum of histological types (teratoma, seminoma, endodermal sinus tumor,

choriocarcinoma, and embryonal carcinoma) and 94 % are located in the anterior mediastinum. The most common germ cell tumor is mature teratoma. On US, the tumor may be mostly cystic or have a complex appearance with echogenic fat, soft tissue components, and calcifications. In contrast to normal thymus, these tumors often compress the neighboring anatomic structures (Fig. 57). CT and MRI are superior to

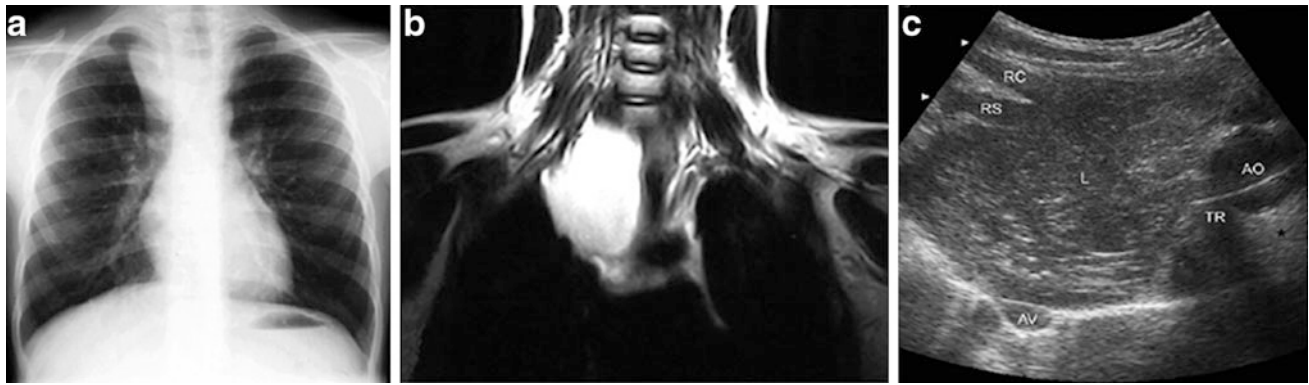


**Fig. 58** Mediastinal lipoma in a 12-year-old girl **a** Chest RX shows mediastinal widening and left tracheal displacement **b** Coronal supra-sternal US view shows an echogenic mass in the paratracheal region, which moved with the heart beat in real time. The aortopulmonary area

is normal (*asterisk*) **c** Coronal T1W MR image confirms fatty nature of the mass (AO aorta; AV azygous vein; L lipoma; RC right carotid artery; RS right subclavian artery; TR trachea)

US for delineating the extension of the tumor and for detecting spread to the pericardium or pleura in cases of tumor rupture, a common occurrence in mediastinal teratoma (Sasaka et al. 1998). Lipomas and lymphangiomas are benign tumors that often extend from the cervical area to the anterior mediastinum through the thoracic inlet (Canonica et al. 2011). Although they can be detected with US, MRI better delineates the entire tumor, including the cervical extension (Castellote et al. 1999; Ching et al. 2002) (Fig. 58).

#### 7.4.2 Middle Mediastinum

The lesions usually found in the middle mediastinum are congenital malformations (including vascular anomalies) and lymphadenopathy. The most common congenital malformations are bronchogenic cysts, esophageal duplication cysts, and neuroenteric cysts. Bronchogenic cysts, generally located in the subcarinal region, are usually seen as solitary thin-walled anechoic masses with a serous content that can vary in shape during respiration. In some cases, fatty material or mucus within the cysts causes internal echoes that simulate a solid mass. Swirling of internal debris seen on real-time examination, the rounded shape and well-defined wall are the clues that differentiate bronchogenic cyst from a solid mass. Patients are usually asymptomatic, but internal bleeding or infection can produce a sudden increase in size and associated symptoms of airway compression (Davis and Umlas 1992).

Most esophageal duplication cysts are found along the lower third of the esophagus. Neuroenteric cysts are the least common type of congenital cysts and are due to incomplete separation of the notochord from the foregut. Although they may be found in the middle mediastinum, they are more common in the posterior mediastinum (paravertebral region) and are often associated with congenital defects of the spine. Due to the different growth patterns of the spine and the

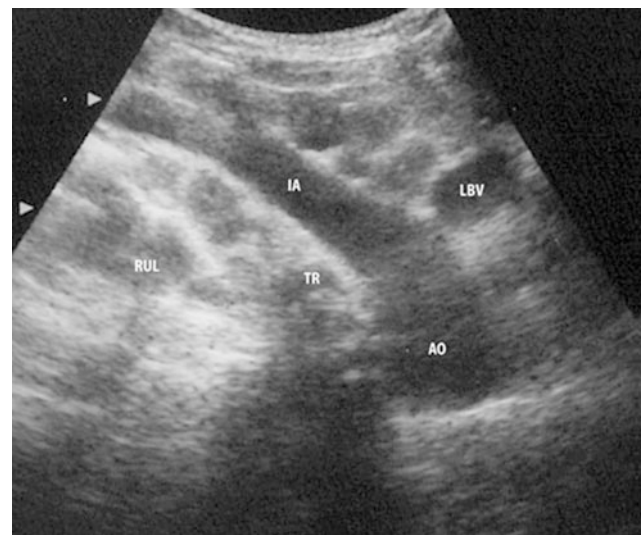


**Fig. 59** Mediastinal lymphadenopathy in a 6-year-old boy with lymphoma. Oblique coronal view through the suprasternal space shows multiple, enlarged, hypoechoic lymph nodes at both sides of the innominate artery (IA) (AO aorta; LBV left brachiocephalic vein; RUL right upper lobe; TR trachea)

thoracic cage, the level of the cyst may not coincide with that of the associated spinal defect. The sonographic features of both esophageal and neuroenteric cysts are identical to those of bronchogenic cysts.

Vascular malformations, including double aortic arch, aberrant left pulmonary artery, and anomalous venous return, can also be detected by US. However, multidetector CT (MDCT) and MRI are the techniques of choice for the study of these malformations.

Lymphadenopathy, secondary to infectious, neoplastic, immunologic, toxic, or metabolic processes is the most common mass found in the middle mediastinum. At US, lymphadenopathy is seen as scattered or clustered nodules

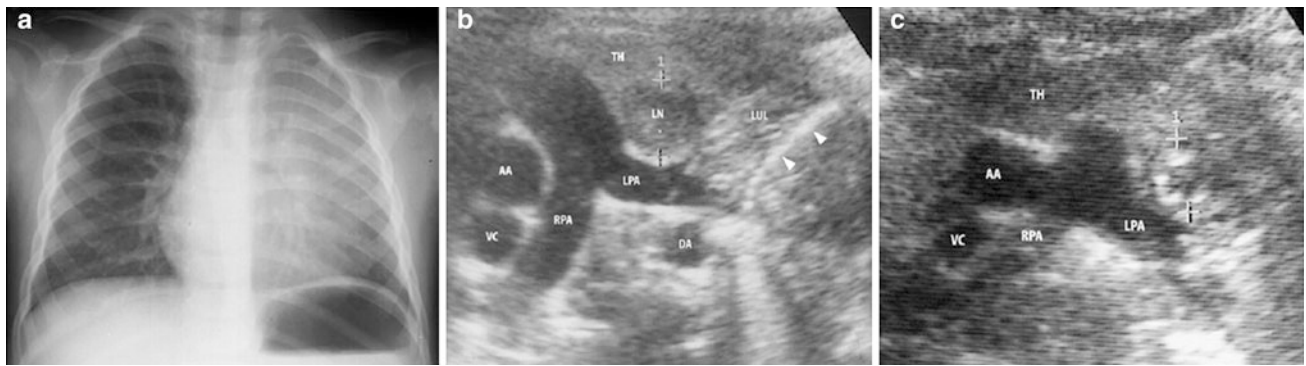


**Fig. 60** Mediastinal lymphadenopathy in an 8-year-old boy with tuberculosis **a** Chest radiograph shows opacity and loss of volume due to left upper lobe collapse **b** US left parasternal axial view demonstrates enlarged lymph nodes (LN) anterior to the left pulmonary artery (LPA). The atelectatic left upper lobe (LUL) and

left pulmonary fissure (*arrowheads*) are also seen. Note mirror artifact showing the echogenic collapse on both sides of the fissure **c** On follow up US study after 2 months of treatment, the node (between calipers) presents a multilayered appearance (AA ascending aorta; VC superior vena cava; DA descending aorta; TH thymus)

with varying degrees of echogenicity. These clusters are more easily identified by US than CT where they can simulate a simple solid mass. The right paratracheal region, pulmonary hilum, and subcarinal space are the most common sites of pathologic lymph nodes (Fig. 59). Most mediastinal lymphadenopathies are of infectious origin. We have observed them in 83 % of children with pneumonia of undetermined cause, 94 % of children with tuberculosis disease (positive PPD, clinical symptoms, and abnormalities on chest X-ray), and 50 % of children infected by tuberculosis (positive PPD, no respiratory symptoms and normal chest X-ray). In our experience, US is more sensitive than chest X-ray for the detection of mediastinal lymphadenopathy in children with tuberculosis and is also useful for follow-up (Bosch-Marcet et al. 2004, 2007). The US appearance of tuberculous nodes can change following treatment and present a hypoechoic center and echogenic halo, probably due to internal caseous material (Fig. 60). Mediastinal lymphadenopathy can also be found in patients with immunologic processes, such as Kawasaki disease (Bosch et al. 1998), Castelman disease and autoimmune thyroiditis.

Leukemia and lymphoma are the most frequent neoplastic processes in children that result in lymphadenopathy, which when massive, can extend to the anterior mediastinum. In an attempt to distinguish benign or reactive from malignant adenopathy, color and power Doppler has been recently applied to study the perfusion patterns within the nodes (Tschammler et al. 1998; Steinkamp et al. 2002). Although good results have been obtained in individual cases, more experience with this method is required to obtain conclusive data as to its value for this purpose.

### 7.4.3 Posterior Mediastinum

Among the three mediastinal regions, the posterior mediastinum is the least suitable for study by ultrasound. The

majority of lesions located in this region are neurogenic tumors, which frequently extend to the spinal canal, a region that is better studied by MRI or CT. However, lesions located in the lower part of the posterior mediastinum (juxtaphrenic or paravertebral masses) can be studied with ultrasound using subxiphoid or transdiaphragmatic approach. These approaches may be particularly helpful for examining children with paravertebral soft tissue widening (Donnelly et al. 2000) in order to differentiate normal patients from those with tumor, atelectasis in the area of the pulmonary ligament or azygos continuation of the inferior vena cava. In neurogenic tumors, US demonstrates a solid mass with frequent granular or fleck-like calcifications. In atelectasis, one will encounter typical signs described for lung consolidation. The vascular nature of the lesion is readily assessed by color Doppler without administration of intravenous contrast material.

## 8 Conclusion

Sonography is a useful technique for rapid assessment of a large variety of chest conditions in children. Use of color, power, and pulsed Doppler enables noninvasive visualization and characterization of vascular structures, a valuable capability for the study of congenital malformations, consolidations, and tumors. US is superior to CT for characterizing pleural fluid collections, thus providing important information for establishing proper treatment. It is the method of choice for screening patients with mediastinal widening, thereby avoiding more invasive study of a normal thymus. Sonography can characterize the solid versus cystic nature of a mediastinal mass in doubtful cases and detect the presence of lymphadenopathy in the paratracheal, aortopulmonary and subcarinal regions.



## References

- Acunas B, Celik L, Acunas A (1989) Chest sonography. Differentiation of pulmonary consolidation from pleural disease. *Acta Radiol* 30:273–275
- Agricola E, Bove T, Oppizzi M et al (2005) “Ultrasound comet-tail images”: a marker of pulmonary edema: a comparative study with wedge pressure and extravascular lung water. *Chest* 127:1690–1695. doi:10.1378/chest.127.5.1690
- Alkrinawi S, Chernick V (1996) Pleural infection in children. *Semin Respir Infect* 11:148–154
- Annessi V, Paci M, De Franco S et al (2003) Diagnosis of anterior mediastinal masses with ultrasonically guided core needle biopsy. *Chir Ital* 55(3):379–384
- Aoki AA, Mock CN, Talner LB (1998) Traumatic rupture of the right hemidiaphragm in an automobile accident victim. *AJR Am J Roentgenol* 171:386. doi:10.2214/ajr.171.2.9694457
- Avila NA, Mueller BU, Carrasquillo JA et al (1996) Multilobar thymic cysts: imaging features in children with human immunodeficiency virus infection. *Radiology* 201:130–134
- Avni EF, Braude P, Pardou A, Matos C (1990) Hyaline membrane disease in the newborn: diagnosis by ultrasound. *Pediatr Radiol* 20:143–146
- Avni EF, Cassart M, de Maertelaer V et al (1996) Sonographic prediction of chronic lung disease in the premature undergoing mechanical ventilation. *Pediatr Radiol* 26:463–469
- Aziz D, Langer JC, Tuuha SE et al (2004) Perinatally diagnosed asymptomatic congenital cystic adenomatoid malformation: to resect or not? *J Pediatr Surg* 39:329–334
- Barillari A, Kiuru S (2010) Detection of spontaneous pneumothorax with chest ultrasound in the emergency department. *Intern Emerg Med* 5:253–255. doi:10.1007/s11739-010-0347-z
- Ben-Ami TE, O'Donovan JC, Yousefzadeh DK (1993) Sonography of the chest in children. *Radiol Clin North Am* 31:517–531
- Bosch J, Serres X, Peñas M et al (1998) Mediastinal lymphadenopathy: a variant of incomplete Kawasaki disease. *Acta Paediatr* 87(11):1200–1202
- Bosch-Marcet J, Serres-Crèixams X, Borrás-Pérez V et al (2007) Value of sonography for follow-up of mediastinal lymphadenopathy in children with tuberculosis. *J Clin Ultrasound* 35:118–124. doi:10.1002/jcu.20304
- Bosch-Marcet J, Serres-Crèixams X, Zuasnarab-Cotro A et al (2004) Comparison of ultrasound with plain radiography and CT for the detection of mediastinal lymphadenopathy in children with tuberculosis. *Pediatr Radiol* 34:895–900. doi:10.1007/s00247-004-1251-3
- Bulas D, Egloff AM (2011) Fetal chest ultrasound and magnetic resonance imaging: recent advances and current clinical applications. *Radiol Clin North Am* 49:805–823. doi:10.1016/j.rcl.2011.06.005
- Bush A, Hogg J, Chitty LS (2008) Cystic lung lesions—prenatal diagnosis and management. *Prenat Diagn* 28:604–611. doi:10.1002/pd.2039
- Büsing KA, Kilian AK, Schaible T et al (2008) MR lung volume in fetal congenital diaphragmatic hernia: logistic regression analysis—mortality and extracorporeal membrane oxygenation. *Radiology* 248:233–239. doi:10.1148/radiol.2481070934
- Calder A, Owens CM (2009) Imaging of parapneumonic pleural effusions and empyema in children. *Pediatr Radiol* 39:527–537. doi:10.1007/s00247-008-1133-1
- Cannie M, Jani J, Chaffiotte C et al (2008a) Quantification of intrathoracic liver herniation by magnetic resonance imaging and prediction of postnatal survival in fetuses with congenital diaphragmatic hernia. *Ultrasound Obstet Gynecol* 32:627–632. doi:10.1002/uog.6146
- Cannie M, Jani J, Meersschaert J et al (2008b) Prenatal prediction of survival in isolated diaphragmatic hernia using observed to expected total fetal lung volume determined by magnetic resonance imaging based on either gestational age or fetal body volume. *Ultrasound Obstet Gynecol* 32:633–639. doi:10.1002/uog.6139
- Cannie M, Jani JC, De Keyser F et al (2006) Fetal body volume: use at MR imaging to quantify relative lung volume in fetuses suspected of having pulmonary hypoplasia. *Radiology* 241:847–853. doi:10.1148/radiol.2413051228
- Cannie MM, Jani JC, Van Kerkhove F et al (2008c) Fetal body volume at MR imaging to quantify total fetal lung volume: normal ranges. *Radiology* 247:197–203. doi:10.1148/radiol.2471070682
- Canonica F, Patassini M, Malaspina C (2011) Nonmyxoid mediastinal lipoblastoma in a 2-year-old girl: case report with US, CT, and MRI findings. *J Ultrasound* 14:14–17. doi:10.1016/j.jus.2011.01.002
- Castellote A, Mencho S, Carreras E et al (2011) Correlation between US and MRI for prenatal lung volumetry in diaphragmatic hernia, and use of Doppler to identify the ipsilateral lung cap. *Pediatr Radiol* 41:1569–1577. doi:10.1007/s00247-011-2200-6
- Castellote A, Vazquez E, Vera J et al (1999) Cervicothoracic lesions in infants and children. *Radiographics* 19:583–600
- Cattarossi L, Copetti R, Poskurica B, Miserocchi G (2010) Surfactant administration for neonatal respiratory distress does not improve lung interstitial fluid clearance: echographic and experimental evidence. *J Perinat Med* 38:557–563. doi:10.1515/JPM.2010.096
- Cavoretto P, Molina F, Poggi S et al (2008) Prenatal diagnosis and outcome of echogenic fetal lung lesions. *Ultrasound Obstet Gynecol* 32:769–783. doi:10.1002/uog.6218
- Coakley FV, Lopoo JB, Lu Y et al (2000) Normal and hypoplastic fetal lungs: volumetric assessment with prenatal single-shot rapid acquisition with relaxation enhancement MR imaging. *Radiology* 216:107–111
- Coley B (2002) Ultrasound-guided interventional procedures. In: Siegel MJ (ed) *Pediatric sonography*, 3rd edn. Lippincott Williams & Wilkins, Philadelphia
- Coley BD (2011) Chest sonography in children: current indications, techniques, and imaging findings. *Radiol Clin North Am* 49:825–846. doi:10.1016/j.rcl.2011.06.008
- Conran RM, Stocker JT (1999) Extralobar sequestration with frequently associated congenital cystic adenomatoid malformation, type 2: report of 50 cases. *Pediatr Dev Pathol* 2:454–463
- Copetti R, Cattarossi L (2007) The “double lung point”: an ultrasound sign diagnostic of transient tachypnea of the newborn. *Neonatology* 91:203–209. doi:10.1159/000097454
- Copetti R, Cattarossi L, Macagno F et al (2008) Lung ultrasound in respiratory distress syndrome: a useful tool for early diagnosis. *Neonatology* 94:52–59. doi:10.1159/000113059
- Correia-Pinto J, Gonzaga S, Huang Y, Rottier R (2010) Congenital lung lesions—underlying molecular mechanisms. *Semin Pediatr Surg* 19:171–179. doi:10.1053/j.sempedsurg.2010.03.003
- Ching ASC, Lee SF, Chan YL (2002) Diagnosing paediatric mediastinal lipoblastoma using ultrasound-guided percutaneous needle biopsy: review and report. *Clin Imaging* 26:23–26
- Daltro P, Werner H, Gasparetto TD et al (2010) Congenital chest malformations: a multimodality approach with emphasis on fetal MR imaging. *Radiographics* 30:385–395. doi:10.1148/rg.302095113
- Davenport M, Warne SA, Cacciaguerra S et al (2004) Current outcome of antenally diagnosed cystic lung disease. *J Pediatr Surg* 39:549–556
- Davis SD, Umlas SL (1992) Radiology of congenital abnormalities of the chest. *Curr Opin Radiol* 4:25–35
- De Pascale A, Giorcelli R, Garofalo G et al (2006) Follow-up of mediastinal lymphoma: role of ultrasonography. *Radiol Med* 111:759–772. doi:10.1007/s11547-006-0070-z



- Donnelly LF, Frush DP (1999) Abnormalities of the chest wall in pediatric patients. *AJR Am J Roentgenol* 173:1595–1601
- Donnelly LF, Frush DP, Zheng J-Y et al (2000) Differentiating normal from abnormal inferior thoracic paravertebral soft tissues on chest radiography in children. *AJR Am J Roentgenol* 175:477–483
- Donnelly LF, Klosterman LA (1997) Pneumonia in children: decreased parenchymal contrast enhancement—CT sign of intense illness and impending cavitory necrosis. *Radiology* 205:817–820
- Dubois J, Garel L, David M, Powell J (2002) Vascular soft-tissue tumors in infancy: distinguishing features on Doppler sonography. *AJR Am J Roentgenol* 178:1541–1545
- Durand C, Garel C, Nuges F, Baudain P (2001) Sonography of thoracic diseases in children. *J Radiol* 82:729–737; discussion 739–740
- Eibenberger K, Dock W, Metz V et al (1991) Value of supine thoracic radiography in the diagnosis and quantification of pleural effusions: comparison with sonography. *Rofo* 155:323–326. doi:[10.1055/s-2008-1033271](https://doi.org/10.1055/s-2008-1033271)
- Enriquez G, Cadavid L, Garcés-Iñigo E et al (2012) Tracheobronchomegaly following intrauterine tracheal occlusion for congenital diaphragmatic hernia. *Pediatr Radiol* 42:916–922. doi:[10.1007/s00247-012-2362-x](https://doi.org/10.1007/s00247-012-2362-x)
- Epelman M, Kreiger PA, Servaes S et al (2010) Current imaging of prenatally diagnosed congenital lung lesions. *Semin Ultrasound CT MR* 31:141–157. doi:[10.1053/j.sult.2010.01.002](https://doi.org/10.1053/j.sult.2010.01.002)
- Epelman M, Navarro OM, Daneman A et al (2005) M-mode sonography of diaphragmatic motion: description of technique and experience in 278 pediatric patients. *Pediatr Radiol* 35:661–667. doi:[10.1007/s00247-005-1433](https://doi.org/10.1007/s00247-005-1433)
- Feola GP, Shaw LCA, Coburn L (2003) Management of complicated parapneumonic effusions in children. *Tech Vasc Interv Radiol* 6:197–204
- Fitoz S, Atasoy C, Türköz E et al (2001) Sonographic findings in ectopic cervical thymus in an infant. *J Clin Ultrasound* 29:523–526
- Frazier AA, Rosado de Christenson ML, Stocker JT, Templeton PA (1997) Intralobar sequestration: radiologic-pathologic correlation. *Radiographics* 17:725–745
- Gassner I, Geley TE (2005) Sonographic evaluation of oesophageal atresia and tracheo-oesophageal fistula. *Pediatr Radiol* 35:159–164. doi:[10.1007/s00247-004-1329-y](https://doi.org/10.1007/s00247-004-1329-y)
- García-Peña P, Lucaya J, Hendry GMA, et al. (1998) Spontaneous involution of pulmonary sequestration in children: a report of two cases and review of the literature. *Pediatr Radiol* 28:266–270
- Gorguner M, Misirlioglu F, Polat P et al (2003) Color Doppler sonographically guided transthoracic needle aspiration of lung and mediastinal masses. *J Ultrasound Med* 22:703–708
- Hamrick-Turner Saif MF, Powers CI et al (1994) Imaging of childhood non-Hodgkin lymphoma: assessment by histologic subtype. *Radiographics* 14:11–28
- Hasiotou M, Polyviou P, Strantzia CM et al (2004) Pleuropulmonary blastoma in the area of a previously diagnosed congenital lung cyst: report of two cases. *Acta Radiol* 45:289–292
- Hedlund GL, Navoy JF, Galliani CA, Johnson WH Jr (1999) Aggressive manifestations of inflammatory pulmonary pseudotumor in children. *Pediatr Radiol* 29:112–116
- Hogan MJ, Coley BD (2008) Interventional radiology treatment of empyema and lung abscesses. *Paediatr Respir Rev* 9:77–84; quiz 84. doi:[10.1016/j.prrv.2007.12.001](https://doi.org/10.1016/j.prrv.2007.12.001)
- Jani J, Cannie M, Done E et al (2007a) Relationship between lung area at ultrasound examination and lung volume assessment with magnetic resonance imaging in isolated congenital diaphragmatic hernia. *Ultrasound Obstet Gynecol* 30:855–860. doi:[10.1002/uog.5168](https://doi.org/10.1002/uog.5168)
- Jani J, Nicolaides KH, Keller RL et al (2007b) Observed to expected lung area to head circumference ratio in the prediction of survival in fetuses with isolated diaphragmatic hernia. *Ultrasound Obstet Gynecol* 30:67–71. doi:[10.1002/uog.4052](https://doi.org/10.1002/uog.4052)
- Kerem E, Bar Ziv Y, Rudenski B et al. (1994) Bacteremic necrotizing pneumococcal pneumonia in children. *Am J Respir Crit Care Med* 149:242–244
- Kilian AK, Büsing K-A, Schuetz E-M et al (2009) Fetal MR lung volumetry in congenital diaphragmatic hernia (CDH): prediction of clinical outcome and the need for extracorporeal membrane oxygenation (ECMO). *Klin Padiatr* 221:295–301. doi:[10.1055/s-0029-1192022](https://doi.org/10.1055/s-0029-1192022)
- Kim OH, Kim WS, Kim MJ et al (2000) US in the diagnosis of pediatric chest diseases. *Radiographics* 20:653–671
- Ko SF, Ng SH, Lee TY et al (2000) Noninvasive imaging of bronchopulmonary sequestration. *AJR Am J Roentgenol* 175:1005–1012
- Kocijancic I, Vidmar K, Ivanovi-Herceg Z (2003) Chest sonography versus lateral decubitus radiography in the diagnosis of small pleural effusions. *J Clin Ultrasound* 31:69–74. doi:[10.1002/jcu.10141](https://doi.org/10.1002/jcu.10141)
- Koh D-M, Burke S, Davies N, Padley SPG (2002) Transthoracic US of the chest: clinical uses and applications. *Radiographics* 22:e1
- Kohzaki S, Tsurusaki K, Uetani M et al (2003) The aurora sign: an ultrasonographic sign suggesting parenchymal lung disease. *Br J Radiol* 76:437–443
- Koumanidou C, Vakaki M, Theophanopoulou M et al (1998) Aberrant thymus in infants: sonographic evaluation. *Pediatr Radiol* 28:987–989
- Kurian J, Levin TL, Han BK et al (2009) Comparison of Ultrasound and CT in the Evaluation of Pneumonia Complicated by Parapneumonic Effusion in Children. <http://dx.doi.org/10.2214/AJR.09.2791>
- Laberge J-M, Bratu I, Flageole H (2004) The management of asymptomatic congenital lung malformations. *Paediatr Respir Rev* 5(Suppl A):S305–312
- Langston C (2003) New concepts in the pathology of congenital lung malformations. *Semin Pediatr Surg* 12:17–37. doi:[10.1053/spsu.2003.00001](https://doi.org/10.1053/spsu.2003.00001)
- Lecomte B, Hadden H, Coste K et al (2009) Hyperechoic congenital lung lesions in a non-selected population: from prenatal detection till perinatal management. *Prenat Diagn* 29:1222–1230. doi:[10.1002/pd.2407](https://doi.org/10.1002/pd.2407)
- Lemaitre L, Leclerc F, Marconi V et al (1987) Ultrasonographic findings in thymic lymphoma in children. *Eur J Radiol* 7:125–129
- Lichtenstein D, Mezière G, Biderman P, Gepner A (2000) The “lung point”: an ultrasound sign specific to pneumothorax. *Intensive Care Med* 26:1434–1440
- Lichtenstein D, Mezière G, Seitz J (2009) The dynamic air bronchogram. A lung ultrasound sign of alveolar consolidation ruling out atelectasis. *Chest* 135:1421–1425. doi:[10.1378/chest.08-2281](https://doi.org/10.1378/chest.08-2281)
- Lobo L (2006) The neonatal chest. *Eur J Radiol* 60:152–158. doi:[10.1016/j.ejrad.2006.07.018](https://doi.org/10.1016/j.ejrad.2006.07.018)
- Lovrenski J (2012) Lung ultrasonography of pulmonary complications in preterm infants with respiratory distress syndrome. *Ups J Med Sci* 117:10–17. doi:[10.3109/03009734.2011.643510](https://doi.org/10.3109/03009734.2011.643510)
- Manson DE, Daneman A (2001) Pitfalls in the sonographic diagnosis of juxtadiaphragmatic pulmonary sequestrations. *Pediatr Radiol* 31:260–264
- Maruyama K, Koizumi T (2006) Hydromediastinum associated with a peripherally inserted central venous catheter in a newborn infant. *J Clin Ultrasound* 34:195–198. doi:[10.1002/jcu.20194](https://doi.org/10.1002/jcu.20194)
- May DA, Barth RA, Yeager S et al (1993) Perinatal and postnatal chest sonography. *Radiol Clin North Am* 31:499–516
- McHugh K, Afaq A, Broderick N et al (2010) Tracheomegaly: a complication of fetal endoscopic tracheal occlusion in the treatment of congenital diaphragmatic hernia. *Pediatr Radiol* 40:674–680. doi:[10.1007/s00247-009-1437-9](https://doi.org/10.1007/s00247-009-1437-9)
- Mong A, Johnson AM, Kramer SS et al (2008) Congenital high airway obstruction syndrome: MR/US findings, effect on management, and

- outcome. *Pediatr Radiol* 38:1171–1179. doi:[10.1007/s00247-008-0962-2](https://doi.org/10.1007/s00247-008-0962-2)
- Newman B (2006) Congenital bronchopulmonary foregut malformations: concepts and controversies. *Pediatr Radiol* 36:773–791. doi:[10.1007/s00247-006-0115-4](https://doi.org/10.1007/s00247-006-0115-4)
- Osada H, Kaku K, Masuda K et al (2004) Quantitative and qualitative evaluations of fetal lung with MR imaging. *Radiology* 231:887–892. doi:[10.1148/radiol.2313021689](https://doi.org/10.1148/radiol.2313021689)
- Paek BW, Coakley FV, Lu Y et al (2001) Congenital diaphragmatic hernia: prenatal evaluation with MR lung volumetry-preliminary experience. *Radiology* 220:63–67
- Papagiannopoulos KA, Sheppard M, Bush AP, Goldstraw P (2001) Pleuropulmonary blastoma: is prophylactic resection of congenital lung cysts effective? *Ann Thorac Surg* 72:604–605
- Pariente G, Aviram M, Landau D, Herskovitz R (2009) Prenatal diagnosis of congenital lobar emphysema: case report and review of the literature. *J Ultrasound Med* 28:1081–1084
- Peralta CFA, Kazan-Tannus JF, Bunduki V et al (2006) Evaluation of the agreement between 3-dimensional ultrasonography and magnetic resonance imaging for fetal lung volume measurement. *J Ultrasound Med* 25:461–467
- Pieper CH, Smith J, Brand EJ (2004) The value of ultrasound examination of the lungs in predicting bronchopulmonary dysplasia. *Pediatr Radiol* 34:227–231. doi:[10.1007/s00247-003-1102-7](https://doi.org/10.1007/s00247-003-1102-7)
- Pumberger W, Hörmann M, Deutinger J et al (2003) Longitudinal observation of antenatally detected congenital lung malformations (CLM): natural history, clinical outcome and long-term follow-up. *Eur J Cardiothorac Surg* 24:703–711
- Raptopoulos V, Davis LM, Lee G et al (1991) Factors affecting the development of pneumothorax associated with thoracocentesis. *AJR Am J Roentgenol* 156:917–920
- Riccabona M (2008) Ultrasound of the chest in children (mediastinum excluded). *Eur Radiol* 18:390–399. doi:[10.1007/s00330-007-0754-3](https://doi.org/10.1007/s00330-007-0754-3)
- Ruano R, Aubry M-C, Dumez Y et al (2008) Predicting neonatal deaths and pulmonary hypoplasia in isolated congenital diaphragmatic hernia using the sonographic fetal lung volume-body weight ratio. *AJR Am J Roentgenol* 190:1216–1219. doi:[10.2214/AJR.07.3078](https://doi.org/10.2214/AJR.07.3078)
- Ruano R, Joubin L, Sonigo P et al (2004) Fetal lung volume estimated by 3-dimensional ultrasonography and magnetic resonance imaging in cases with isolated congenital diaphragmatic hernia. *J Ultrasound Med* 23:353–358
- Rudick MG, Bp Wood (1980) The use of ultrasound in the diagnosis of a large thymic cyst. *Pediatr Radiol* 10:113–115
- Rypens F, Metens T, Rocourt N et al (2001) Fetal lung volume: estimation at MR imaging-initial results. *Radiology* 219:236–241
- Sanchez de Toledo J, Munoz R, Landsittel D et al (2010) Diagnosis of abnormal diaphragm motion after cardiothoracic surgery: ultrasound performed by a cardiac intensivist vs. fluoroscopy. *Congenit Heart Dis* 5:565–572. doi:[10.1111/j.1747-0803.2010.00431.x](https://doi.org/10.1111/j.1747-0803.2010.00431.x)
- Sasaka K, Kurihara Y, Nakajima Y et al (1998) Spontaneous rupture: a complication of benign mature teratoma of the mediastinum. *AJR Am J Roentgenol* 170:323–328
- Seibert JJ, Glasier CH, Leithieser RE (1998) The pediatric chest. In Shankar et al. (2000)
- Seo T, Ando H, Kaneko K et al (2006) Two cases of prenatally diagnosed congenital lobar emphysema caused by lobar bronchial atresia. *J Pediatr Surg* 41:e17–e20. doi:[10.1016/j.jpedsurg.2006.08.037](https://doi.org/10.1016/j.jpedsurg.2006.08.037)
- Shankar S, Gulati M, Kang M et al (2000) Image-guided percutaneous drainage of thoracic empyema: can sonography predict the outcome? *Eur Radiol* 10:495–499
- Siegel MJ. (2002) Chest. In: Siegel MJ (ed) *Pediatric sonography*, 3rd edn. Lippincott Williams & Wilkins, Philadelphia pp 167–211
- Smeets AJ, Robben SG, Meradji M (1990) Sonographically detected costo-chondral dislocation in an abused child. A new sonographic sign to the radiological spectrum of child abuse. *Pediatr Radiol* 20:566–567
- Song I, Yoo S-Y, Kim JH et al (2011) Aberrant cervical thymus: imaging and clinical findings in 13 children. *Clin Radiol* 66:38–42. doi:[10.1016/j.crad.2010.04.023](https://doi.org/10.1016/j.crad.2010.04.023)
- Steinkamp HJ, Wissgott C, Rademaker J et al. (2002) Current status of power Doppler and color Doppler sonography in the differential diagnosis of lymph nodes lesions. *Eur Radiol* 12:1785–1793
- Stefanidis K, Dimopoulos S, Nanas S (2011) Basic principles and current applications of lung ultrasonography in the intensive care unit. *Respirology* 16:249–256. doi:[10.1111/j.1440-1843.2010.01885.x](https://doi.org/10.1111/j.1440-1843.2010.01885.x)
- Stocker JT, Madewell JE, Drake RM (1977) Congenital cystic adenomatoid malformation of the lung. Classification and morphologic spectrum. *Hum Pathol* 8:155–171
- Stocker JT (1994) Congenital and developmental diseases. In: Dail DH, Hammar SP (eds) *Pulmonary pathology*, 2nd edn. Springer, Berlin, pp 155–190
- Swischuk LE, John SD (1996) Normal thymus extending between the right brachiocephalic vein and the innominate artery. *AJR Am J Roentgenol* 166:1462–1464. doi:[10.2214/ajr.166.6.8633465](https://doi.org/10.2214/ajr.166.6.8633465)
- Tanigaki S, Miyakoshi K, Tanaka M et al (2004) Pulmonary hypoplasia: prediction with use of ratio of MR imaging-measured fetal lung volume to US-estimated fetal body weight. *Radiology* 232:767–772. doi:[10.1148/radiol.2323030359](https://doi.org/10.1148/radiol.2323030359)
- Tschammler A, Ott G, Schang T et al (1998) Lymphadenopathy: differentiation of benign from malignant disease—color Doppler US assessment of intranodal angioarchitecture. *Radiology* 208:117–123
- Vijayaraghavan SB, Rao PS, Selvarasu CD, Rao TMS (2003) Prenatal sonographic features of intralobar bronchopulmonary sequestration. *J Ultrasound Med* 22:541–544
- Volpicelli G (2011a) Sonographic diagnosis of pneumothorax. *Intensive Care Med* 37:224–232. doi:[10.1007/s00134-010-2079-y](https://doi.org/10.1007/s00134-010-2079-y)
- Volpicelli G (2011b) The double lung point. *Am J Emerg Med* 29:832–833. doi:[10.1016/j.ajem.2011.04.014](https://doi.org/10.1016/j.ajem.2011.04.014)
- Ward VL, Nishino M, Hatabu H et al (2006) Fetal lung volume measurements: determination with MR imaging—effect of various factors. *Radiology* 240:187–193. doi:[10.1148/radiol.2393050583](https://doi.org/10.1148/radiol.2393050583)
- Wedegaertner U, Tchirikov M, Habermann C et al (2004) Fetal sheep with tracheal occlusion: monitoring lung development with MR imaging and B-mode US. *Radiology* 230:353–358. doi:[10.1148/radiol.2302021095](https://doi.org/10.1148/radiol.2302021095)
- Weinberg B, Diakoumakis EE, Kass EG et al (1986) The air bronchogram: sonographic demonstration. *AJR Am J Roentgenol* 147:593–595
- Wells RG, Havens PL (2003) Intrapleural fibrinolysis for parapneumonic effusion and empyema in children. *Radiology* 228:370–378. doi:[10.1148/radiol.2282020486](https://doi.org/10.1148/radiol.2282020486)
- Werneck K (2000) Ultrasound study of the pleura. *Eur Radiol* 10:1515–1523
- Williams G, Coakley FV, Qayyum A et al (2004) Fetal relative lung volume: quantification by using prenatal MR imaging lung volumetry. *Radiology* 233:457–462. doi:[10.1148/radiol.233203156](https://doi.org/10.1148/radiol.233203156)
- Winters WD, Effmann EL, Nghiem HV, Nyberg DA (1997) Disappearing fetal lung masses: importance of postnatal imaging studies. *Pediatr Radiol* 27:535–539
- Witlox RSGM, Lopriore E, Walther FJ et al (2009) Single-needle laser treatment with drainage of hydrothorax in fetal bronchopulmonary sequestration with hydrops. *Ultrasound Obstet Gynecol* 34:355–357. doi:[10.1002/uog.7316](https://doi.org/10.1002/uog.7316)
- Yang PC, Luh KT, Chang DB et al (1992) Ultrasonographic evaluation of pulmonary consolidation. *Am Rev Respir Dis* 146:757–762

---

# The Contribution of Nuclear Medicine to Pulmonary Imaging

Michael J. Gelfand and David L. Gilday

## Contents

<b>1</b>	<b>Introduction.....</b>	<b>65</b>
<b>2</b>	<b>Technique: Planar Scintigraphy and Single Photon Emission Computed Tomography (SPECT) .....</b>	<b>66</b>
2.1	Aerosol Ventilation Imaging.....	66
2.2	Ventilation Imaging with Noble (Inert) Gases.....	66
2.3	Qualitative Lung Perfusion Scintigraphy .....	66
2.4	Quantitative Lung Perfusion Scintigraphy .....	66
2.5	Salivagram .....	66
<b>3</b>	<b>Clinical Interpretation: Planar Imaging and SPECT.....</b>	<b>67</b>
<b>4</b>	<b>Technique: PET and PET/CT Imaging.....</b>	<b>70</b>
<b>5</b>	<b>Clinical Interpretation: PET and PET/CT Imaging.....</b>	<b>72</b>
	<b>References .....</b>	<b>72</b>

---

## Abstract

A variety of nuclear medicine imaging techniques have been applied to imaging of the chest. Several radiopharmaceuticals were designed specifically to diagnose changes in pulmonary physiology caused by pathologic processes. Intravenous injection of  $^{99m}\text{Tc}$  macroaggregated albumin (MAA) permits identification of local and regional changes in pulmonary arterial perfusion, initially used to identify changes related to pulmonary embolism and later applied to evaluation of pulmonary arterial flow distribution in patients with congenital heart disease. Ventilation studies with noble gases such as  $^{133}\text{Xe}$  and  $^{81m}\text{krypton}$  allow recognition of local and regional changes in ventilation and are used with  $^{99m}\text{Tc}$  MAA perfusion imaging for the identification of pulmonary emboli. Radioaerosols, particularly  $^{99m}\text{Tc}$  DTPA, can also demonstrate local and regional ventilation abnormalities. Aspiration of saliva can be detected by the radionuclide salivagram. Positron emission tomography (PET) after intravenous injection of [ $^{18}\text{F}$ ]fluoro-2-deoxyglucose (FDG) can be used to localize and follow neoplastic and inflammatory processes in the chest.

---

## 1 Introduction

One of the oldest nuclear medicine tests is perfusion lung scintigraphy, which was introduced to diagnose pulmonary embolism. Until recently, pulmonary embolism was considered rare in pediatrics. Another important indication for lung scintigraphy is to evaluate pulmonary perfusion in children with either congenital or acquired pulmonary artery stenosis. Quantifying the distribution of  $^{99m}\text{Tc}$  MAA is especially useful in following up the results of stenting or dilatation of a pulmonary artery, and to evaluate pulmonary perfusion after unifocalization procedures. Similarly, pulmonary artery branch narrowing can be followed up with

---

M. J. Gelfand (✉)  
Department of Radiology,  
Cincinnati Children's Hospital Medical Center,  
University of Cincinnati College of Medicine,  
3333 Burnet Avenue, Cincinnati, OH 45229-3039, USA  
e-mail: michael.gelfand@cchmc.org

D. L. Gilday  
Medical Imaging, Toronto Nuclear Medical Services,  
Suite 210, 123 Edward Street,  
Toronto, ON M5G 1E2, Canada

this technique. It has the advantage of being simple and easy to perform even with the most uncooperative young child or infant. Using ventilation techniques, bronchial obstructive diseases can be evaluated, although computed tomography (CT) has largely supplanted this technique.

Investigation of respiratory problems using nuclear medicine techniques involves assessing the perfusion (Q) and ventilation (V) of the lungs. Ventilation and perfusion studies (V/Q) are used together to better detect and evaluate lung abnormalities. Multiple views are obtained as part of both the ventilation and perfusion portion of the study. The ventilation study can be done with either a noble (inert) gas such as  $^{81\text{m}}$ krypton or  $^{133}$ xenon, or with  $^{99\text{m}}$ Tc diethylene-triamine pentaacetic acid (DTPA) aerosol.

Positron emission tomography (PET) using [ $^{18}\text{F}$ ]2-fluoro-2-deoxyglucose (FDG) is often used for tumor imaging; this has been the most important application of FDG-PET to date. Imaging of pulmonary inflammatory processes with FDG is also useful in some circumstances.

## 2 Technique: Planar Scintigraphy and Single Photon Emission Computed Tomography (SPECT)

### 2.1 Aerosol Ventilation Imaging

Aerosol imaging is the technique most commonly used for imaging of pulmonary ventilation. It is also the easiest and cheapest, and is widely available. The equipment needed to perform an aerosol study consists of a commercial nebulizer, which produces droplets that will be deposited on the surface of the bronchioles. This results in a very accurate picture of the pattern of ventilation. These droplets are produced from a liquid containing  $^{99\text{m}}$ Tc DTPA that is placed in the nebulizer. An aerosol ventilation study can be performed if the child is able to maintain a tight seal around the mouthpiece that is connected to the nebulizer. Studies in patients who are unable to cooperate and in patients on a ventilator present significant technical challenges. Up to eight images are obtained in anterior, posterior, left lateral, right lateral, 45° left anterior oblique (LAO), left posterior oblique (LPO), right anterior oblique (RAO), and right posterior oblique (RPO) projections.

### 2.2 Ventilation Imaging with Noble (Inert) Gases

The commonly used radioactive noble gases are  $^{133}$ xenon and  $^{81\text{m}}$ krypton (a generator-produced radiotracer). The gas is inhaled using a plastic breathing bag equipped with a one-way valve connected to a mouthpiece and another one-way

valve connected to a waste collection bag. The imaging study is obtained as follows: the patient inhales from the bag containing the radioactive noble gas and then exhales into the collection bag. The one-way valves permit inhaling only from the breathing bag and the exhaled air can only go to the collection bag. After equilibrium is attained, the child breathes in room air until all the radioactive gas is washed out.

If  $^{133}$ xenon is used, a wash in phase, an equilibrium phase, and a washout phase can be imaged. With  $^{133}$ xenon, only a single projection is acquired. If  $^{81\text{m}}$ krypton is available, then additional views in each of the eight standard lung views may be obtained, but only the wash in phase is evaluated.

### 2.3 Qualitative Lung Perfusion Scintigraphy

A chest radiograph done within the previous 24 h should be available for review. The radiopharmaceutical,  $^{99\text{m}}$ Tc MAA, is injected with the patient supine. Immediately following injection, eight images are obtained in the anterior, posterior, left lateral, right lateral, 45° LAO, LPO, RAO, and RPO projections. There should be a symmetrical appearance of both perfusion and ventilation in both lungs (Fig. 1). In selected cases, SPECT can provide additional diagnostic information (Touya et al. 1986).

### 2.4 Quantitative Lung Perfusion Scintigraphy

This procedure is carried out on patients with pulmonary artery stenosis to assess pulmonary arterial perfusion to each lung (Glass et al. 1991). Follow-up studies are also performed after surgery or balloon dilatation to assess perfusion. A quantitative perfusion study may also be useful after unifocalization or Fontan procedures (Fukuda et al. 2010).

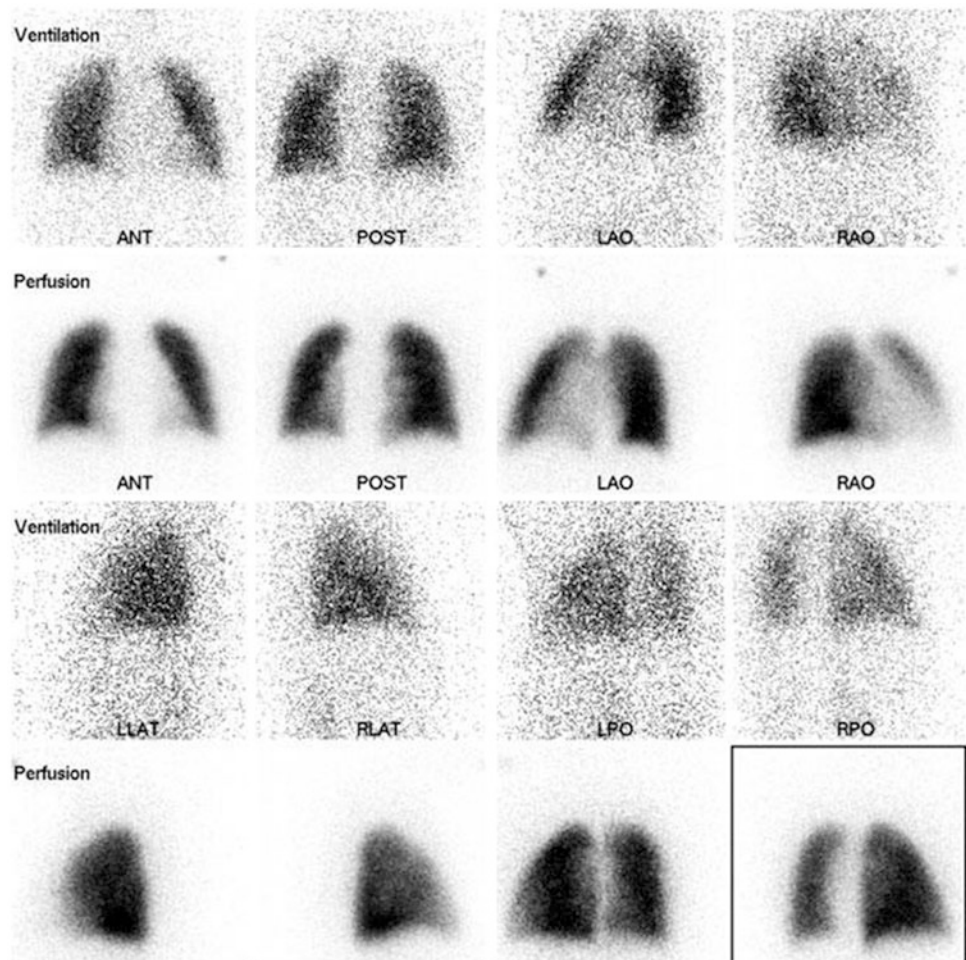
The radiopharmaceutical is injected into the patient using the technique previously described. The amount of  $^{99\text{m}}$ Tc MAA is reduced for this technique, and in infants and patients with right to left shunts, the number of particles injected should be significantly reduced (Gelfand 1978). Immediately following injection, anterior and posterior projections are acquired. The relative perfusion to each lung is calculated using comparable regions of interest on both the anterior and posterior images, using a geometric mean of the values determined from the two images. Additional oblique and lateral images are acquired as needed.

### 2.5 Salivagram

Initial nuclear medicine attempts to detect aspiration were accomplished by imaging the chest after administering a radiotracer labeled drink (usually milk or formula)



**Fig. 1** Normal ventilation and perfusion scan. There is a very close match in the distribution of the tracer between the ventilation and the perfusion images. *ANT* anterior, *POST* posterior, *LAO* left anterior oblique, *RAO* right anterior oblique, *LLAT* left lateral, *RLAT* right lateral, *LPO* left posterior oblique, *RPO* right posterior oblique



(McVeagh et al. 1987). Although this did detect some cases of aspiration secondary to reflux, it was unable to do so if reflux was not present. The salivagram was introduced as a means of detecting aspiration secondary to disordered pharyngeal motility (Heyman 1989; Heyman and Respondek 1989).

The patient is placed in a supine position on the imaging table, beneath which the camera is positioned. The infant or child must be well restrained to minimize motion during the study acquisition. A small dosage of  $^{99m}\text{Tc}$  sulfur colloid is placed under the patient's tongue or in each buccal pouch and allowed to mix with the saliva. Sequential images are acquired until the activity clears from the mouth. The imaging sequence may be repeated to optimize the chance of detecting aspiration. If activity is seen anywhere in the chest area, the patient's clothing may be removed and repeat images acquired to ensure that there is no external contamination. If activity is still seen, a lateral image of the appropriate side is acquired.

### 3 Clinical Interpretation: Planar Imaging and SPECT

Ventilation perfusion scintigraphy continues to be useful in the evaluation of children for the presence of pulmonary emboli. CT angiography (CTA) supplanted V/Q scintigraphy for this purpose in many institutions, in both adults and children. Evidence subsequently emerged that adult patients, who have a normal chest radiograph and no history of chronic lung disease, have a low incidence of indeterminate V/Q studies, only slightly higher than the incidence of indeterminate CTA studies (Daftary et al. 2005; Forbes et al. 2001; Jones and Wittram 2005; Eyer et al. 2005). This was also demonstrated to be true in pediatric patients as well (Gelfand et al. 2008). Depending on the CTA technique, V/Q imaging can have a lower effective radiation dose than CTA and a much lower dose to the female breast (Studler et al. 2005; Parker et al. 2005; Stabin and Gelfand 1998). For this reason, it may be preferred as the first test

for evaluating suspected pulmonary embolism in children and adolescents, as long as there is no prior history of lung disease and the chest radiograph is normal or nearly normal.

Although not nearly as common in children as in adults, pulmonary embolism is increasing in incidence. This is in part due to better recognition that pulmonary embolism occurs in childhood, but, even more importantly, due to increased use of therapies that can predispose to pulmonary embolism, including the increased use of central venous access catheters. The main indication for V/Q imaging is to determine whether pulmonary embolism is present. The diagnosis is usually made according to PIOPED II and PISAPED criteria (Sostman et al. 2008; Miniati et al. 2008). However, these criteria were established for adults and have not been validated in a pediatric population (Fig. 2).

Lung scintigraphy can also be used to map those portions of the lung that function well. V/Q imaging may be used for this purpose, and when ventilation imaging cannot be performed, perfusion imaging alone may be adequate. With rare exceptions, in patients who do not have a history of pulmonary emboli, who are not wheezing and who are relatively free of secretions in their bronchi, ventilation and perfusion imaging are nearly identical (Hayward et al. 2007). SPECT perfusion imaging can be used to demonstrate functioning lung tissue in a tomographic format, and may demonstrate significantly more extensive perfusion abnormalities than are appreciated on planar perfusion scintigraphy, as has been shown in cystic fibrosis patients (Donnelly et al. 1997).

Quantitative perfusion imaging alone can be used to evaluate the relative perfusion to each lung or lobe due to pulmonary artery stenosis (Fig. 3) (Glass et al. 1991). The technique is especially valuable in following up the effects of intervention for the correction of pulmonary arterial narrowing. In some children's hospitals, this is the most common indication for nuclear medicine imaging in pediatric lung disease. It should be remembered that only pulmonary arterial perfusion is evaluated after intravenous injection with  $^{99m}\text{Tc}$  MAA. In children with a history of cyanotic heart disease, nonsegmental perfusion defects may also be due to predominant bronchial arterial perfusion to a volume of lung.

In same way that perfusion abnormalities can be evaluated in patients with pulmonary stenosis, patients with lung disease may be evaluated with ventilation perfusion or perfusion imaging to determine regional lung function after lung injury. This approach has been used in patients with bronchopulmonary dysplasia and cystic fibrosis (Soler et al. 1997). Perfusion and ventilation to each lung can also be evaluated in patients with severe scoliosis, pectus excavatum, and after repair of congenital diaphragmatic hernia (Blickman et al. 1985; Jeandot et al. 1989; Hayward et al. 2007). Congenital diaphragmatic hernia is one of the few

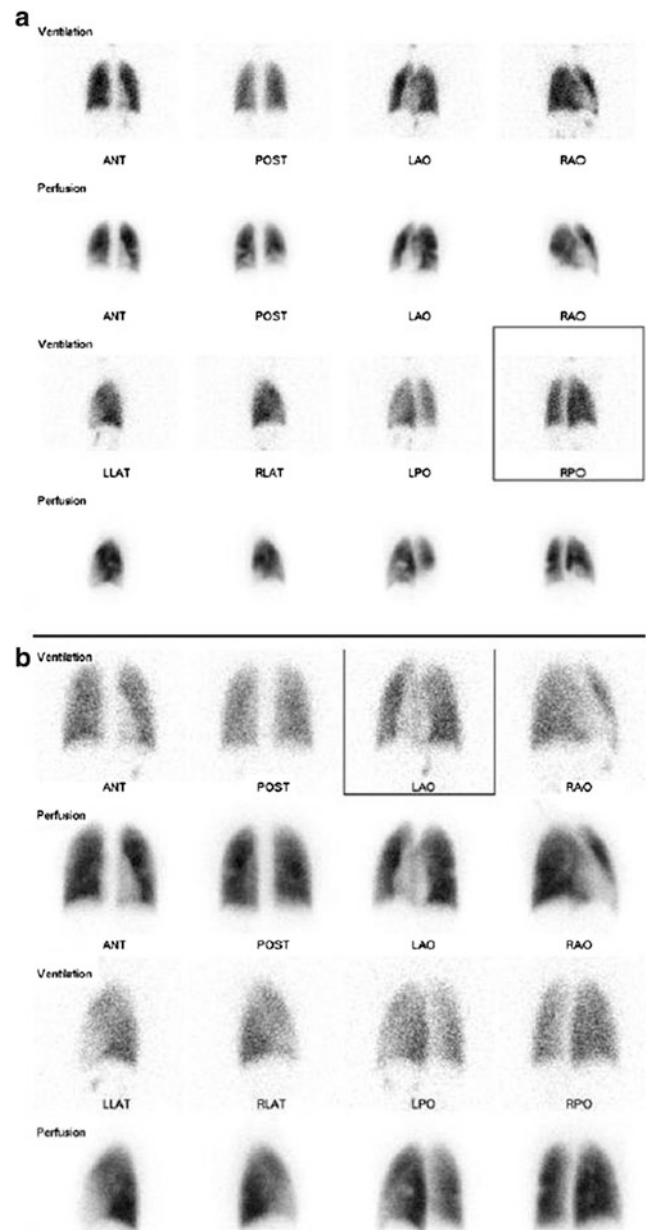
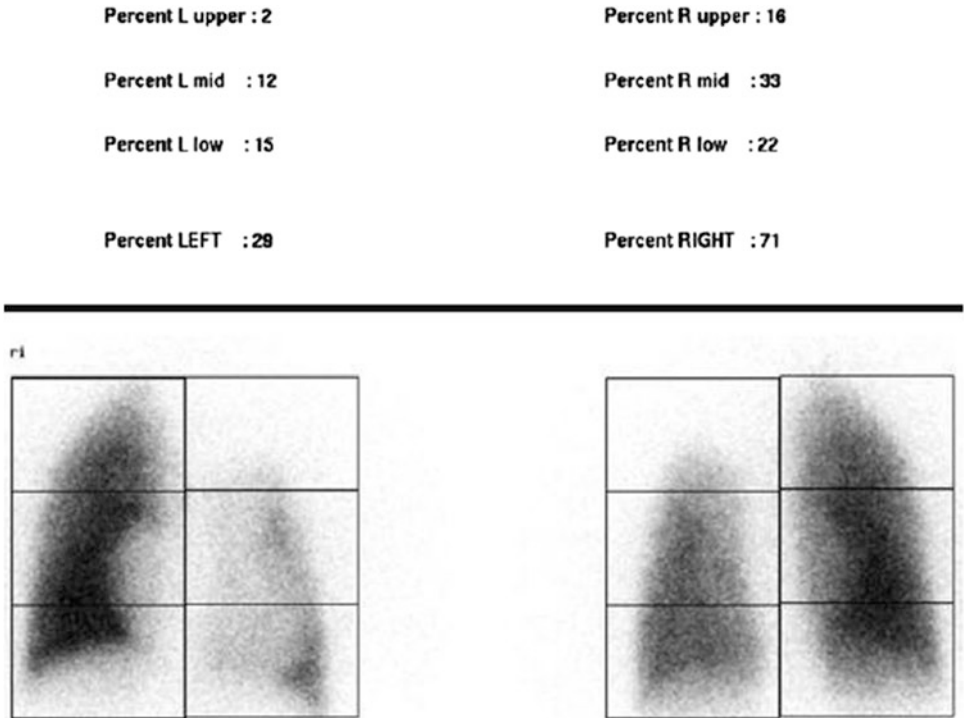


**Fig. 2** Pulmonary embolism. **a** In the initial study, there are perfusion defects present in both lower lobes that are not present in the ventilation images. **b** In the follow-up study, the perfusion defects have decreased in size. *ANT* anterior, *POST* posterior, *LAO* left anterior oblique, *RAO* right anterior oblique, *LLAT* left lateral, *RLAT* right lateral, *LPO* left posterior oblique, *RPO* right posterior oblique

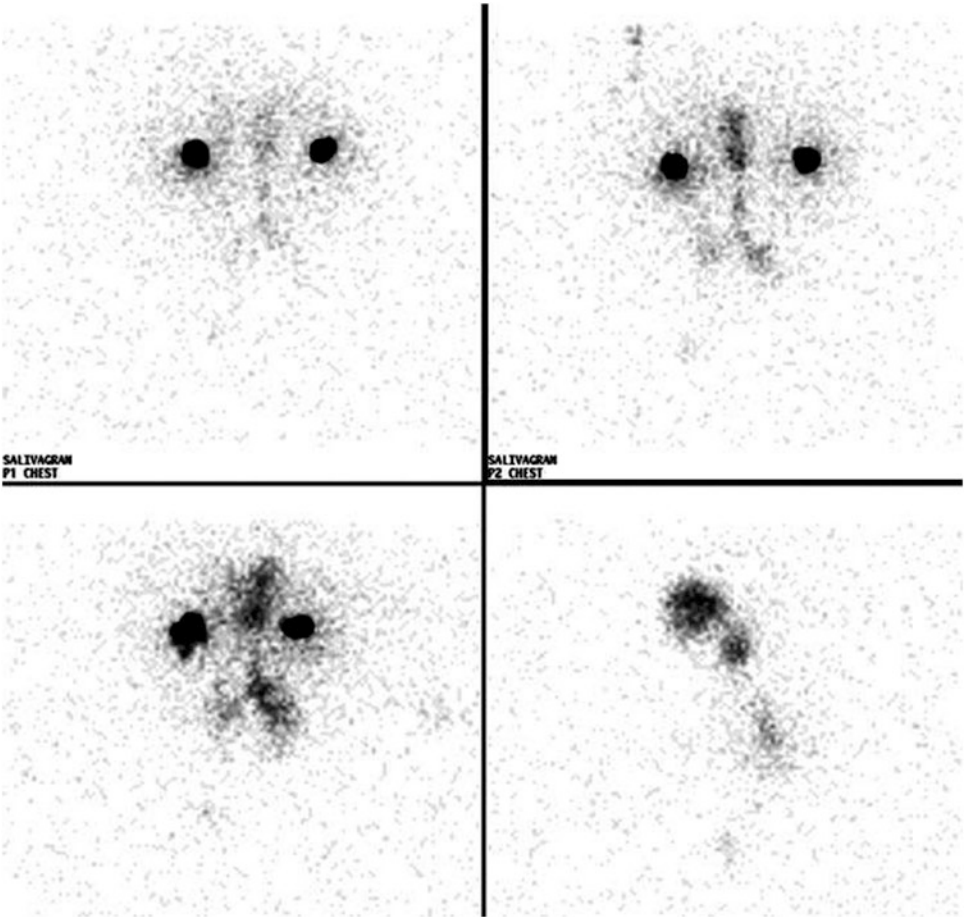
conditions in which a patient may have a ventilation perfusion mismatch in the absence of pulmonary arterial or airway obstruction.

The diagnosis of aspiration in infants is difficult. Gastroesophageal (GE) reflux imaging and pH probe studies are done to determine whether GE reflux is present. The “milk scan” was invented to try to document aspiration after reflux (McVeagh et al. 1987). A limitation of this study is that the only aspiration detectable is that secondary to GE reflux.

**Fig. 3** Quantitative lung perfusion. Each lung is quantitated in both the anterior and posterior images



**Fig. 4** Tracheal and bronchial aspiration. After swallowing of the radiolabeled saliva, some tracer entered the trachea and then entered the bronchi





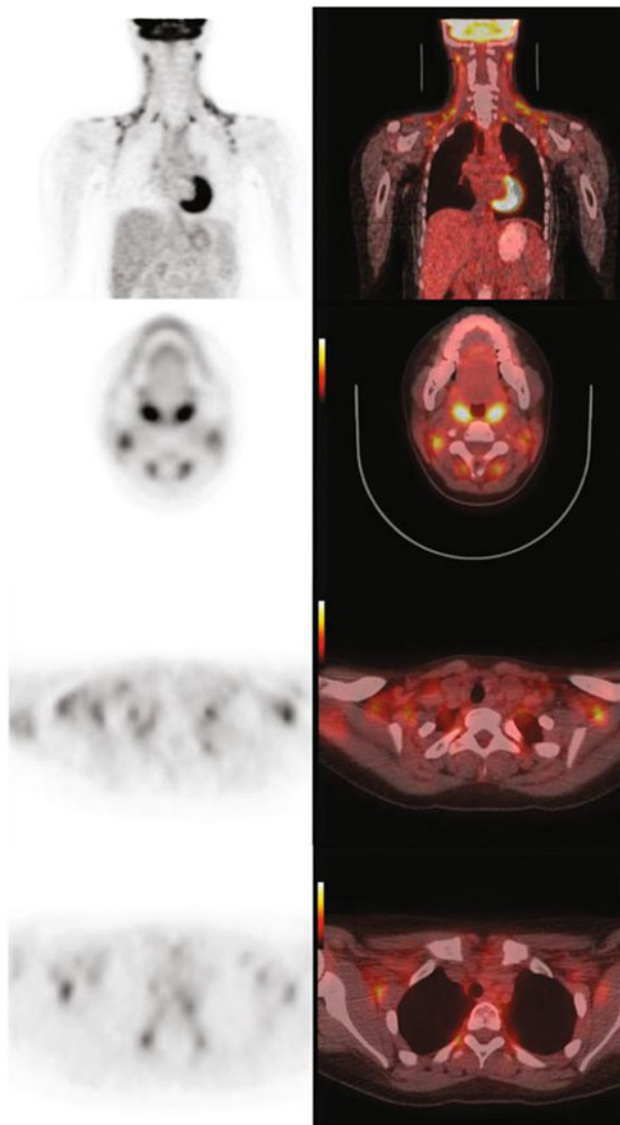


**Fig. 5** Brown adipose tissue. PET/CT demonstrates brown adipose tissue uptake of FDG on coronal views and at three levels on axial views. PET images are on the *left* and co-registered fused PET/CT images are on the *right*

The salivagram is a simple study that was devised to see if saliva was being aspirated in children with pharyngeal dysfunction (Heyman 1989; Heyman and Respondek 1989). It has proved to be a very sensitive and specific study (Fig. 4).

#### 4 Technique: PET and PET/CT Imaging

PET imaging is performed at a minimum of 40 min and preferably at 60 min after intravenous injection of FDG. The patient should be kept quiet at rest between the time of FDG injection and the beginning of imaging to prevent uptake in skeletal muscles that have been actively used

**Fig. 6** Primitive neuroectodermal tumor (PNET) of the right chest wall. An FDG-PET image demonstrates intense tumor uptake of FDG



during the FDG absorption period. All PET studies should be attenuation-corrected to avoid artifactual low grade uptake in the lungs and more prominent artifactual uptake near the skin surface; this is accomplished in older PET-only studies by measuring attenuation of the 511 keV photons using an isotopic source, and in PET/CT scanners by using the absorption data generated by the CT scan. The CT portion of the PET/CT study also provides accurate co-localization information, as long as the patient does not move between the CT and PET acquisitions. Depending on the CT acquisition parameters, the effective dose to the patient from the CT portion of a PET/CT study may be significantly less than, equal to, or greater than the effective dose from the PET portion of the study.

The techniques used for PET and PET/CT imaging of the chest are usually identical to those used for PET imaging of the rest of the body. In most cases, the PET examination of the chest is part of a study that may extend from the base of the brain either to the thighs or ankles. Key technical factors in PET imaging of the chest are mostly related to the CT portion of the PET/CT examination.

CT chest radiation exposure is typically lower than that used for the abdomen and pelvis. If the PET examination is limited to the chest, the CT exposure parameters should be appropriate for chest imaging, and lower than those used for imaging of abdomen and pelvis (with a saving in radiation dose attributable to the CT portion of the study).

The optimum position of the diaphragm for detection of pulmonary nodules on CT is during full inspiration. The PET portion of the study must be performed during tidal respiration because of the much longer duration of the PET imaging phase of the study. The best anatomic match of diaphragmatic position during a PET/CT study occurs when the CT is performed during end tidal respiration or quiet tidal respiration (Goerres et al. 2003). Pulmonary nodules are best detected when the CT is acquired at full inspiration, but there will be a significant anatomic mismatch with PET



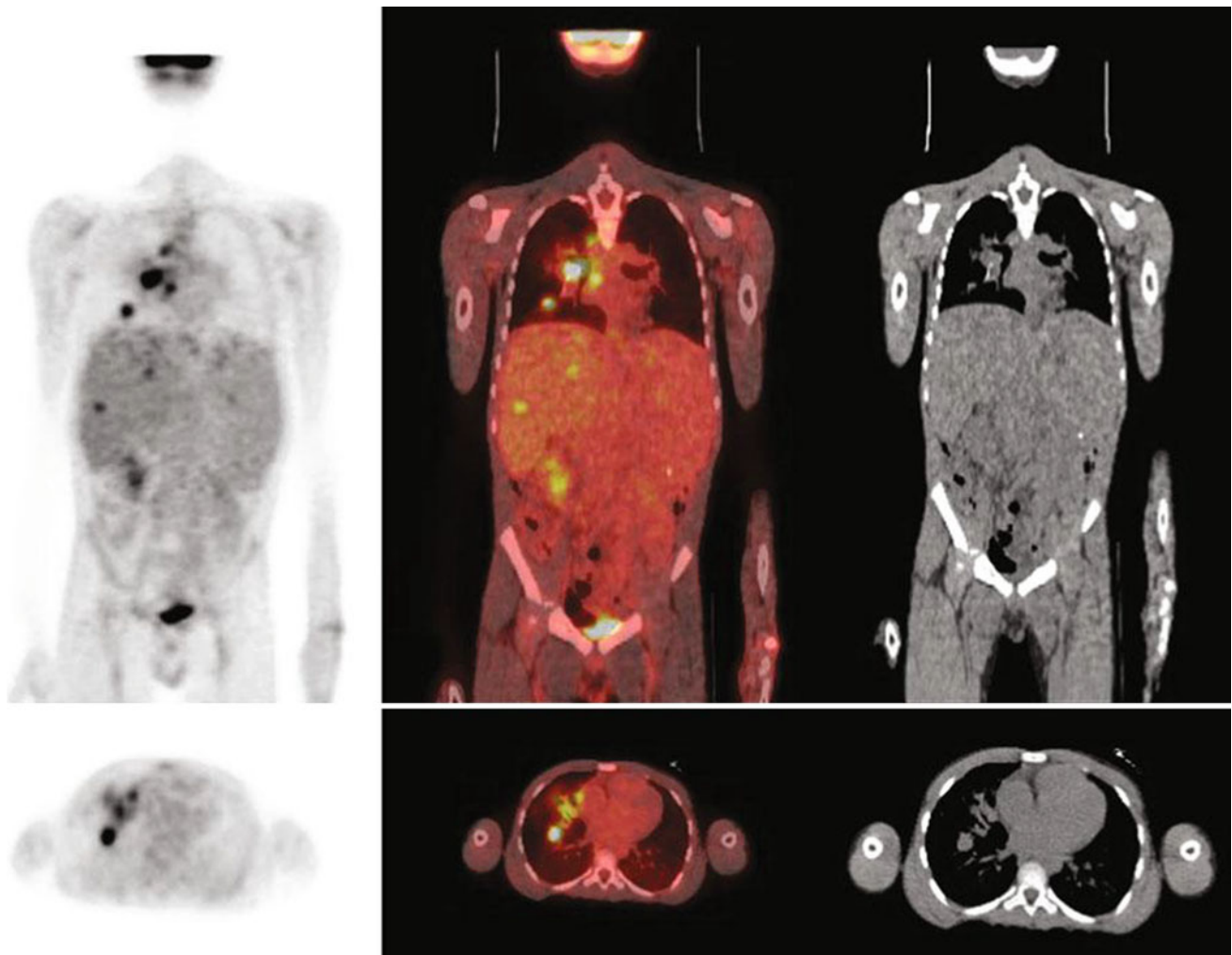


**Fig. 7** Chronic granulomatous disease. Coronal (*top row*) and axial (*bottom row*) FDG-PET images demonstrate uptake in lesions in the mediastinum, right hilum, lung, and liver. PET images are in the *left*

*column*, co-registered fused PET/CT images are in the *middle column*, and CT images are in the *right column*

images acquired during tidal respiration (Allen-Auerbach et al. 2006; Sharp et al. 2007). It may be impossible to acquire both an optimal diagnostic CT study and an accurately co-registered PET examination at the same time. At the diaphragm, co-registration errors may be as great as 3 cm. When there is a significant anatomic mismatch between PET and CT, attenuation-corrected PET images will have artifacts that will likely adversely affect image interpretation and/or mask FDG uptake abnormalities.

Brown adipose tissue is present in children and adolescents. Exposure to a cold environment will activate sympathetically mediated nonshivering thermogenesis in brown adipose tissue, and activated brown adipose tissue utilizes not only fatty acids, but also large amounts of glucose. The cold exposure may be as subtle as a mild chill from hospital air conditioning. Avid glucose uptake in brown adipose tissue may be seen in 15–30 % of children and adolescents undergoing FDG-PET imaging. Brown adipose tissue in the

neck, supraclavicular regions, axillae, and mediastinum is found immediately adjacent to many lymph node groups (Gelfand et al. 2005). Uptake in brown adipose tissue is sometimes present adjacent to costovertebral junctions and may also occasionally be seen in the upper abdomen near the kidneys. Although PET/CT should permit localization of FDG uptake to fat, this is not always possible because of small amounts of patient movement. In addition, the added sensitivity of FDG-PET in identifying tumor in some lymph nodes smaller than 1 cm is compromised when there are multiple foci of brown adipose tissue uptake in the region of the same lymph nodes (Fig. 5).

FDG uptake in brown adipose tissue can be prevented by physical and pharmacological means in most patients. Warming the patient for 30–60 min prior to FDG injection has been used in some institutions (Garcia et al. 2004, 2006; Zukotynski et al. 2009). A variety of medications may be used to prevent transmission of cold stimuli mediated

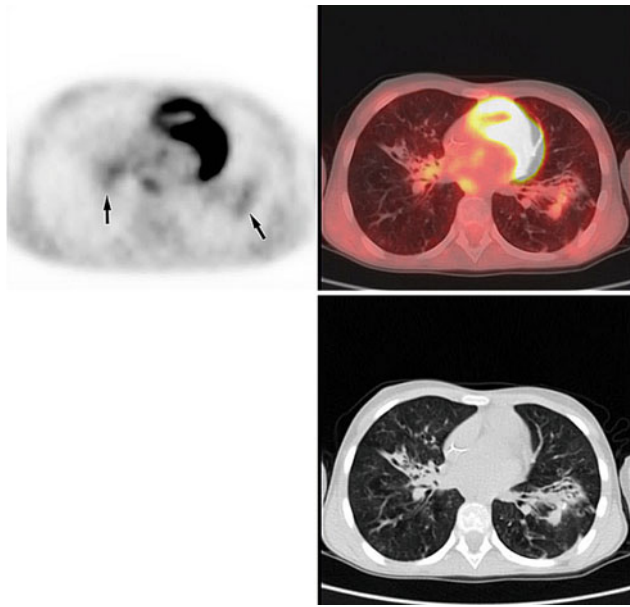


**Fig. 8** Cystic fibrosis. Axial FDG-PET (*upper left*), axial fused PET/CT (*upper right*), and axial CT (*lower right*) images in a child with cystic fibrosis demonstrate bronchiectasis and peribronchial air space disease, with abnormally increased FDG uptake at sites (*arrows*) of focally increased inflammation. Myocardial FDG uptake is physiologic

through the hypothalamus. In children and adolescents, fentanyl and diazepam have been used, with an apparent reduction in incidence of brown adipose tissue uptake of FDG strong enough to create problems in scan interpretation (Barrington and Maisey 1996; Tatsumi et al. 2004; Gelfand et al. 2005). Because of the high incidence of significant uptake of FDG in brown adipose tissue on PET scans in children and adolescents, an attempt should be made to suppress brown fat uptake in most children who undergo FDG-PET and PET/CT imaging.

## 5 Clinical Interpretation: PET and PET/CT Imaging

FDG-PET now plays a major role in the evaluation and follow-up of lymphoma. Use of FDG-PET in lymphoma is detailed in the chapter entitled Imaging of the Pediatric Thymus and Thymic Disorders by Sams and Voss in this book.

FDG-PET imaging is useful in other chest neoplasia. FDG-PET may be used for initial evaluation and follow-up of patients with chest wall tumors such as Ewing sarcoma, primitive neuroectodermal tumor (PNET), and rhabdomyosarcoma (Fig. 6). Patients can be evaluated at diagnosis to determine if metastases are present and confirm that the tumor is FDG avid. They can be followed with FDG-PET imaging to detect metastatic involvement, evaluate response to chemotherapy, and radiation and monitor for recurrence.

Detection of FDG uptake in small lung metastases is inconsistent; therefore, diagnostic quality CT imaging is recommended instead for the detection of lung metastases.

FDG uptake is not only seen in neoplasia. FDG is also taken up by cold-stimulated brown adipose tissue, by normal structures such as the thymus gland and by inflammatory processes (Hany et al. 2002).

Uptake of FDG in inflammatory processes is another example of the nonspecificity of FDG uptake. However, FDG uptake in the lung, unrelated to tumor, usually does not pose a diagnostic problem. Rather lung uptake of FDG may be used to diagnostic advantage. FDG uptake often represents an inflammatory process when seen in a region of parenchymal opacity on CT.

Increased FDG localization has been noted in a wide variety of pulmonary inflammatory processes, including sarcoidosis and many forms of pneumonitis (Bleeker-Rovers et al. 2004, 2005; Mackie and Pohlen 2005; Mascarenhas et al. 2006). FDG uptake in lung has been also used to map lung inflammation in children with cystic fibrosis, and foci of lung infection in chronic granulomatous disease (Fig. 7) (Ozsahin et al. 1998; Gungor et al. 2001). FDG uptake in lung may be demonstrated in sites of active inflammation in patients with cystic fibrosis, and follow-up FDG-PET imaging may be used to evaluate therapeutic response (Klein et al. 2009; Amin et al. 2012; Chen et al. 2013) (Fig. 8).

Uptake in inflammatory lymph nodes, however, may sometimes cause confusion, particularly low level uptake in axillary and cervical nodes. In contrast, intense uptake may be seen in mediastinal lymph nodes affected by histoplasmosis (Perko et al. 2010). FDG uptake may also be seen in cutaneous and soft tissue inflammatory processes. Uptake in recent surgical incisions is distinguished with an appropriate history, physical examination, and/or reference to CT images.

## References

- Allen-Auerbach M, Yeom K, Park J et al (2006) Standard PET/CT of the chest during shallow breathing is inadequate for comprehensive staging of lung cancer. *J Nucl Med* 47:298–301
- Amin R, Charron M, Grinblat L et al (2012) Cystic fibrosis: detecting changes in airway inflammation with FDG PET/CT. *Radiology* 264:868–875
- Barrington SF, Maisey MN (1996) Skeletal muscle uptake of fluorine-18-FDG: effect of oral diazepam. *J Nucl Med* 37:1127–1129
- Bleeker-Rovers CP, de Kleijn EM, Corstens FH et al (2004) Clinical value of FDG PET in patients with fever of unknown origin and patients suspected of focal infection or inflammation. *Eur J Nucl Med Mol Imaging* 31:29–37
- Bleeker-Rovers CP, Vos FJ, Wanten GJA et al (2005) 18F-FDG PET in detecting metastatic infectious disease. *J Nucl Med* 46:2014–2019
- Blickman JG, Rosen PR, Welch KJ et al (1985) Pectus excavatum in children: pulmonary scintigraphy before and after corrective surgery. *Radiology* 156:781–782

- Chen DL, Atkinson JJ, Ferkol TW (2013) FDG PET imaging in cystic fibrosis. *Semin Nucl Med* 43:412–419
- Daftary A, Gregory M, Daftary A et al (2005) Chest radiograph as a triage tool in the imaging-based diagnosis of pulmonary embolism. *AJR Am J Roentgenol* 185:132–134
- Donnelly LF, Gelfand MJ, Brody AS et al (1997) Comparison between morphologic changes seen on high-resolution CT and regional pulmonary perfusion seen on SPECT in patients with cystic fibrosis. *Pediatr Radiol* 27:920–925
- Eyer BA, Goodman LR, Washington L (2005) Clinicians' response to radiologists' reports of isolated subsegmental pulmonary embolism or inconclusive interpretation of pulmonary embolism using MDCT. *Radiology* 184:623–628
- Forbes KP, Reid JH, Murchison JT (2001) Do preliminary chest X-ray findings define the optimum role of pulmonary scintigraphy in suspected pulmonary embolism? *Clin Radiol* 56:397–400
- Fukuda Y, Momoi N, Mitomo M et al (2010) Increasing the accuracy of lung perfusion scintigraphy in children with bidirectional Glenn circulation. *Pediatr Radiol* 40:1890–1894
- Garcia CA, Van Nostrand D, Majd M et al (2004) Benzodiazepine-resistant "brown fat" pattern in positron emission tomography: two case reports of resolution with temperature control. *Mol Imag Biol* 6:368–372
- Garcia CA, Van Nostrand D, Atkins F et al (2006) Reduction of brown fat 2-deoxy-2-[F-18]fluoro-D-glucose uptake by controlling environmental temperature prior to positron emission tomography scan. *Mol Imag Biol* 8:24–29
- Gelfand MJ (1978) Shunts of the heart and great vessels. In: *Proceedings of the 19th annual meeting and continuing education lectures of the southeastern chapter, society of nuclear medicine*, Atlanta, Georgia, pp 9.1–9.23
- Gelfand MJ, O'Hara SM, Curtwright LA et al (2005) Premedication to block [(18)F]FDG uptake in the brown adipose tissue of pediatric and adolescent patients. *Pediatr Radiol* 35:984–990
- Gelfand MJ, Gruppo RA, Nasser MP (2008) Ventilation-perfusion scintigraphy in children and adolescents is associated with a low rate of indeterminate studies. *Clin Nucl Med* 33:606–609
- Glass T, Heyman S, Seliem M et al (1991) Use of Tc-99 m MAA in determining the etiology of increasing cyanosis following SVC-PA anastomosis for the hypoplastic left heart syndrome. *Clin Nucl Med* 16:410–412
- Goerres GW, Burger C, Schwitter MR et al (2003) PET/CT of the abdomen: optimizing the patient breathing pattern. *Eur Radiol* 13:734–739
- Gungor T, Engel-Bicik I, Eich G et al (2001) Diagnostic and therapeutic impact of whole body positron emission tomography using fluorine-18-fluoro-2-deoxy-D-glucose in children with chronic granulomatous disease. *Arch Dis Child* 85:341–345
- Hany TF, Gharehpapagh E, Kamel EM et al (2002) Brown adipose tissue: a factor to consider in symmetrical tracer uptake in the neck and upper chest region. *Eur J Nucl Med Mol Imag* 29:1393–1398
- Hayward MJ, Kharasch V, Sheils C et al (2007) Predicting inadequate long-term lung development in children with congenital diaphragmatic hernia: an analysis of longitudinal changes in ventilation and perfusion. *J Pediatr Surg* 42:112–116
- Heyman S (1989) The radionuclide salivagram for detecting the pulmonary aspiration of saliva in an infant. *Pediatr Radiol* 19:208–209
- Heyman S, Respondek M (1989) Detection of pulmonary aspiration in children by radionuclide "salivagram". *J Nucl Med* 30:697–699
- Jeandot R, Lambert B, Brendel AJ et al (1989) Lung ventilation and perfusion scintigraphy in the follow up of repaired congenital diaphragmatic hernia. *Eur J Nucl Med* 15:591–596
- Jones SE, Wittram C (2005) The indeterminate CT pulmonary angiogram: imaging characteristics and patient clinical outcome. *Radiology* 237:329–337
- Klein M, Cohen-Cymbarknoh M, Armoni S et al (2009) 18F-fluorodeoxyglucose-PET/CT imaging of lungs in patients with cystic fibrosis. *Chest* 136:1220–1228
- Mackie GC, Pohlen JM (2005) Mediastinal histoplasmosis: F-18 FDG PET and CT findings simulating malignant disease. *Clin Nucl Med* 30:633–635
- Mascarenhas NB, Lam D, Lynch GR et al (2006) PET imaging of cerebral and pulmonary Nocardia infection. *Clin Nucl Med* 31:131–133
- McVeagh P, Howman-Giles R, Kemp A et al (1987) Pulmonary aspiration studied by radionuclide milk scanning and barium swallow roentgenography. *Am J Dis Child* 141:917–921
- Miniati M, Sostman HD, Gottschalk A et al (2008) Perfusion lung scintigraphy for the diagnosis of pulmonary embolism: a reappraisal and review of the Prospective Investigative Study of Acute Pulmonary Embolism Diagnosis methods. *Semin Nucl Med* 38:450–461
- Ozsahin H, von Planta M, Muller I et al (1998) Successful treatment of invasive aspergillosis in chronic granulomatous disease by bone marrow transplantation, granulocyte colony-stimulating factor-mobilized granulocytes, and liposomal amphotericin-B. *Blood* 92:2719–2724
- Parker MS, Hui FK, Camacho MA et al (2005) Female breast radiation exposure during CT pulmonary angiography. *AJR Am J Roentgenol* 185:1228–1233
- Perko R, Messinger Y, Moertel C (2010) Pseudometastasis secondary to histoplasmosis infection: false-positive PET/CT findings. *Pediatr Blood Cancer* 54:621–623
- Sharp SE, Helton KJ, Gelfand MJ, Brody AS (2007) Detection of pulmonary nodules on localization CT scans acquired during PET/CT imaging. *Pediatr Radiol* 37(1):S60
- Soler C, Figueras J, Roca I et al (1997) Pulmonary perfusion scintigraphy in the evaluation of the severity of bronchopulmonary dysplasia. *Pediatr Radiol* 27:32–35
- Sostman HD, Miniati M, Gottschalk A et al (2008) Sensitivity and specificity of perfusion scintigraphy combined with chest radiography for acute pulmonary embolism in PIOPED II. *J Nucl Med* 49:1741–1748
- Stabin MG, Gelfand MJ (1998) Dosimetry of pediatric nuclear medicine procedures. *Q J Nucl Med* 12:93–112
- Studler U, Gluecker T, Bongartz G et al (2005) Image quality from high-resolution CT of the lung: comparison of axial scans and of sections reconstructed from volumetric data acquired using MDCT. *AJR Am J Roentgenol* 185:602–607
- Tatsumi M, Engles JM, Ishimori T et al (2004) (18)F-FDG uptake in brown fat can be reduced pharmacologically. *J Nucl Med* 45:1189–1193
- Touya JJ, Corbus HF, Savala KM et al (1986) Single photon emission computed tomography in the diagnosis of pulmonary thromboembolism. *Semin Nucl Med* 16:306–336
- Zukotynski KA, Fahey FH, Laffin S et al (2009) Constant ambient temperature of 24 degrees C significantly reduces FDG uptake by brown adipose tissue in children scanned during the winter. *Eur J Nucl Med Mol Imag* 36:602–606

---

# Helical Multidetector Chest CT

Pilar García-Peña, Tom A. Watson, and Catherine M. Owens

## Contents

<b>1</b>	<b>Introduction</b> .....	75
<b>2</b>	<b>Technical Considerations</b> .....	76
2.1	Helical Technique.....	76
2.2	Personnel and Environment Requirements.....	79
2.3	Previous Exam Evaluation.....	79
2.4	Preparation of the Patient: Fasting Requirements.....	80
2.5	Immobilization and Other Practical Tips.....	80
2.6	Breath-Holding Information.....	80
2.7	Sedation.....	80
2.8	Intravenous Contrast Material Administration.....	83
2.9	Technical Parameters and Protocols.....	86
2.10	Image Postprocessing.....	89
2.11	Newer Advances in CT.....	95
<b>3</b>	<b>Helical Chest CT Main Applications</b> .....	98
3.1	Evaluation of Pulmonary Nodules and Chest Masses.....	99
3.2	Evaluation of Vascular Anatomy: CT Angiography.....	101
3.3	Evaluation of Central Airways.....	104
3.4	Evaluation of Difficult Areas: Cervicothoracic Junction, Peridiaphragmatic Area, and Chest Wall.....	106
3.5	Evaluation of Critically Ill Patients.....	106
3.6	Evaluation of Inconclusive Images on Chest Radiography.....	106
<b>4</b>	<b>Conclusions</b> .....	106
	<b>References</b> .....	107

---

## Abstract

There has been a revolution in the technology of helical computed tomography, with increased speed of acquisition of the CT examinations, improvements in image quality, reduction in volume of intravenous contrast material required and a significant reduction in the need for sedation. All of these technological improvements have particular clinical benefits for children. Indeed many of the significant advances in CT technology are invaluable when studying the airways and cardiovascular structures. These improvements in CT angiography, with consequent isotropic resolution, allow excellent quality multiplanar reconstructions, with holographic three-dimensional reformatted images, available to clinicians that will facilitate best clinical diagnostic and surgical planning. The positive benefits of CT must be considered in the light of potential radiation exposure risks. We are obliged to produce low-dose, weight-based paediatric protocols, which are optimised to provide images that are ‘fit for diagnostic purpose’. We use this chapter as an opportunity to outline the technical aspects of helical MDCT technique, the many potential clinical indications where thoracic CT may benefit children, and we suggest protocols which may be used in children—a very precious commodity!

---

P. García-Peña (✉)  
Professor Emeritus in Paediatric Radiology,  
Department of Paediatric Radiology, Vall d’Hebron Hospitals,  
Ps. Vall d’Hebron 119–129, 08035 Barcelona, Spain  
e-mail: plgarciapeña@gmail.com

T. A. Watson  
Department of Paediatric Radiology,  
Great Ormond Street Hospital for Children,  
NHS Trust, Great Ormond Street, London, WC1N 3JH, UK

C. M. Owens  
Department of Cardiorespiratory Radiology,  
Great Ormond Street Hospital for Children,  
NHS Trust, Great Ormond Street, London, WC1N 3JH, UK

---

## 1 Introduction

There has been much (adverse) publicity over the last decade regarding the use of computed tomography in the medical setting (Brenner and Hall 2007), which has raised public awareness on a global scale. This has resulted in an increased public interest in the importance of justification of computed tomography (CT) by the referring clinical teams. It is important to perform a risk benefit analysis at this time, and to assess whether CT is the only modality that can answer the clinical question posed. Other modalities such as MRI or US



can be used in the abdomen and pelvis, but chest CT is still the preferred choice for imaging lung parenchymal disease.

Once CT has been deemed the most appropriate test, the radiology team must optimize the CT technique so that the best quality images (which are “fit for diagnostic purpose”) are acquired at as low a radiation dose as is possible (García-Peña and Lucaya 1999). This will follow the ALARA, i.e., As Low as is Reasonably Achievable principle.

With this in mind we set out to address important issues, which will help to address the current status of chest CT and its importance in clinical practice and also to provide tips and tricks to enhance image quality via optimization of acquisition and prudent use of post-processing techniques.

Computed tomography in children poses a set of unique problems that are not encountered in adults. The relative lack of visceral fat combined with motion inherent to the small child, (cardiac respiratory and otherwise) results in degradation of image quality, making the recognition of normal anatomical structures and some pathologies more difficult.

The recent major advances in technology, in conjunction with meticulous attention paid to CT technique, and enhanced training of radiologists and technicians have all combined together to improve the sensitivity and specificity of pediatric CT imaging, and have resulted in more precise diagnostic possibilities.

The introduction of helical CT, and more specifically, multidetector CT (MDCT), has further increased the utility, and hence extended the indications for CT in the evaluation of pediatric patients.

Many of the significant changes in current diagnostic practice are solely related to the introduction of helical CT technology and MDCT, which have enabled the study of airway and vascular structures, the development of CT angiography and virtual endoscopy, and improvements in the quality of multiplanar reconstructions.

Helical CT technology has demonstrated real and significant benefits for pediatric patients.

The use of IV contrast agents can be optimized, sedation rates reduced, and radiation exposure to the patient can be decreased, by using extended pitch and by eliminating the need to rescan nondiagnostic data.

MDCT radiation doses can be significantly reduced using custom designed, in-house modification of manufacturers’ protocols, balancing adequate signal-to-noise ratio with diagnostic image quality which are “fit for diagnostic purpose.”

MDCT also improves the overall image quality of two- and three-dimensional (2D and 3D) reconstructions, an important factor when analyzing specific diseases in children.

## 2 Technical Considerations

### 2.1 Helical Technique

In contrast to conventional CT, which is based on the collection of data from sequential scans, helical CT data is obtained continuously during table motion and results in a volumetric acquisition of scan data. If direct reconstruction were performed on these data the resulting images would be of poor quality, being compromised by motion artifacts.

Thus, to compensate for the problems induced by table motion, the image data is interpolated prior to reconstruction (Brink et al. 1994b; Brink 1995; Napel 1995; Siegel and Luker 1995; Siegel 2003).

When compared to conventional section-by-section CT, helical CT has a number of advantages in the examination of pediatric patients. By using the reconstruction capabilities of helical CT we can obtain overlapping slices, a fact that improves lesion depiction without increasing radiation exposure. Post processing of overlapping slices provides high-quality 2D and 3D images, extending the diagnostic applications.

Fortunately in children, due to the possibility of very thin data acquisition with MDCT equipment, it is usually unnecessary to use overlapping slices to obtain a better quality of image for reconstruction.

As a result of isotropic data set acquisition image reconstruction can be performed along any slice using z-axis interval scanning (Singh et al. 2012).

The very short scanning times allow more precise temporal delivery of contrast medium and as a result, contrast-enhanced studies can be performed during peak vascular enhancement. This also may allow a reduction of at least 25 % in the volume of contrast agent needed (Costello et al. 1992a).

As the speed of scanning a particular anatomic area is determined by the collimation thickness and the pitch (defined as the ratio of the table speed, expressed in millimeters per second to collimation thickness, expressed in millimeters multiplied by the time to acquire 360° of data), shorter scan times may help to eliminate or decrease motion artifacts (Rubin et al. 1998).

Some MDCT equipment, instead of using the pitch concept, use the table feed concept expressed in millimeters (millimeters that table moves after each acquisition). High-speed acquisition allows high-quality 2D and 3D image reconstruction and decreases the need for sedation (a very important consideration in pediatric patients).

Radiation dose can be reduced in helical scanning without compromising diagnostic image quality (Takahashi et al. 1998). This is more pertinent, as children are relatively more radiosensitive than adults and have a longer life span in which to manifest radiation-related disease.

Radiation dose is a contentious issue in pediatrics. It is claimed that high cumulative radiation doses may be associated with an increased lifetime risk of brain tumors (Pearce et al. 2012).

As proposed by the ALARA “as low as reasonably achievable” principle, the selection of appropriate scanning parameters focuses on the optimization of image quality, while delivering the lowest possible radiation dose and shifting the risk–benefit balance toward benefit (Shrimpton and Edyream 1998; Callahan 1998; Paterson et al. 2001; Oddone et al. 2005).

The various technical parameters that need to be selected for any scan include: thickness of collimation, tube current—milliamperage and kilovoltage.

The thickness of collimation is the minimum section thickness that can be acquired once the scan is finished and in a 64-row MDCT scanner is 0.6 mm. (See Tables 1, 2, and 3).

The axial images are reconstructed at 1 mm and archived to the PACS system within our hospitals. In recent years, we have made efforts to standardize low-dose protocols for the children scanned in our institution, and the currently applied parameters are summarized in the Tables 1, 2, 3, and 4.

Methods adopted to minimize radiation dose in MDCT are multiple.

#### Automatic exposure control (AEC)

This system focuses on the average amount of noise per slice seen as acceptable and “fit for diagnostic purpose” by the user. The mAs is adjusted accordingly and can result in significant dose reduction (that is when the mAs can be reduced).

Automated tube current modulation systems have been produced by all of the major MDCT scanner manufacturers (Greess et al. 2004).

The tube current is modified to follow the anatomy of the patient, maintaining the same noise level within the images acquired.

Two methods are available, modulation in the x- and y-axes (angular modulation) and z-axis modulation.

**Angular modulation** adjusts the tube current, while the X-ray tube passes around the patient’s body, e.g., in an adult the mAs is reduced in the AP versus the lateral position. This is more beneficial in older patients who may be wider in the side to side, compared to anteroposterior directions, whereas baby’s bodies are more spherical.

In adults, effective doses can be reduced by up to 30 % (Greess et al. 2002, 2004).

Radiation dose reduction in CT examinations of children can be achieved by an attenuation-based on-line modulation of tube current (CARE dose) (Greess et al. 2002).

**Table 1** Protocol: Chest survey

Standard chest CT (‘combiscan’)	
Scan mode	Helical
Indication	CVS anomalies
	Strictures and small tracheobronchial stenoses
	Peripheral airways disease
	Tracheomalacia
	Tumors and metastases
Anatomic coverage	Congenital lung abnormalities
	Thoracic inlet to diaphragm
	The upper abdomen is included if sequestration is suspected
Tube collimation	0.6 mm
Tube rotation	0.5 s
Slice reconstruction	1 mm
Pitch	1
Scan parameters	1–9 kg—80 kV, 60 QmAs, CTDIvol 0.88 mGy
	10–15 kg—100 kV, 30 QmAs, CTDIvol 1.0 mGy
	16–25 kg—100 kV, 38 QmAs, CTDIvol 1.26 mGy
	26–35 kg—100 kV, 42 QmAs, CTDIvol 1.4 mGy
	36–45 kg—100 kV, 48 QmAs, CTDIvol 1.6 mGy
	Over 46 kg—100 kV, 55 QmAs, CTDIvol 1.83 mGy
Intravenous contrast	2 mls/kg (max 100 ml)
	Scan delay of 20–30 s from start of injection depending on patient weight
Reconstruction kernels	B30f 1 mm (mediastinal window)
	B60f 1 mm (lung window)
Tube current modulation	On

Imaging of the pediatric chest with a 64-row MDCT scanner

This **z-axis current modulation** needs the selection of an acceptable noise level and a maximum and minimum tube current, which are chosen before the examination. Thence, the scanner can adjust the tube current within the selected range and maintain the noise level, using data from the scout view or during gantry rotation. The reduction in tube current can be around 40 % using this technique (Karla et al. 2004).

However, the choice of tube current must be accurate prior to the examination as the automated dose control is set to preferentially overexpose to ensure good quality images and may in fact result in a dose increase (Gudjónsdóttir et al. 2010).

**Table 2** Protocol: HRCT chest scanning parameters on a 64 slice system

	HRCT
Scan mode	Sequential
Scan parameter	100 kVp 1–25 kg—30 QmAs, CTDIvol 0.18 mGy 26–35 kg—35 QmAs, CTDIvol 0.21 mGy 36–50 kg—42 QmAs, CTDIvol 0.25 mGy Over 50 kg—60 QmAs, CTDIvol 0.36 mGy
Tube rotation time	0.5 s
Tube collimation	2 × 1 mm
Table feed	Inspiration—10 mm Expiration—25–35 mm dependent on size of child
Coverage	Inspiration—apices to base of lungs Expiration—3 evenly spaced slices to cover upper/middle/lower lobes Nonbreath-hold—2 slices each in R & L decubitus position
Tube current modulation	On
Recon slice width	1 mm
Recon Kernel	1st recon—B60 2nd recon—B30
Window width/level	1st recon—high-resolution lung parenchyma setting 2nd recon—mediastinum setting
Contrast media	–
Scan delay	–

### Reduction of the kilovoltage to 100 kVp when imaging the thorax

Further reduction to 80 kVp is possible for CT Angiography, but as resolution of the lung parenchyma is not always ideal (especially when looking for subtle patterns of interstitial lung disease) the 80 kVp option is applied only if lung pathology is unlikely and vascular anatomy is of paramount importance.

### Iterative reconstruction

One of the most important advances in CT technique has been the development and utilization of new iterative reconstruction techniques which have resulted in a dramatic reduction in CT examination dose (Silva et al. 2010).

Iterative reconstruction techniques attempt to accurately rebuild images by focusing on noise reduction. One type of iterative reconstruction technique, Adaptive Statistical Iterative reconstruction (ASIR), uses information obtained from the Filtered Back Projection (FBP) algorithm as an initial building block for image reconstruction. The ASIR

**Table 3** Protocol: CT angiography scanning parameters on a 64 slice system

	CT Angiography
Scan mode	Helical
Scan parameter	1–15 kg—80 kV, 60 QmAs, CTDIvol 0.88 mGy 16–25 kg—100 kV, 30 QmAs, CTDIvol 1.0 mGy 26–35 kg—100 kV, 36 QmAs, CTDIvol 1.2 mGy 36–45 kg—100 kV, 45 QmAs, CTDIvol 1.5 mGy 46–55 kg—100 kV, 52 QmAs, CTDIvol 1.7 mGy Over 56 kg—100 kV, 62 QmAs, CTDIvol 2.1 mGy
Tube rotation	0.5 s
Tube collimation	64 × 0.6 mm
Pitch	1
Coverage	Dependent on indication
Tube current modulation	On
Recon slice width	1 mm
Recon Kernel	1st recon—B30 2nd recon—B60
Window width/level	1st recon—medium soft, mediastinum 2nd recon—high-resolution for lung parenchyma
Contrast media	2 mL/kg to maximum 150 mL
Scan delay	Bolus tracked—ROI outside body

model then uses matrix algebra to transform the measured value of each pixel ( $y$ ) to a new estimate of the pixel value ( $y'$ ). This pixel value is then compared with the ideal value that the noise model predicts. The process is repeated in successive iterative steps until the final estimated and ideal pixel values ultimately converge.

Using this method, ASIR is able to selectively identify and then subtract noise from an image. Thus, ASIR reconstructs images with lower image noise compared with FBP.

When there are specific clinical indications, for example when high-contrast lesions are surrounded by low-contrast structures, dedicated low-dose protocols have been routinely used in the past in an effort to minimize radiation dose. For example, studies have suggested that low-dose CT is adequate for CT colonography (Cohnen et al. 2004), pulmonary CT angiography, and tracheobronchial evaluation (Heyer et al. 2007).

It is important to remember that although satisfactory for the dedicated evaluation of the intended specific anatomy,

**Table 4** Dose comparison for different scanning protocols, based on actual patient data from GOSH

Effective dose per study (mSv)					
	Standard chest	HRCT	CTA	CXR	
<15 kg	1.6	0.4	1	0.00487	0.00799
<25 kg	1.5	0.4	1.9	0.00874	0.01086
<35 kg	2.2	0.6	2.6	0.01163	0.00968
35–44 kg	2.5	1.1	2.8	0.01769	0.01452

these protocols were implemented by knowing that image quality would be significantly reduced outside the immediate area of interest.

The application of the ASIR algorithm to these low-dose studies can significantly reduce image noise and improve overall image quality when compared with low-dose standard FBP techniques.

### Pitch

Unlike the helical single-row scanner, an increase or decrease in table feed on the MDCT scanner only affects the overall scanning time when Automated Exposure Control is enabled. The tube current is automatically compensated to ensure that the present effective and total mAs is delivered. In other words, an increase in table speed triggers a concomitant increase in mA and this has no impact on the effective dose delivered.

Anatomical coverage for imaging of the pediatric thorax extends from the thoracic inlet to the diaphragm, but a greater degree of coverage may be warranted in certain clinical cases, such as an extralobar pulmonary sequestration, that may be present in the upper abdominal cavity.

In order to increase spatial resolution, the **field of view (FOV)** should closely approximate the cross-sectional area of the body part being studied. A large FOV would result in waste of matrix space and partial volume averaging would generate poor quality images (Callahan 1998).

Helical equipment is remarkably silent as compared to conventional scanners. For this reason, pediatric patients are not usually frightened and remain calm and still. This in itself reduces the need for sedation and improves image quality.

The quality of multiplanar reformatted images, MPR (coronal, sagittal, and curved) and 3D images is significantly improved with MDCT, which decreases motion-related artifacts and provides a smoothing effect of overlapped image reconstruction or due to the thin collimation of the new equipment, reducing stair-step artifacts. Such 3D images can be optimally rotated to display specific normal and abnormal structures allowing analysis of selected parts.

### 2.1.1 Limitations and Disadvantages of Helical CT Technique

The technical limitations previously associated with Helical CT technology have been rendered largely obsolete. The new generation of helical MDCT scanners provides a vast

improvement in volume coverage speed with better resulting diagnostic image quality (Hu et al. 2000).

### 2.1.2 Pitfalls of Helical CT Technique

A common technical artifact associated with traditional helical data acquisition is the stair-step artifact (Wang and Vannier 1994). These occur along high-contrast interfaces that are oriented obliquely to the direction of patient travel. Stair casing causes the edges of longitudinally oriented structures to appear as steps rather than as straight lines. The thinner slice acquisition with MDCT scanners minimizes this technical artifact and image reconstructions are now very smooth and of very high-quality, the more detectors available the better the quality of the image.

Another potential pitfall with MDCT is related to commencing scanning before optimal organ or vessel enhancement by the contrast agent occurs in homogeneous fashion (Sillverman et al. 1995). These flow artifacts, caused by the mixing of contrast material and nonopacified blood are much more frequent in abdominal studies than in chest CT, in part because the circulation of blood is faster in the chest compared with abdominal blood circulation.

## 2.2 Personnel and Environment Requirements

The optimal team for performing pediatric MDCT includes a pediatric radiologist, a technician and a nurse trained in pediatric care. It is important to ensure an optimal environment for pediatric patients in the scanning area and every effort should be made to create a warm welcoming atmosphere that minimizes patient and parental anxiety. Soft lighting, toys, a quiet room decorated with children in mind, and the presence of a relative can help to comfort and console a child.

It is essential to have immediate access to a resuscitation cart with appropriate drugs and equipment for pediatric patients of all ages.

## 2.3 Previous Exam Evaluation

It is mandatory to check the patient's clinical records and all available previous imaging studies before performing a helical CT scan. This helps to decide if the indication is correct and allows the exam to be tailored to the specific requirements of the patient. It is particularly important with regard to the need for sedation and IV contrast administration. Careful planning can prevent difficulties during the study and minimize the potential for unanswered questions afterward. The radiologist/radiographer should explain all aspects of the procedure and the objectives of the study to the parents before obtaining parental consent. At our institution, outpatients are contacted by the nursing team prior to the scan date to assess the needs of each patient, i.e., sedation requirements, etc.



## 2.4 Preparation of the Patient: Fasting Requirements

The patients, parents, and nursing staffs should be informed of fasting requirements before the day of the procedure. Sometimes, no preparation is required (e.g., when studying pulmonary metastasis). When children need sedation during the examination, standard fasting regimens are similar to those for a general anesthetic, water or breast milk can be given up to 2 h prior to sedation, and food up to 4 h beforehand.

## 2.5 Immobilization and Other Practical Tips

Sandbags, adhesive bandages, or blankets wrapped around the patient can all be used to immobilize the patient. It is advisable to wrap a lead apron around the child in the regions adjacent to those to be scanned. This protects them from scattered radiation and, at the same time, can help to immobilize the patient. Overlying radio protective bismuth latex can be placed on breasts and thyroid gland to minimize local radiation absorption to these radiosensitive tissues. However, it should be noted that the use of these devices can increase the overall mAs with some scanners if automatic dose modulation is used and therefore increase overall dose. There is evidence to suggest that performing an initial scout view without shielding prevents the scanner increasing the dose (Coursey et al. 2008).

Toys hanging from the gantry and films or image projection on the gantry can be used to attract the attention of the child and help to keep them quiet. A system for maintaining body temperature such as warming lamps or heating blankets should be used in infants.

## 2.6 Breath-Holding Information

Children under 6 years of age who cannot follow breath-holding commands are examined under normal quiet breathing. In this age group, attempts at breath holding usually result in exams severely compromised by artifacts. Older children are carefully instructed in breath holding before the study.

## 2.7 Sedation

Helical CT and MDCT have reduced the need for sedation (White 1995; Kaste et al. 1997; Sacchetti et al. 2005). Since the introduction of silent helical CT and high-speed MDCT in our institutions, our overall rate of sedation is only 1 % of patients for MDCT versus 18 % for our previous

**Table 5** Protocol: Suggested delay times from the injection of contrast medium

	Manual injection	Pressure injector
Scan initiation time delay	Immediately from termination of injection	20–30 s from start of injection. If a central line is used, this time will be reduced. Bolus tracked studies are operator dependent
Flow rate		1.5–2 ml/s
Age range	All age groups	All age groups

**Table 6** Protocol: Rate of contrast media injection depending on catheter or needle gauge

Catheter/Cannula		Needle	
Gauge (g)	Flow rate (ml/s)	Gauge (g)	Flow rate (ml/s)
26	1.0	25	0.5
24	2.0	23	0.5–0.8
22	3.0	21	0.8–2.0
20	4.0	19	2.0–4.0

conventional CT studies. In 2012, using new generation CT equipments, we performed only 1 % of our thoracic CT studies with sedation.

Previously, in patients under the age of 6 years, 50 % required sedation with conventional CT and only 8 % with helical CT and 2 % with MDCT. Among the patients in this age group who needed IV contrast, 77 % had to be sedated with conventional CT, only 18 % with single slice helical CT and 3 % with MDCT. Finally, among those who did not need IV contrast material, 24 % required sedation with conventional CT, only 2 % with helical CT and 1 % with MDCT. We believe that the relative silence of the helical equipment and the high speed of acquisition have determined this reduced need for sedation. It has been widely reported that with multidetector CT the rate of sedation can be reduced (Pappas et al. 2000).

In outpatients, the need for sedation is assessed by the clinician prior to the investigation and by a dedicated nursing sedation team who telephone the parents prior to admission. A standardized questionnaire is used to evaluate the need for potential sedation.

Despite this, there will still be a need for a final sedation assessment once inside the gantry.

In our experience, infants less than 3 months of age can be successfully imaged after normal feeding and swaddling. Sleep deprivation, the night before the examination has proven to be of no benefit in either decreasing the dose of sedative drugs, or the number of sedation procedures, and can be disruptive for patients and parents.

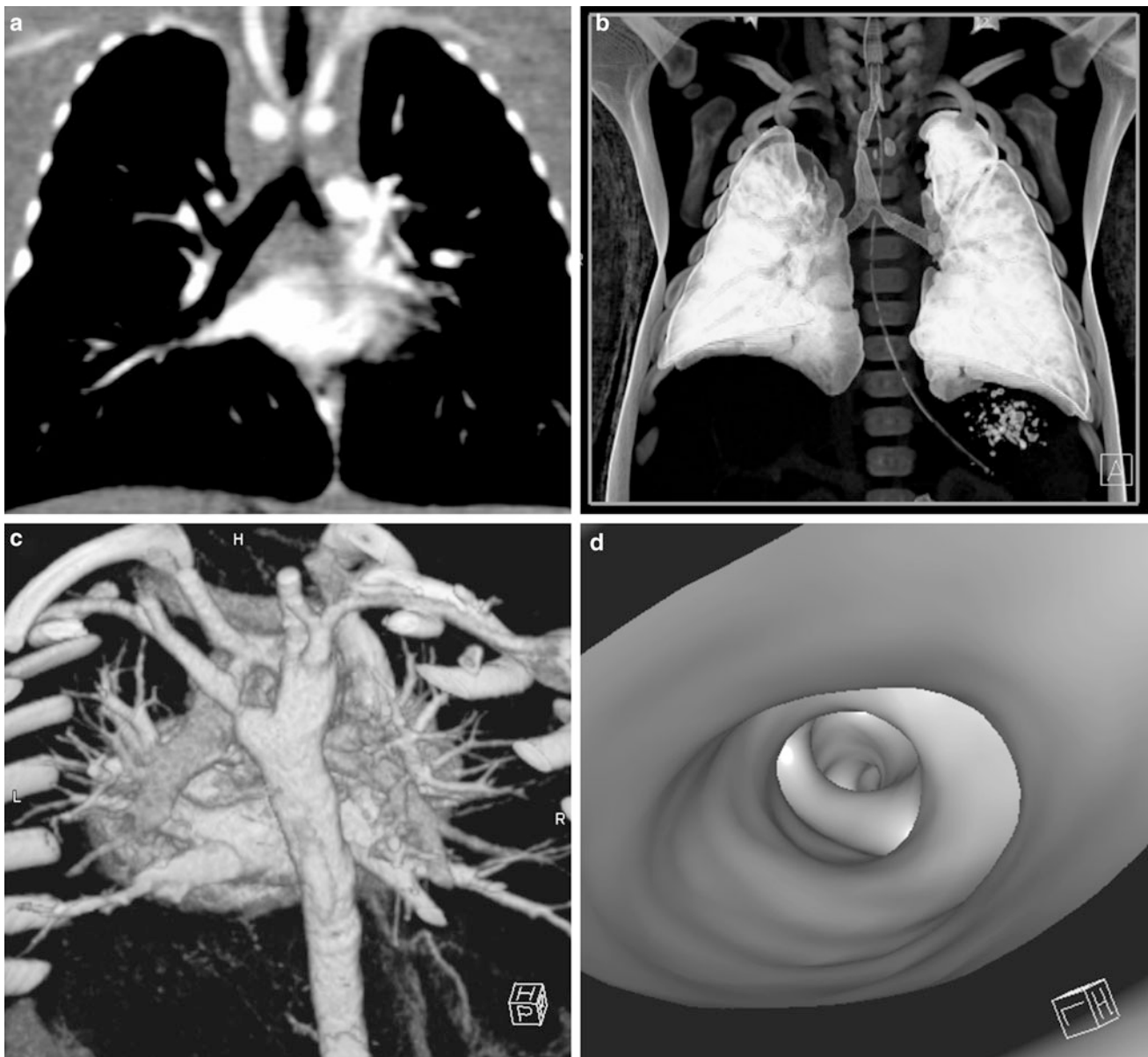


**Fig. 1** Post-processing techniques. **a** Multi-planar reformats (MPR). MPR initially in coronal and sagittal planes should be the initial post-processing technique: with pixel isotropy, no information is lost, and the reformatted plane often gives a better depiction of the anatomical relationships. The coronal image shows a double aortic arch and its effect on the airway. **b** Multiplanar volume reconstructions (MPVRs). MPVRs combine volume rendered images with multi-planar imaging to produce 3D 'slabs' of the area of interest. By applying a minimal intensity projection technique a view of the airways can be produced such as this example of a congenital tracheal and left main bronchial stenosis in a 3-year-old boy with bronchiolitis. This technique is sometimes referred to as a "virtual bronchogram". Historic stair-step artefact in traditional single slice volume-rendered image (bronchographic anteroposterior

view). The artefact occurs along the left bronchus, which is oriented obliquely to the direction of patient travel during data acquisition. **c** Three-dimensional (3D) volume rendering (VR) is an excellent technique for giving an overview of complex vascular anatomy. This example, image weighted on SSD technique is a posterior view of the great vessels with the spine and posterior ribs 'cut-away', showing a double aortic arch with a dominant right arch. **d** Virtual bronchoscopy is a supplementary volume rendering technique that produces images simulating the view from fiberoptic bronchoscopy. The point of view is placed in the airway. This example demonstrates complete tracheal rings in congenital tracheal stenosis: note the abnormally rounded shape to the airway, which is normally ovoid

Before performing an examination with the use of sedation, the radiologist must decide whether benefits outweigh the potential associated risks, and verify that fasting requirements have been observed. In our institution, informed

consent for sedation is covered by the standard consent for admission and CT scan examination.

There are several contraindications to the use of sedation at our institution. These include: raised intracranial pressure,

**Fig. 2** CT angiography of a pulmonary sequestration in a 6-year-old boy who was asymptomatic, but had a persistent dense image in the left pulmonary base. **a** Axial CT image. A large vessel is seen arising from the aorta, with multiple branches supplying a pulmonary mass.

**b** Anteroposterior maximum intensity projection image. Three systemic vessels coming from the aorta are seen to feed the pulmonary sequestration.

**c** Posteroanterior shaded surface display (SSD) image. The 3D depth perception created by SSD technique improves recognition of spatial relationships of the three vessels arising from the aorta. Two veins are also shown in the upper area of the image. With a cine-loop rotating image, the origin and the course of vessels can be better depicted



airway obstruction, gastroesophageal reflux with aspiration risk, and severe renal/hepatic failure.

We do not sedate children under 45 weeks gestation, and a “feed and wrap” protocol is usually sufficient at this age.

In children older than 45 weeks gestation but under 15 kgs we use oral Chloral Hydrate at a dose of 50 mg/kg (to a maximum dose 2000 mg).

When using this regimen and if IV contrast injection is contemplated, the intravenous line is placed in the preparation room before the patient is brought to the CT unit.

In our hospital in Spain, patients of 18 months of age and older, who need sedation, are given intravenous sodium pentobarbital, 6 mg/kg to a maximum dose of 200 mg, diluted in 10 ml saline. The syringe containing the sedation must be appropriately labeled with the drug name. A dose of 2–3 mg/kg should be given initially as slow bolus over 1–2 min. In most children, this dose is adequate and they will fall asleep within the next 4–5 min. If not, an additional dose of 2–3 mg/kg may be given. If the patient still remains awake an additional dose of 2 mg/kg can be given some 30 min later. However, this is rarely necessary. Occasionally, in some patients over 6 months of age who need IV contrast, sodium pentobarbital in the above-mentioned doses is used.

**Sedation Protocol GOSH:** (February 2012): Great Ormond Street Hospital for Children, London UK.

<45 weeks gestation—Feed and wrap only. No sedation.

>45 weeks gestation but <15 kgs—50 mg/kg Oral Chloral Hydrate.

Intravenous “top ups”

If the sedation is not effective, supplementary sedation may only be given by a doctor who is skilled in pediatric resuscitation according to the anesthesiologists practice and expertise, which will vary locally.

Intravenous midazolam is used at incremental doses of 100 µg/kg in children under 20 kgs. The dose must not exceed 300 µg/kg or 10 mg.

NB sedation will sometimes fail and these doses must not be exceeded.

If sedation fails, an anesthesia service must be booked for another day.

Every child undergoing sedation in the CT suite should receive oxygen and be monitored during and after the examination.

Pediatric sedation techniques have been extensively described in the literature (Cook et al. 1992; Frush et al. 1996; Egelhoff et al. 1997).

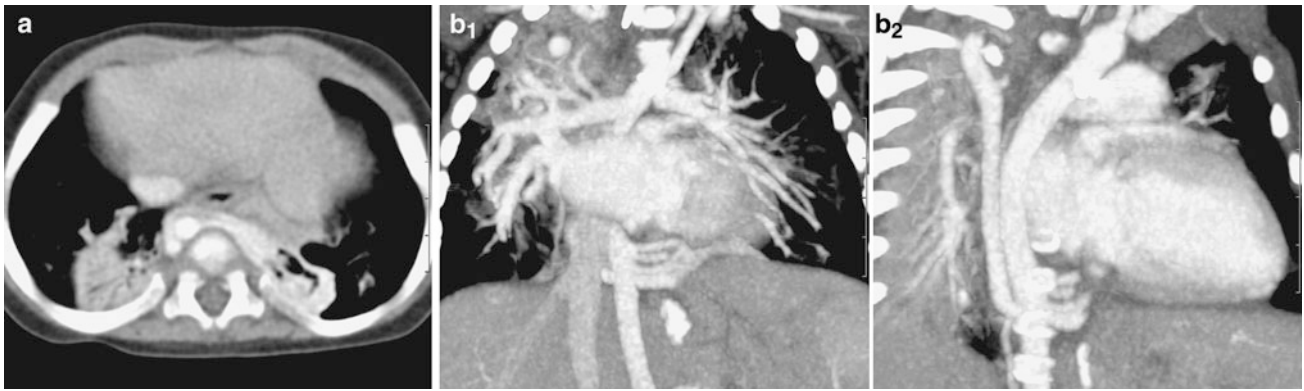


**Fig. 3** Left lower lobe extralobar sequestration in a 10-month old with multiple congenital abnormalities. **a** Axial CT maximum-intensity projection images shows a large artery arising from the aorta, supplying a L lower lobe pulmonary mass. **b** Anteroposterior

(**b<sub>1</sub>**) and sagittal oblique (**b<sub>2</sub>**) maximum intensity projection images show three systemic vessels arising from the aorta to feed the pulmonary sequestration, which drains into the azygous (systemic venous) system

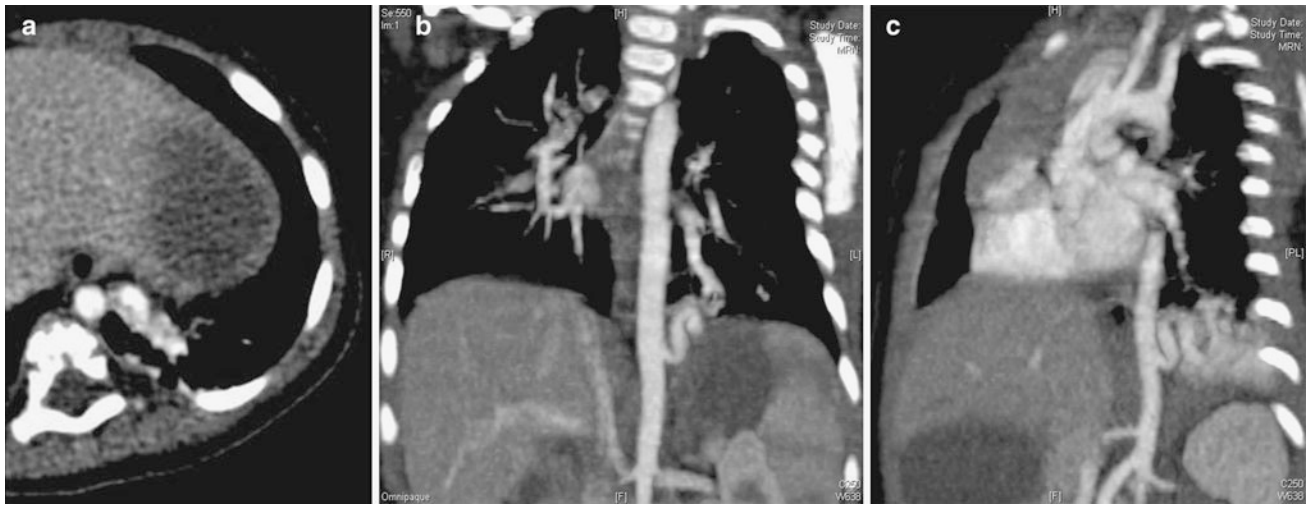


**Fig. 4** Intralobar pulmonary sequestration in a 6-month-old boy. **a** Enhanced axial CT shows a difficult-to-assess lesion in the left lower lobe. **b** and **c** Oblique MIP images better depict the lesion as an

intralobar sequestration with a looping feeding vessel from the aorta and venous drainage to the inferior pulmonary vein

## 2.8 Intravenous Contrast Material Administration

Intravenous administration of a bolus of contrast material for helical CT studies in children can be more complicated than in adults, because of the greater variations in vessel and patient size in the pediatric population. Dosage is based on the patient's body weight. Contrast material is administered by hand or power injector, depending on these variations (Kaste and Young 1996; Frush et al. 1997). To avoid the artifact caused by contrast in the axillary vein just after the injection, the syringe is placed vertically downward and filled with contrast first and then saline solution. Since saline is less dense than contrast material, it will remain in the syringe until

the end of the injection and then flush the vein free of contrast. This will help to obtain better images (Hopper et al. 2000).

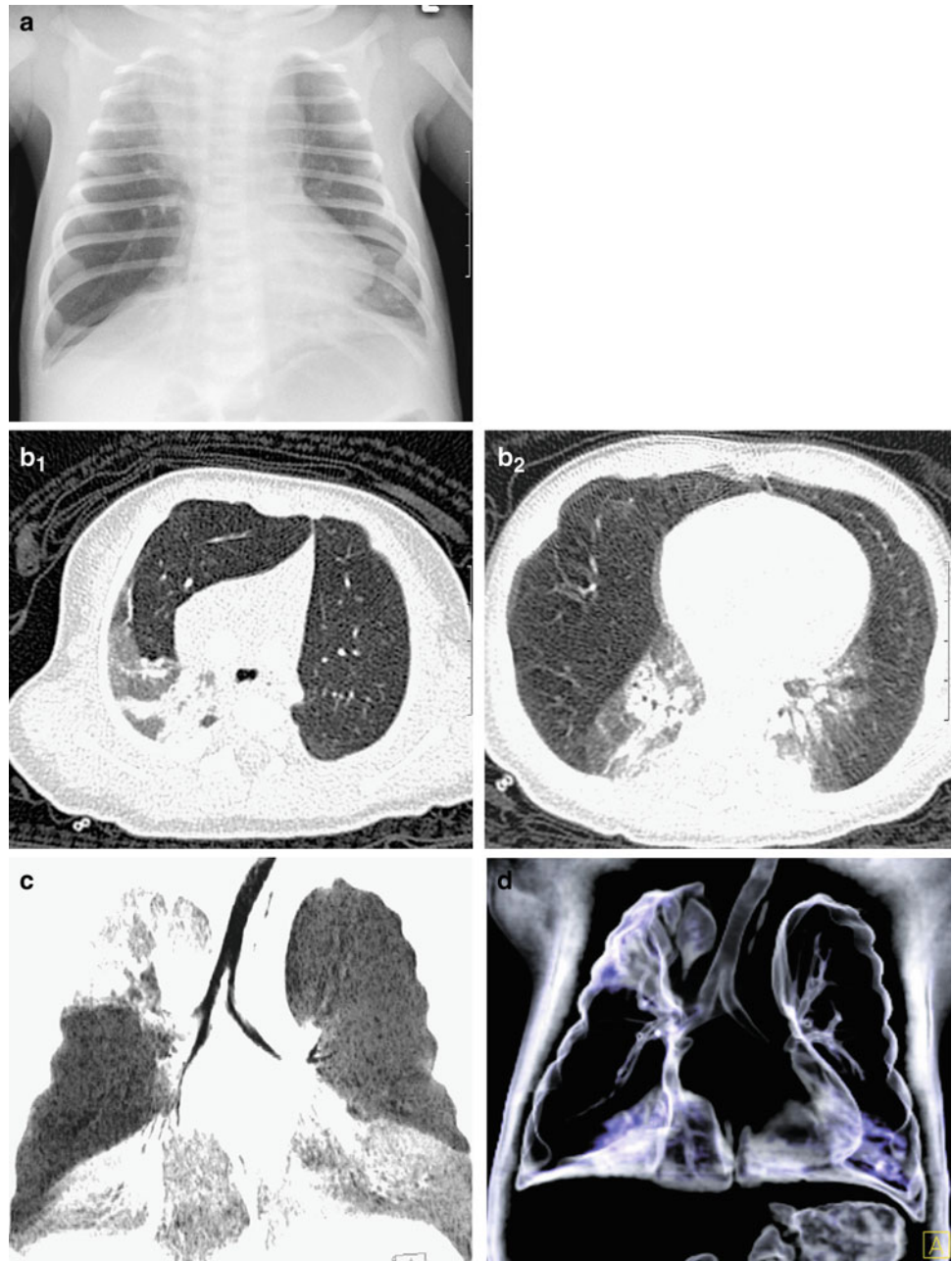
Newer power injectors have a double system of syringes, one syringe for contrast material, and a second syringe for saline solution.

Usually, the double power injector is programmed to inject the contrast material first followed by 5–10 cc of saline solution. It is necessary to check that the venous line is functioning prior to contrast media injection to prevent extravasation occurring.

If contrast material is to be given, an intravenous catheter or a butterfly needle should be placed before the child arrives in the CT suite. This will avoid the distress associated with venepuncture performed immediately before



**Fig. 5** Congenital lobar overinflation. **a** CXR. **b** (**b<sub>1</sub>** and **b<sub>2</sub>**) Axial CT images performed on high resolution (bony algorithm) show the attenuated, over-expanded lung in the right middle and left upper lobes, causing significant overdistension of the hemithorax. This is more easily perceived on the coronal MinIPs (**c**) and coronal VRTs (**d**) confirming the findings in a bronchographic fashion



scanning begins, and help to reduce the need for sedation. Local topical analgesics, such as lidocaine cream, can be applied to the intended venepuncture site to minimize the pain from cannula placement.

Usually, we use catheters 20–26 Gauge, permitting injection rates of 4.0–1.0 ml/s. Butterfly needles 19–25 Gauge, which give injection rates of 4.0–0.5 ml/s can also be used. (Tables 5 and 6).

One should always use the largest cannula suitable for each patient, though rates as low as 0.5–1.0 ml/s in children can still result in excellent enhanced studies. If the patient

already has a central intravenous line in situ, it should be used to gain venous access, using aseptic technique.

Nonionic, low- (240 mg of iodine per milliliter), or high- (300 mg of iodine per milliliter) osmolar contrast media can be used for CT examinations in children (Stokberger et al. 1998). In our practice, we use 240 mg/ml in infants and 300 mg/ml in older children.

The usual dose of contrast media is 1–3 ml/kg, to a maximum dose of 100 ml. In newborns the dose used is 2–3 ml/kg, in infants 2 ml/kg, in children 1.5 ml/kg, and in adolescents 1 ml/kg.

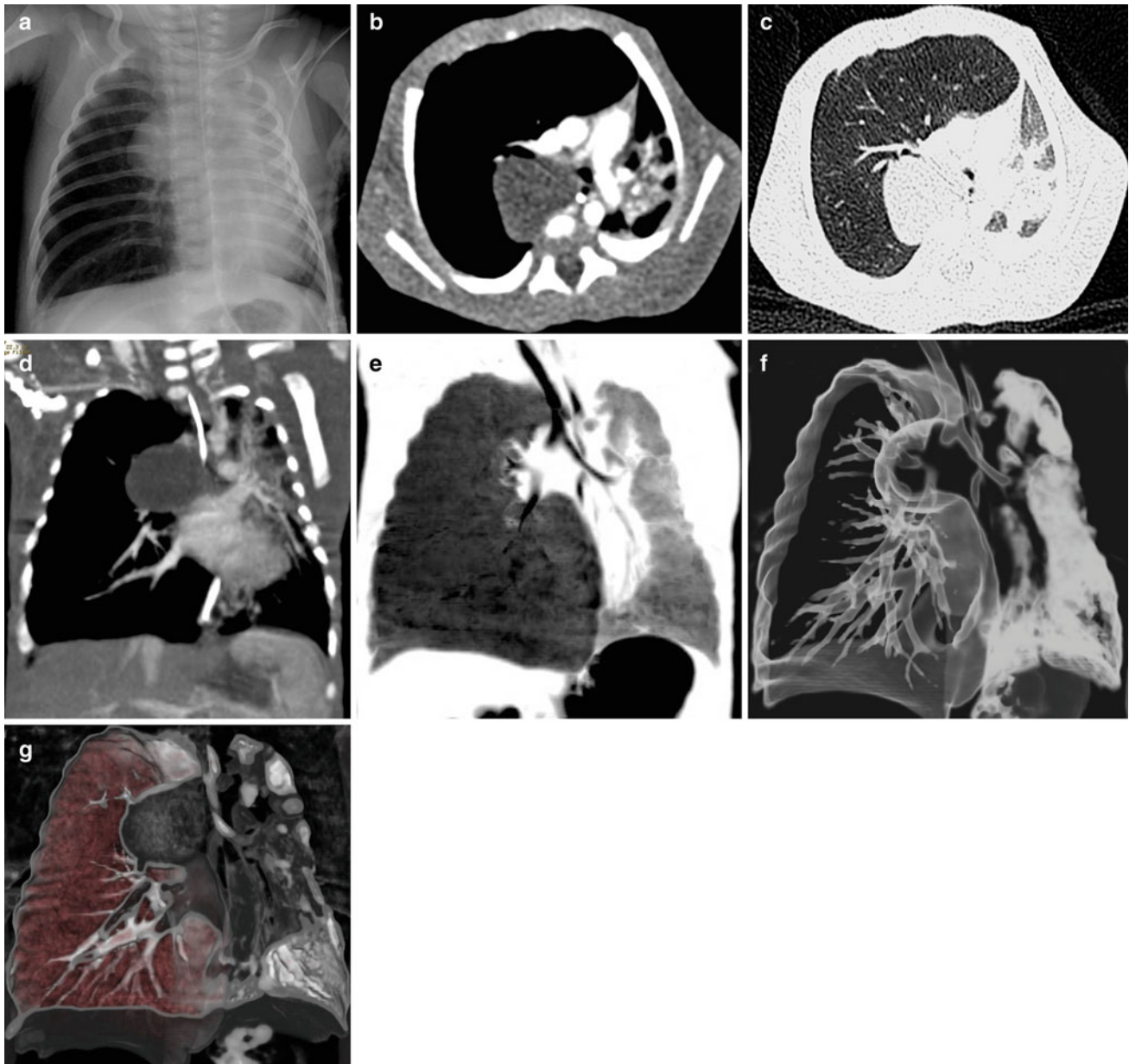


**Fig. 6** Lung over-inflation secondary to an obstructive bronchogenic cyst. One-month-old boy with respiratory distress **a** On chest X-ray, there is over-inflation of the right lung with mediastinal displacement to the opposite side. A mediastinal mass can be seen on the right side. **b** Enhanced axial CT shows a hypodense mediastinal mass on the right side, with substantial over-inflation of the right lung, and mediastinal and lung displacement to the left side. **c** Axial CT B60f for high-resolution

lung parenchyma detail shows right lung over-inflation secondary to right bronchus compression, and left lung atelectasis. **d** Coronal MPR depicts the hypodense mass and mediastinal displacement with lung atelectasis. **e** Coronal MinIP shows right lung over-inflation and right main bronchus compression. This is the best technique to evaluate the central airways and lung attenuation. **f** and **g** VR images of the bronchogram and mediastinum show similar findings

In our experience, helical CT has allowed a 20 % reduction in the volume of intravenous contrast medium given when compared to conventional CT. Similar findings have been described in the literature (Costello et al. 1992a). Optimal contrast enhancement during helical scanning depends on careful selection of the appropriate time of

scanning, as well as on choosing the precise amount of contrast material and the optimal injection rate. The rate of injection depends on the needle or catheter size (Table 6). The timing of the onset of scanning is a crucial factor in successful imaging, but is also one of the trickiest aspects of performing pediatric helical CT.

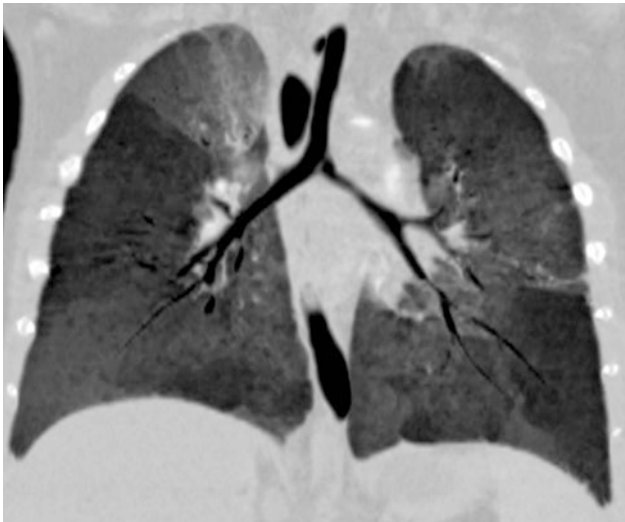


**Fig. 7** Small airway disease in constrictive obliterative bronchiolitis in a 2-year-old boy. Coronal MinIP is a good technique to demonstrate the heterogeneous attenuation of both lungs

## 2.9 Technical Parameters and Protocols

Helical CT has essentially replaced conventional CT for examinations in which the entire chest is to be evaluated. A role for low-dose high-resolution sequential CT remains with the evaluation of the pulmonary parenchyma in cases of suspected diffuse lung disease (García-Peña et al. 2011).

This technique allows scanning at spaced intervals and thus significantly reduces radiation to the patient, while providing excellent spatial and contrast resolution of the lung parenchyma.

In our institutions, we tend to use the sequential HRCT studies in the follow-up assessment of children with chronic lung disease such as cystic fibrosis and interstitial pneumonia (Ambrosino et al. 1994; Lucaya et al. 2000b; García-Peña and Lucaya 2004).

Several techniques are used for data acquisition in helical studies of the chest: standard helical CT, high-resolution helical CT, dynamic helical CT, and low-dose helical CT.

With newer MDCT scanners with multiple detector banks (64 slice +) the narrow collimation (0.6 mm) allows for a study to be performed, of high enough contrast and spatial resolution to allow optimal imaging for both mediastinal and lung parenchymal anatomy without the dose penalty that is incurred with older MDCT scanners.

The modern scanner and the dose reduction methods described above have reduced the dose of this protocol, to such a level that the value in terms of high quality parenchymal and mediastinal imaging in a single study, far outweighs the negligible increase in dose compared to the thicker collimated studies previously performed. We term this a “combiscan.”

This protocol (Table 1) has largely replaced the ‘routine chest protocol’ at our institution for most indications. This study has particular value in the assessment of vascular anomalies, tracheobronchial stenosis, dehiscence, endobronchial lesions, and central airway disease. The thinner collimation allows for excellent Multiplanar and 3D reconstructions. These can be useful in the evaluation of airway abnormalities, certain vascular lesions and cervicothoracic or diaphragmatic and peri-diaphragmatic lesions. 3D images can be rotated to optimally display pathologic entities and selected parts of the reconstruction that can then be analyzed separately.

Helical high-resolution CT scanning of the lung is performed with thin sections (0.5–1 mm) using a high-resolution reconstruction algorithm. This technique is similar to high-resolution CT scanning, but involves continuous data acquisition (Engeler et al. 1994). Lowering the milliamperage setting reduces radiation dose, but the continuous data acquisition of helical CT still delivers more radiation than the low-dose interval high-resolution CT technique (Table 2), in which acquisition is performed with thin collimation and wide sampling intervals.

Dynamic helical CT has enabled scanning at maximum inspiration (TLC, i.e., total lung capacity) and rescanning with an additional spiral acquisition at maximum expiration. This volumetric expiratory method has been used to evaluate lung attenuation in patients with air trapping and emphysema. However, it requires cooperation with breath holding at end expiration, and in young patients <5 years breath holding is problematic.

In our practice, we do not use this technique routinely to evaluate air trapping and emphysema.

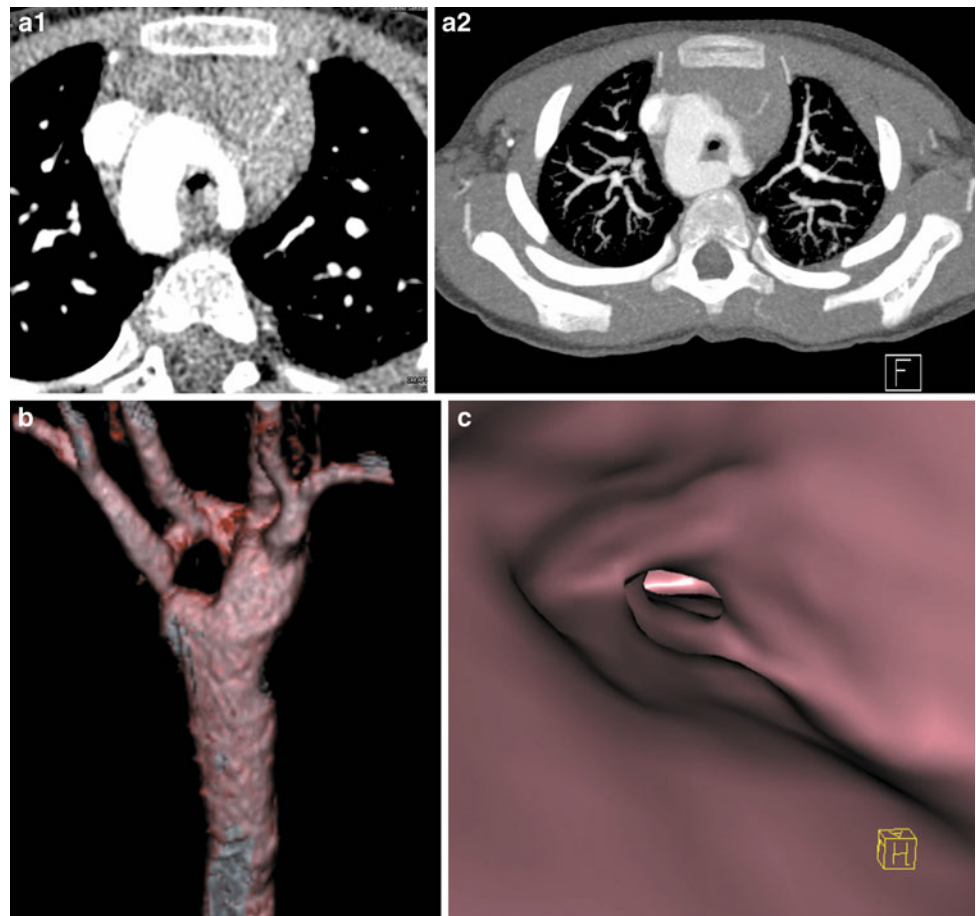
We prefer three spaced expiratory scans with a low-dose high-resolution technique (Lucaya et al. 2000a). In a non-cooperative child, 2 decubitus slices with the child lying on both sides, i.e., 2 in the right, and 2 in left decubitus positions, shows expiration in the dependent lung (Papaioannou et al. 2007).

Minimum Intensity Projections (MinIP) reconstructions of standard volume acquisitions are also an excellent method for the evaluation of heterogeneous lung parenchymal attenuation where the hyperlucent lung is a reflection of air trapping.

Software programs (available on some helical scanners) have enabled dynamic CT densitometry of the lungs (Johnson et al. 1998b). Dynamic helical CT can also be used to demonstrate respiratory changes in the cross-sectional area of the central airway, e.g., in patients with tracheobronchomalacia (Lee et al. 2009). Dynamic airway assessment may also be achieved with newer techniques such as cine MDCT and four-dimensional (4D) MDCT (Lee et al. 2010b, 2013).



**Fig. 8** Double aortic arch in a 1-month-old boy with important respiratory distress. This illustrates the more common right dominant double aortic arch on CTA: the right arch is larger than the left which is stenotic at the origin of the left subclavian artery. Note the marked narrowing of the airway at this level. **a** Thin axial image (**a<sub>1</sub>**) and axial maximal intensity projection (MIP) (**a<sub>2</sub>**). **b** Posterior volume rendered tomogram (VRT) image of the aorta showing the double aortic arch encasing the trachea. **c** Virtual bronchoscopic image shows concentric tracheal narrowing related to complete encirclement of the trachea by the double arch



Dynamic CT has been used in adults in the preoperative assessment of tracheomalacia, but the high-radiation dose has previously limited its use in children. However, the advent of 320 slice scanners allows the whole thorax to be scanned in a single tube rotation or less. The effective doses for these studies have been shown to be reduced in comparison to scanners with less coverage (Lee et al. 2009, 2010a; Joosten et al. 2012).

Low-dose helical CT scanning can be used in many situations. The X-ray tube current should be as low as possible, without compromising image quality (Takahashi et al. 1998; Rogalla et al. 1999). With helical CT technique, a further reduction in radiation dose can be achieved by increasing table speed if automated dose modulation is not available or not enabled. Use of a targeted approach to image localized processes can also reduce the radiation dose administered.

The performance of high-quality helical CT requires proper selection of technical parameters, including collimation (section thickness), field of view (FOV), table speed (or pitch), reconstruction intervals, reconstruction algorithms, scan time duration, exposure factors (kilovoltage and milliamperage), and scan initiation (Brink 1995; Frush and Donnelly 1998; Frush et al. 2002). These parameters

should be based on the patient's size and the body part to be examined. However, reduction in some of these parameters can lead to problems. Noise increases with decreasing collimation. Scan coverage decreases with reductions in collimation and table speed. Radiation dose increases with reductions in table speed and with reduction in collimation. Decreasing the reconstruction intervals increases processing time.

So, the final choice of parameters always involves a balance between these options to achieve diagnostic image resolution and a low effective dose to the patient.

MDCT scanners have subsecond gantry rotation times. So, reducing rotation time from 1 to 0.5 s, we will halve the radiation dose and the scan time if the mA is fixed (i.e., ADM is not enabled).

The kVp has not routinely been adjusted historically for body CT exams in children. Reducing the kVp reduces the radiation dose substantially, that is in an exponential fashion. In our experience, when the voltage is dropped from 120 down to 80, the radiation dose is decreased by 40 %.

The effect on image quality is important, as both image noise and tissue contrast are affected. The kVp can be reduced (to 80 or 100), related to the child's size or when scanning body regions with high inherent contrast such as



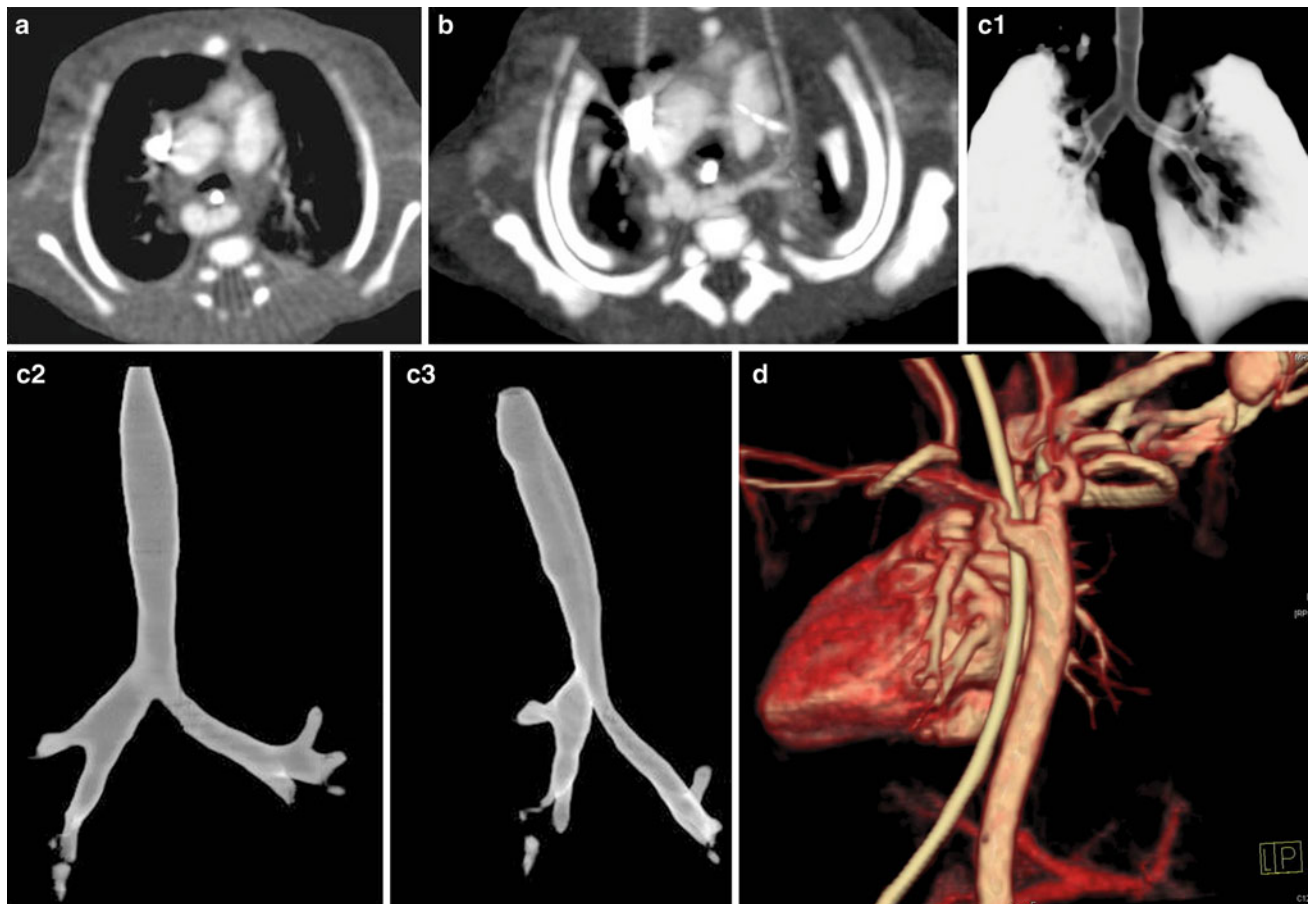


**Fig. 9** Kommerell diverticulum with dominant right aortic arch and aberrant left subclavian artery (SCA) arising from the diverticulum in an 8-month-old girl. **a** On axial CT, a vascular structure is seen behind the esophagus. **b** Axial MIP image depicts a right aortic arch, the diverticulum, and left subclavian artery behind the esophagus. **c1, c2, c3** VR

bronchogram demonstrate the tracheobronchial tree, with narrowing of the trachea and left main bronchus. A round structure should be always checked in different planes (coronal, sagittal, and oblique). **d** Posterior oblique VRT image of the mediastinum better shows the right aortic arch and Kommerell diverticulum with left subclavian artery

the chest, airways, and in skeletal studies and CT angiography (Heyer et al. 2007).

The number of detector rows can also affect effective dose via radiation exposure. MDCT scanners have an inherent dose problem in relation to the X-ray beam, which extends beyond the confines of the detector rows (over-scanning). This effect decreases with more detector rows.

In modern scanners, the X-ray beam is filtered, contouring its shape very closely to remove photons that otherwise will be absorbed by the patient, thus decreasing the radiation dose to the patient.

This process is known as z-axis collimation and is most effective over short scan distances and with greater pitch. This is obviously of particular relevance in pediatrics (Christner et al. 2010).

Post-processing techniques using noise reduction filters can allow the use of low mAs (lowering effective dose) and thus improve the quality of the images for diagnostic purposes (Kalra et al. 2003).

Nowadays, most of the MDCT scanner manufacturers make efforts to help with radiation dose control. They have made changes in their equipment to give information on dose and on how to use modulation dose systems to maintain image quality. They have produced age and (much more appropriately) size/diameter adjusted protocols, which are useful as a guide for pediatric dose reduction.

The image reconstruction interval is usually set at an interval equal to the collimation. If multiplanar or 3D reconstructions are required, reconstruction with 50 % overlap can be performed for better definition. Moreover, overlapping images increase lesion depiction, which is useful in the evaluation of small pulmonary nodules.

The raw volumetric data is currently reconstructed using an algorithm based on filtered back projection. This algorithm is not able to consistently produce diagnostic quality images with low mAs (i.e., low-dose examinations) as the background noise produced is excessive. The more recent algorithm for noise reduction in low dose studies has been

discussed above, i.e., adaptive statistical iterative reconstruction (ASIR).

ASIR uses a series of statistical models to reduce image noise and produce studies with dose savings in excess of 30 % (Silva et al. 2010; Yanagawa et al. 2010).

The most frequent reconstruction algorithm used is the low-spatial frequency (standard) algorithm. As routine in our institution, the pulmonary parenchyma is analyzed with a high-spatial frequency algorithm (bone algorithm).

Scan duration should be tailored as much as possible to the breath-holding ability of the child. The scan delay time varies with the region of interest and the clinical indication of the study (Table 1). The scan delay time for CT angiography (Table 3) is more complex and will be the arterial time, obtained by monitoring the contrast enhancement in the descending aorta. This is done by acquiring very low mA scans at the same level (one scan every 3 s over 15 s) and determining the time of peak contrast when the spiral data acquisition should be commenced.

Alternatively, an automated bolus-tracking technique can be used to monitor contrast enhancement and initiate scanning. Scanning begins once an arbitrary threshold level of contrast enhancement is reached within a predefined region of interest (ROI chosen as 100 HU in our institutions). There are limitations with this technique if the scanner protocol is not adjusted for the relatively high heart rates of children. This can result in optimal contrast enhancement being missed due to erroneous (delayed) scan initiation.

Specific recommendations for the selection of parameters are given in the examination protocols presented above (Tables 1, 2, and 3).

## 2.10 Image Postprocessing

Standard post-processing techniques include four reconstruction displays: Multiplanar Reformats or reconstructions (MPRs), 3D Shaded-Surface-Displays (SSDs), Multiprojective Volume Reconstructions (MPVRs), and 3D Volume Renderings (VRs) (Fig. 1).

The axial images include all the information about the anatomy that is provided with 2D and 3D reformats and it is this information that should be used for most diagnostic purposes. However, postprocessing gives added value to imaging when analyzing oblique structures as well as interfaces and surfaces parallel to the axial plane which are poorly demonstrated and sometimes occult on standard views. 2D and 3D reconstructions are also useful for display of pertinent findings to clinicians and for preoperative planning.

**Multiplanar Reformations (MPRs)** (Fig. 1a) provide additional diagnostic information in different planes and are as accurate as the axial scans because the data is acquired isotomographically. MPRs are 1-voxel-thick, 2D tomographic

sections that can be displayed in standard coronal and sagittal planes, but can in fact be reconstructed in any plane required or in a single tomographic “curved” plane, along the axis of a structure of interest, e.g., a bronchus or a feeding vessel (Salvolini et al. 2000; Siegel 2003). They are real-time, easy-to-reconstruct images, producible as soon as the axial sections are completed. They generally improve our perception of images and give information that although contained in transverse images, is less effectively displayed. Their diagnostic value is substantial in demonstrating and documenting the presence of small focal lesions, defining the vertical extent of a bronchial stenosis, which may go undiagnosed from the axial source CT images, and are invaluable prior to surgical remodeling of vascular rings and the tracheobronchial tree. However, to avoid misinterpretations due to partial volume effect, e.g., overestimation of the degree of a stenosis, overlapping and thinner cuts should be applied when processing the raw data. Likewise, when processing curved MPRs, the trace should be centered within the lumen of interest to avoid anatomic distortion.

Three-dimensional (3D) imaging is a diagnostic tool necessary only in certain cases as it usually requires more time and post-processing skills to provide information already included and demonstrated in the axial images and the MPRs. There is no doubt however that the 3D reformatted images may further increase the diagnostic confidence.

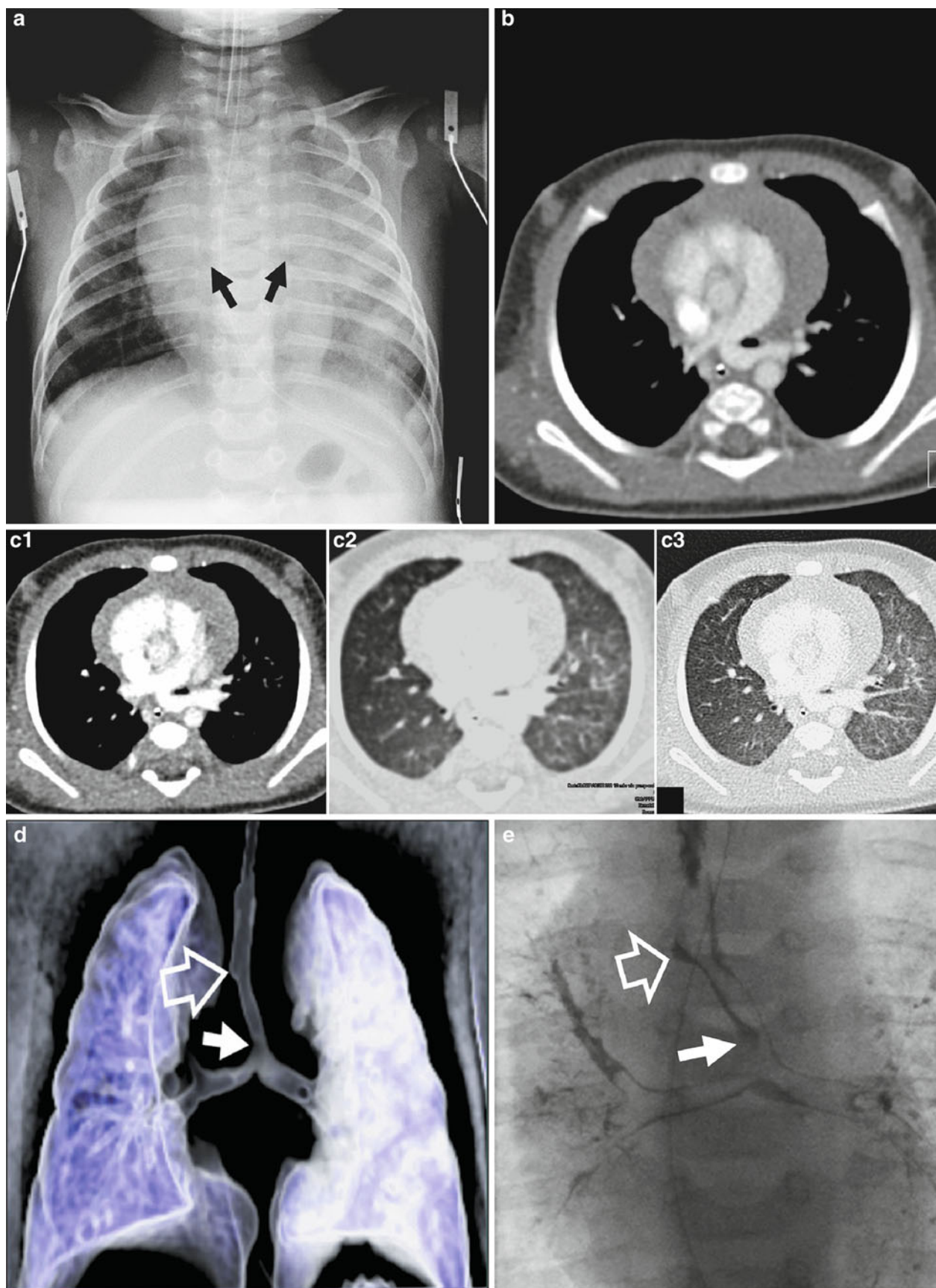
**Shaded-Surface-Display 3D Techniques (SSDs)** (Figs. 1c, 2c) are applied in the imaging of the central airways, vessels, and bone structures and they are usually more visually impressive than clinically useful.

SSD generates images with depth and 3D information. Using binary classification, voxels with attenuation values above a preset threshold are set to white and voxels with lower attenuation values are set to black (Brink 1995). This method first computes a mathematical model of a surface that connects neighboring pixels with CT intensities above a preset threshold.

Depth or 3D perception is created by shading techniques using an imaginary light source that can be arbitrarily positioned. Such data can be then rotated, allowing the image to be viewed from any perspective.

Their generation from original data is time-consuming and they carry the risk of loss of density information due to problems with thresholding. The threshold must be carefully chosen and should be based on the intensity of the contrast material in the area of interest. The choice of threshold will strongly affect the evaluation of some lesions, such as the degree of stenosis. Choosing too low a threshold may increase noise and also allow the higher density soft tissue to obscure the target vasculature. Choosing a too high threshold may result in small vessels disappearing and/or stenoses being falsely implied.

Another problem encountered with SSD is that the reduction of CT volume data to a single surface removes the

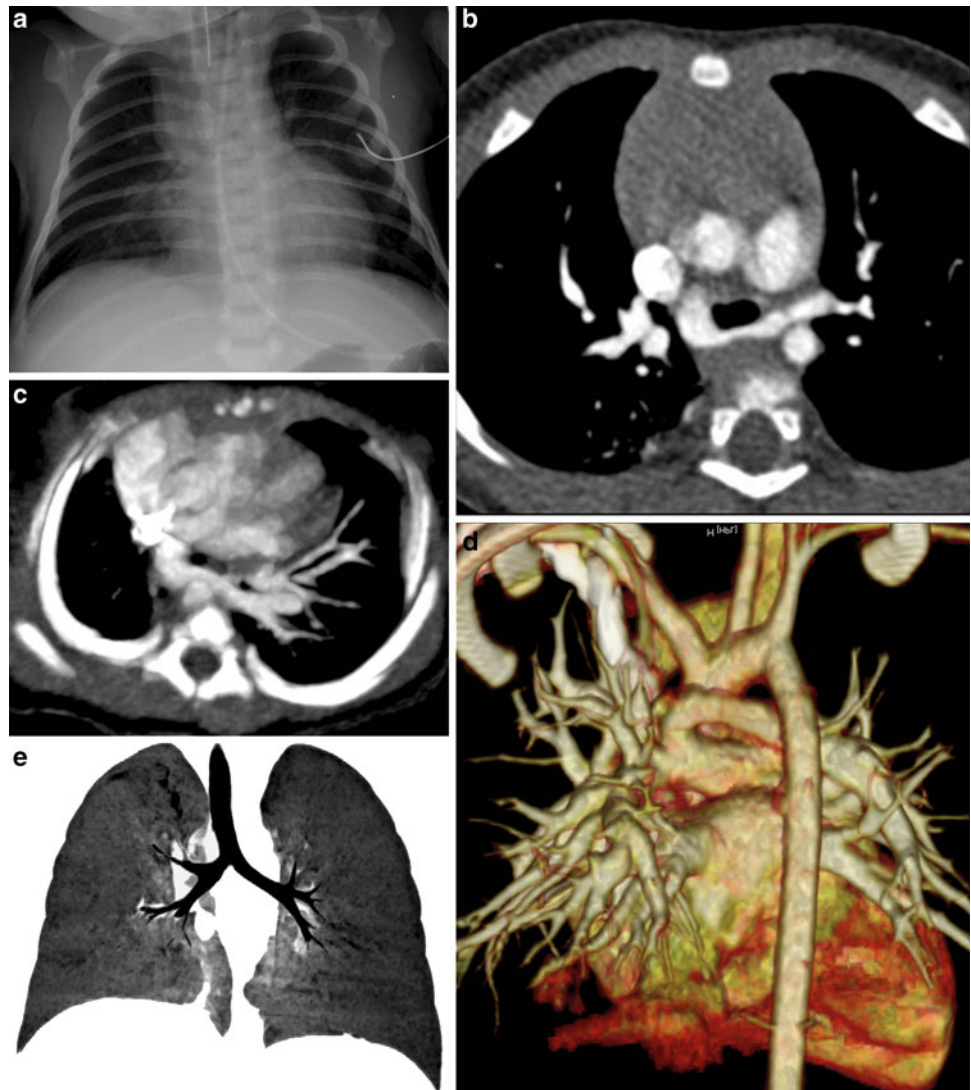




◀ **Fig. 10** Pulmonary artery sling. **a** CXR shows widening of the carinal angle due to associated long segment tracheal stenosis and left lung atelectasis. **b** Axial image CTA demonstrates the left pulmonary artery arising from the right pulmonary artery, running between the oesophagus and trachea, which is narrowed. The tracheal narrowing is in fact due predominantly to intrinsic long segment (complete

cartilaginous ring) tracheal stenosis. **c** Axial images showing various post processing algorithms on which the data can be viewed at B30f for soft tissue (**c<sub>1</sub>**) and lung parenchyma (**c<sub>2</sub>**), and at B60f for high resolution lung parenchymal detail (**c<sub>3</sub>**). **d** VR image ‘virtual bronchogram’ shows long segment tracheal narrowing and stenosis alongside. **e** The conventional invasive tracheobronchogram

**Fig. 11** Pulmonary sling in a 2-year-old boy with stridor. **a** Chest X-ray with tracheal tube looks normal. **b** On enhanced axial CT and MIP image **c**, the left pulmonary artery is seen to cross the mediastinum between the trachea and esophagus. **d** VR image demonstrates a pulmonary sling, in which the left pulmonary artery arises from the right pulmonary artery. **e** In the MinIP image, there is narrowing of the right bronchus due to vascular compression



inherent CT quantitative density values, losing gray-scale levels. With this threshold technique one cannot differentiate between solid organ intraparenchymal vasculature and enhancing parenchyma, or between high attenuation structures in vessel walls and intraluminal contrast enhancement.

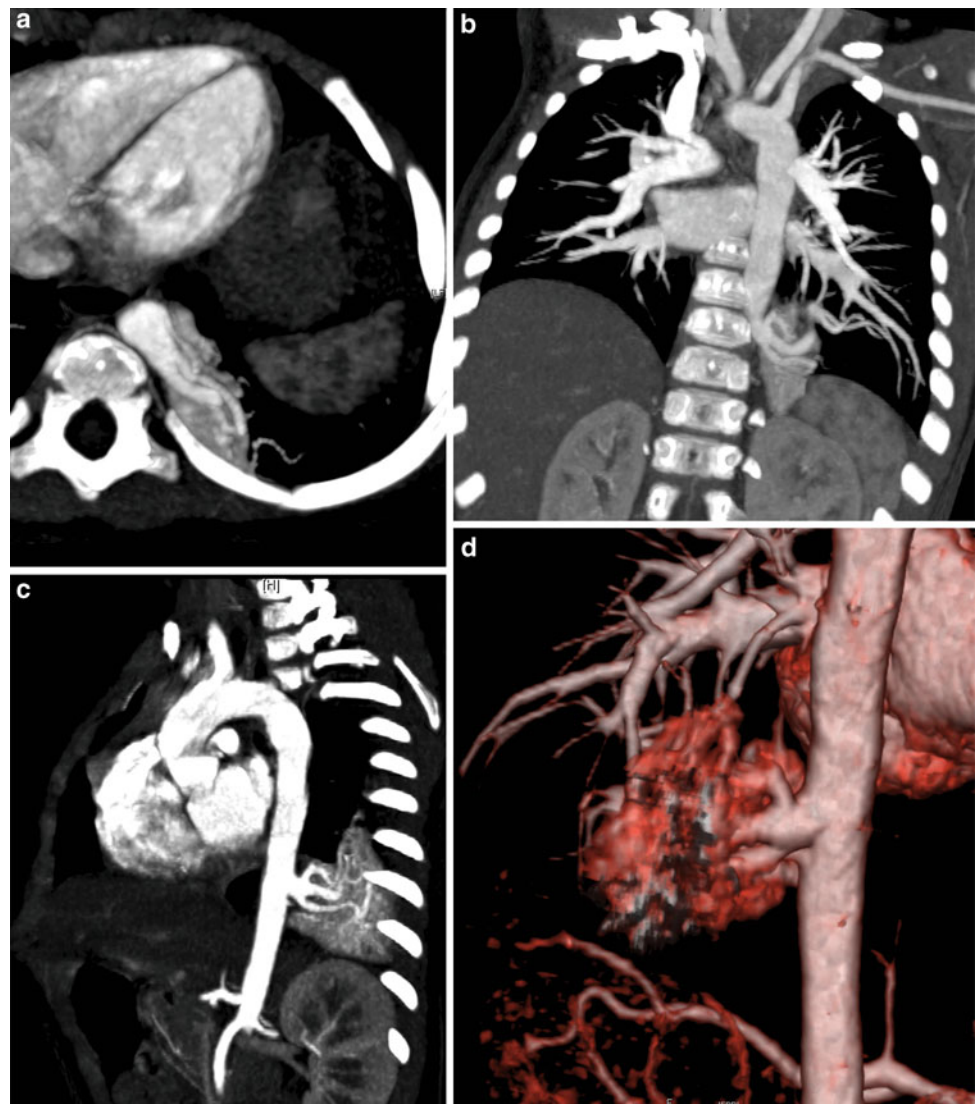
**Multiplanar Volume Reconstructions (MPVR)** (Fig. 1b) allow a combination of the spatial resolution of thin sections with the anatomical display of thicker slices and all the information acquired in the raw data set is used. The routine CT images are combined in multiples to create an image thicker in voxels, the volume “slab”, which constitutes

an interactive sum of axial, coronal, and sagittal reconstructed sections (Siegel 2003; Salvolini et al. 2000). By using different algorithms and setting thresholds, maximum (MIP) or minimum intensity (MiniP) voxels can be highlighted within the slab (STS-MIP, STS-MinIP). The sections are typically thin 2–3 mm sections rendered into approximately 20–30 mm slabs (Napel and Jeffrey 1993).

**Maximum Intensity Projections (MIP, STS-MIP) Images** are generated by mapping the maximum attenuation value along each ray to produce a gray-scale image. Thus, bone and calcified structures are bright and are



**Fig. 12** Intralobar pulmonary sequestration in a 1-year-old boy. **a** Axial MIP image shows a solid left lower lobe lesion with possibly two systemic vessels arising from the aorta. **b** Coronal and **c** sagittal MIP images clearly depict a single systemic vessel arising from the aorta and diving into three branches to feed the sequestration. **d** VR image better shows 3D depth perception of the vessel and venous drainage to the left inferior pulmonary vein



distinguishable from both iodinated contrast material and soft tissue. In a vascular examination, it will be necessary to postprocess the image to avoid bone images (Brink 1995).

MIP images are useful for displaying vascular structures, for CT angiography, and for separate parenchymal nodules from surrounding pulmonary vasculature. They reliably display vessel caliber, metallic stents, and wall calcifications, but provide poor separation of overlapping vessels because 3D relationships are lost (Fig. 2). Vascular anatomy is frequently difficult to comprehend from standard cross-sectional images. Blood vessels that are perpendicular or oblique to the section will appear as small circles or ellipses, and may mimic the appearance of a pulmonary nodule. With MIP, one can integrate the path of vessels and their connections with other structures into the larger picture of vascular anatomy (Fig. 3).

The display of MIP images in a cine loop to simulate a rotating viewing direction improves the lack of 3D depth. This allows visualization of 3D relationships and may provide clues to the nature of eccentric stenosis, and the crossing or looping of vessels (Fig. 4).

#### Minimum Intensity Projections (MinIP, STS-MinIP) Images

MiniP images map the minimal attenuation value to a grayscale image.

MinIP images are valuable in examinations of the central airways (Figs. 5, 6) and in analyzing mild forms of uneven attenuation of the lungs (Remy-Jardin et al. 1993).

MinIPs enable airway anatomy to be visualized and are also useful for displaying the whole volume of parenchymal cysts, bullae, or over inflation. They are also very valuable

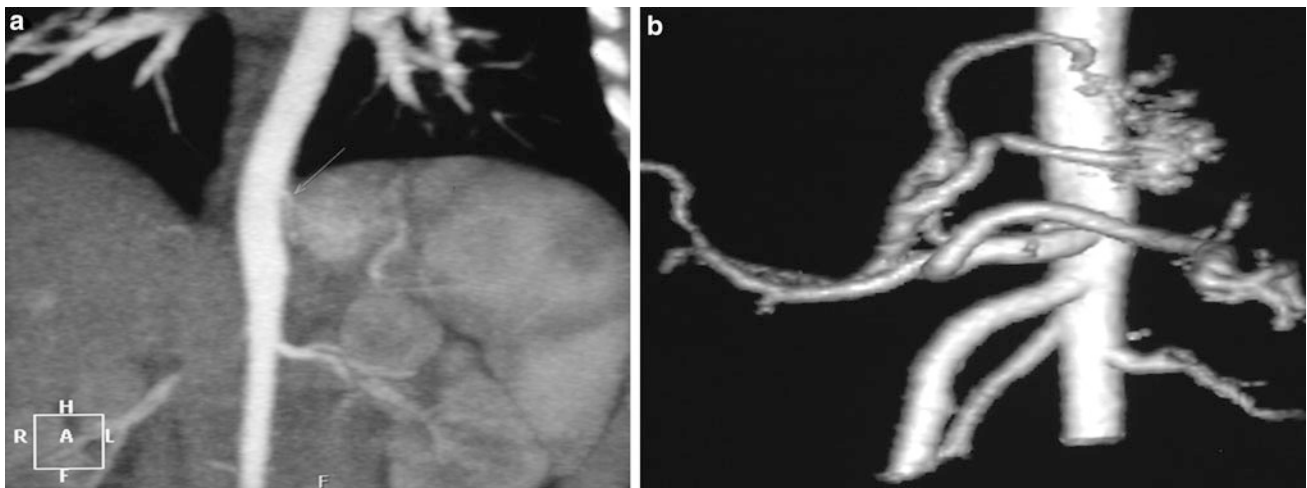


**Fig. 13** Extralobar pulmonary sequestration. Prenatal diagnosis of congenital pulmonary malformation. Postnatal CXR was normal. **a** Coronal MIP image shows an enhanced left mass in a subdiaphragmatic

location, and a small systemic vessel arising from the aorta and feeding the mass. **b** VRT demonstrates another systemic vessel from the celiac trunk feeding the mass, and venous drainage to the portal vein

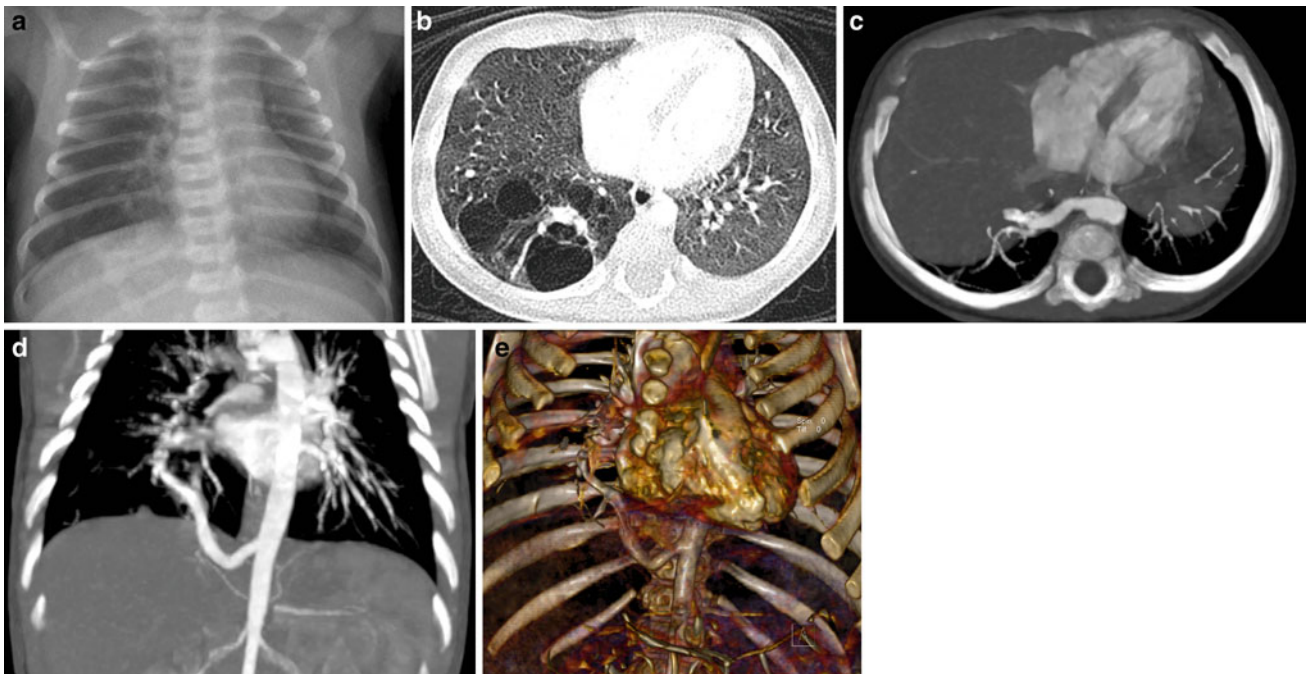


**Fig. 14** Congenital pulmonary airway malformation (CPAM) with a systemic vessel in a 6-month-old girl. Prenatal diagnosis of pulmonary malformation. **a** Chest X-ray looks nearly normal, with some linear images superimposed on the liver silhouette. **b** On axial CT of the lungs, multiple cystic areas are seen in the right lower lobe. **c** Axial

MIP demonstrates a systemic vessel arising from the aorta and feeding the right lung base. **d** Coronal MIP image depicts a prominent systemic vessel from the aorta, and a drainage vein to the right inferior pulmonary vein. **e** VR shows similar findings

for delineation of the branching pattern of the tracheo-bronchial tree and the presence of lung isomerism, tracheal bronchi, and airway narrowing.

Visualization of the heterogeneous attenuation of the lung parenchyma as a result of constrictive obliterative bronchiolitis is well portrayed in the coronal plane particularly (Fig. 7).

### Volume Rendered Tomography (VRT)

Three-dimensional (3D) volume renderings (VRs) represent the main technique for 3D reformatting of the airways and the vascular structures of the mediastinum.

The VR technique is particularly useful for displaying structures that course parallel or oblique to the transverse

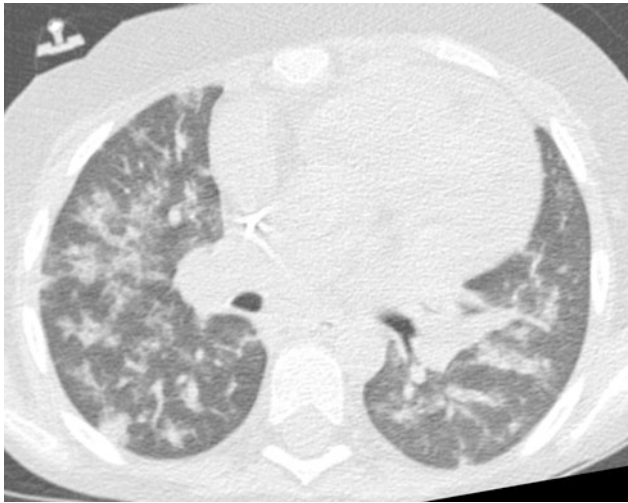


**Fig. 15** Bronchiolitis obliterans with organizing pneumonia (BOOP) in an immunocompromised patient. A 10-year-old boy who underwent renal transplantation 1 year previously with mild respiratory distress. On axial CT, there are multiple poorly-defined nodules and areas of ground glass. The lesions disappeared with steroid therapy

plane and those that develop or extend into multiple planes (Salvolini et al. 2000; Siegel 2003) (Figs. 1, 8, 9, 10, 11). Thus the added value in cardiothoracic imaging to depict complex anatomy of the heart, great vessels, and lungs in 3D has revolutionized cardiothoracic imaging (Figs. 12, 13, 14). However, preliminary editing is still necessary and can be time-consuming, altering work patterns in CT.

In VRT, different anatomical tissues are represented by proportional values that are assigned to every voxel and depend on the range of tissue attenuation values in the original data set. Voxels are selected by the probability of belonging to the object of interest; thus they are displayed in different colors or several shades of gray, different transparency, or opacity. Transition from the reconstructed surface to the surrounding media is gradual and the depiction of interfaces, like the inner tracheal lining, is supposed to approach the true appearances.

VRT from extraluminal visualization of the tracheobronchial tree creates images similar to conventional bronchograms and is applicable in clinical practice without the concomitant administration of a contrast agent (Figs. 5d, 6f, 9c, 10d). Other clinical applications include cardiovascular imaging and chest wall disease (Johnson et al. 1998a).

Albeit this 3D segmentation technique is better and more complicated than the others previously mentioned, some information is still lost during processing so that the axial images are still indispensable for the radiologist to assess extraluminal disease and identify artifacts. Three-dimensional VRT reconstructed images are attractive and appealing to the clinicians as they may better illustrate short

focal areas of narrowing, the craniocaudal length of a tracheobronchial stenosis, and complex congenital cardiovascular and tracheobronchial anomalies.

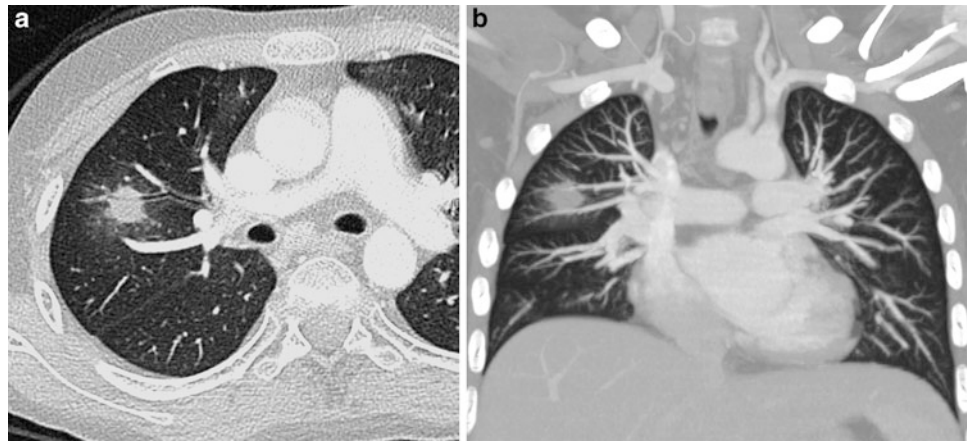
The inner surface of air-containing tracheobronchial tree can be displayed with Virtual Bronchoscopy (VB) (Figs. 1d, 8c) which is performed with either polygonal SSD or direct VR. VB is a noninvasive and accurate technique that can provide “bronchoscopic” views of the central and the peripheral airways.

This technique is considered supplementary both to CT and the gold-standard of flexible bronchoscopy. Referral to the axial sections is again valuable to recognize artifacts and to gain perception of the orientation within the virtual airways. VB uses perspective surface rendering, which takes advantage of the natural contrast between the airway and the surrounding tissues (Heyer et al. 2004). The point for viewing is located intraluminally so that external structures do not overlap and editing takes shorter time periods. Submillimeter (0.625 mm, 0.75 mm) slice thickness allows deeper penetration and visualization of the bronchial surface down to the bronchial diameters of below 5 mm (Khan et al. 2004; Heyer et al. 2004; Venkatraman et al. 2006). In practice, VB is of limited value, reserved for cases where bronchoscopy is not applicable (children at risk of undergoing traditional bronchoscopy) or precise navigation is not possible to guide airway interventional procedures and in emergencies such as infant airway (tracheal) stenosis that cannot be evaluated otherwise (Khan et al. 2004). The produced images resemble the true bronchoscopic images and can additionally “advance” distally to an airway obstruction, where the real endoscope cannot penetrate (Salvolini et al. 2000; Hoppe et al. 2004). However, when compared to fiberoptic bronchoscopy, VB precludes any therapeutic maneuvering, it is incapable of detecting endoluminal lesions smaller than 2–3 mm, and provides limited information about mucosal details (morphology, vascularity, and color) making differentiation between pathologic processes and retained secretions difficult (Heyer et al. 2004). There is consensus that measurements should be better performed in 2D sections as they may be otherwise inaccurate. The technique is additionally affected by the partial volume effect, which may lead to misinterpretation of severe stenoses as occlusions, and the threshold level is therefore of importance for displaying accurate simulations (Hoppe et al. 2004).

Dynamic and functional inspiratory and expiratory scanning with single breath-hold MDCT helps identification of strictures, areas of air-trapping and tracheobronchomalacia, but is rarely applied in pediatric practice because of the associated radiation burden (Johnson et al. 1998b; Siegel 2003). The advent of the newer dose reduction techniques and more detector rows per scanner make the use of dynamic scanning possible.



**Fig. 16** Pulmonary nodules. Post-BMT fungal lesion (*Aspergillus* infection). A 7-year-old boy with BMT due to leukemia. Chest X-ray was normal. **a** Axial CT shows a small nodule in the right upper pulmonary lobe, surrounded by a halo of ground glass. **b** Coronal MIP image better depicts the relationship of the nodule with the minor fissure, and confirms no other nodules



## 2.11 Newer Advances in CT

Newer developments in Computed Tomography leads to improve their applications within pediatric thoracic imaging.

In essence two basic CT scanner configurations exist:

1. Multidetector CT (MDCT) with up to 320 detector rows
2. Dual-Source CT (DSCT) utilizing MDCT technology.

Advantages of the newer scanners on the market include subsecond tube rotation time (down to 0.33 s), and this increased acquisition speed has the potential to reduce motion and respiratory artifact (particularly problematic in children) and also to improve image quality. The availability of even smaller detector elements (0.5 mm) combined with thin-slice collimation, provides isotropic resolution with accurate reformatted images in any orthogonal plane, and displayed as either 2 or 3D images, that have the same spatial resolution as the base axial data set and with reduced partial volume artifact.

### 320-Slice MDCT

The advent of 320 MDCT allows larger volume scanning coverage of up to 16 cms. This is manifest as coverage within and above the clinical range of thoracic imaging in neonates and young children. This allows imaging of the entire chest in a single volume cone-beam acquisition, during one tube rotation of 0.35 s (Kroft et al. 2010). This acquisition time is much faster when compared with either helical MDCT or DSCT acquisition. The acquired axial volumetric datasets allow potential for radiation dose reduction related to the large nominal beam width used, so that the contribution of the penumbra effect is less of a problem as it is less prominent.

In addition unlike helical scanning, over-ranging in the longitudinal axis does not apply, as the exposed range

corresponds exactly to the imaged range and so there is more effective use of the radiation exposure for image formation.

Axial volumetric acquisition can be well suited to other clinical situations, such as cardiac imaging in children, where using prospective ECG-gating the entire heart can be imaged in a single tube rotation.

### Dual-Source CT (DSCT)

Now in its second generation, the DSCT (Siemens Flash, Forchheim, Germany) is currently the latest in CT technology, incorporating two X-ray tubes and corresponding 64-row detector systems (each contributing 128 slices by means of a z flying focal spot) mounted at an angular offset of 90° relative to one another. Primarily designed for cardiac imaging, the two tube-detector system operates in tandem and not simultaneously. Data from the second detector system is collected a quarter of a rotation later following the first set of detectors, thus allowing gapless volume high-pitch scanning (up to 3.2 pitch), avoiding overlapping slices, and with significant reduction in radiation dose.

This enables a 75 ms temporal resolution, which together with a fast gantry rotation time of 0.28 s, allows helical prospective ECG-triggered cardiac imaging.

The result is that imaging children with high heart rates is no longer a limiting factor, and this is invaluable in both pre- and postsurgical assessment of a wide variety of congenital heart diseases and diseases affecting the pulmonary vasculature.

Improved visualization of the coronary arteries can also be achieved even when data is captured during the less favorable, i.e., systolic phase of cardiac motion (Ben Saad et al. 2009) even in younger children.



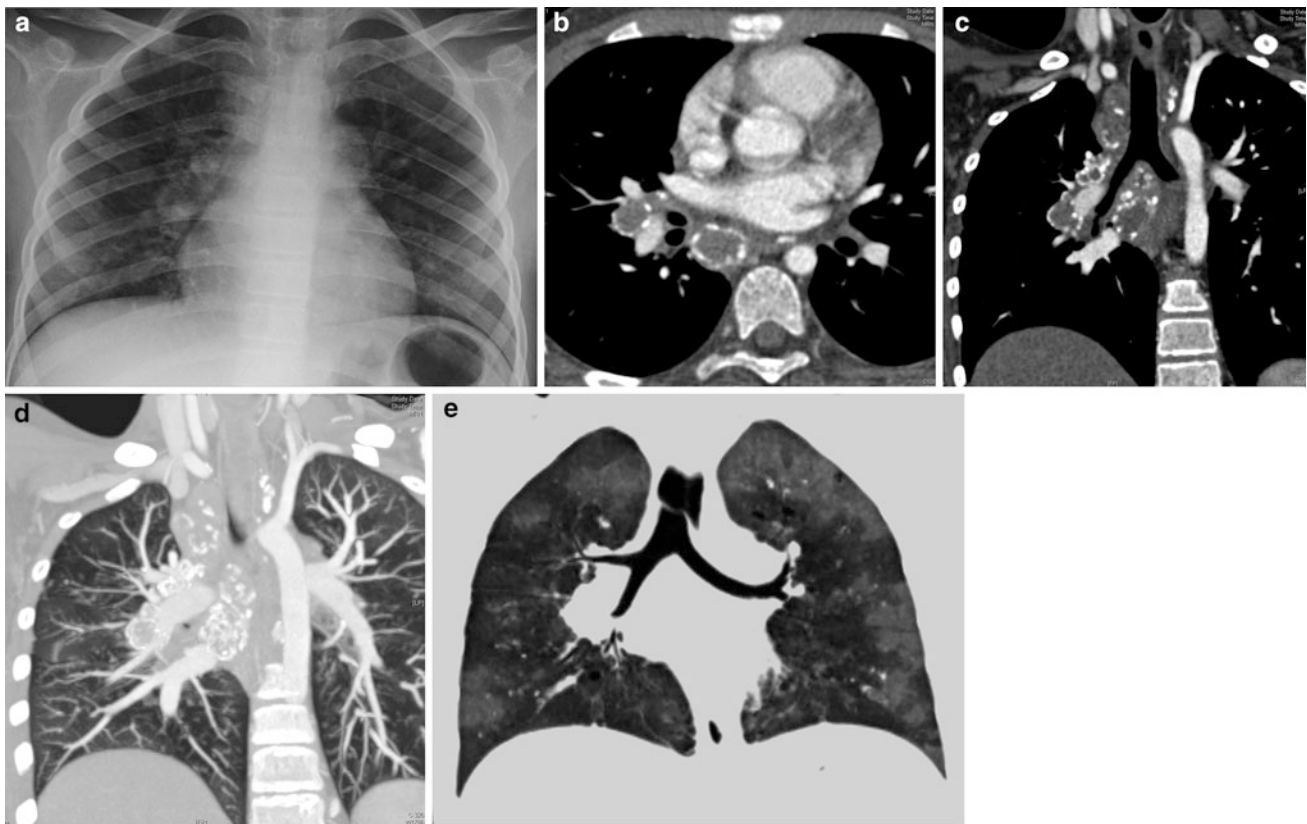


**Fig. 17** Mediastinal and hilar lymph nodes in multidrug-resistant TB. A 6-year-old boy with several weeks of fever. **a** Chest X-ray demonstrates multiple masses in the mediastinum and pulmonary hila, with calcifications **b** Enhanced axial CT shows multiple ring-calcified lymph nodes in the right hilum and below the carina,

differentiating masses from vessels. **c** Coronal MPR additionally depicts the extension of the calcified lesions to the right paratracheal space and the left mediastinum. **d** MIP better depicts the relationship between the lymph nodes and the vessels. **e** MinIP image demonstrates bronchial airway compression, and heterogeneous lung attenuation

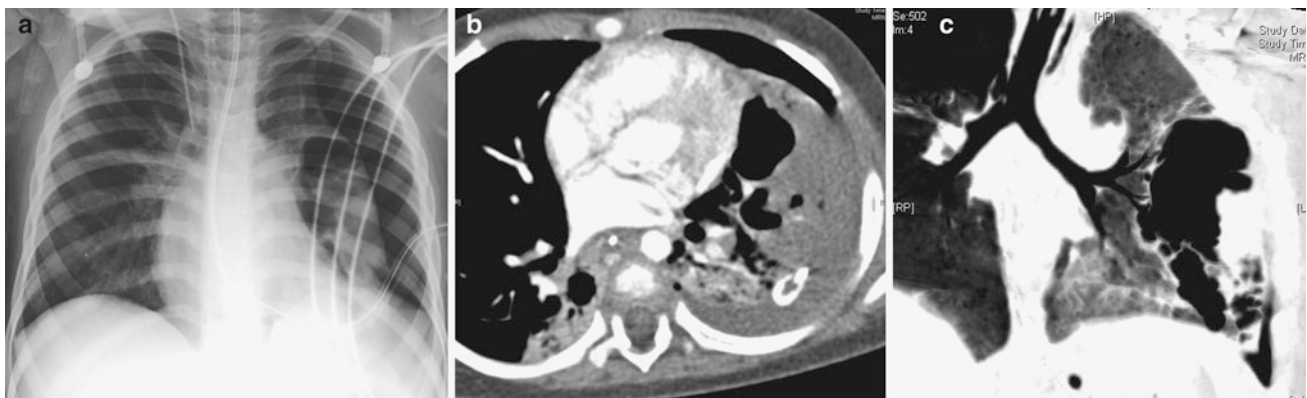


**Fig. 18** Bronchopulmonary fistula in pulmonary infection. A 7-year-old boy with fever of several days duration and respiratory distress. **a** Chest X-ray shows a left lung consolidation with pneumothorax. **b** Enhanced axial CT demonstrates considerable left lung

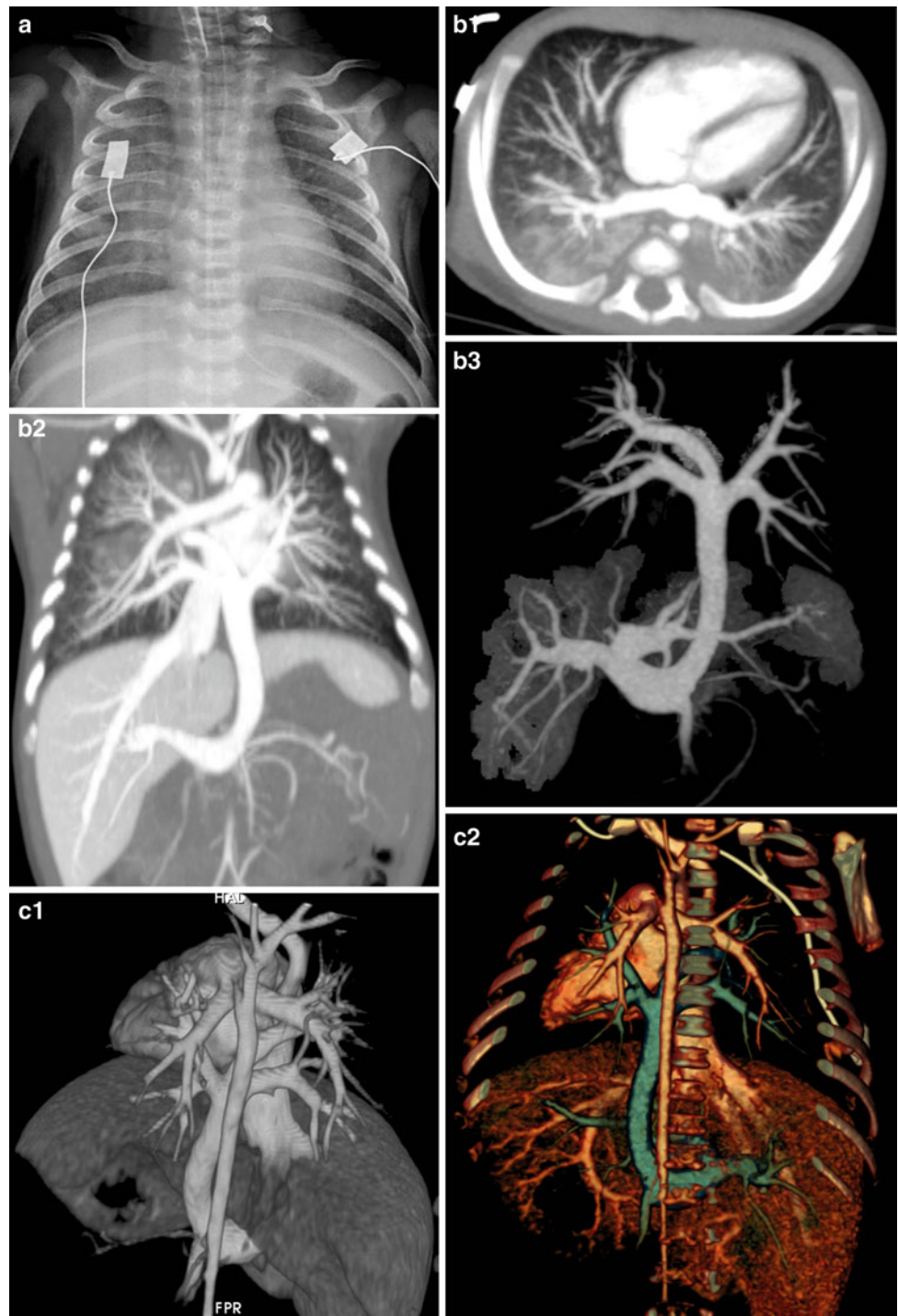
hypoperfusion with necrotic areas, pleural fluid (pleural tube), and a pneumothorax. There is also a small right lung consolidation. **c** Coronal MinIP image better depicts a bronchopulmonary fistula, multiple necrotic air lesions, and a pneumothorax

### Dual-Energy Dual-Source CT

The availability of two X-ray tubes allows simultaneous acquisition of two data sets at different tube potentials (80 and 140 kVp) during the same phase of contrast

enhancement. This will exclude both temporal changes and spatial misregistration. The dual energy technique takes advantage of differences between material and tissue composition, and in differences of their photon absorption

**Fig. 19** Total anomalous pulmonary venous return to IVC. Newborn with severe respiratory distress. **a** Chest X-ray shows increased density in both lungs due to pulmonary edema, with no cardiomegaly. **b1, b2, b3** MIP images and **c1, c2** VR images disclose that the pulmonary veins do not enter the left atrium. The four pulmonary veins join to a collector that drains into the portal vein. Hepatic veins are also prominent



characteristics. In particular, material with high atomic numbers (like iodine) will exhibit a different degree of attenuation between the two different tube potentials.

By applying a specific post-processing algorithm to the acquired data, virtual unenhanced and virtual angiographic data sets can be generated based on the three-material

composition principle, i.e., within the chest, soft tissue, air, and iodine are analyzed. By application of a bone removal algorithm, an angiographic dataset without overlying bony structures for easy interpretation can be viewed. Overall radiation dose associated with dual-energy CT (DECT) is noted to be comparable to that of single source MDCT system.

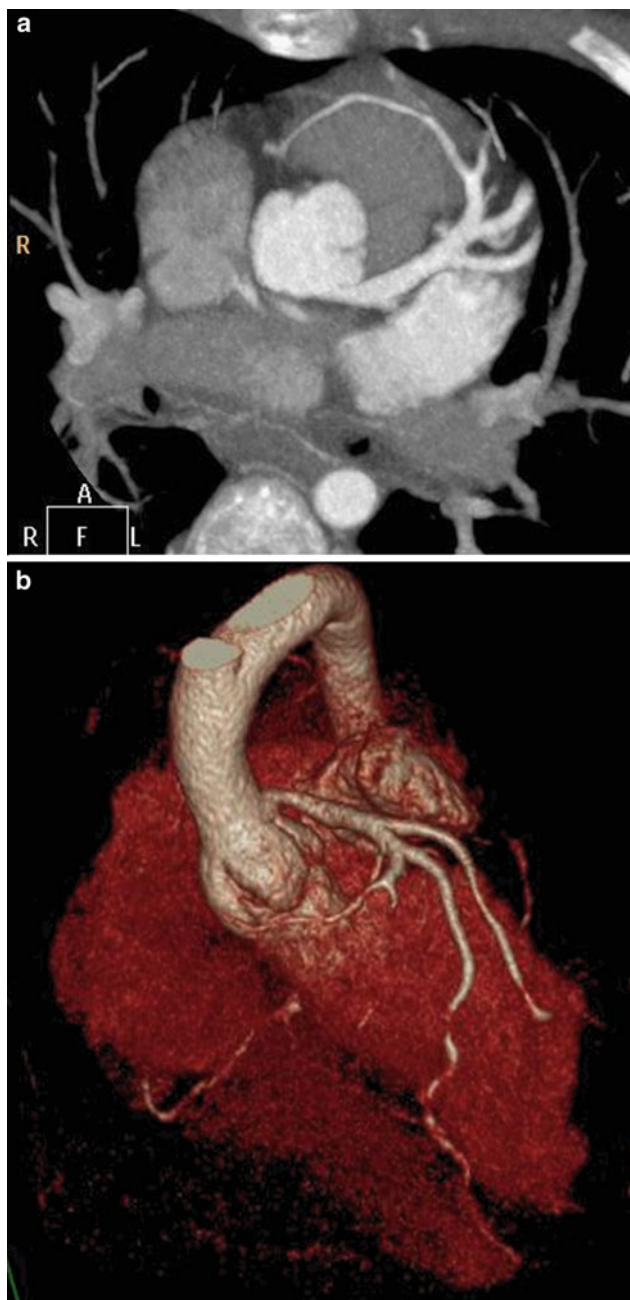


**Fig. 20** Congenital coronary anomalies. Single coronary artery in a 6-year-old boy. Coronary MDCT angiography. **a** Axial MIP image shows a single prominent left coronary artery. There is no ostium for the right coronary artery. **b** VR image displays the left coronary artery and one of its branches supplying the apex and right ventricle

Other clinical dual-energy application includes characterization of abdominal masses, chemical composition of renal calculi, myocardial and pulmonary perfusion imaging.

Within thoracic CT an important area for dual energy imaging is in the depiction of iodine distribution for the detection of peripheral lung perfusion defects, which result from pulmonary emboli. This application adds important

additional functional information to conventional structural pulmonary CT angiography and has an application in the evaluation of subsegmental pulmonary emboli (Johnson et al. 2007; Hoey et al. 2009).

When advanced post-processing software is applied to the acquired data set, an iodine distribution map is generated and overlaid onto a gray-scale image. Normal perfusion images show homogeneous color distribution extending to the lung periphery and when displayed in a multiplanar format can be manipulated manually.

The presence of a filling defect or hypoperfusion of lung parenchyma will indicate an obstructed pulmonary vessel supplying the relevant lung segment. Review of the gray-scale image will help to determine the anatomical site.

### Xenon Ventilation in Chest Imaging

Another potential for the use of DECT is its application with the use of xenon ventilation in thoracic imaging. This technique has been described as more sensitive in the evaluation of both regional and global airway/lung abnormalities in children (Goo et al. 2010).

Conventional CT requires both inspiratory and expiratory acquisitions in order to demonstrate air trapping within the lung parenchyma.

Xenon ventilation, which demonstrates regional ventilation defects on inspiration will obviate the need for an additional expiratory phase acquisition and hence show a reduction in radiation dose.

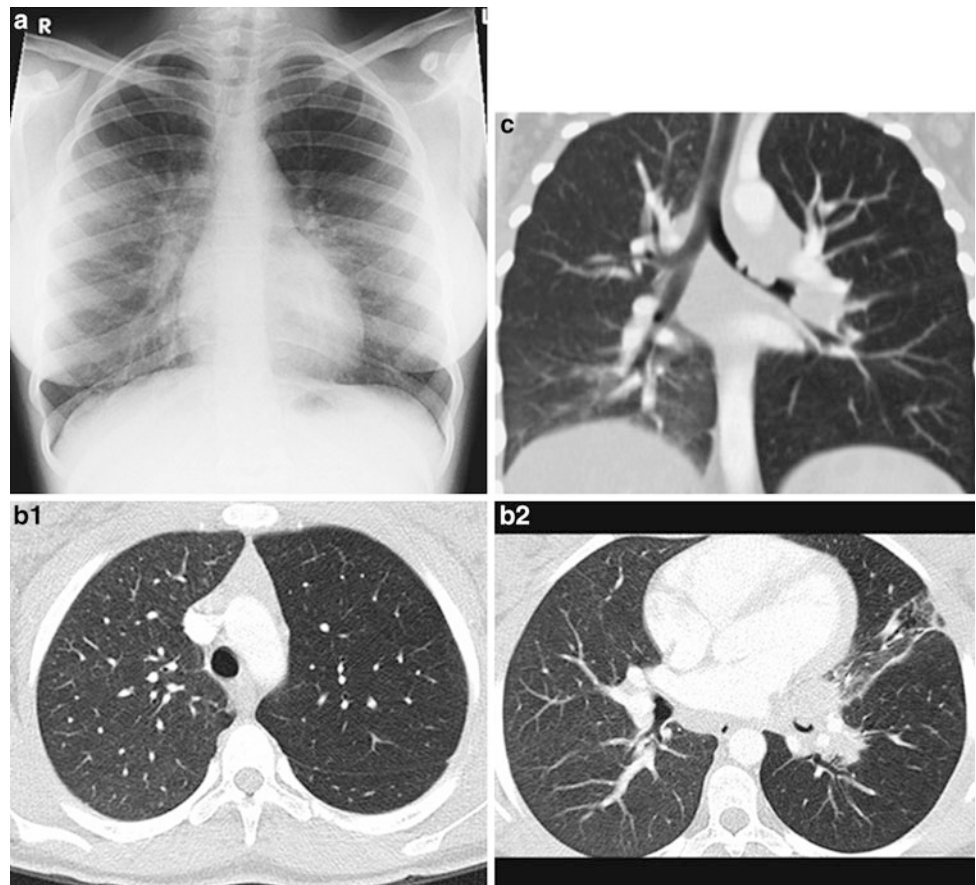
Also problematic in children is the quantitative evaluation of lung density on CT, which is highly age dependent, and varies with the level of cooperation of the patient to breath hold at total lung capacity (TLC). The use of xenon with its insensitivity to degree of lung expansion can provide more accurate assessment.

## 3 Helical Chest CT Main Applications

The introduction of helical technology has extended the clinical indications of chest CT (García-Peña and Owens 2008). The most important diagnostic indications in children include evaluation of pulmonary nodules and thoracic masses (Agrons et al. 1998; Bal et al. 2004; Paterson 2005; Valencia et al. 2006; Mc Hugh 2008), lesions located in difficult areas (e.g., cervico-thoracic, diaphragmatic, peridiaphragmatic, or chest wall regions) (Ahn et al. 2010) and in the central airways (Berrocal et al. 2004; Yedururi et al. 2008), definition of vascular anatomy, and study of critically ill patients, including trauma patients. In our institution, the most common indications for chest studies are the detection and characterization of pulmonary nodules and definition of mediastinal masses in children with known or suspected malignancies, investigation of infection



**Fig. 21** Intrabronchial aspergillus infection with persistent overinflation of the left lung related to delayed diagnosis of bronchopulmonary aspergillosis secondary to chronic granulomatous disease (CGD). **a** CXR relatively unremarkable. **b** Axial CT images (**b<sub>1</sub>** and **b<sub>2</sub>**). The left main bronchus shows an endoluminal polypoid mass with distal overinflation of the left lung due to ball valve effect. **c** Coronal multiplanar reformation (MPR) image through the left main bronchus show overinflation of the left lung compared to the right and the soft tissue images show endoluminal bronchial wall thickening causing ball valve effect in the left lung



in immunocompetent and immunocompromised child (Fig. 15), congenital malformations, combined airway and vascular studies (Figs. 1, 8, 9, 10, 11), and cardiovascular studies (Harty and Kramer 1998; Lobo and Antunes 2012; Dillman et al. 2011; Garcia-Peña et al. 2013). The diagnosis and follow-up of bronchiectasis and diffuse lung disease can also be carried out by MDCT, but an HRCT technique is preferable, because radiation dose should be low when evaluating chronic disease (Lucaya et al. 2000a; Garcia-Peña and Lucaya 2004; Brody et al. 2004; Lucaya and Decou Le Pointe 2008; Klusmann and Owens 2009; Garcia-Peña et al. 2011).

### 3.1 Evaluation of Pulmonary Nodules and Chest Masses

Several studies have demonstrated that at least 10 % more pulmonary nodules can be identified with helical than with conventional CT (Costello et al. 1991; Remy-Jardin et al. 1993). The ability to obtain overlapping reconstructions at smaller intervals with the contiguous volume data acquired increases the certainty that scans are obtained through the

center of any lesion. These images depict the lesion without volume-averaging effect.

In patients with suspected metastatic disease, use of helical CT with a single breath-hold technique eliminates respiratory misregistration caused by variations in the depth of respiration. This results in better ability to detect small nodules. In children unable to breath-hold who must be scanned during quiet respiration, helical CT has shown no significant loss of accuracy in the detection of pulmonary metastasis (Coakley et al. 1997a). The problem of variable respiratory excursion is further minimized by volume acquisition and the possibility of overlapping image reconstruction (Buckley et al. 1995; Coakley et al. 1997b).

The volumetric data created during helical CT and the coronal and sagittal images reconstructed from them are useful for delineating the anatomy of vascular lesions that appear similar to nodules. MIP images are extremely useful for differentiating nodules from vessels. Detection of small nodules on MDCT may be improved with the use of MIP and sliding thick slab MIP (Coakley et al. 1998; Valencia et al. 2006; Kawel et al. 2009). Multiplanar image reconstructions can clarify the spatial relationships of a nodule to the pleura or diaphragm (Brink et al. 1994a; Ahn et al.



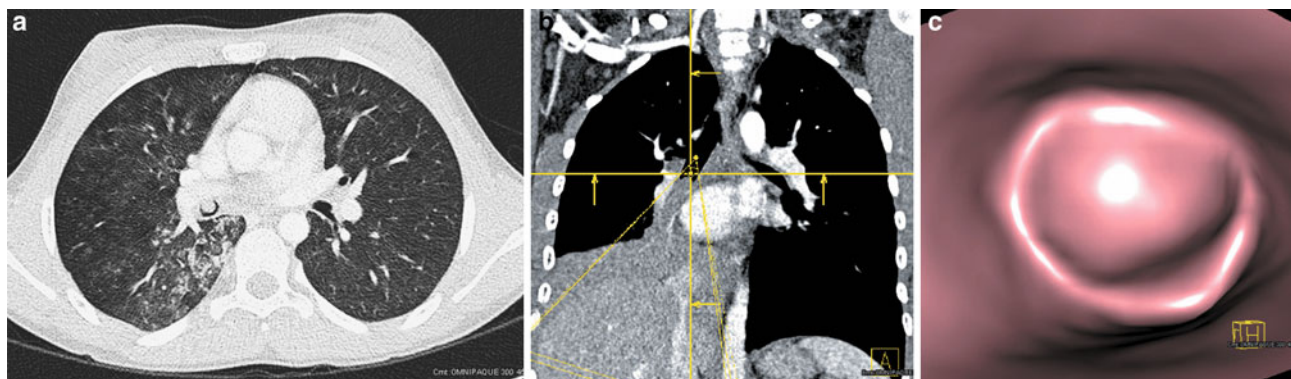


**Fig. 22** An HIV infected patient with TB and massive haemoptysis secondary to endo bronchial and cavitary TB shows polypoid obstruction of the R main bronchus seen on the a–c images. **a** Axial CT image. **b** Coronal MPRs with a tubular soft tissue mass in the

RMB. **c** Virtual bronchoscopy (view from the carina) shows the obstructing mass in the RMB. The coronal MPR image indicates the viewpoint

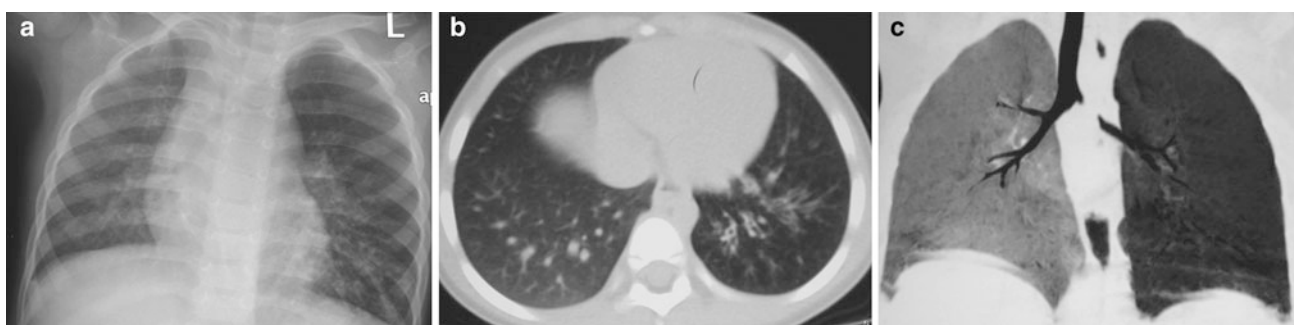


**Fig. 23** Intrabronchial hamartoma in the left main bronchus in a 2-year-old boy with repeated pneumonia of the left lung. **a** Chest X-ray shows hyperaeration of the left hemithorax with increased density of

the LLL. **b** Coronal CT depicts the left emphysema and bronchial thickening secondary to repeated infections. **c** MinIP image confirms the obstructive emphysema due to a left bronchial hamartoma

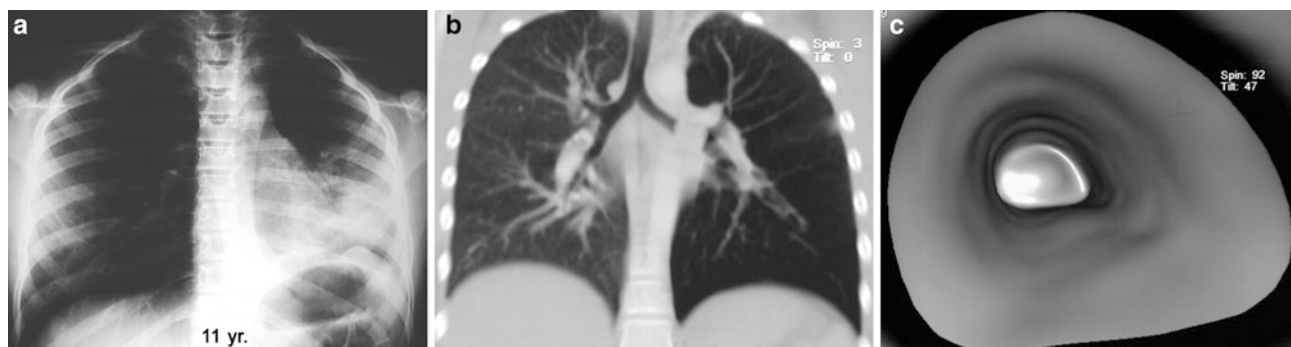


**Fig. 24** Intrabronchial mucoepidermoid carcinoma in an 11-year-old boy with repeated left lung atelectasis. **a** Chest X-ray shows increased density of the left pulmonary base, with elevation of the left diaphragm

due to left lung atelectasis. **b** Coronal MPR depicts obstructive emphysema, and a mass within the left bronchus. **c** On virtual bronchoscopy (VB), the mass is seen to occupy the left bronchus

2010), a task that is especially difficult with conventional section-by-section CT because of the large excursion of the diaphragm between breaths. CT detection of small pulmonary nodules usually causes less of a dilemma in children than in adults, but the differentiation between benign and malignant pulmonary nodules can also be difficult (Fig. 16) (Mc Carville et al. 2006).

Low-dose helical CT of the chest is highly sensitive for detecting pulmonary nodules, and could be an ideal alternative to conventional-dose helical CT for screening purposes (Gartenschläger et al. 1998). Recommendations for the selection of parameters are given in the “Routine Chest Protocol” (Table 1). Intravenous contrast agents are not usually needed in the evaluation of pulmonary nodules.

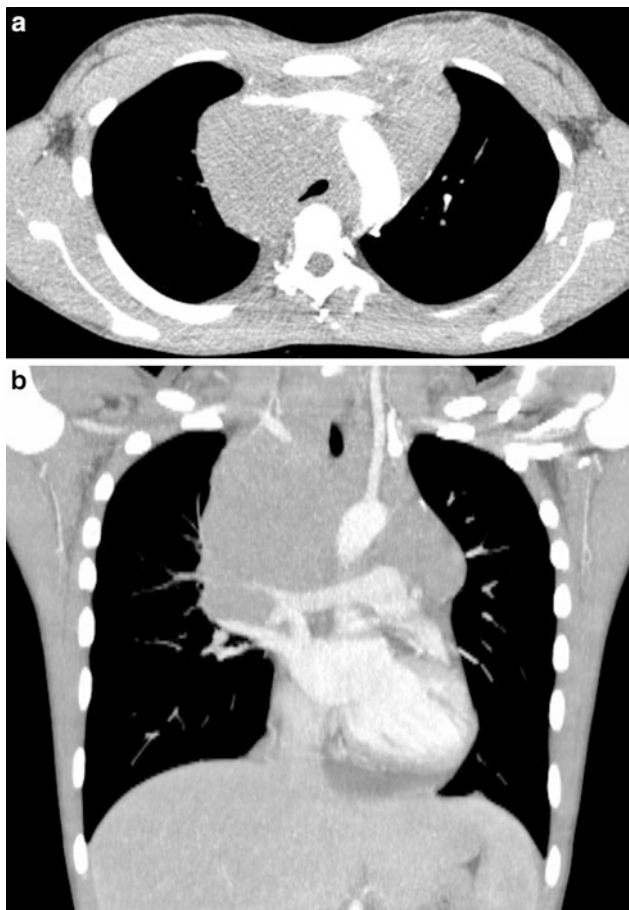


**Fig. 25** Lymphoma with mediastinal and cervicothoracic masses in a 10-year-old boy with fatigue and fever. **a** Axial CT shows a bilateral mediastinal mass and considerable tracheal compression. **b** Coronal MIP better demonstrates the cervical extension of the mass and the tracheal compression

To assess solitary pulmonary masses and mediastinal lesions, another indication of helical CT, we recommend the Routine Chest Protocol with IV contrast material (Table 1). The rapid scanning speed facilitates scanning during the time of peak contrast enhancement, permitting optimal definition of anatomic features. This is particularly important in children, who have little fat and lack intrinsic contrast differences.

Scanning during peak contrast levels optimizes the evaluation of mediastinal and hilar lymph nodes and masses. Mediastinal vascular structures and masses are easily differentiated (Fig. 17). Helical CT is an excellent modality for assessing anterior or middle mediastinal masses and possible lung parenchyma involvement, but MRI is increasingly taking its place in evaluating masses. Posterior mediastinal masses can also be studied by helical CT, but MRI is the procedure of choice in these cases, as mostly they are neurogenic tumors. Special attention should be given to intraspinal extension.

CT provides excellent spatial resolution and considerable detail. The pulmonary parenchyma is optimally visualized on CT as opposed to MR imaging (Newman 2011), and calcification is better seen on CT.

Other important indications for helical CT are tumor staging and follow-up evaluation of treatment, and particularly, assessment of lung metastasis. As compared with conventional CT, helical CT can facilitate identification of infiltration, vascular encasement, airway displacement, and enlarged hilar lymph nodes. Multiplanar reconstructions can be very useful for identifying infiltration, encasement, or compression of vital structures, and intraspinal extension. The resulting information facilitates surgical planning and radiation therapy. Another advantage is that chest and abdominal studies can be performed in a single session with a single dose of IV contrast material. This is especially important in the evaluation of patients with lymphoma.

Other abnormalities that are well seen on helical CT studies at peak contrast enhancement include congenital large vessel abnormalities (Trinavarat 2011) (Figs. 8, 9, 10, 11), congenital chest masses (pulmonary sequestration, cystic congenital pulmonary airway malformation) (Garcia-Peña et al. 2013) (Figs. 12, 13, 14), pulmonary and pleural infections (Fig. 18), chest trauma, surgical shunts and postoperative vascular anatomy, vascular masses (angio-mas, lung fistula, varix), central pulmonary thromboemboli (Remy-Jardin et al. 1992; Lee et al. 2012), and cardiac and coronary evaluation (Goo et al. 2009; Saad et al. 2009).

### 3.2 Evaluation of Vascular Anatomy: CT Angiography

CT angiography is relatively new, and possibly one of the most important applications of helical CT (Choo et al. 2006; Lawrence 2008; Marini et al. 2009; Poole and Ferguson 2010; Chung et al. 2010; Khandelwal et al. 2011). CT angiography provides high-quality vascular imaging, and can depict congenital and acquired vascular abnormalities of the chest in children. Standardized CT angiography and arterial timing bolus test (or bolus-tracking technique) protocols are recommended in such cases (Table 3). Optimal contrast enhancement is best achieved using a power injector, which should be used whenever possible. With CT angiography, one can analyze vascular abnormalities of the pulmonary arteries, aortic arch and great vessels (double aortic arch, pulmonary sling, etc.) (Figs. 1, 8, 9, 10, 11) (Katz et al. 1995; Ghersin et al. 2005; Turner et al. 2005), pulmonary vein anomalies (Fig. 19) (Ou et al. 2009; Vyas et al. 2012), cardiac and coronary lesions (Fig. 20) (Saad et al. 2009; Goo et al. 2009; Lapierre et al. 2010; Siripornpitak et al. 2011), cardiac surgery postoperative status (Marini et al. 2009), and vascular lesions (Khandelwal et al.

**Fig. 26** Diaphragmatic lesion due to reherniation after congenital diaphragmatic hernia repair. A 1-year-old boy with successful previous repair of a congenital diaphragmatic hernia, again presented an abnormal left diaphragm. **a** Chest X-ray after neonatal surgery shows a normally located left diaphragm. **b** Chest X-ray 1 year later depicts opacification of the left pulmonary base, a poorly-defined diaphragm, and the nasogastric tube in the thoracic base. **c** Enhanced axial CT show the gastric bubble up to the chest. It is difficult to determine whether the finding might be due to eventration of the diaphragm or diaphragmatic reherniation. **d** Coronal and **(b)** sagittal MIP images demonstrate the diaphragmatic hole, through which the stomach has herniated



2011). Furthermore, it is useful for studying congenital lung malformations (pulmonary sequestration, congenital cystic pulmonary airway malformation) (Biyyam et al. 2010), in which depiction of the systemic (aortic feeding) vessel is important for establishing the definitive diagnosis (García-Peña et al. 2013) (Figs. 2, 3, 12, 13, 14).

Cardiac imaging by MDCT is used more frequently in the evaluation of complex congenital pediatric heart diseases (Goo 2011) because of its faster volume coverage and higher

temporal resolution. Retrospective ECG-gated imaging with lower KV and automatic tube current modulation can reduce the effective dose, prospective ECG-gated imaging has been shown to decrease radiation dose to an even greater degree in cardiac CT (Jin et al. 2010; Gao et al. 2012).

The improved contrast enhancement of helical CT and the postprocessing capabilities, such as multiplanar and 3-D reconstructions, are useful for characterizing normal and abnormal vascular anatomy. MRI is usually the technique of



**Fig. 27** Intrathoracic rib in an asymptomatic 3-year-old boy. **a** Anteroposterior chest X-ray. There is an abnormal, dense, elongated structure in a right paravertebral position. **b** Axial CT image at the subcarinal level. The dense bony image is seen to arise from the anterior area of the vertebral body. **c** Shaded surface display image better shows the intrathoracic rib with its anterior vertebral origin and its course, running parallel and oblique to the spine

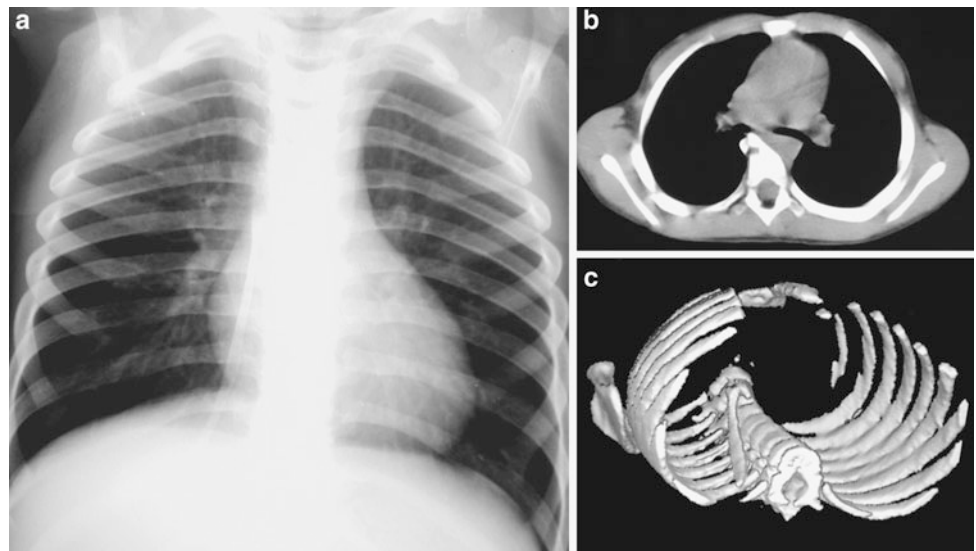
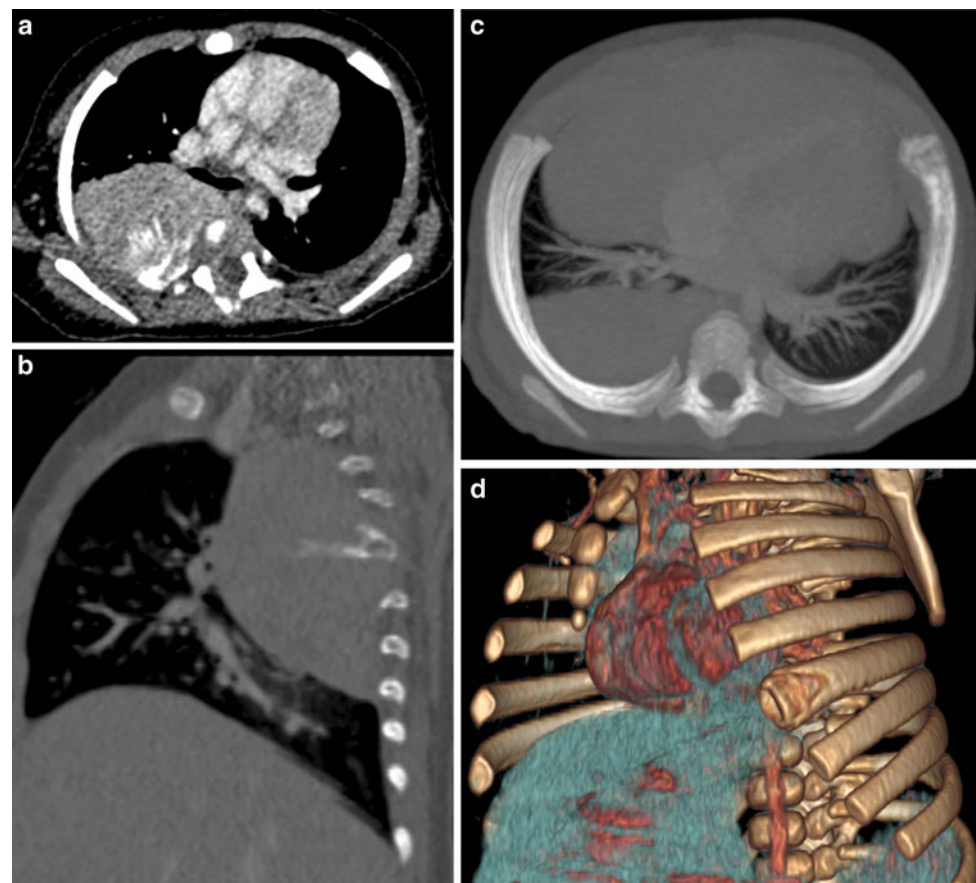


**Fig. 28** Metastatic right chest wall PENET with bony invasion in an 11-year-old girl with chest pain. **a** On enhanced axial CT, a mass is seen in the right hemithorax and a bony lesion in the posterior arch of the rib. There is sunrise periosteal reaction. **b** Sagittal MPR shows a long well-defined mass with extrapleural characteristics (“pregnant belly sign”). **c** Axial MIP image, and **d** VRT depict a metastatic bony lesion in the left anterior arch



choice for evaluating congenital large vessel anomalies and other vascular or cardiac anomalies, but helical CT is a feasible alternative in patients whose clinical condition

requires a quick exam and where a lengthy MRI study would not be advisable (Chandrashekhara et al. 2012). CT is also invaluable as a one-stop shop when combining vascular



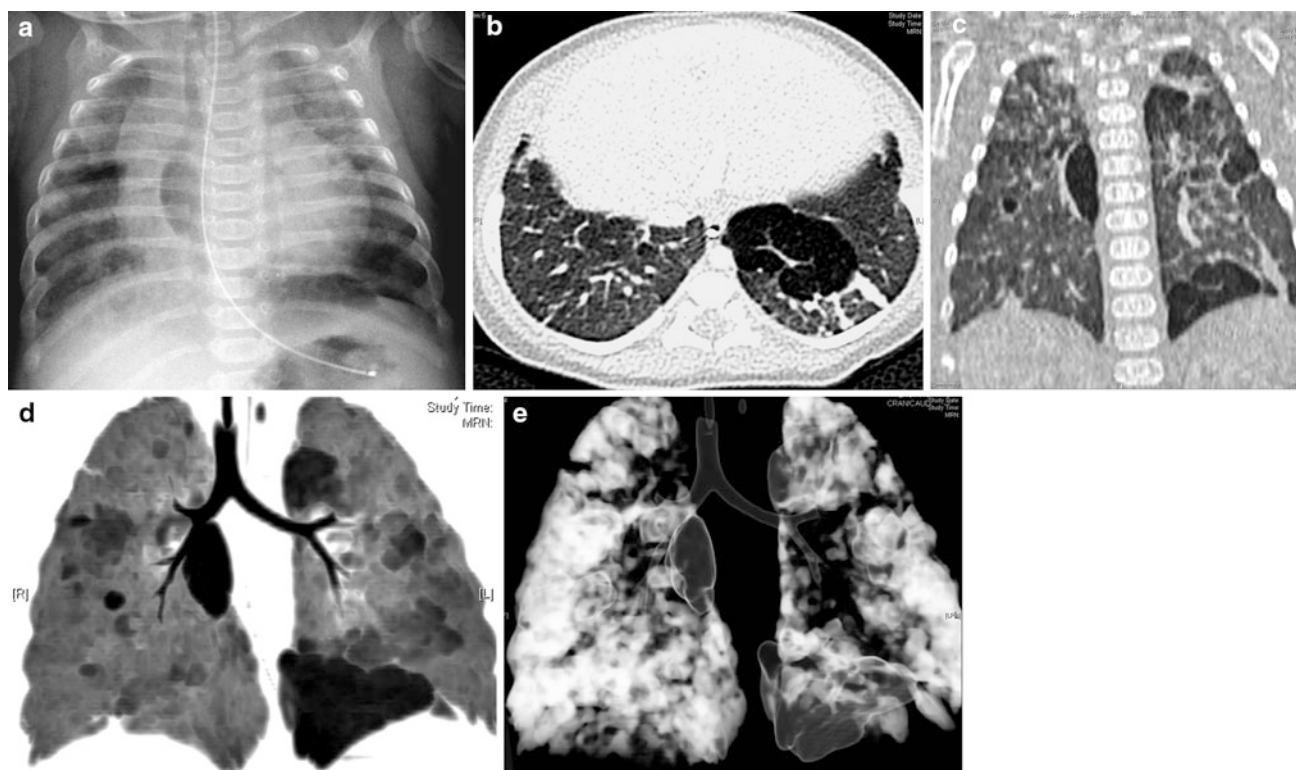


**Fig. 29** Inconclusive image on chest X-ray. A preterm neonate who developed respiratory distress soon after birth. **a** Initial chest X-ray shows multiple cystic abnormalities, which are of uncertain aetiology, cystic lung disease, and focal air trapping are the differentials. **b** Axial CT and **c** coronal MPR eloquently confirms the presence of focal air

trapping secondary to respiratory syndrome. The cystic spaces on CXR are seen as areas of segmental air trapping on axial and coronal lung window CT images. **d** MinIP image and **e** VR “bronchogram” volumetric 3D images highlight the hyperlucent areas of the lung and better shows the tracheobronchial tree

and airway abnormalities. Children benefit from the high-speed scan acquisition and the low sedation requirements (Figs. 1, 8, 9, 10).

Several post-processing techniques are available for analysis of the vascular anatomy. Curved multiplanar reconstructions are useful for displaying serpentine vascular structures, such as a systemic vessel in pulmonary sequestration, but they are highly operator-dependent and time-consuming. STS-MIP requires less computer time and can be used as an alternative to curved MPR to improve the depiction of vessels.

MIP, SSD, and VR images, the ones most frequently used to provide information on vascular anatomy, are comparable to conventional angiograms. Since these 3D images can be rotated in a movie loop, they enable visualization of lesions from innumerable viewing angles. This can facilitate analysis of underlying pathologies and improve display of the vessel origin on superimposed images (Figs. 1, 2, 3, 4, 8, 9, 12, 13, 14, 19, 20). Relationships with other important structures (the airways) can also be perceived.

CT angiography can replace conventional angiography in many applications. Helical CT angiocardigraphy with 3D reconstructions is superior to echocardiography for

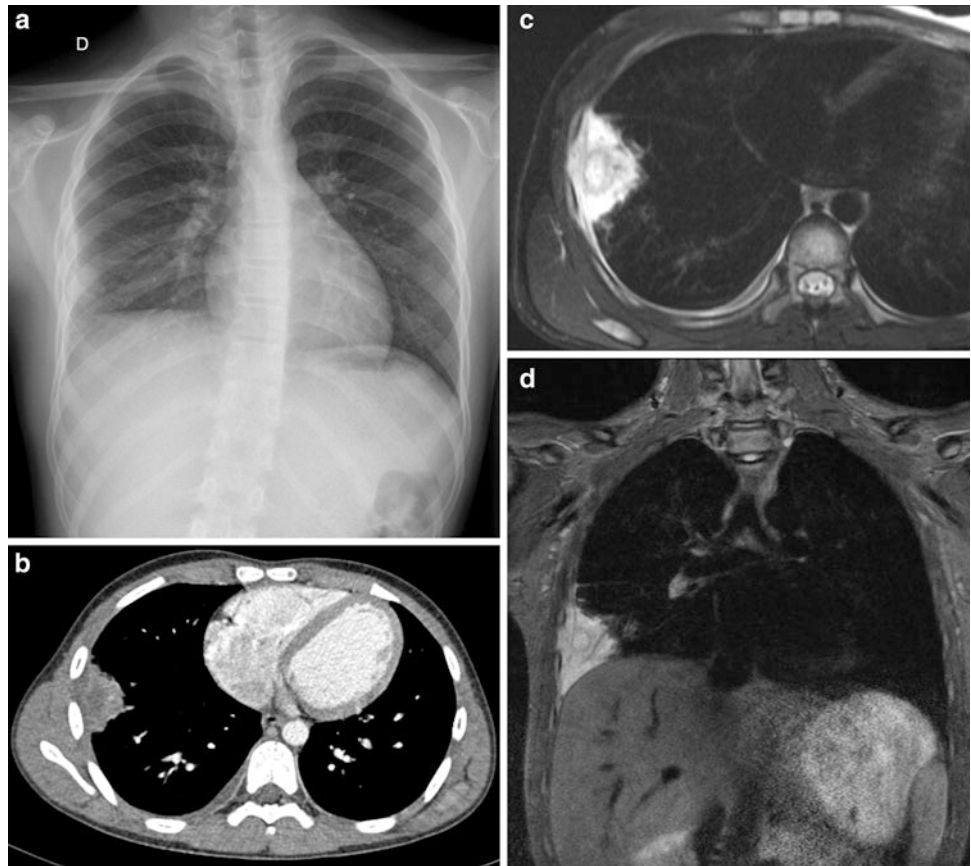
noninvasive assessment of pulmonary artery anatomy and is equal to angiography in patients with complex congenital heart disease (Vestra et al. 1999). As compared to conventional arteriography, CT angiography has the advantages of lower patient morbidity, and reductions in cost and time. Conventional angiography is reserved for angiographic treatment in most cases.

### 3.3 Evaluation of Central Airways

Helical CT of the central airways is performed with thin collimation during one breath-hold or during quiet respiration (Tables 1 and 2). As a result of the thin-section volumetric scanning, more detailed anatomy can be obtained without partial volume effects. A comparison of standard CT at 8 mm contiguous increment and helical CT with thin collimation and reconstruction at 50 % overlap showed that helical CT was the superior imaging technique (Shafer et al. 1991).

Helical CT demonstrates 95 % of the normal segmental bronchial anatomy. The inferior and superior lingular segmental bronchi, which are often difficult to visualize on conventional CT scans, could be seen in 85 % of patients on helical scans (Costello et al. 1992b). MPR, MIP, SSD, and VR

**Fig. 30** Inconclusive images on chest X-ray. A 6-year-old boy with chest pain. Pulmonary abscess was missed on CXR **a** Chest X-ray shows a dense longitudinal image vertically following the chest wall, and obliteration of the right costo-diaphragmatic angle. Pleural or chest wall disease was suspected. US shows a mass of difficult localization. **b** Enhanced axial CT demonstrates a round peripheral lung lesion with a central hypodensity (abscess), and right pleural thickening. A hypodense area was also visible between the right ribs (small chest wall abscess). **c** Axial T2-W FatSat, and **d** Coronal STIR T2-W images show a hyperintense subpleural lung lesion with a hypointense halo area in its center, and a hyperintense lesion going through the ribs on the chest wall. Pleural thickening is also present. *Fusobacterium nucleatum* infection was found in the abscess puncture



images beautifully depict the central airways and are of great clinical value in their assessment (Kauczor et al. 1996; Ferreti et al. 1996; Nicotra et al. 1997; Venkatraman et al. 2006).

Helical CT of the airways is mainly indicated in the study of congenital and acquired abnormalities of the tracheobronchial tree, postpneumectomy complications, complications after lung transplantation, and endobronchial lesions (Berrocal et al. 2004; Kosucu et al. 2004; Choong et al. 2006; Yedururi et al. 2008; Lee et al. 2011; Garcia-Peña et al. 2013) (Figs. 1, 10, 21, 22, 23, 24).

Intensive care and postoperative patients are good candidates for assessment by helical CT. Following pneumectomy, a dehiscence or a bronchopleural fistula can occur at the anastomotic region. Bronchopleural fistula (Fig. 18) is best shown on coronal reformats. Helical CT can demonstrate a bronchopulmonary fistula when conventional axial imaging may be confusing. Two- and three-dimensional images are better than axial images to identify stenotic lesions, especially stenoses in obliquely oriented bronchi. Multiplanar reconstructions along the axis of the bronchus are also useful.

Endobronchial lesions and endobronchial stent location are best shown on multiplanar reconstructions along the axis of the bronchus. Endobronchial lesions (endobronchial tumors, long-standing foreign bodies) can also be shown with virtual endoscopy images (Figs. 22, 24). Intrabronchial

foreign bodies can be difficult to diagnose. There is often no history of foreign body aspiration in children. These patients are usually sent for chest CT examination due to foreign body complications. CT scanning can help in detecting the intrabronchial lesion in these cases.

Helical CT can be useful for evaluating the tracheobronchial tree when using bronchographic images depicted by the VR technique. Tracheobronchography is quite invasive and can carry a significant risk in pediatric patients. This risk is greatest in conditions that compromise the tracheal lumen. Moreover, airway lesions may not be isolated anomalies. It is important to emphasize the possibility offered by helical CT of simultaneously providing bronchographic images and angiographic reconstructions. This combination of data allows evaluation of complex malformations in a single examination and can avoid unnecessary invasive diagnostic procedures (Choo et al. 2006).

Virtual bronchoscopy can be useful for presurgical assessment of strictures that prevent direct passage of a conventional bronchoscope, and for evaluating endoluminal lesions (Honnef et al. 2006) (Figs. 22, 24). Post-processing techniques, such as multiplanar reformatting, volume rendering, and virtual bronchoscopy assist in surgical planning by providing a better representation of 3D anatomy (Yedururi et al. 2008).

MDCT techniques are currently used for noninvasive imaging of patients with suspected tracheobronchomalacia (TBM). Paired end-inspiration, dynamic expiratory MDCT is the examination of choice in these patients (Lee et al. 2009). Dynamic expiratory CT demonstrates a greater degree and extent of airway collapse than standard end-expiratory CT in patients with suspected TBM (Ferretti et al. 2008). Cine CT requires 64-row or greater MDCT scanners, and can be used to rapidly acquire images of the airways throughout the respiratory cycle during free breathing (inspiration and expiration), even in tachypneic patients. In uncooperative patients in whom the controlled-ventilation technique is not feasible, cine CT can be used (Yedururi et al. 2008).

### 3.4 Evaluation of Difficult Areas: Cervicothoracic Junction, Peridiaphragmatic Area, and Chest Wall

Helical CT is useful for imaging lesions in areas that are difficult to evaluate on axial images and are better assessed on 2- or 3-D reformatted images. Multiplanar reconstructions, generated from helical CT data, are particularly helpful in lesions located in cervicothoracic and apical areas (Fig. 25) (Harty and Kramer 1998), peridiaphragmatic and diaphragmatic areas (Fig. 26) (Brink et al. 1994a; Israel et al. 1996; Chavhan et al. 2010), and the chest wall (Figs. 27, 28) (Donnelly et al. 1997). The reformatted images better depict the extension of lesions and their relationship to adjacent anatomic structures.

Although tumors of the chest wall are uncommon in children, they are often malignant and may aggressively invade the pleural space, lung, spinal canal, or mediastinum. The preoperative imaging evaluation should focus on assessment of the size and extent of the primary tumor and any possible bone invasion or involvement of the chest wall musculature. Both CT and MRI can identify bone and soft-tissue involvement by chest wall tumors (Donnelly et al. 1997). CT is more sensitive in detecting cortical bone disruptions and calcifications, but MRI is better at depicting soft-tissue and marrow involvement. Three-dimensional reconstructions also play a role in the depiction of bony structures of the chest wall and the spine. SSD images can be useful in showing the chest wall deformity in pectus excavatum, but VR images are now used more often for this purpose.

### 3.5 Evaluation of Critically Ill Patients

One of the greatest advantages of helical CT, especially MDCT, is its speed; examinations are shorter and the need

for sedation is greatly reduced. This means that some patient groups (e.g., very ill patients and trauma cases) who were not previously considered good candidates can now benefit from CT studies (Westra and Wallance 2005). In these patients, the speed of helical CT allows an enormous amount of information to be obtained in a very short time, and enables both the chest and abdomen to be examined with one data acquisition and a single dose of intravenous contrast material. Helical CT studies in these cases should be done under the supervision of the intensive care physician, who also oversees transport of the child to the CT facilities. The images can be reconstructed and reformatted retrospectively after the patient has been returned to the intensive care unit (Veys and Owens 2002; Moore et al. 2011) (Figs. 5, 10, 21).

### 3.6 Evaluation of Inconclusive Images on Chest Radiography

Helical CT with its technical capabilities of multiplanar and 3D imaging is often useful for defining an inconclusive image seen on chest X-rays and for establishing its exact anatomical location (Figs. 29, 30).

## 4 Conclusions

Helical CT technology has many potential clinical benefits when used in pediatric patients. These include speed, improved image quality and reductions in the volume of contrast material required, and in the use of sedation. Radiation exposure should be controlled by using low-dose pediatric protocols adjusted to the body weight of the patient, dose modulation techniques, noise reduction systems, and extended pitch when possible, remembering the limitations with automated dose. Two- or three-dimensional reformatted images that are of great value in clinical diagnoses can be generated with the available post-processing methods. The technical aspects of this technique, the clinical indications, and the suggested protocols to be used have been set out in this chapter.

### Summary

The increase in radiation burden associated with CT imaging and the potential risk to children cannot be ignored. Therefore, CT requests must be justified with a risk–benefit analysis carried out before undertaking CT examination in children. Imaging techniques and dedicated pediatric protocols must be available to the operators, ensuring adherence to the ALARA principle. The clinical indications have also been set out in this chapter.



## References

- Agrons GA, Rosado-de-Christenson ML, Kirejczyk WM et al (1998) Pulmonary inflammatory pseudotumor: radiologic features. *Radiology* 206:511–518
- Ahn MI, Gleeson TG, Chan IH et al (2010) Perifissural nodules seen at CT screening for lung cancer. *Radiology* 254:949
- Ambrosino MM, Genieser NB, Roche KJ et al (1994) Feasibility of high-resolution low-dose chest CT in evaluating the pediatric chest. *Pediatr Radiol* 24:6–10
- Bal CS, Kumar A, Chandra P et al (2004) Is chest X-ray or high-resolution computed tomography scan of the chest sufficient investigation to detect pulmonary metastasis in pediatric differentiated thyroid cancer? *Thyroid* 14:217–225
- Ben Saad M, Rohnean A, Sigal-Cinqualbre A et al (2009) Evaluation of image quality and radiation dose of thoracic and coronary dual-source CT in 110 infants with CHD. *Pediatr Radiol* 39:668–676
- Berrocal T, Madrid C, Novo S et al (2004) Congenital anomalies of tracheobronchial tree, lung, and mediastinum: embryology, radiology, and pathology. *Radiographics* 24:17
- Brenner DJ, Hall EJ (2007) Computed tomography- an increasing source of radiation exposure. *N Engl J Med* 357:2277–2284
- Biyyam DR, Chapman T, Ferguson MR et al (2010) Congenital lung abnormalities: embryologic features, prenatal diagnosis, and postnatal radiologic-pathologic correlation. *Radiographics* 30:1721–1738
- Brink JA (1995) Technical aspects of helical (spiral) CT. *Radiol Clin North Am* 33:825–841
- Brink JA, Heiken JP, Semenkovich J et al (1994a) Abnormalities of the diaphragm and adjacent structures: findings on multiplanar spiral CT scan. *AJR* 163:307–310
- Brink JA, Heiken JP, Wang G et al (1994b) Helical CT: principles and technical considerations. *Radiographics* 14:887–893
- Brody AS, Klein JS, Molina PL et al (2004) High-resolution computed tomography in young patients with cystic fibrosis: distribution of abnormalities and correlation with pulmonary function tests. *J Pediatr* 145:32–38
- Buckley JA, Scott WWJ, Siegelman SS et al (1995) Pulmonary nodules: effect of increased data sampling on detection with spiral CT and confidence in diagnosis. *Radiology* 196:395–400
- Callahan CW (1998) Primary tracheomalacia and gastro-esophageal reflux in infants with cough. *Clin Pediatr (Phila)* 37:725–731
- Chandrasekhar G, Sodhi KS, Saxena AK et al (2012) Correlation of 64row MDCT, echography and cardiac catheterization angiography in assessment of pulmonary arterial anatomy in children with congenital heart disease. *Eur J Radiol* 81:4211–4217
- Chavhan GB, Babyn PS, Cohen RA et al (2010) Multimodality imaging of the pediatric diaphragm: anatomy and pathologic conditions. *Radiographics* 30:1797–1817
- Christner JA, Zavaletta VA, Eusemann CD et al (2010) Dose reduction in helical CT: dynamically adjustable z-axis X-ray beam collimation. *Am J Roentgenol* 194:49–55
- Choo KS, Lee HD, Ban JE et al (2006) Evaluation of obstructive airway lesions in complex congenital heart disease using composite volume-rendered images from multi-slice CT. *Pediatr Radiol* 36:219–223
- Choong CK, Sweet SC, Zoole JB (2006) Bronchial airways anastomotic complications after pediatric lung transplantation: incidence, cause, management, and outcome. *J Thorac Cardiovas Surg* 131:198–203
- Chung MP, Yi CA, Lee HY et al (2010) Imaging pulmonary vasculitis. *Radiology* 255:322
- Coakley FV, Cohen MD, Waters DJ et al (1997a) The detection of pulmonary metastases with pathologic correlation in canine model: effect of breathing on the accuracy of helical CT. *AJR* 169:1615–1618
- Coakley FV, Cohen MD, Waters DJ et al (1997b) Detection of pulmonary metastases with pathologic correlation: effects of breathing on accuracy of spiral CT. *Pediatr Radiol* 27:576–579
- Coakley FV, Cohen MD, Johnson MS et al (1998) Maximum intensity projection images in the detection of simulated pulmonary nodules by spiral CT. *Br J Radiol* 71:135–140
- Cohnen M, Vogt C, Beck A et al (2004) Feasibility of MDCT colonography in ultra-low-dose technique in the detection of colorectal lesions: comparison with high-resolution video colonoscopy. *AJR* 183:1355–1359
- Cook BA, Bass JW, Nomizu S, Alexander ME (1992) Sedation of children for technical procedures: current standards of practice. *Clin Pediatr* 31:137–142
- Costello P, Anderson W, Blume D (1991) Pulmonary nodule: evaluation with spiral volumetric CT. *Radiology* 179:875–876
- Costello P, Dupuy DE, Ecker CP et al (1992a) Spiral CT of the thorax with reduced volume of contrast material: a comparative study. *Radiology* 183:663–666
- Costello P, Kruskal J, Dupuy D et al (1992b) Evaluation of tracheobronchial tree with spiral CT. *Radiology* 185:355
- Coursey C, Frush DP, Yoshizumi T et al (2008) Pediatric chest MDCT using tube current modulation: effect on radiation dose with breast shielding. *AJR Am J Roentgenol* 190:54–61
- Dillman JR, Sanchez R, Ladino-Torres MF et al (2011) Expanding upon the unilateral hyperlucent hemothorax in children. *Radiographics* 31:723–741
- Donnelly LF, Taylor CNR, Emery KH et al (1997) Asymptomatic, palpable, anterior chest wall lesions in children: is cross-sectional imaging necessary? *Radiology* 202:829–831
- Egelhoff JC, Ball WS Jr, Kock BL et al (1997) Safety and efficacy of sedation in children using a structured sedation program. *AJR* 168:1259–1262
- Engeler CE, Tashjian JH, Engeler CM (1994) Volumetric high-resolution CT in the diagnosis of interstitial lung disease and bronchiectasis: diagnostic accuracy and radiation dose. *AJR* 163:31–35
- Ferretti GR, Vining DJ, Knoplich J et al (1996) Tracheobronchial tree: three-dimensional spiral CT with bronchoscopic perspective. *J Comput Assist Tomogr* 20:777–781
- Ferretti GR, Jankowski A, Perrin MA et al (2008) Multi-detector CT evaluation in patients suspected of tracheobronchomalacia: comparison of end-expiratory with dynamic expiratory volumetric acquisitions. *Eur J Radiol* 68:340–346
- Frush DP, Donnelly LP (1998) Helical CT in children: technical considerations and body applications. *Radiology* 209:37–48
- Frush DP, Bisett GS III, Hall SC (1996) Pediatric sedation in radiology: the practice of safe sleep. *AJR* 167:1381–1387
- Frush DP, Siegel MJ, Bisett GS III (1997) Challenges of pediatric spiral CT. *Radiographics* 17:939–959
- Frush DP, Slack CC, Hollingsworth CL et al (2002) Computed-simulated radiation dose reduction for abdominal multidetector CT of paediatric patients. *AJR Am J Roentgenol* 179:1107–1113
- Gao Y, Lu B, Hou Z et al (2012) Low-dose dual-source CT angiography in infants with complex congenital heart disease: a randomized study. *Eur J Radiol* 81:e789–e795
- García-Peña P, Lucaya J (2004) High-resolution CT in children, technique and indications. *Eur Radiol* 14:13–20
- García-Peña P, Lucaya J (1999) Chest CT-scan in children: main applications and advantages. *Pediatr Pneumonol* 18:56–59
- García-Peña P, Boixadera H, Barber I et al (2011) Thoracic findings of systemic diseases at high-resolution CT in children. *Radiographics* 31:465–482
- García-Peña P, Coma A, Enriquez G (2013) Congenital lung malformations: radiological findings and clues for the differential diagnosis. *Acta Radiol*. doi:10.1177/0284185113475919



- García-Peña P, Owens CM (2008) Helical multidetector chest CT. In: Lucaya J, Strife JL (2nd eds) *Pediatric chest imaging*. Springer-Verlag Berlin, Heidelberg, pp 47–75
- Gartenschläger M, Schweden F, Gast K et al (1998) Pulmonary nodules: detection with low-dose vs conventional-dose spiral CT. *Eur Radiol* 8:609–614
- Ghersin E, Khoury A, Litmanovich D et al (2005) Comprehensive multidetector computed tomography assessment of severe cardiac contusion in a pediatric patient: correlation with echocardiography. *J Comput Assist Tomogr* 29:739–741
- Goo HW, Seo DM, Yun TJ et al (2009) Coronary artery anomalies and clinically important anatomy in patients with congenital heart disease: multislice CT findings. *Pediatr Radiol* 39:265–273
- Goo HW (2011) Cardiac MDCT in children: CT technology overview and interpretation. *Radiol Clin N Am* 49:997–1010
- Goo HW, Yang DH, Hong SJ et al (2010) Xenon ventilation CT using DS & DE technique in children with bronchiolitis obliterans: correlation of xenon and CT density values with pulmonary function test results. *Pediatr Radiol* 40:1490–1497
- Greess H, Nömayr A, Wolf H et al (2002) Dose reduction in CT examinations of children by an attenuation-based online modulation of tube current (CARE dose). *Eur Radiol* 12:1571–1576
- Greess H, Luzte J, Nömayr A et al (2004) Dose reduction in subsecond multislice spiral CT examination in children by online tube current modulation. *Eur Radiol* 14:995–999
- Gudjónsdóttir J, Ween B, Olsen DR (2010) Optimal use of AEC in CT: a literature review. *Radiol Technol* 81(4):309–317
- Harty MP, Kramer SS (1998) Recent advances in pediatric pulmonary imaging. *Curr Opin Pediatr* 10:227–235
- Heyer CM, Kagel T, Lemburg SP et al (2004) Evaluation of tracheobronchial anomalies in children using low-dose multidetector CT: report of a 13-year-old boy with a tracheal bronchus and recurrent pulmonary infections. *Pediatr Pulmonol* 38:168–173
- Heyer CM, Mohr PS, Lemburg SP et al (2007) Image quality and radiation exposure at pulmonary CT angiography with 100- or 120-kVp protocol: prospective randomized study. *Radiology* 245:577–583
- Hoey ETD, Gopalan D, Ganesh V, Agrawal SKB, Qureshi N, Tasker AD, Clements L, Screaton NJ (2009) Dual-energy CT pulmonary angiography: a novel technique for assessing acute and chronic pulmonary thromboembolism. *Clin Radiol* 64:414–419
- Honnef D, Wildberger JE, Das M et al (2006) Value of virtual tracheobronchoscopy and bronchography from 16-slice multidetector-row spiral compute tomography for assessment of suspected tracheobronchial stenosis in children. *Eur Radiol* 16:1684–1691
- Hoppe H, Dinkel HP, Walder B et al (2004) Grading airways stenosis down to the segmental level using virtual bronchoscopy. *Chest* 125:704–711
- Hopper KD, Singapuri K, Finkel A (2000) Body CT and oncologic imaging. *Radiology* 215:27–40
- Hu H, He HD, Foley WD et al (2000) Four multidetector-row helical CT: image quality and volume coverage speed. *Radiology* 215:55–62
- Israel RS, Mayberry JC, Primack SL (1996) Diaphragmatic rupture. Use of helical CT scanning with multiplanar reformations. *AJR* 167:1201–1203
- Jin KN, Park EA, Shin CI et al (2010) Retrospective versus prospective ECG-gated dual-source CT in pediatric patients with congenital heart disease: comparison of image quality and radiation dose. *Int J Cardiovasc Imag* 26:63–73
- Johnson PT, Fishman EK, Duckwall JR et al (1998a) Interactive three-dimensional volume rendering of spiral CT data: current applications in the thorax. *Radiographics* 18:165–187
- Johnson JL, Kramer SS, Mahboubi S (1998b) Air trapping in children: evaluation with dynamic lung densitometry with spiral CT. *Radiology* 206:95–101
- Johnson TRC, Kraub B, Sedlmair M et al (2007) Material differentiation by DECT: initial experience. *Eur Radiol* 17:1510–1517
- Joosten S, MacDonald M, Lau KK et al (2012) Excessive dynamic airway collapse co-morbid with COPD diagnosed using 320-slice dynamic CT scanning technology. *Thorax* 67:95–96
- Kalra MK, Wittram C, Maher MM (2003) Can noise reduction filters improve low-radiation-dose chest CT image? Pilot study. *Radiology* 228:257–264
- Karla MR, Maher MM, Toth TL et al (2004) Comparison of Z-axis automatic tube current modulation technique with fixed tube current CT scanning of abdomen and pelvis. *Radiology* 232:347–353
- Kaste SC, Young CW (1996) Safe use of power injectors with central patient motion and peripheral venous access devices for pediatric CT. *Pediatr Radiol* 26:449–501
- Kaste SC, Young CW, Holmes TP et al (1997) Effect of helical CT on the frequency of sedation in pediatric patients. *AJR* 168:1001–1003
- Katz M, Konen E, Rozenman J, Szeinberg A et al (1995) Spiral CT and 3d image reconstruction of vascular rings and associated tracheobronchial anomalies. *J Comput Assist Tomogr* 19:564–568
- Kauczor HU, Wolcke B, Fisher B et al (1996) Three-dimensional helical CT of the tracheobronchial tree: evaluation of imaging protocols and assessment of suspected stenosis with bronchoscopic correlation. *AJR* 167:419–424
- Kawel N, Seifert B, Luetolf M et al (2009) Effect of slab thickness on the CT detection of pulmonary nodules: use of sliding thin-slab maximum intensity projection and volume rendering. *AJR Am J Roentgenol* 192:1324
- Khan MF, Herzog C, Ackermann H et al (2004) Virtual endoscopy of the trachea-bronchial system: sub-millimeter collimation with 16-row multidetector scanner. *Eur Radiol* 14:1400–1405
- Khandelwal N, Kalra N, Garg MK et al (2011) Multidetector CT angiography in Takayasu arteritis. *Eur J Radiol* 77:S369–S374
- Klusmann M, Owens C (2009) HRCT in paediatric interstitial lung disease—a review for 2009. *Pediatric Radiol* 39:471–481
- Kosucu P, Ahmetoglu A, Koramaz I et al (2004) Low-dose MDCT and virtual bronchoscopy in pediatric patients with foreign body aspiration. *Am J Roentgenol (AJR)* 183:1771–1777
- Kroft LJM, Roelofs JJH, Geleijns J (2010) Scan time and patient dose for thoracic imaging in neonates and small children using axial volumetric 320-detector row CT compared to helical 64, 32, and 16 detector row CT acquisition. *Pediatr Radiol* 40:294–300
- Lapierre C, Déry J, Guérin R et al (2010) Segmental approach to imaging of congenital heart disease. *RadioGraphics* 30:397–411
- Lawrence MB (2008) CT angiography in children: it is accurate, but is it safe? *JACC Cardiovasc Imag* 1:340–342
- Lee EY, Greenberg SB, Boieselle PM (2011) Multidetector computed tomography in pediatric large airway diseases: state-of-the-art. *Radiol Clin North Am* 49:869–893
- Lee EY, Litmanovich D, Boieselle PM (2009) Multidetector CT evaluation of tracheobronchomalacia. *Radiol Clin N Am* 47:261–269
- Lee EY, Strauss KJ, Tracy DA et al (2010a) Comparison of standard-dose and reduced-dose expiratory MDCT techniques for assessment of tracheomalacia in children. *Acad Radiol* 17:504–510
- Lee EY, Tracy DA, Bastos M et al (2010b) Expiratory volumetric MDCT evaluation of air trapping in pediatric patients with and without tracheomalacia. *Am J Roentgenol* 194:1210–1215
- Lee EY, Tse SKS, Zarakowski D et al (2012) Children suspected of having pulmonary Embolism: multidetector CT pulmonary angiography-thromboembolic risk factors and implications for appropriated use. *Radiology* 262:242–251
- Lee EY, Zucker EJ, Restrepo R et al (2013) Advances large airway CT imaging in children: evolution from axial to 4-D assessment. *Pediatr Radiol* 43:285–297

- Lobo L, Antunes D (2012) Chest CT in infants and children. *Eur J Radiol*. doi:10.1016/j.ejrad.2011.12.006
- Lucaya J, Decou Le Pointe (2008) High-resolution CT of the lung in children. In: Lucaya J, Strife JL (2nd eds) *Pediatric chest imaging*. Springer-Verlag Berlin, Heidelberg, pp 77–121
- Lucaya J, Garcia-Peña P, Herrera L et al (2000a) Expiratory chest CT in children. *AJR* 174:1–7
- Lucaya J, Piqueras J, Garcia-Peña P et al (2000b) Low-dose high-resolution CT of the chest in children and young adults: dose, cooperation, artifacts incidence, and image quality. *AJR* 175:985–992
- Marini D, Agnoletti G, Brunelle F et al (2009) Cardiac CT angiography after coronary artery surgery in children using 64-slice CT scan. *Eur J Radiol* 71:492–497
- Mc Carville MB, Lederman HM, Santana VM et al (2006) Distinguishing benign from malignant pulmonary nodules with helical CT in children with malignant tumors. *Radiology* 239:514–520
- Mc Hugh K (2008) Chest tumors other than lymphoma. In: Lucaya J, Strife JL (eds) *Pediatric chest imaging*. Chest imaging in infants and children, 2nd edn. Springer, Berlin, Heidelberg, pp 263–287
- Moore MA, Wallace EC, Westra SJ (2011) Chest trauma in children: current imaging guidelines and techniques. *Radiol Clin N Am* 49:949–968
- Napel SA (1995) Basic principles of spiral CT. In: Fishman EK, Jeffrey RB Jr (eds) *Spiral CT: principles, techniques, and clinical application*. Raven, New York, pp 1–9
- Napel SA, Jeffrey RB Jr (1993) STS-MIP: a new reconstruction technique for CT of the chest. *J Comput Assist Tomogr* 17:832–838
- Newman B (2011) Thoracic neoplasms in children. *Radiol Clin N Am* 49:633–664
- Nicotra JJ, Mahboubi S, Kramer SS (1997) Three-dimensional imaging of the pediatric airway. *Int J Pediatr Otorhinolaryngol* 41:299–305
- Oddone M, Granata C, Vercellino N et al (2005) Multi-modality evaluation of the abnormalities of the aortic arches in children: techniques and imaging spectrum with emphasis on MRI. *Pediatr Radiol* 35:947–960
- Ou P, Marini D, Celermajor DS et al (2009) Non-invasive assessment of congenital pulmonary vein stenosis in children using cardiac-gated CT with 64-slices technology. *Eur J Radiol* 70:595–599
- Papaoiannou G, Young C, Owens C (2007) Multidetector row CT for imaging the paediatric tracheobronchial tree. *Pediatr Radiol* 37:515–529
- Pappas JN, Donnelly LF, Frush DP (2000) Reduced frequency of sedation of young children with multisection helical CT. *Radiology* 215:897–899
- Paterson A (2005) Imaging evaluation of congenital lung abnormalities in infant and children. *Radiol Clin North Am* 43:303–323
- Paterson A, Frush DP, Donnelly LF (2001) Helical CT of the body: are settings adjusted for pediatric patients? *AJR* 176:1–6
- Pearce MS, Salotti JA, Little MP et al (2012) Radiation exposure from CT scans in childhood and subsequent risk of leukaemia and brain tumours: a retrospective cohort study. *Lancet* 4(380):499–505
- Poole PS and Ferguson EC (2010) Revisiting pulmonary arteriovenous malformations. Radiographic and CT-imaging findings and corresponding treatment options. *Contemporary Diagnostic Imaging (CDR)* 8:1
- Remy-Jardin M, Remy J, Watinne L et al (1992) Central pulmonary thromboembolism: diagnosis with spiral volumetric CT with the single-breath-hold technique comparison with pulmonary angiography. *Radiology* 185:381–387
- Remy-Jardin M, Remi J, Giraud F et al (1993) Pulmonary nodules detection with thick-section spiral CT versus conventional CT. *Radiology* 187:513–520
- Rogalla P, Stöver B, Scheer I et al (1999) Low-dose spiral CT: applicability to paediatric chest imaging. *Pediatr Radiol* 28:565–569
- Rubin GD, Leung AN, Robertson VJ et al (1998) Thoracic spiral CT: influence of subsecond gantry rotation on image quality. *Radiology* 208:771–776
- Saad MB, Rohnen A, Sigal-Cinqualbre A et al (2009) Evaluation of image quality and radiation dose of thoracic and coronary dual-source CT in 110 infants with congenital heart disease. *Pediatr Radiol* 39:668–676
- Sacchetti A, Carraccio C, Giardino A et al (2005) Sedation for pediatric CT scanning: is radiology becoming a drug-free zone? *Pediatr Emerg Care* 21:295–297
- Salvolini L, Bichi SE, Costarelli L et al (2000) Clinical applications of 2D and 3D CT imaging of the airways: a review. *Eur J Radiol* 34:9–25
- Shafer CM, Prokop M, Dohring W et al (1991) Spiral CT of the tracheobronchial system: optimized technique and clinical applications. *Radiology* 181:274
- Shrimpton PC, Edyream S (1998) CT scanner dosimetry. *Br J Radiol* 71:1–3
- Siegel MJ (2003) Multiplanar and three-dimensional multidetector row CT of thoracic vessels and airways in the paediatric population. *Radiology* 229:641–650
- Siegel MJ, Luker GD (1995) Pediatric applications of helical (spiral) CT. *Radiol Clin North Am* 33:997–1022
- Silva AC, Lawder HJ, Hara A et al (2010) Innovations in CT dose reduction strategy: application of the adaptive statistical iterative reconstruction algorithm. *AJR Am J Roentgenol* 194:191–199
- Silverman PM, Cooper CI, Welman DI et al (1995) Helical CT: practical considerations and potential pitfalls. *Radiographics* 15:25–36
- Singh S, Kalra MK, Shenoy-Bhangle AS, Saini A, Gervais DA, Westra SJ, Thrall JH (2012) Radiation dose reduction with hybrid iterative reconstruction for pediatric CT. *Radiology* 263(2):537–546
- Siripornpitak S, Pornkul R, Khowsathit P et al (2011) Cardiac CT angiography in children with congenital heart disease. *Eur J Radiol*. doi:10.1016/j.ejrad.2011.11.042
- Stokberger SM Jr, Hicklin JA, Liang Y et al (1998) Spiral CT with ionic and non-ionic contrast material: evaluation of patient motion and scan quality. *Radiology* 208:631–636
- Takahashi M, Maguire WM, Ashtari M et al (1998) Low-dose spiral computer tomography of the thorax. *Invest Radiol* 33:68–73
- Trinavarat P (2011) Computed tomographic angiography (CTA) of major thoracic vessels in children. A pictorial essay on common findings also discussing CTA technique. *Eur J Radiol*. doi:10.1016/j.ejrad.2011.12.002
- Turner A, Gavel G, Coutts J (2005) Vascular rings-presentation, investigation and outcome. *Eur J Pediatr* 164:266–270
- Valencia R, Denecke T, Lehmkuhl L et al (2006) Value of axial and coronal maximum intensity projection (MIP) images in the detection of pulmonary nodules by multislice spiral CT: comparison with axial 1-mm and 5 mm slices. *Eur Radiol* 16:325–332
- Venkatraman R, Raman R, Raman B et al (2006) Fully automated system for three-dimensional bronchial morphology analysis using volumetric multidetector Computed tomography of the chest. *J Digit Imag* 19:132–139
- Vestra SJ, Hill JA, Alejos JC et al (1999) Tree-dimensional helical CT of pulmonary arteries in infants and children with congenital heart disease. *AJR* 173:109–115
- Veys P, Owens C (2002) Respiratory infections following haemopoietic stem cell transplantation in children. *Br Med Bull* 61:151–174
- Vyas HV, Greenberg SB, Krishnamurthy R (2012) MR Imaging and CT evaluation of congenital pulmonary vein abnormalities in neonates and infants. *Radiographics* 32:87–98

- Wang G, Vannier MW (1994) Stair-step artifacts in three-dimensional helical CT: an experimental study. *Radiology* 191:79–83
- Westra SJ, Wallance EC (2005) Imaging evaluation of pediatric chest trauma. *Radiol Clin North Am* 43:267–281
- White KS (1995) Reduced need for sedation in patients undergoing helical CT of the chest and abdomen. *Pediatr Radiol* 25:344–346
- Yanagawa M, Honda O, Yoshida S et al (2010) Adaptive statistical iterative reconstruction technique for pulmonary CT: image quality of the cadaveric lung on standard- and reduced-dose CT. *Acad Radiol* 17:1259–1266
- Yedururi S, Guillerman RP, Chung T et al (2008) Multimodality imaging of tracheobronchial disorders in children. *Radiographics*. doi:[10.1148/rg.e29](https://doi.org/10.1148/rg.e29)

# High-Resolution CT of the Lung in Children: Technique, Indications, Anatomy, and Features of Lung Disease

Javier Lucaya and Ana Coma

## Contents

<b>1</b>	<b>Introduction</b> .....	111
<b>2</b>	<b>Technique</b> .....	112
<b>3</b>	<b>Sedation</b> .....	116
<b>4</b>	<b>Special Techniques</b> .....	119
4.1	“Focused” Chest CT.....	119
4.2	“Limited Slices” Chest CT.....	119
4.3	Expiratory Slices: Lateral Decubitus and Prone Views.....	121
<b>5</b>	<b>Anatomy</b> .....	123
<b>6</b>	<b>HRCT Features of Lung Disease</b> .....	124
6.1	Ground-Glass Opacity .....	124
6.2	Consolidation .....	125
6.3	Pulmonary Nodule.....	125
6.4	Bronchiolar Disease and Tree-in-Bud .....	127
6.5	Air Trapping .....	127
6.6	Septal Thickening .....	128
6.7	Parenchymal Bands .....	128
6.8	Honeycombing.....	130
6.9	Mosaic Attenuation Pattern.....	130
6.10	Architectural Distortion.....	131
6.11	Air-filled Cystic Lung Lesions: Bullae, Pneumocoeles, and Cysts.....	131
6.12	Reversed Ventilatory Pattern .....	131
6.13	Emphysema.....	132
6.14	Halo Sign.....	132
6.15	Reversed Halo Sign.....	132
6.16	Signet Ring Sign.....	132
6.17	Crazy-Paving Pattern.....	132
<b>7</b>	<b>Conclusion</b> .....	132
	<b>References</b> .....	132

## Abstract

High-resolution computed tomography (HRCT) of the chest provides lung images with excellent anatomic detail. HRCT is a valuable technique to gain information on the pattern and anatomical distribution of lung disease, determine the response to therapy, and guide clinical management. Enormous advances in technology in recent years now enable high-quality volumetric CT examinations to be performed at progressively lower radiation doses. Routine use of low-dose techniques is mandatory in pediatric patients to minimize the potential side effects of ionizing radiation exposure. In this chapter, the HRCT features of the normal and abnormal lungs are reviewed and the differential diagnosis of the most common abnormal HRCT patterns is provided. Noncontiguous HRCT with 1 mm slices at 10 or 20 mm intervals remains the technique of choice in the evaluation of many pediatric lung conditions.

## 1 Introduction

High-resolution computed tomography (HRCT) of the chest is a technique able to image the lung with excellent spatial resolution, offering precise anatomic detail (Garcia-peña and Lucaya 2004). HRCT can demonstrate the morphologic characteristics of both the normal and abnormal lung parenchyma and its interstitium (Webb et al. 1996). In this regard, it provides more information than chest radiographs and conventional chest CT. In our experience, classical HRCT study delivers significantly less radiation to the patient than helical CT. Minimizing radiation should be a major focus of research in the coming years. Meanwhile, with this goal in mind, classical HRCT with 1 mm slices at either 10 or 20 mm intervals remains the technique of choice in the evaluation of many pediatric lung disorders.

J. Lucaya (✉)  
Department of Pediatric Radiology  
and Institute of Diagnostic Imaging, Vall d'Hebrón Hospitals,  
Ps. Vall d'Hebrón 119-129, 08035 Barcelona, Spain  
e-mail: xlucaya@gmail.com

A. Coma  
Department of Pediatric Radiology, Vall d'Hebrón Hospitals,  
Ps. Vall d'Hebrón 119-129, 08035 Barcelona, Spain



## 2 Technique

High-resolution CT images can be obtained with a volumetric acquisition technique or a standard acquisition technique (noncontiguous sections). High-resolution CT with a standard protocol allows detailed structural assessment of the lungs with good image quality, while exposing the patient to less radiation than with conventional volumetric CT.

Enormous advances in technology in recent years allow high-quality volumetric CT examinations to be performed at progressively lower radiation doses. Technical advances are just becoming widely available and show considerable promise for additional dose reduction (Kroft et al. 2010; Willemink et al. 2013). Many tools and strategies exist to reduce radiation exposure, and related hardware and software continue to evolve (Sodickson 2012). Current studies affirm that new generation multidetector CT scanners offer methods that reduce the effective dose from routine CT examinations to a minimum of 5 mSv (McCollough et al. 2012a, b). New strategies to minimize radiation in last-generation scanners have lowered the dose in volumetric scanning to levels similar to those used in noncontiguous techniques, giving volumetric CT the advantages of speed and 3D reconstruction capability. Nevertheless, there are still some gaps in our knowledge in this line and the literature remains somewhat controversial, with some recent studies highlighting the problem of a high cumulative radiation dose related to diagnostic CT (Pearce et al. 2012).

Always keeping in mind the ALARA principle, the available equipment will have a significant influence on the decision of whether volumetric CT or a noncontiguous HRCT technique should be used.

To optimize spatial resolution it is necessary to use thin sections. In keeping with most authors, we use 1.0 mm collimation, but good imaging can be obtained with 3 mm collimation. It has been shown that there is no diagnostic difference with use of 1.5 or 3 mm-thick sections (Murata et al. 1988). However, since radiation dose with 1.0 mm at 10 mm intervals is lower than with 3 mm scans at the same intervals (Rothemberg and Pentlow 1992), we recommend using the thinner sections. As a general rule we use 1 mm slices at 10 mm intervals and in premature infants we sometimes use 5 mm intervals.

Use of a high-spatial frequency algorithm (bone algorithm) is critical when performing HRCT of the lungs. The bone algorithm reduces image smoothing and increases spatial resolution, making the structures appear sharper (Mayo et al. 1987). In contrast to what occurs with the lungs, the quality of mediastinal images is poor with all HRCT techniques. This is because low-contrast structures, such as the mediastinum, are affected more by noise than

high-contrast structures, such as the lungs. The quality of mediastinal imaging improves somewhat with use of the low-spatial frequency (standard) algorithm; thus, we always use this filter to reconstruct mediastinal images.

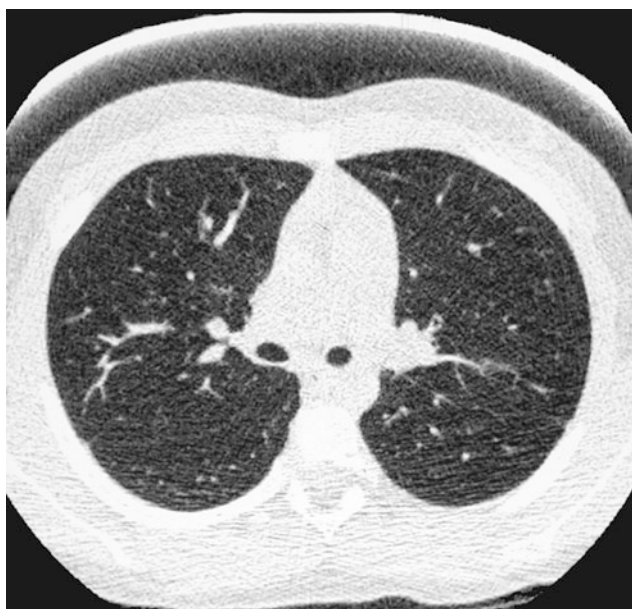
Decreasing the FOV effectively reduces pixel size and improves spatial resolution (Mayo et al. 1987; Murata et al. 1989). The FOV should be reduced as much as possible to the size of the region of interest. The effect of the display FOV is often different, after a certain threshold, pixels are only blown up with no change in spatial resolution (Nivelstein et al. 2010). The combination of a  $512 \times 512$  matrix and 400 cm FOV results in a pixel size of 0.78 mm. With targeted image reconstruction using a FOV of 25 cm, pixel size decreases to 0.49 mm and spatial resolution correspondingly increases. With an 18 cm FOV, pixel size is further reduced to 0.35 mm. We recommend the use of a 15–18 cm FOV for neonates and small infants, 25 cm for larger infants, and 35–45 for older children and adolescents. Generally, the smallest structures visible on HRCT range from 0.3 to 0.5 mm in thickness. Thinner structures, measuring 0.1–0.2 mm are occasionally seen (Webb et al. 1996).

In addition to increasing image sharpness, HRCT techniques increase image noise. Much of this noise is quantum-related and can be reduced by increasing the kilovolt peak or milliamperes used. Kilovoltage increases the energy in each photon, which results in a more penetrating X-ray beam. kVp has an exponential relationship with dose. A decrease of 20 kVp will decrease dose by about 35–40 % (Callahan 2011). However, lowering kVp results in increased noise, and potentially increased artifacts. As a result, the tube current exposure time (mAs) is typically increased to account for the increased noise. Nonetheless, the increased image noise levels are tolerable in high-contrast structures such as lungs, where pathologic conditions are substantially different in attenuation than the surrounding tissue (Sodickson 2012). Thus, we are at an advantage when evaluating the lungs, since good images can be obtained using low kVp and mAs despite an increase in noise. Moreover, owing to the reduced X-ray beam attenuation secondary to lower body mass, lower-weight patients can greatly benefit from radiation dose reductions (Sigal-cinqualbre et al. 2004).

In our experience using 90 kV and 40 mAs, the effective dose for 15 1 mm-thick slices varies from 0.10 to 0.38 mSv depending on the weight of the patient. Using 120 kV and 25 mAs, the dose increases around 35 %, yet the diagnostic quality of the exam does not change significantly, particularly in patients weighing less than 30 kg. At present, we recommend using 90 kV and 25 mAs for neonates. Beyond the neonatal period, we recommend 90 kV and 40 mAs for patients weighing 30 kg or less. For heavier patients, to keep the radiation dose as low as possible, we use 100–120 kVp and 25 mAs and increase the interval

**Table 1** Recommended scanning parameters for HRCT of the chest in children

Slice thickness	1 mm
Interval	10 mm (in premature infants we may use 5 mm) 15–20 mm (in follow-up controls)
kVp	<30 kg 90 ≥30 kg 100–120
mAs	<30 kg 25–40 ≥30 kg 25
Seconds	0.6–1.0
FOV	15–40
Filter	High-spatial-frequency algorithm (bone) Use standard for mediastinum

**Fig. 1** A 10-year-old girl. HRCT of the lungs performed using a 1 mm-thick bismuth-coated latex shield over both nipples. Notice there are no significant artifacts

between sections from 10 mm to 15–20 mm for all follow-up examinations (Table 1).

When examining children, the potential size effects of radiation exposure should always be kept in mind (Lucaya et al. 2000). With use of data obtained in A-bomb survivors, it has been predicted that delivery of 1 Rad (0.01 Gy) of radiation to a woman breast before the age of 35 fractionally increases her risk of breast cancer by 13.6 % over the expected spontaneous rate for the general population. (Land et al. 1993). This is one of the main reasons why we strongly support the use of low-dose techniques for children. Combining HRCT scans at 20 mm intervals with low-dose scans (90 kV and 40 mAs) would result in an average skin dose comparable to that associated with chest radiography (Mayo et al. 1993). Moreover, with properly performed HRCT, one can manage to study the lung with even

**Table 2** HRCT: Indications

Screening of patients with repeated respiratory infections
Bronchiectasis
Cystic fibrosis
Bronchopulmonary dysplasia
Severe asthma
Bronchiolitis obliterans
Diffuse pulmonary disease
Control of some malformations

less radiation to the female breast than with conventional radiography. When examining children with HRCT, we try to either skip the area around the nipple or use shielding. Selective breast shielding has been recommended to achieve significant radiation protection (Fricke et al. 2003). It is particularly useful when performing standard HRCT studies and does not significantly affect image quality (Fig. 1). The use of bismuth shields when performing volumetric exams has been recently questioned. Proponents (Kim et al. 2010) point to significant dose reduction to the breast, whereas opponents (Geleijns et al. 2010) argue that the shields may be counterproductive (McCollough et al. 2012b).

In children under 8 years of age, the mean attenuation value of normal lung ranges from –500 to –700 HU and in those 8 years or older it is about –800 HU, which is similar to the attenuation value in healthy adults (–700 to –800 HU). It should be emphasized that there are no “correct” or ideal windows settings for demonstrating lung anatomy, to be used when photographing an HRCT study. A wide window setting (width of 1500 HU at a center of –500 HU) is recommended for optimally displaying lung parenchyma (Klusmann and Owens 2009). Often the precise windows width and levels chosen are a matter of personal preference. However, it is important that at least one lung window setting be used consistently in all patients. If this is not done, it is difficult to develop an understanding of



**Fig. 2** A 2-week-old premature baby with RDS treated with mechanical ventilation developed localized pulmonary emphysema in left upper lobe. (a) Three months later (b) the lesions have decreased in size. At the age of 10 months (c) CT is normal

**Fig. 3** Bronchopulmonary dysplasia at the age of 2 months (a) shows marked septal thickening, parenchymal bands (arrow), and multiple hyperlucent areas. Repeated HRCT at the age of 2 years (b) shows a mosaic pattern and some residual parenchymal bands (arrow)

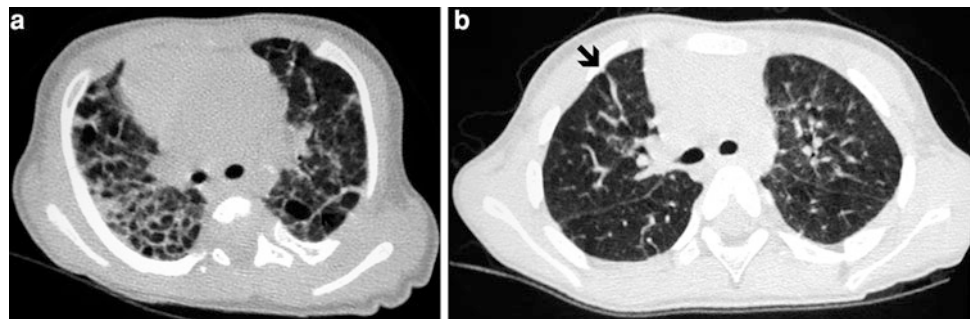


**Fig. 4** A 9-year-old boy with severe asthma. Inspiratory scan (a) shows questionable mosaic pattern, which is evident on expiratory scan (b)

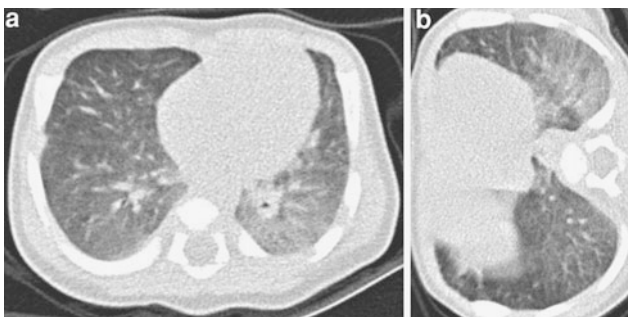
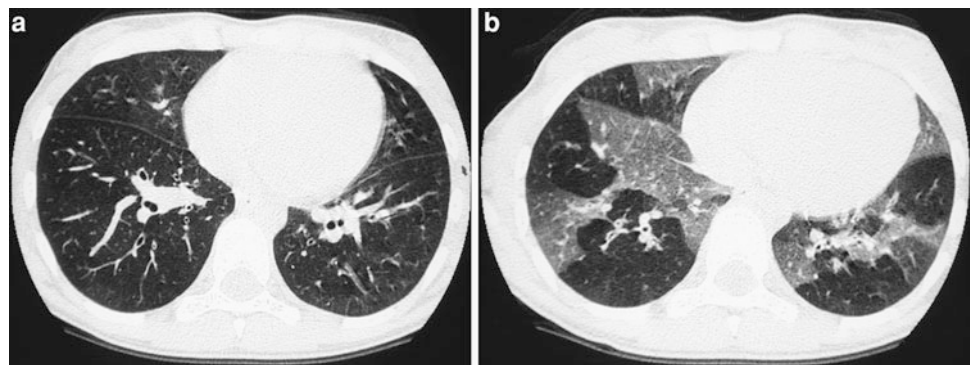


**Fig. 5** HRCT in a 23-day-old baby with meconial aspiration and sepsis. Supine scan (a) shows a ground-glass opacity in the left lower lobe, which persists in the right lateral decubitus scan (b)

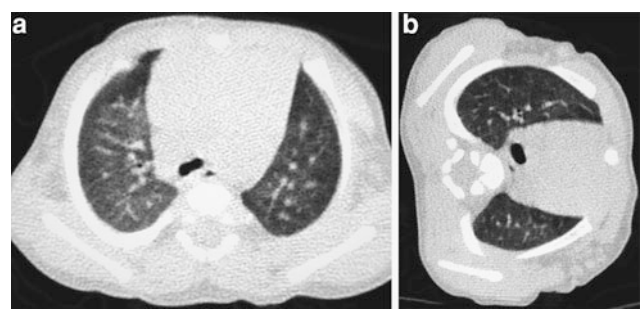


**Fig. 6** A 4-month-old infant with leukemia, fever, and questionable pneumonia. Supine HRCT (a) shows ground glass in right upper lobe, which is no longer identified in the left lateral decubitus view (b)



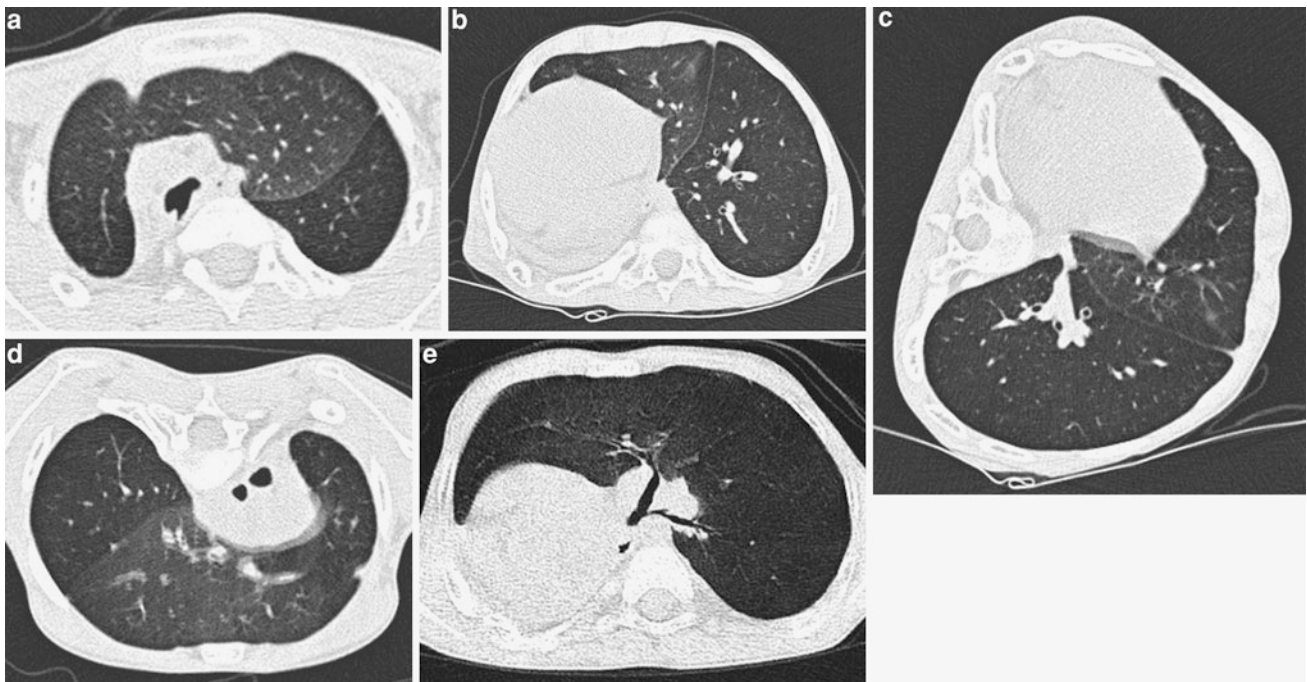


**Fig. 7** A 6-year-old boy with charge syndrome who underwent right pneumonectomy due to repeated infections and bronchiectasis, with progressive respiratory difficulties. HRCT in supine decubitus position

shows left lung herniation to the contralateral hemithorax and left lower lobe air trapping (**a**, **b**) which is confirmed in the lateral (**c**) and prone (**d**) views. Volumetric CT (**e**) shows stenosis of the lower lobe bronchus

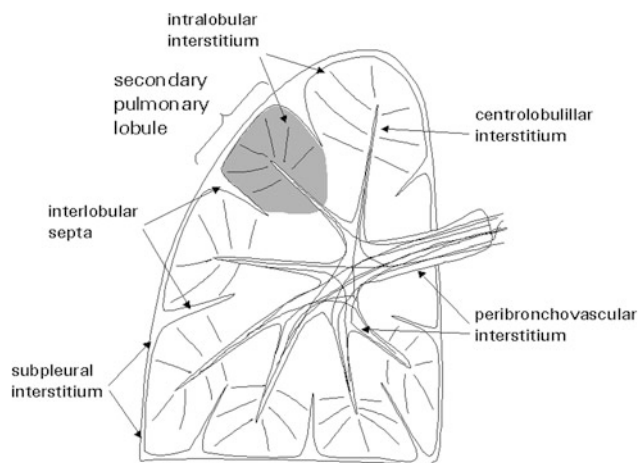


**Fig. 8** Components of the lung interstitium and secondary pulmonary lobule. [Modified and reprinted with permission from Webb et al. (1996)]

what appearances are normal and abnormal, in order to compare cases and to compare sequential examinations in the same patient. Level and width settings of 50/350 are best for evaluating the mediastinum and hila (Webb et al. 1996). The recommended scanning parameters for HRCT of the chest in children are shown in Table 1.

Since the diagnostic sensitivity and specificity of HRCT of the lungs are superior to those of conventional chest X-rays, the indications for HRCT in children have been

increasing. Therefore, we should ensure that the examination is the least aggressive possible. For this purpose, scans should be tailored to the specific clinical problem, the number of sections and exposure parameters should be decreased as much as possible, low-dose techniques should be used routinely and scout views spared. To tailor the examination to diagnostic needs, the radiologist should know the patient's clinical features and previous imaging findings. Furthermore, to obtain the greatest diagnostic information that HRCT can provide, the radiologist should directly supervise the study and decide whether additional or special slices (prone, lateral, decubitus, expiratory, etc.) are required. This approach avoids unnecessary examinations and virtually eliminates incomplete studies. Table 2 shows the main indications of HRCT in children.

Recent developments in radiation dose reduction strategies, which include advances in data acquisition, image reconstruction, and postprocessing algorithms, hold promise for reducing volumetric CT dose (McCollough et al. 2012a; Dougeni et al. 2012). Initial reports suggest that iterative reconstruction may reduce noise and enable substantial reductions in radiation exposure of up to 30–50 % (Sodickson 2012).

The potential for further dose reduction in CT is evident. However, these advances are not universally available on all scanner systems. Moreover, modern multidetector CT scanners made by the various manufacturers differ from one



**Fig. 9** The secondary pulmonary lobule, as defined by Miller. [Modified and reprinted with permission from Webb et al. (1996)]

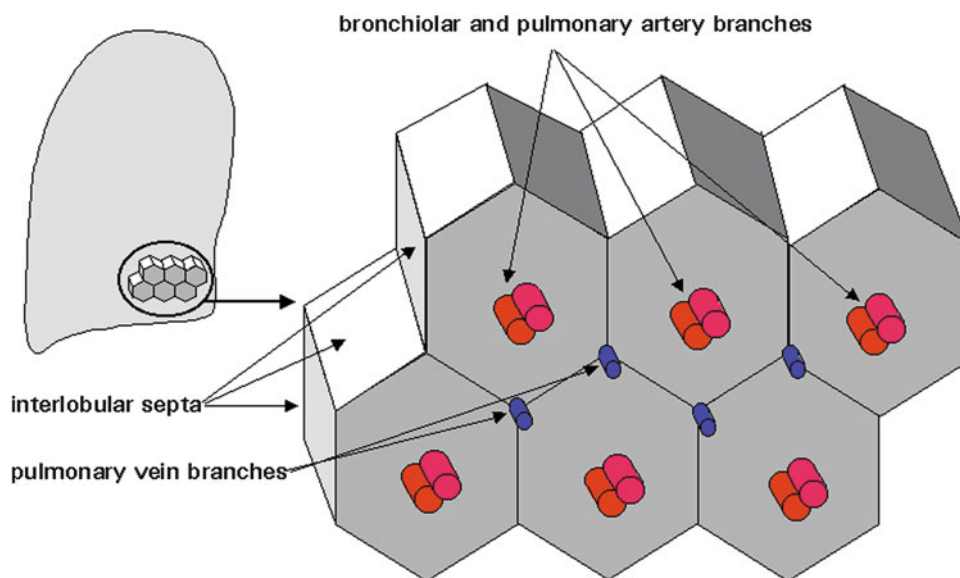


**Fig. 10** A 15-year-old girl with fever and cough of 10 days duration, treated with oral antibiotics. HRCT demonstrates a cavity with thick, irregular wall in the right upper lobe. There is marked interlobular septal thickening around the lesion. Cultures were negatives. The patient responded to intravenous antibiotic therapy

another on essential points (e.g., scanner geometry, detector design, and dose efficiency and collimation technique). This makes comparison between scanners and protocols almost impossible. (Nivelstein et al. 2010). The complexity of new CT scanners adds new challenges. Therefore, substantial research should be focused on this line in the coming years.

Noncontiguous HRCT of the chest is a valuable low-dose tool used to provide information about the pattern and anatomical distribution of lung pathology, determine lung response following therapy, and guide clinical management.

Needless to say, the routine use of low-dose techniques is mandatory to minimize the potential side effects of ionizing radiation exposure. This is extremely important for extending

the indications in children, so they can benefit from the excellent diagnostic information it provides.

### 3 Sedation

Another important measure aimed at reducing the aggressiveness of HRCT is to avoid anesthesia and use of sedation as little as possible. In our practice, we have never used general anesthesia for HRCT in children. Up to 2008 we had reduced the use of sedation in children less than 6 years of age to merely 1.5 %. Since 2008 none of the 1600 HRCT performed have required sedation. We resort to all sorts of tricks to keep the nonsedated patients still. We make sure they are warm and allow the parents to hold their hands and talk to them. To attract a fidgety child's attention, we project and move a spot of light, known TV cartoons onto the gantry or play music throw the gantry speakers. It is also helpful to offer them a bottle with glucose water.

In the past, we used to keep our patients NPO (nothing in mouth) for 4 h before the exam in children younger than 1 year and for 6 h in those 1 year or older because of aspiration risk related to sedation. Nowadays, none of our patients are kept NPO and those who, once in the gantry, behave poorly are rescheduled. Since well-fed infants behave better than hungry ones, this policy has been helpful in reducing our sedation rate to zero. However, as sedation or anesthesia may be needed in hospitals where CT equipment is not as fast as ours or where the technical team is not used to dealing with children, we are including our previous sedation protocols.

We used chloral hydrate p.o. at a dose of 50–75 mg/kg, with a maximum dosage of 2000 mg. Children are given an initial dose of 50 mg/kg and are kept in the sedation area. If

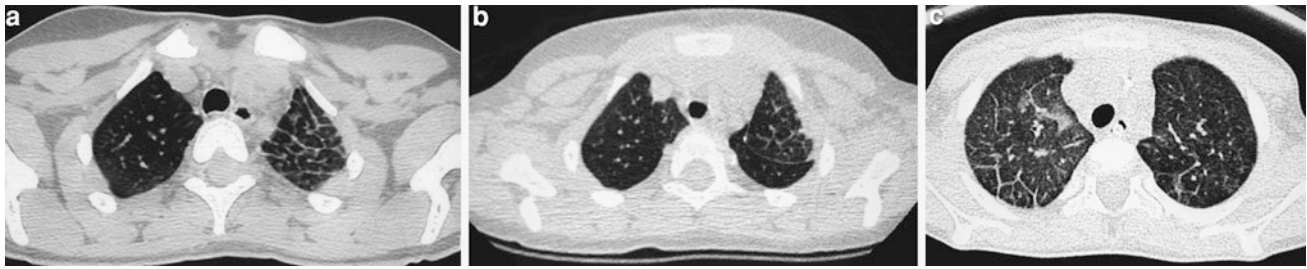


**Fig. 11** Septal thickening delineating the secondary pulmonary lobule in a 2-year-old patient with congenital atresia of the pulmonary veins (a). A 3-year-old boy with stenosis of the left upper pulmonary

vein secondary to radiofrequency catheter ablation of the pulmonary veins for paroxysmal tachycardia (b) and a 5-year-old girl with pulmonary hypertension secondary to veno-occlusive disease (c)

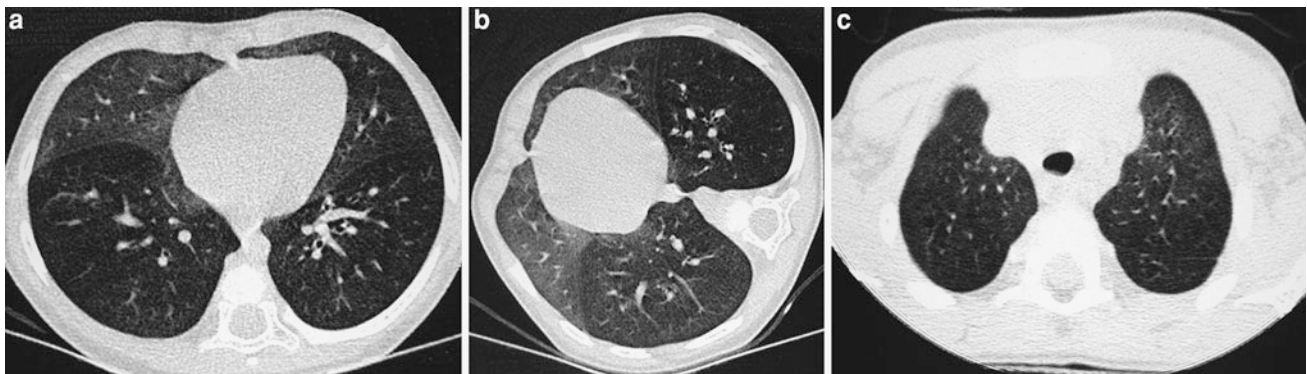


**Fig. 12** Reversal of normal aeration pattern in a 15-month-old girl with biopsy-proven neuroendocrine cell hyperplasia. Axial scan (a) shows the reversal pattern. The right lateral decubitus scan

confirms air trapping in right lower lobe (b). Left decubitus scan (not shown) demonstrated air trapping in the left lower lobe. Similar yet milder findings in a 4-year-old boy with cystic fibrosis (c)

after 20–30 min the patient has not fallen asleep, a second dose of chloral hydrate, usually half the initial dose (25 mg/kg), is given. Exceptionally, we may go up to a total dose of 100 mg/kg. The onset of action is usually within 25–30 min and the duration of sedation is 30–40 min. Chloral hydrate has a bitter taste that children dislike. Attempts to conceal it with sweeteners like cherry syrup are not very helpful. Although the taste improves somewhat, it still remains unpleasant. Furthermore, the total volume of fluid to be administered increases and dose control becomes difficult. Consequently, we always use undiluted chloral hydrate administered directly by syringe or with a nipple connected to a syringe. With time and patience most children swallow it well. Although we use chloral hydrate mainly in children under 2 years of age, it can also be use in older patients.

Chloral is successful sedative in 95–99 % of children (Karian et al. 1999; Pererira et al. 1993) and has a very low rate of side effects. Transient respiratory depression (oxygen desaturation 10 % below baseline for a patient for more than 15 s, despite repositioning of the head and neck to clear airway) is the most common during or after sedation, yet it occurs in less than 1 % of patients. Delayed complications such as vomiting, irritability, and mild respiratory difficulty are also rare (Egelhoff et al. 1997).

Many different models are used in different institutions to provide effective, safe sedation (Chung et al. 2000; Rooks et al. 2003; Shankar 2008; Macias and Chumpitazi 2011; Mason et al. 2011; Henry et al. 2012; Heng Vong et al. 2012). Pentobarbital and chloral hydrate remain the most widely used sedatives for CT. Use of multidrug sedation regimens should be avoided (Sanborn et al. 2005). The radiologist cannot be responsible for sedation. The person providing sedation and monitoring the patient should have proper training to assure patient safety and should not be the person responsible for the imaging procedure (Shankar 2008). All sedated patients are given oxygen by mask or nasal prong to increase pulmonary oxygen reserves and permit prolonged apnea or airway obstruction without hypoxia. Oxygen should be administered to all patients receiving sedative medications with the possible exception of neonates at risk of retinopathy of prematurity, in which case a neonatologist should be consulted. There are no rules about the amount of supplemental oxygen that a patient requires; rather, administration of any amount improves the margin of safety. Thus, there is no legitimate reason to not administer oxygen routinely when patients are sedated (Fisher 1990). Continuous monitoring of the vital signs (at least every 5 min) must be performed and recorded during each use of sedation.

**Fig. 13** HRCT features of lung disease. [Modified and reprinted with permission from Webb et al. (1996)]

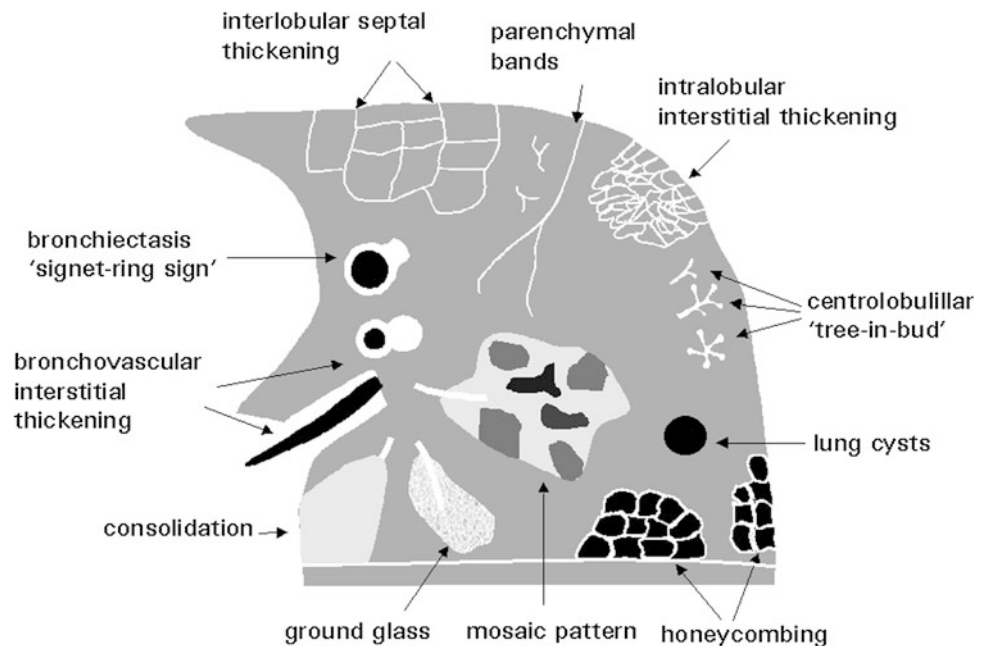


**Fig. 14** Ground-glass pattern due to infectious right middle lobe pneumonia in a 9-year-old girl

The physiologic measurements, we monitor include oxygenation (with pulse oximetry), heart rate, respiratory rate, and temperature. The alarm on the pulse oximeter is usually set at 90 % oxygen saturation, but any decrease below 95 % is immediately investigated. The majority of apparent desaturations are due to patient motion and loss of sensor contact. A small number of patients, however, demonstrate significant decreases in  $pO_2$ . Most of this are transient and are quickly corrected by repositioning the head and extended the neck. Occasionally, a patient requires suctioning of the oral cavity. A suction device and size-appropriate recovery equipment must be on hand during each sedation procedure. Children who have medical

conditions that compromise the airway require special attention with respect to cardiopulmonary monitoring and airway management. These children may not be appropriate candidates for sedation by personnel who do not routinely deal with pediatric airway management and cardiopulmonary resuscitation. Children who fall into this monitoring category include those with anatomic airway anomalies (craniofacial defects), those with airways disease such as obstructive adenotonsillar hyperplasia, acute respiratory infection, uncontrolled asthma, and those with significant cardiopulmonary, neurologic and hepatorenal disorders. Life-threatening airway obstruction or respiratory depression with hypoxia can occur in these children (Vade et al. 1995). Certain patients are difficult to sedate, such as children with mental retardation, patients receiving chemotherapy or antiseizure medication and those habituated to sedation (Hubbard et al. 1992).

Once the examination is over, all sedated patients are discharged home or transported to the inpatient wards, when they meet the postanesthesia care unit discharge criteria recommended by the American Academy of Pediatrics (American Academy of Pediatrics Committee on Drugs 1992):

1. Cardiovascular function and airway patency are satisfactory and stable.
2. The patient is easily arousable, and protective reflexes are intact.
3. The patient can talk (if age-appropriate).
4. The patient can sit unaided (if age-appropriate).
5. The state of hydration is adequate.
6. For a very young or handicapped child, incapable of expected responses, the presedation level of responsiveness



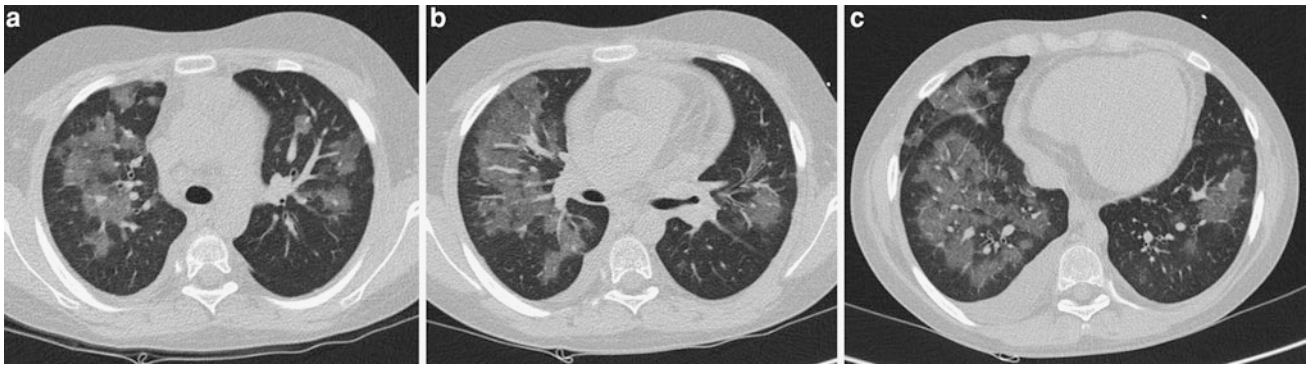


**Fig. 15 a–c** A 10-year-old boy with pulmonary edema. HRCT shows ground-glass opacities with a peribronchovascular distribution and pleural effusion

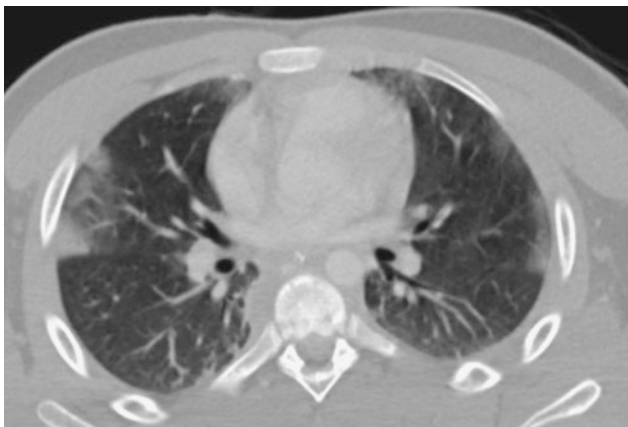


**Fig. 16** A 15-year-old boy sustained lung contusions after a high-energy traumatism. Follow-up HRCT shows multiple peripheral areas of ground glass in both lungs. Also note thickened posterior mediastinum, secondary to thoracic duct rupture, which had been seen on previous volumetric CT

or a level as close as possible to the normal level for that child should be achieved.

Parents are instructed not to feed the children until their level of consciousness and motor function have returned to presedation ranges. When examining critically ill patients, we require the assistance of a pediatrician from the intensive care unit. After the examination is completed, these patients are returned to their wards immediately under the supervision of the specialist. Other sedation regimes (see chapter on Helical CT) are practically never required for HRCT.

## 4 Special Techniques

### 4.1 “Focused” Chest CT

In patients with known “localized” lung disorders we recommend a “focused” technique, performing 1 mm slices at 10 mm intervals through the abnormal area of the lung. The

rest of the lung is not scanned. We believe that study of the entire lung should not be performed in patients being controlled for known localized disease whose clinical symptoms and/or chest radiographs do not suggest progression to other lobes. The “focused” scan is used in the following-up of bronchiectasis, right middle lobe syndrome, cystic emphysema (Fig. 2), cavitated pneumonia, and some pulmonary malformations not considered tributary of surgical treatment. In many of these cases, three or four low-dose HRCT slices will provide more information with less radiation dose to the female breast than PA and lateral radiographs. As always with HRCT, we try to skip the scout of view to save on radiation exposure, though occasionally, and particularly when we want to reduce the exam to a mere of two or three slices, we may use it. We center the exam with the light collimator. When we want to explore the right middle lobe, lingular segments, and both lower lobes, we start the study midway between the sternal manubrium and the xifoid. When examining the upper lobes, we start the study at the level of the clavicles and stop at the inferior border of the abnormal lobe.

### 4.2 “Limited Slices” Chest CT

The “limited slices” technique, consisting of 1 mm slices at 20 mm intervals, is a type of “sampling” technique that can be used for studying generalized lung disorders. Radiation dose is halved with this technique, making it particularly useful for follow-up of patients with chronic lung disorders who require repeated examinations. The main indication for limited slice is in the control of patients with cystic fibrosis, bronchopulmonary dysplasia (Fig. 3), histiocytosis X, alveolar proteinosis, and interstitial pneumonias.

In our experience, use of both “focused” and “limited-slice” techniques has increased steadily over the last few years, particularly when examining female patients with chronic lung disorders. In addition to provide reliable



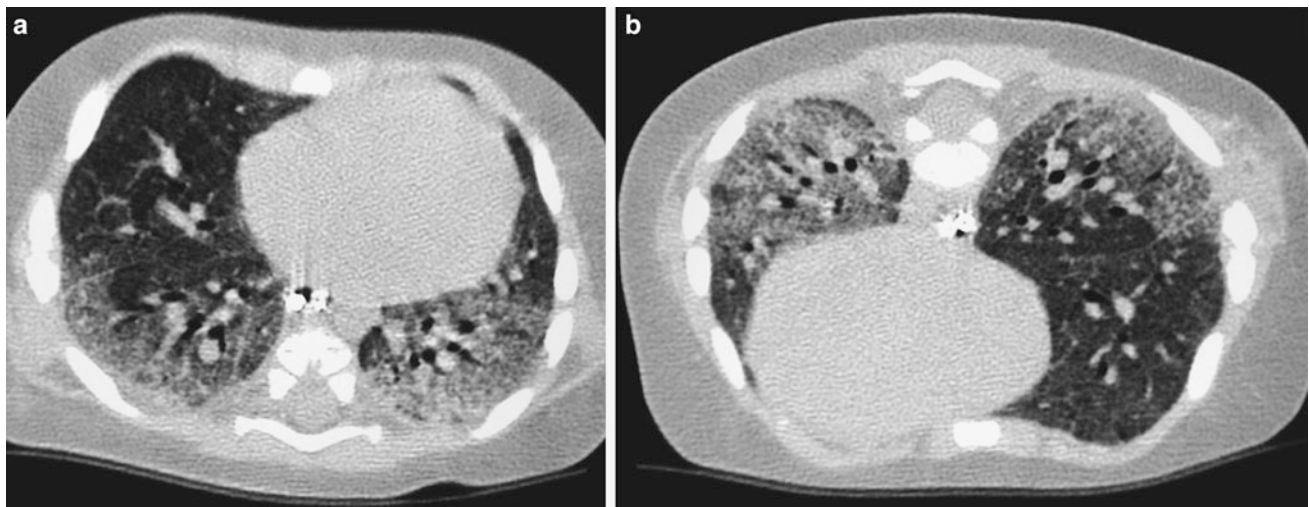


**Fig. 17** Chronic pneumonitis of infancy in a 4-month-old boy. Supine scan shows ground glass in both lower lobes (a). This finding reminded unchanged in prone scans (b)



**Fig. 18** Generalized ground-glass pattern. Chronic pneumonitis of infancy in a 6-month-old boy (a), biopsy-proven alveolar dysplasia in a 2-month-old girl (b), and bleomycin toxicity in 4-year-old girl with a yolk sac tumor (c)

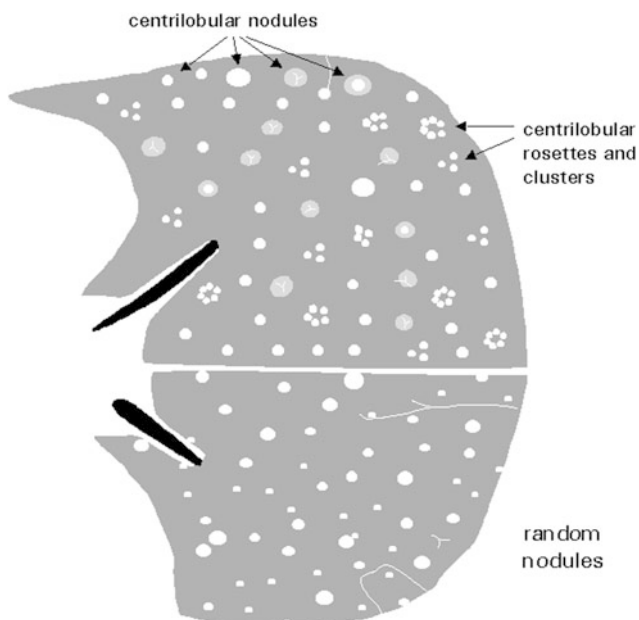


**Fig. 19** Appearance of centrilobular and randomly distributed nodules [Modified and reprinted with permission from Webb et al. (1996)]



**Fig. 20** Centrilobular nodules and tree-in bud in a 13-year-old girl with cystic fibrosis

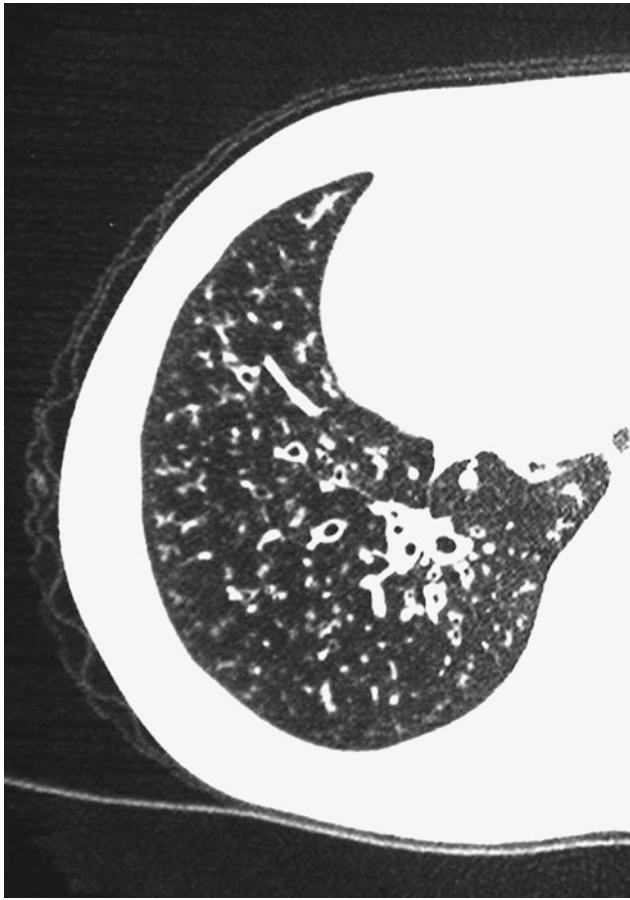


**Fig. 21** A 14-year-old girl with immotile cilia syndrome. HRCT shows centrilobular nodules, bronchiectasis, and peribronchial thickening

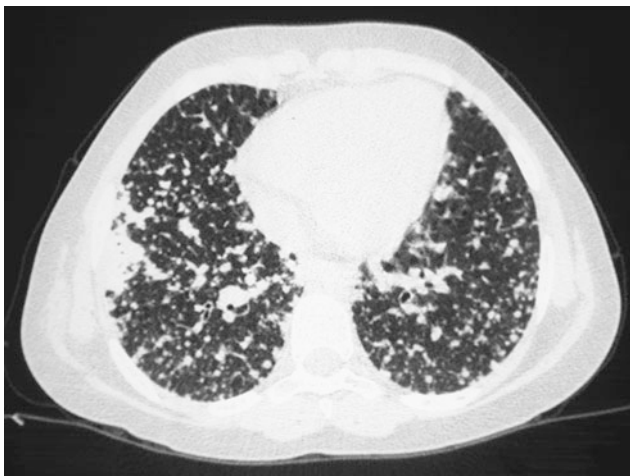


**Fig. 22** Lung metastasis from thyroid carcinoma in a 6-year-old girl. Pulmonary nodules are distributed at random

diagnostic information, these techniques permit a reduction in radiation exposure to the breasts. If radiographs are still required in this group of patients, we obtain the AP or

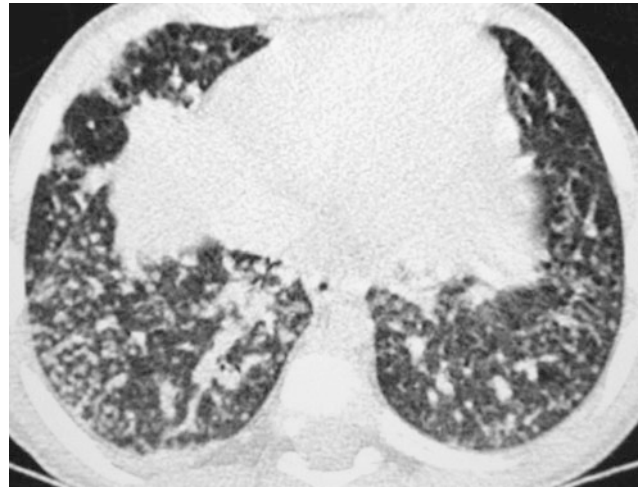


**Fig. 23** Biopsy proven cholesterol granulomas in a 3-year-old boy with rheumatoid arthritis. HRCT shows multiple centrilobular nodules

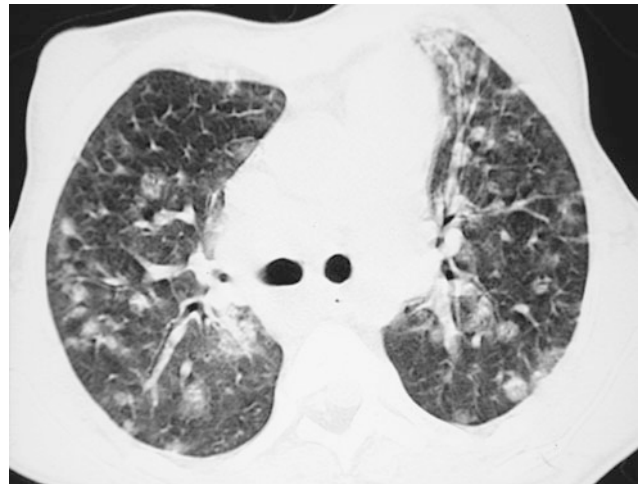


**Fig. 24** Biopsy-proven BOOP in a 15-year-old girl with hypogammaglobulinemia and respiratory difficulty. HRCT shows multiple nodules and some areas of ground glass. Lesions disappeared with steroid therapy

PA views only. The lateral projection is not routinely performed.

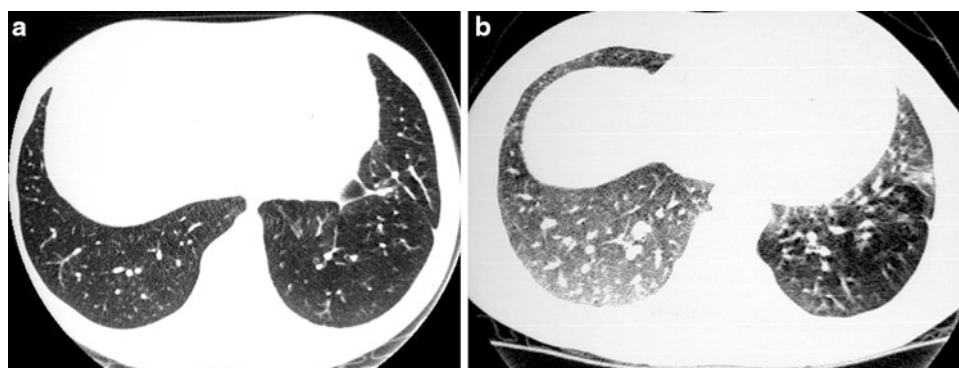
### 4.3 Expiratory Slices: Lateral Decubitus and Prone Views

Expiratory slices are extremely helpful when examining patients suspected of having airway abnormalities or patients with a history of repeated pulmonary infections who are found to have a normal or questionably normal inspiratory CT exam (Lucaya et al. 1999) (Fig. 4). They are also useful when the inspiratory sections demonstrate a mosaic pattern,



**Fig. 25** Example of air trapping in a 9-year-old patient with asthma. Inspiratory scan (a) is normal. Expiratory scan (b) shows severe air trapping. Repeated expiratory scan after bronchodilator therapy (c) is normal

**Fig. 26** A 14-year-old girl with long-standing left lower lobe bronchiectasis treated with physiotherapy and antibiotics. Follow-up inspiratory HRCT (a) shows some architectural distortion and hypovascularity in the left lower lobe. Bronchiectasis is no longer seen. Marked air trapping is evident on the expiratory scan (b)



characterized by visible differences in lung attenuation. Since children do not usually suffer pulmonary thromboembolic disorders, a mosaic pattern is almost always due to small airway disease with obstruction.

When the examining child presents clinical or radiological features commonly associated with small airway disease, we routinely complete the HRCT examination with three additional expiratory slices at three equally-spaced levels, one in the upper, one in the middle, and one in the lower lobes. We use the table level information provided by the inspiratory exam to center these slices. Whereas the “level” of the upper lobes does not change significantly on expiration, the middle lobe, lingular segments, and particularly the lower lobes will “move upwards” significantly, from 2 to 5 cm, depending on the size of the patient. To obtain good expiratory scans it is mandatory to spend some time teaching the child how to exhale well.

A useful method for obtaining expiratory scans in uncooperative children is to use the lateral decubitus technique (Capitanio and Kirkpatrick 1972; Lucaya et al. 1999; Choi et al. 2002). The patients are scanned in both lateral decubitus positions. With the child on his side, the dependent hemithorax is splinted and movement of the thoracic cage is restricted on that side. When movement of the

hemithorax is limited, the lung on the dependent side tends to be underaerated. Conversely, the hemithorax facing upwards is not restricted and the lung is well aerated. If air trapping is present, either diffusely or patchy, the affected lung lobe or segment will remain hyperlucent when that side of the thorax is in the dependent position (Fig. 5). occasionally, in noncooperative patients with normal chest X-rays and known diseases, such as cystic fibrosis or severe asthma, in whom the initial HRCT abnormality is usually of a mosaic pattern secondary to air trapping, we will limit their initial HRCT exam to three scans in each lateral decubitus position.

This simple technique can also be used when trying to obtain good inspiratory examinations in noncooperative patients. As mentioned, the lung facing upwards is usually well aerated. Awareness of this fact is particularly helpful when examining noncooperative patients whose supine scans show a ground-glass pattern consistent either with lung disease or with normal lung on expiration. When the lungs are normal, the ground-glass pattern will no longer persist in the lung facing upwards (Fig. 6). This same principle of gravity-dependent aeration is the rationale for using prone views to obtain good inspiratory scans of the lower lobes (Figs. 7, 17).





**Fig. 27** Septal lines in a 3-month-old boy with bronchopulmonary dysplasia. Also note the heterogeneous aeration



**Fig. 28** A 16-year-old boy with Niemann-Pick disease and respiratory insufficiency. HRCT shows thickening of the interlobular septa. Areas of ground glass were seen in other slices (not shown). Interstitial thickening is due to infiltration of lymphatics and interlobular septa with lipid-laden macrophages. (Courtesy of Dr. Ucar, Argentina)

## 5 Anatomy

The lung is supported by a network of connective tissue fibers known as the lung interstitium (Fig. 8). For the purpose of interpreting HRCT images and identifying abnormal findings, the interstitium can be thought of as having several components. The peribronchovascular interstitium is a system of fibers that invests the large bronchi and pulmonary arteries in the parahilar regions and forms a continuum with the centrilobular interstitium, surrounding the small centrilobular bronchi, arteries, and lymphatic

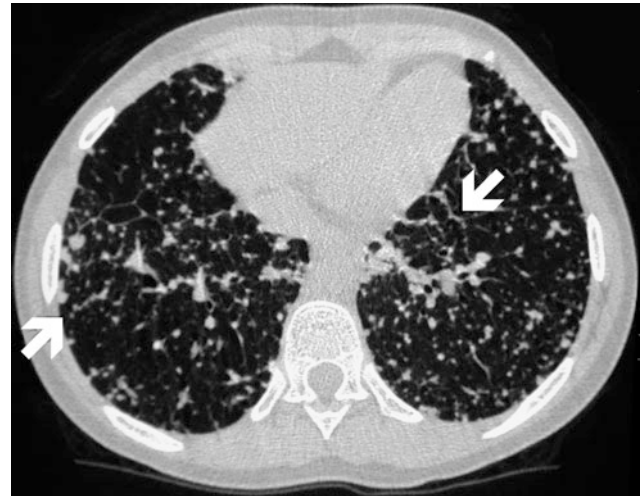


**Fig. 29** A 14-year-old girl with thyroid carcinoma. HRCT demonstrates irregular nodular thickening of interlobular septa (arrows) corresponding to lymphangitic spread. Small nodules randomly distributed through both lungs, characteristic of hematogenous metastasis, are also seen

vessels. The subpleural interstitium is located beneath the visceral pleura and envelops the lung in a fibrous sac from which connective tissue septa (interlobular septa) invaginate into the lung parenchyma. The pulmonary veins and lymphatic vessels travel in the interlobular septa. The last component is the intralobular interstitium, a network of thin fibers in the walls of the alveoli bridging the gap between the centrilobular interstitium and the interlobular septa or subpleural interstitium (Weibel 1979).

The secondary pulmonary lobule is the smallest lung unit delineated by connective tissue septa and the smallest functional unit that can be directly visualized by HRCT (Fig. 9). With a diameter of 1–2.5 mm, it can have polyhedral or prismatic shape, but more frequently resembles a truncated pyramid. Each secondary lobule has a central supporting tissue (centrilobular interstitium) containing a small bronchiole, pulmonary artery, and lymphatic vessel (bronchovascular bundle) and is margined by interlobular septa that contains pulmonary veins and lymphatic branches. The substance of the secondary lobule, surrounding the lobular core and contained within the interlobular septa, consists of a variable number of lung acinis (ranging from 3 to 24) and the associated capillary bed, supplied by small airways and branches of the pulmonary arteries and veins (Giovagnorio and Cavallo 1995). Secondary lobules are difficult to visualize in HRCT scans of children except in patients with abnormal septal thickening (Figs. 10, 11, 27, 28, 45, and 46).

The terminal bronchiole and the artery supplying the lobule are located in its center and give off smaller branches at intervals along their courses. On HRCT scans the vessels can be seen as linear, branching, or dot-like structures near



**Fig. 30** Parenchymal bands in a 4-year-old boy with bronchopulmonary dysplasia (a). Typical features of bronchopulmonary dysplasia were present on initial CT scan performed at the age of 3 months (b)

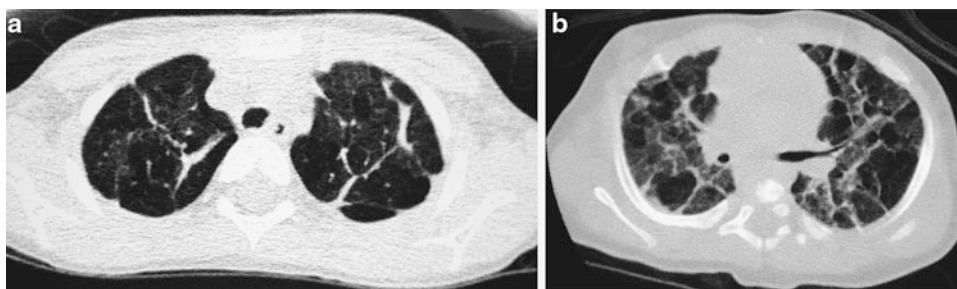


**Fig. 31** Typical features of bronchopulmonary dysplasia on HRCT performed at the age of 3 months. HRCT shows septal thickening, parenchymal bands, pseudocystic pattern, and heterogeneous aeration

the center of the secondary pulmonary lobule extending to within 5–10 mm of the pleural surface; the smallest arteries resolved are as small as 0.2 mm. Normal intralobular bronchioles cannot be identified because their walls are less than 0.15 mm thick. Bronchiolar abnormalities could be detected only when there was thickening of the bronchiolar wall, peribronchiolar inflammation, fibrosis, or bronchioloectasis, with or without filling of the dilated bronchiole with secretions. The sensitivity of last-generation CT scanners, which enables detection of abnormalities even in asymptomatic patients, has created new challenges for the radiologist. Sometimes there is no clear boundary between the normal and abnormal thin-section CT appearance of the lungs and the same finding may be unimportant in one situation, but clinically important in another (Hansell 2010). This is particularly relevant in neonates and young infants who do not follow breath-holding commands and in whom the presence of a diffuse ground-glass pattern most often reflects a normal lung on expiration. The attenuation of the normal air-containing lung varies with the phase of respiration and with the region of the lung being examined. With

the child in a supine position, attenuation is usually higher posteriorly (lower lobes) than anteriorly (right middle lobe and lingular segments). This is due to physiologic hyperemia and the tendency of the dependent lobes to be incompletely expanded. This gravity-dependent density is accentuated at partial expiration, is reversible with full inspiration or with the patient in a prone position, and is most frequently observed in scans of children not following breath-holding commands whose studies are practically never performed on full inspiration. The opposite situation, i.e., anterior lobes denser than the dependent lobes, is always abnormal or air trapping in the dependent lobes (Fig. 12).

## 6 HRCT Features of Lung Disease

The most common HRCT features of lung disease in children are grouped in Fig. 13.

### 6.1 Ground-Glass Opacity

Ground-glass opacity (GGO) refers to hazy increased attenuation of the lung with preservation of the bronchial and vascular margins, caused by partial filling of the air-spaces, interstitial thickening, and partial collapse of alveoli, normal expiration, or increased capillary volume. It is sometimes associated with air bronchograms and can be patchy, resulting in a mosaic pattern of lung attenuation (Collins and Stern 1997). Lung attenuation normally increases with expiration. This increased attenuation can mask underlying GGO from infiltrative lung disease if the expiratory nature of the examination is not recognized. The tracheal configuration changes from round on inspiration to flat or crescent-shaped on expiration and can be used to determine at what phase of respiration HRCT scan was performed (Collins and Stern 1997).

Recognition of GGO is based on subjective assessment of the lung attenuation. When uniform GGO is observed in scans of children not following breath-holding commands, it probably corresponds to normal lung on expiration.

**Fig. 32 a, b** A 6-month-old boy with biopsy-proven pulmonary interstitial glycogenosis. HRCT demonstrates a mosaic perfusion pattern and bilateral linear densities

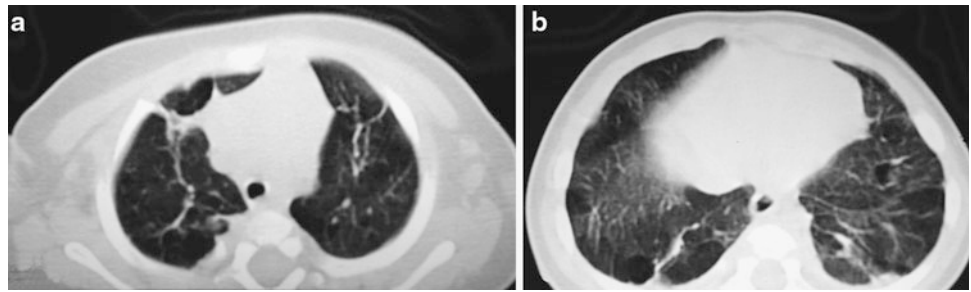


**Fig. 33** A 5-year-old boy with biopsy-proven nonspecific interstitial pneumonia. HRCT shows a mosaic perfusion pattern and multiple bilateral linear densities

Lateral decubitus views can help in this regard (Figs. 5, 6 and 12). When the GGO is patchy, it can cause a mosaic pattern of lung attenuation, which in children is usually due to small airway disease, with the GGO corresponding to areas of normal lung on expiration (Fig. 4b). Again, lateral decubitus views will help to establish whether the mosaic pattern corresponds to patchy ground-glass secondary to lung disease or to patchy air trapping. Assessment of true GGO in the scans of children following breath-holding commands is significantly easier. Its presence in these patients, whose scans are usually obtained in full inspiration, is always abnormal and is due to airspace or interstitial disease or both. The differential diagnosis of pathological GGO in the pediatric age group is extensive, with infectious pneumonia of any etiology being its most common cause (Fig. 14). GGO can also be seen in pulmonary edema (Fig. 15), hemorrhage, leukemic infiltration of the lung, lung contusion (Fig. 16), acute lung transplant rejection, graft-versus-host disease after allogeneic stem cell transplantation (Song et al. 2012), adult respiratory distress syndrome, collagen disease (Garcia-peña et al. 2011), extrinsic allergic alveolitis, interstitial pneumonia (Figs. 17, 18a, b) (Newman et al. 2001; Canakis et al. 2002; Popler

et al. 2012; Lee 2013), drug toxicity (Fig. 18c), sarcoidosis, alveolar proteinosis (Fig. 45), bronchiolitis obliterans organizing pneumonia, idiopathic pulmonary fibrosis, and following bronchoalveolar lavage.

## 6.2 Consolidation

A homogeneous increase in pulmonary parenchymal attenuation that obscures the margins of vessels and airway walls is referred to as consolidation. Air bronchograms may be present. By definition, diseases that produce consolidation are characterized by a replacement of alveolar air by fluid, cells, tissue, or other material. The differential diagnosis of consolidation overlaps that of GGO and, in fact, it is common to find a mixture of both findings. Pneumonia of any etiology, pulmonary edema or hemorrhage, and lung contusion are the most common causes of lung consolidation in children.

## 6.3 Pulmonary Nodule

Pulmonary nodules are focal, rounded opacities of varying size, which can be well or ill defined. They have been described as either airspace or interstitial nodules, but it is more practical to classify them according to their size and distribution. The term micronodule is reserved for round opacities less than 3 mm in diameter. The anatomic distribution may be classified as centrilobular, lymphatic, or random (Fig. 19).

Centrilobular nodules are located in the region of the bronchio arteriolar core of secondary pulmonary lobules. On HRCT they are adjacent to, surround, or obscure the centrilobular arteries, and are centered or clustered 5–10 mm from the periphery of the lobe, pleural surface, or interlobular septa. Most centrilobular nodules in children are secondary to bronchiolar disease that also involves the peribronchiolar interstitium. They are common in cystic fibrosis (Fig. 20), bronchiectasis, infectious bronchitis, and bronchogenic spread of tuberculosis. They may also be present in immotile cilia syndrome (Fig. 21), hypersensitivity

**Fig. 34** Honeycombing. Honeycombing secondary to pulmonary fibrosis in a 10-year-old girl with rheumatoid arthritis (a). Honeycombing secondary to pulmonary fibrosis in a 16-year-old girl with mixed connective tissue disease (b). Honeycombing secondary to scleroderma in a 10-year-old girl at diagnosis (c) and 4 years later (d)

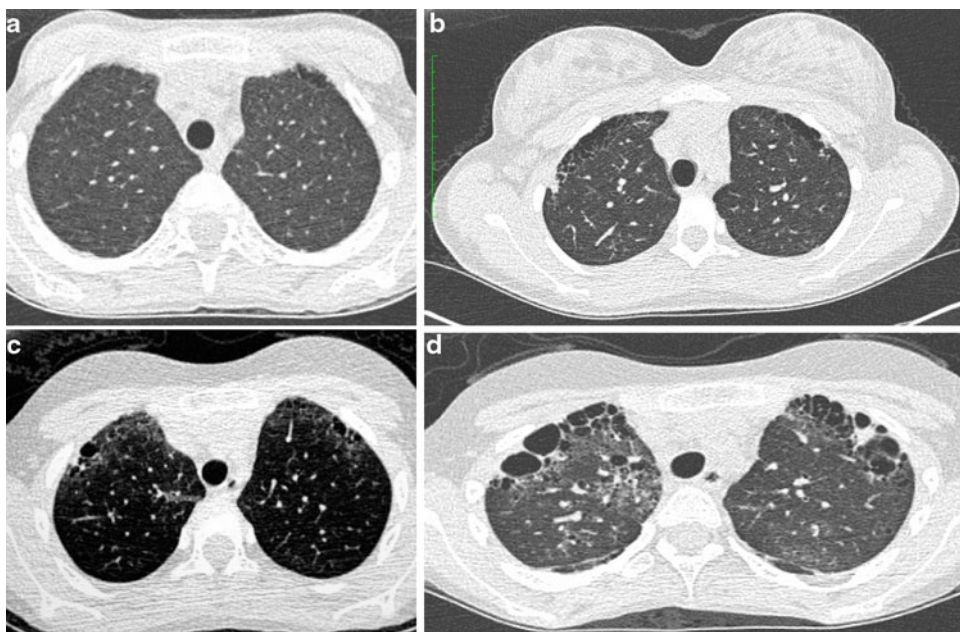


**Fig. 35** Inspiratory (a) and expiratory (b) HRCT scans in a 6-year-old boy with postinfectious bronchiolitis obliterans (Swyer-James syndrome). There is left lower lobe bronchiectasis and a bilateral mosaic pattern with air trapping

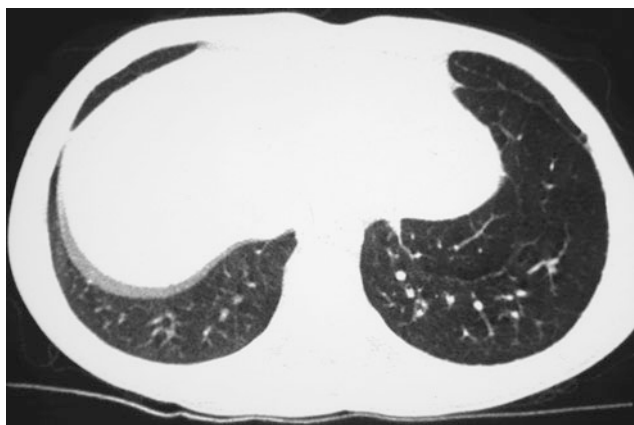
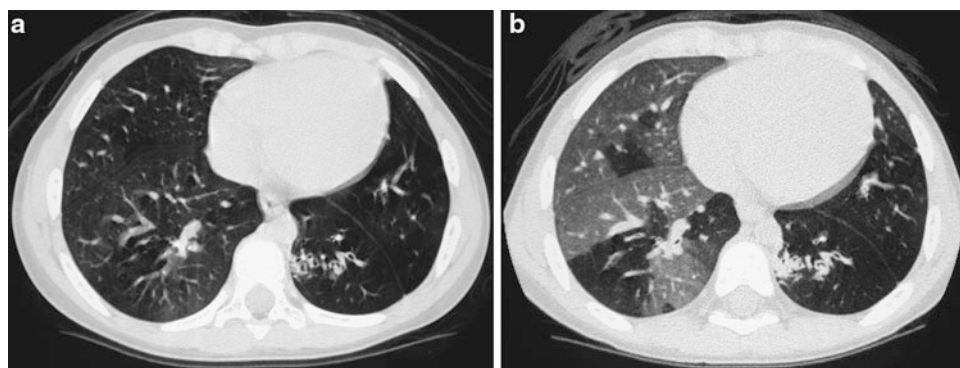


**Fig. 36** Example of architectural distortion of the left lower lobe in a 5-year-old boy with unilateral pulmonary hypoplasia secondary to congenital left-sided diaphragmatic hernia operated in the neonate period

pneumonia, asthma (especially when there is superimposed infection), histiocytosis, lymphocytic interstitial pneumonitis (LIP) in immunocompromised patients, congenital pulmonary lymphangiectasia, bronchiolitis obliterans, Wegener's granulomatosis (Levine et al. 2007), and pulmonary hemosiderosis (Gruden et al. 1994).

Lymphatic nodules are seen as small opacities distributed along the visceral pleura, interlobular septa, or bronchovascular bundles. They may be found in sarcoidosis (Klusmann and Owens 2009) and have also been reported in a patient with osteosarcoma and lymphangitic carcinomatosis (Rastogi et al. 2008).

Nodules that appear randomly distributed in relation to secondary lobule structures are often seen in patients with miliary tuberculosis, (Choi et al. 1999) fungal infections, metastasis (Fig. 22), and histiocytosis X (Moon et al. 1996). Contrary to what occurs with centrilobular nodules, these





**Fig. 37** A 4-year-old boy with history of cystic adenomatoid malformation of the right lower lobe. HRCT performed following right lower lobe lobectomy shows an unusual distribution of the pulmonary vessels in the right lung

can be seen in close proximity to the interlobular septa and the pleural surfaces (Silva et al. 2010).

The differential diagnosis of multiple, larger (>5 mm) nodules includes metastatic disease, tuberculosis, histoplasmosis, mycotic infections, lymphoproliferative disorders, pulmonary spread of laryngeal papillomatosis, septal emboli, vasculitis, histiocytosis, bleomycin lung (Rimmer et al. 1985), lipid granulomas in patients with total parenteral nutrition (Landry and Melhem 1989), cholesterol granulomas in rheumatoid arthritis (Schultz et al. 2001) (Fig. 23), Wegener's granulomatosis (Levine et al. 2007), and bronchiolitis obliterans with organizing pneumonia (Fig. 24).

#### 6.4 Bronchiolar Disease and Tree-in-Bud

The direct CT findings of bronchiolar disease include bronchiolar wall thickening, bronchiolar dilatation, and luminal impaction. Assessment of bronchial wall thickening on HRCT is quite subjective. Moreover, the apparent thickening of the bronchial wall represents not only the wall itself, but also the surrounding peribronchovascular interstitium. Peribronchovascular interstitial thickening, also known as peribronchial cuffing, can result in apparent bronchial wall thickening on HRCT. Bronchial wall/peribronchial thickening should be suspected when the bronchial "walls" are clearly seen in the distal third of the lung or when the walls of the more proximal aspects represent more than one third of the bronchial diameter (Ambrosino et al. 1994).

Small airways that are dilated and/or filled with mucus, pus, or inflammatory material appear in some patients as small, well-defined, centrilobular, nodular, linear, or branching structures of soft-tissue opacity. The "tree-in-bud" pattern represents severe bronchiolar impaction with "clubbing" of distal bronchioles. Seen in profile, the pattern resembles the "finger-in-glove" appearance of impacted bronchi. In cross section, tree-in-bud patterns may resemble childhood toy jacks. The tree-in-bud pattern is most commonly seen in infectious bronchiolitis of any etiology, endobronchial spread of tuberculosis, cystic fibrosis (Fig. 20), allergic bronchopulmonary aspergillosis, and immotile cilia syndrome (Rossi et al. 2005). Occasionally, it will be seen in bronchiolitis obliterans (Aquino et al. 1996).

#### 6.5 Air Trapping

The retention of excess air in all or part of the lung (especially during expiration), as a result of complete or partial airway obstruction or local abnormalities in pulmonary compliance, is known as air trapping. Partial airway obstruction is particularly frequent in children. Recognition of a mosaic pattern on the inspiratory scans can suggest its presence. However, the expiratory scans often demonstrate marked air trapping, while the inspiratory scans show normal findings or only subtle abnormalities, such as decreased vascularity of the affected segment or lobe (Arakawa and Webb 1998). In our experience, the diagnostic yield of inspiratory scans is lower than that of expiratory scans in children with peripheral airway disease. The latter should always be included when performing HRCT of the lungs in cooperative children with clinical features suggesting airway disease (Figs. 4, 25).

Air trapping is particularly common in bronchiolitis, cystic fibrosis, bronchiectasis (Fig. 26), and asthma (Fig. 4), in which it can disappear following bronchodilator therapy (Fig. 25). It has also been reported in children with follicular hyperplasia of a bronchus (Oh et al. 1999) and in neuroendocrine cell hyperplasia of infancy. Since bronchiolitis obliterans distal to bronchiectasis is a universal finding (Shepard 1995), air trapping is always found in the segments or lobes harboring bronchiectasis. This is a feature of significant diagnostic value, particularly when examining children whose studies show "questionable" bronchiectasis. In such cases, the presence of associated air trapping favors the diagnosis (Hansell et al. 1994). It also helps in the follow-up evaluation of children with known cylindrical bronchiectasis that have been treated and maintained infection-free. Occasionally,



**Fig. 38** a, b Bilateral pulmonary pneumatoceles, which appeared 6 days after hydrocarbon ingestion in a 18-month-old girl

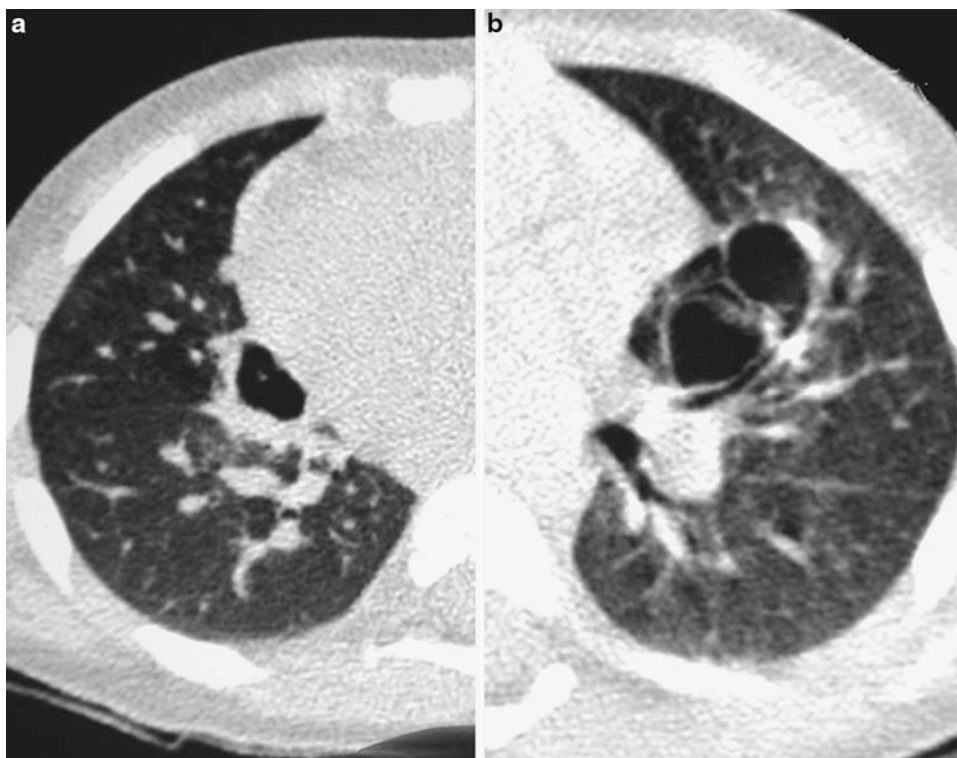


**Fig. 39** Infectious pneumatocele in a 3-month-old infant

the bronchiectasis becomes difficult to identify, yet the air trapping persists (Fig. 26).

## 6.6 Septal Thickening

Interlobular septal thickening, also known as septal lines, is defined as abnormal widening of an interlobular septum or septa. On HRCT it presents as short (1–2 cm in length), fine

linear opacities perpendicular to and abutting the pleural surface (Fig. 27), or as fine, polygonal pattern of lines in the more central lung (Figs. 10, 11, 28). Interlobular septal thickening is usually due to interstitial edema of any cause (Fig. 11), but it is also seen in neoplasms, infectious processes (Fig. 10), pulmonary fibrosis, bronchopulmonary dysplasia (Fig. 27), pulmonary lymphangiectasia, Niemann-Pick disease (Fig. 28) (Ferretti et al. 1996), Gaucher's disease, collagen vascular disorders, tuberous sclerosis, alveolar proteinosis (Fig. 45), sarcoidosis, and pulmonary venous obstruction (Fink et al. 2003; Newman et al. 2001) (Fig. 11). Septal thickening is usually smooth. It can be irregular in cases of fibrosis and irregular or nodular in sarcoidosis or lymphangitis spread of tumor (Fig. 29) (Lynch et al. 1999; Moon et al. 1996). Affected peripheral acini in contiguous lobules may simulate septal thickening (Klusmann and Owens 2009).

Intralobular lines, rarely observed in children, correspond to thickening of intralobular interstitium and they may be seen in interstitial fibrosis and alveolar proteinosis. When numerous, they may appear as a fine reticular pattern.

## 6.7 Parenchymal Bands

Visualized as elongated opacities, parenchymal bands are usually 2–5 cm in length and often represent several contiguous thickened septa. They can also correspond to areas



**Fig. 40** Cystic pulmonary lesions and treated left pneumothorax in a 16-year-old boy with Langerhans cell histiocytosis (a). Cystic pulmonary lesions in a 14-year-old boy with Langerhans cell

histiocytosis. Note the dot sign (arrows) in the center of some of the lesions (b). Cystic lesions in a 10-year-old boy with destructive emphysema secondary to nonspecific interstitial disease (c)

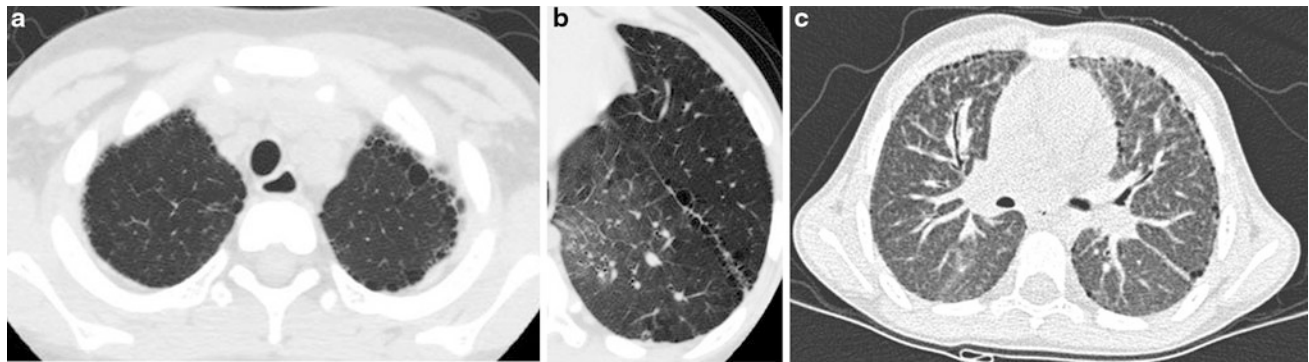


**Fig. 41** HRCT of a 4-year-old girl with Down's syndrome shows multiple subpleural cystic images (a, b). Similar changes can be seen in honeycombing, as in this 3-year-old boy with biopsy-proven chronic

pneumonitis of infancy (c), in whom HRCT shows generalized ground glass with septal thickening and honeycombing producing a subpleural line

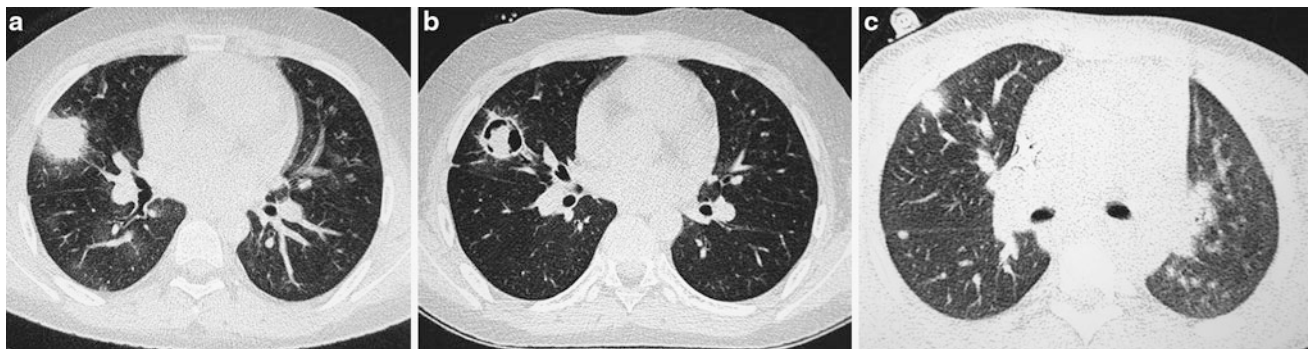


**Fig. 42** A 14-year-old girl with leukemia and pulmonary aspergillosis. Initial CT shows a nodule surrounded by a halo of ground glass (a). Follow-up CT performed 5 weeks later shows cavitation of the nodule (b). Follow-up CT 3 months later shows the nodule smaller in size (c)

of peribronchovascular fibrosis, coarse scars, or atelectasis associated with lung or pleural fibrosis. Parenchymal bands can extend to the pleura, which may be thickened and retracted at the site of contact. The pleural retraction as visualized as pleural-based triangular opacities. These features are commonly seen in children with long-standing bronchopulmonary dysplasia. Most parenchymal bands in bronchopulmonary dysplasia are in the upper lobes (Figs. 3b,

30) (Aquino et al. 1999; Oppenheim et al. 1994). Pleural-based triangular opacities have been observed in the HRCTs of toddlers as the only residual anomaly of previous bronchopulmonary dysplasia (Fig. 31). Similar findings have been reported in adolescents born prematurely even without having suffered bronchopulmonary dysplasia (Aukland et al. 2006). We have also seen linear opacities in patients with interstitial pneumonia (Figs. 32, 33).



**Fig. 43** A 7-year-old boy with cryptogenic organizing pneumonia. Inspiratory (a) and expiratory (b) scans show a subpleural ground-glass opacity with reversed halo sign in left upper lobe. One month later, following steroid therapy, CT findings were normal (c)

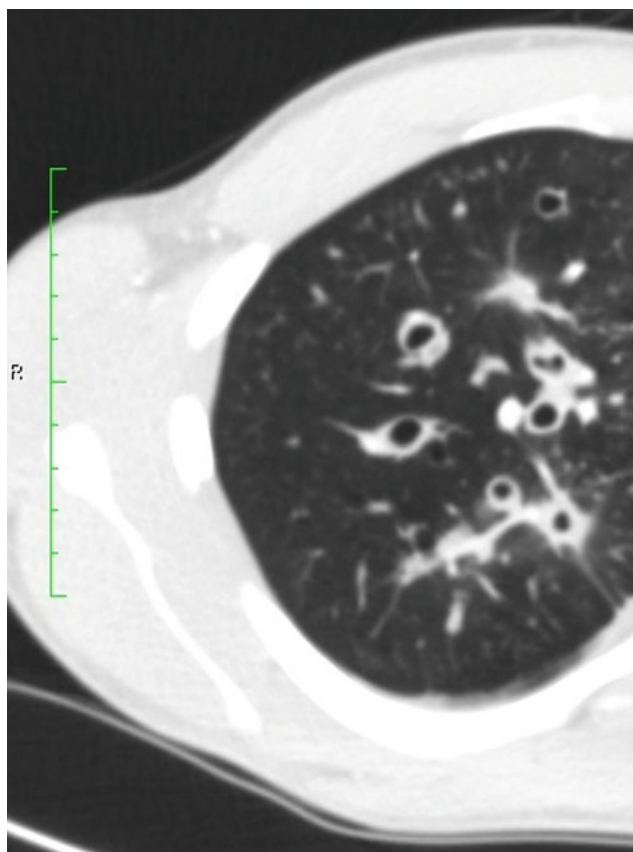


**Fig. 44** Signet ring sign in a 14-year-old patient with cystic fibrosis and right bronchiectasis

## 6.8 Honeycombing

A sign of destroyed, fibrotic, and cystic lung, honeycombing represents complete loss of acinar and bronchiolar architecture at the end stage of fibrosing lung disease. On HRCT of the lung it presents as clustered cystic airspaces with clearly definable walls, measuring 1–3 mm in thickness and predominantly found in peripheral and subpleural lung regions. It is often distributed in several contiguous



**Fig. 45** A 3-year-old girl with alveolar proteinosis. HRCT shows thickened interlobular septa in background of ground-glass opacification (crazy-paving pattern). [Reprinted with permission, from Copley et al. (2000)]

layers, but it can also be seen as a single subpleural line (Fig. 41c). True honeycombing cysts do not change in size during exhalation (Johkoh et al. 1999a). Honeycombing is not a common finding in children, but it can be seen in chronic interstitial lung disorders, such as nonspecific interstitial pneumonitis, desquamative interstitial pneumonitis (Copley et al. 2000), scleroderma (Seely et al. 1998), systemic sclerosis (García-Peña et al. 2011), lupus, and end-stage pulmonary fibrosis (Fig. 34).

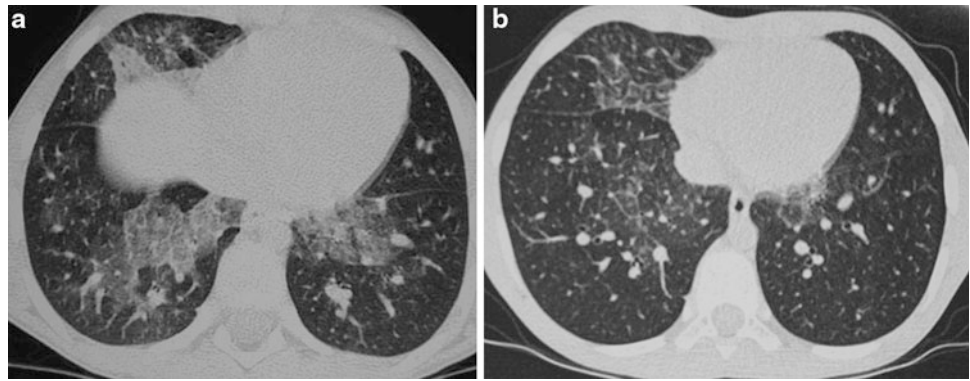
When present, the characteristics and distribution of the honeycombing pattern may have significant prognostic value (Edey et al. 2011).

## 6.9 Mosaic Attenuation Pattern

A patchwork of varied attenuation, mosaic pattern has been interpreted as secondary to regional differences in perfusion. The HRCT mosaic pattern of lung attenuation is a nonspecific finding that can reflect the presence of airway abnormalities, parenchymal ground-glass opacities, or



**Fig. 46** Crazy-paving pattern due to lipoid pneumonia by oil-aspiration in a 10-year-old boy (a). Follow-up HRCT 2 months later shows improvement of the pulmonary lesions (b)



vascular disease (Stern et al. 1995). In small airway disease and pulmonary vascular disease, the pulmonary vessels within the lucent regions of the lung are small relative to the vessels in the more opaque lung. In primary vascular diseases, such as thromboembolism or pulmonary hypertension, which are exceedingly rare in children, the reduced vascularity in the lucent lesions results from the primary vascular disease. In contrast, when mosaic pattern is due to small airway disease, the commonest cause of this pattern in children, the reduced vascularity in the lucent areas results from abnormal ventilation, air trapping, and secondary hypoxic vasoconstriction. Recognition of a mosaic pattern secondary to airway disease is enhanced with the use of expiratory slices. Asthma (Figs. 4, 25), bronchiolitis obliterans (Fig. 35), cystic fibrosis, and bronchopulmonary dysplasia are the most common causes of a mosaic pattern in the pediatric age group.

The third cause of HRCT mosaic pattern of lung attenuation is infiltrative lung disease, producing areas of ground-glass attenuation in a lobular or multilobular distribution. The areas of ground glass can be due to interstitial or airspace infiltrates, or both. In these cases the vessel caliber and number are similar in both the normal lower attenuation regions and the abnormal higher attenuation regions of the lung. Furthermore, there is no air trapping on expiration.

## 6.10 Architectural Distortion

Architectural distortion refers to abnormal morphology, position, or distribution of bronchi, pulmonary vessels, fissures, and/or septa.

Usually, there are fewer vessels and their branching pattern is anomalous. This finding can be observed in pulmonary hypoplasia (Fig. 36), but it is most common in lung diseases associated with small-airway obstruction (Fig. 26). In the latter, architectural distortion may be the only abnormality seen in the inspiratory slices; expiratory scans will demonstrate air trapping (Fig. 26).

In our experience, previous lobectomy may cause an evident abnormal vascular branching pattern in the remaining lobes (Fig. 37).

## 6.11 Air-filled Cystic Lung Lesions: Bullae, Pneumotoles, and Cysts

Air-filled cystic lung lesions correspond to intrapulmonary air collections surrounded by a visible wall of varying thickness. In our experience, it is extremely difficult, if not impossible, to differentiate between air-filled cysts, bullae, pneumotoles, and even some cases of cystic bronchiectasis or localized emphysema on imaging findings alone. Clinical features and evolution are essential to establish the diagnosis.

The differential diagnosis of air-filled cystic lung lesions in children includes congenital cyst, inflammatory pneumotoles secondary to hydrocarbon ingestion (Fig. 38) or infectious pneumonia (Fig. 39), interstitial emphysema due to barotraumas (Fig. 2), Langerhans' cell histiocytosis (Fig. 40), tuberous sclerosis, papillomatosis, septic pulmonary emboli, Wegener's granulomatosis, Ehler-Danlos, Marfan or Williams-Campbell syndromes (Hartman et al. 1994), and trisomy 21 (Fig. 41) (Tyrrell et al. 1999). The dot sign has been described as typical of pulmonary emphysema (Bonelli et al. 1998; Koyama et al. 2003; Seaman et al. 2011), yet we have also seen it in patients with pulmonary Langerhans cell histiocytosis (arrows in Fig. 40b).

## 6.12 Reversed Ventilatory Pattern

Increased subpleural attenuation occurs in a region of the dependent lung and disappears when the lung is nondependent. Dependent increased attenuation is a normal finding. It can be particularly evident in patients who have been examined using deep sedation or general anesthesia. The opposite, i.e., the posterior lung being more



hyperlucent than the anterior on CT scan of a noncooperative patient examined in the supine position is always abnormal and indicative of airway disease (Fig. 12). This has been described in cases of follicular bronchitis (Oh et al. 1999) and in neuroendocrine cell hyperplasia of infancy (Brody 2005; Brody and Crotty 2006; Deterding et al. 2005). We have also seen it in patients with cystic fibrosis (Fig. 12c) or bronchiolitis obliterans.

### 6.13 Emphysema

Emphysema is characterized by permanent, abnormal enlargement of the airspaces distal to the terminal bronchioles, accompanied by destruction of their walls. It is visible on HRCT as a focal region or regions of low attenuation, usually without visible walls, resulting from actual or perceived enlarged airspaces and destroyed alveolar walls (Hansell et al. 2008). It can be associated with air trapping. Emphysema is classified morphologically relative to the pulmonary lobule as centrilobular, panlobular, or paraseptal.

### 6.14 Halo Sign

The halo sign is a ground-glass opacity surrounding the circumference of a nodule or mass. It can be seen in patients with invasive pulmonary aspergilosis (Fig. 42), tuberculosis, lymphoproliferative disorders, bacterial and viral infections (Escuissato et al. 2005), Wegener's, pulmonary hemorrhage, metastatic osteosarcoma (Tomiya et al. 1994; Pinto 2004), pulmonary visceral larva migrans (Sakai et al. 2006), and paragonimiasis (Henry et al. 2012).

### 6.15 Reversed Halo Sign

The reversed halo sign is a ring of consolidation surrounding a focal ground-glass area (Fig. 43). It was initially reported to be specific for cryptogenic organizing pneumonia (Kim et al. 2003) but numerous other conditions including sarcoidosis, Wegener's granulomatosis, and paracoccidioidomycosis have also been described (Robertson and Hansell 2011; Marchiori et al. 2011).

### 6.16 Signet Ring Sign

A ring opacity (usually representing a dilated, thick-walled bronchus) associated with a smaller, round, soft-tissue opacity (the adjacent pulmonary artery) is known as the signet ring sign. In children this finding indicates bronchiectasis (Fig. 44) (Ouellette 1999).

### 6.17 Crazy-Paving Pattern

Crazy-paving pattern is a combination of areas of ground-glass attenuation and smoothly thickened interlobular septa, within the areas of airspace disease (Fig. 45). This finding has been considered to be strongly suggestive of alveolar proteinosis. However, it can occur in other diseases such as lipoid pneumonia (Fig. 46), adult respiratory distress syndrome, acute interstitial pneumonia, drug-induced pneumonitis, bacterial pneumonia, radiation pneumonitis, and pulmonary hemorrhage (Franquet et al. 1998; Johkoh et al. 1999b; Lee et al. 2005, 2007).

## 7 Conclusion

High-resolution computed tomography of the chest enables imaging of the lung with excellent spatial resolution. HRCT with mandatory low-dose protocols is a valuable technique to provide information on the pattern and anatomical distribution of lung disease, determine the response to therapy, and guide clinical management. Classical HRCT with 1 mm slices at 10 or 20 mm intervals remains the technique of choice in the evaluation of many pediatric lung disorders.

## References

- Ambrosino NM, Genieser NB, Roche KJ et al (1994) Feasibility of high-resolution, low-dose chest CT in the evaluation of the pediatric chest. *Pediatr Radiol* 24:6–10
- Aquino SL, Gamsu G, Webb WR et al (1996) Tree-in-bud pattern: frequency and significance on thin section CT. *J Comput Assist Tomogr* 20:594–599
- Aquino SL, Schechter MS, Chiles C et al (1999) High-resolution inspiratory and expiratory CT in older children and adults with bronchopulmonary dysplasia. *AJR Am J Roentgenol* 173:963–967
- Arakawa H, Webb WR (1998) Air-trapping on expiratory high-resolution CT scans in the absence of inspiratory scan abnormalities. *AJR Am J Roentgenol* 170:1012–1018
- Aukland SM, Halvorsen T, Fosse KR et al (2006) High resolution CT of the chest in children and young adults who were born prematurely: findings in a population-based study. *Am J Roentgenol* 187:1012–1018
- Bonelli FS, Hartman TE, Swensen SJ et al (1998) Accuracy of high-resolution CT in diagnosing lung diseases. *AJR Am J Roentgenol* 170:1507–1512
- Brody AS (2005) Imaging considerations: interstitial lung disease in children. *Radiol Clin North Am* 43:391–403
- Brody AS, Crotty EJ (2006) Neuroendocrine cell hyperplasia of infancy (NEHI). *Pediatr Radiol* 36:1328
- Callahan MJ (2011) CT dose reduction in practice. *Pediatr Radiol* 41:S488–S492
- Canakis AM, Cutz E, Mason D et al (2002) Pulmonary interstitial glycogenosis. a new variant of neonatal interstitial lung disease. *Am J Respir Crit Care Med* 165:1557–1565
- Capitanio MA, Kirkpatrick JA (1972) Lateral decubitus film: an aid in determining air-trapping in children. *Radiology* 103:460–462

- Choi D, Lee KS, Suh GY et al (1999) Pulmonary tuberculosis presenting as acute respiratory failure: radiologic findings. *J Comput Assist Tomogr* 23:107–113
- Choi SJ, Choi BK, Kim HJ et al (2002) Lateral decubitus HRCT: a simple technique to replace expiratory CT in children with air trapping. *Pediatr Radiol* 32:179–182
- Chung T, Hoffer FA, Connor L et al (2000) The use of oral pentobarbital sodium (Nembutal) versus oral chloral hydrate in infants undergoing CT and MR imaging—a pilot study. *Pediatr Radiol* 30:332–335
- Collins J, Stern EJ (1997) Ground-glass opacity at CT: the ABCs. *AJR Am J Roentgenol* 169:355–367
- Copley SJ, Coren M, Nicholson AG et al (2000) Diagnostic accuracy of thin-section CT and chest radiography of pediatric interstitial lung disease. *AJR Am J Roentgenol* 174:549–554
- Deterding RR, Pye C, Fan LL et al (2005) Persistent tachypnea of infancy is associated with neuroendocrine cell hyperplasia. *Pediatr Pulmonol* 40:157–165
- Dougeni E, Faulkner K, Panayiotakis G (2012) A review of patient dose and optimisation methods in adult and paediatric CT scanning. *Eur J Radiol* 81:665–683
- Edey AJ, Devaraj AA, Barker RP et al (2011) Fibrotic idiopathic interstitial pneumonias: HRCT findings that predict mortality. *Eur Radiol* 21:1586–1593
- Egelhoff JC, Ball WS, Koch BL et al (1997) Safety and efficacy of sedation in children using a structured sedation program. *AJR Am J Roentgenol* 168:1259–1262
- Escuissato DL, Gasparetto EL, Marchiori E et al (2005) Pulmonary infections after bone marrow transplantation: high-resolution CT findings in 111 patients. *AJR Am J Roentgenol* 185:608–615
- Ferretti GR, Lantejuol S, Brambilla E et al (1996) Pulmonary involvement in Niemann-Pick disease subtype B: CT findings. *J Comput Assist Tomogr* 20:990–992
- Fink C, Schmaelh A, Bock M et al (2003) Pulmonary vein stenosis after radiofrequency ablation for atrial fibrillation. Image findings with multiphasic pulmonary magnetic resonance angiography. *Circulation* 107:e129–e130
- Fisher DM (1990) Sedation of pediatric patients: an anesthesiologist's perspective. *Radiology* 175:613–615
- Franquet T, Gimenez A, Brodes R et al (1998) The crazy paving pattern in exogenous lipid pneumonia. CT-pathologic correlation. *AJR Am J Roentgenol* 170:315–317
- Fricke BL, Donnelly LF, Frush DP et al (2003) In-plane bismuth breast shields for pediatric CT: effects on radiation dose and image quality using experimental and clinical data. *AJR Am J Roentgenol* 180:407–411
- García-Peña P, Boixadera H, Barber I et al (2011) Thoracic findings of systemic diseases at high-resolution CT in children. *Radiographics* 31:465–482
- García-Peña P, Lucaya J (2004) HRCT in children: technique and indications. *Eur Radiol* 14:L13–L30
- Giovagnorio F, Cavallo V (1995) HRCT evaluation of secondary lobules and acini of the lung. *J Thorac Imaging* 10:129–133
- Geleijns J, Wang J, McCollough C (2010) The use of breast shielding for dose reduction in pediatric CT: arguments against the proposition. *Pediatr Radiol* 40:1744–1747
- Gruden JF, Webb WR, Warnock M et al (1994) Centrilobular opacities in the lung on high-resolution CT: diagnostic considerations and pathologic correlation. *AJR Am J Roentgenol* 162:569–574
- Hansell DM (2010) Thin-section CT of the lungs: the hinterland of normal. *Radiology* 256:695–711
- Hansell DM, Bankier AA, MacMahon H et al (2008) Fleischner society: glossary of terms for thoracic imaging. *Radiology* 246:697–722
- Hansell DM, Wells AU, Rubens MB et al (1994) Bronchiectasis: functional significance of areas of decreased attenuation at expiratory CT. *Radiology* 193:369–374
- Hartman TE, Primack SL, Lee KS et al (1994) CT of bronchial and bronchiolar diseases. *Radiographics* 14:991–1003
- Heng Vong C, Bajard A, Thiesse P et al (2012) Deep sedation in pediatric imaging: efficacy and safety of intravenous chlorpromazine. *Pediatr Radiol* 42:552–561
- Henry TS, Lane MA, Weil GJ et al (2012) Chest CT features of North American paragonimiasis. *AJR Am J Roentgenol* 198:1076–1083
- Hubbard AM, Markowitz RI, Kimmel B et al (1992) Sedation for pediatric patients undergoing CT and MRI. *J Comput Assist Tomogr* 16:3–6
- Johkoh T, Müller NL, Ichikado K et al (1999a) Respiratory change in size of honeycombing: inspiratory and expiratory spiral volumetric CT analysis of 97 cases. *J Comput Assist Tomogr* 23:174–180
- Johkoh T, Müller NL, Pickford HA et al (1999b) Lymphocytic interstitial pneumonia: thin-section CT findings in 22 patients. *Radiology* 212:567–572
- Karian VE, Burrows PE, Zurakowski D et al (1999) Sedation for pediatric radiological procedures: analysis of potential causes of sedation failure and paradoxical reactions. *Pediatr Radiol* 29:869–873
- Kim S, Frush DP, Yoshizumi TT (2010) Bismuth shielding in CT: support for use in children. *Pediatr Radiol* 40:1739–1743
- Kim SJ, Lee KS, Ryu YH et al (2003) Reversed halo sign on high-resolution CT of cryptogenic organizing pneumonia: diagnostic implications. *AJR Am J Roentgenol* 180:1251–1254
- Klusmann M, Owens C (2009) HRCT in paediatric diffuse interstitial lung disease—a review for 2009. *Pediatr Radiol* 39:S471–S481
- Koyama M, Johkoh T, Honda O et al (2003) Chronic cystic lung disease: diagnostic accuracy of high-resolution CT in 92 patients. *AJR Am J Roentgenol* 180:827–835
- Kroft L, Roelofs J, Geleijns J (2010) Scan time and patient dose for thoracic imaging in neonates and small children using 320-detector row CT compared to helical 64-, 32-, and 16-detector row CT acquisitions. *Pediatr Radiol* 40:294–300
- Land CE, Tokunaga M, Tokuda AS et al (1993) Early-onset breast cancer in A-bomb survivors. *Lancet* 342:237
- Landry BA, Melhem RE (1989) Pulmonary nodules secondary to total parenteral alimentation. *Pediatr Radiol* 19:456–457
- Lee KH, Kim WS, Cheon JE et al (2005) Squalene aspiration pneumonia in children: radiographic and CT findings as the first clue to diagnosis. *Pediatr Radiol* 35:619–623
- Lee C (2007) The crazy-paving sign. *Radiology* 243:905–906
- Lee EY (2013) Interstitial lung disease in infants: new classification system, imaging technique, clinical presentation and imaging findings. *Pediatr Radiol* 43:3–13
- Levine D, Akikusa J, Manson D et al (2007) Chest CT findings in pediatric Wegener's granulomatosis. *Pediatr Radiol* 37:57–62
- Lucaya J, García-Peña P, Herrera L et al (1999) Expiratory chest CT in children. *AJR Am J Roentgenol* 174:235–241
- Lucaya J, Piqueras J, García-Peña P et al (2000) Low-dose high-resolution CT in children and young adults: dose, cooperation, artifact incidence, and image quality. *AJR Am J Roentgenol* 175:985–992
- Lynch DA, Hay T, Newel JD et al (1999) Pediatric diffuse lung disease. *AJR Am J Roentgenol* 173:713–718
- Macias CG, Chumtazi CE (2011) Sedation and anesthesia for CT: emerging issues for providing high-quality care. *Pediatr Radiol* 41:S517–S522
- Marchiori E, Zanetti G, Mereilles GS et al (2011) The reversed halo sign on high-resolution CT in infectious and noninfectious pulmonary diseases. *AJR Am J Roentgenol* 197:69–75

- Mason KP, Prescilla R, Fontaine PJ et al (2011) Pediatric CT sedation: comparison of dexmedetomidine and pentobarbital. *AJR Am J Roentgenol* 196:194–198
- Mayo JR, Webb WR, Gould R et al (1987) High-resolution CT of the lungs: an optimal approach. *Radiology* 163:507–510
- Mayo JR, Jackson SA, Müller NL (1993) High-resolution CT of the chest: radiation dose. *AJR Am J Roentgenol* 160:479–481
- McCollough CH, Chen GH, Kalender W et al (2012a) Achieving routine submillisievert CT scanning: report from the summit on management of radiation dose in CT. *Radiology* 264:567–580
- McCollough CH, Wang J, Gould RG et al (2012b) Point/counterpoint. the use of bismuth breast shields for CT should be discouraged. *Med Phys* 39:2321–2324
- Moon WK, Kim Ws, Kim IO et al (1996) Diffuse pulmonary disease in children. High-resolution CT findings. *AJR Am J Roentgenol* 167:1405–1408
- Murata K, Khan A, Rojas KA et al (1988) Optimization of computed tomography technique to demonstrate the fine structure of the lung. *Invest Radiol* 23:170–175
- Murata K, Khan A, Herman PG (1989) Pulmonary parenchymal diseases: evaluation with high resolution CT. *Radiology* 170:629–635
- Newman B, Kuhn JP, Kramer SS et al (2001) Congenital surfactant protein B deficiency. Emphasis on imaging. *Pediatr Radiol* 31:327–331
- Nievelstein RA, van Dam IM, van der Molen AJ (2010) Multidetector CT in children: current concepts and dose reduction strategies. *Pediatr Radiol* 40:1324–1344
- Oh YW, Effmann EL, Redding GJ et al (1999) Follicular hyperplasia of bronchus-associated lymphoid tissue causing severe air-trapping. *AJR Am J Roentgenol* 172:745–747
- Oppenheim C, Mamou-Mani T, Sayegh N et al (1994) Bronchopulmonary dysplasia: value of CT in identifying pulmonary sequelae. *AJR Am J Roentgenol* 163:169–172
- Ouellette H (1999) The signet ring sign. *Radiology* 212:67–68
- Pearce MS, Salotti JA, Little MP et al (2012) Radiation exposure from CT scans in childhood and subsequent risk of leukaemia and brain tumours: a retrospective cohort study. *Lancet* 380:499–505
- Pererira JK, Burrows PE, Rickards HM et al (1993) Comparison of sedation regimens for pediatric outpatient CT. *Pediatr Radiol* 23:341–344
- Pinto PS (2004) The halo sign. *Radiology* 230:109–110
- Popler J, Lesnick B, Dishop MK et al (2012) New coding in the international classification of diseases, ninth revision, for children's interstitial lung disease. *Chest* 142:774–780
- Rastogi R, Garg R, Thulkar S et al (2008) Unusual thoracic CT manifestations of osteosarcoma: review of 16 cases. *Pediatr Radiol* 38:551–558
- Rimmer MJ, Dixon AK, Flower DR et al (1985) Bleomycin lung: computed tomographic observations. *Br J Radiol* 58:1041–1045
- Robertson BJ, Hansell DM (2011) Organizing pneumonia: a kaleidoscope of concepts and morphologies. *Eur Radiol* 21:2244–2254
- Rooks VJ, Chung T, Connor N et al (2003) Comparison of oral pentobarbital sodium (neumbutal) and oral chloral hydrate for sedation of infants during radiologic imaging. Preliminary results. *AJR Am J Roentgenol* 180:1125–1128
- Rossi SE, Franquet T, Volpacchio M et al (2005) Tree- in bud pattern and thin section CT of the lungs: radiologic-pathologic overview. *Radiographics* 25:289–901
- Rothemberg LN, Pentlow KS (1992) Radiation dose in CT. *Radiographics* 12:1225–1243
- Sakai S, Shida Y, Takahashi N et al (2006) Pulmonary lesions associated with visceral larva migrans due to *ascaris suum* or *toxocara canis*: imaging of six cases. *AJR Am J Roentgenol* 186:1697–1702
- Sanborn PA, Michna E, Zurazowski D et al (2005) Adverse cardiovascular and respiratory events during sedation of pediatric patients for imaging examinations. *Radiology* 237:288–294
- Schultz R, Mattila J, Gappa M et al (2001) Development of progressive pulmonary interstitial and intra-alveolar cholesterol granulomas associated with therapy-resistant chronic systemic juvenile arthritis. *Pediatr Pulmonol* 32:397–402
- Seaman DM, Meyer CA, Gilman MD et al (2011) Diffuse cystic lung disease at high-resolution CT. *AJR Am J Roentgenol* 196:1305–1311
- Seely JM, Jones LT, Wallace C (1998) Systemic sclerosis: using high-resolution CT to detect lung disease in children. *AJR Am J Roentgenol* 170:691–697
- Shankar VR (2008) Sedating children for radiological procedures: an intensivist's perspective. *Pediatr Radiol* 38:S213–S217
- Shepard JA (1995) The bronchi: an imaging perspective. *J Thorac Imaging* 10:236–254
- Sigal-Cinqualbre AB, Hennequin R, Abada HT et al (2004) Low-kilovoltage multi-detector row chest CT in adults: feasibility and effect on image quality and iodine dose. *Radiology* 231:169–174
- Silva CT, Amaral JG, Moineddin R et al (2010) CT characteristics of lung nodules present at diagnosis of extrapulmonary malignancy in children. *AJR Am J Roentgenol* 194:772–778
- Sodickson A (2012) Strategies for reducing radiation exposure in multi-detector row CT. *Radiol Clin North Am* 50:1–14
- Song I, Yi CA, Han J et al (2012) CT findings of late-onset noninfectious pulmonary complications in patients with pathologically proven graft-versus-host disease after allogeneic stem cell transplant. *AJR Am J Roentgenol* 199:581–587
- Stern EJ, Müller NL, Swensen SJ et al (1995) CT mosaic pattern of lung attenuation: etiologies and terminology. *J Thorac Imaging* 10:294–297
- Tomiyama N, Ikezoe J, Miyamoto M et al (1994) CT halo sign in metastasis of osteosarcoma. *AJR Am J Roentgenol* 162:468
- Tyrrell VJ, Asher MI, Chan Y (1999) Subpleural lung cysts in down's syndrome. *Pediatr Pulmonol* 28:145–148
- Vade A, Sukhani R, Dolenga M et al (1995) Chloral hydrate sedation of children undergoing CT and MR imaging: safety as judged by American academy of pediatrics guidelines. *AJR Am J Roentgenol* 165:905–909
- Webb WR, Müller NL, Naidich DP (1996) High-resolution CT of the lung, 2nd edn. Lippincott-Raven Publishers, Philadelphia
- Weibel ER (1979) Looking into the lungs: what can it tell us? *AJR Am J Roentgenol* 133:1021–1031
- Willeminck MJ, Leiner T, de Jong PA et al (2013) Iterative reconstruction techniques for computed tomography part 2: initial results in dose reduction and image quality. *Eur Radiol* 16



---

# High-Resolution CT of the Lung in Children: Clinical Applications

Hubert Ducou Le Pointe

## Contents

<b>1</b>	<b>Airway</b> .....	135
1.1	Bronchiectasis .....	136
1.2	Asthma: Allergic Bronchopulmonary Aspergillosis.....	138
1.3	Constrictive Bronchiolitis.....	139
1.4	Bronchiolitis Obliterans Organizing Pneumonia: Organizing Pneumonia .....	140
<b>2</b>	<b>HRCT Findings in Specific Diseases</b> .....	141
2.1	Chronic Diffuse Infiltrative Lung Disease .....	141
2.2	Air-Space Diseases .....	150
<b>References</b>	.....	151

---

## Abstract

High-Resolution CT of the Lung in children: Clinical Applications (HRCT) of the chest allows a detailed structural assessment of secondary pulmonary lobules and intrapulmonary interstitium. Based on characteristic patterns and distribution of pathology, it has proved to be of great value for the diagnosis and management of adult patients with lung disease. More recently in the pediatric population HRCT was also recognized to be a valuable tool for exploring lung diseases. Airway diseases and air-space disease are now well known and described. In the recent past, progresses were done in the comprehension of pediatric interstitial lung disease. In the pediatric population, a developmental or genetic origin could be shown. So, classification of interstitial lung disease is now specific to the pediatric population. In this chapter we revisited well-known pediatric lung diseases and introduced notions about the newest childhood interstitial lung diseases.

High-Resolution CT (HRCT) has proved to be of great value for the diagnosis and management of patients with lung disease, particularly when the chest X-ray is normal. Volumetric HRCT is possible with the introduction of multidetector computed tomography (MDCT) and could allow better diagnosis. In this chapter, we discuss airway disease, chronic diffuse infiltrative lung disease, and air-space disease.

---

## 1 Airway

HRCT is the imaging technique of choice for the evaluation of most lesions of the bronchial tree: bronchiectasis, constrictive bronchiolitis, bronchiolitis obliterans organizing pneumonia (BOOP), and asthma.

---

H. Ducou Le Pointe (✉)  
Service de Radiologie Pédiatrique,  
Hôpital d'Enfants Armand-Trousseau,  
26, Avenue du Docteur-Arnold-Netter, 75012 Paris, France  
e-mail: hubert.ducou-le-pointe@trs.ap-hop-paris.fr

## 1.1 Bronchiectasis

Bronchiectasis is defined pathologically as the irreversible dilatation of the bronchial tree. In children, a radiological diagnosis should be considered with caution. Reversible bronchial dilatation or improvement in appearance with medical treatment has been reported (Gaillard et al. 2003). Numerous disorders are associated with bronchiectasis (postinfective bronchial damage, bronchial obstruction, immune deficiency, mucociliary clearance defect, fibrosis, etc.). HRCT has proved to be a reliable, noninvasive technique for assessing the presence, severity, and extension of bronchiectasis and has largely eliminated the need for bronchography in children (Herman et al. 1993; Rossi and Owens 2005). High-resolution MDCT using 1 mm contiguous slices improves the presence, extent, and severity of bronchiectasis compared with conventional bronchiectasis (Dodd et al. 2006). Despite this fact some authors do not recommend this technique in children due to a considerably higher radiation dose delivered. In noncystic fibrosis bronchiectasis, a stronger correlation between the extent and severity of bronchiectasis explored by HRCT and pulmonary function test was observed, than when they are explored by chest X-ray (Edwards et al. 2003).

The HRCT criteria for diagnosing bronchiectasis have been well described (Hansell 1998): internal diameter of the bronchus larger than the diameter of the adjacent pulmonary artery branch, absence of normal tapering of bronchi, bronchial wall thickening, and visualization of a bronchus in the lung periphery. This last criterion is not clearly defined in the literature. Several authors (Grenier et al. 1986; Webb 1994; McGuinness and Naidich 1995) consider all bronchi visible within 2–3 cm from the pleural surface to be abnormal. Kim et al. (1997) defined the visualization of bronchi within 1 cm of costal or paravertebral pleura or visualization of bronchi abutting the mediastinal pleura as abnormal. These differences in criteria could be related to improvements in CT technology. We consider abnormal the visualization of bronchi in the peripheral 1 cm of the lung.

Bronchiectasis has been classified into three types—cylindrical, varicose, and cystic—based on the morphology of the abnormal bronchi. Cylindrical bronchiectasis is diagnosed when there is a lack of bronchial tapering and bronchial walls are smooth or slightly irregular (Fig. 1). Varicose bronchiectasis is easily recognized when bronchi are parallel to the scan plane, as the dilated bronchi have a beaded appearance (Fig. 2). Cystic bronchiectasis has a cystic or saccular appearance (Fig. 3). Air-fluid levels caused by retained secretions are sometimes seen in the dilated bronchi. Cystic and varicose bronchiectasis implies more bronchial destruction than cylindrical bronchiectasis.

Retained bronchial secretions, atelectasis, and/or mosaic perfusion, can also be seen in HRCT scans of patients with



**Fig. 1** A 14-year-old boy with cylindrical bronchiectasis in the middle lobe. Bronchi are dilated and slightly irregular

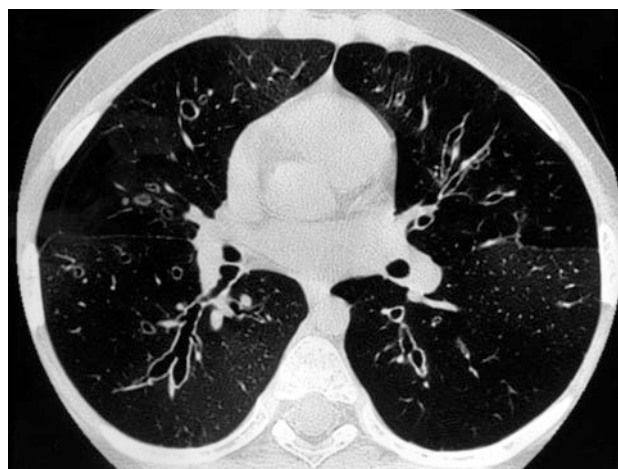


**Fig. 2** An 11-year-old boy with varicose bronchiectasis. In the right lower lobe. Bronchi have an irregular and beaded appearance

bronchiectasis. When the bronchus is perpendicular to the scan plane, retained bronchial secretions in the central lung appear as nodular or oval-shaped opacities. When the bronchus is parallel to the scan plane, they are recognized as lobulated linear or branching structures. In the peripheral bronchi, retained mucus is visualized as centrilobular nodules or tree-in-bud appearance (Grenier et al. 1990). Mosaic perfusion, secondary to air-trapping and reflecting the presence of small airway disease distal to the bronchiectasis, is extremely common.

The pattern and distribution of abnormalities revealed by HRCT in patients with bronchiectasis are influenced by the underlying cause, and distinctive HRCT appearances have

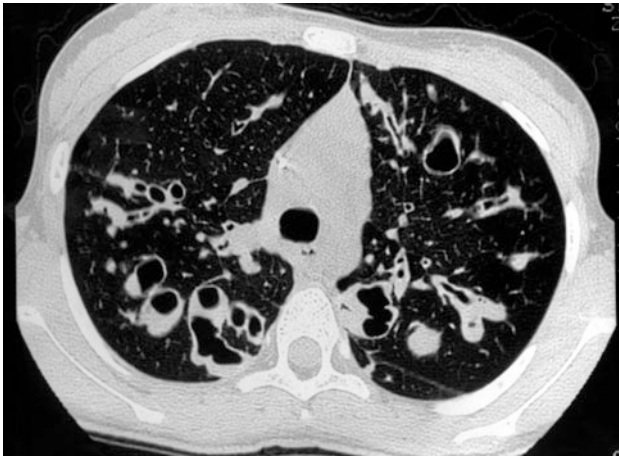


**Fig. 3** A 14-year-old girl with cystic bronchiectasis. Saccular bronchiectasis with retained secretions are seen in both *upper lobes*

been well described in a few conditions: cystic fibrosis, immotile cilia, allergic asthma, bronchopulmonary aspergillosis, tuberculosis, and hypogammaglobulinemia (Cartier et al. 1999).

Bilateral, predominantly upper lobe bronchiectasis is seen most commonly in patients with cystic fibrosis and allergic bronchopulmonary aspergillosis, unilateral upper lobe predominance in patients with tuberculosis, and lower lobe predominance as a sequela of childhood pulmonary infections.

### 1.1.1 Cystic Fibrosis

Cystic fibrosis is the most common cause of pulmonary insufficiency in childhood (Ruzal-Shapiro 1998). HRCT and High-resolution MDCT technique have been used for the evaluation of cystic fibrosis lung disease. HRCT technique allows lower dose CT scanning and may be useful for qualitative evaluation. HRCT images at interval greater than 10 mm underestimate the severity of the disease (de Jong et al. 2006). High-resolution MDCT is recommended for longitudinal evaluation and for quantitative evaluation (Brody et al. 2005). This opinion is not accepted by all authors. They still prefer to reduce the dose using preselected CT cuts (Jiménez et al. 2006). Bronchiectasis in cystic fibrosis is usually widespread, with upper lobe involvement being almost universal and both central and peripheral bronchiectasis being present in approximately two-thirds of patients. Although cystic and varicose types are not uncommon, cylindrical bronchiectasis usually predominates, particularly in young children. Peribronchial thickening, mucoid impaction, and a mosaic perfusion pattern secondary to air-trapping are common in cystic fibrosis (Fig. 4). Mosaic perfusion may be the initial (and only) HRCT abnormality early in the course of the disease. Mucoid impaction can present as large nodules in the central lung or as centrilobular or tree-in-bud pattern in the lung periphery. Mucus plugging may lead to lobar and segmental atelectasis. Partial or total

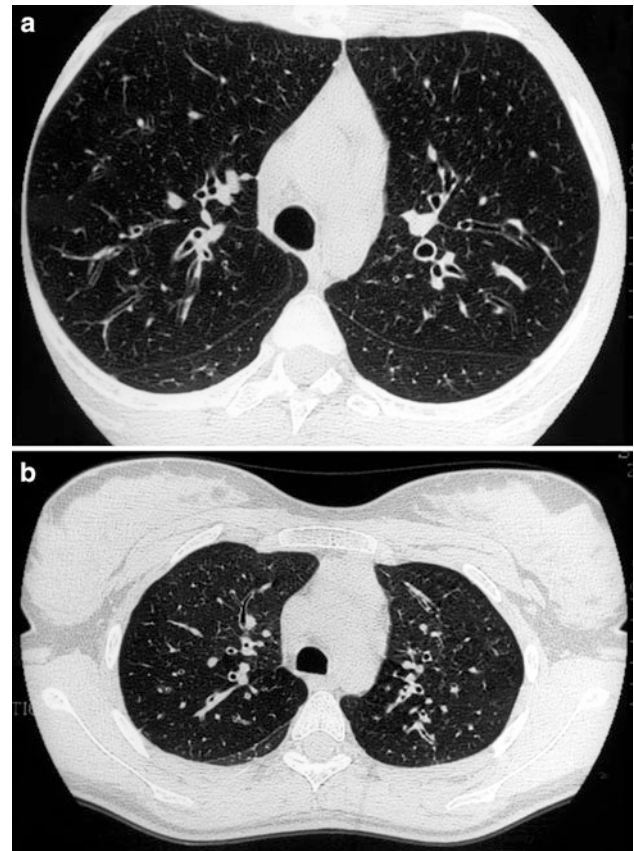


**Fig. 4** A 15-year-old girl with cystic fibrosis. HRCT detects cylindrical bronchiectasis with bronchial wall thickening (a). Expiratory air-trapping reflects the presence of small airways disease (b)

resolution of mucus plugging is a finding that can reflect therapeutic efficacy and is useful for monitoring.

Several authors have devised scoring systems based on chest X-ray findings to assess the severity of the disease (Nathanson et al. 1991; Sockrider et al. 1994; Cleveland et al. 1998). The Brasfield method is one of the most commonly used (Brasfield et al. 1980). New scoring systems based on HRCT have been proposed (Shah et al. 1997; Brody et al. 1999; Helbich et al. 1999). The most popular is the Bhalla method (Bhalla et al. 1991), which attempts to provide an objective assessment of the severity and extension of lung disease. Dissociation between CT score and lung function was reported by authors (de Jong et al. 2004; Brody et al. 2004). HRCT is a more sensitive technique than pulmonary function tests to detect structural changes and disease progression. However, the clinical relevance of HRCT scoring systems has not yet been demonstrated (Brody et al. 2005). Low-dose HRCT is now considered as an appropriate method for the evaluation of bronchiectasis in cystic fibrosis pediatric patients (O'Connor et al. 2010). But one must be aware that MRI gains increasing importance in the assessment and scoring of cystic fibrosis lung disease (Eichinger et al. 2012).



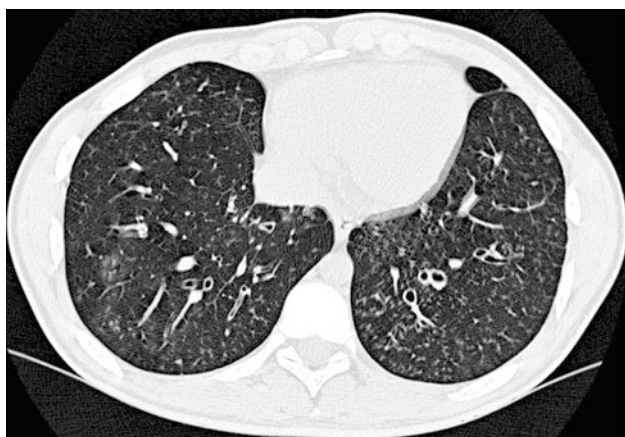


**Fig. 5** A 15-year-old girl with primary ciliary dyskinesia. Cylindrical bronchiectasis with mucus plugging (*tree-in-bud pattern*) is seen in both lower lobes

### 1.1.2 Immotile Cilia

Immotile cilia or primary ciliary dyskinesia (PCD) is a term including diseases that occur as a direct result of congenital defects in the airway cilia (Meeks and Bush 2000). The main features of PCD are recurrent sinopulmonary infections, situs inversus, and subfertility. The association between chronic respiratory disease and PCD is well-recognized. Kartagener's syndrome, characterized by situs inversus totalis, bronchiectasis, and paranasal sinusitis accounts for 50 % of all patients with PCD (Hiddema and Engelshove 1999). The radiological and clinical features of PCD are similar to those of cystic fibrosis but are less severe and progressive. Hyperinflation and bronchial thickening are the most common abnormalities. Bronchiectasis (particularly in the right middle lobe), mucus plugging (Fig. 5), atelectasis, and consolidation are also frequent (Nadel et al. 1985; Fauré et al. 1986; Reyes de La Rocha et al. 1987). HRCT is currently used to monitor the disease progression despite the fact that CT monitoring affects poorly pulmonary outcome in PCD (Barbato et al. 2009).

## 1.2 Asthma: Allergic Bronchopulmonary Aspergillosis

Asthma is a disorder of the tracheobronchial tree characterized by inflammation, reversible airway obstruction and tracheobronchial mucosal hyperreactivity to numerous stimuli. Asthma often coexists with other allergic disorders (e.g. allergic rhinitis and atopic dermatitis). Radiography is indicated to exclude other causes of wheezing and to detect complications. Air-trapping due to small airway disease is the most common HRCT feature in children with asthma (Fig. 6) (Fig. 4, “[High-Resolution CT of the Lung in Children: Technique, Indications, Anatomy, and Features of Lung](#)

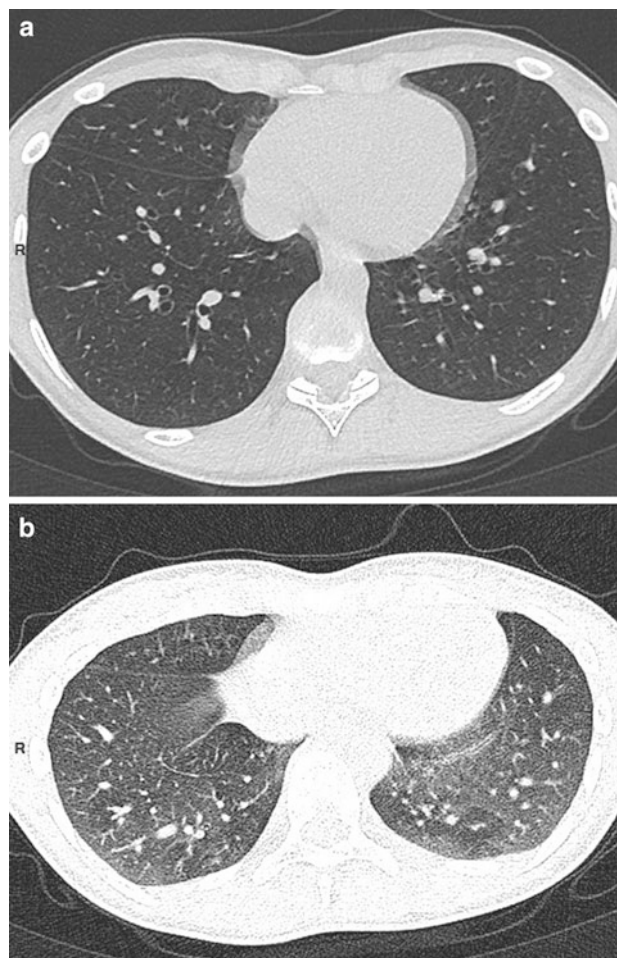


**Fig. 6** A 12-year-old boy with severe asthma. Inspiratory scan (a) shows no mosaic pattern. This pattern is clear on expiratory scan (b)

Disease”) and can disappear after therapy with bronchodilators (Lucaya et al. 2000) (Fig. 25, “[High-Resolution CT of the Lung in Children: Technique, Indications, Anatomy, and Features of Lung Disease](#)”). The sensitivity of HRCT for asthma is likely superior to pulmonary function test; patchy subsegmental involvement can be detected by HRCT even when pulmonary function tests are normal (Sharma et al. 2002). Atelectasis, particularly in the right middle lobe, is also common (Altamirano et al. 1991).

Other reported HRCT features include bronchial wall thickening, bronchiectasis, and mucoid impaction (McLean et al. 1998; Paganin et al. 1992; Grenier et al. 1996). The pathogenesis of bronchial wall thickening in asthmatic patients is not clear. Lynch (1998) has suggested that it is due to inflammation, muscle hypertrophy, and peribronchial fibrosis. The prevalence of bronchiectasis seems to be associated with disease severity (Paganin et al. 1992; Grenier et al. 1996). In contrast with adults with severe asthma, pediatric patients did not have CT evidence

bronchiectasis, mucoid impaction, emphysema; but bronchial wall thickening seems to be a criterion of asthma severity in children (Marchac et al. 2002). Jain et al. showed that air trapping on CT scans (percentage of low-density pixels) was correlated with the percentage of predicted total lung capacity and total gas volume and was inversely correlated with the forced expiratory volume in 1 s (FEV1)/forced vital capacity (FVC) and forced expiratory flow at 25–75 % of forced vital capacity (Jain et al. 2005).

According to Bandeira no isolated HRCT findings (increased lung volume, inspiratory decreased attenuation, expiratory air trapping, and mosaic pattern), could accurately differentiate severe asthma and bronchiolitis obliterans (Bandeira et al. 2011).

Central bronchiectasis associated with asthma is considered to be highly suggestive of allergic bronchopulmonary aspergillosis (ABPA) (Shah et al. 1992; Silva et al. 2004). ABPA is an immunological disorder characterized by immediate hypersensitivity due to endobronchial growth of *Aspergillus fumigatus*. In patients with IgE-mediated asthma, *A. fumigatus* may trigger an asthmatic reaction. The diagnosis of ABPA is based on a clinical history of asthma, skin test reactivity, elevated IgE, and measurement of serum precipitins. The presence of randomly distributed, predominantly central, moderate to severe bronchiectasis affecting three or more lobes, bronchial wall thickening, and centrilobular nodules in an asthmatic patient is highly indicative of ABPA (Ward et al. 1999; Mitchell et al. 2000). However, normal HRCT cannot exclude the diagnosis of ABPA (Agarwal et al. 2012).

### 1.3 Constrictive Bronchiolitis

Constrictive bronchiolitis (bronchiolitis obliterans) is a rare disease characterized by thickening of the bronchiole walls due to submucosal collagenization, with few changes in the distal parenchyma (Colby 1998). Progressive bronchiole narrowing is associated with distortion of the lumen, mucostasis, and chronic inflammation. Bronchiolectasis and bronchiolar smooth-muscle hypertrophy may also be seen.

Constrictive bronchiolitis can be idiopathic or secondary to various insults, such as viral, bacterial, or mycoplasma infections, bone marrow or lung transplantation, collagen vascular diseases or toxic fume inhalation (Chang et al. 1998; Lau et al. 1998; Sargent et al. 1995; Siegel 1999). It has also been reported to occur in association with Stevens-Johnson syndrome (Kim and Lee 1996). Chest X-rays are usually normal, although hyperaeration and vascular attenuation are sometimes seen. HRCT demonstrates a mosaic perfusion pattern due to oligemia and air-trapping, which is better detected on expiratory scans. Central or peripheral bronchiectasis, bronchial thickening, and mucus plugging of the

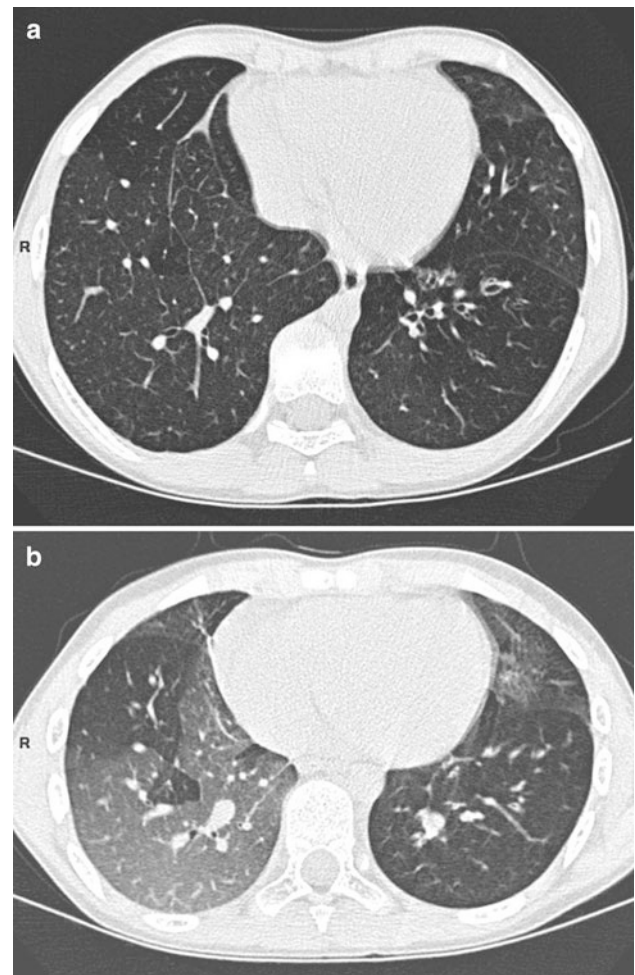


**Fig. 7** Inspiratory (a) and expiratory (b) HRCT scans in a 10-year-old boy with postinfectious bronchiolitis obliterans (mycoplasma infection). CT shows bronchiectasis in the lingula and in the left lower lobe. It also demonstrates bilateral mosaic perfusion pattern with air trapping

centrilobular bronchioles may also be noted. A recent study using xenon ventilation CT technique demonstrates impaired regional ventilation and its heterogeneity accurately in children with constrictive bronchiolitis (Goo et al. 2010).

Swyer-James or Macleod's syndrome is a variant of postinfectious constrictive bronchiolitis (Marti-Bonmati et al. 1989), and is characterized by unilateral small or normal-sized hyperlucent lung with air-trapping (Stern and Samples 1992; Moore et al. 1992). It is usually the result of a viral or mycoplasma respiratory infection in early childhood. HRCT reveals unilateral hyperlucency and decreased pulmonary vascularity in all patients. Other common findings are a mosaic perfusion pattern and bronchiectasis, each of which is seen in approximately 70 % of patients. Expiratory HRCT scans show air-trapping in the hyperlucent lung in all cases. Contralateral lung involvement, characterized by patchy areas of air-trapping, is present in half the patients (Fig. 7). Bronchiectasis can be cylindrical or



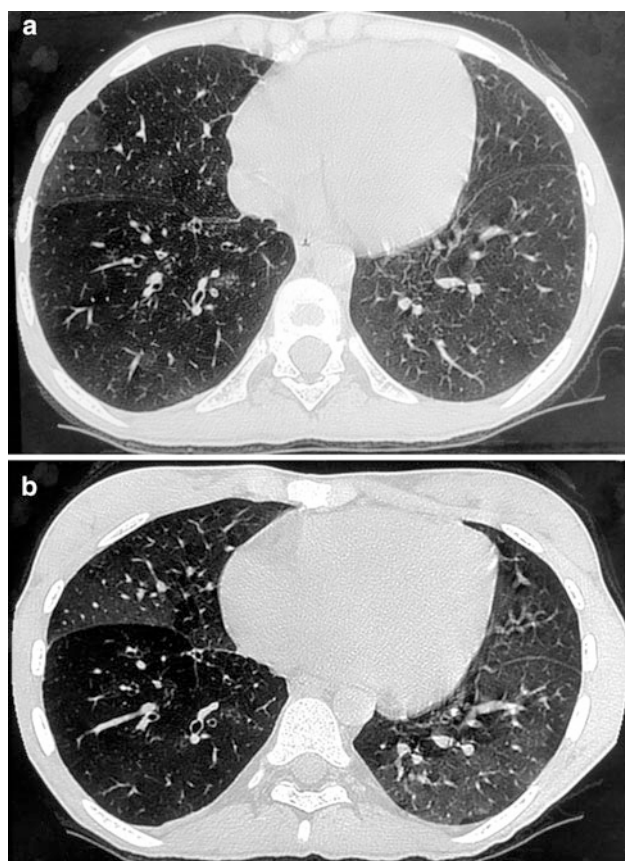


**Fig. 8** A 17-year-old girl with constrictive bronchiolitis after heart-lung transplantation. Bronchial dilatation in the right lower lobe with bronchial wall thickening are seen on inspiratory HRCT (a). Mosaic perfusion is better seen on expiratory HRCT (b)

varicose and may be associated with collapse. Children without bronchiectasis or with cylindrical bronchiectasis had a lower incidence of pneumonia episodes than those with varicose bronchiectasis (Lucaya et al. 1998). Several authors reported that the disease might occur in various forms including partial involvement of one lung or bilateral disease (Lucaya et al. 1998; Arslan et al. 2001).

Constrictive bronchiolitis may occur after heart-lung transplantation (50 % of patients) or bone marrow transplantation (10 % of patients). It is thought to be the consequence of repeated episodes of rejection. Clinically, the patients may present with cough and dyspnea. The triad of mosaic perfusion pattern, bronchial dilatation, and bronchial wall thickening after lung transplantation is indicative of constrictive bronchiolitis (Fig. 8). A mosaic perfusion pattern without the associated bronchial changes has been observed in a large percentage of transplant patients with normal pulmonary function tests (Lau et al. 1998). In lung transplant recipients, the extent of air trapping (in excess of 32 % of the parenchyma) seems to be suggestive of constrictive bronchiolitis (Bankier et al. 2001).

#### 1.4 Bronchiolitis Obliterans Organizing Pneumonia: Organizing Pneumonia

Bronchiolitis obliterans organizing pneumonia (BOOP) is characterized pathologically by the presence of granulation tissue within the lumen of bronchioles and alveolar ducts and associated patchy areas of organizing pneumonia. BOOP rarely occurs in children. It may be idiopathic but is more commonly seen in children after chemotherapy. It can also occur after bone marrow transplantation or as a response to toxic inhalants, drugs, radiotherapy or viral, mycoplasmal, or bacterial infection (Inoue et al. 1996; Mathew et al. 1994; Kleinau et al. 1997). The main symptoms are cough, dyspnea, fever, and weight loss. Physical examination is unremarkable except for crackles on auscultation of the lungs. Pulmonary function tests show a restrictive ventilatory defect with impaired gas transfer.

The HRCT findings in BOOP most commonly consist of patchy consolidation or ground glass opacities, often with a subpleural and/or peribronchial distribution changing in location over a matter of weeks (Muller et al. 1990; Flowers et al. 1992; Akira et al. 1998; Robertson and Hansell 2011) (Fig. 24, “[High-Resolution CT of the Lung in Children: Technique, Indications, Anatomy, and Features of Lung Disease](#)”). The reverse halo sign was initially considered to be an HRCT scan finding characteristic of this disease. This sign was demonstrated in a variety of conditions, including infectious diseases such as tuberculosis, invasive pulmonary disease, pneumocystis jiroveci pneumonia, and noninfectious disease such as pulmonary embolism, sarcoidosis, pulmonary edema, or Wegener disease (Marchiori et al. 2012). Peripheral nodular opacities, irregular linear opacities, bronchial wall thickening and dilatation, and small pleural effusions may also be present (Webb et al. 1996; Lee et al. 1994a). Although nonspecific, the HRCT findings can suggest the diagnosis and help to select the site for biopsy.

In adults, a new classification and terminology is now preferred. The preferred term is organizing pneumonia. Organizing pneumonia is defined pathologically by the presence in the distal airspaces of buds of granulation tissue progressing from fibrin exudates to loose collagen containing fibroblast. The lesions occur predominantly within alveolar spaces but are associated with buds of granulation tissue occupying the bronchiolar lumen (Cordier 2000). The organizing pneumonia, in adult population, is often secondary to a known cause (rheumatoid arthritis, viral pneumonia, drug reactions). The term cryptogenic organizing pneumonia is used when histologic features are demonstrated and the cause is idiopathic (Wittram et al. 2003; Ujita et al. 2004). This new terminology is not widely used in the pediatric literature.



## 2 HRCT Findings in Specific Diseases

### 2.1 Chronic Diffuse Infiltrative Lung Disease

A specific diagnosis of chronic diffuse infiltrative lung disease (CDILD) is essential to prescribe treatment. The diagnosis is based on clinical information, pulmonary function tests, bronchoalveolar lavage, and chest imaging. Studies in adults have demonstrated the superiority of HRCT over radiography for obtaining the correct diagnosis of CDILD because many of these patients have distinguishing features (characteristic appearances and distributions) when evaluated with this technique (Grenier et al. 1994; Lee et al. 1994b; Bonelli et al. 1998; Swensen et al. 1997). According to numerous publications the same results were obtained in children (Lynch et al. 1999; Copley et al. 2000; Koh and Hansell 2000). In some cases, lung biopsy can be avoided. HRCT can also be useful to determine the optimal site for biopsy and to assess the extent of the disease. CDILD is uncommon in children. The prevalence of CDILD is estimated between 1.32 and 3.6 per 1,000,000 (Dinwiddie et al. 2002; Griese et al. 2009). During a long period of time, pediatric CDILD description was based on small series. Two main groups were proposed: disorders of known etiology (aspiration, extrinsic allergic alveolitis) and disorders of unknown etiology. In 2004, a task force (Clement et al. 2004) classified CDILD into four groups (interstitial lung diseases of unknown etiology, idiopathic interstitial pneumonias, other forms of interstitial pneumonia and congenital disorders). In 2007, a new classification for infants was proposed by a study group formed by clinicians and pathologists (Deutsch et al. 2007). This classification is divided into four main groups: diffuse developmental disorders, growth abnormalities, surfactant dysfunction disorders, and related abnormalities or specific conditions of unknown or poorly understood etiology (Lee 2013). The understanding of the pathogenesis and diagnosis is due to advances in genetics. Some respiratory diseases in infants (surfactant or some diffuse lung developmental disorders) have a genetic basis (Cazzato et al. 2013). The applications of HRCT are less developed. Our experience suggests that HRCT contributes to the diagnosis and monitoring of pediatric CDILD.

#### 2.1.1 Langerhans' Cell Histiocytosis

Infiltration and accumulation of monocytes and large histiocytes in various tissues and organs characterize the histological appearance of Langerhans' Cell Histiocytosis (LCH). Pulmonary involvement is present in 23–50 % of children with the multisystemic form (Smets et al. 1997; Odame et al. 2006). Localized LCH is the mildest and most common form (70 % of all cases) and involves either bone

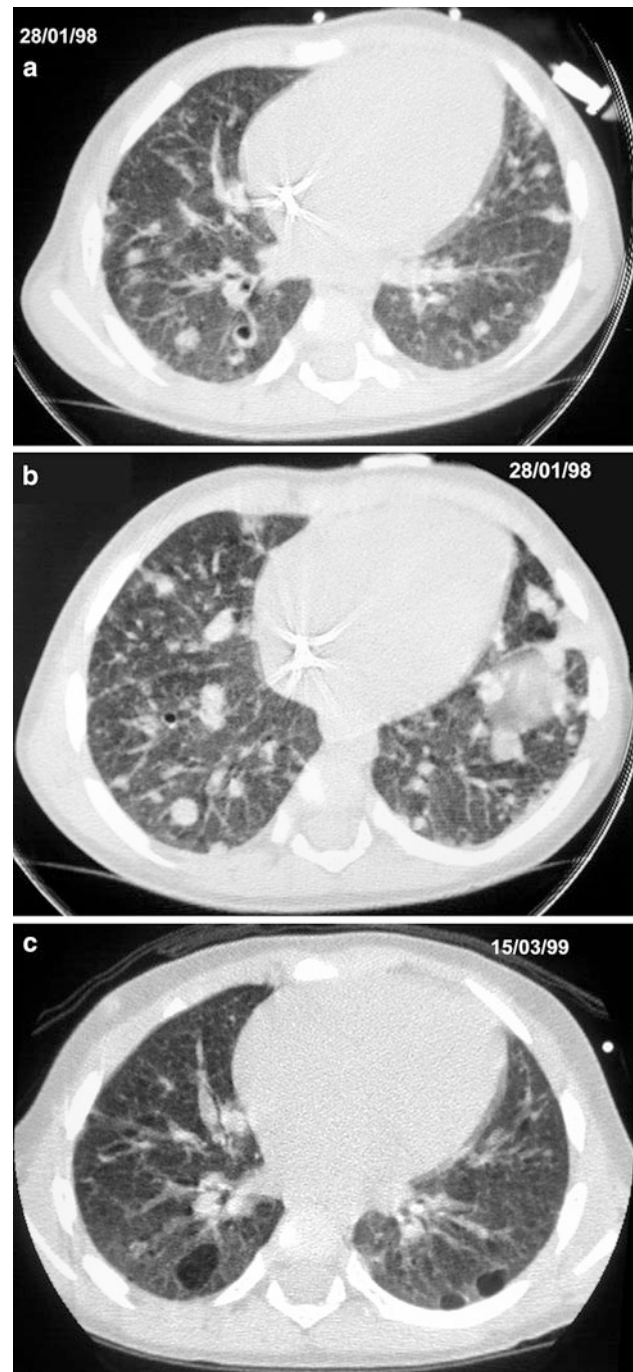


**Fig. 9** A 14-month-old girl with Langerhans' cell histiocytosis. Initial HRCT (a, b) shows nodules and small cystic lesions. Follow-up HRCT (c) at the age of 30 months shows larger cystic lesions

or lung. The lung is the second most common site of LCH (Sminiopoulou et al. 1999). HRCT detects centrilobular, peribronchial or peribronchiolar granulomas, usually 1–10 mm in diameter; larger nodules are less common. These nodules can disappear or cavitate (Brauner et al. 1989b) and become thick-walled cysts that can progress to thin-walled cysts (Brauner et al. 1997) (Fig. 9).

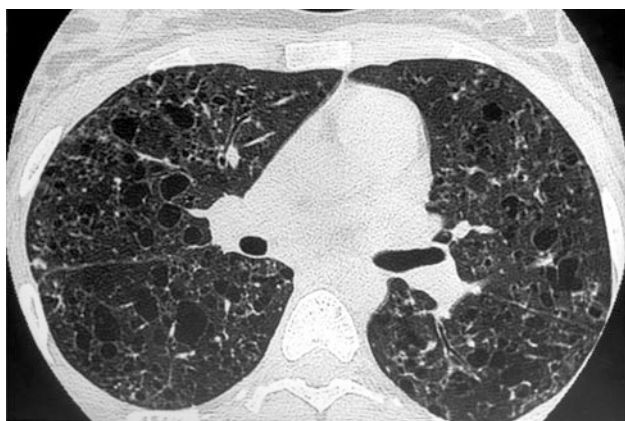


**Fig. 10** A 16-year-old girl with Langerhans' cell histiocytosis. HRCT shows thick- and thin-walled cysts; a few micronodules are also seen

Thick (wall thickness  $>2$  mm) or thin-walled pulmonary cysts are the main feature of LCH. They may be round or irregularly shaped, probably due to the fusion of several cysts (Fig. 10). LCH lesions are mostly found in the upper and middle lung zones. The costophrenic angles are generally spared in adults (Moore et al. 1989) and involved in children (Seeley et al. 2012). Rupture of subpleural cysts may cause pneumothorax (Fig. 11). Pneumothorax occurs in up to 25 % of patients over the course of their disease (Abbott et al. 2004). In children, LCH lesions may remain stable over long periods or progress rapidly, leading to destruction of the pulmonary parenchyma within a few weeks or months after diagnosis (Seely et al. 1997). In our experience, patients with a poor lung involvement are asymptomatic.

Thymic involvement associated with parenchymal lesions has been also reported (Donnelly 2000). Prognosis of primary pulmonary LCH in pediatric age group remains unclear because of limited number of cases (Bano et al. 2014). In the multisystemic form of LCH pulmonary involvement does not mean that the disease is more severe or suggests a poorer prognosis (Smets et al. 1997; Braier et al. 2004), yet it may influence the choice of treatment.

### 2.1.2 Extrinsic Allergic Alveolitis

Extrinsic allergic alveolitis (EAA) is caused by the repeated inhalation of particulate organic antigens. Farmer's lung is the best-known EAA syndrome and is a rare entity in young children (Stauffer et al. 2006). The development of EEA requires massive acute or prolonged low-grade exposure. Many inhaled responsible antigens have been described, including animal and plant proteins, and fungal microorganisms (thermophilic actinomycetes). Extrinsic allergic alveolitis is divided into acute, subacute, and chronic forms (Vincent et al. 1992). The diagnosis of EAA in its earliest stages is controversial and remains primarily clinical.



**Fig. 11** A 15-year-old boy with Langerhans' cell histiocytosis, with multiple skin lesions, diabetes insipida, and recurrent bilateral pneumothoraces. Chest CT shows multiple pulmonary cystic lesions, some located subpleurally, and bilateral pneumothorax

Symptoms occur 4–8 h after exposure, and include shortness of breath, dry cough, malaise, and fever. Subacute and chronic forms have an insidious onset with progressive shortness of breath and cough.

HRCT abnormalities are suggestive of the disease and depend on the stage of the disease. HRCT could be useful to evaluate the inflammatory activity of the disease (Sterclova et al. 2006). HRCT could allow the diagnosis in asymptomatic family members of an index case (Ceviz et al. 2006). HRCT is rarely performed in the early stage. In the acute and subacute stages EAA presents as airway disease characterized by small poorly defined centrilobular nodules ( $<5$  mm in diameter) and areas of ground glass (Hansell and Moskovic 1991) (Fig. 12). Ground-glass opacities are slightly more marked in the middle and lower lung zones. Areas of decreased attenuation and air-trapping, consistent with small airway disease, are also common findings (Small et al. 1996). Areas of ground-glass opacities and centrilobular nodules decreased during the follow-up (Tateishi et al. 2011). Chronic EAA is characterized by fibrosis that seems to spare the lung bases.

### 2.1.3 Sarcoidosis

Sarcoidosis is a chronic granulomatous disorder of unknown etiology. It is uncommon in children and occurs most often in young adults (Pattishall and Kendig 1996). The majority of pediatric patients are 9–18 years of age (Grossman et al. 1985). Prognosis is more severe in younger children and in case of multi-organ involvement (Fauroux and Clément 2005). Respiratory symptoms include cough, dyspnea, and, sometimes, chest pain. Mediastinal and/or bilateral hilar adenopathy, often isolated, is the most common intrathoracic finding in sarcoidosis. The characteristic HRCT finding



**Fig. 12** A 12-year-old boy with extrinsic allergic alveolitis. HRCT shows small, ill-defined rounded opacities with patchy ground-glass opacities

consists in small 2–10 mm nodules with irregular margins distributed along the lymphatics in the bronchovesicular sheath and in the interlobar septa and pleura. This distribution can produce a beaded appearance of the bronchovesicular bundles and interlobular septa and fissural nodularity (Brauner et al. 1989a; Dawson and Muller 1990; Traill et al. 1997) (Fig. 13).

Confluence of granulomas may result in large opacities with poorly defined contours, or areas of frank consolidation. Air-bronchograms may be seen within these opacities. Large nodules can cavitate, but this is uncommon. Patchy areas of ground-glass opacity may also be present and may be due to the presence of numerous sarcoid granulomas below the resolution of HRCT (Nishimura et al. 1995). Micronodules and ground-glass opacities are the most frequent features observed in children with sarcoidosis (Sileo et al. 2013).

Ground-glass opacities, architectural distortion, displacement of interlobar fissures, traction bronchiectasis, cystic air spaces, and honeycombing are signs of advanced disease with fibrosis (Abekhser et al. 2000). Posterior displacement of the main or upper lobe bronchus is a classical finding, which indicates loss of volume in the posterior segment of the upper lobes.

HRCT could assess the severity of the disease. The appearance and the extent of the disease on HRCT (thickening of the bronchovesicular bundle, intraparenchymal nodules, septa and nonseptal lines, and focal pleural thickening are associated with parameters of respiratory functional impairment (Drent et al. 2003).

#### 2.1.4 Pulmonary Alveolar Proteinosis

Pulmonary Alveolar Proteinosis (PAP) is a rare intrinsic lung disease characterized by alveolar filling with amorphous lipoproteinaceous material (Schumacher et al. 1989).

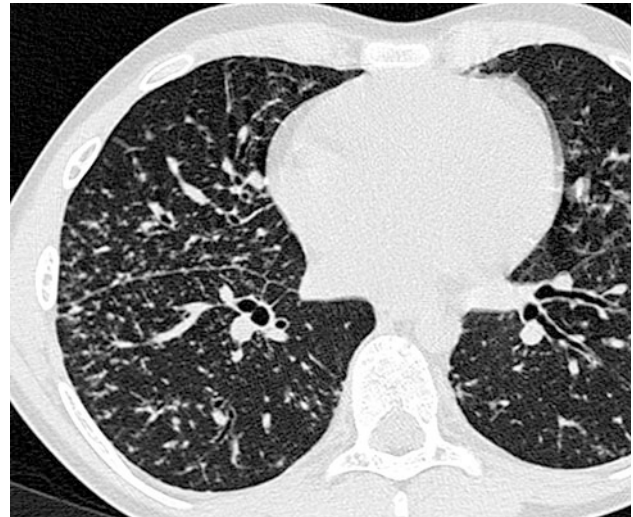


**Fig. 13** An 11-year-old boy with sarcoidosis. HRCT detects small nodules in a perilymphatic distribution (note the beaded appearance of the bronchovascular bundles and subpleural nodularity)

The cause of alveolar proteinosis is unclear. One possible cause may be dysfunction of intra-alveolar macrophages, another cause relates to an abnormal surfactant C protein function which predisposes certain patients to diffuse lung disease (Nowers et al. 2002). Plain films show alveolar infiltrates, a reticulonodular pattern or both. Pleural effusion and adenopathy are absent (McCook et al. 1981). HRCT shows areas of consolidation or ground glass, often with a geographic distribution, and/or widespread miliary nodules (Godwin et al. 1988; Murch and Carr 1989; Albaladejo et al. 1999) (Fig. 14). Smooth thickening of the interlobular septa within the areas of air space disease resulting in a crazy paving appearance (Fig. 45, “[High-Resolution CT of the Lung in Children: Technique, Indications, Anatomy, and Features of Lung Disease](#)”) is suggestive of, but not specific to, alveolar proteinosis (Coullier et al. 1999; Johkoh et al. 1999b; Rossi et al. 2003). Quantitative CT is proposed for detecting the response to therapeutic interventions such as whole lung lavage (Guan et al. 2012).

#### 2.1.5 Pulmonary Fibrosis and Chronic Interstitial Pneumonias

Pulmonary fibrosis is a chronic inflammatory interstitial lung disorder, characterized by an initial accumulation of inflammatory and immunoregulatory cells in the pulmonary interstitium and the alveolar space. Inflammation leads to modification of the alveolar structures with progression to interstitial fibrosis and thickening of alveolar walls. In children, pulmonary fibrosis is the result of a heterogeneous group of disorders that share common histological features (Osika et al. 1997). The known causes include infectious disorders, reactions to environmental exposures, drugs, collagen-vascular disorders, or gastroesophageal reflux with



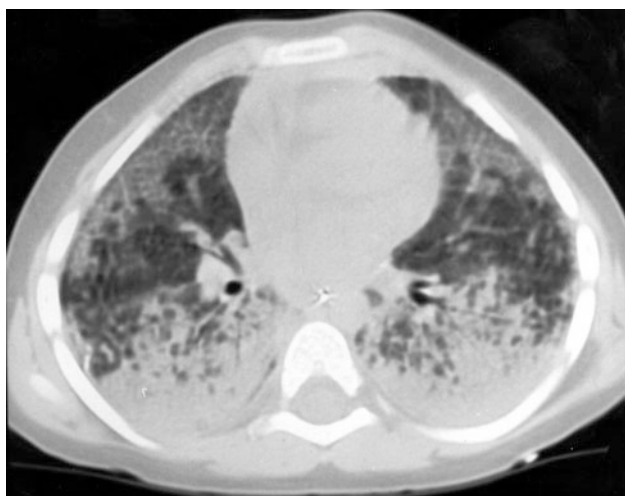


**Fig. 14** A 3-year-old boy with biopsy-proven pulmonary alveolar proteinosis. Despite the 5 mm slice thickness alveolar consolidation and alveolar infiltrates are clearly visualized

chronic aspiration. For idiopathic pulmonary fibrosis (IPF), classification by histological features into usual interstitial pneumonitis (UIP) and desquamative interstitial pneumonitis (DIP) has been proposed. The distinction between these two forms of fibrosing alveolitis is now questioned (UIP and DIP can be seen simultaneously). These entities may represent different stages of a lung injury (Webb et al. 1996) with associated thickening of alveolar walls and many mononuclear cells in the alveolar space.

Because of the rarity of these entities in children, most HRCT findings have been reported in adults. On HRCT, the main sign in DIP is the presence of bilateral and symmetric areas of ground-glass opacity (the predominant lesion in DIP is alveolar spaces filled with macrophages) (Hartman et al. 1993). The ground-glass areas of attenuation are seen mainly in lower lung zones. Other findings in DIP are those of UIP: reticular opacities, which correspond to areas of irregular fibrosis, honeycombing, and traction bronchiectasis (Nishimura et al. 1992). Less common HRCT findings include discrete nodules and interlobular septal thickening. Mild enlargement of mediastinal lymph nodes is commonly seen, whereas large lymph nodes are uncommon.

The main HRCT findings of IPF in children are areas of ground-glass attenuation involving mostly the subpleural regions Seely et al. (1997). Large subpleural air cysts in the upper lobes adjacent to areas of ground-glass opacities seem to be unique to childhood IPF. These cysts are interpreted as paraseptal or irregular emphysema (Fig. 15). Intralobular lines, irregular interlobular septal thickening and honeycombing seem to be less common findings and, thus, less contributive to diagnosis.

Recently, two new forms of idiopathic interstitial pneumonia have been described: acute interstitial pneumonia



**Fig. 15** A 13-year-old boy with biopsy-proven idiopathic pulmonary fibrosis. HRCT shows ground-glass attenuation, intralobular lines, and air cysts and involving mostly the subpleural regions

(AIP) (Katzenstein et al. 1986) and nonspecific interstitial pneumonia and fibrosis (NIPF) (Katzenstein and Fiorelli 1994).

AIP is a fulminant disease of unknown etiology that is histologically characterized as diffuse alveolar damage. The latter manifests as injury to the alveolar lining and endothelial cells, pulmonary edema, hyaline membrane formation and, later, proliferative changes involving alveolar and bronchiolar lining cells, and interstitial cells. The histologic appearance of AIP can be separated into acute exudative, subacute proliferative and chronic fibrotic phases. The radiological finding on chest radiographs is progressive parenchymal consolidation. HRCT images include diffuse air-space consolidation and patchy or diffuse ground-glass opacities, traction bronchiectasis, and, occasionally, focal honeycombing (Primack et al. 1993; Ichikado et al. 1997). These findings are usually bilateral, symmetrical, and basilar in distribution. Ground-glass opacities are seen in all three histological phases and reflect different histological findings. During the acute exudative phase, they reflect the presence of alveolar septal edema and hyaline membranes along the alveolar walls. During the subacute proliferative phase, ground-glass opacities are due to intra-alveolar and interstitial organization. During the fibrotic phase, ground-glass attenuation results from alveolar septal fibrosis. Bronchiectasis within areas of ground-glass attenuation may correspond to fibrosis and its severity (Johkoh et al. 1999a, c).

NIPF describes the group of interstitial pneumonias that cannot be classified as UIP, DIP, AIP, or BOOP. NIPF is essentially a diagnosis of exclusion. It is characterized by varying degrees of interstitial inflammation and fibrosis that persist (Müller and Colby 1997). Copley et al. (2000) reported six cases of NIPF in children. In three of them, HRCT showed a predominantly upper-zone honeycomb pattern with parenchymal distortion superimposed on a background of widespread ground-glass opacification (Fig. 16). For the

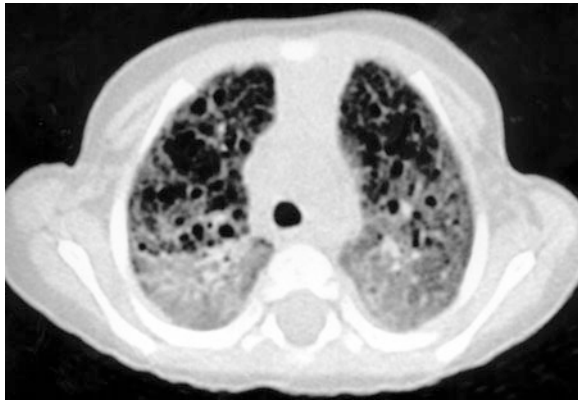


**Fig. 16** A 10-month-old female infant with biopsy-proven nonspecific interstitial pneumonitis. HRCT shows ground glass and honeycombing. [Reprinted with permission from Copley et al. (2000)]

other three patients with NIPF, one had widespread ground-glass opacification, honeycombing with mid- and lower-zone predominance, and traction bronchiectasis; another had widespread ground-glass opacification; and the last patient had widespread ground-glass opacification with peripheral consolidation. None of the patients had interlobular septal thickening.

Genetic studies will perhaps help us to better understand these entities in children. Recently, mutations in the gene encoding surfactant protein C associated with familial interstitial lung disease have been identified in familial cases (Nogee et al. 2001). Few authors report familial cases of NIPF and UIP with mutation in surfactant protein C (Thomas et al. 2002; Chibbar et al. 2004).

### 2.1.6 Lymphocytic Interstitial Pneumonia

LIP is a benign lymphoproliferative disorder described by Liebow and Carrington (1973) and characterized by pulmonary infiltration of lymphocytes and plasma cells. LIP occurs in patients who have systemic disorders, such as Sjögren's syndrome, multicentric Castleman's disease or acquired immunodeficiency syndrome (AIDS). In children, LIP has been reported to be frequently associated with AIDS. In a series of 77 human immunodeficiency virus-positive (HIV+) children evaluated by Amorosa et al. (1992), 32 were diagnosed as having LIP. The appearance of LIP on chest radiography is nonspecific and includes a fine reticular pattern and nodular opacities or a diffuse confluent pattern. HRCT findings include extensive bilateral ground-glass attenuation, focal air-space consolidation, ill-defined, micronodules with a perilymphatic distribution, and thin-walled cystic lesions (Carignan et al. 1995; McGuinness and Naidich 1995; Becciolini et al. 2001) (Fig. 17). Associated bronchiectasis and hilar or mediastinal lymphadenopathy may be present (Johkoh et al. 1999b). No pleural effusion is seen in LIP (Honda 1999).

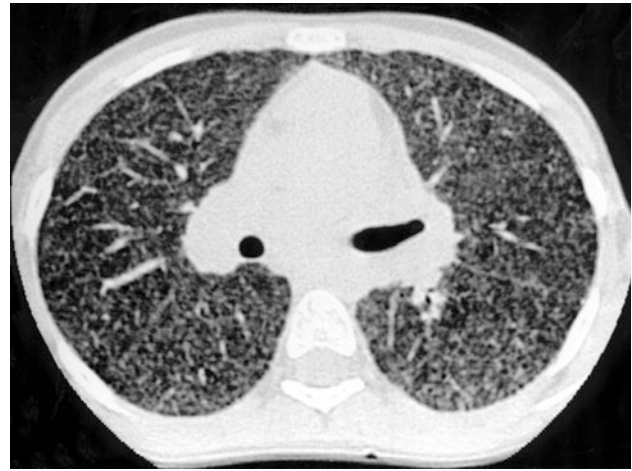


**Fig. 17** A 13-year-old girl with biopsy-proven lymphocytic interstitial pneumonia. The patient was immunocompromised because of postviral neutropenia. HRCT shows profuse nodules with random distribution. [Reprinted with permission from Copley et al. (2000)]

### 2.1.7 Pulmonary Lymphangitic Carcinomatosis

Pulmonary lymphangitic carcinomatosis (PLC) refers to tumor growth in the lymphatics of the lung. The histological findings are characterized by thickening of the interlobular septa and the peribronchovascular interstitium. In most cases, the primary tumor disseminates hematogenously to the lungs and secondarily penetrates vessel walls and invades the surrounding interstitium and lymphatics. In children PLC is uncommon but can occur in lymphoma, thyroid carcinoma, sarcoma, and neuroblastoma (Kuhn 1993). In our experience, PLC was most common in lymphoma.

Chest X-ray findings are normal or show nonspecific findings in many patients with PLC (Munk et al. 1988). HRCT findings (Johkoh et al. 1992) correlate well with the two types of lymphatic drainage systems described by pathologists. Axial drainage is seen on HRCT as smooth or nodular peribronchovascular interstitial thickening in the parahilar lung and enhanced visibility of the branching arteries in the pulmonary lobule. Peripheral drainage (interlobular and subpleural) is seen as interlobular septal thickening or as thickening of fissures, which may be smooth or nodular. HRCT abnormalities can be focal, unilateral, or diffuse (Fig. 22, "High-Resolution CT of the Lung in Children: Technique, Indications, Anatomy, and Features of Lung Disease") (Fig. 18). Despite axial and peripheral interstitial abnormalities, lung architecture remains normal, a finding that is useful to differentiate between PLC and sarcoidosis.

### 2.1.8 Collagen-Vascular Disease and Pulmonary Vasculitis

Pulmonary vasculitis can be due to primary systemic vasculitides, such as Wegener's granulomatosis, Churg-Strauss angiitis, or microscopic polyangiitis. In addition, pulmonary

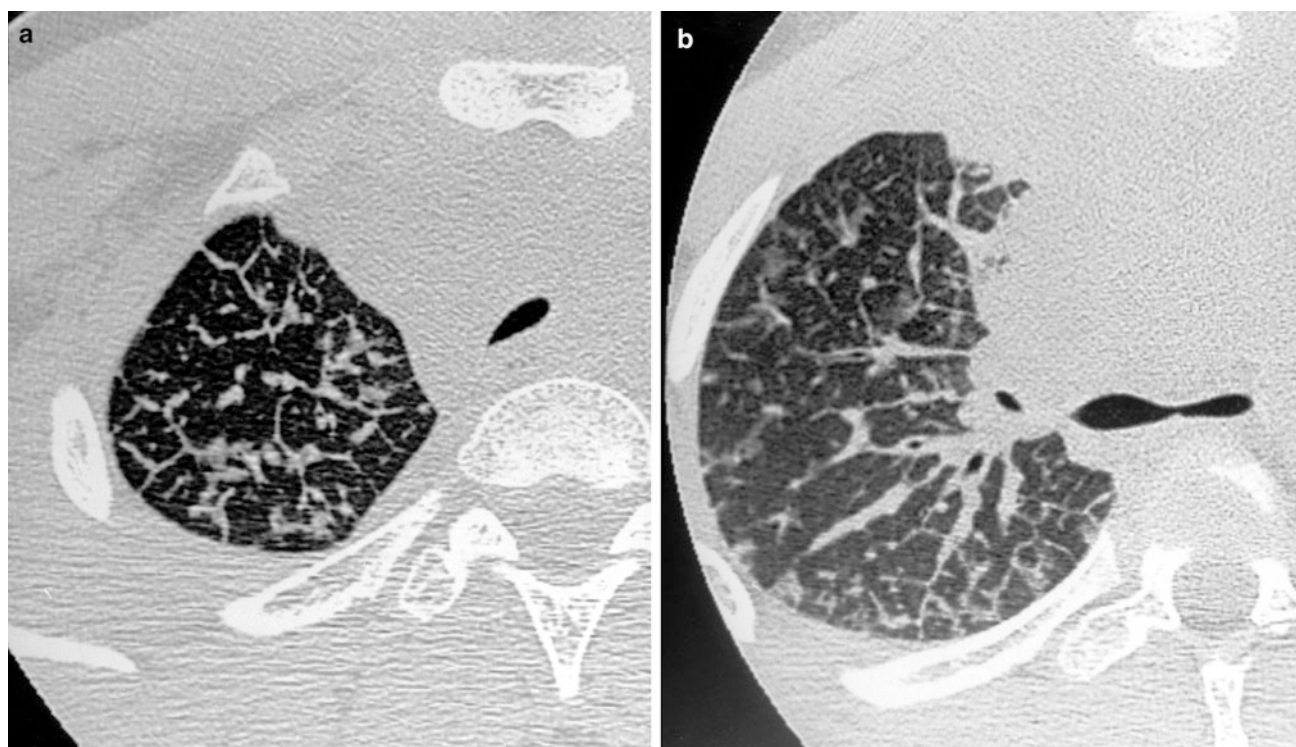


**Fig. 18** A 14-year-old boy with Hodgkin's disease. HRCT shows thickening of the interlobular septa (a), smooth peribronchovascular interstitial thickening (b), and ground-glass attenuation

vasculitis may accompany systemic connective tissue disease, including systemic lupus erythematosus, dermatomyositis, or systemic sclerosis. Connolly et al. (1996) identified a pattern on HRCT of perivascular, centrilobular, ill-defined densities in eight children with vasculitis. In the appropriate clinical setting this pattern indicates pulmonary involvement and may obviate the need for lung biopsy.

Collagen-vascular disease, especially progressive systemic sclerosis (PSS), is commonly associated with pulmonary fibrosis in children. Seely et al. (1998) described a series of 11 patients with PSS who had interstitial lung disease. HRCT revealed abnormality in 91 % of the patients. The main features were ground-glass opacities, subpleural micronodules, nonseptal linear opacities, honeycombing, and subpleural cysts. HRCT was able to demonstrate interstitial lung disease in 53 % of patients with lupus erythematosus (Fenlon et al. 1996) (Fig. 19). In the pediatric population, the frequency of pulmonary involvement is lower (8 %) than in adult one (Lilleby et al. 2006). Juvenile rheumatoid arthritis, on the other hand, seldom leads to pulmonary fibrosis in children (Seely et al. 1998). The HRCT pattern of fibrosis associated with collagen-vascular disease is similar to that of idiopathic pulmonary fibrosis and consists predominantly of areas of ground-glass involving mostly the subpleural lung regions, large and thin-walled cysts or bullae in the affected upper-lung zones, and smooth or irregular intralobular septal thickening.



**Fig. 19** A 16-year-old girl with systemic lupus erythematosus. HRCT shows honeycombing, predominantly in the periphery, and pleural effusion. Note the right pneumomediastinum

### 2.1.9 Pulmonary Lymphangiectasia

According to Noonan et al. (1970), pulmonary lymphangiectasia can be divided into three groups. In the first, pulmonary lymphangiectasia is part of a generalized disease, the major clinical manifestations being related to the intestinal involvement. The pulmonary involvement is less severe and is associated with a better prognosis than for the following two groups. In the second group with associated heart disease, dilatation of the lung lymphatics occurs secondary to obstruction of pulmonary venous flow. The third



group, termed congenital pulmonary lymphangiectasia (CPL), includes patients with a primary developmental defect of lung lymphatics, which are dilated. Histological examination is characterized by subpleural, interlobar, perivascular, and peribronchial lymphatic dilatation. Radiological findings include bilateral pulmonary hyperinflation and a reticulonodular pattern throughout the lung fields. Occasional small cystic areas, representing aerated distal bronchial and alveolar ducts, may also be present. Pleural effusion and pneumothorax may be associated. Unilateral or lobar involvement has been reported (Verlaet et al. 1994; Li et al. 1985; Rettwitz-Volk et al. 1999).

Prolonged survival of patients with CPL is rare. The chest radiograph and HRCT findings in survivors have recently been reviewed by Chung et al. (1999). Chest radiograph findings include increased interstitial markings, hyperinflation that generally increases with age, pleural effusion, and pectus excavatum. The presence of patchy subpleural or perihilar ground-glass opacities that are fixed in location and tend to decrease with time was the most characteristic HRCT feature. Hyperinflation and interstitial thickening were often seen.

#### 2.1.10 Lymphangiomatosis and Gorham's Disease

Lymphangiomatosis, a malformation of the lymphatic system, is a rare entity that occurs mainly in children and adolescents. It is believed to be caused by either a developmental defect or obstruction of the lymphatic channels. The main abnormalities seen on HRCT are thickening of the interlobular septa and vascular bundles, and areas of ground-glass opacification (Swensen et al. 1995). Bilateral pleural effusions or smooth thickening of the pleura and increased attenuation of the mediastinal fat are also seen in most patients (Mitchell et al. 1993; Dutheil-Doco et al. 1997). Chest involvement in Gorham's or "vanishing bone" disease, in which there is replacement of a single or several contiguous bones by lymphangiomatous tissue, may present with severe and progressive osteolysis associated with septal thickening (Fig. 20) and chylothorax (Konez et al. 2000). The presence of chylous pleural effusion usually indicates a poor prognosis (Yang and Goo 2006).

#### 2.1.11 Pulmonary Hemorrhage

Pulmonary hemorrhage is frequently found in children with idiopathic hemosiderosis (Kiper et al. 1999; Koh and Hansell 2000) and may also be seen in systemic lupus erythematosus, Wegener's granulomatosis and Goodpasture's syndrome (Ramirez et al. 1984; Von Vigier et al. 2000). Pulmonary hemorrhage appears on HRCT as patchy, frequently bilateral areas of ground-glass attenuation or consolidation (Fig. 21). Idiopathic hemosiderosis is characterized by recurrent pulmonary hemorrhages. The etiology

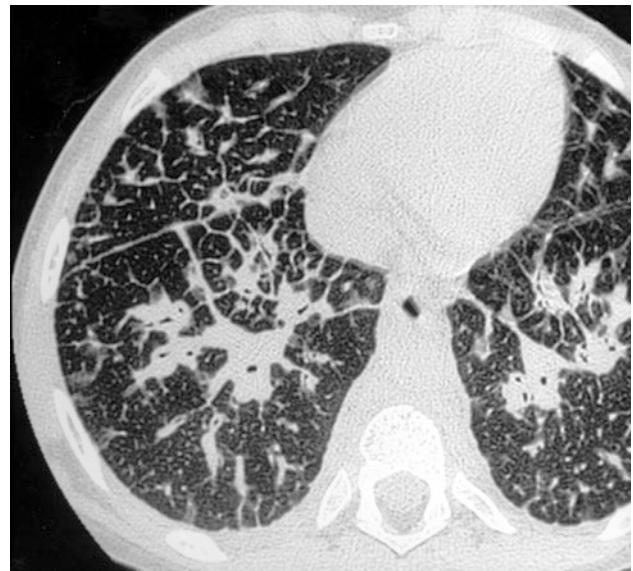


**Fig. 20** A 6-year-old girl with Gorham's disease. Note the prominent diffuse smooth septal thickening, bronchovascular bundles, and ground-glass attenuation



**Fig. 21** A 3-year-old girl with hemosiderosis. HRCT shows ground-glass attenuation due to pulmonary hemorrhage

remains unknown and prognosis is poor since pulmonary fibrosis develops rapidly (Primack et al. 1995) (Fig. 22).

#### 2.1.12 Pulmonary Alveolar Microlithiasis

Pulmonary alveolar microlithiasis (PAM) is characterized by calcium deposits within the alveoli of both lungs with a predominantly symmetrical middle- and lower-lung zone distribution. The etiology is unknown, but evidence supporting an autosomal recessively inherited defect is accumulating (Wallis et al. 1996). HRCT findings are ground-glass opacities

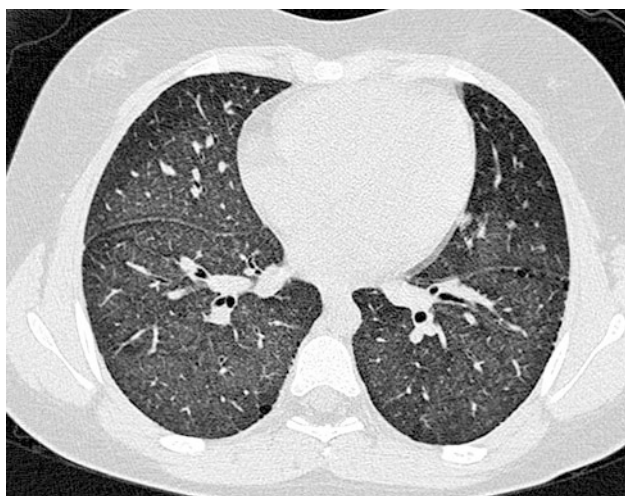


**Fig. 22** An 11-year-old-girl with hemosiderosis. HRCT shows ground-glass attenuation and air cysts, involving subpleural regions

and tiny calcifications along the bronchovesicular bundles, pleura and interlobular septa (Cluzel et al. 1991). Parenchymal calcifications are described as nodular in adults and as micronodular in children. Parenchymal and subpleural cysts have also been reported as signs of fibrosis in PAM. However, in the two pediatric cases studied by Helbich et al. (1997), no intraparenchymal cysts were seen. In PAM a proportional relationship between profusion of micronodules and parenchymal alterations is found and a correlation between the parenchymal alterations and the degree of pulmonary function loss (Deniz et al. 2005).

### 2.1.13 Pulmonary Gaucher's Disease

Gaucher's disease is a genetic disorder characterized by beta-glucocerebrosidase deficiency with secondary accumulation of glucocerebrosides in the reticuloendothelial system. The liver, spleen, bone marrow, brain, and lungs may be involved. Three clinical forms have been described. In the adult form (type I), the central nervous system is intact and pulmonary involvement is rare. The infantile form (type II) is characterized by early CNS involvement and death within 2 years. The juvenile form (type III) is a subacute variant of the disease that comprises cases with combined involvement of the CNS and other organs. Pulmonary involvement is not unusual in the infantile form but is particularly rare in the adult form. However, HRCT pulmonary findings have only been reported in the adult type (Tunaci et al. 1995; Aydin et al. 1997; Yassa and Wilcox 1998). These include interlobular and intralobular septal thickening, ground-glass opacities, and small nodules within the secondary lobules. Thickening of the septa reflects infiltration of the pulmonary interstitium by

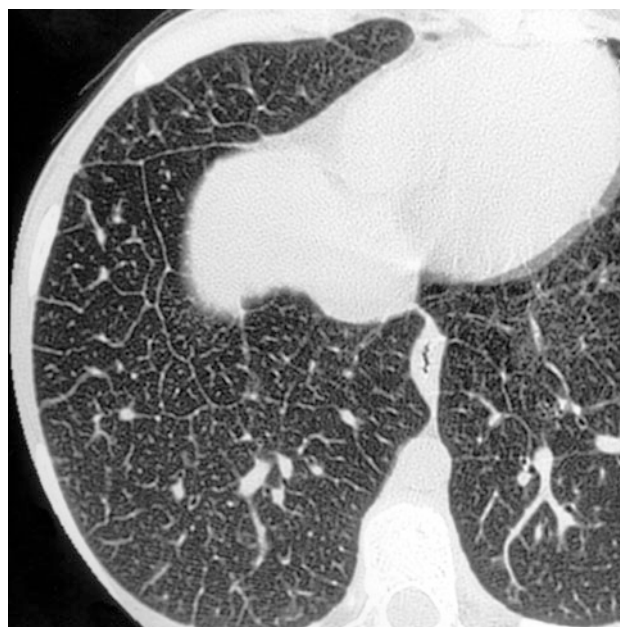


**Fig. 23** A 13-year-old girl with Gaucher's disease. Interlobular septal and intralobular interstitial thickening are seen on HRCT

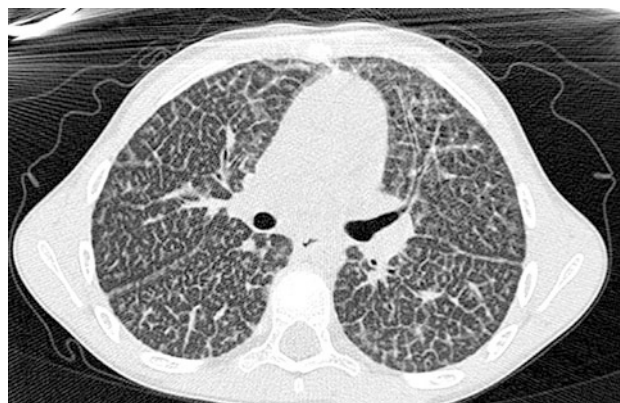


**Fig. 24** A 7-year-old-boy with Niemann-Pick. HRCT shows a crazy paving pattern (ground-glass attenuation with superimposed interlobular septal thickening)

Gaucher cells (Fig. 23). Ground-glass opacities may indicate interstitial or intra-alveolar involvement and micronodules are probably due to accumulation of Gaucher cells within air-spaces. Enzyme treatment could improve hematological parameters and decrease dyspnea and hepatosplenomegaly. Radiological findings are poorly improved by the treatment even in pediatric patients (Goiten et al. 2001). Similar HRCT features have been reported in patients with Niemann-Pick disease (Fig. 24) (Feretti et al. 1996; Duchateau et al. 2001).

### 2.1.14 Bronchopulmonary Dysplasia

Bronchopulmonary dysplasia (BPD) occurs in premature infants and as the chronic sequela of lung disease (mostly surfactant deficiency) and its treatment. In the early phase HRCT shows thickening of the peribronchial and interlobular interstitium, subpleural parenchymal bands, and hyper-expanded cyst-like areas, corresponding to hyperaerated lung and atelectasis that give the lung a “cobblestone” appearance (Fig. 3, “[High-Resolution CT of the Lung in Children: Technique, Indications, Anatomy, and Features of Lung Disease](#)”). In most survivors of BPD respiratory symptoms and radiologic abnormalities show a slow but continuous improvement. After the age of 2 years HRCT scans in children who have had BPD will be abnormal and characterized by the presence of a mosaic attenuation pattern due to air-trapping, parenchymal bands, thickened interlobular septa, peripheral wedge-shaped subpleural opacities, and architectural distortion (Fig. 30, “[High-Resolution CT of the Lung in Children: Technique, Indications, Anatomy, and Features of Lung Disease](#)”) (Oppenheim et al. 1994; Aquino et al. 1999). In the experience of AQUINO, the correlation between these findings and physiologic evidence of air-trapping and obstructive lung disease was statistically significant. According to Auckland neonatal history of prolonged requirements for oxygen treatment predicted subsequent structural abnormalities on the HRCT scan, as well as lung function abnormalities (Aukland et al. 2009). HRCT score for infants proposed by SHIN is related to the incidence of home oxygen on discharge and that of rehospitalization for respiratory problems in BPD patients (Shin et al. 2013). The HRCT features of BPD in older children may resemble those seen in constrictive bronchiolitis. Whereas parenchymal bands and architectural distortion are more common in BPD, bronchiectasis is significantly more frequent in constrictive bronchiolitis.

### 2.1.15 Neuroendocrine Cell Hyperplasia

Neuroendocrine cell hyperplasia of infancy (persistent tachypnea of infancy) was first described by Deterding et al. (2001). The etiology of the disease is unknown. Clinically, it is characterized by tachypnea, retraction, crackles, and hypoxemia. The diagnostic gold standard is lung biopsy demonstrating increased numbers of bombesin-immunopositive pulmonary neuroendocrine cells (PNECs) within bronchioles and alveolar ducts without evidence of other abnormalities, and limited or absent inflammation. Diagnosis of neuroendocrine cell hyperplasia of infancy is possible using clinical presentation, HRCT scan findings, and consistent infant pulmonary function data (Deterding 2012). The term “NEHI syndrome” is used when diagnosis is proposed without lung biopsy.

Ground-glass opacification and air-trapping with a mosaic pattern are the most common findings. The right middle lobe and lingula are the most commonly involved (Brody 2010).

### 2.1.16 Pulmonary Interstitial Glycogenosis

Pulmonary interstitial glycogenosis was first reported by Canakis in seven infants (Canakis 2002). All infants presented with tachypnea, hypoxemia, and diffuse interstitial infiltrates with overinflated lungs on chest radiographs in the first month of life. Lung biopsies show interstitial thickening with immature glycogen-laden mesenchymal cells without inflammation or fibrosis. Radiographically, changes of bilateral hyperinflation and diffuse interstitial markings on chest radiographs are not specific and are reported in other pediatric interstitial lung diseases of infancy (Castillo et al. 2010). HRCT findings are not yet clearly defined in the literature. HRCT demonstrates distortion of the lung architecture with linear and ground-glass opacities mixed with hyperinflated or hyperlucent areas (Guillerman 2010). The imaging appearance can be variable and is likely impacted by the presence of coexisting lung disease. Caution in interpretation is warranted, as findings of septal thickening and diffuse ground-glass opacities can overlap with other disorders, including infection or potentially lung disease related to surfactant gene mutations (Castillo et al. 2010; Deutsch and Young 2010; Deutsch et al. 2007). Multiple small scattered cystic changes of variable size might be present in pulmonary interstitial glycogenosis associated with underlying growth abnormalities (Lee 2013).

### 2.1.17 Surfactant Dysfunction Diseases

Surfactant dysfunction diseases are caused by genetic abnormalities. They encompass a large number of diseases such as: autosomal-recessive surfactant protein B (Sp-B), autosomal dominant surfactant protein C (Sp-C), autosomal-recessive ATP-binding cassette transporter protein A3 (ABCA3), and abnormalities of TTF1 (thyroid transcription factor 1), another rare genetic disorder impacting surfactant function.

SP-B deficiency was the first recognized genetic defect associated with surfactant dysfunction. The typical presentation involves a full-term infant with diffuse lung disease that clinically and radiographically resembles respiratory distress syndrome in premature infants, in the absence of risk factors associated with respiratory distress syndrome (Gower and Noguee 2011). Imaging findings on chest radiograph are characterized by diffuse hazy granular opacities resembling respiratory distress syndrome of prematurity. HRCT finding is a crazy paving appearance (ground-glass opacity with smooth interlobular septal thickening) (Newman et al. 2001). The lung disease is progressive and unresponsive to medical therapy, with death resulting from respiratory failure usually within 3 months of birth (Gower and Noguee 2011).

Mutations in the gene encoding ABCA3 and in the gene encoding SFTPC affect infants or older children. Affected infants may present the same clinical presentation as SP-B



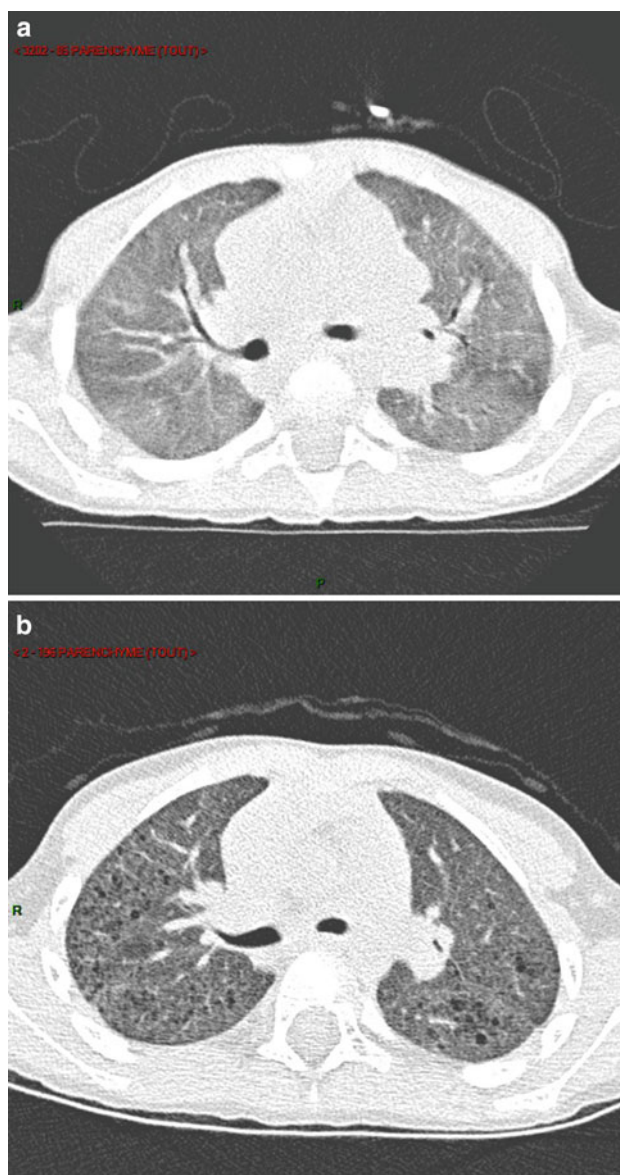


**Fig. 25** **a** 1-year-old with proven mutations in the gene encoding SFTPC. HRCT shows diffuse ground-glass pattern. **b** Repeated HRCT 2 years later. Ground-glass opacities remain and small air-filled parenchymal lung cysts appear

deficiency. Older children may have a history of neonatal lung disease and present with symptoms of infiltrative lung disease such as tachypnoea, failure to thrive, crackles, hypoxemia, or pectus excavatum (Gower and Noguee 2011). Both diseases typically present with diffuse or patchy hazy granular opacities on chest radiograph and with diffuse ground-glass or consolidating opacity, and septal thickening on CT. In some patients the intensity of the ground-glass opacification decreased with age. Patients may develop small air-filled parenchymal lung cysts (Fig. 25) and tend to increase in number and size over time (Doan et al. 2008; Mechri et al. 2010).

NKX2-1/TTF1 mutation could be associated with congenital hypothyroidism, basal ganglia maldevelopment, and respiratory distress in neonatal period (Krude et al. 2002). Recurrent pulmonary infection and chronic interstitial lung disease are common manifestations (Carre et al. 2009; Galambos et al. 2010). HRCT finding is bilateral diffuse ground-glass appearance with alveolar condensations (Guillot et al. 2012).

## 2.2 Air-Space Diseases

### 2.2.1 Invasive Pulmonary Aspergillosis

Invasive pulmonary aspergillosis is a common complication in immunocompromised patients (acute leukemia with neutropenia, organ transplantation, use of immunosuppressive drugs, etc.) (Bomelburg et al. 1992; Taccone et al. 1993). The invasive form is characterized by occlusion of large or medium caliber arteries by plugs of hyphae. Lesions caused by *Aspergillus* microorganisms are endobronchial at the beginning followed by transbronchial vascular invasion.

Radiographic findings are initially nonspecific: patchy nodular opacities or lobar-type air-space disease. The two most common HRCT findings of invasive pulmonary aspergillosis are segmental consolidation with surrounding ground-glass attenuation and nodules surrounded by a halo corresponding to pulmonary hemorrhage (Logan et al. 1994; Thompson et al. 1995). These two signs are not specific and have been reported in other entities, such as mucormycosis, lymphoma, organizing pneumonia, and pulmonary hemorrhage (Won et al. 1998).

Cavitation occurs in half of the cases as a consequence of pulmonary infarction and increased granulocytic response associated with bone-marrow recovery. The cavitation process is characterized on HRCT by the air-crescent sign (Fig. 26), which represents air between retracted infarcted lung and the adjacent parenchyma. In the appropriate clinical setting though this sign is suggestive, but not diagnostic, of the disease. It may be seen in other diseases, such as tuberculosis, actinomycosis, bacterial abscess, or septic emboli.

Despite good diagnostic value of galactomannan assessment in bronchoalveolar lavage, chest HRCT and bronchoalveolar lavage cultures remain the most accurate diagnostic methods to identify invasive pulmonary aspergillosis (De Mol et al. 2013).

### 2.2.2 Pneumocystic Carinii Pneumonia

PCP is the most common pulmonary opportunistic infection in immunosuppressed children, occurring in up to 90 % of HIV+ patients during the course of their illness (Sivit et al. 1995). Radiographically, PCP presents as diffuse bilateral, progressively coalescing pulmonary infiltrates. In about

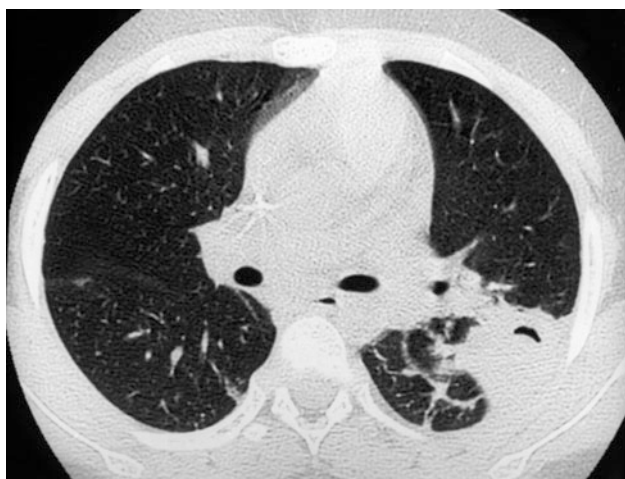


**Fig. 26** A 7-year-old girl with acute leukemia and invasive pulmonary aspergillosis. HRCT shows pulmonary consolidation with an air crescent sign

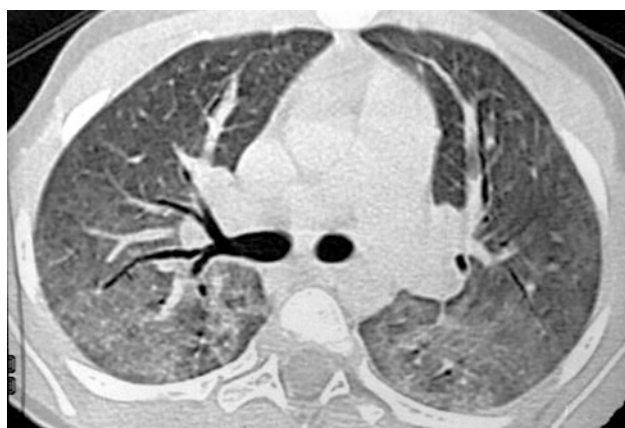


**Fig. 27** A 6-year-old HIV+ girl with *Pneumocystis carinii* pneumonia. Diffuse homogeneous ground-glass opacities are seen on the HRCT scan

10–20 % of microbiologically documented cases, the chest radiograph remains normal.

HRCT is considered to be more sensitive than chest radiography for the detection of early parenchymal disease. HRCT findings include patchy air-space disease with a geometric or mosaic pattern and diffuse homogeneous ground-glass opacities (Fig. 27). Interlobular septal thickening and reticular densities have also been reported. Cysts are frequently observed and are highly suggestive of the diagnosis. Lymphadenopathy, pleural effusion, and pulmonary nodules are uncommon.

HRCT is now a well-established technique for evaluating pediatric airway diseases. HRCT findings have also been described in most chronic diffuse infiltrative lung disease despite the fact that diffuse lung disease is relatively uncommon in children and that the range of disease is more heterogeneous than in adults. Concerning pulmonary fibrosis

and chronic interstitial pneumonias, more definitive categorization of the histopathology is needed to increase diagnostic accuracy of HRCT.

## References

- Abbott GF, Rosado-de-Christenson ML, Franks TJ et al (2004) Pulmonary Langerhans cell histiocytosis. *Radiographics* 24: 821–841
- Abehsera M, Valeyre D, Grenier P et al (2000) Sarcoidosis with pulmonary fibrosis: CT patterns and correlation with pulmonary function. *AJR* 174:1751–1757
- Agarwal R, Khan A, Garg M et al (2012) Chest radiographic and computed tomographic manifestations in allergic bronchopulmonary aspergillosis. *World J Radiol* 28:141–150
- Akira M, Yamamoto S, Sakatani M (1998) Bronchiolitis obliterans organizing pneumonia manifesting as multiple large nodules or masses. *AJR* 170:291–295
- Albafouille V, Sayegh N, de Coudenhove S et al (1999) CT scan patterns of pulmonary alveolar proteinosis in children. *Pediatr Radiol* 29:147–152
- Altamirano HG, McGeady SJ, Mansmann HC (1991) Right middle lobe syndrome in asthmatic children. *Pediatr Asthma Allergy Immunol* 5:33–37
- Amorosa JK, Miller RW, Laraya-Cuasay L et al (1992) Bronchiectasis in children with lymphocytic interstitial pneumonia and acquired immune deficiency syndrome. *Pediatr Radiol* 22:603–607
- Aquino SL, Schechter MS, Chiles C et al (1999) High-resolution inspiratory and expiratory CT in older children and adults with bronchopulmonary dysplasia. *AJR* 173:963–967
- Arslan N, Ilgan S, Ozkan M et al (2001) Utility of ventilation and perfusion scan in the diagnosis of young military recruits with an incidental findings of hyperlucent lung. *Nucl Med Commun* 22:525–530
- Aukland SM, Rosendahl K, Owens CM et al (2009) Neonatal bronchopulmonary dysplasia predicts abnormal pulmonary HRCT scans in long-term survivors of extreme preterm birth. *Thorax* 64:405–410
- Aydin K, Karabulut N, Demirkazik F et al (1997) Pulmonary involvement in adult Gaucher's disease: high-resolution CT appearance. *Br J Radiol* 70:93–95
- Bandeira T, Negreiro F, Ferreira R et al (2011) Clinical, radiological, and physiological differences between obliterative bronchiolitis and problematic severe asthma in adolescents and young adults: the early origins of the overlap syndrome? *Pediatr Pulmonol* 46:573–580
- Bankier AA, van Muylen A, Knoop C et al (2001) Bronchiolitis obliterans syndrome in heart-lung transplant recipients: diagnosis with expiratory CT. *Radiology* 218:533–539
- Bano S, Chaudhary V, Narula MK et al (2014) Pulmonary Langerhans cell histiocytosis in children: a spectrum of radiologic findings. *Eur J Radiol* 83:47–56
- Barbato A, Frischer T, Kuehni CE et al (2009) Primary ciliary dyskinesia: a consensus statement on diagnostic and treatment approaches in children. *Eur Respir J* 34:1264–1276
- Becciolini V, Gudinchet F, Cheseaux JJ et al (2001) Lymphocytic interstitial pneumonia in children with AIDS: high-resolution CT findings. *Eur Radiol* 11:1015–1020
- Bhalla M, Turcios N, Aponte V et al (1991) Cystic fibrosis: scoring system with thin-section CT. *Radiology* 179:783–788
- Bomelburg T, Roos N, von Lengerke HJ et al (1992) Invasive aspergillosis complicating induction chemotherapy of childhood leukaemia. *Eur J Pediatr* 151:485–487

- Bonelli FS, Hartman TE, Swensen SJ et al (1998) Accuracy of high-resolution CT in diagnosing lung diseases. *AJR* 170:1507–1512
- Braier J, Latella A, Balancini B et al (2004) Outcome in children with pulmonary Langerhans cell histiocytosis. *Pediatr Blood Cancer* 43:765–769
- Brasfield D, Hicks G, Soong SJ et al (1980) Evaluation of scoring system of the chest radiograph in cystic fibrosis: a collaborative study. *AJR* 134:1195–1198
- Brauner MW, Grenier P, Mompont D et al (1989a) Pulmonary sarcoidosis: evaluation with high-resolution CT. *Radiology* 172:467–471
- Brauner MW, Grenier P, Mouelhi MM et al (1989b) Pulmonary histiocytosis X: evaluation with high-resolution CT. *Radiology* 172:255–258
- Brauner MW, Grenier P, Tijani K et al (1997) Pulmonary Langerhans cell histiocytosis: evolution of lesions on CT scans. *Radiology* 204:497–502
- Brody AS, Molina PL, Klein JS et al (1999) High-resolution computed tomography of the chest in children with cystic fibrosis: support for use as an outcome surrogate. *Pediatr Radiol* 29:731–735
- Brody AS, Klein JS, Molina PL et al (2004) High-resolution computed tomography in young patients with cystic fibrosis: distribution of abnormalities and correlation with pulmonary function test. *J Pediatr* 145:32–38
- Brody AS, Tiddens HA, Castile RG et al (2005) Computed tomography in the evaluation of cystic fibrosis lung disease. *Am J Respir Crit Care Med* 172:1246–1252
- Brody AS, Guillerman RP, HaY TC et al (2010) Neuroendocrine cell hyperplasia of infancy: diagnosis with high-resolution CT. *Am J Roentgenol* 194:238–244
- Canakis AM, Cutz E, Manson D (2002) Pulmonary interstitial glycogenosis: a new variant of neonatal interstitial lung disease. *Am J Respir Crit Care Med* 165:1557–1565
- Carignan S, Staples CA, Müller NL (1995) Intrathoracic lymphoproliferative disorders in the immunocompromised patient: CT findings. *Radiology* 197:53–58
- Carré A, Szinnai G, Castanet M et al (2009) Five new TTF1/NKX2.1 mutations in brain-lung-thyroid syndrome: rescue by PAX8 synergism in one case. *Hum Mol Genet* 18:2266–2276
- Cartier Y, Kavanagh PV, Johkoh T et al (1999) Bronchiectasis: accuracy of high-resolution CT in the differentiation of specific diseases. *AJR* 173:47–52
- Castillo M, Vade A, Lim-Dunham JE et al (2010) Pulmonary interstitial glycogenosis in the setting of lung growth abnormality: radiographic and pathologic correlation. *Pediatr Radiol* 40:1562–1565
- Cazzato S, di Palmo E, Ragazzo V et al (2013) Interstitial lung disease in children. *Early Hum Dev* 89(Suppl 3):S39–S43
- Ceviz N, Kaynar H, Olgun H et al (2006) Pigeon breeder's lung in childhood: is family screening necessary? *Pediatr Pulmonol* 41:279–282
- Chang AB, Masel JP, Masters B (1998) Post-infectious bronchiolitis obliterans: clinical, radiological and pulmonary function sequelae. *Pediatr Radiol* 28:25–29
- Chibbar R, Shih F, Baga M et al (2004) Non specific interstitial pneumonia and usual interstitial pneumonia with mutation in surfactant protein C in familial pulmonary fibrosis. *Modem Pathol* 17:973–980
- Chung CJ, Fordham LA, Barker P et al (1999) Children with congenital pulmonary lymphangiectasia: after infancy. *AJR* 173:1583–1588
- Clement A, Task Force ERS (2004) Task force on chronic interstitial lung disease in immunocompetent children. *Eur Respir J* 24:686–697
- Cleveland RH, Staub Neish A, Zurakowski D et al (1998) Cystic fibrosis: a system for assessing and predicting progression. *AJR* 170:1067–1072
- Cluzel P, Grenier P, Bernadac P et al (1991) Pulmonary alveolar microlithiasis: CT findings. *J Comput Assist Tomogr* 15:938–942
- Colby TV (1998) Bronchiolitis pathologic considerations. *Am J Clin Pathol* 109:101–109
- Connolly B, Manson D, Eberhard A et al (1996) CT appearance of pulmonary vasculitis in children. *AJR* 167:901–904
- Copley SJ, Coren M, Nicholson AG et al (2000) Diagnostic accuracy of thin-section CT and chest radiography of pediatric interstitial lung disease. *AJR* 174:549–554
- Cordier JF (2000) Organising pneumonia. *Thorax* 55:318–328
- Coulier B, Mailleux P, Mairesse M et al (1999) Pulmonary alveolar proteinosis, high-resolution CT findings and evolution in 5 patients. *JBR-BTR* 82:277–281
- Dawson WB, Müller NL (1990) High-resolution computed tomography in pulmonary sarcoidosis. *Semin Ultrasound CT MR* 11:423–429
- de Jong PA, Ottink MD, Robben SG et al (2004) Pulmonary disease assessment in cystic fibrosis: comparison if CT scoring systems and value of bronchial and arterial dimension measurements. *Radiology* 231:434–439
- de Jong PA, Nakano Y, Lequin MH et al (2006) Dose reduction for CT in children with cystic fibrosis: is feasible to reduce the number of images per scan. *Pediatr Radiol* 36:50–53
- de Mol M, de Jongste JC, van Westreenen M et al (2013) Diagnosis of invasive pulmonary aspergillosis in children with bronchoalveolar lavage galactomannan. *Pediatr Pulmonol* 48:789–796
- Deniz O, Ors F, Tozkoparan E et al (2005) High-resolution computed tomographic features of pulmonary alveolar microlithiasis. *Eur J Radiol* 55:452–460
- Deterding RR (2012) Infants and young children with children's interstitial lung disease. *Pediatr Allergy Immunol Pulmonol* 23:25–31
- Deterding RR, Fan LL, Morton R et al (2001) Persistent tachypnea of infancy (PTI)—a new entity. *Pediatr Pulmonol* 23:72–73
- Deutsch GH, Young LR (2010) Pulmonary interstitial glycogenosis: words of caution. *Pediatr Radiol* 40:1471–1475
- Deutsch GH, Young LR, Deterding RR et al (2007) Diffuse lung disease in young children: application of a novel classification scheme. *Am J Respir Crit Care Med* 176:1120–1128
- Dinwiddie R, Sharief N, Crawford O (2002) Idiopathic interstitial pneumonitis in children: a national survey in the United Kingdom and Ireland. *Pediatr Pulmonol* 34:23–29
- Doan ML, Guillerman RP, Dishop M et al (2008) Clinical, radiological and pathological features of ABCA3 mutations in children. *Thorax* 63:366–373
- Dodd JD, Souza CA, Muller NL (2006) Conventional high-resolution CT versus helical high-resolution MDCT in the detection of bronchiectasis. *AJR* 187:414–420
- Donnelly LF (2000) Langerhan's cell histiocytosis showing low-attenuation mediastinal mass and cystic lung disease. *AJR* 174:877–878
- Drent M, de Vries J, Lenters M et al (2003) Sarcoidosis: assessment of disease severity using HRCT. *Eur Radiol* 13:2462–2471
- Duchateau F, Dechambre S, Coche E (2001) Imaging of pulmonary manifestations in subtype B of Niemann-Pick disease. *Br J Radiol* 74:1059–1061
- Dutheil-Doco A, Ducou le Pointe H, Larroquet M et al (1997) Maladie de Gorham à manifestation pleuro-pulmonaire prédominante. *J Radiol* 78:665–667
- Edwards EA, Metcalfe R, Milne DG (2003) Retrospective review of children presenting with non cystic fibrosis bronchiectasis: HRCT features and clinical relationships. *Pediatr Pulmonol* 36:87–93
- Eichinger M, Optazait DE, Kopp-Schneider A et al (2012) Morphologic and functional scoring of cystic fibrosis lung disease using MRI. *Eur J Radiol* 81:1321–1329



- Fauré C, Verderi D, Schmit P et al (1986) The chest film in immobile cilia syndrome in children. *Ann Radiol* 29:301–311
- Fauroux B, Clément A (2005) Paediatric sarcoidosis. *Paediatr Respir Rev* 6:128–133
- Fenlon HM, Doran M, Sant SM et al (1996) High-resolution chest CT in systemic lupus erythematosus. *AJR* 166:301–307
- Ferretti GR, Lantuejoul S, Brambilla E et al (1996) Pulmonary involvement in Niemann-Pick disease subtype B: CT findings. *J Comput Assist Tomogr* 20:990–992
- Flowers JR, Clunie G, Burke M et al (1992) Bronchiolitis obliterans organizing pneumonia: the clinical and radiological features of seven cases and a review of the literature. *Clin Radiol* 45:371–377
- Gaillard EA, Carty H, Heaf D et al (2003) Reversible bronchial dilatation in children: comparison of serial high-resolution computer tomography scans of the lungs. *Eur J Radiol* 47:215–220
- Galambos C, Levy H, Cannon CL et al (2010) Pulmonary pathology in thyroid transcription factor-1 deficiency syndrome. *Am J Respir Crit Care Med* 182:549–554
- Godwin JD, Müller NL, Takasugi JE (1988) Pulmonary alveolar proteinosis: CT findings. *Radiology* 169:609–613
- Goitein O, Elstein D, Abrahamov A et al (2001) Lung involvement and enzyme replacement therapy in Gaucher's disease. *QJM* 94:407–415
- Goo HW, Yang DH, Hong SJ et al (2010) Xenon ventilation CT using dual-source and dual-energy technique in children with bronchiolitis obliterans: correlation of xenon and CT density values with pulmonary function test results. *Paediatr Radiol* 40:1490–1497
- Gower WA, Noguee LM (2011) Surfactant dysfunction. *Paediatr Respir Rev* 12:223–229
- Grenier P, Maurice F, Musset D et al (1986) Bronchiectasis: assessment by thin-section CT. *Radiology* 161:95–99
- Grenier P, Lenoir S, Brauner M (1990) Computed tomographic assessment of bronchiectasis. *Semin Ultrasound CT MR* 11:430–441
- Grenier P, Chevret S, Beigelman C et al (1994) Chronic diffuse infiltrative lung disease: determination of the diagnostic value of clinical data, chest radiography, and CT with Bayesian analysis. *Radiology* 191:383–390
- Grenier P, Mourey-Gerosa I, Benali K et al (1996) Abnormalities of the lung and lung parenchyma in asthmatics: CT observations in 50 patients and inter- and intraobserver variability. *Eur Radiol* 6:199–206
- Griese M, Haug M, Brasch F et al (2009) Incidence and classification of pediatric diffuse parenchymal lung diseases in Germany. *Orphanet J Rare Dis* 4:26
- Grossman H, Merten DF, Spock A et al (1985) Radiographic features of sarcoidosis in pediatric patients. *Semin Roentgenol* 20:393–399
- Guan Y, Zeng Q, Yang H et al (2012) Pulmonary alveolar proteinosis: quantitative CT and pulmonary functional Correlations. *Eur J Radiol* 81:2430–2435
- Guillerman RP (2010) Imaging of childhood interstitial lung disease. *Paediatr Allergy Immunol Pulmonol* 23:43–68
- Guillot L, Carré A, Szinnai G et al (2012) NKX2-1 mutations leading to surfactant protein promoter dysregulation cause interstitial lung disease in "Brain-Lung-Thyroid Syndrome". *Hum Mutat* 31:E1146–E1162
- Hansell DM (1998) Bronchiectasis. *Radiol Clin North Am* 36:107–128
- Hansell DM, Moskovic E (1991) High-resolution computed tomography in extrinsic allergic alveolitis. *Clin Radiol* 43:8–12
- Hartman TE, Primack SL, Swenson SJ et al (1993) Desquamate interstitial pneumonia: thin-section CT findings in 22 patients. *Radiology* 187:787–790
- Helbich TH, Wojnarovsky C, Wunderbaldinger P et al (1997) Pulmonary alveolar microlithiasis in children: radiographic and high-resolution CT findings. *AJR* 168:63–65
- Helbich TH, Heinz-Peer G, Fleischmann D et al (1999) Evolution of CT findings in patients with cystic fibrosis. *AJR* 173:81–88
- Herman M, Michalkova K, Kopriva F (1993) High-resolution CT in the assessment of bronchiectasis in children. *Paediatr Radiol* 23:376–379
- Hiddema A, Engelshove HA (1999) Kartagener's syndrome. *JBR-BTR* 82:112
- Honda O, Johkoh T, Ichikado K et al (1999) Differential diagnosis of lymphocytic interstitial pneumonia and malignant lymphoma on high-resolution CT. *AJR* 173:71–74
- Ichikado K, Johkoh T, Ikezoe J et al (1997) Acute interstitial pneumonia: high-resolution CT findings correlated with pathology. *AJR* 168:333–338
- Inoue T, Toyochiro K, Kikui M (1996) Idiopathic bronchiolitis obliterans organizing pneumonia (idiopathic BOOP) in childhood. *Paediatr Pulmonol* 22:67–72
- Jain N, Covar RA, Gleason MC et al (2005) Quantitative computed tomography detects peripheral airway disease in asthmatic children. *Paediatr Pulmonol* 40:211–218
- Jimenez S, Jimenez JR, Crespo M et al (2006) Computed tomography in children with cystic fibrosis: a new way to reduce radiation dose. *Arch Dis Child* 91:388–390
- Johkoh T, Ikezoe J, Tomiyama N et al (1992) CT findings in lymphangitic carcinomatosis of the lung: correlation with histologic findings and pulmonary function tests. *AJR* 158:1217–1222
- Johkoh T, Müller NL, Cartier Y et al (1999a) Idiopathic interstitial pneumonias: diagnostic accuracy of thin-section CT in 129 patients. *Radiology* 211:555–560
- Johkoh T, Müller NL, Pickford HA et al (1999b) Lymphocytic interstitial pneumonia: thin-section CT findings in 22 patients. *Radiology* 212:567–572
- Johkoh T, Müller NL, Taniguchi H et al (1999c) Acute interstitial pneumonia: thin section CT findings in 36 patients. *Radiology* 211:859–863
- Katzstein AL, Fiorelli RF (1994) Nonspecific interstitial pneumonia/fibrosis. Histologic features and clinical significance. *Am J Surg Pathol* 18:136–147
- Katzstein AL, Myers JL, Mazur MT (1986) Acute interstitial pneumonia. A clinicopathologic, ultrastructural, and cell kinetic study. *Am J Surg Pathol* 10:256–267
- Kim MJ, Lee KY (1996) Bronchiolitis obliterans in children with Stevens-Johnson syndrome: follow-up with high-resolution CT. *Paediatr Radiol* 26:22–25
- Kim JS, Müller NL, Park CS et al (1997) Cylindrical bronchiectasis: diagnostic findings on thin-section CT. *AJR* 168:751–754
- Kiper N, Gocmen A, Ozcelik U et al (1999) Long-term clinical course of patients with idiopathic pulmonary hemosiderosis (1979–1994): prolonged survival with low-dose corticosteroid therapy. *Paediatr Pulmonol* 27:180–184
- Kleinau I, Perez-Canto A, Schmid HJ et al (1997) Bronchiolitis obliterans organizing pneumonia and chronic graft-versus-host disease in a child after allogeneic bone marrow transplantation. *Bone Marrow Transplant* 19:841–844
- Koh DM, Hansell DM (2000) Computed tomography of diffuse interstitial lung disease in children. *Clin Radiol* 55:659–667
- Konec O, Vyas PK, Goyal M (2000) Disseminated lymphangiomatosis presenting with massive chylothorax. *Paediatr Radiol* 30:35–37
- Krude H, Schütz B, Biebermann H et al (2002) Chorioathetosis, hypothyroidism, and pulmonary alterations due to human NKX2-1 haploinsufficiency. *J Clin Invest* 109:475–480
- Kuhn JP (1993) High-resolution computed tomography of pediatric pulmonary parenchymal disorders. *Radiol Clin North Am* 31:533–551
- Lau DM, Siegel MJ, Hildebolt CF et al (1998) Bronchiolitis obliterans syndrome: thin-section CT diagnosis of obstructive changes in

- infants and young children after lung transplantation. *Radiology* 208:783–788
- Lee EY (2013) Interstitial lung disease in infants: new classification system, imaging technique, clinical presentation and imaging findings. *Pediatr Radiol* 43:3–13
- Lee KS, Kullnig P, Hartman TE et al (1994a) Cryptogenic organizing pneumonia: CT findings in 43 patients. *AJR* 162:543–546
- Lee KS, Primack SL, Staples CA et al (1994b) Chronic infiltrative lung disease: comparison of diagnostic accuracies of radiography and low- and conventional-dose thin-section CT. *Radiology* 191:669–673
- Li YW, Snow J, Smith W et al (1985) Localized pulmonary lymphangiectasia. *AJR* 145:269–270
- Liebow AA, Carrington CB (1973) Diffuse pulmonary lymphoreticular infiltrations associated with dysproteinemia. *Med Clin North Am* 57:809–843
- Lilleby V, Aaløkken TM, Johansen B (2006) Pulmonary involvement in patients with childhood-onset systemic lupus erythematosus. *Clin Exp Rheumatol* 24:203–208
- Logan PM, Primack SL, Miller RR et al (1994) Invasive aspergillosis of the airways: radiographic, CT and pathologic findings. *Radiology* 193:383–388
- Lucaya J, Gartner S, Garcia-Pena P et al (1998) Spectrum of manifestations of Swyer-James-MacLeod syndrome. *J Comput Assist Tomogr* 22:592–597
- Lucaya J, Garcia-Pena P, Herrera L et al (2000) Expiratory chest CT in children. *AJR* 174:235–241
- Lynch DA (1998) Imaging of asthma and allergic bronchopulmonary mycosis. *Radiol Clin North Am* 36:129–142
- Lynch DA, Hay T, Newell JD Jr et al (1999) Pediatric diffuse lung disease: diagnosis and classification using high-resolution CT. *AJR* 173:713–718
- Marchac V, Emond S, Mamou-Mani T et al (2002) Thoracic CT in pediatric patients with difficult-to-treat asthma. *AJR* 179:1245–1252
- Marchiori E, Zanetti G, Escuissato DL et al (2012) Reversed halo sign: high-resolution CT scan findings in 79 patients. *Chest* 141:1260–1266
- Marti-Bonmati L, Ruiz Perales F, Catala F et al (1989) CT findings in Swyer-James syndrome. *Radiology* 172:477–480
- Mathew P, Bozeman P, Krance RA et al (1994) Bronchiolitis obliterans organizing pneumonia (BOOP) in children after allogeneic bone marrow transplantation. *Bone Marrow Transplant* 13:221–223
- McCook TA, Kirks DR, Merten DF et al (1981) Pulmonary alveolar proteinosis in children. *AJR* 137:1023–1027
- McGuinness G, Naidich DP (1995) Bronchiectasis: CT/clinical correlations. *Semin Ultrasound CT MR* 16:395–419
- McLean AN, Sproule MW, Cowan MD et al (1998) High-resolution computed tomography in asthma. *Thorax* 53:308–314
- Mechri M, Epaud R, Emond S et al (2010) Surfactant protein C gene (SFTPC) mutation-associated lung disease: high-resolution computed tomography (HRCT) findings and its relation to histological analysis. *Pediatr Pulmonol* 45:1021–1029
- Meeks M, Bush A (2000) Primary ciliary dyskinesia (PCD). *Pediatr Pulmonol* 29:307–316
- Mitchell CS, Parisi MT, Osborn RE (1993) Gorham's disease involving the thoracic skeleton. *Pediatr Radiol* 23:543–544
- Mitchell TA, Hamilos DL, Lynch DA et al (2000) Distribution and severity of bronchiectasis in allergic bronchopulmonary aspergillosis (ABPA). *J Asthma* 37:65–72
- Moore AD, Godwin JD, Müller NL et al (1989) Pulmonary histiocytosis X: comparison of radiographic and CT findings. *Radiology* 172:249–254
- Moore AD, Godwin JD, Dietrich PA (1992) Swyer-James syndrome: CT findings in eight patients. *AJR* 158:1211–1215
- Müller NL, Colby TV (1997) Idiopathic interstitial pneumonias: high-resolution CT and histologic findings. *RadioGraphics* 17:1016–1022
- Müller NL, Staples CA, Miller RR (1990) Bronchiolitis obliterans organizing pneumonia: CT features in 14 patients. *AJR* 154:983–987
- Munk PL, Müller NL, Miller RR et al (1988) Pulmonary lymphangitic carcinomatosis: CT and pathologic findings. *Radiology* 166:705–709
- Murch CR, Carr DH (1989) Computed tomography appearances of pulmonary alveolar proteinosis. *Clin Radiol* 40:240–243
- Nadel HR, Stringer DA, Levison H et al (1985) The immotile cilia syndrome: radiological manifestations. *Radiology* 154:651–655
- Nathanson I, Conboy K, Murphy S et al (1991) Ultrafast computerized tomography of the chest in cystic fibrosis: a new scoring system. *Pediatr Pulmonol* 11:81–86
- Newman B, Kuhn JP, Kramer SS et al (2001) Congenital surfactant protein B deficiency—emphasis on imaging. *Pediatr Radiol* 31:327–331
- Nishimura K, Kitaichi M, Izumi T et al (1992) Usual interstitial pneumonia: histologic correlation with high-resolution CT. *Radiology* 182:337–342
- Nishimura K, Itoh H, Kitaichi M et al (1995) CT and pathological correlation of pulmonary sarcoidosis. *Semin Ultrasound CT MR* 16:361–370
- Nogee LM, Dunbar AE, Wert SE et al (2001) A mutation in the surfactant protein C gene associated with familial interstitial lung disease. *N Engl J Med* 344:573–579
- Noonan JA, Walters LR, Reeves JT (1970) Pulmonary lymphangiectasis. *Am R Dis Child* 120:314–319
- Nowers K, Rasband JD, Berges G et al (2002) *Semin Ultrasound CT MR* 23:302–323
- O'Connor OJ, Valeur M, McGarrigle AM et al (2010) Development of low-dose protocols for thin-section CT assessment of cystic fibrosis in pediatric patients. *Radiology* 257:820–829
- Odame I, Li P, Lau L et al (2006) Pulmonary Langerhans cell histiocytosis: a variable disease in childhood. *Pediatr Blood Cancer* 47:889–893
- Oppenheim C, Mamou-Mani T, Sayegh N et al (1994) Bronchopulmonary dysplasia: value of CT in identifying pulmonary sequelae. *AJR* 163:169–172
- Osika E, Muller MH, Boccon-Gibod L (1997) Idiopathic pulmonary fibrosis in infants. *Pediatr Pulmonol* 23:49–54
- Paganin F, Trussard V, Seneterre E et al (1992) Chest radiography and high-resolution computed tomography of the lungs in asthma. *Am Rev Respir Dis* 146:1084–1087
- Pattishall EN, Kendig EL (1996) Sarcoidosis in children. *Pediatr Pulmonol* 22:195–203
- Primack SL, Hartman TE, Ikezoe J et al (1993) Acute interstitial pneumonia: radiographic and CT findings in nine patients. *Radiology* 188:817–820
- Primack SL, Miller RR, Müller NL (1995) Diffuse pulmonary hemorrhage: clinical, pathologic, and imaging features. *AJR* 164:295–300
- Ramirez RE, Glasier C, Kirks D et al (1984) Pulmonary hemorrhage associated with systemic lupus erythematosus in children. *Radiology* 152:409–412
- Rettwitz-Volk W, Schlober R, Ahrens P et al (1999) Congenital unilobar pulmonary lymphangiectasis. *Pediatr Pulmonol* 27:290–292
- Reyes de la Rocha S, Pysher TJ, Leonard JC (1987) Dyskinetic cilia syndrome: clinical, radiographic and scintigraphic findings. *Pediatr Radiol* 17:97–103
- Robertson BJ, Hansell DM (2011) Organizing pneumonia: a kaleidoscope of concepts and morphologies. *Eur Radiol* 21:2244–2254
- Rossi UG, Owens CM (2005) The radiology of chronic lung disease in children. *Arch Dis Child* 90:601–607
- Rossi SE, Erasmus JJ, Volpacchio M et al (2003) *RadioGraphics* 23:1509–1519

- Ruzal-Shapiro C (1998) Cystic fibrosis. An overview. *Radiol Clin North Am* 36:143–161
- Sargent MA, Cairns RA, Murdoch MJ et al (1995) Obstructive lung disease in children after allogeneic bone marrow transplantation: evaluation with high-resolution CT. *AJR* 164:693–696
- Schumacher RE, Marrogi AJ, Heidelberger KP (1989) Pulmonary alveolar proteinosis in a newborn. *Pediatr Pulmonol* 7:178–182
- Seely JM, Effmann EL, Müller NL (1997) High-resolution CT of pediatric lung disease: imaging findings. *AJR* 168:1269–1275
- Seely JM, Jones LT, Wallace C (1998) Systemic sclerosis: using high-resolution CT to detect lung disease in children. *AJR* 170:691–697
- Seely JM, Salahudeen S Sr, Cadaval-Goncalves AT et al (2012) Pulmonary Langerhans cell histiocytosis: a comparative study of computed tomography in children and adults. *J Thorac Imaging* 27:65–67
- Shah A, Pant CS, Bhagat R et al (1992) CT in childhood allergic bronchopulmonary aspergillosis. *Pediatr Radiol* 22:227–228
- Shah RM, Sexauer W, Ostrum BJ et al (1997) High-resolution CT in the acute exacerbation of cystic fibrosis: evaluation of acute findings, reversibility of those findings, and clinical correlation. *AJR* 168:375–380
- Sharma V, Shaaban AM, Berges G et al (2002) The radiological spectrum of small-airway diseases. *Semin Ultrasound CT MR* 23:339–351
- Shin SM, Kim SW, Cheon JE et al (2013) Bronchopulmonary dysplasia: new high resolution computed tomography scoring system and correlation between the high resolution computed tomography score and clinical severity. *Korean J Radiol* 14:350–360
- Siegel MJ (1999) Pediatric body CT. Lippincott Williams and Wilkins, Philadelphia, p. 126
- Sileo C, Epaud R, Mahloul M et al (2013) Sarcoidosis in children: HRCT findings and correlation with pulmonary function tests. *Pediatr Pulmonol*. doi: [10.1002/ppul.22956](https://doi.org/10.1002/ppul.22956)
- Silva CI, Colby T, Muller NL (2004) Asthma and associated conditions: high resolution CT and pathologic findings. *AJR* 183:817–824
- Sivit CJ, Miller CR, Rakusan TA et al (1995) Spectrum of chest radiographic abnormalities in children with AIDS and pneumocystis carinii pneumonia. *Pediatr Radiol* 25:389–392
- Small JH, Flower CD, Traill ZC et al (1996) Air-trapping in extrinsic allergic alveolitis on computed tomography. *Clin Radiol* 51:684–688
- Smets A, Mortelé K, de Praeter G et al (1997) Pulmonary and mediastinal lesions in children with Langerhans cell histiocytosis. *Pediatr Radiol* 27:873–876
- Sminiopoulou JG, Lonergan GJ, Abbott RM et al (1999) Image interpretation session: 1998. *RadioGraphics* 19:205–233
- Sockrider MM, Swank PR, Seilheimer DK et al (1994) Measuring clinical status in cystic fibrosis: internal validity and reliability of the modified NIH score. *Pediatr Pulmonol* 17:86–96
- Stauffer Ettlin M, Pache JC, Renevey F et al (2006) Bird breeder's disease: a rare diagnosis in young children. *Eur J Pediatr* 165:55–61
- Sterclova M, Vasakova M, Dutka J et al (2006) Extrinsic allergic alveolitis: comparative study of the bronchoalveolar lavage profiles and radiological presentation. *Postgrad Med J* 82:598–601
- Stern EJ, Samples TL (1992) Dynamic ultrafast high-resolution CT findings in a case of Swyer-James syndrome. *Pediatr Radiol* 22:350–352
- Swensen SJ, Hartman TE, Mayo JR et al (1995) Diffuse pulmonary lymphangiectasis: CT findings. *J Comput Assist Tomogr* 19:348–352
- Swensen SJ, Aughenbaugh GL, Myers JL (1997) Diffuse lung disease: diagnostic accuracy of CT in patients undergoing surgical biopsy of the lung. *Radiology* 205:229–234
- Taccone A, Occhi M, Garaventa A et al (1993) CT of invasive pulmonary aspergillosis in children with cancer. *Pediatr Radiol* 23:177–180
- Tateishi T, Ohtani Y, Takemura T et al (2011) Serial high-resolution computed tomography findings of acute and chronic hypersensitivity pneumonitis induced by avian antigen. *J Comput Assist Tomogr* 35:272–279
- Thomas AQ, Lane K, Philipps J et al (2002) Heterozygosity for a surfactant protein C gene mutation associated with usual interstitial pneumonitis and cellular nonspecific interstitial pneumonitis in one kindred. *Am J Respir Crit Care Med* 165:1322–1328
- Thompson BH, Stanford W, Galvin JR et al (1995) Varied radiologic appearances of pulmonary aspergillosis. *RadioGraphics* 15:1273–1284
- Traill ZC, Maskell GF, Gleeson FV (1997) High-resolution CT findings of pulmonary sarcoidosis. *AJR* 168:1557–1560
- Tunaci A, Berkmen YM, Gokmen E (1995) Pulmonary Gaucher's disease: high-resolution computed tomographic features. *Pediatr Radiol* 25:237–238
- Ujita M, Renzoni EA, Veeraraghavan S et al (2004) Organizing pneumonia: peribular pattern at thin-section CT. *Radiology* 232:757–761
- Verlaet CW, Peters HM, Semmekrot BA et al (1994) Congenital pulmonary lymphangiectasis presenting as a unilateral hyperlucent lung. *Eur J Pediatr* 153:202–205
- Vincent JM, Armstrong P, Wilson AG (1992) Extrinsic allergic alveolitis and eosinophilic pneumonia. *Imaging* 4:5–13
- von Vigier RO, Trummler SA, Laux-End R et al (2000) Pulmonary renal syndrome in childhood: a report of twenty-one cases and a review of the literature. *Pediatr Pulmonol* 29:382–388
- Wallis C, Whitehead B, Malone M et al (1996) Pulmonary alveolar microlithiasis in childhood: diagnosis by transbronchial biopsy. *Pediatr Pulmonol* 21:62–64
- Ward S, Heyneman L, Lee MJ et al (1999) Accuracy of CT in the diagnosis of allergic bronchopulmonary aspergillosis in asthmatic patients. *AJR* 173:937–942
- Webb WR (1994) High-resolution computed tomography of obstructive lung disease. *Radiol Clin North Am* 32:745–757
- Webb WR, Müller NL, Naidich DP (1996) High-resolution CT of the lung, 2nd edn. Lippincott-Raven, Philadelphia
- Wittram C, Mark EJ, McLoud TG (2003) CT-Histologic correlation of the ATS/ERS 2002 classification of idiopathic interstitial pneumonias. *RadioGraphics* 23:1057–1071
- Won HJ, Lee KS, Cheon JE et al (1998) Invasive pulmonary aspergillosis: prediction at thin-section CT in patients with neutropenia—a prospective study. *Radiology* 208:777–782
- Yang DH, Goo HW (2006) Generalized lymphangiomatosis: radiologic findings in three pediatric patients. *Korean J Radiol* 7:287–291
- Yassa NA, Wilcox AG (1998) High-resolution CT pulmonary findings in adults with Gaucher's disease. *Clin Imaging* 22:339–342



---

# Fetal MR Imaging of the Chest

Pedro Daltro, Heron Werner, and Taísa Davaus Gasparetto

## Contents

<b>1</b>	<b>Introduction</b> .....	157
<b>2</b>	<b>MR Imaging Technique and Normal Anatomy Patterns</b> .....	158
<b>3</b>	<b>Indications for Fetal MR Imaging of the Chest</b> .....	159
<b>4</b>	<b>Pulmonary Lesions</b> .....	159
4.1	Congenital Pulmonary Airway Malformation.....	159
4.2	Bronchopulmonary Sequestration.....	159
4.3	Bronchogenic Cyst.....	162
4.4	Neurenteric Cyst.....	162
4.5	Pulmonary Arteriovenous Malformations.....	162
4.6	Congenital Pulmonary Lymphangiectasia.....	162
<b>5</b>	<b>Hydrothorax</b> .....	162
<b>6</b>	<b>Congenital Diaphragmatic Hernia</b> .....	164
<b>7</b>	<b>Congenital Laryngeal Atresia</b> .....	168
<b>8</b>	<b>Cardiac Malformations</b> .....	168
<b>9</b>	<b>Hemangiomas</b> .....	170
<b>10</b>	<b>Conclusions</b> .....	170
	<b>References</b> .....	171

---

## Abstract

Magnetic resonance (MR) imaging is nowadays widely used in more complex cases of fetal malformation as an important complement to prenatal ultrasound. Due to the higher contrast resolution than ultrasound, the fetal MR imaging allows better differentiation of normal from abnormal tissue, providing detailed imaging information of the fetal structures, particularly the lungs. Congenital chest malformations may affect the foregut, pulmonary airway, and vasculature. Hybrid conditions are commonly seen with interrelated chest malformations having various radiologic and pathologic features. To date, fetal MR imaging has shown to have an important role in the evaluation of lung abnormalities sonographically suspected, leading to a more specific diagnosis and helping to access the development of the remaining lung parenchyma.

---

## 1 Introduction

Congenital chest malformations are rare, and they may involve the lung parenchyma, bronchi, arterial supply, and venous drainage (Daltro et al. 2010). The most common congenital chest anomalies include congenital pulmonary airway malformation (CPAM), congenital diaphragmatic hernia (CDH), bronchopulmonary sequestration (BPS), and congenital hydrothorax.

Magnetic resonance (MR) imaging is a noninvasive technique that allows the acquisition of high-definition images of fetal anatomy, adding important information to the routine prenatal ultrasound (US). The prenatal US is currently the gold standard imaging technique during pregnancy, since it is patient friendly, useful, cost-effective, and considered to be safe. However, MR imaging has several advantages, which has led to its increasing use for further characterization of fetal anatomy. MR images are usually not affected by fetal position, and image quality

---

P. Daltro (✉) · H. Werner · T. D. Gasparetto  
Clínica de Diagnóstico por Imagem-CDPI, Rio de Janeiro, Brazil  
e-mail: daltro.pedro@gmail.com

P. Daltro  
Hospital dos Servidores do Estado-H.S.E., Rio de Janeiro, Brazil

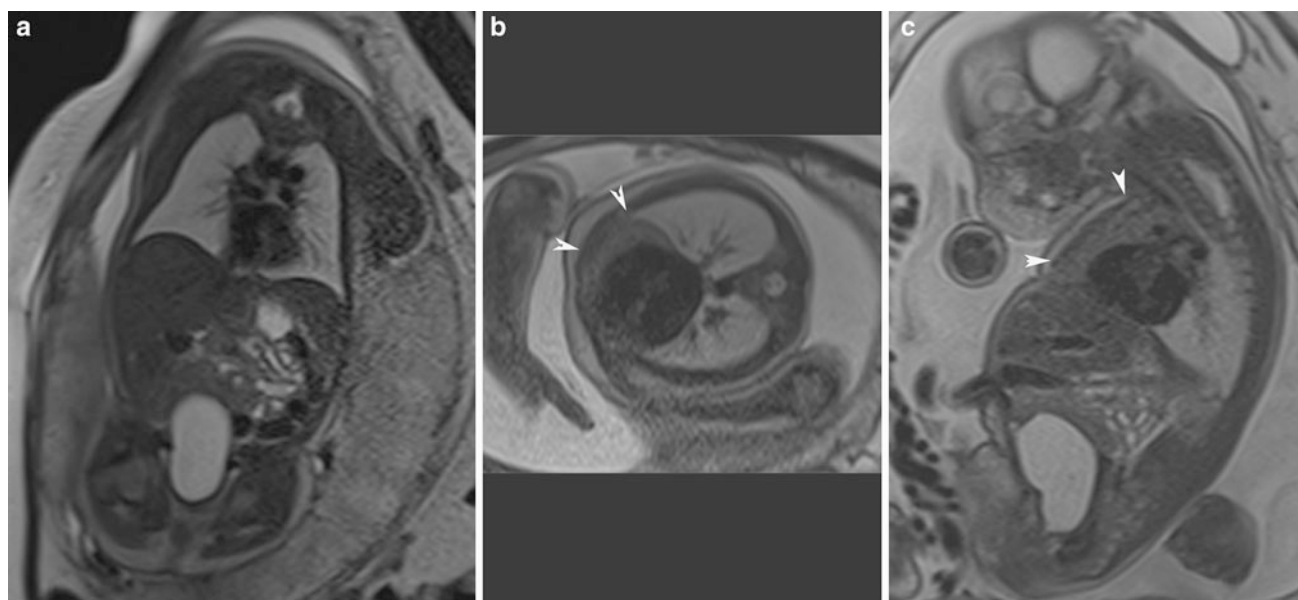


**Fig. 1** Normal lung. **a** Coronal T2-weighted image (33 weeks) showing great vessels and lungs with normal volume and signal intensity. **b** Axial T2-weighted image showing the normal high signal intensity suggestive of habitual pulmonary development. Note the

normal thymus (*arrowheads*). **c** Sagittal T2-weighted showing the high signal intensity of the lungs due to the presence of amniotic fluid within the parenchyma. Note the thymus anteriorly to the heart (*arrowheads*)

does not depend on the amount of amniotic fluid (Hubbard et al. 1999; Matsuoka et al. 2003). In addition, MR imaging can provide more accurate information than US alone, and may therefore assist decisions regarding the continuation of pregnancy, the method or site of delivery, and whether to perform a high-risk but potentially life-saving fetal intervention (Guo and Luo 2006; Werner et al. 2010, 2011; Kul et al. 2012).

## 2 MR Imaging Technique and Normal Anatomy Patterns

To obtain quality fetal chest MR images, it is essential to use fast sequences such as HASTE (Half-Fourier Single shot Turbo spin-Echo), FSSE (Fast Single Shot Echo), or true-FISP (Free Induction Steady-state Precession). These sequences permit quick image acquisition, avoiding artifacts related to fetal movement. The examination should begin with T2-weighted images of the thorax in axial, coronal, and sagittal planes, allowing an anatomic study of this region. T1-weighted images can be obtained to evaluate the liver and small bowel in patients with CDH. Fluid-filled structures usually have low signal on T1- and high signal on T2-weighted sequences. Solid organs demonstrate intermediate signal on T1- and T2-weighted images and the fat-containing structures have high-signal on T1- and T2-weighted images.

The T2-weighted sequences are most useful for evaluating the fetal chest. The lungs contain a significant amount of fluid, which increases with the gestational age. As a consequence, the signal of the lungs is homogeneously high on T2-weighted images, in contrast to the chest wall and mediastinal structures (Daltro et al. 2010; Bulas and Egloff 2011). In addition, the trachea and bronchi are well seen due to the amniotic fluid inside them. The thymus demonstrates intermediate signal on T2-weighted images and the heart is not well seen due to motion artifacts. To avoid heart artifacts movements, balanced MR images sequences such as steady-state free precession improve blood-pool homogeneity and allow faster acquisition, which results in better image resolution and fewer motion artifacts (Saleem 2008) (Fig. 1).

At the moment, there are no known biological effects of MR imaging on the fetus. The current recommendations by the Safety Committee of the Society of Magnetic Resonance Imaging regarding MR imaging safety during pregnancy suggest using this technique only in patients with inconclusive US. However, several imaging centers avoid acquiring MR imaging during the first trimester of the pregnancy, because there are no benefits in fetal diagnosis. Gadolinium-based contrast media are not recommended because they cross the placenta and penetrate the fetal circulation within seconds after intravenous administration (Shellock and Kanal 1991; Guo and Luo 2006).

### 3 Indications for Fetal MR Imaging of the Chest

Although US remains the gold standard imaging technique for screening of fetal malformations, MR imaging has been advancing in the last two decades as a complementary method for studying fetal anatomy (Hubbard et al. 1999; Shinmoto et al. 2000; Coakley et al. 2004). One of the most important advantages of MR imaging is soft tissue contrast. In addition, in cases of severe oligohydramnios or maternal obesity, this method can provide essential information not possible with US studies.

Improvements in US resolution over the past two decades have increased the ability to diagnose fetal chest anomalies. However, recent advances in MR imaging techniques have also increased the value of MR in evaluating these malformations, especially for atypical lesions and masses (Levine et al. 2003; Kasprian et al. 2006).

There are many factors that influence normal fetal lung growth, such as adequate size and shape of the fetal thorax, fetal breathing, movements, and an adequate amount of amniotic fluid. Pulmonary hypoplasia can occur when any of these factors are abnormal, but it is most commonly seen in patients with intrathoracic space occupying lesions. The most common space occupying lesions in the fetal thorax are CDH, CPAM, BPS, and fetal hydrothorax (Hubbard et al. 1999; Levine et al. 2003; Newman 2006).

## 4 Pulmonary Lesions

### 4.1 Congenital Pulmonary Airway Malformation

The CPAM, previously known as congenital adenomatoid malformation, is the most common congenital lung malformation. It is a lesion characterized by abnormal branching of immature bronchioles that may communicate with the tracheobronchial tree. The CPAM usually has arterial blood supply originating from the normal pulmonary circulation and venous drainage into normal pulmonary veins. However in hybrid lesions, a systemic blood supply may be evidenced. These lesions are often diagnosed on prenatal US or MR imaging (Daltro et al. 2004; Bulas and Egloff 2011). Fetal MR imaging is helpful in its ability to distinguish CPAM from other entities such as CDH, BPS, bronchogenic cyst, neurenteric/enteric cyst, laryngeal or tracheal atresia, and mediastinal cystic teratomas.

For clinical management, the classification into micro- or macrocystic appearance has been used. Adzick et al. (1985) suggested classifying CPAMs into two types: macrocystic

(>5 mm) and microcystic (<5 mm). However, the original classification of Stocker et al. (1977) remains more commonly used. These authors divided the lesions into three types: type I, macrocystic (>2 cm); type II, multiple small cysts; and type III, solid form (microscopic cysts). A newer classification proposed by Stocker (2002, 2009) considered also the pathologic analysis to the categorization, with the lesions that have been classified according to cyst size and histologic similarity to segments of the developing bronchial tree and airspaces. Five types were proposed by these authors: type 0 a tracheal or bronchial origin and is pathologically defined as acinar dysgenesis or dysplasia; type 1 is defined as large cystic lesions (2–10 cm) with a bronchial or bronchiolar origin; type 2 represents the small cystic lesions (0.5–2 cm) with a bronchiolar origin; type 3 has a bronchiolar–alveolar duct origin (adenomatoid type) with microscopic cysts; and type 4 with distal acinar origin and usually localized to one lobe and demonstrated large cysts with mediastinal shift. Given the controversial and occasionally confusing terminology and the paucity of literature correlating pathology, it is best to carefully describe the anatomy of the malformation and associated changes related to large lesions to guide any surgery or management (Epelman et al. 2010). Depending on the type of the CPAM, the US and MR imaging may vary. The cystic components will present as an anechoic mass by US and will be bright on T2-weighted MR images (Figs. 2 and 3). On the other hand, solid components of CPAM will present as a homogeneous echogenic mass by US and hyperintense lesions on T2-weighted MR images.

The natural history and prognosis of CPAM are variable. Maximum growth of a CPAM lesion typically occurs between 20 and 26 weeks of gestation. In the late second trimester, the mass often decreases in size (Bulas and Egloff 2011). The prognosis associated with this lesion is dependent on the size, rather than the histologic type of the lesion. Larger lesions are associated with higher frequency of mediastinal shift, pulmonary hypoplasia, vascular compromise, hydrops, and also hydramnios (Hubbard et al. 1999; Witlox et al. 2011; Schrey et al. 2012; Biyyam et al. 2010).

### 4.2 Bronchopulmonary Sequestration

Bronchopulmonary sequestration is a mass of pulmonary tissue that does not communicate with the central airway through a normal bronchial connection, and that receives its blood supply through an anomalous systemic artery, resulting in a nonfunctioning lung tissue. The arterial supply may arise from the descending thoracic or abdominal aorta, or from one of its branches (Daltro et al. 2010). Bronchopulmonary sequestration may be extralobar or intralobar, although most often the BPS present as hybrid lesions with



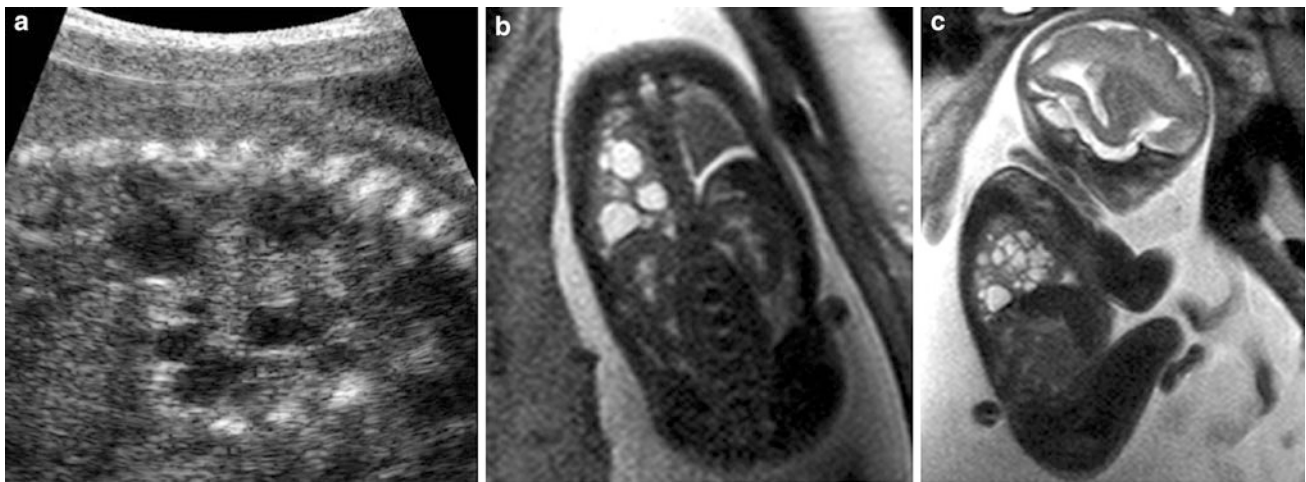


**Fig. 2** Cystic lung lesion. **a** Ultrasound view of multiple cysts of different sizes in the right lung. **b, c** Coronal and sagittal T2-weighted view shows cysts in the right lung. Note the low intensity signal in the left lung and small left hemothorax

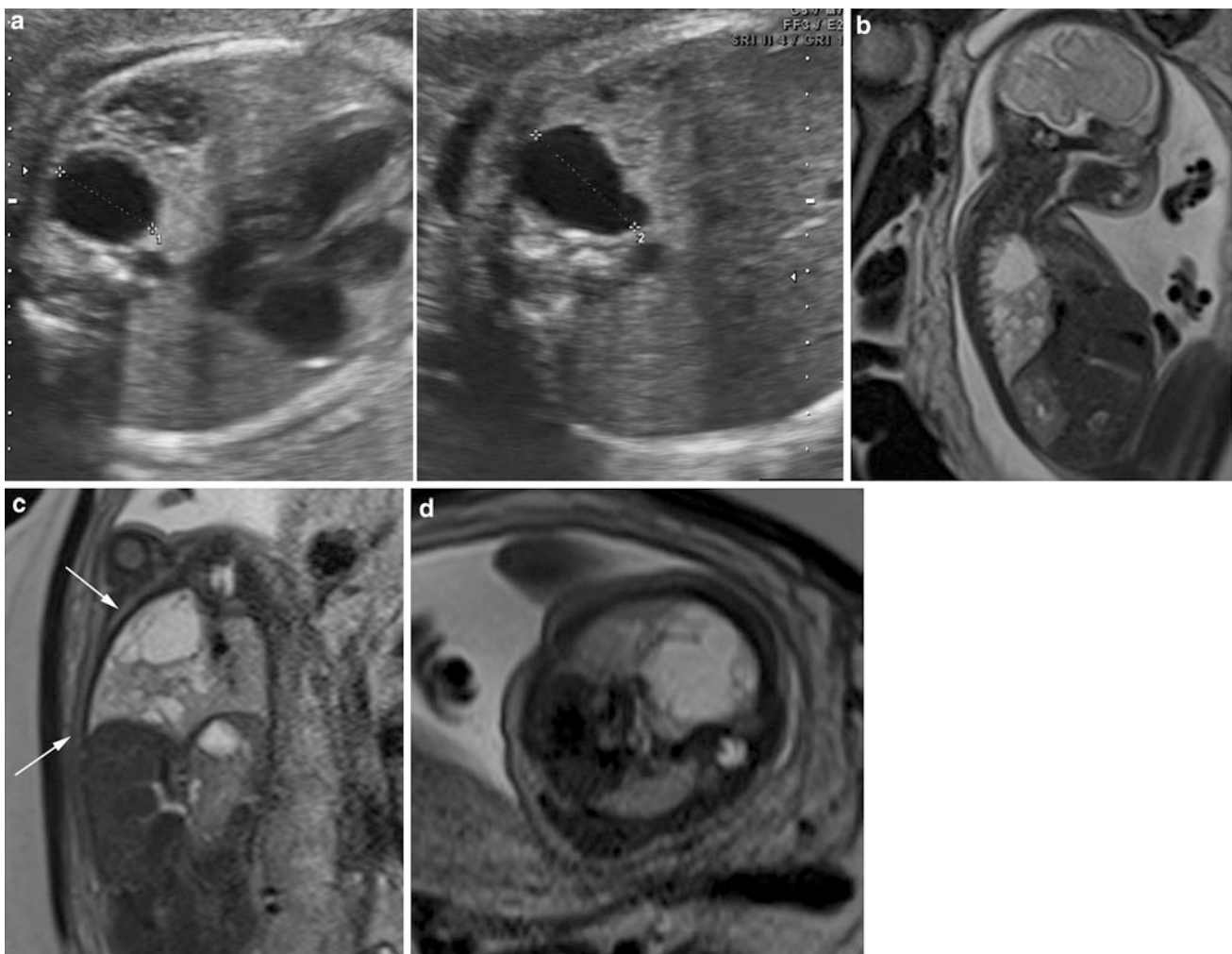


**Fig. 3** Cystic lung lesion with mass effect. **a** Ultrasound view of multiple cysts of different sizes in the right lung. **b–d** Sagittal, coronal, and axial T2-weighted images demonstrate multiple cysts in the right lung (*white arrow*). Note the mass effect of the lesion, displacing the mediastinum and compressing the left lung parenchyma

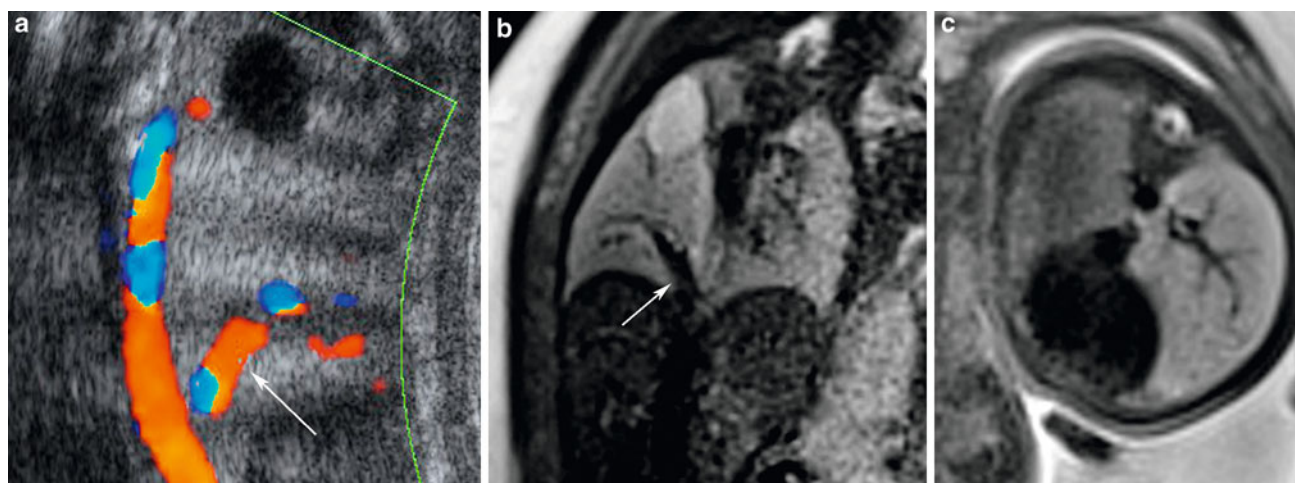
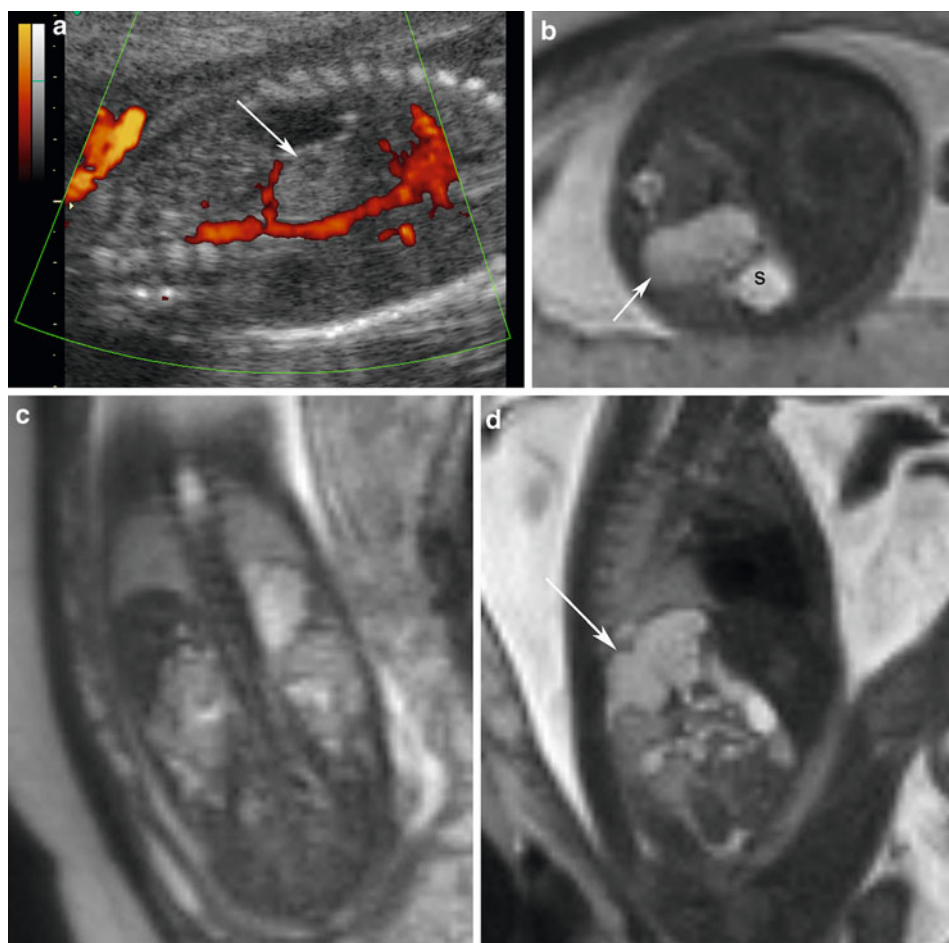


**Fig. 4** Hybrid lung lesion. **a** Ultrasound image of a hybrid lesion composed of an intralobar sequestration and a CPAM lesion. Note the hyperechoic lesion with arterial supply from the aorta (*white arrow*).

**b, c.** Coronal and axial T2-weighted images showing a hyperintense mass in the lung, with arterial supply from the aorta (*white arrow*) associated with a cystic lesion in the upper lobe

**Fig. 5** Pulmonary sequestration. **a** Prenatal ultrasound (27 weeks) reveals hyperechoic image with arterial supply from the aorta (*white arrow*). **b–d** Axial, coronal and sagittal T2-weighted images showing hyperintense signal mass in the base of the left lung. Axial view shows the lesion close to the stomach



components of both sequestration and CPAM. The hybrid cases are described as a cystic lesion with a feeding systemic vessel (Fig. 4). The extralobar form is most commonly diagnosed in the prenatal and neonatal periods,

whereas the intralobar form, although nowadays could be seen in the prenatal period, is more commonly seen in childhood. Some of the BPS lesions may regress in utero (Daltro et al. 2004; Epelman et al. 2010).

Prenatal US demonstrates bronchopulmonary sequestration as a homogeneously hyperechogenic mass in the lower lobes of the lung. On MR imaging, sequestered lung tissue has markedly high signal on T2- and low signal on T1-weighted images. The characterization of the anomalous vessels is possible by US but very difficult by MR imaging (Fig. 5).

The differential diagnosis of pulmonary sequestration may include neuroblastoma and adrenal hemorrhage to the infradiaphragmatic lesions. Pulmonary sequestration is more commonly seen as a solid lesion located on the left side, and can be seen with US during the second trimester. On the other hand, neuroblastoma usually contains cystic areas, which occurs more frequently on the right side and is more commonly diagnosed in the third trimester (Kays et al. 2006; Biyyam et al. 2010).

### 4.3 Bronchogenic Cyst

The bronchogenic cyst is the most common cystic lesion of the mediastinum. It is classified as an anomaly of the ventral bud of the primitive gut that occurs between the 26th and 40th days of embryonic development. The walls of bronchogenic cysts are thin, covered by respiratory epithelium and contain mucinous material. Most of the cysts are seen in the mediastinum or near the carina (Fig. 6). Less commonly, the cysts may occur within the lung parenchyma, pleura, or diaphragm. When the cysts are seen in the lung parenchyma, they are usually located in the inferior lobes. Bronchogenic cysts are sometimes found in association with other congenital pulmonary malformations such as sequestration or lobar overinflation (Daltro et al. 2004; Stocker 2009).

### 4.4 Neurenteric Cyst

The neurenteric cyst is the main lesion included in the differential diagnosis of bronchogenic cysts. The walls of neurenteric cysts have nervous and gastrointestinal elements, with intestinal epithelium that may be ciliated. They are usually seen in the posterior mediastinum, and may communicate with the esophagus, stomach, or duodenum. Neuroenteric cysts are frequently associated with anomalies of vertebral segmentation, and they can be asymptomatic at birth or present minimal respiratory distress (Fig. 7) (Newman 2006).

### 4.5 Pulmonary Arteriovenous Malformations

Pulmonary arteriovenous malformations (PAVMs) result from an abnormal communication between the pulmonary



**Fig. 6** Bronchogenic cyst. Coronal T2-weighted image shows cystic lesion in the base of the left lung

arteries and veins. Most of the lesions are congenital in origin and the female: male ratio is around 2:1. Infants and children with PAVMs may be asymptomatic; however, if the lesions are large enough to cause a significant right-to-left shunt, the patient may present with cyanosis or heart failure. Between 50 and 70 % of PAVMs occur in the lower lobes and about 2/3 of the patients have multiple lesions (Hansell et al. 2005) (Fig. 8).

### 4.6 Congenital Pulmonary Lymphangiectasia

Congenital pulmonary lymphangiectasia is a generalized dilation of otherwise histopathologically normal lymphatic vessels. The condition may occur primarily, or secondary to severe pulmonary venous obstruction in cases of total anomalous pulmonary venous return or hypoplastic left heart syndrome. Congenital pulmonary lymphangiectasia is frequently associated with genetic diseases, including Noonan, Turner, Ehlers-Danlos, and Down syndromes (Faul et al. 2000) (Fig. 9).

## 5 Hydrothorax

Hydrothorax is the accumulation of fluid in the pleural space, and can be primary or secondary in origin. Most hydrothoraces are primary, with chylothorax being the most



**Fig. 7** Neuroenteric cyst. **a** Ultrasound view of the spine shows an associated segmental anomaly (*arrow*). **b** Sagittal T2-weighted image showing the cyst close to the spine. Note the dilated bowel loop (\*)

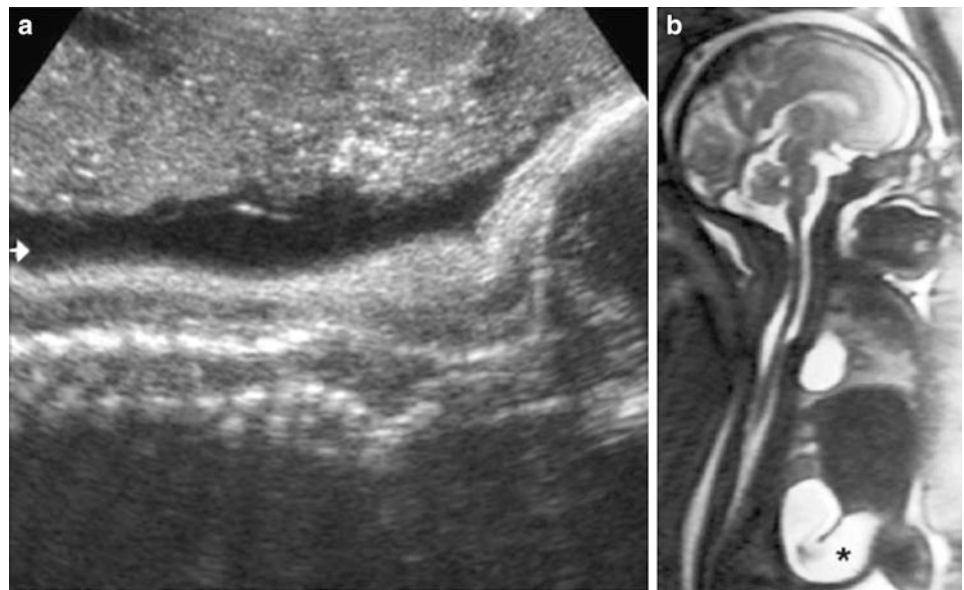


**Fig. 8** **a** Pulmonary arteriovenous malformation. Ultrasound view shows a vascular lesion close to the heart. **b–d** Axial, coronal, and sagittal T2-weighted images reveal a low signal intensity lesion in the middle of the right lung

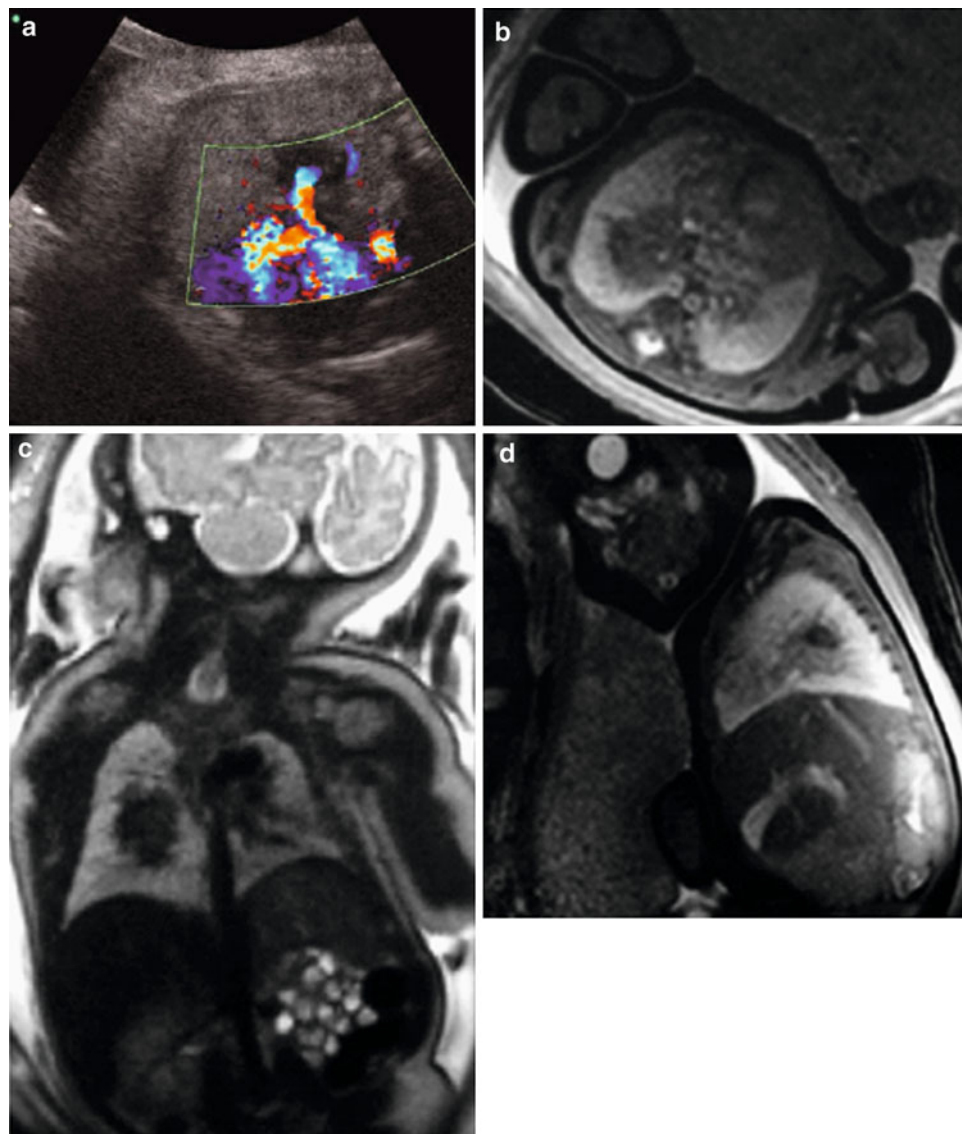
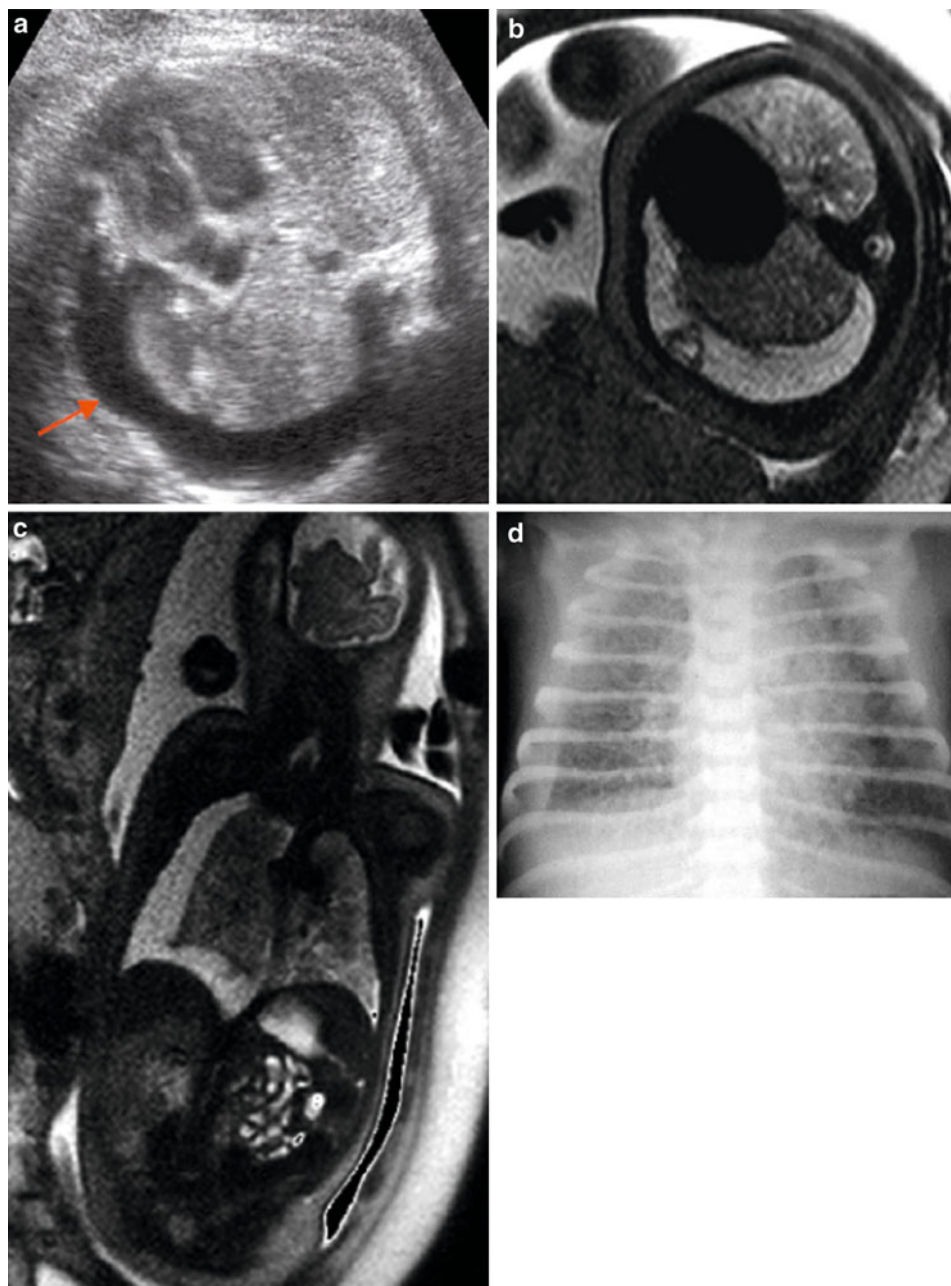


**Fig. 9** Congenital pulmonary lymphangiectasia. **a** Ultrasound view shows right hydrothorax (arrow). **b, c.** Axial and coronal T2-weighted images demonstrate right hydrothorax compressing the homolateral lung. Note the low signal intensity of the both lungs. **d** Conventional X-ray some hours after delivery reveals diffuse reticular infiltrate and right pleural effusion



common. The chylothorax occurs because of an abnormality in the formation of the thoracic lymphatic ducts, with resultant abnormal drainage. It is usually unilateral, occurring more frequently on the right side. In patients with secondary pleural effusions, the most common causes are chromosomal abnormalities (Down or Turner syndrome) or infectious diseases (cytomegalovirus, toxoplasmosis). Hydrothorax may also be seen in cases of fetal hydrops.

The diagnosis of hydrothorax can be made with US, which can also help to guide treatment, including drainages and shunts (Fig. 10).

## 6 Congenital Diaphragmatic Hernia

Congenital diaphragmatic hernia is defined as a partial or complete lack of development of the diaphragm, allowing the migration of abdominal structures into the thorax; these structures can compress the lungs and affect their development (Paek et al. 2001; Kays 2006). The CDH can be divided in two forms: an early form, in which the abdominal organs develop inside the thorax, and a late form, which is associated with secondary migration of the abdominal organs to the thorax. The fetal MR imaging is important in

**Fig. 10** Hydrothorax. **a**, **b** Coronal T2-weighted image of the fetus (26 weeks) shows a large bilateral hydrothorax. Note also the cutaneous edema and small lungs



these cases allowing an anatomic evaluation and also helping to determinate the specific type of CDH and the effect of the hernia contents on adjacent structures. The fetal MR imaging may also be used to calculate lung volume and liver herniation measurements as well as to the calculation of the diameters of the pulmonary arteries and aorta (Mehollin-Ray et al. 2012; Recio Rodríguez et al. 2012).

The most common type of CDH occurs through the Bochdalek foramina, and occurs more frequently on the left side (Fig. 11). US can suggest this diagnosis between the 2nd and 3rd trimesters, demonstrating the stomach and small bowel loops in the left hemi-thorax, and the heart deviated to the right side. Around 12 % of the cases of CDH occur on the right. In most of these cases the liver is seen in the right hemi-thorax, compressing the heart in the left hemi-thorax (Fig. 12). The migration of small bowel loops into the right hemi-thorax is uncommon (Okazaki et al. 2003; Bedoyan et al. 2004; Hedrick et al. 2004). An extreme form of congenital diaphragmatic hernia is associated with the complete bilateral agenesis of the diaphragm (Fig. 13). In these cases, the lack of mediastinal shift may be evident and the lung parenchyma may be completely compressed by the abdominal content herniated (Hiasa et al. 2012; Jasnosz et al. 1994; Wang et al. 1997; Mehollin-RAY et al. 2012).

Even after recent improvements in diagnosis and treatment of CDH, the mortality remains around 58 % (Harrison et al. 1994; Paulson et al. 1995). Both the gestational age at which the CDH develops, and the organs that have migrated affect the prognosis. In cases of late CDH (>25 weeks), the prognosis is better because lung development is less affected. On the other hand, CDHs that occur earlier (<25 weeks) are usually associated with severe lung

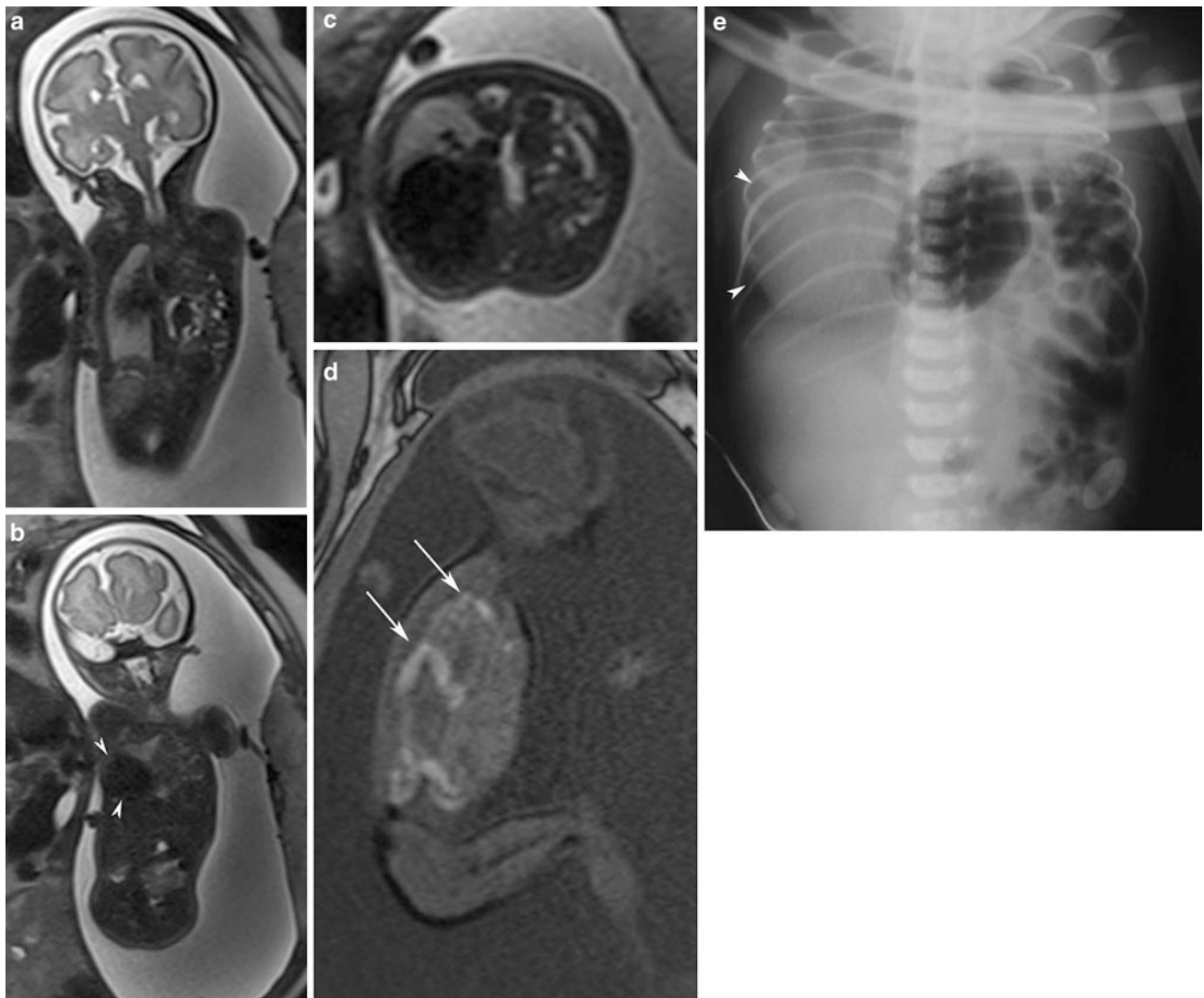
abnormalities, and have a worse prognosis (Leung et al. 2000; Kays 2006).

The pathogenesis of pulmonary hypoplasia is poorly understood. Fetal lung fluid plays an important role in normal lung development. Kuwashima et al. (2001) found a close relationship between fetal lung intensity on MR imaging and pulmonary growth. Low intensity of the fetal lung suggested the presence of pulmonary hypoplasia, whereas high intensity was consistent with normal pulmonary development.

Several studies have demonstrated the potential use of 3D US and MR imaging in measuring the lung volumes. Nowadays, MR volumetry is considered more trusty for identifying ipsilateral lung and, therefore, for calculating precise fetal lung volumes (Jani et al. 2007). These techniques involve accessing three orthogonal planes to allow an accurate determination of organ volume (Mahieu-Caputo et al. 2001; Ruano et al. 2004; Peralta et al. 2005). To obtain the total lung volume by MR imaging, the cross-sectional area of the lung is measured on each transverse section. To calculate the volume for each section, the value of the cross-sectional area is multiplied by the section thickness and intersection gap combined. The volumes of all of the sections are then added to obtain the volume of the entire lung. The calculation is repeated for the contralateral lung, and then the volumes of both lungs are added to obtain the total lung volume (Figs. 14, 15, and 16).

Another way to evaluate for pulmonary hypoplasia is to calculate the lung-head ratio (LHR). It can be obtained by US multiplying the orthogonal diameters of the right lung at the level of the four heart chambers at 24–26 weeks gestational age, and dividing by the head circumference (in millimeters). An LHR of <1.0 is associated with mortality

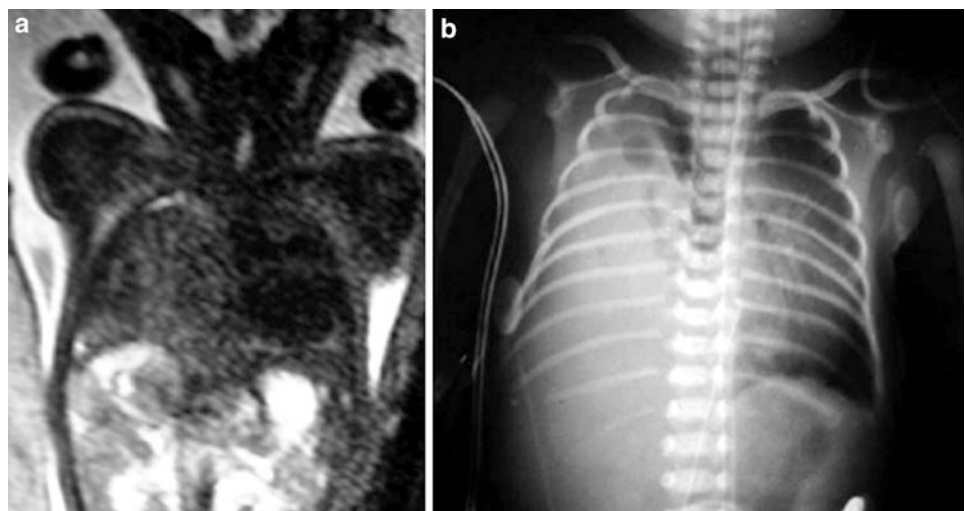




**Fig. 11** Diaphragmatic hernia. **a–c** Coronal and axial T2-weighted views showing a left diaphragmatic hernia. Note a small stomach and multiple bowel loops in the left hemithorax displacing the heart to the right side (*arrowheads* in **b**). The liver maintained the abdominal position and the right lung present normal signal intensity. **d** Sagittal

T1-weighted view showing bowel loops in the hemithorax presenting high signal intensity due to the meconium content. **e** The postnatal X-ray showing the bowel loops into the left hemithorax displacing the heart to the right (*arrowheads*)

**Fig. 12** Right diaphragmatic hernia. **a** Coronal T2-weighted view shows the liver in the right hemi-thorax compressing the heart to the left hemi-thorax. **b** The postnatal X-ray showing similar findings



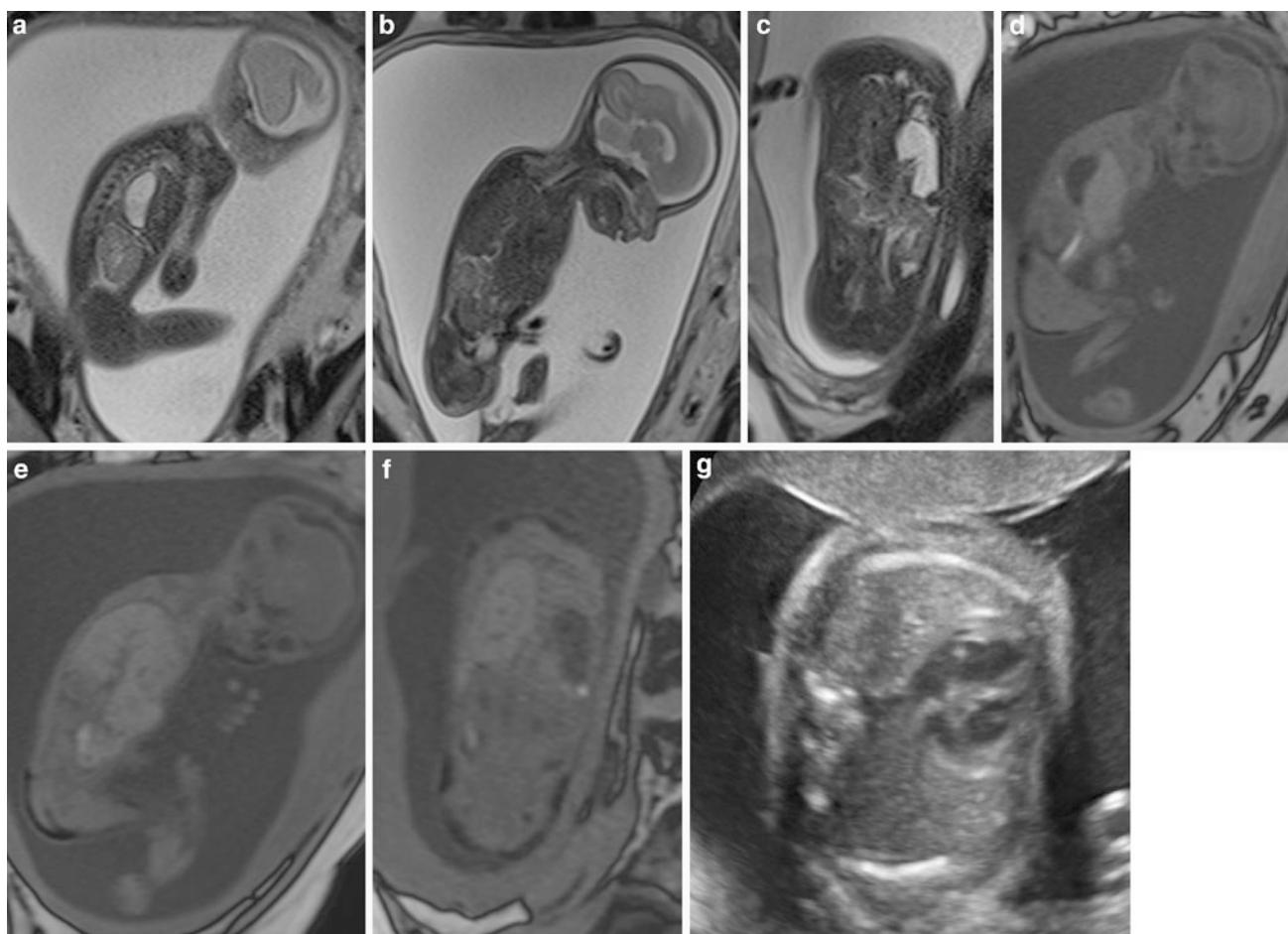


**Fig. 13** Bilateral diaphragmatic hernia. **a–c** Sagittal and coronal T2-weighted images showing stomach, spleen, and liver in the thorax. **d–f** Sagittal and coronal T1-weighted images well demonstrates the liver and spleen occupying the thorax. **g** Ultrasound image at the same day

showing the heart and mediastinum well positioned due to the bilateral herniation. Note that the echogenicity of the herniated liver is very similar to the normal lung

**Fig. 14** **a–c** Normal lung volume (axial, coronal, and sagittal) measured by MRI at 32 weeks



of approximately 100 %. Conversely, an LHR of more than 1.4 is associated with a good prognosis. The mortality rate seen in patients with LHR between 1.0 and 1.4 is around 60 % (Metkus et al. 1996; Jani et al. 2006, 2012).

The most important factors for determining prognosis in patients with pulmonary hypoplasia are early diagnosis, the presence of associated malformations, chromosomal

anomalies, migration of the liver to the thorax, and the LHR (Albanese et al. 1998).

Many efforts have been made to improve survival of infants born with CDH. The first intrauterine surgery for CDH was performed by Harrison in 1990. However, due to poor outcome, the technique was abandoned. Subsequently, tracheal occlusion was developed as a promising new

**Fig. 15** a–c Lung volume measured in axial, coronal, and sagittal in a case of left diaphragmatic hernia with liver down (28 weeks)

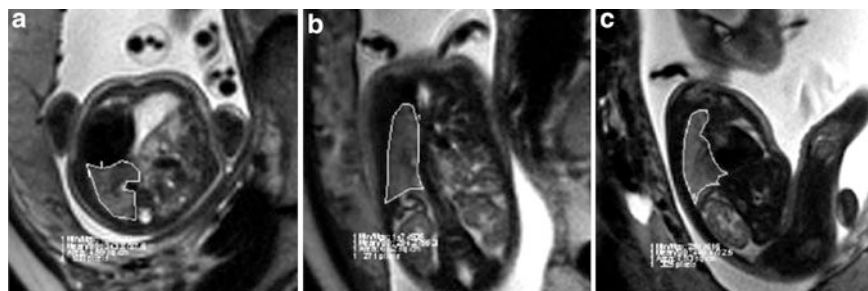
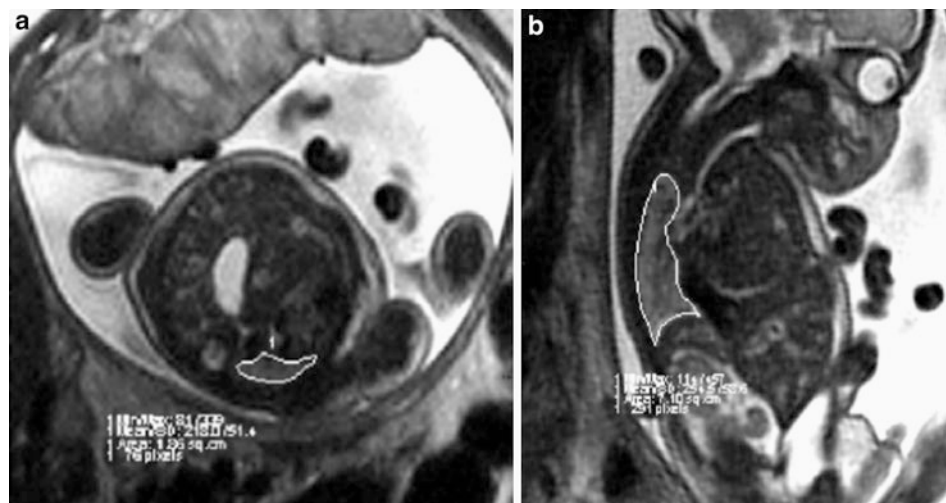


**Fig. 16** a, b Lung volume measured in axial and sagittal in a case of left diaphragmatic hernia with liver up (28 weeks)



treatment option aimed at increasing lung volumes for the intrauterine treatment of CDH in patients with poor prognosis. Although some authors have demonstrated good results with this technique, further studies have to be conducted to clarify the advantages of the intrauterine management of CDH (Deprest et al. 2006a, b; Harrison et al. 2003). Postnatal management with surfactants and extra corporeal membrane oxygenation are also improving prognosis for these patients.

## 7 Congenital Laryngeal Atresia

Congenital laryngeal atresia is a rare anomaly, with few cases of prenatal diagnosis in the literature. In cases of upper airway stenosis, US demonstrate bilateral and homogeneous hyperechogenicity of the lungs, which have increased volume. In addition, the diaphragm cupules are inverted and inferiorly deviated. Most of the patients develop ascites and anasarca, probably related to abnormal venous return (right heart failure). The amniotic fluid volume may be normal, increased, or reduced. Oligohydramnios may be related to lack of pulmonary drainage, and polyhydramnios to esophageal compression by the lungs (Kassanos et al. 1997). The increased lung volumes seen in

patients with congenital laryngeal atresia are demonstrated on MR imaging as marked high signal of the lung parenchyma on T2-weighted images (Fig. 17). In addition, the heart is centered in the thorax and the diaphragmatic cupules are inverted.

## 8 Cardiac Malformations

Magnetic resonance imaging is less useful than US for the diagnosis of cardiac malformations (Hata et al. 1995). The lack of gating for the heartbeats results in images with significant motion artifacts. However, although the anatomy and the function of the heart are not well studied with MR imaging, the size and position of the heart should always be evaluated (Fig. 18).

The most common cardiac tumors in the fetal age are rhabdomyomas and teratomas. Rhabdomyomas are usually small intracardiac tumors. Although they are well seen with MR imaging, this technique is more useful for evaluating the associated brain lesions in patients with rhabdomyomas and tuberous sclerosis (Werner et al. 1994). Teratomas are a common fetal neoplasm; around 10 % of them occur in the thorax and abdomen. Most of the thoracic teratomas involve the pericardium and mediastinum. The identification of



**Fig. 17** Congenital laryngeal atresia. **a.** Ultrasound of the fetal thorax (27 weeks) demonstrates the echogenic lung and inverted diaphragms. Note four chamber view of the heart and ascites. **b, c** Coronal oblique T2-weighted images of the fetal thorax (28 weeks) show the augmentation of the lungs and inverted diaphragmatic couple. Note the ascites

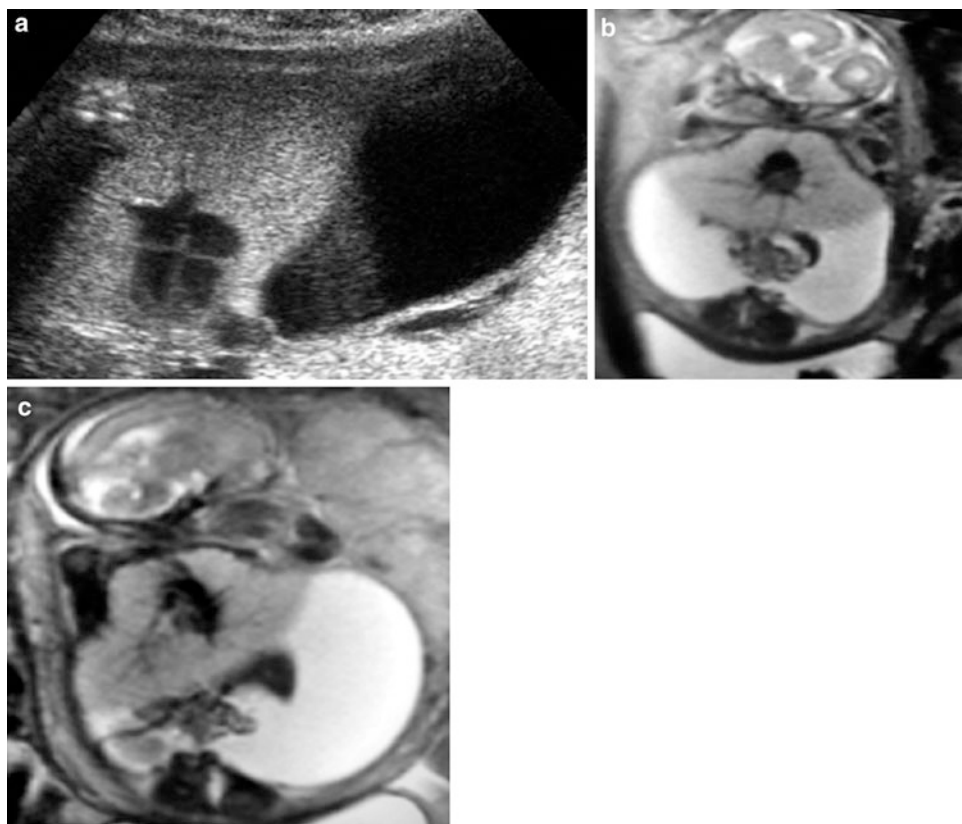
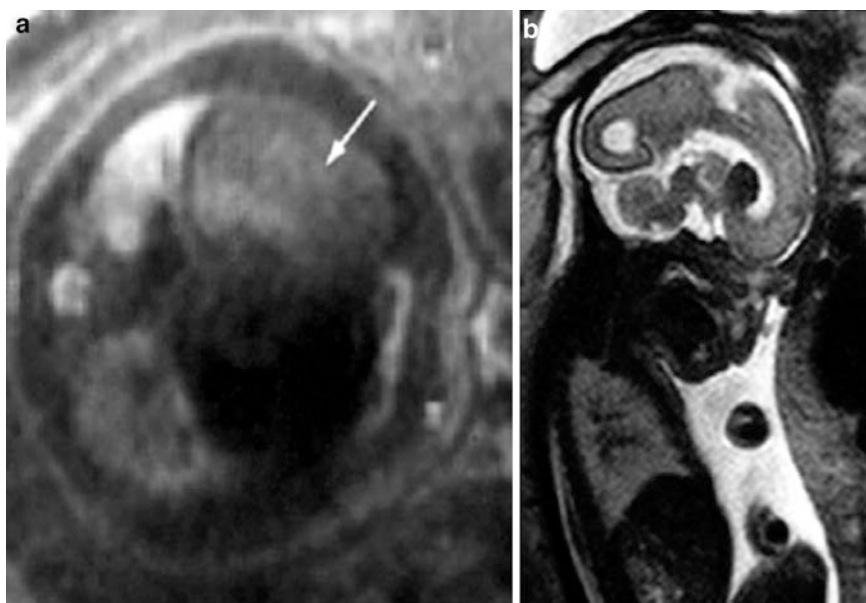
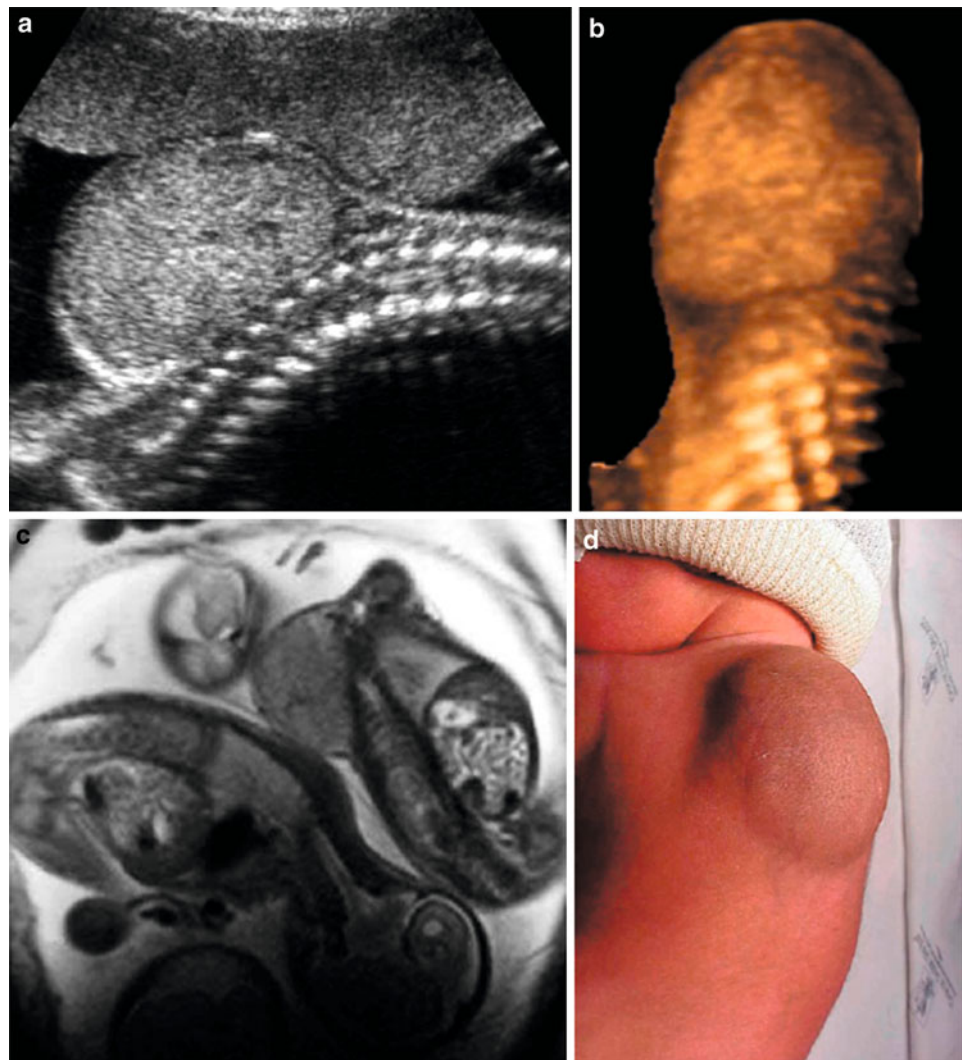


**Fig. 18** Cardiac rhabdomyosarcoma. **a** Axial T2-weighted image of the fetal thorax shows a cardiac rhabdomyoma. **b** Sagittal T2-weighted image of the fetal head shows a typical subependymal nodule in a case of tuberous sclerosis



calcification in teratomas helps the differential diagnosis with CPAM and extra-lobar pulmonary sequestration (Woodward et al. 2005).

**Fig. 19** a, b. Hemangioma. 2D and 3D ultrasound images of the 28-week fetus with a mass behind the back. c Prenatal MRI shows three fetuses, one of them with homogeneous mass in the back (arrow). d Postnatal image



## 9 Hemangiomas

Hemangiomas are benign tumors of blood vessels. They are classified as: cavernous, capillary (strawberry), or mixed. The cavernous hemangiomas are masses of dilated vessels located deep in the skin, containing large blood-filled spaces. They appear as pale, skin-colored, red or blue masses. These lesions can cause hydrops during the prenatal period. Strawberry hemangiomas are bright red protuberant masses that may occur in any area of the body, especially the face, scalp, back, and chest. They vary in size from pinhead to several centimeters in diameter, and may be flat or slightly raised (Dubois et al. 1998) (Fig. 19).

## 10 Conclusions

The extraordinary advances in fetal MR imaging in recent years have occurred more quickly than with any other imaging technique. MR imaging provides images of the

fetus that are easier to visualize and understand than US images, both for physicians and parents.

Prenatal diagnosis of congenital thoracic lesions can be critical; these lesions can range from small and asymptomatic to large space occupying lesions that require immediate surgical treatment. Currently, the diagnosis of chest abnormalities is made more frequently with US. However, MR imaging is an important adjunct in the evaluation of fetal chest pathologies. The increased knowledge gained from MR imaging of these pathologies allows more objective prenatal counseling and more efficient treatment during the postnatal period. The indication and timing of surgical or conservative treatments are now better defined based on the advances of the imaging tools.

Far from being a static imaging technique, MR imaging has been and will continue to be constantly advancing as an imaging alternative for the investigation of fetal chest pathologies.

## References

- Adzick NS, Harrison MR, Glick PL (1985) Fetal cystic adenomatoid malformation: prenatal diagnosis and natural history. *J Pediatr Surg* 20:483–488
- Albanese CT, Lopoo J, Goldstein RB (1998) Fetal liver position and perinatal outcome for congenital diaphragmatic hernia. *Prenat Diagn* 18:1138–1142
- Bedoyan JK, Blackwell SC, Treadwell MC, Johnson A, Klein MD (2004) Congenital diaphragmatic hernia: associated anomalies and antenatal diagnosis. *Pediatr Surg Int* 20:170–176
- Biyyam DR, Chapman T, Ferguson MR, Deutsch G, Dighe MK (2010) Congenital lung abnormalities: embryologic features, prenatal diagnosis, and postnatal radiologic-pathologic correlation. *Radiographics* 30:721–738
- Bulas D, Egloff AM (2011) Fetal chest ultrasound and magnetic resonance imaging: recent advances and current clinical applications. *Radiol Clin North Am* 49:805–823. This bibliography is not mentioned on the text
- Coakley FV, Glenn OA, Qayyum A, Barkovich AJ, Goldstein R, Filly RA (2004) Fetal MRI: a developing technique for the developing patient. *AJR Am J Roentgenol* 182:243–252
- Daltro P, Fricke BL, Kuroki I, Domingues R, Donnelly LF (2004) CT of congenital lung lesions in pediatric patients. *AJR* 183:1479–1506
- Daltro P, Werner H, Gasparetto TD, Domingues RC, Rodrigues L, Marchiori E, Gasparetto E (2010) Congenital chest malformations: a multimodality approach with emphasis on fetal MR imaging. *RadioGraphics* 30:385–395
- Deprest J, Jani J, Van Schoubroeck et al (2006a) Current consequences of prenatal diagnosis of congenital diaphragmatic hernia. *J Pediatr Surg* 41:423–430
- Deprest J, Jani J, Van Schoubroeck et al (2006b) Prenatal intervention for isolated congenital diaphragmatic hernia. *Curr Opin Obstet Gynecol* 18:203–215
- Dubois J, Patriquin HB, Garel L, Powell J, Filiatrault D, David M, Grignon A (1998) Soft-tissue hemangiomas in infants and children: diagnosis using Doppler sonography. *AJR Am J Roentgenol* 171(1):247–252
- Epelman M, Kreiger PA, Servaes S, Victoria T, Hellinger JC (2010) Current imaging of prenatally diagnosed congenital lung lesions. *Semin Ultrasound CT MR* 31:141–157
- Faul JL, Berry GJ, Colby TV et al (2000) Thoracic lymphangioma, lymphangiectasis, lymphangiomatosis, and lymphatic dysplasia syndrome. *Am J Respir Crit Care Med* 161:1037–1046
- Guo Y, Luo B (2006) The state of the art of fetal magnetic resonance imaging. *Chin Med J* 119(15):1294–1299
- Hansell DM, Armstrong P, Lynch DA, McAdams HP (2005) Congenital anomalies. In: *Imaging of the diseases of the chest*, 4th edn. Elsevier, Mosby
- Harrison MR, Adzick NS, Estes JM, Howell LJ (1994) A prospective study of the outcome for fetuses with diaphragmatic hernia. *JAMA* 271:382–384
- Harrison MR, Keller RL, Hawgood SB et al (2003) A randomized trial of fetal endoscopic tracheal occlusion for severe fetal congenital diaphragmatic hernia. *N Engl J Med* 349(20):1916–1924
- Hata K, Hata T, Manabe A (1995) Hypoplastic left heart syndrome: color Doppler sonographic and magnetic resonance imaging features in utero. *Gynecol Obstet Invest* 39:70–72
- Hedrick HL, Crombleholme TM, Flake AW et al (2004) Right congenital diaphragmatic hernia: prenatal assessment and outcome. *J Pediatr Surg* 39(3):319–323
- Hiasa KI, Fujita Y, Fukushima K, Nagata K, Taguchi T, Wake N (2012) Ultrasound and MR images of prenatally diagnosed bilateral congenital diaphragmatic hernia, a rare variation of CDH. *Clin Imaging* 36(5):639–642
- Hubbard AM, Adzick NS, Crombleholme TM et al (1999) Congenital chest lesions: diagnosis and characterization with prenatal MR Imaging. *Radiology* 212:48–49
- Jani J, Peralta CF, Van Schoubroeck D et al (2006) Relationship between lung-to-head ratio and lung volume in normal fetuses and fetuses with diaphragmatic hernia. *Ultrasound Obstet Gynecol* 27:545–550
- Jani JC, Cannie M, Peralta CFA, Deprest JA, Nico-laides KH, Dymarkowski S (2007) Lung volumes in fetuses with congenital diaphragmatic hernia: comparison of 3D US and MR imaging assessments. *Radiology* 244:575–582
- Jani JC, Peralta CF, Nicolaides KH (2012) Lung-to-head ratio: a need to unify the technique. *Ultrasound Obstet Gynecol* 39:2–6
- Jasnosc KM, Hermansen MC, Snider C et al (1994) Congenital complete absence (bilateral agenesis) of the diaphragm: a rare variant of congenital diaphragmatic hernia. *Am J Perinatol* 11:340–343
- Kasprian G, Balassy C, Brugger P, Prayer D (2006) MRI of normal and pathological fetal lung development. *Eur Radiol* 16:261–270
- Kassanos D, Christodoulou CV, Agapitos E et al (1997) Prenatal ultrasonographic detection of the tracheal atresia sequence. *Ultrasound Obstet Gynecol* 10:133–136
- Kays DW (2006) Congenital diaphragmatic hernia and neonatal lung lesions. *Sur Clin N Am* 86:329–352
- Kul S, Korkmaz HA, Cansu A et al (2012) Contribution of MRI to ultrasound in the diagnosis of fetal anomalies. *J Magn Reson Imaging* 35:882–890
- Kuwashima S, Nishimura G, Iimura F et al (2001) Low-intensity fetal lungs on MRI may suggest the diagnosis of pulmonary hypoplasia. *Pediatr Radiol* 31:669–672
- Leung JWT, Coakley FV, Hricak H et al (2000) Prenatal MR imaging of congenital diaphragmatic hernia. *Am Roentgen* 174:1607–1612
- Levine D, Banewolt CE, Mehta TS et al (2003) Fetal thoracic abnormalities: MR imaging. *Radiology* 228:379–388
- Mahieu-Caputo D, Sonigo P, Dommergues M et al (2001) Fetal lung volume measurement by magnetic resonance imaging in congenital diaphragmatic hernia. *BJOG* 108:863–868
- Matsuoka S, Takeuchi K, Yamanaka Y et al (2003) Comparison of magnetic resonance imaging and ultrasonography in the prenatal diagnosis of congenital thoracic abnormalities. *Fetal Diagn Ther* 18:447–453
- Mehollin-Ray AR, Cassady CI, Cass DL, Olutoye OO (2012) Fetal MR imaging of congenital diaphragmatic hernia. *Radiographics* 32:1067–1084
- Metkus AP, Filly RA, Stringer MD et al (1996) Sonographic predictors of survival in fetal diaphragmatic hernia. *J Pediatr Surg* 31:148–151
- Newman B (2006) Congenital bronchopulmonary foregut malformations: concepts and controversies. *Pediatr Radiol* 36:773–791
- Okazaki T, Kohno S, Hasegawa S et al (2003) Congenital diaphragmatic hernia: efficacy of ultrasound examination in its management. *Pediatr Surg Int* 19:176–179
- Paulson TE, Spear RM, Peterson BM (1995) New concepts in the treatment of children with acute respiratory distress syndrome. *J Pediatr* 127:163–175
- Paek BW, Coakley FV, Yiung Lu et al (2001) Congenital diaphragmatic hernia: prenatal evaluation with MR lung volumetry—preliminary experience. *Radiology* 220:63–67
- Peralta CF, Cavoretto P, Csapo B et al (2005) Assessment of lung area in normal fetuses at 12–32 weeks. *Ultrasound Obstet Gynecol* 26:718–724
- Recio Rodríguez M, Martínez de Vega V, Cano Alonso R, Carrascoso Arranz J, Martínez Ten P, Pérez Pedregosa J (2012) MR imaging



- of thoracic abnormalities in the fetus. *Radiographics* 32:E305–E321
- Ruano R, Joubin L, Sonigo P et al (2004) Fetal lung volume estimated by 3-dimensional ultrasonography and magnetic resonance imaging in cases with isolated congenital diaphragmatic hernia. *J Ultrasound Med* 23:353–358
- Saleem SN (2008) Feasibility of MRI of the fetal heart with balanced steady-state free precession sequence along fetal body and cardiac planes. *AJR* 191:1208–1215
- Schrey S, Kelly EN, Langer JC et al (2012) Fetal thoracoamniotic shunting for large macrocystic congenital cystic adenomatoid malformations of the lung. *Ultrasound Obstet Gynecol* 39:515–520
- Shellock FG, Kanal E (1991) Policies, guidelines, and recommendations for MR imaging safety and patient management. *SMRI safety committee. J Magn Reson Imaging* 1:97–101
- Shinmoto H, Kashima K, Yuasa Y et al (2000) MR imaging of non-CNS fetal abnormalities: a pictorial essay. *RadioGraphics* 20(5):1227–1243
- Stocker JT, Madewell JE, Drake RM (1977) Congenital cystic adenomatoid malformation: prenatal diagnosis and natural history. *J Pediatr Surg* 8:155–158
- Stoker JT (2002) Congenital pulmonary airway malformation: a new name for and an expanded classification of congenital cystic adenomatoid malformation of the lung. *Symposium 24: non-neoplastic lung disease. Histopathology* 41:424–30
- Stocker JT (2009) Cystic lung disease in infants and children. *Fetal Pediatr Pathol* 28:155–184
- Wang SM, Lin CH, Lin YJ et al (1997) Congenital bilateral agenesis of diaphragm: report of a case. *Eur J Pediatr* 156:572–574
- Werner H, Dos Santos JRL, Fontes R, Daltro P, Gasparetto E, Marchiori E, Campbell S (2010) Additive manufacturing models of fetuses built from three-dimensional ultrasound, magnetic resonance imaging and computed tomography scan data. *Ultrasound Obstet Gynecol* 36:355–361
- Werner H, Dos Santos JRL, Fontes R, Daltro P, Gasparetto E, Marchiori E, Campbell S (2011) Virtual bronchoscopy in the fetus. *Ultrasound Obstet Gynecol* 37:113–115
- Werner H, Mirlesse V, Jacquemard F et al (1994) Prenatal diagnosis of tuberous sclerosis. Use of magnetic resonance imaging and its implications for prognosis. *Prenat Diagn* 14:1151–1154
- Witlox RS, Lopriore E, Oepkes D (2011) Prenatal interventions for fetal lung lesions. *Prenat Diagn* 31:628–636
- Woodward PF, Sohaey R, Kennedy A et al (2005) A comprehensive review of fetal tumors with pathologic correlation. *RadioGraphics* 25:215–242

---

# Neonatal Chest Imaging

Eric J. Crotty

## Contents

<b>1</b>	<b>Introduction</b> .....	173
<b>2</b>	<b>Technique</b> .....	173
<b>3</b>	<b>Systematic Approach</b> .....	174
<b>4</b>	<b>Medical Disease</b> .....	176
4.1	Transient Tachypnea of the Newborn .....	176
4.2	Respiratory Distress Syndrome .....	176
4.3	Bronchopulmonary Dysplasia .....	180
4.4	Meconium Aspiration Syndrome .....	182
4.5	Neonatal Pneumonia.....	183
<b>5</b>	<b>Air Leak Phenomenon</b> .....	187
5.1	Pulmonary Interstitial Emphysema .....	187
5.2	Pneumothorax .....	188
5.3	Pneumomediastinum.....	189
5.4	Pneumopericardium .....	189
<b>6</b>	<b>Lines and Tubes</b> .....	189
<b>7</b>	<b>Summary</b> .....	194
	<b>References</b> .....	194

---

## Abstract

Neonatal lung disease is a common problem with potential for significant morbidity and mortality. Chest radiographs remain the most important imaging tool for investigation of these diseases. Many of these diseases can have a similar appearance on radiographs, but differentiation can be often be achieved by noting differentiating and sometimes subtle imaging findings, and taking into consideration pertinent clinical information such as the gestational age and perinatal history. As these patients are often critically ill, radiographs also need to be evaluated for adequate positioning of the support tubes and catheters. Many complications of these diseases, such as air leak related to mechanical ventilation, can also be assessed with radiographs. This chapter will describe and illustrate the imaging findings of diseases of the neonatal lung and complications of their management.

---

## 1 Introduction

The chest radiograph is the most frequent imaging study performed on neonates. This reflects respiratory distress being a very common sign in an ill neonate, especially in premature infants. A wide spectrum of medical and surgical disorders can present in the neonatal period with respiratory distress. This chapter will focus on the common pulmonary conditions, as the cardiac and surgical conditions will be discussed in other chapters.

---

## 2 Technique

Although the radiation dose from an individual chest radiograph is low, it is important that the ALARA principals are observed. While patients in the neonatal intensive care unit are ill, they often do not require a daily chest radiograph, and

---

E. J. Crotty (✉)  
Department of Radiology,  
Cincinnati Children's Hospital Medical Center,  
University of Cincinnati College of Medicine,  
3333 Burnet Avenue, Cincinnati, OH 45229-3039, USA  
e-mail: eric.crotty@cchmc.org

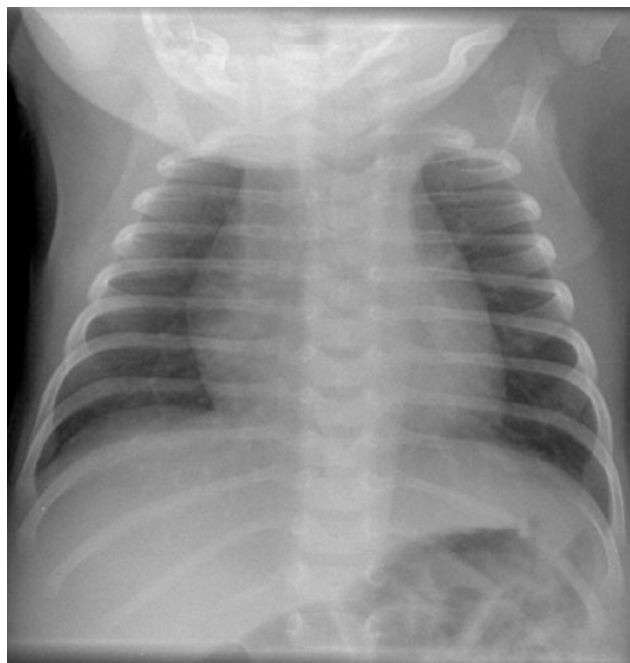


**Fig. 1** Normal anteroposterior (AP) chest radiograph in a neonate. Symmetrically inflated lungs are seen with sharp costophrenic angles. The configuration of the cardiothymic silhouette is normal

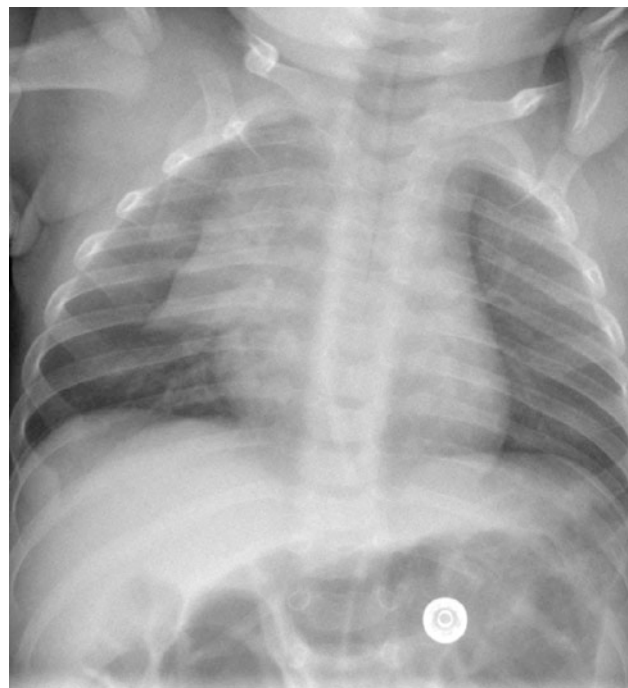


**Fig. 2** Thymic wave sign. Undulating lateral border of the soft thymus from deformation by the overlying ribs. The thymus also projects like a sail away from the other mediastinal structures

judicious ordering of imaging is the best method to decrease exposure to ionizing radiation. When a chest radiograph is obtained, proper technique is important. Images are obtained anteroposterior (AP) with the patient in the supine position. Care should be taken to avoid rotation. Imaging is centered at the nipple line and should extend from the lung apices superiorly to L1/L2 level inferiorly. An AP view usually suffices for evaluation of the chest. Occasionally a cross-table lateral view or a lateral decubitus view can be helpful, most often in the evaluation for an anterior pneumothorax.

### 3 Systematic Approach

A systematic method of evaluating radiographs is recommended. The lungs should demonstrate symmetrical aeration and radiolucency. Patient rotation will lead to asymmetrically increased or decreased density and a unilateral hyperlucent lung can mimic a pneumothorax or a congenital overinflation lesion. Pulmonary vasculature should be inconspicuous in the periphery of the lungs but should be visible in the central two-thirds. The hemidiaphragms should be dome-shaped and the costophrenic angles should be sharp. The transverse cardiothoracic ratio can be up to 60 % in neonates (Fig. 1). The normal thymus can have a varied appearance and can mimic a mass or consolidation. Various signs can be used to identify a normal thymus. These include a wavy lateral border due to

impression by the anterior ribs, a notch between the thymus and the heart, and a sail-like appearance of the thymus projecting off the mediastinum (Fig. 2). The thymus should be visible in a normal neonate. However, stress and illness can lead to rapid involution of the thymus. Confirmation of the presence of a thymus and differentiation of a thymus from a mass can usually be made by ultrasound, as a normal thymus has a typical sonographic appearance (Fig. 3) (Han et al. 2001).

Patients in the neonatal intensive care unit often have catheters and tubes and evaluation of this support apparatus is an important part of reviewing chest radiographs in these infants. Review should include not only the chest cavity, but also the osseous structures and the soft tissues of the chest wall. The upper abdomen should also be reviewed for comorbid conditions such as necrotizing enterocolitis, a common disease in patients with respiratory distress syndrome (RDS). The signs of this condition include pneumatosis intestinalis, portal venous gas, and free intraperitoneal air, all of which may be identified on a chest radiograph (Fig. 4). Abdominal heterotaxy with malposition of the stomach and liver can be accompanied by asplenia or polysplenia and is strongly associated with congenital heart disease. The osseous structures need to be evaluated for vertebral and rib abnormalities. The Vertebral anomalies, Anal atresia, Cardiac anomalies, Tracheoesophageal abnormalities, Renal anomalies, and Limb anomalies (VACTERL)



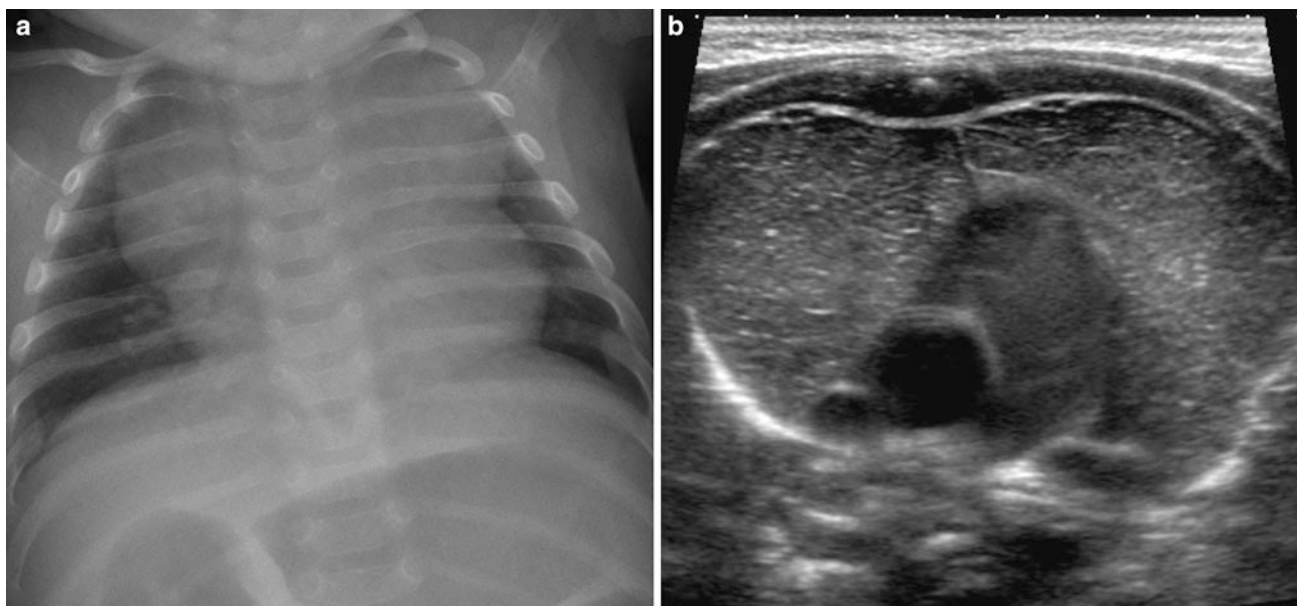


**Fig. 3** Prominent thymus confirmed with ultrasound. **a** Neonate with a prominent lobulated mediastinal contour on a chest radiograph. **b** Ultrasound demonstrates a normal thymus with the typical appearance of echogenic lines and punctate foci on a hypoechoic stroma

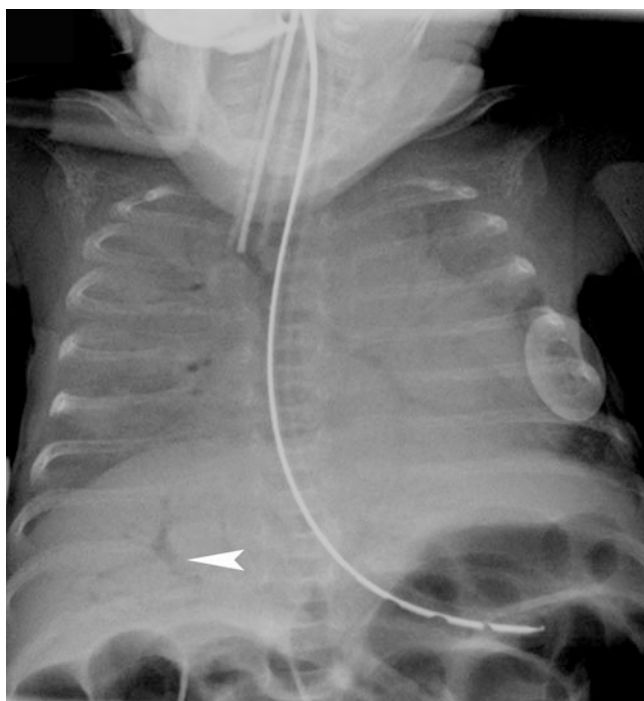


**Fig. 4** Abdominal pathology on a chest radiograph. Chest radiograph in a 3 week old former 27 week gestation premature infant with necrotizing enterocolitis demonstrating branching lucent structures in the liver (arrowhead) consistent with portal venous gas

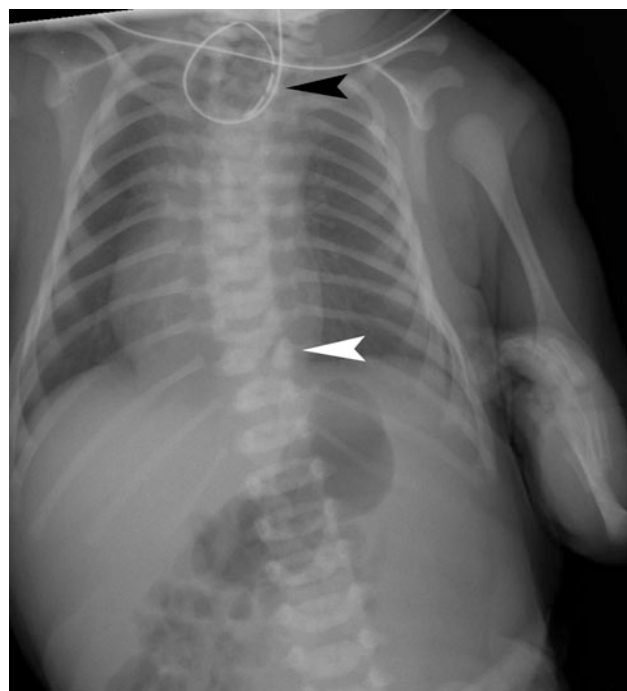


**Fig. 5** VACTERL association. Notice the vertebral segmentation anomaly (white arrowhead). An enteric tube is coiled in the atretic proximal esophagus (black arrowhead) and there is gas in the bowel consistent with esophageal atresia with a tracheoesophageal fistula. The patient also has a deformity of the left upper extremity

association may be suggested by a dilated esophagus, absent bowel gas, and vertebral anomalies (Fig. 5). Rib anomalies can be associated with conditions with restrictive physiology such as asphyxiating thoracic dystrophy and thanatophoric

dwarfism. In cases where the gestational age is unknown or where the provided history is limited, examination of the humeri may help, as the proximal humeral epiphysis is ossified in 80 % of term infants.

## 4 Medical Disease

### 4.1 Transient Tachypnea of the Newborn

Transient tachypnea of the newborn (TTN), also known as “wet lung,” is a common cause of respiratory distress in infants who are either near-term, term, or postterm. It is secondary to retention of fetal fluid in the newborn’s lung and occurs with an incidence of 5.9 % (Tutdibi et al. 2010).

The production of fetal lung fluid decreases as gestation approaches full term. The remaining fluid is cleared from the lungs during labor by active resorption of fluid from the air spaces through epithelial sodium channels. Hormones, including epinephrine, glucocorticoids, and thyroid hormones released during the stress of labor, as well as inhaled oxygen in the postnatal period trigger this resorptive process (Barker and Olver 2002). The removal of lung fluid is practically completed by 2 h of life (Aherne and Dawkins 1964). If the epithelial sodium transport mechanism is immature or the lungs are not exposed to the stress of labor, fluid resorption may be inadequate. The retained fluid in the interstitium leads to decreased compliance of the lungs. The majority of this fluid is removed from the interstitium via the pulmonary veins and lymphatics (Humphreys et al. 1967; Bland et al. 1982). Epinephrine has also been demonstrated to cause the release of surfactant (Lawson et al. 1978), which increases pulmonary compliance and decreases the effect of any retained fluid. Pressure transmitted to the lungs by compression of the chest wall during delivery with resultant clearance of fetal lung fluid via the tracheobronchial tree, the so-called “vaginal squeeze” contributes minimally to removal of this fluid.

Transient tachypnea of the newborn is seen more often in patients that are born by cesarean section, especially elective cesarean section without preceding labor. It is also seen more commonly in infants of mothers who have been sedated, in infants of diabetic mothers with poor glucose control and in infants of mothers with asthma, in large or small for gestational age infants, and in male infants (Schatz et al. 1991; Persson and Hanson 1998; Tutdibi et al. 2010). The severity of TTN also correlates with elective cesarean section and shorter duration of labor as well as lower gestational age (Tutdibi et al. 2010).

Infants with TTN present with signs of respiratory distress and they may require supplemental oxygen. More severe complications including pneumothorax, the need for positive pressure ventilation or extracorporeal membrane oxygenation, and death have been recorded (Ramachandrapa and Jain 2008). The condition is usually self-limiting, most patients recovering in 24–72 h, but occasionally patients need longer to become asymptomatic. The majority of patients with TTN recover fully without long-term morbidity,

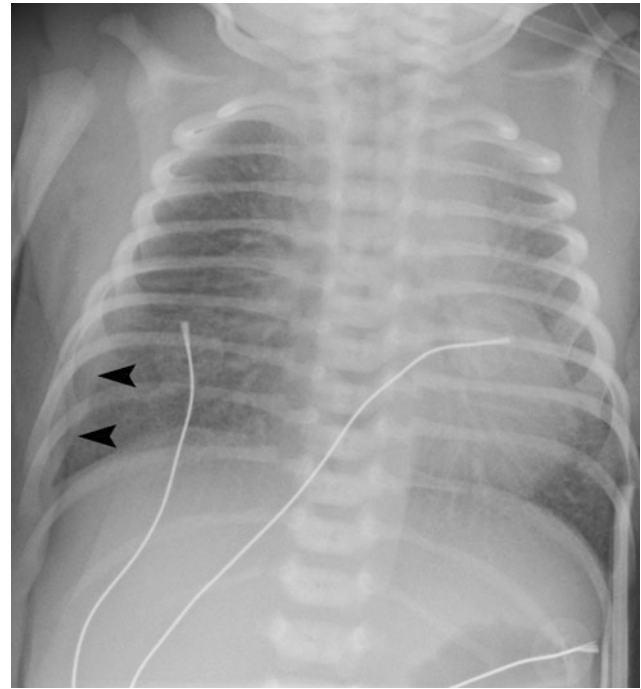


**Fig. 6** Term infant with transient tachypnea of the newborn. The lungs are well inflated with prominent interstitial opacities radiating from the hila. There is a small right pleural effusion (arrowheads)

although some studies have shown an increased incidence of childhood asthma in these patients (Birnkranz et al. 2006).

Transient tachypnea of the newborn is a clinical diagnosis and radiographs of the chest are primarily performed in these infants to exclude other causes of respiratory distress. On imaging, the lungs are well inflated. Symmetrically prominent interstitial opacities radiating from the hila are most commonly seen (Fig. 6). Diffuse fine granular opacities may be present bilaterally and can be confused with RDS if attention is not paid to the patient’s gestational age and the degree of inflation. Small pleural effusions may be evident, another finding not seen in RDS (Fig. 7). A follow up radiograph is usually not indicated as the patients clinically improve, but if performed it demonstrates rapid clearance of the radiographic abnormalities (Swischuk 1970; Wesenberg et al. 1971).

### 4.2 Respiratory Distress Syndrome

Respiratory Distress Syndrome (RDS) is a disease of neonates resulting from surfactant deficiency. RDS is primarily a disease of premature infants born at less than 36 weeks of gestation, although it can rarely be seen in term infants and also in infants of diabetic mothers with poor glucose control. Other factors that increase the risk of developing RDS include intrapartum asphyxiation, multiple gestation births,

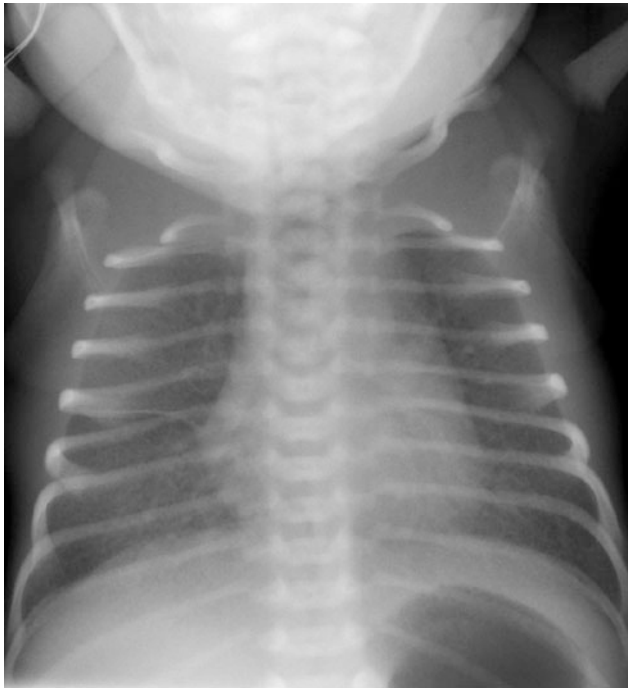


**Fig. 7** Term infant with transient tachypnea of the newborn. The appearance could be confused with respiratory distress syndrome as there are fine granular opacities. However, the lungs are well inflated and there is a small amount of pleural fluid along the minor pulmonary fissure

sepsis, and maternal and fetal hemorrhage. Male and Caucasian infants have an increased incidence of RDS (Anadkat et al. 2012). The lower the gestational age, the greater the incidence of RDS; it occurs with an incidence of 93 % in infants less than 28 weeks gestation (Stoll et al. 2010), 10 % at 34 weeks, and 0.3 % at greater than 38 weeks gestation (Hibbard et al. 2010).

Alveoli begin to form during the later part of the canalicular stage of lung development, at about 24–28 weeks gestation (Agrons et al. 2005) and are lined by Type II pneumocytes which express surfactant, a complex lipoprotein, into the alveoli. Surfactant becomes activated when it combines with surface surfactant proteins which are also produced by Type II pneumocytes. This activated surfactant reduces surface tension within the alveoli, not only preventing them from collapsing but also allowing collapsed alveoli to expand with less applied force. In preterm infants, an insufficient amount of surfactant results in collapse of the alveoli and atelectasis with resultant development of hypoxia and acidosis. An inflammatory reaction ensues, often exacerbated by oxygen therapy and barotrauma from positive pressure ventilation. This inflammation results in damage to both the respiratory epithelium and capillary endothelium with loss of integrity of these structures. Interstitial edema ensues along with formation of a membrane along the terminal bronchioles and alveolar ducts

(Stocker 1992). These hyaline membranes prevent gas exchange and result in ventilation–perfusion mismatching, leading to hypoxia and acidemia. Over time this can lead to arteriolar vasoconstriction and pulmonary hypertension.

Clinically, infants become symptomatic soon after birth and develop progressive worsening of symptoms over the first 48 h of life with signs of respiratory distress. The increased effort required for breathing leads to fatigue often necessitating support with positive pressure ventilation. The natural history for the majority of infants with uncomplicated RDS is gradual improvement as endogenous surfactant production is induced. Superimposed neonatal pneumonia, a patent ductus arteriosus, persistent pulmonary hypertension, and sepsis can all lead to prolongation of symptoms and a more complicated clinical course, including the development of an air leak. Long term, the infants are at risk of developing bronchopulmonary dysplasia.

The administration of steroids to the expectant mother for 12–36 h while in preterm labor has been shown to accelerate lung maturation in fetuses over 28 weeks gestation with decreased severity of RDS (Liggins and Howie 1972). A similar decrease in the severity of RDS has not been shown to occur in infants born between 24 and 28 weeks gestation following prenatal steroid administration to the mother (Garite et al. 1992). However, infants born at this gestation have been shown to have a reduced incidence of other diseases of prematurity following steroid administration, such as necrotizing enterocolitis, high-grade intracranial hemorrhage, and also decreased mortality (Crowley et al. 1990). A further reduction in the severity of RDS can be achieved by the administration of exogenous surfactant to the neonate via an endotracheal tube (Suresh and Soll 2005). Exogenous surfactant therapy results in decreased surface tension in the alveoli and subsequent lessening of respiratory symptoms as the work of breathing lessens. In addition, the infant does not require as high concentrations of therapeutic oxygen or as high positive airway pressures if they are being mechanically ventilated.

The classic description of RDS on radiographs is diffuse fine granularity bilaterally (Fig. 8), effacement of normal pulmonary vascularity, and central air bronchograms. Untreated lungs are low in volume due to the diffuse acinar collapse (Fig. 9), although this is less commonly seen now as patients are usually intubated, receive positive pressure ventilation and are administered surfactant prior to an initial radiograph. Occasionally this may be more severe with near complete whiteout of the lungs (Fig. 10). Following administration of surfactant and application of positive airway pressure, these appearances may change, with improved lung volumes and clearance of the diffuse granularity (Fig. 11). This improvement can be rapid and can result in complete clearance, partial and symmetric clearance, or patchy and asymmetric clearance (Dinger et al. 1997;



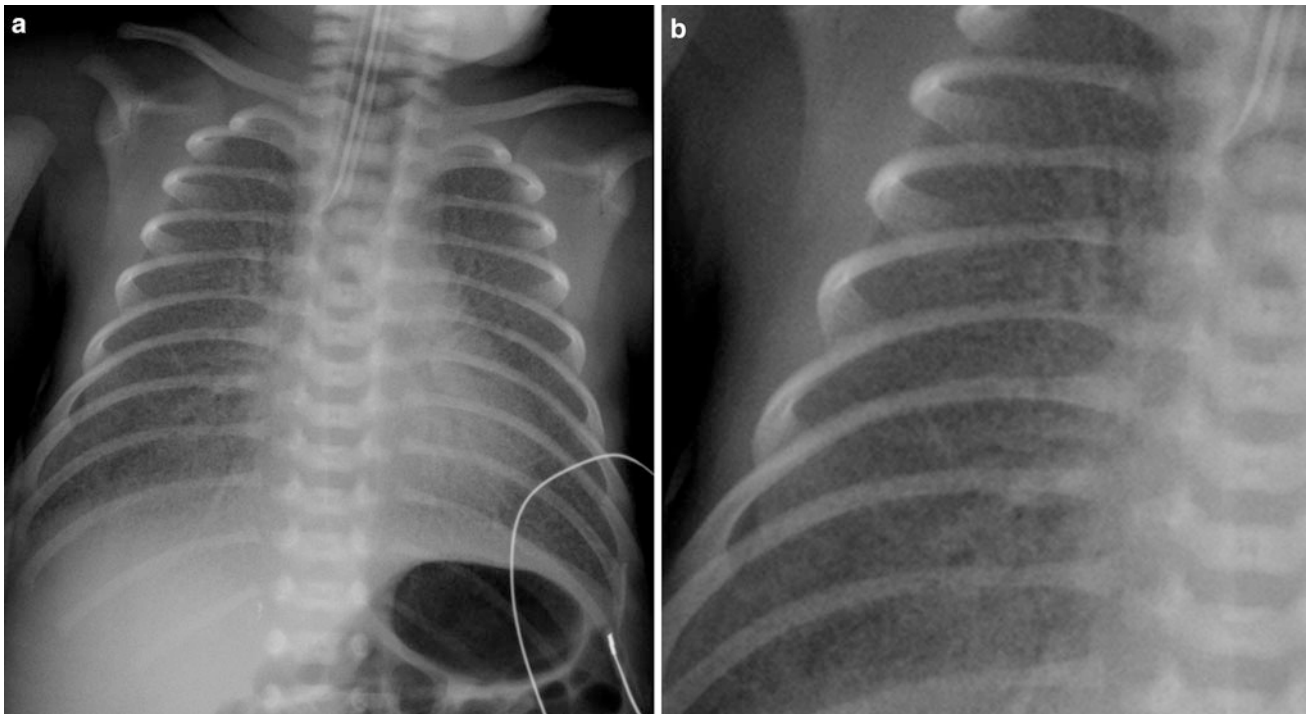


**Fig. 8** Newborn with respiratory distress syndrome. **a** There are hazy opacities diffusely distributed bilaterally. **b** The granular nature of these opacities is well seen on the magnified image



**Fig. 9** Newborn with untreated respiratory distress syndrome. The lungs are low in volume with increased density bilaterally and subtle central air bronchograms

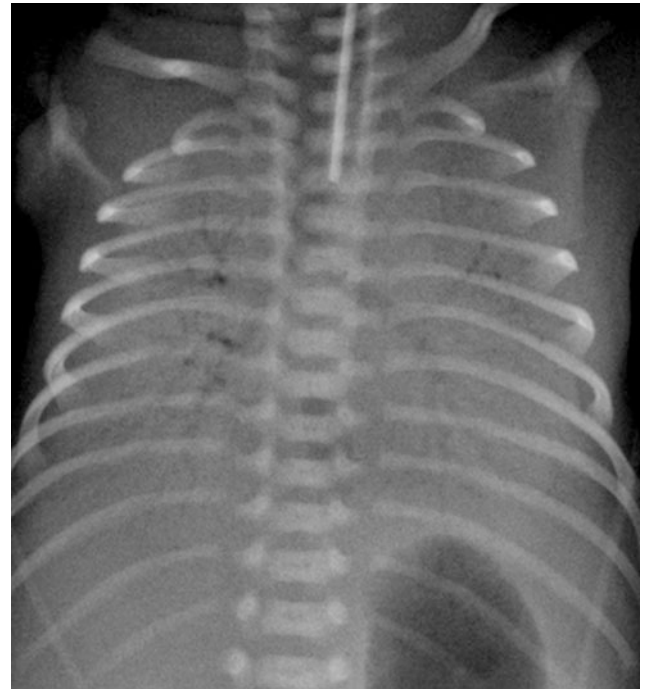


**Fig. 10** Newborn with a “whiteout” appearance from respiratory distress syndrome. The lungs are densely opacified, obscuring the cardiac and diaphragmatic contours, and there are prominent air bronchograms bilaterally

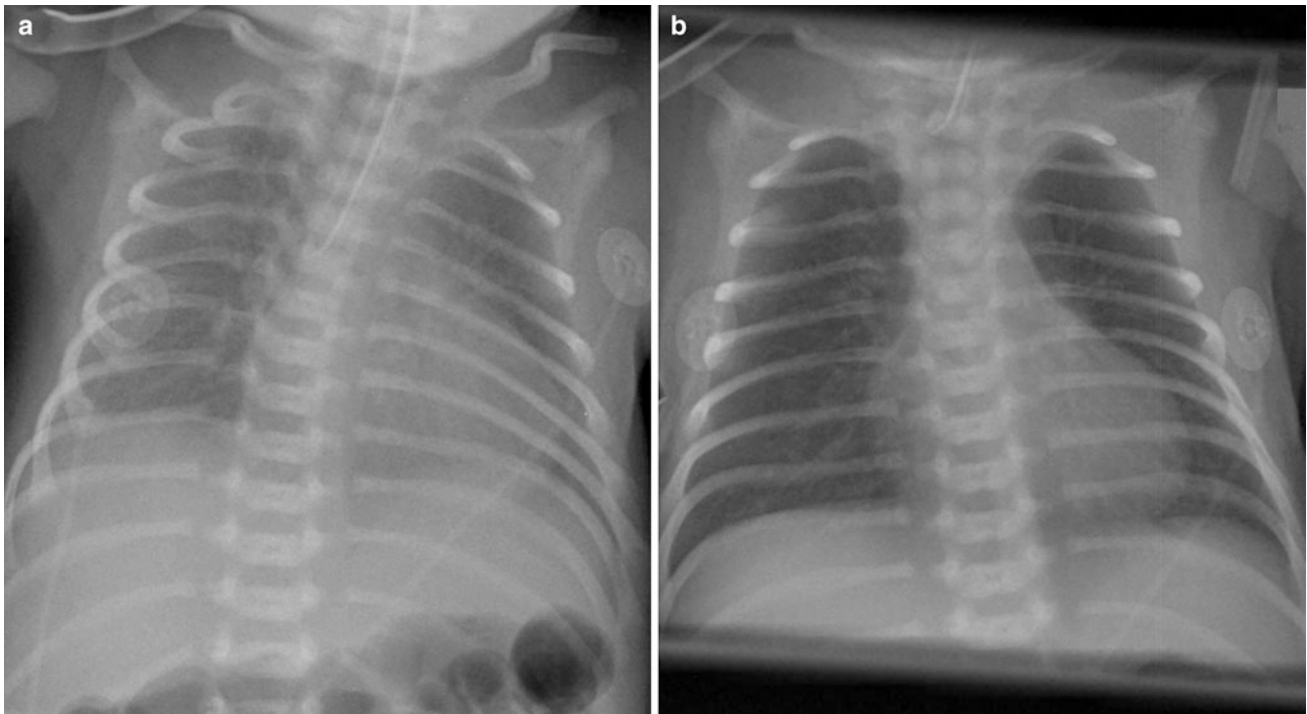


**Fig. 11** Effect of surfactant administration. **a** Initial radiograph of a newborn with respiratory distress syndrome (RDS) taken following intubation. Fine granular opacities are present bilaterally. **b** Radiograph

taken 12 h later demonstrates rapid clearing of these opacities following the administration of surfactant

Slama et al. 1999), which may reflect uneven distribution of the administered surfactant, insufficient surfactant administration, and regional differences in aeration (Slama et al. 1999) (Fig. 12). This uneven clearance can mimic other entities such as neonatal pneumonia. Over time, the radiographic appearance may reflect complications of RDS and prematurity such as an air leak phenomenon, superimposed infection, chronic lung disease related to the surfactant deficiency, i.e., bronchopulmonary dysplasia, persistent pulmonary hypertension, and edema. This edema can sometimes be severe and hemorrhagic and is secondary to a left-to-right shunt through a patent ductus arteriosus. This can occur rapidly as pulmonary arterial blood pressure decreases (van Houten et al. 1992). With treatment, localized hyperinflation can rapidly occur, mimicking air leaks (Cleveland 1995).

Very immature infants, less than 27 weeks gestation and weighing less than 1,000 g, may develop mild haziness bilaterally which clears with surfactant therapy. Subsequently, these infants may again develop mild diffuse haziness bilaterally, thought to reflect seepage of lung fluid into the interstitium through damaged arteriolar basement membranes, the so-called “leaky lung” (Swischuk et al. 1996). Because these infants are extremely immature their

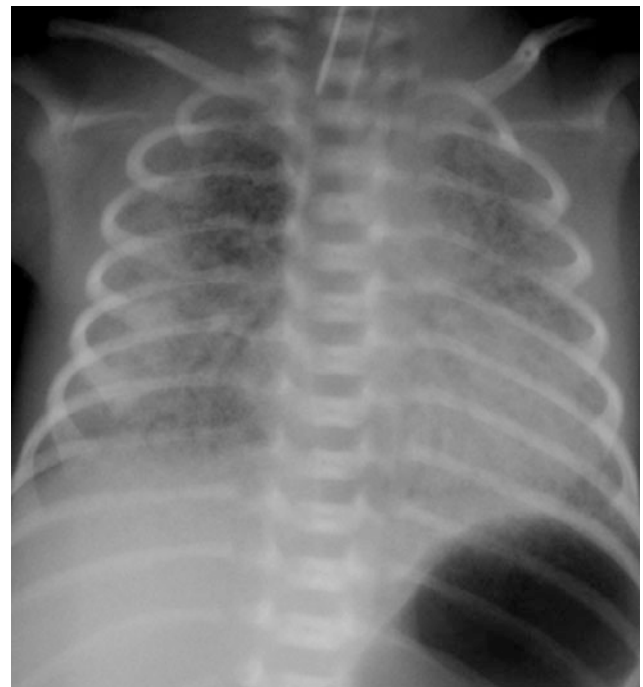


**Fig. 12** Newborn premature infant with uneven aeration following the administration of surfactant. There is relative lucency in the right upper lobe and relatively increased density in both lung bases



**Fig. 13** Early development of chronic lung disease in a premature infant who is now 10 days of age. The lungs are hyperinflated and there are coarse reticular opacities bilaterally with intervening lucencies. These findings are typical of chronic lung disease

lungs are hypoplastic with a deficient number of alveoli and as a result they often require prolonged positive pressure ventilation and high oxygen concentrations. The resultant barotrauma can lead to the early development of coarse irregular reticular opacities bilaterally consistent with chronic lung disease (Cleveland 1995) (Fig. 13).

Respiratory Distress Syndrome was formerly known as Hyaline Membrane Disease, a term that is no longer favored as hyaline membranes are seen in other neonatal lung diseases and are not specific to RDS. It has been suggested that RDS is also a nonspecific descriptive term that could describe the clinical appearance of a number of respiratory illnesses and it has been proposed that the term Surfactant Deficiency Disease be used as this would more accurately reflect the underlying etiology (Swischuk and John 1996).

### 4.3 Bronchopulmonary Dysplasia

Bronchopulmonary dysplasia (BPD) is a chronic disorder of the lungs most commonly seen in low birth weight infants who were born prematurely. The pathogenesis of BPD is not completely understood but is complex and multifactorial in origin. Aside from prematurity, mechanical ventilation, and oxygen therapy, a number of other factors are known to contribute to the development of BPD including a patent ductus arteriosus or fluid overload, inflammation

(alone or associated with infection), poor nutrition, and genetics (Bancalari et al. 2003). Infection may result from chorioamnionitis, may be acquired during delivery, or may be nosocomial.

Bronchopulmonary dysplasia was originally described as a disease of premature infants who were treated with oxygen and mechanical ventilation (Northway et al. 1967). The effects from the surfactant deficiency coupled with the ventilator-induced lung injury and the further damage from oxygen toxicity resulted in changes of alveolar septal fibrosis, alveolar cell hyperplasia, bronchiolar squamous metaplasia, and necrotizing bronchiolitis (Stocker 1986; Husain et al. 1998). This resulted in heterogeneous airway and parenchymal disease with hyperinflated but otherwise normal alveoli alternating with alveoli that are scarred to varying degrees along with smooth muscle hypertrophy and airway damage.

The patient population in this original description of BPD presented with severe RDS, had an average weight of 1,894 g and a gestational age of 33 weeks (Northway et al. 1967). Radiographically, this “old” BPD has four stages of development. Stage I (at 2–3 days) has changes of RDS with a diffuse granular pattern and central air bronchograms. Stage II (at 4–10 days) demonstrates almost complete opacification bilaterally. Stage III (10–20 days) shows small rounded lucencies with intervening areas of irregular opacification, while Stage IV (>1 month) has further enlargement of the lucent areas and thinning of the intervening linear opacities with hyperinflation of the lungs (Northway and Rosan 1968). These stages are less commonly seen today.

With modern therapy, a similar group of patients to that described in the initial description of BPD would have an excellent prognosis and would be unlikely to develop BPD. However, the incidence of BPD is not decreasing. This reflects significantly increased survival rates of neonates of less than 28 weeks gestation. Now the population that most commonly develops BPD has a gestational age of 22 to 28 weeks and weighs as little as 500 g. The lungs of a patient with this “new” BPD are at a more immature and simplified stage of development with fewer alveoli. Exposure to the extrauterine environment leads to a complete or partial arrest in acinar development (Husain et al. 1998). This extreme immaturity coupled with the frequent administration of prenatal maternal glucocorticoid therapy and postnatal extrinsic surfactant to the infant as well as less aggressive positive pressure ventilation and oxygen therapy, has resulted in a different histological and radiographic appearance and has also resulted in changing definitions of BPD. Currently the most widely accepted definition of BPD was issued in 2001 following a workshop held by the National Institute of Child Health and Human Development, the National Heart, Lung and Blood Institute, and the Office of Rare Diseases (Jobe and Bancalari 2001). This defines BPD as the need for supplemental oxygen for at



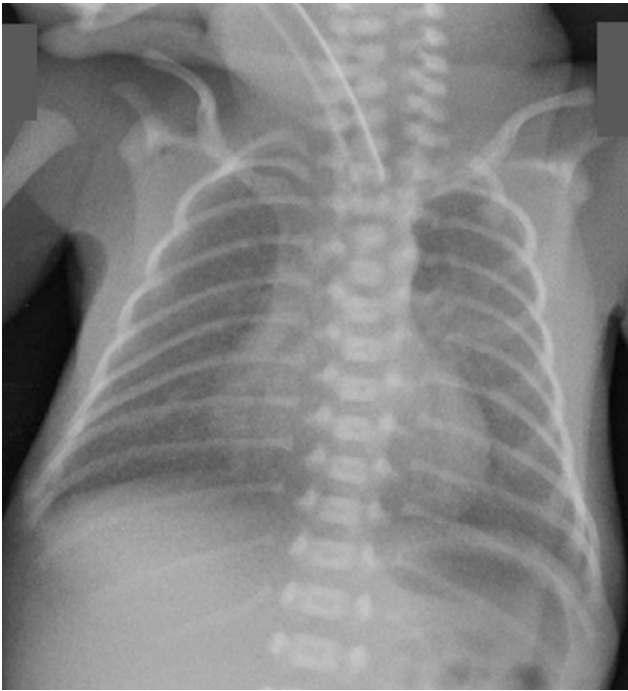


**Fig. 14** Newborn 24 week gestation premature infant, first day of life. Mild hazy opacities are seen diffusely throughout both lungs

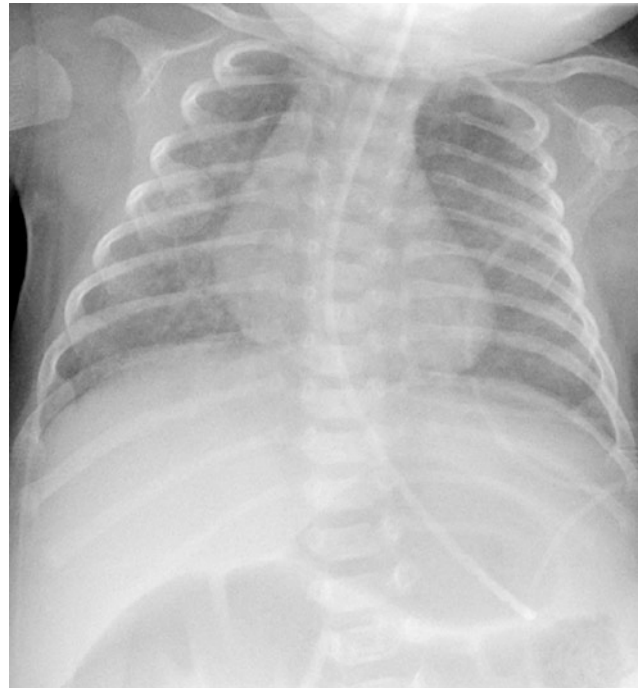


**Fig. 15** Former 25 week gestation premature infant who is now 70 days old. Note the diffuse hazy opacification throughout both lungs. This is consistent with “new” bronchopulmonary dysplasia

least 28 days following birth and its severity is graded according to the extent of oxygen therapy and other respiratory support at 36 weeks postmenstrual age (gestational age at birth plus chronologic age) or at discharge, whichever comes first, if born at <32 weeks gestational age, or at 56 days postnatal age or at discharge, whichever comes first, if born at 32 or >weeks gestational age.

The histology of this “new” BPD in these extremely premature neonates demonstrates fewer but larger alveoli which have a more uniform caliber, with less interstitial inflammation and fibrosis. In these very immature neonates, chest radiographs initially may be clear or may demonstrate subtle diffuse hazy opacities bilaterally (Fig. 14). Over time, because they have fewer alveoli than normal, these neonates often require prolonged ventilator support and oxygen therapy. Although minimized, this support leads to chronic lung changes on chest radiographs. Most commonly this is a diffuse haziness bilaterally (Fig. 15). Less commonly they progress from this diffuse haziness to a more heterogeneous appearance with diffuse cystic lucencies and coarse reticular opacities bilaterally giving a “bubbly” appearance to the lungs similar in appearance to stages III and IV of the original radiographic description of BPD. This has been described as developing within a week of birth (Swischuk et al. 1996) but may also occur later as described in “old” BPD (Fig. 16). This appearance is seen when infants have a difficult post natal course that requires

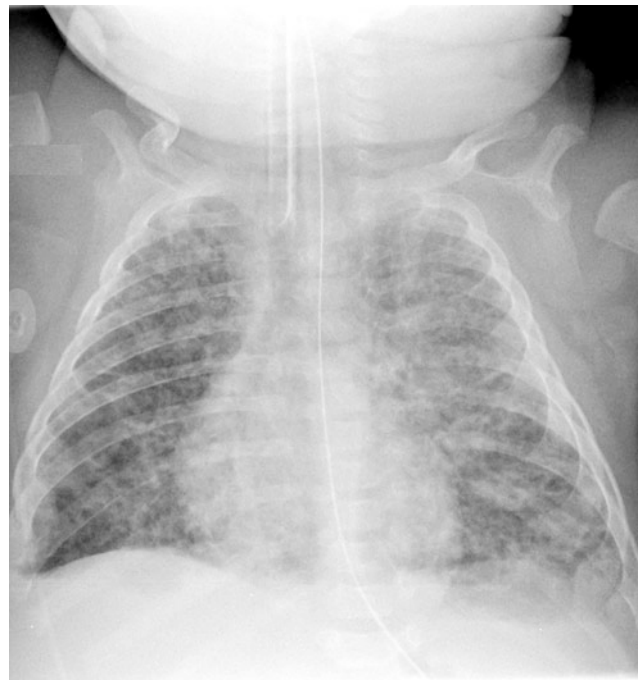


**Fig. 16** Bronchopulmonary dysplasia in a 3-month-old former 24 week gestation infant. The lungs are hyperinflated. Coarse reticular opacities are present bilaterally with intervening small rounded lucencies giving a somewhat “bubbly” appearance to the lungs

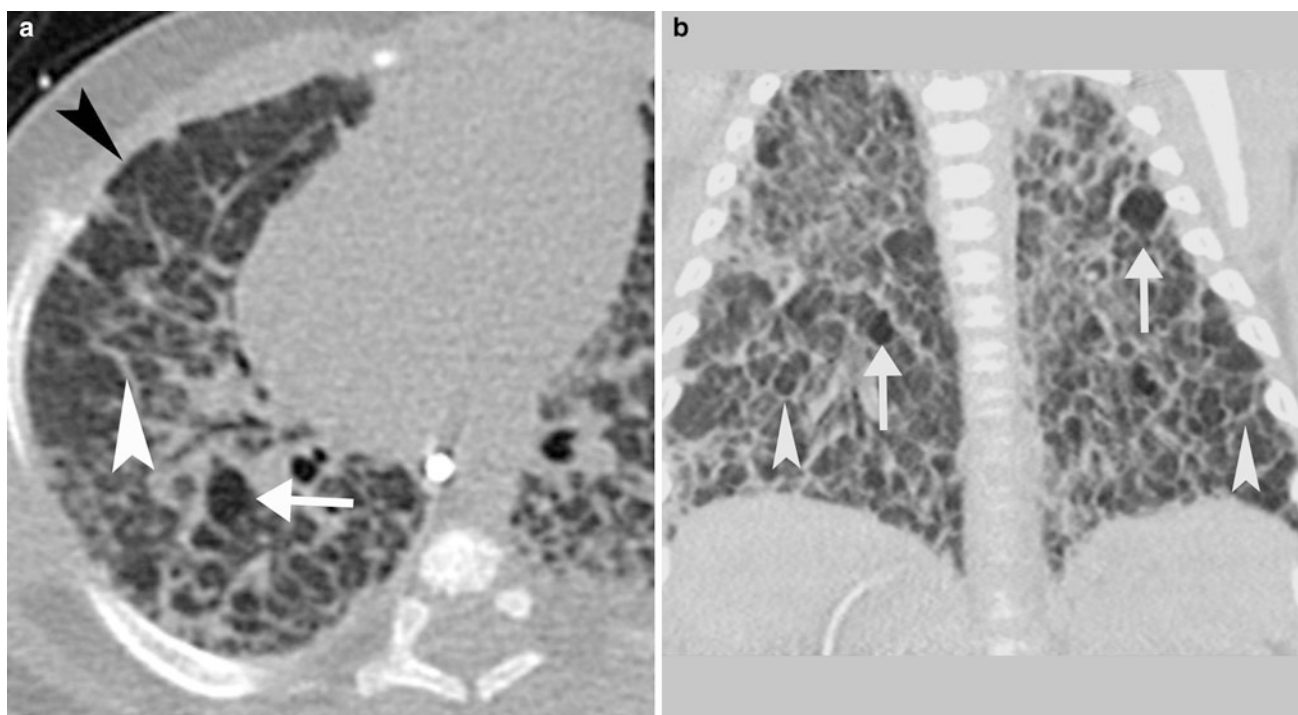


**Fig. 17** CT in a 4-month-old former 24 week gestation infant with BPD. **a** and **b** There are thickened interlobular septa (white arrowhead) surrounding distended secondary pulmonary lobules, some of

which are hyperlucent (arrow). Scattered subpleural cysts (black arrowhead) are also present

intubation and high pressure ventilation and high concentrations of supplemental oxygen.

CT is occasionally performed after the neonatal period in patients with BPD. These studies are sometimes requested in patients with ongoing respiratory difficulty in whom there is concern for a comorbid condition such as aspiration. If performed in infancy or early childhood, BPD will appear as hyperinflated lungs with distended secondary pulmonary lobules that are bounded by thickened interlobular septa (Fig. 17). Small subpleural cysts are frequently present. The distended secondary pulmonary lobules demonstrate air trapping on expiratory images. If imaged later in childhood, patients with longstanding BPD demonstrate overall increased lung volumes with mosaic attenuation and air trapping. There are linear and band-like opacities that represent areas of atelectasis and scarring. Subpleural triangular opacities that sometimes are associated with the linear opacities are thought to represent pseudo-fissuring (Oppenheim et al. 1994) (Fig. 18).

#### 4.4 Meconium Aspiration Syndrome

Meconium aspiration syndrome (MAS) is defined as respiratory distress in an infant born through meconium-stained amniotic fluid with characteristic radiological changes and

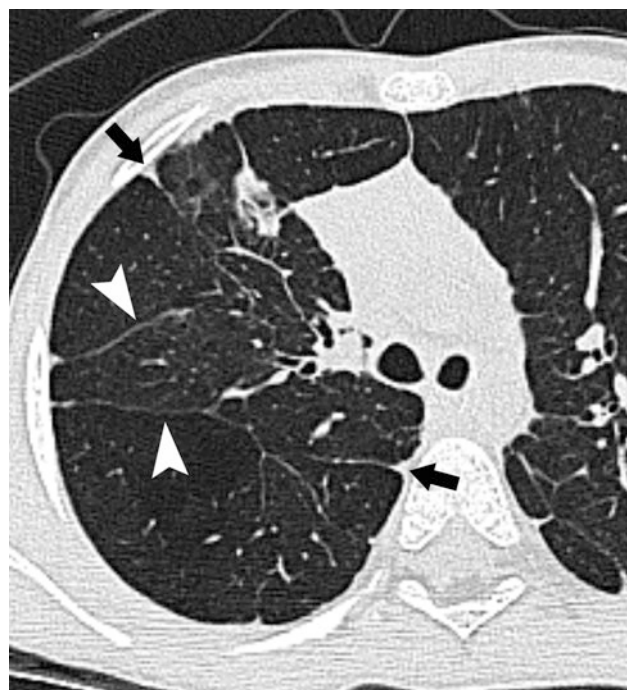


**Fig. 18** CT in a 5-year-old former 24 week gestation premature infant. Axial CT images demonstrates multiple linear bands (white arrowheads), many extending to the pleural surface and many associated with triangular pleural-based opacities (black arrowheads). Subtle mosaic attenuation of the parenchyma is also present

whose symptoms cannot be otherwise explained (Wiswell et al. 1990). MAS occurs when meconium is aspirated into the lungs before or during labor and delivery. Staining of amniotic fluid is seen in 8–20 % of births, with MAS developing in approximately 20 % of these cases (Usta et al. 1995).

Meconium aspiration syndrome is a disease of term and especially of postterm neonates and of small for gestational age infants (Clausson et al. 1999). Passage of meconium in utero is rare before 37 weeks of gestation due to immaturity of the colon (Matthews and Warshaw 1979). Infants with MAS born after 40 weeks of gestation are more likely to require intubation than those born earlier (Dargaville et al. 2006). Factors predisposing to in utero passage of meconium include advanced maternal age, placental insufficiency, fetal distress, oligohydramnios, preeclampsia, and maternal drug use, particularly of cocaine (Swarnam et al. 2012).

Aspiration of meconium affects the lungs in a number of ways. If an airway is completely occluded, this can result in atelectasis. Partial occlusion of the airway may result in a ball-valve phenomenon with hyperinflation of the portion of the lung that is distal to the meconium plug. This can result in an air leak phenomenon if there is progressive overinflation. Although the primary constituent of meconium is water, it also contains many compounds such as pancreatic juices, bile, and gastrointestinal secretions that irritate the airways and alveoli, resulting in a chemical pneumonitis. Although the aspiration may be focal, the influx of inflammatory cells and chemical mediators in inflammation such as interleukins and tumor necrosis factors can induce a more widespread pneumonitis involving much of the lung (Cleary and Wiswell 1998). Surfactant lining the alveoli is deactivated by meconium which also may decrease the amount of surfactant produced (Dargaville et al. 2001; Janssen et al. 2006). This combination results in surfactant dysfunction, further promoting atelectasis and diminished aeration. The resultant hypoxia, hypercapnia, and respiratory acidosis lead to pulmonary arterial vasoconstriction. This may be compounded by the effects of preexisting chronic intrauterine hypoxia leading to thickening of the arteriolar walls. The increased resistance in the pulmonary vascular bed can result in persistent pulmonary hypertension of the newborn (PPHN), further worsening the degree of hypoxia and difficulty with ventilation.

Supplemental oxygen is the mainstay of therapy and may be all that is required (Singh et al. 2009) but more aggressive support is not unusual; intubation and mechanical ventilation is required in up to one-third of patients (Cleary and Wiswell 1998). In cases where adequate oxygenation cannot be achieved with mechanical ventilation, extracorporeal membrane oxygenation may be needed. Surfactant therapy, corticosteroids, and nitric oxide have been used as adjuvant therapies (Dargaville 2012).

Over the past decades, a reduction in the risk of MAS has been attributed to better obstetric practices, in particular, to avoidance of postmaturity and to expeditious delivery when fetal distress has been noted (Yoder et al. 2002). However, the mortality in patients with MAS remains considerable at 7 % (Dargaville et al. 2006), usually related to pulmonary hypertension and cerebral hypoxic ischemic injury. Approximately 10 % of patients intubated for MAS will develop a pneumothorax. This is an indicator of disease severity with a mortality rate of 42 % (Dargaville et al. 2006).

The most significant long-term morbidity in MAS is neurological injury. A diagnosis of MAS in the neonatal period confers a considerable risk of cerebral palsy (5–10 %) and global developmental delay (15 %) (Beligere and Rao 2008). Pulmonary sequelae are also seen. In the first year of life, up to half of infants will demonstrate respiratory symptoms with wheezing and coughing (Yuksel et al. 1993). Older children may exhibit evidence of airway obstruction, hyperinflation, and airway hyperreactivity, but appear to have normal aerobic capacity (Swaminathan et al. 1989).

On imaging a variety of appearances may be seen. The lungs are usually well inflated. Some cases may demonstrate symmetric fine reticular opacities bilaterally or may have more streaky opacities in the perihilar regions bilaterally, a radiographic appearance that can be difficult to differentiate from TTN (Fig. 19). In more severe cases, the lungs are hyperinflated with coarser linear and band-like opacities bilaterally reflecting atelectasis alternating with lucent areas corresponding to air trapping (Fig. 20). More ill-defined confluent opacities can be seen and relate to pneumonitis (Fig. 21). Findings may be symmetric but can be quite asymmetric. Small pleural effusions may be present (Gooding and Gregory 1971) (Fig. 22). Because of difficulty with ventilation and adequate oxygenation, air leaks are not uncommon and result in pneumothorax and/or pneumomediastinum in approximately 10 % of patients (Wiswell et al. 1990). Depending on the severity of the aspiration, the findings may resolve within 48 h or they may persist with more gradual improvement. However, the severity of the appearances on imaging does not always correlate with the clinical findings.

## 4.5 Neonatal Pneumonia

Neonatal pneumonia results from infection that can arise by a number of routes. Infection can be acquired in utero either transplacentally or via an ascending infection of amniotic fluid, in the perinatal period by inhalation of infected material during or immediately following birth, or in the neonatal period. Predisposing factors to neonatal pneumonia



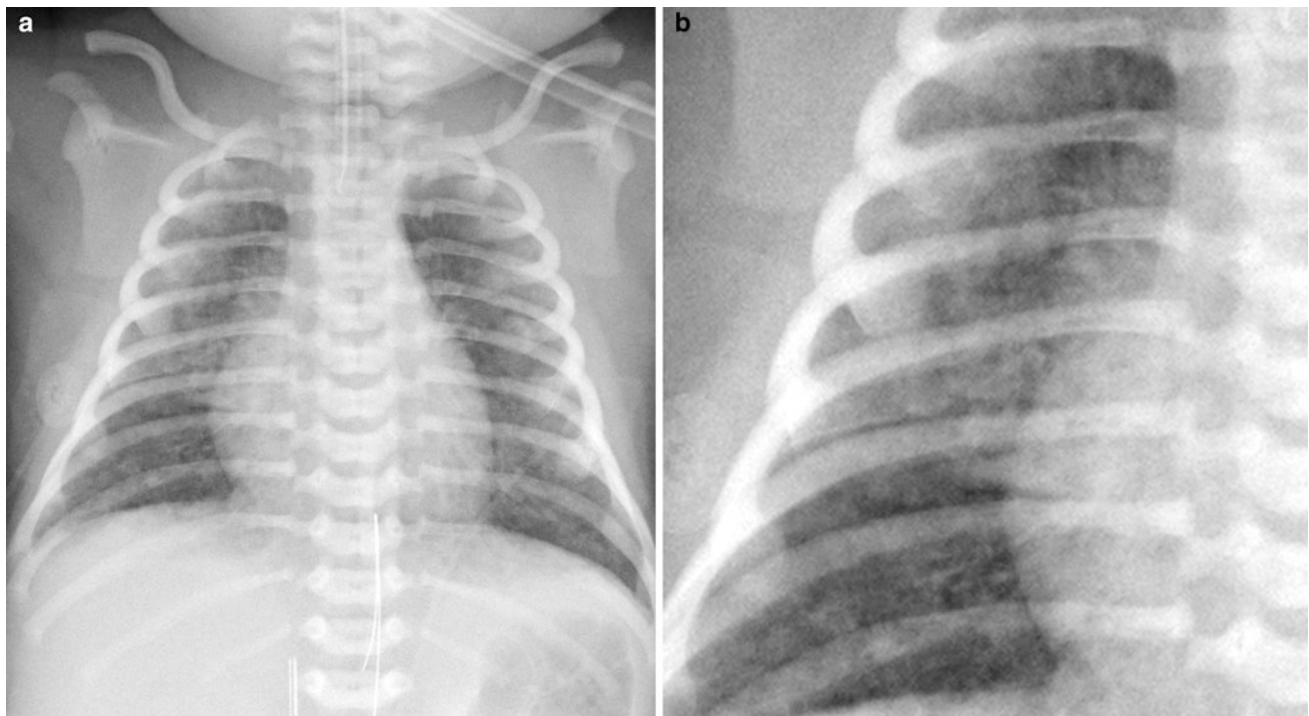


**Fig. 19** Mild changes of meconium aspiration. **a** and **b** Mildly coarsened reticulonodular opacities are present bilaterally, most prominent in the right perihilar region. Without the history of

meconium aspiration the appearance could be mistaken for transient tachypnea of the newborn or neonatal pneumonia

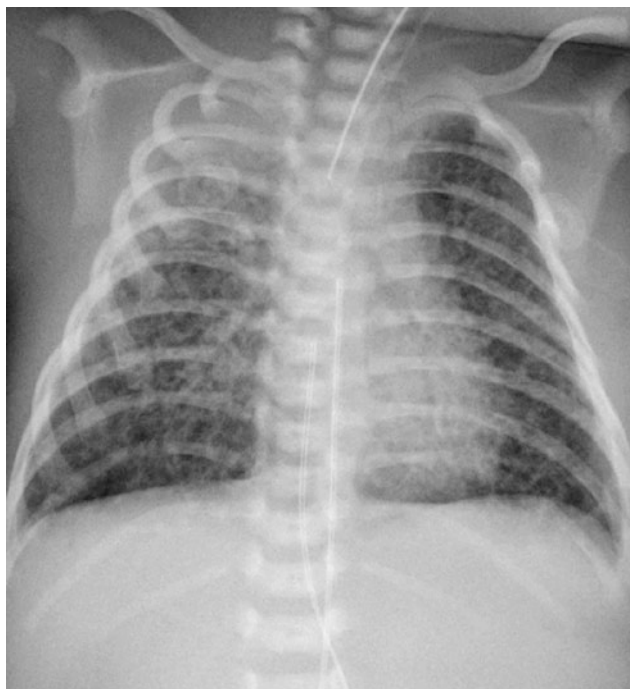


**Fig. 20** Newborn term infant with meconium aspiration. The lungs are hyperinflated. Coarse reticulonodular opacities are present throughout both lungs with more confluent opacification in the right upper lobe

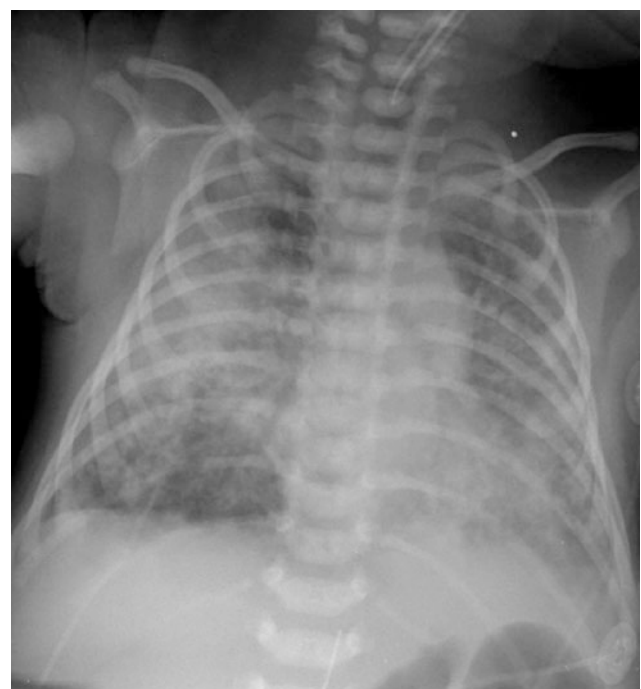


**Fig. 21** Meconium aspiration with pneumonitis. The lungs are diffusely abnormal bilaterally with confluent opacities in the right mid lung and the left lower lobe. These confluent opacities are consistent with areas of pneumonitis and atelectasis



**Fig. 22** Meconium aspiration with an effusion. Coarse reticular opacities are present bilaterally. More focal opacities are present in the peripheral left mid lung and in the left lower lobe with relative lucency at the right lung base suggesting air trapping. In addition, there is a small right pleural effusion (arrowhead)

include prolonged rupture of membranes, chorioamnionitis, maternal vaginal colonization, prematurity, and prolonged hospitalization.

In the developing world, neonatal infection accounts for significant morbidity and mortality. WHO figures estimates 800,000 neonatal deaths per year from respiratory infection in developing nations (Garenne et al. 1992). The estimated incidence in developed countries is less than 1 % in term infants and closer to 10 % in preterm and low birth weight infants (Dennehy 1987).

Neonatal pneumonia is termed as early onset if it manifests within the first 7 days of life, and the majority present within 48–72 h. Early onset pneumonia, especially when presenting in the immediate postnatal period, is often associated with generalized sepsis and a poorer prognosis. Pneumonia occurring beyond 7 days is considered late-onset, is usually not associated with sepsis, and generally has a better prognosis. Bacteria are the cause of most early and late-onset pneumonias.

The majority of early onset pneumonias in term and near-term neonates are caused by group B beta hemolytic streptococcus (GBS), a common colonizer of the female genitourinary tract. The incidence of GBS pneumonia has decreased due to increased testing for GBS colonization of the mother's genitourinary tract and increased use of intrapartum antibiotics (Jeffery and Moses Lahra 1998).

*Escherichia coli* is now the most common cause of pneumonia in very low birth weight infants (<1500 g) (Stoll et al. 2005). Numerous other bacteria can cause ascending infection and include *Hemophilus influenza*, other gram-negative bacilli, *Listeria monocytogenes*, *Enterococcus*, and *Staphylococcus*. In very low birth weight infants, *Ureaplasma urealyticum* is frequently recovered from endotracheal aspirates shortly after birth. It has been associated with the development of early onset of chronic lung disease and a poor prognosis (Kotecha et al. 2004). Viral and fungal organisms are rare causes of neonatal pneumonia. The most common viral pathogens include herpes simplex virus, respiratory syncytial virus, and adenovirus.

Most late-onset pneumonias are also caused by bacteria. These infections are usually nosocomial, especially in pre-term infants, but can also be community-acquired following discharge. Organisms involved include *Pseudomonas aeruginosa*, *E. coli*, *Streptococcus pyogenes*, *Staphylococcus aureus*, and *Streptococcus pneumoniae*. Chlamydia trachomatis, an obligate intracellular parasite, causes a late-onset pneumonia that can manifest between 4 and 12 weeks of age (Hammerschlag 1994).

Early onset neonatal pneumonia can present with non-specific signs of infection, including temperature instability, apnea or tachypnea, tachycardia or bradycardia, hypoglycemia, abdominal distension, and listlessness. More specific signs of respiratory infection including grunting, retractions, and nasal flaring are variably present. Infected neonates may be gravely ill as septicemia is common in early onset pneumonia. In utero infection can result in the infant being still-born.

Chest radiographs in neonatal pneumonia are often non-specific as the appearance can overlap with other neonatal illnesses such as RDS, TTN, and meconium aspiration. The radiographic appearance can also vary depending on the responsible organism. As a consequence, the findings of neonatal pneumonia on imaging can be quite varied and radiographic diagnosis is difficult especially if not correlated with the clinical setting. Unlike pneumonia in older children, an isolated focal consolidation is rare in neonatal pneumonia (Haney et al. 1984). Most commonly, radiographs demonstrate bilateral ill-defined air-space opacities (Fig. 23) but these opacities can be diffuse and homogeneous (Haney et al. 1984). Multifocal coarse opacities may also be seen, similar to meconium aspiration (Fig. 24). A pattern very similar to RDS with diffuse granular opacities with central air bronchograms can be seen, usually with GBS infection (Ablow et al. 1976) (Fig. 25). However, small pleural effusions may be present which suggest infection rather than surfactant deficiency (Leonidas et al. 1977) (Fig. 26). In addition, the lungs are usually well inflated, rather than the low lung volumes seen in RDS (Ablow et al. 1976). Chlamydia trachomatis pneumonia may be preceded by conjunctivitis.

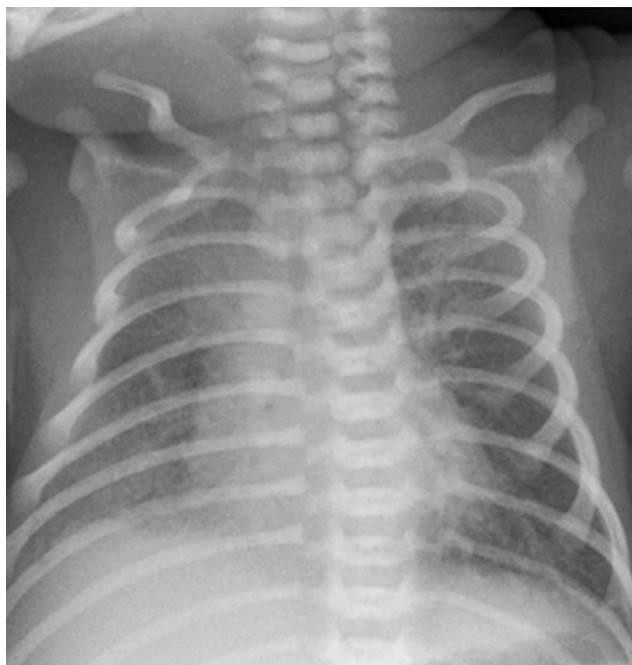


**Fig. 23** Neonatal pneumonia. The patient was born at 39 weeks gestation. The lungs are well inflated and there are diffuse fine reticulonodular opacities bilaterally. More confluent opacities are seen in the bilateral upper and right lower lobes. Blood cultures grew group B streptococcus

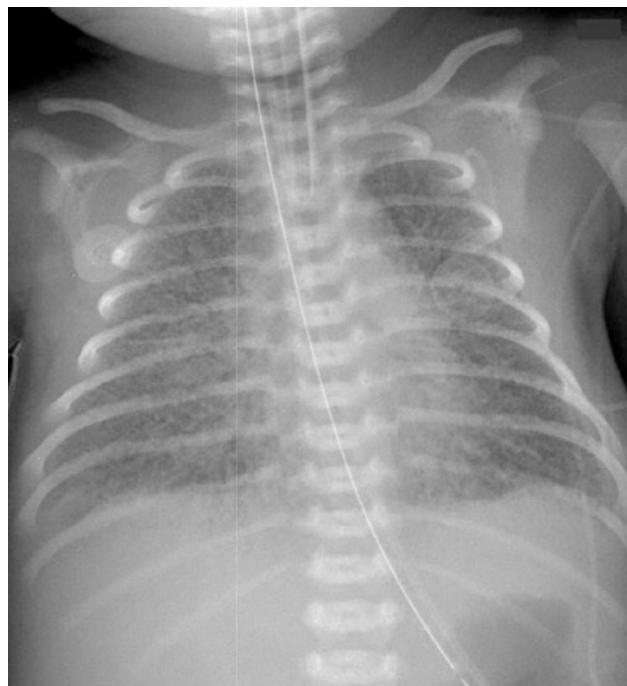


**Fig. 25** Neonatal pneumonia appearing like respiratory distress syndrome. There are diffuse symmetrical fine reticular and granular opacities bilaterally, findings that can be seen with respiratory distress syndrome. However, the patient was a term infant and grew group B streptococcus from blood cultures

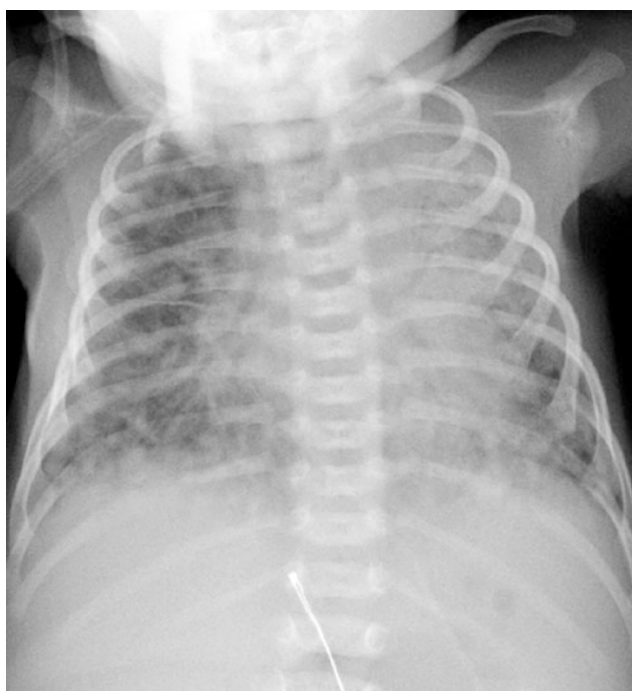


**Fig. 24** Neonatal pneumonia appearing like meconium aspiration. Bilateral coarse reticular and nodular opacities are present diffusely, most confluent in the left upper lobe. Washings from a bronchoalveolar lavage isolated herpes simplex virus

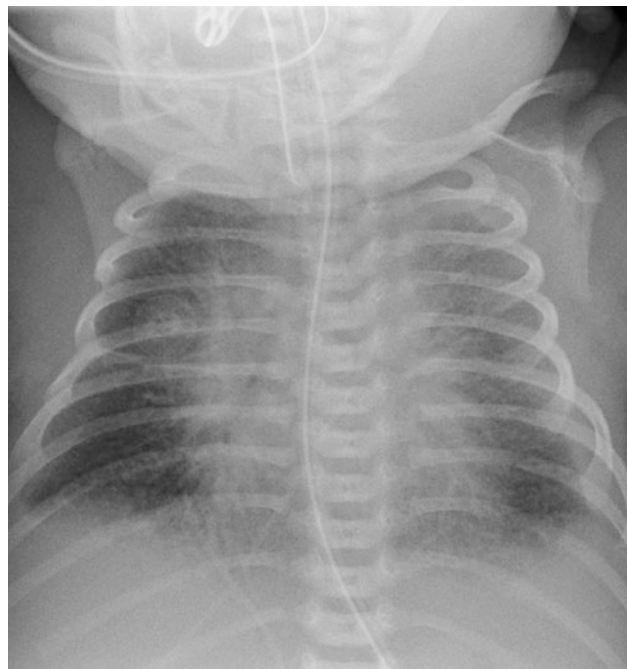


**Fig. 26** Neonatal pneumonia and effusions. Fine reticular and granular opacities are present bilaterally which suggest respiratory distress syndrome. However, there are bilateral pleural effusions which make neonatal pneumonia more likely. Cerebrospinal fluid cultures grew group B streptococcus



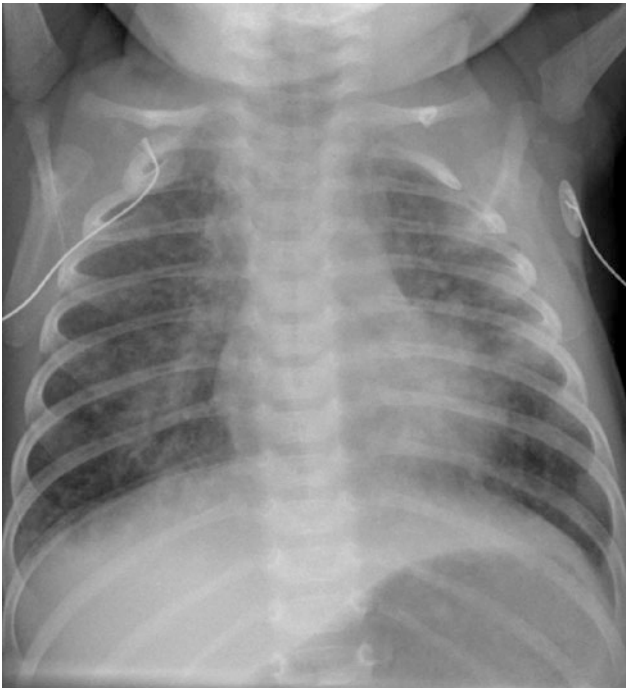


**Fig. 27** Eight week old term female with chlamydia pneumonia. The lungs are hyperinflated and there are coarse reticular opacities bilaterally with more focal opacities in the lingula

Radiographs demonstrate hyperinflation with bilateral ill-defined opacities, especially in the perihilar regions (Hammerschlag 1994) (Fig. 27).

## 5 Air Leak Phenomenon

Pulmonary air leaks occur when air escapes from the lung into surrounding structures or compartments. Airway overdistension results in rupture of the alveoli and passage of air into the perivascular and peribronchial spaces, resulting in pulmonary interstitial emphysema (PIE). Alternatively, it can track peripherally to the pleural surface and rupture into the pleural space to create a pneumothorax or it can track centrally and enter the mediastinum to create a pneumomediastinum. Rarely, the air will track into the pericardial space to form a pneumopericardium, track inferiorly into the abdomen to form a pneumoperitoneum, or enter one of the pulmonary veins and create an air embolus which can be rapidly fatal. An air leak most often occurs as a result of intubation and mechanical ventilation. However, it can also occur in patients who only have had continuous positive airway pressure (CPAP) applied (Fig. 28). Air leaks are most often associated with RDS, meconium aspiration syndrome, and conditions that cause pulmonary hypoplasia.

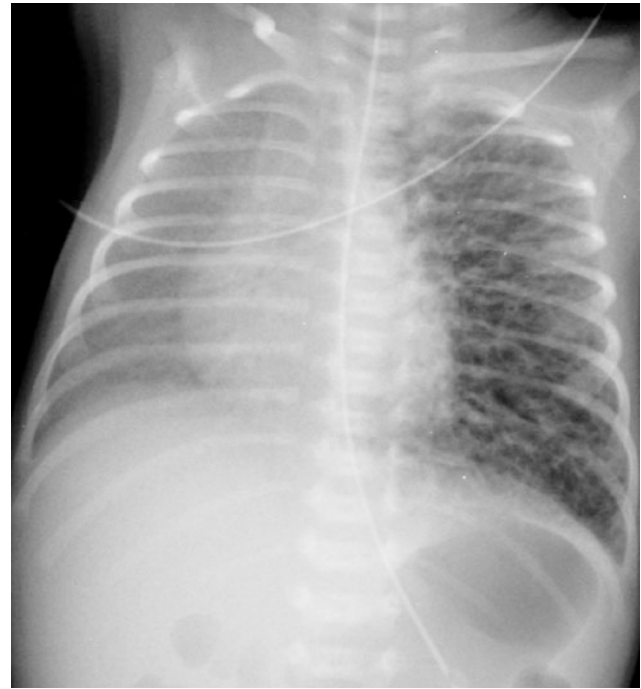


**Fig. 28** Pulmonary interstitial emphysema in a patient on CPAP. Lucencies are seen throughout the left lung with intervening coarse reticular opacities. The patient was on continuous positive airway pressure for respiratory distress syndrome and had never been intubated

### 5.1 Pulmonary Interstitial Emphysema

Pulmonary interstitial emphysema can compress the airways resulting in poorly compliant lungs that are difficult to ventilate as they will not inflate and deflate with respiration. The increased pressure in the interstitium can also compress pulmonary veins resulting in impaired venous return and diminished cardiac output (Plenat et al. 1978).

Radiographically, PIE is seen as tubular lucencies extending towards the mediastinum and small cystic lucencies (Fig. 29). PIE can be unilateral or bilateral, focal or diffuse. Diffuse unilateral PIE can result in mediastinal shift into the collateral hemithorax. Occasionally the small cystic lucencies may coalesce into a larger focal intra-parenchymal lucency termed a pneumatocoele (Fig. 30). Usually PIE resolves over time, but it can persist and form a cystic mass that may result in mass effect and respiratory compromise and mimic a congenital pulmonary airway malformation (Donnelly et al. 2003). Without clinical history and comparing to prior imaging, diffuse PIE may be difficult to differentiate from bronchopulmonary dysplasia.

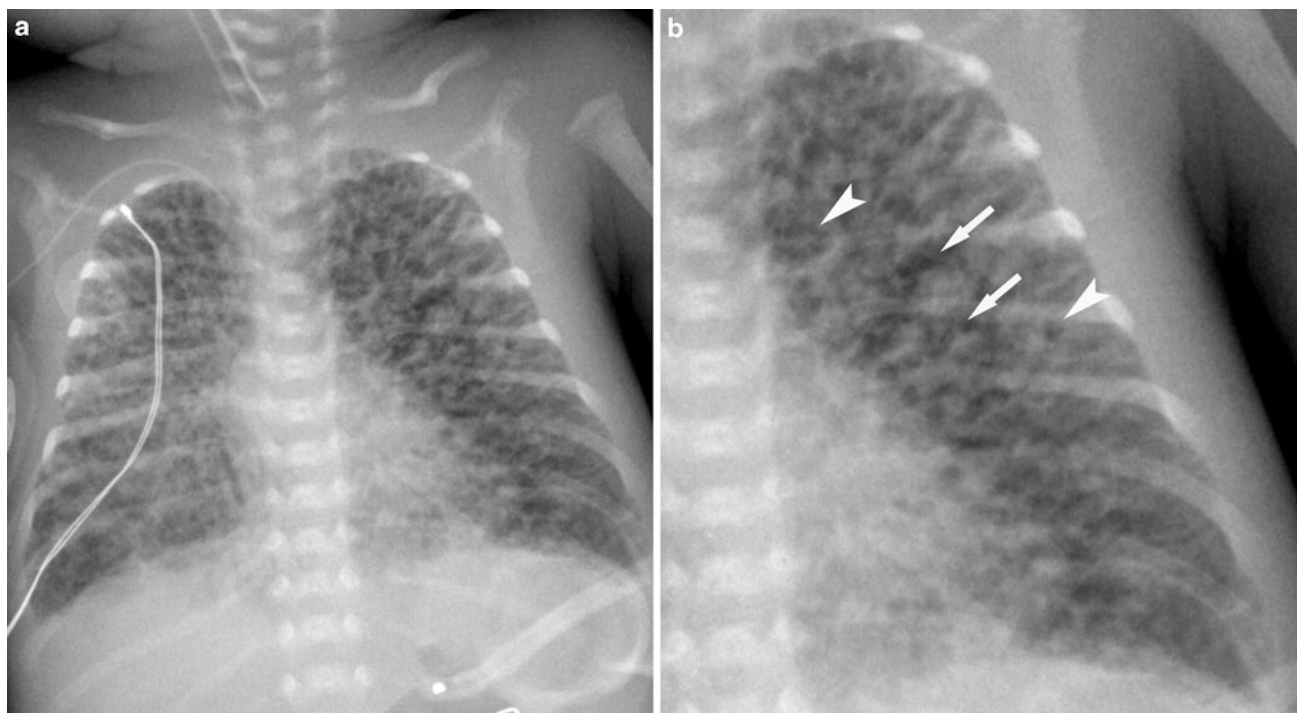


**Fig. 29** Diffuse bilateral pulmonary interstitial emphysema. **a** There are mixed lucencies and streaky opacities diffusely throughout both lungs. **b** On the magnified view, tubular lucencies are seen radiating from the hilum (*arrows*) as well as scattered cystic lucencies (*arrowheads*)

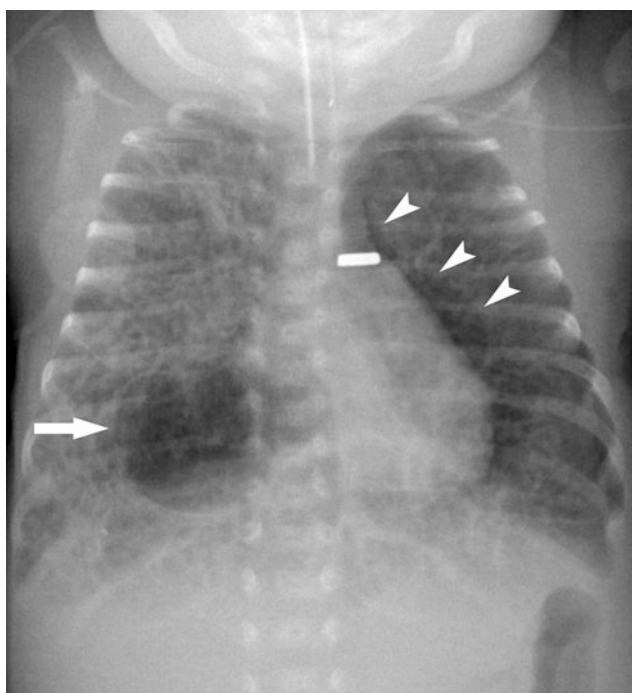


**Fig. 30** Pulmonary interstitial emphysema and a pneumatocele. There is PIE and a rounded lucency in the right lung base consistent with a pneumatocele (*arrow*). There is also a subtle left pneumothorax indicated by overall mild decreased attenuation of the left hemithorax as well as a lucency adjacent to the left heart border (*arrowheads*)

## 5.2 Pneumothorax

When the air leak results in air entering the pleural space, a pneumothorax is formed. The lung collapses toward the hilum and a sharp interface is seen between the collapsed lung and the air in the pleural space. If air enters the pleural space under positive pressure and cannot exit, a tension pneumothorax may develop. This results in deviation of the mediastinum to the contralateral side and flattening or inversion of the ipsilateral hemidiaphragm (Fig. 31). This is a potentially life threatening emergency as systemic venous return may be obstructed by the increased intrathoracic pressure. Obstruction to venous return may result in a narrow appearance of the heart (Fig. 32). Fortunately, large tension pneumothoraces are easily identified. Less easily appreciated are smaller pneumothoraces. This is especially true in neonates in the intensive care setting as these images are obtained with the patient in the supine position. This results in pleural air preferentially collecting anteriorly and medially and an air-pleural interface may not be appreciable at the periphery of the lung (Moskowitz and Griscom 1976). On radiographs, a subtle lucency either focally or diffusely may overlie the lung. Often this lucency is anteromedially positioned and results in sharp margination of the heart, other mediastinal structures or the hemidiaphragm (Fig. 30).

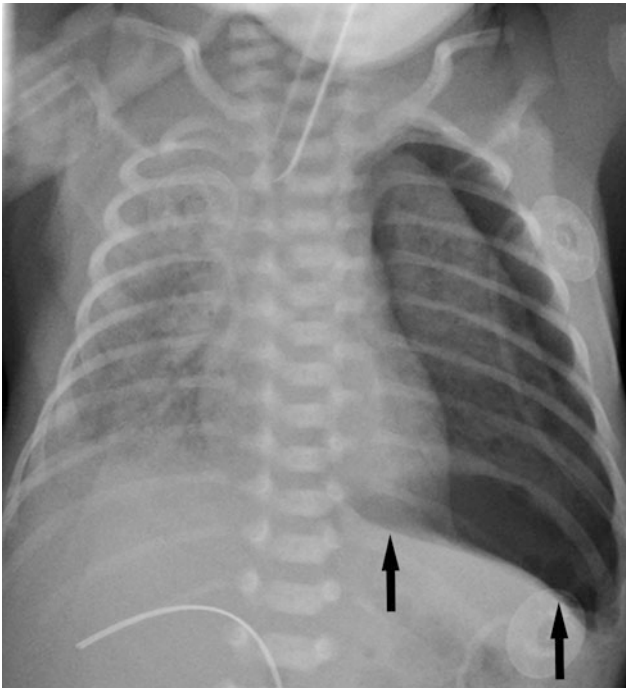


**Fig. 31** Respiratory distress syndrome complicated by a tension pneumothorax. The left hemidiaphragm is flattened (arrows) and the mediastinal structures are displaced into the right hemithorax

Occasionally, the ipsilateral costophrenic angle may be asymmetrically prominent and well-defined, the “deep sulcus sign” (Fig. 33). Confirmation of the presence or absence of a pneumothorax may be obtained by performing a cross-table lateral or lateral decubitus view.

Occasionally skin folds can mimic the appearance of a pneumothorax. On closer examination, they can usually be correctly identified as the folds often extend beyond the edge of the thoracic cavity and usually do not follow the expected contour of the lung edge (Fig. 34).

Spontaneous pneumothoraces that are not associated with pulmonary disease usually occur in the immediate postnatal period. These are seen in 1 % of neonates with approximately 10 % of these infants being symptomatic (Greenough et al. 1992).

### 5.3 Pneumomediastinum

If interstitial air tracks centrally, it can enter the mediastinum and form a pneumomediastinum. An isolated pneumomediastinum is usually not a clinical problem. Radiographs demonstrate a lucent line sharply marginating the mediastinal structures. In neonates the prominent thymus can be outlined and occasionally elevated, giving a characteristic appearance that has been termed the “angel wing” sign (Fig. 35). This is usually easily identified, but if the lobes of the thymus are

markedly displaced then they can simulate upper lobe opacification (Fig. 36). Another sign of a pneumomediastinum is the “continuous diaphragm” sign that is seen when air is interposed between the diaphragm and the inferior surface of the heart. Mediastinal air, if extensive, can track superiorly into the neck or inferiorly into the peritoneal cavity (Fig. 37).

### 5.4 Pneumopericardium

Air tracking medially can enter the pericardial sac. A small amount of air in the pericardial sac is very difficult to distinguish from pneumomediastinum. A large pneumopericardium is more easily differentiated from a pneumomediastinum as the air is confined to the pericardial sac, creating a focal lucency around the heart which does not extend beyond the confines of the pericardium (Fig. 38). The pericardium itself may be visualized as a thin stripe separate from the surface of the heart. A large pneumopericardium can result in a pericardial tamponade and decreased cardiac output. Very rarely, pulmonary interstitial air can enter the pulmonary veins and result in an air embolus that is often fatal.

## 6 Lines and Tubes

When evaluating a chest radiograph, it is important to closely study the position of the support apparatus. Many patients in neonatal care units have umbilical venous and arterial catheters (UVC and UAC, respectively), endotracheal tubes (ETT), and gastric tubes, and malpositioning of these devices can lead to complications with resultant prolonged hospital stay, long-term morbidity, and even death. It can be easy to overlook the position of these devices, especially when they overlap or when there are confounding distractions like external wires and leads.

A correctly placed umbilical venous catheter follows the single anteriorly positioned umbilical vein that courses cephalad from the umbilicus into the liver along the free edge of the falciform ligament, usually at or slightly to the right of midline. Within the liver, the umbilical vein intersects with the left branch of the portal vein before continuing cranially as the ductus venosus to the middle or left hepatic vein, ultimately draining into the inferior vena cava (IVC) and right atrium. Optimal positioning of the tip of a UVC is below the right atrium within the suprahepatic IVC, between the T9 and T12 vertebral body levels (Fig. 39). A UVC can take an abnormal course prior to reaching its optimal position in the IVC or it can be advanced beyond the IVC. Abnormal positions prior to reaching the IVC include within the right or left branches of the portal vein (Fig. 40), the main portal vein, the superior mesenteric vein



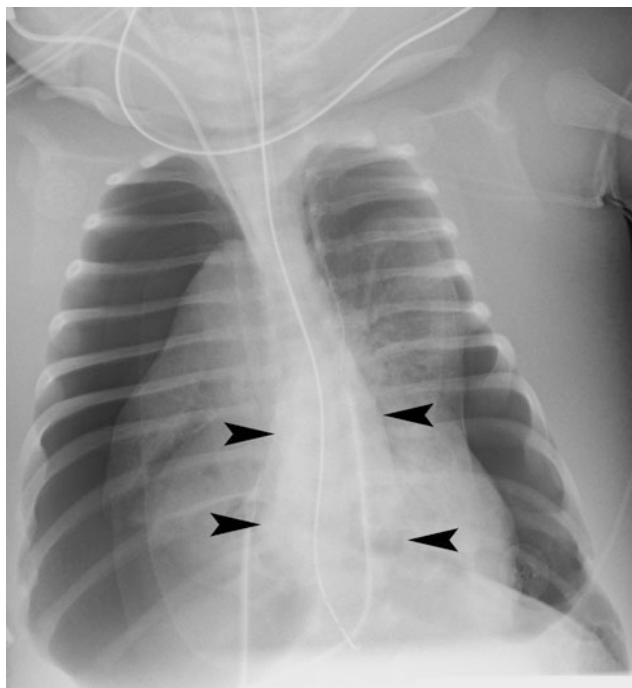


**Fig. 32** Bilateral tension pneumothoraces with impaired venous return. Both hemidiaphragms are inverted and the heart has a narrow configuration (*arrowheads*) related to diminished central venous return

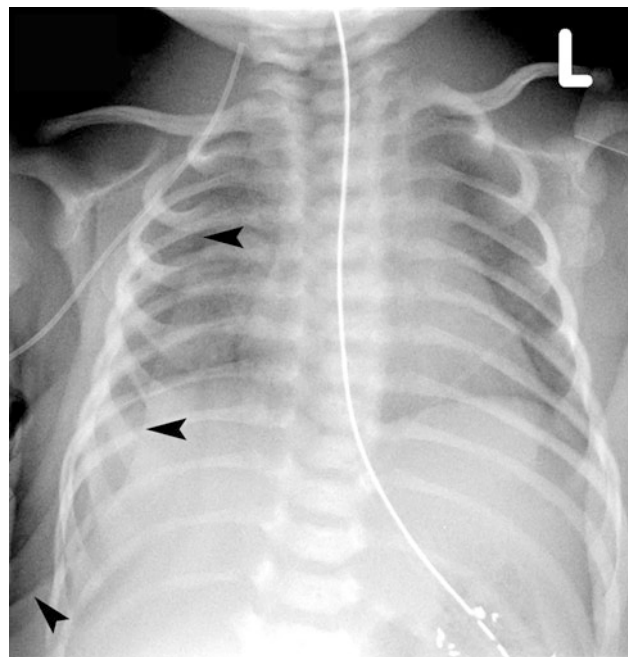


**Fig. 34** Skin folds mimicking a pneumothorax. Relative lucency is seen in the periphery of the right hemithorax, raising the concern for a pneumothorax. However, the “edge” of the air-soft tissue interface can be followed beyond the ribs and into the chest wall (*arrowheads*), consistent with a skin fold. On closer inspection, multiple skin folds are visible along the right chest wall

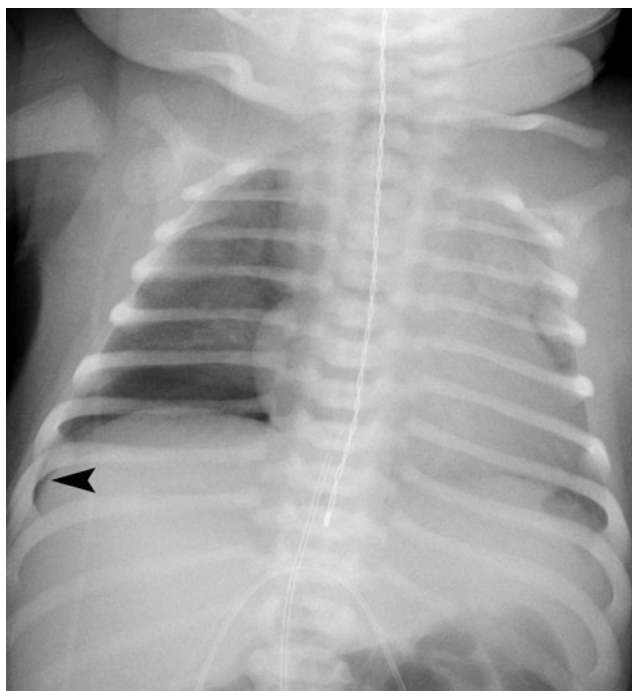


**Fig. 33** Deep sulcus sign. Notice the asymmetric lucency of the right hemithorax, the lucent margination of the right side of the mediastinum and right hemidiaphragm, and the deeper than usual appearance of the right costophrenic sulcus (*arrowhead*)

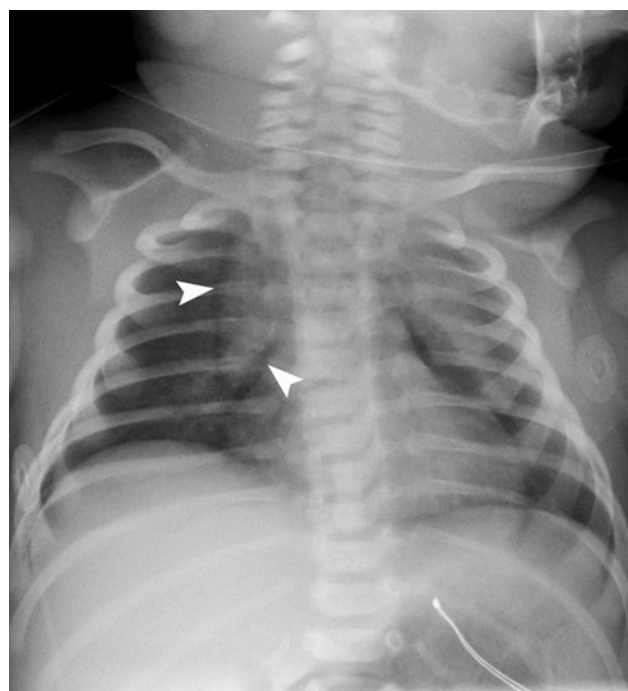


**Fig. 35** Pneumomediastinum and angel wing sign. There is a lucent band outlining the right side of the superior mediastinum and extending under the right lobe of the thymus, slightly elevating it from the heart (*arrowheads*). A slightly more exaggerated appearance is seen on the left side. The elevated thymic lobes have the configuration of “angels’ wings”



**Fig. 36** Lobes of thymus simulating upper lobe opacification. The lobes of the thymus are lifted superiorly away from the heart and could be mistaken for upper lobe opacities. The apical position of the left thymic lobe could also be mistaken for a loculated pleural effusion

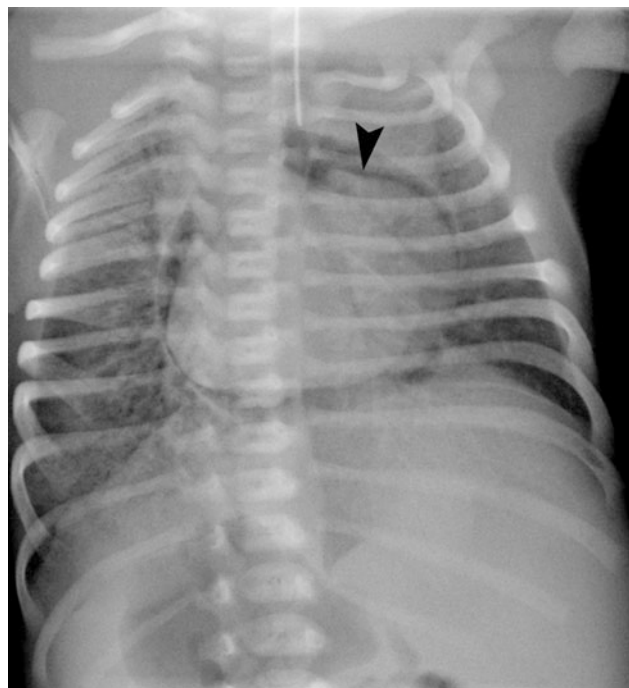


**Fig. 38** Pneumopericardium. Interstitial air has tracked centrally and entered the pericardial sac, surrounding the heart. Note the air outlining the left atrial appendage (*arrowhead*)



**Fig. 37** Newborn premature infant with pneumoperitoneum secondary to a pneumomediastinum. Air has collected centrally in the mediastinum (*black arrowheads*) and has extended inferiorly into the abdomen (*black arrow*) and into the neck (*white arrowhead*)

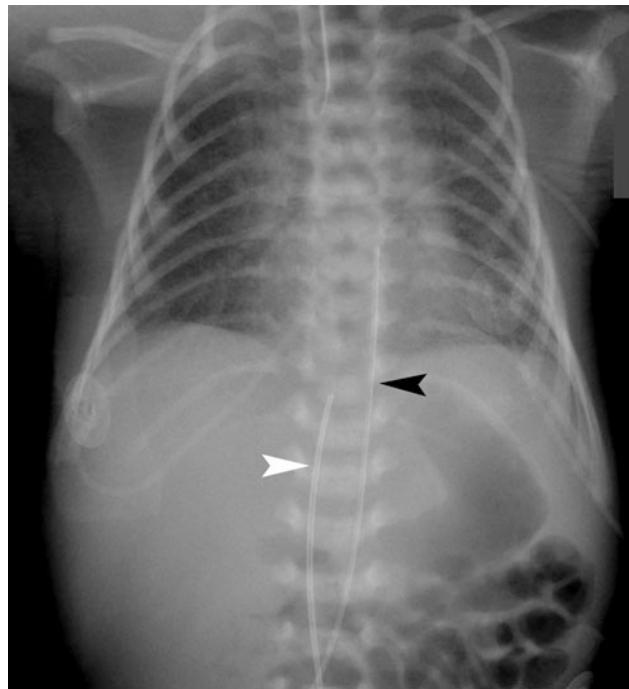


**Fig. 39** Appropriate positioning of umbilical arterial and venous catheters. The tip of the UAC (*black arrowhead*) is at the level of the T7 vertebral body and the tip of the UVC (*white arrowhead*) is at the level of the suprahepatic IVC

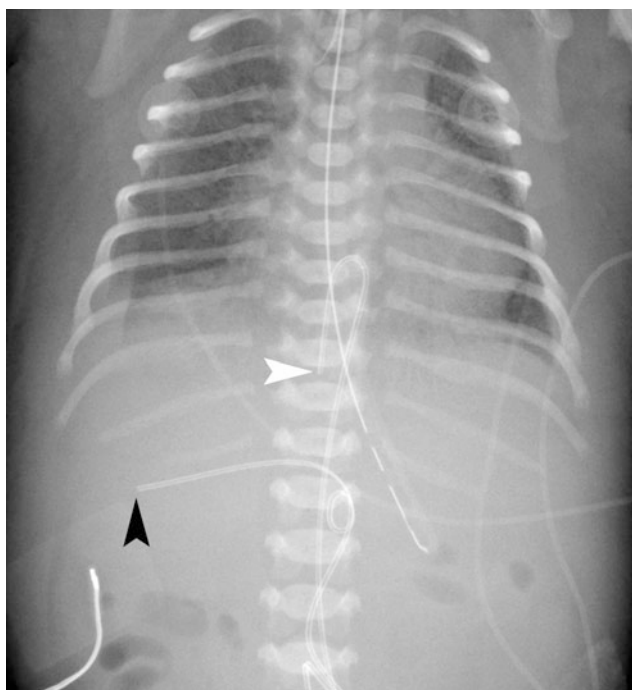


**Fig. 40** Abnormal position of umbilical arterial and venous catheters. The UAC loops back on itself within the aorta (*white arrowhead*). Having looped in the umbilical recess, the UVC courses into the right portal vein (*black arrowhead*)

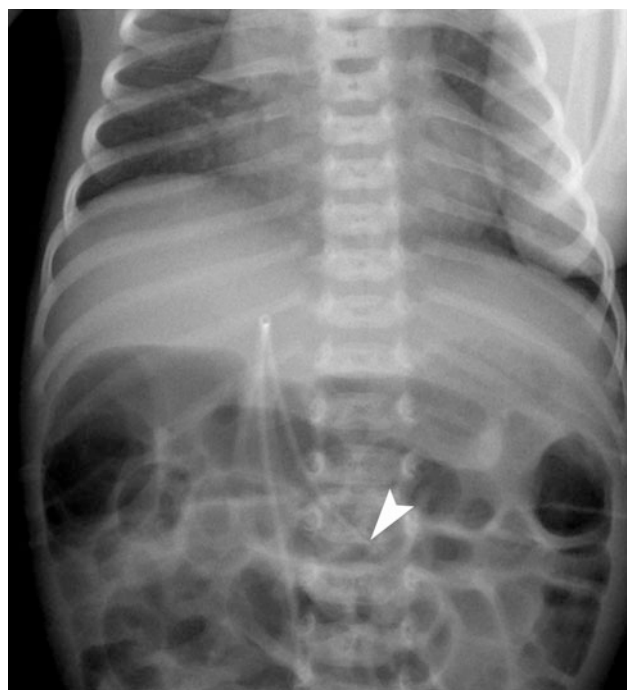


**Fig. 41** Abnormal position of an umbilical venous catheter. The catheter courses inferiorly along the main portal vein to terminate in the superior mesenteric vein (*arrowhead*)

(Fig. 41), or the splenic vein. There is increased likelihood of the UVC being abnormally positioned if it loops in the liver (Fig. 40). This looping often occurs in the umbilical recess, a dilated segment of the umbilical vein situated immediately prior to the junction with the left portal vein. Abnormal positioning of a UVC in a portal vein may cause damage to the liver from the infused fluids. The UVC can also perforate the hepatic venous structures and terminate in the liver parenchyma.

If the UVC is advanced too far then it may terminate in the right atrium or, progress through the foramen ovale into the left atrium and from there into the left upper pulmonary vein (Fig. 42). Rarely, it may pass through the tricuspid valve into the right ventricle (Fig. 43) and from there it may enter the pulmonary arterial system. Alternatively, it may traverse the right atrium and enter the central veins above the heart (Fig. 44).

A correctly placed UAC follows one of the paired umbilical arteries which course caudad and posteriorly from the umbilicus to the internal iliac arteries. The UAC passes into the internal iliac artery, then the common iliac artery and aorta. Favored positioning of the tip of the UAC is between the T6 and T10 levels, proximal to the origin of the aortic branches that supply the abdominal organs (Fig. 39).

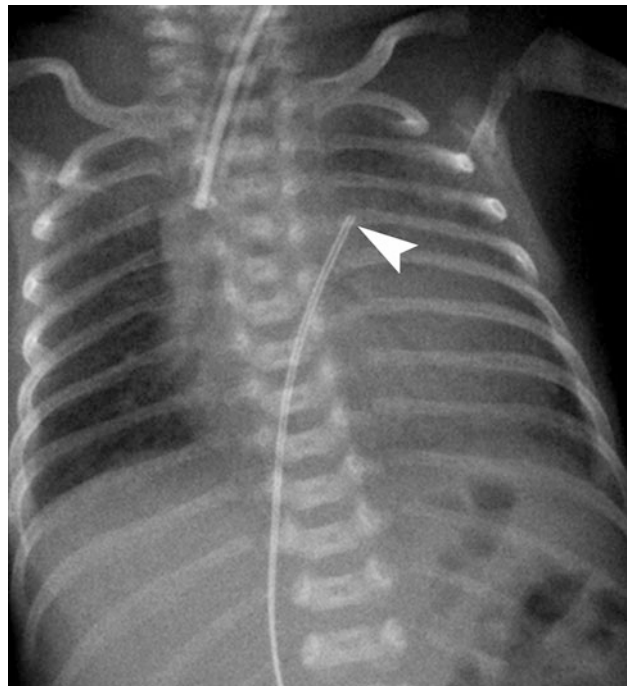


**Fig. 42** Umbilical venous catheter in the left upper pulmonary vein. The UVC has crossed through a patent foramen ovale into the left atrium and then into the left upper pulmonary vein (*arrowhead*)



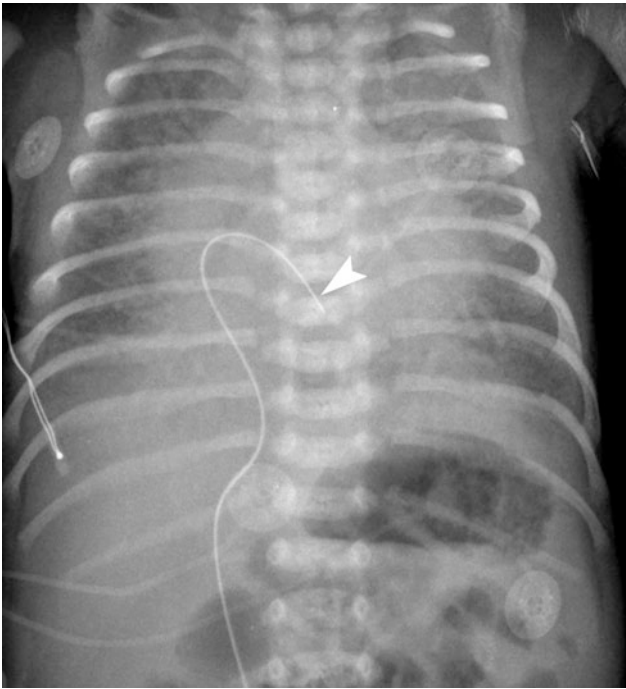


**Fig. 43** Umbilical venous catheter in the right ventricle. The UVC has looped in the right atrium and courses through the tricuspid valve, terminating in the right ventricle (*arrowhead*)

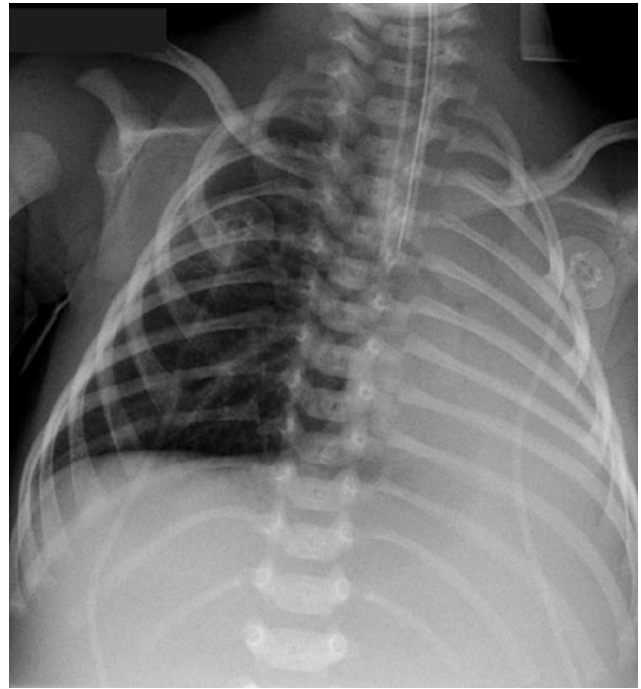


**Fig. 45** Endotracheal tube in the right mainstem bronchus. The endotracheal tube has been advanced beyond the carina into the right mainstem bronchus, resulting in collapse of the left lung

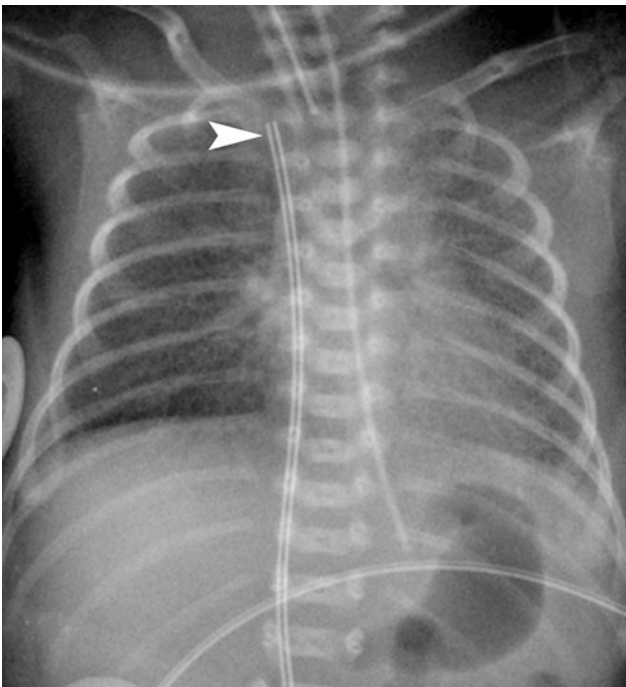


**Fig. 44** Umbilical venous catheter above the heart. The catheter has been advanced through the right atrium and terminates in the right brachiocephalic vein (*arrowhead*)

If this position cannot be obtained, then the catheter tip may be positioned below the origin of these branches between the L3 and L5 vertebral body levels. The high position is preferred because it is associated with a lower incidence of complications, such as thrombosis (Mokrohisky et al. 1978). Abnormal positioning of the UAC includes looping in the aorta (Fig. 40) or positioning in the ipsilateral or contralateral common iliac, external iliac, or femoral artery, or within a branch of the abdominal aorta.

Endotracheal tubes should be positioned in the intrathoracic trachea above the carina. Positioning too high in the trachea increases the risk of accidental extubation. A low position of the ETT may cause collapse of the contralateral lung (Kuhns and Poznanski 1971) (Fig. 45) or overinflation of the ipsilateral lung with a resultant increased risk of an air leak (Thibeault et al. 1973). Unintended intubation of the esophagus can be recognized by gaseous distension of the esophagus, stomach, and bowel with volume loss of the lungs (Fig. 46).

Nasogastric and orogastric tubes should follow the course of the esophagus and terminate in the stomach. Occasionally, they may terminate in the esophagus or be ectopically positioned in the tracheobronchial tree (Fig. 47). If these tubes are used to administer nutrition, then positioning in the

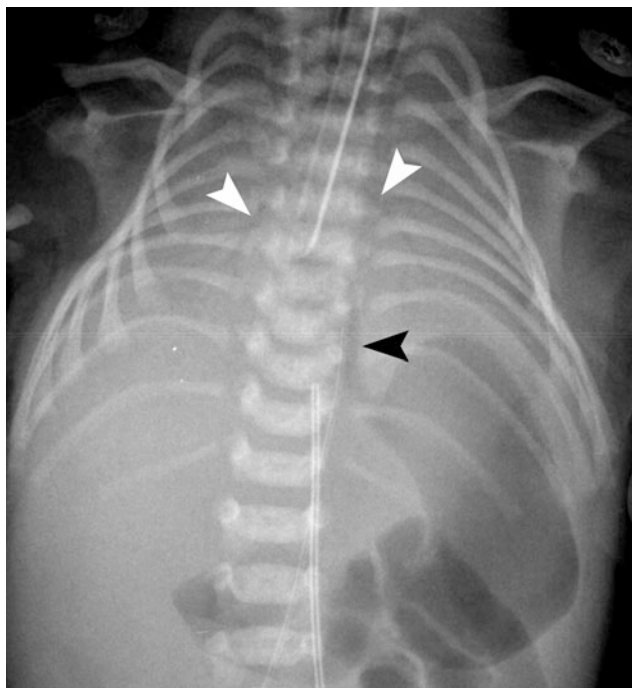


**Fig. 46** Esophageal intubation. The tip of the endotracheal tube is not in the trachea or either mainstem bronchus (*white arrowheads*). Air is visible in the distal esophagus (*black arrowhead*), and the stomach and proximal small bowel are distended with air



**Fig. 47** Abnormal position of an enteric tube. A nasogastric tube is looped in the esophagus with the tip in the oropharynx (*black arrowhead*) while the tip of an endotracheal tube is in the right mainstem bronchus (*white arrowhead*)

tracheobronchial tree or esophagus may lead to aspiration and chemical pneumonitis. Esophageal perforation can occur, usually at the level of the piriform sinuses, especially in premature infants (Sapin et al. 2000).

## 7 Summary

Imaging of neonatal lung disease continues to play an important role in the care of ill infants. Although the radiographic appearances of many of the conditions can overlap, the clinical history including gestational age, maternal history, and birth history combined with the radiographic findings most often allow the radiologist to correctly diagnose the patient's illness. Attention to the support apparatus as well as extra-pulmonary findings is an important part of image interpretation.

## References

- Ablow RC, Driscoll SG, Effmann EL et al (1976) A comparison of early-onset group B streptococcal neonatal infection and the respiratory-distress syndrome of the newborn. *N Engl J Med* 294(2):65–70
- Agrons GA, Courtney SE, Stocker JT et al (2005) From the archives of the AFIP: lung disease in premature neonates: radiologic-pathologic correlation. *Radiographics* 25(4):1047–1073
- Aherne W, Dawkins MJ (1964) The removal of fluid from the pulmonary airways after birth in the rabbit, and the effect on this of prematurity and pre-natal hypoxia. *Biol Neonatal* 7:214–229
- Anadkat JS, Kuzniewicz MW, Chaudhari BP et al (2012) Increased risk for respiratory distress among white, male, late preterm and term infants. *J Perinatol* 32(10):780–785
- Bancalari E, Claure N, Sosenko IR (2003) Bronchopulmonary dysplasia: changes in pathogenesis, epidemiology and definition. *Semin Neonatal* 8(1):63–71
- Barker PM, Olver RE (2002) Invited review: clearance of lung liquid during the perinatal period. *J Appl Physiol* 93(4):1542–1548
- Beligere N, Rao R (2008) Neurodevelopmental outcome of infants with meconium aspiration syndrome: report of a study and literature review. *J Perinatol* 28(Suppl 3):S93–S101
- Birnkrant DJ, Picone C, Markowitz W et al (2006) Association of transient tachypnea of the newborn and childhood asthma. *Pediatr Pulmonol* 41(10):978–984
- Bland RD, Hansen TN, Haberkern CM et al (1982) Lung fluid balance in lambs before and after birth. *J Appl Physiol* 53(4):992–1004
- Clausson B, Cnattingius S, Axelsson O (1999) Outcomes of post-term births: the role of fetal growth restriction and malformations. *Obstet Gynecol* 94(5 Pt 1):758–762
- Cleary GM, Wiswell TE (1998) Meconium-stained amniotic fluid and the meconium aspiration syndrome. An update. *Pediatr Clin North Am* 45(3):511–529
- Cleveland RH (1995) A radiologic update on medical diseases of the newborn chest. *Pediatr Radiol* 25(8):631–637
- Crowley P, Chalmers I, Keirse MJ (1990) The effects of corticosteroid administration before preterm delivery: an overview of the evidence from controlled trials. *Br J Obstet Gynaecol* 97(1):11–25
- Dargaville PA (2012) Respiratory support in meconium aspiration syndrome: a practical guide. *Int J Pediatr* 2012:965159

- Dargaville PA, Copnell B, Australian et al (2006) The epidemiology of meconium aspiration syndrome: incidence, risk factors, therapies, and outcome. *Pediatrics* 117(5):1712–1721
- Dargaville PA, South M, McDougall PN (2001) Surfactant and surfactant inhibitors in meconium aspiration syndrome. *J Pediatr* 138(1):113–115
- Dennehy PH (1987) Respiratory infections in the newborn. *Clin Perinatol* 14(3):667–682
- Dinger J, Schwarze R, Rupprecht E (1997) Radiological changes after therapeutic use of surfactant in infants with respiratory distress syndrome. *Pediatr Radiol* 27(1):26–31
- Donnelly LF, Lucaya J, Ozelame V et al (2003) CT findings and temporal course of persistent pulmonary interstitial emphysema in neonates: a multiinstitutional study. *AJR Am J Roentgenol* 180(4):1129–1133
- Garenne M, Ronsmans C, Campbell H (1992) The magnitude of mortality from acute respiratory infections in children under 5 years in developing countries. *World Health Stat Q* 45(2–3):180–191
- Garite TJ, Rumney PJ, Briggs GG et al (1992) A randomized, placebo-controlled trial of betamethasone for the prevention of respiratory distress syndrome at 24 to 28 weeks' gestation. *Am J Obstet Gynecol* 166(2):646–651
- Gooding CA, Gregory GA (1971) Roentgenographic analysis of meconium aspiration of the newborn. *Radiology* 100(1):131–140
- Greenough A, Morley C, Robertson N (1992). Acute respiratory diseases in the newborn. In: Robertson N (ed) *Textbook of Neonatology*. Churchill Livingstone, London, pp 385–504
- Hammerschlag MR (1994) Chlamydia trachomatis in children. *Pediatr Ann* 23(7):349–353
- Han BK, Suh YL, Yoon HK (2001) Thymic ultrasound. I. Intrathymic anatomy in infants. *Pediatr Radiol* 31(7):474–479
- Haney PJ, Bohlman M, Sun CC (1984) Radiographic findings in neonatal pneumonia. *AJR Am J Roentgenol* 143(1):23–26
- Hibbard JU, Wilkins I, Sun L et al (2010) Respiratory morbidity in late preterm births. *JAMA* 304(4):419–425
- Humphreys PW, Normand IC, Reynolds EO et al (1967) Pulmonary lymph flow and the uptake of liquid from the lungs of the lamb at the start of breathing. *J Physiol* 193(1):1–29
- Husain AN, Siddiqui NH, Stocker JT (1998) Pathology of arrested acinar development in postsurfactant bronchopulmonary dysplasia. *Hum Pathol* 29(7):710–717
- Janssen DJ, Carnielli VP, Cogo P et al (2006) Surfactant phosphatidylcholine metabolism in neonates with meconium aspiration syndrome. *J Pediatr* 149(5):634–639
- Jeffery HE, Moses Lahra M (1998) Eight-year outcome of universal screening and intrapartum antibiotics for maternal group B streptococcal carriers. *Pediatrics* 101(1):E2
- Jobe AH, Bancalari E (2001). Bronchopulmonary dysplasia. *Am J Respir Crit Care Med* 163:1723–1729
- Kotecha S, Hodge R, Schaber JA et al (2004) Pulmonary Ureaplasma urealyticum is associated with the development of acute lung inflammation and chronic lung disease in preterm infants. *Pediatr Res* 55(1):61–68
- Kuhns LR, Poznanski AK (1971) Endotracheal tube position in the infant. *J Pediatr* 78(6):991–996
- Lawson EE, Brown ER, Torday JS et al (1978) The effect of epinephrine on tracheal fluid flow and surfactant efflux in fetal sheep. *Am Rev Respir Dis* 118(6):1023–1026
- Leonidas JC, Hall RT, Beatty EC et al (1977) Radiographic findings in early onset neonatal group b streptococcal septicemia. *Pediatrics* 59 Suppl(6 Pt 2):1006–1011
- Liggins GC, Howie RN (1972) A controlled trial of antepartum glucocorticoid treatment for prevention of the respiratory distress syndrome in premature infants. *Pediatrics* 50(4):515–525
- Matthews TG, Warshaw JB (1979) Relevance of the gestational age distribution of meconium passage in utero. *Pediatrics* 64(1):30–31
- Mokrohisky ST, Levine RL, Blumhagen JD et al (1978) Low positioning of umbilical-artery catheters increases associated complications in newborn infants. *N Engl J Med* 299(11):561–564
- Moskowitz PS, Griscom NT (1976) The medial pneumothorax. *Radiology* 120(1):143–147
- Northway WH Jr, Rosan RC (1968) Radiographic features of pulmonary oxygen toxicity in the newborn: bronchopulmonary dysplasia. *Radiology* 91(1):49–58
- Northway WH Jr, Rosan RC, Porter DY (1967) Pulmonary disease following respirator therapy of hyaline-membrane disease. Bronchopulmonary dysplasia. *N Engl J Med* 276(7):357–368
- Oppenheim C, Mamou-Mani T, Sayegh N et al (1994) Bronchopulmonary dysplasia: value of CT in identifying pulmonary sequelae. *AJR Am J Roentgenol* 163(1):169–172
- Persson B, Hanson U (1998) Neonatal morbidities in gestational diabetes mellitus. *Diabetes Care* 21(Suppl 2):B79–B84
- Plenat F, Vert P, Didier F et al (1978) Pulmonary interstitial emphysema. *Clin Perinatol* 5(2):351–375
- Ramachandrapa A, Jain L (2008) Elective cesarean section: its impact on neonatal respiratory outcome. *Clin Perinatol* 35(2):373–393, vii
- Sapin E, Gumpert L, Bonnard A et al (2000) Iatrogenic pharyngoesophageal perforation in premature infants. *Eur J Pediatr Surg* 10(2):83–87
- Schatz M, Zeiger RS, Hoffman CP et al (1991) Increased transient tachypnea of the newborn in infants of asthmatic mothers. *Am J Dis Child* 145(2):156–158
- Singh BS, Clark RH, Powers RJ et al (2009) Meconium aspiration syndrome remains a significant problem in the NICU: outcomes and treatment patterns in term neonates admitted for intensive care during a ten-year period. *J Perinatol* 29(7):497–503
- Slama M, Andre C, Huon C et al (1999) Radiological analysis of hyaline membrane disease after exogenous surfactant treatment. *Pediatr Radiol* 29(1):56–60
- Stocker J (1992). The respiratory tract. In: Stocker J, Dehner LP (eds) *Pediatric pathology*. Lippincott, Philadelphia, pp 505–573
- Stocker JT (1986) Pathologic features of long-standing “healed” bronchopulmonary dysplasia: a study of 28 3- to 40-month-old infants. *Hum Pathol* 17(9):943–961
- Stoll BJ, Hansen NI, Bell EF et al (2010) Neonatal outcomes of extremely preterm infants from the NICHD neonatal research network. *Pediatrics* 126(3):443–456
- Stoll BJ, Hansen NI, Higgins RD et al (2005) Very low birth weight preterm infants with early onset neonatal sepsis: the predominance of gram-negative infections continues in the National Institute of Child Health and Human Development Neonatal Research Network, 2002–2003. *Pediatr Infect Dis J* 24(7):635–639
- Suresh GK, Soll RF (2005) Overview of surfactant replacement trials. *J Perinatol* 25(Suppl 2):S40–S44
- Swaminathan S, Quinn J, Stabile MW et al (1989) Long-term pulmonary sequelae of meconium aspiration syndrome. *J Pediatr* 114(3):356–361
- Swarnam K, Soraisham AS, Sivanandan S (2012) Advances in the management of meconium aspiration syndrome. *Int J Pediatr* 2012:359571
- Swischuk LE (1970) Transient respiratory distress of the newborn (TRDN). A temporary disturbance of a normal phenomenon. *Am J Roentgenol Radium Ther Nucl Med* 108(3):557–563
- Swischuk LE, John SD (1996) Immature lung problems: can our nomenclature be more specific? *AJR Am J Roentgenol* 166(4):917–918



- Swischuk LE, Shetty BP, John SD (1996) The lungs in immature infants: how important is surfactant therapy in preventing chronic lung problems? *Pediatr Radiol* 26(8):508–511
- Thibeault DW, Lachman RS, Laul VR et al (1973) Pulmonary interstitial emphysema, pneumomediastinum, and pneumothorax. Occurrence in the newborn infant. *Am J Dis Child* 126(5):611–614
- Tutdibi E, Gries K, Bucheler M et al (2010) Impact of labor on outcomes in transient tachypnea of the newborn: population-based study. *Pediatrics* 125(3):e577–e583
- Usta IM, Mercer BM, Sibai BM (1995) Risk factors for meconium aspiration syndrome. *Obstet Gynecol* 86(2):230–234
- van Houten J, Long W, Mullett M et al (1992) Pulmonary hemorrhage in premature infants after treatment with synthetic surfactant: an autopsy evaluation. The american exosurf neonatal study group I, and the Canadian exosurf neonatal study group. *J Pediatr* 120(2 Pt 2):S40–S44
- Wesenberg RL, Graven SN, McCabe EB (1971) Radiological findings in wet-lung disease. *Radiology* 98(1):69–74
- Wiswell TE, Tuggle JM, Turner BS (1990) Meconium aspiration syndrome: have we made a difference? *Pediatrics* 85(5):715–721
- Yoder BA, Kirsch EA, Barth WH et al (2002) Changing obstetric practices associated with decreasing incidence of meconium aspiration syndrome. *Obstet Gynecol* 99(5 Pt 1):731–739
- Yuksel B, Greenough A, Gamsu HR (1993) Neonatal meconium aspiration syndrome and respiratory morbidity during infancy. *Pediatr Pulmonol* 16(6):358–361

---

# Pulmonary Malformations Beyond the Neonatal Period

Josep M. Mata and Amparo Castellote

## Contents

<b>1</b>	<b>Introduction</b> .....	197
<b>2</b>	<b>Focal Malformations</b> .....	197
2.1	Congenital Lobar Overinflation: Lobar Emphysema and Bronchial Atresia.....	198
2.2	Single Congenital Thoracic Cyst.....	200
2.3	Congenital Pulmonary Airway Malformation: Pulmonary Sequestration Complex.....	201
2.4	Isolated Systemic Supply to Normal Lung .....	207
<b>3</b>	<b>Dysmorphic Lung</b> .....	208
3.1	Lung Agenesis–Hypoplasia Complex.....	208
3.2	Lobar Agenesis–Aplasia Complex.....	209
	<b>References</b> .....	215

---

## Abstract

Congenital lung malformations are not infrequent. It is necessary to know their radiological manifestations in order to avoid diagnostic errors. We classify the congenital lung malformations into two main groups: Focal malformations and Dysmorphic lung. We review the radiological findings and the role of radiological techniques.

---

## 1 Introduction

Congenital lung malformations include a heterogeneous group of anomalies affecting the lung parenchyma, the arterial supply to the lung and its venous drainage (Heitzman 1984). From the morphological-radiological viewpoint, these malformations can be divided into two groups: focal malformations (bronchial atresia, single congenital thoracic cyst, congenital pulmonary airway malformation (CPAM), pulmonary sequestration, and isolated systemic supply to normal lung), and dysmorphic lung (lung agenesis–hypoplasia complex and lobar agenesis–aplasia complex).

---

## 2 Focal Malformations

Focal congenital malformations usually involve only a part of the lung. They are a heterogeneous group, whose boundaries are not well defined and whose radiologic and pathologic manifestations vary and can be difficult to classify, especially if infection is present. They may cause symptoms in early life or be discovered incidentally.

Focal congenital malformations can be separated according to their radiologic and pathologic manifestations, with the understanding that significant degrees of overlap may occur. They can be considered a spectrum: at one extreme we find isolated bronchopulmonary anomaly (congenital lobar overinflation: lobar emphysema and bronchial atresia, single congenital thoracic cyst, CPAM);

---

J. M. Mata (✉)

UDIAT, Servei de Diagnòstic per la Imatge,  
Corporació Parc Taulí, Parc Taulí s/n,  
08208 Sabadell, Spain  
e-mail: jmata@tauli.cat

A. Castellote

Servei de Radiologia Pediàtrica, Hospital Vall d'Hebron,  
Ps. Vall d'Hebron 119–129, 08035 Barcelona, Spain

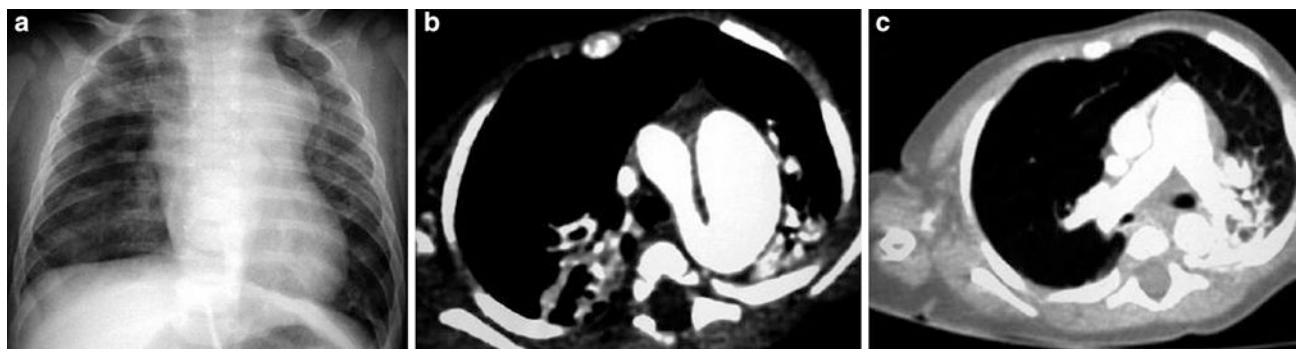


**Fig. 1** Patent ductus arteriosus in a 3-month-old girl with pulmonary hypertension. **a** Chest X-ray shows right pulmonary hyperinflation and a bulge in the left upper cardiac silhouette. **b** CT demonstrates that it

corresponds to a huge patent ductus. **c** The right main pulmonary bronchus is compressed by the right pulmonary artery causing obstructive emphysema of the right lung

next, associated systemic vascularization in the diseased lung (pulmonary sequestration); and at the other extreme isolated systemic arterial anomalies (isolated systemic supply to normal lung).

Although these developmental lesions usually are isolated, there are too many cases of the concurrent association of two or more of these anomalies, to be on the basis of chance alone. The theory of a variably level, completeness, and timing of the obstruction with secondary pulmonary dysplastic changes may help in understanding this overlap malformations (Langston 2003; Newman 2006).

The prenatal ultrasound (US) and magnetic resonance (MR) examination of the fetus has facilitated recognition and has added new information of many intrathoracic malformations. Nowadays, in countries where fetal US is routinely used, most congenital malformations are discovered antenatally, and confirmed in the neonatal period.

## 2.1 Congenital Lobar Overinflation: Lobar Emphysema and Bronchial Atresia

### 2.1.1 Congenital Lobar Emphysema

Congenital lobar emphysema (CLE) is characterized by progressive hyperexpansion of a lobe, usually the left upper or the right middle lobe. Its basic pathologic abnormality is overdistension of otherwise normal alveoli without destruction of alveolar walls. Proposed etiologies include focally deficient bronchial wall cartilage, deficient connective tissue stroma resulting in abnormal support of alveolar walls, and intrinsic or extrinsic obstruction of an affected bronchus. These abnormalities are believed to result in a check-valve mechanism, with progressive hyperinflation of the involved lobe after birth. Infrequently, lobar emphysema can be acquired. It can be caused by extrinsic compression from a vascular anomaly such as an enlarged pulmonary artery or vein (Figs. 1, 2), a patent ductus

arteriosus or a mediastinal mass (Winters and Effmann 2001). Clinically, most infants with CLE present within the first 6 months of life, with symptoms and signs of respiratory distress. Radiographs obtained beyond the neonatal period always demonstrate hyperlucency and overexpansion of the affected lobe and variable degrees of atelectasis of the ipsilateral lobe or lobes with associated mediastinal shift. CT is useful to exclude other causes of lobar emphysema, such as vascular anomalies or a mediastinal mass. CT findings of CLE are an expanded hemithorax, an overinflated low-attenuation lobe with stretching and attenuation of the pulmonary vessels, and atelectasis of the adjacent lobes. The paucity of vascular shadows within the overexpanded lung is in itself diagnostic of obstructive emphysema. Expiratory slices will confirm severe air-trapping in the affected lobe. Follow-up scans of patients who have minimal or no symptoms and, therefore, are treated conservatively, usually demonstrate either no changes or a progressive reduction in the degree of overexpansion of the affected lobe. However, significant air-trapping on expiration persists. Bilateral or multifocal involvement is rare (Hugosson et al. 1995).

### 2.1.2 Bronchial Atresia

Bronchial atresia (BA) is an anomaly characterized by obliteration of the proximal lumen of a segmental bronchus, with preservation of the distal structures. Its pathogenesis is unknown, although it may be due to a vascular insult. Most pediatric BA cases are congenital, but the condition may be acquired secondary to traumatic or infectious injury to the bronchus (Wasilewska et al. 2012). Air enters the affected segment via collateral channels, producing overinflation and air-trapping. The mucus secretions generated in the bronchi accumulate at the point of obstruction, originating mucus impaction (Lemire et al. 1970; Felson 1979). The mucocele can be linear, branched, ovoid, or spherical. BA almost always affects just one segment, and rarely affects a lobar





**Fig. 2** 17-year-old boy with chest pain. **a** Chest radiograph shows a hyperinflation of the lingula and a vascular linear shadow (*arrow*) **b**, **c** CT demonstrates that this structure corresponds to a huge single pulmonary vein going to the left atrium. Hyperinsufflation of the lingula is also seen



**Fig. 3** Bronchial atresia in a 17-year-old girl. Expiratory CT image with lung window shows the bronchocele and hyperinflation of the right upper lobe

bronchus. Involvement of multiple segments has been reported in a few cases (Ward and Morcos 1999). BA is characteristically located in the left upper lobe (apico-posterior segment), but can involve any lobe (Remy-Jardin et al. 1989; Medelli et al. 1979) and can be associated with other congenital anomalies. It is usually asymptomatic and is an incidental finding on radiological study. Infection of the unconnected lung is rare.

The chest plain film usually demonstrates pulmonary insufflation with trapped air during expiration, accompanied by a tubular, branched, or spherical image in a central position, which corresponds to the mucocoele (Jederlinic et al. 1986). CT shows the segmental overinflation and mucous impaction with great precision. When BA does not



**Fig. 4** Bronchial atresia in a 4-year-old boy. CT scan imaged with lung window shows a cystic lesion containing gas and fluid at the right hilum (*arrow*) corresponding to the dilated right upper lobe bronchus and hyperinflated right upper lobe

involve the left upper lobe or when it does not present characteristic radiological findings in the plain film, CT is diagnostic, demonstrating the combination of emphysema and bronchial impaction that is the hallmark of this condition (Pugatch and Gale 1983; Finck and Milne 1988) (Fig. 3). In some cases, a cystic lesion containing gas and fluid corresponding to a severely dilated bronchus just distal to segmental bronchial atresia can also be seen (Griscom 1993) (Fig. 4).

When the mucocoele cannot be identified, radiological diagnosis of bronchial atresia versus CLE may be impossible. In both these entities symptoms may be absent and radiological features may progressively improve. Nonetheless, the degree of mediastinal shift and collapse of the ipsilateral lobes is much more significant in most cases of lobar emphysema than in bronchial atresia (Castellote et al. 2005).

MRI is not commonly used to evaluate bronchial atresia after birth, but this malformation can be depicted on pre-natal MRI. The obstructed lobe appears hyperintense on T2-weighted images. This appearance can also be seen in CLE, type III CPAM, and BPS (Recio Rodríguez et al. 2012; Biyyam et al. 2010).

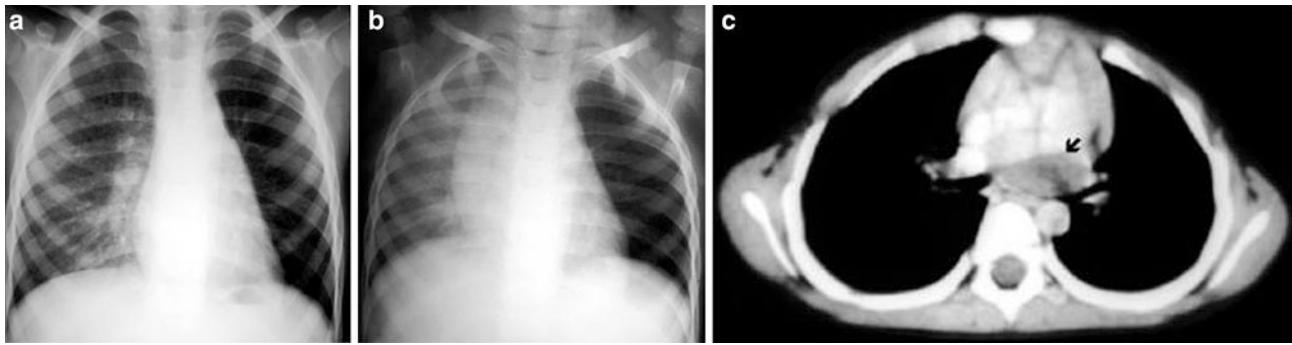


**Fig. 5** Bronchogenic cyst in a 3-year-old boy. **a** Inspiratory chest radiograph shows hyperlucency and decreased vascular perfusion in the left lung. **b** Expiratory chest radiograph demonstrates air-trapping

in the left lung. **c** A subcarinal cyst compressing the left main bronchus is seen in the CT scan (*arrow*)

## 2.2 Single Congenital Thoracic Cyst

We include under the term single congenital thoracic cyst (SCTC) all congenital cysts located in the mediastinum (bronchogenic cysts, duplication cysts, and pleuropéricardial cysts) and lung parenchyma. Treatment of SCTC depends on the symptoms. The best approach in asymptomatic patients with mediastinal cysts is periodic control, avoiding surgery. For practical purposes of clinical management, all cysts located within the lung parenchyma can be considered bronchogenic cysts requiring surgery. The definitive diagnosis of SCTC should be established on the basis of the study of the cyst wall. When there is associated inflammation and in some cases of mediastinal cysts, diagnosis can be difficult.

The most frequent location of bronchogenic cyst varies according to the published series (DuMontier et al. 1985; Baker 1989; Patcher and Lattes 1963; Rogers and Osmer 1964). In the most recent series including 68 bronchogenic cysts (McAdams et al. 2000), 58 (85 %) were mediastinal, and seven were intrapulmonary (10 %), demonstrating a clear predominance of mediastinal cysts. Mediastinal cysts are most often found in a subcarinal location, whereas intrapulmonary bronchogenic cysts are most frequently located in the lower lobes. Bronchogenic cysts can be found in the diaphragm, below the diaphragm (Braffman et al. 1988) and even in the liver (Kimura et al. 1990) or neck and can be associated with pericardial agenesis (Kwak et al. 1971). They are usually solitary and spherical in shape with thin walls of bronchial epithelium, and have a viscous gelatinous, mucoid, hemorrhagic or watery, translucent fluid content. They occasionally contain calcium, have calcified walls, or are completely calcified and they can be air-filled when they communicate with the bronchial tree (Rogers and Osmer 1964; Reed and Sobonya 1975). Bronchogenic cysts are sometimes found in association with

other congenital pulmonary malformations such as sequestration, lobar emphysema, or BA (Kuhn and Khun 1992; Grewal and Yip 1994).

In infants mediastinal SCTC tend to compress or distort the esophagus, the trachea, and bronchi, resulting in clinical respiratory compromise, but the condition can be asymptomatic and be discovered fortuitously. Compression of a main bronchus may result in obstructive pulmonary hyperinflation of the ipsilateral lung (Fig. 5). These cysts can also compress the pulmonary artery or superior vena cava (Bankoff et al. 1985). Mediastinal and intrapulmonary SCTC can disappear spontaneously (Martin et al. 1988), change form due to decreases in their internal pressure, or diminish in size, making themselves invisible to the chest plain film (Fig. 6).

The basic radiological study used to detect SCTC is the chest plain film. In the majority of cases, this technique detects the lesion and some of the complications (e.g., compression on neighboring structures). Ultrasound, MDCT, and MR allow a better evaluation of SCTC and its anatomic relationship with adjacent structures. CT reveals a round or ovoid mass with water or soft-tissue attenuation. Almost 50 % of SCTC appear iso- or even hyperdense at CT due to intracystic hemorrhage, protein content, or milk of calcium. On MRI, SCTC are homogeneously and markedly hyperintense on T2-weighted images. The intracystic signal intensity on T1-weighted images is more variable, and, depending upon the cyst content, low, intermediate, and high signal intensity cases have been reported (Naidich et al. 1988; Nakata et al. 1993). Relatively high signal intensity on T1 is due to a high protein content and/or the presence of methemoglobin. Fluid–fluid levels have also been reported (Lyon and McAdams 1993). When air–fluid levels are seen within the cyst, it is usually infected, although we have seen cysts with air–fluid levels in asymptomatic patients (Fig. 7). Minimal wall enhancement is expected with gadolinium enhancement.

**Fig. 6** Mediastinal bronchogenic cyst in a 14-year-old boy. **a** Chest radiograph shows an ovoid perihilar mass in the right upper lobe (*arrow*). **b** Chest radiograph performed 1 year later, prior to surgery, is normal. **c** CT scan performed at the same time as (**b**), shows an isodense mass in the right upper lobe (*arrow*). **d** Coronal T1-weighted MR image demonstrates the presence of an intermediate signal intensity ovoid mass (*arrow*). **e** Coronal T2-weighted MR image. The homogeneous high signal intensity of the mass indicates a fluid content (*arrow*)

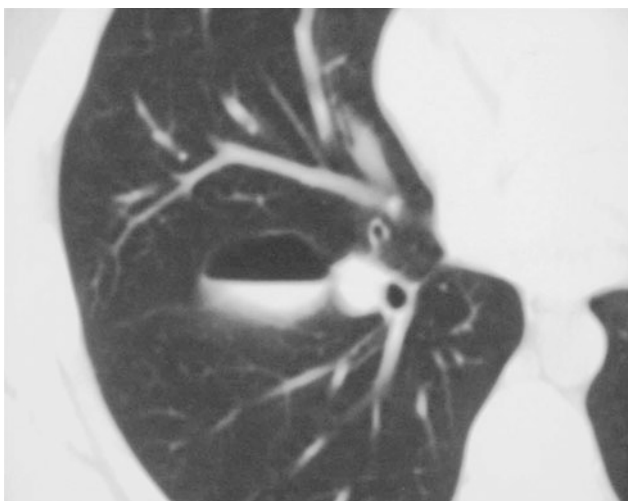
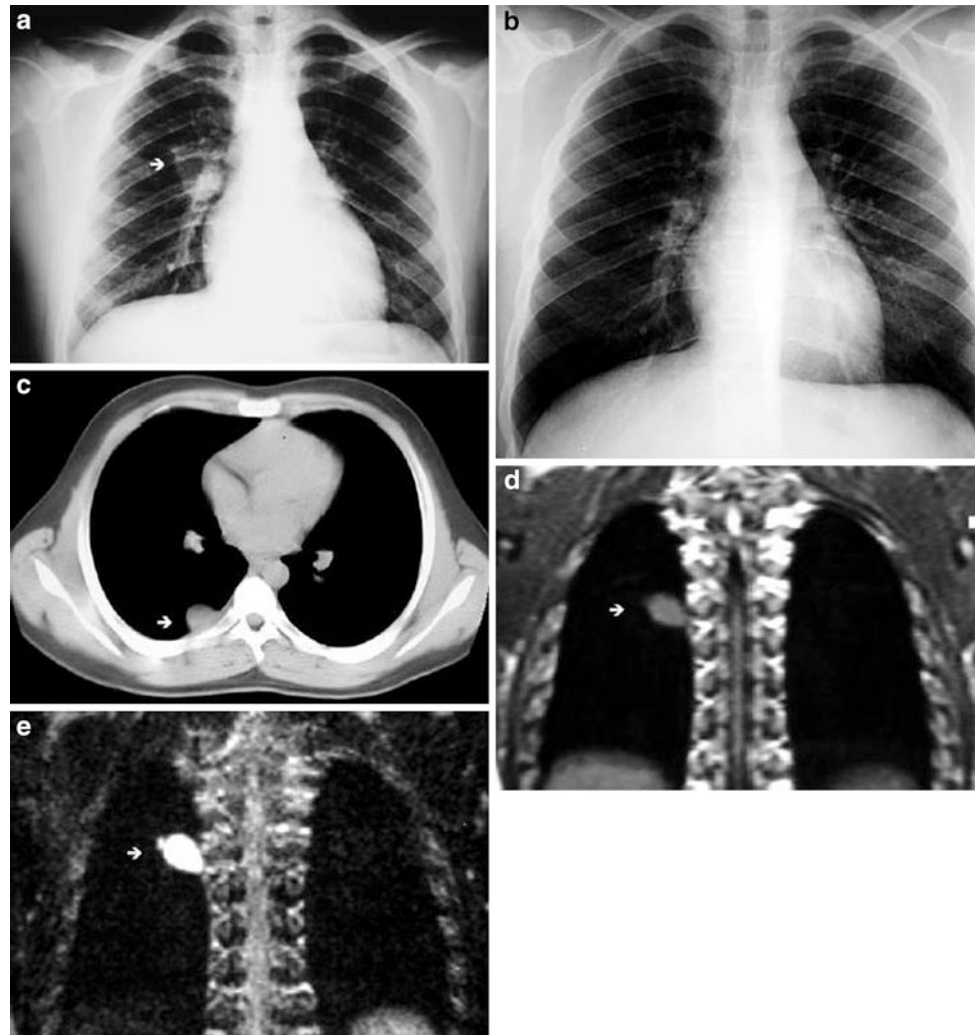


**Fig. 7** Bronchogenic cyst in an asymptomatic 12-year-old boy. CT scan shows an air–fluid level within the cyst

## 2.3 Congenital Pulmonary Airway Malformation: Pulmonary Sequestration Complex

### 2.3.1 Congenital Pulmonary Airway Malformation

Congenital pulmonary airway malformation, previously named congenital cystic adenomatoid malformation (CCAM) consists of an intrapulmonary mass of disorganized pulmonary tissue that may or may not be accompanied by macroscopic cysts (Stocker 2002). When present, the cysts communicate with the airways and their vascular supply comes from pulmonary circulation. However, there are numerous examples of CPAM fed by systemic blood vessels and in these cases it is extremely difficult to differentiate CPAM from pulmonary sequestration, as they correspond to overlapping malformations (Winters et al. 1997). From the radiological viewpoint the differentiation between CPAM with systemic supply and pulmonary sequestration is impossible. These malformations correspond to the same



**Table 1** The extended classification of congenital pulmonary airway malformation

Type	Incidence (%)	Gross appearance	Microscopy	Other features
0	1–3	Solid; both lungs are small and firm	Bronchial-type airways that have cartilage, smooth muscle, and glands are separated by abundant mesenchymal tissue	Incompatibility with life
1	60–70	Large cysts (up to 10 cm)	The cysts are lined by pseudostratified ciliated cells that are often interspersed with rows of mucous cells	May be late; best overall prognosis; less than 1 % carcinomatous change
2	10–15	Sponge-like composed of multiples cysts (up to 2 cm) and solid pale tumor-like tissue	The cysts resemble dilated bronchioles separated by normal alveoli; striated muscle in 5 %	Neonates; cardiac and renal anomalies; poor prognosis
3	5	Solid	Scattered bronchiolar/alveolar duct-like structures are lined by low cuboidal epithelium and surrounded by alveoli lined by cuboidal epithelium	Neonates, almost exclusively in males; poor prognosis
4	15	Large cysts (up to 10 cm) generally at the periphery of the lung	The cysts are lined by a flattened epithelium resting on loose mesenchymal tissue	Neonates and infants; good prognosis; overlap with PPB

Adapted from Macsweeney et al. (2003)

clinical and radiological entity, although they have a different anatomic-pathological expression.

Ch'in and Tang applied the name “congenital cystic adenomatoid malformation” to a congenital cystic pulmonary anomaly for the first time in 1949. The essential discovery is an adenomatoid proliferation of the terminal bronchioles that produces cysts of varying sizes coated with bronchial epithelium. There is considerably controversy over classification and nomenclature. CPAM has recently been recommended as a preferred term to congenital cystic adenomatoid malformation because not all the lesions are cystic and only type III is adenomatoid. In 1977 Stocker et al. divided CCAM into three groups, depending on whether the cysts were larger than 2 cm (type I), smaller than 2 cm (type II), or the malformation was solid without cysts (type III). (Stocker et al. 1977). An expanded classification (types 0–4) has been proposed representing malformations of larger through smaller airways. In an attempt to maintain a similar ordering of the three types published in 1977, type I, II, and III become type 1, 2, and 3 and the “distal acinar” lesion added is type 4, presenting features of a large cyst generally located at the periphery of the lung. Type 0 is characterized by its involvement of all lobes of the lung and its incompatibility with life (Table 1). A number of reports have been suggesting a relationship between CPAM and pleuropulmonary blastoma (PPB) and it is unclear at this time. Anyway, although Stocker feels based in his experience that they are separate lesions, other authors (MacSweeney et al. 2003) consider that both lesions show histologic overlap.

CPAM can be associated with other congenital malformations such as pulmonary sequestration, tracheal bronchus, tracheal atresia, tracheal diverticulum (Restrepo et al. 2004), and bronchogenic cyst. CPAM can also be associated

with congenital BA in the same lobe (Cachia and Sobonya 1981) or can involve more than one lobe or be bilateral. In our experience it occurs with more frequency in lower lobes. CPAM can cause severe respiratory distress in the neonatal period. Beyond this time it is usually discovered when it becomes infected or as an incidental radiological finding (Pulpeiro et al. 1987).

The malformation can escape detection on plain films. Although, these days, however, CPAM is increasingly being diagnosed on antenatal (US) examinations, where it is seen as an echogenic mass, which may or may not contain cysts. Antenatal MR imaging may help to evaluate any associated pulmonary hypoplasia and predict the prognosis. The lesions may disappear completely, may remain unchanged or increase in size and be associated with the development of polyhydramnios or fetal nonimmune hydrops fetalis (Fig. 8) (Paterson 2005).

The appearance of CPAM on radiographs and CT depends on the relative presence of cystic and solid components and whether there is superimposed infection. On plain films, type I presents as one or more dominant cysts with adjacent smaller cysts and solid tissue elements. Type II displays smaller, more evenly sized and spaced cysts. Type III, which is very rare, appears as a solid mass. Large masses produce significant mediastinal displacement. Air-fluid levels are often seen, mainly, but not always, associated with infection. On chest CT, CPAM is seen as multiple thin- or thick-walled, air- or fluid-filled cysts of variable size, expanding the affected lung. Air-fluid levels are often present (Rosado-de-Christenson and Stocker 1991). CPAM may mimic cystic pleuropulmonary blastoma. PPB is probably the same tumor that several authors have reported as mesenchymal sarcoma or rhabdomyosarcoma arising in congenital lung cysts (Ueda et al. 1977). It has also been stated that PPB can arise from

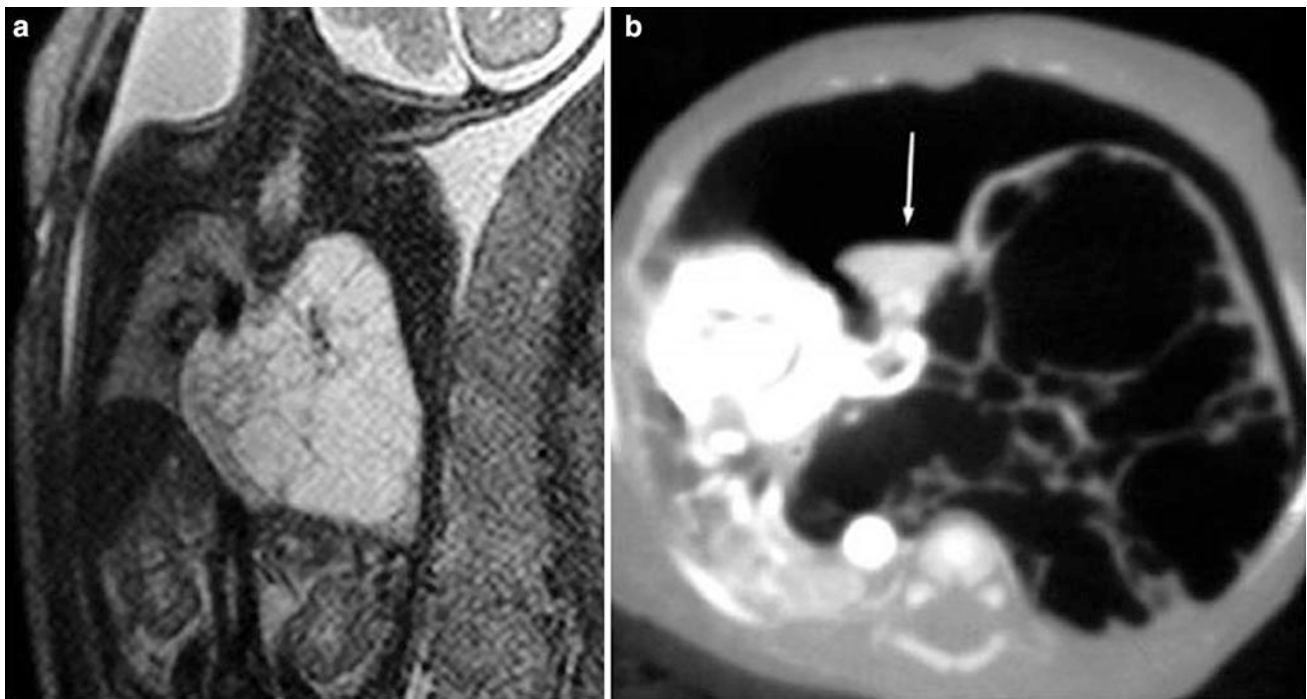


**Fig. 8** CPAM type 1. **a** Coronal MR hASTE image in a 27-week-old fetus shows a large high signal intensity slightly heterogeneous mass with multiple septa arising from the left lung and crossing the midline. **b** A CT done when the patient was 5-day-old shows an anterior

pneumothorax and multiple cysts occupying the left hemithorax, crossing the midline, displacing the heart to the right. A small collapsed superior lobe is seen (*arrow*)

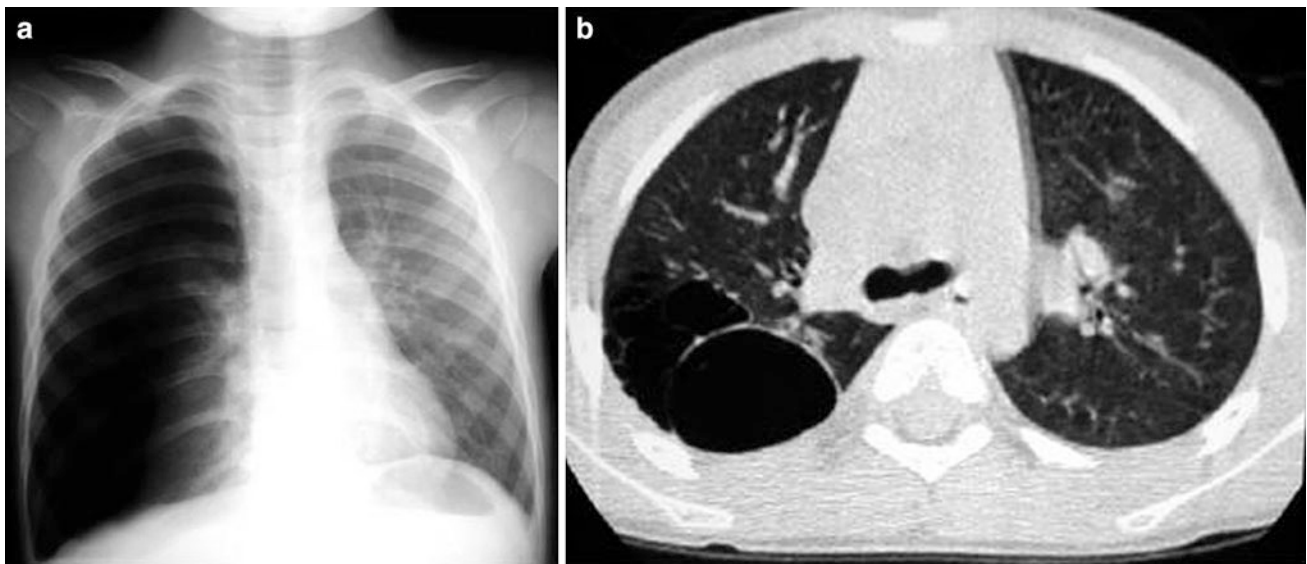


**Fig. 9** Congenital pulmonary airway malformation type I in a 6-year-old girl with chest pain and dyspnea. **a** Chest radiograph shows right-sided pneumothorax. A chest tube was inserted and the lung was re-

expanded. **b** Chest CT performed 1 week later reveals multiple cysts at the right upper lobe

preexisting cystic lung disease, but is reasonable to assume that the cystic changes are a component of the PPB, itself (Murphy et al. 1992). As the initial manifestation, pneumothorax is more frequently seen in PPB than in CPAM (Fig. 9)

(Senac et al. 1991). However, pneumothorax can be found associated with both entities and the available information does not support the use of this finding as a differentiating diagnostic criteria (Lejeune et al. 1999).

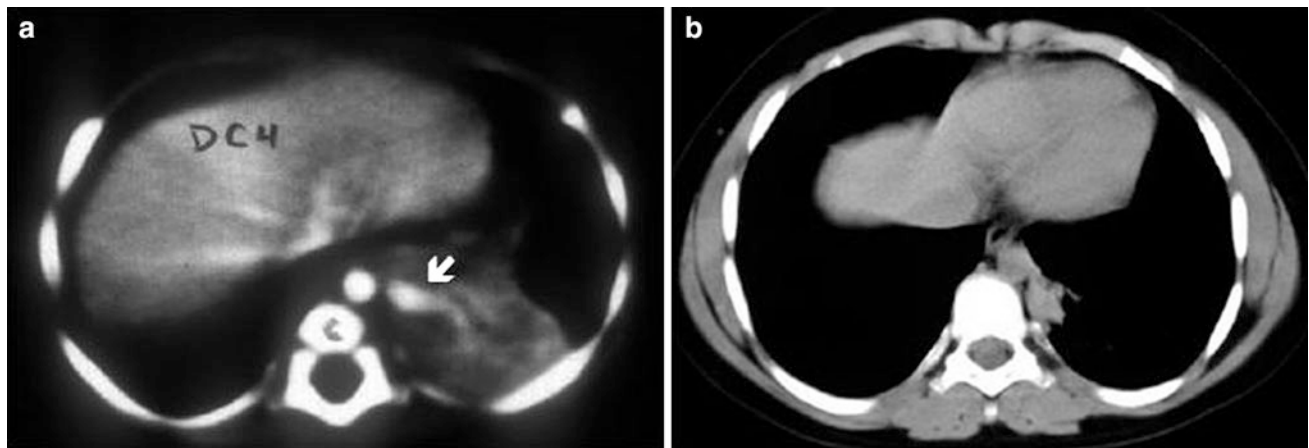


**Fig. 10** Spontaneous involution of a pulmonary sequestration. **a** Contrast-enhanced chest CT at the age of 3 months shows a soft tissue density mass with a large feeding vessel originating from the aorta (arrow). **b** Significant shrinkage of the mass is seen in the scan at the age of 10 years

Cases of CPAM/pulmonary sequestration that dramatically decreased in size or disappear completely during pregnancy and infancy have been reported (Fig. 10). However, the clinical management of an asymptomatic child with a congenital mass of the lung remains controversial. Some authors advocate close clinical observation and radiological surveillance (MacGillivray et al. 1993), whereas others, considering the possibility that cystic pulmonary lesions may be infected (Garcia-Peña et al. 2013), or may harbor or develop PPB, favor elective surgical resection (Samuel and Burge 1999).

### 2.3.2 Pulmonary Sequestration

Pulmonary sequestration consists of a mass of pulmonary tissue disconnected from the bronchial tree that receives its blood supply from the systemic circulation (Heitzman 1984). Pulmonary sequestration is divided into two groups: intralobar sequestration, in which the tissue is surrounded by normal lung and found in the interior of the visceral pleura, and extralobar sequestration, in which the tissue is disconnected from the bronchial tree and has its own pleural coating. In 1946 Pryce identified intralobar sequestration as a clinical-pathological entity. He was the first to apply the term “sequestration” and further classified the lesion as intralobar or extralobar on the basis of the morphologic patterns of the malformation. There are also mixed cases with characteristics of both intralobar and extralobar sequestration.

Pulmonary sequestration is an uncommon anomaly; the intralobar form is more frequent than the extralobar. Intralobar sequestration constitutes 75 % of all pulmonary sequestrations and is located in the left lower lobe in 60 % of the cases. Only 2 % occur in the upper lobes and 0.25 % in the middle lobe. The affected lung can maintain the normal lung architecture, behave like a mass, or present as internal cysts. Vascularization in the majority of cases is

through the thoracic aorta (Savic et al. 1979), or less commonly, through systemic vessels originating from the abdominal aorta or one of its branches (Pedersen et al. 1988). The systemic supply can be formed by multiple, small-caliber blood vessels or by a single vessel, which are histologically similar to the pulmonary artery. This favors the early appearance of atherosclerosis (Ikezo et al. 1990). Intralobar sequestration does not receive blood from the pulmonary arteries and it drains through pulmonary veins. In exceptional cases it communicates with the digestive tract (bronchopulmonary foregut malformation) (Hruban et al. 1989). It can be bilateral, or associated with other congenital malformations.

Since Pryce’s description of pulmonary sequestration, there has been considerable controversy about its origin. Some authors contend that intralobar sequestration is, in fact, acquired (Gebauer and Mason 1959; Holder and Langston 1986), resulting from endobronchial obstruction leading to chronic pulmonary infection and hypertrophy of the systemic arteries in and around the area of the pulmonary ligament. This explains why, in the past, when infections were poorly controlled, intralobar sequestration was overdiagnosed. However, congenital intralobar sequestration does occur, since this anomaly has been recognized on prenatal US and has been detected in newborns (West et al. 1989; Laurin and Hägerstrand 1999) (Fig. 11).

Intralobar sequestration is usually discovered because the patient has developed a pulmonary infection, although some patients are asymptomatic when the lesion is found. In a small number of cases intralobar sequestration debuts as a pulmonary hemorrhage (Fig. 12), pleural effusion (Kim et al. 1997; Lucaya et al. 1984), or pleural bleeding secondary to infarction of the sequestered lung (Zumbro et al. 1974). On plain films, intralobar sequestration appears as a homogenous opacity mostly in the lower lobes. This opacity can simulate a mass with a well-defined border, or show





**Fig. 11** Intralobar pulmonary sequestration in a 10-day-old boy with an echogenic mass in the left lower lobe seen on prenatal US. **a** Coronal MIP CT reconstructed image shows two anomalous arteries arising from thoracic aorta. **b** The drainage is through the lower left pulmonary vein

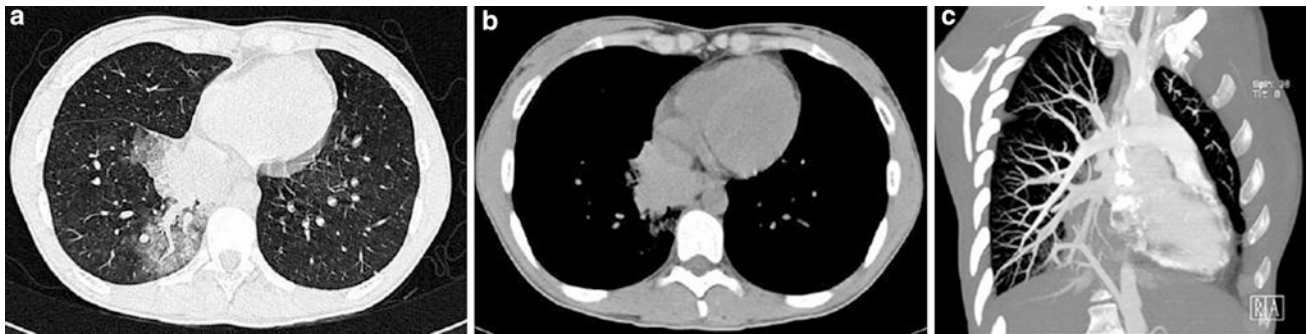


**Fig. 12** Pulmonary sequestration in a 18-year-old with hemoptysis. **a** CT demonstrates the presence of ground glass area due to hemorrhage in the right lower lobe with a central vessel. **b** Shows a

hyperdense mass secondary to hemorrhage into sequestration. **c** Angio-CT with MIP reconstructions shows that the vessel originates from the abdominal aorta

internal air–fluid levels and a poorly defined border. In rare cases calcifications are present within the sequestration or in the systemic blood vessel. An unusual presentation of intralobar sequestration is localized emphysema without an associated opacity or mass (Ko et al. 2000).

Extralobar sequestration is usually located between the lower lobe and the diaphragm, more frequently at the left thoracic base, in 77 % of cases (Savic et al. 1979). To a much lesser degree it has also been found in the mediastinum, pericardium (Stocker and Kagan-Hallet 1979), diaphragm, or retroperitoneum (Baker et al. 1982). Vascular supply occurs through a systemic artery and venous drainage through the azygos or portal system (Rees 1981), although nearly 25 % are completely or partially drained by pulmonary veins. Extralobar sequestration is associated with other congenital malformations in 65 % of cases, such as diaphragmatic hernia, bronchogenic cyst, BA, scimitar syndrome, pericardial defect and as previously stated,

CCAM (Savic et al. 1979), and these are much more frequent than those associated with the intralobar form. Both types of sequestration occasionally can connect with the digestive tract (bronchopulmonary foregut malformation) (Hruban et al. 1989). The presence of air bronchograms within a mass thought to be ELS should suggest the diagnosis of bronchopulmonary foregut malformation. Communication between the tracheobronchial tree and the GI should be examined by upper GI series or MDCT. Extralobar sequestration is usually detected fortuitously and can also be associated with pleural effusion. It may be seen as a homogeneous mass or a small bump on the posterior hemidiaphragm that may be subtle and occasionally inapparent on the chest radiograph.

Ultrasound, CT, and MRI are useful in the study of sequestrations (Fig. 13). Multidetector CT angiography is considered the imaging technique of choice for preoperative evaluation of pulmonary sequestration. MDCT with

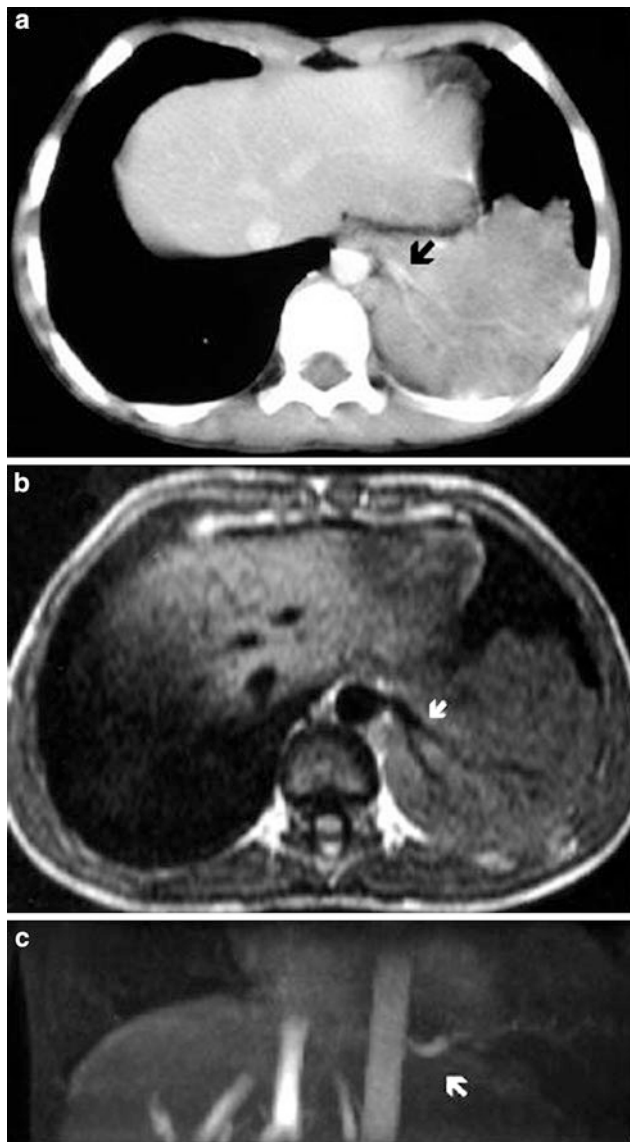


**Fig. 13** Intralobar pulmonary sequestration of the left lower lobe in a 2-year-old boy. **a** Contrast-enhanced chest CT shows the sequestration and a systemic branching vessel originating from the aorta (arrow). **b** Axial SE T1-weighted and **c** coronal 2D TOF MIP reconstruction images demonstrate a branching feeding vessel originating from the descending aorta and supplying the pulmonary sequestration (arrows)

supplementary multiplanar and 3D images has the advantage of being able to show the pulmonary parenchyma abnormality, as well as the arterial and venous angioarchitecture of the sequestration (Lee et al. 2004, 2011a). CT has some advantages over MR angiography for evaluating pulmonary sequestrations in children. CT scan times are significantly shorter, and resolution of small vessels and lung parenchyma is better. CT in a single phase of contrast injection is adequate for evaluation of both the arterial and the venous anatomy, using low dose to minimize radiation (Abbey et al. 2009; Lee et al. 2011b). Intralobar sequestration typically manifests as a homogeneous or

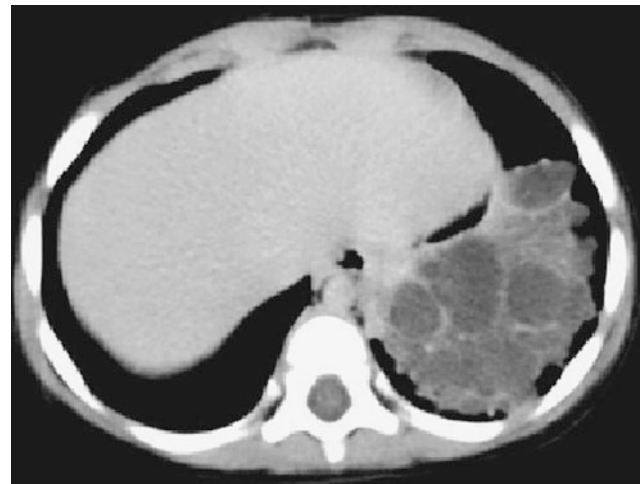


**Fig. 14** Intralobar pulmonary sequestration in a 2-year-old boy. CT scan shows a mass with multiple fluid-filled cysts in the left lower lobe

inhomogeneous solid mass, with or without definable cystic changes. It can also appear as an aggregate of multiple small cystic lesions with air or fluid content (Fig. 14), a well-defined cystic mass, or a large cavitary lesion with air–fluid level. The lesion may enhance with contrast material (Frazier et al. 1997; Rosado-De-Christenson et al. 1993). An appearance simulating emphysema, possibly resulting from collateral ventilation and air-trapping, can sometimes be seen in sequestration. Expiratory CT scans are helpful for delineating the extent of the malformation (Fig. 15) (Stern et al. 2000; Lucaya et al. 2000). Extralobar sequestration is seen on chest CT as a homogeneous, well-delimited mass, sometimes with internal cystic areas (Rosado-De-Christenson et al. 1993).

MR imaging is a safe and noninvasive imaging method, which may be useful in some specific cases of pulmonary sequestration (Naidich et al. 1988; Yu et al. 2010). In MR, this anomaly is seen as a well-defined, irregular, or branch-like mass. MR can also reveal the presence of cystic areas, as well as the variable solid, fluid, hemorrhagic, and mucus-containing components. However, MR imaging cannot delineate focal thin-walled cysts or the emphysematous changes of sequestration as clearly as CT. The size, origin, and course of the aberrant systemic artery and the venous drainage can be demonstrated by MR imaging. Breath-hold (if possible) or nonbreath-hold three-dimensional contrast-enhanced MR angiography offer excellent display of the aberrant vessel without flow artifacts (Ko et al. 2000). The advantage of MRI over CT is the absence of radiation. However, long scan times, sedation requirements, and suboptimal evaluation of lung parenchyma are the disadvantages of this method.

Nowadays, there is no place for conventional angiography in the diagnosis of pulmonary sequestration. Vascular

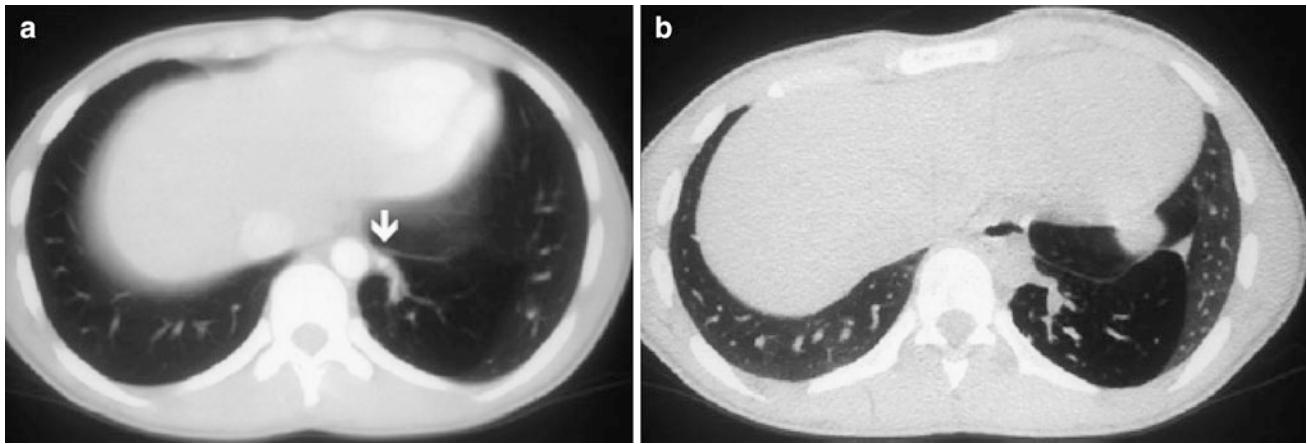


**Fig. 15** Intralobar pulmonary sequestration in left lower lobe in a 15-year-old boy. **a** Enhanced CT scan shows hyperlucency in left lower lobe. A systemic vessel (*arrow*) originating from the aorta and feeding

the sequestration is well defined. **b** In an expiratory high-resolution CT scan at same level as (**a**), air-trapping can be seen within the sequestered lung. (Reprinted with permission)

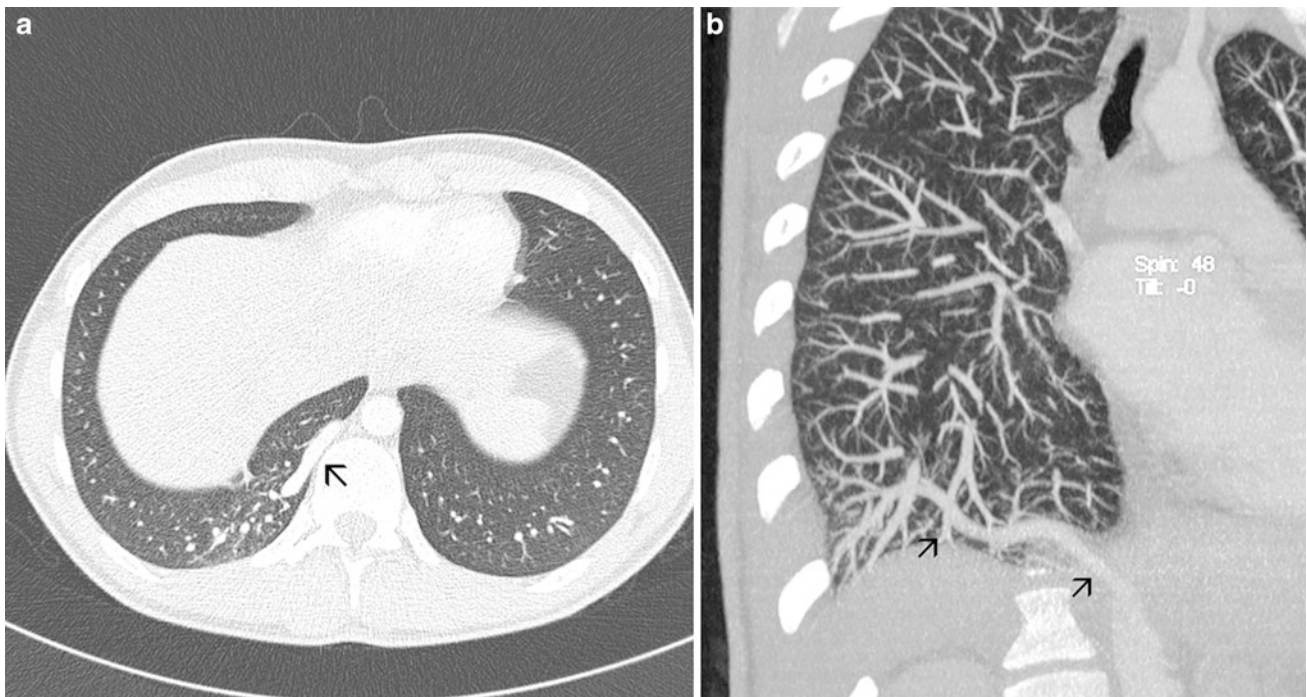


**Fig. 16** Isolated systemic supply to normal lung in a 18-year-old. CT scan in **a** shows the anomalous vessel as a large tubular structure in the right lower lobe (*arrow*). The vessels in the tissue supplied by the

systemic artery are larger than the remaining pulmonary artery vessels. CT angiogram with MIP reconstruction **b** shows the course of the anomalous systemic vessel from the abdominal aorta (*arrows*)

studies should be limited to cases in which embolization of feeding vessels is contemplated.

The treatment of bronchopulmonary sequestration (BPS) is controversial. Some authors consider that even in asymptomatic patients, BPS should be resected (Cho et al. 2012). Others consider endovascular treatment with selective embolization of the inflow arteries an attractive and minimally invasive therapeutic option (Marine et al. 2011). Nevertheless, other authors recommend nonsurgical management in asymptomatic patients due to the fact that BPS

can decrease and even spontaneously disappear (see Fig. 10) (Garcia-Peña et al. 1998, 2013).

## 2.4 Isolated Systemic Supply to Normal Lung

Isolated systemic supply to normal lung is a variant of pulmonary sequestration. This malformation corresponds to type I of Pryce's classification (Pryce et al. 1947). The artery is typically large and supplies the normal lung



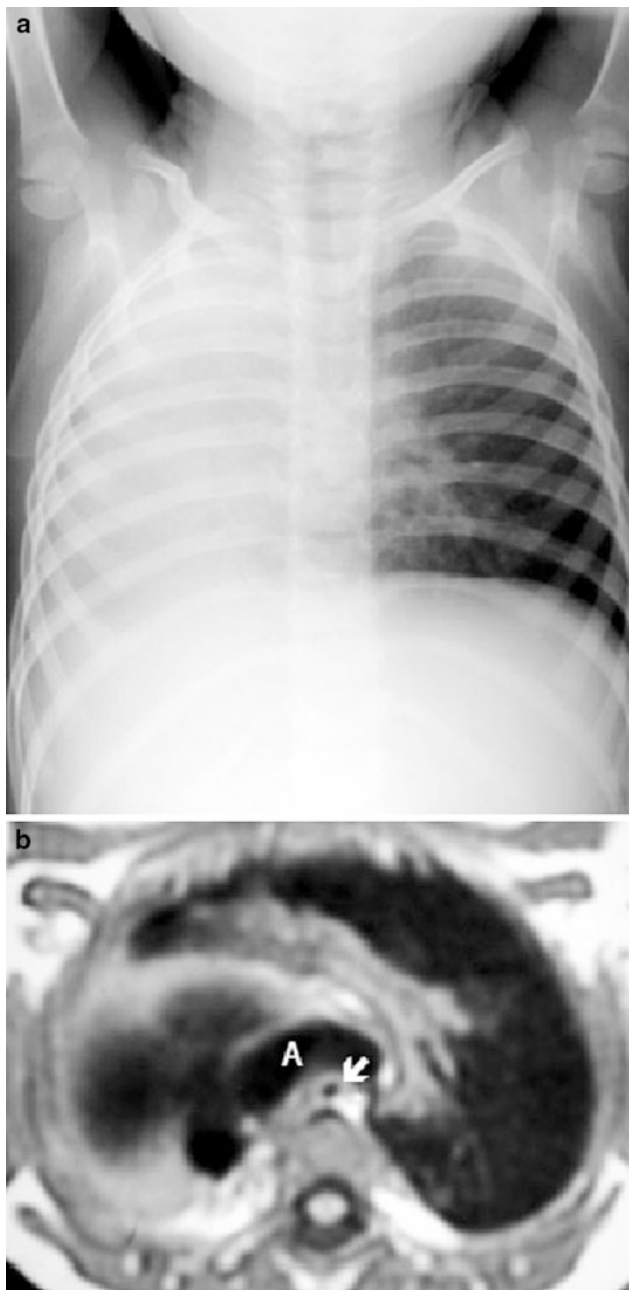


**Fig. 17** Right lung aplasia in a 2-year-old boy with respiratory symptoms. **a** Chest radiograph shows opaque right hemithorax with cardiomeastinal displacement and left lung hyperinflation. **b** Axial MR image at the level of the aortic arch demonstrates severe narrowing and posterior displacement of the distal trachea (arrow) by the crossing arch (A)

connected to the bronchial tree; the lung bases are affected more often (Mäkinen et al. 1981). Patients are usually asymptomatic, although there may be a continuous murmur on the thoracic wall or heart failure secondary to left-to-left shunt. Associated hemoptysis occurs occasionally.

Chest radiographs show increased opacity due to the systemic artery. Sometimes well-defined tubular or rounded

images produced by the anomalous vessels can be recognized. The pulmonary parenchyma does not present any other changes, unless there is associated hemorrhage. Definitive diagnosis can be established with MDCT identification of a systemic artery originating in the thoracic or abdominal aorta and absence of pathology of the underlying lung (Fig. 16) (Mata et al. 1991; Jiang et al. 2011).

### 3 Dysmorphic Lung

Dysmorphic lung (DL) is characterized by arrested development of either a whole lung (lung agenesis–hypoplasia complex) or a lobe (lobar agenesis–aplasia complex). Absence of a lobe may be associated with other abnormalities, some of them common and others highly unusual. DL can be recognized on chest radiographs when we are aware of its existence and it is sometimes possible to reach a diagnosis based solely on plain film evidence. In doubtful cases it is advisable to use CT (Mata et al. 1990; Woodring et al. 1994), or MRI (Baxter et al. 1990) to confirm the diagnosis.

#### 3.1 Lung Agenesis–Hypoplasia Complex

Arrested development of a whole lung (lung agenesis–hypoplasia complex) is uncommon and occurs equally often in either hemithorax. Although the terms agenesis (absence of bronchus and lung), aplasia (absence of lung with bronchus present), and hypoplasia (bronchus and rudimentary lung present) describe different anomalies (Boyden 1955), we group all three under the term “agenesis–hypoplasia complex” because all have a similar radiologic appearance on the chest radiograph. In pediatric patients the prognosis for right-sided agenesis is worse than for left-sided lesions, due to a greater shift of the heart and mediastinum, resulting in a greater distortion of the airway and great vessels. Respiratory distress and recurrent infections are common in children with right-lung agenesis. Airway compression by vascular structures, such as the aortic arch, pulmonary artery and patent ductus arteriosus, as well as intrinsic tracheobronchial anomalies and tracheobronchomalacia have been described in patients with right-lung agenesis (Newman and Gondor 1997) (Fig. 17). A similar appearance has been reported in patients with the so-called right post-pneumonectomy syndrome.

Lung agenesis–hypoplasia complex can be associated with malformations in other systems, including the skeletal, digestive, cardiac and urinary systems, and even in the contralateral lung (Brünner and Nissen 1963). The incidence of lung agenesis–hypoplasia with malformations in the skeleton or other organs is very high in some series

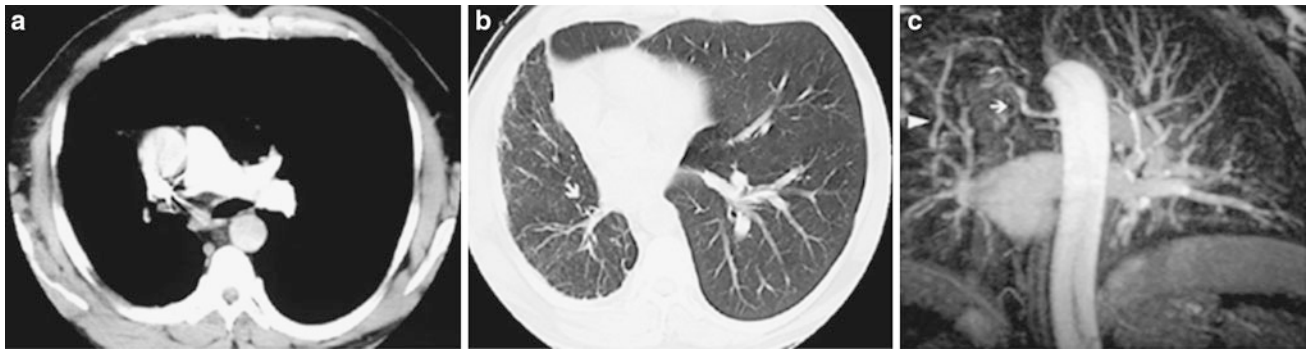


**Fig. 18** Absence of proximal right pulmonary artery. **a** Contrast-enhanced CT scan reveals absence of the right pulmonary artery. **b** Axial CT image at lung window shows volume loss on right side with shift of heart and mediastinum and a tiny pulmonary vein

(arrow). **c** Breath-hold coronal 3D GRE MIP reconstruction after dynamic gadolinium injection shows the presence of intercostal vessels (arrowhead) and bronchial arteries (arrow) arising from the aorta supplying the right lung

(Osborne et al. 1989). A common origin, such as insult to the neural crest in the embryo has been postulated to explain these phenomena, giving rise to the VACTERL syndrome of anomalies (Knowles et al. 1988).

Characteristically, lung agenesis–hypoplasia complex appears on the posteroanterior view as a diffuse opacity of one hemithorax with mediastinal shift, reminiscent of the appearance of whole lung atelectasis. Occasionally it presents an atypical appearance that is more difficult to recognize on plain film. The small hemithorax, aerated lung and apparent pleural thickening, simulate chronic pleural disease (Calenoff and Friederici 1964). This appearance results from the marked herniation of the contralateral lung. Typical and atypical cases show the same radiological appearance on the lateral chest view: retrosternal hyperclarity with the heart and large mediastinal vessels displaced backwards (Mata and Cáceres 1996).

CT demonstrates the reasons for the two distinct radiological presentations. Pulmonary herniation takes place behind the sternum in both groups and accounts for the retrosternal hyperclarity. Mediastinal rotation explains the posterior displacement of the heart and mediastinum. If the herniation of the contralateral lung is not severe, the plain film shows the typical appearance of a small opaque hemithorax. In atypical cases, the extensive herniation of the contralateral lung crosses the midline to penetrate deep into the malformed hemithorax, giving the appearance of aerated lung on plain films. The pseudo-thickening of the pleura is produced by accumulation of subpleural fatty tissue, filling the space left by the absent or underdeveloped lung (Mata et al. 1990). Lung agenesis, aplasia, and hypoplasia can be differentiated with use of CT, although the distinction is of little clinical significance. CT reveals the presence or absence of bronchi and pulmonary tissue, and allows measurement of the ipsilateral pulmonary artery (Mata and Cáceres 1996). Although lung agenesis–

hypoplasia complex is said to go together with a small ipsilateral pulmonary artery, on CT or MRI studies a small number of patients show a near normal-sized pulmonary artery with substantial blood flow.

Absence (atresia or interruption) of the main right or left pulmonary artery (APA) is an isolated vascular malformation that goes together with small homolateral lung, but should not be considered a part of lung agenesis–hypoplasia complex. It usually occurs in association with cardiac anomalies; isolated APA is rare (Kleinman 1979). During childhood APA produces substantial bronchial and transpleural (intercostal arteries) collateral circulation. The enlarged bronchial and intercostal arteries that feed the lung sometimes produce hemoptysis. At radiologic study, APA is seen as a small lung with mediastinal shift and no identifiable pulmonary artery. Collateral systemic supply produces peripheral linear opacities and pleural thickening. CT and MRI show absence of the pulmonary artery and can identify the enlarged systemic arteries (Fig. 18).

### 3.2 Lobar Agenesis–Aplasia Complex

Lobar agenesis–aplasia complex is a group of pulmonary malformations affecting, almost exclusively, the right hemithorax. All of these malformations present pulmonary anomalies in the form of one or more absent or underdeveloped pulmonary lobe. Depending upon the associated venous malformation, we can look at this group as a continuum. At one extreme, the pulmonary malformation is isolated and the veins are normal (hypogenetic lung syndrome). The second step in the continuum includes the anomalous unilateral single pulmonary vein, which drains all the lung parenchyma into the left atrium (Hasuo et al. 1981). Next in line is the levo-atriocardinal vein; in this malformation there is an anomalous vein that drains the entire lung and connects the left atrium with a systemic vein

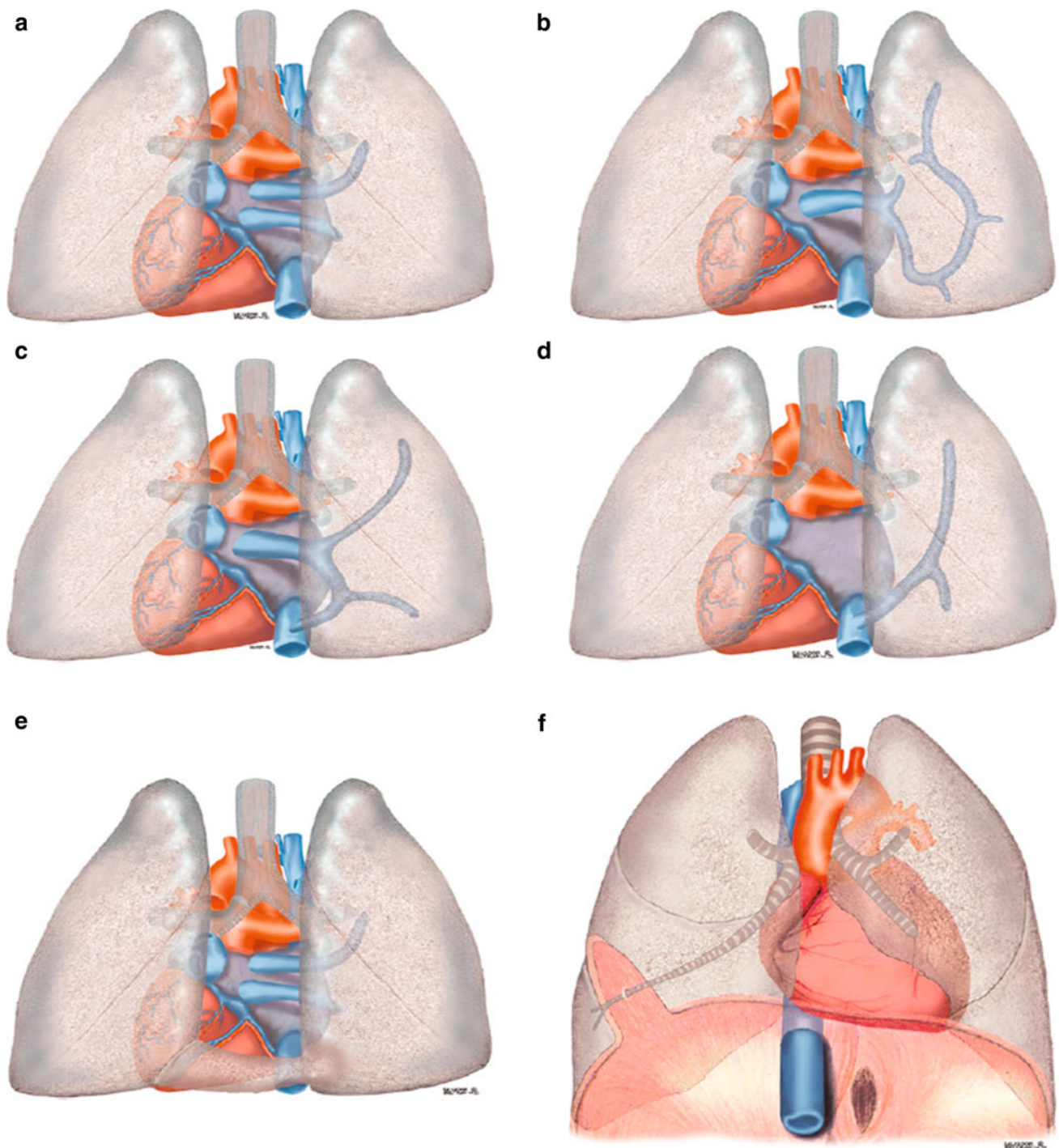


**Fig. 19** The term lobar agenesis–aplasia comprises a complex group of pulmonary malformations with one or more absent or underdeveloped pulmonary lobes. Depending on the associated venous malformation, this group can be viewed as a continuum. At one extreme, the pulmonary malformation is isolated, and the veins are normal and drain into the left atrium (a). The second step of the continuum includes the anomalous unilateral single pulmonary vein, which drains the entire lung parenchyma into the left atrium (b). Next in line is the levo-atriocardinal vein, in which there is an anomalous vein that

drains the entire lung and connects the left atrium with a systemic vein (inferior vena cava in the drawing) (c). Last in the continuum is an anomalous vein draining into the systemic venous system (venolobar syndrome) (d). Horseshoe lung (tissue from the malformed lung crossing the mediastinum to meet or fuse with the left lower lobe) (e) and accessory diaphragm (part of the right lung trapped by a membranous duplication of the diaphragm) (f) can accompany any of these malformations



**Fig. 20** Multiplanar reformation image. Congenital venolobar syndrome. We can see the scimitar vein (*arrow*) and the systemic supply from the abdominal aorta going to the right pulmonary base (*arrowheads*)



(Edwards and DuShane 1950). Last in the continuum is an anomalous vein draining into the systemic venous system (venolobar syndrome). Accessory diaphragm (part of the right lung trapped by a membranous duplication of the diaphragm) (Nazarian et al. 1971) and horseshoe lung (tissue from the malformed lung crossing the mediastinum to meet or fuse with the left lower lobe) (Dische et al. 1974) can accompany any of these malformations (Fig. 19). Systemic supply from the thoracic aorta is almost always present, although it is hardly ever seen on plain film or CT scans (Fig. 20). Sometimes the systemic artery is thick, mimicking a scimitar vein (Partridge et al. 1988).

### 3.2.1 Hypogenetic Lung Syndrome

In hypogenetic lung syndrome there is agenesis or aplasia of one or two pulmonary lobes. Patients are usually asymptomatic. This entity almost always occurs in the right hemithorax; left hemithorax involvement is exceptional.

The chest radiograph shows a small right hemithorax with mediastinal shift to the right and haziness of the right cardiac border. In some cases, the right hilum is hidden by mediastinal rotation and cannot be seen, and in others the shape of the hilum is reminiscent of the left hilum. In most cases, lateral chest films show a retrosternal band caused by the interface between the shifted mediastinum and the anterior border of the underdeveloped lung (Ang and Proto 1984).

CT provides a wealth of information (Godwin and Tarver 1986; Mata and Cáceres 1996) by demonstrating the size of the pulmonary artery, the branching of the bronchi, and accompanying anomalies of the diaphragm (diaphragmatic hernias). If underdevelopment is very pronounced, one can observe extrapleural fat deposits along the thoracic wall simulating pleural thickening similar to, though not as striking as, those seen in the lung agenesis–hypoplasia complex (Mata et al. 1990). The right upper lobe is the most often affected. This gives a bronchial pattern of the right lung similar to that observed in the left lung in normal conditions (hypoarterial bronchus) (Fig. 21). CT demonstrates the pulmonary veins draining into their normal location, ruling out venous anomalies.



**Fig. 21** Hypogenetic lung syndrome. CT scan shows left bronchial pattern in both lungs. The right lung is smaller than the left lung (Reprinted with permission)

### 3.2.2 Lobar Agenesis–Aplasia with Anomalous Unilateral Single Pulmonary Vein

The second step in the continuum is a symptom-free malformation, first described by Benfield et al. in 1971. It has received several names since its description: pulmonary varix, meandering right pulmonary vein, or scimitar sign with normal pulmonary venous drainage. In our experience, in most cases this malformation consists of a hypogenetic lung with a single anomalous vein draining the entire lung parenchyma into the left atrium. The vein follows an unusual pathway before it meets the left atrium.

In the chest radiograph anomalous unilateral single pulmonary vein usually has the same appearance as hypogenetic lung syndrome, plus a tubular and serpiginous shadow due to the anomalous vein. In rare cases the anomalous vein mimics a scimitar vein (Herer et al. 1988). MDCT and MRI provide the right diagnosis, showing a serpiginous shadow running through the lung and ending in the left atrium (Mata and Cáceres 1996) (Fig. 22). In some cases of anomalous unilateral single pulmonary vein, the vein drains into an extracardiac chamber located behind the left atrium (cor triatriatum).

Exceptionally we can see atypical cases with anomalous pulmonary veins affecting both lungs. This has been described as idiopathic prominence of pulmonary veins or “meandering pulmonary veins” (Kriss et al. 1995; Mata et al. 2000). The veins of both lungs follow an unusual pathway and drain into the left atrium. Meandering pulmonary veins is occasionally associated with hypogenetic lung.



**Fig. 22** Anomalous right unilateral single pulmonary vein. Axial SE T1-weighted images at two different levels (**a**, **b**) reveal an enlarged and serpiginous right pulmonary vein (arrows) draining at the left

atrium. **c** Coronal MR GRE 2D demonstrates the huge and tortuous single right pulmonary vein (arrow)



**Fig. 23** Multiplanar reformation image showing a levo-atriocardinal vein (arrow) connecting an anomalous vein draining into the inferior vena cava vein and a pulmonary vein draining into the left atrium (Courtesy of José Cáceres M.D.)

### 3.2.3 Lobar Agenesis-Aplasia with Levo-atriocardinal Vein

Levo-atriocardinal vein is defined as an anomalous vein that connects the left atrium and one vein of the systemic venous system. The systemic venous system derives from the embryological system known as cardinal veins. The malformation consists of a hypogenetic lung with the anomalous vein connecting the left atrium and one of the main systemic veins. Levo-atriocardinal vein would be the mid-point in the continuum between anomalous unilateral single pulmonary vein and venolobar syndrome. It is a very uncommon malformation.

On chest radiography the levo-atriocardinal vein looks very similar to the anomalous unilateral single pulmonary vein. CT demonstrates the usual findings of hypogenetic

lung syndrome and the vein joining the left atrium and a systemic vein (Fig. 23). The anomalous vein drains all the pulmonary veins, and MRI shows the pathway of the vein as well as the points where it meets with the systemic vein and the left atrium (Fig. 24) (Mata et al. 2000). MRI can demonstrate that there is no gradient between the left atrium and the systemic vein.

### 3.2.4 Congenital Venolobar Syndrome

In congenital venolobar syndrome (CVS), also known as scimitar syndrome, partial anomalous venous return (PAVR) is associated with hypogenetic lung syndrome. This malformation is one of the extremes of the DL continuum. Other components of the syndrome are an absent or small right pulmonary artery, anomalous systemic arterial supply of the lung from the thoracic or abdominal aorta, absence of the inferior vena cava, and anomalies of the hemidiaphragm (hernia, eventration, partial absence, accessory diaphragm). Bronchial tree anomalies (abnormal distribution, stenosis), esophageal and gastric lung (communication between sequestered lung and the esophagus or stomach), horseshoe lung, anomalous superior vena cava, and absence of the left pericardium are less frequently seen.

Congenital heart disease, most commonly atrial septal defects, is present in approximately 25 % of patients. Ventricular septal defects, patent ductus, tetralogy of Fallot, endocardial cushion defects, and aortic coarctation have also been reported.

Most adults and older children are asymptomatic. The left–right shunt produced by the anomalous drainage is usually small and has no clinical repercussions, though on rare occasions it can lead to pulmonary hypertension (Haworth et al. 1983). When scimitar syndrome presents during infancy, symptoms are usually severe and there are complex associated anomalies such as cardiac defects and anomalous systemic supply to the lung. (Canter et al. 1986). CVS occurs almost exclusively in the right hemithorax.



**Fig. 24** Levo-atriocardinal vein in the right lung. Axial MR GRE 2D images at three different levels (**a–c**) show the tortuous vein that goes from the left atrium to the inferior vena cava (*arrows*)

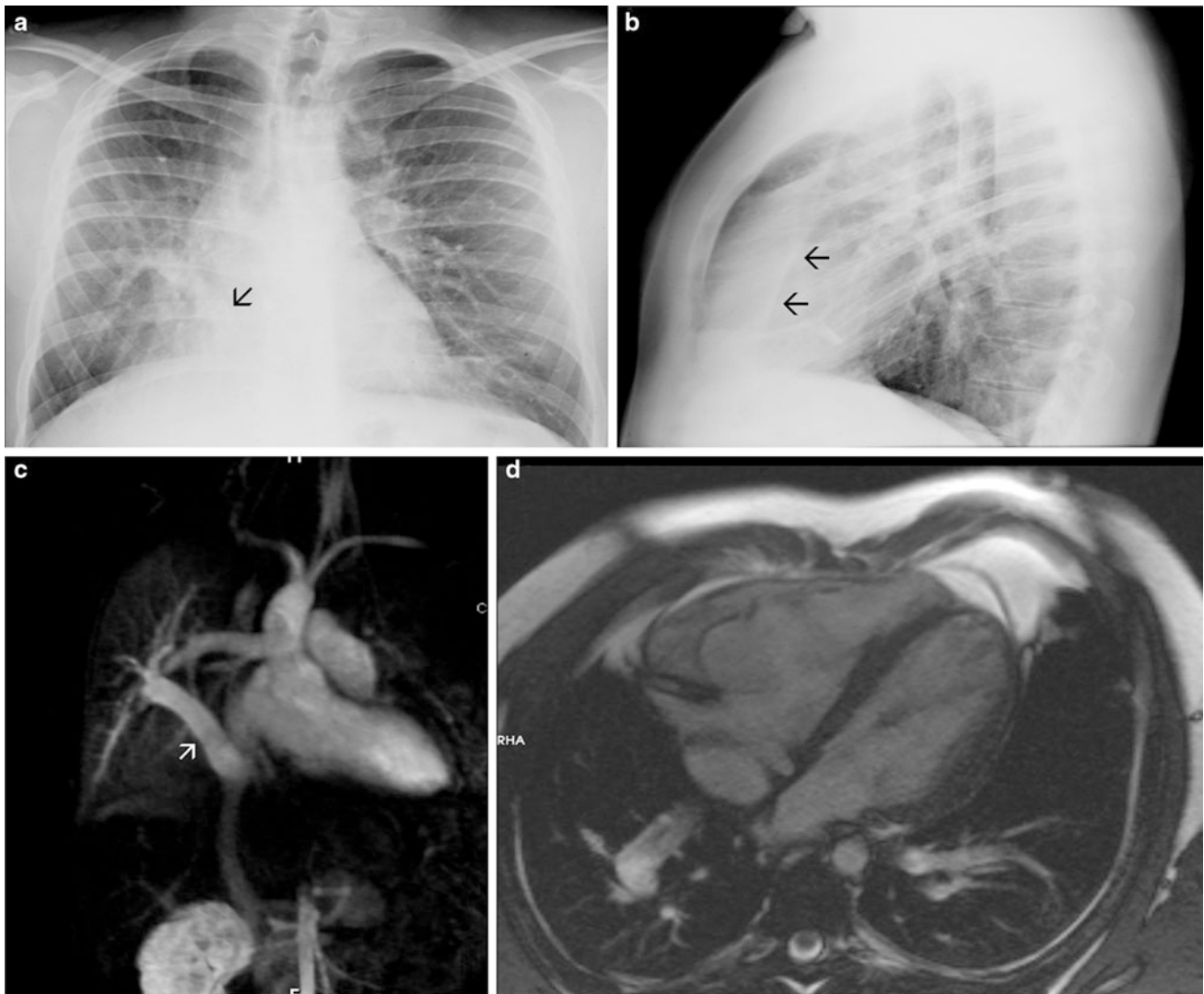


**Fig. 25** Venolobar syndrome **a** Chest plain film shows a tubular image in the right pulmonary base (*arrow*) and an elevation of right diaphragm secondary to diaphragmatic eventration; the right lung is smaller than the left lung. The lateral view **b** shows a retrosternal band

(*arrows*) **c** MR angiogram reveals the scimitar vein (*arrow*) draining to the suprahepatic portion of the inferior vena cava. **d** Bright-blood MR image shows right ventricular dilatation

Plain film findings are similar to those of hypogenetic lung. The differential finding is the anomalous vein. The vessel is seen as a widening tubular shadow that extends

toward the base of the lung, originating the term scimitar syndrome. The anomalous vein usually drains into the inferior vena cava or the right atrium. Less commonly,





**Fig. 26** Horseshoe lung. Plain film **a** shows a small right hemithorax and a linear image in the left pulmonary base (*arrow*). CT demonstrates the anomalous pattern of right bronchial tree and the

mediastinal shift (**b**). In **c** we can see the mediastinal discontinuity behind the heart and right lower lobe arteries and bronchus (*arrows*) crossing the midline, going to the left pulmonary base

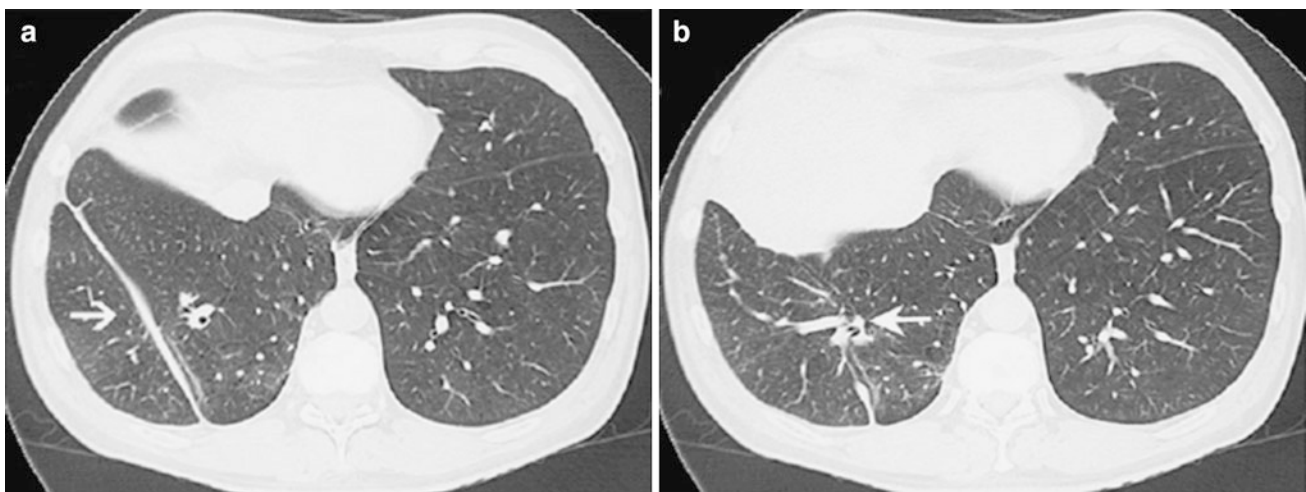


**Fig. 27** Accessory diaphragm. **a** The accessory diaphragm can be seen by CT as a line, simulating a fissure (*arrow*). **b** The vessels and bronchus are crowded together as they go through the central hole (*arrow*)

PAVR drains into the hepatic or portal veins, azygos system or coronary sinus. This drainage can be stenotic at its implantation. The fact there may be more than one vein or that a single vein may be hidden behind the displaced heart, accounts for the fact that the PAVR is not seen on plain films in half the cases.

Contrast-enhanced MDCT and gadolinium-enhanced MR angiography will show the anomalous pulmonary venous return, its course and drainage, the pulmonary artery, the systemic circulation to the lung (Mata et al. 1990; Woodring et al. 1994; Castellote et al. 2005) (Fig. 25), and the absence of pulmonary veins. PAVR is associated with an accessory pulmonary fissure that is visible on CT study (Godwin and Tarver 1986). MDCT scan may add information about bronchial anatomy and tracheobronchial abnormalities, septal lines (when the anomalous pulmonary return is obstructed), horseshoe lung, and other diaphragm malformations. Nevertheless, MR imaging provides functional data such as ventricular volumetry,

ventricular function, flow analysis, and flow quantification, which may be used to calculate the left-to-right shunt fraction. These functional data enable the cardiologist to determine the functional importance of the lesion.

Surgery is reserved for patients with severe symptoms, usually due to a substantial left-to-right shunt with right ventricular dilatation (from volume overload) (Vyas et al. 2012).

### 3.2.5 Horseshoe Lung

Horseshoe lung is associated with hypogenetic lung syndrome and occurs when a small quantity of right pulmonary tissue arising from the lower lobe crosses the midline and joins the left lower lung. The right and left lower lobes may fuse, or be separated by a fissure. The isthmus of pulmonary tissue crosses the mediastinum behind the pericardium, in front of the aorta and the esophagus, and it is supplied by the right lower lobe vessels and bronchus (Frank et al. 1986; Freedom et al. 1986).

The chest radiograph shows hypogenetic lung syndrome or CVS together with an anomalous fissure in the base of the left lung. This finding suggests the correct diagnosis on the PA chest film (Frank et al. 1986). Sometimes the anomalous fissure can be seen as a thick opacity due to internal fat. CT shows the typical findings of hypogenetic lung, with or without abnormal veins, plus two additional findings: mediastinal discontinuity behind the heart, with the vessels of the right lower lobe crossing the midline and, when present, an anomalous fissure located at the base of the left lung (Fig. 26) (Beitzke et al. 1982).

### 3.2.6 Accessory Diaphragm

Accessory diaphragm, also known as diaphragmatic duplication, is a rare congenital anomaly associated with the lobar agenesis-aplasia complex. It does not occur as an isolated malformation. Accessory diaphragm was first described by Drake et al. in 1950. These authors postulated that the anomaly is produced in the initial stages of embryonic development when the septum transversum, which gives rise to the diaphragm, is in a very high position. If for some reason the descent of the septum transversum is arrested, part of the primitive lung can be trapped by it. The septum transversum would remain anchored to the posterior wall, creating an additional diaphragmatic leaf.

Accessory diaphragm is a thin fibromuscular membrane fused anteriorly with the diaphragm and coursing posterosuperiorly to join the posterior chest wall. It produces two compartments in the right hemithorax, trapping part of the lung parenchyma (Wille et al. 1975). The vessels and bronchi that supply the trapped lung pass through a central hole in the accessory diaphragm.

The accessory diaphragm can have two different appearances in the chest radiograph. When the central hiatus is very narrow, the trapped lung is not aerated and appears as a mass. When the trapped lung is aerated, the accessory diaphragm appears in plain film as a thin oblique line in either the posteroanterior or lateral chest view. In some patients a haziness is visible where the duplicated diaphragm joins the normal one.

When the lung is aerated, CT scans show the accessory diaphragm as a fissure-like line with a hole in the center (Woodring et al. 1994; Hidalgo et al. 2006) (Fig. 27). Depending upon the size of the central hole, the CT appearance varies. When the hole is large, it may be difficult to identify the accessory diaphragm. When the hole is small, the trapped lung may be opaque or hyperlucent, due to air-trapping. Vessels and bronchi are crowded together when they go through the central hiatus.

## References

- Abbey P, Das CJ, Pangtey GS, Seith A, Dutta R, Kumar A (2009) Imaging in bronchopulmonary sequestration. *J Med Imaging Radiat Oncol* 53:22–31
- Ang JGP, Proto A (1984) CT demonstration of congenital pulmonary venolobar syndrome. *J Comput Assist Tomogr* 8:753–757
- Baker EM (1989) Intrathoracic duplication cysts: a review of 17 patients. *J Med Imaging* 3:127–134
- Baker EL, Gore RM, Moss AA (1982) Retroperitoneal pulmonary sequestration: computed tomographic findings. *Am J Roentgenol* 138:956–957
- Bankoff MS, Daly BDT, Johnson HA, Carter BL (1985) Bronchogenic cyst causing superior vena cava obstruction: CT appearance. *J Comput Assist Tomogr* 9:951–952
- Baxter R, McFadden PM, Gradman M, Wright A (1990) Scimitar syndrome: cine magnetic resonance imaging demonstration of anomalous pulmonary venous drainage. *Ann Thorac Surg* 50:121–123
- Beitzke VA, Gypser G, Sager WD (1982) Scimitarsyndrom mit Hufeisenlunge. *ROFO* 136:265–269
- Benfield JR, Gots RE, Mills D (1971) Anomalous single left pulmonary vein mimicking a parenchymal nodule. *Chest* 59:101–102
- Biyyam DR, Chapman T, Ferguson MR, Deutsch G, Dighe MK (2010) Congenital lung abnormalities: embryologic features, prenatal diagnosis, and postnatal radiologic-pathologic correlation. *Radiographics* 30:1721–1738
- Boyden EA (1955) Developmental anomalies of the lung. *Am J Surg* 89:79–89
- Braffman B, Keller R, Stein Gendal E, Finkel SI (1988) Subdiaphragmatic bronchogenic cyst with gastric communication. *Gastrointest Radiol* 13:309–311
- Brünner S, Nissen E (1963) Agenesis of the lung. *Am Rev Respir Dis* 78:103–106
- Cachia R, Sobonya RE (1981) Congenital cystic adenomatoid malformation of the lung with bronchial atresia. *Hum Pathol* 12:947–950
- Calenoff L, Friederici HH (1964) Unilateral pulmonary hypoplasia in an adult. *Am J Roentgenol* 91:265–272
- Canter CE, Martin TC, Spray TL, Weldon CS, Strauss AW (1986) Scimitar syndrome in childhood. *Am J Cardiol* 58:652–654
- Castellote A, Enriquez G, Lucaya J (2005) Congenital malformations of the chest beyond the neonatal period. In: Carty H, Brunelle F, Stringer DA, Kao SC-S (eds) *Imaging children*, Elsevier, Amsterdam
- Ch'in KY, Tang MY (1949) Congenital adenomatoid malformation of one lobe of the lung with general anasarca. *Arch Pathol* 48:221–229
- Cho MJ, Kim DY, Kim SC et al (2012) Embolization versus surgical resection of pulmonary sequestration: clinical experience with a thorascopic approach. *J Pediatr Surg* 12:2228–2233
- Dische MR, Teixeira ML, Winchester PA, Engle MA (1974) Horseshoe lung associated with a variant of the “scimitar” syndrome. *Br Heart J* 36:617–620
- Drake EH, Portland ME, Lynch JP (1950) Bronchiectasis associated with anomaly of the right pulmonary vein and right diaphragm. *J Thorac Surg* 19:433
- DuMontier C, Graviss ER, Silberstein MJ, McAlister WH (1985) Bronchogenic cysts in children. *Clin Radiol* 36:431–436

- Edwards JE, DuShane JW (1950) Thoracic venous anomalies. *Arch Pathol* 49:517
- Felson B (1979) Mucoid impaction (inspissated secretions) in segmental bronchial obstruction. *Radiology* 133:9–16
- Finck S, Milne ENC (1988) A case report of segmental atresia: Radiologic evaluation including computed tomography and magnetic resonance imaging. *J Thorac Imag* 3:53–57
- Frank JL, Poole CA, Rosas G (1986) Horseshoe lung: clinical, pathologic, and radiologic features and a new plain film finding. *Am J Roentgenol* 146:217–226
- Frazier AA, Rosado-de-Christenson M, Stocker JT, Templeton PA (1997) Intralobar sequestration: radiologic-pathologic correlation. *Radiographics* 17:725–745
- Freedom RM, Burrows PE, Moes CAF (1986) “Horseshoe” lung: report of five new cases. *Am J Roentgenol* 146:211–215
- García-Peña P, Lucaya J, Hendry GMA et al (1998) Spontaneous involution of pulmonary sequestration in children: a report of two cases and review of the literature. *Pediatr Radiol* 28:266–270
- García-Peña P, Coma A, Enriquez G (2013) Congenital lung malformations: radiological findings and clues for differential diagnosis. *Acta Radiol*. doi:10.1177/0284185113475919
- Gebauer PW, Mason CB (1959) Intralobar pulmonary sequestration associated with anomalous pulmonary vessels: a nonentity. *Dis Chest* 35:282–287
- Godwin JD, Tarver RD (1986) Scimitar syndrome: four new cases examined with CT. *Radiology* 159:15–20
- Grewal RG, Yip CK (1994) Intralobar pulmonary sequestration and mediastinal bronchogenic cyst. *Thorax* 49:615–616
- Griscom NT (1993) Diseases of the trachea, bronchi, and smaller airways. *Radiol Clin North Am* 31:605–615
- Hasuo K, Numaguchi Y, Kishikawa T, Ikeda J, Matsuura K (1981) Anomalous unilateral single pulmonary vein mimicking pulmonary varices. *Chest* 79:602–604
- Haworth SG, Sauer U, Bühlmeier K (1983) Pulmonary hypertension in scimitar syndrome in infancy. *Br Heart J* 50:182–189
- Heitzman ER (1984) The lung: radiologic-pathologic correlations. Mosby, St Louis
- Herer B, Jaubert F, Delaisements C, Huchon G, Chretien J (1988) Scimitar sign with normal pulmonary venous drainage and anomalous inferior vena cava. *Thorax* 43:651–652
- Hidalgo A, Franquet T, Gimenez A (2006) 16-MDCT and MR angiography of accessory diaphragm. *AJR* 187:149–152
- Holder PD, Langston C (1986) Intralobar pulmonary sequestration (a nonentity?). *Pediatr Pulmonol* 2:147–153
- Hruban RH, Shumway SJ, Orel SB, Dumler JS, Baker RR, Hutchins M (1989) Congenital pulmonary foregut malformations. Intralobar and extralobar pulmonary sequestration communicating with the foregut. *Am J Clin Pathol* 91:403–408
- Hugosson C, Rabeah A, Al-Rawaf A et al (1995) Congenital bilobar emphysema. *Pediatr Radiol* 25:649–651
- Ikezoe J, Murayama S, Godwin JD, Done SL, Verschakelenm JA (1990) Bronchopulmonary sequestration: CT assessment. *Radiology* 176:375–379
- Jederlinic PJ, Sicilian LS, Baigelman W, Gaensler EA (1986) Congenital bronchial atresia. *Medicine* 65:73–83
- Jiang S, Shi JY, Zhu XH et al (2011) Endovascular embolization of the complete type of anomalous systemic arterial supply to normal basal lung segments: a report of four cases and literature review. *Chest* 139:1506–1513
- Kim WS, Lee KS, Kim IO et al (1997) Congenital cystic adenomatoid malformation of the lung. CT-pathologic correlation. *Am J Roentgenol* 168:47–53
- Kimura A, Makuuchi M, Takayasu K, Sakamoto M, Hirohashi S (1990) Ciliated hepatic foregut cyst with solid tumor appearance on CT. *J Comput Assist Tomogr* 14:1016–1018
- Kleinman PK (1979) Pleural telangiectasia and absence of a pulmonary artery. *Radiology* 132:281–284
- Knowles S, Thomas RM, Lindenbaum RH, Keeling JW, Winter RM (1988) Pulmonary agenesis as part of the VACTERL sequence. *Arch Dis Child* 63:723–726
- Ko SF, Ng SH, Lee TZ et al (2000) Noninvasive imaging of bronchopulmonary sequestration. *Am J Roentgenol* 175:1005–1012
- Kriss VM, Woodring JH, Cottrill CM (1995) “Meandering” pulmonary veins: report of a case in an asymptomatic 12-year-old girl. *J Thorac Imaging* 10:142–145
- Kuhn C, Khun JP (1992) Coexistence of bronchial atresia and bronchogenic cyst: diagnostic criteria and embryologic considerations. *Pediatr Radiol* 22:568–570
- Kwak GL, Stork WI, Greenberg SD (1971) Partial defect of the pericardium associated with a bronchogenic cyst. *Radiology* 101:287–288
- Langston C (2003) New concepts in the pathology of congenital lung malformations. *Semin Pediatr Surg* 12:17–37
- Laurin S, Hägerstrand I (1999) Intralobar bronchopulmonary sequestration in the newborn—a congenital malformation. *Pediatr Radiol* 29:174–178
- Lee EY, Siegel MJ, Sierra LM et al (2004) Evaluation of angioarchitecture of pulmonary sequestration in pediatric patients using 3D MDCT angiography. *AJR Am J Roentgenol* 183:183–188
- Lee EY, Tracy DA, Mahmood SA et al (2011a) Preoperative MDCT evaluation of congenital lung anomalies in children: comparison of axial, multiplanar and 3 D images. *Am J Roentgenol* 196:1040–1046
- Lee EY, Dorkin H, Vargas SO (2011b) Congenital pulmonary malformations in pediatric patients: review and update on etiology, classification, and imaging findings. *Radiol Clin North Am* 49:921–948
- Lejeune C, Deschildre A, Thumerelle C et al (1999) Pneumothorax revealing cystic adenomatoid malformation of the lung in a 13 year old boy. *Arch Pediatr* 6:863–866
- Lemire P, Trepanier A, Hebert G (1970) Bronchocele and blocked bronchiectasis. *Am J Roentgenol* 110:687–693
- Lucaya J, García-Conesa JA, Bernadó L (1984) Pulmonary sequestration associated with unilateral pulmonary hypoplasia and massive pleural effusion. *Pediatr Radiol* 14:228–229
- Lucaya J, García-Peña P, Herrera L et al (2000) Expiratory chest CT in children. *Am J Roentgenol* 174:235–241
- Lyon RD, McAdams HP (1993) Mediastinal bronchogenic cyst demonstration of a fluid–fluid level at MR imaging. *Radiology* 186:427–428
- MacGillivray TE, Harrison MR, Goldstein RB, Adzik SA (1993) Disappearing fetal lung lesions. *J Pediatr Surg* 28:1321–1325
- MacSweeney F, Papagiannopoulos K, Goldstraw P (2003) An assessment of the expanded classification of congenital cystic adenomatoid malformations and their relationship to malignant transformation. *Am J Surg Pathol* 27(8):1139–1146
- Mäkinen EO, Merikanto J, Rikainen H, Satokari K (1981) Intralobar pulmonary sequestration occurring without alteration of pulmonary parenchyma. *Pediatr Radiol* 10:237–240
- Marine LM, Valdes FE, Mertens RM et al (2011) Endovascular treatment of symptomatic pulmonary sequestration. *Ann Vasc Surg* 25:696.e11–5
- Martin KW, Siegel MJ, Chesna E (1988) Spontaneous resolution of mediastinal cysts. *Am J Roentgenol* 150:1131–1132
- Mata JM, Cáceres J (1996) The dysmorphic lung: imaging findings. *Eur Radiol* 6:403–414
- Mata JM, Cáceres J, Lucaya J, García-Conesa JA (1990) CT of congenital malformations of the lung. *Radiographics* 10:651–674



- Mata JM, Cáceres J, Lucaya X (1991) CT diagnosis of isolated systemic supply to the lung: a congenital broncho-pulmonary vascular malformation. *Eur J Radiol* 13:138–142
- Mata JM, Cáceres J, Castañer E, Gallardo X, Andreu J (2000) The dysmorphic lung: imaging findings. *Postgrad Radiol* 20:3–15
- McAdams HP, Kirejczyk WM, Rosado-de-Christenson ML, Matsumoto S (2000) Bronchogenic cyst: imaging features with clinical and histopathologic correlation. *Radiology* 217:441–446
- Medelli J, Lattaignant JC, Bertoux JP, Goudot B, Remond A (1979) L'atrésie bronchique segmentaire. *Poumon* 35:53–58
- Murphy JJ, Blair GK, Fraser GC et al (1992) Rhabdomyosarcoma arising within congenital pulmonary cysts: report of three cases. *J Pediatr Surg* 27:1364–1367
- Naidich DP, Rumancick WM, Ettenger NA et al (1988) Congenital anomalies of the lung in adults: MR diagnosis. *Am J Roentgenol* 151:13–19
- Nakata H, Egashira K, Warnanake H (1993) MRI of bronchogenic cysts. *J Comput Assist Tomogr* 17:267–270
- Nazarian M, Currarino G, Webb WR, Willis K, Kiphart RJ, Wilson HE (1971) Accessory diaphragm: report of a case with complete physiological evaluation and surgical correction. *J Thorac Cardiovasc Surg* 61:293
- Newman B (2006) Congenital bronchopulmonary foregut malformations: concepts and controversies. *Pediatr Radiol* 36:773–791
- Newman B, Gondor M (1997) MR evaluation of right pulmonary agenesis and vascular airway compression in pediatric patients. *Am J Roentgenol* 168:55–58
- Osborne J, Masel J, McCredie J (1989) A spectrum of skeletal anomalies associated with pulmonary agenesis: possible neural crest injuries. *Pediatr Radiol* 19:425–432
- Partridge JB, Osborne JM, Slaughter RE (1988) Scimitar etcetera: the dysmorphic lung. *Clin Radiol* 39:11–19
- Patcher MR, Lattes R (1963) Mediastinal cysts: a clinicopathologic study of twenty cases. *Dis Chest* 44:416–422
- Paterson A (2005) Imaging evaluation of congenital lung abnormalities in infants and children. *Radiol Clin North Am* 43:303–323
- Pedersen ML, LeQuire MH, Spies JB, Ladd WA (1988) Computed tomography of intralobar bronchopulmonary sequestration supplied from the renal artery. *J Comput Assist Tomogr* 12:874–875
- Pryce DM (1946) Lower accessory pulmonary artery with intralobar sequestration of lung, report of seven cases. *J Pathol Bacteriol* 58:457–467
- Pryce DM, Holmes Sellors T, Blair LG (1947) Intralobar sequestration of lung associated with an abnormal pulmonary artery. *Br J Surg* 35:18–29
- Pugatch RD, Gale ME (1983) Obscure pulmonary masses: bronchial impaction revealed by CT. *Am J Roentgenol* 141:909–914
- Pulpeiro JR, López I, Sotelo T, Ruiz JC, García-Hidalgo E (1987) Congenital cystic adenomatoid malformation of the lung in a young adult. *Br J Radiol* 60:1128–1130
- Recio Rodríguez M, Martínez de Vega V, Cano Alonso R, Carrascoso Arranz J, Martínez Ten P, Pérez Pedregosa J (2012) MR imaging of thoracic abnormalities in the fetus. *Radiographics* 32(7):E305–E321
- Reed JC, Sobonya RE (1975) RCP from the AFIP. *Radiology* 117:315–319
- Rees S (1981) Arterial connections of the lung. *Clin Radiol* 32:1–15
- Remy-Jardin M, Remy J, Ribet M, Gosselin B (1989) Bronchial atresia: diagnostic criteria and embryologic considerations. *Diagn Interv Radiol* 1:45–51
- Restrepo S, Villamil MA, Rojas JC (2004) Association of two respiratory congenital anomalies: tracheal diverticulum and cystic adenomatoid malformation of the lung. *Pediatr Radiol* 34:263–266
- Rogers LE, Osmer JC (1964) Bronchogenic cyst. A review of 46 cases. *Am J Roentgenol* 91:273–283
- Rosado-de-Christenson M, Stocker JT (1991) Adenomatoid malformation. *Radiographics* 11:865–886
- Rosado-de-Christenson M, Frazier AA, Stocker JT, Templeton PA (1993) Extralobar sequestration: radiologic-pathologic correlation. *Radiographics* 13:425–441
- Samuel M, Burge DM (1999) Management of antenatally diagnosed pulmonary sequestrations associated with congenital cystic adenomatoid malformation. *Thorax* 54:701–706
- Savic B, Birtel FJ, Tholen W, Funke HD, Knoche R (1979) Lung sequestration: report of seven cases and review of 540 published cases. *Thorax* 34:96–101
- Senac MO, Wood BP, Isaacs H, Weller M (1991) Pulmonary blastoma: a rare childhood malignancy. *Radiology* 179:743–746
- Stern EJ, Webb WR, Warnock ML et al (2000) Bronchopulmonary sequestration: dynamic, ultrafast, high-resolution CT evidence of air trapping. *Am J Roentgenol* 74:235–241
- Stocker JT (2002) Congenital pulmonary airway malformation: a new name and an expanded classification of congenital cystic adenomatoid malformation of the lung. *Histopathology* 41(suppl): 424–431
- Stocker JT, Kagan-Hallet K (1979) Extralobar pulmonary sequestration. Analysis of 15 cases. *Am J Clin Pathol* 72:917–925
- Stocker JT, Madewell JE, Drake RM (1977) Congenital cystic adenomatoid malformation of the lung. *Hum Pathol* 8:155–171
- Ueda K, Gruppo R, Unger F, Martin L, Bove K (1977) Rhabdomyosarcoma of the lung arising in congenital cystic adenomatoid malformation. *Cancer* 40:383–388
- Vyas HV, Greenberg B, Krishnamurthy R (2012) MR imaging and CT evaluation of congenital pulmonary vein abnormalities in neonates and infants. *Radiographics* 32:87–98
- Ward S, Morcos SK (1999) Congenital bronchial atresia. Presentation of three cases and a pictorial review. *Clin Radiol* 54:144–148
- Wasilewska E, Lee EY, Eisenberg RL (2012) Unilateral hyperlucent lung in children. *AJR Am J Roentgenol* 198:400–414
- West MS, Donaldson JS, Shkolnik A (1989) Pulmonary sequestration. Diagnosis by ultrasound. *J Ultrasound Med* 8:125–129
- Wille L, Holthusem W, Willich E (1975) Accessory diaphragm: report of 6 cases and a review of the literature. *Pediatr Radiol* 4:14–20
- Winters WD, Effmann EL (2001) Congenital masses of the lung: prenatal and postnatal imaging evaluation. *J Thorac Imaging* 16:196–206
- Winters WD, Effmann EL, Nghiem HV et al (1997) Disappearing fetal lung masses: importance of postnatal imaging studies. *Pediatr Radiol* 27:535–539
- Woodring JH, Howard TA, Kanga JF (1994) Congenital pulmonary venolobar syndrome revisited. *Radiographics* 14:349
- Yu H, Li HM, Liu SY, Xiao XS (2010) Diagnosis of arterial sequestration using multidetector CT angiography. *Eur J Radiol* 76:274–278
- Zumbro GL, Green DC, Brott W, Tresaure RL (1974) Pulmonary sequestration with spontaneous intrapleural hemorrhage. *J Thorac Cardiovasc Surg* 68:673–674

# Congenital and Acquired Large Airway Disorders in Pediatric Patients

Evan J. Zucker, Monica Epelman, Ricardo Restrepo, and Edward Y. Lee

## Contents

<b>1</b>	<b>Introduction</b> .....	219
<b>2</b>	<b>Imaging Algorithm</b> .....	220
<b>3</b>	<b>Imaging Techniques</b> .....	220
3.1	Conventional Radiographs .....	220
3.2	Airway Fluoroscopy .....	220
3.3	Computed Tomography.....	220
<b>4</b>	<b>Spectrum of Imaging Findings</b> .....	222
4.1	Congenital Large Airway Disorders.....	222
4.2	Acquired Large Airway Disorders.....	228
<b>5</b>	<b>Mimic of Focal Large Airway Abnormalities</b> .....	237
5.1	Physiological Tracheal Buckling .....	237
5.2	Mucus.....	237
<b>6</b>	<b>Conclusion</b> .....	237
	<b>References</b> .....	238

## Abstract

Timely and accurate airway assessment is essential in infants and children who present with respiratory distress. With smaller and more compressible airways than their adult counterparts, more prone symptomatic airway obstruction. Failure to promptly recognize and treat airway disease can lead to substantial short-term morbidity or even mortality as well as long-term detrimental sequelae. In this chapter, currently available imaging methods for large airway assessment are discussed, followed by an overview of congenital and acquired large airway disorders affecting infants and children.

## 1 Introduction

Timely and accurate airway assessment is essential in infants and children who present with respiratory distress. With smaller and more compressible airways than their adult counterparts, children are more prone to symptomatic airway obstruction (Laya and Lee 2012; Lee et al. 2012). Failure to promptly recognize and treat airway disease can lead to substantial short-term morbidity or even mortality as well as long-term detrimental sequelae. While in many cases, children with suspected acute airway disease respond to empiric therapy without the need for further work-up, in other instances the diagnosis remains unclear despite the most thorough clinical evaluation. In these situations, imaging plays a pivotal role in the evaluation, detecting airway disease earlier, helping to narrow the differential diagnosis or suggest the exact diagnosis, directing management, obviating unnecessary interventions, and assisting in preprocedural planning. Due to recent and robust technical advances, computed tomography (CT) has become the gold standard for noninvasive evaluation of the pediatric large airway (Lee et al. 2011b, 2013). In this chapter, currently available imaging methods for large airway

E. J. Zucker  
Department of Radiology, Floating Hospital for Children,  
Tufts Medical Center, 800 Washington Street,  
Boston, MA 02111, USA

M. Epelman  
Department of Radiology, Nemours Children's Hospital,  
Orlando, FL, USA

R. Restrepo  
Department of Radiology, Miami Children's Hospital,  
2100 SW 62nd Avenue, Miami, FL 33155, USA

E. Y. Lee (✉)  
Department of Radiology and Medicine, Pulmonary Division,  
Boston Children's Hospital and Harvard Medical School,  
300 Longwood Avenue, Boston, MA 02115, USA  
e-mail: Edward.Lee@childrens.harvard.edu

assessment are discussed, followed by an overview of congenital and acquired large airway disorders affecting infants and children.

## 2 Imaging Algorithm

Imaging evaluation of the pediatric patient with clinically suspected large airways disease typically begins with plain radiographs of the neck and/or chest. Cheap and widely accessible, conventional radiography can help exclude radiopaque foreign body and assess for respiratory pathology simulating airways disease. Airway fluoroscopy may follow, helping to confirm radiographic abnormalities (e.g., prevertebral soft tissue swelling) represent true findings rather than artifacts created by improper patient positioning. Fluoroscopy also allows real-time assessment of the large airway and is useful in evaluating such dynamic conditions as tracheobronchomalacia (TBM) in infants and young children (Laya and Lee 2012; Lee et al. 2012, 2013).

Ultimately, further evaluation with cross-sectional imaging is often necessary due to the limited anatomical precision of conventional radiography and fluoroscopy compounded by the difficulties of poor patient cooperation. Although magnetic resonance imaging (MRI) would seem ideal due to the lack of ionizing radiation, in general it has limited ability to assess the airways and is less appealing due to long scan times and the potential need for patient sedation. CT, particularly multidetector CT (MDCT) with shorter scan times, higher spatial resolution, and the capability to evaluate both the lungs and airways simultaneously, is currently the imaging modality of choice for diagnosis, preprocedural planning, and follow-up of most pediatric large airway disorders (Laya and Lee 2012; Lee et al. 2011b, 2012, 2013).

## 3 Imaging Techniques

### 3.1 Conventional Radiographs

Plain radiographs remain first-line in the imaging assessment of children with suspected large airways disease. The typical examination consists of frontal and lateral radiographs of the neck and/or chest. A high kilovoltage (kV) magnification technique is preferred when imaging the airway to reduce conspicuity of the bones (Slovic 1977). The lateral neck radiograph should be taken with moderate neck extension during inspiration. Care should be taken to avoid patient expiration, flexion, or rotation, which may lead to inaccurate interpretation. Inspiratory-expiratory and/or lateral decubitus views are often obtained to assess for air trapping, an indirect sign of foreign body obstruction,

depending on the degree of patient cooperation (Laya and Lee 2012; Lee et al. 2012). Judicious use of immobilization devices can help achieve satisfactory images while preventing unnecessary retakes. However, children should never be forced to maintain a position that is uncomfortable and could in fact precipitate acute airway compromise.

### 3.2 Airway Fluoroscopy

Airway fluoroscopy is useful in confirming radiographic abnormalities and evaluating dynamic airway disorders such as TBM. In frontal, lateral, and oblique projections, the entire airway from nasopharynx to main bronchi may be assessed in real-time, safely, rapidly, and noninvasively. In addition to fiberoptic nasolaryngoscopy, airway fluoroscopy is commonly performed in infants and young children with stridor and is able to screen for fixed and dynamic airway obstruction below the level of vocal cords. Barium swallow may be performed simultaneously to assess for such conditions as tracheoesophageal fistula that may present with upper airway symptoms. Following the “As Low As Reasonably Achievable” (ALARA) principle, radiation dose-reduction techniques such as pulsed fluoroscopy and restricting time spent using the fluoroscopic pedal should be performed whenever possible. Achieving diagnostic fluoroscopy in uncooperative or obese patients can be technically challenging. Ultimately, more advanced modalities such as MDCT may be required for accurate assessment (Laya and Lee 2012; Lee et al. 2012).

### 3.3 Computed Tomography

Offering precise anatomical detail, rapid scan times, and the ability to create multiplanar two-dimensional (2D) and three-dimensional (3D) reconstructions on-demand, MDCT has become the noninvasive gold standard for evaluating the pediatric airway. Additionally, dynamic airway assessment may be achieved with newer techniques such as paired inspiratory-expiratory MDCT, cine MDCT, and four-dimensional (4D) MDCT (Laya and Lee 2012; Lee 2008; Lee and Boiselle 2009; Lee et al. 2010b, 2012, 2013; Lee and Siegel 2007). Technical considerations for performing high-quality airway CT in children are discussed in detail below.

#### 3.3.1 Patient Preparation

Patient preparation for CT differs according to age. Traditionally, sedation often with intubation was routinely recommended for infants and young children ( $\leq 5$ -years old), allowing a controlled ventilation (breath-hold) technique for end-inspiratory and end-expiratory airway imaging. End-inspiratory and end-expiratory images could be acquired by alternatively applying and withholding 15–20 cm H<sub>2</sub>O



**Table 1** Tube current and kV by patient weight for central airway MDCT

Weight (kg)	Tube current (mAs) Insp./exp.	Kilovoltage (kV)
<10	40/20	80
10–14	50/25	80
15–24	60/30	80
25–34	70/35	80
35–44	80/40	80
45–54	90/40	90
55–70	100–120/40	100–120

Reprinted with permission from Lee and Boiselle (2009)

*Insp* inspiratory; *Exp* expiratory; *mA* milliamperage; *kV* kilovoltage; *MDCT* multidetector computed tomography

For tube current and kilovoltage by patient weight for end-expiratory MDCT examination, mAs should be reduced by 50 % to a maximum of 40 mA while maintaining the same level of kV for end-inspiratory MDCT examination.

positive pressure ventilation during inspiration and expiration, respectively. Children >5-years old are usually able to follow instructions for respiratory maneuvers (end-inspiration, end-expiration, forced expiration, and coughing). After a practice session with the technologist or radiologist prior to imaging, these patients can generally undergo CT successfully without sedation even on older scanners (Lee et al. 2010b, 2013). However, scan times are now so rapid with modern 320-detector MDCT that satisfactory imaging can be obtained without sedation or intubation, even during breathing or crying episodes.

For routine evaluation of the large airways, intravenous (IV) contrast is not necessary. However, in certain situations it is recommended, e.g., to assess concurrent vascular anomalies, mediastinal masses, or central airway tumors. In these cases, appropriate IV access is necessary, with the volume of contrast administered weight-based and the injection rate dependent on the size and stability of IV catheter as well as method of injection. Mechanical is preferred to hand or central venous injection when possible in order to obtain more uniform contrast enhancement. The contrast dose ranges from 2 to 4 mL/kg, to a maximum of 125 mL. Typical injection rates range from 1 to 1.5 mL/s (by hand) for a 24-gauge catheter to 4–5 mL/s (mechanically) for an 18-gauge catheter (Lee et al. 2011a, b, 2013).

### 3.3.2 MDCT Parameters

MDCT parameters for large airway imaging are dependent on the type of CT scanner. A minimum of 16 detectors are recommended. Suggested parameters are: 0.75 mm collimation for a 16-MDCT scanner, 0.625 mm collimation for a 32-MDCT scanner, and 0.6 mm collimation for a 64-

MDCT scanner; high-speed mode; and a pitch equivalent of 1.0–1.5. Radiation-limiting measures should be utilized whenever possible, such as age- or weight-adjusted milliamperage (mA), lowest possible kV, and anatomically based real-time automated exposure control. The natural contrast between the airways and surrounding soft tissues allows for a lower-dose technique. Tube current and kV guidelines from Boston Children's Hospital are shown in Table 1. For cine MDCT, a gantry rotation time of  $\leq 0.5$  s, a detector collimation of 0.5–0.625 mm, and anatomic coverage up to 4 cm in the z-axis are recommended. For 4D dynamic MDCT, imaging is performed with 80 kVp,  $\text{mA} = (2.5 \times \text{kg} + 5)/0.35$ , and continuous scanning for 1.4 s (350 ms/rotation  $\times$  4 cycles) (Laya and Lee 2012; Lee and Boiselle 2009; Lee et al. 2011b, 2012, 2013).

### 3.3.3 Postprocessing Techniques

Three main currently available postprocessing techniques for evaluation of large airway disorders include 2D, 3D and 4D reconstructions.

#### 3.3.3.1 2D Reconstruction Imaging

Single-voxel-thick 2D multiplanar reformatted (MPR) images can be readily created at the CT console or at a distant postprocessing workstation in any desired plane (e.g., coronal, sagittal, oblique). Curved reformation along the long axis of the large airways may be obtained by drawing a reference line through the airway center on sagittal MPRs (Figs. 1a, 2b). Such reconstruction is invaluable for obtaining accurate airway measurements as are often needed prior to invasive interventions. Thick slab (generally 3–10 mm) or MPR volume reformation may be obtained by adding adjacent thin slices to balance spatial with contrast resolution to the desired level. Minimum intensity projection (MinIP) volume-rendered images, formed by choosing the lowest attenuation voxels, may be obtained to help increase conspicuity of the airways and lung parenchyma (Laya and Lee 2012; Lee and Boiselle 2009; Lee et al. 2011b, 2012, 2013).

#### 3.3.3.2 3D Reconstruction Imaging

3D airway reconstruction is typically obtained using volume rendering. This is a computational method that analyzes all available data voxels with an edge detection algorithm to create external and internal renderings of the large airways. External 3D renderings (i.e., virtual bronchography) show the relationship of the outer airway surfaces to nearby structures (Fig. 1c). Internal 3D renderings (i.e., virtual bronchoscopy) provide intraluminal views of the airways on par with conventional (direct) bronchoscopy (Fig. 1d). Virtual bronchoscopy is useful in preoperative

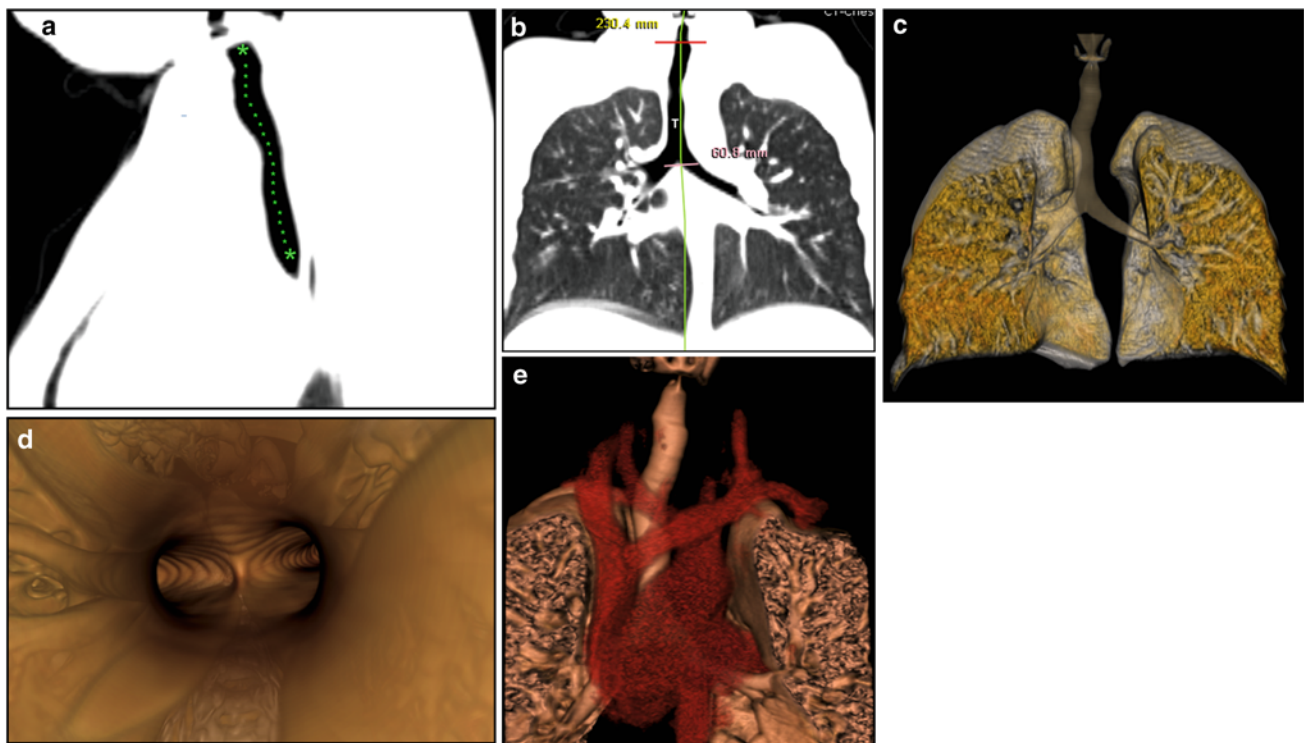


**Fig. 1** Normal large airways of a 6-year-old girl, **a** Sagittal reformatted CT image of the large airways shows a reference position (green asterisks) through the center of the airway for reconstruction of a curved coronal reformatted CT image, **b** Curved coronal reformatted CT image demonstrates a straighten view of the entire trachea (T), **c** 3D external volume rendering image (i.e., virtual bronchography) of

the large airways, **d** 3D internal volume rendering (i.e., virtual bronchoscopy) image obtained at the level of carina. Bilateral main stem bronchi are patent, **e** Combined 3D external volume rendering image of the large airways and surrounding cardiovascular structures (red)

planning. Moreover, it may even substitute for traditional diagnostic bronchoscopy, thus potentially avoiding an invasive procedure and the need for general anesthesia (Lee et al. 2012, 2013). For preoperative evaluation of underlying mediastinal vascular anomalies resulting in large airway compression, a combined view of both large airways and vascular structures can provide comprehensive assessment (Fig. 1e).

### 3.3.3.3 4D Reconstruction Imaging

4D MDCT combines 3D renderings with real-time evaluation, which is considered as the fourth dimension. The large airways are depicted in real-time as a continuously moving 3D image. Innovative 320 MDCT scanners can display the large airways up to a 16-cm-long craniocaudal extent (sufficient even for most older children) with true isometric, isophasic, and isovolumetric 4D imaging throughout the respiratory cycle. 4D techniques are particularly useful for evaluating dynamic airway abnormalities such as TBM, assessing anatomical changes with time (Lee et al. 2012, 2013).

## 4 Spectrum of Imaging Findings

### 4.1 Congenital Large Airway Disorders

#### 4.1.1 Non-vascular Congenital Large Airway Disorders

##### 4.1.1.1 Tracheobronchial Branching Anomalies Ectopic Bronchus: Tracheal, Esophageal, Cardiac Bronchus

Tracheal bronchus, accessory cardiac bronchus (ACB), and esophageal bronchus are the three major congenital tracheobronchial branching anomalies, in descending order of frequency. Tracheal bronchus describes a spectrum of anomalies characterized by an aberrant bronchus originating from the trachea or main bronchi directed toward the upper lobes (Fig. 2). Previously, it was narrowly defined as a right upper lobe bronchus arising from the trachea, hence its eponym “bronchus suis” due to a similar morphology in pigs. ACB refers to an extra bronchus arising from the inner

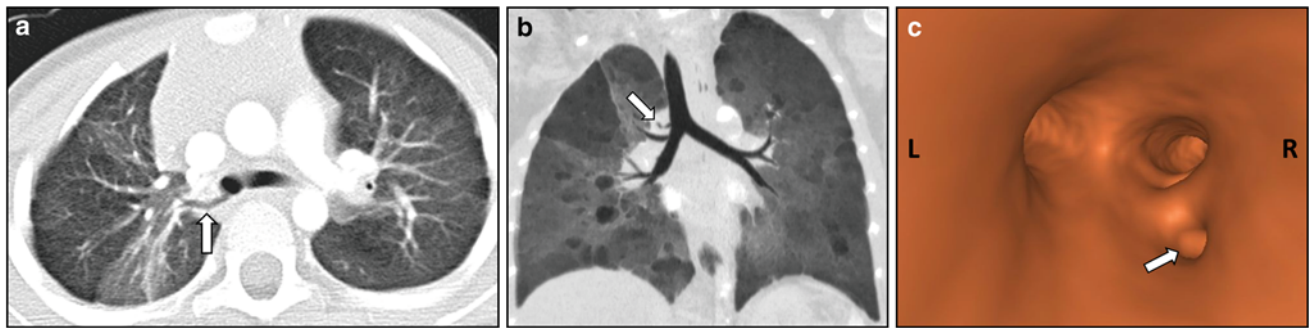


**Fig. 2** Tracheal bronchus in a 4-year-old girl who presented with recurrent right upper lobe pneumonia. Axial lung window CT image (a), coronal minimum intensity projection image (b), and 3D virtual

bronchoscopy image (c) show an anomalous bronchus (arrow) supplying the posterior segment of the right upper lobe bronchus directly arising from the right lateral wall of the trachea

wall of the right main bronchus or bronchus intermedius opposite the right upper lobe bronchus origin and advancing 1–5 cm caudally toward the pericardium, parallel to the bronchus intermedius (Berrocal et al. 2004; Ghaye et al. 2001; Lee et al. 2011b, 2012, 2013). Esophageal bronchus is characterized by a lobar bronchus originating from the esophagus, usually supplying the right lower lobe medial basal segment (Pimpalwar and Hassan 2012; Verma et al. 2008).

Of these tracheobronchial branching anomalies, tracheal bronchus is most common, with a prevalence of 0.1–2 % on the right and 0.3–1 % on the left. The frequency of ACB is 0.08 % (Ghaye et al. 2001). Esophageal bronchus is extremely rare with data limited to case reports. All of these entities may present with recurrent pulmonary infection, although tracheal and accessory cardiac bronchi may be incidental and asymptomatic (Ghaye et al. 2001; McGuinness et al. 1993; Pimpalwar and Hassan 2012; Yildiz et al. 2006). A characteristic history for tracheal bronchus is persistent right upper lobe pneumonia or atelectasis following endotracheal intubation (O’Sullivan et al. 1998).

Chest radiographs occasionally depict the anomalous bronchus but often are normal. They may show consolidation or atelectasis in the portion of the lung supplied by the anomalous bronchus. Barium swallow is diagnostic for esophageal bronchus, establishing the abnormal communication. For all of the entities, MDCT with 2D and 3D reformats accurately characterizes the aberrant bronchus, assisting in preoperative planning, and documents any associated anomalies (Fig. 2b, c). In symptomatic patients, surgical resection of the anomalous bronchus and affected lung tissue is recommended. There is also a potential role for bronchial reimplantation when the aberrant bronchus is detected early but expected to produce substantial future lung damage (Ghaye et al. 2001; McGuinness et al. 1993; Lee et al. 2011b, 2012, 2013; Pimpalwar and Hassan 2012; Verma et al. 2008; Yildiz et al. 2006).

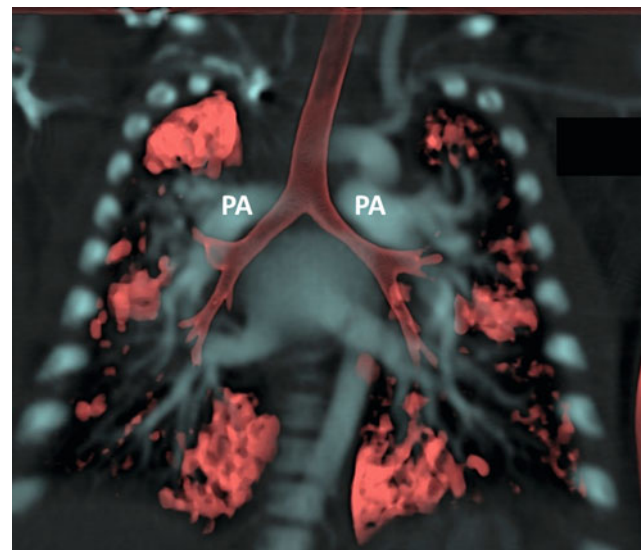


**Fig. 3** Heterotaxy patient with hyperarterial bronchial in left isomerism. Coronal volume rendered CT image shows both main stem bronchi coursing inferior to their ipsilateral pulmonary artery (PA) on each side

### Heterotaxy: Left Isomerism and Right Isomerism

Heterotaxy, or situs ambiguus, refers to an abnormal arrangement and development of the visceral organs. This is in contrast to the normal organ position (situs solitus) or its complete mirror image (situs inversus). While heterotaxy has many variations, there are two major subdivisions: left isomerism (“double left-sidedness”) and right isomerism (“double right-sidedness”). In each condition, there is a relative duplication of the structures normally located on one side of the body on the opposite side. Findings in left isomerism include a midline liver, multiple spleens (polysplenia), bilateral bilobed lungs with hyperarterial bronchi (located below the ipsilateral pulmonary artery), and bilateral pulmonary atria (receiving blood from the pulmonary veins like the normal left atrium) (Fig. 3). Findings in right



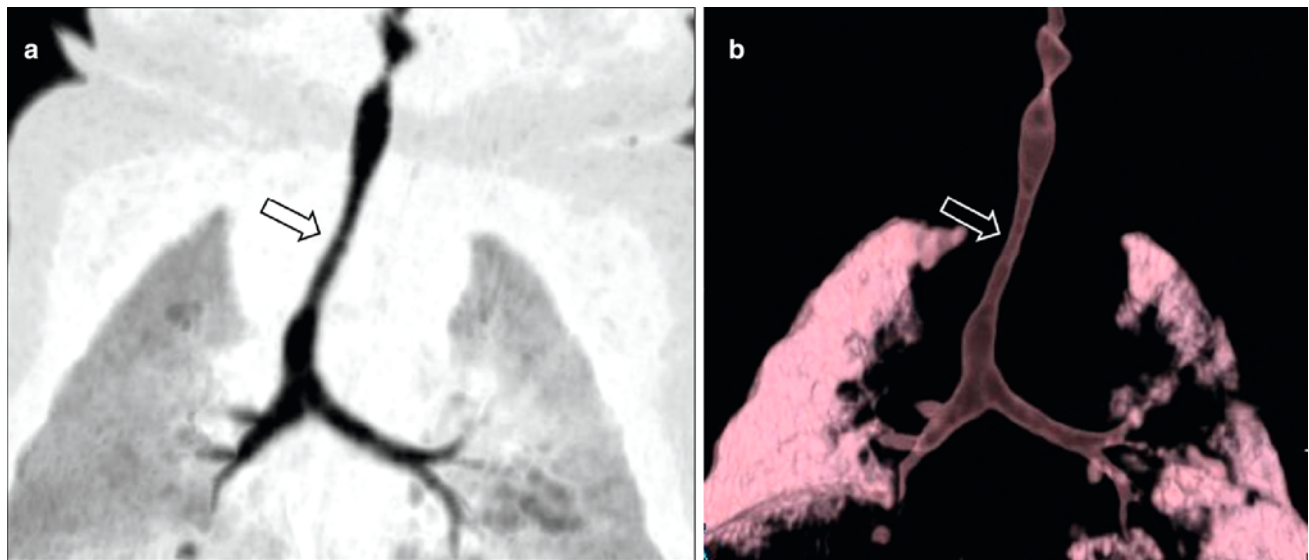


**Fig. 4** Infant girl with congenital long segment tracheal stenosis who presented with severe respiratory distress. Coronal minimum intensity projection image (a) and 3D external volume rendered image (b) shows an approximately 2 cm long segment concentric stenosis

(arrow) of the trachea. At bronchoscopy, multiple complete tracheal rings in the region of the tracheal narrowing seen on CT images were identified

isomerism include a midline liver, an absent spleen (asplenia), bilateral trilobed lungs with bilateral minor fissures and eparterial bronchi (above the ipsilateral pulmonary artery, and bilateral systemic atria (receiving blood from the inferior vena cava [IVC] like the normal right atrium). Heterotaxy is overall very rare and associated with a variety of anomalies including congenital heart disease in 50–100 % of cases and intestinal malrotation. An interrupted IVC with azygous/hemiazygos continuation is frequently observed in right isomerism but not in left isomerism (Applegate et al. 1999).

Chest radiography is the first step in diagnosis and is able to establish the position of the aortic arch, cardiac apex, and stomach bubble. If these structures are not located on the left (situs solitus) or the reverse (situs inversus), then heterotaxy is present. The imaging work-up should next extensively confirm and detail the aberrant anatomy and any associated anomalies. Specifically, the position of the atria, venous drainage below the diaphragm relative to midline, aorta relative to midline, stomach, liver, gallbladder, and cardiac apex should be assessed. Additionally, the presence of intestinal malrotation and bilobed versus trilobed lungs as well as number and appearance of spleens should be documented. For these purposes, a variety of imaging modalities may be utilized including upper gastrointestinal (GI) series, ultrasound/echocardiography, CT, MRI, and when necessary angiography (Applegate et al. 1999). Treatment and prognosis depend on the extent and severity of anomalies. Patients with left isomerism generally have less severe cardiac defects than do patients with right isomerism with better chance of surgical repair (Kim 2011).

#### 4.1.1.2 Congenital Tracheal Stenosis

Congenital tracheal stenosis (CTS) is a rare anomaly in which focal or diffuse complete tracheal cartilage rings result in deficient or absent tracheal membranes, causing fixed tracheal narrowing (Lee et al. 2011b, 2012, 2013; Lee and Siegel 2007). There are three major types: generalized total tracheal hypoplasia but normal bronchi (type I); funnel-like stenosis and gradual airway tapering with a normal subglottic but stenotic carinal end of the trachea (type II); and short-segment airway stenosis, approximately 2–5 cm in length (type III). These variations occur in 30, 20, and 50 % of cases, respectively (Cantrell and Guild 1964; Herrera et al. 2007; Lee et al. 2011b, 2013). Concurrent cardiovascular defects occur in most patients, the most common being left pulmonary artery sling (Lee et al. 2012; Antón-Pacheco et al. 2012). Patients present typically by age 1 with recurrent pneumonia, wheezing, and biphasic stridor (Lee et al. 2011b).

Chest radiography and fluoroscopy may show tracheal narrowing but are often insensitive. MDCT with 2D and 3D reformations is superior to chest radiograph and fluoroscopy for accurate detection and characterization (Fig. 4). CT precisely depicts the location and extent of stenosis and can also evaluate for other congenital anomalies. CT virtual bronchoscopy closely mirrors images from conventional bronchoscopy and may in the future be sufficient for diagnosis (Herrera et al. 2007; Lee et al. 2011b, 2012, 2013; Lee and Siegel 2007).

In symptomatic patients, CTS is managed surgically when feasible. Short stenoses ( $\leq 5$  cm) are treated with segmental resection and end-to-end anastomosis. Longer stenoses were

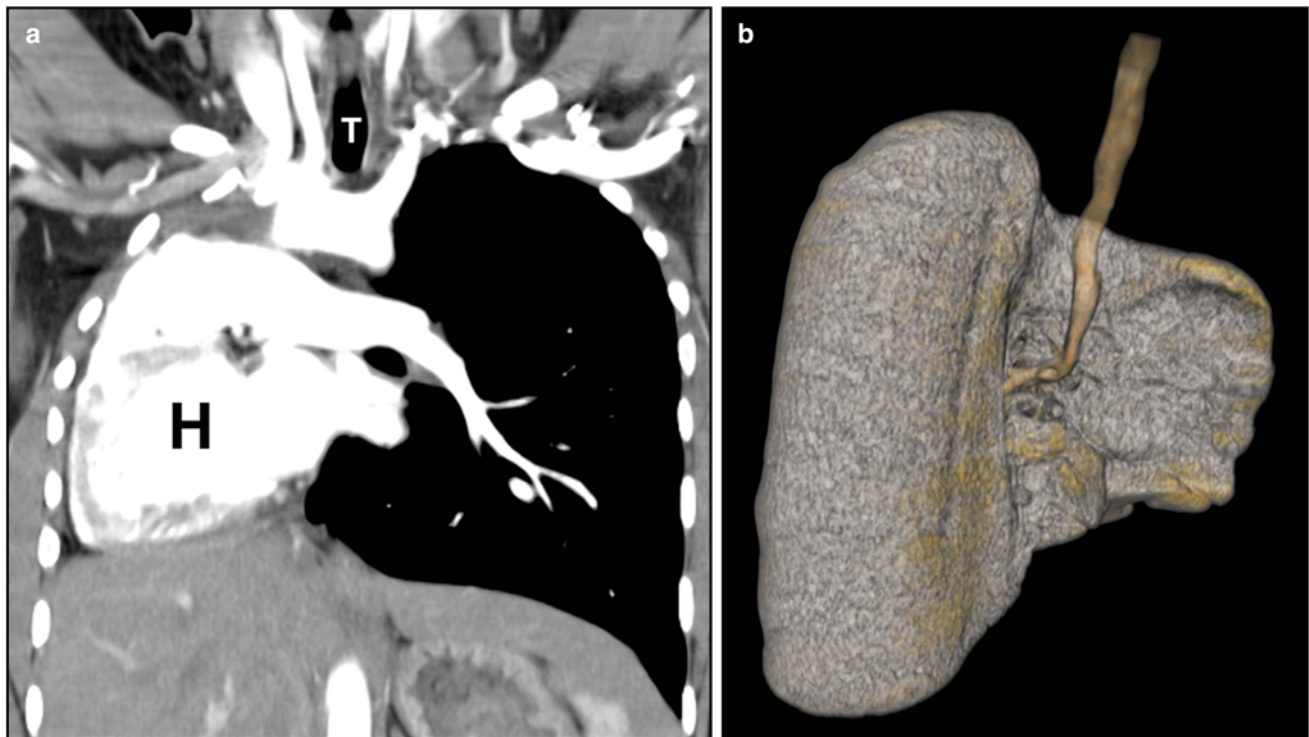


**Fig. 5** Right lung agenesis in a 16-year-old girl who presented with respiratory distress and abnormal chest radiograph. CT was subsequently obtained for further evaluation. **a** Enhanced coronal CT image shows the entire mediastinal structure shifted to the right side of

hemithorax. *H* heart. *T* trachea, **b** 3D volume rendered image of the large airway from the posterior view demonstrates absent right bronchus and right lung. Compensatory hypertrophy and hyperinflation of the left lung is also seen

previously treated with patch or tracheal autograft repair but now slide tracheoplasty is preferred (Antón-Pacheco et al. 2012; Herrera et al. 2007; Lee et al. 2012).

#### 4.1.1.3 Pulmonary Agenesis, Aplasia, and Hypoplasia

This spectrum of rare congenital disorders, referred to as the agenesis-aplasia-hypoplasia complex, is characterized by large airway underdevelopment. Pulmonary hypoplasia, generally caused by lesions that preclude normal lung growth, is the least severe form, characterized by bronchial, lung, and pulmonary artery hypoplasia. Pulmonary aplasia is intermediate severity, with absence of the lung and pulmonary artery, but a preserved although primitive main bronchus. Pulmonary agenesis is the most severe with total absence of the bronchus, lung, and pulmonary artery (Lee 2007; Lee et al. 2008a, 2010a, b, c, 2011a, b, 2012, 2013) (Fig. 5). Associated cardiovascular, gastrointestinal, or skeletal anomalies are seen in >50 % of cases (Biyyam et al. 2010). Affected pediatric patients may be asymptomatic or present with recurrent pulmonary infection, cough, and dyspnea (Lee et al. 2008a, 2010a, b, c, 2011b, 2013).

Radiographs show widespread opacification of the affected hemithorax with ipsilateral shift of the mediastinum (Biyyam et al. 2010). CT with 2D, 3D, and 4D reformats accurately characterizes the extent of hypoplasia

or aplasia of the pulmonary arteries, airways, and lungs. In symptomatic pediatric patients for whom surgical correction is indicated, CT is ideal for preoperative planning (Lee et al. 2008a, 2010a, b, c, 2011b, 2012, 2013).

#### 4.1.2 Vascular Congenital Large Airway Disorders

Many mediastinal vascular anomalies cause symptomatic extrinsic compression of the large airways. They may be broadly classified into innominate artery compression syndrome (detailed below), vascular rings (vascular and ligamentous structures that encircle the esophagus and trachea), and vascular slings (typified by pulmonary artery sling) (Hernanz-Schulman 2005; Lee et al. 2013). In general, the imaging work-up begins with chest radiography to discern the laterality or bilaterality of the aortic arch and then barium esophagram to determine if there is any abnormal impression on the trachea and/or esophagus. A normal esophagram generally excludes a vascular ring or sling but if abnormal, further evaluation with MDCT (or MRI) is often pursued to better characterize the anomaly particularly before surgical ligation (Hernanz-Schulman 2005).

##### 4.1.2.1 Innominate Artery Compression Syndrome

In this disorder, there is an anomalous innominate artery that originates on the left side of the aortic arch and courses

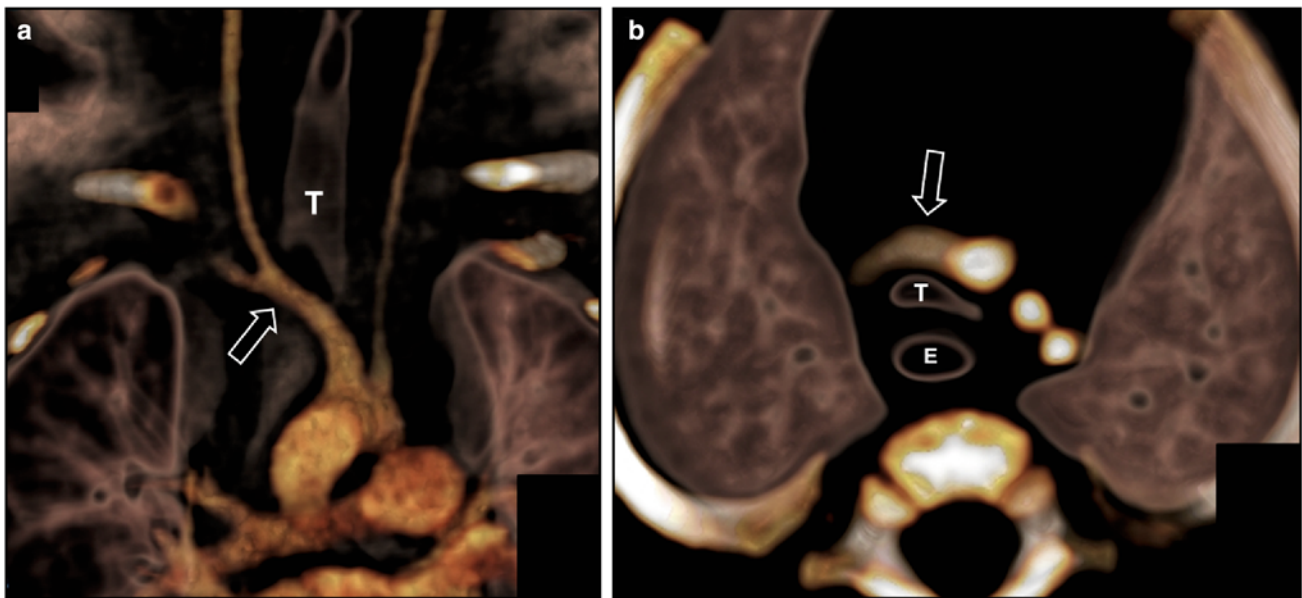


**Fig. 6** Innominate artery compression syndrome in a 1-month old boy with stridor, respiratory distress, and acute life threatening event. Frontal view (a) and superior view (b) of the 3D volume rendered

images of the large airways and vascular structures show the compression of the trachea (T) by an innominate artery (arrow). E esophagus

obliquely from left to right, compressing the anterior trachea. Patients presents with variable respiratory distress ranging from mild stridor to near-death episodes. The classic appearance on barium swallow is anterior tracheal compression without esophageal compression. Pulsatile anterior tracheal compression seen on bronchoscopy should heighten suspicion and prompt CT for accurate characterization (Fig. 6). Mild symptoms usually resolve by age 2. In more severe cases, surgical correction with inominopexy or aortopexy (suspension of the innominate artery or aorta in front of the sternum, respectively) may be necessary (Lee et al. 2010a, 2011b, 2012, 2013).

#### 4.1.2.2 Double Aortic Arch

The most symptomatic cause of vascular tracheoesophageal compression, double aortic arch is a true vascular ring in which persistent bilateral aortic arches encircle the trachea and esophagus. Secondary tracheomalacia due to extrinsic compression also occurs. Patients present with cough, wheezing, stridor, and dysphagia. On barium swallow, there is anterior tracheal compression and posterior esophageal compression (Fig. 7a). MRI and MDCT accurately depicts the anomaly and identifies the dominant arch, essential information in presurgical planning (Hernanz-Schulman 2005; Lee et al. 2010a, 2011b, 2012, 2013; Kondrachuk et al. 2012) (Fig. 7b).

#### 4.1.2.3 Right Aortic Arch with Aberrant Left Subclavian Artery

This anomaly is also a vascular ring characterized by a right aortic arch and posterior left subclavian artery originating from a diverticulum of Kommerell (equivalent to a left arch remnant). In 90 % of cases, there is a left-sided ductal ligament arising from the left pulmonary artery that completes the ring (Hernanz-Schulman 2005). As in double aortic arch, symptoms include dysphagia and/or respiratory distress, and secondary tracheomalacia may occur (Lee et al. 2013). On barium swallow, there is a posterior impression on the esophagus only. MDCT provides precise assessment in anticipation of surgical correction (Hernanz-Schulman 2005; Lee et al. 2010a, 2011b, 2012, 2013; Kondrachuk et al. 2012).

#### 4.1.2.4 Pulmonary Artery Sling

Pulmonary sling is a rare disorder characterized by an anomalous origin of the left pulmonary artery from the right pulmonary artery. The aberrant left main pulmonary artery travels to the left chest between the trachea and esophagus (Fig. 8). Presenting symptoms include stridor, hypoxia, and apneic episodes. On barium swallow, there is posterior tracheal compression and anterior esophageal compression. MDCT demonstrates not only the primary anomaly in anticipation of surgical correction but also commonly associated malformations of the airway and/or heart (Lee et al. 2010a, 2011b, 2012, 2013; Kondrachuk et al. 2012).



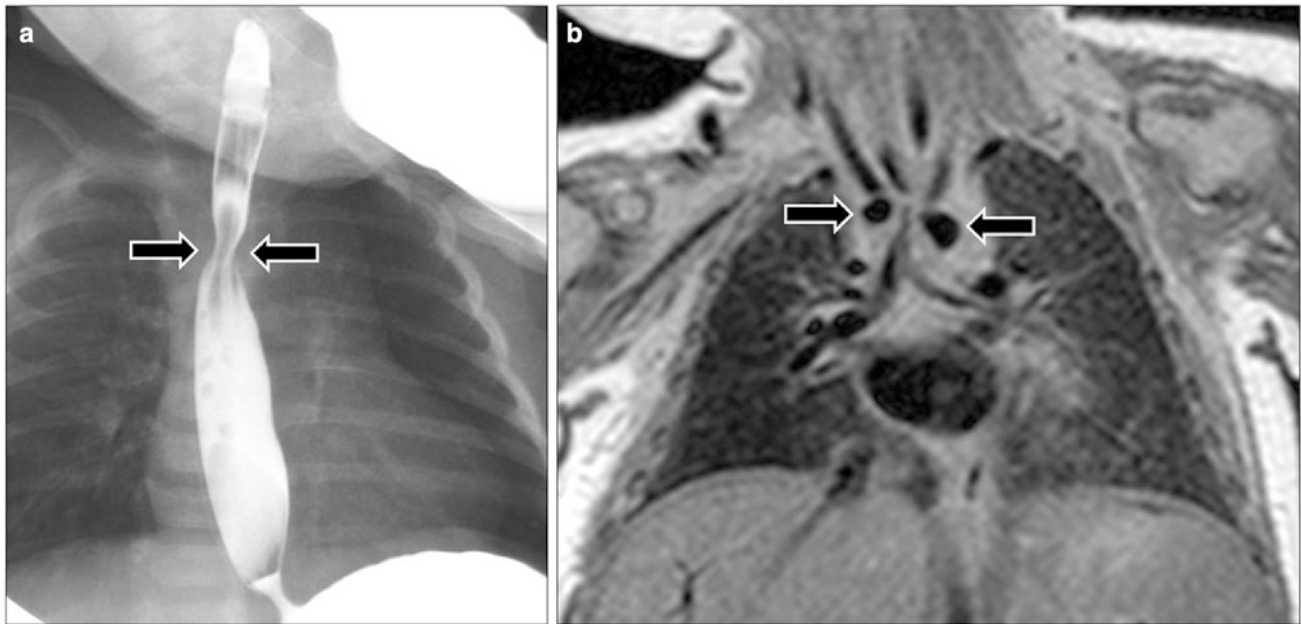


**Fig. 7** Double aortic arch in a 1-month-old girl who presented with respiratory distress and feeding difficulty. **a** Frontal radiograph obtained during barium swallow study shows a narrowing (arrows)

in the upper esophagus. **b** Coronal proton density MR image shows two aortic arches (arrows) consistent with double aortic arch with tracheal narrowing at this level

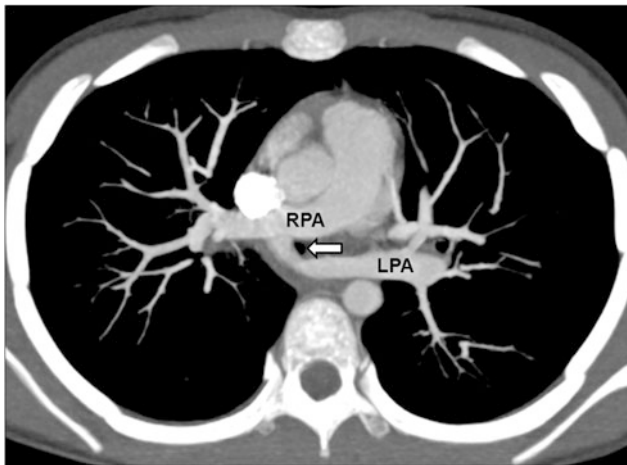


**Fig. 8** Pulmonary artery sling in an 8-year-old girl who presented with chronic respiratory distress. Axial maximum intensity projection CT image shows an anomalous left main pulmonary artery (LPA) arising from the right main pulmonary artery (RPA). Tracheal compression (arrow) by the anomalous left pulmonary artery is seen at this level

#### 4.1.2.5 Tetralogy of Fallot with Absent Pulmonary Valve

This congenital disorder combines the usual features of tetralogy of Fallot (TOF) (overriding aorta, pulmonic stenosis, right ventricular hypertrophy, and an anterior ventricular septal defect [VSD]) with absence of the pulmonary valve (APVS). It accounts for 3–6 % of TOF cases. Affected pediatric patients develop aneurismal dilation of

the main and branch pulmonary arteries leading to secondary large airway narrowing and/or tracheobronchomalacia. Up to half present in infancy with variable respiratory distress requiring mechanical ventilation in severe cases. The rest are clinically indistinguishable from other TOF patients and may experience cyanotic episodes and/or congestive heart failure. On chest radiography, the characteristic “boot-shaped” heart of TOF is often not present because the dilated pulmonary arteries overlap with the left heart border. While echocardiography is the major imaging modality for all TOF patients, CT is an important tool for preoperative planning in TOF-APVS (Kirshbom and Kogon 2004; Vincenti et al. 2012) (Fig. 9).

### 4.1.3 Dynamic Congenital Large Airway Disorder

#### 4.1.3.1 Tracheobronchomalacia

Tracheobronchomalacia (TBM) is characterized by abnormal collapse of the trachea or bronchi on expiration due to airway wall softening, supporting cartilage weakening, and/or supporting muscle hypotonia. It may be congenital (primary) or acquired (secondary) due to such causes as prior infection, surgery, or extrinsic mediastinal vascular compression (as previously discussed) (Laya and Lee 2012; Lee and Boiselle 2009; Lee et al. 2008b, c, 2009, 2010a, b, c, 2011b, 2012, 2013). TBM may be associated with cardiac anomalies, bronchopulmonary dysplasia, gastroesophageal reflux, and neurologic problems (Carden et al. 2005). Presenting symptoms, exacerbated during forced expiration, or

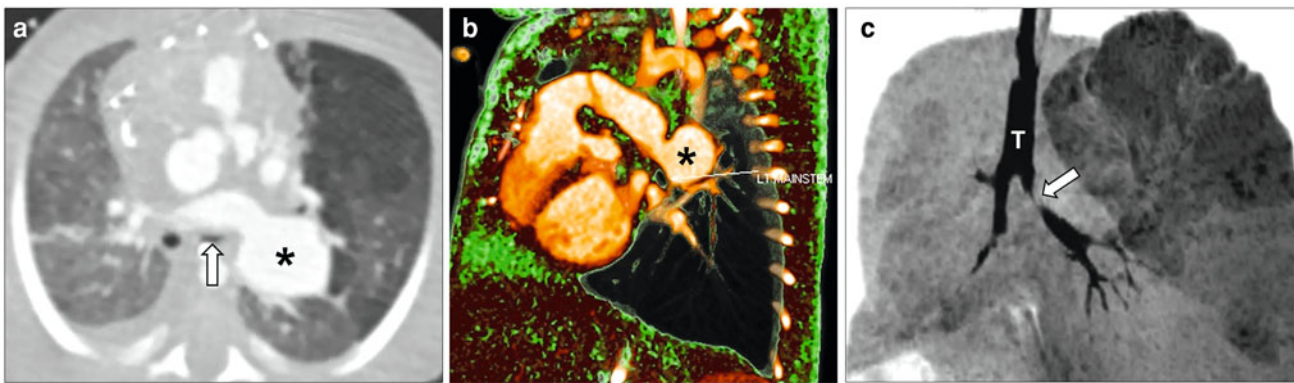


**Fig. 9** Tetralogy of Fallot with absent pulmonary valve and aneurysmal dilatation of left pulmonary artery in a neonate boy who presented with severe respiratory distress. Axial lung window CT image (a), 3D volume rendered image (b), and minimum intensity projection image (c) show an aneurysmal dilatation of the left

pulmonary artery (*asterisk*) compressing and inferiorly displacing the left upper lobe bronchus (*arrow*). Also noted is air-trapping in the left upper lobe best seen on minimum intensity projecting image (c). T trachea

crying, include cough, wheezing, stridor, dyspnea, cyanosis, and recurrent respiratory infections (Laya and Lee 2012).

Whether diagnosed by bronchoscopy or imaging, TBM is defined as >50 % airway collapse on expiration.

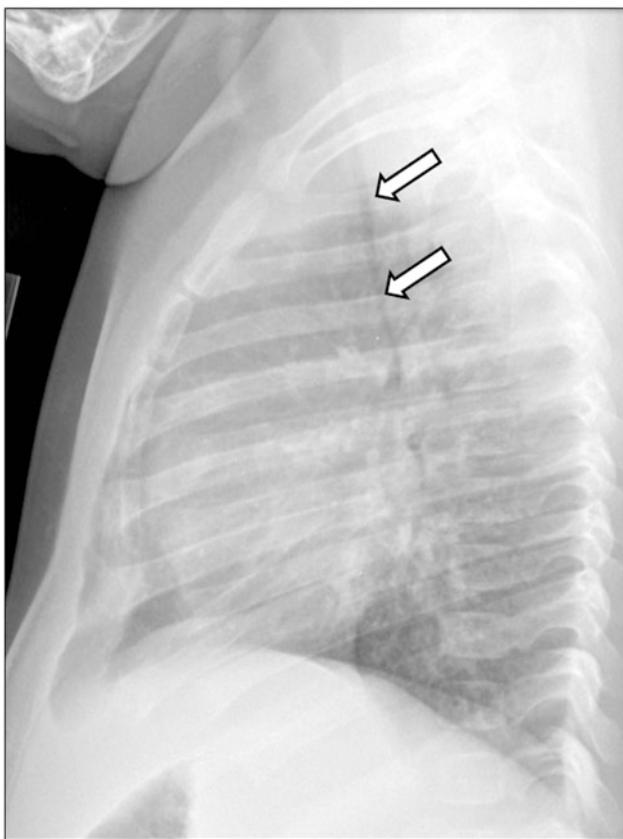


**Fig. 10** Tracheomalacia in an infant girl who presented with respiratory distress and wheezing. Lateral chest radiograph obtained at end expiration shows markedly decreased caliber of the intrathoracic trachea (*arrows*)

Noninvasive evaluation historically was limited to chest radiography and airway fluoroscopy (Fig. 10). MDCT with multiplanar 2D and 3D reformats has now become the gold standard, combining superior anatomical detail with the ability to perform quantitative measurements (Fig. 11). Additionally, it can also detect air-trapping and any associated anomalies often detected in pediatric patients with TBM. Most often performed is paired inspiratory–expiratory MDCT. Notably, on expiration the tube current may be reduced by half without compromising diagnostic ability (Lee et al. 2010a, b, c). Real-time dynamic 4D assessment is also now possible with cine 64-MDCT and true 4D imaging with the 320-MDCT (Laya and Lee 2012; Lee and Boiselle 2009; Lee et al. 2008b, c, 2009, 2010a, b, c, 2011b, 2012, 2013).

Mild to moderate TBM symptoms may substantially improve or even completely abate because the tracheal cartilage grows stronger with age. Conservative measures include pulmonary physiotherapy, humidified oxygen, and antibiotics for concomitant pulmonary infections. In patients with more severe disease, options may include continuous positive airway pressure (CPAP) tracheostomy, airway stenting, and surgical tracheoplasty or aortopexy (Carden et al. 2005; Laya and Lee 2012; Lee et al. 2012; Lee and Boiselle 2009).

## 4.2 Acquired Large Airway Disorders

### 4.2.1 Infectious Large Airway Disorders

#### 4.2.1.1 Croup

A common cause of acute pediatric airway obstruction, croup is characterized by diffuse laryngeal and tracheal inflammation as well as severe subglottic laryngeal swelling

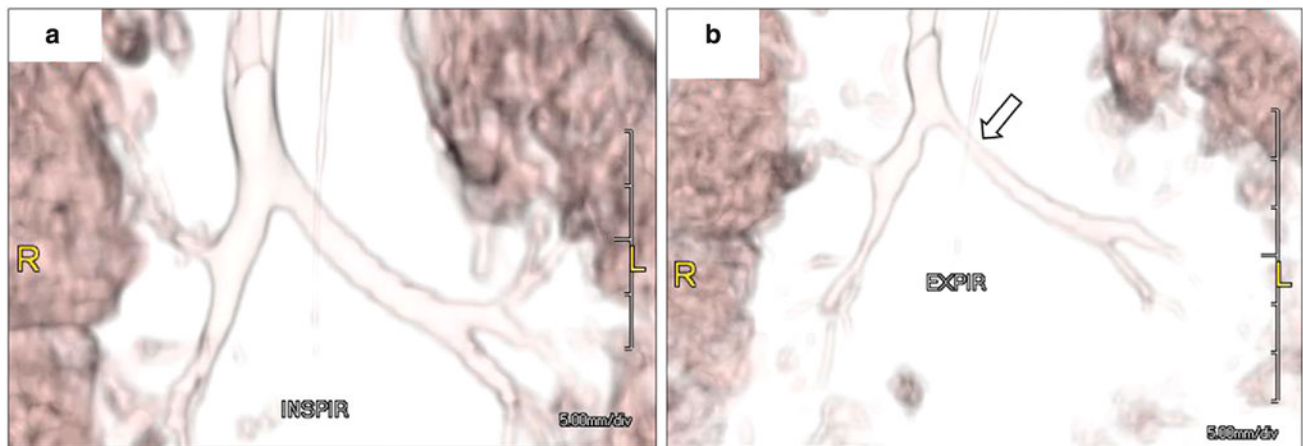


**Fig. 11** Bronchomalacia in a 4-month-old ex-25 week premature infant with chronic lung disease and tracheobronchomalacia. 3D volume rendered images of the large airways obtained at end inspiration (a) and at end expiration (b) show decrease (>50 %) in

caliber of the bronchial tree, particularly proximal left main stem bronchus (arrow) as well as the left upper lobe and right upper lobe bronchi

and narrowing. It may be caused directly by a virus (typically parainfluenza virus 1) or an allergic inflammatory response to a virus. Patients generally 7 months to 3-years old present with barking cough, inspiratory stridor, and hoarseness (Currarino and Williams 1982; Chapman et al. 2012; Cherry 2008).

The classic appearance on AP neck radiographs is termed the “steeple sign” with loss of the normal shouldering edges of the subglottic airway with tapered narrowing to the level of the glottis (Fig. 12). On the lateral view, the normally sharp margins of the subglottic airway are obliterated. Also characteristic are distention of the hypopharynx and larynx and cervical tracheal narrowing that improve or even resolve with expiration. It should be cautioned that 50 % of neck radiographs in croup are normal (Currarino and Williams 1982; Chapman et al. 2012; Salour 2000; Huang and Shih 2012). Higher-level imaging is only pursued if more complex pathology is anticipated.

Croup is generally self-limited. Medical management is tailored to the severity of disease. Options include corticosteroids, nebulized or L-epinephrine, and heliox therapy (Pitluk et al. 2011).

#### 4.2.1.2 Bacterial Tracheitis

This large airway disorder is characterized by potentially life-threatening acute airway obstruction due to thick, adherent tracheal membranes. Previously, *Staphylococcus aureus* was the most common causative pathogen but now many strains of bacteria are implicated. Patients generally 3–8 years old present with cough and stridor with subsequent hoarseness, fever, and tachypnea, often rapidly declining despite medical therapy (Miranda et al. 2011; Shargorodsky et al. 2010).

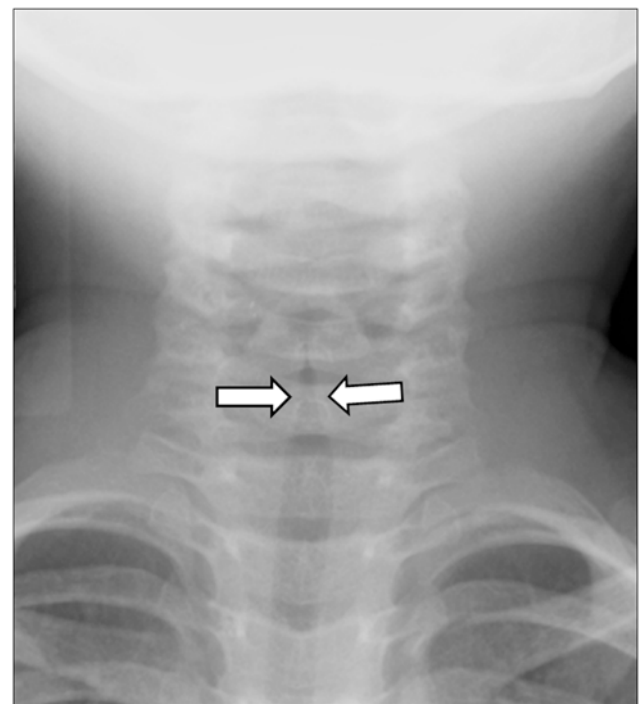


**Fig. 12** Croup in a 1-year old boy who presented with barking cough. Anteroposterior radiograph shows a steeple appearance of the subglottic trachea due to symmetric subglottic narrowing (arrows) with loss of the normal shoulders of the upper airway

Neck and chest radiographs demonstrate subglottic tracheal narrowing and contour irregularity of the proximal trachea (Fig. 13). Characteristic are tracheal membranes, typically linear, which may detach and resemble foreign bodies (Han et al. 1979; Sammer and Pruthi 2010). Pneumomediastinum is a rare radiographic presentation (Hedlund et al. 1998).



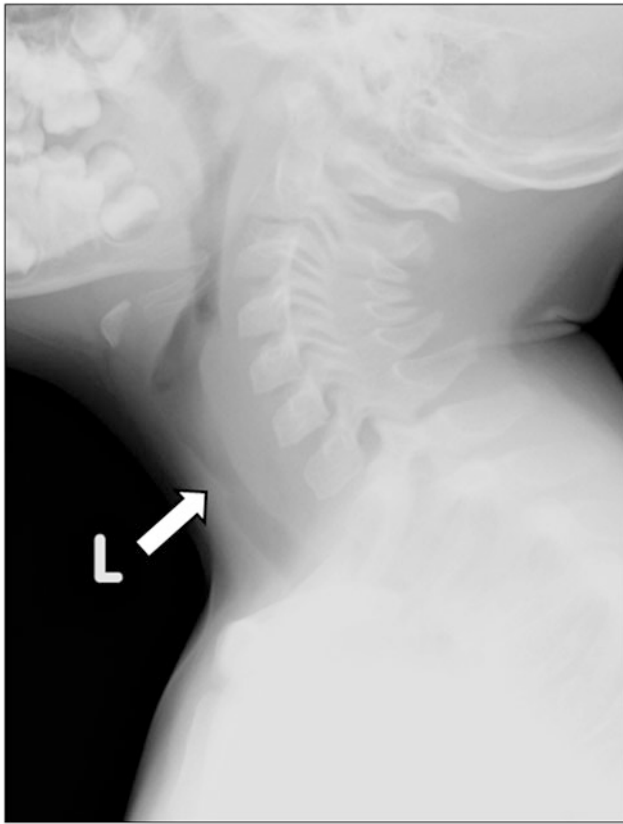


**Fig. 13** Bacterial tracheitis in a 5-year-old boy who presented with cough, stridor and fever. Lateral soft tissue neck radiograph shows a subglottic tracheal narrowing and contour irregularity (arrow)

In managing bacterial tracheitis, there should be a low threshold to perform endotracheal intubation or establish a surgical airway due to the high risk of airway compromise. Broad-spectrum IV antibiotics and often corticosteroids are administered. However, most crucial are rigid laryngoscopy and bronchoscopy allowing direct debridement of purulent debris as well as sampling for microbiological culture (Miranda et al. 2011; Shargorodsky et al. 2010).

#### 4.2.1.3 Epiglottitis

Epiglottitis is a relatively rare bacterial infection of the epiglottis and surrounding structures (aryepiglottic folds, arytenoids, and supraglottic larynx) resulting in potentially life-threatening acute airway obstruction. Prior to vaccination against *Haemophilus influenza* type b (Hib), previously the most common causative pathogen, the disease presented in children ages 2–5 years old with drooling, dysphagia, dyspnea, and dysphonia (“4 Ds”) and high fever. Since vaccination became available, the incidence has dropped 40-fold, and children present at a mean age of approximately 12-years old with milder symptoms such as low-grade fever and croup-like cough (Chapman et al. 2012; John and Swischuk 1992; Wheeler et al. 2008).

Characteristic findings on neck radiography are marked thickening of the epiglottis and aryepiglottic folds (Chapman et al. 2012; John and Swischuk 1992). The impression of the inflamed epiglottis on the airway known as the “thumbprint sign” is classic (Grover 2011; Podgore and Bass 1976). The frontal neck radiograph may show a funnel or steeples configuration of the glottic and subglottic airway (John and Swischuk 1992). The omega epiglottis, a normal variant in which the epiglottis is uniformly thickened with a horseshoe shape, may mimic epiglottitis. However, in true epiglottitis the aryepiglottic folds are thickened (Chapman et al. 2012).

To prevent airway compromise, patients should not be forced to maintain an uncomfortable position. Laryngoscopy under anesthesia is needed, allowing endotracheal intubation and supraglottic culture. Broad-spectrum antibiotics are given and then tailored to culture data (Wheeler et al. 2008).

#### 4.2.1.4 Tuberculosis

Tuberculosis (TB) is a leading cause of death worldwide, usually affects the airways through extrinsic compression by infectious mediastinal and/or hilar lymphadenopathy. It also may directly inoculate the airways, generally the trachea and proximal main bronchi (Lee et al. 2011b, 2012). TB may cause airway obstruction from caseation, mucus plugging, or granulomatous change; tracheobronchial narrowing due to mucosal edema; and in late stages fibrostenosis or fistula formation (Lee et al. 2012; Wong et al. 2006).

Pediatric primary TB presents radiographically as lymphadenopathy potentially with lung parenchymal abnormalities (Leung et al. 1992; Weber et al. 1968). Intrinsic or extrinsic airway involvement may be evident but is often not apparent. MDCT clearly depicts any airway findings such as tracheobronchial narrowing and thickening (Fig. 14). Additionally, it can demonstrate associated lung findings such as “tree-in-bud” nodular opacities and consolidation as well as extrapulmonary sequelae (Lee et al. 2011b, 2012). TB lymph nodes characteristically demonstrate low attenuation centrally with rim enhancement or calcification (Kim et al. 1997).

Early, aggressive anti-TB medication should be urged to prevent airway complications (Lee et al. 2011b). When endobronchial involvement is already present, a variety of treatments may be tried including steroids, bronchoscopic dilation, and stenting with variable success. Fibrostenosis requires surgical correction either with excision and anastomosis or bronchoplasty (Ochoa et al. 2006).

#### 4.2.1.5 Histoplasmosis

Most prevalent in the Ohio River Valley region, histoplasmosis is a fungal infection that may cause airway

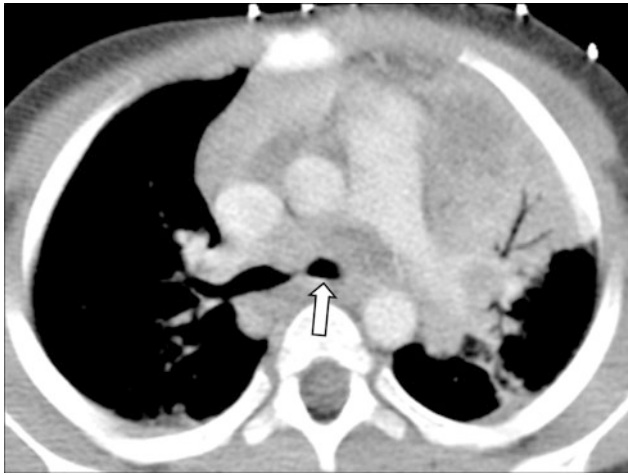


**Fig. 14** Tuberculosis infection in a 32-month-old boy who presented with cough, weight loss and low grade fever. After abnormal chest radiograph, enhanced CT study was obtained which showed an extensive low attenuation mediastinal lymph node compressing the left main stem bronchus (*arrow*)

obstruction (Fischer et al. 2009; Lee et al. 2011b, 2012). This obstruction may occur through external compression either from mediastinal lymphadenopathy or uncommonly via development of fibrosing mediastinitis, an excessive production of fibrous tissue and collagen in the mediastinum (Devaraj et al. 2007; Lee et al. 2011b; Rossi et al. 2001; Sherrick et al. 1994). In general, patients with histoplasmosis are either asymptomatic or present with mild symptoms such as cough, malaise, and fever (Fischer et al. 2009; Kirchner et al. 1991).

Potential findings on plain radiography include parenchymal consolidation and hilar or mediastinal lymphadenopathy (Fischer et al. 2009). CT is superior for assessment, showing mediastinal and/or hilar lymphadenopathy typically with calcification, pulmonary nodules (1–3 cm), and possible vascular or airway involvement (Lee et al. 2012). One important variant is the mediastinal granuloma consisting of a several-centimeter lobulated conglomerate of lymph nodes encased by a thin capsule and possibly containing calcification (Fischer et al. 2009; Kirchner et al. 1991). Fibrosing mediastinitis usually appears as a right paratracheal, subcarinal, or hilar focal soft tissue mass often with calcification, although an infiltrative diffuse form also exists (Lee et al. 2011b).

Uncomplicated histoplasmosis often requires no treatment. For disseminated disease, antifungals (amphotericin B) are indicated (Fischer et al. 2009). In patients with fibrosing mediastinitis, corticosteroids and even surgery may be necessary (Lee et al. 2011b).



**Fig. 15** Subglottic hemangioma in a 2-month-old boy who presented with recurrent biphasic stridor and cough. Bronchoscopy confirmed subglottic hemangioma. Coronal CT image shows an enhancing subglottic lesion (*arrow*) arising from the left side of the subglottic trachea narrowing the upper airway at this level

## 4.2.2 Neoplastic Large Airway Disorders

### 4.2.2.1 Primary Airway Neoplasms

#### Hemangioma

The most common benign large airway neoplasm in children, hemangioma is a rare but important cause of acute airway obstruction, with up to 50 % mortality if untreated (Javia et al. 2011; Lee et al. 2011b, 2012; Raol et al. 2011). Affected patients typically present between 6 and 12-weeks old with feeding difficulties, respiratory distress, and inspiratory or biphasic stridor (Javia et al. 2011; Lee et al. 2012). Occasionally, they may have hemoptysis (Lee et al. 2011b).

Asymmetric narrowing of the subglottic trachea on frontal neck radiography is characteristic but neither sensitive nor specific for the diagnosis. In fact, subglottic hemangioma may cause symmetric subglottic tracheal narrowing, and other lesions such as cysts and granulomas can cause asymmetric narrowing (Sutton and Nogrady 1973; Cooper et al. 1992). CT demonstrates an intensely enhancing, circumscribed, round soft tissue mass that typically arises from the posterolateral subglottic trachea (Koplewitz et al. 2005; Lee et al. 2011b, 2012) (Fig. 15).

For small subglottic hemangiomas, laser treatment is the standard of care (Javia et al. 2011; Lee et al. 2011b, 2012).

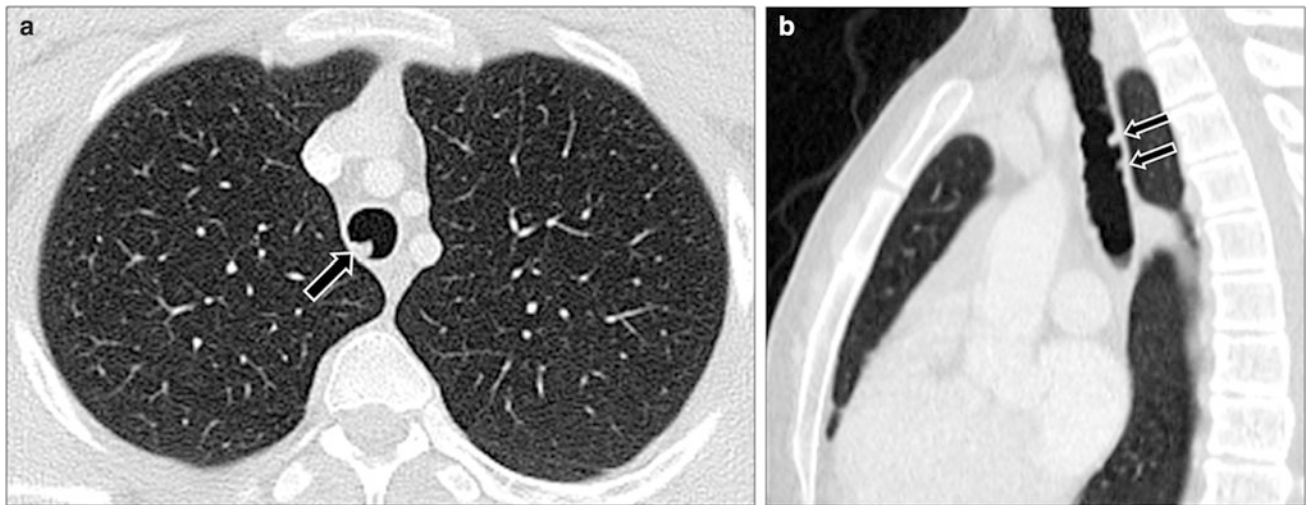


**Fig. 16** Recurrent tracheal papillomatosis in a 17-year-old male. Axial (a) and coronal (b) CT images show multiple intratracheal nodular lesions (arrows). Case courtesy of Hedieh K. Eslamy, MD,

Department of Radiology, Lucile Packard Children's Hospital, Stanford, CA. Reprint with permission from *Seminars in Roentgenology*, 2012, volume 47, No 2

Other options that have been used include systemic steroids, interferon therapy, external radiation, sclerotherapy, cryotherapy, radium implantation, tracheotomy, and surgical excision. Propranolol may be effective, but most experience with this medication to date is for cutaneous hemangiomas (Javia et al. 2011; Lee et al. 2011b, 2012; Raol et al. 2011).

#### Recurrent Respiratory Papillomatosis

This large airway disorder is characterized by multiple laryngeal or tracheal papillomas, representing the second most common benign pediatric large airway tumors. It is caused by human papillomavirus (HPV) types 6 and 11 infection, usually acquired via the birth canal. The larynx is affected in nearly all cases. Typical presenting symptoms include voice changes and stridor (Lee et al. 2011b, 2012; Venkatesan et al. 2012).

The preferred noninvasive imaging modality for assessment is CT, which demonstrates numerous intraluminal airway lesions consistent with papillomas (Fig. 16). Papillomas are generally indistinguishable by imaging from endobronchial leiomyomas, rare benign smooth muscle neoplasms associated with Epstein-Barr virus (EBV) infection. However, EBV-associated leiomyomas occur almost exclusively in patients with immunodeficiency states such as human immunodeficiency virus (HIV) infection. Lung involvement consisting of multiple cystic and/or solid nodules is also present in 1 of 20 patients affected with papillomatosis (Glikman and Barody 2005; Hatano et al. 2006; Lee et al. 2011b, 2012; User et al. 2010; Williams et al. 1994). Rarely, however, papillomas may undergo malignant degeneration, which should be suspected if there is substantial change on follow-up imaging or increased uptake on 2-[<sup>18</sup>F]-fluoro-2-deoxy-D-glucose (F-18 FDG)

positron-emission tomography (PET) (Lui et al. 1995; Szyszko et al. 2009).

Methods for eradicating papillomas include carbon dioxide (CO<sub>2</sub>) laser, cryotherapy, and electrocautery. Cytotoxic and antiviral agents help slow papilloma growth (Lee et al. 2011b, 2012). It is possible the advent of the HPV vaccine will lead to a decrease in the disease in the future (Venkatesan et al. 2012).

#### Carcinoid Tumor

A neuroendocrine tumor, carcinoid is the most prevalent malignant large airway neoplasm in children. Affected patients present with wheezing, cough, airway obstruction, and even hemoptysis. Of note, the well-known "carcinoid syndrome" consisting of facial flushing and diarrhea due to tumor serotonin production rarely occurs in pediatric bronchial carcinoid (Moraes et al. 2003; Lee et al. 2011b, 2012).

On CT, carcinoid appears as a round, oval, or polypoid endobronchial lesion with mild to intense enhancement (Fig. 17). It usually occurs within the main or lobar bronchi but in 15 % of cases is located within the lung periphery or segmental bronchi (Lee et al. 2011b, 2012). Airway obstruction by the tumor may lead to hyperinflation distally (Curtis et al. 1998). Bronchial carcinoids often demonstrate increased uptake on somatostatin receptor scintigraphy using [<sup>111</sup>In-DTPA-D-Phe<sup>1</sup>]-octreotide (Hervás Benito et al. 2010; Moraes et al. 2003) (Fig. 17c).

Surgical resection is the gold standard treatment. Because lesions often penetrate the bronchial wall more deeply than might be apparent on direct visualization ("iceberg phenomenon"), laser and endoscopic ablation are usually unsatisfactory. Lymph node involvement is also often overlooked (Avanzini et al. 2012).



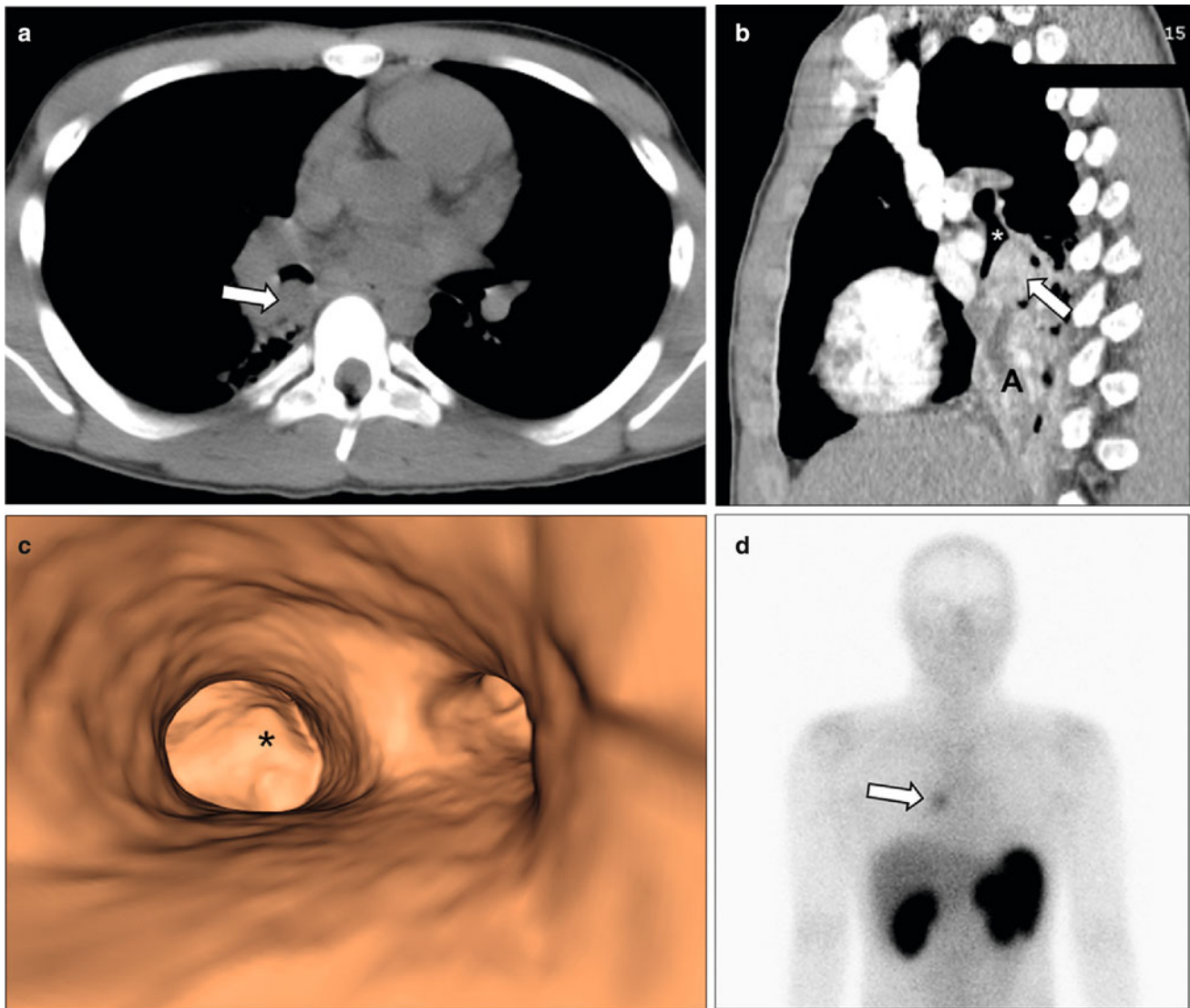


**Fig. 17** Endobronchial carcinoid tumor in a 15-year-old boy who presented with cough and abnormal chest radiographs. Surgical pathology confirmed the diagnosis of endobronchial carcinoid tumor. **a** Non-enhanced axial CT image obtained at an outside hospital shows an endobronchial mass (arrow). **b** Enhanced sagittal CT image demonstrates an enhancing endobronchial mass (arrow) compressing

the bronchus intermedius (asterisk). **A** postobstructive atelectasis with mucus plugging, **c** Virtual bronchoscopy image shows an obstruction of the bronchus intermedius by an endobronchial mass (asterisk), **d** Octreotide scan shows a focal area of increased activity (arrow) corresponding to the endobronchial mass seen in CT study

### Mucoepidermoid Tumor

The second most common malignant primary airway tumor in children, mucoepidermoid arises from the minor salivary glands of the large airways. Typically occurring in the main stem or proximal lobar bronchi, the lesion may appear as a sessile, polypoid, or pedunculated exophytic intraluminal mass. Histologically, it may be either high-grade or more commonly low-grade (Lee et al. 2007, 2011b, 2012; Park et al. 2009). Affected pediatric patients present with cough, wheezing, chest pain, fever, hemoptysis, and rarely clubbing (Liu and Adams 2007).

Radiographs, while insensitive, may show an endoluminal or pulmonary lesion or central mass with postobstructive atelectasis and/or pneumonia. CT demonstrates an oval or lobulated endotracheal or endobronchial mass, sharply marginated, following the airway contours, mild to diffusely enhancing, and generally 1–4 cm in size. Calcification is seen in 50 % of cases. A crescent of air corresponding to the remaining ectatic bronchus may be present around the tumor (Kim et al. 1999; Lee et al. 2011b; Yikilmaz and Lee 2007). High-grade mucoepidermoid should be anticipated in larger masses (>5 cm) that

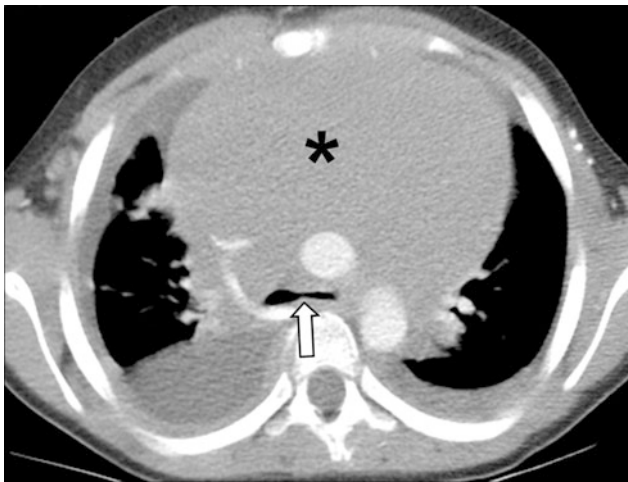


**Fig. 18** Hodgkin's lymphoma in an 8-year-old boy who presented with chest pain, weight loss, and shortness of breath. Enhanced axial CT image shows a large anterior mediastinal mass (*asterisk*) compressing central airway (*arrow*). Also noted are bilateral pleural effusions, right side larger than the left side

demonstrate irregular borders and infiltration of adjacent mediastinal structures (Lee et al. 2012).

Similar to carcinoid, mucoepidermoid is “iceberg-like,” extending deeper than it might appear. Thus, endoscopic removal is generally unsatisfactory (Granata et al. 1997). Total surgical excision with primary reanastomosis or sleeve resection is the current surgical management of choice (Lee et al. 2012).

#### 4.2.2.2 Secondary Airway Neoplasms

##### Intraluminal Metastasis

In children, hematogenous metastases to the large airways are extremely infrequent. Direct airway extension from metastatic mediastinal lymphadenopathy or lymphoma may occur. Potential primary malignancies include neuroblastoma, Wilms tumor, sarcomas, and testicular tumors. CT is effective at demonstrating the extent of involvement (Lee et al. 2011b, 2012). Treatment and prognosis are dependent on the primary tumor.

##### Extraluminal Metastasis (in the mediastinum)

Mediastinal lymphoma or metastatic mediastinal lymphadenopathy causing extrinsic airway compression is a much more common scenario (Figs. 18, 19). Affected pediatric patients may present with cough and dyspnea. Greater than 50 % of tracheal narrowing is associated with a high risk of cardiopulmonary failure during sedation. Findings on chest radiography may include an anterior and/or middle mediastinal mass corresponding to lymphadenopathy or primary lymphoma. CT better depicts the often homogeneous lymph node conglomerates and associated mass effect on the airway and adjacent mediastinal structures (Figs. 18, 19). Ossified lymph nodes should raise the possibility of



**Fig. 19** Mediastinal metastatic lung cancer in a 14-year-old boy who presented with chest pain and shortness of breath. Coronal CT image shows metastatic lung cancer in the mediastinum resulting in right main stem bronchial narrowing (*arrow*)

metastatic osteosarcoma (Lee et al. 2011b, 2012). Although lymphoma is chemo- and radiosensitive, surgical debulking may be needed if the tumor causes substantial airway compromise (Jaggers and Balsara 2004).

#### 4.2.3 Traumatic Large Airway Disorder

##### 4.2.3.1 Tracheal Stenosis

Pediatric tracheal stenosis is usually caused by prior surgery or instrumentation and most commonly due to long-term endotracheal tube or tracheostomy placement, occurring in up to 15 % of patients. Pressure ischemia from the tube eventually results in tracheal necrosis, fibrosis, and finally stenosis (Lee et al. 2011b, 2012; Lee and Siegel 2007). CT is highly accurate for detecting postintubation stricture, with the sensitivity and specificity reported at 92 and 100 % using conventional bronchoscopy as the gold standard (Lee et al. 2011b; Sun et al. 2007). Characteristic findings on MDCT are focal proximal tracheal narrowing with concentric or eccentric soft tissue thickening typically at the level of the endotracheal tube balloon or tracheostomy stoma (Fig. 20). Management options include stenting versus surgical resection with end-to-end anastomosis (Lee et al. 2011b, 2012).

##### 4.2.3.2 Bronchial Stenosis

In children, acquired bronchial stenoses usually occur in the setting of prior lung transplantation at the surgical anastomotic site. MDCT accurately characterizes the



**Fig. 20** Acquired tracheal stenosis caused by previous long-term placement of endotracheal tube in a 15-year-old boy. 3D external volume rendered image of the airways demonstrates a short-segment irregular narrowing (arrows) at the thoracic inlet level where the endotracheal tube balloon was placed



**Fig. 21** Post-surgical bronchial narrowing in a 13-year-old girl who underwent bilateral lung transplant for an end-stage lung disease related to underlying cystic fibrosis. 3D external volume-rendered CT image shows a right main stem bronchial narrowing (arrows) at the surgical anastomosis site

extent of disease. The use of 2D and 3D reformats is particularly useful for obliquely oriented stenoses (McAdams et al. 1998; Medina et al. 1994; Lee et al. 2011b, 2012) (Fig. 21). Treatment options include angioplasty, stenting, and surgery (Brown et al. 1987; Lee et al. 2011b, 2012). MDCT effectively demonstrates post-intervention complications such as stent migration or fracture (Dialani et al. 2008).



**Fig. 22** Tracheal laceration in a 17-year-old male with motor vehicle accident. Enhanced axial CT image shows a disruption (arrow) of the left lateral tracheal wall. Left upper lung consolidation, bilateral hemothoraces, endotracheal tube tip, and left sided chest tube are also seen

#### 4.2.3.3 Tracheobronchial Laceration

Although occurring in <1 % of pediatric patients with thoracic trauma, tracheobronchial injury is nonetheless critical to detect with delayed diagnosis in 25 % of cases and resultant mortality in up to 30 %. Tracheal injuries generally take place just above the carina (Fig. 22). Bronchial injuries are usually located within 2.5 cm of the carina and typically disrupt the proximal right main bronchus (Hammer et al. 2012; Lee et al. 2012).

Potential radiographic findings include extensive pneumomediastinum and/or pneumothorax despite functioning mediastinal and chest tubes. MDCT is far superior for precise diagnosis and preoperative planning. The injured bronchus may be enlarged, and if completely avulsed may collapse dependently (“fallen lung sign”). Fractures of the first through third anterior ribs and an abnormal endotracheal tube position should also raise suspicion (Hammer et al. 2012; Harvey-Smith et al. 1980; Lee et al. 2012; Epelman et al. 2002).

For injuries involving <33 % circumference of the airway, conservative measures with chest tube or intubation across the tracheal tear may be sufficient. In more severe cases, surgical correction is required with primary reanastomosis or reimplantation. Early repair helps prevent later scarring and infection (Bingol-Kologlu et al. 2006; Lee et al. 2012).

#### 4.2.4 Foreign Body Aspiration

Foreign body aspiration is a very common and yet potentially life-threatening cause of acute airway obstruction affecting children between 6 months and 3-years of age. Foreign bodies tend to lodge in the right main bronchus, as it is directly aligned with the trachea in upright patients and typically larger than the left main bronchus. Affected



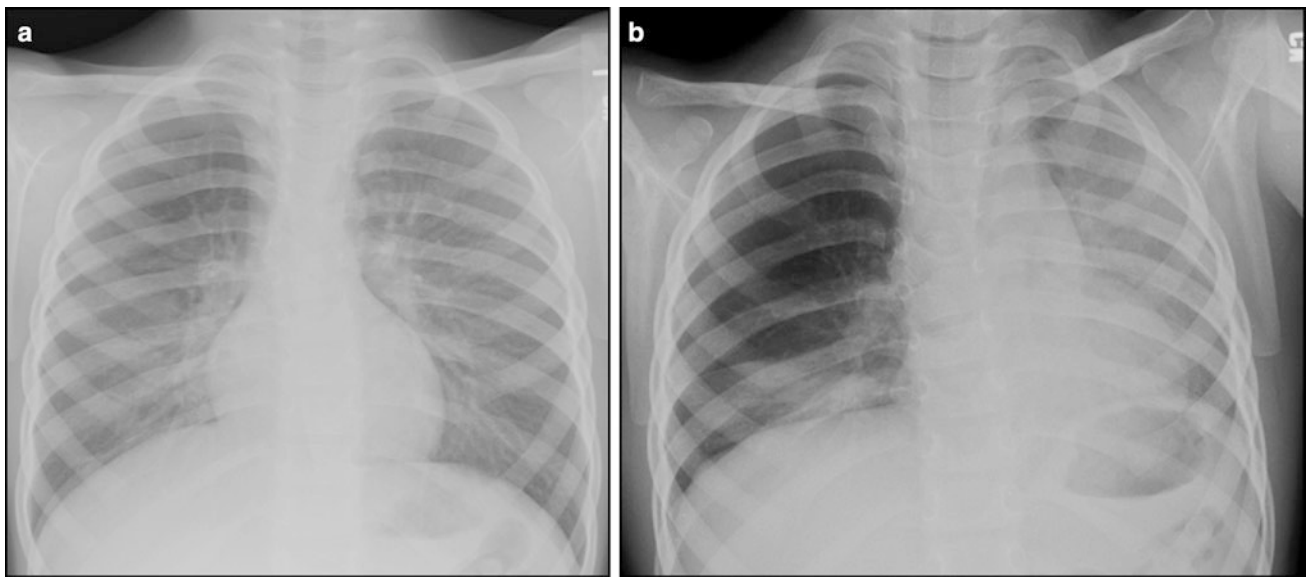


**Fig. 23** Non-radio-opaque foreign body aspiration in a 2-year-old boy who presented with acute respiratory distress after accidentally swallowing popcorns. Popcorn kernels lodged in the right main stem bronchus were bronchoscopically removed. **a** Frontal chest radiograph obtained at end inspiration shows symmetric aeration in both lungs,

**b** Frontal chest radiograph obtained at end expiration demonstrates an air trapping manifested by lucency in the right lung. Normal decompression of the left lung is seen on this end expiratory chest radiograph



**Fig. 24** Non-radio-opaque foreign body aspiration in a 3-year-old boy who presented with acute coughing and respiratory distress after eating chicken nuggets. Bronchoscopy confirmed retained chicken nuggets fragments in the left main stem bronchus. Enhanced axial CT image shows endobronchial low-attenuation material (*arrow*) within the left main stem bronchus. Also noted is left lung atelectasis

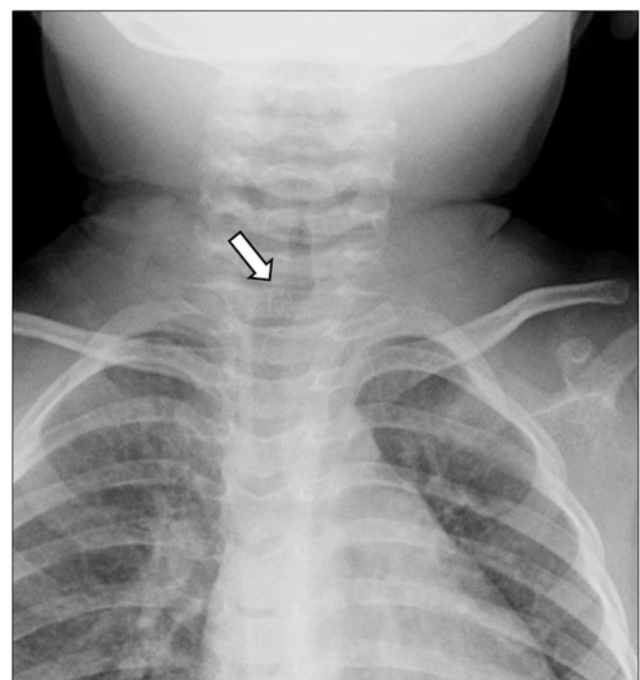


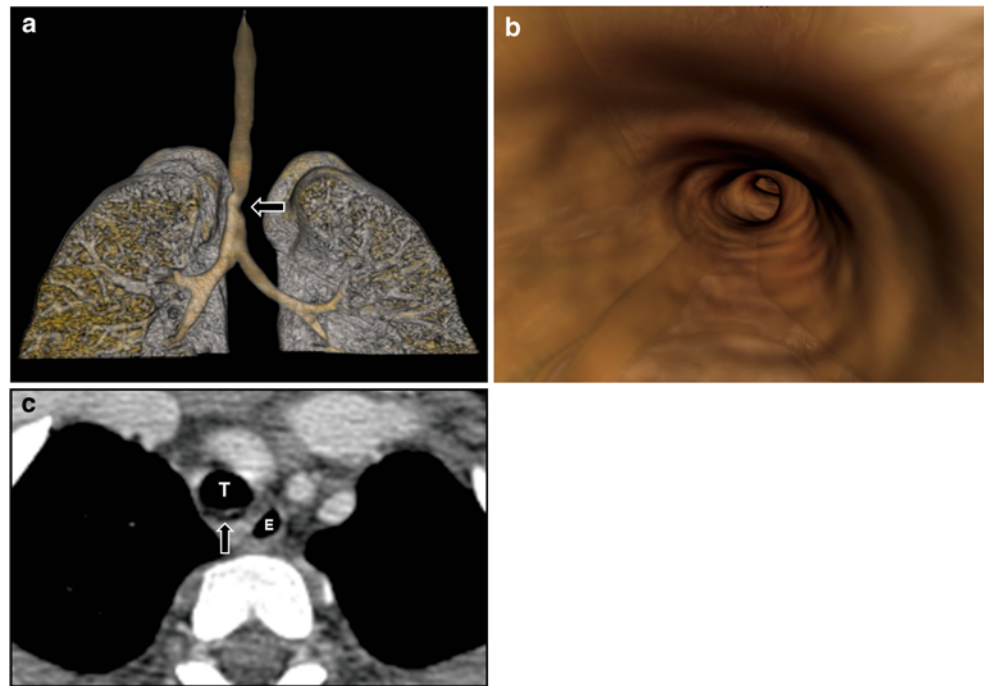
**Fig. 25** Normal physiologic tracheal buckling or deviation (*arrow*) of the trachea in a 22-month-old girl who underwent chest radiograph for evaluation of pneumonia. Frontal chest radiograph shows normal deviation (*arrow*) of the trachea to the right of midline at the thoracic inlet level

pediatric patients may be asymptomatic but classically presenting with acute choking, coughing, wheezing, and possibly stridor (Grover et al. 2011; Lee et al. 2011b, 2012).

Approximately 10 % of aspirated foreign bodies are radiopaque and therefore readily visible on chest radiographs. However, secondary signs such as hyperinflation, unilateral emphysema, localized air-trapping, mediastinal shift, pleural effusion, focal consolidation, or pneumothorax

help suggest the diagnosis. The presence of air-trapping may be further assessed with bilateral decubitus or forced expiratory radiographs, although recent research questions

**Fig. 26** Mucus mimicking an intra-tracheal lesion in a 9-year-old girl who underwent CT for evaluation of possible underlying interstitial lung disease. **a** 3D external volume-rendered CT image shows a narrowing (*arrow*) in the mid tracheal level, **b** 3D internal volume-rendered CT image also demonstrates a narrowing of the mid trachea, **c** Enhanced axial CT image shows small amount of hypoattenuating material mixed with air, creating a “bubbly” appearance, and layering dependently in the trachea, consistent with mucus



the utility of such maneuvers (Brown et al. 2013; Chapman et al. 2012; Grover et al. 2011; Lee et al. 2011b, 2012) (Fig. 23). If radiographs are negative or equivocal and clinical concern remains, CT may be pursued particularly if bronchoscopy would be considered too invasive. CT shows an endoluminal mass of variable attenuation with an accuracy of close to 100 % and any associated post-obstructive air-trapping or consolidation (Lee et al. 2011b, 2012; Lee and Siegel 2007) (Fig. 24). Multiplanar reformats and virtual bronchoscopy assist in preprocedural planning (Jung et al. 2012; Koşucu et al. 2004).

The treatment of choice is rigid bronchoscopy with removal of the foreign body (Grover et al. 2011). If bronchoscopy is unsuccessful, other measures may be attempted including postural drainage, tapotement (rhythmic percussion), and administration of bronchodilators and corticosteroids (Cataneo et al. 2008). MDCT effectively demonstrates any residual foreign body after attempt at removal (Lee et al. 2011b; Shin et al. 2009).

tracheal length in relation to the child's short rib cage and neck (Fig. 25). Importantly, however, the same finding is abnormal in children over 5 and should prompt further investigation to exclude a vascular or neoplastic lesion (Chang et al. 1970; Lee et al. 2012). Another normal variant is expiratory anterior buckling of the trachea combined with widening of the retropharyngeal soft tissues, features that may be mistaken for a retropharyngeal abscess (Eslamy and Newman 2009).

## 5.2 Mucus

Mucus is a common potential mimic of airway neoplasm. Usually, it is hypoattenuating on CT and mixed with air, creating a “bubbly” appearance, and layers dependently in the airway, allowing for confident diagnosis (Fig. 26). Thick mucus is more likely to be confused with tumor. To distinguish these possibilities, the CT can be repeated after the patient coughs vigorously; mucus should resolve, while tumor will not (Marom et al. 2001).

## 5 Mimic of Focal Large Airway Abnormalities

### 5.1 Physiological Tracheal Buckling

Lateral deviation or buckling of the trachea is a normal variant occurring in children under 6-years of age. Occurring at or just superior to the thoracic inlet opposite the aortic arch, this phenomenon is thought related to the long

## 6 Conclusion

A multitude of congenital and acquired disorders affect the pediatric large airway. Clinically, these entities are often indistinguishable. Imaging allows early and precise diagnosis, helping to prevent potentially life-threatening complications such as acute airway obstruction. Imaging evaluation of the pediatric patient with clinically suspected

large airways disease typically begins with plain radiographs of the neck and/or chest, sometimes followed by fluoroscopy. For inconclusive cases or for confirmation and further characterization of lesions seen on plain radiographs or fluoroscopy, in recent years, MDCT with 2D and 3D reconstructions has become the noninvasive test of choice for anatomic localization and preprocedural planning. Newer techniques such as 4D MDCT now allow dynamic airway assessment for such conditions as TBM. As CT technology continues to advance in concert with radiation dose-limiting measures, delays in diagnosis and invasive or inappropriate procedures should only continue to decline. Up-to-date knowledge of advantages and disadvantages of currently available imaging modalities for evaluating large airway disorders as well as clear understanding of characteristic imaging appearances of these abnormalities can result in optimal patient care.

## References

- Antón-Pacheco JL, Kalicinski P, Kansy A, Maruszewski P (2012) Slide tracheoplasty in an infant with congenital tracheal stenosis and oesophageal atresia with tracheoesophageal fistula. *Eur J Cardiothorac Surg* 42:892–893
- Applegate KE, Goske MJ, Pierce G, Murphy D (1999) Situs revisited: imaging of the heterotaxy syndrome. *Radiographics* 19:837–852
- Avanzini S, Pio L, Buffa P et al (2012) Intraoperative bronchoscopy for bronchial carcinoid parenchymal-sparing resection: a pediatric case report. *Pediatr Surg Int* 28:75–78
- Berrocal T, Madrid C, Novo S, Gutiérrez J, Arjonilla A, Gómez-León N (2004) Congenital anomalies of the tracheobronchial tree, lung, and mediastinum: embryology, radiology, and pathology. *Radiographics* 24:e17
- Bingol-Kologlu M, Fedakar M, Yagmurlu A, Fitoz S, Dindar H, Gokcora IH (2006) Tracheobronchial rupture due to blunt chest trauma: report of a case. *Surg Today* 36:823–826
- Biyyam DR, Chapman T, Ferguson MR, Deutsch G, Dighe MK (2010) Congenital lung abnormalities: embryologic features, prenatal diagnosis, and postnatal radiologic-pathologic correlation. *Radiographics* 30:1721–1738
- Brown SB, Hedlund GL, Glasier CM, Williams KD, Greenwood LH, Gilliland JD (1987) Tracheobronchial stenosis in infants: successful balloon dilation therapy. *Radiology* 164:475–478
- Brown JC, Chapman T, Klein EJ et al (2013) The utility of adding expiratory or decubitus chest radiographs to the radiographic evaluation of suspected pediatric airway foreign bodies. *Ann Emerg Med* 61:19–26
- Carden KA, Boisselle PM, Waltz DA, Ernst A (2005) Tracheomalacia and tracheobronchomalacia in children and adults: an in-depth review. *Chest* 127:984–1005
- Cataneo AJ, Cataneo DC, Ruiz RL Jr (2008) Management of tracheobronchial foreign body in children. *Pediatr Surg Int* 24:151–156
- Chang LW, Lee FA, Gwinn JL (1970) Normal lateral deviation of the trachea in infants and children. *Am J Roentgenol Radium Ther Nucl Med* 109:247–251
- Chapman T, Sandstrom CK, Parnell SE (2012) Pediatric emergencies of the upper and lower airway. *Appl Radiol* 41:10–17
- Cherry JD (2008) Clinical practice. Croup. *N Engl J Med* 358:384–391
- Cooper M, Slovis TL, Madgy DN, Levitsky D (1992) Congenital subglottic hemangioma: frequency of symmetric subglottic narrowing on frontal radiographs of the neck. *Am J Roentgenol* 159:1269–1271
- Currarino G, Williams B (1982) Lateral inspiration and expiration radiographs of the neck in children with laryngotracheitis (croup). *Radiology* 145:365–366
- Curtis JM, Lacey D, Smyth R, Carty H (1998) Endobronchial tumours in childhood. *Eur J Radiol* 29:11–20
- Devaraj A, Griffin N, Nicholson AG, Padley SP (2007) Computed tomography findings in fibrosing mediastinitis. *Clin Radiol* 62:781–786
- Dialani V, Ernst A, Sun M et al (2008) MDCT detection of airway stent complications: comparison with bronchoscopy. *Am J Roentgenol* 191:1576–1580
- Epelman M, Ofer A, Klein Y et al (2002) CT diagnosis of traumatic bronchial rupture in children. *Pediatr Radiol* 32(12):888–891
- Eslamy HK, Newman B (2009) Imaging of the pediatric airway. *Paediatr Anaesth* 19(Suppl 1):9–23
- Fischer GB, Mocelin H, Severo CB, Oliveira Fde M, Xavier MO, Severo LC (2009) Histoplasmosis in children. *Paediatr Respir Rev* 10:172–177
- Ghaye B, Szapiro D, Fanchamps JM, Dondelinger RF (2001) Congenital bronchial abnormalities revisited. *Radiographics* 21:105–119
- Glikman D, Baroody FM (2005) Images in clinical medicine. Recurrent respiratory papillomatosis with lung involvement. *N Engl J Med* 352:e22
- Granata C, Battistini E, Toma P et al (1997) Mucoepidermoid carcinoma of the bronchus: a case report and review of the literature. *Pediatr Pulmonol* 23:226–232
- Grover C (2011) Images in clinical medicine. “Thumb sign” of epiglottitis. *N Engl J Med* 365:447
- Grover S, Bansal A, Singhi SC (2011) Airway foreign body aspiration. *Indian J Pediatr* 78:1401–1403
- Hammer MR, Dillman JR, Chong ST, Strouse PJ (2012) Imaging of pediatric thoracic trauma. *Semin Roentgenol* 47:135–146
- Han BK, Dunbar JS, Striker TW (1979) Membranous laryngotracheobronchitis (membranous croup). *Am J Roentgenol* 133:53–58
- Harvey-Smith W, Bush W, Northrop C (1980) Traumatic bronchial rupture. *Am J Roentgenol* 134:1189–1193
- Hatano M, Takada H, Nomura A et al (2006) Epstein-Barr virus-associated bronchial leiomyoma in a boy with cellular immunodeficiency. *Pediatr Pulmonol* 41:371–373
- Hedlund GL, Wiatrak BJ, Prankoff T (1998) Pneumomediastinum as an early radiographic sign in membranous croup. *Am J Roentgenol* 170:55–56
- Hernanz-Schulman M (2005) Vascular rings: a practical approach to imaging diagnosis. *Pediatr Radiol* 35:961–979
- Herrera P, Caldarone C, Forte V et al (2007) The current state of congenital tracheal stenosis. *Pediatr Surg Int* 23:1033–1044
- Hervás Benito I, Bello Arques P, Loaiza JL, et al (2010) Somatostatin receptor scintigraphy in pediatric bronchial carcinoid tumor. [Article in Spanish]. *Rev Esp Med Nucl* 29:25–28
- Huang CC, Shih SL (2012) Images in clinical medicine. Steeple sign of croup. *N Engl J Med* 367:66
- Jagers J, Balsara K (2004) Mediastinal masses in children. *Semin Thorac Cardiovasc Surg* 16:201–208
- Javia LR, Zur KB, Jacobs IN (2011) Evolving treatments in the management of laryngotracheal hemangiomas: will propranolol supplant steroids and surgery? *Int J Pediatr Otorhinolaryngol* 75:1450–1454
- John SD, Swischuk LE (1992) Stridor and upper airway obstruction in infants and children. *Radiographics* 12:625–643



- Jr Cantrell (1964) Guild HG. Congenital stenosis of the trachea. *Am J Surg* 108:297–305
- Jung SY, Pae SY, Chung SM, Kim HS (2012) Three-dimensional CT with virtual bronchoscopy: a useful modality for bronchial foreign bodies in pediatric patients. *Eur Arch Otorhinolaryngol* 269:223–228
- Kim SJ (2011) Heterotaxy syndrome. *Korean Circ J* 41:227–232
- Kim WS, Moon WK, Kim IO et al (1997) Pulmonary tuberculosis in children: evaluation with CT. *Am J Roentgenol* 168:1005–1009
- Kim TS, Lee KS, Han J et al (1999) Mucoepidermoid carcinoma of the tracheobronchial tree: radiographic and CT findings in 12 patients. *Radiology* 212:643–648
- Kirchner SG, Hernanz-Schulman M, Stein SM, Wright PF, Heller RM (1991) Imaging of pediatric mediastinal histoplasmosis. *Radiographics* 11:365–381
- Kirshbom PM, Kogon BE (2004) Tetralogy of Fallot with absent pulmonary valve syndrome. *Semin Thorac Cardiovasc Surg Pediatr Card Surg Annu* 7:65–71
- Kondrachuk O, Yalynska T, Tamm R et al (2012) Multidetector computed tomography evaluation of congenital mediastinal vascular anomalies in children. *Semin Roentgenol* 47:127–134
- Koplewitz BZ, Springer C, Slasky BS et al (2005) CT of hemangiomas of the upper airways in children. *Am J Roentgenol* 184:663–670
- Koşucu P, Ahmetoğlu A, Koramaz I et al (2004) Low-dose MDCT and virtual bronchoscopy in pediatric patients with foreign body aspiration. *Am J Roentgenol* 183:1771–1777
- Laya BF, Lee EY (2012) Congenital causes of upper airway obstruction in pediatric patients: updated imaging techniques and review of imaging findings. *Semin Roentgenol* 47:147–158
- Lee EY (2007) MDCT and 3D evaluation of type 2 hypoplastic pulmonary artery sling associated with right lung agenesis, hypoplastic aortic arch, and long segment tracheal stenosis. *J Thorac Imaging* 22:346–350
- Lee EY (2008) Advancing CT and MR imaging of the lungs and airways in children: imaging into practice. *Pediatr Radiol* 38(Suppl 2):S208–S212
- Lee EY, Boiselle PM (2009) Tracheobronchomalacia in infants and children: multidetector CT evaluation. *Radiology* 252:7–22
- Lee EY, Siegel MJ (2007) MDCT of tracheobronchial narrowing in pediatric patients. *J Thorac Imaging* 22:300–309
- Lee EY, Vargas SO, Sawicki GS, Boyer D, Grant FD, Voss SD (2007) Mucoepidermoid carcinoma of bronchus in a pediatric patient: (18)F-FDG PET findings. *Pediatr Radiol* 37:1278–1282
- Lee EY, Boiselle PM, Cleveland RH (2008a) Multidetector CT evaluation of congenital lung anomalies. *Radiology* 247:632–648
- Lee EY, Mason KP, Zurakowski D et al (2008b) MDCT assessment of tracheomalacia in symptomatic infants with mediastinal aortic vascular anomalies: preliminary technical experience. *Pediatr Radiol* 38:82–88
- Lee EY, Zurakowski D, Waltz DA et al (2008c) MDCT evaluation of the prevalence of tracheomalacia in children with mediastinal aortic vascular anomalies. *J Thorac Imaging* 23:258–265
- Lee EY, Litmanovich D, Boiselle PM (2009) Multidetector CT evaluation of tracheobronchomalacia. *Radiol Clin North Am* 47:261–269
- Lee EY, Boiselle PM, Shamberger RC (2010a) Multidetector computed tomography and 3-dimensional imaging: preoperative evaluation of thoracic vascular and tracheobronchial anomalies and abnormalities in pediatric patients. *J Pediatr Surg* 45:811–821
- Lee EY, Strauss KJ, Tracy DA, Bastos M, Zurakowski D, Boiselle PM (2010b) Comparison of standard-dose and reduced-dose expiratory MDCT techniques for assessment of tracheomalacia in children. *Acad Radiol* 17:504–510
- Lee EY, Tracy DA, Bastos M, Casey AM, Zurakowski D, Boiselle PM (2010c) Expiratory volumetric MDCT evaluation of air trapping in pediatric patients with and without tracheomalacia. *Am J Roentgenol* 194:1210–1215
- Lee EY, Dorkin H, Vargas SO (2011a) Congenital pulmonary malformations in pediatric patients: review and update on etiology, classification, and imaging findings. *Radiol Clin North Am* 49:921–948
- Lee EY, Greenberg SB, Boiselle PM (2011b) Multidetector computed tomography of pediatric large airway diseases: state-of-the-art. *Radiol Clin North Am* 49:869–893
- Lee EY, Restrepo R, Dillman JR, Ridge CA, Hammer MR, Boiselle PM (2012) Imaging evaluation of pediatric trachea and bronchi: systematic review and updates. *Semin Roentgenol* 47:182–196
- Lee EY, Zucker EJ, Restrepo R, Daltro P, Boiselle PM (2013) Advanced large airway CT imaging in children: evolution from axial to 4-D assessment. *Pediatr Radiol* 43:285–297
- Leung AN, Müller NL, Pineda PR, FitzGerald JM (1992) Primary tuberculosis in childhood: radiographic manifestations. *Radiology* 182:87–91
- Liu X, Adams AL (2007) Mucoepidermoid carcinoma of the bronchus: a review. *Arch Pathol Lab Med* 131:1400–1404
- Lui D, Kumar A, Aggarwal S, Soto J (1995) CT findings of malignant change in recurrent respiratory papillomatosis. *J Comput Assist Tomogr* 19:804–807
- Marom EM, Goodman PC, McAdams HP (2001) Focal abnormalities of the trachea and main bronchi. *Am J Roentgenol* 176:707–711
- McAdams HP, Palmer SM, Erasmus JJ et al (1998) Bronchial anastomotic complications in lung transplant recipients: virtual bronchoscopy for noninvasive assessment. *Radiology* 209:689–695
- McGuinness G, Naidich DP, Garay SM, Davis AL, Boyd AD, Mizrahi HH (1993) Accessory cardiac bronchus: CT features and clinical significance. *Radiology* 189:563–566
- Medina LS, Siegel MJ, Glazer HS et al (1994) Diagnosis of pulmonary complications associated with lung transplantation in children: value of CT vs histopathologic studies. *Am J Roentgenol* 162:969–974
- Miranda AD, Valdez TA, Pereira KD (2011) Bacterial tracheitis: a varied entity. *Pediatr Emerg Care* 27:950–953
- Moraes TJ, Langer JC, Forte V, Shayan K, Swezey N (2003) Pediatric pulmonary carcinoid: a case report and review of the literature. *Pediatr Pulmonol* 35:318–322
- Ochoa TJ, Rojas R, Gutierrez M, Porturas D (2006) Severe airway obstruction in a child with Pott's disease. *Pediatr Infect Dis J* 25:649–651
- O'Sullivan BP, Frassica JJ, Rayder SM (1998) Tracheal bronchus: a cause of prolonged atelectasis in intubated children. *Chest* 113:537–540
- Park CM, Goo JM, Lee HJ, Kim MA, Lee CH, Kang MJ (2009) Tumors in the tracheobronchial tree: CT and FDG PET features. *Radiographics* 29:55–71
- Pimpalwar AP, Hassan SF (2012) Esophageal bronchus in an infant—a rare cause of recurrent pneumonia. *J Pediatr Surg* 47:e5–e8
- Pitluk JD, Uman H, Safranek S (2011) Clinical inquiries. What's best for croup? *J Fam Pract* 60:680–681
- Podgore JK, Bass JW (1976) Letter: the “thumb sign” and “little finger sign” in acute epiglottitis. *J Pediatr* 88:154–155
- Raol N, Metry D, Edmonds J, Chandy B, Sulek M, Larrier D (2011) Propranolol for the treatment of subglottic hemangiomas. *Int J Pediatr Otorhinolaryngol* 75:1510–1514
- Rossi SE, McAdams HP, Rosado-de-Christenson ML, Franks TJ, Galvin JR (2001) Fibrosing mediastinitis. *Radiographics* 21:737–757
- Salour M (2000) The steeple sign. *Radiology* 216:428–429
- Sammer M, Pruthi S (2010) Membranous croup (exudative tracheitis or membranous laryngotracheobronchitis). *Pediatr Radiol* 40:781

- Shargorodsky J, Lee GS, Whittemore KR (2010) Bacterial tracheitis: a therapeutic approach. *Laryngoscope* 120:2498–2501
- Sherrick AD, Brown LR, Harms GF, Myers JL (1994) The radiographic findings of fibrosing mediastinitis. *Chest* 106:484–489
- Shin SM, Kim WS, Cheon JE et al (2009) CT in children with suspected residual foreign body in airway after bronchoscopy. *Am J Roentgenol* 192:1744–1751
- Slovic TL (1977) Noninvasive evaluation of the pediatric airway: a recent advance. *Pediatrics* 59:872–880
- Sun M, Ernst A, Boiselle PM (2007) MDCT of the central airways: comparison with bronchoscopy in the evaluation of complications of endotracheal and tracheostomy tubes. *J Thorac Imaging* 22:136–142
- Sutton TJ, Nogrady MB (1973) Radiologic diagnosis of subglottic hemangioma in infants. *Pediatr Radiol* 1:211–216
- Szysko T, Gnanasegaran G, Barwick T, Breen R, Cane P, Rankin S (2009) Respiratory papillomatosis of lung and F-18 FDG PET-CT. *Clin Nucl Med* 34:521–522
- User IR, Dogru D, Talim B, Orhan D, Karnak I (2010) Endobronchial, pulmonary and liver leiomyomata in a child with primary immune deficiency. *Eur J Pediatr Surg* 20:423–425
- Venkatesan NN, Pine HS, Underbrink MP (2012) Recurrent respiratory papillomatosis. *Otolaryngol Clin North Am* 45:671–694
- Verma A, Mohan S, Kathuria M, Baijal SS (2008) Esophageal bronchus: case report and review of the literature. *Acta Radiol* 49:138–141
- Vincenti M, Jacquot A, Guillaumont S, Milési C et al (2012) Thoracic computed tomography in absent pulmonary valve syndrome management. *Pediatr Int* 54:938–941
- Weber AL, Bird KT, Janower ML (1968) Primary tuberculosis in childhood with particular emphasis on changes affecting the tracheobronchial tree. *Am J Roentgenol Radium Ther Nucl Med* 103:123–132
- Wheeler DS, Dauplaise DJ, Giuliano JS Jr (2008) An infant with fever and stridor. *Pediatr Emerg Care* 24:46–49
- Williams SD, Jamieson DH, Prescott CA (1994) Clinical and radiological features in three cases of pulmonary involvement from recurrent respiratory papillomatosis. *Int J Pediatr Otorhinolaryngol* 30:71–77
- Wong JS, Ng CS, Lee TW, Yim AP (2006) Bronchoscopic management of airway obstruction in pediatric endobronchial tuberculosis. *Can Respir J* 13:219–221
- Yikilmaz A, Lee EY (2007) CT imaging of mass-like nonvascular pulmonary lesions in children. *Pediatr Radiol* 37:1253–1263
- Yildiz H, Ugurel S, Soylu K, Tasar M, Somuncu I (2006) Accessory cardiac bronchus and tracheal bronchus anomalies: CT-bronchoscopy and CT-bronchography findings. *Surg Radiol Anat* 28:646–649

---

# Congenital and Acquired Mediastinal Vascular Disorders in Children

Monica Epelman, Oleksandr Kondrachuk, Ricardo Restrepo,  
and Edward Y. Lee

## Contents

<b>1</b>	<b>Introduction</b> .....	241
<b>2</b>	<b>Imaging Techniques</b> .....	242
2.1	Multidetector-Row Computed Tomography.....	242
2.2	Magnetic Resonance Imaging: Magnetic Resonance Angiography .....	242
<b>3</b>	<b>Spectrum of Imaging Findings</b> .....	243
3.1	Congenital Mediastinal Vascular Anomalies .....	243
3.2	Acquired Mediastinal Vascular Abnormalities .....	258
	<b>References</b> .....	262

---

## Abstract

Congenital thoracic vascular anomalies may involve the thoracic aorta and its branches, pulmonary arteries and veins, as well as the thoracic systemic veins. Technical improvements in multidetector-row computed tomography (MDCT) and magnetic resonance imaging (MRI), now allow for the noninvasive preoperative and postoperative imaging evaluation of the majority of these anomalies. The addition of 3D imaging provides comprehensive 3D displays for real-time and interactive interpretation and treatment guidance (Hellinger et al. 2011; Kondrachuk et al. 2012; Lee et al. 2010). In this chapter, the current imaging techniques of MDCT and MRI are reviewed, followed by a discussion on the commonly encountered thoracic congenital and acquired mediastinal vascular anomalies in pediatric patients.

---

## 1 Introduction

Congenital thoracic vascular anomalies may involve the thoracic aorta and its branches, pulmonary arteries and veins, as well as the thoracic systemic veins. Technical improvements in multidetector-row computed tomography (MDCT) and magnetic resonance imaging (MRI), now allow for the noninvasive preoperative and postoperative imaging evaluation of the majority of these anomalies. The addition of 3D imaging provides comprehensive 3D displays for real-time and interactive interpretation and treatment guidance (Hellinger et al. 2011; Kondrachuk et al. 2012; Lee et al. 2010). In this chapter, the current imaging techniques of MDCT and MRI are reviewed, followed by a discussion on the commonly encountered thoracic congenital and acquired mediastinal vascular anomalies in pediatric patients.

---

M. Epelman

Department of Radiology, Nemours Children's Hospital,  
13535 Nemours Parkway, Orlando 32827, Florida

O. Kondrachuk

Department of Radiology, Ukrainian Children's Cardiac Center,  
28/1 Chornovola Street, Kyiv 01135, Ukraine

R. Restrepo

Department of Radiology, Miami Children's Hospital,  
2100 SW 62nd Avenue, Miami 33155, Florida

E. Y. Lee (✉)

Department of Radiology, Boston Children's Hospital  
and Harvard Medical School, 300 Longwood Avenue,  
Boston, MA 02115, US

e-mail: Edward.Lee@childrens.harvard.edu



## 2 Imaging Techniques

Chest radiographs are usually the initial method for investigation of congenital thoracic vascular anomalies; however, echocardiograms or other cross-sectional imaging modalities are often needed, particularly for surgical planning. In the past, catheter angiography has been regarded as the reference standard for the evaluation of these abnormalities. However, in recent years, magnetic resonance angiography (MRA) and computed tomography angiography (CTA) have gradually replaced catheter angiography for diagnostic purposes, and catheter angiography is currently primarily reserved for direct hemodynamic assessment and endovascular interventions.

Interpretation of vascular abnormalities, either with MRA or CTA, should always include a review of the axial source images, along with a review of the datasets in advanced workstations and using 3D visualization techniques (Kondrachuk et al. 2012; Epelman et al. 2010; Hellinger et al. 2010a, b, 2011; Lee et al. 2008a). The use of interactive workstations not only assists in overcoming the noise that one may encounter in low-dose studies but also enables the evaluation of vascular structures, which are better displayed in the z-plane (Hellinger et al. 2010a, b; Lee et al. 2011b; Epelman et al. 2010). 3D volume renderings (VR) and 2D thin slab maximum intensity projection (MIP) images are particularly useful for (1) adequately depicting the complex spatial relationship between the interrogated vessels and the extravascular structures; (2) providing accurate orthogonal and longitudinal measurements of vascular stenosis; and (3) improving the communication and conveyance of the findings to the referring clinicians and families (Kondrachuk et al. 2012).

### 2.1 Multidetector-Row Computed Tomography

Thoracic MDCT for the evaluation of extracardiac congenital or acquired mediastinal vascular disorders in children can generally be obtained without electrocardiographic gating. This technique is usually performed under suspended respiration or during quiet breathing. Anatomic coverage should be tailored to the clinical question, and if possible, radiosensitive organs, such as the thyroid, should be avoided or limited in the scan. Highly concentrated iodine contrast medium (300–350 mg I/mL) is administered according to weight (2 mL/kg, not to exceed 4 or 100 mL/kg) at the highest weight-based injection rate possible via a pressure-limiting power injector (e.g., a pressure limit set to 200–250 psi). Initially, we evaluate the peripheral intravenous (IV) access with saline using a flow rate similar to that

planned for the contrast medium. If the test injection is uneventful, we proceed with the contrast injection, followed by a saline chase to clear the venous inflow and optimize the volume of contrast that reaches the target region. The flow rate used varies according to the patient's weight and IV access. In infants and young children, we use 0.8–1.5 cc/sec, while in larger, adult-sized patients, we can inject at 4.5–5 cc/sec. We trigger our CT studies using automated bolus tracking, which results in lower radiation dose from the monitoring slices and decreases the total amount of contrast agent used (Epelman et al. 2010; Fleischmann and Kamaya 2009). For automated detection, a region of interest (ROI) is placed in the vessel to be evaluated, and the scan is triggered automatically once a predefined enhancement threshold is achieved (e.g., 100–150 HU). The tube current and exposure time (mAs) and tube voltage (kVp) are determined by weight to minimize the overall radiation dose, with 80 kVp usually sufficient for most patients under 60 kg. MDCT imaging using 80 kVp results in increased attenuation of the vascular structures scanned, as 80 kVp is closer to the k-edge of iodine (33.2 keV) (Kalva et al. 2006). Similarly, MDCT evaluation of the extracardiac congenital mediastinal vascular anomalies can be performed using weight-based low-dose milliamperage following the as-low-as-reasonably achievable principles. We typically use a thin collimation (1.2 mm), a pitch of 1.3–1.5, and a gantry rotation time of 0.33 s. Datasets are usually reconstructed into 3 or 5 mm-thick axial images for routine viewing and into 1.5 mm axial images with 50 % overlap for reconstructions (Epelman et al. 2010). An exception is when very thin collimation (0.5–1.0 mm) is used because such thin collimation provides an isotropic data set, in which spatial resolution is the same regardless of whether CT images are reviewed in the axial, sagittal, or coronal plane (Honda et al. 2002).

### 2.2 Magnetic Resonance Imaging: Magnetic Resonance Angiography

MRI is rarely used as the sole initial test for the evaluation of thoracic vascular disorders, and this technique usually complements echocardiography as a noninvasive alternative to conventional catheter angiography. MRI should include preferably ECG-gated “black-blood” and “bright blood” sequences accompanied by an angiographic sequence, preferably a time-resolved sequence, which facilitates the assessment of collateralization and hemodynamics (Nael et al. 2009; Lee et al. 2012). Dark-blood imaging refers to the low signal exhibited by the vascular structures and is used primarily to delineate the vascular anatomy and evaluate the central airway (Hellinger et al. 2011). Black- and bright-blood MRI sequences provide comprehensive

anatomical detail, particularly of the vessel course, caliber, and arterial branching or venous drainage pattern. In the 1980 and 1990s, spin echo sequences were used for dark-blood imaging; currently, these techniques have been largely replaced by fast spin echo (FSE) and turbo spin echo (TSE) techniques. Slow-flowing blood or the presence of Gadolinium interfere with nulling of the blood signal and appear bright on this sequence, and they could potentially result in artifacts and misinterpretation. Bright-blood imaging is usually achieved either with GRE sequences or with steady-state-free precession (SSFP). These techniques demonstrate a high-signal intensity for fast-flowing blood and are commonly used to evaluate the vasculature. Phase contrast (PC)-imaging with velocity-encoded imaging is an optional sequence used to evaluate the flow direction and velocity and to estimate the pulmonary blood flow (Qp) and systemic blood flow (Qs). These values can ultimately be used to calculate the pulmonary-to-systemic flow ratio (Qp:Qs) and determine the shunt fraction. A Qp:Qs greater than 1.5 usually indicates a significant left-to-right shunt that may require intervention. Angiographic techniques include time of flight (TOF) MRA, PC-MRA, multiphase (arterial and venous) 3D T1 weighted contrast-enhanced (CE) MRA, and time-resolved MRA. Contrast-enhanced acquisitions are usually conducted in the coronal plane, depending on the required anatomical coverage and breath-hold duration. To maximize 3D displays, the CE-MRA slice thickness should not be greater than 1.5–2.0 mm, as maximum intensity projections (MIPs) and 3D volume renderings are useful adjuncts for enhancing interpretation (Hellinger et al. 2010a, b, 2011). In those cases where Gadolinium administration is not an option, ECG-gated balanced SSFP without arterial spin labeling may be used as a nonenhanced angiographic technique. A limitation of SSFP for angiography is sensitivity to field inhomogeneities (Ginat et al. 2011; Hellinger et al. 2011).

## 3 Spectrum of Imaging Findings

### 3.1 Congenital Mediastinal Vascular Anomalies

#### 3.1.1 Vascular Rings and Slings

Vascular rings and slings refer to congenital anomalies in which the trachea and esophagus are encircled by vessels or their atretic portions and can result in compression of these structures (Weinberg 2006; Kellenberger 2010; Hernanz-Schulman 2005; Hellinger et al. 2011; Weinberg and Whitehead 2010; Weinberg et al. 1998, 2012). These vessels may include the aortic arch or arches, aortic arch branch vessels, pulmonary branch arteries, and the ductus arteriosus or the ligamentum arteriosum (Weinberg 2006;

Weinberg and Whitehead 2010). Clinical presentation can vary widely, as these anomalies may be asymptomatic and incidentally discovered in older patients while pursuing a contrast esophagogram, or the airway may be constricted enough to cause respiratory symptoms, such as the characteristic stridor worsening during feedings in neonates and young infants (Weinberg 2006; Kellenberger 2010; Hernanz-Schulman 2005). An increased association with a chromosomal deletion at 22q11.2 and the DiGeorge syndrome has been reported with aortic arch anomalies (Weinberg and Whitehead 2010; Hellinger et al. 2011; Weinberg et al. 2012). Furthermore, approximately 25 % of the patients with arch anomalies and without associated intracardiac defects have 22 q 11 deletion (McElhinney et al. 2001). Most vascular rings are either a double aortic arch or a right aortic arch with an aberrant left subclavian artery and a ligamentum arteriosum completing the ring (Berdon 2000; Hernanz-Schulman 2005).

During the early 1930s, Barium esophagography was the principal imaging modality used in the evaluation of these abnormalities. In the 1960s, catheter angiography became the reference standard, however, it has been largely replaced by CT and MRI in the past 20 years.

#### 3.1.1.1 Double Aortic Arch

Double aortic arch (DAA) is the most common form of symptomatic vascular ring in both pediatric and adult population. It is the result of persistence of both, the right and left embryonic 4th arches. While in most cases, both arches remain patent (Figs. 1 and 2), in some cases, an atretic segment may be present in either arch, usually the left arch and typically following the take-off of the left subclavian artery (Fig. 3) (Weinberg 2006; Weinberg and Whitehead 2010; Kondrachuk et al. 2012; Hellinger et al. 2011). In most cases, the right arch is dominant and on coronal images appears slightly more superiorly located than the left arch. In these cases, the descending aorta is slightly more commonly observed on the left side (Weinberg 2006). When this occurs, the right arch classically gives origin to the right common carotid and right subclavian artery, either as a brachiocephalic artery or as two separate vessels, while the left arch generally gives origin to the left common carotid and left subclavian arteries. Less frequently, both arches are equal in size or the right arch is atretic and the left arch is dominant (Weinberg 2006; Weinberg and Whitehead 2010; Hellinger et al. 2011).

DAA is rarely associated with congenital heart disease, although when present, is usually tetralogy of Fallot. When considering surgical correction, it should be kept in mind that either a ligamentum arteriosum or, less commonly, a patent ductus arteriosus, typically on the left side, may be present and should be divided in addition to one of the arches. If not, the ligamentum may still form a vascular ring

**Fig. 1** Double aortic arch with dominant *left* arch in a neonate with severe respiratory distress. Posterior oblique (a) and posterior cranial (b) volume rendered, axial (c) and coronal (d) CT images show a complete vascular ring with a dominant *left* arch (green arrow), which is unusual, completely encircling the trachea (yellow arrow) and the esophagus (red arrow). The trachea is severely compressed at the level of the ring (white arrow in c). Coronal (e) and sagittal (f) minimum intensity projection images show pronounced hyperinflation, evidenced by flattening of the hemidiaphragms and bulging of lung tissue between the ribs (asterisks). Note the extent and severity of the tracheal compression (black arrow). The esophagus is air distended (white arrows) and is also collapsed, and likely compressed at the level of the ring (arrowhead). The narrowing is so severe that on virtual bronchoscopy (g) the trachea appears to end blindly (arrow)





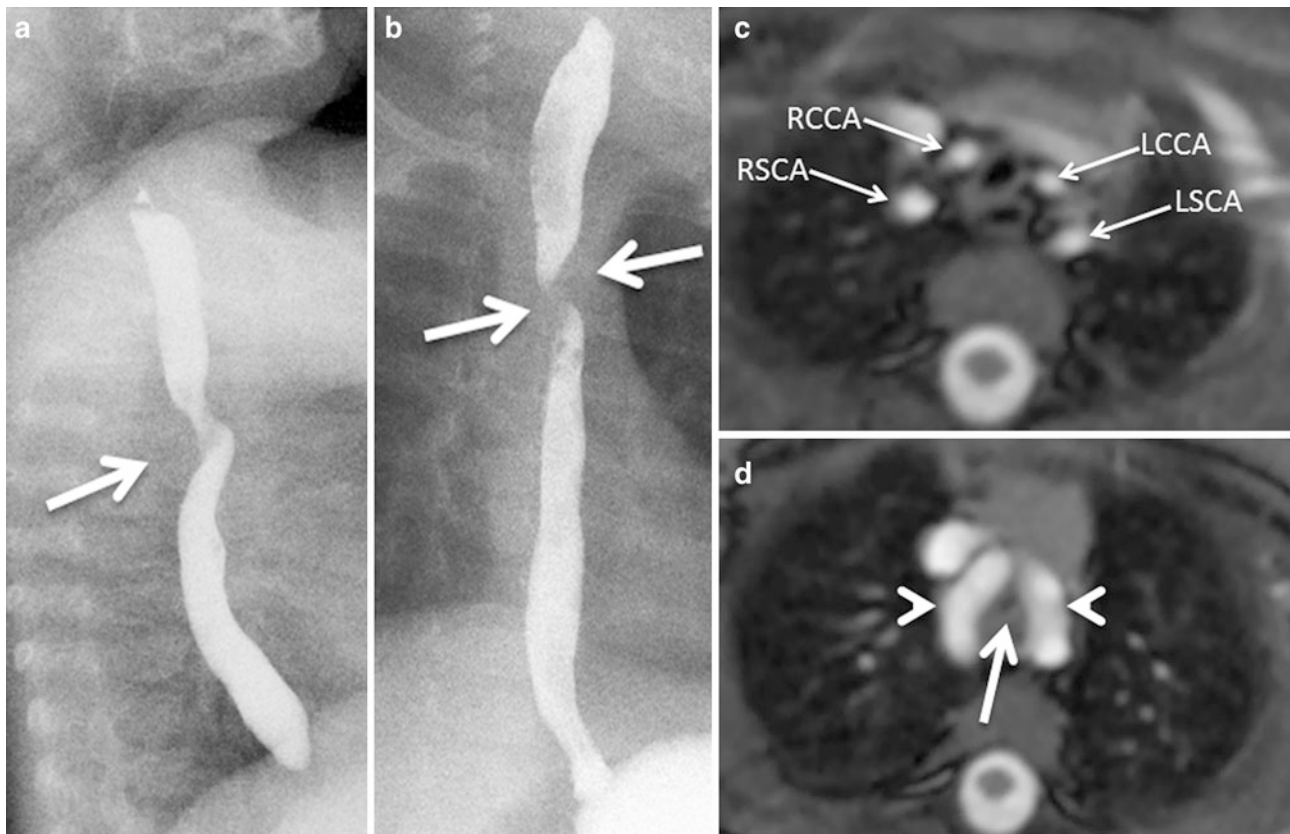


**Fig. 2** A 6-month-old with worsening stridor and double aortic arch with equal arches. Lateral (a) and frontal (b) esophagogram images show broad posterior (a) and bilateral (b) indentations consistent with vascular impressions on the esophagus. c. Axial white-blood MR image shows symmetrical origins of the four arch vessels arising separately from the two arches. RCCA right common carotid artery;

RSCA right subclavian artery; LCCA left common carotid artery; LSCA left subclavian artery. d. More inferior axial image reveals two nearly equal aortic arches (arrowheads) encircling the narrowed trachea (arrow). This type of double aortic arch, although it is not the more common type found in clinical practice, it is usually associated with significant tracheal compression

once the arches are divided (Weinberg 2006; Weinberg and Whitehead 2010).

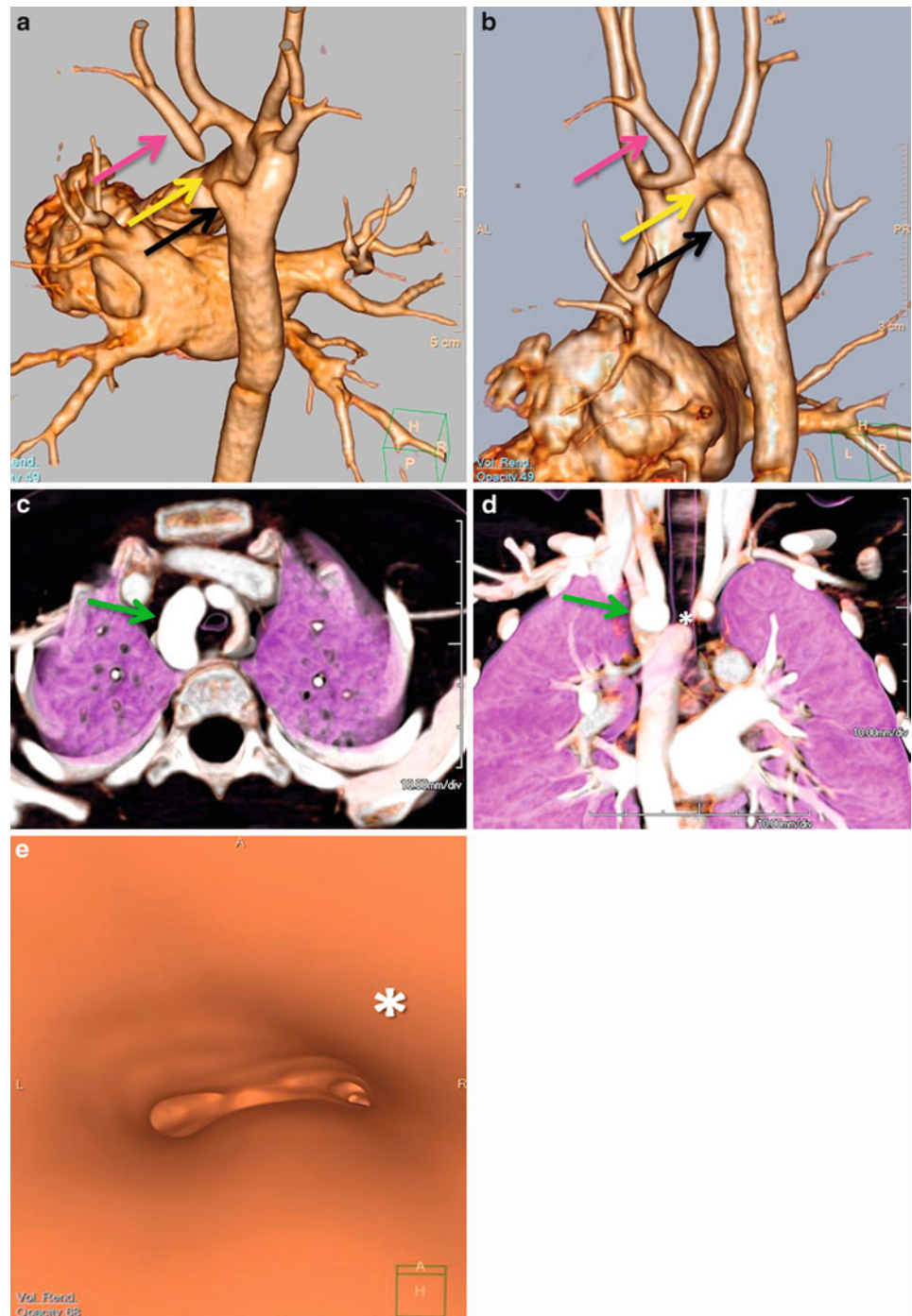
### 3.1.1.2 Right Aortic Arch Anomalies

There are three major types of right aortic arch anomalies associated with vascular rings. These anomalies include the following: (1) *right aortic arch with an aberrant left subclavian artery off a Kommerell diverticulum* (2) *right aortic arch with left descending aorta (right circumflex aortic arch)* and (3) *right aortic arch with a mirror image branching and a left retroesophageal ductus arteriosus or ligamentum arteriosum*.

The *right aortic arch with an aberrant left subclavian artery off a Kommerell diverticulum* is the second most common form of symptomatic vascular rings after double aortic arch (Figs. 4 and 5). In this anomaly, the right aortic arch gives rise to, in the order of occurrence, the left common carotid artery, the right common carotid artery, the right subclavian artery, and an aberrant left subclavian artery, which originates from a diverticulum of Kommerell.

It is important to recognize that a diverticulum of Kommerell is associated with the presence of a left ligamentum arteriosum, which is not visible using current imaging modalities but that attaches the pulmonary artery to the aortic diverticulum constituting a vascular ring. The so-called diverticulum of Kommerell is the result of the embryonic origin of the left aberrant subclavian artery off the patent ductus arteriosus (Fig. 6). The ductus arteriosus carries a significant amount of flow during fetal life into the descending aorta, while the aberrant subclavian artery only carries a small amount of flow into the left upper extremity. Following birth and once the ductus involutes, the distal portion of the subclavian artery remains small, while the proximal portion, which originates from the ductus, remains relatively larger in size, resulting in this aortic diverticulum. Although the flow in the proximal and distal subclavian arteries is similar, the difference in caliber persists. Therefore, an aortic diverticulum implies the presence of a ligamentum arteriosum in the side of the diverticulum, and if located in the contralateral side of the aortic arch, a vascular

**Fig. 3** Double aortic with atretic left arch. Posterior oblique (a) and lateral oblique (b) 3D volume-rendered images show a double aortic arch with a dominant right arch and a small atretic portion (yellow arrow) in the left arch. There is tethering of the left subclavian artery (pink arrow) posteriorly opposite to an aortic dimple (black arrow) by the atretic segment (yellow arrow). Axial (c) and coronal (d) volume-rendered 3D images show a right dominant arch (green arrow). Note the compression on the airway (\*) on the coronal (d) and virtual bronchoscopy (e) images. Most double aortic arches have a dominant right arch, and unlike this case, on coronal images it appears slightly more superiorly located. 3d volume rendered images make it easier to quickly evaluate arch dominance and location



ring can be inferred (Weinberg 2006; Weinberg et al. 1998; Weinberg and Whitehead 2010; Hellinger et al. 2011; Kondrachuk et al. 2012).

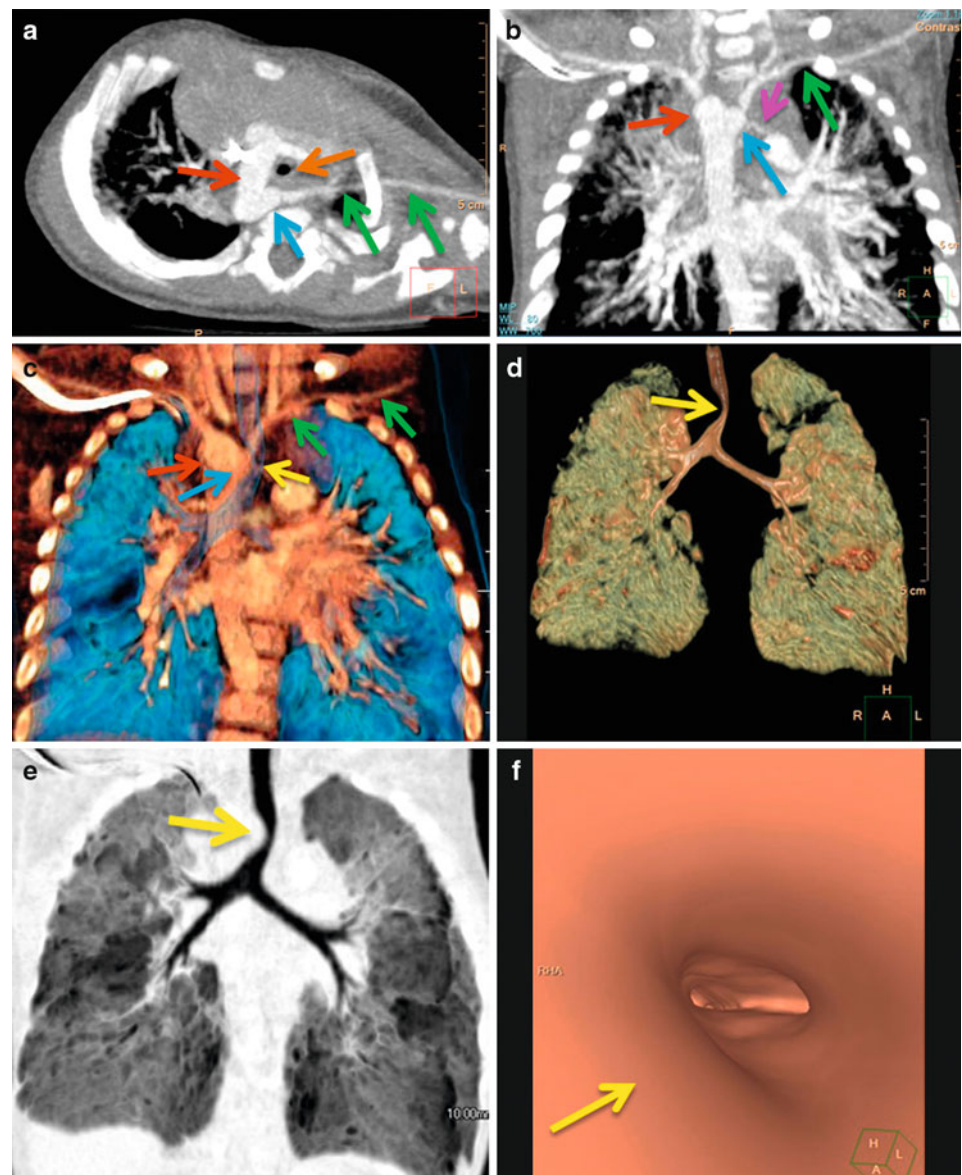
Conversely, in the case of a right aortic arch with an aberrant left subclavian artery, in which the caliber of the aberrant left subclavian vessel is uniform all along its course, no vascular ring can be anticipated. In these cases, the ductus or ligamentum arteriosum will presumably be right-sided, and it will not tether the aberrant left subclavian

artery. Therefore, no complete, constrictive vascular ring is formed (Weinberg 2006; Weinberg and Whitehead 2010; Weinberg et al. 1998).

A right aortic arch with a left descending aorta (right circumflex aortic arch) and a left ductus or ligamentum arteriosum is the third most common type of vascular ring. In these cases, the arch courses behind the trachea and esophagus, so-called circumflex aortic arch, and then following an acute turn inferiorly the descending aorta courses



**Fig. 4** A 5-month-old with noisy breathing since birth, who developed worsening stridor and significant respiratory distress with recurrent upper respiratory infections. Axial oblique (a) and coronal (b) maximum intensity projection and coronal volume-rendered (c) images show a right aortic arch (red arrows) with an aberrant left subclavian artery (green arrows) off a Kommerell diverticulum (blue arrows). Note the decrease caliber of the trachea (orange arrow) in (a) and the compression on the right wall of the trachea (yellow arrows) seen on the volume rendered (c, d), minimum intensity projection (e), and virtual bronchoscopic images. A tiny, patent left ductus arteriosus (pink arrow in b) is present confirming the presence of a vascular ring



along the left of the midline. This is unlike cases of right aortic arch in which the descending aorta after coursing over the right mainstem bronchus gradually descends for some distance on the right, and then progressively courses into the left before reaching the aortic hiatus (Weinberg and Whitehead 2010; Weinberg 2006; Weinberg et al. 2012).

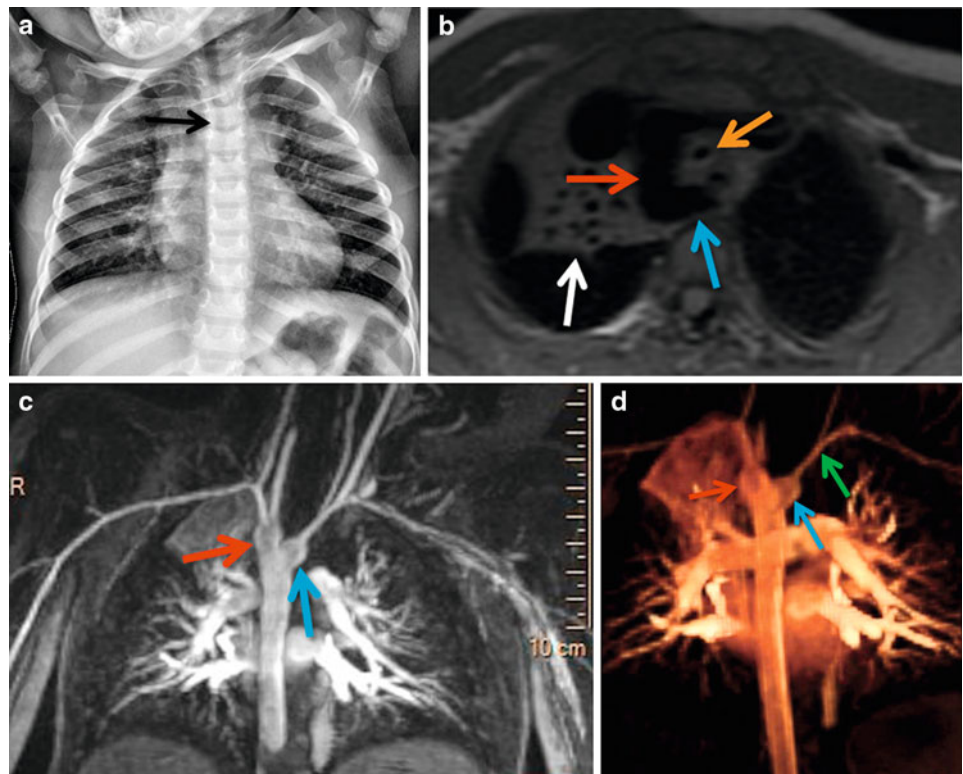
A right aortic arch with mirror image branching and a left retroesophageal ductus arteriosus or ligamentum arteriosum is an uncommon anomaly, and the only type of right aortic arch with mirror image branching forming a vascular ring. The usual right aortic arch with mirror image branching, but without vascular ring, is typically seen in cases of congenital heart disease, usually tetralogy of Fallot. In right aortic arch with mirror image branching and a left retroesophageal ductus arteriosus or ligamentum arteriosum the branching pattern has the brachiocephalic artery (left

common carotid and left subclavian arteries) as the first branch, followed by the right common carotid and the right subclavian arteries. The ring is completed by a patent ductus arteriosus or a ligamentum arteriosum originating typically from a prominent aortic diverticulum that courses leftward and behind the esophagus to reach the left pulmonary artery. As stated before, this anomaly may be easily confused with a right aortic arch with mirror image branching, which is typically found in patients with congenital heart disease, characteristically tetralogy of Fallot, but this anomaly *does not* constitute a vascular ring in the majority of the cases as in these instances, the ductus or ligamentum are usually right-sided. Less commonly, it may be left-sided, however, in these cases it most commonly originates from the base of the innominate artery and not from the aortic arch, consequently it does not encircle the



**Fig. 5** A 3-year-old with recurrent pulmonary infections underwent cardiac MRI for vascular ring evaluation noted on UGI (image not shown).

(a) Frontal chest radiograph shows the presence of a *right* aortic arch (arrow) evidenced by mild effacement of the right wall of the trachea. (b) Axial dark-blood image shows a *right* aortic arch (red arrow) and the presence of a retroesophageal Kommerell diverticulum (blue arrow). Note the small caliber of the trachea (orange arrow) and the presence of right upper lobe airspace opacification (white arrow). Maximum intensity projection (c) and 3D volume-rendered (d) images depict a *right* aortic arch with an aberrant *left* subclavian artery (green arrows) arising from a prominent a diverticulum of Kommerell (blue arrow) and conforming a vascular ring. Note the difference in size between the diverticulum and the aberrant *left* subclavian artery



airway and esophagus and does not form a vascular ring. If this is the case, one could expect to identify a quite prominent innominate artery, because of the large amount of blood flow being shunted from the left pulmonary artery and right heart across the patent ductus into the innominate artery during fetal life. Therefore, in the cases in which the ductus is closed, it is extremely helpful to identify the *ductus dimple*. If the ductus dimple is ipsilateral to the right aortic arch and directed toward the right, no ring is present, while if it is directed toward the left, the presence of a vascular ring can be inferred (Weinberg 2006; Weinberg and Whitehead 2010; Hellinger et al. 2011; Weinberg et al. 2012).

### 3.1.1.3 Left Aortic Arch Anomalies

A *left aortic arch with an aberrant right subclavian artery* is the most common arch anomaly, but it does *not* constitute a vascular ring, as the trachea and esophagus are not completely encircled by vessels and/or ligaments. In these cases, the arch gives rise to, in sequence, the right common carotid artery, the left common carotid artery, the left subclavian artery, and the right subclavian artery (*arteria lusoria*), which takes a retroesophageal course (Fig. 7). In older literature, the presence of this variant was reported to result in dysphagia in elderly patients. In these cases, the right aberrant subclavian artery is smooth in its contours, it is nearly equal in caliber throughout its intrathoracic course

and tapers gradually (Weinberg 2006; Weinberg and Whitehead 2010). Very rarely, a left-sided aortic arch may coexist with a right Kommerell diverticulum giving origin to an aberrant right subclavian artery, indicating that a right-sided ligament is present, forming a complete vascular ring (Weinberg and Whitehead 2010; Kellenberger 2010).

### 3.1.1.4 Pulmonary Artery Sling

In a pulmonary artery sling (PAS), the left pulmonary artery (LPA) arises from the posterior aspect of the right pulmonary artery, instead of the main pulmonary artery, and courses between the trachea and the esophagus to reach the left hilum, forming a sling around the distal trachea and the proximal right mainstem bronchus. The coexisting presence of a left ligamentum arteriosum connecting the main or right pulmonary artery and the left descending aorta results in a complete vascular ring that encircles the trachea but spares the esophagus (Castañer et al. 2006; Hellinger et al. 2011; Lee et al. 2011a). It is believed that PAS is the result of proximal-left-sixth arch involution, with development of a secondary connection to the right-sixth branchial arch through the embryonic peritracheal primitive mesenchymal vessels (Newman and Ya 2010; Hellinger et al. 2011; Castañer et al. 2006).

There are two main types of PASs. In type I, the position of the carina is normally situated at the T4-5 level. In most instances, the airway is intrinsically normal with or without

**Fig. 6** Right aortic arch with left descending aorta in a 4-day-old presenting with respiratory distress. Axial oblique maximum intensity projection (a) and coronal volume-rendered (b) CT images shows the ascending aorta (AAo), a right-sided aortic arch (RAoA), and a retro esophageal distal circumflex aortic arch (yellow arrow) coursing into a left-sided descending aorta. Note the position of the descending aorta with respect to the spine. Posterior (c) and posterior oblique (d) 3D volume-rendered images demonstrate a prominent, patent ductus arteriosus (PDA) completing the ring. Note that an aberrant left subclavian artery (LSCA) originates from the PDA. Compare the caliber of the LSCA with that of the PDA, this explains the discrepant size of the LSCA with respect to any aortic, Kommerell diverticulum (asterisk), which is an embryologic remnant of the ductus. MPA main pulmonary artery; LPA left pulmonary artery; RPA right pulmonary artery; RSCA right subclavian artery; LSCA left subclavian artery

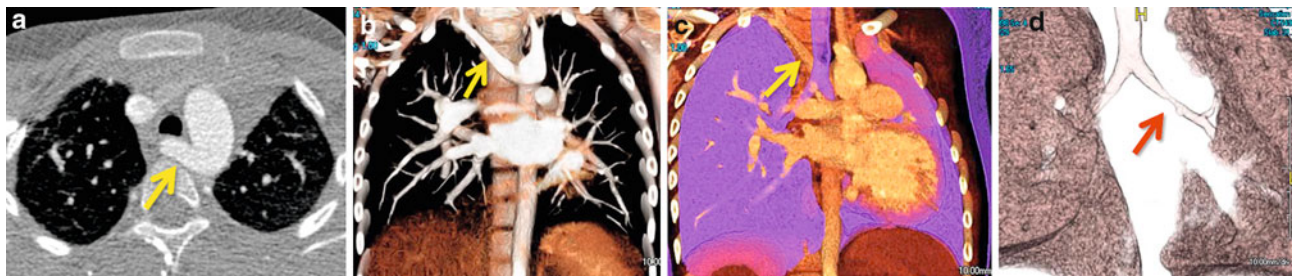
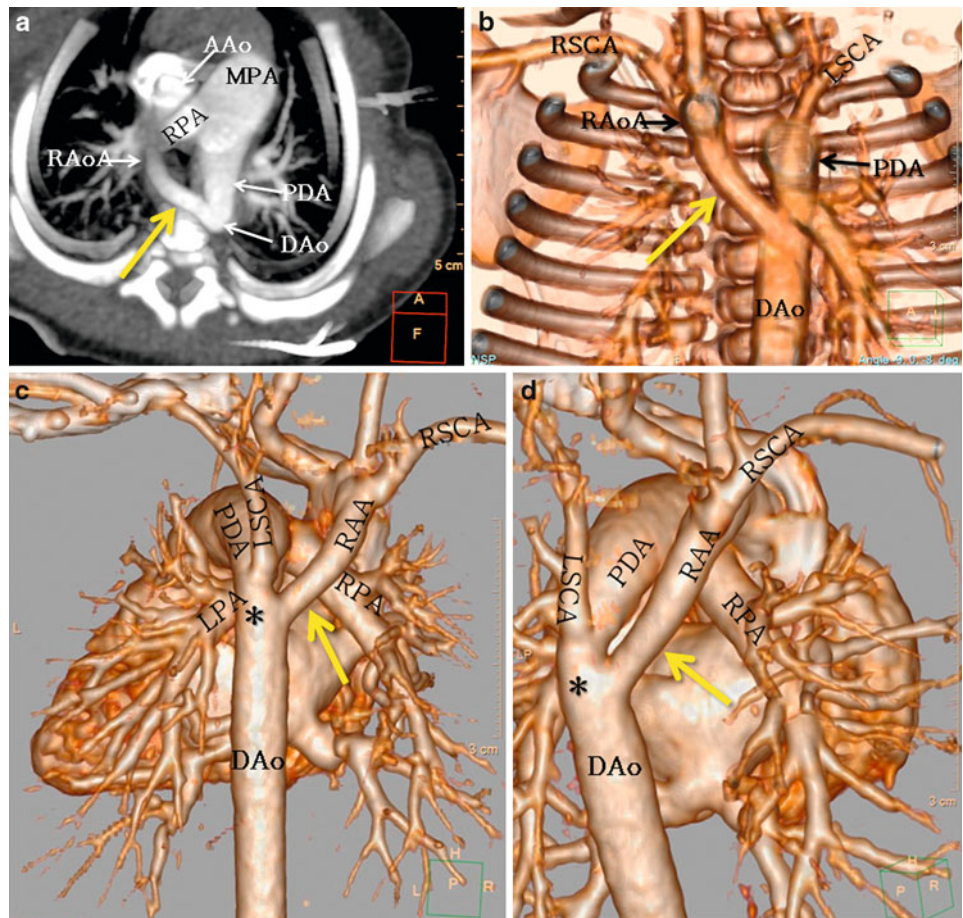


**Fig. 7** History of recurrent left pneumonias and concern for vascular ring. (a) Axial CTA and (b, c) volume-rendered CT images reveal an aberrant right subclavian artery (yellow arrows), which is smooth in caliber and without evidence of a Kommerell diverticulum or airway compression. The presence or not of a Kommerell diverticulum and a vascular ring is typically better appreciated on 3D imaging. In this case

there is no diverticulum, the aberrant subclavian vessel is smooth in contours and caliber and this type of arch anomaly does not constitute a vascular ring. (d) However, volume-rendered CT image dedicated to the airway demonstrates a high-grade left mainstem bronchus narrowing (red arrow)

an associated tracheal bronchus. In these cases, the aberrant LPA potentially compresses the posterior wall of the distal trachea and the lateral aspect of the right mainstem bronchus, resulting in tracheobronchomalacia and leading to right lung air-trapping (Newman 2006; Newman and Ya 2010; Lee et al. 2011a). Type II is more common and is associated with a more inferiorly located carina at the T6

level; it is characteristically associated with long-segment tracheal stenosis with complete cartilaginous rings and abnormal bronchial branching, including a T-shaped carina and a right-bridging bronchus. Other cardiovascular, gastrointestinal, and right-lung anomalies may coexist, including lung hypoplasia, aplasia, agenesis, and scimitar syndrome (Lee et al. 2008a; Newman and Ya 2010).



Patients with PAS characteristically present as infants with respiratory symptoms, such as stridor, apneic spells, or hypoxia. The timing and severity of the symptoms are dictated by the severity of the accompanying airway abnormalities, which may be triggered by an acute upper respiratory infection (Newman and Ya 2010; Newman 2006).

Imaging findings in PASs depend on its type and other coexisting congenital anomalies. In type I, significant right-sided hyperinflation due to partial obstruction and right bronchomalacia may be appreciated. Although the right lung may be fluid-filled and appear radio-dense in the early neonatal period due to prolonged fetal fluid retention, a right-sided tracheal bronchus above the carina may occasionally be observed. On occasion, on the lateral projection in both types, a small, rounded, soft-tissue density may be present between the mid trachea and esophagus, representing the LPA coursing between these two structures. In type II PASs, bilateral hyperinflation may be observed in cases of long-segment tracheal stenosis. In cases of unexplained right-sided volume loss, if the trachea appears narrow or difficult to see and the carina appears low and horizontal on frontal chest radiographs, these findings should raise suspicion of type II PAS.

MDCT and a cardiac MRI with 3D reconstructions are excellent imaging tests for the assessment of PASs, because the origin, size, and entire course of the aberrant LPA, as well as the associated central airway anomalies, can be accurately depicted on the 3D renderings on both modalities (Figs. 8 and 9). When concomitant lung anomalies are suspected, a CT should be obtained for accurate assessment of the lung parenchyma; the MRI resolution is still not useful, although the gap is narrowing. Paired inspiratory/expiratory CT scans can accurately demonstrate tracheo-bronchomalacia often associated with PAS (Hellinger et al. 2011; Lee et al. 2008b).

Asymptomatic patients may be followed clinically. Patients with type I PAS and respiratory symptoms may benefit from re-implantation of the LPA and excision of the patent ductus arteriosus or ductal ligament. In type II PAS, re-implantation or anterior translocation of the LPA alone will not result in improvement of respiratory symptoms if the long-segment airway stenosis is not addressed, usually by slide tracheoplasty. In mildly symptomatic cases, there are some anecdotic reports of spontaneous improvement (Newman 2006; Newman and Ya 2010).

### 3.1.2 Obstructive Lesions of the Aortic Arch

The aortic arch is divided into three main segments: (1) the proximal transverse arch, extending from the origin of the innominate artery to the left common carotid artery; (2) the distal transverse arch, extending from the left common carotid artery to the left subclavian artery; and (3) the aortic

isthmus, which is the aortic segment extending distal from the left subclavian artery to the ligamentum or ductus insertion (Backer and Mavroudis 2000; Restrepo et al. 2012). In general, all three major supraaortic branches, the brachiocephalic artery, the left common carotid artery and the left subclavian artery originate off the aortic arch fairly close together, and a distance between each segment exceeding the 5 mm is considered abnormal (Moulaert et al. 1976).

Obstructive abnormalities may affect the aortic arch or its segments. The obstruction may be in the form of a discrete, shelf-like coarctation, typically in a juxtaductal location and affecting a focal area of the arch versus a diffuse, smooth, tubular hypoplastic narrowing involving a longer portion of the arch (Matsui et al. 2007). The narrowing becomes significant when a pressure gradient is measured across the area of narrowing, and it usually occurs when there is more than a 50 % reduction in luminal cross-sectional area. Although gradual tapering of the aortic isthmus is normal up to 3 months after birth, persistence beyond this limit should be considered abnormal (Ho and Anderson 1979; Restrepo et al. 2012).

There are four main types of obstructive lesions of the aortic arch (Matsui et al. 2007; Epelman and MacDonald 2010): (1) Discrete coarctation of the aorta, (2) Tubular hypoplasia of the aortic arch, (3) Combined hypoplasia and discrete coarctation, which usually coexist in approximately 30 % of instances (Brown et al. 2009), and (4) Interruption of the aortic arch (Matsui et al. 2007).

#### 3.1.2.1 Coarctation of the Aorta

Coarctation of the aorta is the 6th most common type of congenital heart disease, accounting for approximately 7 % of all congenital heart anomalies in children with a male–female ratio of 2:1 (Tanous et al. 2009; Restrepo et al. 2012; Murillo et al. 2012). Coarctation of the aorta is defined as a hemodynamically significant, focal, shelf-like narrowing of the descending aorta typically distal to the takeoff of the left subclavian artery in the region of the ligamentum arteriosum. The shelf of the coarctation is most often juxtaductal, but it may be pre- or postductal (Backer and Mavroudis 2000; Tanous et al. 2009; Murillo et al. 2012). Coarctation of the aorta may be a feature of Turner's syndrome and is associated with a bicuspid aortic valve in more than 70 % of patients (Tanous et al. 2009; Murillo et al. 2012). Other intracardiac abnormalities may also be found in association with coarctation, especially in patients who present in infancy and are more likely to have associated left ventricular outflow obstruction and/or associated ventricular septal defects, which may be perimembranous, muscular or misalignment. Mitral valve abnormalities resulting in mitral stenosis, such as a supravulvar mitral ring, dysplastic mitral valve leaflets, or a parachute mitral valve may also be



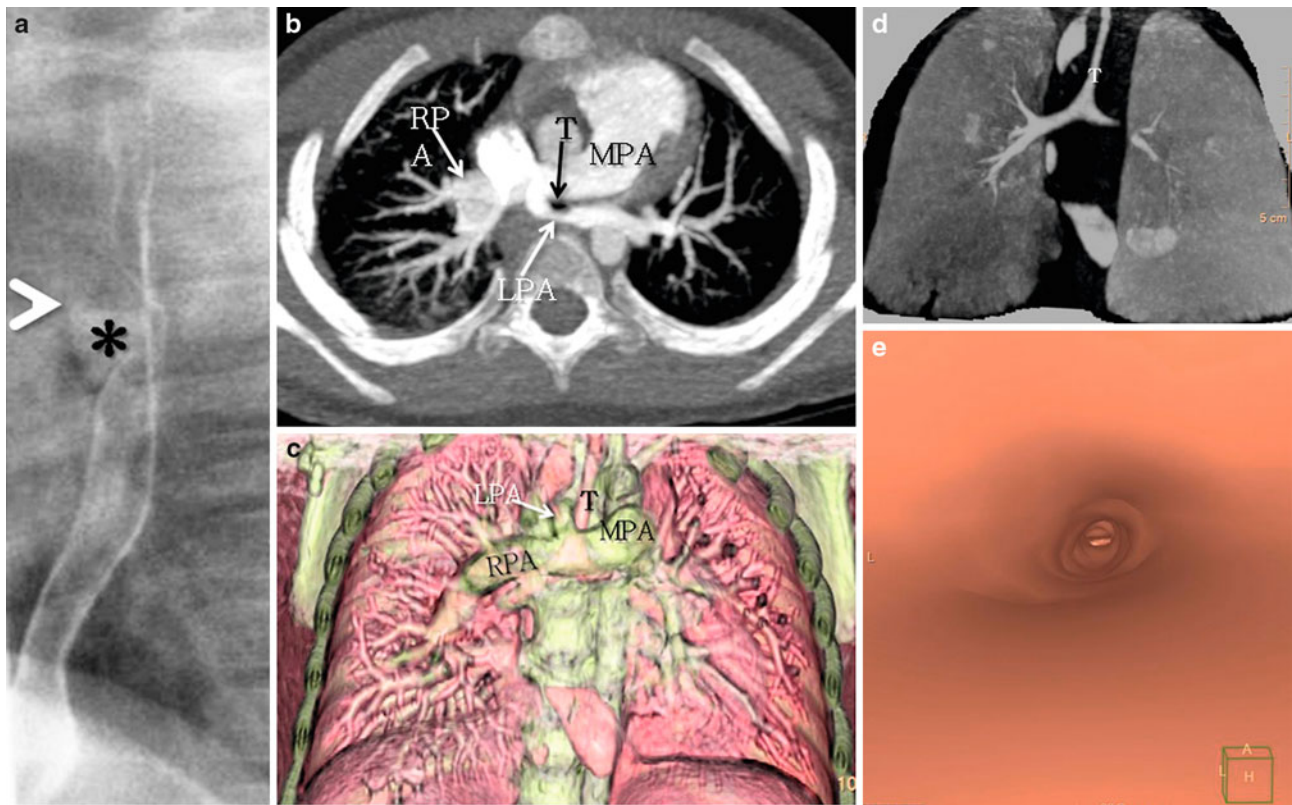


**Fig. 8** A 3-year-old female with a history of trisomy 21 and stridor. **a.** Lateral esophagogram image shows a classic anterior indentation (\*) on the esophagus with narrowing and anterior displacement of the distal trachea (T). **Axial** maximum intensity projection (**b**) and coronal volume rendered (**c**) CT images show anomalous origin of the left pulmonary artery (LPA) from the right pulmonary artery (RPA) instead of the main pulmonary artery (MPA) and coursing between the trachea

and esophagus forming a sling around the trachea. Coronal minimum intensity projection (**d**) and virtual bronchoscopy (**e**) CT images show findings consistent with long-segment tracheal stenosis and a rounded appearance of complete tracheal rings. There is in addition complete effacement of the *left* mainstem bronchus, the result of a combination of vascular compression as the bronchus courses between the left main pulmonary artery and descending aorta, and tracheobronchomalacia

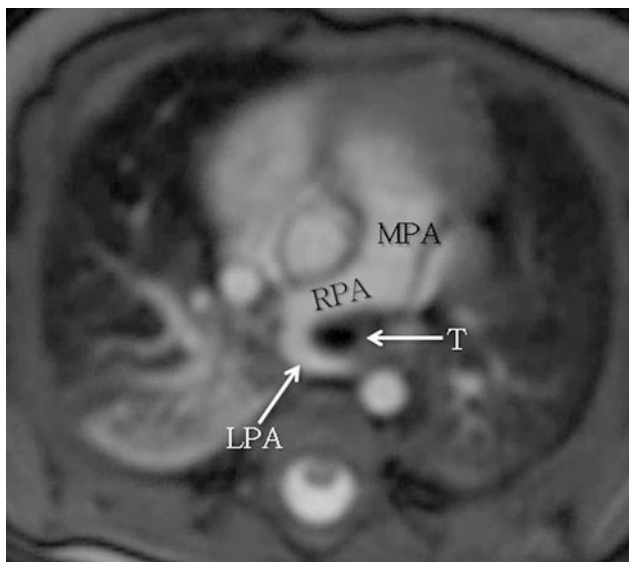


**Fig. 9** Axial white-blood MRI image shows anomalous origin of the left pulmonary artery (LPA) off the right pulmonary artery (RPA) instead from the main pulmonary artery (MPA) with imaging findings consistent with LPA sling

present in patients with coarctation. Subaortic stenosis is also a potentially associated lesion. When this group of left-sided obstructive lesions occurs together, they are referred to as the Shone complex (Moene et al. 1987; Rosenquist 1974; Shone et al. 1963; Moulaert et al. 1976).

Unless corrected in infancy, collateral circulation gradually develops between the proximal aorta and the distal aorta to bypass the coarctation. The vessels contributing to the collateral circulation may become markedly enlarged and tortuous by early adulthood (Hellinger et al. 2011; Restrepo et al. 2012).

The age of presentation and symptoms depends on the severity, rather than on the site, of the coarctation, the presence or absence of associated lesions and, most importantly, the patency of the ductus arteriosus, as the ductus acts as a bypass for blood distal to the coarctation. Once the ductus closes, in cases of high-grade stenosis, congestive heart failure symptoms develop. The blood pressure is elevated in the vessels originating proximal to the coarctation; the blood pressure as well as the pulse pressure below the coarctation are typically lower (Epelman

and MacDonald 2010; Jenkins and Ward 1999). Coarctation of the aorta recognized after infancy is rarely associated with significant symptoms. Older children are frequently referred to a cardiologist when they are found to be hypertensive on routine physical examination. Arterial pulses in the legs are either absent or weak and delayed, and there is hypertension in the arm, or blood pressure readings in the arm are higher than those in the leg. In normal children, the systolic pressures in the thigh or calf are higher by 5–10 mm Hg than that in the arm.

If aortic coarctation is left untreated, it is expected that 90 % of the patients will die before the age of 50 (Campbell 1970). The most common causes of death are congestive heart failure, aortic rupture, bacterial endocarditis, and intracranial hemorrhage (Campbell 1970).

On chest radiography, the findings will vary according to the severity of the coarctation and the presence of the associated pathology. Abnormality in the contour of the isthmus region is the most important sign in coarctation, and it may be the only finding. The contour of the proximal descending aorta may resemble a number 3 (“Figure of 3 sign”); the upper portion of the 3 is related to the combined shadows of the pre-stenotic aortic knob and the dilated proximal portion of the left subclavian artery; the waist of the “figure of 3” represents the coarctation itself; and the lower portion corresponds to the poststenotic dilatation of the descending aorta (Epelman and MacDonald 2010). Rib notching between the fourth and eighth ribs may be observed in older children but rarely before the age of seven. Rib notching is the result of pressure erosion caused by dilated or tortuous intercostal arteries, which serve as collaterals between the internal mammary arteries and the descending aorta. The first, second, and third ribs do not typically exhibit rib notching, as the intercostal arteries at these level originate from the thyrocervical trunk, which originates above the coarctation (Epelman and MacDonald 2010).

Critical preoperative information to be evaluated with cross-sectional imaging (Figs. 10 and 11) includes (1) the anatomy of the transverse aorta and the aortic isthmus, including the orthogonal dimensions and the relationship to other arch vessels; (2) the presence and extent of any pre-coarctation hypoplasia; (3) the severity of the obstruction and hemodynamics, including quantification of collateral flow, flow velocity, flow volume, and pressure gradients across the stenosis, by phase contrast MR imaging; (4) the presence of previously mentioned associated intracardiac anomalies, such as bicuspid aortic valve and mitral valve abnormalities (Konen et al. 2004); and (5) the presence of aneurysm, particularly in cases after prior surgical or endovascular interventions (Weinberg and Whitehead 2010; Restrepo et al. 2012; Konen et al. 2004; Hom et al. 2008).

While surgery is the mainstay of treatment in infants, endovascular repair with balloon angioplasty and stenting is being increasingly used, particularly in older children (Holzer et al. 2010). Commonly used surgical procedures include resection and end-to-end anastomosis, subclavian flap aortoplasty, synthetic patch repair, and aortic bypass interposition grafting or bypass grafting (Jenkins and Ward 1999). The continued monitoring of patients with stents is required to assess for complications such as aneurysm formation or the need for reintervention (Holzer et al. 2010).

### 3.1.2.2 Tubular Hypoplasia of the Aortic Arch

Tubular hypoplasia of the aortic arch may involve one or all segments and characteristically presents in association with other intracardiac anomalies, ranging in severity from a bicuspid aortic valve to a more complex left-sided obstructive lesion or hypoplastic left heart syndrome (Brown et al. 2009). A common rule of thumb for determining aortic arch hypoplasia in neonates on echocardiography is an internal luminal diameter of less 1 mm/kg (Brown et al. 2009). This finding may coexist with associated discrete, focal coarctation in nearly 30 % of the cases (Brown et al. 2009). The narrowing is smooth and usually affects the isthmus, although in rare occasions, it may affect the entire arch (Brown et al. 2009; Matsui et al. 2007). Recognition of this instance is important, as it may affect the operative approach, and in some complex patients, the surgeon may opt for a median sternotomy instead of the classic left thoracotomy (Brown et al. 2009) (Fig. 12).

### 3.1.2.3 Interruption of the Aortic Arch

Interruption of the aortic arch (IAA) is an uncommon, hemodynamically critical, obstructive aortic arch anomaly. In this condition, the left and right fourth embryonic arches have regressed and there is lack of luminal continuity between the ascending and descending aorta. It accounts for 1.5 % of all congenital heart disease. In IAA, the flow between the ascending and descending aorta and the lower body is maintained only by a ductal arch (patent ductus arteriosus) or collateral circulation once the ductus closes (Kellenberger 2010; Hellinger et al. 2011; Weinberg and Whitehead 2010; Weinberg et al. 1998; Mishra 2009). The affected neonates are typically not cyanotic and normal appearing at birth, but they present usually later on, characteristically during the first 2 weeks of life, with congestive heart failure that worsens as the ductus closes (Hellinger et al. 2011; Kellenberger 2010).

The classification system proposed by Celoria and Patton (Celoria and Patton 1959) is the most widely accepted and classifies these anomalies in three types according to the point of interruption: (1) in type A, the interruption occurs distal to the left subclavian artery origin at the aortic isthmus;

**Fig. 10** Sagittal oblique (candy-cane) white-blood (a) and volume-rendered (b) MR images show a discrete aortic coarctation (arrow) with multiple hypertrophied collaterals

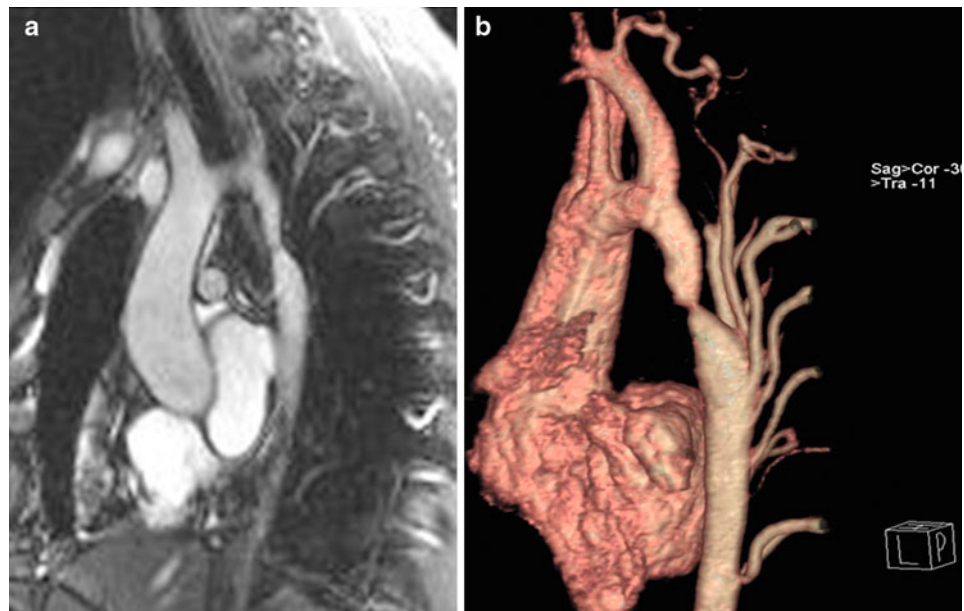
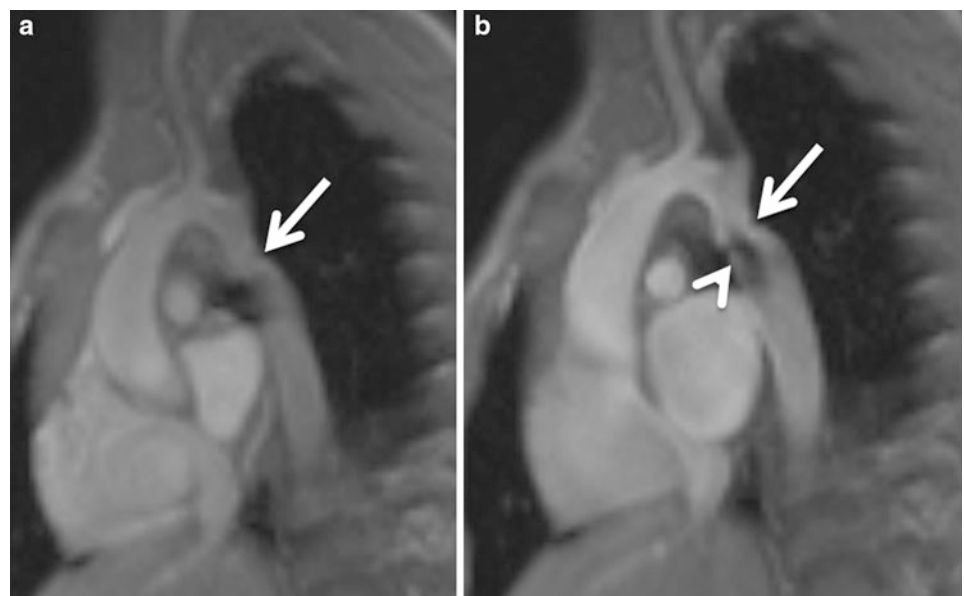


**Fig. 11** A 4-year-old with a moderate discrete coarctation of the aorta. Diastolic (a) and systolic (b) frames of steady-statefree precession MR images show a posterior indentation at the coarctation site (arrow). Note signal void (arrowhead) due to turbulent flow at the coarctation site



(2) in type B, the interruption takes place between the origins of the left common carotid artery and the left subclavian artery (Fig. 13); and (3) in type C, the interruption takes place proximal to the left common carotid artery, between the origins of the innominate and left common carotid arteries (Weinberg and Whitehead 2010; Kellenberger 2010; Hellinger et al. 2011). Type B is the most common type, and it accounts for approximately two-thirds of the cases. Type C is the least common type, occurring in less than 2 % of the cases (Collins-Nakai et al. 1976; Norwood et al. 1983; Vouhe et al. 1990; Jonas et al. 1994; Serraf et al. 1996; Tlaskal et al. 1998; Brown et al. 2006; Flint et al. 2010; Hellinger et al. 2011). Similar to other arch anomalies involving the fourth

embryonic arch, Type B interruption is commonly observed in patients with DiGeorge syndrome (Goldmuntz et al. 1998; Momma 2010). In addition, IAA rarely occurs in isolation and a patent ductus arteriosus is always present. VSD, as well as a left ventricular outflow tract obstruction, are commonly present. Less commonly, IAA may be associated with aortopulmonary window, truncus arteriosus, and double outlet right ventricle (Mishra 2009; Restrepo et al. 2012). These patients are surgically treated early in life; if left untreated, death may ensue at a median age of 4–10 days (Kellenberger 2010; Mishra 2009). Imaging should be tailored to identify the precise type of IAA, to measure the distance between the segments, to assess the dimensions of the left ventricular



**Fig. 12** A 4-day-old with tubular hypoplasia of the aortic arch (AA). Lateral (a) and (b) cranial posterior volume rendered MR images show diffuse, severe narrowing of the transverse aorta and isthmus proximal to the patent ductus arteriosus (PDA). The ductus is quite prominent in size and is similar in caliber to the descending aorta (DAo) as the systemic circulation is ductal dependent

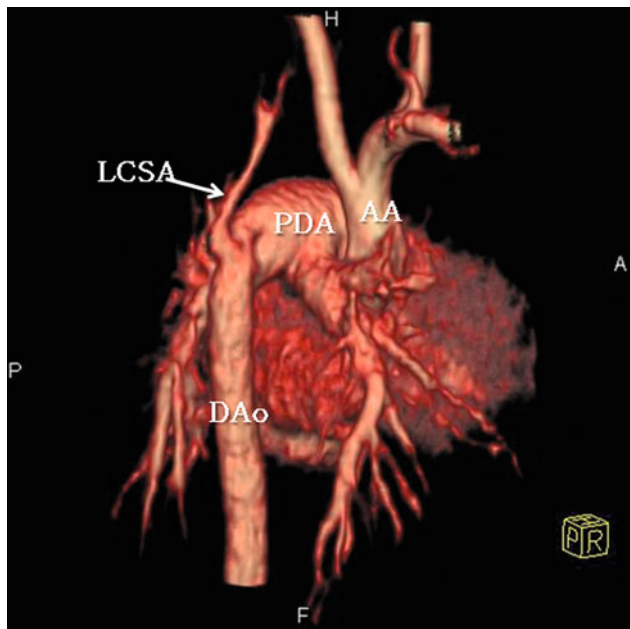
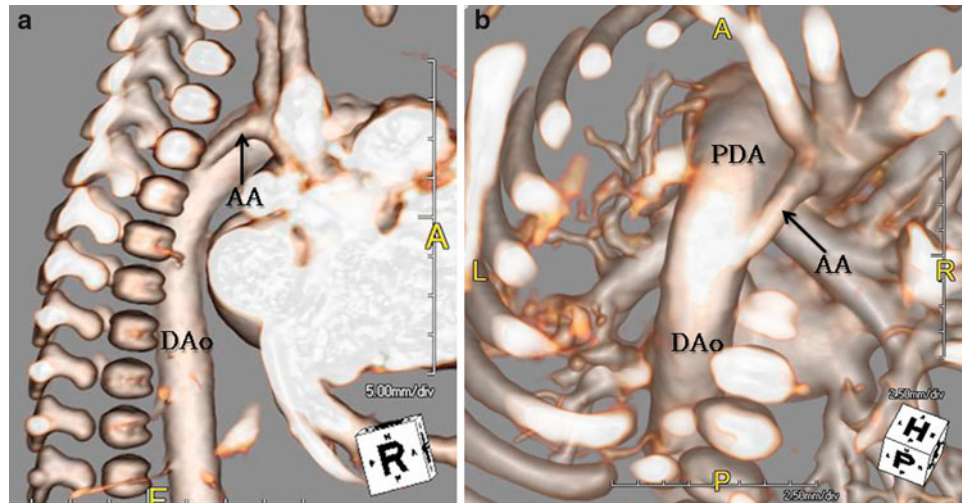


**Fig. 13** A 11-day-old patient with interrupted aortic arch. Volume-rendered CT image shows complete lack of continuity between the proximal aortic arch (AA) and the descending aorta (DAo), with imaging findings consistent with aortic arch interruption between the origins of the left common carotid artery and the left subclavian artery (LSCA). The descending aorta is reconstituted via a patent ductus arteriosus (PDA)

outflow tract, and to describe the morphological characteristics of the patent ductus arteriosus and any associated anomalies.

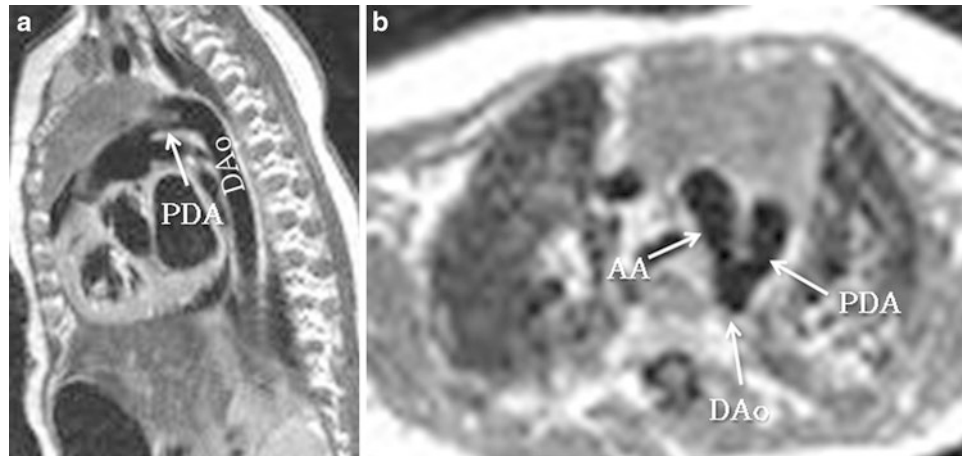
### 3.1.3 Shunt Lesions

#### 3.1.3.1 Patent Ductus Arteriosus

Patent ductus arteriosus (PDA) is the most common heart defect in neonates, and it is defined as incomplete closure of the ductus arteriosus beyond functional closure after birth.

Its incidence is quite high in premature infants, being as high as 60 % in those born before 28 weeks of gestation (Corno and Festa 2009b). PDA consists of a vascular connection usually between the left proximal pulmonary artery and the descending thoracic aorta (Fig. 14), just distal and opposite to the left subclavian artery ostium bypassing the deflated lungs. However, the precise point of connections can vary substantially (Backer and Mavroudis 2000; Berko and Haramati 2012; Kondrachuk et al. 2012). Rarely, the PDA can insert onto the right pulmonary artery. The PDA usually connects to the left pulmonary artery, even in the presence of a right aortic arch. Bilateral patent ducti have also been rarely described (Corno and Festa 2009b). The ductus arteriosus usually closes within 72 h of birth, but if it does not, it is considered unlikely that it will close spontaneously (Berko and Haramati 2012). It typically closes beginning from the pulmonary end, leaving a diverticulum on the aortic side, which eventually closes as well (Corno and Festa 2009b). This anomaly usually persists in patients with underlying congenital heart disease, commonly ASD or VSD, but it is also seen in diseases that are ductus-dependent, such as hypoplastic left heart syndrome, aortic arch interruption, and pulmonary atresia with or without an intact ventricular septum (Corno and Festa 2009b). On cross-sectional imaging, the ductus arteriosus appears as a tubular structure joining the aorta and the proximal left pulmonary artery (Fig. 14), which can be easily missed if only axial imaging is used (Kondrachuk et al. 2012). Conversely, the location, caliber, and morphology of the PDA can be easily depicted with multiplanar reconstructions in isolated defects or in complex cardiac malformations. PDA in older patients may be potentially complicated by aneurysm formation, calcification, and rupture. An increased risk for bacterial endarteritis has also been reported (Moore and Brook 2012; Berko and Haramati 2012). Premature infants are given a trial of prostaglandin inhibitors. If this fails,

**Fig. 14** Patent ductus arteriosus in a 3-month-old girl. Sagittal oblique (candy cane) and *axial* black-blood MR images show a patent ductus arteriosus (PDA) connecting the pulmonary artery with the descending aorta (Dao). AA Aortic arch



surgical ligation is performed via a left posterolateral thoracotomy. Percutaneous coil occlusion is reserved for older children (Kondrachuk et al. 2012; Corno and Festa 2009b).

### 3.1.3.2 Aortopulmonary Collaterals

Major aortopulmonary (systemic to pulmonary) collateral arteries (MAPCAs) characteristically develop in the setting of severe pulmonary stenosis/atresia or right ventricular outflow tract obstruction serving as the primary source of blood flow to the lungs (Kondrachuk et al. 2012; Flamm 2010). MAPCAs are highly variable in their presence, size, and origin. They may originate more frequently from the descending aorta or, less frequently, from the arch vessels, or the subclavian, internal mammary or intercostal arteries (Lofland 2004; Kondrachuk et al. 2012). MAPCAs may be diminutive or extremely large, resulting in over-circulation to the portion of the lung supplied by them. They may exhibit focal areas of stenosis either at their origin or anywhere along their course. MAPCAs may also have connections with the native pulmonary arteries (Lofland 2004, 2009). Multidetector CT or contrast-enhanced MRI with 3D reconstructions are extremely helpful for their full depiction and mapping prior to unifocalization or interventional embolization (Fig. 15) (Corno and Festa 2009c; Lofland 2004, 2009).

### 3.1.4 Venous Lesions

#### 3.1.4.1 Anomalies of the Pulmonary Veins

The embryology of the left atrium and central and peripheral pulmonary veins is a complicated process that initially occurs separately. The primitive pulmonary venous system draining the lung buds is part of the splanchnic plexus, which initially connects to the cardinal veins (precursors of the right- and left-sided SVCs) and umbilicovitelline veins (precursors of the IVC, portal system, and ductus venosus). During the first month of gestation, a small outpouching

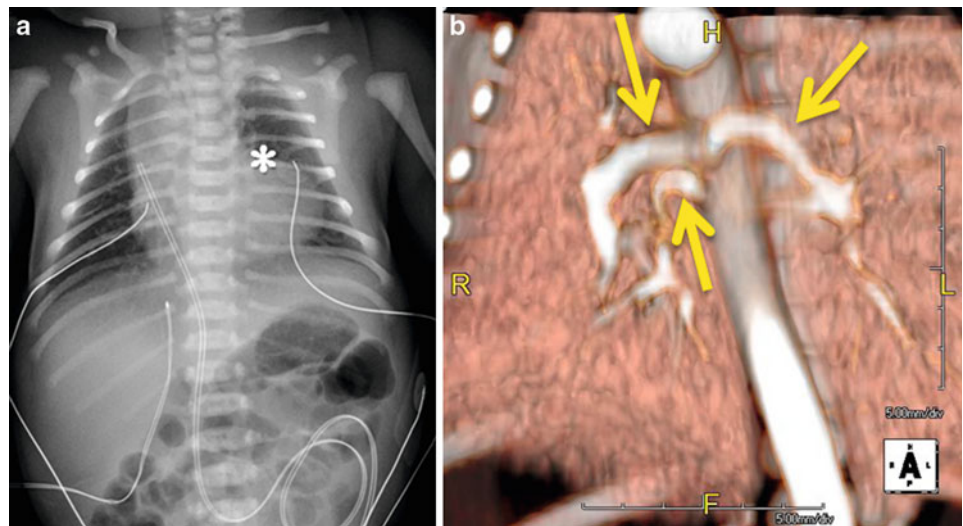
develops from the dorsal wall of the developing left atrium, resulting in the common pulmonary vein (CPV). By the thirtieth day of gestation, the CPV connects to the pulmonary venous system. Connections with the cardinal venous system and the umbilicovitelline veins involute, resulting in the expected direct pulmonary venous drainage into the left atrium (Dillman et al. 2011; Hellinger et al. 2011; Vyas et al. 2012; Latson and Prieto 2007).

If any of these processes fail to occur, pulmonary venous anomalies result. Incomplete incorporation of the CPV into the left atrium results in pulmonary vein stenosis/atresia or cor triatriatum. If the CPV fails to connect to the splanchnic plexus and communications between the splanchnic plexus and the cardinal or umbilicovitelline vein persist, some type of total or partial anomalous pulmonary venous return (TAPVR or PAPVR) will occur. If the connections between the splanchnic plexus that drain the lung buds to the cardinal and umbilicovitelline venous systems are destroyed and the CPV fails to develop or to incorporate into the left atrium, the result is the very rare condition of pulmonary vein atresia (Dillman et al. 2011; Hellinger et al. 2011; Vyas et al. 2012; Latson and Prieto 2007).

#### Pulmonary Vein Atresia/Hypoplasia

Pulmonary vein atresia is an uncommon anomaly associated with high morbidity and mortality. It is typically unilateral (Newman 2006), as if bilateral and surgical repair is not performed on an emergency basis, the condition is typically fatal (Dominguez Garcia et al. 2009; Vyas et al. 2012). The etiology is believed to represent the result of unsuccessful incorporation of the CPV into the left atrium resulting in the absence of long segments of the central pulmonary veins (Newman 2006). If unilateral, the condition may be asymptomatic or may manifest in infancy or childhood with recurrent episodes of pneumonia in the affected side, hemoptysis due to rupture of the bronchial varices, which develop as collateral circulation for the

**Fig. 15** Newborn with respiratory distress. (a) Frontal chest radiograph shows moderate cardiomegaly on account of the right chambers, an absent main pulmonary artery segment (asterisk), and decreased peripheral pulmonary vascularity. Echocardiography demonstrated tetralogy of Fallot. (b). Volume-rendered CTA image was obtained to map out the aortopulmonary collateral arteries (arrows) prior to unifocalization and demonstrates three prominent MAPCAs supplying both lungs



obstructed pulmonary veins, exercise intolerance or pulmonary hypertension (Newman 2006; Heyneman et al. 2001; Mataciunas et al. 2009; Wiebe et al. 2003). Nearly half of the cases are associated with other forms of congenital heart disease (Pourmoghadam et al. 2003; Newman 2006; Heyneman et al. 2001).

Chest radiographs show a small affected hemithorax with ipsilateral mediastinal shift and a small ipsilateral hilum. The affected lung shows circumferential pleural thickening, diffuse reticular opacities, and septal lines reminiscent of pulmonary edema, which is most pronounced in the lower lung fields (Newman 2006; Heyneman et al. 2001). On enhanced CT examination of these patients, the margins of the left atrium at the expected level of the pulmonary vein ostia appear smooth, and some adjacent enhancing soft tissue density may be present reflecting collateral pulmonary-to-systemic venous channels. The ipsilateral pulmonary artery appears diminutive in size. Systemic collaterals may be present in the mediastinum. On lung window CT images, diffuse ground-glass attenuation and smooth thickening of the interlobular septa and bronchovascular bundles may be observed (Heyneman et al. 2001). The overall findings are believed to represent prominent bronchial veins, dilated lymphatics and patchy parenchymal fibrosis, secondary to pulmonary infarcts (Heyneman et al. 2001).

In cases of unilateral pulmonary venous atresia and depending on the age at diagnosis, surgical repair will not be possible. Most of the patients reported in the literature present late in life once irreversible changes affected the lungs and vasculature. Although the mainstay of therapy should be a surgical reestablishment of the pulmonary venous drainage to the left atrium (Wiebe et al. 2003), this may not always be an option. Therefore, pneumonectomy might be necessary to prevent repeated pulmonary infections, to relieve the left-to-right shunt, and to remove the

dead space contributing to exercise intolerance (Pourmoghadam et al. 2003; Argueta-Morales et al. 2009).

### Pulmonary Vein Stenosis

Congenital pulmonary vein stenosis (PVS) is believed to be the result of uninhibited proliferation of myofibroblast-like cells and matrix deposition resulting in expanded intimas, endoluminal thickening, and narrowing of the pulmonary veins (Riedlinger et al. 2006; Lee et al. 2008a). However, the term “primary” pulmonary vein stenosis would be more accurate, as there is increasing evidence that the disease is progressive and may even not be present at the time of delivery. The association with other congenital heart diseases is high, ranging from 30 to 80 % (Lee et al. 2008a; Latson and Prieto 2007). Therefore, echocardiographic evaluations of all forms of congenital heart defects should include an assessment of the pulmonary veins, as some studies demonstrated worsening pulmonary vein stenosis in patients with prior normal pulmonary venous flow patterns (Breinholt et al. 1999; Drossner et al. 2008).

A strong association with prematurity has been reported, with a preponderance in premature infants with cardiac shunt lesions (Drossner et al. 2008). However, PVS may also occur in isolation, and in these cases, PVS usually shows a rapid course. Generally, the age at diagnosis and the severity of symptoms are contingent on the number of pulmonary veins involved and the severity of pulmonary venous obstruction to the individual pulmonary veins (Vyas et al. 2012; Latson and Prieto 2007). Patients with only three or four stenotic pulmonary veins have a poorer prognosis, as their mortality rate approaches 85 versus 0 % in patients with 1 or 2 stenosed pulmonary veins (Breinholt et al. 1999). Most cases of PVS present in infancy with a history of worsening respiratory distress and recurrent pneumonias. With disease progression, pulmonary



hypertension develops and becomes increasingly prominent. Therefore, an evaluation for stenotic pulmonary veins should always be performed in young patients with unexplained pulmonary hypertension. Hemoptysis may ensue, particularly in older patients (Latson and Prieto 2007).

Unlike in adults, in whom secondary PVS is most frequently associated with radiofrequency ablation for atrial fibrillation, in pediatric patients, secondary PVS typically occurs following the surgical repair of anomalous pulmonary vein connections. Approximately 10 % of these patients develop substantial stenosis, either at the anastomotic site or within the central portions of the pulmonary veins (Hancock Friesen et al. 2005; Caldarone et al. 1998).

In young children, echocardiography can usually visualize all pulmonary veins. Turbulent flow on color Doppler with flow velocities  $>1.6$  m/s may potentially indicate hemodynamically significant obstruction (Smallhorn et al. 1985). Findings on chest radiographs include patchy reticular opacities and thickened septa, reflecting the impaired venous drainage in the affected lung. On MDCT images, PVS manifests with pulmonary vein narrowing and wall thickening, although it typically affects the pulmonary venous—left atrial junction, which may extend and involve more central and peripheral segments, resulting in long-segment narrowing, particularly in cases of advanced disease (Lee et al. 2011a, 2008a). In advanced cases, the findings may be indistinguishable from pulmonary venous atresia, with smooth septal thickening, reticular opacities, patchy ground glass centrilobular opacities, and pleural thickening, which may be smooth or nodular (Miller 2012). A pattern of diffuse, multifocal regions of mosaic attenuation may be present, with oligemia in the hypoattenuating regions, reflecting a vascular motive to this mosaic pattern, rather than small airways disease (Swensen et al. 1996). Enlarged mediastinal lymph nodes, related to vascular congestion may be present (Bailey et al. 2000). PVS may show a mottled appearance on V/Q scans with a patchy distribution of the radionuclide tracer but without discrete segmental or subsegmental defects that could be demonstrated on pulmonary angiograms. This is estimated to represent the result of increased downstream resistance to the flow of the macroaggregated albumin particles but not to the injection of the contrast under pressure in CT angiography or pulmonary angiograms (Bailey et al. 2000; Miller 2012). MRI may show similar findings, although to a lesser extent, as CT has better spatial resolution (Fig. 16). However, MRI may provide additional physiological information (Vyas et al. 2012).

PVS may be amenable to balloon angioplasty, with or without stent placement, although restenosis seems universal. Care should be taken, as stent implantation before surgery may complicate and limit the surgical approach. Restenosis following surgery occurs in approximately 10 %

of cases, despite the advent of new techniques based on the premise of reducing trauma to the veins to avoid any stimulus for regrowth of obstructive tissue. In severe cases, transplantation of the lung or combined heart–lung transplantation may be necessary (Latson and Prieto 2007; O’Callaghan et al. 2011).

### Pulmonary Varix

Congenital pulmonary varix is a rare vascular anomaly resulting in focal aneurysmal dilatation of a segment of a pulmonary vein that may be easily mistaken with the more common pulmonary arteriovenous malformation (PAVM) (Maillard et al. 2007; Kumazoe et al. 2008). Unlike PAVM, pulmonary varices do not result in right-to-left shunting. Pulmonary varix may be congenital or acquired, the latter is found in patients who have underlying cardiac conditions, resulting in pulmonary venous hypertension, such as mitral valve disease, aortic coarctation and pulmonary vein stenosis (Kumazoe et al. 2008). In most instances, pulmonary varices are incidental findings in otherwise asymptomatic patients. On rare occasions, the varix may potentially function as a thrombogenic nidus, and the patients may become symptomatic, due to complications such as rupture and thromboembolism (Lee et al. 2008a, 2011a).

On chest radiographs, pulmonary varices may appear as well-defined pulmonary or mediastinal lesions in close proximity to the cardiac silhouette and should be differentiated from other etiologies for space occupying lesions in the pediatric patient, such as a congenital lung anomaly, a neoplasm, or round pneumonia. MDCT studies with 3D reconstructions are useful for characterization of these lesions (Fig. 17). The radiological features favor the diagnosis of pulmonary varix, including contiguity between the pulmonary vein and varix, simultaneous contrast enhancement within both structures, and the lack of a feeding artery contiguous with the pulmonary artery (Lee et al. 2008a, 2011a). Some authors advocate for the use of modalities that are able to demonstrate the flow direction and pattern within the lesion, such as US, MR, or conventional angiography, to avoid confusion with a PAVM (Abujudeh 2004; Kumazoe et al. 2008; Maillard et al. 2007). Surgical resection is only indicated for symptomatic patients or complications (Abujudeh 2004; Lee et al. 2011a).

#### 3.1.4.2 Anomalous Systemic Venous Connections

Clinically significant anomalous systemic connections are uncommon in patients with normal situs solitus. However, their incidence in patients with heterotaxy is increased (Geva 2012; Corno and Festa 2009a).

The most common anomaly of systemic venous return is a *persistent left superior vena cava* with a prevalence of 0.3 % in normal individuals and 4.4 % in patients with congenital heart disease (Gonzalez-Juanatey et al. 2004). It

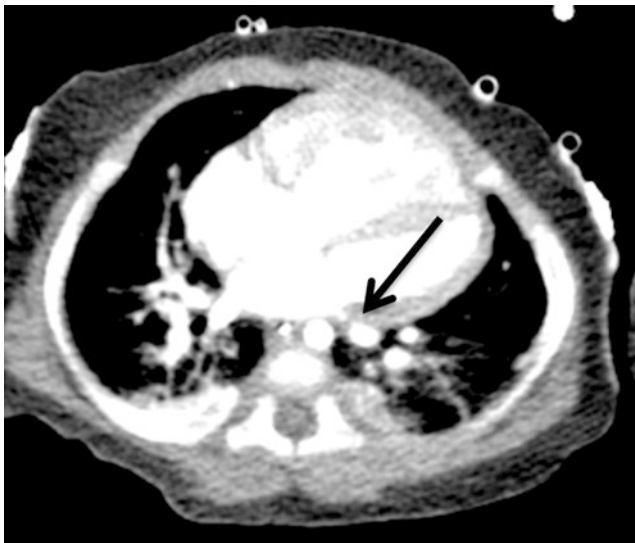


**Fig. 16** A 3-month-old boy with pulmonary vein stenosis who presented with persistent desaturation and tachypnea. Enhanced axial CT image shows a marked narrowing (*arrow*) of the left inferior pulmonary vein. Right inferior pulmonary vein is normal in size and patent. Note the enlarged right cardiac chambers with right ventricular hypertrophy, the result of pulmonary hypertension

is the result of incomplete resorption of the embryonic vasculature (Gonzalez-Juanatey et al. 2004). In most instances, the persistent left superior vena cava drains into the right atrium via a dilated coronary sinus (Fig. 18). However, in some instances, it may drain into the left atrium and result in a right-to-left shunt (Gonzalez-Juanatey et al. 2004; Geva 2012). Cardiac abnormalities associated with a persistent left superior vena cava include juxtaposition of the right atrial appendage, atrioventricular septal defects, mitral atresia, and tetralogy of Fallot (Geva 2012). Identification of this abnormality is of the utmost importance, as the strategy for cardiopulmonary bypass may need to be changed depending on whether a concomitant bridging innominate vein to a right-sided superior vena cava is present (Corno and Festa 2009a; Corno 2007). If the bridging innominate vein is present, the customary direct cannulation of the superior and inferior vena cava (IVC) will suffice to provide adequate venous return. If no bridging innominate vein is present, other, more complex strategies will need to be instituted to warrant adequate venous return (Corno 2007). In addition, if a bidirectional Glenn is needed and the bridging innominate vein is absent, bilateral bidirectional Glenn surgeries will be needed to be performed (Corno and Festa 2009a). An additional anomaly of the systemic venous return that may influence the strategy of cardiopulmonary bypass or the type of surgery if total cavopulmonary connection is needed in the *interruption of the IVC with azygous continuation* (Corno and Festa 2009a). Therefore, it is particularly important to describe

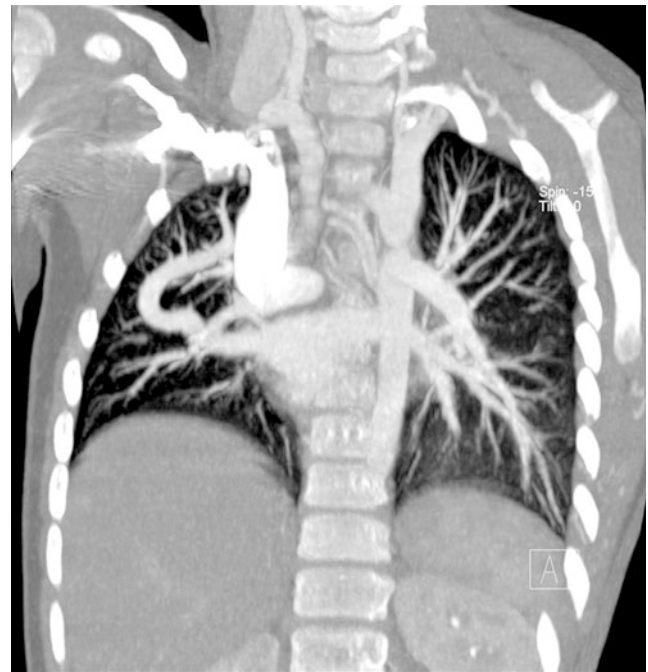


**Fig. 17** A 4-year-old boy with an abnormal chest radiograph obtained for evaluation of pneumonia. Subsequently obtained coronal reformatted maximum intensity projection CT image shows an incidental finding of an enlarged and tortuous right inferior pulmonary vein, consistent with pulmonary varix

this anomaly in candidates for cardiac surgery. Anomalous systemic venous connection to IVC or portal vein occurs in association with congenital venolobar syndrome, also known as scimitar syndrome.

### 3.2 Acquired Mediastinal Vascular Abnormalities

#### 3.2.1 Traumatic Lesions

Traumatic injury to the thoracic aorta is a potentially fatal injury and is the second most common cause of death from trauma following head injuries (Mirka et al. 2012). Violent deceleration is the most common mechanism of injury by applying shearing forces to the aorta at sites of relative immobility, typically the ligamentum arteriosum, aortic root, and diaphragmatic hiatus (Steenburg et al. 2008). The aortic isthmus is the most common site of injury in clinical practice (Fig. 19). However, on autopsy series, the involvement of the ascending aorta has been reported in 20–25 % of the cases, which is related to the fact that 80 % of the traumatic injuries to the ascending aorta result in fatal injuries, such as hemopericardium with tamponade, aortic valve rupture, or coronary artery dissection (Groskin 1992). Aortic injuries, which are more commonly transverse tears, may range from intimal laceration to complete transection

depending on how many layers of the aortic wall are involved. Partial tears usually involve only the inner two layers and result in a contained rupture, while complete transections typically involve all three layers and are usually fatal due to exsanguination (Steenburg et al. 2008). CT is the most important type of imaging modality for this sort of injury with a diagnostic sensitivity and a negative predictive value for the detection of a traumatic aortic injury approaching 100 % (Steenburg et al. 2008; Dyer et al. 1999).

Direct signs of aortic trauma include pseudoaneurysm formation, intimal flap, irregular contour, mural thrombus, sudden change in aortic caliber (so-called pseudocoarctation) and rarely, direct extravasation of contrast, especially if located in the juxtaductal regions (Dyer et al. 1999; Steenburg et al. 2008; Mirvis 2005; Mirka et al. 2012; Mirvis and Shanmuganathan 2007). Traumatic pseudoaneurysms manifest as rounded bulges with irregular margins projecting anteriorly and originating from the isthmus region. These features indicate a contained rupture by the adventitia, resulting in bulging as a result of the dissection of blood through an intimal and medial tear. The torn intima may present as a flap across the base of the pseudoaneurysm. The finding of a juxtaductal pseudoaneurysm nearly always indicates aortic injury. An aortic intimal tear must be differentiated from the normal ductus diverticulum or ductus bump (Fig. 20), which is an embryological remnant at the site of the ligamentum arteriosum in the aortic isthmus and manifests as a focal bulge along the anteromedial aspect of the aortic isthmus (Berko and Haramati 2012; Fisher et al. 1997). This is a normal variant that may be easily mistaken for a post-traumatic pseudoaneurysm, which also takes place at the aortic isthmus. The ductus bump has smooth contours and exhibits obtuse angles, while a tear usually has irregular contours and more acute angles. Indirect signs of aortic trauma include periaortic mediastinal hematoma, which may be the result of hemorrhage of the aorta vasa vasorum, hemothorax, and hemopericardium (Mirka et al. 2012; Mirvis and Shanmuganathan 2007).

The use of multiplanar, maximum intensity projection, volume rendered, and virtual angioscopic 3D images significantly aids in determining the precise anatomy (Hellinger et al. 2011; Mirvis 2005). Surgical repair remains the mainstay of therapy, although in recent years, the use of percutaneous endovascular stent grafting as an alternative to surgery has been expanded in many trauma centers (Steenburg et al. 2008).

### 3.2.2 Infectious Lesions

#### 3.2.2.1 Mycotic Aneurysm

Mycotic aneurysm or infected aneurysm represents any aortic dilatation of infectious etiology, irrespective of size or

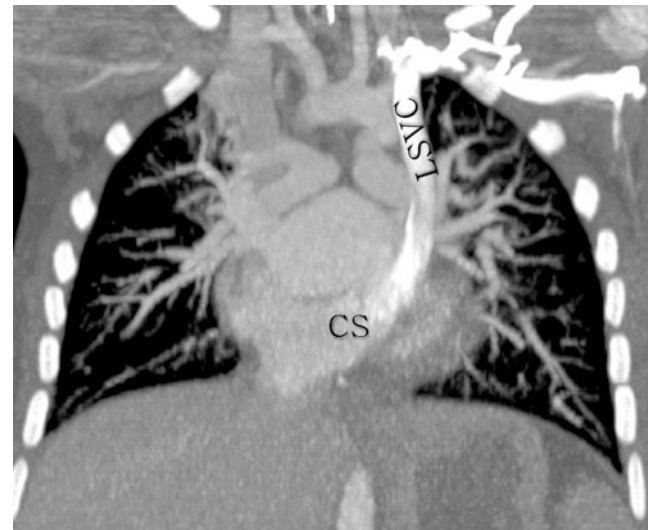


**Fig. 18** A 10-month-old male with congenital heart disease and bilateral superior vena cava. Coronal reformatted CTA image shows bilateral superior vena cava present. Contrast was injected from the left upper extremity and delineates a left-sided superior vena cava (LSVC) draining into a prominent coronary sinus (CS). No bridging vein joining both SVCs is seen

etiology. Mycotic aneurysms are uncommon lesions representing less than 3 % of all aortic aneurysms (Restrepo et al. 2011; Katabathina and Restrepo 2012), and they rarely affect children (Mengozi et al. 2001). *Staphylococcus aureus*, *Salmonella* sp., and enterococci are the most common causative organisms. Other less common pathogens include *Pneumococcus*, *Listeria*, *Bacteroides fragilis*, and *Treponema pallidum* and *Mycobacterium tuberculosis* in adults (Restrepo et al. 2011; Katabathina and Restrepo 2012; Litmanovich et al. 2012). The mechanisms of infection include contiguous spread from the neighboring infected structures, such as mediastinitis, infectious pericarditis, empyema, or a paravertebral abscess; septic emboli to the aortic vasa vasorum; bacteremic seeding of an intimal injury and direct bacterial inoculation at the time of trauma (Litmanovich et al. 2012; Restrepo et al. 2011; Lopes et al. 2009; Katabathina and Restrepo 2012). On imaging, most aneurysms are saccular and have irregular, thickened walls. Air trapped in the walls may be observed on rare occasions. Periaortic fluid and fat stranding of the surrounding soft tissues are early findings of infection. A rapid progression or change in shape of a saccular aneurysm is highly concerning for super-imposed infection (Litmanovich et al. 2012; Katabathina and Restrepo 2012; Restrepo et al. 2011).

#### 3.2.3 Vasculitis

Childhood vasculitis comprises a group of uncommon, multisystemic disorders characterized by the presence of inflammation in the blood vessel walls, which if left untreated may potentially result in tissue ischemia from



**Fig. 19** Enhanced axial CT image (a) shows traumatic aortic injury at the classic location of the aortic isthmus (arrow) in a 15-year-old post motor vehicle accident. The resultant pseudoaneurysm formation is more easily appreciated in the subsequent angiogram (b)

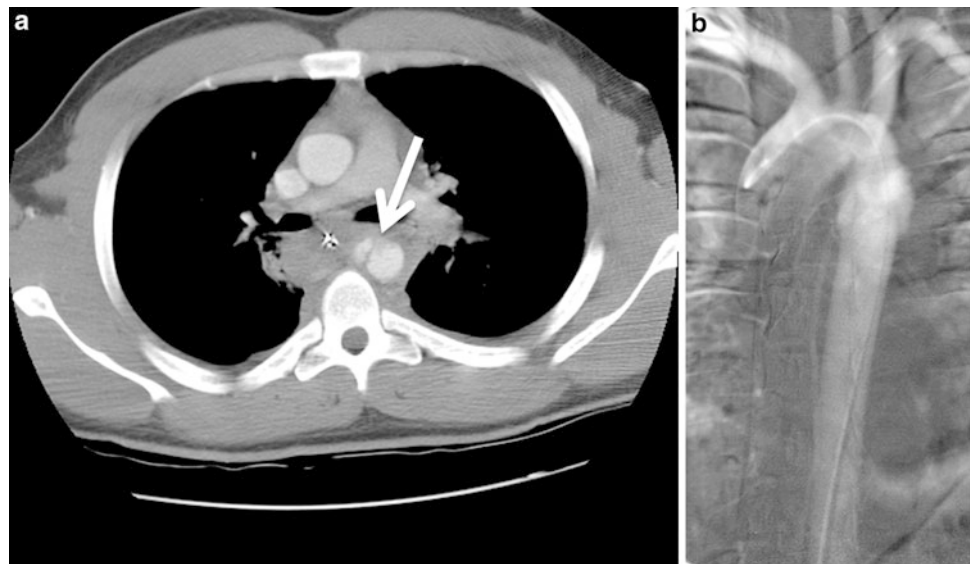
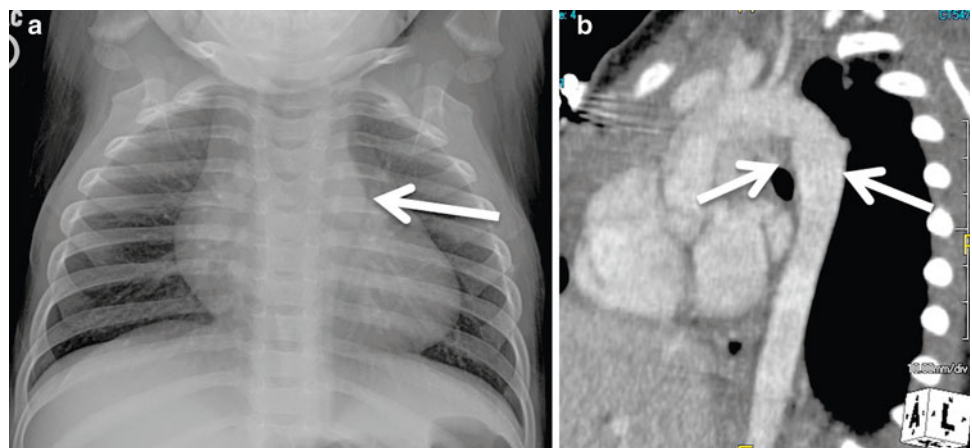


**Fig. 20** Ductus bump in a young child with URI. Chest radiograph (a) shows a prominent ductus bump. Corresponding sagittal oblique reformatted CT image (b) demonstrates the ductus diverticulum or ductus bump (arrows). The ductus arteriosus typically closes commencing on the pulmonary arterial side leaving sometimes an outpouching on the aortic side, abnormal, developmental variant



vascular stenosis, occlusion, aneurysm, or rupture (Eleftheriou and Brogan 2009; Eleftheriou et al. 2009). The incidence of vasculitis in children is approximately 23 per 100,000 (Gardner-Medwin et al. 2002). Vasculitis in children may occur secondary to infection, malignancy, drug, or radiation exposure and to other rheumatologic disorders, such as lupus or juvenile dermatomyositis (Weiss 2012). The classification of vasculitis in children is primarily based on the size of the affected vessels and the presence or absence of granulomatous changes (Ozen et al. 2006). Henoch-Schonlein purpura and Kawasaki disease are the most common vasculitides in the pediatric setting. However, Takayasu arteritis more frequently affects the large vessels.

### 3.2.3.1 Takayasu Arteritis

Takayasu arteritis is a large-vessel granulomatous vasculitis that primarily affects the aorta and its major branches. There is a female predilection for this condition. Early diagnosis is challenging because the clinical manifestations

are nonspecific. The most common complaints at presentation are in order of frequency: headaches, dizziness, abdominal pain, lower extremity claudication, fever, and weight loss (Weiss 2012; Eleftheriou and Brogan 2009; Eleftheriou et al. 2009). T cell mediated panarteritis extends from the adventitial vasa vasorum inwards. Clinically, Takayasu arteritis is divided into two phases. An early, systemic, “prepulseless” phase and a late, occlusive, “pulseless” phase. During the early, “prepulseless” phase, constitutional, so-called B-symptoms, malaise, fever, night sweats, and weight loss, are more common. On physical examination, hypertension is present in nearly 90 % of the patients, and bruits or weakened blood pulses may be detected in involved vessels.

The symptoms of the chronic phase are determined by the vessels involved, and symptoms of ischemia present once vascular occlusions or high-grade stenosis develop. Depending on the vascular territories affected, children may have hypertension, ischemic heart disease, testicular pain,

**Fig. 21** Chest radiograph (a) in a 15-year-old with malaise and low-grade fevers show a prominent descending aorta (arrows). Subsequent sagittal oblique black-blood MR image (b) shows corresponding fusiform aneurysmatic dilation of the descending aorta, which exhibits diffusely thickened walls

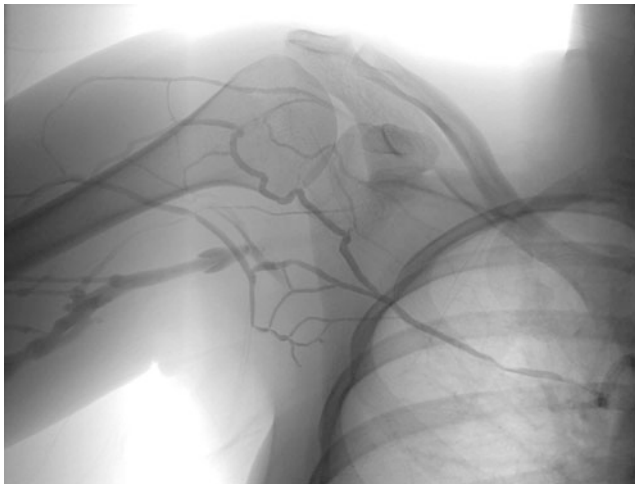
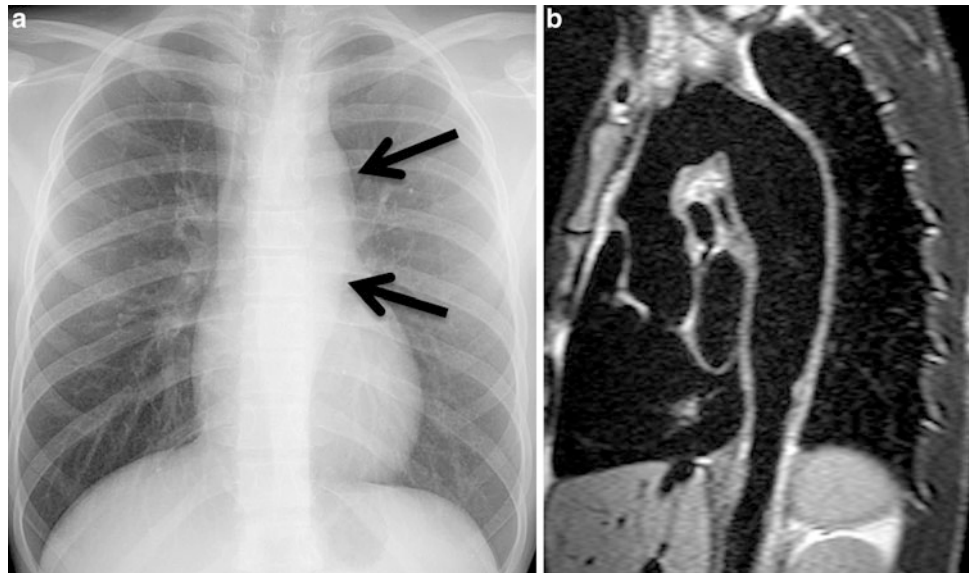


**Fig. 22** Right subclavian vein thrombosis in a 17-year-old boy who is a baseball pitcher with Paget Schroetter syndrome. Venography image shows occlusive thrombosis in the right proximal subclavian vein

abdominal pain, hematuria, or proteinuria (Litmanovich et al. 2012; Weiss 2012; Katabathina and Restrepo 2012; Restrepo et al. 2011).

Cross-sectional imaging, and preferably MR angiography, is used to evaluate Takayasu arteritis. Both modalities, MDCT and MRI, can depict the luminal and the mural thickening (Fig. 21). Maximum intensity projection and volume-rendered 3D reconstructions are particularly helpful to delineate the degree of stenosis or aneurysmatic dilation in the vessels involved. Additionally, with MRI, contrast enhancement of the thickened wall may be depicted, a finding that usually correlates with disease activity, which is difficult to adequately evaluate. Recently, Papa et al. (2012) published promising results to more accurately evaluate

disease activity using the blood pool agent, Gadofosveset trisodium, for the assessment of disease activity and follow-up of the response to therapy. In addition, occasionally, mural edema may be seen on T2-weighted MR sequences as a concentric rim of high signal intensity (Katabathina and Restrepo 2012; Litmanovich et al. 2012). The limitations of MRI include the poor depiction of vascular branch points, which may be misinterpreted as vascular occlusions; the poor depiction of calcifications, which may occur in late-stage Takayasu arteritis; and the relatively poor sensitivity for the evaluation of smaller vessels as well as the limited areas that can be scanned in each station, as opposed to CTA. Furthermore, one may be limited in the amount of gadolinium that can be injected (Litmanovich et al. 2012; Gotway et al. 2005; Papa et al. 2012). Steroids are the mainstay for treatment. Methotrexate, azathioprine, and infliximab have also been used in children (Weiss 2012; Eleftheriou et al. 2009).

### 3.2.4 Thrombotic Lesions

Paget Schroetter syndrome, also known as effort-induced thrombosis, is a condition usually found in young, otherwise healthy individuals and is characterized by the development of axillary-subclavian vein thrombosis, usually in the dominant upper extremity following strenuous sporting activities involving sustained upper extremity movements, such as wrestling, weight lifting, pitching, rowing, gymnastics, and swimming, or after execution of repetitive overhead activities, such as painting (Fig. 22). Microtrauma to the endothelium and activation of the coagulation cascade are believed to occur following retroversion, hyperabduction, and extension of the arm in these sporting activities. Patients are typically symptomatic and complain of a blue, heavy, painful, swollen upper extremity

(Engelberger and Kucher 2012; Alla et al. 2010; Thompson et al. 2011; Illig and Doyle 2010).

A chest radiograph should be obtained in these individuals to evaluate for the presence of a mediastinal mass or any osseous abnormality, such as a cervical rib. Duplex sonography is an excellent initial imaging modality for evaluating this condition, although it is operator dependent. Significant venous compression during hyperabduction may be identified when there is complete interruption of flow or flattening of the waveform with loss of the transmitted cardiac and respiratory dynamics on spectral display (Longley et al. 1992). Evaluation of the contralateral side is important to study. If significant arterial or venous compression is noted, an anatomical predisposition may be inferred. CT or MR venography, if performed during neutral and provocative maneuvers, with the arms at rest and in the “surrender” position, are helpful, as they can depict the vascular anatomy as well as any other causes of extraanatomical vascular compression (Ersoy et al. 2012). The drawbacks are the need of double doses of contrast material and a second additional scan, which not only doubles the time but also the radiation dose in the case of CT.

Treatment goal of Paget Schroetter syndrome is aimed at preventing irreversible fibrotic changes in the vein, which may result in chronic edema and significant disability. A multidisciplinary approach consisting of anticoagulation therapy, thrombolysis, and subsequent surgical decompression is the current standard of care (Engelberger and Kucher 2012; Alla et al. 2010; Thompson et al. 2011; Illig and Doyle 2010).

## References

- Abujudeh H (2004) Pulmonary varix: blood flow is essential in the diagnosis. *Pediatr Radiol* 34(7):567–569. doi:10.1007/s00247-004-1142-7
- Alla VMMD, Natarajan NMD, Kaushik MMD, Warriar RMD, Nair CKMD (2010) Paget-Schroetter Syndrome: review of pathogenesis and treatment of effort thrombosis. *West J Emerg Med* 11(4):0
- Argueta-Morales IR, Garg R, DeCampli WM (2009) Diagnosis and management of congenital right pulmonary venous atresia. *Cardiol Young* 19(6):648–651. doi:10.1017/s1047951109991867
- Backer CL, Mavroudis C (2000) Congenital heart surgery nomenclature and database project: patent ductus arteriosus, coarctation of the aorta, interrupted aortic arch. *Ann Thorac Surg* 69(4):S298–S307
- Bailey CL, Channick RN, Auger WR, Fedullo PF, Kerr KM, Yung GL, Rubin LJ (2000) “High probability” perfusion lung scans in pulmonary venoocclusive disease. *Am J Respir Crit Care Med* 162(5):1974–1978
- Berdon WE (2000) Rings, slings, and other things: vascular compression of the infant trachea updated from the midcentury to the millennium—the legacy of Robert E. Gross, MD, and Edward B. D. Neuhauser, MD. *Radiology* 216(3):624–632
- Berko NS, Haramati LB (2012) Simple cardiac shunts in adults. *Semin Roentgenol* 47(3):277–288. doi:10.1053/j.ro.2011.12.003
- Breinholt JP, Hawkins JA, Minich L, Tani LY, Orsmond GS, Ritter S, Shaddy RE (1999) Pulmonary vein stenosis with normal connection: associated cardiac abnormalities and variable outcome. *Ann Thorac Surg* 68(1):164–168
- Brown JW, Rodefeld MD, Ruzmetov M (2009) Transverse aortic arch obstruction: when to go from the front. *Semin Thorac Cardiovasc Surg: Pediatr Cardiac Surg Ann* 12(1):66–69. doi:10.1053/j.pcsu.2009.01.024
- Brown JW, Ruzmetov M, Okada Y, Vijay P, Rodefeld MD, Turrentine MW (2006) Outcomes in patients with interrupted aortic arch and associated anomalies: a 20-year experience. *Eur J Cardiothorac Surg* 29(5):666–673; discussion 673–664. doi:10.1016/j.ejcts.2006.01.060, S1010-7940(06)00146-1 [pii]
- Caldarone CA, Najm HK, Kadletz M, Smallhorn JF, Freedom RM, Williams WG, Coles JG (1998) Relentless pulmonary vein stenosis after repair of total anomalous pulmonary venous drainage. *Ann Thorac Surg* 66(5):1514–1520
- Campbell M (1970) Natural history of coarctation of the aorta. *Br Heart J* 32(5):633–640
- Castañer E, Gallardo X, Rimola J, Pallardó Y, Mata JM, Perendreu J, Martin C, Gil D (2006) Congenital and acquired pulmonary artery anomalies in the adult: radiologic overview I. *Radiographics* 26(2):349–371. doi:10.1148/rg.262055092
- Celoria GC, Patton RB (1959) Congenital absence of the aortic arch. *Am Heart J* 58:407–413
- Collins-Nakai RL, Dick M, Parisi-Buckley L, Fyler DC, Castaneda AR (1976) Interrupted aortic arch in infancy. *J Pediatr* 88(6):959–962
- Corno AF (2007) Systemic venous drainage: can we help Newton? *Eur J Cardiothorac Surg* 31(6):1044–1051. doi:10.1016/j.ejcts.2007.01.066
- Corno AF, Festa P (2009a) Anomalous systemic venous connections. In: Corno AF, Festa P (eds) *Congenital heart defects: decision making for surgery*, vol 3. Springer, Berlin pp 18–22
- Corno AF, Festa P (2009b) Patent ductus arteriosus. In: Corno AF, Festa P (eds) *Congenital heart defects: decision making for surgery*, vol 1. Springer, Berlin
- Corno AF, Festa P (2009c) Pulmonary atresia with intact ventricular septum. In: Corno AF, Festa P (eds) *Congenital heart defects: decision making for surgery*, vol 3. Springer, Berlin, pp 154–161
- Dillman JR, Sanchez R, Ladino-Torres MF, Yarram SG, Strouse PJ, Lucaya J (2011) Expanding upon the unilateral hyperlucent hemithorax in children. *Radiographics* 31(3):723–741. doi:10.1148/rg.313105132
- Dominguez Garcia O, Granados Ruiz M, Sanchez-Redondo M, Lázaro Salvador M, Juárez Tosina R (2009) A difficult emergency surgical diagnosis: atresia of the common pulmonary vein. *Pediatr Cardiol* 30(7):989–991. doi:10.1007/s00246-008-9320-2
- Drossner DM, Kim DW, Maher KO, Mahle WT (2008) Pulmonary vein stenosis: prematurity and associated conditions. *Pediatrics* 122(3):e656–e661. doi:10.1542/peds.2008-0075
- Dyer DS, Moore EE, Mestek MF, Bernstein SM, Iklé DN, Durham JD, Heinig MJ, Russ PD, Symonds DL, Kumpe DA, Roe EJ, Honigman B, McIntyre RC, Eule J (1999) Can chest CT be used to exclude aortic injury? *Radiology* 213(1):195–202
- Eleftheriou D, Brogan PA (2009) Vasculitis in children. *Best Pract Res Clin Rheumatol* 23(3):309–323. doi:10.1016/j.berh.2009.02.001
- Eleftheriou D, Dillon MJ, Brogan PA (2009) Advances in childhood vasculitis. *Curr Opin Rheumatol* 21(4):411–418. doi:10.1097/BOR.0b013e32832c49f2
- Engelberger RP, Kucher N (2012) Management of deep vein thrombosis of the upper extremity. *Circulation* 126(6):768–773. doi:10.1161/circulationaha.111.051276
- Epelman M, Kreiger PA, Servaes S, Victoria T, Hellinger JC (2010) Current imaging of prenatally diagnosed congenital lung lesions.



- Semin Ultrasound CT MR 31(2):141–157 doi:[10.1053/j.sult.2010.01.002](https://doi.org/10.1053/j.sult.2010.01.002), S0887-2171(10)00004-1 [pii]
- Epelman M, MacDonald C (2010) Obstructive lesions of the aortic arch. In: Yoo SJ, MacDonald C, Babyn PS (eds) Chest radiographic interpretation in pediatric cardiac patients. Thieme, New York, pp 229–233
- Ersoy H, Steigner ML, Coyner KB, Gerhard-Herman MD, Rybicki FJ, Bueno R, Nguyen LL (2012) Vascular thoracic outlet syndrome: protocol design and diagnostic value of contrast-enhanced 3D MR angiography and equilibrium phase imaging on 1.5- and 3-T MRI scanners. *Am J Roentgenol* 198(5):1180–1187. doi:[10.2214/ajr.11.6417](https://doi.org/10.2214/ajr.11.6417)
- Fisher RG, Sanchez-Torres M, Whigham CJ, Thomas JW (1997) “Lumps” and “bumps” that mimic acute aortic and brachiocephalic vessel injury. *Radiographics* 17(4):825–834
- Flamm SD (2010) Chapter 5: contrast cardiac MR—anatomy, physiology, viability and perfusion. In: Fogel MA (ed) Principles and practice of cardiac magnetic resonance in congenital heart disease: Form, function and flow. 1st edn. Wiley-Blackwell, pp 79–81
- Fleischmann D, Kamaya A (2009) Optimal vascular and parenchymal contrast enhancement: the current state of the art. *Radiol Clin North Am* 47(1):13–26. doi:[10.1016/j.rcl.2008.10.009](https://doi.org/10.1016/j.rcl.2008.10.009), S0033-8389(08)00191-7 [pii]
- Flint JD, Gentles TL, MacCormick J, Spinetto H, Finucane AK (2010) Outcomes using predominantly single-stage approach to interrupted aortic arch and associated defects. *Ann Thorac Surg* 89(2):564–569. doi:[10.1016/j.athoracsur.2009.10.036](https://doi.org/10.1016/j.athoracsur.2009.10.036), S0003-4975(09)02147-X [pii]
- Gardner-Medwin JMM, Dolezalova P, Cummins C, Southwood TR (2002) Incidence of Henoch-Schönlein purpura, Kawasaki disease, and rare vasculitides in children of different ethnic origins. *The Lancet* 360(9341):1197–1202. doi:[10.1016/S0140-6736\(02\)11279-7](https://doi.org/10.1016/S0140-6736(02)11279-7)
- Geva T (2012) Abnormal systemic venous connections. In: Allen H, Driscoll D, Shaddy R, Feltes T (eds) Moss & Adams’ heart disease in infants, children, and adolescents: including the fetus and young adult. Lippincott Williams & Wilkins, Agree, Philadelphia
- Ginat DT, Fong MW, Tuttle DJ, Hobbs SK, Vyas RC (2011) Cardiac imaging: part 1, MR pulse sequences, imaging planes, and basic anatomy. *Am J Roentgenol* 197(4):808–815. doi:[10.2214/ajr.10.7231](https://doi.org/10.2214/ajr.10.7231)
- Goldmuntz E, Clark BJ, Mitchell LE, Jawad AF, Cuneo BF, Reed L, McDonald-McGinn D, Chien P, Feuer J, Zackai EH, Emanuel BS, Driscoll DA (1998) Frequency of 22q11 deletions in patients with conotruncal defects. *J Am Coll Cardiol* 32(2):492–498, S0735-1097(98)00259-9 [pii]
- Gonzalez-Juanatey C, Testa A, Vidan J, Izquierdo R, Garcia-Castelo A, Daniel C, Armesto V (2004) Persistent left superior vena cava draining into the coronary sinus: report of 10 cases and literature review. *Clin Cardiol* 27(9):515–518
- Gotway MB, Araoz PA, Macedo TA, Stanson AW, Higgins CB, Ring EJ, Dawn SK, Webb WR, Leung JW, Reddy GP (2005) Imaging findings in Takayasu’s arteritis. *AJR Am J Roentgenol* 184(6):1945–1950, 184/6/1945 [pii]
- Groskin SA (1992) Selected topics in chest trauma. *Radiology* 183(3):605–617
- Hancock Friesen CL, Zurkowski D, Thiagarajan RR, Forbess JM, del Nido PJ, Mayer JE, Jonas RA (2005) Total anomalous pulmonary venous connection: an analysis of current management strategies in a single institution. *Ann Thorac Surg* 79(2):596–606
- Hellinger JC, Daubert M, Lee EY, Epelman M (2011) Congenital thoracic vascular anomalies: evaluation with state-of-the-art MR imaging and MDCT. *Radiol Clin North Am* 49(5):969–996 doi:[10.1016/j.rcl.2011.06.013](https://doi.org/10.1016/j.rcl.2011.06.013), S0033-8389(11)00083-2 [pii]
- Hellinger JC, Medina LS, Epelman M (2010a) Pediatric advanced imaging and informatics: state of the art. *Semin Ultrasound CT MR* 31(2):171–193. doi:[10.1053/j.sult.2010.01.003](https://doi.org/10.1053/j.sult.2010.01.003), S0887-2171(10)00005-3 [pii]
- Hellinger JC, Pena A, Poon M, Chan FP, Epelman M (2010b) Pediatric computed tomographic angiography: imaging the cardiovascular system gently. *Radiol Clin North Am* 48(2):439–467 doi:[10.1016/j.rcl.2010.03.005](https://doi.org/10.1016/j.rcl.2010.03.005) [pii]: S0033-8389(10)00028-X
- Hernanz-Schulman M (2005) Vascular rings: a practical approach to imaging diagnosis. *Pediatr Radiol* 35(10):961–979. doi:[10.1007/s00247-005-1529-0](https://doi.org/10.1007/s00247-005-1529-0)
- Heyneman LE, Nolan RL, Harrison JK, McAdams HP (2001) Congenital unilateral pulmonary vein atresia. *Am J Roentgenol* 177(3):681–685
- Ho SY, Anderson RH (1979) Coarctation, tubular hypoplasia, and the ductus arteriosus. Histological study of 35 specimens. *Br Heart J* 41(3):268–274
- Holzer R, Qureshi S, Ghasemi A, Vincent J, Sievert H, Gruenstein D, Weber H, Alday L, Peirone A, Zellers T, Cheatham J, Slack M, Rome J (2010) Stenting of aortic coarctation: acute, intermediate, and long-term results of a prospective multi-institutional registry—congenital cardiovascular interventional study consortium (CCISC). *Catheter Cardiovasc Interv* 76(4):553–563. doi:[10.1002/ccd.22587](https://doi.org/10.1002/ccd.22587)
- Hom JJ, Ordovas K, Reddy GP (2008) Velocity-encoded cine MR imaging in aortic coarctation: functional assessment of hemodynamic events. *Radiographics* 28(2):407–416 doi:[10.1148/rg.282075705](https://doi.org/10.1148/rg.282075705) [pii]
- Honda O, Johkoh T, Yamamoto S, Koyama M, Tomiyama N, Kozuka T, Hamada S, Mihara N, Nakamura H, Muller NL (2002) Comparison of quality of multiplanar reconstructions and direct coronal multidetector CT scans of the lung. *AJR Am J Roentgenol* 179(4):875–879
- Illig KA, Doyle AJ (2010) A comprehensive review of Paget-Schroetter syndrome. *J Vasc Surg* 51(6):1538–1547. doi:[10.1016/j.jvs.2009.12.022](https://doi.org/10.1016/j.jvs.2009.12.022)
- Jenkins NP, Ward C (1999) Coarctation of the aorta: natural history and outcome after surgical treatment. *QJM* 92(7):365–371. doi:[10.1093/qjmed/92.7.365](https://doi.org/10.1093/qjmed/92.7.365)
- Jonas RA, Quaegebeur JM, Kirklin JW, Blackstone EH, Daicoff G (1994) Outcomes in patients with interrupted aortic arch and ventricular septal defect. A multiinstitutional study. *Congenital Heart Surgeons Society. J Thorac Cardiovasc Surg* 107(4):1099–1109; discussion 1109–1013, S0022522394000139 [pii]
- Kalva SP, Sahani DV, Hahn PF, Saini S (2006) Using the K-edge to improve contrast conspicuity and to lower radiation dose with a 16-MDCT: a phantom and human study. *J Comput Assist Tomogr* 30(3):391–397
- Katabathina VS, Restrepo CS (2012) Infectious and noninfectious aortitis: cross-sectional imaging findings. *Semin Ultrasound CT MR* 33(3):207–221 doi:[10.1053/j.sult.2011.12.001](https://doi.org/10.1053/j.sult.2011.12.001), S0887-2171(11)00162-4 [pii]
- Kellenberger C (2010) Aortic arch malformations. *Pediatr Radiol* 40(6):876–884. doi:[10.1007/s00247-010-1607-9](https://doi.org/10.1007/s00247-010-1607-9)
- Kondrachuk O, Yalynska T, Tammo R, Lee EY (2012) Multidetector computed tomography evaluation of congenital mediastinal vascular anomalies in children. *Semin Roentgenol* 47(2):127–134. doi:[10.1053/j.ro.2011.11.004](https://doi.org/10.1053/j.ro.2011.11.004)
- Konen E, Merchant N, Provost Y, McLaughlin PR, Crossin J, Paul NS (2004) Coarctation of the aorta before and after correction: the role of cardiovascular MRI. *AJR Am J Roentgenol* 182(5):1333–1339
- Kumazoe H, Komori M, Ochiai R, Egashira R, Nakazono T, Kudo S (2008) Pulmonary varix mimicking arteriovenous malformation. *Clin Imag* 32(1):61–64. doi:[10.1016/j.clinimag.2007.05.004](https://doi.org/10.1016/j.clinimag.2007.05.004)

- Latson LA, Prieto LR (2007) Congenital and acquired pulmonary vein stenosis. *Circulation* 115(1):103–108. doi:[10.1161/circulationaha.106.646166](https://doi.org/10.1161/circulationaha.106.646166)
- Lee EY, Boisselle PM, Cleveland RH (2008a) Multidetector CT evaluation of congenital lung anomalies. *Radiology* 247(3):632–648 doi:[10.1148/radiol.2473062124](https://doi.org/10.1148/radiol.2473062124), 247/3/632 [pii]
- Lee EY, Boisselle PM, Shamberger RC (2010) Multidetector computed tomography and 3-dimensional imaging: preoperative evaluation of thoracic vascular and tracheobronchial anomalies and abnormalities in pediatric patients. *J Pediatr Surg* 45(4):811–821 doi:[10.1016/j.jpedsurg.2009.12.013](https://doi.org/10.1016/j.jpedsurg.2009.12.013), S0022-3468(09)01069-0 [pii]
- Lee EY, Browne LP, Lam W (2012) Noninvasive magnetic resonance imaging of thoracic large vessels in children. *Semin Roentgenol* 47(1):45–55 doi:[10.1053/j.ro.2011.07.005](https://doi.org/10.1053/j.ro.2011.07.005), S0037-198X(11)00066-6 [pii]
- Lee EY, Dorkin H, Vargas SO (2011a) Congenital pulmonary malformations in pediatric patients: review and update on etiology, classification, and imaging findings. *Radiol Clin North Am* 49(5):921–948
- Lee EY, Zucker EJ, Tsai J, Tracy DA, Cleveland RH, Zurakowski D, Boisselle PM (2011b) Pulmonary MDCT angiography: value of multiplanar reformat images in detecting pulmonary embolism in children. *AJR Am J Roentgenol* 197(6):1460–1465 doi:[10.2214/AJR.11.6886](https://doi.org/10.2214/AJR.11.6886), 197/6/1460 [pii]
- Lee EY, Zurakowski D, Waltz DA, Mason KP, Riaz F, Ralph A, Boisselle PM (2008b) MDCT evaluation of the prevalence of tracheomalacia in children with mediastinal aortic vascular anomalies. *J Thorac Imag* 23(4):258–265 doi:[10.1097/RTI.0b013e31817fbd7f](https://doi.org/10.1097/RTI.0b013e31817fbd7f), 00005382-200811000-00006 [pii]
- Litmanovich D, Yildirim A, Bankier A (2012) Insights into imaging of aortitis. *Insight Imag* 3(6):545–560. doi:[10.1007/s13244-012-0192-x](https://doi.org/10.1007/s13244-012-0192-x)
- Lofland GK (2004) Pulmonary atresia, ventricular septal defect, and multiple aorta pulmonary collateral arteries. *Semin Thorac Cardiovasc Surg Pediatr Cardiac Surg Ann* 7(1):85–94. doi:[10.1053/j.pcsu.2004.02.012](https://doi.org/10.1053/j.pcsu.2004.02.012)
- Lofland GK (2009) An overview of pulmonary atresia, ventricular septal defect, and multiple aorta pulmonary collateral arteries. *Prog Pediatr Cardiol* 26(2):65–70
- Longley DG, Yedlicka JW, Molina EJ, Schwabacher S, Hunter DW, Letourneau JG (1992) Thoracic outlet syndrome: evaluation of the subclavian vessels by color duplex sonography. *Am J Roentgenol* 158(3):623–630
- Lopes RJ, Almeida J, Dias PJ, Pinho P, Maciel MJ (2009) Infectious thoracic aortitis: a literature review. *Clin Cardiol* 32(9):488–490. doi:[10.1002/clc.20578](https://doi.org/10.1002/clc.20578)
- Maillard JO, Cottin V, Etienne-Mastroianni B, Frolet JM, Revel D, Cordier JF (2007) Pulmonary varix mimicking pulmonary arteriovenous malformation in a patient with turner syndrome. *Respiration* 74(1):110–113
- Mataciunas M, Gumbiene L, Cibiras S, Tarutis V, Tamosiunas A (2009) CT angiography of mildly symptomatic, isolated, unilateral right pulmonary vein atresia. *Pediatr Radiol* 39(10):1087–1090. doi:[10.1007/s00247-009-1291-9](https://doi.org/10.1007/s00247-009-1291-9)
- Matsui H, Adachi I, Uemura H, Gardiner H, Ho SY (2007) Anatomy of coarctation, hypoplastic and interrupted aortic arch: relevance to interventional/surgical treatment. *Expert Rev Cardiovasc Ther* 5(5):871–880. doi:[10.1586/14779072.5.5.871](https://doi.org/10.1586/14779072.5.5.871)
- McElhinney DB, Clark BJ 3rd, Weinberg PM, Kenton ML, McDonald-McGinn D, Driscoll DA, Zackai EH, Goldmuntz E (2001) Association of chromosome 22q11 deletion with isolated anomalies of aortic arch laterality and branching. *J Am Coll Cardiol* 37(8):2114–2119, S0735-1097(01)01286-4 [pii]
- Mengozzi E, Sartoni Galloni S, Giovannini G, Bronzetti G (2001) Mycotic aneurysm of the thoracic aorta presenting as pneumonia. *Pediatr Radiol* 31(7):488–490. doi:[10.1007/s002470100487](https://doi.org/10.1007/s002470100487)
- Miller C (2012) Pulmonary veno-occlusive disease: a misnomer? *Pediatr Radiol* 42(6):647–652. doi:[10.1007/s00247-012-2350-1](https://doi.org/10.1007/s00247-012-2350-1)
- Mirka H, Ferda J, Baxa J (2012) Multidetector computed tomography of chest trauma: indications, technique and interpretation. *Insight Imag* 3(5):433–449. doi:[10.1007/s13244-012-0187-7](https://doi.org/10.1007/s13244-012-0187-7)
- Mirvis SE (2005) Imaging of acute thoracic injury: the advent of MDCT screening. *Semin Ultrasound CT MRI* 26(5):305–331. doi:[10.1053/j.sult.2005.08.001](https://doi.org/10.1053/j.sult.2005.08.001)
- Mirvis SE, Shanmuganathan K (2007) Diagnosis of blunt traumatic aortic injury 2007: still a nemesis. *Eur J Radiol* 64(1):27–40. doi:[10.1016/j.ejrad.2007.02.016](https://doi.org/10.1016/j.ejrad.2007.02.016)
- Mishra PK (2009) Management strategies for interrupted aortic arch with associated anomalies. *Eur J Cardiothorac Surg* 35(4):569–576. doi:[10.1016/j.ejcts.2008.12.044](https://doi.org/10.1016/j.ejcts.2008.12.044)
- Moene RJ, Gittenberger-de Groot AC, Oppenheimer-Dekker A, Bartelings MM (1987) Anatomic characteristics of ventricular septal defect associated with coarctation of the aorta. *Am J Cardiol* 59(9):952–955, 0002-9149(87)91132-5 [pii]
- Momma K (2010) Cardiovascular anomalies associated with chromosome 22q11.2 deletion syndrome. *Am J Cardiol* 105(11):1617–1624. doi:[10.1016/j.amjcard.2010.01.333](https://doi.org/10.1016/j.amjcard.2010.01.333)
- Moore P, Brook MM (2012) Patent ductus arteriosus and aortopulmonary window. Moss & Adams' heart disease in infants, children, and adolescents: including the fetus and young adult. Lippincott Williams & Wilkins, Philadelphia
- Moulaert AJ, Bruins CC, Oppenheimer-Dekker A (1976) Anomalies of the aortic arch and ventricular septal defects. *Circulation* 53(6):1011–1015. doi:[10.1161/01.cir.53.6.1011](https://doi.org/10.1161/01.cir.53.6.1011)
- Murillo H, Lane MJ, Pun R, Fleischmann D, Restrepo CS (2012) Imaging of the aorta: embryology and anatomy. *Semin Ultrasound CT MR* 33(3):169–190 doi:[10.1053/j.sult.2012.01.013](https://doi.org/10.1053/j.sult.2012.01.013), S0887-2171(12)00014-5 [pii]
- Nael K, Krishnam M, Ruehm SG, Michaely HJ, Laub G, Finn JP (2009) Time-resolved MR angiography in the evaluation of central thoracic venous occlusive disease. *Am J Roentgenol* 192(6):1731–1738. doi:[10.2214/ajr.08.1919](https://doi.org/10.2214/ajr.08.1919)
- Newman B (2006) Congenital bronchopulmonary foregut malformations: concepts and controversies. *Pediatr Radiol* 36(8):773–791. doi:[10.1007/s00247-006-0115-4](https://doi.org/10.1007/s00247-006-0115-4)
- Newman B, Ya Cho (2010) Left pulmonary artery sling—anatomy and imaging. *Semin Ultrasound CT MRI* 31(2):158–170. doi:[10.1053/j.sult.2010.01.004](https://doi.org/10.1053/j.sult.2010.01.004)
- Norwood WI, Lang P, Castaneda AR, Hougen TJ (1983) Reparative operations for interrupted aortic arch with ventricular septal defect. *J Thorac Cardiovasc Surg* 86(6):832–837
- O'Callaghan DS, Dorfmueller P, Jaïs X, Mouthon L, Sitbon O, Simonneau G, Humbert M, Montani D (2011) Pulmonary veno-occlusive disease: the bête noire of pulmonary hypertension in connective tissue diseases? *La Presse Médicale* 40 (1, Part 2):e87–e100. doi:[10.1016/j.lpm.2010.10.017](https://doi.org/10.1016/j.lpm.2010.10.017)
- Ozen S, Ruperto N, Dillon MJ, Bagga A, Barron K, Davin JC, Kawasaki T, Lindsley C, Petty RE, Prieur AM, Ravelli A, Woo P (2006) EULAR/PRES endorsed consensus criteria for the classification of childhood vasculitides. *Ann Rheum Dis* 65(7):936–941. doi:[10.1136/ard.2005.046300](https://doi.org/10.1136/ard.2005.046300)
- Papa M, De Cobelli F, Baldissera E, Dagna L, Schiani E, Sabbadini M, Del Maschio A (2012) Takayasu arteritis: intravascular contrast medium for MR angiography in the evaluation of disease activity. *Am J Roentgenol* 198(3):W279–W284. doi:[10.2214/ajr.11.7360](https://doi.org/10.2214/ajr.11.7360)

- Pourmoghadam KK, Moore JW, Khan M, Geary EM, Madan N, Wolfson BJ, Chadarevian JP, Holsclaw DS, Jacobs ML (2003) Congenital unilateral pulmonary venous atresia: definitive diagnosis and treatment. *Pediatr Cardiol* 24(1):73–79. doi:[10.1007/s00246-002-0220-6](https://doi.org/10.1007/s00246-002-0220-6)
- Restrepo CS, Melendez-Ramirez G, Kimura-Hayama E (2012) Multidetector computed tomography of congenital anomalies of the thoracic aorta. *Semin Ultrasound CT MR* 33(3):191–206 doi: [10.1053/j.sult.2011.11.002](https://doi.org/10.1053/j.sult.2011.11.002), S0887-2171(11)00146-6 [pii]
- Restrepo CS, Ocasionez D, Suri R, Vargas D (2011) Aortitis: imaging spectrum of the infectious and inflammatory conditions of the aorta. *Radiographics* 31(2):435–451 doi:[10.1148/rg.312105069](https://doi.org/10.1148/rg.312105069) [pii]
- Riedlinger WF, Juraszek AL, Jenkins KJ, Nugent AW, Balasubramanian S, Calicchio ML, Kieran MW, Collins T (2006) Pulmonary vein stenosis: expression of receptor tyrosine kinases by lesional cells. *Cardiovasc Pathol* 15(2):91–99 doi:[10.1016/j.carpath.2005.11.006](https://doi.org/10.1016/j.carpath.2005.11.006), S1054-8807(05)00170-5 [pii]
- Rosenquist GC (1974) Congenital mitral valve disease associated with coarctation of the aorta: a spectrum that includes parachute deformity of the mitral valve. *Circulation* 49(5):985–993
- Serraf A, Lacour-Gayet F, Robotin M, Bruniaux J, Sousa-Uva M, Roussin R, Planche C (1996) Repair of interrupted aortic arch: a ten-year experience. *J Thorac Cardiovasc Surg* 112(5):1150–1160, S0022-5223(96)70128-9 [pii]
- Shone JD, Sellers RD, Anderson RC, Adams P Jr, Lillehei CW, Edwards JE (1963) The developmental complex of “parachute mitral valve,” supraaortic ring of left atrium, subaortic stenosis, and coarctation of aorta. *Am J Cardiol* 11:714–725
- Smallhorn JF, Pauperio H, Benson L, Freedom RM, Rowe RD (1985) Pulsed doppler assessment of pulmonary vein obstruction. *Am Heart J* 110(2):483–486. doi:[10.1016/0002-8703\(85\)90174-7](https://doi.org/10.1016/0002-8703(85)90174-7)
- Steenburg SD, Ravenel JG, Ikonomidis JS, Schönholz C, Reeves S (2008) Acute traumatic aortic injury: imaging evaluation and management. *Radiology* 248(3):748–762. doi:[10.1148/radiol.2483071416](https://doi.org/10.1148/radiol.2483071416)
- Swensen SJ, Tashjian JH, Myers JL, Engeler CE, Patz EF, Edwards WD, Douglas WW (1996) Pulmonary venoocclusive disease: CT findings in eight patients. *Am J Roentgenol* 167(4):937–940
- Tanous D, Benson LN, Horlick EM (2009) Coarctation of the aorta: evaluation and management. *Curr Opin Cardiol* 24(6):509–515. doi:[10.1097/HCO.0b013e328330cc22](https://doi.org/10.1097/HCO.0b013e328330cc22)
- Thompson JF, Winterborn RJ, Bays S, White H, Kinsella DC, Watkinson AF (2011) Venous thoracic outlet compression and the Paget-Schroetter syndrome: a review and recommendations for management. *Cardiovasc Intervent Radiol* 34(5):903–910. doi: [10.1007/s00270-011-0148-4](https://doi.org/10.1007/s00270-011-0148-4)
- Taskal T, Hucin B, Hruda J, Marek J, Chaloupecky V, Kostelka M, Janousek J, Skovranek J (1998) Results of primary and two-stage repair of interrupted aortic arch. *Eur J Cardiothorac Surg* 14(3):235–242, S1010794098001845 [pii]
- Vouhe PR, Mace L, Vernant F, Jayais P, Pouard P, Mauriat P, Leca F, Neveux JY (1990) Primary definitive repair of interrupted aortic arch with ventricular septal defect. *Eur J Cardiothorac Surg* 4(7):365–370
- Vyas HV, Greenberg SB, Krishnamurthy R (2012) MR imaging and CT evaluation of congenital pulmonary vein abnormalities in neonates and infants. *Radiographics* 32(1):87–98. doi:[10.1148/rg.321105764](https://doi.org/10.1148/rg.321105764)
- Weinberg PM (2006) Aortic arch anomalies. *J Cardiovasc Magn Reson* (Taylor & Francis Ltd) 8(4):633–643. doi:[10.1080/10976640600713756](https://doi.org/10.1080/10976640600713756)
- Weinberg PM, Hubbard AM, Fogel MA (1998) Aortic arch and pulmonary artery anomalies in children. *Semin Roentgenol* 33(3):262–280. doi:[10.1016/S0037-198X\(98\)80008-4](https://doi.org/10.1016/S0037-198X(98)80008-4)
- Weinberg PM, Natarajan S, Rogers L (2012) Aortic arch and vascular anomalies. *Moss & Adams' heart disease in infants, children, and adolescents: including the fetus and young adult*. Lippincott Williams & Wilkins, Philadelphia
- Weinberg PM, Whitehead KK (2010) Aortic arch anomalies. In: Fogel MA (ed) *Principles and practice of cardiac magnetic resonance in congenital heart disease: form, function and flow*. 1st edn. Wiley-Blackwell, pp 183–208
- Weiss PF (2012) Pediatric vasculitis. *Pediatr Clin N Am* 59(2):407–423. doi:[10.1016/j.pcl.2012.03.013](https://doi.org/10.1016/j.pcl.2012.03.013)
- Wiebe S, Maclusky I, Manson D, Holowka S, Yoo SJ (2003) Hemoptysis: a rare cause can be related to a bronchial varix due to pulmonary venous obstruction. *Pediatr Radiol* 33(12):884–886. doi:[10.1007/s00247-003-0971-0](https://doi.org/10.1007/s00247-003-0971-0)



# Acute Chest Diseases: Infection and Trauma

José Fonseca Santos

## Contents

<b>1</b>	<b>Introduction</b> .....	268
<b>2</b>	<b>Thoracic Infection</b> .....	268
2.1	Imaging Techniques .....	268
2.2	Physiological Considerations .....	269
2.3	Characterization of Pulmonary Infiltrates .....	269
2.4	Evaluation of Children with Pneumonia .....	270
2.5	Differential Diagnosis According to Clinical Character of Illness and Age of Patient .....	271
2.6	Viral Pneumonias .....	271
2.7	Atypical Pneumonia .....	272
2.8	Bacterial Pneumonias .....	273
2.9	Fungal Pneumonias.....	274
2.10	Parasitic Lung Infection .....	275
2.11	Follow-up Controls in Pneumonia.....	275
2.12	Complications of Pneumonia .....	276
<b>3</b>	<b>Thoracic Trauma</b> .....	277
3.1	Imaging Techniques .....	278
3.2	Chest Wall Injuries.....	279
3.3	Diaphragmatic Rupture .....	279
3.4	Tracheobronchial Injuries.....	280
3.5	Pneumothorax .....	280
3.6	Pulmonary Contusion .....	280
3.7	Lung Laceration.....	281
3.8	Mediastinal Injuries .....	281
3.9	Traumatic Lung Cysts.....	281
3.10	Esophageal Rupture.....	281
<b>4</b>	<b>Summary</b> .....	282
	<b>References</b> .....	283

## Abstract

Acute chest diseases include clinical situations with infectious and traumatic etiology. Pulmonary infection is the most common indication for performing chest radiography. Radiological imaging often confirms the diagnosis and allows the evaluation of the location and extent of infection. Chest radiography is the primary imaging procedure and the starting point for the evaluation of all children with acute chest disease. Accurate interpretation of pediatric chest films also requires a basic understanding of the physiologic and anatomic differences among adults, neonates, and infants and their most important differences will be referred. Characterization of pulmonary infiltrates is important, because patterns of abnormality suggest specific organisms and aetiologies. Although providing evidence suggestive of the causative agent, the chest radiograph cannot confirm viral infection, confirm or exclude bacterial etiology. In fact, in infancy, pneumonia usually produces a combination of alterations of the airspace and interstitium. However, some aspects may be useful in distinguishing between viral and bacterial pneumonia. Close attention to CT technique is crucial for imaging evaluation of pneumonia in pediatric patients, namely those with persistent symptoms and/or progressive symptoms despite medical or surgical therapy, or in immunocompromised patients. CT with low radiation dose technique should be carefully performed in these cases. CT examination with IV contrast is very useful for the evaluation of complications of chest infection. Thoracic trauma in children is rare, only 4–6 % of children are hospitalized following severe trauma. Only a small number of children with trauma have thoracic injury (14 %), but the injuries tend to be of serious nature. About 25–50 % of thoracic trauma cases occur in combination with other trauma locations. Pulmonary contusion and lacerations, tracheobronchial injuries, pneumothorax, and esophageal rupture are referred as

J. F. Santos (✉)  
Hospital de Santa Maria, Av. Professor Egas Moniz,  
1649-035 Lisbon, Portugal  
e-mail: jfonsecasantos@gmail.com

the main consequences of trauma. The decision for the appropriate use of imaging techniques must consider the specific case under review. Chest radiography should be the initial screening method. The decision to use CT is determined by the nature of the trauma, the clinical circumstances, and the prediction of future reevaluation, always taking into account the radiation dose applied to the child.

## 1 Introduction

Acute chest diseases include all the clinical situations with infectious and traumatic etiology.

In considering the multiple entities of infectious cause in the pediatric age groups, two approaches to the differential diagnosis are available based on the clinical character of symptoms and on the age of the patient.

Accurate interpretation of pediatric chest films also requires a basic understanding of the physiologic and anatomic differences among adults, neonates, and infants and the most important differences will be referred. Characterization of pulmonary infiltrates (interstitial, alveolar, and mixed) is important, because patterns of abnormality suggest specific organisms and etiologies.

A small number of children with trauma have thoracic injury, but the injuries tend to be of a serious nature.

Pulmonary contusion, tracheobronchial injuries, pneumothorax, and esophageal rupture will be referred as consequences of trauma.

The decision for the appropriate use of imaging techniques must be due to the specific case under review. Chest radiography should be the initial screening method. The decision to use CT is determined by the nature of the trauma, the clinical circumstances, and the prediction of future reevaluation, taking into account the use of radiation in children.

## 2 Thoracic Infection

One of the most common acute chest diseases in children is the respiratory tract infection.

### 2.1 Imaging Techniques

#### 2.1.1 Radiography

This is the primary imaging procedure and the starting point for all children. The film should be well inspired, correctly centered, and coned. A supine film is preferable until the child is old enough to cooperate fully with an erect position. When the child is old enough, the film should be acquired in

posteroanterior position to reduce the breast radiation. Unlike in adults, hidden pathology is unlikely. The localization of the focus of infection is usually easy on frontal film and lateral view is not routinely used (Carty 2000).

#### 2.1.2 Ultrasound

Ultrasound (US) was initially applied to detect pleural fluid, however in recent years the applications of US for the chest have been widely extended. The technique has several advantages that are particularly beneficial in children. US does not use ionizing radiation and permits visualization of the lesions in real time in different planes (Enriquez et al. 2008). US has been advocated as an important initial aid in categorizing the pleural fluid (simple and complicated), and making therapeutic decisions for parapneumonic effusions, acute complication of pneumonia. US can also be used to provide imaging guidance for pleural fluid drainage, especially when is loculated. US is very useful initially to study patients presenting with an opaque hemithorax on plain film.

Patients with lung consolidation associated to pleural fluid can be initially evaluated at the same time by US. Color and power Doppler can analyze the perfusion of the lung parenchyma. It could be well vascularized and poorly vascularized with or without necrosis. Initially, US can provide diagnostic and prognostic information which may influence therapy.

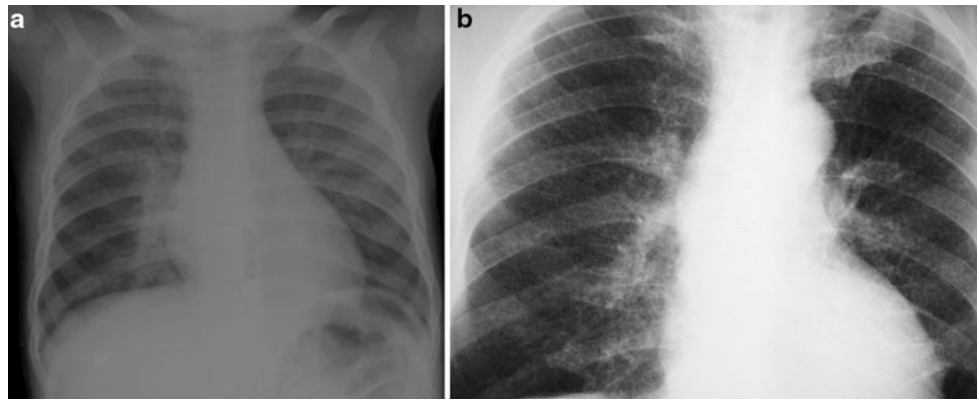
#### 2.1.3 Computed Tomography

CT can play an important role and is crucial for imaging evaluation of pneumonia in pediatric patients with persistent or progressive clinical symptoms or in immunocompromised patients. Close attention to CT technique is mandatory and CT with low radiation dose technique should be carefully performed in these cases.

Lung high resolution computed tomography (HRCT) gives exquisite pulmonary parenchymal detail and is of increasing importance in imaging infection particularly in its complications. The advent of spiral scanners with very fast scan times has made HRCT a practical proposition in most children without the need for sedation. The main indication in children with infection is the diagnosis of bronchiectasis and mapping its extent, particularly when assessing the effect of treatment or considering resection, confirming the presence of suspected areas of collapsed lung, and in the more acute situation confirming the presence of a lung abscess or empyema. Occasionally, CT is helpful in identifying appropriate placement of pleural drains. HRCT has been used to identify the extent of disease associated with opportunistic infections in children who are immunocompromised.

Contrast-enhanced CT should be performed for the evaluation of mediastinum, pleura, and lung parenchyma with suspected necrosis. CT allows easy identification of

**Fig. 1** Interstitial involvement in a child of 12 months with viral infection. **a** Chest radiograph shows an enlarged *right* hilum, with linear images. **b** Interstitial nodular pattern in a 17-year-old boy with CMV infection after BM transplant



mediastinal lymph nodes in tuberculosis or in other infection with lymphadenopathy, pleural fluid, and lung parenchyma hypoperfusion or necrosis. These findings are difficult to evaluate by chest X-ray (Carty 2000).

Focal CT scan should be tailored to the area of interest (especially if following a specific lesion serially over time) to further decrease the overall radiation dose (Hedieh et al. 2011).

#### 2.1.4 Magnetic Resonance Imaging

Magnetic Resonance Imaging (MRI), with its combination of good resolution and multiplanar facilities, is the preferred first-choice tool for visualizing the mediastinum. MRI is useful for confirming the presence and the extent of nodal disease and for evaluating vascular anomalies or mass lesions associated with infection such as pulmonary sequestrations (Carty 2000).

Peltola and colleagues (Peltola et al. 2008) recently published their experience with MR imaging of lung infections in children using free-breathing T2-weighted, short tau inversion recovery, and T1-weighted with fat saturation precontrast and postcontrast sequences. Children with chronic lung conditions and recurrent infection, such as cystic fibrosis, who are often subjected to substantial radiation exposure from repeated CT studies, would benefit the most from MR imaging evaluation of the lungs instead of CT (Hedieh et al. 2011).

#### 2.1.5 Fluoroscopy

Neurologically compromised children have a high incidence of aspiration fluid, saliva, and food, and have severe and recurrent infections. Videofluoroscopy of swallowing when challenged with liquids and food of varying consistencies is required to identify aspiration or gastroesophageal reflux. Children with tracheoesophageal fistula (TOF) are also prone to chest infections. The causes include an unrecognized H fistula, recurrent fistula, tracheomalacia, dysmotility, gastroesophageal reflux, and anastomotic stricture with proximal dilatation. The latter three are

associated with aspiration which is maximal in the supine position (Carty 2000).

## 2.2 Physiological Considerations

Accurate interpretation of pediatric chest films also requires a basic understanding of the physiologic and anatomic differences among adults, neonates, and infants.

The most important differences include the following: (1) the peripheral airways of infants are relatively smaller than those of adults, and collateral pathways of ventilation are less developed; (2) the airways of infants are more prone to collapse in response to pressure changes than those of adults; (3) Infants also have relatively more mucous glands and a greater mucous production. For these reasons, the peripheral airways of infants are more susceptible to inflammatory narrowing than adult airways. In older children and adults, respiratory infections most commonly involve the interstitium and alveoli. Lower respiratory infections in infants, on the other hand, manifest their primary effects in the smaller airways, producing peripheral mucous obstruction and disproportionately severe respiratory distress. This is revealed on the chest films by generalized hyperaeration (air trapping) with focal irregularities of aeration that reflects atelectasis from mucous plugging. True consolidative (alveolar) pneumonia is a much less frequent occurrence (Wesenberg et al. 2006).

## 2.3 Characterization of Pulmonary Infiltrates

Characterization of pulmonary infiltrates is important because patterns of abnormality suggest specific organisms and aetiologies. The three basic kinds of infiltrates are interstitial, alveolar, and mixed.

The interstitial pattern has been described with a variety of confusing radiographic terms. When mild, an interstitial infiltrate is characterized by a string collection of densities



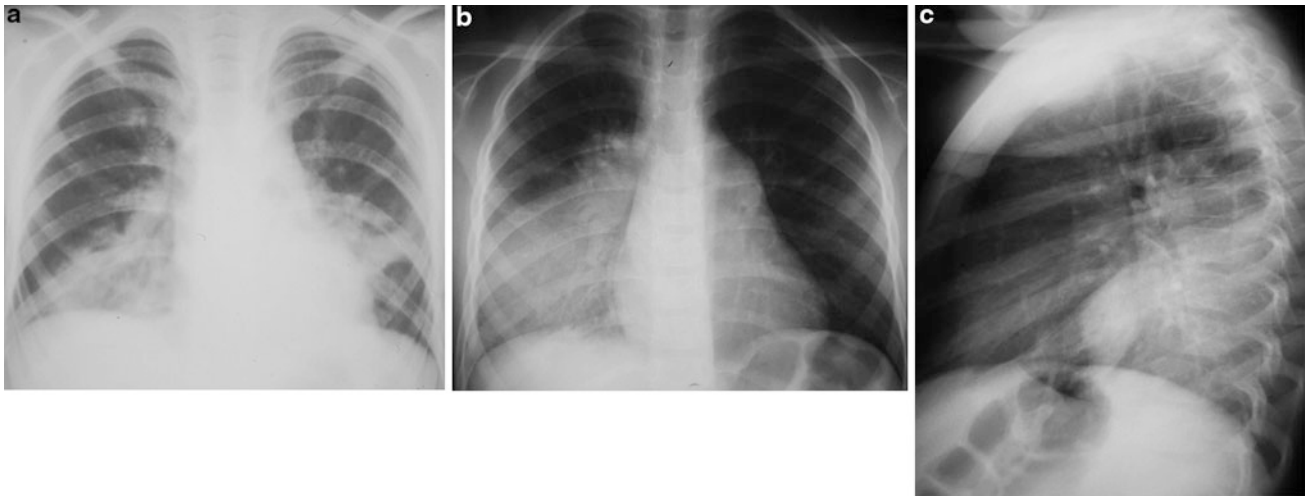


**Fig. 2** Alveolar pattern on chest radiograph in a 10-year-old child with pneumococcal pneumonia. **a** Heterogeneous opacity with ill-defined boundaries air bronchogram in the *right* base and *lower third*

of the *left* lung field. **b** and **c** Another similar case with alveolar pattern in a 11-year-old child with lobar pneumococcal pneumonia

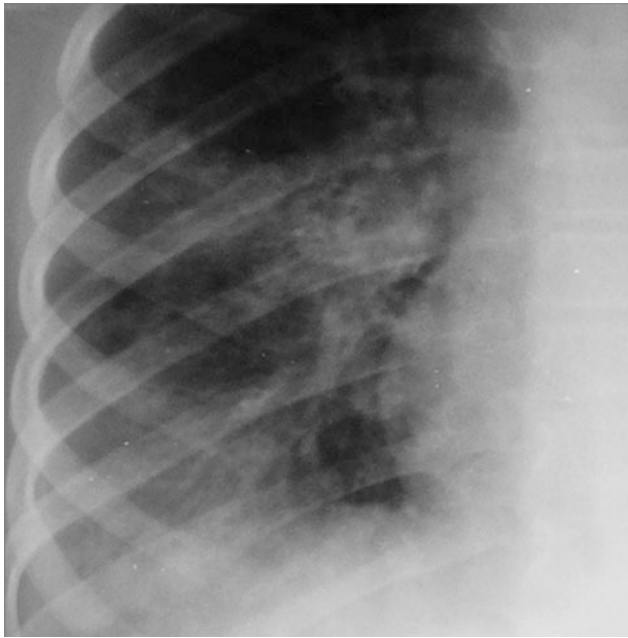


**Fig. 3** Mixed infiltrate on a chest radiograph in an 8-year-old girl with streptococcus pneumonia. There is an ill-defined area of mildly increased density (containing finely dilated air bronchioles). There is usually no significant pleural effusion

that run out from the hila (Fig. 1a), seen on the frontal projection as apparent enlargement and poor (fuzzy) definition of the hila.

When the pneumonia is severe, the pattern shows a diffuse, bilateral, sharply defined reticular (stringy) or nodular infiltrate (Fig. 1b). There is no air bronchogram and associated pleural effusion.

Alveolar (airspace) disease is characterized by a plethora of descriptive names. The typical alveolar infiltrate is a

smooth, homogeneous increase in density (whiteness) of the lungs (Fig. 2). The most common alveolar infiltrate is well-defined, dense homogeneous lobar or segmental consolidation, with an air bronchogram within it. There is commonly associated pleural effusion.

Mixed infiltrates, not surprisingly, have features of both alveolar and interstitial patterns. If an unknown pulmonary infiltrate cannot comfortably be classified as either alveolar or interstitial, it is considered to have the mixed pattern (Fig. 3). The prototype of a mixed infiltrate is an ill-defined area of mildly increased density containing finely dilated air bronchioles. There is usually no significant pleural effusion.

## 2.4 Evaluation of Children with Pneumonia

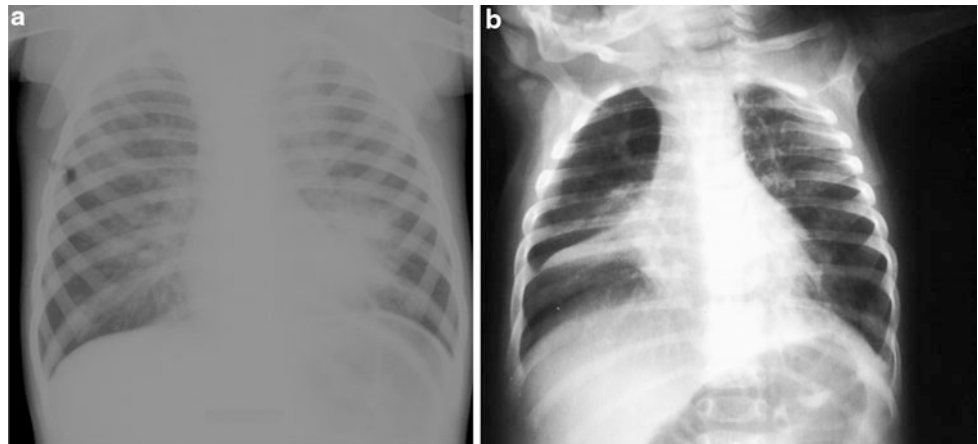
Pulmonary infection is the most common indication for performing chest radiography. It is the radiological imaging that confirms the diagnosis and allows evaluating the location and extent of infection.

The common difficulties in the etiologic diagnosis of pneumonia led pediatricians and radiologists to a need to specify the causative infectious agents based on radiological patterns.

In this respect, special importance was placed on the distinction between viral and bacterial pneumonias, attributing to the viral disease interstitial pattern and the bacterial infection involving airspace.

Although providing evidence suggestive of the causative agent, the chest radiograph cannot confirm viral infection nor confirm or eliminate bacterial etiology. In fact, in infancy, pneumonia usually produces a combination of changing the airspace and interstitium. However, some

**Fig. 4** Viral infection in a 22-month-old boy with fever and increased respiratory distress. **a** Radiography of the 4th day of hospitalization shows exuberant bilateral interstitial pattern. Serology revealed adenovirus infection. **b** Another similar case in a 12-month-old child with RSV infection. Atelectasis of the middle lobe is also shown



aspects may be useful in distinguishing between viral and bacterial pneumonia.

The roles of imaging in the evaluation of immunocompetent children with Community-acquired pneumonia are multiple: confirmation or exclusion of pneumonia, characterization and prediction of infectious agents, exclusion of other symptoms, evaluation when there is failure to resolve, and evaluation of all related complications (Donnelly and Klosterman 1997a).

Concerning characterization and prediction of infectious agents, the previously described patterns of radiographic and CT findings which suggest a specific infectious agent are rarely of clinical relevance in the previously healthy child who is imaged for suspected pneumonia (Donnelly 2002).

Cough and fever are two of the most common symptoms of illness in the pediatric age group and suggest respiratory pathogenesis, particularly pneumonia. Radiographic findings in combination with clinical evaluation are vital in deciding whether treatment with antibiotics or further study is indicated. The character of pneumonia that it is revealed radiographically, in combination with the clinical pattern of the disease, assists the physician in deciding whether antibiotics are indicated. Despite numerous advances in pediatric care and imaging modalities, the plain chest radiography remains the most valuable tool available for evaluating airway and the lungs and for assessing the site and gross character of pulmonary disease (Wesenberg et al. 2006).

In considering the multiple entities that cause cough and fever in the pediatric age groups, two approaches to the differential diagnosis are available.

The first is based on the clinical character of symptoms, specifically acute illness versus illness that is chronic or recurrent.

The second approach is based on the age of the patient, because there are distinct age predilections of agents that cause cough and fever in children.

## 2.5 Differential Diagnosis According to Clinical Character of Illness and Age of Patient

The three main causes of community-acquired pneumonia (CAPs) in pediatric patients are viral, atypical, and bacterial.

As a group, viruses account for approximately 65 % of all pneumonias that occur in pediatric patients. Respiratory syncytial virus (RSV) is the responsible organism in approximately 50 % of the cases.

The epidemic and seasonal occurrence of pneumonias and lower tract infections is a well-known phenomenon. RSV and metapneumovirus are responsible for yearly outbreaks, during winter.

The respiratory viruses, as a group, account for approximately 90 % of the agents recovered from children younger than 4 years of age (Wesenberg et al. 2006).

The most common specific agent that produces demonstrable pneumonia in pediatric age group is mycoplasma pneumonia, the most prevalent in school-age children. It is one of the main causes of atypical pneumonia. In children younger than 4 years of age, the incidence drops to approximately 5 %.

The most common cause of other bacterial pneumonia in pediatric age group is *Streptococcus pneumoniae*. In addition, there has been a recent increase in the prevalence of pneumonias caused by community-acquired methicillin-resistant staphylococcus aureus (MRSA). Less common causative bacteria are *S. pyogenes*, *Klebsiella* species, and gram-negative organisms (Wesenberg et al. 2006).

## 2.6 Viral Pneumonias

Viral pneumonia usually originates interstitial dispersed patterns, sometimes bilateral. They are frequently ill-defined opacities, involving one or more lobes, being located mainly

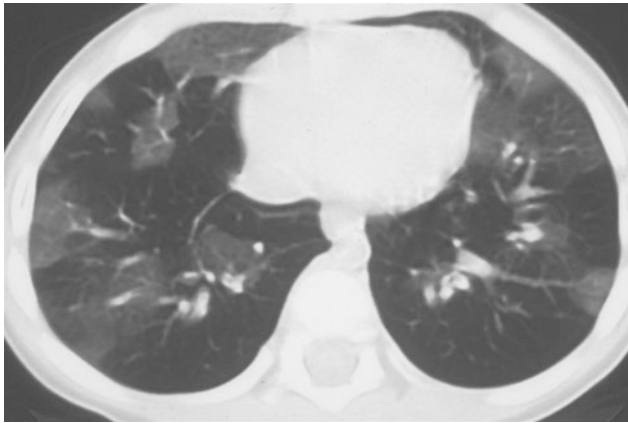


**Fig. 5** Obliterative Bronchiolitis as sequelae of adenovirus pneumonia in an 8-year-old girl. Follow-up CT image shows a mosaic pattern with some patchy air-trapping areas and a normal expiratory ground-glass areas

in the perihilar regions. There is often thickening of the bronchial wall and densities and peribronchial opacities scattered non-confluent and areas of atelectasis affecting predominantly the upper lobes and middle lobe.

Often the small airways are involved causing anterior prolapse with hypersuflation of the lungs, prolapsed of the sternum, and lowering the of diaphragm.

The most common radiographic findings are bilateral, symmetrical, parahilar, and bronchial opacities with or without atelectasis and air trapping (Fig. 4). Focal and asymmetrical disease is not uncommon. Lymph node enlargement can occur, but pleural effusion is rare (Daltro et al. 2011).

Recently, viral infection has been recognized as a cause of severe pneumonias leading to respiratory failure and death. Higher mortality rates are associated to coronavirus A (SARS, severe acute respiratory syndrome), and influenza virus type A H5N1 (bird flu) and type A H1N1. As with other viral pneumonias, focal or diffuse interstitial opacities are the initial chest radiograph presentation, but they can progress rapidly to bilateral areas of consolidation (Daltro et al. 2011).

The radiographic findings in RSV bronchiolitis are predominantly those of hyperaeration of the lungs with a variable degree of perihilar interstitial infiltrate. Usually the lungs are clear peripherally. Typically the bilateral, perihilar interstitial infiltrate is suggestive of mild to moderate hilar enlargement that it is indistinct on both projections. A more widespread interstitial infiltrate occurs in more severe infections, and areas of subsegmental atelectasis are common, reflecting mucous plugging.

The lungs in pneumonia commonly are also hyperaerated but generally less so than in RSV bronchiolitis. Radiographic clearing is not as rapid as clinical recovery, and complete clearing may take as long as 2–5 months.



**Fig. 6** *Mycoplasma pneumoniae* in a 11-year-old girl with cough and fever. Chest radiograph shows areas of hypotransparencies and lung densities in both lungs. Serology was positive for *M. pneumoniae* and antibiotic therapy instituted led to clinical and radiological resolution

The initial radiographic findings in adenoviral pneumonia are nonspecific and are shared with the other viral pneumonias. The most common manifestation is bilateral, perihilar interstitial infiltrate.

The pulmonary sequelae of adenovirus pneumonia are usually evident on follow-up controls (Fig. 5). A mild form of adenoviral pneumonia is chronic pneumonitis, with associated fibrosis and mild bronchiectasis. In severe disease, necrotizing bronchiolitis progress to obliterative bronchiolitis, which leads to unilateral hyper lucent lung (Swyer-James syndrome) or bilateral hyperlucent lung, with or without areas of associated bronchiectasis and chronic atelectasis.

## 2.7 Atypical Pneumonia

A wide variety of infectious agents (virus and bacteria) may be the cause of atypical pneumonia. Atypical features in pneumonia include prominent extrapulmonary features (e.g., headache, sore throat, and pharyngeal exudates), minimal or disparate chest signs on physical examination, subacute onset, non focal lung opacity on chest radiographs, lack of clinical response to antibiotics, lack of substantial leukocytosis, and a slow disease course. On chest radiographs, the pulmonary opacity is seen as either airspace, reticular (linear), or band-like opacities in a non focal, patchy, or mottled distribution, with various degrees of



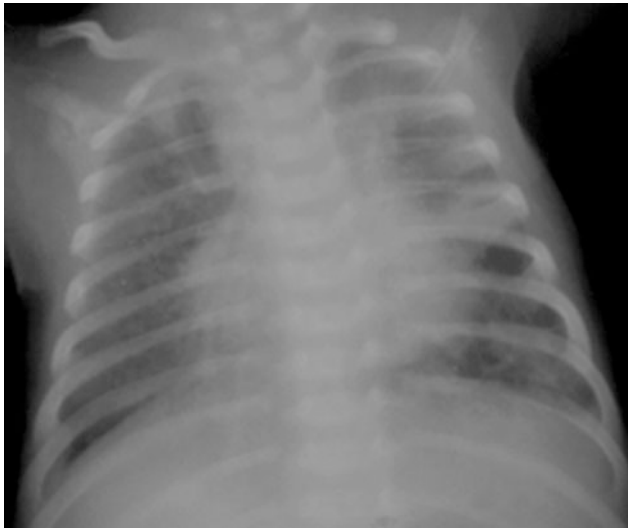


**Fig. 7** Newborn with conjunctivitis and polipnea, with abnormal pulmonary auscultation. Chest radiography showed a bilateral interstitial linear pattern and consolidation. Serology was positive for *C. trachomatis* and clinical evolution was favorable with antibiotics

density, usually without a single dense area of consolidation (Hedieh et al. 2011).

The most specific agent that produces demonstrable pneumonia in the pediatric age group is a bacterium, *Mycoplasma pneumoniae*, most prevalent in school-age children.

The radiographic pattern produced by *M. pneumoniae* is most commonly an ill-defined, mildly increased density segmental or lobar consolidation with involvement that is usually in the lower lobes. Acutely, a perihilar interstitial pattern is present. Typically, there are areas bronchiolar and acinar dilatations, commonly within the consolidation, that suggest mild micro cyst formation. A patchy, alveolar bronchopneumonic pattern may occasionally be seen. There is usually no pleural effusion (Wesenberg et al. 2006).

In the mycoplasma pneumonia, radiological aspects are not specific. Often there are bronchopneumonic opacities mainly affecting the lower lobes. There may also be interstitial or peribronchial densities as well as segmental or subsegmental atelectasis. Pleural effusions are not uncommon and are usually minor and transient. Often there is discrepancy between the exuberant symptoms, the poor objective examination and marked radiographic lesions (Fig. 6).

Patients who have *Chlamydia trachomatis* pneumonia have a fairly typical bilateral, perihilar interstitial pattern of infiltrate. Patchy fluffy-appearing alveolar infiltrates are usually bilaterally superimposed on this pattern, and radiographic findings are often more severe than clinical symptoms.

*Chlamydia pneumoniae* causes an atypical pneumonia virtually indistinguishable from that caused by *Mycoplasma* (Wesenberg et al. 2006).

In *C. trachomatis* pneumonia, the chest radiograph often shows hyperinflation and diffuse interstitial or alveolar opacities.

There are also the aspects of clinical pneumonia (cough in infants 3 weeks to 4 months prior afebrile and conjunctivitis), the epidemiological context (mother gynecological infection in the last trimester of pregnancy), and the specific laboratory tests (hemogram with eosinophilia), which will lead us to the possible causing agent (Fig. 7).

## 2.8 Bacterial Pneumonias

Bacterial pneumonias account for only 3–5 % of all childhood pneumonias. In general, bacterial pneumonias have a sudden onset. The epidemic and seasonal occurrence of pneumonias and lower respiratory tract infections is a well-known phenomenon. A viral infection commonly precedes the bacterial pneumonia by several days to a week.

Radiologically, bacterial pneumonias usually cause dense lobar or segmental consolidation that frequently contains an air bronchogram. Patchy pneumonia is the second most common pattern. When present, findings that suggest bacterial rather than viral pneumonia include significant pleural effusion, abscess, and pneumatocele formation within pneumonic infiltrates.

The pattern of epidemic occurrence for school-age children (4–18 years) is distinctly different from that of preschool children.

The most common cause of other bacterial pneumonia in the pediatric age group is *S. pneumoniae*.

The bacterial pneumonia usually originates scattered opacities in infants, the segmental or lobar condensation is the most typical finding being located predominantly in the middle or at the periphery of the lung fields, especially when the agent is *S. pneumoniae* or *Haemophilus influenzae* (Fig. 8). Hilar engorgement is more common in pneumonia by *H. influenzae* or *Staphylococcus aureus* pneumonia, but can also occur in pneumococcal pneumonia. Pneumothorax or pleural effusion, including empyema, can occur particularly in staphylococcal infections and other purulent agents. Generally, the infection affects one lung but also can be bilateral (Fig. 9).

Certain bacterial specimens originate necrotic foci in the parenchyma that communicate with the lumen of the airways, forming thin-walled and well-defined bubbles called pneumatoceles. In the course of pneumonia, an abscess can also arise, which differs from pneumatocele by presenting itself as an image with thick-walled cavitation that fades in

**Fig. 8** Bacterial pneumonia in a 6-year-old boy with fever and thoracic pain. **a** The chest radiograph shows rounded opacity of the *right* lung and small lamellar spill along the *right* chest wall. A *S. pneumonia* was isolated. **b** Similar case of rounded pneumonia in a 7-year-old child with streptococcus infection

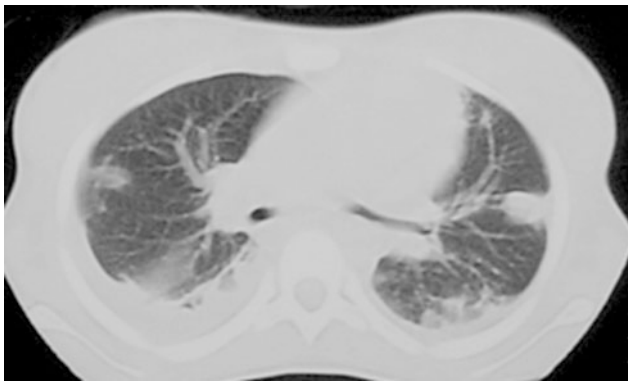
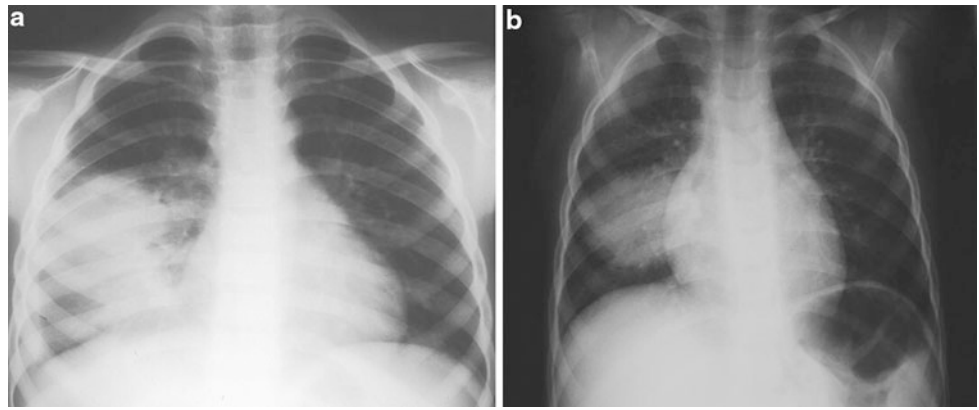


**Fig. 9** Bacterial pneumonia in a 10-year-old girl, after cutaneous wound in the foot, developed fever and respiratory distress. Chest radiograph (not shown) and CT showed round opacities, and pleural fluid. A *Staphylococcus aureus* was isolated

the condensation surroundings, and often with liquid content (Fig. 10). Pneumotocels are more common in staphylococcal pneumonia, particularly in the convalescent phase, but other agents are also associated with bullous images, including *Klebsiella pneumoniae*, *H. influenzae*, *S. pyogenes* and *S. pneumoniae*. Sometimes bacterial pneumonia may present as spherical opacities (Fig. 8). Usually the edge of these pneumonias is not well-defined and the image does not look so round in two planes (PA and lateral). An X-ray follow-up days later often reveals a condensation without the initial round appearance.

Therefore, the presence of a segmental or lobar condensation, pleural effusion, necrotic foci, abscess, or pneumatocele in children with high fever and signs of toxicity suggest bacterial etiology.

*S. pneumoniae* pneumonia manifests as a dense, homogeneous, alveolar lobar, or segmental consolidation of lung parenchyma (Fig. 11). The consolidation begins in the

peripheral air spaces and thus almost invariably abuts a pleural surface. The consolidation usually has an air bronchogram and middle well-defined border. Pleural effusion or empyema is common.

*S. pneumoniae* is one of the common organisms that produce a so-called “round pneumonia”, seen almost exclusively in children (Fig. 8). Sometimes, because of the lack of collateral air drift openings, the exudates take the appearance of a spherical consolidation—a “round pneumonia”. The inflammatory cells are confined under a mild degree of pressure, and these infants often have high fever. The radiographic appearance can be alarming because a round pneumonia can look like a neoplasm (Bransom et al. 2005).

Pneumatocels may form during resolution and are considered a favorable prognostic sign.

The radiographic findings of staphylococcal pneumonia are indistinguishable from those of other bacterial pneumonias. There is a tendency, however, for staphylococcal pneumonia to manifest initially as a patchy bronchopneumonia, with dense alveolar consolidation developing rapidly, and usually involving a whole lobe or multiple lobes (Fig. 9). Pleural effusion (or empyema) occurs in more than 90 % of the cases and pneumatoceles occur in 40–60 % of the cases. Usually, pneumatoceles appear late in the first week of pneumonia and disappear spontaneously, generally within 6 weeks.

## 2.9 Fungal Pneumonias

Pulmonary fungal infections are rare in children, especially in immunocompetent patients. Fungal infection is suspected, when dealing with pneumonia that is usually localized and chronically persisting, despite antibiotic treatment.

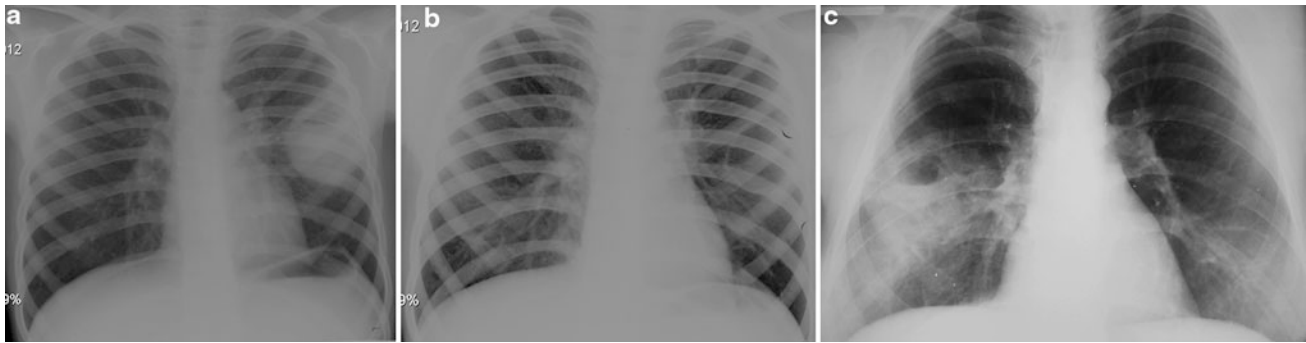


**Fig. 10** Necrotic pneumonia in a 10-year-old boy with productive cough, fever and thoracic pain (**a**, **b**). **a** Chest radiograph revealed cavitated round opacity which evolved into pneumatocele after

antibiotic therapy. **b** A *S. pneumonia* was isolated. **c** Similar case of necrotic pneumonia in a 16-year-old boy with *Staphylococcus aureus* infection



**Fig. 11** *S. pneumonia* in a 45-day-old-girl, with fever, nasal obstruction, and respiratory distress. Chest radiograph showed bilateral opacities of the upper lobes.  $\beta$ -hemolytic *Streptococcus* was isolated in blood culture

The hallmark of CT findings, which is associated with possible fungal infection, is the presence of nodules, often clustered, with poorly defined margins, cavitation, or surrounding halo of ground-glass opacity (Donnelly 2002).

Pulmonary aspergillosis is the most common and can occur in three clinical forms: allergic, invasive, or cavity. Allergic aspergillosis is predominant in patients with asthma and especially as a complication in patients with cystic fibrosis. The radiological identification in these patients is difficult, but in general they have more mucous plugging. The invasive form is very severe and occurs predominantly in immunocompromised patients, such as those in treatment for leukemia or lymphoma, post bone marrow transplant, and other organ transplantation (Fig. 12). Pulmonary consolidation, central bronchiectasis, mucoid impaction, and appearance on secondarily infecting a preexisting pulmonary cavity are the most characteristic findings for fungal infection.

Certain lung infections occur mainly in patients with immunological problems, including congenital or acquired immune defects, or therapy with corticosteroids or immunosuppressants. These are infections by opportunistic agents such as *Pneumocystis*, *Cytomegalovirus*, or *Herpes simplex*.

## 2.10 Parasitic Lung Infection

The parasitic lung infections are rare in infancy. The most common is *Echinococcus granulosus* infection (hydatid disease). Radiologically present as one or more homogeneous, well-defined round opacities, which are replaced by liquid level when the cyst ruptures (Fig. 13).

## 2.11 Follow-up Controls in Pneumonia

In general, the clinical healing of pneumonia is not parallel to radiological resolution which is typically slow. In the respiratory syncytial virus pneumonia (RSV) and parainfluenza with uncomplicated clinical course, radiological healing occurs up to 3–4 weeks. Adenoviral pneumonia is often severe (Fig. 5) with prolonged evolution. In these cases, the radiological changes may still persist after 6–12 months and sequelae are common.

In *M. pneumoniae* pneumonia and *C. trachomatis*, the response to therapeutic and healing is usually quick with no radiological sequelae consequences.

In most cases of bacterial pneumonia, where the agent is *S. pneumoniae* or *H. influenzae*, a normal chest radiography and follow-up control without complications are expected 3–4 weeks after treatment. The remaining cases usually normalize in 3–4 months. When the clinical course is slow or complications arise (pleural effusion, empyema, necrosis, pneumatoceles), control radiographs are useful. These are particularly important in staphylococcal pneumonia in which these complications are very common, requiring radiological controls and sometimes thoracic CT.



**Fig. 12** Fungal infection in a 6-year-old-girl, with acute lymphatic leukemia and bone marrow aplasia. **a** Chest radiograph showed a rounded opacity with peripheral cavitation at the *middle* third of the *right* lung field. **b** CT showed bilateral lesions related to invasive aspergillosis

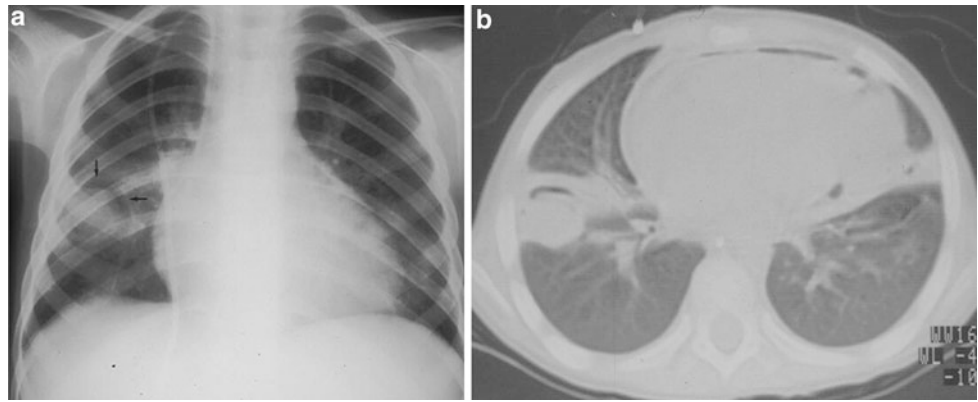
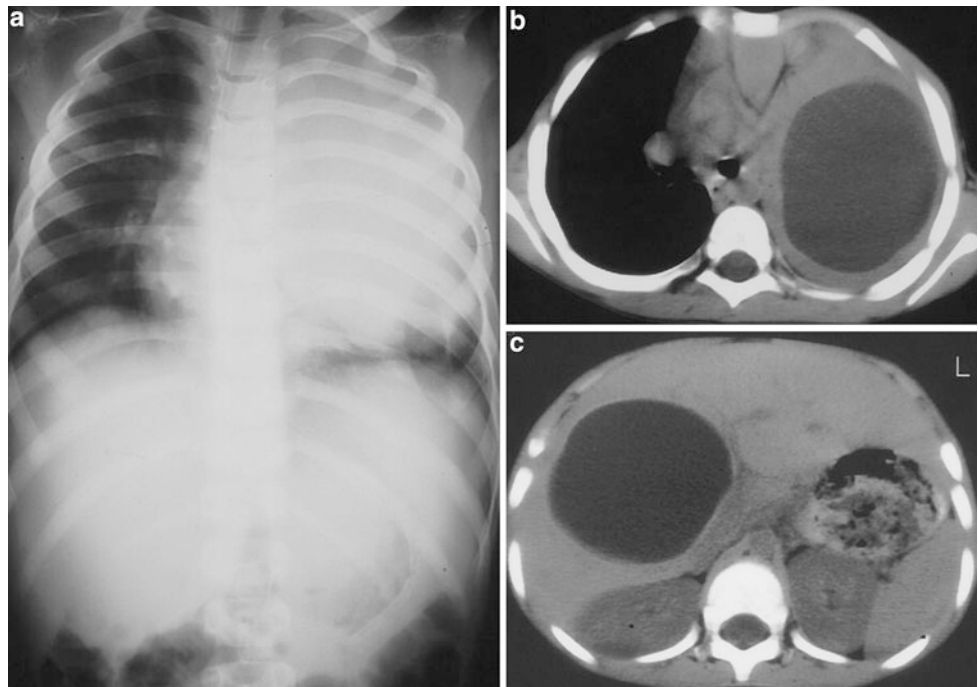


**Fig. 13** Echinococcus infection in a 10-year-old boy with fever and progressive respiratory distress. **a** Chest radiograph revealed a round dense lesion in the *left* lung, located in CT in the posterior *lower* lobe, showing the mass as a cystic lesion (**b**). **c** CT shows another intrahepatic cystic lesion. Serology for hydatid disease was positive, and resection of the cysts was performed



Pneumatocèles or pleural thickening can take 6–12 months to resolve.

Follow-up radiographs should be reserved for those children who have persistent or recurrent symptoms and those who have an underlying condition such as immunodeficiency. When follow-up radiographs are indicated, they should be obtained at least 2–3 week after treatment (Hedlund et al. 1997).

Development lung masses, such as sequestration, bronchogenic cyst, and cystic congenital malformation, may become infected and present as a recurrent or persistent pneumonia. CT is helpful in confirming and characterizing the presence of developmental masses. In cases of sequestration, CT is capable of identifying the characteristic systemic arterial supply.

## 2.12 Complications of Pneumonia

CT has an important role in the evaluation of complications related to pneumonia when the child has persistent or progressive symptoms despite medical or surgical therapy.

Imaging pleural effusion reflects the patterns of management at specific institutions. Traditionally, the aggressiveness of therapy has been based on categorizing **parapneumonic effusions** as empyema or transudative effusion (Donnelly and Klosterman 1997a; Donnelly 2002). The differentiation has been based on US findings and analysis of pleural fluid.

No individual CT findings (pleural enhancement, pleural thickening, extrapleural subcostal tissue abnormally, or adjacent chest wall edema) nor a score based on a

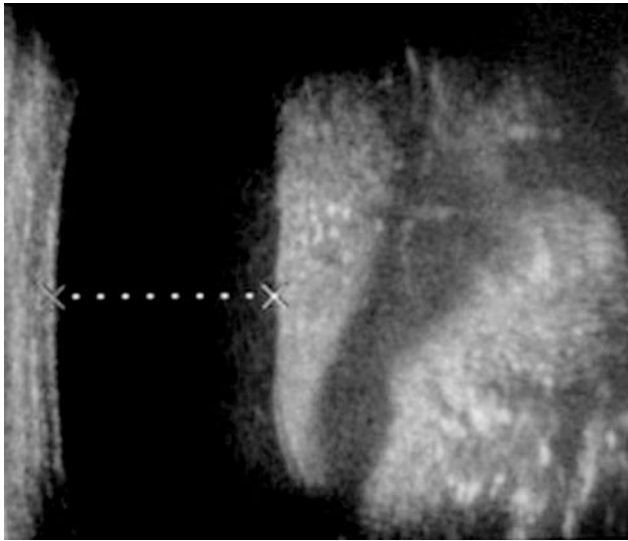


**Fig. 14** Pleural fluid in a boy with an opaque hemithorax. US shows an anechoic band of pleural fluid. There is a lung consolidation

combination of CT findings could accurately separate empyema from effusion (Donnelly and Klosterman 1997a).

The use of sonography in characterizing the pleural fluid (simple or complicated) in making therapeutic decisions for parapneumonic effusions has been advocated. Massive pleural effusion is one of the main causes of opaque hemithorax seen on chest X-ray films. Ultrasound is extremely useful for studying children with this radiological finding, which can be due to other entities, such as pulmonary and chest wall masses or consolidation.

US can also be used to provide imaging guidance for pleural drainage procedures, particularly when the pleural fluid is loculated. With US, one can determine the depth of the collection and decide on the safest manner to approach to drain it (Fig. 14) (Enriquez et al. 2008).

In the setting of a child with a noncontributory radiograph who has not responded appropriately to therapy, contrast-enhanced CT has been shown to be useful in detecting clinically significant suppurative complications. CT can help differentiate whether the reason for persistent illness is pleural or related to lung parenchyma, directing therapy in the appropriate direction (Donnelly and Klosterman 1997b).

On contrast-enhanced CT, uncomplicated pneumonia usually enhance the lung parenchyma. Enhancement is not a reliable way to differentiate atelectasis from pneumonia (Donnelly and Klosterman 1997b). On contrast-enhanced CT, complicated pneumonia shows a decrease and heterogeneous parenchymal enhancement (Donnelly 2008).

Suppurative lung parenchymal complications represent a spectrum of abnormalities and include cavitory necrosis,

lung abscess, pneumatocele, bronchopleural fistula, and pulmonary gangrene (Donnelly and Klosterman 1998a, b).

**Cavitory necrosis** represents a dominant area of necrosis of a consolidated lobe associated with a variable number of thin wall cysts. Unlike in adults, among whom the mortality rate of cavitory necrosis is high and early surgical removal of the affected lung has been advocated, the long-term outcome in children with cavitory necrosis is favorable with medical management alone (Donnelly 2002).

**Lung abscess** represents a dominant focus of suppuration surrounded by a well-formed fibrous wall. On contrast-enhanced CT, lung abscesses appear as fluid- or air-filled cavities with definable enhancing walls (Donnelly 2008).

On chest radiography, it is often difficult to determine how much of a detected opacity is due to pleural effusion and how much is due to consolidated lung, when both are present. Accurate determination of the amount of pleural fluid and its location, provided by CT also affects therapeutic decisions regarding drainage (Donnelly and Klosterman 1998b; Enriquez et al. 2008). CT gives helpful information depicting loculated pleural collections not in communication with the chest tube, or poor chest tube placement.

There are a number of potential complications from pneumonia that can cause chronic respiratory difficulties. These include bronchiectasis, Swyer-James syndrome or bronchiolitis obliterans, parenchymal scarring, and fibrothorax.

**Swyer-James syndrome** is defined as the presence of unilateral hyperlucent lung in association with decreased pulmonary vasculature. It is thought to represent an obliterative bronchiolitis that occurs secondary to viral infection, often related with adenovirus. Bilateral lung involvement is quite frequent (Lucaya et al. 1998, 1999; Garcia-peña and Lucaya 2004).

**Bronchiectasis** is probably the most common chronic complication of childhood pneumonia. Reversible bronchiectasis can occur during acute pneumonia. Chronic bronchiectasis most commonly occurs due to adenovirus or bacterial infection. (Donnelly 2008; Lucaya and Ducou Le Point 2008).

### 3 Thoracic Trauma

Thoracic trauma in children is rare, with only 4–6 % of children hospitalized with an indication of severe trauma. Only a small number of children with trauma have thoracic injury (14 %), but the injuries tend to be of a serious nature.

It occurs in 15 % of cases in isolation and in 25–50 % of cases in combination with other trauma locations (Chaumoitre et al. 2008).

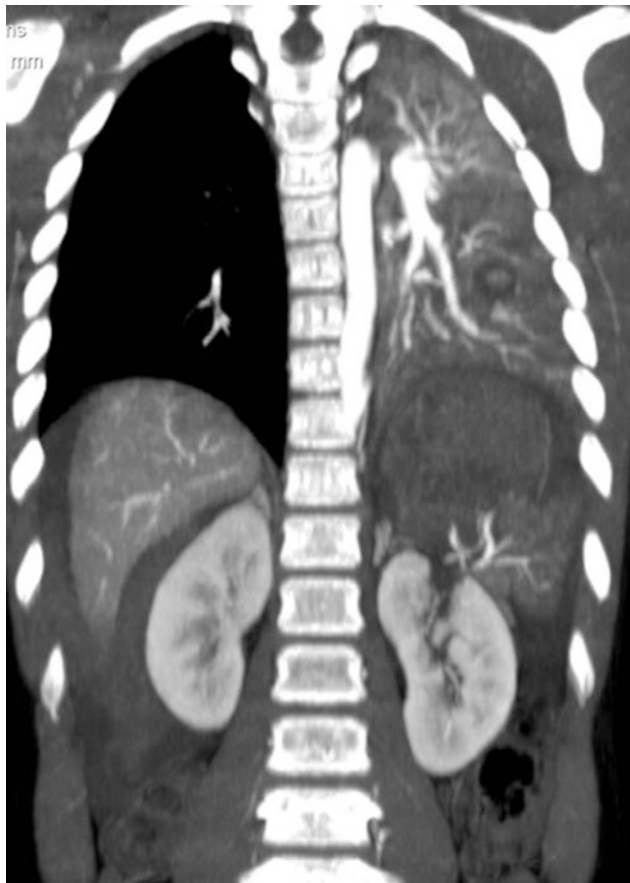


**Fig. 15** Polytrauma by car accident in 10-year-old boy. Coronal MCDT image shows pulmonary laceration, spleen fracture, kidney fracture and hemoperitoneum

Polytraumatized children have a great risk of mortality and thoracic trauma is the second leading cause of death (the first is the CNS).

In more than 85 % of cases the trauma is closed, as a result of car accidents, pedestrian accidents or falls from a height.

The most common chest injuries are pulmonary contusion, laceration, hemothorax, pneumothorax, and rib fractures. Less common lesions are the aortic arch lesion, cardiac contusion, tracheobronchial tree rupture, esophageal rupture, and diaphragmatic rupture. Most of traumatic thoracic lesions are treated conservatively, not requiring surgery.

Because of the plasticity of the pediatric rib cage, rib fractures are infrequent, and severe parenchymal injuries can be present in the absence of rib fracture.

Mediastinal lesions are unusual. The increased mobility of solid intra-abdominal organs combined with a weaker abdominal wall is specific to pediatric patients (Chaumoitre et al. 2008).

Children are different from adults due to the small body surface area, the compliance of the chest wall, the mediastinal mobility, and high vascular elasticity. The reliable

diagnosis of chest injuries in the acutely injured patient is often clinically difficult.

Cardiopulmonary symptoms may not be present in the first 24 h and there is no consistent relationship between external chest wall injuries and underlying abnormalities. This is particularly true with children in whom increased compliance of the bony thorax allows major internal injury to occur without associated skeletal injury. (Sivit et al. 1989).

High physiological reserves can compensate up to 40 % loss of volume and can obscure serious injury.

Children and adults can have the same type of injury, but with different patterns.

Rib fractures, flail chest, aortic injury, and diaphragmatic rupture are more common in adults, whereas pulmonary contusion, pneumothorax, and intrathoracic injury without bony injury predominate in children.

The differing pattern of injury may be explained by the anatomic and physiologic differences between children and adults.

The smaller size of the tracheobronchial tree in children leads to greater respiratory distress for small caliber changes.

The trachea is relatively narrow, short, and more readily compressible in children, so that small changes in airway caliber from external compression or inhaled foreign body may result in more significant respiratory compromise (Moore et al. 2011).

Taking into account that major trauma does not respect anatomic boundaries and may lead to multisystemic injury, this approach should be diagnostically accurate, cost effective, and provide efficient treatment decisions, using the lowest possible radiation dose (Moore et al. 2011).

### 3.1 Imaging Techniques

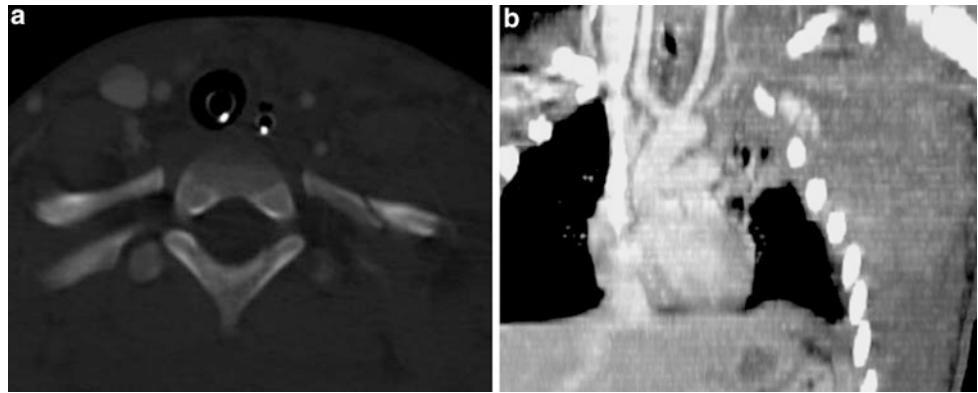
Chest radiograph is basic and important, often conditioned by artifacts and technical limitations. Chest radiograph allows rapid analysis of the lungs, pleura, mediastinum, chest wall, and drainage systems in place. It is often a means of fast diagnosis in circumstances of severe instability.

Chest radiography plays an important role in the initial evaluation of blunt and penetrating chest trauma, providing rapid imaging information to supplement the history and physical examination. In the emergency department, familiarity with the spectrum of injuries that can occur in the chest and upper abdomen is important for accurate interpretation of chest radiographs as well as establishment of appropriate recommendations for management and follow up (Mai-Lan 2009).

CT of the chest is the most reliable and sensitive instrument to assess the trauma, allowing a detailed analysis of all intrathoracic organ. It has a variable clinical impact,



**Fig. 16** Arterial axilar injury by car accident in a 12-year-old girl. **a** Left rib fracture in axial CT. **b** Laceration of left axilar artery with chest wall hematoma in coronal contrast enhanced CT



however it can use high doses of radiation and should therefore be reserved for selected patients (Markel et al. 2009).

When CT is being performed to evaluate traumatic injury to either the abdominal contents or mediastinum, it is important to evaluate the lung for lung contusion or other trauma-related lung opacity.

The MDCT used in trauma provides a large amount of information in a short time interval (Fig. 15). It is the ideal technique for severe multiple trauma with greater sensitivity than chest radiography. The use of the MDCT in detecting chest injuries should wonder about their impact on the clinical management and the final result, taking into account the radiation burden.

Initial indications for the use of CT include fractures of ribs, sternum or shoulder, abnormal mediastinum on chest radiograph, penetrating trauma or positive pressure ventilation. Delayed CT indications are persistent hemorrhagic drainage and progressive pneumomediastinum.

The use of CT in trauma should consider an adapted pediatric protocol, efficient immobilization, and avoid multiple phases. The optimization of radiation should be adjusted for age and weight, considering the mAs and the kVp, scan times, collimation, pitch, and the use of modulation systems.

The other imaging techniques (US, angiography, and MRI) are more limited and present more precise indications.

Ultrasound is useful in the assessment of pleural collections in mediastinal deviation and allows quick analysis of the lower chest. Angiography is reserved for intervention in cases of acute bleeding, and MRI should be considered when there is suspicion of spinal cord injury.

### 3.2 Chest Wall Injuries

The rib fractures are uncommon in children. They are more frequent in the posterior arcs and can be multiple. When there is fracture of the three first ribs (Fig. 16) and the sternum, associated vascular injury should be suspected (Durant et al. 2005).

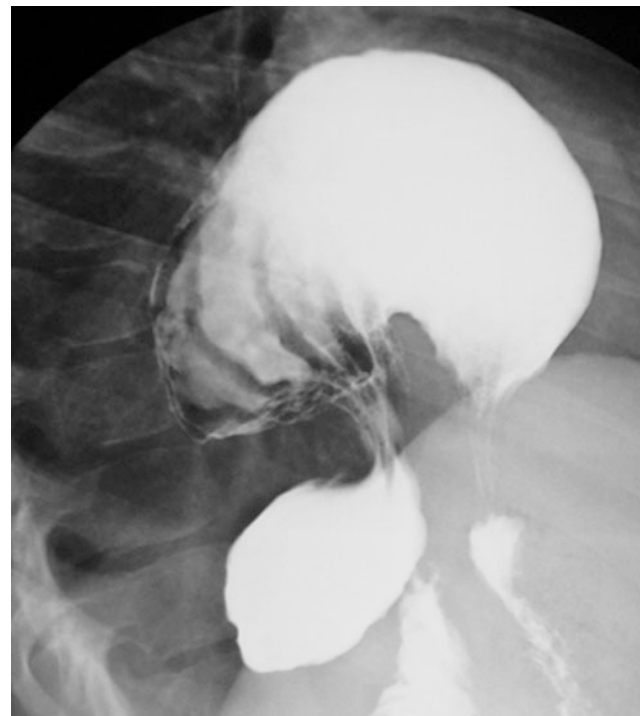


**Fig. 17** Traumatic intrathoracic gastric hernia by car accident in a 10-year-old boy. Contrast GI shows a gastric hernia going into the chest cavity through a small diaphragmatic rupture

### 3.3 Diaphragmatic Rupture

Diaphragmatic rupture is rare, the diagnosis can be delayed, often overlooked with herniated viscera complication (Fig. 17).

Diaphragmatic rupture is most frequently caused by compressive blunt trauma to the abdomen but it is also described with penetrating trauma. Left diaphragmatic hernias are more common due to the protective effect of the liver on the right side.

CT may show the diaphragmatic rupture and air in the bowel loops above the diaphragm. If CT is equivocal or unavailable and if the patient's condition permits,

**Fig. 18** Tracheobronchial tear by car accident in a 10-year-old boy. **a** Axial lung window CT image mainly shows consolidation of *left* lower lobe and small *right* consolidation. **b** Contrast enhanced CT better shows *left* lower lobe bronchial tear

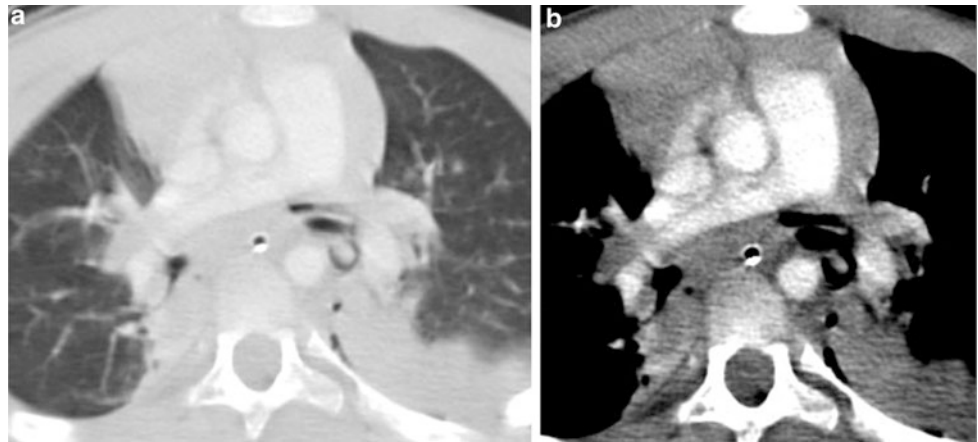


**Fig. 19** Left traumatic tension pneumothorax in a 13-year-old boy. Chest radiograph shows a hyperlucent hemithorax with mediastinal shift to the *right* and descent *left* diaphragm. Lung is collapsed

water-soluble contrast studies are extremely helpful and can show the hollow viscus (Duncan 2002).

### 3.4 Tracheobronchial Injuries

Tracheobronchial injuries are rare and, if proximal, cause mediastinal and cervical emphysema. More distal damage is intrapleural and causes a pneumothorax. Patients with trauma, who have hoarseness or stridor in addition to dyspnoea, cough, and haemoptysis should be suspected of having tracheobronchial injury. These clinical signs with pneumothorax or mediastinal subcutaneous emphysema should alert to the possibility of tracheobronchial injury (Duncan 2002) (Fig. 18).

### 3.5 Pneumothorax

CT is the most sensitive technique in the pneumothorax evaluation.

Pneumothorax may be secondary to injury to the lung, airways or esophagus, or to be due to direct penetration of the chest. Lack of response to drainage may indicate tracheal or bronchial tear.

A tension pneumothorax in addition to the hyperlucent hemithorax on the chest radiograph can produce shift of the mediastinum. Lung contusion and hematoma may, however, prevent total collapse of the lung and it is possible to have a marked tension pneumothorax without the ipsilateral lung being totally collapsed (Fig. 19).

A large opaque hemithorax is not always due to a hemothorax. Rupture of the hemidiaphragm can allow abdominal viscera to herniate into the chest, giving an opaque hemithorax appearance on the chest film (Duncan 2002).

### 3.6 Pulmonary Contusion

Lung contusion is defined as hemorrhage and edema formation in the alveoli and interstitium secondary to blunt chest trauma, without accompanying parenchymal laceration. On CT, lung contusions are characteristically non-segmental in distribution, not following segmental or lobar anatomic boundaries (Sivit et al. 1989; Donnelly and Klosterman 1997c; Wylie et al. 2009).

Contusions are usually located posteriorly, crescentic, or amorphous in shape and mixed confluent nodular quality.

The lung contusions of children may also demonstrate a 1–2 mm region of uniformly non-opacified subpleural lung, separating the area of lung consolidation from the adjacent chest wall (Donnelly and Klosterman 1997c) (Fig. 20).

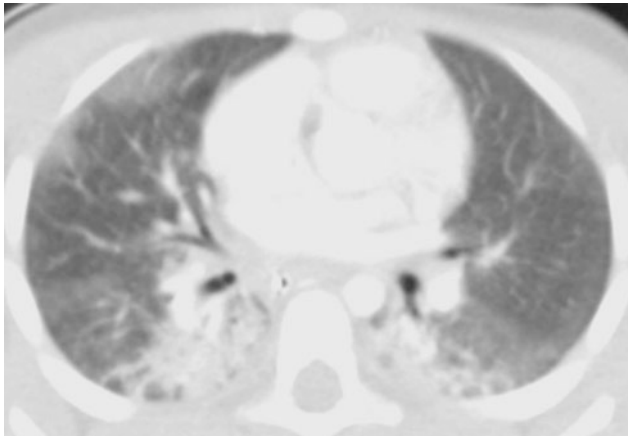


**Fig. 20** Bilateral lung contusion with subpleural sparing in a 10-year-old boy. CT shows bilateral areas of contusion of *lower lobes*

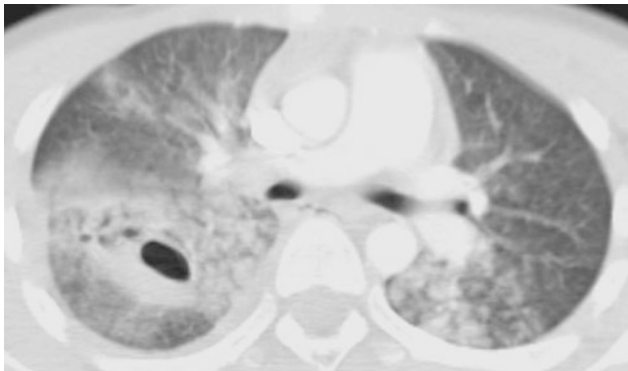


**Fig. 21** Lung laceration in a 10-year-old boy. CT image shows bilateral consolidations with blood- and air-filled cavities due to alveolar disruption

Lung contusions are a result of alveolar capillary damage with extravasation of edema and hemorrhage into alveoli and interstitial spaces.

### 3.7 Lung Laceration

Pulmonary laceration differs from contusion in that with laceration there is a frank tear within the lung parenchyma. The characteristic CT finding of pulmonary laceration is the presence of an air- or fluid-filled cavity (Fig. 21).

Lacerations result from penetrating injuries, such as adjacent displaced rib fractures, or shearing blunt forces to the lung. Initially, they may be indistinguishable from surrounding contusion. Because of the disruption of the lung tissue, one or more air cavities develop over time and may contain a central density or fluid level because of intrapulmonary hematoma. Pulmonary lacerations tend to heal more slowly than contusions, and, especially in children, they may leave behind a persistent cavity called

a posttraumatic pulmonary pseudocyst (Westra and Wallace 2005).

### 3.8 Mediastinal Injuries

Pneumomediastinum is recognized by streaky air collections outlining mediastinal structures such as the thymus and mediastinal vessels, or the superior surface of the diaphragm. It can be due to benign causes and be self-limiting, or it can be a sign of serious trauma, such as penetrating injury and tracheobronchial and esophageal rupture (Westra and Wallace 2005).

Detection of mediastinal hematoma is extremely important, because it may be a clue to an occult traumatic aortic injury, which is often clinically silent (Westra and Wallace 2005) (Fig. 22). The aortic lesion is extremely rare in children, but early detection improves the outcome.

Tracheobronchial laceration is a life-threatening emergency, rare and if proximal, can cause mediastinal and cervical emphysema. Distal damage is intrapleural and causes a pneumothorax. Emphysema and pneumothorax should alert to the possibility of tracheobronchial injury (Duncan 2002). Pleural fluid could accompany distal esophageal damage.

### 3.9 Traumatic Lung Cysts

Traumatic lung cysts have a similar radiological appearance to pneumatoceles and are often referred to as traumatic pneumatoceles (Fig. 23). They are usually due to blunt trauma without associated rib fracture. The etiology is thought to be fracture of small bronchi due to a sudden compression restricting the air outflow at the same time as compressing the lung. This causes distal lung tissue to burst in a balloon-like manner. They appear on a chest X-ray or CT within 1–3 days of injury as the pulmonary contusion or hematoma resolves and, like inflammatory pneumatoceles, they resolve spontaneously within 2–16 weeks. Rupture will cause a pneumothorax (Duncan 2002).

### 3.10 Esophageal Rupture

Except in cases of direct injury, esophageal rupture is extremely rare; this is especially true in children, and can be easily missed. When rupture occurs, it usually involves the lower third of the esophagus and the content enters to the mediastinum, aided by the negative pressures of inspiration. Pneumomediastinum, pneumothorax, and pleural effusions are radiographic signs (Fig. 24).



**Fig. 22** Postraumatic aortic injury in a 15-year-old boy. **a** Axial enhanced CT scan shows dissection of aortic arch. **b** Coronal enhancement CT scan shows aortic pseudoaneurism

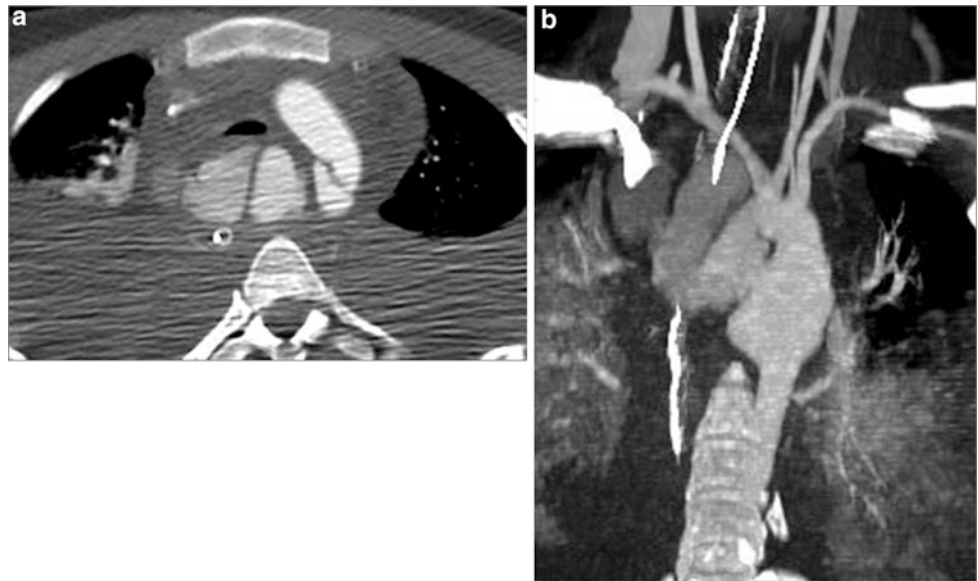


**Fig. 23** Traumatic pneumatocel post pulmonary hematoma in a 13-year-old girl. **a** CT shows a round density in RLL. **b** CT scan control after 30 days shows a cystic lesion

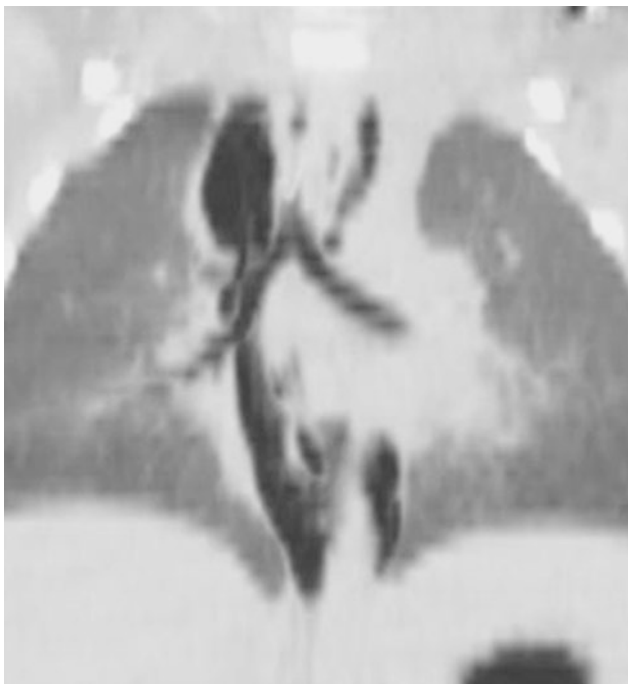
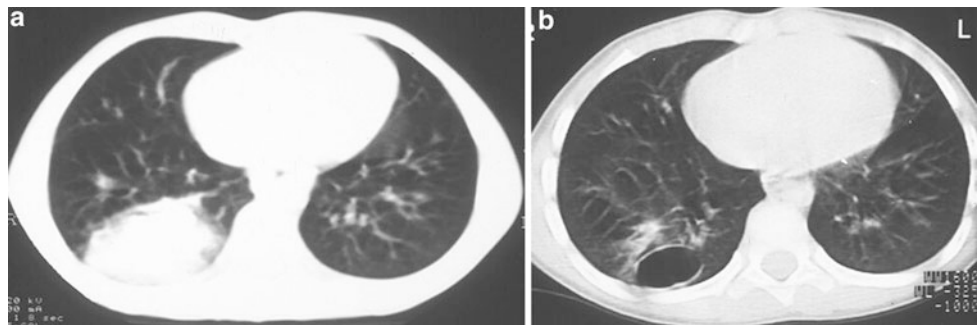


**Fig. 24** Esophageal rupture, post penetrating trauma in a 9-year-old-boy. Coronal reconstruction CT image shows pneumomediastinum

Most esophageal ruptures are iatrogenic in children and caused during the passage of a nasogastric tube or occur as the result of impaction of a foreign body or during endoscopy removal.

#### 4 Summary

Pulmonary infection is caused by a variety of agents, and incidence and frequency are variable in different age groups of children. Chronic infection may have underlying congenital lung malformations or sequelae of previous infections. It is important to know the different patterns of presentation and their complications, which lead to an appropriate use of imaging techniques and therapeutic.

The decision for the appropriate use of imaging techniques in thoracic trauma must depend on the specific case under review. Chest radiography should be the initial screening method. The decision to use CT is determined by the nature of the trauma, the clinical circumstances, and the prediction of future reevaluation, taking into account the use of radiation in children.

## References

- Bransom RT, Griscom NT, Cleveland RH (2005) Interpretation of chest radiographs in Children with cough and fever. *Radiology* 236:22–29
- Carty H (2000) Imaging infection. In: Fonseca-Santos J, Aragão-Machado M, Santos C (eds) *Pediatric radiology—The State of the Art in 2000—ESPR—Syllabus—Bracco—Education in Diagnostic Imaging*—ed. Springer pp 3–5
- Chaumoitre K, Merrot T, Petit P, Paniel M (2008) Particularités des traumatismes thoraciques et abdominaux chez l'enfant. *J Radiol* 89:1871–1888
- Daltro P, Santos EN, Gasparetto MEUC et al (2011) Pulmonary infections. *Pediatr Radiol* 41:S69–S82. doi:[10.1007/s00247-011-2012-8](https://doi.org/10.1007/s00247-011-2012-8)
- Donnelly LF, Klosterman LA (1997a) CT appearance of parapneumonic effusions in children: findings are not specific for empyema. *AJR Am J Roentgenol* 169:179–182
- Donnelly LF, Klosterman LA (1997b) Pneumonia in children: decreased parenchymal contrast enhancement- CT sign of intense illness and impending cavity necrosis. *Radiology* 205:817–820
- Donnelly LF, Klosterman LA (1997c) Subpleural sparing: a CT finding of lung contusion in children. *Radiology* 204:385–387
- Donnelly LF, Klosterman LA (1998a) Cavity necrosis complicating pneumonia in children: sequential findings on chest radiography. *AJR Am J Roentgenol* 171:253–256
- Donnelly LF, Klosterman LA (1998b) The yield of CT of children who have complicated pneumonia and non-contributory chest radiograph. *AJR Am J Roentgenol* 170:1627–1631
- Donnelly LF (2002) CT of acute pulmonary infection/trauma. In: Lucaya J, Strife J (eds) *Pediatric chest imaging*, 1st edn. Springer-Verlag, Berlin, pp 113–127
- Donnelly LF (2008) CT of acute pulmonary disease: infection, infarction, and trauma. In: Lucaya J, Strife J (eds) *Pediatric chest imaging*, 2nd edn. Springer-Verlag, Berlin, pp 147–164
- Duncan AW (2002) Emergency chest radiology in children. In: Carty H (ed) *Emergency pediatric radiology*, 2nd edn. Springer-Verlag, Berlin, pp 33–116
- Durant C, Piolat C, Nagues F, Bessaguet S, Alvarez C, Baudin P (2005) Imagerie thoracique en urgence chez l'enfant. *J Radiol* 86:198–206
- Enriquez G, Aso C, Serres X (2008) Chest US. In: Lucaya J, Strife J (eds) *Pediatric chest imaging*, 2nd edn. Springer-Verlag, Berlin, pp 1–35
- Garcia-Peña P, Lucaya J (2004) HRCT in children: technique and indications. *Eur Radiol* 14:L13–L30
- Eslamy HK, Beverley Newman MD (2011) Pneumonia in normal and immunocompromised Children: an overview and update. *MD Radiol Clin N Am* 49:895–920. doi:[10.1016/j.rcl.2011.06.007](https://doi.org/10.1016/j.rcl.2011.06.007)
- Hedlund GL, Griscom NT, Cleveland RH et al (1997) Respiratory system. In: Kirks DR (ed) *Practical pediatric imaging*, vol 3., LittleBrown and Company, Boston, pp 619–821
- Lucaya J, Gartner S, Garcia-Peña P et al (1998) Spectrum of manifestations of Swyer-James-McLeod syndrome. *J Comp Assist Tomogr* 22:592–597
- Lucaya J, Garcia-Peña P, Herrera L et al (1999) Expiratory chest CT in children. *AJR Am J Roentgenol* 174:235–241
- Lucaya J, Ducou le Point H (2008) High-resolution CT of the lung in children. In: Lucaya J, Strife J (eds) *Pediatric chest imaging*, 2nd edn. Springer-Verlag, Berlin, pp 77–121
- Ho M-L, Gutierrez FR (2009) Chest radiography in thoracic polytrauma. *AJR* 192:599–612
- Markel TA, Kumar R, Koontz NA (2009) The utility of computed tomography as a screening tool for the evaluation of pediatric blunt chest trauma. doi:[10.1097/TA.0b013e318184ba9a](https://doi.org/10.1097/TA.0b013e318184ba9a)
- Moore MA, Wallace EC, Westra J (2011) Chest trauma in children: current imaging guidelines and techniques *Radiol Clin N Am* 49:949–968. doi:[10.1016/j.rcl.2011.06.002](https://doi.org/10.1016/j.rcl.2011.06.002)
- Peltola V, Ruuskanen O, Svedström E (2008) Magnetic resonance imaging of lung infections in children. *Pediatr Radiol* 38(11):1225–1231
- Sivit CJ, Taylor GA, Eichelberg MR (1989) Chest injury in children with abdominal trauma: evaluation with CT. *Radiology* 171:815–818
- Wesenberg RL, Figarola MS, Estrada B (2006) Child with cough and fever. In: Hilton S, Edwards D (eds) *Practical pediatric radiology*, 3rd edn. Saunders-Elsevier, USA, pp 311–349
- Westra SJ, Wallace EC (2005) Imaging evaluation of pediatric chest trauma. *Radiol Clin N Am* 43:267–281
- Wylie J, Morrison GC, Nalk K et al (2009) Lung contusion in children—early computed tomography versus radiography. *Ped Crit Care Med* 10(6):643–646

# Pediatric Tuberculosis

Pedro Daltro, Eloá Nunez-Santos, and Bernard F. Laya

## Contents

<b>1</b>	<b>Introduction and Historical Aspects</b> .....	286
<b>2</b>	<b>Epidemiology</b> .....	286
<b>3</b>	<b>Pathogenesis</b> .....	287
3.1	Infection .....	287
3.2	Disease .....	288
<b>4</b>	<b>Clinical Aspects</b> .....	288
<b>5</b>	<b>Imaging Techniques</b> .....	290
5.1	Chest X-Ray .....	290
5.2	Computed Tomography.....	290
5.3	Magnetic Resonance Imaging .....	290
5.4	Ultrasound.....	290
<b>6</b>	<b>Imaging Features of Intrathoracic Tuberculosis</b> .....	290
6.1	Infection: The Primary Complex .....	290
6.2	Primary Pulmonary Tuberculosis: Spectrum of Disease Progression.....	291
6.3	Unusual Presentations and Complications.....	299
<b>7</b>	<b>Tuberculosis and Human Immunodeficiency Virus Infection</b> .....	299
<b>8</b>	<b>Response to Treatment</b> .....	300
<b>9</b>	<b>Conclusions</b> .....	300
	<b>References</b> .....	301

## Abstract

Tuberculosis (TB) is a transmittable chronic disease caused by infection with the *Mycobacterium tuberculosis* complex. It is a global public health problem with one-third of the world's population being infected, and is a leading cause of death and disability from infection. Children are amongst the most vulnerable group because of their immature immune status. A child usually gets TB infection after being exposed to a sputum-positive adult and it can have devastating effects if left untreated. Depending on many factors, the infection can lead to latency or TB disease. Clinical signs and symptoms can be diverse and could depend on the location of the lesions, extent of disease, as well as the age, and state of patient's immune status. TB can affect every organ in the body, but pulmonary infection is by far the most common. TB in children remains a diagnostic challenge. In addition to history of TB exposure, signs and symptoms, laboratory and microbiologic tests, medical imaging remains a valuable tool in its diagnosis. In some instances, particularly in difficult cases, imaging offers the only way to a thorough evaluation of the extent of the disease and to reach a correct diagnosis. Radiograph is the most commonly ordered initial imaging tool for screening and diagnosis of pulmonary involvement but other imaging modalities especially computed tomography offers more detailed assessment of lung, adenopathy, pericardial, and pleural disease. Medical imaging is also utilized to follow-up patients during or after anti-TB treatment. Knowledge of the common imaging patterns, pitfalls, and dilemma are very important in establishing the diagnosis of TB in children. The chapter discusses the pathophysiology of pediatric TB as it correlates with imaging findings. The wide spectrum of imaging manifestations on thoracic tuberculosis is presented.

P. Daltro  
Instituto Fernandes Figueira-Fiocruz and Clinica  
de Diagnóstico por Imagem – Barrashopping,  
Av. das Américas 4666, sala 325-Barra da Tijuca,  
Rio de Janeiro, Rj-Brasil 22649-900, Brazil

E. Nunez-Santos  
Instituto Fernandes Figueira-Fiocruz,  
Rua Almirante Guillobel 93/402 Lagoa,  
Rio de Janeiro, Rj-Brasil 22471-150, Brazil

B. F. Laya (✉)  
St. Luke's Medical Center-Global City,  
Institute of Radiology, 32nd Street,  
Bonifacio Global City, Taguig City 1634, Philippines  
e-mail: bernielaya@gmail.com



## 1 Introduction and Historical Aspects

Tuberculosis (TB) is a transmittable chronic disease caused by infection with the *Mycobacterium tuberculosis* complex. Pathologically it is characterized by the formation of granulomas. Clinical signs and symptoms can be diverse and could depend on the location of the lesions, extent of disease, as well as the age and state of patient's immune status. TB can affect every organ in the body, but pulmonary infection is by far the most common.

TB has been known to affect man as far back as historical data can record. Skeletal remains of prehistoric humans dating back to 8000 BC and Egyptian mummies dating from between 2500 and 1000 BC have revealed clear evidence of the disease in the spine (Cremin and Jamieson 1995). The best-documented confirmation of TB infection has come from DNA studies of an 8-year-old male Inca mummy who lived in around 700 AD. Radiographic study of his lumbar spine showed evidence of Pott's disease and smears of the lesion revealed acid-fast bacilli, most likely *Mycobacterium bovis* (Dutt and Stead 1999).

Jean Antoine Villemin (1827–1892) was the first to prove the infectious nature of TB by passing it from humans to cattle, and from cattle to rabbits. In 1882, Robert Koch in Germany identified the actual agent of TB, the tubercle bacillus. The TB vaccine, bacille Calmette-Guérin (BCG), was developed in the early part of the twentieth century by the French researchers Calmette and Guérin. Effective therapy against TB became available in 1943 with Waksman's discovery of streptomycin, the first antituberculosis drug.

## 2 Epidemiology

*Mycobacterium tuberculosis* is the most devastating bacterial pathogen of all time. Approximately one-third of the world's population is infected with TB, and therefore at risk of developing the disease (Cremin and Jamieson 1995). Without treatment, TB is often fatal, and it is estimated that 50–60 % of the untreated patients are likely to die within 5 years after diagnosis (Maher and Raviglione 1999). In 1993, more than a century after the TB causal agent discovery, followed by decades of research on implementation of appropriate chemical therapy, the World Health Organization (WHO) declared TB a global emergency. This was the first time in the history of the organization that such a document was issued.

TB has always been a public health problem especially among young people. The global incidence rates have been stable from 1990 to 2001 but, thereafter, it started to decline. From 2010 to 2011, the rate of decline in incidence

was 2.2 %, and the TB mortality has also decreased by 41 % since 1990. Despite of this, the global TB burden remains enormous. In 2011 alone, there were an estimated 8.7 million incident cases of TB globally, which is equivalent to 125 cases per 100,000 population. The burden is highest in Asia (59 %) and Africa (26 %), but also seen in Eastern Mediterranean Region (7.7 %), Europe (4.3 %), and America (3 %) (WHO Global Tuberculosis Report 2012a). Challenges to estimating the burden of TB in children include: difficulty in establishing definitive diagnosis, increased presence of extrapulmonary disease in young children, lack of standard case definition, and the lower public health priority given to childhood TB compared to that of adult disease (Nelson and Wells 2004). In 2012, the WHO report on global TB care and control for the first time, included the estimated TB burden in children (<15 years), which is 490,000 cases (6 % of 8.7 million cases a year) and 64,000 deaths per year.

In 1997, in response to the growing concern about global TB control, the WHO adopted a new strategy, Directly Observed Treatment Short Course (DOTS) which aims to prevent the emergence of resistant strains of *M. tuberculosis* and to detain their spread. The DOTS program is based on five pillars including: governmental political support, microscopic detection of the cases by sputum-smear examination, short and supervised therapy, regular supply of antituberculosis drugs, and a standardized recording and reporting system for program supervision and evaluation.

There are many reasons for the alarming worldwide resurgence of TB. Poverty and poor living conditions (resulting in malnutrition and crowding), associated with lack of appropriate anti-TB drugs and sometimes governmental lack of interest in the control of TB, are the most important causes in many developing countries. In developed countries, the disease has been mainly reported in HIV-positive patients, intravenous drug users, groups of people living in enclosed, crowded settings (prisons, shelters, and nursing homes), people living in outer unsanitary city areas, as well as among immigrants or refugees from countries where TB is endemic (Cremin and Jamieson 1995). The most recent factor allowing for the increase of TB is the human immunodeficiency virus (HIV) pandemic, affecting both developed and developing countries. In African countries and South-East Asia, the association between TB and HIV has progressively increased. People living with HIV who got infected by TB are more likely to develop TB disease. Of the estimated 8.7 million new TB cases in 2011, an estimated 1.1 million or 13 % were among people living with HIV, which is highest in the African region (80 %). In 2011 alone, there were 0.4 million HIV-associated TB deaths reported globally (WHO Global Tuberculosis Report 2012a). Published studies of children with TB in sub-Saharan Africa and elsewhere have shown a

co-infection rate with HIV of 11–64 % (Nelson and Wells 2004; Coovadia et al. 1998).

Multidrug-resistant tuberculosis (MDR-TB), defined as resistance to isoniazid and rifampicin, is a new face of the disease. Drug resistance results from inappropriate drug treatment or patient non-adherence to treatment and has a potentially dramatic impact on the epidemiology and control of TB worldwide. Drug-resistant strains of TB have emerged and are spreading. Globally in 2011, there were an estimated 630,000 cases of MDR-TB among the world's 12 million prevalent cases of TB. It is estimated that 3.7 % of new TB cases and 20 % of previously treated cases have MDR-TB (WHO Global Tuberculosis Report 2012b). Transmission of TB infection from adult MDR index cases to children in close household contact and subsequent development of disease in children has been established (Schaaf 2002). The diagnosis of pediatric MDR-TB is often delayed due to reliance on the diagnosis of the adult contact case of MDR-TB. Resistance patterns in children have generally been found to be similar to those of adults from same areas and similar background but there is limited published information available about MDR-TB in children (Nelson and Wells 2004). Treatment of drug-resistant TB is still inadequate in many countries. In some, laboratory diagnosis is of poor quality, others lack national policies on MDR-TB management, first and second-line drugs of uncertain quality are widely available, and large numbers of MDR-TB patients are treated outside the National Tuberculosis Programmes (NTPs) to inappropriate diagnostic and treatment procedures. Extensively drug resistant TB (XDR-TB), defined as MDR-TB plus resistance to a fluoroquinolone and at least one of three injectable second-line drugs (amikacin, kanamycin or capreomycin) has been identified in 84 countries and the average proportion of MDR-TB with XDR-TB is 9 % (WHO Global Tuberculosis Report 2012b). Another source of alarm is the few but very important reports of cases resistant to all licensed anti-TB drugs available, termed totally drug resistant TB or TDR-TB. The imaging appearance of drug resistant TB is the same as non drug-resistant TB. Moreover, it is no more infective than usual TB.

Since TB is a global emergency, the disease will be only defeated by a global alliance, bringing together public health agencies, the pharmaceutical industry and the academia. Effective control programs must foster private–public partnership in order to succeed.

---

### 3 Pathogenesis

#### 3.1 Infection

Humans are the only species in which *M. tuberculosis* is a self-perpetuating pathogen. In more than 95 % of cases, the

entrance door of TB infection is the lung, by inhalation of bacilli. Infection through the oro-pharynx, throat, eye or skin, rarely occurs. The exposed child inhales the infected aerosolized droplet containing 1–3 bacilli. These bacillary particles can be moved up the bronchial tree by cilia and might eventually be swallowed, causing no infection. They can also reach the alveoli (Ghon focus), where they will be ingested by the alveolar macrophages. The bacilli can be killed or inhibited by these cells. If the bacilli are quite virulent, they grow and multiply inside the alveolar macrophage until it bursts, releasing a greater number of pathogens. These bacilli will be then ingested by other alveolar and blood macrophages (i.e. monocytes), forming the *tubercle*, which consists of an aggregation of macrophages, epithelioid cells and lymphocytes. Central necrosis inside the tubercle is formed by destruction of macrophages. This immune response is mainly tissue-damaging delayed-type hypersensitivity, and at this time, usually 3–8 weeks after infection, the tuberculin skin test (TST) will usually be positive. Eventually, sclerosis and calcification of the lesion may develop (Dannenberg 1999; Marais et al. 2004a). The bacilli escapes from the edge of the caseous necrosis, multiply again and spread from the tubercle to nearby mediastinal lymph nodes. These three items together: the alveolar site of infection (Ghon focus), the infected lymph nodes and associated lymphangitis—form the “primary (Ranke's) complex”.

At this time, the primary focus becomes encapsulated, perifocal inflammation increases and manifests as a granuloma, which may be visible on chest radiograph. In most cases, cellular immunity controls the spread of infection. The pathologic events associated include caseous necrosis, fibrosis, and healing of the primary complex components with or without calcification. The extent of calcification depends on the degree of necrosis and caseation. After exposure, most children do not develop disease but instead develop latent tuberculosis infection (LTBI), which implies that an effective immune response has contained the infection but it is presumed that there are low numbers of viable tubercle bacilli that are dormant. These children usually have a reactive TST and/or interferon-gamma release assays (IGRA), no clinical evidence of TB, and generally no abnormalities on chest radiograph apart from the primary complex residual, which can sometimes be apparent (Onur et al. 2012). It is important to always bear in mind that TB-infected children, left untreated, will house the bacilli for longer periods of time than adults and can become a source of TB in future years (Inselman 1996).

TB spreads more easily among family members or among people who share the same facilities. However, contact alone is not bound to develop the disease. Immunologic and genetic factors affect the child's response to the initial infection (Starke 1999; Fejia and Saiman 2005).

Children under 5 years of age, and especially those under two, are less resistant to the organism; therefore, disseminated forms of the disease are more common in this age group. There is less risk of progressive primary disease in later childhood, between 6 and 12 years of age. Pediatric TB infection almost invariably occurs by contact with an adult or adolescent with cavitary pulmonary TB, most often at home, but also in school or day-care center. In the outside air, the bacilli are rapidly killed by ultraviolet light and viable bacilli are so widely dispersed that inhalation of even a single bacillus is extremely improbable.

TB transmission from a child has only been rarely reported but it could occur especially in children with cavitary pulmonary lesions and laryngeal disease (Curtis et al. 1999; Van Hest et al. 2004). In general, the incidence of child-to-child transmission is virtually unknown because children do not show the tussive force of an adult and have only sparse secretions. However, they play a peculiar role in the transmission of TB, because they may harbor a partially healed infection that lies dormant, only to be reactivated as infectious pulmonary TB many years later (Starke 1999). Thus, children constitute a long-lasting reservoir of TB in the population from which future generations will be infected (Cremin and Jamieson 1995).

### 3.2 Disease

Primary TB disease is defined as the disease progression of any component of the primary complex, and is most common in children. If the host is unable to contain the tubercle bacilli, progressive parenchymal caseation occurs in the lung parenchyma surrounding the Ghon focus. Pulmonary primary disease is the progression of disease in the lungs, which may occur from the primary site or may extend to the adjacent lung and disseminate further. The primary focus, may be initially small and not radiographically visible, but it can grow and may caseate centrally, liquefy, and empty into the adjacent bronchi (Feja and Saiman 2005). The area of caseation may discharge into bronchus, resulting in the formation of a cavity with possible endobronchial spread. Similarly, the regional lymph nodes may continue to enlarge, resulting in lymphobronchial involvement, in which affected bronchus may become partially or totally obstructed. Symptoms vary according to the degree of airway involvement (Fig. 1).

From the infected lymph nodes, bacilli can travel via the lymphatics or bloodstream to many parts of the body, such as the liver, spleen, kidneys, bone metaphysis, brain and other organs, or return to the lungs causing secondary lung lesions. Infants and young children have poor cell-mediated immunity, so when infected, they show a higher incidence of TB than adults or older children.

In children, the disease usually develops soon after the primary infection (primary TB disease) but the bacilli can also lie dormant in tissue macrophages for many years, only to develop the disease some decades later (secondary or reactivation TB). Complete eradication of the bacillus by the immune system never occurs, and it is still very difficult even with the use of effective antituberculosis therapy (Ehlers 1999). Calcified lesions are sterile in 85 % and fibrotic lesions in 86 %. In contrast, solid caseous lesions are sterile in only 50 % (Moulding 1999).

## 4 Clinical Aspects

Humans display a wide spectrum of immunologic response to TB, reflected in the diverse clinical manifestation ranging from asymptomatic infection to hematogenous dissemination with severe fatal disease. Numerous factors determine an individual's risk of developing disease once infected including malnutrition, recently acquired infection, immune suppression including human immunodeficiency (HIV) infection, and age. Children < 5 years of age infected with TB are at a higher risk of developing TB disease. Among infants (age < 1 year), 43 % of those infected will develop disease compared to 24 % in children aged 1–5 years, 15 % of adolescents, and 5–10 % of adults over a lifetime (Nelson and Wells 2004).

Most infants and children who become infected with *M. tuberculosis* will have LTBI. These children have a reactive TST, normal or minimal chest radiograph findings, no clinical evidence of TB, and presumed with low numbers of viable tubercle bacilli that are dormant. Recently, new diagnostic techniques have been developed to diagnose TB infection in vitro: the IGRA to quantify the IFN- $\gamma$  released by sensitized T cells stimulated with specific *M. tuberculosis* antigens (Dominguez et al. 2009). Those children who are symptomatic demonstrate few symptoms or signs of pulmonary disease at the outset. Fewer than half develop non-specific symptoms such as fever, anorexia, and weight loss. Most develop cough and many wheeze. If untreated, symptoms and signs of pulmonary bronchopneumonia and extrapulmonary disease may become apparent. Children with LTBI should be treated because of the high risk of disease progression, more years of developing active disease later in life, and the potential of spreading the disease (Mandalakas and Starke 2005). Disease progression is usually indicated by persistent, non-remitting symptoms, although the rate of progression is variable. In a majority of cases (>90 %), disease occurs within a year after primary infection, with the youngest children at greatest risk of progression (Marais et al. 2004a).



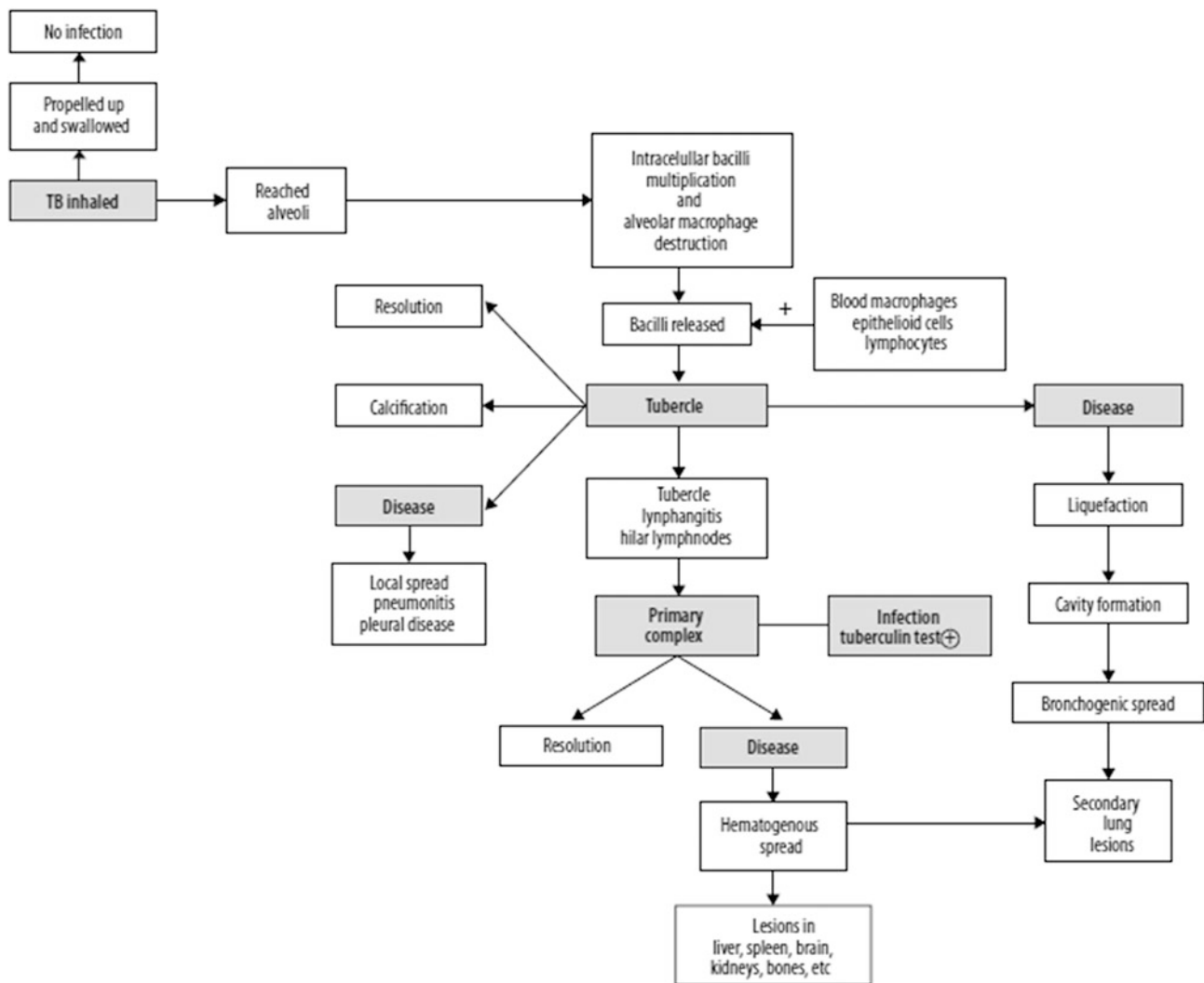


**Fig. 1** Pathogenesis of Tuberculosis

For the absolute diagnosis of TB, the demonstration on culture of *M. tuberculosis* in secretions or tissue of the patient is required. A positive TST demonstrates that the individual has been infected with *M. tuberculosis* but it cannot tell whether the bacilli are living in a quiescent latent state or actively replicating and causing disease. When the pathology is virtually confined to the lungs, as is usually the case in adults with pulmonary TB, it is relatively easy to confirm the diagnosis by sputum culture. When the principal focus of infection is the intrathoracic lymph nodes, as often is the situation in infants and young children, the organisms are inaccessible and it becomes difficult to prove that the patient has TB. Furthermore, children produce little sputum, which, in addition, contains few microorganisms, and they generally swallow it. Because of these factors and the difficulties associated with obtaining adequate samples of swallowed sputum from the stomach, the diagnosis of TB

is confirmed bacteriologically in considerably less than half (range 10–75 %) of infants and young children who are treated for TB (Klein and Iseman 1999; Marais 2008). Thus, the triad of a positive TST, abnormal chest radiographs and a history of exposure to an adult with TB remains the most effective method for diagnosing TB in children.

Primary TB has been used to describe pediatric pulmonary disease that arises as a complication of the TB infection. In children, disease frequently complicates the initial infection immediately, making the distinction between the two stages impossible. Miliary and meningeal TB can develop any time, but they are more likely to occur during the initial 3 months following the primary infection. Endobronchial TB can also develop at this time. Tuberculosis of the pleura and peritoneum characteristically occurs 3–7 months after demonstration of a positive skin test (Inselman 1996).

## 5 Imaging Techniques

Imaging methods such as chest X-ray, chest US, and chest CT are extremely important tools for the diagnosis of pediatric pulmonary TB. In some instances, particularly in difficult cases, they offer the only way to reach a correct diagnosis and a thorough evaluation of the extent of the disease.

### 5.1 Chest X-Ray

Chest radiography remains the first and most widely used imaging technique for the evaluation of pulmonary TB in children. Although it has low sensitivity and specificity (Smuts et al. 1994; Swinger et al. 2005) and the radiographic findings vary, pronounced lymphadenopathy with or without airway compression is suggestive of TB. Both anterior and lateral views are required for optimal lymph node visualization, although it may remain difficult to visualize enlarged lymph nodes with certainty (De Villiers et al. 2004). A normal chest X-ray in a patient suspected with TB could be misleading because a subtle primary lesion maybe small, diffuse, or obscured by normal structures (Andronikou et al. 2004). An apparently normal chest X-ray cannot exclude presence of pulmonary TB, but when positive, the X-ray findings although not specific, closely reflect the pathological changes of the disease (Lamont et al. 1986).

### 5.2 Computed Tomography

CT is the examination of choice in unusual, complicated, or disseminated presentations of the disease. It is also helpful for the evaluation of infants with positive skin test and normal chest X-rays, and for older children with either a history of recent exposure to TB or a positive skin test and inconclusive chest X-ray findings. In small children with disseminated or miliary TB, head CT should always be performed as well. Recognition of brain lesions, which commonly occur in these patients, can influence therapy.

CT scan is very good in the assessment of subtle lung parenchymal disease as well as lymph nodes, which may not be apparent on radiographs (Swaminathan et al. 2005). The advantages of CT over conventional radiographs in defining the extent of the disease and its possible complications (bronchial, pleural, pericardiac, and chest wall involvement) have been well documented in the literature (Kim et al. 1997). Since the search for lymph nodes is crucial in the study of chest TB in children, contrast-enhanced scans are preferred. Unenhanced scans are not

routinely obtained. Multiplanar and 3D reconstructions are also helpful in some cases, particularly in the evaluation of tracheobronchial disease.

CT scans cannot be routinely recommended because of the high cost, and risks associated with intravenous contrast administration. Another important issue is the radiation-associated risks, so therefore a clear indication for the procedure has to be present. Radiation dose reduction measures including the use of automatic dose modulation techniques and the adaption of weight-based pediatric CT protocols are recommended.

### 5.3 Magnetic Resonance Imaging

MRI is an excellent method for detecting mediastinal lymph node, pleural disease, and pericardial involvement. MRI also has the advantage of multiplanar imaging capability. However, high cost, need for sedation in most cases and poor visualization of the lung parenchyma limits its use.

### 5.4 Ultrasound

US is an easy to use, inexpensive, non-aggressive technique that is useful for identifying mediastinal lymph nodes (Bosch-Marcet et al. 2004) and differentiating them from a large normal thymus in patients who present mediastinal widening. It is also helpful for detecting pleural and pericardial effusion. Ultrasound is also an excellent tool for image-guided interventions.

---

## 6 Imaging Features of Intrathoracic Tuberculosis

### 6.1 Infection: The Primary Complex

Infection will result in pathologic changes and associated clinical disease. The tubercle bacilli that reach the terminal airway induce a local inflammatory process referred to as parenchymal focus (Ghon focus). Bacilli originating from the focus drain via local lymphatics to the regional lymph nodes. The triad of the Ghon focus, local tuberculous lymphangitis and involved regional lymph nodes is referred to as “primary complex” (Fig. 2). Bacilli located in the regional lymph nodes may enter the systemic circulation directly or via the lymphatic duct, which may disseminate bacilli to a variety of target organs, where the bacilli may survive for decades (Mandalakas and Starke 2005). Of infected children, 95 % will be subclinical and will not develop disease. The primary focus becomes encapsulated, and perifocal inflammation increases and manifests as a

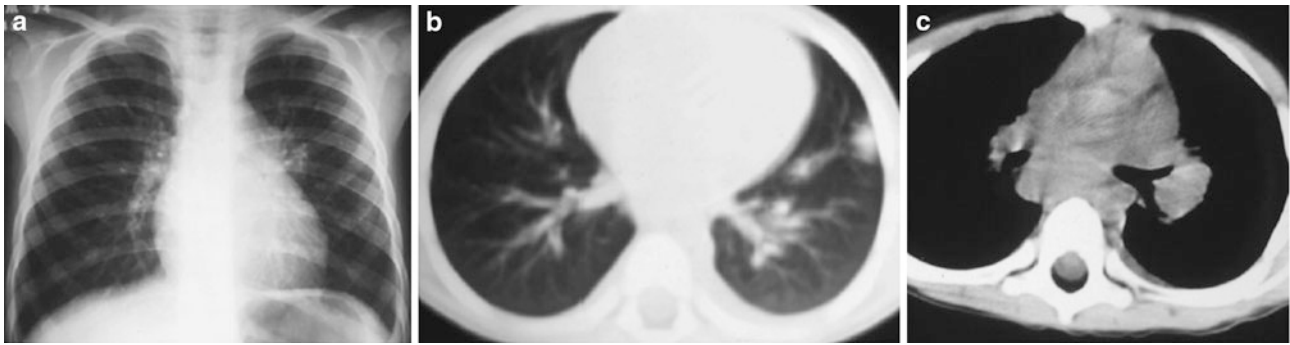


**Fig. 2** **a** Chest X-ray of an 8-year-old boy shows slight enlargement of the left hilum. **b** Unenhanced CT of the same patient demonstrates peripheral pulmonary focus in the left lower lobe and lymphangitis. **c** Mediastinal window shows left hilar adenopathy

granuloma. The pathologic events associated include caseous necrosis, fibrosis, and healing of the primary complex components with or without calcification depending on the degree of necrosis and caseation. Although these sequences of events occur in LTBI, the resolution may not be complete and viable TB bacilli may persist for many years, potentially reactivating and causing TB disease months to years later (Feja and Saiman 2005).

Lymphadenopathy (present in 92 %) with or without a visible Ghon focus is the radiographic hallmark of TB infection. Typically, it involves the hilar and paratracheal regions (Leung et al. 1992). The right side is more commonly affected than the left because of the usual pattern of lymphatic circulation within the lungs (Fig. 3). A left-sided parenchymal focus often leads to bilateral hilar adenopathy, whereas a right-sided focus is usually associated only with right-sided lymphadenitis (Starke 1999). With serial radiographs, 40 % of these lesions cleared within 6 months, a further 30 % within 1 year, and the remainder persisted for up to 4 years. Calcification, an indication of clinical quiescence, which usually occurs between 12 and 14 months, developed in 20–50 % of children with visible lymph node involvement (Marais et al. 2004a). Lateral views are particularly useful in detecting hilar lymphadenopathy, and both frontal and lateral views should be obtained (Fig. 4).

The Ghon foci may be too small to be radiographically visible but can also undergo caseation and calcify. There is no predilection for any specific part of the lung but a right-sided predominant distribution is well recognized (Leung et al. 1992) and approximately 70 % of the primary foci are subpleural in location (Mandalakas and Starke 2005).

## 6.2 Primary Pulmonary Tuberculosis: Spectrum of Disease Progression

### 6.2.1 Progressive Ghon Focus

Disease progression may occur at the site of the organism deposition (Ghon focus), within the regional lymph nodes,

or following disease spread. Ghon focus represents the first site of possible disease progression and is a sign of poor disease containment. Parenchymal involvement in primary pulmonary TB most commonly appears as homogeneous consolidation, although it can appear patchy, linear, nodular, and mass like (Fig. 5). Caseation necrosis, liquefaction, or calcifications can be seen within the consolidation and can progress into extensive lung damage (Fig. 6). Discharge of the caseated material from a Ghon focus into a bronchus results in the formation of a parenchymal cavity and infants and the immunocompromised are most vulnerable (Marais et al. 2004a) (Fig. 7). Another rare complication is the appearance of bullous or cystic lesions in the lung (Fig. 8). These have been reported to occur during treatment (Matsaniotis et al. 1967), but they were also observed before therapy was initiated. Occasionally peripheral bullous lesions will lead to pneumothorax.

Parenchymal lesions can be uni or multi-focal and are usually seen in areas of greatest ventilation: the middle lobe, the lower lobes, and the anterior segments of upper lobes. This pattern differs from the reactivation TB in adults, which is typically in the apical and posterior segments of the upper lobes (Kim et al. 1997). Parenchymal opacities occur in association with and affect the same side as the nodal enlargement (Leung et al. 1992).

### 6.2.2 Progressive Lymph Node Disease

Another possible site of disease progression is within the regional lymph nodes, which enlarges due to central caseation and surrounding inflammatory edema. Children 0–3 years of age had higher prevalence of lymphadenopathy (Leung et al. 1992). The small airway size makes children most vulnerable to development of lymphobronchial TB that refers to a spectrum of airways involvement and associated complications that may arise following lymph node disease (Marais 2008). Enlarged and edematous hilar, paratracheal, and sub-carinal lymph nodes may encroach upon the regional bronchus. Intraluminal obstruction results from the granulomatous tissue that



**Fig. 3** **a** Frontal view Chest X-ray of a 7-year-old girl with positive tuberculin skin test shows a prominent right perihilar shadow compatible with lymphadenopathy. No appreciable lung parenchymal abnormality is seen. **b** Lateral view confirms the lymphadenopathy superimposed on the mediastinal vessels

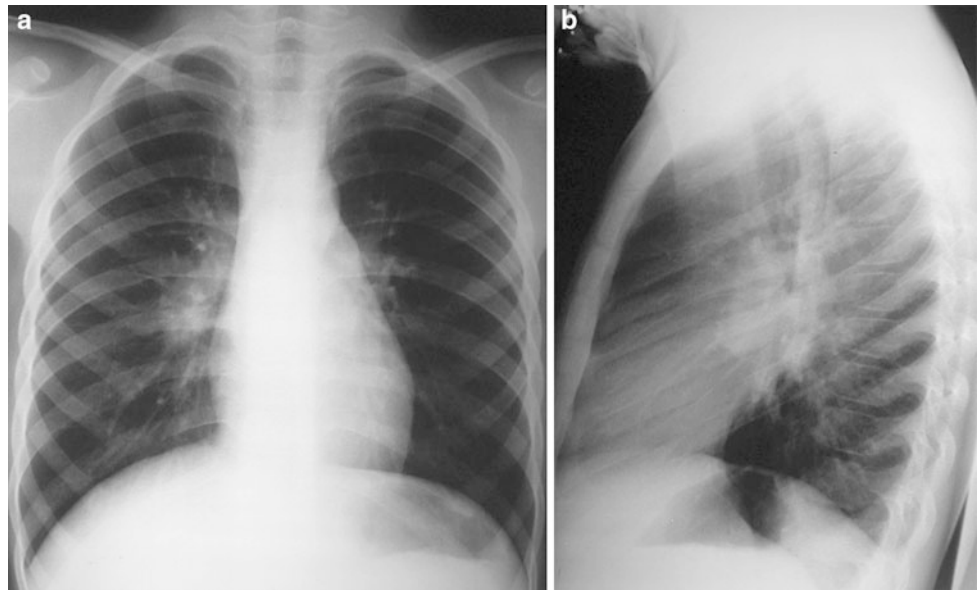


**Fig. 4** **a** Primary complex with calcified pulmonary focus in a 6-year-old child. **b** Calcified right hilar lymph nodes in a 5-year-old boy with latent tuberculosis infection

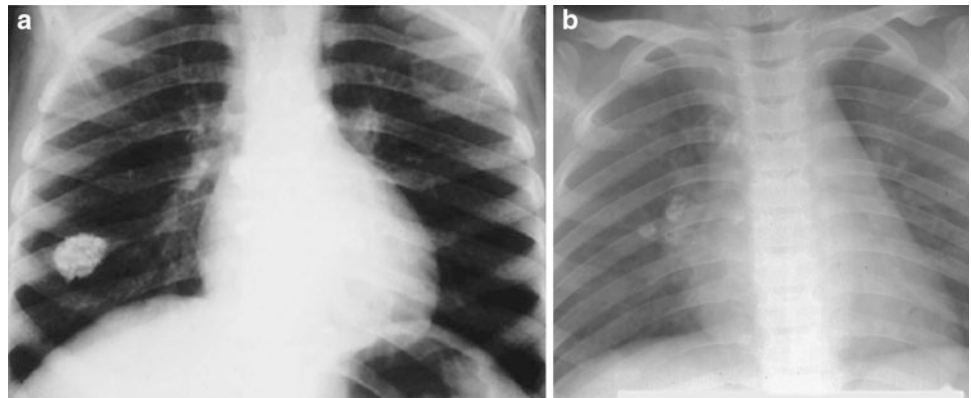
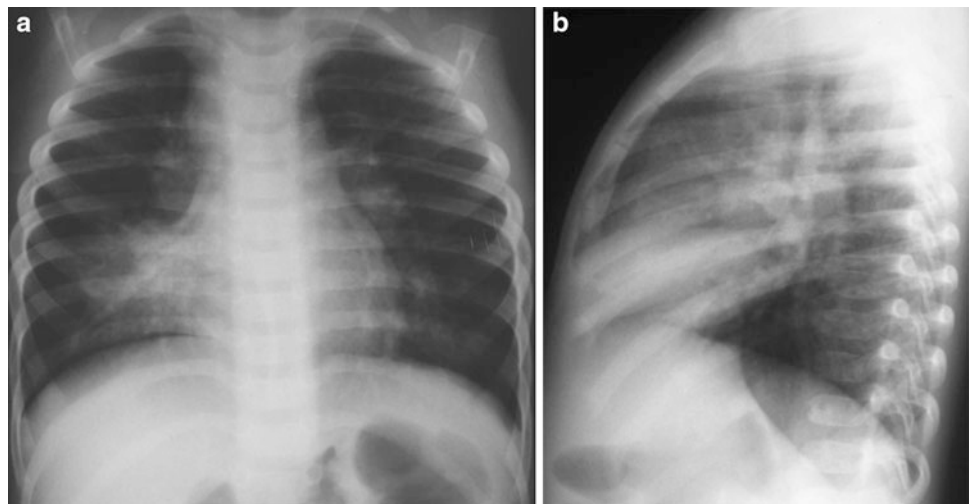


**Fig. 5** **a** Frontal and **b** lateral views of the chest on a 3-year-old child with chronic cough, fever, and positive tuberculin skin test showing right middle lobe opacity compatible with Ghon focus progression. Bilateral perihilar fullness represents concomitant lymphadenopathy



develops secondary to inflammatory changes in the bronchial wall, or from caseous material deposited on the eruption of caseated lymph node into the airway. This

compression can cause bronchial stenosis and lead to hyperinflation in the distal lung secondary to air trapping, or completely occlude an airway and produce lung collapse.

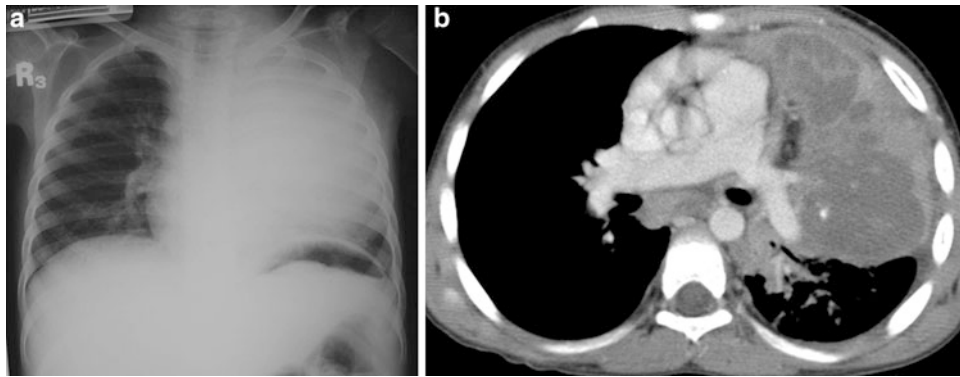


**Fig. 6** **a** Chest X-ray reveals complete opacification of the left upper lobe in this 9-year-old malnourished boy with TB disease. **b** Contrast-enhanced CT scan in axial view demonstrates consolidation of the left

upper lobe with low density areas of non-enhancement compatible with necrosis and early liquefaction. Prominent lymph nodes are seen in the subcarinal region

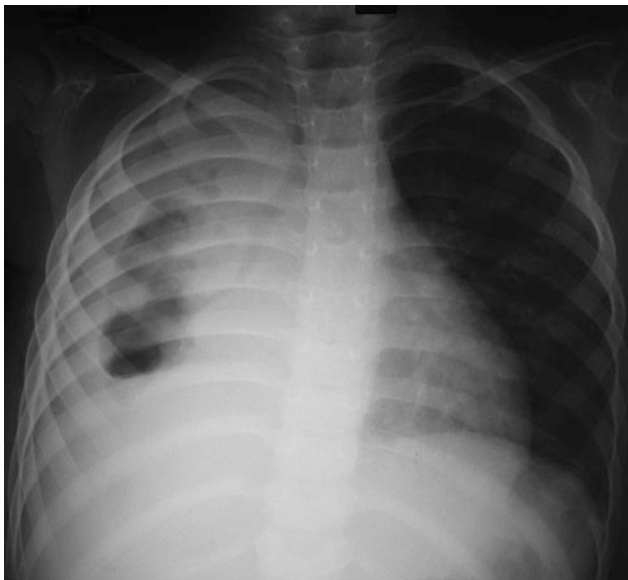


**Fig. 7** Completely opacified right lung with a large cavity communicating with the right bronchus



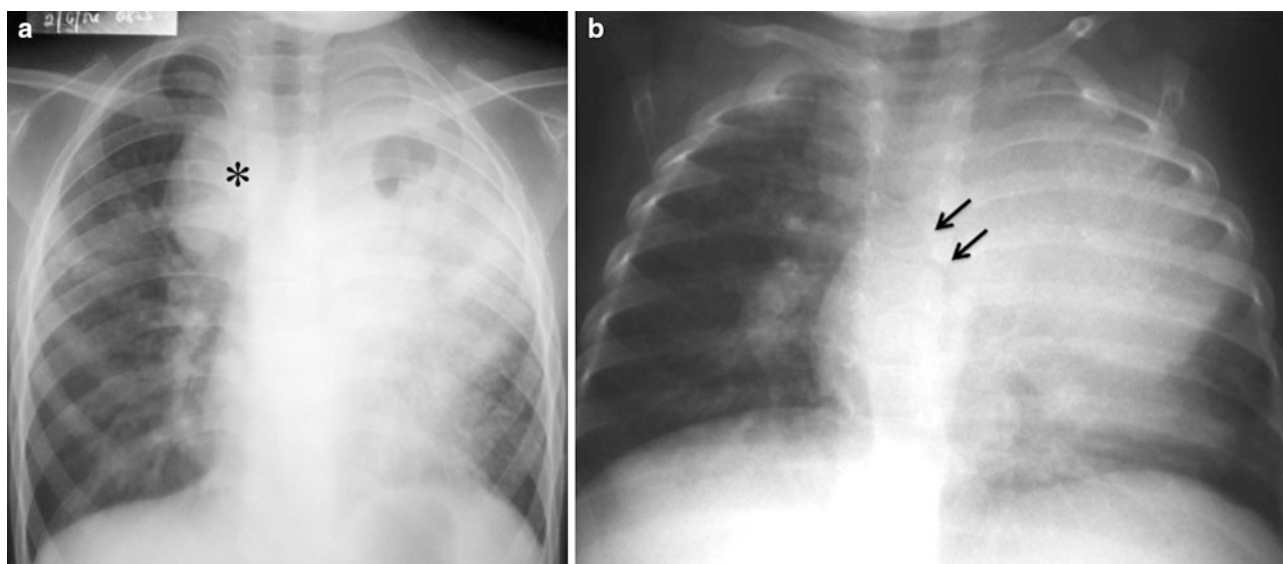
**Fig. 8** A large peripherally located cyst in the left hemithorax in a 3-year-old diagnosed with TB disease

On chest plain films lymphadenopathy usually presents as asymmetrically distributed paratracheal, hilar and/or subcarinal lobulated nodes with sharp or ill-defined borders. The enlarged lymph nodes can compress and stretch the bronchi, or compress and displace the trachea (Fig. 9). Sub-carinal lymph node involvement can cause splaying of the mainstem bronchi. Shift of the mediastinum may not occur because of the fixed nature of these lymph nodes (Inselman 1996).

Lymphadenopathy is not always easy to detect on conventional radiographs and CT has a higher sensitivity. On contrast-enhanced CT, TB lymphadenopathy, especially when nodal size exceeds 2 cm in diameter, may have a characteristic appearance consisting of central areas of low attenuation with peripheral rim enhancement and obliteration of perinodal fat. Calcification within the nodes is seen

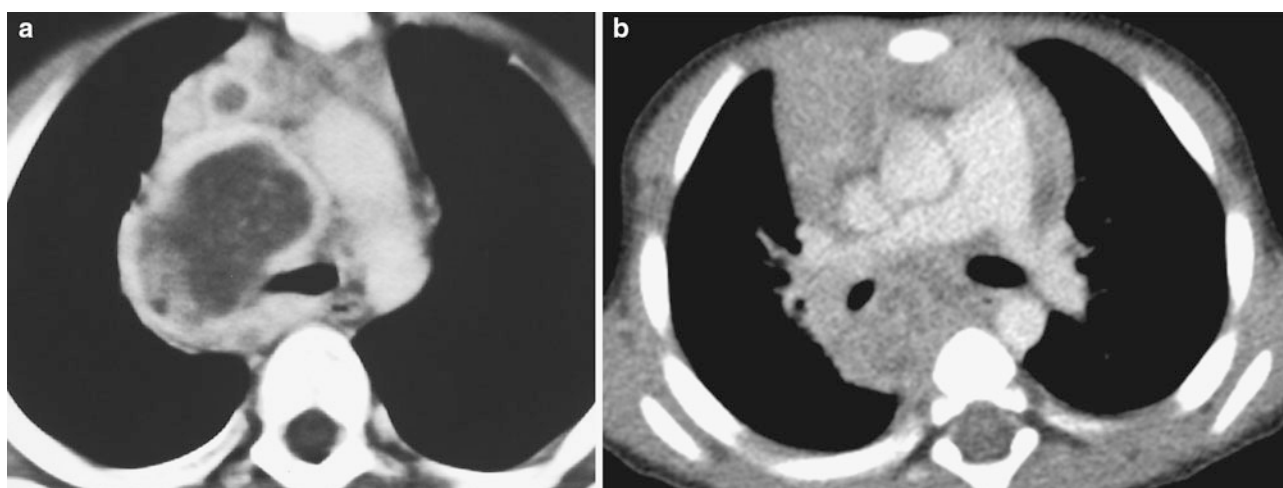
in 15 % (Kim et al. 1997). Another study shows a ghost-like pattern of enhancement of enlarged lymph nodes (Andronikou et al. 2004) (Figs. 10, 11). A study comparing CT and fiberoptic tracheobronchoscopy (FOT) in children with pulmonary TB showed lymph node enlargement resulting in extrinsic compression of the central airways in 86 %. It also showed that CT is 92 % sensitive and 85 % specific in the detection of the degree of airway narrowing as compared to FOT bronchoscopy (Du Plessis et al. 2009) (Fig. 12).

Bronchopneumonic consolidation could result from intrabronchial spread of a parenchymal cavity with a high organism load or after eruption of a caseated lymph node with variable organism load into the bronchial tree. The radiographic pattern shows large irregular patchy infiltration usually involving more than one lobe of a single lung



**Fig. 9** **a** Frontal view chest X-ray of a child with primary progressive TB demonstrating significantly enlarged nodes in the right paratracheal region (*asterisk*) effacing the trachea to the left. There is also

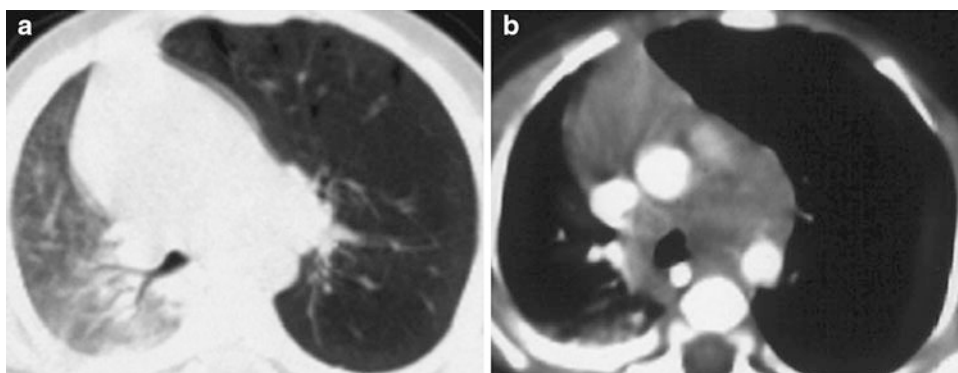
progression of lung parenchymal disease with cavitation on the left upper lobe. **b** Chest X-ray of an 18-month-old boy with enlarged left perihilar lymph nodes effacing the left bronchus (*arrows*)



**Fig. 10** Contrast-enhanced CT scan demonstrating appearance of TB lymphadenopathy. **a** Enlarged right perihilar lymph node with central low attenuation and peripheral contrast enhancement. **b** Enlarged

subcarinal lymph nodes widening the carinal angle, displaying a heterogeneous ghost-like pattern of enhancement

**Fig. 11** **a, b** CT of a 4-month-old boy with obstructive emphysema of the left lung caused by hilar adenopathy





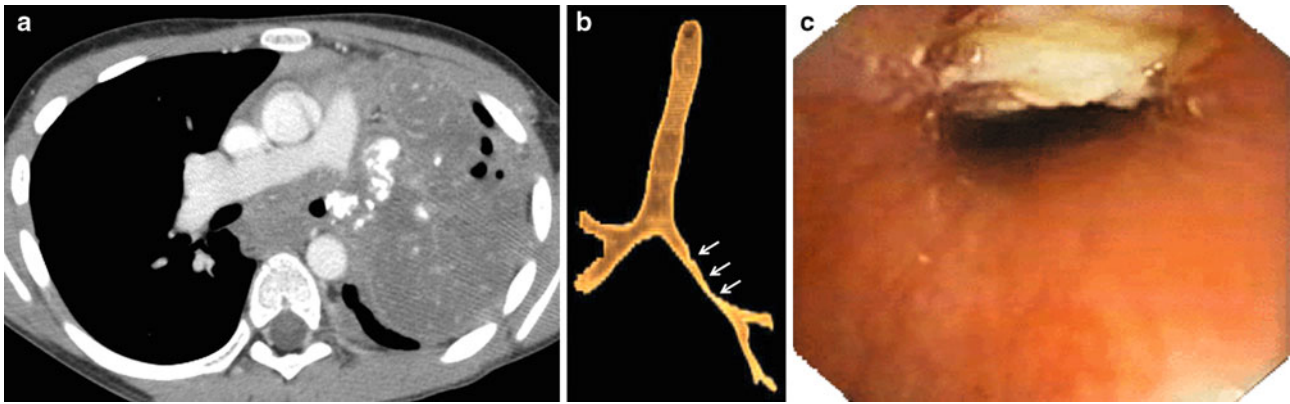


**Fig. 12** **a** Axial CT image showing subcarinal and calcified left hilar adenopathy eroding into the left main bronchus. **b** CT external surface 3D reconstruction shows irregular narrowing of the left bronchus.

**c** Corresponding image from fiberoptic bronchoscopy shows the caseating lymph node eroding into the bronchus. Courtesy of Dr. Marion O. Sanchez; St. Luke's Medical Center, Philippines

(Lamont et al. 1986; Marais et al. 2004a). On CT, this will manifest as poorly defined nodules or rosettes of nodules, 2–10 mm in diameter that can be identified as centrilobular or branching centrilobular opacities mimicking the “tree in bud” image. Coalescence of the centrilobular opacities results in focal areas of bronchopneumonia (Webb et al. 1996). Extensive bronchogenic spread can cause other patterns, such as pulmonary consolidation, or multiple nodules throughout the lungs (Fig. 13).

Expansile pneumonia is due to lymph node eruption into a bronchus with distal aspiration of caseous material into the affected segment or lobe. The result is a consolidation due to viable mycobacterial organisms and tuberculo-protein along with allergic response. This was also referred to as allergic consolidation or Epi-tuberculosis. These children are ill, with high fever, acute respiratory symptoms, and even hemoptysis. Secondary bacterial infection often complicates the clinical picture. Chest radiograph shows a dense consolidation, mostly the upper lobes with bulging fissures (Fig. 14). Enlarged lymph nodes are usually present but are obscured on the radiographs. CT scan picture shows mostly homogeneous opacification with areas of necrotic liquefaction, along with mediastinal lymph nodes (Goussard et al. 2004).

### 6.2.3 Disseminated (Miliary) Disease

Miliary spread complicating the primary infection occurs most often in infants and small children, usually no later than 3–6 months after the infection. The organs most commonly seeded are the lungs, liver, spleen, meninges, peritoneum, lymph nodes, pleura, and bones. Pulmonary dissemination leads to the formation of pulmonary nodular interstitial granulomas, usually 1–2 mm in size, widely disseminated throughout the lungs.

Chest radiographs demonstrate the usual miliary nodular pattern but the nodules maybe too small and difficult to recognize. The nodules can also be numerous that they seem

to form larger nodules greater than 2 mm or even appear as consolidation with air bronchograms. CT is more sensitive than chest X-ray for the detection of miliary TB (Kim et al. 1997), which shows numerous small, well defined, non-calcified nodules of up to several millimeters in diameter uniformly distributed throughout the lungs. A random distribution of nodules with respect to the lobule is observed (Webb et al. 1996; Marais et al. 2004b). In addition, CT can reveal hilar or mediastinal lymph nodes and occasionally small pleural effusions (Oh et al. 1994; Kwong et al. 1996). Exceptionally, pulmonary involvement by the miliary nodules will be asymmetrical. Brain involvement is common in miliary TB (Schuit 1979), and therefore head CT scan should be performed in all children with miliary TB especially if there are neurological symptoms (Fig. 15).

### 6.2.4 Pleural Disease

Tuberculous pleural effusion results from rupture of a subpleural lesion into the pleural space, spread from caseous lymph nodes or an adjacent spinal lesion (Hulnick et al. 1983). In primary TB, effusions develop 3–6 months after infection and believed to result from hypersensitivity response to a small amount of tuberculo-protein released into the pleural space. Pleural fluid will yield positive cultures in only 20–40 % (Fonseca-Santos 2005). Tuberculous pleural effusion is infrequent in children under 6 years of age and rare in those under 2. The prevalence of effusion increases with age and is reported to be 6–11 % in children and 29–38 % in adults (Leung 1999). The fluid is usually unilateral to the primary parenchymal lesion, but may occur in both pleural spaces with bilateral primary complexes and with miliary dissemination (Inselman 1996). Chronic TB empyema is persistent and grossly purulent pleural fluid containing numerous tubercle bacilli, which remain dormant within the pleural space (Moon et al. 1999).

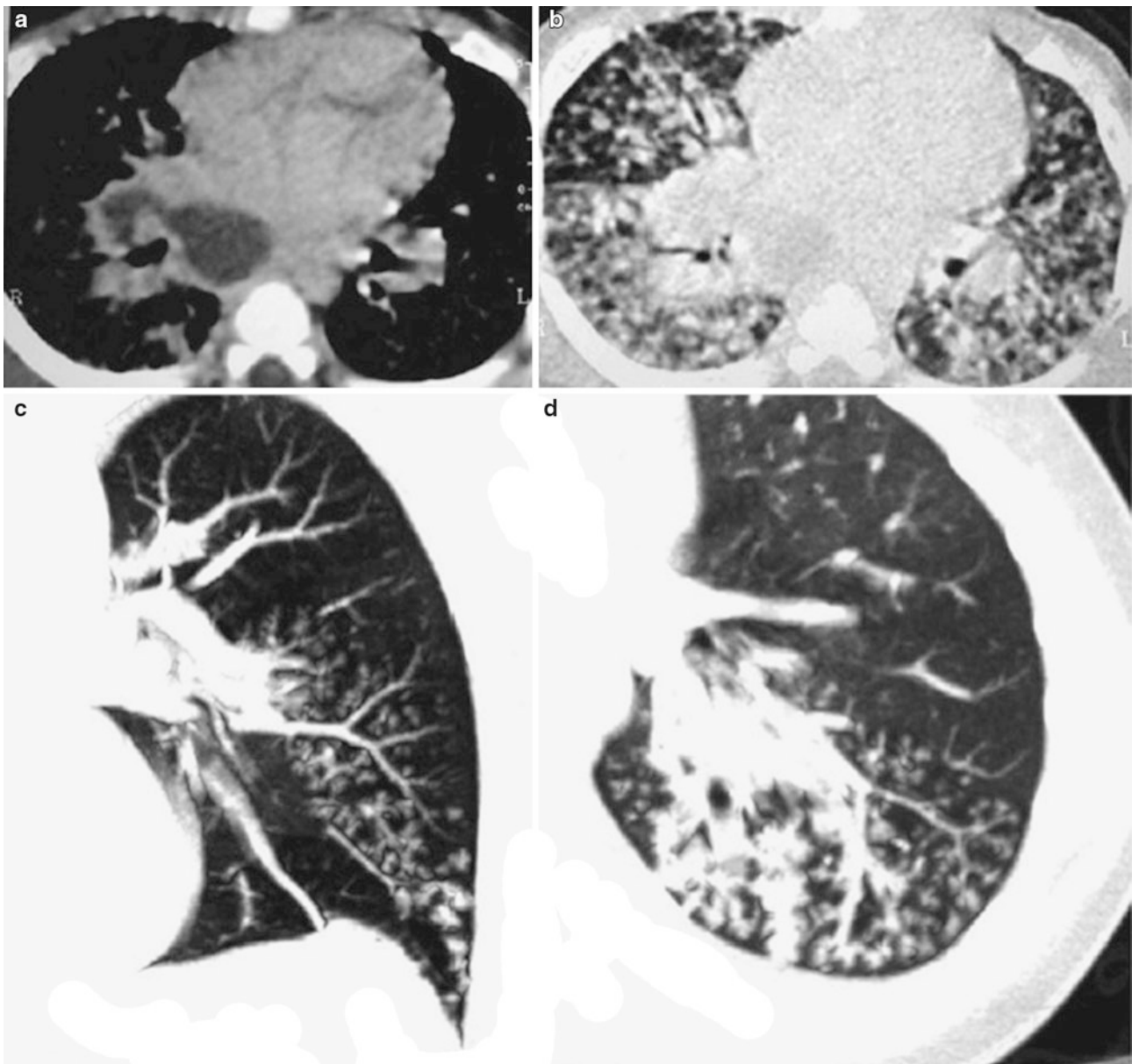


**Fig. 13** Unenhanced CT (mediastinal window) (a) in a 6-month-old boy shows right hilar lymph node with hypodense center (caseum) with fistulous tract to the right main bronchus, causing bronchogenic spread with multiple pulmonary nodules of different sizes (b). CT scan

of a 7-year-old boy, MIP reconstructed images reveals bronchogenic spread with tree-in-bud pattern (c). Note the secondary pulmonary lobule and centrilobular opacities (d)

Chest X-ray appearance of TB pleural effusion is not particularly different from that caused by other etiologies. It varies in size from small to massive, and is sometimes difficult to exclude lesions in the lung. Loculated effusion or empyema can be confused with an intrapulmonary mass on radiographs. The CT features of complicated pleural TB in children are pleural thickening, enhancement, and pleural fluid collection with associated parenchymal abnormalities

and lymphadenopathy (Moon et al. 1999). Pleural calcification can also be seen (Fig. 16).

#### 6.2.5 Pericardial Disease

Pericarditis and pericardial effusion are complications resulting from secondary extension of infected peribronchial nodes to the pericardium (Andronikou et al. 2004). Chest X-ray may show cardiac shadow enlargement with a



**Fig. 14** Frontal chest X-ray of a 4-year-old girl with TB disease shows a dense expansile consolidation of the right upper and middle lobes. Presence of tracheal and right bronchial effacement is also indicative of underlying lymphadenopathy

suggestive globular appearance. Ultrasound is a sensitive way to confirm the diagnosis and assess sequelae including constrictive pericarditis (Marais 2008). CT or MRI can quantitate and characterize the pericardial fluid, but can also characterize the thickness and irregularity of the affected pericardium (Fig. 17).

### 6.2.6 Congenital Tuberculosis

Congenital tuberculosis (CTB) could be defined as an infection due to the *M. tuberculosis* transmitted from the mother to the fetus (Stallworth et al. 1980). It is extremely rare, even in countries with high prevalence of TB, with less than 300 reported cases (Asensi et al. 1990).

Transmission could occur transplacental, with the primary complex developing in the liver, with involvement of periportal lymph nodes and further dissemination to numerous organs. The hypoxic intra-uterine medium avoids the mycobacterium growing, with the lungs being latent until the delivery. As a result, children being infected during the pregnancy can be asymptomatic until 2–4 weeks after the delivery. Another way of transmission is the genital tract of the mother. During the delivery, mycobacterium can be swallowed, resulting in primary complex on the lungs, or the amniotic fluid ingestion could result in gastrointestinal primary complex (Machin et al. 1992). There is also emerging evidence that congenital TB is increasing in the era of TB/HIV co-infection in expectant mothers (Nelson and Wells 2004).

Early diagnosis requires high suspicious level (Myers et al. 1981; Souza et al. 2006). All the newborns with pneumonia unresponsive to the treatment, mostly those with mothers with history of TB and from endemic areas, should be considered at risk for CTB (Resinger et al. 1974). The maternal endometrial biopsy could improve the diagnostic accuracy of CTB (Nemir et al. 1985; Rajiv et al. 2005).

The symptoms can be demonstrated at the birth, but commonly occur during the second and fourth weeks of life. The chest radiographs can be normal during the early infection. However, the lesions are usually progressive and present a miliary pattern. Parenchymal opacities and mediastinal lymph nodes enlargement may also be seen (CDC 2005; Neyaz et al. 2008) (Fig. 18).

The diagnostic criteria for CTB were first proposed by Beitzke in 1935, and further modified by Cantwell and colleagues. They defined the diagnosis of CTB in the patients with at least one of the following: lesions during the first week of life, hepatic primary complex or hepatic granulomas (Fig. 18), confirmation of TB infection on the placenta or genital tract of the mother, and exclusion of post-natal transmission through investigation of contacts, including hospital staff. (Cantwell et al. 1994).

The specific treatment for CTB should be immediately initiated in suspicious cases due to the risk of disease progression and death (Mazade et al. 2001; Souza et al. 2006; Welsoly et al. 2004).

### 6.2.7 Adult Type Disease

Adult type disease results from primary infection, endogenous reactivation, or exogenous reinfection. Adult type disease presentation is common after primary infection in children over 10 years of age. Endogenous reactivation or post-primary TB occurs in patients previously sensitized to *M. tuberculosis* with reactivation of dormant bacilli during periods of immunosuppression, malnutrition, and debilitation. Postprimary TB in the pediatric age group mainly occurs in adolescents. The interval from primary infection to adult type disease is widely variable from 3 month to 20 years and depends mostly on the age at primary infection (Fonseca-Santos 2005). Development of adult type disease from exogenous reinfection is uncommon.

The initial presentation may be a cloudy opacification in the involved lung followed by coalescence and parenchymal breakdown. There is usually cavitation and associated fibrosis. Complications include progressive cavity formation and intrabronchial spread with bronchopneumonic consolidation (Fig. 19) (Marais et al. 2004b).

On chest radiograph, bilateral ill-defined parenchymal disease is common mainly involving the apical segments of the upper lobes, with lower lobe involvement less frequent. Predilection of post-primary TB in the upper lobes is likely due to a combination of factors including the relatively





**Fig. 15** A 10-year-old girl presents fever, shortness of breath and two episodes of seizure. Frontal chest X-ray (**a**) demonstrates innumerable tiny nodules scattered throughout both lungs compatible with military

TB as seen on the axial CT scan (**b**). Gadolinium-enhanced Axial T1 image (**c**) shows several contrast enhancing lesions compatible with multiple tuberculomas on this patient with disseminated TB disease

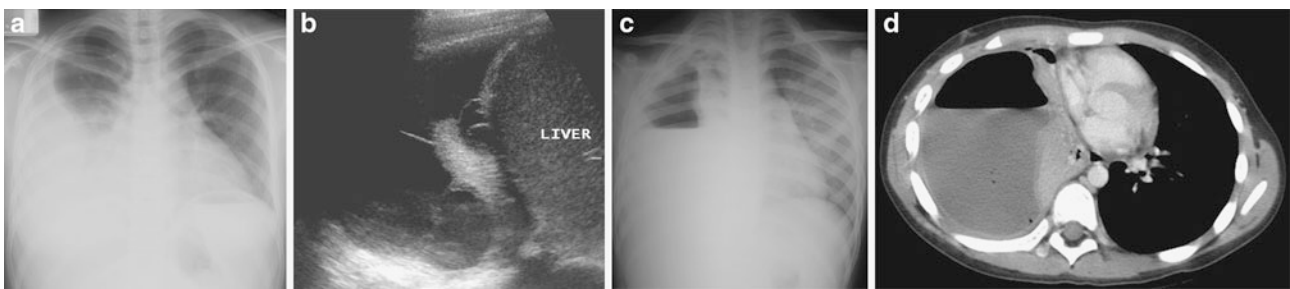
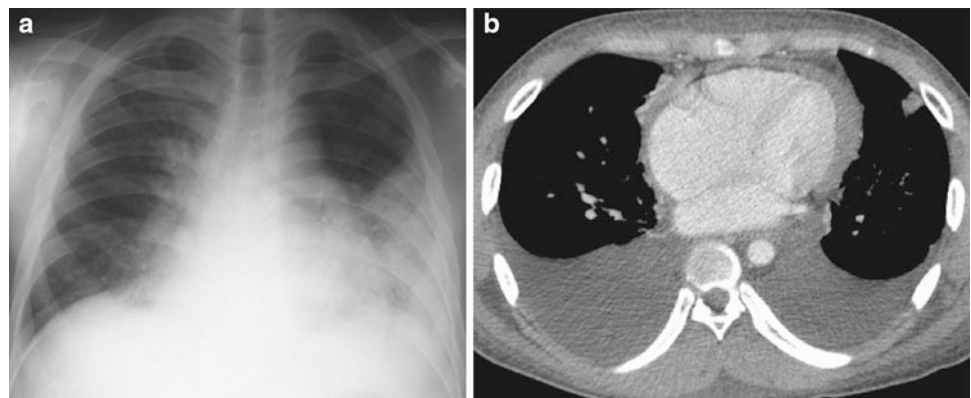


**Fig. 16** Pleural involvement in TB. **a** Chest X-ray reveals a right-sided pleural effusion in a 13-year-old boy. **b** Ultrasound of the right chest reveals a large pleural fluid collection with sediments and fine septations. **c** Chest X-ray on patient being treated for TB demonstrates

large pleural fluid collection on the right with air-fluid levels. **d** Contrast-enhanced axial CT image reveals a thick pleural fluid collection, mildly enhancing pleura and pneumothorax. Aspirated fluid confirms TB empyema

**Fig. 17** **a** Chest X-ray of a 17-year-old male being treated for TB shows a prominent cardiac shadow and bilateral pleural effusion. **b** Contrast-enhanced axial image demonstrate thick pericardium compatible with TB constrictive pericarditis



higher oxygen tension and impaired lymphatic drainage (Fonseca-Santos 2005). It is usually associated with nodular and linear fibrosis radiating from the hilum to the periphery, which can result in distortion of mediastinal and broncho-vascular structures. Cavitation in a single or multiple sites can be seen and air-fluid levels could be present (Leung 1999). Radiographic evidence of original primary infection in the form of calcified lymph node and/or upper lobe fibrotic changes can be seen. Because fibrosis and

calcification can be found in both healed and active disease, radiographic determination of disease status based on their presence is unreliable (Palmer 1979) (Fig. 20).

The lung lesions are often smaller in adolescents than adults and lordotic views or even CT may be necessary to demonstrate small lesions (Starke 1999). The CT findings of post-primary TB include lobular consolidation, cavitation, and bronchial wall thickening. Bronchogenic spread of disease is commonly seen in adult type disease. On CT

**Fig. 18** **a** Unenhanced CT of a 2-month-old boy with bronchogenic spread causing huge parenchymal opacities. **b** Same patient, 3 months later, shows left hilar nodal calcification

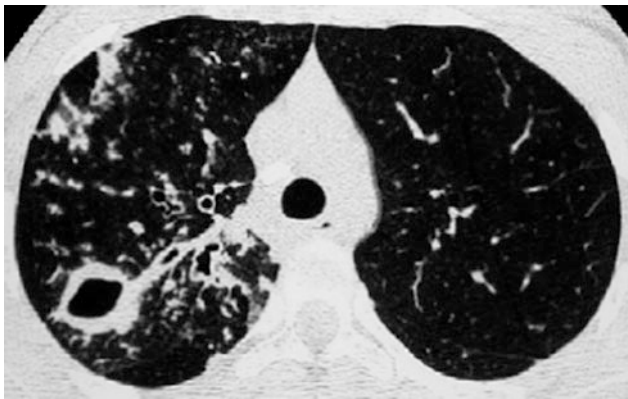
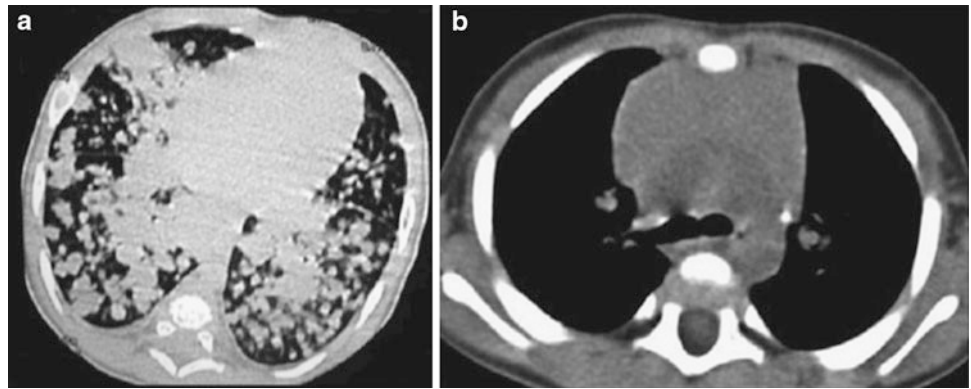


**Fig. 19** A 10-year-old girl with secondary apical tuberculosis. CT demonstrates nodules (some with a hazy halo), ground glass and cavity

scan, it manifests as ill-defined centrilobular nodules and sharply margined linear branching opacities in segmental or lobar distribution. This typical tree-in-bud pattern has been shown to represent caseous necrosis within and around terminal and respiratory bronchioles (Im et al. 1993).

Pleural effusions, which are typically loculated and commonly unilateral in distribution are also observed while hilar and mediastinal lymphadenopathy are uncommon manifestations of post-primary TB. Dissemination during post-primary TB is rare among immunocompetent adolescents, but is very common in HIV-infected or immunocompromised adolescents. Bronchiectasis and progressive cavity formation, which predisposes to colonization with *Aspergillus* species have also been observed (Leung 1999).

### 6.3 Unusual Presentations and Complications

Pneumothorax, hemothorax, and bronchopleural or bronchoesophageal fistulas are unusual complications of pulmonary TB. Aortic rupture, which can result from spread of lymph nodes into the vessel, is even more rare (Inselman 1996). TB infection of the endothoracic fascia is highly

uncommon. It is a peripleuritis caused by peripleural inflammation of the endothoracic fascia (Broglia et al. 2006). The peripleura is a mass of lax cell tissue that supports the parietal pleura in areas corresponding to the chest wall, thorax vertex, and mediastinal-suprahilar region. CT scan can show round images on the front, lateral, and back regions of the thorax, projecting toward the parietal pleura in the corresponding peripleura region (Fig. 21).

Rasmussen aneurysm is an exceedingly unusual complication of TB in children. It corresponds to a pseudoaneurysm caused by erosion of a peripheral pulmonary artery branch by an adjacent tuberculous cavity lesion (Kim et al. 2001). It is almost exclusively seen in advanced pulmonary cavity forms of TB in adults and can occur despite adequate treatment. The typical Rasmussen aneurysm is a peripheral, solitary lesion in the upper lobes, but uncommon presentations can also be seen (Fig. 22).

## 7 Tuberculosis and Human Immunodeficiency Virus Infection

Children with HIV often have other lung disease related to their HIV infection, including infection with *Pneumocystis*, lymphocytic interstitial pneumonitis (LIP), and other viral or bacterial pneumonias. Because of the inherent difficulties of diagnosing TB in young children, this may result in an over-diagnosis of TB in HIV-infected children if the index of suspicion is high. Children with HIV infection can have several lung diseases at the same time. Thus, an HIV-infected child who improves with empiric antibiotics may still have TB. Children with TB and HIV co-infection also appear to have poorer treatment outcomes and higher rates of relapse in several studies (Nelson 2004; Jeena et al. 2002). Early initiation of antiretroviral therapy is the single most important intervention for reducing overall mortality and the risk of TB among HIV-infected infants with isoniazid preventive therapy providing additional benefit (Perez-Velez and Marais 2012).

**Fig. 20** Adult Type TB Disease on two different patients. **a** Chest X-ray on 15-year-old girl reveals a hazy opacity involving the apical segment of the right upper lobe. **b** Chest radiograph of a 13-year-old boy with chronic cough and shortness of breath demonstrates advance TB disease of the right lung with apical fibronodular densities, severe pleural thickening, and decreased right lung volume

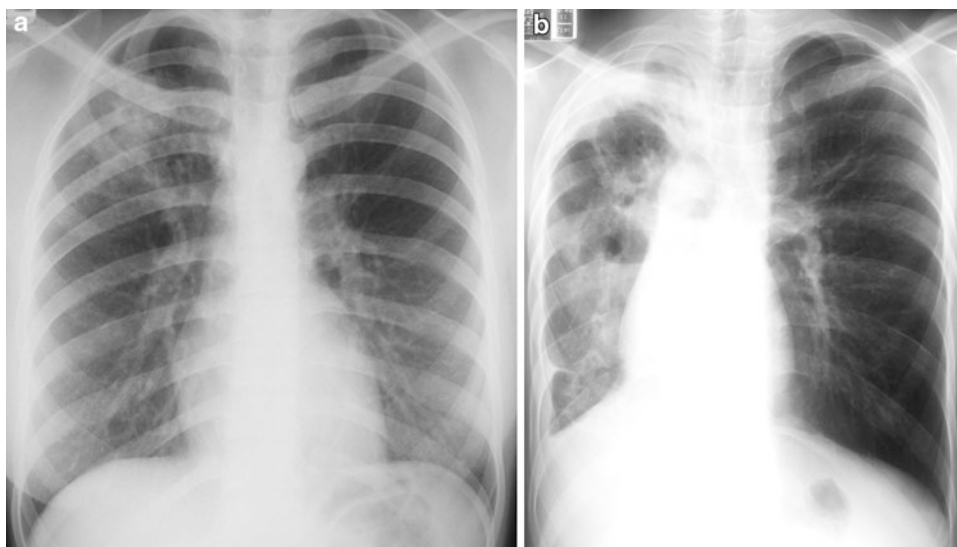


**Fig. 21** Enhanced CT scan of a child showing round contrast enhancing lesions at the anterior and lateral aspect of the right chest wall, projecting toward the parietal pleura

The radiographic manifestations of HIV-associated TB are dependent on the level of immune suppression at the time of overt disease. Patients with relatively intact immune function demonstrate radiographic findings similar to those non-HIV-infected individuals. At severe levels of immune suppression, normal radiographs can be seen but it also demonstrates findings associated with primary disease. Significantly higher prevalence of mediastinal and/or hilar lymphadenopathy and lower prevalence of cavitation is seen in patients with T-lymphocyte count of less than 200/mm<sup>3</sup> (Perlman 1997). Chest radiograph interpretation in children with TB/HIV co-infection is complicated further by co-morbid conditions usually associated with HIV (Marais et al. 2010). CT patterns in HIV seropositive patients include, multiple nodules, tuberculoma, and lymphadenopathy (Leung et al. 1996) (Fig. 23).

The TST was less sensitive and the chest radiography was less specific in HIV-infected patients (Palme et al. 2002). In HIV positive patients, findings of low attenuation nodes are considered sufficient to warrant instituting empirical anti-TB therapy (Pastores et al. 1993).

## 8 Response to Treatment

Treatment response of pulmonary TB is best assessed by means of repeated sputum evaluation in patients with positive bacteriology. In persons with negative pre-treatment sputum and in children in whom bacteriologic confirmation is possible in only one-third of cases, radiographic and clinical evaluation become major indicators of response to therapy. Regression is a slow process and radiographic findings may show worsening in the first 3 months of treatment, which may be related to hypersensitivity reaction that normally occurs 2–10 weeks after initial infection. Resolution of parenchymal abnormalities has been observed from 6 months to 2 years on radiographs and up to 15 months on CT scans. Lymphadenopathy may persist for several years after treatment (Leung et al. 1992).

## 9 Conclusions

Diagnosis of pulmonary TB presents a continuing challenge to pediatricians and radiologists. Careful clinical history, tuberculin skin testing, and chest radiography remain the basic elements for establishing diagnosis. Chest US, MRI, and particularly chest CT can provide information not available with conventional imaging, and thereby clarify diagnosis and influence therapy.



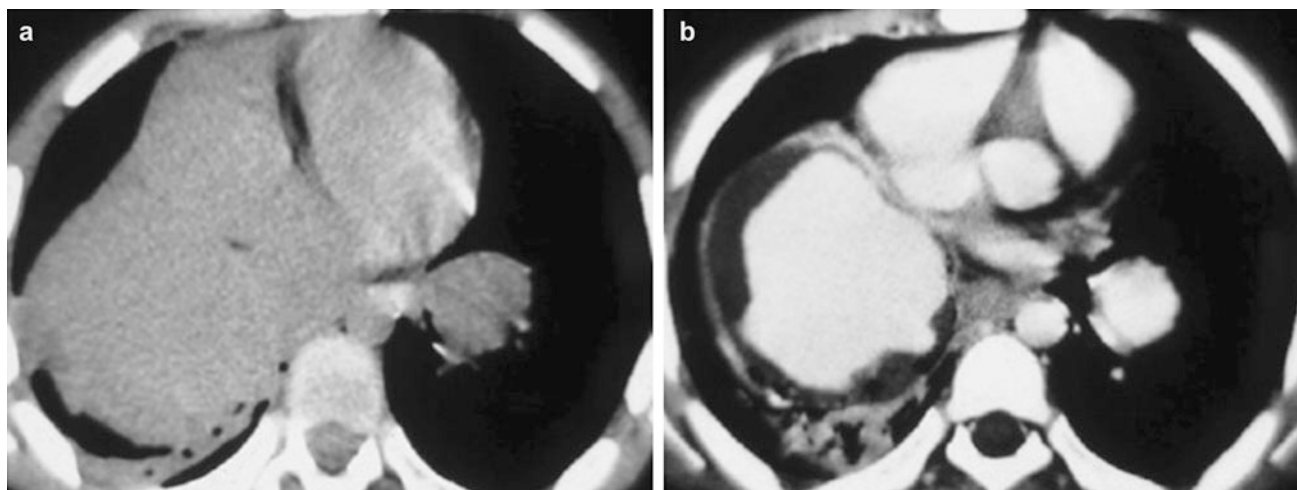


**Fig. 22** **a** Unenhanced CT performed in an 11-year-old girl demonstrates extensive opacity in the right hemithorax and a small nodular lesion on the left side. **b** Following contrast enhancement, opacification of a huge right pulmonary artery with peripheral thrombus can be

seen. There is a smaller aneurysmal dilatation of the left pulmonary artery. The patient died 15 days later due to severe hemoptysis (Courtesy of Dr. Alexandre Kalil; Hospital São Rafael, Salvador, Brazil)

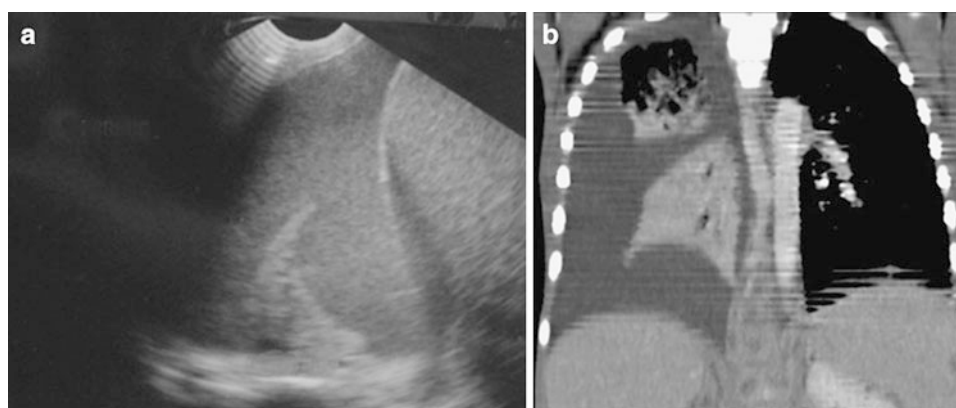


**Fig. 23** Tuberculosis in an HIV-positive 4-year-old girl. **a** US and **b** coronal MPR CT images show right-side chylothorax caused by erosion of the thoracic duct by several adjacent thoracic-abdominal

lymph nodes with intense peripheral enhancement. Reprinted with permission courtesy of Daltro et al. (2011)

## References

- Andronikou S, Joseph E, Lucas S et al (2004) CT scanning for the detection of tuberculous mediastinal and hilar lymphadenopathy in children. *Pediatr Radiol* 34:232–236
- Asensi F, Otero MC, Perez-Tamarit D et al (1990) Congenital tuberculosis, still a problem. *Pediatr Infect Dis J* 9:223–224
- Bosch-Marcet J, Serres X, Zuasnarab A et al (2004) Comparison of ultrasound with plain radiography and CT for the detection of mediastinal lymphadenopathy in children with tuberculosis. *Pediatr Radiol* 34:895–900
- Broglia B, Bisero E, Sclavo L, Andreozzi P (2006) Tuberculosis of the Endothoracic Fascia. *Pediatr Pulmonol* 41:441–444
- Cantwell MF, Shehab ZM, Costello AM et al (1994) Brief report: congenital tuberculosis. *N Engl J Med* 330:1051–1054
- CDC Centers for Disease Control and Prevention (2005) Congenital pulmonary tuberculosis associated with maternal cerebral tuberculosis, Florida, 2002. *MMWR Morb Mortal Wkly Rep* 54(10):249–250
- Coovadia HM, Jeena P, Wilkinson D (1998) Childhood human immunodeficiency virus and TB co-infections: reconciling conflicting data. *Int J Tuberc Lung Dis* 2:844–851
- Cremin BJ, Jamieson DH (1995) Imaging of pulmonary tuberculosis. In: Cremin BJ, Jamieson DH (eds) *Childhood tuberculosis: modern imaging and clinical concepts*. Springer, Berlin, pp 19–50
- Curtis AB, Ridzon R, Vogel R et al (1999) Extensive transmission of *Mycobacterium tuberculosis* from a child. *N Engl J Med* 341:1491–1495

- Daltro P, Santos EN, Gasparetto TD et al (2011) Pulmonary infections. *Pediatr Radiol* 41(Suppl 1):S69–S82
- Dannenbergh AM Jr (1999) Pathophysiology: basis aspects. In: Schlossberg D (ed) *Tuberculosis and nontuberculous mycobacterial infections*, 4th edn. Saunders, Philadelphia, pp 17–47
- De Villiers RVP, Andronikou S, Van de Westhuizen S (2004) Specificity and sensitivity of chest radiographs in the diagnosis of paediatric pulmonary tuberculosis and the value of additional high-kilovolt radiographs. *Australas Radiol* 48:148–153
- Dominguez J, Latorre I, Altet N, Mateo L, de Souza-Galvão M, Ruiz-Manzano J, Ausina V (2009) Interferon-gamma release assays to diagnose tuberculosis infection in the immunocompromised individual. *Expert Rev Respir Med* 3(3):309–327
- Du Plessis J, Goussard P, Andronikou S et al (2009) Comparing three-dimensional volume rendered CT images with fiberoptic tracheobronchoscopy in the evaluation of airway compression caused by TB lymphadenopathy in children. *Pediatr Radiol* 39:694–702
- Dutt AK, Stead WW (1999) Epidemiology and host factors. In: Schlossberg D (ed) *Tuberculosis and nontuberculous mycobacterial infections*, 4th edn. Saunders, Philadelphia, pp 3–16
- Ehlers S (1999) Immunity to tuberculosis: a delicate balance between protection and pathology. *FEMS Immun Med Microbiol* 23:149–158
- Feja K, Saiman L (2005) Tuberculosis in children. *Clin Chest Med* 26:295–312
- Fonseca-Santos J (2005) Tuberculosis in children. *Eur J Radiol* 55:202–208
- Goussard P, Gie RP, Kling S, Beyers N (2004) Expansile pneumonia in children caused by *Mycobacterium tuberculosis*: clinical, radiological, and bronchoscopic appearances. *Pediatr Pulmonol* 38:451–455
- Hulnick DH, Naidich DP, McCauley DI (1983) Pleural tuberculosis evaluated by computed tomography. *Radiology* 149:759–765
- Im JG, Itoh H, Sim Y et al (1993) Pulmonary tuberculosis: CT findings—early active disease and sequential change with antituberculous therapy. *Radiology* 186:653–660
- Inselman LS (1996) Tuberculosis in children: an update. *Pediatr Pulmonol* 21:101–120
- Jeena PM, Pillay P, Pillay T et al (2002) Impact of HIV-1 co-infection on presentation and hospital-related mortality in children with culture proven pulmonary tuberculosis in Durban, South Africa. *Int J Tuberc Lung Dis* 6(8):672–678
- Kim WS, Moon WK, Kim IO et al (1997) Pulmonary tuberculosis in children: evaluation with CT. *AJR* 168:1005–1009
- Kim HY, Song KS, Goo JM et al (2001) Thoracic sequelae and complications of tuberculosis. *Radiographics* 21(4):839–858
- Klein M, Iseman MD (1999) *Mycobacterial infections*. In: Taussig LM, Landau LI (eds) *Pediatric respiratory medicine*. Mosby, St Louis, pp 702–732
- Kwong JS, Carignan S, Kang E, Muller NL, Fitzgerald JM (1996) Miliary tuberculosis: diagnostic accuracy of chest radiography. *Chest* 110:339–342
- Lamont AC, Cremin BJ, Pelteret RM (1986) Radiological patterns of pulmonary tuberculosis in the pediatric age group. *Pediatr Radiol* 16:2–7
- Leung AN (1999) Pulmonary tuberculosis: the essentials. *Radiographics* 210:307–322
- Leung AN, Muller NL, Pinerda PR, Fitzgerald JM (1992) Primary tuberculosis in childhood: radiographic manifestations. *Radiology* 182:87–91
- Leung AN, Brauner MW, Gamsu G et al (1996) Pulmonary tuberculosis: comparison of CT findings in HIV-seropositive and HIV-seronegative patients. *Radiology* 198:68–691
- Machin GA, Honoré LH, Fanning EA, Molesky M (1992) Perinatally acquired neonatal tuberculosis: report of two cases. *Pediatr Pathol* 12:707–716
- Maier D, Raviglione MC (1999) The global epidemic of tuberculosis: a World Health Organization Perspective. In: Schlossberg D (ed) *Tuberculosis and nontuberculous mycobacterial infections*, 4th edn. Saunders, Philadelphia, pp 104–115
- Mandalakas AM, Starke JR (2005) Current concepts of childhood tuberculosis. *Semin Pediatr Infect Dis* 16:93–104
- Marais BJ (2008) State of the Art series: global pediatric pulmonary issues—tuberculosis in children. *Pediatr Pulmonol* 43:322–329
- Marais BJ, Gie RP, Schaaf HS, Hesselning AC et al (2004a) The natural history of childhood intrathoracic tuberculosis: a critical review of prechemotherapy literature. *Int J Tuberc Lung Dis* 8:392–402
- Marais BJ, Gie RP, Schaaf HS, Starke JR et al (2004b) A proposed radiological classification of childhood intrathoracic tuberculosis. *Pediatr Radiol* 34:886–894
- Marais BJ, Rabie H, Cotton MF (2010) TB and HIV in children—advances in prevention and management. *Paediatr Respir Rev* 12:39–45
- Matsaniotis N, Kattamis C, Economou-Mavrou C et al (1967) Bullous emphysema in childhood tuberculosis. *J Pediatr* 71:703–707
- Mazade MA, Evans EM, Starke JR et al (2001) Congenital tuberculosis presenting as sepsis syndrome: case and review of the literature. *Pediatr Infect Dis J* 20:439–442
- Moon WK, Kim WS, Kim IO (1999) Complicated pleural tuberculosis in children: CT evaluation. *Pediatr Radiol* 29:153–157
- Moulding T (1999) Pathogenesis, pathophysiology, and immunology: clinical orientations. In: Schlossberg D (ed) *Tuberculosis and nontuberculous mycobacterial infections*, 4th edn. Saunders, Philadelphia, pp 48–56
- Myers JP, Perlstein PH, Light IJ, Towbin RB, Dinesoy HP, Dinesoy MY (1981) Tuberculosis in pregnancy with fatal congenital infection. *Pediatrics* 67:9–94
- Nelson LJ, Wells CD (2004) Global epidemiology of Childhood TB. *Int J Tuberc Lung Dis* 8(5):536–647
- Nemir RL, O'Hare D (1985) Congenital tuberculosis. Review and diagnostic guidelines. *Am J Dis Child* 139:139–287
- Neyaz Z, Gadodia A, Gamanagatti S et al (2008) Imaging findings of congenital tuberculosis in three infants. *Singap Med J* 49(2):e42–e46
- Oh YW, Kim YH, Lee NJ et al (1994) High-resolution CT appearance of miliary tuberculosis. *J Comput Assist Tomogr* 18:862–866
- Onur H, Hatipoglu S, Arica V et al (2012) Comparison of quantiferon test with tuberculin skin test for the detection of tuberculosis infection in children. *Inflammation* 35(4):1518–1524. doi: 10.1007/s10753-012-9466-1
- Palme IB, Gudetta B, Bruchfield J et al (2002) Impact of human immunodeficiency virus-1 infection on clinical presentation, treatment outcome, and survival in a cohort of Ethiopian children with tuberculosis. *Pediatr Infect Dis J* 21:1053–1061
- Palmer PES (1979) Pulmonary tuberculosis: usual and unusual radiographic presentations. *Semin Roentgenol* 12:204–243
- Pastores SM, Naidich DP, Aranda CP et al (1993) Intrathoracic adenopathy associated with pulmonary tuberculosis in patients with human immunodeficiency virus infection. *Chest* 103:1433–1437
- Perez-Velez CM, Marais BJ (2012) Tuberculosis in children: current concepts. *N Engl J Med* 367:348–361
- Perlman DC, El-Sadr WM, Nelson ET et al (1997) Variation of chest radiographic patterns in pulmonary tuberculosis by degree of human immunodeficiency virus related immune suppression. *Clin Infect Dis* 25:242–246
- Ravij K, Nomeeta G, Arvind S et al (2005) Congenital tuberculosis. *Indian J Pediatr* 72:631–633
- Resinger KS, Evans P, Yost G, Rogers KD (1974) Congenital tuberculosis: report of a case. *Pediatrics* 54:74–76
- Schaaf HS, Gie RP, Kennedy M, Eyers N, Hesselning PB, Donald PR (2002) Evaluation of young children in contact with adult

- multidrug-resistant pulmonary tuberculosis: a 30-Month Follow-up. *Pediatrics* 109:765–771
- Schuit KE (1979) Miliary tuberculosis in children. Clinical and laboratory manifestations in 19 patients. *Am J Dis Child* 133:583–585
- Smuts NA, Beyers N, Gie RP et al (1994) Value of lateral chest radiograph in tuberculosis in children. *Pediatr Radiol* 24(7):478–480
- Souza ELS, Moreira LMO, Silva MF (2006). Perinatal tuberculosis: a diagnostic challenge. *BJID* 10:228–229
- Stallworth JR, Brasfield DM, Tiller RE (1980) Congenital miliary tuberculosis proved by open lung biopsy specimen and successfully treated. *Am J Dis Child* 134:320–321
- Starke JR (1999) Tuberculosis in infants and children. In: Schlossberg D (ed) *Tuberculosis and nontuberculous mycobacterial infections*, 4th edn. Saunders, Philadelphia, pp 303–324
- Swaminathan S, Raghavan A, Datta M et al (2005) Computerized tomography detects pulmonary lesions in children with normal radiographs diagnosed to have tuberculosis. *Indian Pediatr* 42:258–261
- Swingler GH, Du Toit G, Andronikou S et al (2005) Diagnostic accuracy of chest radiography in detecting mediastinal lymphadenopathy in suspected pulmonary tuberculosis. *Arch Dis Child* 2005(90):1153–1156
- Van Hest R, De Vries G, Morbano G et al (2004) Cavitating tuberculosis in an infant: case report and literature review. *Pediatr Infect Dis J* 23(7):667–670
- Webb R, Muller N, Naidich D (1996) *High resolution CT of the lung*, 2nd edn. Lippincott-Raven, Philadelphia
- Welsoly DL, Khan AM, Elidemir O et al (2004) Congenital tuberculosis requiring extracorporeal membrane oxygenation. *Pediatr Pulmonol* 37:470–473
- World Health Organization, Global Tuberculosis Report (2012a) The burden of disease caused by TB. World Health Organization, Geneva, WHO/HTM/TB/2012.6
- World Health Organization, Global Tuberculosis Report (2012b) Drug resistant TB. World Health Organization, Geneva, WHO/HTM/TB/2012.6



---

# Foreign Body Aspiration: Imaging Aspects

Benjamin Z. Koplewitz and Jacob Bar-Ziv

## Contents

1	Introduction.....	306
2	Etiology/Types of Foreign Bodies.....	306
3	Mechanisms of Airway Obstruction.....	310
4	Clinical Findings and Differential Diagnosis.....	312
5	Imaging Techniques .....	313
6	Imaging Findings .....	317
7	Complications.....	318
8	Conclusion .....	321
	References.....	321

---

## Abstract

Foreign body aspiration is the most frequent pediatric domestic accident, and has serious and sometimes fatal sequelae. Most cases occur under the age of 4 years. The history of choking followed by persistent cough is the most reliable clue for the diagnosis, but many patients present with various nonspecific clinical symptoms. When the history of a foreign body aspiration is definite, bronchoscopy is the modality of choice for both diagnosis and management. In the absence of such a history diagnosis can be overlooked, and many children present with unresolved pneumonia, atelectasis, or other complications. The role of the radiologist in such cases is not only to confirm a clinically suspected diagnosis, but also to suggest the diagnosis in patients with nonspecific clinical symptoms and radiologic features that could be related to long-standing foreign bodies. Many clinical and imaging findings are the result of a one-way obstruction mechanism. A normal inspiratory chest radiograph does not rule out a foreign body. Expiratory films are important to demonstrate air-trapping. The high kilo-voltage (kV) copper filter technique is valuable for demonstrating a nonopaque foreign body, and fluoroscopy can be very useful. Computed Tomography (CT) has become more valuable by virtue of its wide availability, high resolution, and the multiplanar, three-dimensional and additional image reconstruction capabilities. CT can indicate the exact location of a foreign body, suggest alternative diagnoses, and can demonstrate any associated complications. The role of other imaging modalities is not as well established. An understanding of the mechanisms of obstruction and their resultant clinical and imaging manifestations, can lead to earlier diagnosis and lower the complication rate. This chapter discusses imaging techniques and findings related to the various types and mechanisms of obstruction and to the complications of foreign body aspiration.

---

B. Z. Koplewitz (✉) · J. Bar-Ziv  
Department of Medical Imaging,  
Hadassah-Hebrew University Medical Centre,  
POB 12000, 91120, Jerusalem, Israel  
e-mail: BenjaminK@hadassah.org.il; ben\_kop@hadassah.org.il

## 1 Introduction

Aspiration of foreign bodies into the respiratory tract can occur at any age, but is most common in young children and in the elderly population. Foreign body aspiration is the most frequent pediatric domestic accident, and has serious and sometimes fatal sequelae (Black et al. 1984; Fitzpatrick and Guarisco 1998; Bhana et al. 2000; Ciftci et al. 2003; Qureshi and Mink 2003; Li et al. 2009; Gang et al. 2012; Pan et al. 2012; Foltran et al. 2013; Bamber et al. 2013). Most cases occur under the age of 4 years (Mantel and Butenandt 1986; Esclamado and Richardson 1987; Piepsz 1988; Schmidt and Manegold 2000; Oguz et al. 2000; Lima and Fischer 2002; Roda et al. 2008; Kitcher 2009; de Sousa et al. 2009; Tang and Chen 2009; Goktas et al. 2010; Orji and Akpeh 2010; Paksu et al. 2012; Pan et al. 2012; Boufersaoui et al. 2013). When the history of a foreign body aspiration is definite, bronchoscopy is the modality of choice for both diagnosis and management (Cohen et al. 2009; Ezer et al. 2011; Mortellaro et al. 2013; Samkani et al. 2013). Until recently, rigid or flexible bronchoscopy was used for diagnosis, while removal of foreign bodies was carried out by rigid bronchoscopy only (Friedman 2000; Lima and Fischer 2002; Ayed et al. 2003; Ciftci et al. 2003; Lima et al. 2008; Cohen et al. 2009; Albirmawy and Elsheikh 2011). With the advance of technology, removal of foreign bodies can now be done by flexible bronchoscopy, which is a shorter and safer procedure (Swanson and Edell 2001; Tang et al. 2006; Zhijun et al. 2008; Rodrigues et al. 2012a; Falase et al. 2013). The complication rate of bronchoscopy varies between 1 and 8 % (Black et al. 1984; Steen and Zimmermann 1990; Zerella et al. 1998; Zaytoun et al. 2000; Ayed et al. 2003; Ciftci et al. 2003; Cohen et al. 2009; Kiyan et al. 2009), and the mortality rate is as low as 0.25–1 % (Mu et al. 1990, 1991; Steen and Zimmermann 1990; Hoeve and Rombout 1992; Ciftci et al. 2003; Zhijun et al. 2008; Tang and Chen 2009; Tang et al. 2009; Rodrigues et al. 2012b).

In many cases, however, the aspiration event is not witnessed, and the classical triad of choking followed by cough, focal decreased breath sounds, and wheeze is missing. Diagnosis is then delayed or overlooked, and many children present with unresolved pneumonia, atelectasis, or other complications. The role of the radiologist in cases of foreign body aspiration is not only to confirm a clinically suspected diagnosis, but also to suggest the diagnosis in patients with nonspecific clinical symptoms and radiologic features that could be related to long-standing foreign bodies. Often the radiologist is the first to raise the possibility of foreign body aspiration.

This chapter discusses imaging techniques and findings related to the various types and mechanisms of obstruction and to the complications of foreign body aspiration.

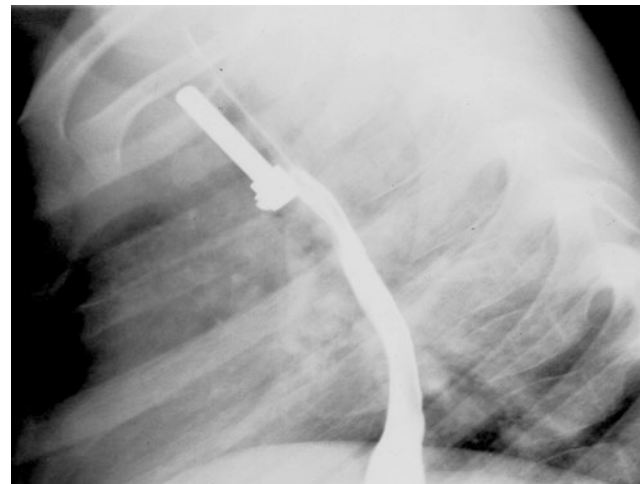


**Fig. 1** Lateral view of a barium swallow shows a metallic bolt in the trachea of a 2-year-old boy

## 2 Etiology/Types of Foreign Bodies

Most cases of foreign body aspiration occur between the age of 6 months and 3 years, with the highest incidence during the second year of life (Mantel and Butenandt 1986; Piepsz 1988; Fitzpatrick and Guarisco 1998; Lima and Fischer 2002; Witt 1985; Roda et al. 2008; Kitcher 2009; de Sousa et al. 2009; Tang et al. 2009; Orji and Akpeh 2010; Pan et al. 2012; Paksu et al. 2012; Boufersaoui et al. 2013; Sidell et al. 2013; Tenjovic et al. 2013). Infants and toddlers in this age group are already ambulatory and can therefore “disappear” from parent or guardian supervision for varying periods of time. They tend to act as “vacuum cleaners,” and examine new objects of any size or shape by inserting them into their mouth. The combination of natural curiosity, lack of posterior dentition, inadequate control of deglutition, and a startle response facilitates entry of solids into the larynx (Witt 1985; Byard 1994). The size and variety of objects that can pass through the vocal cords are quite astonishing (Fig. 1) (Blazer et al. 1980).

*Food particles and organic materials* constitute the vast majority of aspirated objects (Blazer et al. 1980; Keith et al. 1980; Svensson 1985; Mantel and Butenandt 1986; Piepsz 1988; Mu et al. 1990; Linegar et al. 1992; Black et al. 1994; Baharloo et al. 1999; Metrangelo et al. 1999; Diaz et al. 2000; Siddiqui et al. 2000; Brkic et al. 2001; Lima and Fischer 2002; Ayed et al. 2003; Roda et al. 2008; Ugrinovic et al. 2009; Chik et al. 2009; de Sousa et al. 2009; Albirmawy and Elsheikh 2011; Huankang et al. 2012). The nature of the aspirated material varies according to geographic and sociologic circumstances. Peanuts are the most common aspirated particles in North America, Europe, India, and South Africa (Teixidor de Otto et al. 1980; Mantel and Butenandt 1986; Mu et al. 1990; Linegar et al. 1992; Diaz

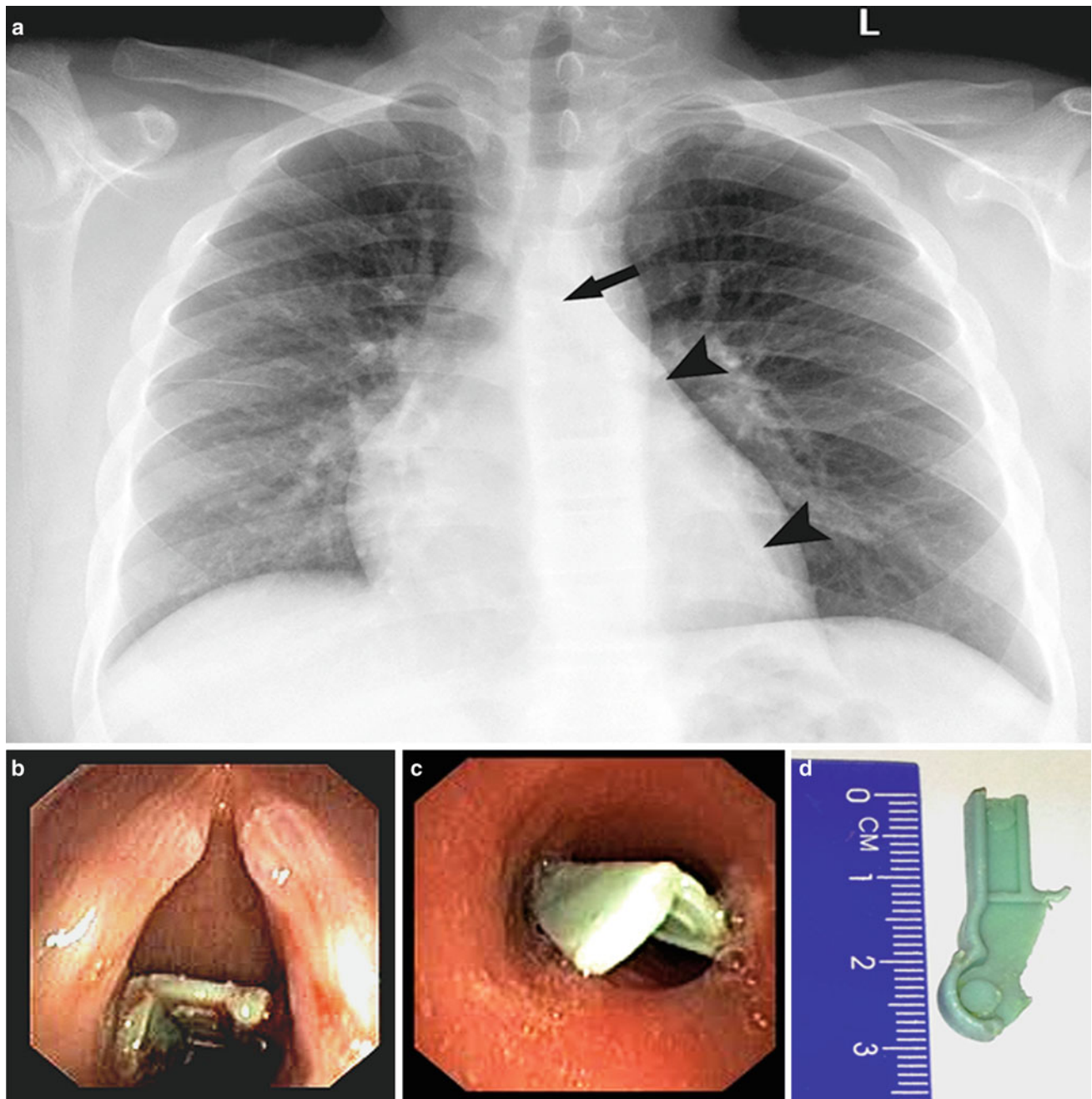


**Fig. 2** Posteroanterior chest radiograph demonstrating “absence” of the left main bronchus (“interrupted bronchus” sign, *arrow*, (a)) in a 13-year-old boy who held a plastic piece of a toy between his lips while playing a computer game. Note resultant left lower lobe

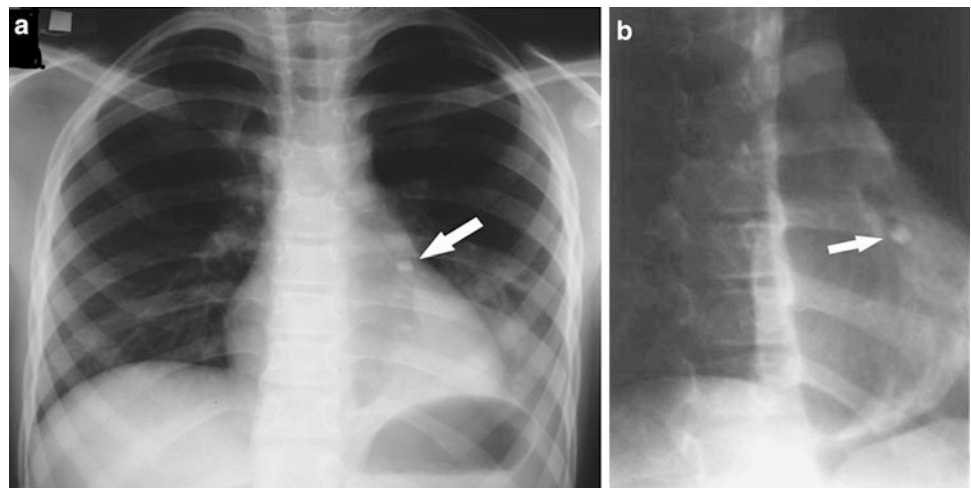
atelectasis (*arrowheads*) as well as left upper lobe hyperinflation. At bronchoscopy, the plastic was initially seen under the vocal cords (b), then migrated to the orifice of the left lower bronchus (c). Note the size of the extracted piece (d)

et al. 2000; Sehgal et al. 2002; Shivakumar et al. 2003), whereas earthnuts, grains, sunflower seeds, and watermelon seeds are more common in the South America, Middle East, and eastern Asia (Farkash et al. 1982; Elhassani 1988; Oguz et al. 2000; Pasaoglu et al. 1991; Cataneo et al. 2008; Zhijun et al. 2008; Chik et al. 2009; Saki et al. 2009; Oncel et al. 2012; Gang et al. 2012; Pan et al. 2012). Due to their high protein concentration, most organic foreign bodies absorb

water from bronchial secretions and tend to increase in size. Candies have been reported to have a similar effect due to their high sugar concentration (Mearns et al. 1975). Oil, salt, and vegetable proteins in cooked food irritate the mucosa, causing edema and formation of granulation tissue with resultant narrowing of the bronchial lumen. Hence, an organic foreign body can grow to be larger than the original diameter of the bronchus, and what was initially a partial



**Fig. 3** Posteroanterior chest radiograph (a) of a 10-year-old girl and an oblique view (b) (obtained at fluoroscopy): a deciduous tooth (arrow) is present in the left lower lobe bronchus obstructing some of the basal segments and causing volume loss. Bronchiectasis, evident in the left lower lobe, is better demonstrated by the oblique projection



obstruction can progress to become a complete obstruction (Fig. 2a) (Aytac et al. 1977; Cataneo et al. 1997).

*Grass inhalation* is not uncommon and has some unique characteristics. The literature contains reports describing aspiration of several types of grass heads, all with the same structure of side spurs along the main stem. When inhaled stump-first, the spikes carry the grass heads distally into the bronchial tree and lung parenchyma. Being resistant to organic decay, they can remain in the chest for a long time and can cause unusual infections, as well as other complications (Spencer et al. 1981; Maayan et al. 1993; Dindar et al. 1994; Basok et al. 1997; Newson et al. 1998; Ammari et al. 2000).

*Nonorganic objects* comprise 5–20 % of the foreign bodies aspirated by children (Farkash et al. 1982; Mortellaro et al. 2013). Of these, coins are the most common (Reilly and Walter 1992), followed by plastic toy pieces and sharp objects such as pencils and pull-tabs from aluminum cans (Rogers and Igini 1975; Burrington 1976; Blazer et al. 1980; Strickland et al. 1987; Applegate et al. 2001). Inert foreign bodies have little effect on the bronchial mucosa and, unless they cause an obstruction by virtue of their size, can remain undiagnosed for long periods of time (Adegboye et al. 2003). Aspiration of pacifiers is not uncommon among toddlers (Jain et al. 1986; Barrett and Debelle 1995). Partially inflated balloons and Nylon bags are particularly hazardous (Abdel-Rahman 2000; Anas and Perkin 1983).

A tooth can be aspirated by a sleeping child at the age of permanent tooth eruption. This happened to a 10-year-old girl who had a loose deciduous tooth when she fell asleep at night. When she woke up the next morning the tooth had disappeared from her mouth. The episode was forgotten; 10 days later she developed symptoms of left lower lobe pneumonia, with no response to antibiotic therapy over several months. When she was admitted to the hospital, the missing tooth was evident in the left lower lobe bronchus on

a chest radiograph, with atelectasis of most of the basal segments (Fig. 3). The tooth was removed by bronchoscopy; 2 months later residual bronchiectatic changes could still be seen in the left lower lobe.

Aspiration of tooth, dental fillings, crowns, or dental treatment equipment can also occur during dental treatment (Steelman et al. 1997), following minor trauma (Holan and Ram 2000), during anesthesia, and intubation or resuscitation procedures, especially in victims of road traffic accidents, and following tracheostomy canula replacement in debilitated patients.

Aspiration of gravel, dirt, or sand can happen during a traffic accident, in a cave-in or accidental burial, in a near-drowning event, or while playing in sand (Bergeson et al. 1978; Wales et al. 1983; Avital et al. 1989; Choy and Idowu 1996; Glinjongol et al. 2004; Arun Babu and Ananthakrishnan 2013). Airway obstruction has also been reported as a result of nonaccidental trauma, when forcible introduction of a foreign body caused tracheal obstruction, with a resultant death reported in one case (Barrett and Debelle 1995; Nolte 1993). Aspiration of headscarf needles (Turban pins) has been reported in young girls and adolescents in Islamic populations (Ucan et al. 1996; Kaptanoglu et al. 1999; Murthy et al. 2001; Kaptanoglu et al. 2007; Al-Sarraf et al. 2009; Hamad et al. 2010; Albirmawy and Elsheikh 2011; Ilan et al. 2012). Aspiration of other sharp metallic objects occurs more commonly among adolescents (Ludemann and Riding 2007; Walz et al. 2013). Such an aspirated pin, an office thumbtack, or a sewing needle can get stuck in the bronchial wall in one or both ends, a condition in which simple bronchoscopic extraction is not possible. In such cases, the use of additional, advanced endoscopic techniques is necessary in order to enable a successful bronchoscopic extraction and obviate the need for possible thoracotomy (Jabbardarjani et al. 2010).

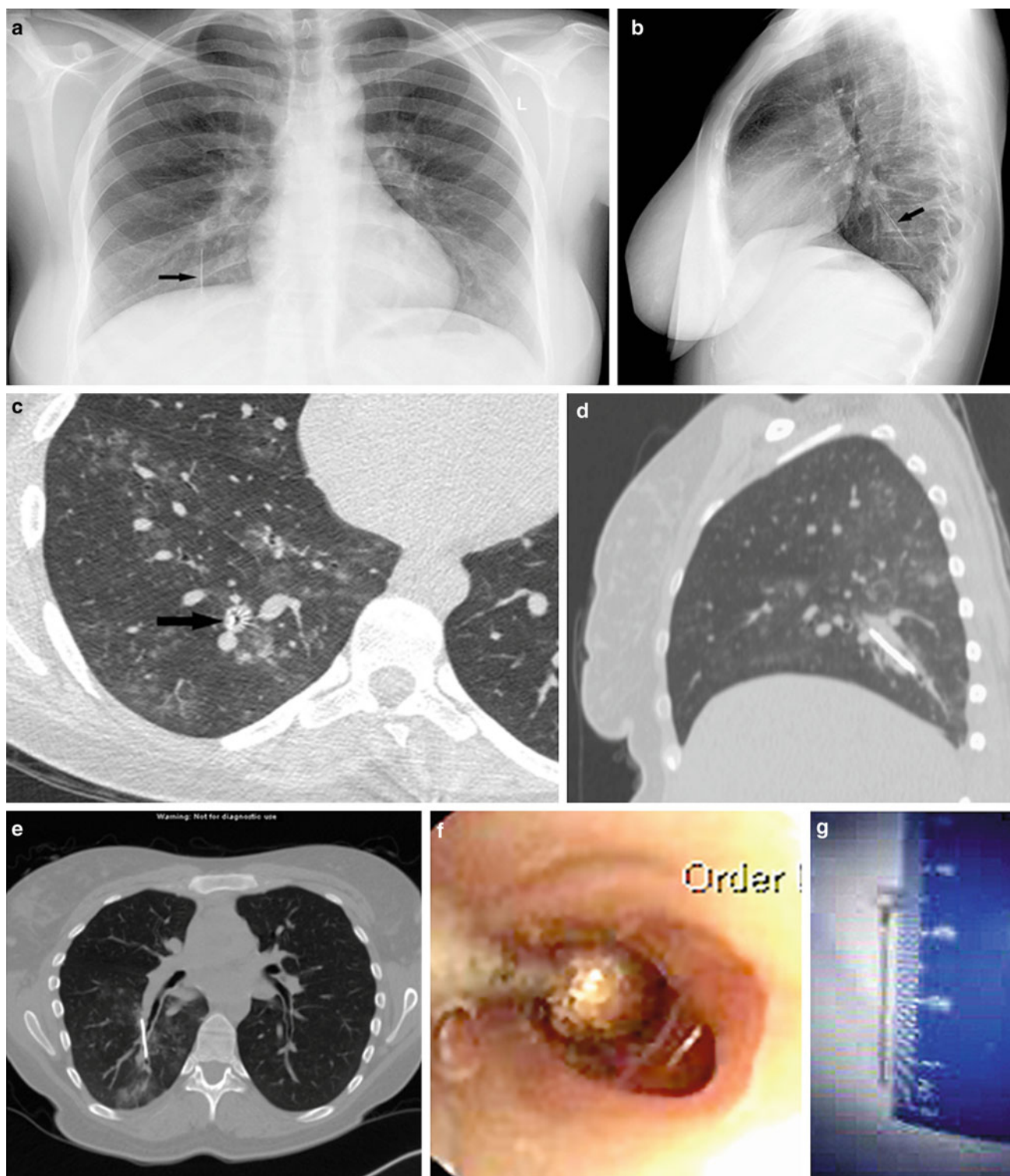


**Fig. 4** Posteroanterior (a) and lateral (b) chest radiograph demonstrating a hairpin aspirated into the right lower lobe (arrow). Axial (c), semicoronal (d), and sagittal (e) reformats of a CT scan demonstrated the oblique position of the pin with its end protruding through the

bronchial wall, as demonstrated at bronchoscopy (f). Extraction of the pin (g) was accomplished without further bronchial wall destruction only after it was heated and bent

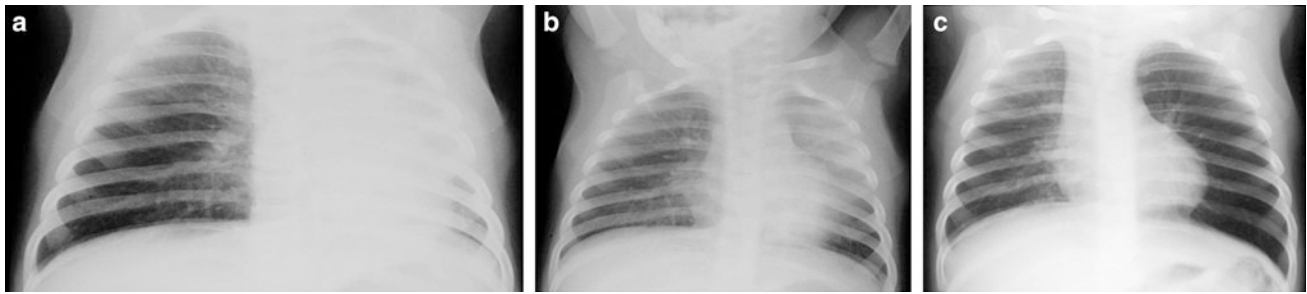
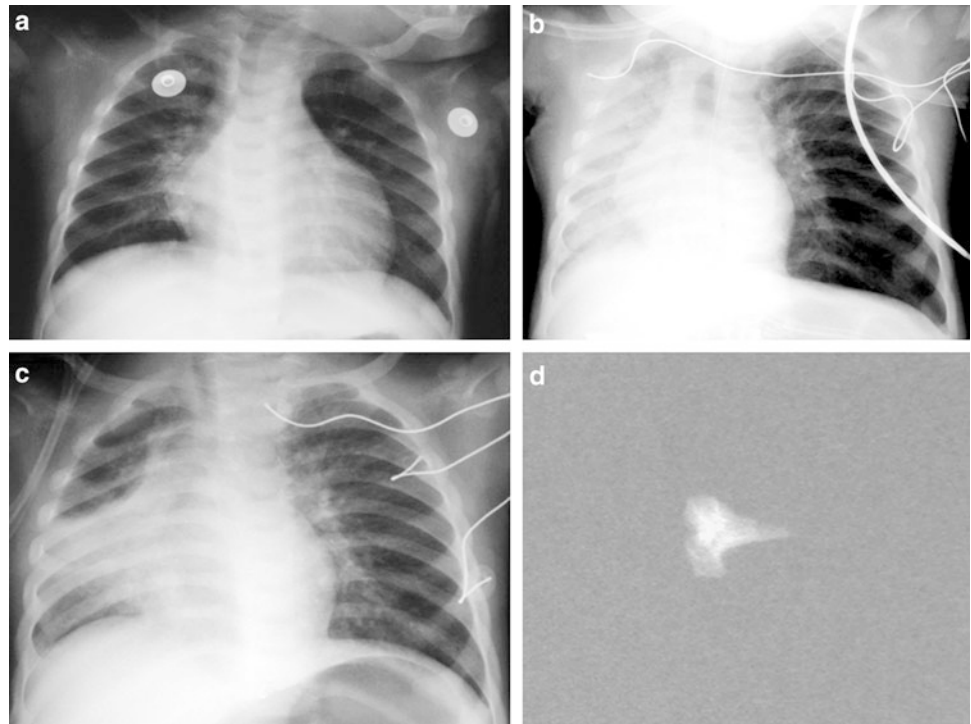


**Fig. 5** A 10-month-old girl with cough, low fever, and mild tachypnea for 4 days. Initial chest radiograph was normal. Follow-up chest radiographs 24 h later, on day 5 (a), showed collapsed left lung.

24 h later, on day 6 (b), there was left upper lobe collapse; 48 h later, on day 8 (c), emphysema of the left lung was seen. Bronchoscopy found two foreign bodies: a wood splinter and a piece of plastic

**Fig. 6** A 10-month-old boy with rickets aspirated a chicken bone. Initial chest radiograph (a) was normal (the chicken bone was missed). Follow-up chest radiographs 24 h (b) and 48 h (c) later showed progressive collapse of the right lung. A chicken bone (d) was removed from the right main bronchus on bronchoscopy



### 3 Mechanisms of Airway Obstruction

A foreign body in the respiratory tract does not necessarily cause an obstruction, i.e., air can be inhaled and exhaled freely around the foreign body. This is known as a “two-way valve mechanism,” and occurs when the foreign body, which is usually located in the trachea, is small in relation to the airway. A foreign body can cause complete obstruction when air entry is blocked during inspiration and the air cannot be exhaled during expiration. This is called a “no-way valve mechanism.” A foreign body can allow air entry during inspiration but prevent the exit of air during expiration in a “one-way valve mechanism.” This mechanism is explained by the larger diameter of the airway during inspiration due to higher intrathoracic negative pressure, and the smaller diameter during expiration.

Chest X-rays performed in cases of a nonobstructive tracheal or bronchial foreign body demonstrate uniform aeration bilaterally both in inspiration and expiration. In partial obstruction due to the one-way valve mechanism, the chest radiograph usually demonstrates air-trapping. Inspiratory films are often normal, and the air-trapping may become evident only in an expiratory study. In cases of complete airway obstruction (most commonly at the level of a bronchus), we often notice a combination of air-trapping in the non-dependent lobes with atelectasis of the dependent lobes. This is due to mucus plugging and the accumulation of secretions in the bronchial tree of the dependent segments (Figs. 2, 4, 5).

The incidence of right and left bronchial foreign bodies is almost equal in infants and young children (Mu et al. 1990; Black et al. 1994; Burton et al. 1996; Cataneo et al. 1997;



**Fig. 7** A broken piece of a metal zipper partially blocking the distal trachea of a 2.5-year-old girl causing bilateral hyperinflation as seen in an AP (a) and lateral (b) chest radiograph. During rigid bronchoscopy, the foreign body got stuck between the vocal cords and the child could neither be ventilated nor intubated. Bradycardia and decrease in oxygen saturation necessitated resuscitation and emergency tracheostomy. The foreign body was pushed down to the right bronchus (c). Following completion of tracheostomy, the metal piece (d) was pulled up to the level of the cords by flexible bronchoscopy and dislodged using surgical forceps

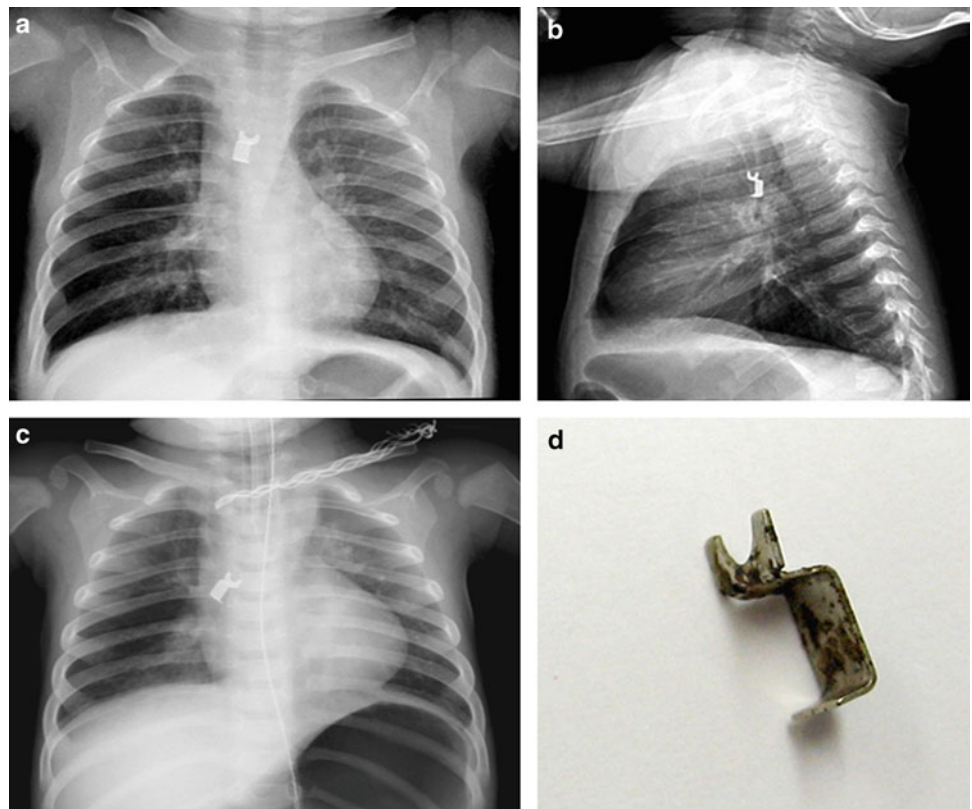
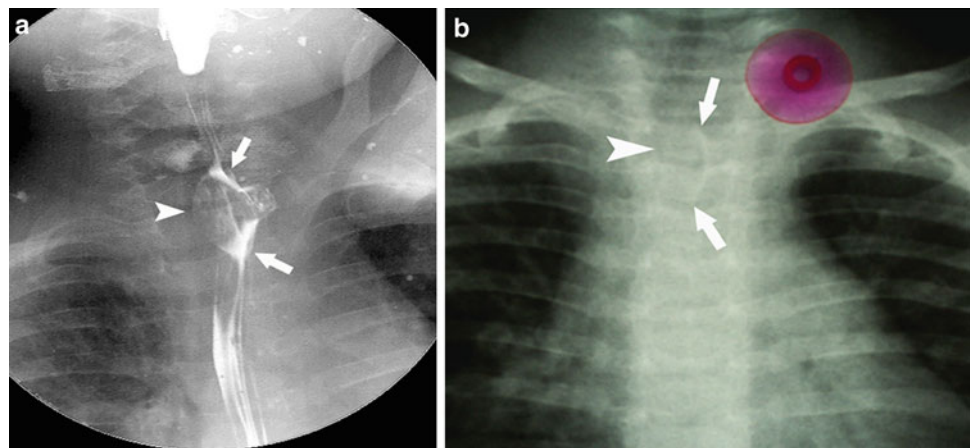


**Fig. 8** A rubber-made vacuum hanger was swollen by a 2-year-old boy causing stridor and salivation. Oblique view of a barium swallow study (a) demonstrated the rubber hanger in the proximal esophagus (arrows), causing marked posterior compression and narrowing of the trachea (arrowhead). Magnified AP chest radiograph (b) demonstrated the rubber hanger in the upper esophagus, with a similar one illustrated on the top left corner of the film



Senkaya et al. 1997; Metrangelo et al. 1999; Oguz et al. 2000; Van Looij et al. 2003; Ayed et al. 2003; Pinto et al. 2006; Zhijun et al. 2008; Cohen et al. 2009; Rodriguez et al. 2013), as opposed to predominance of the right bronchial tree in older children, adolescents, and adults (Baharloo et al. 1999; Fraga Ade et al. 2008; Roda et al. 2008; Kitcher 2009; de Sousa et al. 2009; Tang et al. 2009; Saki et al. 2009; Falase et al. 2013; Sidell et al. 2013). These differences can partly be explained by the almost symmetrical tracheobronchial angle in younger children (Cleveland 1979) and by the position of the carina that is more

commonly seen left to the midline (Tahir et al. 2009). Migration of a small foreign body within the airways during different phases of the respiratory cycle, secondary to alterations of posture or following cough is rare, but does occur, and can change the clinical and imaging findings (Figs. 5, 6) (Metrangelo et al. 1999). The authors witnessed a case in which a foreign body that was located in the right main bronchus migrated to the right upper lobe bronchus when the father of the child turned her upside down in an attempt to expel the foreign body from the airway. Since in those days only rigid bronchoscopy was available, the

foreign body could not be endoscopically removed and the patient required thoracotomy and lobectomy. Migration of a foreign body can also occur during bronchoscopy, if the foreign body detaches from the bronchoscopic forceps on its way out or if it is partially lodged into the tracheal or bronchial wall and has to be manipulated prior to its extraction.

#### 4 Clinical Findings and Differential Diagnosis

The clinical manifestations of aspirated foreign bodies vary according to the location and degree of obstruction.

*Laryngeal and subglottic foreign bodies* make up about 5 % of foreign bodies in the airways (Mantel and Butenandt 1986; Esclamado and Richardson 1987; Cohen et al. 1993; Black et al. 1994; Baharloo et al. 1999). When large enough, their presence in the major airway causes dyspnea, and when located adjacent to the vocal cords they may induce hoarseness, sudden loss of voice, and inspiratory stridor (Blazer et al. 1980; Hanukoglu et al. 1986; Laks and Barzilay 1988). Cyanosis may occur secondary to laryngeal spasm (Halvorson et al. 1996; Baharloo et al. 1999; Ciftci et al. 2003). Similar symptoms can be induced by other processes such as a laryngeal web (Chen et al. 1998), viral or bacterial croup, epiglottitis, papilloma or hemangioma, angioneurotic edema, or hypocalcemic tetany (Grad and Taussig 1990; Ibrahimov et al. 2013). Laryngeal or tracheal hirudiniasis following leech infestation while drinking infected stream water can cause the same symptoms due to mechanical obstruction. In addition, the combination of the grasp of the mucosa by the leech cutting plates and secretion of an anticoagulant causes hemorrhage that can result in prolonged hemoptysis and anemia (Mohammad et al. 2002; Yazici et al. 2012).

*Tracheal foreign bodies* constitute 4–13 % of foreign bodies in the airways (Mu et al. 1990, 1991; Black et al. 1994; Burton et al. 1996; Metrangelo et al. 1999) (Figs. 1, 7). In one series, they represented 23 % of the cases with early diagnosis and 7 % of the cases with late diagnosis (Oguz et al. 2000). In most patients there is a history of choking and dyspnea, yet they tend to be diagnosed later than bronchial foreign bodies, probably because they cause less severe respiratory symptoms (Esclamado and Richardson 1987). Inspiratory or biphasic stridor and wheeze can also be caused by tracheomalacia or external compression on the trachea by a vascular structure. Vascular rings usually cause a focal narrowing, but can have a hazardous effect by blocking a small foreign body that would have otherwise be aspirated into a more distal bronchus, thus turning a partial, distal bronchial obstruction to a

potentially fatal tracheal obstruction. Other causes of external compression include bronchogenic cysts, enlarged lymph nodes (secondary to viral or bacterial infection or due to tuberculosis), mediastinal tumors (e.g., lymphoma), or an esophageal foreign body (Fig. 8). A hollow foreign body located in the larynx or trachea can be almost asymptomatic and thus presents a unique diagnostic challenge (Jain et al. 2013).

*Bronchial foreign bodies* The majority of aspirated foreign bodies (67–85 %) are found in the main bronchi (Blazer et al. 1980; Mantel and Butenandt 1986). A history of sudden choking is the most important clue for diagnosis (Esclamado and Richardson 1987; Silva et al. 1998; Zerella et al. 1998; Metrangelo et al. 1999; Oguz et al. 2000; Ciftci et al. 2003). Such a history, however, was documented in only about one third of the cases in one series (Oguz et al. 2000). The classical triad of a choking episode, cough, and wheeze was found in over 90 % of the patients in another series (Blazer et al. 1980). Hemoptysis can be a presenting symptom (even in cases of a blunt foreign body) (Scully et al. 1983; Maayan et al. 1993; Fabian and Smitheringale 1996; Cataneo et al. 1997; Zuniga et al. 2000; Abellan Martinez et al. 2000; Mohammad et al. 2002). Physical examination will reveal unequal chest expansion during inspiration, as well as decreased breath sounds over the obstructed lung (Laks and Barzilay 1988; Oguz et al. 2000; Orji and Akpeh 2010; Roda et al. 2008; Huankang et al. 2012). Occasionally, a slapping sound of a loose foreign body can be heard (Felman 1982).

In cases of delayed diagnosis, pneumonia is a common presentation. The presence of an aspirated foreign body should be suspected in any patient with unexplained chronic pulmonary symptoms. Foreign body aspiration, however, is by no means the most common cause of recurrent pneumonia. Recurrent or persistent pneumonia can also result from bacterial infections, gastroesophageal reflux, impaired clearance of secretions from the tracheobronchial tree as in asthma, ciliary dysmotility (primary ciliary dyskinesia), cystic fibrosis, infected bronchiectasis or secondary to an immune deficiency (Kumar et al. 2009). Tumors of the tracheobronchial tree are uncommon in children, but, when present, may cause a varying degree of airway obstruction. Foreign bodies can sometimes coexist with other medical conditions that elicit similar symptoms such as allergic asthma, recurrent infections, or acute bronchiolitis (Ezer et al. 2011). Persistent symptoms and lack of improvement despite appropriate medical therapy should raise suspicion for the presence of a foreign body.

*Esophageal foreign bodies* can mimic foreign bodies in any location of the airway due to external compression of the larynx, trachea, or bronchi (Fig. 8). Such compression can cause laryngeal or tracheal spasm, resulting in respiratory

**Fig. 9** Anteroposterior chest fluoroscopy at inspirium (a) and expirium (b) demonstrating minimal change in volume and lucency of the hyperinflated, obstructed right lung as opposed to volume loss and change in opacity of the deflated left lung in expiration (b). Note the arched and more superior position of the left hemidiaphragm and the mediastinal shift toward the unobstructed left lung at expiration

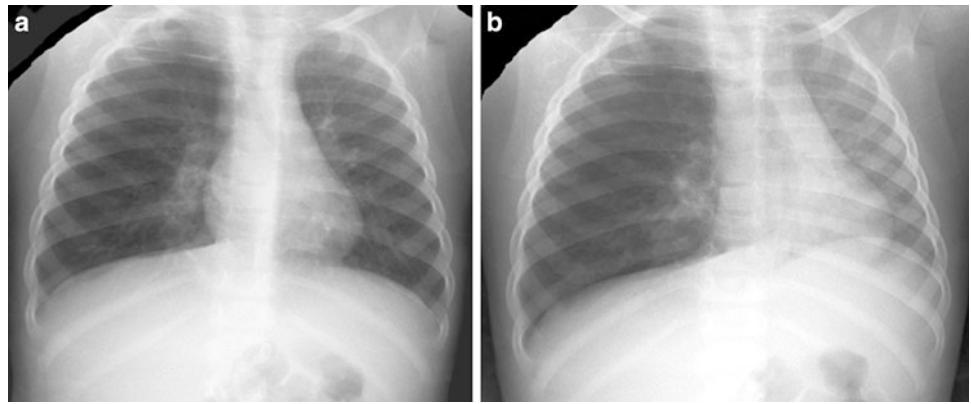
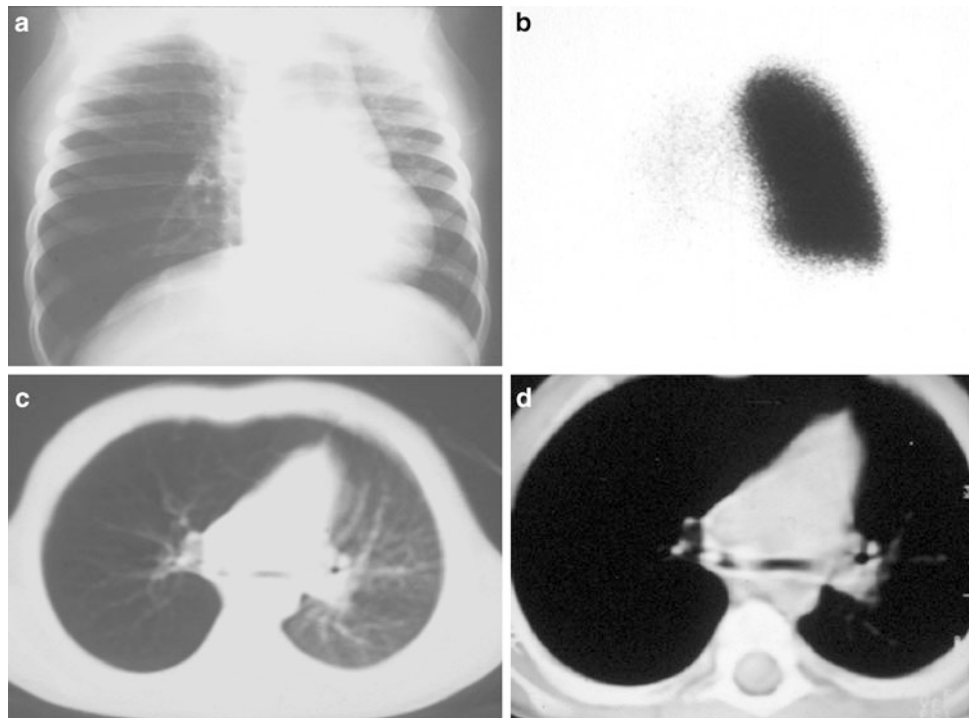


**Fig. 10** A 20-month-old boy had a choking episode. Initial chest radiograph (a) demonstrated obstructive emphysema of the right lung; bronchoscopy failed to reveal a foreign body. Lung scan (b) showed lack of perfusion to the right lung. Chest CT demonstrated obstructive emphysema of the right lung with contralateral mediastinal shift (c), as well as a foreign body in the right main bronchus (d). Repeat bronchoscopy identified a lentil



distress, stridor, or wheeze (Smith et al. 1974). In infants operated for congenital esophageal atresia, the combination of esophageal dilatation proximal to a stenotic anastomosis and an inherent tracheomalacia can result in severe tracheal narrowing, stridor, and a respiratory arrest. A tracheoesophageal fistula may develop as a result of a decubitus ulcer caused by an esophageal foreign body of long-standing duration (Szold et al. 1991; Li et al. 2009).

*Nasal foreign bodies*, when present for a long time, usually cause swelling of the nostrils or nasal discharge that may be foul smelling. They can ulcerate and damage the nasal septum, dislodge into the nasopharynx, and seldom can be aspirated into the tracheobronchial tree (Cohen et al. 1993; Fini-Storchi and Ninu 1996; Qureshi et al. 2009).

## 5 Imaging Techniques

*Chest Radiograph.* The plain chest X-ray remains the initial study in the evaluation of a suspected aspirated foreign body. Abnormal findings are found in 40–88 % of chest X-rays in children with proven foreign bodies (Laks and Barzilay 1988; Mu et al. 1990; Black et al. 1994; Oguz et al. 2000; Cataneo et al. 2008; Fraga Ade et al. 2008; Sidell et al. 2013). These rates increase when using inspiratory–expiratory techniques (Black et al. 1984, 1994; Losek 1990). Opaque foreign bodies are easily identified, but most are radiolucent (Figs. 1, 2, 11).



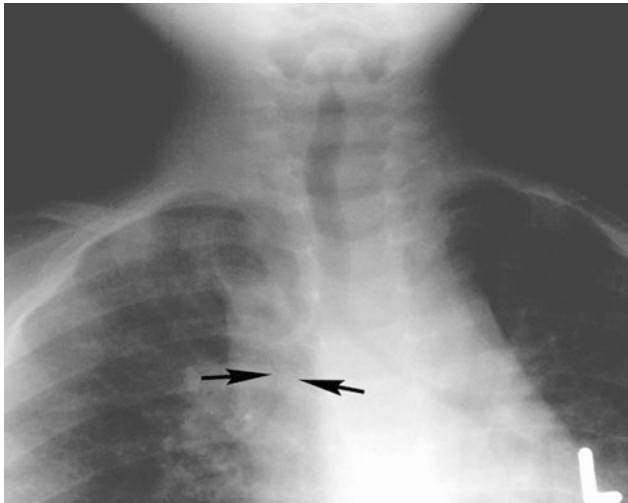


**Fig. 11** High kV copper filter technique of the tracheobronchial tree of a 15-month-old girl. A nonopaque foreign body (arrows) surrounded by air is seen at the carina and in the right main bronchus. The inspiration and expiration films did not reveal air trapping or any other pulmonary pathology

In cases of a nonopaque foreign body, inspiratory and expiratory films can provide important information. Comparison of the two hemithoraces is mandatory. The inspiratory film is often normal or near normal, while the expiratory film shows obvious air-trapping. The obstructed lung is of larger volume and more radiolucent. The decrease in ventilation of the obstructed lobe causes an increase in  $p\text{CO}_2$ . The higher  $p\text{CO}_2$  leads to arterial vasoconstriction and therefore to reduced pulmonary perfusion. Thus, the vessels in the obstructed region become narrow and sparse. This finding, characteristic of obstructive emphysema, can be seen on both plain films and Computed Tomography (CT). There is usually a mediastinal shift to the opposite side in expiration, as well as a lower ipsilateral hemi diaphragm (Figs. 9, 10).

In young children, whose cooperation is not always optimal, two lateral decubitus films, one on each side, can replace the inspiratory–expiratory films (Capitanio and Kirkpatrick 1972). An unobstructed, dependent lung shows smaller volume and crowded vessels as a result of gravitational forces on the abdominal and mediastinal organs. In cases of partial obstruction, the dependent lung does not deflate as expected. The relative hyperinflation of the dependent lung thus indicates the presence of partial bronchial obstruction.

Alternatively, expiratory films can be obtained in non-cooperative patients by applying manual pressure on the upper abdomen using a lead glove during the examination (Wesenberg and Blumhagen 1979). In infants this can also be done by inflating a blood pressure cuff, wrapped around the abdomen. Careful monitoring must be performed to

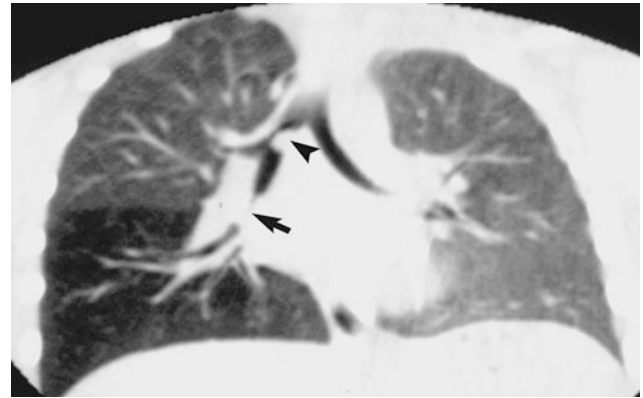


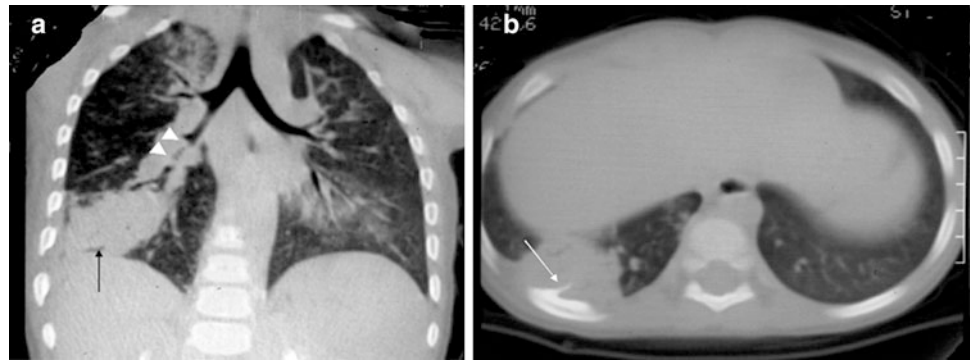
**Fig. 12** A semicoronal chest CT (lung settings) of a 2-year-old boy, obtained in expiration. Soft tissue density is demonstrated in the bronchus intermedius causing a partial obstruction (arrow). This is the equivalent of the “absent segment” sign that results from the presence of an obstructing foreign body and inflammatory changes in the adjacent bronchial wall. Note also the obvious air trapping in the right lower lobe as compared to the normal-sized right upper lobe and left lung. Another partially obstructing foreign body is seen adjacent to the medial wall of the right main bronchus (arrowhead)

ascertain that at no time the pressure in the cuff exceeds the child’s systolic blood pressure. Oblique projections enable better visualization of the trachea and main bronchi, and may demonstrate an otherwise “hidden” foreign body or discontinuation of the air column, depicted as an “absent segment” of the airway (Figs. 2, 3).

*The High kilo-voltage (kV) Copper Filter Technique* increases the visibility of the major airways and of non-opaque foreign bodies (Fig. 11). This technique combines the use of high kV with filters that absorb most of the low energy photons. As a result, the contrast between soft tissue and bone is reduced and the contrast between air and all other tissues is increased. Thus, the airway and its contents are sharply delineated over the background of the other tissues. Various filters have been used; however, the combination of 0.4 mm of tin, 0.5 mm of copper, and 0.75 mm of aluminum is probably the most useful. The use of this technique enables improved visualization of the major airways with reduced radiation dose (Joseph et al. 1976).

The sensitivity, specificity, and accuracy of chest radiographs for the detection and diagnosis of aspirated foreign bodies have been shown to be low when compared to bronchoscopy or to clinical signs in several retrospective studies (Svedstrom et al. 1989; Hoeve and Rombout 1992; Hoeve et al. 1993; Barrios Fontoba et al. 1997; Silva et al. 1998; Zerella et al. 1998; Sehgal et al. 2002; Ayed et al. 2003; Pinto et al. 2006; Cataneo et al. 2008; Kiyani et al. 2009; Zupa et al. 2009; Hitter et al. 2011). In some series, up to 50 % of chest X-rays obtained in children with proven foreign bodies were found to be normal when filmed in the early period (within 3 days) following aspiration; however, expiratory

**Fig. 13** A 3-year-old boy aspirated a branch of Timothy grass. Semicoronal (a) and axial (b) chest CT demonstrate narrowing and irregularity of the bronchus intermedius (arrowheads), distal atelectasis, and abscess formation (arrow). Also note sclerosis of the adjacent rib representing osteomyelitis (white arrow in (b))



radiographs were not routinely obtained in these studies (Zerella et al. 1998; Oncel et al. 2012). Expiratory films have a high diagnostic value, but without clinical suspicion of foreign body aspiration, they will not be routinely performed. Therefore, it is mandatory that the clinician provide this sort of information to the radiologist in charge of the exam. Chest X-rays can also be normal in cases of a radiolucent tracheal foreign body that is not large enough to cause obstruction (Chang and Pereira 2013) and in cases of bilateral bronchial foreign bodies (Wiseman 1984; Musemeche and Kosloske 1986; Laks and Barzilay 1988).

*Fluoroscopy* can still raise a significant contribution to the investigation of foreign body aspiration. The proponents of this modality advocate its use because it is widely available, easy to use, and rapidly diagnostic in up to 90 % of cases of a bronchial foreign body (Blazer et al. 1980; Zerella et al. 1998). In our practice, fluoroscopy is seldom used. Nevertheless, the radiologist can optimally visualize the airways and detect obstruction or the presence of an opaque foreign body with fluoroscopy (Fig. 3b), especially if a copper filter is used adjacent to the X-ray tube or close to the patient (W.E. Berdon, personal communication). Mediastinal shift toward the obstructed side during inspiration and towards the contralateral side during expiration is easily recognized (Fig. 9) (Theander 1970; Laks and Barzilay 1988; Mu et al. 1990). Unequal descent or ascent of the hemidiaphragms on inspiration and expiration can be seen and is more easily noticed in crying babies and in older children when requested to sniff rapidly. Diminished excursions of the diaphragmatic leaflets are invariably seen on the affected side, either with hyperinflation (in partial obstruction) or with volume loss (in complete obstruction) (Theander 1970). Use of any technique for assisted expiration, as described earlier, can facilitate demonstration of air-trapping. Digital subtraction fluoroscopy has been described as a sensitive method for the demonstration of tracheal and bronchial narrowing secondary to the presence of a radiolucent aspirated foreign body (Ikeda et al. 2001). The use of “last image hold” and “last fluoroscopy hold” applications currently installed in most modern fluoroscopy

machines enables quick exclusion or confirmation of suspected bronchial obstruction with minimal radiation exposure.

*Computed tomography (CT)*, due to its high contrast resolution, enables demonstration of foreign bodies that are frequently not visible on the chest X-ray. CT is usually utilized as a part of work-up for unclear cases of persistent, nonresolving respiratory symptoms, for which foreign body aspiration can be one of the reasons. When initial imaging studies or bronchoscopy are negative, CT may reveal the presence and location of a previously undiagnosed foreign body (Berger et al. 1980; Bertolani et al. 1999). CT is a very sensitive modality for demonstrating small dense objects, such as thin fish or chicken bones, that may not be detected on plain films (Braverman et al. 1993; Mignon et al. 1997; Bai et al. 2011; Hitter et al. 2011; Sattar et al. 2011; Manach et al. 2013).

CT is also an efficient tool for the demonstration of small plastic toy particles such as LEGO pieces (Applegate et al. 2001) or rubber products. The presence and location of an intraluminal lesion can easily be detected and multiple intrabronchial findings can at times be identified (Figs. 4, 10, 12, 13), as well as the “interrupted bronchus” sign. Intravenous contrast administration can enhance discrimination between an intraluminal foreign body and other endobronchial, bronchial wall, or extrinsic findings, such as a hemangioma or lymph nodes. By varying window width and level, one can see not only the foreign body, but also the reaction of the tissue around and distal to it. One can also assess the presence and extent of complications such as air-trapping, atelectasis, pneumonia, alveolar hemorrhage, empyema, bronchiectasis, or chest wall involvement (Figs. 4, 10, 12, 14) (Haliloglu et al. 2003; Kosucu et al. 2004; Adaletli et al. 2007). Air-trapping is well demonstrated by decubitus scans (Fig. 15) (Garcia-Pena et al. 1999; Lucaya et al. 2000; Choi et al. 2002). Scanning in the semicoronal plane had been used to demonstrate accurate localization of the obstructing foreign body (Figs. 12, 13) (Bar-Ziv and Solomon 1990). However, with current helical, multidetector scanners using volumetric acquisition of

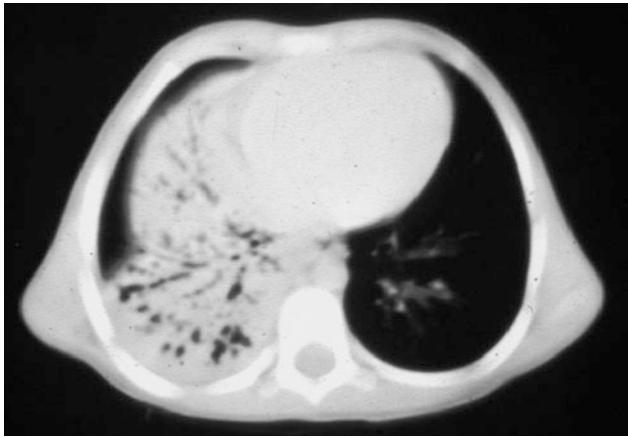


**Fig. 14** Axial CT of the lower chest in a case of chronic foreign body aspiration into the right intermediate bronchus, causing collapse and bronchiectasis in the right middle lobe and right lower lobe

data, a high pitch and a short scanning time, accurate multiplanar reconstructions can be obtained, thereby replacing the semicoronal scans.

We routinely use a helical technique with 3-mm collimation, 3-mm reconstructions for adolescents and children, with the smallest possible field of view. For infants and toddlers we may use 2-mm collimation with 1-mm reconstructions. Tube current can be reduced to as low as 25–30 mA for such studies, and kV can be reduced to as low as 80–90, depending on child age and weight. Multiplanar reconstructions are helpful in detecting airway foreign bodies (Kosucu et al. 2004; Kocaoglu et al. 2006; Adaletli et al. 2007; Bai et al. 2011). Virtual bronchoscopy can further contribute to the diagnosis and location of a presumed aspirated foreign body when a chest radiograph is not informative (Konen et al. 1998; Haliloglu et al. 2003; Kosucu et al. 2004; Kocaoglu et al. 2006; Adaletli et al. 2007; Cevizci et al. 2008). Virtual bronchoscopy has the advantage of demonstrating smaller airways than possible to view with conventional bronchoscopy, as well as the airways beyond an obstructed bronchus (Haliloglu et al. 2003; Kosucu et al. 2004; Adaletli et al. 2007; Cevizci et al. 2008; Bhat et al. 2010). However, reconstructions are time consuming and have not been shown to contribute additional information over multiplanar reconstructions (Kosucu et al. 2004; Kocaoglu et al. 2006). The major disadvantage of CT examinations is the inherent radiation exposure of the young patient, despite improved technology and increasing awareness of both manufacturers and radiologists to minimize radiation dose. Therefore, it is imperative to weight the potential benefit of the additional data yielded as a result of each study against the potential risk, especially in cases when conventional bronchoscopy, that might be both diagnostic and therapeutic, is to be carried out as well (McHugh 2005; Manach et al. 2013).



**Fig. 15** Right lateral decubitus chest CT demonstrates air-trapping in the right (dependent) lung, following aspiration of a piece of an eraser

*Nuclear medicine* is not recommended for the diagnosis of a bronchial foreign body. When used, however, the lung scan can be helpful in defining regional decrease in ventilation and perfusion (Fig. 10b), as well as air-trapping, and can thus guide endoscopy to the area of suspected obstruction (Holland and Trumbull 1979; Lull et al. 1980; Balink et al. 2012).

*Magnetic resonance imaging (MRI)* studies are also rarely used for investigating suspected foreign body aspiration, especially because at present the use of sedation is mandatory. Nevertheless, several reports have described the utility of MRI in the management of foreign body aspiration. Due to the multiplanar nature of this modality, MRI can accurately locate the foreign body prior to bronchoscopy, and can also reveal foreign bodies in multiple sites during the same study (Imaizumi et al. 1994; Morijiri et al. 1994). The high fat content of aspirated peanuts, as well as the high water content of most organic foreign bodies enable clear delineation of their size and site (O'Uchi et al. 1992; Tashita et al. 1998).

*Ultrasound (US)* can be of value in defining the presence, nature, and extent of complications of foreign bodies, such as consolidation with an air bronchogram, pleural effusion or empyema, loculated pockets of fluid, chest wall abscess, or rib osteomyelitis (Seibert et al. 1986; Giudicelli et al. 1996). Ultrasound can presumably demonstrate the foreign



body within the collapsed lung; however, the authors do not have experience in this.

## 6 Imaging Findings

Imaging findings in cases of foreign body aspiration are determined by the presence and the degree of airway obstruction, the site of the foreign body, its type, and the time that has elapsed between aspiration and the performance of imaging studies.

A foreign body can be present in the airway without causing obstruction. This situation almost always involves an oblong foreign body in the trachea, small enough to have been aspirated yet not large enough to block the (relatively) larger airway. In such a case the chest radiograph and fluoroscopy will usually be negative, although pneumonia might be present (Esclamado and Richardson 1987; Mu et al. 1990; Cataneo et al. 1997). Fluoroscopy or a high kV soft tissue technique with a copper filter may reveal the foreign body (Fig. 11). CT (Gupta and Berry 1991; Malis and Hayes 1995; Bertolani et al. 1999) and MR imaging (O'Uchi et al. 1992; Imaizumi et al. 1994; Morijiri et al. 1994; Tashita et al. 1998) can demonstrate the presence and often the nature of such a foreign body when the initial imaging is negative.

Obstruction of the airway can vary in severity and occur at different levels of the tracheobronchial tree. Laryngeal or subglottic foreign bodies tend to be thinner and are often arranged in an anteroposterior direction (sagittal plane) in the region of the vocal cords, as opposed to esophageal foreign bodies, which lie in a transverse direction (coronal plane). If the foreign body is a thin, rounded object (e.g., a coin or an egg shell), it will be seen as a thin line on the anteroposterior chest radiograph when located between the vocal cords, and as a rounded shadow when located in the esophagus. Tracheal foreign bodies usually cause no obstruction or incomplete obstruction. The imaging findings, when present, are often bilateral: either bilateral volume loss or bilateral hyperinflation (Fig. 7). In the latter case, the diaphragms are flattened and in a low position. When small enough, the foreign body may move in the tracheobronchial tree during the different phases of the respiratory cycle, as a result of coughing or following treatment with inhaled bronchodilators, with consequent changes in the clinical and imaging findings (Figs. 5, 6) (Metrangelo et al. 1999).

About three quarters of airway foreign bodies are found in the main bronchi (Blazer et al. 1980; Mantel and Butenandt 1986; Zhijun et al. 2008; Kitcher 2009; Saki et al. 2009), where they cause partial or complete obstruction. Plain films and fluoroscopy seldom demonstrate a nonopaque foreign body. An oblique projection obtained with these modalities,

placing the upper airway over the mediastinal soft tissues, creates better contrast and enhances demonstration of the foreign body (Fig. 3). This technique may also indirectly reveal the presence of a foreign body by virtue of focal absence of the air column in the obstructed bronchus, the so-called "absent segment" or the "interrupted bronchus" sign (Fig. 2) (Grunebaum et al. 1979; Lim-Dunham and Youssefzadeh 1999). Partial obstruction results in localized air-trapping distal to the site of the foreign body, with resultant widening of the intercostal spaces, and flattening of the ribs and diaphragms, and blunting of the costophrenic angles (Laks and Barzilay 1988; Mu et al. 1990; Ernst and Mahmud 1994; Black et al. 1994; Oguz et al. 2000). Segmental or lobar emphysema due to air trapping has been reported to be present in ~40 % of children with proven foreign body aspiration (Bai et al. 2011; Sattar et al. 2011; Boufersaoui et al. 2013; Mortellaro et al. 2013); in some studies, this is indicated as the most specific finding in the chest radiograph (Hitter et al. 2011; Sattar et al. 2011; Boufersaoui et al. 2013). Pulmonary hyperexpansion with sparse vascularity or displacement of the mediastinum to the contralateral side on expiration indicates the presence of obstructive emphysema (Figs. 2, 5, 6, 9, 10) (Mu et al. 1990). Complete obstruction also causes segmental or lobar atelectasis (Figs. 2, 3, 5, 6), or even total collapse of the ipsilateral lung (Figs. 5, 6). The collapsed area may initially be homogeneously opaque, due to the absence of air in the alveoli and bronchi. Collateral diffusion of air to the bronchioles distal to the obstructing foreign body may result in a faint air bronchogram. In cases with lobar atelectasis, compensatory emphysema of the ipsilateral respected lobes and of the contralateral lung is often present (Theander 1970). In contrast to obstructive emphysema, pulmonary vessels are prominent in compensatory emphysema.

The presence of lobar collapse with localized pneumothorax should suggest the diagnosis of acute bronchial obstruction of any etiology (Berdon et al. 1984; Nimkin et al. 1995) (Fig. 16). The combination of increased pressure and the presence of a sharp object in the bronchi can result in a bronchopleural fistula. This complication, as well as pneumonia secondary to focal obstruction, may give rise to pleural effusion or empyema (Dogan et al. 1999). Pleural effusion as the only imaging sign of foreign body aspiration has also been reported (Auerback 1990). In prolonged cases, localized or multifocal bronchiectasis may develop and be evident on the plain radiograph (Fig. 3) or on CT (Fig. 14); these are best evaluated by high-resolution CT with thin section collimation (Kuhn 1993). Subacute or chronic infection and inflammatory response may form a parenchymal abscess adjacent or distal to the foreign body, or a chest wall abscess and rib osteomyelitis (Fig. 13).



**Fig. 16** Collapsed right lower lobe with localized pneumothorax due to acute foreign body aspiration

## 7 Complications

Complications of foreign body aspiration can be immediate or long term. A foreign body can cause *fatal asphyxia and death* when there is complete obstruction of the major airways (Buntain et al. 1979; Black et al. 1984, 1994; Byard 1994; Bhana et al. 2000; Ciftci et al. 2003). This occurrence is rare, although it was described in 5–7.5 % of foreign body aspiration cases in one report (Menendez et al. 1991; Foltran et al. 2013). This high incidence has not been observed in the author's experience and is not corroborated in most other reports. Complete obstruction can develop abruptly when a relatively small foreign body is aspirated into a trachea with a pre-existing (sometimes unknown) focal narrowing caused by a vascular ring, tracheomalacia or external compression. Complete obstruction can also occur during bronchoscopy for extraction of a foreign body (Fig. 7).

Asphyxia and hypoxemia can result in hypoxic-ischemic encephalopathy, convulsions, severe neurologic deterioration over varying period of time and death within several days or following several months or years (Northcote 1983; Bamber et al. 2013).

*Atelectasis* is reported by some as the most common complication of foreign body aspiration (Mu et al. 1990; Cataneo et al. 1997; Oguz et al. 2000), and is seen in 21–50 % of the patients who are diagnosed 24 h or more after the suspected aspiration event (Figs. 2, 3, 5, 6, 16) (Wiseman 1984; Mortellaro et al. 2013). Though atelectasis usually develops gradually, collapse of the entire lung may occur within an hour. When this happens on the right side,

kinking of the superior vena cava may cause a sudden decrease of venous return to the heart and lead to loss of consciousness. Elevation of jugular venous pressure should alert the examining physician to the possibility of such a complication.

*Pneumonia* appears in 20–50 % of patients with an aspirated foreign body diagnosed 3 days or later consequent to the aspiration event (Cataneo et al. 1997; Oguz et al. 2000; Diaz et al. 2000; Tenjovic et al. 2013). The pneumonia in these cases is usually located in the lower lobes, does not resolve following antibiotic therapy and is frequently associated with a pleural effusion. Pneumonia may at times be due to uncommon pathogens (Cavens et al. 1973; Baethge et al. 1990), and can be accompanied with the formation of multiple lung abscesses. Dirt or shallow water aspiration can lead to diffuse pneumonitis (Mangge et al. 1993; Li et al. 2009).

*Air leak* A sudden increase in alveolar pressure due to proximal obstruction can cause an air leak into the interstitial space, leading to interstitial emphysema, pneumomediastinum (Hanukoglu et al. 1980; Burton et al. 1989; Ramadan et al. 1992; Bratton and O'Rourke 1993; Oliveira et al. 2002; Ciftci et al. 2003; Otgun et al. 2008; Li et al. 2009; Zielinski et al. 2011; Nimrey-Atrash et al. 2012; Hu et al. 2013), pneumothorax (Fig. 16) (Berdon et al. 1984; Esclamado and Richardson 1987; Ramadan et al. 1992; Nimkin et al. 1995; Cataneo et al. 1997; Newson et al. 1998; Carron and Derkay 2000; Ciftci et al. 2003) or pneumopericardium (Tjhen et al. 1978; Bro and Thamsen 1989). The abrupt onset of an air leak in a child under 2 years of age, without a history of chest trauma or asthma, should raise the suspicion of an aspirated foreign body (Cataneo et al. 1997).

*Long-term complications* The incidence and severity of long-term complications are directly related to the length of time that has passed between the actual event of aspiration and establishment of the diagnosis (Auerback 1990; Linegar et al. 1992; Schmidt and Manegold 2000; Karakoc et al. 2002). Positive radiological findings are more common in cases diagnosed 24 h later consequent to the suspected aspiration (Esclamado and Richardson 1987; Mu et al. 1990); the longer the delay in diagnosis, the higher the rate of complications (Levy et al. 1983; Mu et al. 1990; Karakoc et al. 2002; Shlizerman et al. 2010). In most cases of delayed diagnosis, the original episode passed unnoticed and the parents or physician do not relate recent, recurrent signs and symptoms as being linked to such an episode or to each other (Mantel and Butenandt 1986). In such cases the presentation can be that of recurrent events of hyper-reactive airway disease, with incomplete response to treatment,

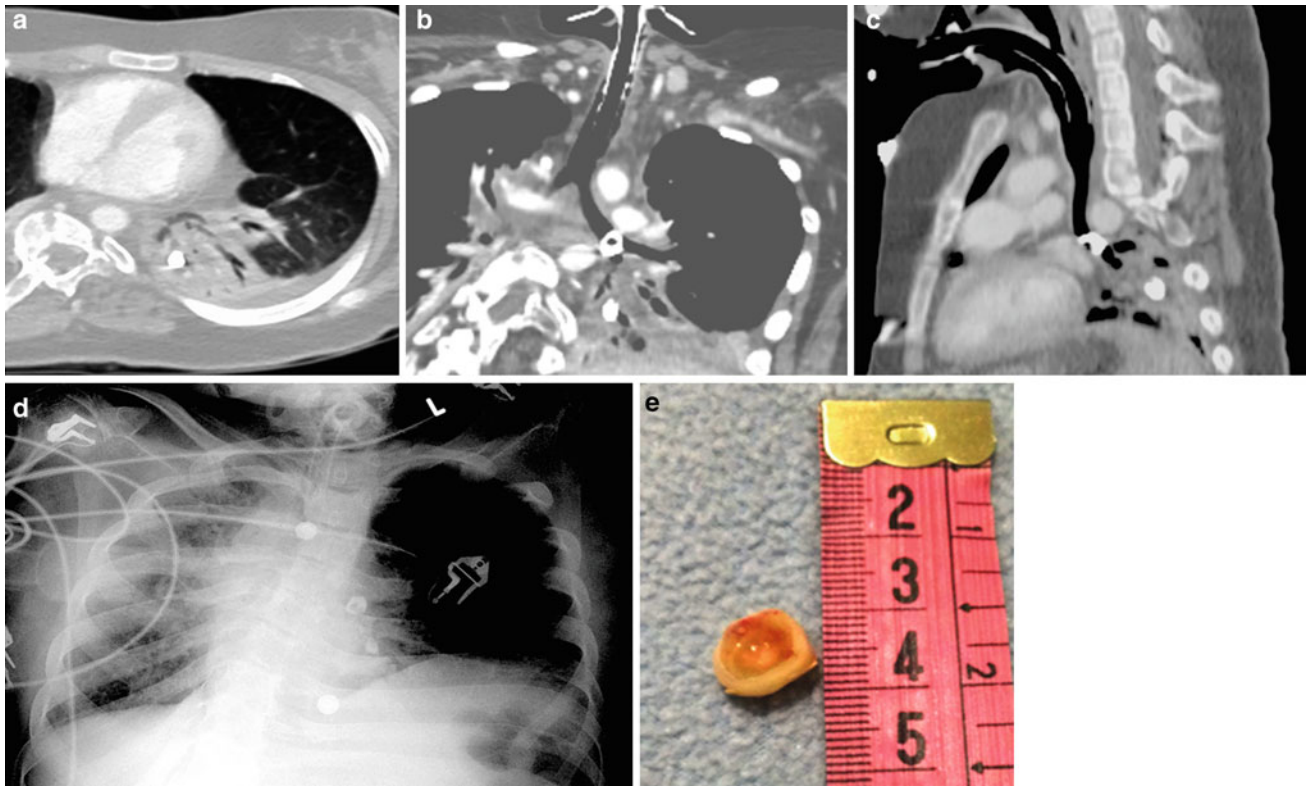


**Fig. 17** 7-year-old debilitated girl was referred from another institution for a chest, abdomen, and pelvis CT scan as part of an evaluation for acute deterioration and suspected intestinal obstruction. Left lower lobe atelectasis and bronchiectasis were noted in the axial images (a) and the curved coronal (b) and sagittal (c) reformats, as well as two bronchial opaque structures resembling teeth, one in the left main

bronchus and one in the left lower lobe. These were in retrospect identified in a previous chest radiograph (d) and were thought to have dropped into the trachea during a previous tracheal cannula replacement. A dental crown (e) was extracted from the left main bronchus at bronchoscopy; extraction of the more distal crown was not carried out as it was considered too complicated and risk-bearing

or of recurrent pneumonia, with or without abscess formation, pleural effusion, or empyema (Burton et al. 1989; Auerback 1990; Dogan et al. 1999; Li et al. 2009).

*Chronic bronchitis and bronchiectasis* (Figs. 3, 14, 17) secondary to long-standing foreign body aspiration constitute approximately 5 % of chronic suppurative lung disease. The presence of a bronchial foreign body of long duration causes atelectasis that can become infected and lead to the development of bronchiectasis. This can become so severe that bronchoscopic extraction of the foreign body might not be possible, and surgical treatment may eventually be required (Spencer et al. 1981; Gatch et al. 1987; Maayan et al. 1993; Nikolaizik and Warner 1994; Cataneo et al. 1997; Scully et al. 1998; Karakoc et al. 2002; Adegbeye et al. 2003).

*Grass heads* of different types have been reported to cause a unique sequence of complications (Ammari et al. 2000). If they have spikes that are soft and close together, as is the case of Timothy grass, they will soften with moisture following aspiration and will not penetrate into the lung

periphery. The grass head may lodge in the bronchial tree and occlude it causing obstructive emphysema, collapse, pneumonia, and lung abscess. If the spikes are stiff and do not become soft when moistened, or when inhaled stump-first, respiratory actions and cough can cause them to advance. Being carried by the spikes distally into the bronchial tree, they can penetrate the lung tissue and ultimately even extrude spontaneously through the chest wall (Hilman et al. 1980). During this process they can cause lung abscess (Fig. 13), bronchocutaneous fistula (Cavens et al. 1973; Baethge et al. 1990; Maayan et al. 1993; Dindar et al. 1994), rib osteomyelitis (Figs. 13, 18), chest wall abscess, or pneumocutaneous fistula (Cheng et al. 1991). Among several of our patients who suffered such a complication, one was a 3-year-old boy who had aspirated a branch of Timothy grass. Subsequently, the child developed cough and fever. A chest radiograph obtained several weeks later showed consolidation and volume loss in the right lower lobe. A semi-coronal chest CT study revealed irregularity and narrowing of the right lower lobe bronchus, partial consolidation, and



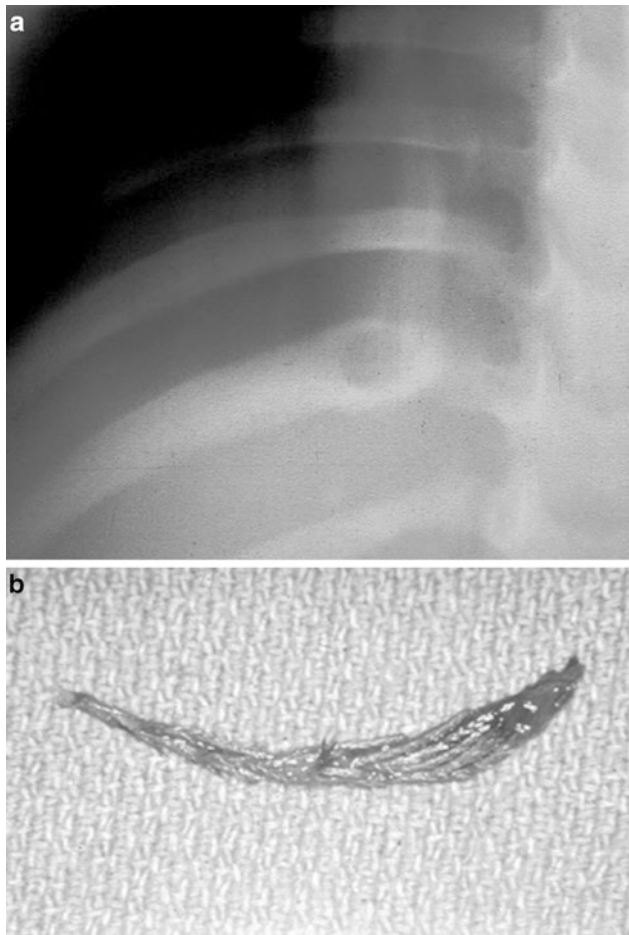


**Fig. 18** A 2-year-old girl had repeated episodes of right lower lobe pneumonia for several months following an episode of choking around Christmas. Chest radiograph (a) showed an osteolytic lesion with thickening and sclerosis in a rib at the right lower chest. At surgery, a pine tree needle (b) was found in the rib, with osteomyelitis

atelectasis of the right lower lobe with abscess formation. Thickening, sclerosis, and irregularity of the inner border of the adjacent rib were also noted (Fig. 13). Pathology of the resected right lower lobe revealed the presence of Timothy grass within the bronchus of the lateral basal segment with bronchiectasis and abscess formation.

*Brain abscesses* have been reported in association with foreign body aspiration, presumably due to faulty pulmonary capillary filter mechanisms (Spencer et al. 1981; Sane et al. 1999; Fuentes et al. 2001; Shachor-Meyouhas et al. 2009; Dabbah et al. 2009).

Prolonged presence of a tracheal or an esophageal foreign body can result in a decubitus ulcer that can progress to a *tracheoesophageal fistula* (Fig. 19) with possible mediastinitis, which might require surgery (Szold et al. 1991; Li et al. 2009).



**Fig. 19** A 6-week-old baby girl had suffered from respiratory symptoms since the age of 2 weeks. Tube esophagogram demonstrated a filling defect in the upper esophagus and a tracheoesophageal fistula. A pistachio nutshell was surgically removed and the fistula excised

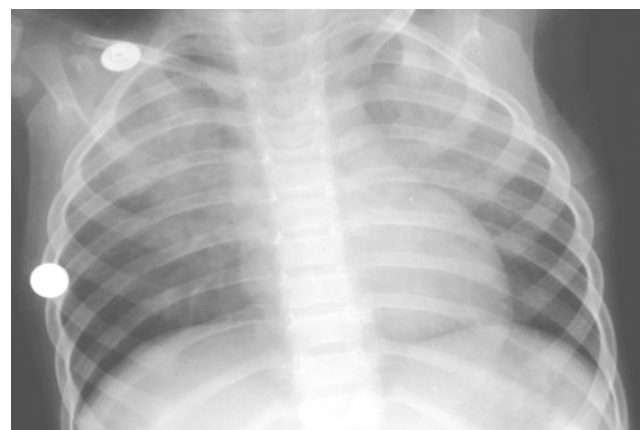


**Fig. 20** Anteroposterior chest radiograph demonstrating ill-defined increased capacity of the upper zones bilaterally as a result of pulmonary edema following relief of obstruction after extraction of a foreign body

*Pulmonary edema* may occur subsequent to relief of an upper airway obstruction, regardless of the etiology (Fig. 20). The pathophysiology of the pulmonary edema in these cases is not fully understood. It is thought that pulmonary congestion develops during obstruction as a result of raised pleural negative pressure, which increases venous return to the heart, in the presence of decreased left ventricular function. The hypoxia causes pulmonary hypertension and increased capillary permeability. This combination leads to greater pulmonary vascular volume, which may be

radiographically difficult to detect because of associated air trapping. Once the obstruction is relieved and lung aeration returns to normal, the pulmonary edema becomes apparent (Sofer et al. 1984a, b, 1985).

## 8 Conclusion

A wide variety of opaque or nonopaque foreign bodies can be aspirated by infants and young children. The history of choking is the most reliable clue for the diagnosis of foreign body aspiration, but many patients reach medical attention because of various nonspecific clinical symptoms. The role of the radiologist in these cases is crucial. Knowledge of the imaging features of a foreign body in the respiratory tract is essential for diagnosis. Many clinical and imaging findings are the result of a one-way obstruction mechanism, most commonly affecting one of the main bronchi. A normal inspiratory chest radiograph does not rule out an endotracheobronchial foreign body. Hence, expiratory films are extremely important to demonstrate air trapping. Alternatively, lateral decubitus or assisted expiration films can be used. The high kV copper filter technique is valuable for demonstrating the foreign body, and for indirectly showing an area of deficient aeration in the tracheobronchial tree, the “absent segment” sign.

Fluoroscopy can be very useful, but unfortunately the art of fluoroscopy is now almost lost. CT has become more valuable by virtue of its wide availability, high resolution, and the multiplanar, three-dimensional, and additional image reconstruction capabilities. CT can establish the diagnosis of a foreign body, indicate its exact location, and often show its composition, as well as any associated complications. Other imaging modalities can be used, though their role is not as well established. Nuclear scans are of some value only in cases of obstructive endobronchial foreign body. MRI has great potential and may be used extensively in the future. Currently, however, it is not widely available and usually requires sedation of the child. Ultrasound is being used to demonstrate complications such as pleural effusion or chest wall abscesses.

An understanding of the mechanisms of obstruction and their resultant clinical and imaging manifestations, especially when foreign body aspiration is highly suspected, can lead to earlier diagnosis and lower the complication rate.

**Acknowledgments** The authors thank Prof. C. Springer and Prof. B.S. Slasky for reviewing the manuscript; Prof. P. Mogle for his comments and for the contribution of the case described in Fig. 19; Prof. J. Lucaya for the cases presented in Figs. 5–6, 10, 12, 14–16; Prof. J. Strife for the case described in Fig. 18; and Mr. E. Koplewitz and Mrs. B. Koplewitz for their editorial comments and their continuous support.

## References

- Abdel-Rahman HA (2000) Fatal suffocation by rubber balloons in children: mechanism and prevention. *Forensic Sci Int* 108(2): 97–105
- Abellan Martinez MC, Mendez Martinez P, Sanchez Gascon F, Hernandez Martinez J, Ruiz Lopez FJ (2000) Repeated hemoptysis for foreign body bronchial aspiration: presentation of a case and review of literature. *Ann Med Intern* 17(12):652–654
- Adaletli I, Kurugoglu S, Ulus S, Ozer H, Elicevik M, Kantarci F, Mihmanli I, Akman C (2007) Utilization of low-dose multidetector CT and virtual bronchoscopy in children with suspected foreign body aspiration. *Pediatr Radiol* 37(1):33–40
- Adegboye VO, Osinowo O, Adebo OA (2003) Bronchiectasis consequent upon prolonged foreign body retention. *Cent Afr J Med* 49(5–6):53–58
- Al-Sarraf N, Jamal-Eddine H, Khaja F, Ayed AK (2009) Headscarf pin tracheobronchial aspiration: a distinct clinical entity. *Interact Cardiovasc Thorac Surg* 9(2):187–190
- Albirmawy OA, Elsheikh MN (2011) Foreign body aspiration, a continuously growing challenge: Tanta University experience in Egypt. *Auris Nasus Larynx* 38(1):88–94
- Ammari FF, Faris KT, Mahafza TM (2000) Inhalation of wild barley into the airways: two different outcomes. *Saudi Med J* 21(5):468–470
- Anas NG, Perkin RM (1983) Aspiration of a balloon by a 3-month-old infant. *JAMA* 250(3):385–386
- Applegate KE, Dardinger JT, Lieber ML, Herts BR, Davros WJ, Obuchowski NA, Maneker A (2001) Spiral CT scanning technique in the detection of aspiration of LEGO foreign bodies. *Pediatr Radiol* 31(12):836–840
- Arun Babu T, Ananthakrishnan S (2013) Unusual presentation of sand aspiration in a 14-month-old child. *Indian J Pediatr* 80(9):786–788
- Auerback ML (1990) Pleural effusion due to unsuspected aspiration of vegetable matter in a three-year-old boy. *N Engl J Med* 322(17):1238
- Avital A, Springer C, Mogle P, Godfrey S (1989) Successful treatment after ‘drowning’ in sand. *Arch Dis Child* 64(4):615–616
- Ayed AK, Jafar AM, Owayed A (2003) Foreign body aspiration in children: diagnosis and treatment. *Pediatr Surg Int* 19(6):485–488
- Aytac A, Yurdakul Y, Ikizler C, Olga R, Saylam A (1977) Inhalation of foreign bodies in children. Report of 500 cases. *J Thorac Cardiovasc Surg* 74(1):145–151
- Baethge BA, Eggerstedt JM, Olash FA Jr (1990) Group F streptococcal empyema from aspiration of a grass inflorescence. *Ann Thorac Surg* 49(2):319–320
- Baharloo F, Veyckemans F, Francis C, Bietlot MP, Rodenstein DO (1999) Tracheobronchial foreign bodies: presentation and management in children and adults. *Chest* 115(5):1357–1362
- Bai W, Zhou X, Gao X, Shao C, Califano JA, Ha PK (2011) Value of chest CT in the diagnosis and management of tracheobronchial foreign bodies. *Pediatr Int* 53(4):515–518
- Balink H, Collins J, Korsten-Meijer AG, Rottier BL (2012) Unilateral hyperlucent lung in a child caused by a foreign body identified with v/q scintigraphy. *Clin Nucl Med* 37(9):916–917
- Bamber AR, Pryce J, Ashworth M, Sebire NJ (2013) Fatal aspiration of foreign bodies in infants and children. *Fetal Pediatr Pathol* (Epub ahead of print Oct 21 2013)
- Bar-Ziv J, Solomon A (1990) Direct coronal CT scanning of tracheobronchial, pulmonary and thoraco-abdominal lesions in children. *Pediatr Radiol* 20(4):245–248

- Barrett TG, Debelle GD (1995) Near-fatal aspiration of a child's dummy: design fault or deliberate injury? *J Accid Emerg Med* 12(2):154–155
- Barrios Fontoba JE, Gutierrez C, Lluna J, Vila JJ, Poquet J, Ruiz-Company S (1997) Bronchial foreign body: should bronchoscopy be performed in all patients with a choking crisis? *Pediatr Surg Int* 12(2–3):118–120
- Basok O, Yaldiz S, Kilincer L (1997) Bronchiectasis resulting from aspirated grass inflorescences. *Scand Cardiovasc J* 31(3):157–159
- Berdon WE, Dee GJ, Abramson SJ, Altman RP, Wung JT (1984) Localized pneumothorax adjacent to a collapsed lobe: a sign of bronchial obstruction. *Radiology* 150(3):691–694
- Berger PE, Kuhn JP, Kuhns LR (1980) Computed tomography and the occult tracheobronchial foreign body. *Radiology* 134(1):133–135
- Bergeson PS, Hinchcliffe WA, Crawford RF, Sorenson MJ, Trump DS (1978) Asphyxia secondary to massive dirt aspiration. *J Pediatr* 92(3):506–507
- Bertolani MF, Marotti F, Bergamini BM, Pellegrino M, Balli R, Calandra Buonaura PL (1999) Extraction of a rubber bullet from a bronchus after 1 year: complete resolution of chronic pulmonary damage. *Chest* 115(4):1210–1213
- Bhana BD, Gunaselvam JG, Dada MA (2000) Mechanical airway obstruction caused by accidental aspiration of part of a ballpoint pen. *Am J Forensic Med Pathol* 21(4):362–365
- Bhat KV, Hegde JS, Nagalotimath US, Patil GC (2010) Evaluation of computed tomography virtual bronchoscopy in paediatric tracheobronchial foreign body aspiration. *J Laryngol Otol* 124(8):875–879
- Black RE, Choi KJ, Syme WC, Johnson DG, Matlak ME (1984) Bronchoscopic removal of aspirated foreign bodies in children. *Am J Surg* 148(6):778–781
- Black RE, Johnson DG, Matlak ME (1994) Bronchoscopic removal of aspirated foreign bodies in children. *J Pediatr Surg* 29(5):682–684
- Blazer S, Naveh Y, Friedman A (1980) Foreign body in the airway. A review of 200 cases. *Am J Dis Child* 134(1):68–71
- Boufarsaoui A, Smati L, Benhalla KN, Boukari R, Smail S, Anik K, Aouameur R, Chaouche H, Baghrich M (2013) Foreign body aspiration in children: experience from 2624 patients. *Int J Pediatr Otorhinolaryngol* 77(10):1683–1688
- Bratton SL, O'Rourke PP (1993) Spontaneous pneumomediastinum. *J Emerg Med* 11(5):525–529
- Braverman I, Gomori JM, Polv O, Saah D (1993) The role of CT imaging in the evaluation of cervical esophageal foreign bodies. *J Otolaryngol* 22(4):311–314
- Brkic F, Delibegovic-Dedic S, Hajdarovic D (2001) Bronchoscopic removal of foreign bodies from children in Bosnia and Herzegovina: experience with 230 patients. *Int J Pediatr Otorhinolaryngol* 60(3):193–196
- Bro H, Thamsen H (1989) Pneumopericardium after aspiration of a pea into the respiratory tract. *Ugeskr Laeger* 151(42):2733
- Buntain WL, Benton JW, Gutierrez JF (1979) Christmas bow tragedies. *South Med J* 72(11):1471–1472
- Burrington JD (1976) Aluminum "pop tops". A hazard to child health. *JAMA* 235(24):2614–2617
- Burton EM, Brick WG, Hall JD, Riggs W Jr, Houston CS (1996) Tracheobronchial foreign body aspiration in children. *South Med J* 89(2):195–198
- Burton EM, Riggs W Jr, Kaufman RA, Houston CS (1989) Pneumomediastinum caused by foreign body aspiration in children. *Pediatr Radiol* 20(1–2):45–47
- Byard RW (1994) Unexpected death due to acute airway obstruction in daycare centers. *Pediatrics* 94(1):113–114
- Capitanio MA, Kirkpatrick JA (1972) The lateral decubitus film. An aid in determining air-trapping in children. *Radiology* 103(2):460–462
- Carron JD, Derkay CS (2000) Potpourri aspiration presenting as tension pneumothorax. *Am J Otolaryngol* 21(5):349–351
- Cataneo AJ, Cataneo DC, Ruiz RL Jr (2008) Management of tracheobronchial foreign body in children. *Pediatr Surg Int* 24(2):151–156
- Cataneo AJ, Reibschheid SM, Ruiz Junior RL, Ferrari GF (1997) Foreign body in the tracheobronchial tree. *Clin Pediatr (Phila)* 36(12):701–706
- Cavens TR, McGee MD, Miller RR, Bowen DA (1973) Pneumocutaneous fistula secondary to aspiration of grass. *J Pediatr* 82(4):737–738
- Cevizci N, Dokucu AI, Baskin D, Karadag CA, Sever N, Yalcin M, Bahadir E, Basak M (2008) Virtual bronchoscopy as a dynamic modality in the diagnosis and treatment of suspected foreign body aspiration. *Eur J Pediatr Surg* 18(6):398–401
- Chang AE, Pereira KD (2013) Tracheal foreign bodies: are radiographs misleading? *Pediatr Emerg Care* 29(4):515–517
- Chen YT, Singh R, Brett RH (1998) Diagnostic red herring in an infant with stridor. *Singapore Med J* 39(10):471–472
- Cheng T, Herman G, Coulter K (1991) A tale of two diseases: pneumonia and chest wall abscess. *Pediatr Infect Dis J* 10(5):414–415, 417–418
- Chik KK, Miu TY, Chan CW (2009) Foreign body aspiration in Hong Kong Chinese children. *Hong Kong Med J* 15(1):6–11
- Choi SJ, Choi BK, Kim HJ, Lee SH, Choi SH, Park SJ, Goo HW, Lee JS, Yoon CH (2002) Lateral decubitus HRCT: a simple technique to replace expiratory CT in children with air trapping. *Pediatr Radiol* 32(3):179–182
- Choy IO, Idowu O (1996) Sand aspiration: a case report. *J Pediatr Surg* 31(10):1448–1450
- Ciftci AO, Bingol-Kologlu M, Senocak ME, Tanyel FC, Buyukpamukcu N (2003) Bronchoscopy for evaluation of foreign body aspiration in children. *J Pediatr Surg* 38(8):1170–1176
- Cleveland RH (1979) Symmetry of bronchial angles in children. *Radiology* 133(1):89–93
- Cohen HA, Goldberg E, Horev Z (1993) Removal of nasal foreign bodies in children. *Clin Pediatr (Phila)* 32(3):192
- Cohen S, Avital A, Godfrey S, Gross M, Kerem E, Springer C (2009) Suspected foreign body inhalation in children: what are the indications for bronchoscopy? *J Pediatr* 155(2):276–280
- Dabbah H, Elias N, Bentur L (2009) Foreign-body aspiration as an aetiology for brain abscess. *Arch Dis Child* 94(8):601
- de Sousa ST, Ribeiro VS, de Menezes Filho JM, dos Santos AM, Barbieri MA, de Figueiredo Neto JA (2009) Foreign body aspiration in children and adolescents: experience of a Brazilian referral center. *J Bras Pneumol* 35(7):653–659
- Diaz GA, Valledor L, Seda F (2000) Foreign bodies from the upper-aero digestive tract of children in Puerto Rico. *Bol Asoc Med P R* 92(9–12):124–129
- Dindar H, Konkan R, Cakmak M, Barlas M, Gokcora H, Yucsan S (1994) A bronchopleurocutaneous fistula caused by an unusual foreign body aspiration simulating acute abdomen. *Eur J Pediatr* 153(2):136–137
- Dogan K, Kaptanoglu M, Onen A, Saba T (1999) Unusual sites of uncommon endobronchial foreign bodies. Reports of four cases. *Scand Cardiovasc J* 33(5):309–311
- Elhassani NB (1988) Tracheobronchial foreign bodies in the Middle East. A Baghdad study. *J Thorac Cardiovasc Surg* 96(4):621–625
- Ernst KD, Mahmud F (1994) Reversible cystic dilatation of distal airways due to foreign body. *South Med J* 87(3):404–406
- Esclamado RM, Richardson MA (1987) Laryngotracheal foreign bodies in children. A comparison with bronchial foreign bodies. *Am J Dis Child* 141(3):259–262
- Ezer SS, Oguzkurt P, Ince E, Temiz A, Caliskan E, Hicsonmez A (2011) Foreign body aspiration in children: analysis of diagnostic criteria and accurate time for bronchoscopy. *Pediatr Emerg Care* 27(8):723–726



- Fabian MC, Smitheringale A (1996) Hemoptysis in children: the hospital for sick children experience. *J Otolaryngol* 25(1):44–45
- Falase B, Sanusi M, Majekodunmi A, Ajose I, Oke D (2013) Preliminary experience in the management of tracheobronchial foreign bodies in Lagos. *Nigeria Pan Afr Med J* 15:31
- Farkash J, Liberman A, Bar-Ziv J et al (1982) Respiratory tract foreign bodies in children. *Harefuah* 10:383–387
- Felman AH (1982) *The pediatric chest*. Thomas, Springfield, pp 411–423
- Fini-Storchi I, Ninu MB (1996) Atypical intranasal foreign body. *Ear Nose Throat J* 75(12):796–799
- Fitzpatrick PC, Guarisco JL (1998) Pediatric airway foreign bodies. *J La State Med Soc* 150(4):138–141
- Foltran F, Ballali S, Rodriguez H, Sebastian van As AB, Passali D, Gulati A, Gregori D (2013) Inhaled foreign bodies in children: a global perspective on their epidemiological, clinical, and preventive aspects. *Pediatr Pulmonol* 48(4):344–351
- Fraga Ade M, Reis MC, Zambon MP, Toro IC, Ribeiro JD, Baracat EC (2008) Foreign body aspiration in children: clinical aspects, radiological aspects and bronchoscopic treatment. *J Bras Pneumol* 34(2):74–82
- Friedman EM (2000) Tracheobronchial foreign bodies. *Otolaryngol Clin North Am* 33(1):179–185
- Fuentes S, Bouillot P, Regis J, Lena G, Choux M (2001) Management of brain stem abscess. *Br J Neurosurg* 15(1):57–62
- Gang W, Zhengxia P, Hongbo L, Yonggang L, Jiangtao D, Shengde W, Chun W (2012) Diagnosis and treatment of tracheobronchial foreign bodies in 1024 children. *J Pediatr Surg* 47(11):2004–2010
- Gatch G, Myre L, Black RE (1987) Foreign body aspiration in children. Causes, diagnosis, and prevention. *AORN J* 46(5):850–861
- Garcia-Pena P, Lucaya J (1999) Chest CT in children: main applications and advantages. *Pediatr Pulmonol* S18:56–59
- Giudicelli J, Chapelon C, Louis D, Andre C, Bellon G (1996) Intrabronchial inhaled seed migration. Value of ultrasonography in the diagnosis of pleural-cutaneous fistula. *Rev Mal Respir* 13(4):428–429
- Glinjongol C, Kiatchaipipat S, Thepharoeniran S (2004) Severe sand aspiration: a case report with complete recovery. *J Med Assoc Thai* 87(7):825–828
- Goktas O, Snidero S, Jahnke V, Passali D, Gregori D (2010) Foreign body aspiration in children: field report of a German hospital. *Pediatr Int* 52(1):100–103
- Grad R, Taussig LM (1990) Acute infections producing upper airway obstruction. In: Chenick V, Kendig EL (eds) *Disorders of the respiratory tract in children*. Saunders, Philadelphia, pp 336–348
- Grunebaum M, Adler S, Varsano I (1979) The paradoxical movement of the mediastinum. A diagnostic sign of foreign-body aspiration during childhood. *Pediatr Radiol* 8(4):213–218
- Gupta AK, Berry M (1991) Detection of a radiolucent bronchial foreign body by computed tomography. *Pediatr Radiol* 21(4):307–308
- Haliloglu M, Ciftci AO, Oto A, Gumus B, Tanyel FC, Senocak ME, Buyukpamukcu N, Besim A (2003) CT virtual bronchoscopy in the evaluation of children with suspected foreign body aspiration. *Eur J Radiol* 48(2):188–192
- Halvorson DJ, Merritt RM, Mann C, Porubsky ES (1996) Management of subglottic foreign bodies. *Ann Otol Rhinol Laryngol* 105(7):541–544
- Hamad AM, Elmistekawy EM, Ragab SM (2010) Headscarf pin, a sharp foreign body aspiration with particular clinical characteristics. *Eur Arch Otorhinolaryngol* 267(12):1957–1962
- Hanukoglu A, Fried D, Hadas E (1980) Pneumomediastinum and subcutaneous emphysema following foreign body aspiration. *Harefuah* 98:262–264
- Hanukoglu A, Fried D, Segal S (1986) Loss of voice as sole symptom of subglottic foreign-body aspiration. *Am J Dis Child* 140(10):973
- Hilman BC, Kurzweg FT, McCook WW Jr, Liles AE (1980) Foreign body aspiration of grass inflorescences as a cause of hemoptysis. *Chest* 78(2):306–309
- Hitter A, Hullo E, Durand C, Righini CA (2011) Diagnostic value of various investigations in children with suspected foreign body aspiration: review. *Eur Ann Otorhinolaryngol Head Neck Dis* 128(5):248–252
- Hoeve LJ, Rombout J (1992) Pediatric laryngobronchoscopy. 1332 procedures stored in a data base. *Int J Pediatr Otorhinolaryngol* 24(1):73–82
- Hoeve LJ, Rombout J, Pot DJ (1993) Foreign body aspiration in children. The diagnostic value of signs, symptoms and pre-operative examination. *Clin Otolaryngol Allied Sci* 18(1):55–57
- Holan G, Ram D (2000) Aspiration of an avulsed primary incisor. A case report. *Int J Paediatr Dent* 10(2):150–152
- Holland NJ, Trumbull HR (1979) Chronic foreign body aspiration diagnosed by lung scan. *Clin Pediatr (Phila)* 18(8):497–500
- Hu M, Green R, Gungor A (2013) Pneumomediastinum and subcutaneous emphysema from bronchial foreign body aspiration. *Am J Otolaryngol* 34(1):85–88
- Huankang Z, Kuanlin X, Xiaolin H, Witt D (2012) Comparison between tracheal foreign body and bronchial foreign body: a review of 1,007 cases. *Int J Pediatr Otorhinolaryngol* 76(12):1719–1725
- Ibrahimov M, Yollu U, Akil F, Aydin F, Yener M (2013) Laryngeal foreign body mimicking croup. *J Craniofac Surg* 24(1):e7–e8
- Ikeda M, Himi K, Yamauchi Y, Ikui A, Shigihara S, Kida A (2001) Use of digital subtraction fluoroscopy to diagnose radiolucent aspirated foreign bodies in infants and children. *Int J Pediatr Otorhinolaryngol* 61(3):233–242
- Ilan O, Eliashar R, Hirshoren N, Hamdan K, Gross M (2012) Turban pin aspiration: new fashion, new syndrome. *Laryngoscope* 122(4):916–919
- Imaizumi H, Kaneko M, Nara S, Saito H, Asakura K, Akiba H (1994) Definitive diagnosis and location of peanuts in the airways using magnetic resonance imaging techniques. *Ann Emerg Med* 23(6):1379–1382
- Jabbardarjani H, Kiani A, Arab A, Masjedi M (2010) Foreign body removal using bronchoscopy and argon plasma coagulation. *Arch Iran Med* 13(2):150–152
- Jain L, Sivieri E, Bhutani VK (1986) Aspiration of pacifiers. *Pediatrics* 78(5):955–956
- Jain S, Kashikar S, Deshmukh P, Gosavi S, Kaushal A (2013) Impacted laryngeal foreign body in a child: a diagnostic and therapeutic challenge. *Ann Med Health Sci Res* 3(3):464–466
- Joseph PM, Berdon WE, Baker DH, Slovis TL, Haller JO (1976) Upper airway obstruction in infants and small children. Improved radiographic diagnosis by combining filtration, high kilovoltage, and magnification. *Radiology* 121(1):143–148
- Kaptanoglu M, Dogan K, Onen A, Kunt N (1999) Turban pin aspiration: a potential risk for young Islamic girls. *Int J Pediatr Otorhinolaryngol* 48(2):131–135
- Kaptanoglu M, Nadir A, Dogan K, Sahin E (2007) The heterodox nature of “Turban Pins” in foreign body aspiration; the central anatolian experience. *Int J Pediatr Otorhinolaryngol* 71(4):553–558
- Karakoc F, Karadag B, Akbenlioglu C, Ersu R, Yildizeli B, Yuksel M, Dagli E (2002) Foreign body aspiration: what is the outcome? *Pediatr Pulmonol* 34(1):30–36
- Keith FM, Charrette EJ, Lynn RB, Salerno TA (1980) Inhalation of foreign bodies by children: a continuing challenge in management. *Can Med Assoc J* 122(1):52, 55–57
- Kitcher ED (2009) Foreign body inhalation: a review of patients at the Korle Bu Teaching Hospital, Accra, Ghana. *West Afr J Med* 28(6):368–370

- Kiyan G, Gocmen B, Tugtepe H, Karakoc F, Dagli E, Dagli TE (2009) Foreign body aspiration in children: the value of diagnostic criteria. *Int J Pediatr Otorhinolaryngol* 73(7):963–967
- Kocaoglu M, Bulakbasi N, Soyulu K, Demirbag S, Tayfun C, Somuncu I (2006) Thin-section axial multidetector computed tomography and multiplanar reformatted imaging of children with suspected foreign-body aspiration: is virtual bronchoscopy overemphasized? *Acta Radiol* 47(7):746–751
- Konen E, Katz M, Rozenman J et al (1998) Virtual bronchoscopy in children: early clinical experience. *Am J Roentgenol* 171:1699–1702
- Kosucu P, Ahmetoglu A, Koramaz I, Orhan F, Ozdemir O, Dinc H, Okten A, Gumele HR (2004) Low-dose MDCT and virtual bronchoscopy in pediatric patients with foreign body aspiration. *AJR Am J Roentgenol* 183(6):1771–1777
- Kuhn JP (1993) High-resolution computed tomography of pediatric pulmonary parenchymal disorders. *Radiol Clin North Am* 31(3):533–551
- Kumar M, Biswal N, Bhuvaneswari V, Srinivasan S (2009) Persistent pneumonia: underlying cause and outcome. *Indian J Pediatr* 76(12):1223–1226
- Laks Y, Barzilay Z (1988) Foreign body aspiration in childhood. *Pediatr Emerg Care* 4(2):102–106
- Levy M, Glick B, Springer C, Mogle P, Vatahsy E, Drexler H, Godfrey S (1983) Bronchoscopy and bronchography in children. Experience with 110 investigations. *Am J Dis Child* 137(1):14–16
- Li Y, Wu W, Yang X, Li J (2009) Treatment of 38 cases of foreign body aspiration in children causing life-threatening complications. *Int J Pediatr Otorhinolaryngol* 73(12):1624–1629
- Lim-Dunham JE, Yousefzadeh DK (1999) The interrupted bronchus: a fluoroscopic sign of bronchial foreign body in infants and children. *AJR Am J Roentgenol* 173(4):969–972
- Lima AG, Santos NA, Rocha ER, Toro IF (2008) Bronchoscopy for foreign body removal: where is the delay? *J Bras Pneumol* 34(11):956–958
- Lima JA, Fischer GB (2002) Foreign body aspiration in children. *Paediatr Respir Rev* 3(4):303–307
- Linegar AG, von Oppell UO, Hegemann S, de Groot M, Odell JA (1992) Tracheobronchial foreign bodies. Experience at red cross children's hospital, 1985–1990. *S Afr Med J* 82(3):164–167
- Losek JD (1990) Diagnostic difficulties of foreign body aspiration in children. *Am J Emerg Med* 8(4):348–350
- Lucaya J, Garcia-Pena P, Herrera L, Enriquez G, Piqueras J (2000) Expiratory chest CT in children. *AJR Am J Roentgenol* 174(1):235–241
- Ludemann JP, Riding KH (2007) Choking on pins, needles and a blowdart: aspiration of sharp, metallic foreign bodies secondary to careless behavior in seven adolescents. *Int J Pediatr Otorhinolaryngol* 71(2):307–310
- Lull RJ, Anderson JH, Telepak RJ, Brown JM, Utz JA (1980) Radionuclide imaging in the assessment of lung injury. *Semin Nucl Med* 10(3):302–310
- Maayan C, Avital A, Elpeleg ON, Springer C, Katz S, Godfrey S (1993) Complications following oat head aspiration. *Pediatr Pulmonol* 15(1):52–54
- Malis DJ, Hayes DK (1995) Retained bronchial foreign bodies: is there a role for high-resolution computed tomography scan? *Otolaryngol Head Neck Surg* 112(2):341–346
- Manach Y, Pierrot S, Couloigner V, Ayari-Khalfallah S, Nicollas R, Venail F, Pondaven S, Baculard F, Tantcheu V (2013) Diagnostic performance of multidetector computed tomography for foreign body aspiration in children. *Int J Pediatr Otorhinolaryngol* 77(5):808–812
- Mangge H, Plecko B, Grubbauer HM, Popper H, Smolle-Juttner F, Zach M (1993) Late-onset military pneumonitis after near drowning. *Pediatr Pulmonol* 15(2):122–124
- Mantel K, Butenandt I (1986) Tracheobronchial foreign body aspiration in childhood. A report on 224 cases. *Eur J Pediatr* 145(3):211–216
- McHugh K (2005) CT dose reduction in pediatric patients. *AJR Am J Roentgenol* 184(5):1706; author reply 1706–1707
- Mearns AJ, England RM, Mearns AJ, England RM (1975) Dissolving foreign bodies in the trachea and bronchus. *Thorax* 30(4):461–463
- Menendez AA, Gotay Cruz F, Seda FJ, Velez W, Trinidad Pinedo J (1991) Foreign body aspiration: experience at the university pediatric hospital. *P R Health Sci J* 10(3):127–133
- Metrangola S, Monetti C, Meneghini L, Zadra N, Giusti F (1999) Eight years' experience with foreign-body aspiration in children: what is really important for a timely diagnosis? *J Pediatr Surg* 34(8):1229–1231
- Mignon F, Mesurolle B, Chambellan A, Duboucher C, Dangeard-Chikhani S, Leclerc P, Lemesle J (1997) Foreign body granuloma mimicking bronchial tumor. Aspects in x-ray computed tomography with views by virtual endoscopy. *J Radiol* 78(11):1181–1184
- Mohammad Y, Rostum M, Dubaybo BA (2002) Laryngeal hirudini-asis: an unusual cause of airway obstruction and hemoptysis. *Pediatr Pulmonol* 33(3):224–226
- Morijiri M, Seto H, Kageyama M, Shimizu M, Nagayoshi T, Watanabe N, Kakishita M (1994) Assessment of peanut aspiration by MRI and lung perfusion scintigram. *J Comput Assist Tomogr* 18(5):836–838
- Mortellaro VE, Iqbal C, Fu R, Curtis H, Fike FB, St Peter SD (2013) Predictors of radiolucent foreign body aspiration. *J Pediatr Surg* 48(9):1867–1870
- Mu L, He P, Sun D (1991) The causes and complications of late diagnosis of foreign body aspiration in children. Report of 210 cases. *Arch Otolaryngol Head Neck Surg* 117(8):876–879
- Mu LC, Sun DQ, He P (1990) Radiological diagnosis of aspirated foreign bodies in children: review of 343 cases. *J Laryngol Otol* 104(10):778–782
- Murthy PS, Ingle VS, George E, Ramakrishna S, Shah FA (2001) Sharp foreign bodies in the tracheobronchial tree. *Am J Otolaryngol* 22(2):154–156
- Musemeche CA, Kosloske AM (1986) Normal radiographic findings after foreign body aspiration. When the history counts. *Clin Pediatr (Phila)* 25(12):624–625
- Newson TP, Parshuram CS, Berkowitz RG, Auld AW, Robinson PJ (1998) Tension pneumothorax secondary to grass head aspiration. *Pediatr Emerg Care* 14(4):287–289
- Nikolaizik WH, Warner JO (1994) Aetiology of chronic suppurative lung disease. *Arch Dis Child* 70(2):141–142
- Nimkin K, Kleinman PK, Zwerdling RG, Spevak MR, O'Sullivan BP (1995) Localized pneumothorax with lobar collapse and diffuse obstructive airway disease. *Pediatr Radiol* 25(6):449–451
- Nimrey-Atrash N, Bentur L, Elias N (2012) Subcutaneous emphysema and pneumomediastinum due to foreign body aspiration in children with asthma. *Pediatr Pulmonol* 47(1):88–90
- Nolte KB (1993) Esophageal foreign bodies as child abuse. Potential fatal mechanisms. *Am J Forensic Med Pathol* 14(4):323–326
- Northcote RJ (1983) Pulmonary aspiration presenting with generalised convulsions. *Scott Med J* 28(4):368–370
- O'Uchi T, Tokumaru A, Mikami I, Yamasoba T, Kikuchi S (1992) Value of MR imaging in detecting a peanut causing bronchial obstruction. *AJR Am J Roentgenol* 159(3):481–482
- Oguz F, Citak A, Unuvar E, Sidal M (2000) Airway foreign bodies in childhood. *Int J Pediatr Otorhinolaryngol* 52(1):11–16
- Oliveira CF, Almeida JF, Troster EJ, Vaz FA (2002) Complications of tracheobronchial foreign body aspiration in children: report of 5 cases and review of the literature. *Rev Hosp Clin Fac Med Sao Paulo* 57(3):108–111

- Oncel M, Sunam GS, Ceran S (2012) Tracheobronchial aspiration of foreign bodies and rigid bronchoscopy in children. *Pediatr Int* 54(4):532–535
- Orji FT, Akpeh JO (2010) Tracheobronchial foreign body aspiration in children: how reliable are clinical and radiological signs in the diagnosis? *Clin Otolaryngol* 35(6):479–485
- Otgun I, Fakioglu E, Arda IS, Hicsonmez A (2008) Subcutaneous emphysema and pneumomediastinum due to foreign body aspiration. *Eur J Pediatr Surg* 18(2):129–130
- Paksu S, Paksu MS, Kilic M, Guner SN, Baysal K, Sancak R, Ozturk F (2012) Foreign body aspiration in childhood: evaluation of diagnostic parameters. *Pediatr Emerg Care* 28(3):259–264
- Pan H, Lu Y, Shi L, Pan X, Li L, Wu Z (2012) Similarities and differences in aspirated tracheobronchial foreign bodies in patients under the age of 3 years. *Int J Pediatr Otorhinolaryngol* 76(6):911–914
- Pasaoglu I, Dogan R, Demircin M, Hatipoglu A, Bozer AY (1991) Bronchoscopic removal of foreign bodies in children: retrospective analysis of 822 cases. *Thorac Cardiovasc Surg* 39(2):95–98
- Piepsz A (1988) Late sequelae of foreign body inhalation. A multicentric scintigraphic study. *Eur J Nucl Med* 13(11):578–581
- Pinto A, Scaglione M, Pinto F, Guidi G, Pepe M, Del Prato B, Grassi R, Romano L (2006) Tracheobronchial aspiration of foreign bodies: current indications for emergency plain chest radiography. *Radiol Med* 111(4):497–506
- Qureshi AA, Lowe DA, McKiernan DC (2009) The origin of bronchial foreign bodies: a retrospective study and literature review. *Eur Arch Otorhinolaryngol* 266(10):1645–1648
- Qureshi S, Mink R (2003) Aspiration of fruit gel snacks. *Pediatrics* 111(3):687–689
- Ramadan HH, Bu-Saba N, Baraka A, Mroueh S (1992) Management of an unusual presentation of foreign body aspiration. *J Laryngol Otol* 106(8):751–752
- Reilly JS, Walter MA (1992) Consumer product aspiration and ingestion in children: analysis of emergency room reports to the national electronic injury surveillance system. *Ann Otol Rhinol Laryngol* 101(9):739–741
- Roda J, Nobre S, Pires J, Estevao MH, Felix M (2008) Foreign bodies in the airway: a quarter of a century's experience. *Rev Port Pneumol* 14(6):787–802
- Rodrigues AJ, Oliveira EQ, Scordamaglio PR, Gregorio MG, Jacomelli M, Figueiredo VR (2012a) Flexible bronchoscopy as the first-choice method of removing foreign bodies from the airways of adults. *J Bras Pneumol* 38(3):315–320
- Rodrigues AJ, Scussiatto EA, Jacomelli M, Scordamaglio PR, Gregorio MG, Palomino AL, Oliveira EQ, Figueiredo VR (2012b) Bronchoscopic techniques for removal of foreign bodies in children's airways. *Pediatr Pulmonol* 47(1):59–62
- Rodriguez H, Cuestas G, Botto H, Nieto M, Cocciaglia A, Passali D, Gregori D (2013) Delayed diagnosis of foreign body in the airway in children: case series. *Arch Argent Pediatr* 111(3):e69–e73
- Rogers LF, Igini JP (1975) Beverage can pull-tabs. Inadvertent ingestion or aspiration. *JAMA* 233(4):345–348
- Saki N, Nikakhlagh S, Rahim F, Abshirini H (2009) Foreign body aspirations in infancy: a 20-year experience. *Int J Med Sci* 6(6):322–328
- Samkani A, Larsen KV, Faber CE, Godballe C (2013) Bronchoscopy should always be performed in children on suspicion of foreign body aspiration. *Dan Med J* 60(10):A4715
- Sane SM, Faerber EN, Belani KK (1999) Respiratory foreign bodies and *Eikenella corrodens* brain abscess in two children. *Pediatr Radiol* 29(5):327–330
- Sattar A, Ahmad I, Javed AM, Anjum S (2011) Diagnostic accuracy of chest x-ray in tracheobronchial foreign body aspiration in paediatric patients. *J Ayub Med Coll Abbottabad* 23(4):103–105
- Schmidt H, Manegold BC (2000) Foreign body aspiration in children. *Surg Endosc* 14(7):644–648
- Scully RE, Mark EJ, McNeely BU (1983) Case records of the Massachusetts general hospital: case 48–1983. *N Engl J Med* 309:1374–1381
- Scully RE, Mark EJ, McNeely BU (1998) Case records of the Massachusetts general hospital: case 31–1998. *N Engl J Med* 339:1144–1151
- Sehgal A, Singh V, Chandra J, Mathur NN (2002) Foreign body aspiration. *Indian Pediatr* 39(11):1006–1010
- Seibert RW, Seibert JJ, Williamson SL (1986) The opaque chest: when to suspect a bronchial foreign body. *Pediatr Radiol* 16(3):193–196
- Senkaya I, Sagdic K, Gebitekin C, Yilmaz M, Ozkan H, Cengiz M (1997) Management of foreign body aspiration in infancy and childhood. A life-threatening problem. *Turk J Pediatr* 39(3):353–362
- Shachor-Meyouhas Y, Guilburd JN, Kassir I (2009) Brain abscess complicating foreign body aspiration. *Isr Med Assoc J* 11(9):564–565
- Shivakumar AM, Naik AS, Prashanth KB, Shetty KD, Praveen DS (2003) Tracheobronchial foreign bodies. *Indian J Pediatr* 70(10):793–797
- Shlizerman L, Mazzawi S, Rakover Y, Ashkenazi D (2010) Foreign body aspiration in children: the effects of delayed diagnosis. *Am J Otolaryngol* 31(5):320–324
- Siddiqui MA, Banjar AH, Al-Najjar SM, Al-Fattani MM, Aly MF (2000) Frequency of tracheobronchial foreign bodies in children and adolescents. *Saudi Med J* 21(4):368–371
- Sidell DR, Kim IA, Coker TR, Moreno C, Shapiro NL (2013) Food choking hazards in children. *Int J Pediatr Otorhinolaryngol*
- Silva AB, Muntz HR, Clary R (1998) Utility of conventional radiography in the diagnosis and management of pediatric airway foreign bodies. *Ann Otol Rhinol Laryngol* 107(10 Pt 1):834–838
- Smith PC, Swischuk LE, Fagan CJ (1974) An elusive and often unsuspected cause of stridor or pneumonia (the esophageal foreign body). *Am J Roentgenol Radium Ther Nucl Med* 122(1):80–89
- Sofer S, Baer R, Gussarsky Y, Lieberman A, Bar-Ziv J (1984a) Pulmonary edema secondary to chronic upper airway obstruction. Hemodynamic study in a child. *Intensive Care Med* 10(6):317–319
- Sofer S, Bar-Ziv J, Mogle P (1985) Pulmonary oedema following choking: report of two cases. *Eur J Pediatr* 143(4):295–296
- Sofer S, Bar-Ziv J, Scharf SM (1984b) Pulmonary edema following relief of upper airway obstruction. *Chest* 86(3):401–403
- Spencer MJ, Millet VE, Dudley JP, Sherrod JL, Bryson YJ (1981) Grassheads in the tracheobronchial tree: two different outcomes. *Ann Otol Rhinol Laryngol* 90(4 Pt 1):406–408
- Steelman R, Millman E, Steiner M, Gustafson R (1997) Aspiration of a primary tooth in a patient with a tracheostomy. *Spec Care Dentist* 17(3):97–99
- Steen KH, Zimmermann T (1990) Tracheobronchial aspiration of foreign bodies in children: a study of 94 cases. *Laryngoscope* 100(5):525–530
- Strickland AL, Elhassani SB, Stowe DG (1987) Aspiration of metallic foil by children: report of two cases. *J S C Med Assoc* 83(2):49–51
- Svedstrom E, Puhakka H, Kero P (1989) How accurate is chest radiography in the diagnosis of tracheobronchial foreign bodies in children? *Pediatr Radiol* 19(8):520–522
- Svensson G (1985) Foreign bodies in the tracheobronchial tree. Special references to experience in 97 children. *Int J Pediatr Otorhinolaryngol* 8(3):243–251
- Swanson KL, Edell ES (2001) Tracheobronchial foreign bodies. *Chest Surg Clin N Am* 11(4):861–872
- Szold A, Udassin R, Seror D, Mogle P, Godfrey S (1991) Acquired tracheoesophageal fistula in infancy and childhood. *J Pediatr Surg* 26(6):672–675



- Tahir N, Ramsden WH, Stringer MD (2009) Tracheobronchial anatomy and the distribution of inhaled foreign bodies in children. *Eur J Pediatr* 168(3):289–295
- Tang FL, Chen MZ, Du ZL, Zou CC, Zhao YZ (2006) Fibrobronchoscopic treatment of foreign body aspiration in children: an experience of 5 years in Hangzhou city China. *J Pediatr Surg* 41(1):e1–e5
- Tang LF, Chen ZM (2009) Fiberoptic bronchoscopy in neonatal and pediatric intensive care units: a 5-year experience. *Med Princ Pract* 18(4):305–309
- Tang LF, Xu YC, Wang YS, Wang CF, Zhu GH, Bao XE, Lu MP, Chen LX, Chen ZM (2009) Airway foreign body removal by flexible bronchoscopy: experience with 1027 children during 2000–2008. *World J Pediatr* 5(3):191–195
- Tashita H, Inoue R, Goto E, Kondo N (1998) Magnetic resonance imaging for early detection of bronchial foreign bodies. *Eur J Pediatr* 157(5):442
- Teixidor de Otto J, Negro F, Gutierrez C (1980) Removal of foreign bodies from the upper airways and the bronchial tree of small children. *Z Kinderchir Grenzgeb* 30(2):137–140
- Tenjavic D, Petrovic S, Dautovic GV, Lovrenski J, Rodic BB (2013) Clinical and radiological characteristics of unrecognised foreign body aspiration into respiratory tract in children. *Med Pregl* 66(5–6):214–219
- Theander G (1970) Motility of diaphragm in children with bronchial foreign bodies. *Acta Radiol Diagn (Stockh)* 10(2):113–129
- Tjhen KY, Schmaltz AA, Ibrahim Z, Nolte K (1978) Pneumopericardium as a complication of foreign body aspiration. *Pediatr Radiol* 7(2):121–123
- Ucan ES, Tahaoglu K, Mogolkoc N, Dereli S, Basozdemir N, Basok O, Turktaş H, Akkoçlu A, Ates M (1996) Turban pin aspiration syndrome: a new form of foreign body aspiration. *Respir Med* 90(7):427–428
- Ugrinovic AB, Djukic VB, Erdevicki LV, Arsenijevic SD, Milovanovic JP, Andric SD, Radoic NN (2009) Foreign bodies of the lower respiratory tract. *Acta Chir Jugosl* 56(3):127–130
- Van Looij MA, Rood PP, Hoeve LJ, Borgstein JA (2003) Aspirated foreign bodies in children: why are they more commonly found on the left? *Clin Otolaryngol Allied Sci* 28(4):364–367
- Wales J, Jackimczyk K, Rosen P (1983) Aspiration following a cave-in. *Ann Emerg Med* 12(2):99–101
- Walz PC, Scholes MA, Merz MN, Elmaraghy CA, Jatana KR (2013) The internet, adolescent males, and homemade blowgun darts: a recipe for foreign body aspiration. *Pediatrics* 132(2):e519–e521
- Wesenberg RL, Blumhagen JD (1979) Assisted expiratory chest radiography: an effective technique for the diagnosis of foreign-body aspiration. *Radiology* 130(2):538–539
- Wiseman NE (1984) The diagnosis of foreign body aspiration in childhood. *J Pediatr Surg* 19(5):531–535
- Witt WJ (1985) The role of rigid endoscopy in foreign body management. *Ear Nose Throat J* 64(2):70–74
- Yazici H, Dogan S, Sunter AV, Yilmaz E, Daskaya H (2012) Surprising cause of respiratory distress in child: laryngeal leech. *J Craniofac Surg* 23(3):e272–e273
- Zaupa P, Saxena AK, Barounig A, Hollwarth ME (2009) Management strategies in foreign-body aspiration. *Indian J Pediatr* 76(2):157–161
- Zaytoun GM, Rouadi PW, Baki DH (2000) Endoscopic management of foreign bodies in the tracheobronchial tree: predictive factors for complications. *Otolaryngol Head Neck Surg* 123(3):311–316
- Zerella JT, Dimler M, McGill LC, Pippus KJ (1998) Foreign body aspiration in children: value of radiography and complications of bronchoscopy. *J Pediatr Surg* 33(11):1651–1654
- Zhijun C, Fugao Z, Niankai Z, Jingjing C (2008) Therapeutic experience from 1428 patients with pediatric tracheobronchial foreign body. *J Pediatr Surg* 43(4):718–721
- Zielinski R, Piotrowska V, Zakrzewska A (2011) Pneumomediastinum and emphysema in a case of a soft bronchial foreign body aspiration in a child. A case report. *Otolaryngol Pol* 65(1):59–61
- Zuniga S, De Manana M, Monge M, Garcia C, Gonzalez S, Iturriaga L, Sanchez I (2000) Vegetal foreign body in the airway: an unusual cause of hemoptysis in childhood. Clinical case. *Rev Med Chil* 128(3):323–329

# Imaging of the Pediatric Thymus and Thymic Disorders

Cassandra M. Sams and Stephan D. Voss

## Contents

<b>1</b>	<b>Introduction</b> .....	327
1.1	Historical Perspective.....	327
1.2	Embryology.....	328
1.3	Histology.....	328
1.4	Function.....	329
1.5	Anatomy.....	329
<b>2</b>	<b>Imaging Appearance</b> .....	329
2.1	Chest Radiography.....	329
2.2	Ultrasound.....	330
2.3	Fluoroscopy.....	330
2.4	Computed Tomography.....	331
2.5	Magnetic Resonance Imaging.....	331
2.6	Nuclear Medicine.....	332
<b>3</b>	<b>Congenital and Developmental Anomalies and Variants</b> .....	333
<b>4</b>	<b>Benign Thymic Masses</b> .....	335
4.1	Thymic Cysts.....	335
4.2	Thymolipoma.....	335
<b>5</b>	<b>Thymic Hyperplasia</b> .....	336
<b>6</b>	<b>Malignant Thymic Masses</b> .....	337
6.1	Thymoma.....	337
6.2	Thymic Carcinomas.....	338
6.3	Thymic Carcinoids.....	338
6.4	Other Masses.....	339
<b>7</b>	<b>Leukemia and Lymphoma</b> .....	339
7.1	Leukemia.....	340
7.2	Lymphoma.....	341
<b>8</b>	<b>Conclusion</b> .....	347
	<b>References</b> .....	347

## Abstract

Imaging of the thymus can prove challenging for the radiologist. The purpose of this chapter is to provide a broad overview of the thymus, its role in normal physiology and pathologic processes. After a brief discussion of the history of the thymus, the embryology, anatomy, and histology of the thymus are reviewed. The normal appearance of the thymus using the various imaging modalities available to the radiologist is then discussed, followed by an overview of congenital thymic variants and benign pathologies involving the thymus, including thymolipoma, thymoma, and thymic rebound. The chapter concludes with a summary of thymic malignancies, with a primary focus on leukemia and lymphoma.

## 1 Introduction

### 1.1 Historical Perspective

Understanding of the thymus has a colorful and storied past. The word thymus derives from the Greek root *thymos* meaning “wartlike excrescence” according to the Oxford English Dictionary. In arriving at this name, anatomists of the time were reminded of the bud of the thyme plant. The Greeks believed the thymus to be the seat of the soul, and thyme leaves were burned at ceremonies as a means of purification. While Galen was the first to note that the size of the thymus varies with age, he was uncertain of its function and referred to it as “the organ of mystery” (Jacobs et al. 1999).

An early description of the thymus is found in Blankaart’s 1684 Physical dictionary in which it is described as “a fleshy Tumor that hangs upon the Body like a Wart.” The function attributed to the thymus was to separate “watry Humour, called Lympha, from the blood, and empties it by

C. M. Sams · S. D. Voss (✉)  
Department of Radiology, Boston Children’s Hospital,  
300 Longwood Avenue, Boston, MA 02115, USA  
e-mail: stephan.voss@childrens.harvard.edu

the Lymphatic Vessels.” Indeed, the true function of the thymus was not discovered until 1961 by the Australian physician Jacques Miller (Varga et al. 2011).

Before the middle of the twentieth century, the thymus remained a poorly understood organ. Two fictional disorders were attributed to its presence: thymic asthma and status thymolympathicus (Jacobs et al. 1999; Varga et al. 2011; Kaufman et al. 2001). The confusion surrounding the (incorrectly) perceived pathology ascribed to the thymus arose from its disproportionately large size during infancy and its proximity to the airway and great vessels. When infants and young children who died suddenly subsequently underwent autopsy, it was noted that the thymus was significantly larger than in children who were chronically ill. Lacking any other explanation for the cause of death, this apparently large, but actually normal, thymus was deemed the cause of death.

In an effort to prevent such deaths, thymic enlargement was treated with surgery and radiation. The first successful radiation therapy consisted of 96 min of radiation to the chest (Jacobs et al. 1999). Recognizing the potential harmful effects of radiation, these doses were subsequently reduced to half of the skin erythema dose. As one would expect, children treated in this manner had an increased rate of malignancy later in life. This unfortunate practice persisted into the 1960s.

The decline of this belief in thymic pathology coincided with the rise of pediatric radiology as a distinct subspecialty. As our subspecialty grew, it was recognized that the thymus could be quite large and create the appearance of a “mass” on chest radiographs in normal, healthy infants. Dr. John Caffey, one of the forefathers in the field of pediatric radiology, felt that one of his greatest contributions to the field of medicine was the “destruction of the thymic myth” (Jacobs et al. 1999). Indeed, one of the first major accomplishments in the field of pediatric radiology was demonstration of the varying sizes and shapes of a normal thymus.

## 1.2 Embryology

Thymic embryology is helpful in understanding the variable appearance of the normal thymus, as well as expected locations for aberrant thymic tissue. The thymus begins its development during the sixth week of gestation and arises from the ventral portion of the paired third pharyngeal pouches, with a variable contribution from the fourth pharyngeal pouch. During the seventh week of development, the thymic primordia detach from the pharyngeal wall and form a central cleft, known as the thymopharyngeal duct. During the eighth week of development, together with the inferior parathyroid anlagen, they descend via this duct along the

carotid sheath into the superior–anterior mediastinum. There the paired structures approach one another, although a thin capsule surrounds each lobe preventing true fusion (Varga et al. 2011; Kaufman et al. 2001).

Until approximately the 10th week of development, the thymus is comprised almost exclusively of epithelial cells. Beginning at 10th week, lymphoid precursor cells migrate from the fetal liver and bone marrow to the developing thymus. By the 13 and 14th weeks of gestation, the distinction between the thymic cortex and medulla becomes obvious, and from the 14th to 16th weeks, Hassall’s corpuscles undergo a striking proliferation, which in part accounts for the rapid early growth of the thymus. For the remainder of gestation, the thymus continues to grow. By birth, the thymus reaches its greatest weight relative to the weight of the body.

## 1.3 Histology

The cortex of the thymus is composed predominantly of thymocytes which are hematopoietic progenitor cells that mature and differentiate into T-cells. A “blood-thymus” barrier in the thymic cortex controls the introduction of antigenic material to the developing T-cells. Only efferent lymphatics, not afferent lymphatics, exist, affecting the distribution of T-cells and serving to provide an environment that allows the maturing immune cells to respond to both positive and negative selective forces. The result is the generation of a repertoire of immune cells able to elicit an appropriate response to foreign pathogens, while remaining immunologically tolerant to self-antigens.

The medulla is composed primarily of epithelial cells, so-called nurse cells, that play a vital role in the maturation of T-cell lymphocytes. Hassall’s corpuscles are also located in the medulla; these structures are composites of medullary epithelial cells and surrounding cell deposits that have a characteristic histological appearance as seen in Fig. 1. Their true function, however, remains unclear (Anastasiadis and Ratnatunga 2007). Other less abundant cell types are also found in the thymus, including antigen-presenting macrophages and myoid cells, the latter being of particular interest given their potential role as a target in the immune-mediated disorder myasthenia gravis. Capillaries, which carry the mature lymphocytes into the systemic circulation, are also present in the medulla. With aging, the thymus involutes and the epithelial cells and thymocytes are replaced by adipose tissue. Despite this age-related decline both in the bulk of thymic tissue and in thymic function, Hassall’s corpuscles persist, allowing the thymus to be identified histologically even in its atrophied state.



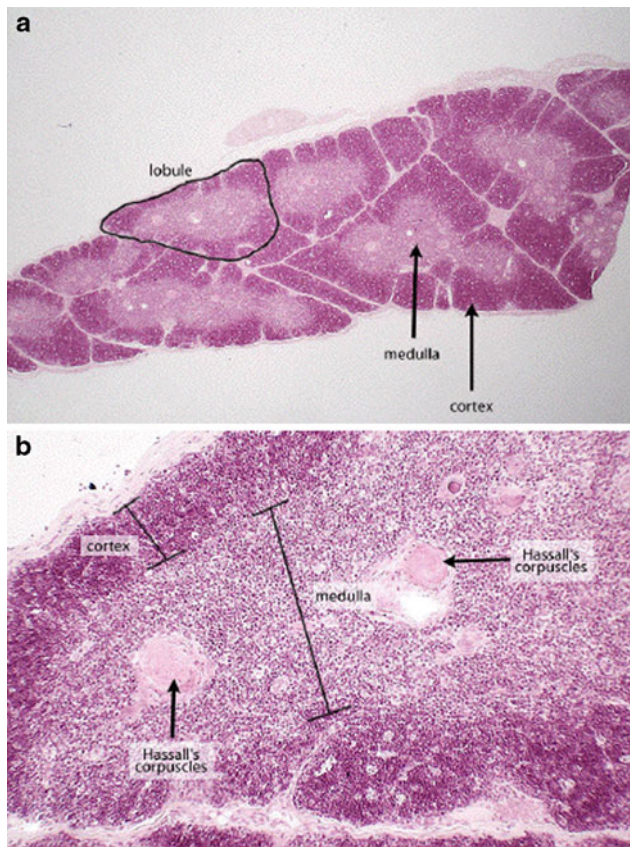


**Fig. 1** Histology of the thymus. **a** The thymus of an infant viewed under low-power microscopy shows the lobulated appearance as well as the clear delineation between cortex and medulla. **b** On higher power, the Hassall's corpuscles are seen with surrounding thymocytes. Reproduced from [http://www.dartmouth.edu/~anatomy/Histo/lab\\_6/lymphoid/DMS117/popup.html](http://www.dartmouth.edu/~anatomy/Histo/lab_6/lymphoid/DMS117/popup.html), by permission of Dr. Rand S. Swenson, MD, PhD, Dartmouth Medical School

## 1.4 Function

The thymus is one of the central lymphoid organs and plays a key role in cellular immunity via the generation of mature, antigen-specific T-cells. Pro-thymocyte precursor cells migrate from the bone marrow into the thymus, which serves as the site of T-cell “education” and maturation. Via highly complex signaling pathways, the thymocytes develop into physiologically useful T-cells that are ideally able to respond to a given foreign pathogen while recognizing and remaining tolerant of normal host cells. Throughout life the thymus serves as the site of T-cell differentiation and maturation, typically beginning this process after the first few months of life and peaking in early/mid childhood. Because we do not require an ever-increasing T-cell immune repertoire, the need for continuous generation of T-cells plateaus, and the thymus begins to undergo a gradual process of atrophy and involution in the second decade of life.

## 1.5 Anatomy

The thymus is a bilobed organ located in the midline behind the sternum and anterior to the pericardium, heart, and great vessels. The thymus has a soft, pliable texture and drapes over the structures of the mediastinum. On gross inspection, the thymus during infancy is pink due to the rich vascular supply but becomes progressively more yellow due to accumulation of fat. Loose connective tissue surrounds both lobes. Each lobe is composed of multiple lobules, the septations of which extend to the corticomedullary junction, so that the medulla is contiguous throughout each lobe (Safieddine and Keshavjee 2011).

The blood supply to the thymus derives from three principle sources: the superior thymic artery, a branch of the inferior thyroid artery; the lateral thymic artery, a branch of the internal mammary artery; and the posterior thymic arteries, branches from the aorta and brachiocephalic artery (Safieddine and Keshavjee 2011). The veins draining the thymus follow the interlobar septa and fuse along the posterior venous plexus, which in turn drains into the brachiocephalic vein (Safieddine and Keshavjee 2011). Variably, the superior aspect of the thymus may drain into the inferior thyroid vein (Safieddine and Keshavjee 2011). The blood supply of the thymus is shown in Fig. 2.

The thymus weighs approximately 13–15 g at birth, increasing to approximately 25–45 g at puberty when it attains its maximum weight (Safieddine and Keshavjee 2011). Subsequently the thymus begins its gradual involution, with an average weight of approximately 6 g by age 70 (Safieddine and Keshavjee 2011). On cross-sectional imaging, the infant thymus has a quadrilateral shape with convex margins. As the child ages and the thymus involutes, the margins of the thymus become concave and assume the triangular configuration typically seen in adults. The thickness of the left lobe of the thymus can be used as an indicator of thymic enlargement, with a maximum dimension of 18 mm perpendicular to the axis of the aortic arch in patients younger than 20 years of age (Restrepo et al. 2005).

## 2 Imaging Appearance

The thymus can be evaluated by a variety of imaging modalities including chest radiography (CXR), fluoroscopy, ultrasound, computed tomography (CT), magnetic resonance imaging (MRI), and nuclear medicine.

### 2.1 Chest Radiography

Familiarity with the wide range of appearances of the normal thymus gland on chest radiography is important for all

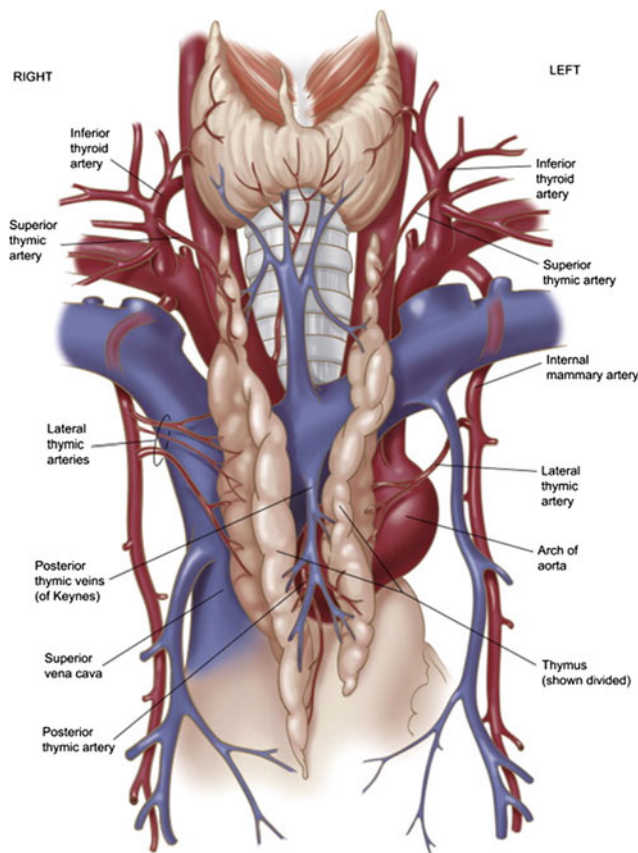


**Fig. 2** Illustration of the arterial blood supply and venous drainage of the thymus. Reproduced from Safieddine and Keshavjee 2011, with permission from Elsevier Limited, Oxford, UK

radiologists. In infants and young children, the thymus can be impressively large on frontal radiographs. The classic “sail” sign, a sharply demarcated pointed base seen most frequently along the right inferior margin of the thymus gland, is actually found in only 5 % of children (Fig. 3a). The wave sign, the smooth undulation of the thymus as it interdigitates along the anterior costal margin, is more frequently seen but is less striking (Fig. 3b). To potentiate the wave sign, decubitus views can be used as a problem-solving tool for determining the etiology of anterior mediastinal mass. In most instances the thymus is seen simply as a smoothly marginated, low-density soft tissue causing widening of the superior mediastinum. This is in contrast to pathologic masses, which commonly have irregular or lobular margins and cause mass effect on adjacent structures, rather than smoothly conforming to the available space in the mediastinum. The thymus becomes less evident on chest radiographs beginning around 2 years of age and typically is not seen in children over 8 years of age (Arthur 2000). In cases of a particularly unusual appearance of the

thymus, further evaluation can be obtained with other imaging modalities as described below.

## 2.2 Ultrasound

Ultrasound is a useful tool in the evaluation of the thymus in infants and young children due to its lack of ionizing radiation and its real-time imaging capabilities. Even after the thymus is no longer apparent radiographically, it may still be visible with ultrasound (Adam and Ignotus 1993). A high frequency, linear transducer works best in the neonatal population with lower frequency transducers used in the older age groups. A variety of approaches can be used in the infant including subxyphoid, parasternal, suprasternal, and transcostal windows (Mong et al. 2012). However, as ossification of the manubrium and sternum progresses, a suprasternal approach provides the best acoustic window.

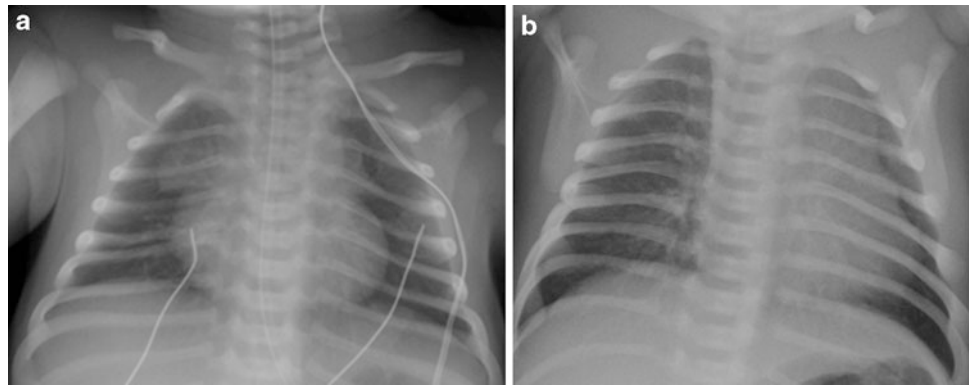
In the neonate and young child, the thymus has a distinctive sonographic signature making it identifiable when present in abnormal locations. The thymus has a heterogeneous, but uniform echotexture, and is predominantly hypoechoic relative to the liver, thyroid, and spleen, with punctate and linear echogenic foci secondary to the fat present (Fig. 4) (Mong et al. 2012; Newman 2011; Kim et al. 2000). As the patient ages, the thymus becomes more homogeneous and echogenic due to increased fat content. It should have a smooth contour due to the capsule surrounding each lobe with no compression of the surrounding structures. During real-time scanning, the thymus should change shape in response to respiratory and cardiac motion reflecting its soft, pliable nature, which further helps to delineate it from a pathologic mediastinal mass.

Particularly in younger children, ultrasound can also be used in the evaluation of thymic masses. Ultrasound can also be used for real-time guidance of biopsies of suspected thymic masses.

## 2.3 Fluoroscopy

Fluoroscopy is of limited use in the dedicated evaluation of the thymus. However, knowledge of the expected fluoroscopic appearance of the thymus can be useful during routine examinations such as airway fluoroscopy and upper GI examinations. As on chest radiography, the thymus is seen as a soft tissue density in the anterior mediastinum. Its size and shape should vary with respiration, and it should never exert substantial mass effect on any of the mediastinal

**Fig. 3** Sail sign and wave sign. **a** AP radiograph of the chest in a neonate demonstrating a bilateral sail sign. **b** AP radiograph in a neonate demonstrating a wave sign along the left thymic border as it interdigitates along the anterior costal margin



structures, i.e., displacement of a contrast filled esophagus should not be attributed to a normal thymus.

## 2.4 Computed Tomography

CT provides excellent visualization of the thymus and thymic pathology. However, given concerns about radiation risk from CT scanning, this modality should be used judiciously in characterizing abnormalities of the thymus. The thymus can typically be seen in the anterior mediastinum on CT imaging throughout childhood, and is still visible in most patients up to the age of 30 years. On CT imaging performed without intravenous contrast administration, the thymus has a homogeneous appearance that, compared to cardiac and chest wall musculature, is hyperdense in infancy and nearly isodense later in childhood (mean Hounsfield Unit values ranging from 80.8 in infancy to 56.4 at 14 years of age) (Sklair-Levy et al. 2000). It demonstrates homogeneous enhancement on post-contrast images. The attenuation of the thymus declines with increasing age as it becomes increasingly replaced with fat (Sklair-Levy et al. 2000).

On cross-sectional imaging, the appearance of the thymus is consistent with its radiographic appearance. The thymus has a quadrilateral configuration with bulging contours in infants and young children, becoming progressively more triangular in shape with concave margins in older children and adolescents (Fig. 5). The relationship of the thymus to its surrounding structures, particularly the presence of compression or invasion in the setting of thymic pathology, is well seen with CT. Internal heterogeneity, calcifications, fat, or abnormal enhancement are also well depicted with CT. For operative planning purposes, the location of the feeding and draining vessels can be delineated on contrast-enhanced CT imaging.

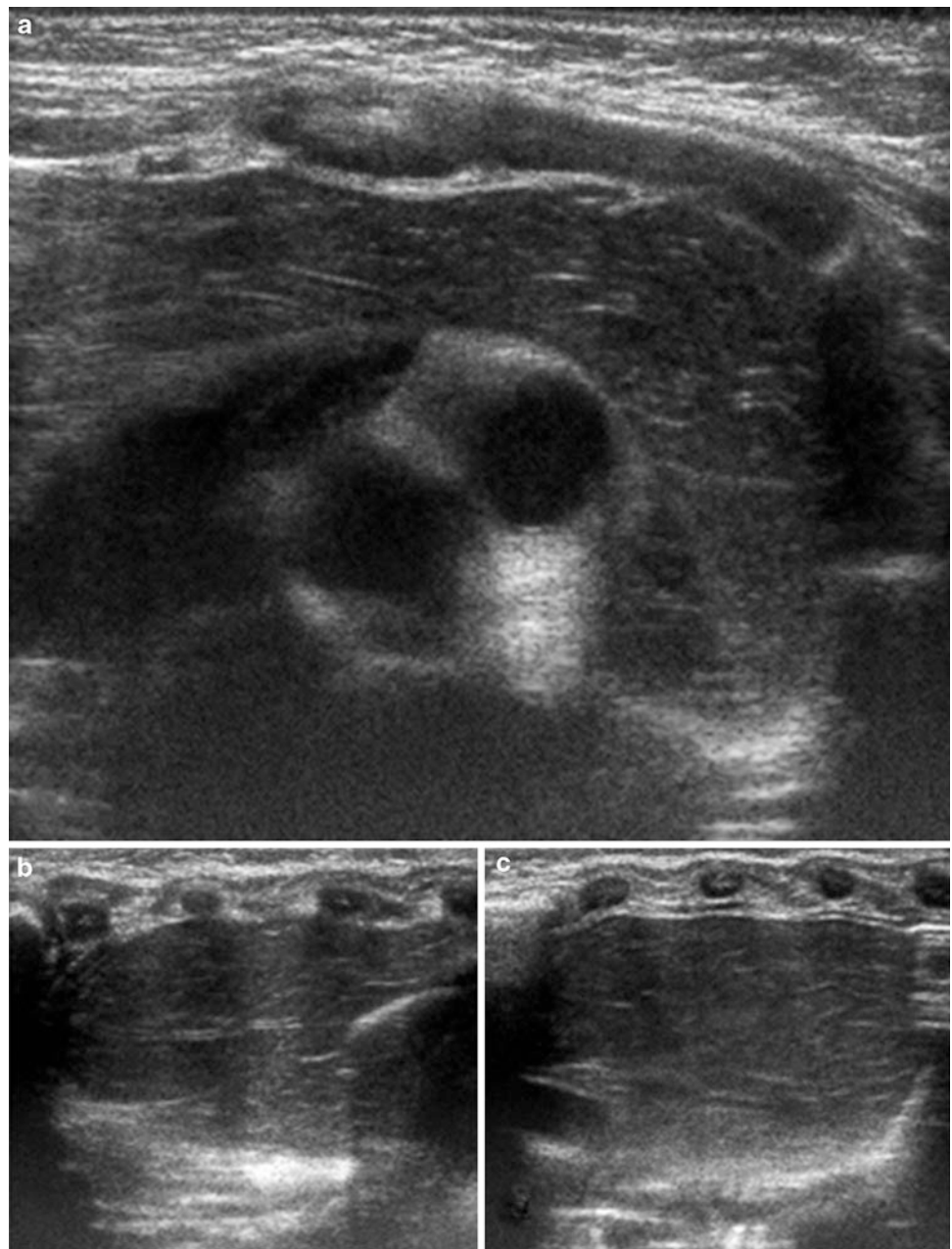
## 2.5 Magnetic Resonance Imaging

MRI can be a valuable tool in the evaluation of patients with suspected thymic pathology. However, due to its relatively greater expense, study length, and variable need for sedation, MRI is not typically the initial choice of imaging modality for evaluation of the thymus. The MRI appearance of the thymus varies as it involutes. Prior to fatty infiltration, the signal intensity of the thymus is slightly greater than that of muscle but less than that of fat on T1-weighted images, while on nonfat suppressed FSE-T2 weighted images (Henkelman et al. 1992), the signal intensity is increased relative to muscle, but lower than subcutaneous fat (Fig. 6) (Molina et al. 1990). As the thymus becomes progressively more fatty its signal intensity approaches with that of pure fat (Ackman and Wu 2011; Siegel et al. 1989). As on CT, there is homogeneous enhancement of the normal thymus on post-contrast images. Due to the presence of fat within non-neoplastic thymus, opposed phase imaging has been studied to differentiate between normal thymus/thymic hyperplasia and a solid mass lesion (Inaoka et al. 2007). This imaging technique has not been studied on the thymus of younger (<16 years of age) patient populations. However, it may be of value since small quantities of fat coexisting with nonfatty soft tissue in the same imaging voxel can be detected by opposed phase imaging, and could provide a sensitive means of characterizing normal thymic tissue in younger age groups, where the quantity of thymic fat is less abundant.

Coil selection depends on the child's size. Both T1- and T2-weighted images in at least two planes should be used for routine evaluation of the thymus. The sagittal plane in particular can nicely demonstrate the anteriorly positioned normal thymus. In order to achieve high-quality MRI images of the thymus, one must keep in mind the proximity of the thymus to the moving heart and lungs. If close scrutiny of the



**Fig. 4** Normal sonographic appearance of the thymus. Transverse (a) and sagittal ultrasound images of the right (b) and left (c) lobes of the thymus from an infant demonstrating the normal hypoechoic echotexture with scattered echogenic lines due to the interspersed fat. Note on transverse image that the thymus drapes over the mediastinal structures without causing any mass effect. On the sagittal images, the thymus has an undulating contour beneath the ribs, the sonographic equivalent of the wave sign

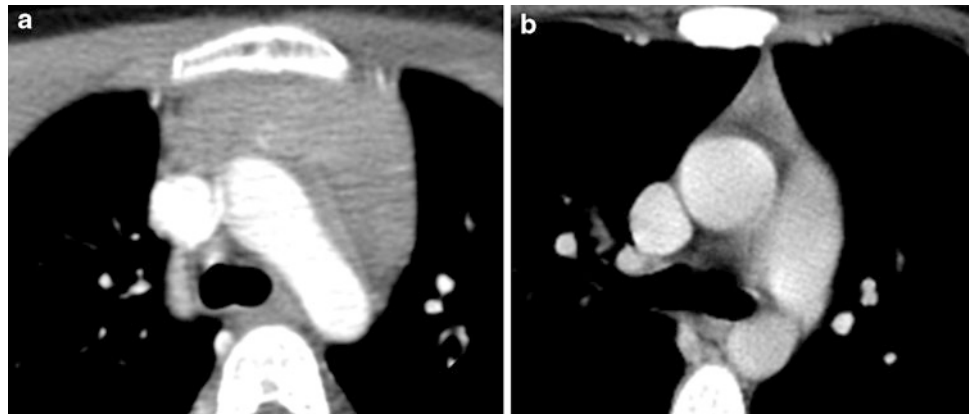


thymus is desired, cardiac gating and breath-hold sequences may be needed. The phase-encoding direction should be in the transverse medial–lateral rather than anterior–posterior direction to prevent motion artifact from interfering in the evaluation of the thymus as shown in Fig. 7.

## 2.6 Nuclear Medicine

- i. *F-18 FDG PET*—On PET imaging in young patients, the thymus is seen as an FDG-avid, bilobed organ with an arrowhead configuration. The degree of FDG uptake varies greatly between normal individuals, but typically decreases with age. Prior studies have demonstrated uptake in the thymus gland in all patients younger than 12 and in 50 % of patients between 12 and 17 years of age (Connolly and Connolly 2003). Rebound thymic hyperplasia, which is discussed later in this article, can demonstrate FDG avidity independent of patient age. Correlation with cross-sectional imaging, typically CT images acquired as part of integrated PET/CT examinations, can be helpful to differentiate normal from abnormal FDG uptake.
- ii. *Other radiopharmaceuticals*—In addition to FDG, the normal thymus can take up a variety of radiotracers. Due to the presence of the sodium-iodide symporter,

**Fig. 5** Age-related changes in normal CT appearance of the thymus. **a** Axial CT image with contrast in a young child demonstrates the normal quadrilateral configuration of the thymus with bulging contours. **b** Axial CT image with contrast in a young adult demonstrates the normal triangular configuration that the thymus assumes as it involutes



the thymus has normal low-level avidity for radioactive iodine (I-123 and I-131) and uptake in this gland should not be mistaken for ectopic thyroid tissue (Connolly and Connolly 2003). In-111 pentetreotide can also localize to the thymus due to the presence of somatostatin receptors; the number of these receptors declines with age with a corresponding decrease in the avidity of this agent (Connolly and Connolly 2003).

Gallium scintigraphy with  $^{67}\text{Ga}$ -citrate enjoyed widespread use for imaging infection and was an effective agent for staging and assessing response in patients with lymphoma (Even-Sapir and Israel 2003). With the increasing use of FDG-PET, gallium scintigraphy is now rarely used. Thymic uptake of gallium has been noted in up to 61 % of children less than 2 years of age, both in patients with lymphoid and nonlymphoid tumors (Connolly and Connolly 2003). As age increases, the degree of gallium uptake in the thymus diminishes, although thymic uptake of gallium may still be seen in adults (Connolly and Connolly 2003). Gallium uptake can also be seen in the setting of thymic hyperplasia and can persist for several years after the inciting event.

### 3 Congenital and Developmental Anomalies and Variants

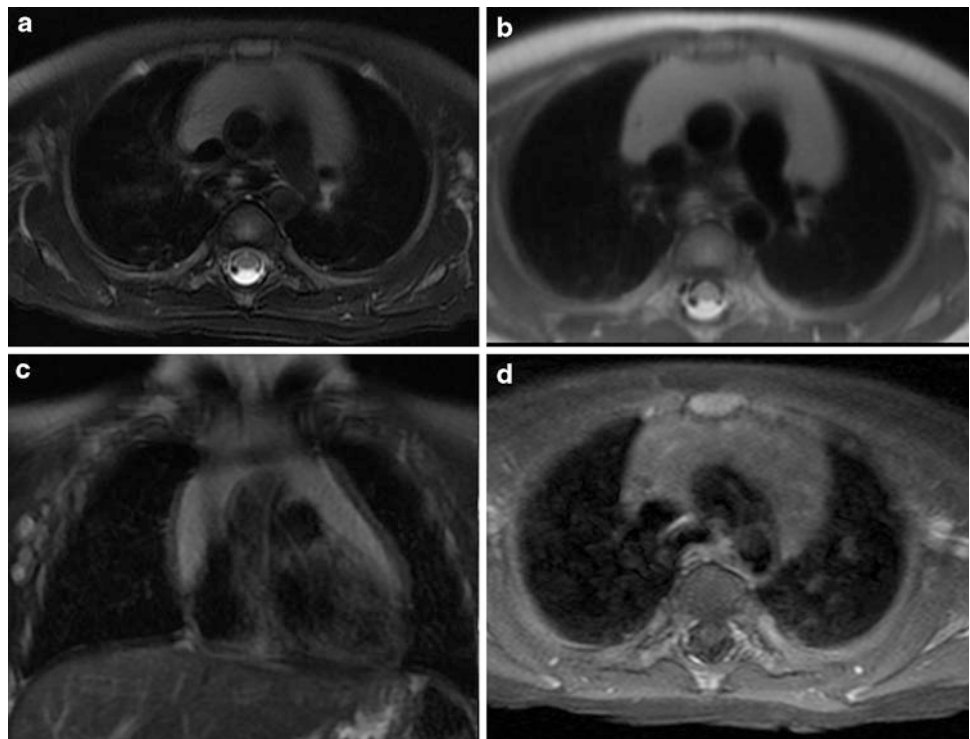
The thymus has a variety of normal configurations that should not be mistaken for pathology. Accessory thymic tissue, which is thymic tissue that arises from rests of thymic cells along their path of normal embryological descent, is considered distinct from ectopic thymic tissue which arises in abnormal locations, such as the base of the skull, presumably due to aberrant migration pathways (Tunkel et al. 2001).

A rare congenital variant is the retrocaval thymus which, as the name would suggest, is posterior extension of the thymus behind the superior vena cava (SVC). This variant can displace the SVC laterally and mimic a mediastinal mass or right upper lobe collapse on chest radiographs. Cross-sectional imaging demonstrates the posterior extent of the normal-appearing thymic parenchyma as seen in Fig. 8, helping to distinguish this normal variant from a pathologic posterior mediastinal mass.

A much more frequently encountered variant is suprasternal extension of the thymus. In up to 2/3 of infants and young children, the thymus can extend superiorly into the neck to the level of the thyroid gland (Fig. 9). While the normal thymus is not commonly appreciated on routine physical examination, during times of increased intrathoracic pressure the suprasternal extension of the thymus can become more apparent, which may be alarming to parents and clinicians alike given its mass-like appearance (Costa et al. 2010). Ultrasound should be the initial imaging modality of choice in this clinical situation. Not only is ultrasound effective at demonstrating normal ectopic thymic tissue, it is also useful for the detection of other mass lesions in the head and neck. As expected, the sonographic appearance of suprasternal thymic tissue is characteristic of normal thymus. By simply redirecting the transducer, this superiorly positioned tissue can be followed inferiorly and is usually contiguous with the normal thymus located in the anterior-superior mediastinum. In more challenging cases, a limited MRI examination can also be used to demonstrate superior extension of normal thymic tissue.

This normal superior extension of the thymus must be distinguished from accessory cervical thymic tissue which can be found anywhere along the path of thymic descent from the angle of the mandible to the superior mediastinum. It is thought to occur secondary to an arrest in its normal descent or sequestration of a thymic rest during its caudal

**Fig. 6** Normal MRI appearance of the thymus. **a** Transverse T2-weighted image with fat suppression shows a homogeneously high-signal intensity thymus draping over the mediastinal structures. **b** Transverse T1-weighted image shows a hyperintense structure that is slightly less intense than the nearby subcutaneous fat. **c** Coronal T2-weighted image with fat suppression shows an arrowhead configuration of the thymus. **d** Post-contrast axial T1-weighted image with fat suppression shows homogeneous uptake of gadolinium contrast material within the thymus



migration (Kaufman et al. 2001). This is an uncommon entity with a reported incidence of 1:6800 (Bale and Sotelo-Avila 1993) and classically presents as a painless, unilateral mass. This accessory tissue can be solid or cystic. Ultrasound is the primary diagnostic tool in children, with MRI or CT reserved for more difficult or equivocal cases. The aberrant solid thymic tissue will have the same echotexture, CT attenuation, and MRI signal intensity as the normally positioned thymus (Fig. 10). The cystic form arises from a patent thymopharyngeal duct and is typically unilocular and located along the carotid sheath. Depending on its size and location, this entity may be difficult to differentiate from other cystic neck masses and may require histologic sampling for a final diagnosis.

In addition to normal variations in size and location, the thymus may be pathologically hypoplastic, or even aplastic, in the setting of certain immunodeficiency syndromes (Yin et al. 2001). The two most common of these syndromes affecting the thymus are Severe Combined immunodeficiency (SCID) and DiGeorge syndrome. In SCID, the absence of functional T-cells to populate the thymus leads to failed thymic development, with a resultant small dysplastic thymus. DiGeorge syndrome, in contrast, results from a chromosomal deletion that directly affects thymic

development from its third and fourth pharyngeal pouch anlagen, with abnormal T-lymphocyte maturation resulting from the absence of the normal thymic environment. As expected, both of these syndromes clinically present with cellular immune dysfunction. In DiGeorge syndrome, other abnormalities include hypocalcemia due to the concomitant maldevelopment of the parathyroid glands (which also arise from the third and fourth pharyngeal pouches). On all imaging modalities, minimal, if any thymic, tissue will be present. This can be most striking on neonatal chest radiographs, where the mediastinal silhouette may adopt an almost adult configuration due to the absence of the expected broad thymic shadow (Fig. 11). The corollary to this observation is that the presence of a normal thymic shadow in a child being evaluated for immunodeficiency virtually excludes SCID and DiGeorge syndrome from the list of considerations (Buckley 2006).

Another cause for an absent or diminutive thymus on imaging studies is a history of surgery via a median sternotomy approach, most frequently seen in children with congenital heart disease. As a part of this approach, to gain access to the heart, the bulk of the thymus is removed, as seen in Fig. 12. In a study by MacDonald et al., less than a third of patients who had undergone surgery with this type



**Fig. 7** Extensive motion artifact on MRI. **a** Axial T2-weighted image of the chest with extensive motion artifact obscuring the thymus. **b** Axial T2-weighted image in a different patient with the phase-encoding direction switched from the anterior–posterior to the medial–lateral transverse plane allowing better visualization of the thymus

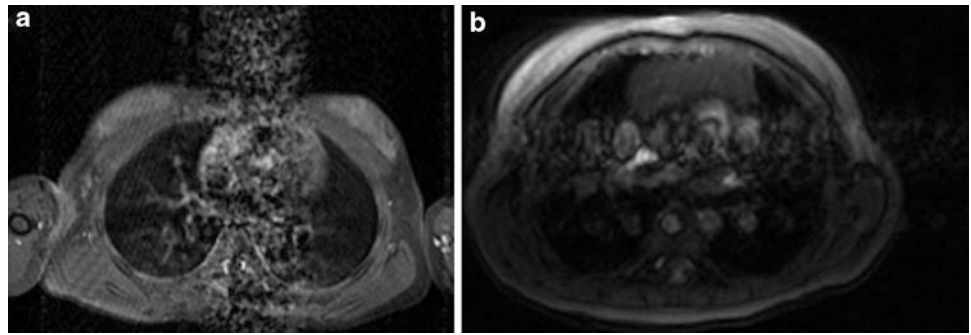
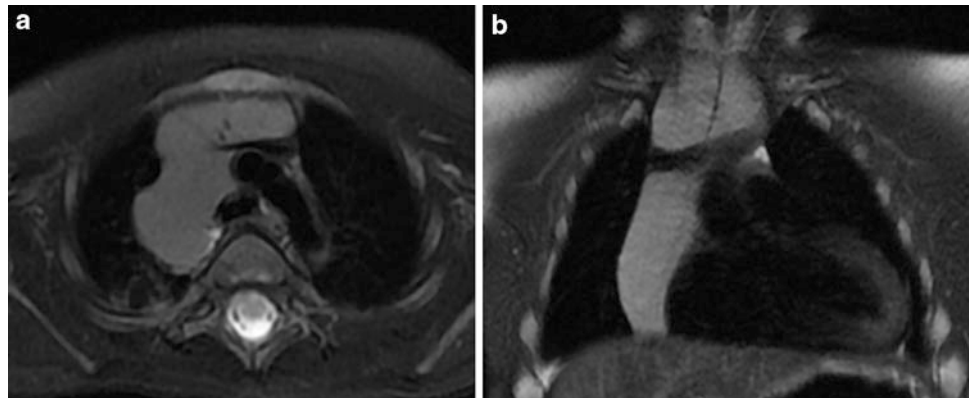


**Fig. 8** Retrocaval and suprasternal extension of the thymus. **a** Axial T2-weighted image with fat suppression shows posterior extension of the normal thymus with splaying of the SVC. **b** Coronal T2-weighted image in the same patient shows superior extension of the thymus above the clavicles



of approach had a thymus that was visible by MRI (MacDonald and Mackenzie 2009).

At the opposite end of the spectrum, rarely congenital thymic hyperplasia can occur, both sporadically and in patients with Beckwith-Weideman syndrome (Balcom et al. 1985). This is distinct from rebound thymic hyperplasia discussed later in this chapter.

## 4 Benign Thymic Masses

### 4.1 Thymic Cysts

Thymic cysts can either be congenital or acquired. As described previously, congenital thymic cysts arise from a patent thymopharyngeal duct and reside along the carotid sheath. If large enough, they can be detected in utero on both ultrasound and MRI. These cysts are lined by ciliated epithelium, typically unilocular, and contain simple fluid if drained (Restrepo et al. 2005; Petroze and McGahren 2012; Mortelmans and Hermans 2005). They rarely measure greater than 6 cm (Hegde et al. 2012), and in most cases they are asymptomatic and are discovered incidentally on imaging. They may present as a base of neck mass if there is sufficient suprasternal extension of the cyst, as shown in Fig. 13. If they are large enough, they can present with chest pain, hoarseness, or dyspnea from mass effect. These

masses are often occult on chest radiographs; however, if they are large enough they can be seen as a smoothly margined mass arising from the upper mediastinum. On ultrasound imaging, they will present as an anechoic mass and may contain a variable amount of debris depending on the presence of inflammation or prior hemorrhage. CT will show a round, fluid-attenuation mass with no solid components, as shown in Fig. 14. On MRI, simple thymic cysts will typically have high-signal intensity on fluid sensitive sequences (Fig. 13). No solid components should be present, and there should be no internal contrast enhancement.

Acquired cysts vary in etiology. Typically, they are postinfectious but can be seen in the setting of prior neoplasm, radiation, or autoimmune diseases such as myasthenia gravis. Children with HIV infection can also present with massive cystic enlargement of the thymus related to aberrant immunoregulation (Kontny et al. 1997). These acquired cysts are more complex than the simple congenital cysts described above. They often have thicker cyst walls, internal septations, and contain a more gelatinous liquid (Restrepo et al. 2005). They tend to be multilocular and can range in diameter from a few millimeters to over 15 cm (Hegde et al. 2012). The complex nature of the acquired cysts is reflected in their appearance on imaging studies. On ultrasound imaging they range from anechoic to hypoechoic, with a variable number of septations. CT or MRI will also demonstrate a variable number of septations that may

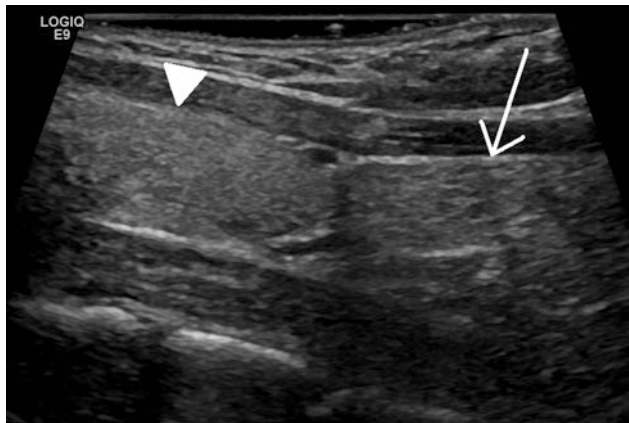


**Fig. 9** Normal superior extension of the thymus to the inferior margin of the thyroid. Sagittal ultrasound image of the neck in a 21-year-old female. The thymus (*arrow*) extends superiorly and abuts the inferior margin of the thyroid gland (*arrowhead*). The thymus is more echogenic in this young woman than in the infant in Fig. 4 due to the presence of more fat

enhance. On MRI, these lesions may be higher in signal intensity on T1-weighted images and lower signal intensity on T2-weighted images, as compared to simple cysts, reflecting the complex nature of the fluid, often due to higher protein content. Regardless of the etiology of these cysts, they are uniformly benign in the pediatric population (Petroze and McGahren 2012).

## 4.2 Thymolipoma

Thymolipoma is a rare, slowly growing tumor composed of thymic elements and adipose tissue, representing less than 10 % of all thymic tumors in adults (Restrepo et al. 2005). These are soft, malleable tumors which can conform to adjacent structures and extend to the cardiophrenic or costophrenic angles. Occasionally, they can grow large enough to fill an entire hemithorax (Nasseri and Eftekhari 2010) and typically weigh over 500 g (Restrepo et al. 2005). Clinically, these masses may present with symptoms secondary to mass effect or, rarely, with paraneoplastic syndromes, including myasthenia gravis. About half of these tumors, however, are found incidentally on chest radiographs.

On chest radiograph they are typically seen as a large anterior mediastinal mass with smooth contours. These masses are characteristically located in the anterior mediastinum and grow caudally toward the diaphragm, conforming to the contours of the inferior thorax (Restrepo et al. 2005). In approximately one-half of cases, low density can be appreciated within the mass on radiographs due to the large amount of fat present. These masses often have a

whorled appearance due to the intermixing of macroscopic fat and soft tissue, which results in a heterogeneous mass with enhancing soft tissue intermixed with low attenuation fat on CT imaging. These lesions will also have a heterogeneous appearance on MRI on both T1- and T2-weighted sequences, as shown in Fig. 15. Due to their characteristic appearance on both CT and MRI, FDG-PET does not have an established role in the diagnosis of these tumors (Sharma et al. 2013).

## 5 Thymic Hyperplasia

There are two forms of thymic hyperplasia: true thymic hyperplasia and lymphoid hyperplasia. Lymphoid or follicular hyperplasia is much more commonly encountered in normal clinical practice and, in addition, is seen in approximately two-thirds of patients with myasthenia gravis (Mizuno et al. 1997). It is characterized by inflammation and proliferation of lymphoid follicles with increased numbers of lymphocytes and epithelial cells. Despite the relatively common occurrence of lymphoid hyperplasia in clinical practice, the involved thymus is usually normal in size and shape on imaging studies. Therefore, lymphoid hyperplasia is typically occult on imaging studies and, when indicated, is confirmed with histologic sampling. Rarely, lymphoid hyperplasia will present as diffuse enlargement of the thymus or as a focal thymic mass. No specific imaging features have been described to differentiate between these forms of hyperplasia.

In true thymic hyperplasia, both the size and weight of the thymus increase, while the histologic architecture is preserved. Depending on the degree of hyperplasia, the thymus may lose its bilobed appearance and become more oval in shape (Nasseri and Eftekhari 2010). While there are no distinguishing features on imaging studies, patients with true thymic hyperplasia can be divided into three clinical groups: patients with no related preexisting condition, patients with a condition known to be associated with thymic hyperplasia, such as sarcoidosis or hyperthyroidism, and patients in whom the thymic hyperplasia is secondary to a rebound phenomenon. Rebound thymic hyperplasia is commonly encountered in clinical practice and can be observed after radiation therapy, chemotherapy, corticosteroid therapy, or a period of physiologic stress. These causes of stress can lead to a rapid and considerable decrease in the size of the thymus, which is presumed to be related to an increase in endogenous steroids released as part of the physiologic response to stress. After recovery, the thymus returns to its original size (thymic rebound) and may even grow up to 50 % greater than its original size, as shown in Fig. 16 (Nasseri and Eftekhari 2010). While affecting all ages in the pediatric population, and even adults, this

**Fig. 10** Ectopic thymic tissue in an infant. **a** Axial CT image with contrast demonstrates a smoothly marginated, homogeneously enhancing soft tissue mass posterior to the left mandible. **b** Sagittal ultrasound image in the same patient shows an ovoid mass with the classic echotexture of the thymus

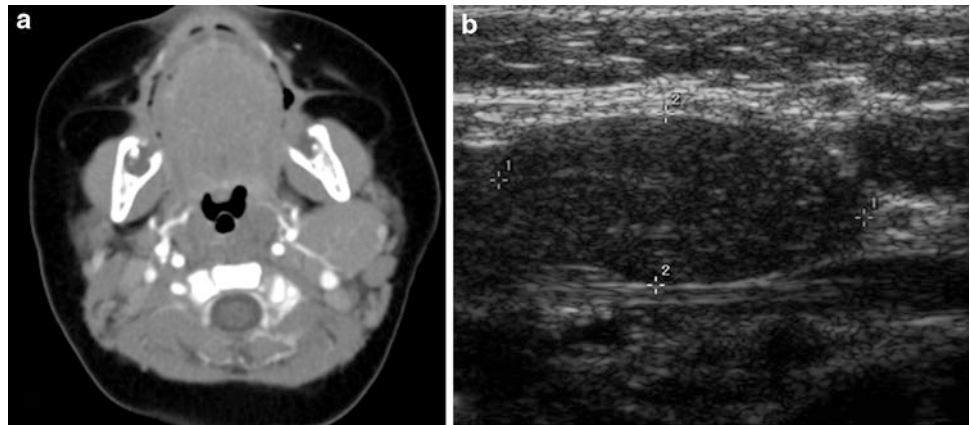
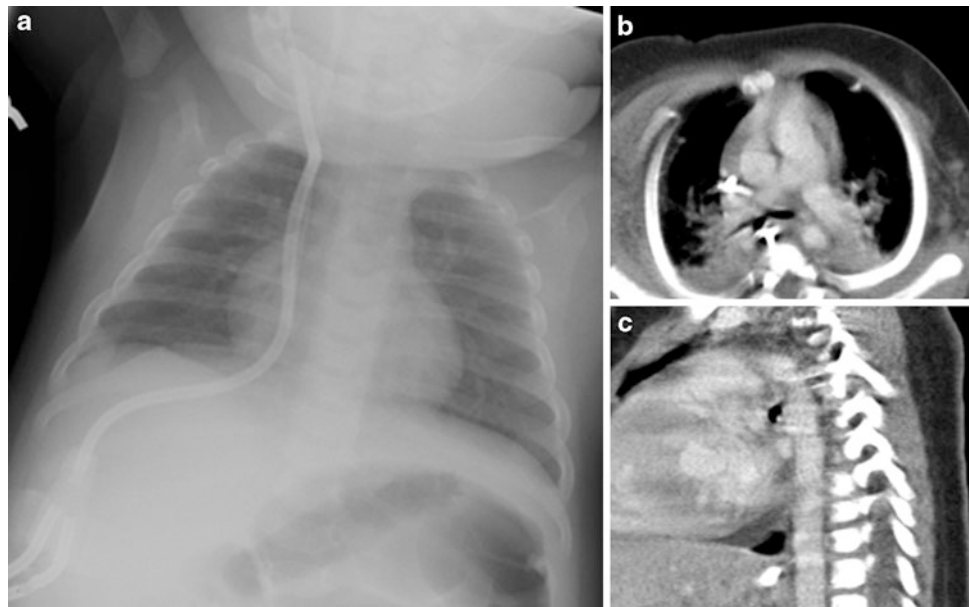


**Fig. 11** Aplasia of the thymus in an infant with severe combined immunodeficiency (SCID). **a** AP chest radiograph shows narrowed mediastinum suggestive of hypoplastic or aplastic thymus. Axial (**b**) and sagittal (**c**) CT images with contrast, obtained for evaluation of recurrent pneumonias, confirms the absence of thymic tissue



rebound phenomenon is seen more frequently in younger children.

On imaging studies, this phenomenon may present a diagnostic dilemma, particularly in the setting of treated lymphoma, where the apparent increase in size of a mediastinal mass may raise concern for disease relapse. Various imaging features have been described in an effort to differentiate hyperplastic thymus from recurrent tumor. On cross-sectional imaging, the hyperplastic thymus should have smooth, nonlobulated contours with no mass effect on the surrounding structures (Fig. 16). On real-time ultrasonography, the enlarged, non-neoplastic thymus should vary in shape with respiration. It should have a homogeneous appearance on CT and MRI. With rebound hyperplasia, the thymus can also demonstrate increased FDG uptake, as seen in Fig. 17. Recently, attempts have been made to use measures of FDG uptake on PET imaging, such as the standardized uptake value (SUV), to help in differentiating

these entities. Gawande et al. suggested that an  $SUV_{max} < 3.4$  is indicative of hyperplasia and not tumor recurrence, although reliance on SUV alone to make this distinction should be undertaken with caution (Gawande et al. 2012).

## 6 Malignant Thymic Masses

### 6.1 Thymoma

Thymomas are the most common primary malignant tumor of the thymus gland and arise from medullary thymic epithelium. These tumors are classically found during the fourth to sixth decades of life and are rarely seen as a cause of mediastinal mass in the pediatric population. As in the adult population, thymoma in children has a strong association with paraneoplastic syndromes. The most common



**Fig. 12** Surgical resection of the thymus during heart surgery. **a** Preoperative AP chest radiograph shows a normal-appearing thymus with a sail sign. **b** Postoperative AP chest radiograph obtained 1 day later shows absence of a thymic silhouette

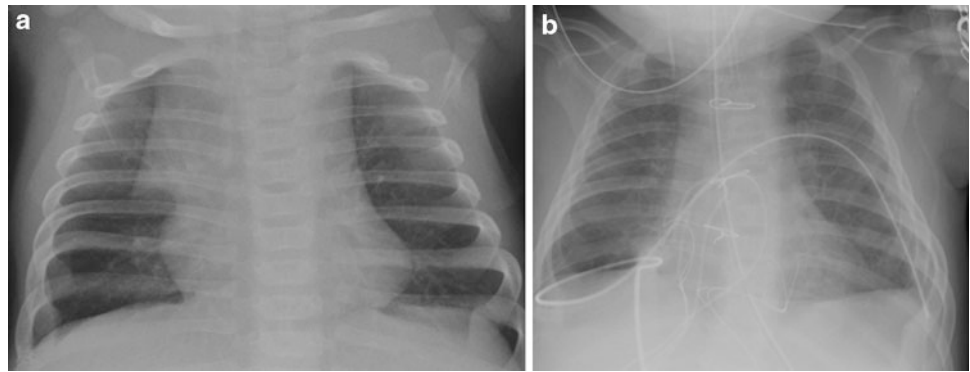
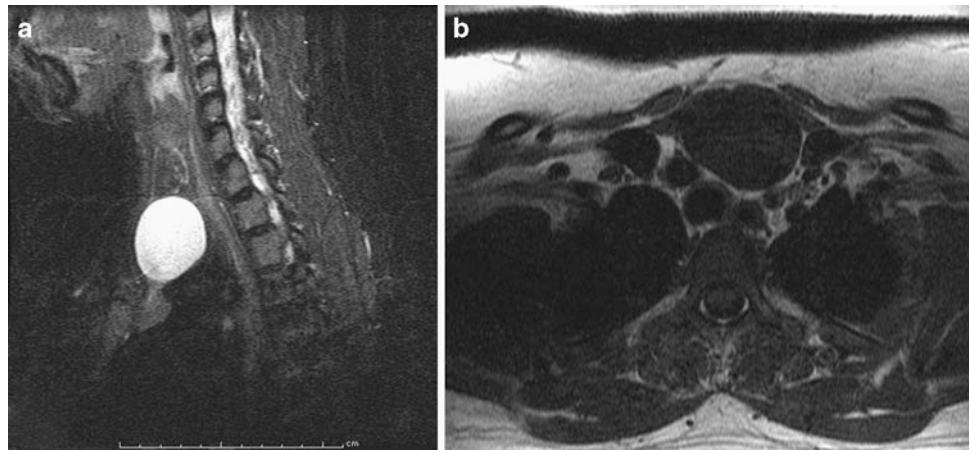


**Fig. 13** Thymic cyst presenting as a base of neck mass. **a** Sagittal T2-weighted image of the neck shows an ovoid T2 hyperintense lesion extending to the base of the neck. **b** Axial T1-weighted image shows a homogeneously low-signal intensity lesion contiguous with the normal-appearing thymus in the superior mediastinum, compatible with a thymic cyst with suprasternal extension



of these is myasthenia gravis, but red cell aplasia and hypogammaglobulinemia can also be seen. These tumors normally present as slow growing mediastinal masses which can invade adjacent structures and, rarely, metastasize. Thymomas can be subdivided into invasive and noninvasive forms depending on whether the tumor extends beyond the confines of the fibrous capsule on microscopic examination. While invasion may be suspected based on imaging, histopathologic confirmation is definitive.

Due to its rarity, imaging features of thymoma specific to the pediatric population have not been reported to our knowledge. Inferring from the adult population, on chest radiographs thymomas present as a nonspecific anterior mediastinal mass that may grow to be quite large (Fig. 18). The CT appearance can vary widely with the less aggressive thymomas having a more homogeneous soft tissue composition, and the more aggressive forms containing calcifications with cystic degeneration, presumably related to necrosis. These characteristics are reflected in the MRI appearance, where they can demonstrate heterogeneous T2 signal intensity. On T1-weighted images, they typically have a homogeneous pattern of enhancement, although those that have undergone cystic degeneration will have a more heterogeneous appearance. Invasive thymomas have a

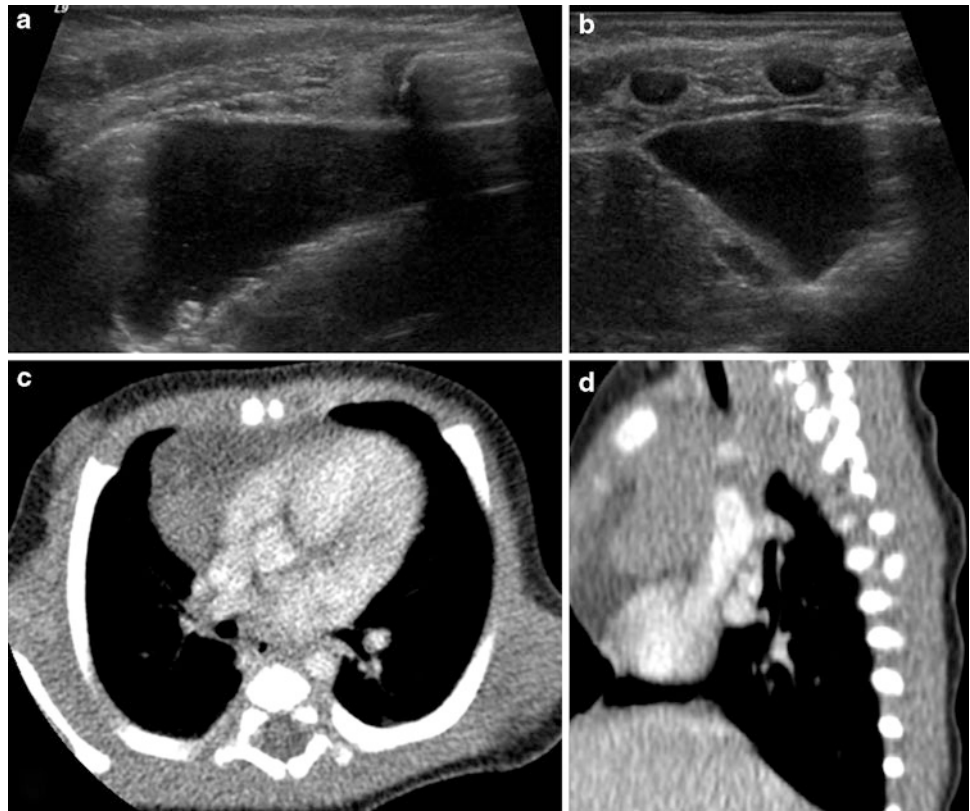
propensity for pleural seeding, creating lobulated soft tissue masses along the periphery of the lung. While of limited use in an individual patient, invasive thymomas generally show higher FDG uptake than their noninvasive counterparts (Sharma et al. 2013).

## 6.2 Thymic Carcinomas

While invasive thymomas may appear aggressive on imaging studies, they lack cytological evidence of malignancy. Thymic carcinomas, in contrast, lose the classic histologic features of thymic tissue and have obvious anaplasia on pathology specimens. These tumors have a much greater rate of metastasis and invasion, and are less frequently associated with paraneoplastic syndrome than thymomas. Although these tumors are extremely rare in the pediatric patient population, limited studies have suggested a dismal prognosis due to the advanced stage of disease at presentation (Yaris et al. 2006).

On imaging studies, these lesions are typically large and more heterogeneous than thymomas, with regions of necrosis and calcification frequently present. Other distinguishing characteristics of these tumors include the

**Fig. 14** Thymic cyst diagnosed prenatally and confirmed after birth. Axial (a) and sagittal (b) ultrasound images demonstrate a thin-walled lesion that contains anechoic fluid and is contiguous with normal-appearing thymus. c, d Axial (c) and sagittal (d) CT images with contrast show a low attenuation structure abutting normally enhancing thymic tissue



presence of lymphadenopathy and distant metastases. On PET imaging, thymic carcinomas are metabolically active and tend to have high levels of FDG uptake ( $SUV_{max}$  of  $>7$ ) (Sharma et al. 2013).

### 6.3 Thymic Carcinoids

Thymic carcinoids are highly aggressive neoplasms that arise from neural crest cells (Restrepo et al. 2005). One report demonstrated that every case of thymic carcinoid studied in the pediatric population presented with Cushing syndrome, in contrast to the adult population in which only 25–40 % presented with an endocrine disorder (Gartner and Voorhess 1993). In addition to presenting with endocrine abnormalities, patients may present with symptoms related to mass effect on mediastinal structures. These tumors can occur in isolation, but are also seen with multiple endocrine neoplasia types 1 and 2.

The appearance on imaging studies is nonspecific, making them difficult to differentiate from other thymic tumors. Chest radiographs will show an anterior mediastinal mass of variable size. CT and MRI typically demonstrate an irregular soft tissue mass with possible invasion of surrounding structures. These masses frequently have a heterogeneous pattern of enhancement with varying degrees of necrosis. Whereas bronchial carcinoids are variably FDG-

avid (Park et al. 2009), thymic carcinoids usually demonstrate increased FDG uptake (Sharma et al. 2013).

### 6.4 Other Masses

The thymus can occasionally be involved in systemic processes such as Langerhans cell histiocytosis or metastatic disease. Other masses, both benign and malignant, such as germ cell tumors, bronchogenic foregut malformations, thyroid lesions, pleural and pericardial-based lesions, and primary mesenchymal neoplasms, can arise in or around the thymus and anterior mediastinum. This can make it challenging to arrive at a definite diagnosis. These lesions are discussed more fully in the chapter on chest tumors.

## 7 Leukemia and Lymphoma

Leukemia and lymphoma account for two of the top three most frequently encountered malignancies in children (Ries 1999). In patients with lymphoid malignancies, the thymus is a frequent site of disease involvement. Depending on the disease, the thymus may be considered an extramedullary nodal site and thymic involvement may not necessarily change the stage of disease (Bae and Lee 2010). In most cases it represents a site of secondary disease involvement

**Fig. 15** Thymolipoma. **a** Axial CT image demonstrates a heterogeneous soft tissue mass abutting the right heart border and containing foci of fat attenuation. Coronal (**b**) and axial (**c**) proton density black blood images show the same mass with foci of hyperintense signal corresponding to the fat noted on the CT image. **d** Axial T2-weighted fat saturated image shows signal dropout corresponding to the foci of high-signal intensity fat seen on the non-fat suppressed images the foci of fat

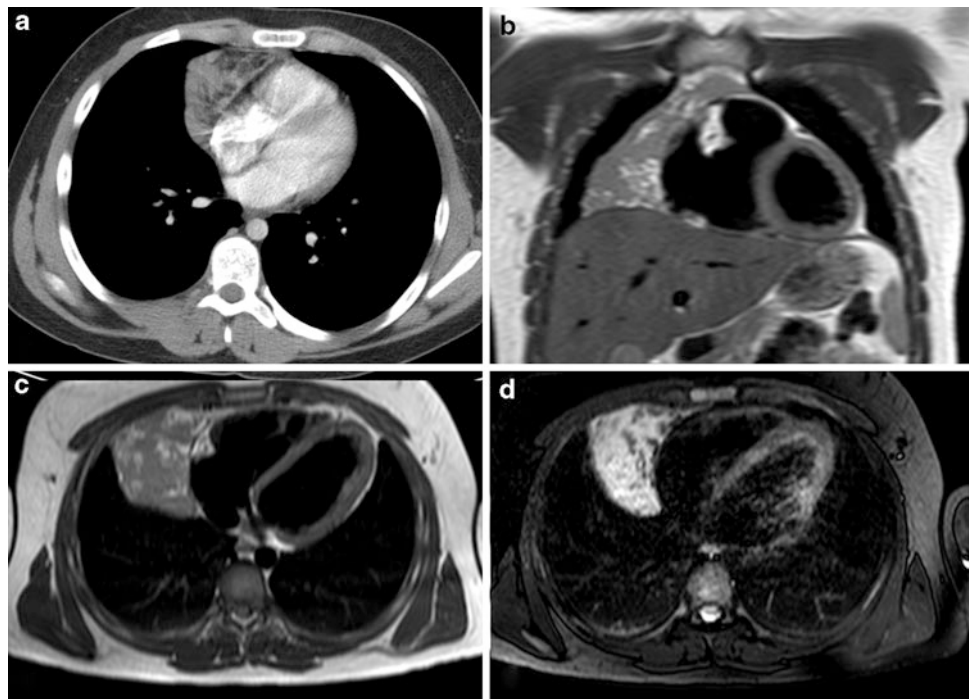
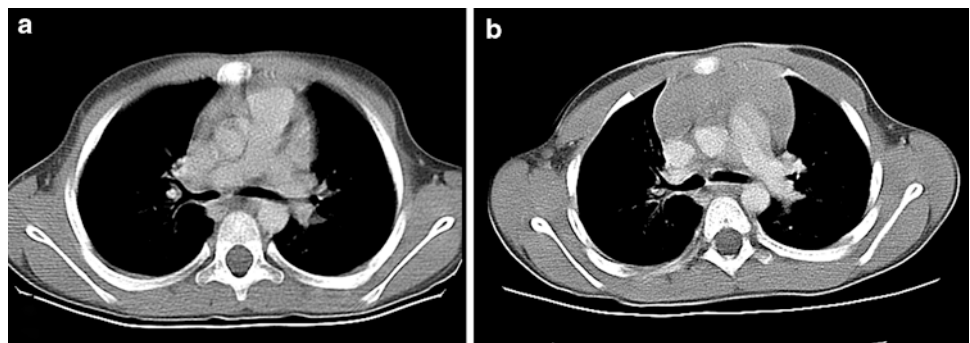


**Fig. 16** Rebound hyperplasia in a 4-year old with Hodgkin lymphoma. **a** Axial CT image with contrast obtained during therapy shows negligible thymic tissue. **b** Axial CT image obtained 6 months after the cessation of therapy shows marked increase in the size of the thymus which maintains a smooth contour and internal homogeneity



but it can also be the primary site of disease. The various manifestations and imaging appearance of these diseases will be discussed below with an emphasis placed on thymic involvement.

## 7.1 Leukemia

Acute lymphoblastic leukemia (ALL) is the most common pediatric malignancy, accounting for 25 % of malignancies in children less than 15 years of age and accounting for 75 % of all childhood leukemias. The World Health Organization subdivides ALL by immunophenotype into B-lymphoblastic (B-ALL) and T-lymphoblastic forms (T-ALL), with the B-lymphoblastic form representing greater than 80 % of all pediatric ALL. Because patients with leukemia typically present with disseminated disease in the blood and bone marrow, the traditional imaging-based

staging paradigm does not apply. Instead, these patients are classified as low risk, standard risk, high risk, and very high risk based on clinical and biological features as well as initial response to therapy (Guillerman et al. 2011). Imaging studies play a lesser role in staging, response assessment, or relapse surveillance in patients with leukemia.

Children with B-ALL can present with a wide range of symptoms ranging from easy bruising and bleeding to bone pain. Although patients with B-ALL can have an associated mediastinal mass, this is uncommon, and there are few other primary manifestations involving the thymus. Consequently, it will not be further discussed in this chapter.

T-ALL tends to be a more aggressive leukemia that typically occurs later in childhood than B-ALL (Bae and Lee 2010; Guillerman et al. 2011). Considerable overlap exists between the presentation and histopathologic features of T-ALL and T-cell lymphoblastic lymphoma (T-LBL) with the differentiating characteristic related to the extent of



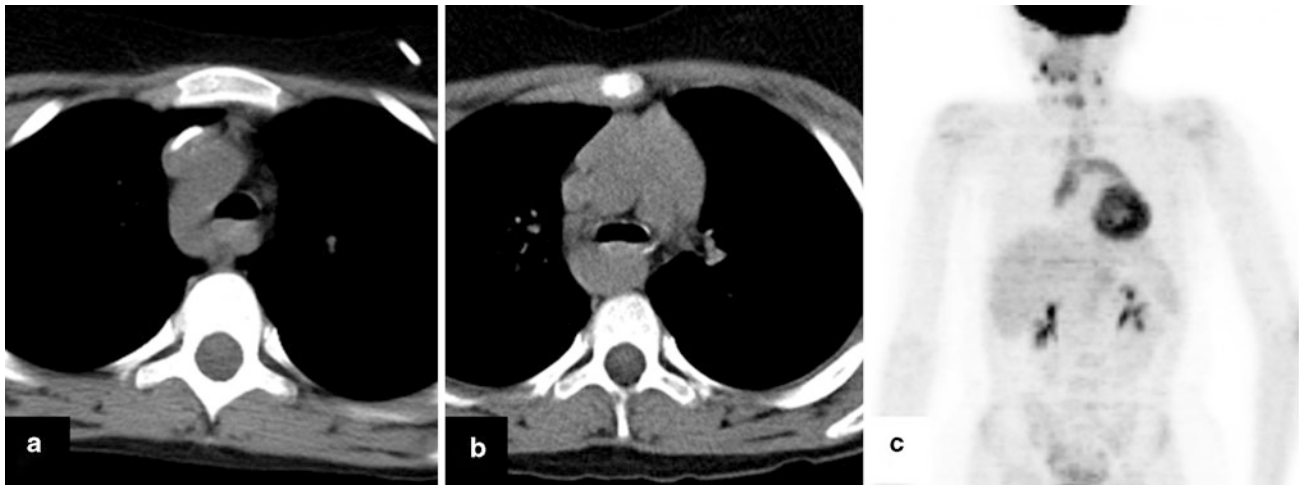
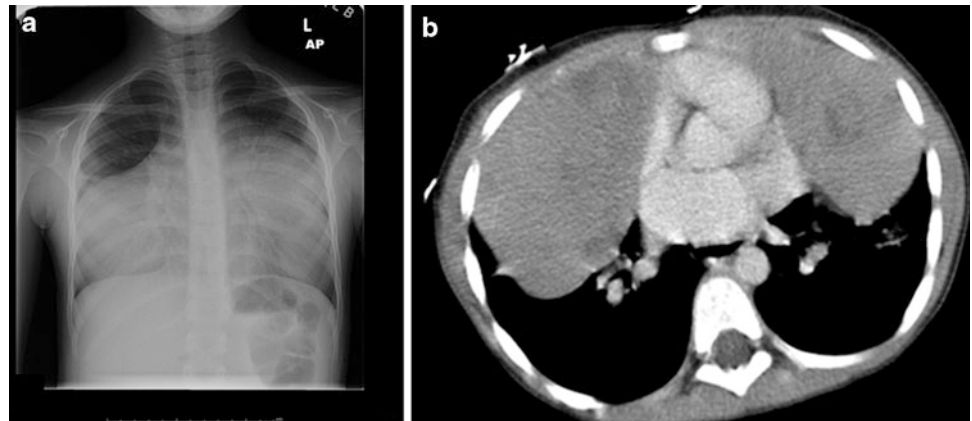


**Fig. 17** Rebound hyperplasia in a 12-year old with rhabdomyosarcoma. **a** Axial CT image obtained while undergoing therapy demonstrates minimal residual thymus. Axial CT image (**b**) and FDG PET

MIP image (**c**) show an increase in the size of the thymus and increased FDG uptake by the thymus

**Fig. 18** Large thymoma in a 5-year old with myasthenia gravis. **a** AP chest radiograph shows a very large mediastinal mass. **b** Axial CT of the chest shows a large, relatively homogenous mass compressing the mediastinal structures



bone marrow involvement. In patients with a mediastinal mass and >25 % marrow involvement with T-cell lymphoblasts, the diagnosis is T-ALL with a mediastinal mass; when there is <25 % marrow involvement the diagnosis of T-LBL is made. Both of these neoplasms are thought to originate from the precursor T-cell lymphoblast found in the thymus. The majority of patients (50–70 %) with T-ALL presents with a mediastinal mass due to diffuse thymic infiltration (Fig. 19). In response to therapy, patients with both T-ALL and T-LBL typically have a rapid shrinkage in their mediastinal mass and improvement in their symptoms. There is no clear role for CT characterization of the mediastinal mass apart from establishing the extent of disease and sites of disease of involvement that may require urgent intervention. Early resolution of the mediastinal mass, either on chest radiograph (Shepherd et al. 1995) or on CT (Termuhlen et al. 2013), is associated with improved outcome, presumably reflecting patients with more chemosensitive disease.

## 7.2 Lymphoma

### 7.2.1 Hodgkin Lymphoma

Approximately 1,100 children under 20 years of age are diagnosed with Hodgkin lymphoma (HL) each year in the US with the 5-year survival rate exceeding 90 % (Kelly et al. 2013). HL is typically seen in older children and adolescents and is staged using the Ann Arbor staging classification that is based on the number of sites of lymph node involvement, presence of extranodal disease, and history of B symptoms, such as fever, night sweats, or weight loss (Table 1). The presence of multinucleated Reed Sternberg cells define HL histologically, but multiple histological subtypes exist with nodular sclerosis being the most common in adolescents and mixed cellularity subtype being most common in children (Kelly et al. 2013).

While HL only represents 40–50 % of all cases of pediatric lymphoma, thoracic manifestation of disease is seen in up to 85 % of patients at the time of diagnosis

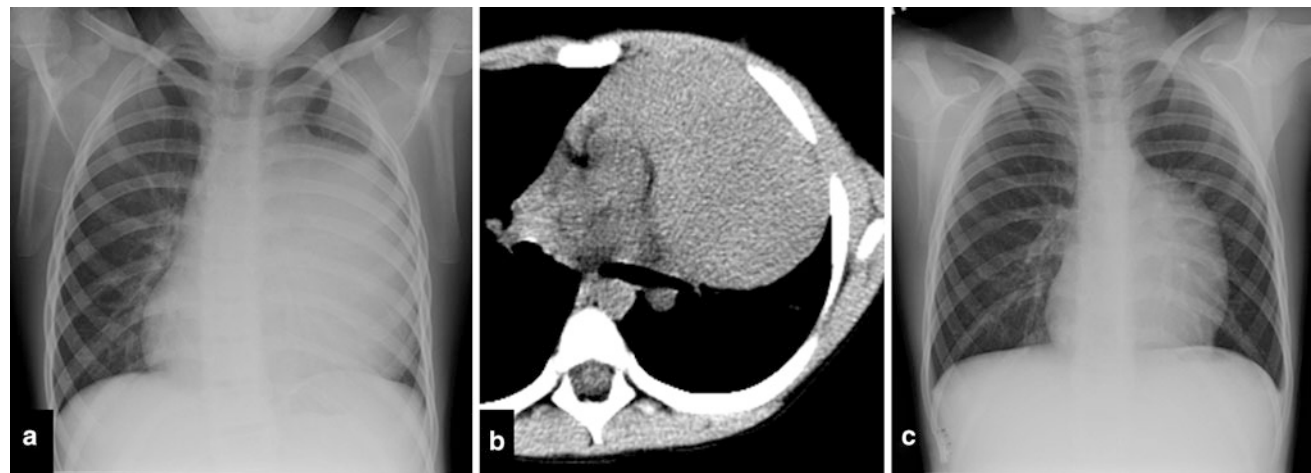


**Fig. 19** Diffuse thymic enlargement from infiltration with T-cell acute lymphoblastic leukemia (ALL). **a** AP radiograph of the chest demonstrates a large, predominantly left-sided mediastinal mass. **b** Axial CT of the chest without contrast shows an enlarged

homogeneous thymus with preservation of the fat plane between the thymus and the great vessels. **c** Chest radiograph obtained 1 week after the initiation of therapy demonstrates marked decrease in the size of the mediastinal mass

**Table 1** Lymphoma staging—Hodgkins lymphoma

Ann Arbor classification for staging
<i>Stage I</i>
Involvement of single lymph node region (I) or localized involvement of a single extralymphatic organ or site (IE)
<i>Stage II</i>
Involvement of two or more lymph node regions on the same side of the diaphragm (II), or
Localized contiguous involvement of a single extralymphatic organ or site and its regional lymph node(s), with involvement of one or more lymph node regions on the same side of the diaphragm (IIIE)
<i>Stage III</i>
Involvement of lymph node regions on both sides of the diaphragm (III). These may also be accompanied by localized contiguous involvement of an extralymphatic organ or site (IIIE), by involvement of the spleen (IIIS), or both (IIIE + S)
<i>Stage IV</i>
Disseminated (multifocal) involvement of one or more extralymphatic organs or tissues, With or without associated lymph node involvement, or
Isolated extralymphatic organ involvement, with distant (non-regional) nodal involvement

*Additional designation*  
“A”: Lack of “B” symptoms  
“B”: At least one of the following  
Unexplained weight loss >10 % over 6 months  
Unexplained fever >38° orally for 3 consecutive days  
Drenching night sweats

(Bae and Lee 2010). HL classically presents on chest radiographs as an anterior mediastinal mass with variable involvement of nodal stations. Bulky disease is defined as

transverse mediastinal diameter greater than one-third of the maximum intrathoracic diameter, as measured on an upright posterior–anterior chest radiograph (Hodgson et al. 2007). On cross-sectional imaging, this mass classically has lobulated contours with a homogeneous soft tissue density as seen in Fig. 20; although with increasing size, these masses may develop central low-density areas compatible with necrosis (Bae and Lee 2010). In contrast to other malignancies, the majority of cells in the mediastinal mass in HL patients is made up of non-malignant lymphocytes, with the malignant Reed Sternberg cells comprising only about 10 % of the mass. These abundant reactive lymphocytes, rather than the infrequent malignant Reed Sternberg cells, likely account for the intense FDG uptake typically seen on PET in HL.

**7.2.2 Non-Hodgkin Lymphoma**

Non-Hodgkin lymphoma (NHL) accounts for approximately 10–15 % of all childhood cancers. T-cell neoplasms account for approximately half of pediatric NHL, whereas in the adult population the majority arises from B-cells (Abramson and Price 2008). NHL is divided into various histologic subtypes by the World Health Organization. In children, the most common of these are the mature B-cell malignancies Burkitt lymphoma (BL) and diffuse large B-cell lymphoma (DLBCL), the mature T-cell neoplasm anaplastic large cell lymphoma (ALCL), and the precursor T-cell neoplasm lymphoblastic lymphoma (T-LBL). BL will not be discussed further in this chapter as it rarely involves the thymus or mediastinum. NHL is more frequent in patients under the age of ten, and males are more frequently affected, making up 70 % of the patient population

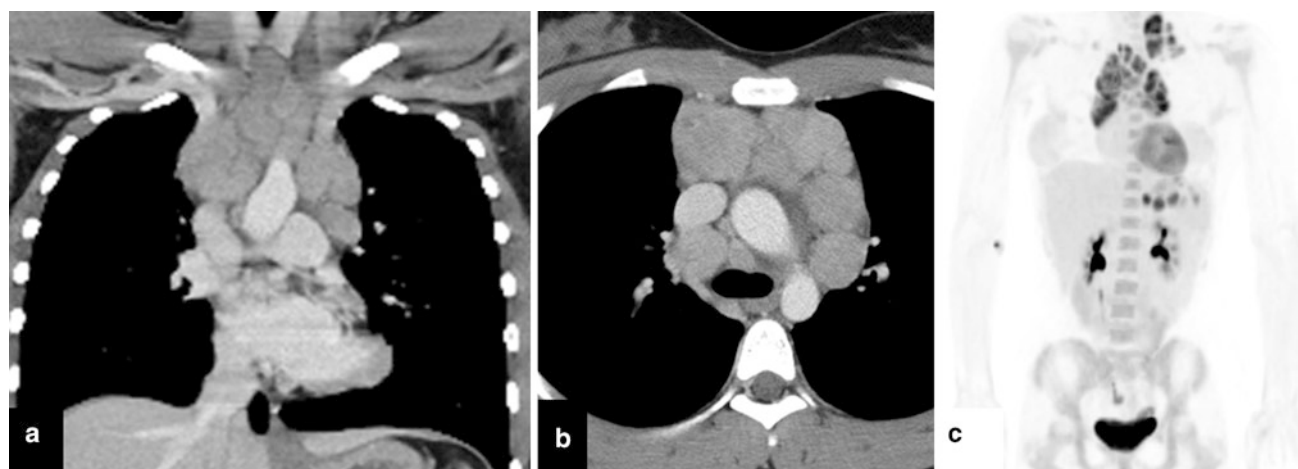


**Fig. 20** Hodgkin lymphoma. Axial (a) and coronal (b) CT images with contrast in a teenage female with Hodgkin lymphoma show a lobulated anterior mediastinal mass. c Coronal FDG-PET image shows

the lobulated involvement of the thymus as well as left cervical and infraclavicular adenopathy and splenic involvement

**Table 2** Lymphoma staging—Non-Hodgkins lymphoma

St. Jude classification
<b>Localized</b>
<i>Stage I</i>
A single tumor (extranodal) or single anatomic area (nodal) with exclusion of the mediastinum or abdomen
<i>Stage II</i>
A single tumor (extranodal) with regional node involvement
Two or more nodal areas on the same side of the diaphragm
Two single (extranodal) tumors with or without regional node involvement on the same side of the diaphragm
A primary gastrointestinal tumor, usually in the ileocecal area, with or without involvement of associated mesenteric nodes, grossly completely resected
<b>Disseminated</b>
<i>Stage III</i>
Two single tumors (extranodal) on opposite sides of the diaphragm
Two or more nodal areas above and below the diaphragm
All primary intra-thoracic tumors (mediastinal, pleural, thymic)
All extensive primary intra-abdominal disease
All paraspinal or epidural tumors, regardless of other tumor site(s)
<i>Stage IV</i>
Any of the above with initial CNS and/or bone marrow involvement

Based on Murphy, Seminars in Oncology (1980) 7:332–339

(Guillerman et al. 2011; Abramson and Price 2008). NHL is staged with the St. Jude staging system (Table 2) that can be divided for prognosis purposes into “limited” (stage 1 and 2) and “extensive” (stage 3 and 4). Most patients present with extensive disease.

DLBCL is composed of two subtypes: primary mediastinal B-cell lymphoma (PMBL) and disseminated disease. PMBL was first recognized as a distinct subtype of DLBCL in the 1980s (Johnson and Davies 2008; Attias et al. 2009). This tumor arises from the thymic medullary B-cells. It is a rare subset, accounting for only 3–5 % of NHL cases, although it represents a higher percentage in adolescents and young adults (Johnson and Davies 2008; Hutchinson and Wang 2011). The median age of pediatric PMBL in a recent study was 14.3 years compared to 9 years in other types of B-cell NHL (Hutchinson and Wang 2011). This tumor may be difficult to differentiate from classic HL, nodular sclerosis type, as they may have similar clinical presentation and immunophenotypes (Hutchinson and Wang 2011). However, this distinction is very important for therapeutic decisions.

Clinically, these tumors present as rapidly growing mediastinal masses with symptoms related to mass effect, namely dyspnea, cough, chest pain, or hoarseness (Hutchinson and Wang 2011). Due to rapid growth of the mass, 80 % of cases present with “limited” disease (Martelli et al. 2008) (Fig. 21). Patients can also present with symptoms of venous or lymphatic obstruction, resulting in SVC syndrome, or pericardial and pleural effusions due to lymphatic blockade. These tumors tend to respect the confines of the thorax without involvement of contiguous lymph node stations or other lymphoid organs at the time of presentation. However, extrathoracic and extranodal manifestations can be seen with increased frequency at the time of disease relapse (Hutchinson and Wang 2011).

As noted previously, considerable overlap exists between T-ALL with a mediastinal mass and T-LBL with the



**Fig. 21** Primary mediastinal B-cell lymphoma. Axial (a) and sagittal (b) images from a chest CT with contrast show a very large, smoothly contoured mass with significant mass effect on the airways and great vessels. c Fused FDG-PET/CT image shows marked FDG avidity of the mass

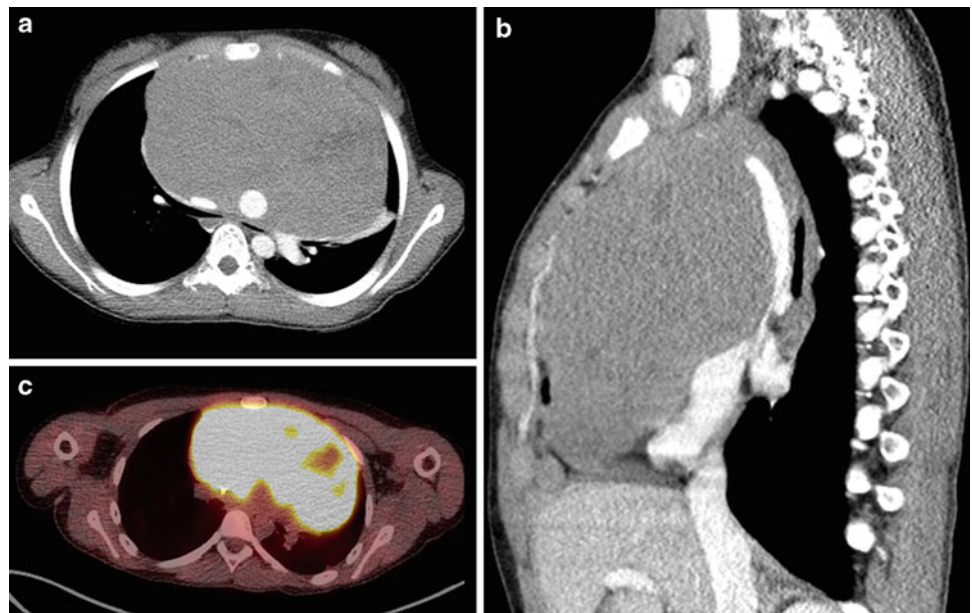
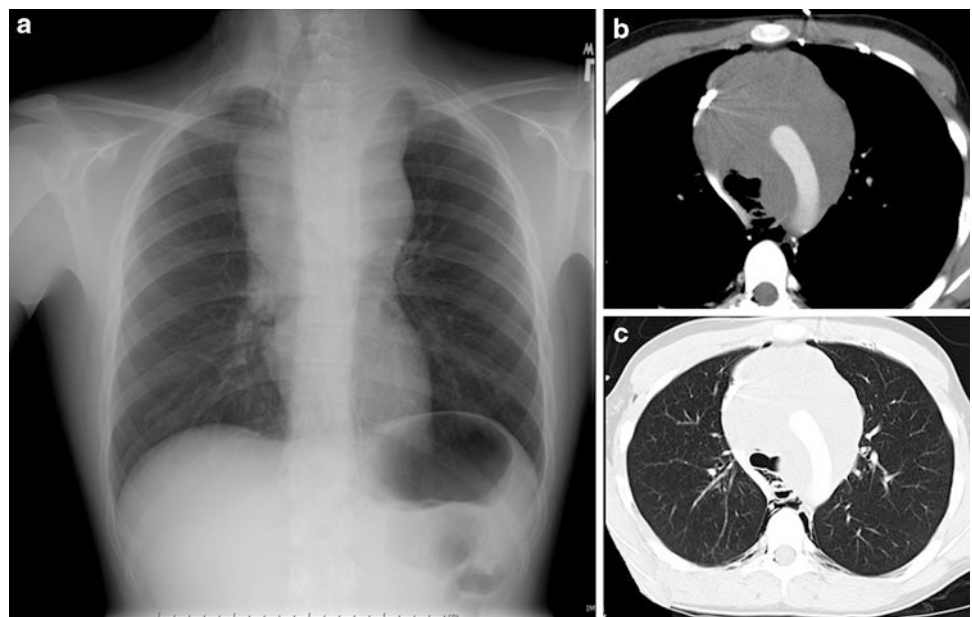


**Fig. 22** Pneumomediastinum in a patient with T-cell ALL. a PA chest radiograph demonstrates a mediastinal mass with air tracking along the right neck. b Axial CT image with contrast shows a homogeneous mediastinal soft tissue mass encasing the aortic arch and compressing the superior vena cava (SVC). Not unexpectedly, patients with these masses may present with SVC syndrome. Compression of the trachea and resultant airway obstruction may result in spontaneous pneumomediastinum (c), and these patients warrant close clinical monitoring for airway compromise



distinguishing feature related to the degree of marrow involvement. Up to 75 % of patients with T-LBL present with a mediastinal mass and related symptoms due to mass effect (Guillerman et al. 2011). Due to the rapid growth and the location of the mass, patients with T-ALL or T-LBL may deteriorate from respiratory compromise when sedated or placed supine; thus, imaging studies should be obtained with caution in this patient subgroup. On cross-sectional imaging, the thymus is diffusely infiltrated by a relatively homogeneous mass (Fig. 22), with a contour that is

smoother than that seen with HL (Fig. 20), which classically manifests as a lobulated mass (Guillerman et al. 2011).

ALCL is a rare subtype of T-cell lymphoma that tends to be extremely aggressive and commonly presents with multifocal disease, as shown in Fig. 23. These patients may have a prolonged course prior to diagnosis with nonspecific, systemic symptoms such as fever and weight loss. At the time of presentation, up to 40 % of patients with ALCL will have a mediastinal mass, which frequently coexists with pleural and pericardial effusions (Guillerman et al. 2011).

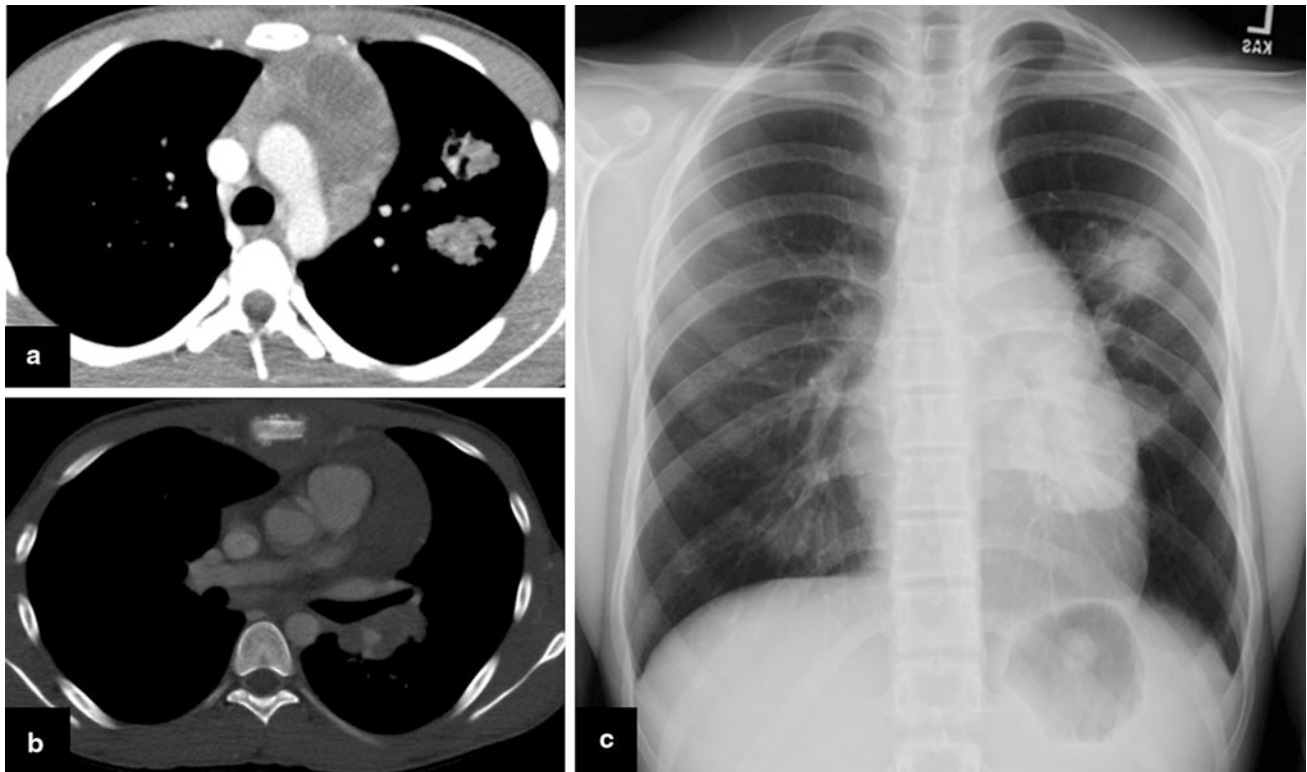


**Fig. 23** Anaplastic large cell lymphoma. **a, b** Axial CT images with contrast show a heterogeneous mediastinal soft tissue mass with invasion of the anterior chest wall and involvement of the sternum.

There is also multifocal involvement of the left lung. **c** PA radiograph of the chest again shows the mediastinal mass and demonstrates the extent of lung involvement

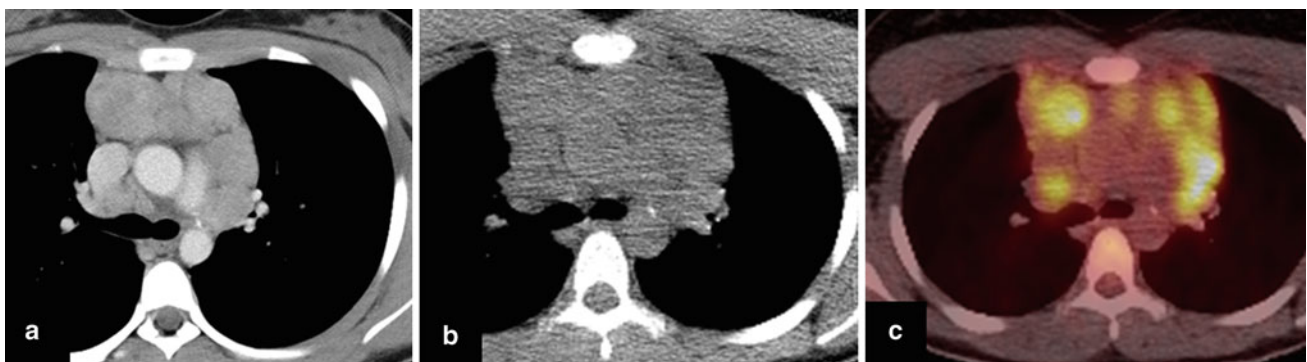


**Fig. 24** Value of contrast in assessing mediastinal mass size. **a** Axial CT image with contrast clearly demarcates the size of the mass. Axial image (**b**) from the attenuation correction CT performed in

conjunction with the FDG-PET and the fused FDG-PET/CT image (**c**) demonstrate the difficulty in obtaining an accurate size measurement of the mass in the absence of intravenous contrast

### 7.2.3 Staging and Initial Follow-Up Examinations

CT has been the most commonly used modality for staging of lymphoma. However, PET/CT has the added advantages of detecting disease in non-enlarged lymph nodes as well as sites of extranodal involvement, assessing potential disease involvement in bone marrow, and helping to guide biopsy of more metabolically active tissue, thus increasing chances for a positive biopsy (Cronin et al. 2010). Additionally, PET/CT

can suggest the aggressiveness of the tumor with more indolent lymphomas having less FDG avidity than their more aggressive counterparts (Cronin et al. 2010). The inclusion of intravenous (IV) contrast at the time of CT scanning is considered necessary for the complete staging of lymphoma patients, regardless of whether FDG-avid disease is present. The use of IV contrast allows for a more accurate measurement of disease burden while simultaneously

**Table 3** Summary of new harmonization project criteria for PET and CT in determining response in lymphoma

Response	Criteria
CR	FDG–PET completely negative
	Residual lymph nodes/nodal masses allowed, if FDG-negative
	Bone marrow biopsy negative
	Splenic/liver involvement must disappear
	No new sites of disease
PR	FDG positivity should be present in at least one previously involved site
	Regression of measurable disease; no new sites of disease
	≥50 % decrease in SPD of 6 dominant LNs/nodal masses
	≥50 % reduction in splenic/hepatic nodules, if present
	Even if CR by other criteria, positive bone marrow biopsy is considered PR
SD	Failure to achieve PR, but not meeting PD criteria
PD/ relapse	Any lesion increased in size by ≥ 50 % from nadir
	Any new lesion
	PET should be positive in new/progressed lesions if ≥1.5 cm

*Notes* New criteria include PET in definition of CR. PET considered positive if uptake is greater than mediastinal blood pool (lesions >2 cm), or above local background (lesions <2 cm)

**Table 4** 5 point Deauville criteria

Score 1	No uptake
Score 2	Uptake ≤ mediastinum
Score 3	Uptake ≥ mediastinum and < liver
Score 4	Uptake ≥ liver at any site
Score 5	Markedly increased uptake at any site, including new sites of disease

allowing better evaluation of solid visceral organs such as the liver, spleen, and kidneys, and the presence of vascular compression, invasion, or thrombosis.

Even after the initial staging examination, there is benefit in using IV contrast material. As the tumor decreases in size, it can become progressively more difficult to distinguish it from surrounding mediastinal structures, particularly on a non-contrast examination. The value of IV contrast in characterizing a mediastinal mass is shown in Fig. 24, where the margins between the mass and normal structures are more accurately defined with IV contrast, as compared to the accompanying non-contrast, attenuation correction CT or even the fused PET/CT image. Non-

contrast attenuation correction CT examinations are routinely obtained at the time of PET/CT, along with contrast-enhanced diagnostic CT imaging. In an effort to reduce radiation burden to the patient, some investigators perform the low dose attenuation correction CT with IV contrast to help better define residual tumor and potentially eliminate the need for an additional, separately acquired diagnostic CT examination. As the emerging modality of PET/MRI becomes more widely studied and available (Kluge et al. 2013), it may eventually be used as an adjunct or even replacement for PET/CT, given its inherently superior soft tissue contrast, lower amount of ionizing radiation, and better ability to characterize residual soft tissue abnormalities, both in terms of their location and cellular physiology. Multiple studies in pediatric patients have shown a correlation between early response to therapy, as defined by early interim resolution of FDG uptake, and improved event free and overall survival. Response or lack thereof can be detected after 1–3 cycles of chemotherapy, which can allow the clinicians to modify therapy early in the course of treatment, thus increasing the patient's odds of survival (Tateishi et al. 2004). However, standardized methods are needed to define such a response. The International Harmonization criteria, developed in 2007, modified the existing criteria for determining response to therapy, with particular attention paid to the role of PET/CT. Although these criteria have not yet been validated in the pediatric population, they serve as a useful framework for thinking about response to therapy. While detailing the full criteria for response is beyond the scope of this chapter, they are summarized in Table 3.

Even with such objective criteria available, the question still remains as to what qualifies as “PET positive.” Various SUV values have been proposed as a quantitative means of assessing FDG uptake, but this approach has not been widely accepted. The recently developed 5-point Deauville criteria provide semiquantitative visual assessment criteria using uptake in the liver and mediastinal blood pool as internal standards for reference (Table 4) (Kluge et al. 2013). These criteria, however, have yet to be validated in large trials or for the pediatric population.

#### 7.2.4 Surveillance Imaging

The need for routine surveillance imaging is currently a topic of intense debate in the pediatric oncologic community. Until recently, the standard practice entailed annual, or even more frequent, CT examinations, typically for up to 5 years after completion of therapy. Some protocols also included PET/CT for routine surveillance, although current data shows no role for PET/CT in surveillance imaging of asymptomatic patients. A recent study by Voss et al. found that the only predictor of overall survival was the time to relapse, with those patients relapsing within the first year



after completing therapy having lower overall survival than those patients with later relapses (Voss et al. 2012). Additionally, regardless of whether these later relapses were detected by routine surveillance imaging, laboratory data, or physical examination, the patient was equally likely to have a positive outcome. These data, confirmed by others (Friedmann et al. 2013; Rathore et al. 2012), suggest most patients with aggressive disease and worse outcome will relapse within the first year, and that routine surveillance imaging after 1 year of therapy is unlikely to impact overall survival (Voss 2013).

## 8 Conclusion

A variety of pathologies can manifest in the thymus. Understanding of the embryology, anatomy, histology, and function of the thymus helps the radiologist to differentiate congenital variants, physiologic reactions, and benign and malignant diseases affecting the thymus. Expertise in imaging of the thymus is particularly important in childhood when the thymus is subject to great variation related to normal growth and development, as well as involvement by leukemia and lymphoma, two of the most common childhood malignancies.

## References

- Abramson SJ, Price AP (2008) Imaging of pediatric lymphomas. *Radiol Clin North Am* 46:313–338, ix
- Ackman JB, Wu CC (2011) MRI of the thymus. *Am J Roentgenol* 197:W15–W20
- Adam EJ, Ignatus PI (1993) Sonography of the thymus in healthy children: frequency of visualization, size, and appearance. *Am J Roentgenol* 161:153–155
- Anastasiadis K, Ratnatunga C (2007) The thymus gland: diagnosis and surgical management. Springer, Berlin
- Arthur R (2000) Interpretation of the paediatric chest X-ray. *Paediatr Respir Rev* 1:41–50
- Attias D, Hodgson D, Weitzman S (2009) Primary mediastinal B-cell lymphoma in the pediatric patient: can a rational approach to therapy be based on adult studies? *Pediatr Blood Cancer* 52:566–570
- Bae YA, Lee KS (2010) Cross-sectional evaluation of thoracic lymphoma. *Thorac Surg Clin* 20:175–186
- Balcom RJ, Hakanson DO, Werner A et al (1985) Massive thymic hyperplasia in an infant with Beckwith-Wiedemann syndrome. *Arch Pathol Lab Med* 109:153–155
- Bale PM, Sotelo-Avila C (1993) Maldevelopment of the thymus: 34 necropsy and 10 surgical cases, including 7 thymuses medial to the mandible. *Pediatr Pathol* 13:181–190
- Buckley RH (2006) Primary immunodeficiency or not? Making the correct diagnosis. *J Allergy Clin Immunol* 117:756–758
- Connolly LP, Connolly SA (2003) Thymic uptake of radiopharmaceuticals. *Clin Nucl Med* 28:648–651
- Costa NS, Laor T, Donnelly LF (2010) Superior cervical extension of the thymus: a normal finding that should not be mistaken for a mass. *Radiology* 256:238–242
- Cronin CG, Swords R, Truong MT et al (2010) Clinical utility of PET/CT in lymphoma. *Am J Roentgenol* 194:W91–W103
- Even-Sapir E, Israel O (2003) Gallium-67 scintigraphy: a cornerstone in functional imaging of lymphoma. *Eur J Nucl Med Mol Imaging* 30(Suppl 1):S65–S81
- Friedmann AM, Wolfson JA, Hudson MM et al (2013) Relapse after treatment of pediatric Hodgkin lymphoma: outcome and role of surveillance after end of therapy. *Pediatr Blood Cancer* 60:1458–1463
- Gartner LA, Voorhess ML (1993) Adrenocorticotrophic hormone—producing thymic carcinoid in a teenager. *Cancer* 71:106–111
- Gawande RS, Khurana A, Messing S et al (2012) Differentiation of normal thymus from anterior mediastinal lymphoma and lymphoma recurrence at pediatric PET/CT. *Radiology* 262:613–622
- Guillerman RP, Voss SD, Parker BR (2011) Leukemia and lymphoma. *Radiol Clin North Am* 49:767–797, vii
- Hegde KV, Suneetha P, Pradeep PV et al (2012) Asymptomatic thymic cyst appearing in the neck on valsalva: unusual presentation of a rare disease. *J Clin Imaging Sci* 2:11
- Henkelman RM, Hardy PA, Bishop JE et al (1992) Why fat is bright in RARE and fast spin-echo imaging. *J Magn Reson Imaging* 2:533–540
- Hodgson DC, Hudson MM, Constine LS (2007) Pediatric Hodgkin lymphoma: maximizing efficacy and minimizing toxicity. *Semin Radiat Oncol* 17:230–242
- Hutchinson CB, Wang E (2011) Primary mediastinal (thymic) large B-cell lymphoma: a short review with brief discussion of mediastinal gray zone lymphoma. *Arch Pathol Lab Med* 135:394–398
- Inaoka T, Takahashi K, Mineta M et al (2007) Thymic hyperplasia and thymus gland tumors: differentiation with chemical shift MR imaging. *Radiology* 243:869–876
- Jacobs MT, Frush DP, Donnelly LF (1999) The right place at the wrong time: historical perspective of the relation of the thymus gland and pediatric radiology. *Radiology* 210:11–16
- Johnson PW, Davies AJ (2008) Primary mediastinal B-cell lymphoma. *Hematol Am Soc Hematol Educ Program* 2008:349–358
- Kaufman MR, Smith S, Rothschild MA et al (2001) Thymopharyngeal duct cyst: an unusual variant of cervical thymic anomalies. *Arch Otolaryngol Head Neck Surg* 127:1357–1360
- Kelly KM, Hodgson D, Appel B et al (2013) Children's Oncology Group's 2013 blueprint for research: Hodgkin lymphoma. *Pediatr Blood Cancer* 60:972–978
- Kim OH, Kim WS, Kim MJ et al (2000) US in the diagnosis of pediatric chest diseases. *Radiographics* 20:653–671
- Kluge R, Kurch L, Montravers F et al (2013) FDG PET/CT in children and adolescents with lymphoma. *Pediatr Radiol* 43:406–417
- Kontny HU, Sleasman JW, Kingma DW et al (1997) Multilobar thymic cysts in children with human immunodeficiency virus infection: clinical and pathologic aspects. *J Pediatr* 131:264–270
- MacDonald K, Mackenzie S (2009) What happens to the thymus in children who have undergone a median sternotomy? *Pediatr Radiol* 39:616–621
- Martelli M, Ferreri AJ, Johnson P (2008) Primary mediastinal large B-cell lymphoma. *Crit Rev Oncol Hematol* 68:256–263
- Mizuno T, Hashimoto T, Masaoka A et al (1997) Thymic follicular hyperplasia manifested as an anterior mediastinal mass. *Surg Today* 27:275–277
- Molina PL, Siegel MJ, Glazer HS (1990) Thymic masses on MR imaging. *Am J Roentgenol* 155:495–500
- Mong A, Epelman M, Darge K (2012) Ultrasound of the pediatric chest. *Pediatr Radiol* 42:1287–1297

- Mortelmans A, Hermans R (2005) Thymopharyngeal duct cyst. *JBR-BTR* 88:99
- Nasseri F, Eftekhari F (2010) Clinical and radiologic review of the normal and abnormal thymus: pearls and pitfalls. *Radiographics* 30:413–428
- Newman B (2011) Ultrasound body applications in children. *Pediatr Radiol* 41(Suppl 2):555–561
- Park CM, Goo JM, Lee HJ et al (2009) Tumors in the tracheobronchial tree: CT and FDG PET features. *Radiographics* 29:55–71
- Petroze R, McGahren ED: *Pediatric chest II* (2012) Benign tumors and cysts. *Surg Clin North Am* 92:645–658, ix
- Rathore N, Eissa HM, Margolin JF et al (2012) Pediatric Hodgkin lymphoma: are we over-scanning our patients? *Pediatr Hematol Oncol* 29:415–423
- Restrepo CS, Pandit M, Rojas IC et al (2005) Imaging findings of expansile lesions of the thymus. *Curr Probl Diagn Radiol* 34:22–34
- Ries LAG, Smith MA, Gurney JG, Linet M, Tamra T, Young JL (1999) Cancer Incidence and Survival among Children and Adolescents: United States SEER Program 1975–1995. In: Bunin GR (ed) *National Cancer Institute SEER Program*. No. 99-4649, Bethesda, MD
- Safieddine N, Keshavjee S (2011) Anatomy of the thymus gland. *Thorac Surg Clin* 21:191–195, viii
- Sharma P, Singhal A, Kumar A et al (2013) Evaluation of thymic tumors with 18F-FDG PET-CT: a pictorial review. *Acta Radiol* 54:14–21
- Shepherd SF, A'Hern RP, Pinkerton CR (1995) Childhood T-cell lymphoblastic lymphoma—does early resolution of mediastinal mass predict for final outcome? The United Kingdom Children's Cancer Study Group (UKCCSG). *Br J Cancer* 72:752–756
- Siegel MJ, Glazer HS, Wiener JJ et al (1989) Normal and abnormal thymus in childhood: MR imaging. *Radiology* 172:367–371
- Sklair-Levy M, Agid R, Sella T et al (2000) Age-related changes in CT attenuation of the thymus in children. *Pediatr Radiol* 30:566–569
- Tateishi U, Muller NL, Johkoh T et al (2004) Primary mediastinal lymphoma: characteristic features of the various histological subtypes on CT. *J Comput Assist Tomogr* 28:782–789
- Termuhlen AM, Smith LM, Perkins SL et al (2013) Disseminated lymphoblastic lymphoma in children and adolescents: results of the COG A5971 trial: a report from the children's oncology group. *Br J Haematol* 162:792–801
- Tunkel DE, Erozan YS, Weir EG (2001) Ectopic cervical thymic tissue: diagnosis by fine needle aspiration. *Arch Pathol Lab Med* 125:278–281
- Varga I, Pospisilova V, Jablonska-Mestanova V et al (2011) The thymus: picture review of human thymus prenatal development. *Bratisl Lek Listy* 112:368–376
- Voss SD, Chen L, Constine LS, Chauvenet A, Fitzgerald TJ, Kaste SC, Slovis T, and Schwartz CL (2012) Surveillance computed tomography imaging and detection of relapse in intermediate- and advanced-stage pediatric Hodgkin's lymphoma: a report from the Children's Oncology Group. *J Clin Oncol* 30(21):2635–2640
- Voss SD (2013) Surveillance imaging in pediatric Hodgkin lymphoma. *Curr Hematol Malig Rep* 8:218–225
- Yaris N, Nas Y, Cobanoglu U et al (2006) Thymic carcinoma in children. *Pediatr Blood Cancer* 47:224–227
- Yin EZ, Frush DP, Donnelly LF et al (2001) Primary immunodeficiency disorders in pediatric patients: clinical features and imaging findings. *Am J Roentgenol* 176:1541–1552

# Pulmonary and Extrathymic Mediastinal Tumors

Karen Lyons, R. Paul Guillerman, and Kieran McHugh

## Contents

<b>1</b>	<b>Introduction</b> .....	349
<b>2</b>	<b>Clinical Features</b> .....	350
<b>3</b>	<b>Imaging</b> .....	350
<b>4</b>	<b>Pulmonary Tumors</b> .....	351
4.1	Pulmonary Metastases .....	352
4.2	Pulmonary Lymphoma and Post-transplantation Lymphoproliferative Disorder.....	354
4.3	Pulmonary Hamartoma.....	355
4.4	Pulmonary Chondroma.....	355
4.5	Fetal Lung Interstitial Tumor.....	355
4.6	Infantile Myofibromatosis .....	356
4.7	Congenital Peribronchial Myofibroblastic Tumor.....	357
4.8	Inflammatory Myofibroblastic Tumor .....	357
4.9	Pleuropulmonary Blastoma .....	359
4.10	Bronchial Carcinoid Tumor .....	360
4.11	Mucoepidermoid Carcinoma .....	361
4.12	NUT Midline Carcinoma .....	361
4.13	Papillomas and Squamous Cell Carcinoma.....	362
4.14	Leiomyoma and Leiomyosarcoma.....	363
<b>5</b>	<b>Extrathymic Mediastinal Tumors</b> .....	363
5.1	Germ Cell Tumors.....	363
5.2	Neuroblastic Tumors .....	364
5.3	Lymphangiomatosis .....	365
5.4	Esophageal Leiomyomatosis .....	367
<b>6</b>	<b>Conclusion</b> .....	367

## Abstract

The most frequently encountered pediatric thoracic tumors are pulmonary metastases from extracranial solid tumors. Primary pulmonary neoplasms are rare in childhood, but can cause considerable morbidity and mortality from mass effect, tissue invasion, and metastatic disease in affected children. Mesenchymal neoplasms are more common than epithelial neoplasms in the pediatric lung, unlike in adults, and some of these neoplasms are associated with predisposing genetic syndromes and certain infections. While lymphoma is the most common mediastinal malignancy, germ cell, neuroblastic, and other mediastinal tumors also manifest with distinctive features that are important to recognize for appropriate management. Many of these tumors are detectable on chest radiography, but chest CT remains the primary imaging modality used to formulate a differential diagnosis for these tumors, define anatomy for preoperative planning, assess tumor response to therapy, and survey for recurrent disease, with MRI and nuclear medicine studies playing a complementary role. This chapter will review the characteristic clinical presentations and imaging findings of selected pulmonary and extrathymic mediastinal tumors of childhood.

## 1 Introduction

Thoracic tumors are often classified, despite some overlap, as originating in one of three major thoracic compartments, namely the lungs, the mediastinum, or the chest wall. In the interests of simplicity and convention, this anatomical approach will be used in this chapter, with the focus on tumors of the lungs and certain tumors of the mediastinum. In this book, lymphoma and thymic tumors are covered in the chapter entitled Imaging Evaluation of the Thymus and Thymic Disorders in Children by Sams and Voss, and chest

K. Lyons · R. Paul Guillerman (✉)  
Department of Pediatric Radiology,  
Texas Children's Hospital,  
Baylor College of Medicine,  
6701 Fannin St, Suite 470,  
Houston, TX 77030, USA  
e-mail: rpguille@texaschildrens.org

K. McHugh  
Department of Radiology,  
Great Ormond Street Hospital for Children NHS Trust,  
Great Ormond Street, London, WC1N 3JH, UK  
e-mail: Kieran.McHugh@gosh.nhs.uk



wall tumors, hemangiomas, lymphatic malformations, and neurofibromas are covered in the chapter entitled Radiology of the Chest Wall by Eich, Kellenberger and Willi, and will not be further addressed in this chapter. An emphasis is placed on imaging features of these thoracic tumors at diagnosis. The subsequent follow-up imaging of benign conditions is governed by the clinical course, and that of malignancies is largely determined by protocols devised by the various pediatric oncology co-operative groups.

---

## 2 Clinical Features

The most frequently encountered pediatric thoracic tumors, particularly in pediatric oncology centers, are pulmonary metastases. These are usually initially found during staging of a known or suspected malignancy and the dominant clinical findings are typically those related to the primary tumor. Primary thoracic neoplasia is uncommon in childhood and seldom an early diagnostic consideration, but a wide variety of tumors do occur within the chest and appropriate management is facilitated by correct recognition on imaging. There is no major difference between the sexes in the incidence of primary chest tumors, and tumors occur with relatively equal frequency in either lung.

Primary chest neoplasms largely manifest either due to pressure effects from compression of adjacent organs, systemic symptoms from disseminated malignancy, or as an incidental finding. Paraneoplastic syndromes are very rare, and usually limited to neuroblastoma or bronchial carcinoid. In the setting of airway obstruction or respiratory symptoms that do not respond to conventional medical treatment, computed tomography (CT) can be very useful in demonstrating a mass lesion occult to chest radiography (CXR). While the presenting symptoms can vary greatly even within the same histological group, some generalizations with regard to the presentation of chest masses can be made.

In both benign and malignant lung tumors, the most frequent presenting complaints are fever, cough, and pneumonitis (Hancock et al. 1993; Hartman and Shochat 1983). Hemoptysis and respiratory distress are more common with malignant pulmonary lesions. In the largest review series to date, 28 % of benign tumors were asymptomatic as compared to 6 % of malignant tumors (Hancock et al. 1993). A child who is truly asymptomatic is twice as likely to harbor a benign pulmonary tumor, and this likelihood is even greater in children over 4 years of age. Endobronchial masses typically result in lung collapse, persistent hyperinflation, or wheezing which fails to respond to conventional treatment and may be complicated by bronchiectasis. The endobronchial location of many such lesions may be apparent only after careful review of multiplanar CT images or bronchoscopy.

Thoracic neurogenic tumors such as neuroblastoma and ganglioneuroma are often found incidentally on a CXR performed for other reasons, while the majority of mediastinal tumors generally present with respiratory symptoms such as airway obstruction, cough, or fever due to a complicating pneumonia. In contrast to many tumors of pulmonary origin, the likely nature of the illness is apparent on CXR. The opacity is generally not typical for pneumonia with often clearly defined margins suggesting an extrapulmonary origin. Mediastinal shift or adenopathy may be seen and rib destruction, in particular, should be sought as this latter finding virtually always indicates an extrapulmonary malignancy. In fact, the majority of mediastinal and chest wall tumors seen in children are malignant.

---

## 3 Imaging

CXR remains the most common initial imaging modality for evaluation of chest masses secondary to its wide availability, low cost, and relatively low associated radiation dose. Radiological investigation should begin with a frontal CXR. When an unusual opacity is evident, a lateral view can be particularly helpful in assessing the trachea for compression and/or displacement, and in accurately defining the location of the abnormality, which aids greatly in establishing a differential diagnosis. Chest CT is used to investigate suspicious or persistent abnormalities seen on CXR, or to detect disease occult on CXR. Compared to CXR, CT is much more sensitive for detecting small lesions and calcifications, and better at defining anatomic relationships and mass effect on critical structures such as the airway and great vessels. Due to its greater sensitivity for small lesions and precision for measuring the size of lesions, CT is routinely used in follow-up of treated malignancy. While CT is highly sensitive, it lacks specificity and cannot reliably differentiate between benign and malignant lung nodules (McCarville et al. 2006; Silva et al. 2010). Correlation with clinical history and serial imaging follow-up improves its specificity. CT is also useful for guiding tissue sampling.

Contemporary multidetector volumetric CT scanners can acquire images of the entire chest of a child within a few seconds or even less than a second, resulting in less need for sedation and less motion artifact (Bastos et al. 2009). These scanners also allow generation of high-resolution multiplanar reconstructions (MPR) and 3D renderings to better depict anatomy for diagnostic and treatment planning. The dose of ionizing radiation from CT is typically much higher than from CXR, but can be reduced without compromising image quality by judicious application of new techniques such as iterative reconstruction (Brady et al. 2014). To better characterize tumors and evaluate the mediastinal/hilar

**Table 1** Spectrum of benign and malignant primary pediatric tumors

Primary Pulmonary Tumors	
Benign	Malignant
Hamartoma	Inflammatory myofibroblastic tumor
Chondroma	Pleuropulmonary blastoma
Fetal lung interstitial tumor	Bronchial carcinoid
Infantile myofibromatosis	Mucoepidermoid carcinoma
Congenital peribronchial myofibroblastic tumor	NUT midline carcinoma
Papilloma	Bronchogenic carcinoma
Leiomyoma	Leiomyosarcoma

structures, intravenous contrast is typically administered for chest CT scans of primary thoracic tumors for initial staging, therapy response assessment, and relapse surveillance. However, chest CT scans performed to detect and follow-up lung metastases from extrathoracic nonlymphomatous tumors can be performed without intravenous contrast (Kuhns and Roubal 1995) at relatively low tube current (Diederich et al. 1999) without loss of sensitivity because of the high inherent contrast of aerated lung parenchyma. Use of maximum intensity projection (MIP) images can improve sensitivity for small pulmonary nodules (Coakley et al. 1998; Kawel et al. 2009). Maximum intensity projection (MIP) processing has several advantages in the detection of small nodules: vascular structures appear as tubular and branching structures rather than as discrete nodules; the MIP slab preserves the inherent resolution of the original images; MIP images can be constructed in any plane; and image numbers are markedly reduced in comparison to the axial image set from a routine MDCT study (Gruden et al. 2002). Use of MIP images should complement but not substitute for axial image review. Computer-aided detection (CAD) has been shown to have good sensitivity for detection of nodules 4 mm in diameter or larger with a low false positive rate (Helm et al. 2009), but is not in widespread use in pediatric imaging. In routine clinical practice, contiguous axial sections are usually adequate for nodule detection, supplemented by coronal or sagittal reformatted images for decision making on questionable small nodules.

CT virtual bronchoscopy (VB) can better define the endobronchial anatomy when an endobronchial lesion is present. The added value of this information is questionable, however. VB can increase total examination time and cost, and may not provide additional clinically useful information over MPR images (Kocaoglu et al. 2006). Despite meticulous technique and attention to detail, post-obstructive pneumonitis, or atelectasis may obscure an endobronchial tumor, resulting in a false negative CT study.

CT after intravenous contrast administration can accurately define mediastinal masses and is sensitive in the detection of adjacent bony destruction from chest wall masses. Magnetic resonance imaging (MRI), however, has become the preferred technique for examining chest wall masses, and in some cases, mediastinal masses. This has come about mainly as a result of faster scanning sequences, improved gating techniques to reduce cardiorespiratory motion artifact, and MR angiography to better depict the vasculature, in addition to the conventional advantages of better soft-tissue contrast and lack of ionizing radiation exposure compared to CT (Newman 2011). Most tumors have intermediate or low signal intensity on T1-weighted sequences, are hyperintense to varying degrees on T2-weighted sequences, and display variable contrast enhancement after gadolinium administration. Rather than actual signal characteristics, it is the site of tumor occurrence and the age of the patient that suggests the most likely tumor in an individual case.

The role of FDG-PET in evaluating nonlymphomatous chest tumors has yet to be clearly established. There may be a limited role for FDG-PET in improving the specificity for malignancy in enlarged lymph nodes or lung nodules visualized on CT (Kleis et al. 2009; Cistaro et al. 2012).

## 4 Pulmonary Tumors

Primary pulmonary neoplasms are unusual in childhood, and far less common than non-neoplastic, mass-like processes. The absence of pyrexia or leukocytosis helps exclude a round pneumonia, lung abscess, or infected congenital pulmonary airway malformation (CPAM). Clinical history and laboratory tests are often valuable in suggesting granulomatous disease, infarction, or hematoma as a cause of pulmonary mass. Metastases from an extra-pulmonary primary malignancy are far more common than

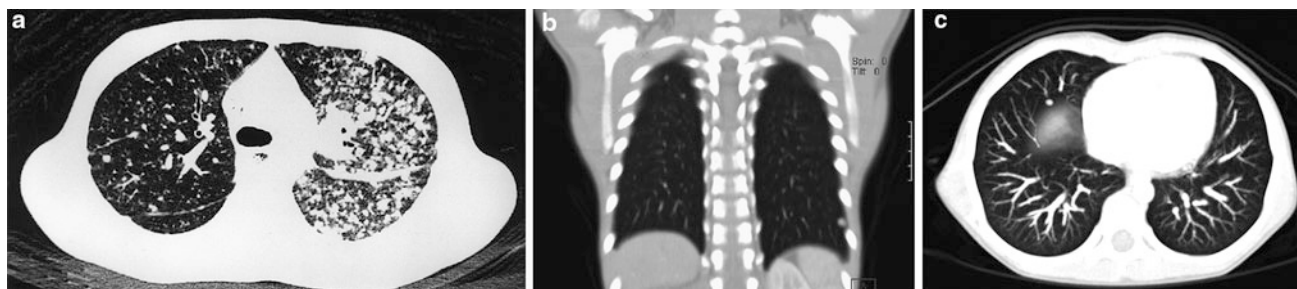


**Fig. 1** Pulmonary metastases. **a** Axial chest CT image demonstrates predominantly left-sided pulmonary nodularity, pleural and interstitial thickening due to neuroblastoma metastases. An unusual lymphatic pattern of tumor spread has occurred in this patient. **b** Two subtle right apical pulmonary nodules and another nodule in the left lower lobe

depicted on a coronal CT image are suspicious for metastatic disease in a different 4-year-old patient with a newly diagnosed renal tumor. **c** Axial MIP CT image from the same patient illustrating how the MIP technique clearly helps differentiate between pulmonary vessels and small lung nodules

primary pulmonary tumors in children (Cohen and Kaschula 1992). A majority (76–88 %) of primary pulmonary tumors in childhood are malignant (Hancock et al. 1993) (Table 1).

#### 4.1 Pulmonary Metastases

The lungs are a common site of metastatic spread of many pediatric solid extracranial malignancies, including (with an approximate percentage incidence of pulmonary metastases at diagnosis) Wilms tumor (10 %), osteosarcoma (15–20 %), Ewing sarcoma (15–20 %), rhabdomyosarcoma (15 %), and hepatoblastoma (10 %) (Paulussen et al. 1998; Kaste et al. 1999). Pulmonary metastases are found in only 1–3 % of cases of neuroblastoma at diagnosis (Cowie et al. 1997), and in 3–4 % of those with stage 4 disease (DuBois et al. 2008), but are a prognostic marker of unfavorable outcome (Kammen et al. 2001; DuBois et al. 2008), as is the case for nearly all pediatric solid extracranial malignancies (Fuchs et al. 2012). Routine chest CT for staging purposes is warranted at diagnosis for these malignancies, as well as for some other less common pediatric malignancies. Staging for metastatic neuroblastoma is, however, best achieved with metaiodobenzylguanidine (MIBG) scanning. Lung metastases usually result from hematogenous dissemination and manifest as multiple, well-defined pulmonary nodules. Lymphatic spread producing a reticular or reticulonodular pattern can also occur in neuroblastoma (McCahon 2006) (Fig. 1).

Diagnostic dilemmas arise when pulmonary nodules are small (a few millimeters in diameter), indistinct, or solitary. Among malignant causes, an incidentally detected nodule is much more likely to represent a metastasis rather than a primary lung tumor in a child. Benign causes of pulmonary nodules are myriad and include granulomas (particularly in areas with a high prevalence of histoplasmosis or tuberculosis), hamartomas, chondromas, intraparenchymal lymph nodes, septic emboli, plugged distal airways, previous varicella infection, vasculitis, Langerhans cell histiocytosis,



**Fig. 2** Intrapulmonary lymph node. Axial chest CT image from a 17-year old with osteosarcoma undergoing staging demonstrates a well-circumscribed, bean-shaped, solid pulmonary nodule (arrow) of the right lower lobe close to the pleura. This nodule proved to be an intrapulmonary lymph node rather than a metastasis upon biopsy

respiratory papillomatosis, opportunistic infections in the setting of immunodeficiency, and fibrotic nodules in the setting of bleomycin or cyclophosphamide toxicity. Clustering of multiple nodules favors an infectious or inflammatory etiology. Spontaneous resolution of pulmonary nodules may be related to a focal inflammatory process, atelectasis, mucoid impaction of small bronchi, or intermittent enlargement of benign intrapulmonary lymph nodes (Diederich et al. 2005). Intrapulmonary lymph nodes tend to be located peripherally below the level of the carina at or near the junction of the pleura and adjacent lung lobules (Wang et al. 2013) (Fig. 2).

In an individual case, it can be very difficult to distinguish benign from metastatic pulmonary nodules in young patients with a solid extracranial malignancy. A study of pediatric oncology patients found that the most significant predictors of a pulmonary nodule being metastatic were peripheral location, size between 5 and 10 mm diameter, location in the right lower lobe, and a history of osteosarcoma, Ewing sarcoma, or hepatocellular carcinoma



(Murrell et al. 2011). Another study found that sharp nodule margins and development of new nodules are significantly associated with malignancy, but that nodules measuring less than 5 mm in diameter are as likely to be malignant as larger nodules, unlike in adults (McCarville et al. 2006). Co-existence of both benign and malignant nodules is also possible. In the setting of pediatric osteosarcoma, over 90 % of malignant nodules are correctly classified, while only 11–30 % of benign nodules are correctly classified on the basis of imaging findings (Brader et al. 2011).

FDG-PET may be a useful adjunct for the evaluation of possible pulmonary metastases in pediatric malignancies. FDG-PET confers significantly higher specificity than CT for pulmonary metastases greater than 5 mm diameter in children (Kleis et al. 2009). A prospective study of FDG-PET/CT in the characterization of pulmonary nodules in children with bone sarcoma demonstrated a sensitivity of 90 % and specificity of 94 % using a  $SUV_{max}$  value around 1, compared to a sensitivity of 90 % and specificity of 81 % using a cut-off value of 6 mm for nodule diameter (Cistaro et al. 2012).

Findings equivocal for pulmonary metastatic disease on chest CT warrant further evaluation, either with FDG-PET, close surveillance with follow-up imaging, or biopsy. Because of the survival advantage conferred by complete resection of pulmonary metastases in selected pediatric malignancies (Tronc et al. 2008) and the difficulty in reliably diagnosing metastatic disease solely by imaging when only one or a few small lung nodules are discovered in a child with a solid tumor, there is a trend toward resecting or performing a biopsy of indeterminate pulmonary nodules. Fine needle aspiration cytology is widely practiced in adult patients with carcinoma and is usually diagnostic. In children, however, sarcomas are much more common, and aspiration cytology is generally regarded as unreliable for the diagnosis of childhood tumors since differentiation from other cells can be extremely difficult on small cytological specimens and architectural information is lost. Core needle biopsies of small pulmonary nodules in children under CT guidance using a co-axial system permit multiple biopsies through a single pleural pass to be obtained, yielding adequate tissue for diagnosis in most cases and reducing the likelihood of complicating hemothorax or pneumothorax (Connolly et al. 1999).

A successful response to chemotherapy should be accompanied by disappearance of pulmonary metastases. Occasionally, nodules may demonstrate incomplete resolution related to residual fibrosis or selection of less mitotically active cells (as in the case of rhabdomyomatous differentiation in Wilms tumors or mature teratoma elements in germ cell tumors), but ultimately proof of a benign nature rests on either biopsy or stability on follow-up, particularly off treatment (Seemayer et al. 1997; Seifert et al. 2012). If the initial chest CT at diagnosis is negative

for metastases, later follow-up for pediatric oncology patients is largely with CXR, with CT reserved for equivocal CXR findings, clinically suspected relapses, or tumors with a high risk of pulmonary relapse.

Patients with osteosarcoma or FDG-PET positive disease at initial presentation appear to be at the highest risk of recurrent pulmonary metastatic disease (Murrell and Dasgupta 2013). As up to 30–40 % of children with osteosarcoma eventually develop pulmonary metastases and complete surgical remission is the main prognostic factor affecting survival, routine chest CT surveillance, and pulmonary metastasectomy of osteosarcoma patients may be justified (Diemel et al. 2009). In an osteosarcoma patient, pulmonary nodules, particularly those that are calcified or greater than 5 mm in diameter, should be regarded as malignant until proven otherwise (McCahon 2006; Brader et al. 2011). CT also tends to underestimate the number of metastatic pulmonary nodules found at thoracotomy in osteosarcoma patients (Kayton et al. 2006). Centrally-located pulmonary metastases of osteosarcoma may be associated with reduced median survival compared with those that are peripherally sited (Letourneau et al. 2011). Osteosarcoma may also metastasize to the mediastinal lymph nodes and pleura, and even to the myocardium. Cavitory metastases are unusual in childhood but are occasionally seen with sarcomas or Wilms tumor, or after chemotherapy or radiotherapy.

Co-operative pediatric oncology groups in North America and Europe once recommended that presumed pulmonary metastases from Wilms tumor could be ignored if they were not visible on CXR. This is no longer the case with current protocols from the Children's Oncology Group (COG) and the International Society of Pediatric Oncology (SIOP). However, the clinical significance of these small nodules that are detectable only with CT in patients with Wilms tumor is uncertain. A retrospective review of National Wilms Tumor Studies (NWTs)-4 and -5 found that patients with pulmonary nodules detected only by CT who received three chemotherapeutic agents had improved 5 year event-free survival, but not overall survival, compared with those receiving only two drugs (Grundy et al. 2012). These so-called CT-only patients represent a small (2–4 %) cohort of all Wilms patients (Smets et al. 2012). It has been argued that this small proportion of CT-only detected lesions makes it difficult to justify the routine use of a relatively high radiation technique such as CT when patient outcomes may not be affected by the CT findings in the setting of Wilms tumor (Smets et al. 2012). In a SIOP Wilms study, patients with CT-only lesions should have been treated as having localized disease but many were not, leading the authors to conclude that current clinical decision-making was based on a fear of under-treatment. The outcome for patients with CT-only lesions, whether treated

as localized or metastatic disease (the latter received more intensive therapy), were no different. Some patients with CT-only lesions may have benign chest disease, yet suffer late toxic effects from more intensive therapy. This underscores the need to devise better diagnostic imaging tests for the detection of metastases and selection of patients for more intensive therapy. Chest CT perhaps could be used in children with Wilms tumor after preoperative chemotherapy and nephrectomy to select those with persisting pulmonary lesions. The finding of persisting pulmonary lesions in combination with high risk histology and/or stage III disease confers a worse prognosis, and therefore these patients might benefit from intensified therapy (Smets et al. 2012). Wilms tumor patients with metastatic lung disease at presentation who are in complete pulmonary remission after chemotherapy with or without metastasectomy have a better outcome than those with unresectable pulmonary metastases. The findings on chest CT help determine which patients should or should not receive radiotherapy, with persisting lung lesions being an indication for radiotherapy (Verschuur et al. 2012).

An aggressive diagnostic approach with chest CT is also advocated in pediatric malignant non-Wilms renal tumors, where survival requires complete clearance of lung metastases, either through chemotherapy, radiotherapy, or metastasectomy (Warmann et al. 2012).

#### 4.2 Pulmonary Lymphoma and Post-transplantation Lymphoproliferative Disorder

Pulmonary involvement occurs in approximately 10 % of cases of pediatric lymphoma and is usually associated with ipsilateral hilar or mediastinal lymphadenopathy. Pulmonary lymphoma is most frequently seen in Hodgkin disease or anaplastic large cell non-Hodgkin lymphoma, and most often manifests as nodules or consolidative masses. A reticular pattern related to lymphatic spread can also be observed (Maturen et al. 2004). In the setting of pediatric Hodgkin lymphoma, direct contiguous involvement of the lung by an adjacent mediastinal mass is considered stage IIE invasive disease rather than disseminated stage IV disease (Guillerman et al. 2011).

Post-transplantation lymphoproliferative disorder (PTLD) is thought to result from an Epstein–Barr virus (EBV)-induced proliferation from B-cell lymphocytes, which is normally opposed by a functioning T-cell system in immunocompetent patients. It is estimated to occur in 2–3 % of all solid organ transplants including both children and adults, but the incidence in children with lung transplants is reported to be 8 % (Pickhardt et al. 2000). Post-transplantation lymphoproliferative disorder (PTLD)

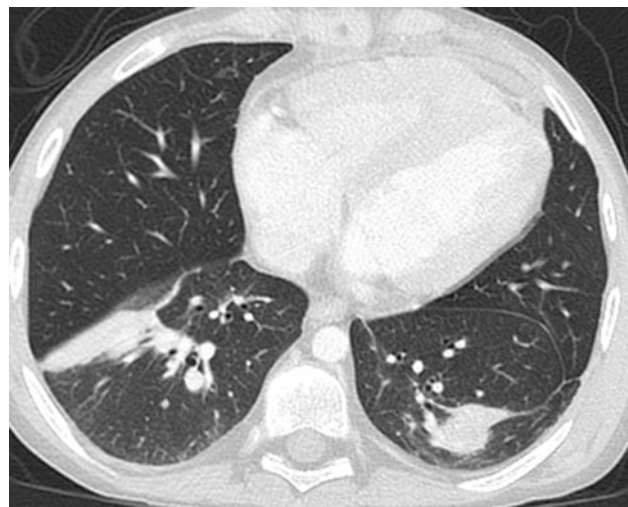


**Fig. 3** Post-transplantation lymphoproliferative disorder (PTLD). Axial chest CT image from a 15-year-old post lung transplantation demonstrates lobular subsegmental masses of the lower lobes. Biopsy revealed monomorphic PTLD, diffuse large B-cell lymphoma type

occurs more often and presents earlier in lung transplants compared with other solid organ transplants, with a median time from transplant to diagnosis of 6–10 months (Wilde et al. 2005; Siegel et al. 2003). The overall prevalence of pulmonary involvement in pediatric PTLD is 29 % (Maturen et al. 2004), and a large majority of pediatric lung transplant recipients with PTLD have intrathoracic involvement of the lungs or mediastinum (Wilde et al. 2005).

The most common presentation of intrathoracic PTLD is asymptomatic pulmonary nodules. Close monitoring of EBV viral load and the degree of immunosuppression via lymphocyte function assays can facilitate an early diagnosis (Elidemir et al. 2009). Children at greatest risk are those who receive EBV-positive donor lungs who were EBV-seronegative prior to transplantation. The typical CT appearance is multiple well-defined, soft-tissue attenuation pulmonary nodules measuring 1–4 cm. They are usually homogeneous but can have central necrosis. In approximately 10 % of cases, multifocal masses or consolidations are the predominant parenchymal finding. Mediastinal lymphadenopathy is often present, and may coalesce into large nodal masses (Wilde et al. 2005).

The principal initial treatment of PTLD is cessation or reduction of immunosuppression. However, PTLD may progress to an aggressive diffuse large B-cell lymphoma (Fig. 3). Only 50 % of pediatric lung transplant patients were reported to survive more than 2 years after diagnosis of PTLD in one study (Siegel et al. 2003), but that figure has likely improved in recent years.

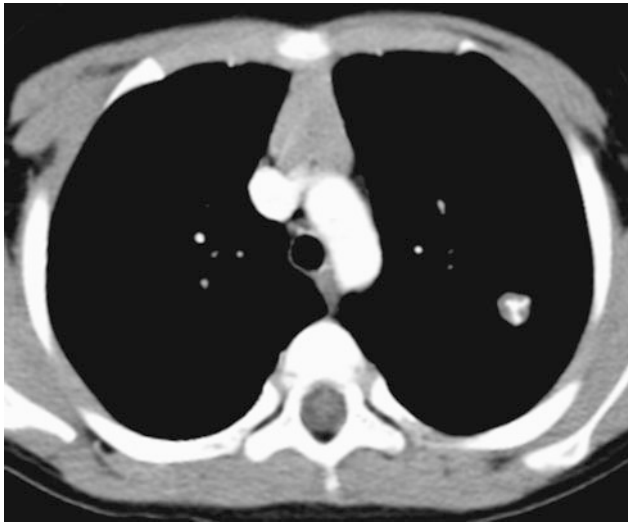


**Fig. 4** Pulmonary hamartoma. Axial contrast-enhanced chest CT image shows a small, well-defined, lobular, left pulmonary nodule with curvilinear calcification

### 4.3 Pulmonary Hamartoma

Hamartomas account for the majority of benign tumors that occur in the lung parenchyma in childhood (Hancock et al. 1993). A pulmonary hamartoma consists of variable mesenchymal tissues that are native to the lung but present in an abnormal configuration. Despite being regarded as possible developmental anomalies, the vast majority of pulmonary hamartomas are discovered in adults and grow very slowly (doubling time longer than 550 days in almost all cases) (Huang et al. 2011), supporting the idea that hamartomas are actually acquired lesions.

Pulmonary hamartomas in adults are frequently asymptomatic and often found incidentally (Hartman and Shochat 1983). The characteristic radiological finding is a clearly defined solid nodular opacity in the lung periphery. Hamartomas measuring less than 1 cm in diameter are more likely to be spherical, and those measuring over 1 cm in diameter are more likely to be lobulated. Approximately 10 % show calcification, often with a speckled or curvilinear configuration (Fig. 4), and sometimes in a “popcorn” pattern. Central fat attenuation is seen in up to 30 % of hamartomas on CT. The likelihood of identifying fat or calcification increases with lesion size and these classic features are rarely seen in lesions measuring less than 2 cm in diameter. Hamartomas typically show no uptake on FDG-PET (Huang et al. 2011). MRI reveals linear or curvilinear clefts along the marginal surface, particularly on T2-weighted imaging. Most lesions demonstrate cleft and rim enhancement with contrast, but fat is usually inconspicuous on MRI (Park et al. 2008).

In contrast to adult patients, many of the reported cases of pulmonary hamartomas in younger children have fared poorly, including fatalities among those in the neonatal period (Hartman and Shochat 1983). Only a minority of the reported pediatric cases have been asymptomatic. Although pulmonary hamartomas typically manifest as isolated pulmonary nodules, these lesions may be quite large in young children.

Endobronchial hamartomas, which are particularly uncommon in childhood, present with respiratory symptoms or infections due to airway obstruction. A few reports of pediatric tracheal hamartomas exist, some of which may have a large extraluminal component manifesting clinically as a neck mass (Gross et al. 1996). Surgery for hamartomas is curative, although endobronchial hamartomas may require lobectomy or even pneumonectomy.

### 4.4 Pulmonary Chondroma

Pulmonary chondromas are benign lesions usually composed of myxoid rather than hyaline cartilage. The presence of a thin fibrous pseudocapsule, frequent bone metaplasia and calcification, and the absence of entrapped respiratory epithelium, smooth muscle, or fat allow distinction of pulmonary chondromas from hamartomas. On imaging, pulmonary chondromas appear as well-circumscribed nodules with or without calcification/ossification (Rodriguez et al. 2007). Pulmonary chondromas are the second most common component of the Carney triad, a rare nonfamilial disorder predominantly occurring in young women that also includes gastrointestinal stromal tumors (GISTs) and extraadrenal paragangliomas (Stratakis and Carney 2009) (Fig. 5). The chondromas associated with the Carney triad are usually asymptomatic and can be multiple (Rodriguez et al. 2007).

### 4.5 Fetal Lung Interstitial Tumor

Fetal lung interstitial tumor (FLIT) is a recently described, very rare tumor composed of immature interstitial mesenchyme in association with irregular airspace-like structures resembling the fetal lung at 20–24 weeks of gestation. In a case series of 10 patients, all presented by 3 months of age, and two were detected by prenatal ultrasound. Other than the two cases detected antenatally, all patients presented with respiratory distress (Dishop et al. 2010). One of the patients detected prenatally presented with a large pulmonary tumor causing fetal hydrops due to inferior vena cava obstruction



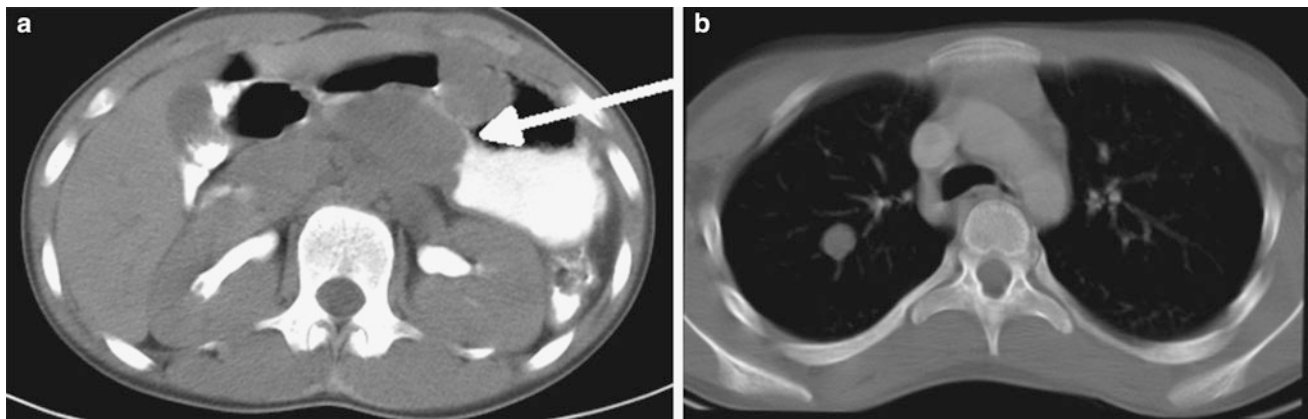


**Fig. 5** Pulmonary chondroma. **a** Axial contrast-enhanced abdominal CT image in a 13-year-old female with incomplete Carney triad demonstrates a solid mass (*arrow*) along the distal wall of the stomach

representing a gastrointestinal stromal tumor (GIST). **b** Axial chest CT image in the same patient shows a well-defined, solid right upper lobe pulmonary nodule without obvious calcification

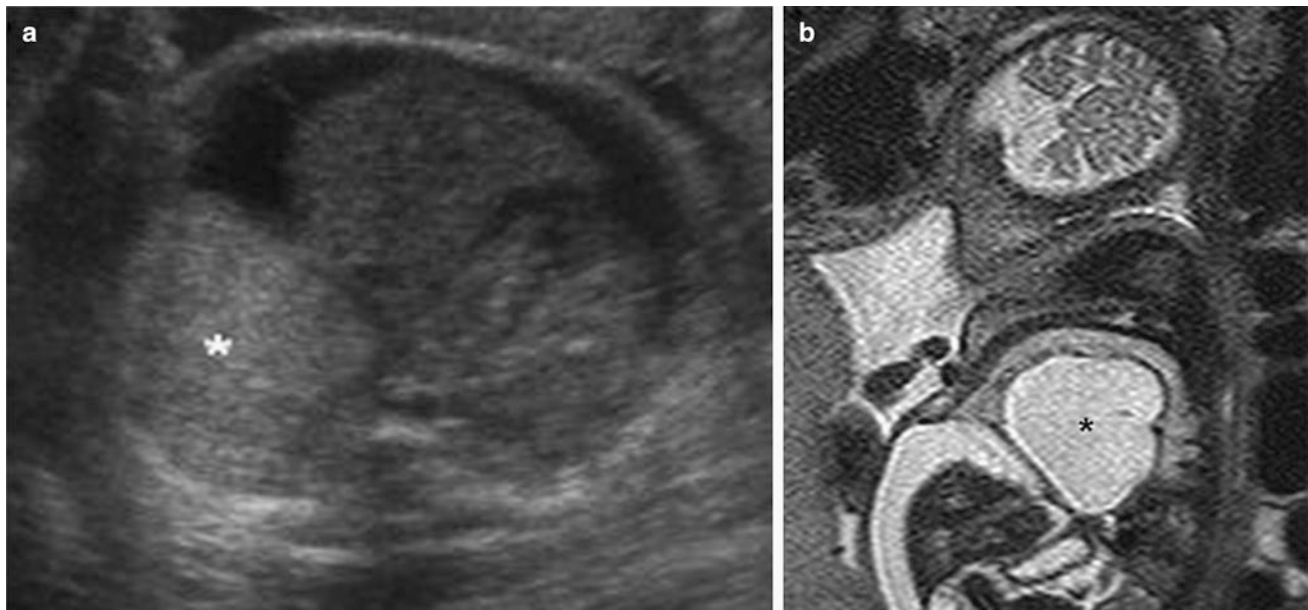


**Fig. 6** Fetal lung interstitial tumor. **a** Transverse image from prenatal ultrasound exam performed at 36 weeks gestation reveals a large, well-circumscribed, solid hyperechoic right basilar lung mass (*asterisk*). **b** T2-weighted sagittal fetal MR image of the same patient

demonstrates a large, well-circumscribed, high signal intensity mass (*asterisk*) compressing the adjacent lung and everting the diaphragm, with associated ascites related to inferior vena cava compression

and had ex utero intrapartum treatment (EXIT procedure) at 37 weeks gestational age (Lazar et al. 2011).

On imaging, these tumors are well-circumscribed, unifocal, and confined to a single lobe with a predilection for the right hemithorax. A majority are solid, although some may be partially cystic. They are homogeneously low in attenuation on CT imaging and the single case evaluated by MRI demonstrated heterogeneously increased signal intensity on T2-weighted images (Fig. 6). Prognosis is favorable, with no reports of malignant transformation or recurrence, even in incompletely resected cases (Dishop et al. 2010).

#### 4.6 Infantile Myofibromatosis

Infantile myofibromatosis, the most common fibrous tumorous condition of infancy, most often presents with a firm nodular mass in the subcutaneous tissues. This entity, defined by a benign proliferation of fibroblasts and myofibroblasts, is subdivided into solitary and multicentric forms that may or may not have visceral involvement (Dishop and Kuruvilla 2008). The median age of presentation is 5 months for multicentric forms and 26 months for solitary forms (Levine et al. 2012). Myofibromas usually appear as a

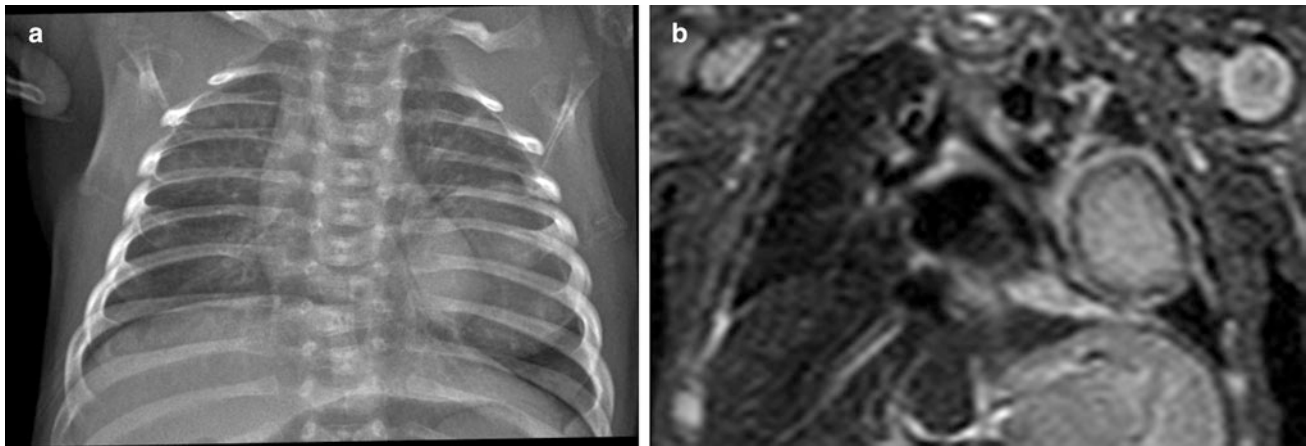


**Fig. 7** Infantile myofibromatosis. **a** Frontal chest radiograph of a 1-month old shows a large, well-circumscribed mass of the left lower lung zone. **b** STIR coronal MR image of the same patient confirms the

presence of a large left lung mass which exhibits central signal hyperintensity and a peripheral low signal intensity rim

mass with a thick-wall and a hypoechoic or anechoic center on ultrasound, and can demonstrate peripheral calcifications and adjacent bony erosion on CT. On MRI, they are usually hypointense on T1-weighted images and hyperintense with variable central hypointensity on T2-weighted images, and exhibit peripheral contrast enhancement (Koujok et al. 2005) (Fig. 7). Pulmonary masses may be a manifestation of multicentric visceral involvement and should not be misinterpreted as metastatic disease. Multicentric myofibromatosis with visceral involvement is associated with high morbidity and mortality despite chemotherapy and surgery, while the prognosis is excellent in other forms with surgery alone (Levine et al. 2012).

#### 4.7 Congenital Peribronchial Myofibroblastic Tumor

Congenital peribronchial myofibroblastic tumor (CPMT) is a very rare tumor that is thought to develop at approximately 12 weeks of gestational age and demonstrates variable degrees of smooth muscle and cartilaginous differentiation (Alobeid et al. 1997). The tumor is typically detected in the neonatal period, and antenatal presentation with fetal hydrops has been reported (Horikoshi et al. 2005). Although histologically benign, CPMT can exhibit certain aggressive features such as frequent mitoses, necrosis, and infiltrative growth, leading some cases to be reported as malignant entities such as bronchopulmonary fibrosarcoma (Kim et al. 2013). No syndromic, genetic, or maternal associations have been identified (Travis et al. 2004).

On imaging, CPMT typically appears as a large, single well-circumscribed pulmonary mass without lobar predilection. The tumors typically measure 5–7 cm in diameter

and occupy the majority of the involved hemithorax, exerting mass effect with mediastinal shift (Travis et al. 2004). Hydrops fetalis is reported in 36 % and polyhydramnios in 27 % of cases (Horikoshi et al. 2005). CPMT has a heterogeneously hyperechoic appearance on ultrasound and a heterogeneous appearance on CT without cysts or calcifications (Travis et al. 2004). The appearance on MRI has not been described.

Patients generally survive CPMT following complete surgical resection. However, some die in the prenatal or neonatal period as a result of hydrops fetalis or respiratory failure (Huppmann et al. 2011). No local recurrence or metastasis of CPMT has been reported.

#### 4.8 Inflammatory Myofibroblastic Tumor

Inflammatory myofibroblastic tumor (IMT) is a borderline or low-grade malignancy that can occur at a variety of sites, with the lungs being second only to the abdomen. Previously known as inflammatory pseudotumor or plasma cell granuloma, the current nomenclature emphasizes the dominant component of spindle cells, accompanied by variable numbers of inflammatory cells, particularly eosinophils, lymphocytes, and plasma cells (Yousem et al. 2004).

The important function of the myofibroblast in tissue repair is consistent with the hypothesis that an aberrant response to tissue injury underlies the pathogenesis of these lesions. A variety of unusual microorganisms have been implicated in individual case reports, including *Mycobacterium avium intra-cellulare*, *Corynebacterium equi*, *Coxiella burnetii*, and *Bacillus sphaericus* (Hedlund et al. 1999). More recently, viruses such as EBV and HHV-8 have also been implicated (Mergan et al. 2005).

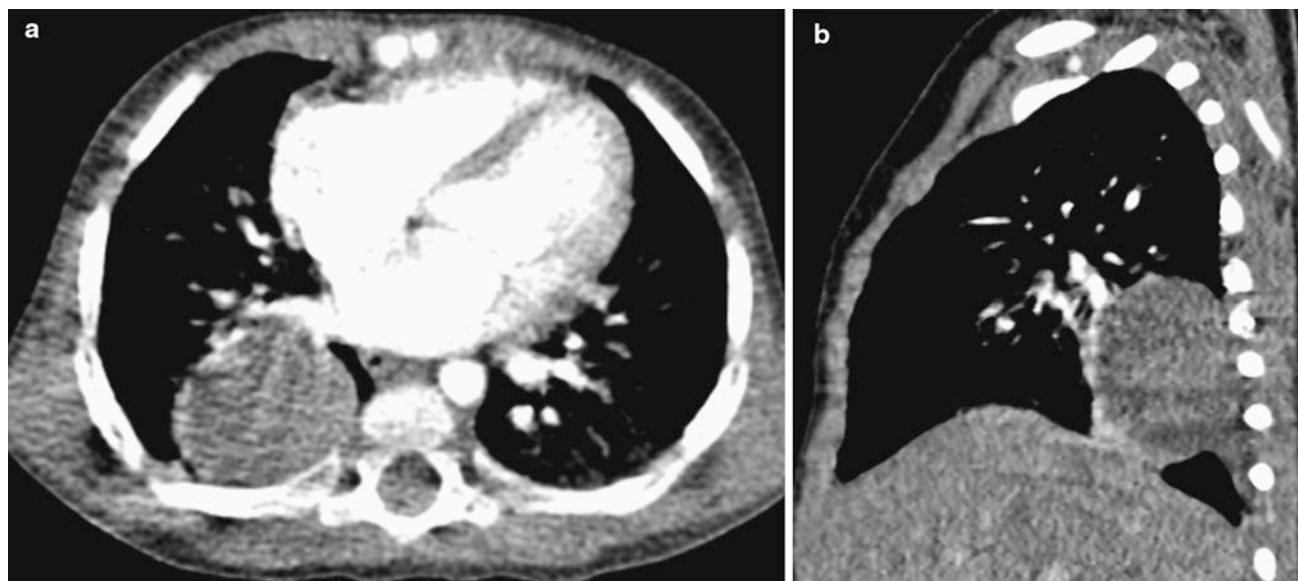


**Fig. 8** Inflammatory myofibroblastic tumor (IMT). **a** Axial contrast-enhanced chest CT image in a 13-month-old girl who had intermittent unexplained fever. A chest radiograph had shown a rounded right

lower lobe mass, confirmed to be solid on CT. **b** Sagittal contrast-enhanced CT image shows pleural extension of the mass posteroinferiorly, but no associated pleural effusion or chest wall invasion

IMT has been reported to account for 14 % of primary lung tumors, a similar proportion to tumors such as pleuropulmonary blastoma and bronchial carcinoid (Hancock et al. 1993). The mean age of presentation is 13 years. Although pulmonary IMT can be asymptomatic, it can also present with cough, chest pain, or a constellation of fever, weight loss, anemia, thrombocytosis, polyclonal hyperglobulinemia, and elevated inflammatory markers (Coffin et al. 2007). An association with hypertrophic pulmonary osteoarthropathy has been reported (Mas Estelles et al. 1995).

The typical imaging appearance of IMT is a well-circumscribed, solitary, upper lobe predominant pulmonary mass, with a mean size of 8.4 cm (Coffin et al. 2007; Siminovich et al. 2012). About 80–85 % is parenchymal, with the remainder being endobronchial (Hancock et al. 1993) (Fig. 8). IMTs typically are low in attenuation on noncontrast CT imaging with slight enhancement on early phase post-contrast imaging and heterogeneous enhancement on delayed phase post-contrast imaging, although single phase contrast-enhanced CT scanning should generally suffice for lesion evaluation (McHugh and Disini 2011). Calcification or cavitation is rarely seen. On MRI, IMTs typically demonstrate homogeneous slightly low signal intensity on T1-weighted images, variable hyperintensity on T2-weighted images, and heterogeneous contrast enhancement that is most pronounced in the delayed phase (Takayama et al. 2008). Hilar lymphadenopathy and pleural effusion are not commonly associated (Mas Estelles et al. 1995). Although bronchi and vessels may be trapped within the pulmonary masses and become narrowed distally or even obliterated,

atelectasis is observed in only 14 % of pediatric patients (Verbeke et al. 1999).

Locally aggressive IMTs are occasionally seen and may invade the mediastinum, chest wall, or diaphragm (Hedlund et al. 1999; Verbeke et al. 1999; Yousem et al. 2004). CT and MRI are both useful in characterizing the extent of these aggressive lesions in relation to the airways, esophagus, cardiovascular structures, and chest wall (Hedlund et al. 1999). Lesions arising solely in the esophagus have been described, and barium esophagography can be useful for characterizing esophageal involvement when suspected.

Over-expression of the ALK1 (anaplastic lymphoma kinase) gene is associated with an increased rate of local recurrence but not distant metastases, and an overall improved prognosis. Recurrent and metastatic IMTs tend to be larger (Coffin et al. 2007). Many IMTs act in a relatively indolent fashion, although about one-quarter recur. Pulmonary resection with removal of all gross evidence of disease is the mainstay of treatment and is usually curative for tumors confined to the lung. Locally aggressive lesions may require more radical surgery including pneumonectomy rather than the more usual segmental or lobar resection. When these tumors extend beyond the organ of origin at diagnosis, up to 46 % relapse locally (Janik et al. 2003). Relapse or invasion of the mediastinum has occasionally been treated with immunosuppressive therapy or even multiagent chemotherapy with good results (Verbeke et al. 1999; Janik et al. 2003). Metastases have been documented to the lung, liver, bone, and brain (Coffin et al. 2007; Siminovich et al. 2012).



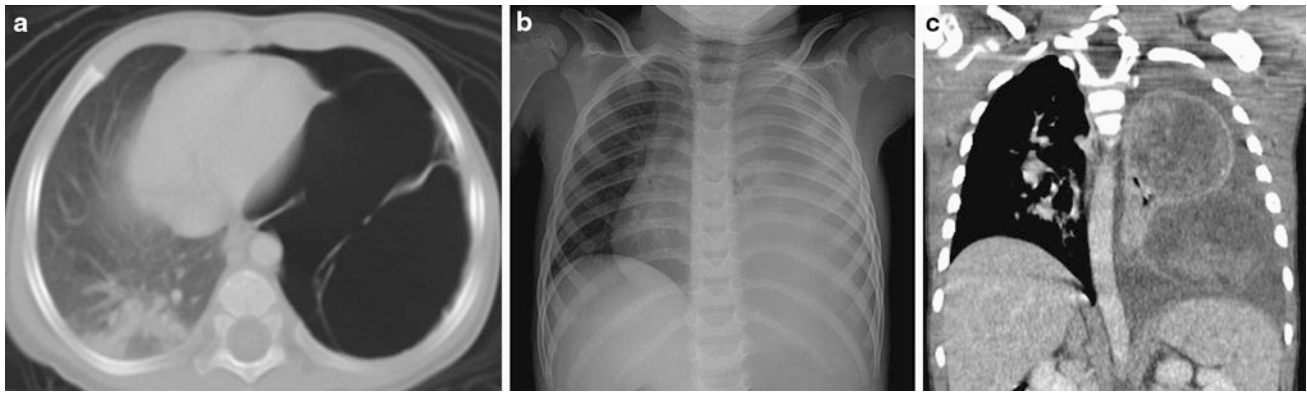


**Fig. 9** Pleuropulmonary blastoma (PPB). **a** Axial chest CT image from a 1-year old with a history of spontaneous pneumothorax demonstrates a large, thin-walled, septated, air-filled, cystic lesion of the left lung representing a Type I (cystic) PPB. **b** Frontal chest radiograph of a different patient at 3 years of age shows near complete

opacification of the left hemithorax with rightward mediastinal shift, findings evocative of complicated pneumonia with empyema. **c** Coronal contrast-enhanced chest CT image reveals a bilobed heterogeneously enhancing mass arising from the left lung representing a Type III (solid PPB), with an associated left pleural effusion

#### 4.9 Pleuropulmonary Blastoma

Although previous reports report a similar incidence to IMTs and bronchial carcinoids (Hancock et al. 1993), pleuropulmonary blastoma (PPB) is likely the most common primary lung malignancy of childhood (Priest et al. 1997). The mean age at presentation is 38 months, and it is rarely seen in children over 6 years of age. Prenatal presentation has also been reported (Miniati et al. 2006). Approximately 30–40 % of PPB patients or their relatives have manifestations of the PPB Family Tumor Dysplasia Syndrome (PPB-FTDS), an autosomal dominant genetic disorder with a distinctive predisposition to certain tumors and dysplasias, including PPB, cystic nephroma, multinodular goiter, Sertoli-Leydig cell tumor, cervical embryonal rhabdomyosarcoma, pituitary blastoma, pineoblastoma, nasal chondromesenchymal hamartoma, and ciliary body medulloepithelioma (Slade et al. 2010; Foulkes et al. 2011). Approximately 70–75 % of patients with PPB have germline mutations in the *DICER1* gene that encodes a protein involved in microRNA processing (Priest 2012).

PPB is composed of a malignant mesenchymal component resembling fetal lung in early gestation with a variably sarcomatous or blastematos appearance, but no malignant epithelial component. Rhabdomyosarcomatous areas in PPB are identical to embryonal rhabdomyosarcoma, and cases of PPB have been misdiagnosed as rhabdomyosarcomas arising in a congenital cystic adenomatoid malformation (CCAM) (Pai et al. 2007) or in normal lung (Schiavetti et al. 2009). Recognition of high grade blastemal elements, cartilage, spindle cell sarcoma, or diffuse-marked anaplasia facilitates the correct diagnosis of PPB in a pediatric lung mass. PPB is distinct from pulmonary blastoma, a biphasic sarcomatoid carcinoma predominantly occurring in adults (Dehner 1994).

Three subtypes of PPB are described based on gross morphology. Type I is a unilocular or multilocular cyst with delicate fibrous septa, Type II PPB is mixed cystic and solid and Type III PPB is entirely solid (Dehner et al. 1995; Priest et al. 2006). There is a significant difference in the age at presentation. The median age at diagnosis is 10 months for type I, 34 months for type II, and 44 months for type III (Priest et al. 2006). Progression of unresected Type I PPB to Type II and III PPB can occur. Type I PPB may also spontaneously regress, whereby it is classified as Type I-regressed PPB (Type Ir PPB). Types I and Ir PPB are indistinguishable on gross inspection from the large-cyst form of CCAM; however, CCAMs do not transform into PPBs (Priest et al. 2009).

The clinical presentation of PPB is varied and nonspecific, ranging from incidental detection to cough, chest pain, and respiratory distress. Type I and Ir PPBs appear as well-defined, air-filled cysts confined to the lung parenchyma or visceral pleura, and the presence of multifocal cysts or spontaneous pneumothorax favors type I PPB over large-cyst CCAM (Priest et al. 2009). Type II and III PPBs typically manifest as a large mass in the hemithorax, often in the lung periphery adjacent to the pleura, with associated mediastinal mass effect and pleural effusion (Priest et al. 2006) (Fig. 9). Invasion of the chest wall or diaphragm is occasionally observed. Local invasion of the bronchi, great vessels, and heart is rare (Goel et al. 2010; Priest et al. 2011). The solid components of the mass demonstrate contrast enhancement on CT and MRI. Some type II and III PPBs are sharply demarcated from adjacent lung parenchyma while others may be more infiltrative. Confident assignment of the site of origin is often difficult to determine with large lesions.

Initial misdiagnosis is common, with Type I PPBs mimicking large-cyst CCAMs, and type II and III PPBs

mimicking other tumors or complicated pneumonia with empyema. These tumors are so friable intraoperatively that empyema may still be suspected during surgery (Buyukavci et al. 2006). The diagnosis depends on histological evaluation that in most cases takes place after attempted or successful surgical resection. The malignant elements in Type I PPBs can be very subtle, requiring meticulous inspection of the pathology specimen to make the correct diagnosis.

Type I PPBs have a better prognosis than the other subtypes. Local recurrence is unusual in Type I PPB, occurring in fewer than 15 %, but develops in more than 45 % of Types II and III. Metastases occur in 11 % of Type II and 55 % of Type III cases (Priest 2012). Metastases have a particular tropism for the central nervous system including the spinal cord (Priest et al. 1997), so that craniospinal MRI is merited at staging and follow-up. The second most common site for metastatic spread is the skeletal system. Metastases to the liver, adrenals, and ovary are also reported (Priest 2012). The use of adjuvant chemotherapy in addition to surgery confers a survival advantage for all three subtypes (Priest et al. 2006). Overall survival is 90 % for Type I and 40–60 % for Types II and III (Priest 2012). Extrapulmonary involvement and incomplete resection confer a worse prognosis (Indolfi et al. 2007).

#### 4.10 Bronchial Carcinoid Tumor

Bronchial carcinoid tumors arise from neuroendocrine Kulchitsky cells in the airways. Although bronchial carcinoid is the most common malignant endobronchial tumor and the second most common primary pediatric malignancy of the lower respiratory tract (Dishop and Kuruvilla 2008), it is still uncommon in children relative to adults. When it occurs in children, it tends to present in adolescents (Al-Qahtani et al. 2003). The actual carcinoid syndrome is very rare in childhood outside the setting of metastatic disease (Hancock et al. 1993). Cushing syndrome from ectopic adrenocorticotrophic hormone secretion has also been described but is similarly uncommon (Wang et al. 1993). Children with bronchial carcinoids are much more likely than their adult counterparts to present with post-obstructive wheezing and atelectasis, in addition to hemoptysis and pneumonitis (Wang et al. 1993). A carcinoid in an asymptomatic patient is more likely to involve a peripheral airway than a central airway (Curtis et al. 1998). Bronchial carcinoids usually have intraluminal, mural, and extrabronchial components. Up to 4 % of carcinoid tumors are associated with other endocrine neoplasias, the most common association being with pituitary tumors (Al-Qahtani et al. 2003).

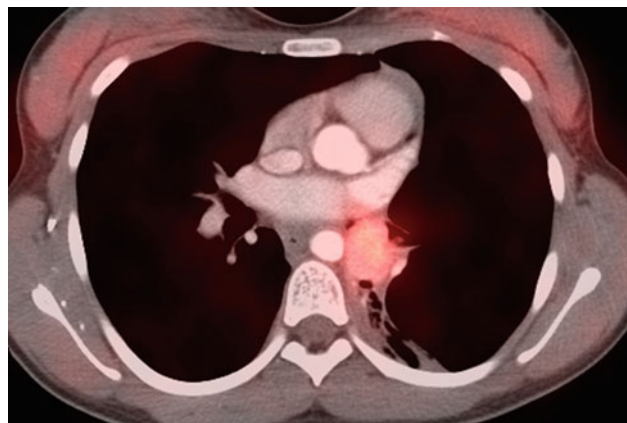


**Fig. 10** Bronchial carcinoid tumor. A fused axial chest image from an In-111 octreotide SPECT-CT scan in a 12-year old shows avid radiopharmaceutical uptake by a hyper-enhancing soft-tissue mass along the distal left mainstem bronchus

The majority of carcinoid tumors are not visible on CXR and their true extent may be difficult to determine even on high-resolution CT. The typical CT appearance is of a single round or lobulated mass that is at least partially endobronchial (Jeung et al. 2002). They are hypervascular polypoid tumors and characteristically show prominent contrast enhancement. Occasionally, the mass external to the bronchus is larger than that in the lumen, and the extrabronchial component may consequently be visible as a hilar mass. The mass resides along the main, lobar, or segmental bronchi in 80 % of cases, with a predilection for branching sites. The mass involves the more peripheral airways in the other 20 % of cases (Chong et al. 2006). Approximately one quarter of carcinoid tumors in adult patients are calcified, but the frequency of calcification is much less in childhood. Bronchial carcinoids typically demonstrate hyperintensity on T2-weighted images and avid homogeneous contrast enhancement on MRI. Bronchial carcinoids show increased octreotide uptake on somatostatin receptor scintigraphy in greater than 85 % of cases (Jeung et al. 2002) (Fig. 10). Although not yet widely available, the novel PET tracers 68-Ga-DOTATOC and 18F-DOPA in combination with integrated CT offer higher spatial resolution than conventional somatostatin scintigraphy and improved sensitivity for the detection of carcinoid tumor (Koopmans et al. 2008; Buchmann et al. 2007). The incidence of metastases with bronchial carcinoids in children is 10–15 % (Wang et al. 1993). Metastases are most commonly seen in the liver, adrenals, brain, and bone. Pediatric bronchial carcinoids generally have an excellent prognosis with complete resection and lymph node excision. Recurrence has been reported in as many as 20 % of cases but usually can be successfully treated surgically (Rizzardi et al. 2009).

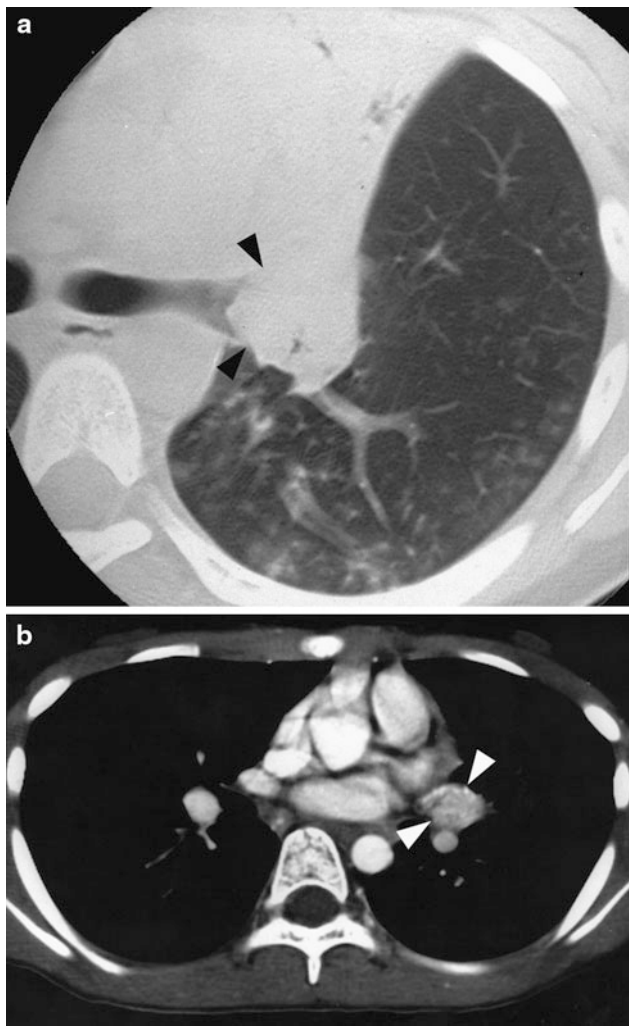


**Fig. 11** Mucoepidermoid carcinoma. **a** Axial chest CT image showing an endobronchial mass (arrowheads) nearly occluding the left mainstem bronchus close to the origin of the upper lobe bronchus with associated upper lobe collapse. **b** Axial contrast-enhanced chest CT image from a different patient demonstrating an enhancing, hypervascular mass (arrowheads) at the origin of the lingular bronchus (Courtesy of Dr. H. Hara, Tokyo)

#### 4.11 Mucoepidermoid Carcinoma

Mucoepidermoid carcinoma, the second most common pediatric endobronchial malignancy (Al-Qahtani et al. 2003), is thought to originate from the minor salivary glands lining the airways. Mucoepidermoid carcinoma is graded by histology similar to other salivary-type neoplasms into low, intermediate, and high grades. Pediatric mucoepidermoid carcinomas are generally low grade, low stage lesions (Andronikou and Kader 2001).

As with other endobronchial lesions, the history is usually that of respiratory infections or lobar collapse with or without air trapping. Up to 25 % of patients are asymptomatic

(Al-Qahtani et al. 2003). The typical imaging appearance is of a single round, lobulated, or polypoid mass in a lobar bronchus (Kim et al. 1999). Calcification is seen in 50 % of tumors. Contrast enhancement may be marked, suggesting hypervascularity (Fig. 11). Although endoscopy remains the diagnostic procedure of choice for endobronchial lesions, their “tip-of-the-iceberg” endobronchial nature makes endoscopic resection inadvisable. Grades are indistinguishable by imaging. Lymphadenopathy and distal metastasis are unusual, being seen in less than 10 % of cases (Wu et al. 2011). Thoracotomy, with lymph node sampling, is the recommended treatment to ensure histologically negative margins (Morini et al. 2003). For low-grade tumors without lymph node metastases, complete resection should result in a good outcome (Xi et al. 2012).

#### 4.12 NUT Midline Carcinoma

NUT midline carcinoma is a poorly differentiated aggressive carcinoma associated with characteristic rearrangement of the nuclear protein in testes (NUT) promoter gene. The largest published series of NUT midline carcinomas to date consisted of 22 cases (French 2010). No clear gender predilection is evident, and the mean age of diagnosis is 25 years. The presenting symptoms vary depending on the primary site of tumor or the presence of metastases.

NUT carcinomas arise in the mediastinum, upper aerodigestive tract, neck, or head in the majority of cases (French 2010). Other reported primary sites include the salivary glands, liver, bladder, pelvic skeleton, and extremity soft tissues (French et al. 2004; den Bakker et al. 2009). Pulmonary cases may originate from basal cells of the bronchiolar epithelium (Tanaka et al. 2012). A midline location is noted in 70 % of cases (Polsani et al. 2012). Apart from the midline location, imaging features are nonspecific. A heterogeneous low attenuation mass with central areas of necrosis has been reported on CT with occasional small central calcifications. On MRI, the mass exhibits decreased signal intensity on T1-weighted images, mildly increased signal intensity on T2-weighted images, and heterogeneous contrast enhancement. Both the primary tumor and metastases are FDG-avid on PET (Rosenbaum et al. 2012). The lungs are the most common site of metastases and metastases to the liver, kidney, brain, spinal cord, and subcutaneous soft tissues have also been reported (Polsani et al. 2012).

Intrathoracic NUT carcinomas have a poor prognosis. Widespread metastases are typically present at diagnosis, and intrathoracic growth produces superior vena cava compression. A mean survival of 9.5 months is reported (French 2010).



### 4.13 Papillomas and Squamous Cell Carcinoma

Papillomas are the most common benign tumor of the lower respiratory tract in children (Dishop and Kuruvilla 2008). Recurrent respiratory papillomatosis (RRP) is primarily caused by vertical transmission of human papillomavirus (HPV), most frequently HPV types 6 and 11 (Cook et al. 2000). Childhood RRP has a bimodal peak of 2 and 10 years of age and no sex predilection has been established (Rabah et al. 2001). Although usually isolated to the larynx, papillomas develop in the lower airways in up to 8 % of RRP cases, with lung parenchymal nodules occurring in approximately 1 % of cases (Soldatski et al. 2005). The occurrence of lower airway and pulmonary lesions may be exacerbated by treatment of the primary laryngeal lesions, including tracheostomy for tracheal stenosis and recurrent intubation. It is hypothesized that detached fragments are carried down the airways during inspiration and can enlarge if not expelled by mucociliary clearance (Kramer et al. 1985).

Airway papillomas may be localized or extensive. Conglomerate lesions typically manifest as endotracheal or endobronchial masses. Papillomas have a classic fimbriated or “salmon egg” appearance on endoscopy. They are predominantly endoluminal, although submucosal infiltration does occur with more extensive papillomas. Pulmonary parenchymal lesions typically have a nodular appearance and may be widely scattered remote from the major bronchi. The nodules may be thin or thick walled and may cavitate (Fig. 12). Air-fluid levels can be seen with superimposed hemorrhage or infection. Some lesions occasionally resemble dilated bronchi or bronchiectasis but close inspection shows no direct communication to more central bronchi (Williams et al. 1994). An intraluminal airway mass with concomitant pulmonary nodules or cavities is highly suggestive of laryngotracheal papillomatosis.

Children with RRP may present with cough and fever due to atelectasis, consolidation, and bronchiectasis related to airways obstruction and recurrent superinfection (Williams et al. 1994). RRP associated with HPV 11 has a more aggressive course and worse prognosis than RRP associated with HPV 6 (Rabah et al. 2001). Severe lung damage from multiple destructive parenchymal lesions may result in symptoms of restrictive lung disease in addition to upper airway obstruction. Malignant transformation into squamous cell carcinoma is another potential complication of RRP (Katz et al. 2005), and is associated with HPV 11 (Cook et al. 2000). Benign papillomas can demonstrate increased FDG uptake on PET and be confused with malignancy (Pipavath et al. 2008). Interval lesion growth,

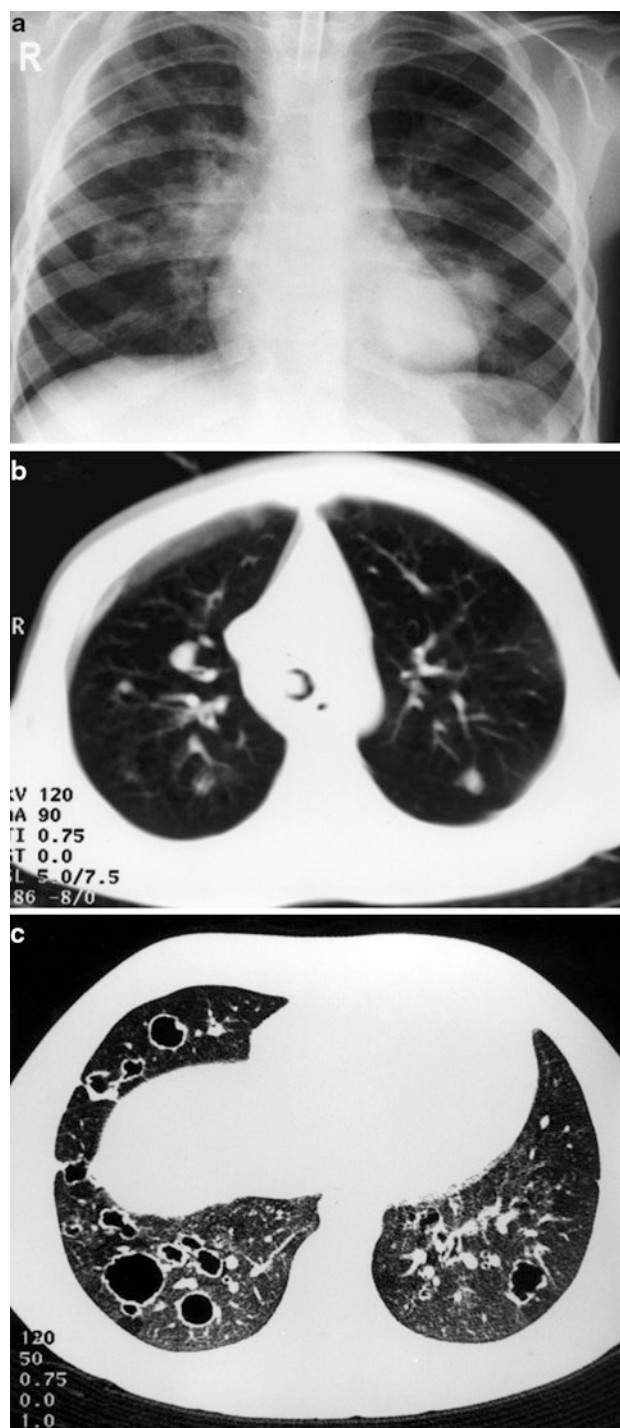


**Fig. 12** Recurrent respiratory papillomatosis (RRP) with lung involvement. **a** Frontal upright chest radiograph showing two cavitary lung nodules, with an air-fluid level in the larger, left-sided lesion. **b** Axial chest CT image demonstrating an endotracheal mass and bilateral pulmonary nodules. **c** Numerous bilateral cavitary pulmonary nodules of varying sizes, many with thick, irregular walls

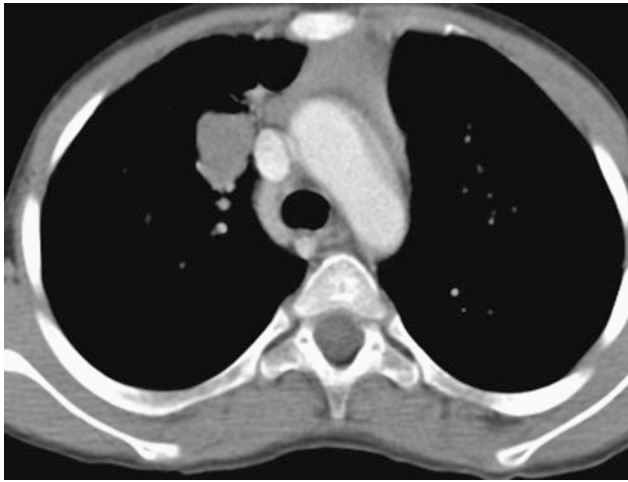


**Fig. 13** Leiomyoma. Axial contrast-enhanced chest CT image from an HIV + 11-year old shows a lobular solid mass of the medial right upper lobe

increasing lesion wall thickening, thoracic lymphadenopathy, and the presence of metastases are findings that suggest malignant transformation.

#### 4.14 Leiomyoma and Leiomyosarcoma

Leiomyoma and leiomyosarcoma of the pediatric lower respiratory tract are very rare and reside along a spectrum of benign to malignant tumors of smooth muscle origin. There is an association between smooth muscle tumors, immunosuppression related to solid organ transplantation or human immunodeficiency virus (HIV) infection (Chadwick et al. 1990), and Epstein–Barr virus (EBV) expression within the tumor cells (McClain et al. 1995). Clonality studies indicate that multifocality of these lesions is often caused by infection of multiple cells rather than metastasis (Parham et al. 2012).

Patients with smooth muscle tumors of the lower respiratory tract usually present with nonspecific respiratory signs and symptoms (Lal et al. 2005). Since most affected patients are immunosuppressed, infection is often the initial concern, leading to a delay in diagnosis (McClain et al. 1995). Although the majority of smooth muscle tumors of the respiratory tract are found in the lung parenchyma and less than one-third of cases manifest as endobronchial lesions, they are thought to arise from smooth muscle of the bronchi or bronchioles. They typically present as single or multiple well-defined solid pulmonary masses (Balsam and Segal 1992) (Fig. 13). The tumor behavior is usually indolent, and treatment consists of some combination of surgery, chemotherapy, and reduction of immunosuppression (Parham et al. 2012).

## 5 Extrathymic Mediastinal Tumors

Lymphoma, leukemia, and primary neoplasms of the thymus are covered in the chapter entitled *Imaging Evaluation of the Thymus and Thymic disorders in Children* by Sams and Voss in this book. Hemangiomas, vascular malformations, and neurofibromas are addressed in the chapter entitled *Radiology of the Chest Wall* by Eich, Kellenberger, and Willi.

### 5.1 Germ Cell Tumors

Primary germ cell tumors (GCT) account for up to 10 % of all mediastinal masses in children and are second only to lymphoma as a cause of an anterior mediastinal mass. (Dulmet et al. 1993). Only 2–3 % of mediastinal GCTs occur in the posterior mediastinum. An intrapulmonary location is exceedingly rare. There is an association among nonseminomatous mediastinal germ cell tumors, hematological malignancies, and Klinefelter syndrome (XXY) (Strollo et al. 1997).

Up to 50 % of affected patients have no symptoms at the time of diagnosis (Sasaka et al. 1998). Large tumors may cause tracheal compression, superior vena cava obstruction, or fetal hydrops. Occasionally, ectopic production of sex hormones or insulin leads to presentation with pseudoprecocious puberty or hypoglycemia before the onset of respiratory symptoms. GCTs, which include teratomas, teratocarcinomas, seminomas, dysgerminomas, embryonal cell carcinomas, endodermal sinus tumors, and choriocarcinomas, usually do not present before the second decade of life, but can be detected by prenatal ultrasound. GCTs are malignant in about 10 % of cases. Malignant GCTs have a male predilection and are frequently associated with elevated serum levels of human chorionic gonadotropin or alpha-fetoprotein. Teratomas account for the vast majority of mediastinal GCTs in children and have varied amounts of mature and immature somatic tissues. Mature teratomas are benign lesions composed of well-differentiated ectodermal, mesodermal, and endodermal derivatives, and are curable by surgical resection. Immature teratomas are potentially malignant but in patients less than 15 years of age have biological and clinical behavior similar to mature teratomas (Dulmet et al. 1993). The prognosis for other malignant mediastinal GCTs in childhood is poor (Yalcin et al. 2012).

CT attenuation values and MR signal intensity for these tumors are highly variable depending on the amount of fat, calcium, fluid, or soft tissue in the mass. Most teratomas have well-defined margins, thick walls, and some fatty tissue and/or calcification (Alper et al. 2005) (Fig. 14). Fatty tissue plus calcification in an anterior mediastinal mass almost invariably indicate a germ cell origin. Seminomas

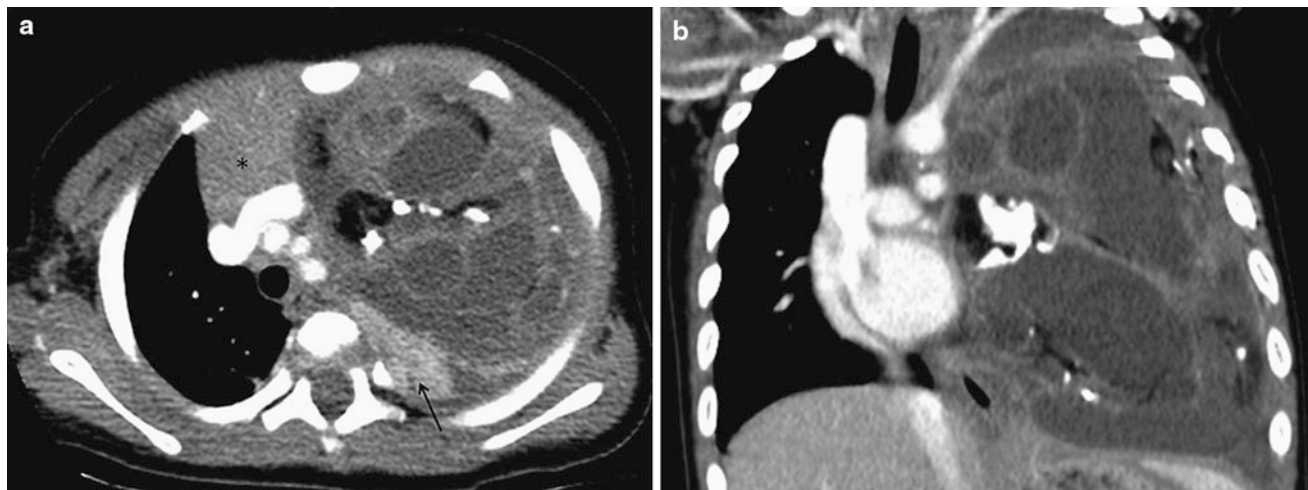


**Fig. 14** Teratoma. **a** Axial contrast-enhanced chest CT image in a 15-month-old girl, who presented with cough and respiratory distress, shows a mixed cystic and solid mass that contains calcific and fatty elements. The mass appears to be separate from the displaced thymus (asterisk), and left lower lobe compressive atelectasis (arrow) is also

evident. **b** A coronal contrast-enhanced chest CT image shows mediastinal displacement by the mass and close proximity of the mass to the heart, but no pericardial effusion. There is no tracheal compression despite the tracheal displacement

typically have more homogeneous, soft-tissue attenuation. Features suggesting malignancy include large size, ill-defined margins, and extensive central necrosis, but there is wide variation in the appearance of these tumors (Strollo et al. 1997).

Teratomas may rupture into adjacent structures such as the pleural space, pericardium, airways, or pulmonary air spaces. Up to one-third of mature benign mediastinal teratomas are reported to rupture, with malignant lesions having a lesser tendency to leak their contents (Sasaka et al. 1998). Severe symptoms such as chest pain or hemoptysis are more commonly found in ruptured than in unruptured tumors (Choi et al. 1998). Proteolytic or digestive enzymes and sebaceous materials within these teratomas are thought to play a role in their tendency to rupture and incite adjacent inflammation. High amylase levels have been found in pleural effusions and in the tumor contents (Sasaka et al. 1998). Ruptured tumors tend to display more heterogeneity in their internal components than unruptured teratomas. Ancillary findings in ruptured tumors depend on the space into which the rupture occurs. Rupture into an airway or lung may cause a chemical pneumonitis or fat-containing masses in the adjacent lung parenchyma. Hemoptysis with expectoration of hair or sebaceous material indicates a fistula between the tumor and the airway (Sasaka et al. 1998; Alper et al. 2005). Rupture into the pleura or pericardium results in pleural or pericardial effusions (Choi et al. 1998). Rupture is important to recognize as inflammation and adhesions secondary to extravasation of tumor contents may result in more hazardous and extensive surgery than had been anticipated.

## 5.2 Neuroblastic Tumors

The majority of posterior mediastinal masses in children are neurogenic tumors arising from the paravertebral sympathetic chain. The major childhood neurogenic tumors are neurofibromas, neuroblastoma, ganglioneuroblastoma, and ganglioneuroma. Neuroblastoma and ganglioneuroblastoma occur in the first decade of life whereas the benign ganglioneuroma, in which all cells are mature, is typically seen in older children and adolescents.

Thoracic neuroblastoma accounts for 15 % of all cases of neuroblastoma and typically has a better outcome than primary abdominal neuroblastoma. In one series of 96 children with thoracic neuroblastoma, the median age at presentation was at 0.9 years, only 20 % had metastatic disease, and actuarial survival was 88 % at 4 years (Adams et al. 1993). In this series, a posterior mediastinal mass was diagnosed incidentally on chest radiographs performed for non-tumor-related symptoms in half the cases.

In most instances, the diagnosis of a neuroblastic tumor is suggested by CXR findings, particularly when posterior rib erosion is seen indicating a posterior mediastinal mass. On CT, most thoracic neuroblastic tumors are well-circumscribed, fusiform masses oriented in a paraspinal location. Approximately 40 % contain some calcification. Only about 2 % of primary thoracic neuroblastomas will have pulmonary metastases visible at diagnosis (DuBois et al. 2008). MRI demonstrates hypointensity on T1-weighted images and variable intermediate or high signal intensity on T2-weighted images, with signal voids corresponding to calcifications or



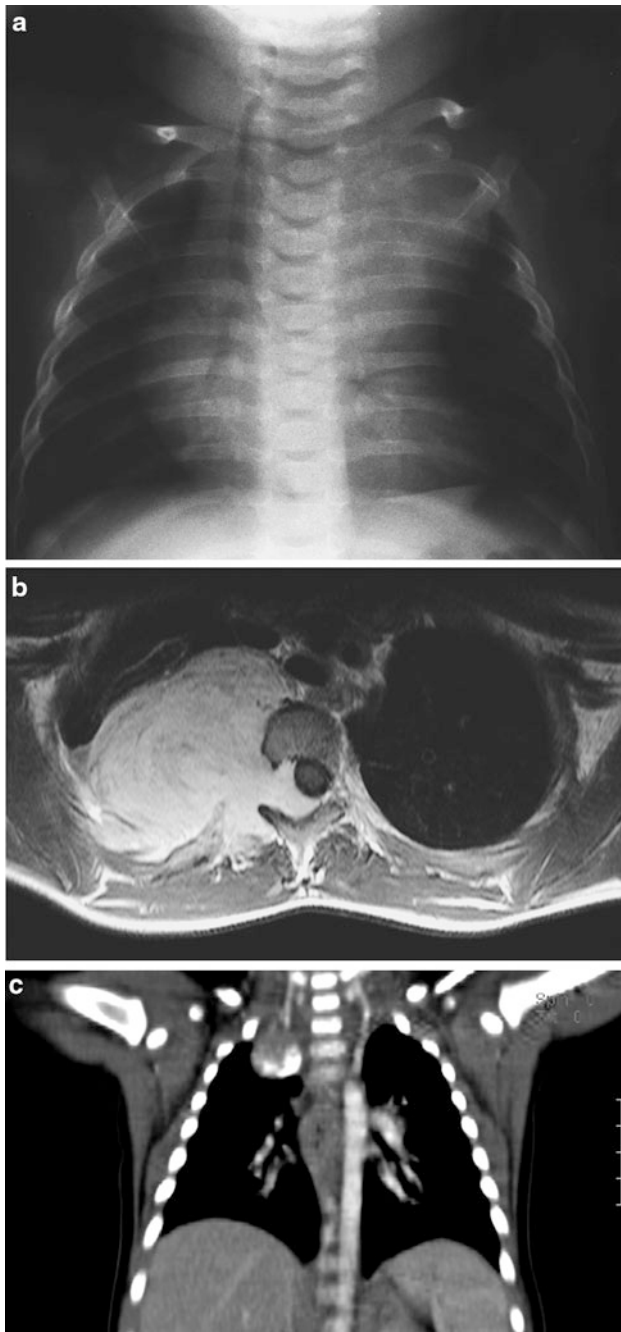


**Fig. 15** Neuroblastoma. **a** Frontal chest radiograph of an infant showing an opacity in the left upper hemithorax and posterior rib erosion indicative of a posterior mediastinal mass. **b** Axial contrast-enhanced T1-weighted chest MR image from a different patient demonstrates a large right-sided mass lesion with intraspinal and posterior chest wall invasion. **c** A coronal contrast-enhanced chest CT image from a different 6-month-old patient shows a calcified mass of the right apical hemithorax

encased vessels (Fig. 15). Non-necrotic portions of neuroblastic tumors demonstrate avid contrast enhancement (Daldrup et al. 1997).

The International Neuroblastoma Risk Group (INRG) Project has proposed the new INRG Staging System

(INRGSS) that shifts the focus from surgicopathologic to imaging findings for neuroblastic tumors. The INRGSS system includes two stages of localized disease that are dependent on whether or not image-defined risk factors (IDRFs) are present at the time of diagnosis (Brisse et al. 2011). Stage L1 tumors are localized tumors that do not involve vital structures, as defined according to the IDRFs, and stage L2 tumors are local–regional tumors with one or more IDRFs. IDRFs in the chest relate to vascular encasement, airway compression, or neural encroachment (Table 2).

There is no current consensus regarding the optimal imaging modality for assessment of local–regional disease in neuroblastic tumors. Although MRI has long been recognized as an effective method for imaging neuroblastoma and provides excellent visualization of the intraspinal contents, superiority of MRI over CT for local–regional staging has not been demonstrated (Siegel et al. 2002). Metaiodobenzylguanidine (MIBG) scintigraphy should be routinely performed to identify metastatic disease, ideally with single photon emission computed tomography (SPECT) or SPECT-CT to allow better identification and localization of small foci of uptake that are difficult to see on planar MIBG scans (Brisse et al. 2011). The role of whole-body MRI and PET in neuroblastic tumors is not yet clearly established.

In the absence of metastatic disease, ganglioneuroma in older children is indistinguishable from neuroblastoma on imaging. When histological assessment is unclear, biopsy is not feasible or the diagnosis is uncertain, MIBG scanning should be considered. MIBG will demonstrate primary tumor uptake in over half of such cases, confirm the presence of a neural crest tumor, and simultaneously screen for metastases.

### 5.3 Lymphangiomatosis

Lymphangiomatosis is a rare disease characterized by is proliferation of complex anastomosing lymphatic channels with secondary lymphatic dilation. The disease is believed to be congenital and the majority of cases are diagnosed in childhood. It may present with single organ or multiorgan involvement, and most frequently involves the thorax (Wunderbaldinger et al. 2000).

Clinical presentation depends on the sites and extent of disease involvement, and may include dyspnea, wheezing, chest pain, or neck swelling. Initial misdiagnosis as asthma or other respiratory diseases is common (Satria et al. 2011). Diffuse, bilateral symmetric interlobular and peribronchovascular thickening, which may be smooth or nodular, is seen on CT, often with an upper lobe predominance (Swenson et al. 1995). CT also reveals edematous mediastinal soft tissues, a very distinctive finding (Fig. 16). MRI shows hyperintense signal on T2-weighted images and heterogeneous

**Table 2** Description of IDRFs applicable to thoracic neuroblastic tumors

Anatomic Region	Description of IDRFs
Multiple body compartments	Ipsilateral tumor extension within two adjacent body compartments (e.g. neck and chest, chest and abdomen)
Cervicothoracic junction	Tumor encasing brachial plexus roots Tumor encasing subclavian vessels, vertebral artery, and/or carotid artery Tumor compressing trachea
Thorax	Tumor encasing aorta and/or major branches Tumor compressing trachea and/or principal bronchi Lower mediastinal tumor infiltrating costovertebral junction between T9 and T12 vertebral levels
Thoracoabdominal junction	Tumor encasing aorta and/or vena cava
Intraspinal tumor extension	Intraspinal tumor extension provided that more than one-third of spinal canal in axial plane is invaded, the perimedullary leptomeningeal spaces are not visible, or the spinal cord signal intensity is abnormal
Infiltration of adjacent organs and structures	Pericardium, diaphragm

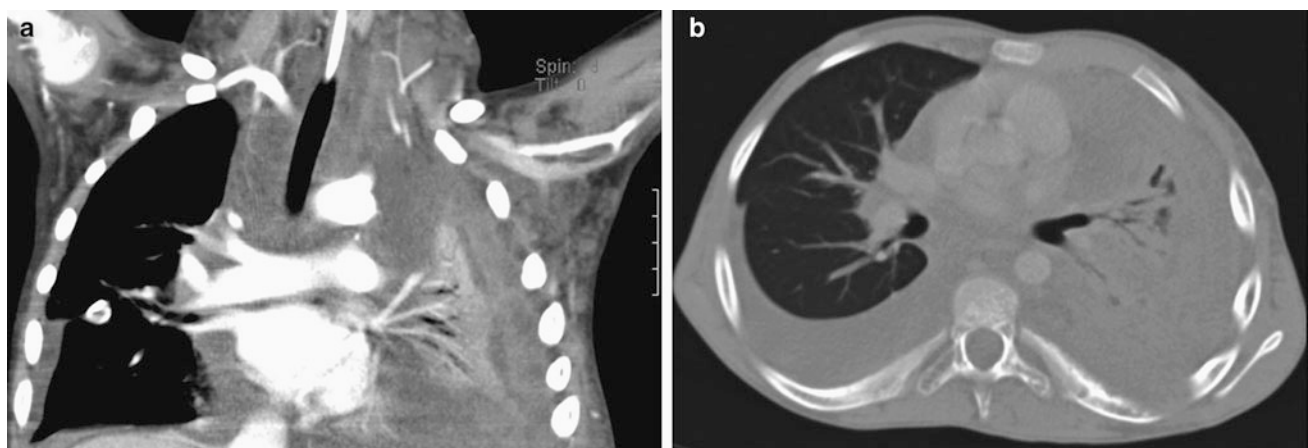


**Fig. 16** Lymphangiomatosis. **a** Coronal contrast-enhanced chest CT image shows a collapsed left lung enveloped by edematous tissue along the pleura that extends into the left axilla and mediastinum.

**b** Axial chest CT image in bone windows from the same patient reveals ill-defined lucencies in a thoracic vertebra and a posterior left rib

enhancement of abnormal soft tissue in the mediastinal and paraspinal regions without extension into the neural foramina or spinal canal (Shah et al. 2011). Pleural or pericardial infiltration is frequently present and chylous effusions are common (Aviv and McHugh 2000). Common extrathoracic findings include osteolytic bone lesions, enlargement of the spleen, and cystic splenic lesions.

The clinical course and prognosis are variable. Some cases show inexorable progression, while others spontaneously arrest. Although lymphangiomatosis is histologically benign, patients with chylothorax associated with osteolytic lesions have a notably poor prognosis. Attempts at surgical excision are rarely curative due to the infiltrative nature of the disease, and may exacerbate chylous leakage. Sclerotherapy, drainage procedures, and medical therapy with

vincristine, sirolimus, interferon  $\alpha$ -2b, or propranolol are palliative or temporizing measures. Intractable effusions, infection, and cardiorespiratory failure frequently supervene (Satria et al. 2011).

A novel subtype, Kaposiform lymphangiomatosis, has recently been described, and is characterized by spindled endothelial cells accompanying the malformed lymphatic channels, along with a propensity for hemorrhage and hematologic abnormalities similar to the Kasabach-Merritt phenomenon seen with Kaposiform hemangioendothelioma. As with classic lymphangiomatosis, the mediastinum, lungs, pleura, bones, and spleen are most commonly involved. The overall survival is reported at 34 % with mean interval of 2.75 years between diagnosis and death (Croteau et al. 2013).

## 5.4 Esophageal Leiomyomatosis

Although quite rare, leiomyomas are the most common benign tumor of the esophagus. Esophageal leiomyomas are more likely to be multiple or diffuse in children than in adults, and pediatric esophageal leiomyomatosis is associated with Alport syndrome. The involved esophagus demonstrates marked circumferential wall thickening that leads to dysphagia. In severe cases, mass effect on the adjacent airway can produce respiratory symptoms (Guest et al. 2000).

## 6 Conclusion

Non-neoplastic masses and pulmonary metastases from extracranial solid tumors are far more common than primary pulmonary neoplasms in childhood. Although rare, primary pulmonary neoplasms are often malignant and can cause considerable morbidity and mortality from mass effect, tissue invasion, and metastatic disease. Mesenchymal neoplasms are more common than epithelial neoplasms in the pediatric lung, unlike in adults, and some of these neoplasms are associated with predisposing genetic syndromes or certain infections. While lymphoma is the most common mediastinal malignancy, germ cell, neuroblastic, and other mediastinal tumors also manifest with distinctive features that are important to recognize for appropriate management. Many of these tumors are detectable on chest radiography, but chest CT remains the primary imaging modality used to formulate a differential diagnosis for these tumors, define anatomy for preoperative planning, assess tumor response to therapy, and survey for recurrent disease, with MRI and nuclear medicine studies playing a complementary role.

## References

- Adams GA, Shochat SJ, Smith EI, Shuster JJ, Joshi VV, Altshuler G, Hayes FA, Nitschke R, McWilliams N, Castleberry RP (1993) Thoracic neuroblastoma: a Pediatric Oncology Group study. *J Pediatr Surg* 28:372–377
- Alobeid B, Beneck D, Sreekantaiah C, Abbi RK, Slim MS (1997) Congenital pulmonary myofibroblastic tumor: a case report with cytogenetic analysis and review of the literature. *Am J Surg Pathol* 21:610–614
- Alper F, Kaynar H, Kantarci M, Onbas O, Polat P, Erdogan F, Akgun M, Okur A (2005) Trichoptysis caused by intrapulmonary teratoma: computed tomography and magnetic resonance imaging findings. *Australas Radiol* 49:53–56
- Al-Qahtani AR, Di Lorenzo M, Yazbeck S (2003) Endobronchial tumors in children: institutional experience and literature review. *J Pediatr Surg* 38:733–736
- Andronikou S, Kader E (2001) Bronchial mucoepidermoid tumour in a child with organomegaly due to secondary amyloidosis: case report and review of the literature. *Pediatr Radiol* 31:348–350
- Aviv R, McHugh K (2000) Mechanisms of chylous effusions in lymphangiomatosis. *AJR Am J Roentgenol* 175:1191
- Balsam D, Segal S (1992) Two smooth muscle tumors in the airway of an HIV-infected child. *Pediatr Radiol* 22:552–553
- Bastos MD, Lee EY, Strauss KJ, Zurakowski D, Tracy DA, Boiselle PM (2009) Motion artifact on high-resolution CT images of pediatric patients: comparison of volumetric and axial CT methods. *AJR Am J Roentgenol* 193:1414–1418
- Brader P, Abramson SJ, Price AP, Ishill NM, Zabor EC, Moskowitz CS, LaQuaglia MP, Ginsberg MS (2011) Do characteristics of pulmonary nodules on computed tomography in children with known osteosarcoma help distinguish whether the nodules are malignant or benign? *J Pediatr Surg* 46:729–735
- Brady SL, Moore BM, Yee BS, Kaufman RA (2014) Pediatric CT: implementation of ASIR for substantial radiation dose reduction while maintaining pre-ASIR image noise. *Radiology* 270:223–231
- Brisse HJ, McCarville BM, Granata C, Krug KB, Wootton-Gorges SL, Kanegawa K, Giammarile F, Schmidt M, Shulkin BL, Matthay KK, Lewington VJ, Sarnacki S, Hero B, Kaneko M, London WB, Pearson AD, Cohn SL, Monclair T (2011) Guidelines for imaging and staging of neuroblastic tumors: consensus report from the International Neuroblastoma Risk Group Project. *Radiology* 261:243–257
- Buchmann I, Henze M, Engelbrecht S, Eisenbut M, Runz A, Schafer M, Schilling T, Haufe S, Herrman T, Haberkorn U (2007) Comparison of 68 Ga-DOTATOC PET and In111-DTPAOC (Octreoscan) SPECT in patients with neuroendocrine tumours. *Eur J Nucl Med Mol Imaging* 34:1617–1626
- Buyukavci M, Atlas S, Salman B, Eren S (2006) An aggressive childhood tumor mimicking pleural empyema: pleuropulmonary blastoma. *J Pediatr Hematol Oncol* 28:257–259
- Chadwick EG, Connor EJ, Hanson IC, Joshi VV, Abu-Farsakh H, Yogev R, McSherry G, McClain K, Murphy SB (1990) Tumors of smooth muscle origin in HIV-infected children. *JAMA* 263:3182–3184
- Chong S, Lee KS, Chung MJ, Han J, Kwon OJ, Kim TS (2006) Neuroendocrine tumors of the lung: clinical, pathologic, and imaging findings. *Radiographics* 26:41–57
- Choi S-J, Lee JS, Song KS, Lim T-H (1998) Mediastinal teratoma: CT differentiation of ruptured and unruptured tumors. *AJR Am J Roentgenol* 171:591–594
- Cistaro A, Lopci E, Gastaldo L, Fania P, Del Prever AB, Fagioli F (2012) The role of 18F-FDG PET/CT in the metabolic characterization of lung nodules in pediatric patients with bone sarcoma. *Pediatr Blood Cancer* 59:1206–1210
- Coakley FV, Cohen MD, Johnson MS, Gonin R, Hanna MP (1998) Maximum intensity projection images in the detection of simulated pulmonary nodules by spiral CT. *Br J Radiol* 71:135–140
- Coffin CM, Hornick JL, Fletcher CD (2007) Inflammatory myofibroblastic tumor: comparison of clinicopathologic, histologic, and immunohistochemical features including ALK expression in atypical and aggressive cases. *Am J Surg Pathol* 31:509–520
- Cohen MC, Kaschula RO (1992) Primary pulmonary tumors in childhood: a review of 31 years' experience and the literature. *Pediatr Pulmonol* 14:222–232
- Connolly BL, Chait PG, Duncan DS, Taylor G (1999) CT guided percutaneous needle biopsy of small lung nodules in children. *Pediatr Radiol* 29:342–346
- Cook JR, Hill DA, Humphrey PA, Pfeifer JD, El-Mofty SK (2000) Squamous cell carcinoma arising in recurrent respiratory papillomatosis with pulmonary involvement: emerging common pattern of clinical features and human papillomavirus serotype association. *Mod Pathol* 13:914–918
- Cowie F, Corbett R, Pinkerton CR (1997) Lung involvement in neuroblastoma: incidence and characteristics. *Med Pediatr Oncol* 28:429–432



- Croteau SE, Kozakewich HPW, Perez-Atayde AR, Fishman SJ, Alomari AI, Chaudry G, Mulliken JB, Trenor CC (2013) Kaposiform lymphangiomatosis: a distinct aggressive lymphatic anomaly. *J Pediatr*. doi: [10.1016/j.jpeds.2013.10.013](https://doi.org/10.1016/j.jpeds.2013.10.013) (Epub ahead of print)
- Curtis JM, Lacey D, Smyth R, Carty H (1998) Endobronchial tumours in childhood. *Eur J Radiol* 29:11–20
- Daldrup HE, Link TM, Wortler K, Reimer P, Rummeny EJ (1997) MR imaging of thoracic tumors in pediatric patients. *AJR Am J Roentgenol* 170:1639–1644
- den Bakker MA, Beverloo BH, van den Heuvel-Eibrink MM, Meeuwis CA, Tan LM, Johnson LA, French CA, van Leenders GJ (2009) NUT midline carcinoma of the parotid gland with mesenchymal differentiation. *Am J Surg Pathol* 33:1253–1258
- Dehner LP (1994) Pleuropulmonary blastoma is THE pulmonary blastoma of childhood. *Semin Diagn Pathol* 11:144–151
- Dehner LP, Watterson J, Priest J (1995) Pleuropulmonary blastoma: a unique intrathoracic-pulmonary neoplasm of childhood. *Perspect Pediatr Pathol* 18:214–226
- Diederich S, Lenzen H, Windmann R, Puskas Z, Yelbuz TM, Henneken S, Klaiber T, Eameri M, Roos N, Peters PE (1999) Pulmonary nodules: experimental and clinical studies at low dose CT. *Radiology* 213:289–298
- Diederich S, Hansen J, Wormanns D (2005) Resolving small pulmonary nodules: CT features. *Eur Radiol* 15:2064–2069
- Diemel KD, Klippe HJ, Branscheid D (2009) Pulmonary metastasectomy for osteosarcoma: is it justified? *Recent Results Cancer Res* 179:183–208
- Dishop MK, Kuruvilla S (2008) Primary and metastatic lung tumors in the pediatric population: a review and 25-year experience at a large children's hospital. *Arch Pathol Lab Med* 132:1079–1103
- Dishop MK, McKay EM, Kreiger PA, Priest JR, Williams GM, Langston C, Jarzembowski J, Suchi M, Dehner LP, Hill DA (2010) Fetal lung interstitial tumor (FLIT): a proposed newly recognized lung tumor of infancy to be differentiated from cystic pleuropulmonary blastoma and other developmental pulmonary lesions. *Am J Surg Pathol* 34:1762–1772
- DuBois SG, London WB, Zhang Y, Matthay KK, Monclair T, Ambros PF, Cohn SL, Pearson A, Diller L (2008) Lung metastases in neuroblastoma at initial diagnosis: a report from the International Neuroblastoma Risk Group (INRG) project. *Pediatr Blood Cancer* 51:589–592
- Dulmet EM, Macchiarini P, Suc B, Verley JM (1993) Germ cell tumours of the mediastinum: a 30 year experience. *Cancer* 72:1894–1901
- Elidemir O, Kancherla BS, Schecter MG, McKenzie ED, Morales DL, Heinle JS, Mallory GB (2009) Post-transplant lymphoproliferative disease in pediatric lung transplant recipients: recent advances in monitoring. *Pediatr Transplant* 13:606–610
- Foulkes WD, Bahubeshi A, Hamel N, Pasini B, Asioli S, Baynam G, Choong CS, Charles A, Frieder RP, Dishop MK, Graf N, Ekim M, Bouron-Dal Soglio D, Arseneau J, Young RH, Sabbaghian N, Srivastava A, Tischkowitz MD, Priest JR (2011) Extending the phenotypes associated with DICER1 mutations. *Hum Mutat* 32:1381–1384
- French CA (2010) NUT midline carcinoma. *Cancer Genet Cytogenet* 203:16–20
- French CA, Kutok JL, Faquin WC, Toretsky JA, Antonescu CR, Griffin CA, Nose V, Vargas SO, Moschovi M, Tzortzidou-Stathopoulou F, Miyoshi I, Perez-Atayde AR, Aster JC, Fletcher JA (2004) Midline carcinoma of children and young adults with NUT rearrangement. *J Clin Oncol* 22:4135–4139
- Fuchs J, Seitz G, Handgretinger R, Schafer J, Warmann SW (2012) Surgical treatment of lung metastases in patients with embryonal pediatric solid tumors: an update. *Semin Pediatr Surg* 21:79–87
- Goel P, Panda S, Srinivas M, Kumar D, Seith A, Ahuja A, Sarkar C, Chowdhury S, Agarwala S (2010) Pleuropulmonary blastoma with intrabronchial extension. *Pediatr Blood Cancer* 54:1026–1028
- Gross E, Chen MK, Hollabaugh RS, Joyner RE (1996) Tracheal hamartoma: report of a child with a neck mass. *J Pediatr Surg* 31:1584–1585
- Gruden JF, Ouanounou S, Tigges S, Norris SD, Klausner TS (2002) Incremental benefit of maximum-intensity-projection images on observer detection of small pulmonary nodules revealed by multidetector CT. *AJR Am J Roentgenol* 179:149–157
- Grundy PE, Green DM, Dirks AC, Berendt AE, Breslow NE, Anderson JR, Dome JS (2012) Clinical significance of pulmonary nodules detected by CT and not CXR in patients treated for favorable histology Wilms tumor on national Wilms tumor studies-4 and -5: a report from the Children's Oncology Group. *Pediatr Blood Cancer* 59:631–635
- Guest AR, Strouse PJ, Hiew CC, Arca M (2000) Progressive esophageal leiomyomatosis with respiratory compromise. *Pediatr Radiol* 30:247–250
- Guillerman RP, Voss SD, Parker BR (2011) Leukemia and lymphoma. *Radiol Clin N Am* 49:767–797
- Hancock BJ, Di Lorenzo M, Youssef S, Yazbeck S, Marcotte JE, Collin PP (1993) Childhood primary pulmonary neoplasms. *J Pediatr Surg* 28:1133–1136
- Hartman GE, Shochat SJ (1983) Primary pulmonary neoplasms of childhood: a review. *Ann Thorac Surg* 36:108–119
- Hedlund GL, Navoy JF, Galliani CA, Johnson WH Jr (1999) Aggressive manifestations of inflammatory pseudotumor in children. *Pediatr Radiol* 29:112–116
- Helm EJ, Silva CT, Roberts HC, Manson D, Seed MT, Amaral JG, Babyn PS (2009) Computed-aided detection for the identification of pulmonary nodules in pediatric oncology patients: initial experience. *Pediatr Radiol* 39:685–693
- Horikoshi T, Kikuchi A, Matsumoto Y, Tatsumatsu M, Takae K, Ogiso Y, Nakayama M, Unno N (2005) Fetal hydrops associated with congenital pulmonary myofibroblastic tumor. *J Obstet Gynaecol Res* 31:552–555
- Huang Y, Xu DM, Jirapatnakul A, Reeves AP, Farooqi A, Zhang Lj, Giunta S, Zulueta J, Aye R, Miller A, Mendelson DS, Aylesworth C, Sheppard B, Klingler K, Yankelevitz DF, Henschke CI (2011) CT- and computer-based features of small hamartomas. *Clin Imaging* 35:116–122
- Huppmann AR, Coffin CM, Hoot AC, Kahwash S, Pawel BR (2011) Congenital peribronchial myofibroblastic tumor: comparison of fetal and postnatal morphology. *Pediatr Dev Pathol* 14:124–129
- Indolfi P, Bisogno G, Casale F, Cecchetto G, De Salvo G, Ferrari A, Donfrancesco A, Donofrio V, Martone A, Di Martino M, Di Tullio MT (2007) Prognostic factors in pleuro-pulmonary blastoma. *Pediatr Blood Cancer* 48:318–323
- Janik JS, Janik JP, Lovell MA, Hendrickson RJ, Bensard DD, Grefe BS (2003) Recurrent inflammatory pseudotumors in children. *J Pediatr Surg* 38:1491–1495
- Jeung MY, Gasser B, Gangi A, Charneau D, Ducroq X, Kessler R, Quiox E, Roy C (2002) Bronchial carcinoid tumors of the thorax: spectrum of radiologic findings. *Radiographics* 22:351–365
- Kammen BF, Matthay KK, Pacharn P, Gerbing R, Brasch RC, Gooding CA (2001) Pulmonary metastases at diagnosis of neuroblastoma in pediatric patients: CT findings and prognosis. *AJR Am J Roentgenol* 176:755–759
- Kaste SC, Pratt CB, Cain AM, Jones-Wallace DJ, Rao BN (1999) Metastases detected at the time of diagnosis of primary pediatric extremity osteosarcoma: imaging features. *Cancer* 86:1602–1608
- Katz SL, Das P, Ngan BY, Manson D, Pappo AS, Sweezey NB, Solomon MP (2005) Remote intrapulmonary spread of recurrent

- respiratory papillomatosis with malignant transformation. *Pediatr Pulmonol* 39:185–188
- Kayton ML, Huvo AG, Casher J, Abramson SJ, Rosen NS, Wexler LH, Meyers P, LaQuaglia MP (2006) Computed tomographic scan of the chest underestimates the number of metastatic lesions in osteosarcoma. *J Pediatr Surg* 41:200–206
- Kawel N, Seifert B, Luetolf M, Boehm T (2009) Effect of slab thickness on the CT detection of pulmonary nodules: use of sliding thin-slab maximum intensity projection and volume rendering. *AJR Am J Roentgenol* 192:1324–1329
- Kim TS, Lee KS, Han J, Im JG, Seo JB, Kim JS, Kim HY, Han SW (1999) Mucoepidermoid carcinoma of the tracheobronchial tree: radiographic and CT findings in 12 patients. *Radiology* 212:643–648
- Kim Y, Park HY, Cho J, Han J, Cho EY (2013) Congenital peribronchial myofibroblastic tumor: a case study and literature review. *Korean J Pathol* 47:172–176
- Kleis M, Daldrop-Link H, Matthay K, Goldsby R, Lu Y, Schuster T, Schreck C, Chu PW, Hawkins RA, Franc BL (2009) Diagnostic value of PET/CT for the staging and restaging of pediatric tumors. *Eur J Nucl Med Mol Imaging* 36:23–36
- Kocaoglu M, Bulakbasi N, Soyly K, Demirbag S, Tayfun C, Somuncu I (2006) Thin section axial multidetector computed tomography and multiplanar reformatted imaging of children with suspected foreign body: is virtual bronchoscopy overemphasized? *Acta Radiol* 47:746–751
- Koopmans KP, Neels OC, Kema IP, Elsinga PH, Sluiter WJ, Vanghillewe K, Brouwers AH, Jager PL, de Vries EG (2008) Improved staging of patients with carcinoid and islet cell tumors with 18F-dihydroxy-phenyl-alanine and 11C-5-hydroxy-tryptophan positron emission tomography. *J Clin Oncol* 26:1489–1495
- Koujok K, Ruiz RE, Hernandez RJ (2005) Myofibromatosis: imaging characteristics. *Pediatr Radiol* 35:374–380
- Kramer SS, Wehunt WD, Stocker JT, Kashima H (1985) Pulmonary manifestations of juvenile laryngotracheal papillomatosis. *AJR Am J Roentgenol* 144:687–694
- Kuhns LR, Roubal S (1995) Should intravenous contrast be used for chest CT in children with nonlymphomatous extrathoracic malignancies? *Pediatr Radiol* 25(Suppl 1):S184–S186
- Lal DR, Clark I, Shalkow J, Downey RJ, Shorter NA, Klimstra DS, La Quaglia MP (2005) Primary epithelial lung malignancies in the pediatric population. *Pediatr Blood Cancer* 45:683–686
- Lazar DA, Cass DL, Dishop MK, Adam K, Olutoye OA, Ayres NA, Cassady CI, Olutoye OO (2011) Fetal lung interstitial tumor: a cause of late gestation fetal hydrops. *J Pediatr Surg* 46:1263–1266
- Letourneau PA, Xiao L, Harting MT, Lally KP, Cox CS Jr, Andrassy RJ, Hayes-Jordan AA (2011) Location of pulmonary metastasis in pediatric osteosarcoma is predictive of outcome. *J Pediatr Surg* 46:1333–1337
- Levine E, Freneaux P, Schleiermacher G, Brisse H, Pannier S, Teissier N, Mesples B, Orbach D (2012) Risk-adapted therapy for infantile myofibromatosis in children. *Pediatr Blood Cancer* 59:115–120
- Mas Estelles F, Andres V, Vallcanera A, Muro D, Cortina H (1995) Plasma cell granuloma of the lung in childhood: atypical radiologic findings and association with hypertrophic osteoarthropathy. *Pediatr Radiol* 25:369–372
- Maturen KE, Blane CE, Strouse PJ, Fitzgerald JT (2004) Pulmonary involvement in pediatric lymphoma. *Pediatr Radiol* 34:120–124
- McCahon E (2006) Lung tumours in children. *Paediatr Respir Rev* 7:191–196
- McCarville MB, Lederman HM, Santana VM, Daw NC, Shochat SJ, Li CS, Kaufman RA (2006) Distinguishing benign from malignant pulmonary nodules with helical chest CT in children with malignant solid tumors. *Radiology* 239:514–520
- McClain KL, Leach CT, Jenson HB, Joshi VV, Pollock BH, Parmley RT, DiCarlo FJ, Chadwick EG, Murphy SB (1995) Association of Epstein-Barr virus with leiomyosarcomas in children with AIDS. *N Engl J Med* 332:12–18
- McHugh K, Disini L (2011) Commentary: for the children's sake, avoid non-contrast CT. *Cancer Imaging* 11:16–18
- Mergan F, Jaubert F, Sauvat F, Hartmann O, Lortat-Jacob S, Revillon Y, Nihoul-Fekete C, Sarnacki S (2005) Inflammatory myofibroblastic tumor in children: clinical review with anaplastic lymphoma kinase, Epstein-Barr virus and human herpes virus 8 detection analysis. *J Pediatr Surg* 40:1581–1586
- Miniati DN, Chintagumpala M, Langston C, Dishop MK, Olutoye OO, Nuchtern JG, Cass DL (2006) Prenatal presentation and outcome of children with pleuropulmonary blastoma. *J Pediatr Surg* 41:66–71
- Morini F, Quattrucci S, Cozzi DA, Tancredi G, Cicconi AM, Guidi R, Midulla F (2003) Bronchial adenoma: an unusual cause of recurrent pneumonia in childhood. *Ann Thorac Surg* 76:2085–2087
- Murrell Z, Dasgupta R (2013) What predicts the risk of recurrent lung metastases. *J Pediatr Surg* 48:1020–1024
- Murrell Z, Dickie B, Dasgupta R (2011) Lung nodules in pediatric oncology patients: a prediction rule for when to biopsy. *J Pediatr Surg* 46:833–837
- Newman B (2011) Thoracic neoplasms in children. *Radiol Clin North Am* 49:633–664
- Pai S, Eng HL, Lee SY, Hsiao CC, Huang WT, Huang SC, Hill DA, Dehner LP, Priest JR (2007) Correction: pleuropulmonary blastoma, not rhabdomyosarcoma in a congenital lung cyst. *Pediatr Blood Cancer* 48:370–371
- Parham DM, Alaggio R, Coffin CM (2012) Myogenic tumors in children and adolescents. *Pediatr Dev Pathol* 15:211–238
- Park KY, Kim SJ, Noh TW, Cho SH, Lee DY, Paik HC, Ryu YH (2008) Diagnostic efficacy and characteristic feature of MRI in pulmonary hamartoma: comparison with CT, specimen MRI and pathology. *J Comput Assist Tomogr* 32:919–925
- Paulussen M, Ahrens S, Craft AW, Dunst J, Frohlich B, Jabar S, Rube C, Winkelmann W, Wissing S, Zoubek A, Jurgens H (1998) Ewing's tumour with primary lung metastases: survival analysis of 114 (European Intergroup) Cooperative Ewing's Sarcoma Studies patients. *J Clin Oncol* 16:3044–3052
- Pickhardt PJ, Siegel MJ, Hayashi RJ, Kelly M (2000) Post-transplantation lymphoproliferative disorder in children: clinical, histopathologic, and imaging features. *Radiology* 217:16–25
- Pipavath SN, Manchanda V, Lewis DH, Schmidt RA, Martins RG, Godwin JD (2008) 18F FDG-PET/CT findings in recurrent respiratory papillomatosis. *Ann Nucl Med* 22:433–436
- Polsani A, Braithwaite KA, Alazraki AL, Abramowsky C, Shehata BM (2012) NUT midline carcinoma: an imaging case series and review of literature. *Pediatr Radiol* 42:205–210
- Priest JR (2012) Pleuropulmonary blastoma. In: Schneider DTBI, Olson TA, Ferrari A (eds) *Rare tumors in children and adolescents, pediatric oncology*. Springer, Berlin, pp 213–221
- Priest JR, McDermott MB, Bhatia S, Watterson J, Manivel JC, Dehner LP (1997) Pleuropulmonary blastoma: a clinicopathologic study of 50 cases. *Cancer* 80:147–161
- Priest JR, Hill AD, Williams GM, Moertel CL, Messinger Y, Finkelstein MJ, Dehner LP (2006) Type I pleuropulmonary blastoma: a report from the International Pleuropulmonary Blastoma Registry. *J Clin Oncol* 24:4492–4498
- Priest JR, Williams GM, Hill DA, Dehner LP, Jaffe A (2009) Pulmonary cysts in early childhood and the risk of malignancy. *Pediatr Pulmonol* 44:14–30
- Priest JR, Andic D, Arbucke S, Gonzalez-Gomez I, Hill DA, Williams G (2011) Great vessel/cardiac extension and tumor embolism in

- pleuropulmonary blastoma: a report from the International Pleuropulmonary Blastoma Registry. *Pediatr Blood Cancer* 56:604–609
- Rabah R, Lancaster WD, Thomas R, Gregoire L (2001) Human papillomavirus-11-associated recurrent respiratory papillomatosis is more aggressive than human papillomavirus-6-associated disease. *Pediatr Dev Pathol* 4:68–72
- Rizzardi G, Marulli G, Calabrese F, Rugge M, Rebusso A, Sartori F, Rea F (2009) Bronchial carcinoid tumours in children: surgical treatment and outcome in a single institution. *Eur J Pediatr Surg* 19:228–231
- Rodriguez FJ, Aubry MC, Tazelaar HD, Slezak J, Carney JA (2007) Pulmonary chondroma: a tumor associated with Carney triad and different from pulmonary hamartoma. *Am J Surg Pathol* 31:1844–1853
- Rosenbaum DG, Feldstein JT, Price AP, Meyers P, Abramson S (2012) Radiologic features of NUT midline carcinoma in an adolescent. *Pediatr Radiol* 42:249–252
- Sasaka K, Kurihara Y, Nakajima Y, Seto Y, Endo I, Ishikawa T, Takagi M (1998) Spontaneous rupture: a complication of benign mature teratomas of the mediastinum. *AJR Am J Roentgenol* 170:323–328
- Satria MN, Pacheco-Rodriguez G, Moss J (2011) Pulmonary lymphangiomas. *Lymphat Res Biol* 9:191–193
- Schiavetti A, Indolfi P, Hill DA, Priest JR (2009) Primary pulmonary rhabdomyosarcoma in childhood: clinic-biologic features in two cases with review of the literature—erratum. *Pediatr Blood Cancer* 52:146
- Seemayer TA, Harper JL, Shickell D, Gross TG (1997) Cytodifferentiation of a Wilms' tumor pulmonary metastasis: theoretic and clinical implications. *Cancer* 79:1629–1634
- Seifert RP, McNab P, Sexton WJ, Sawczyn KK, Smith P, Coppola D, Bui MM (2012) Rhabdomyomatous differentiation in Wilms tumor pulmonary metastases: a case report and literature review. *Ann Clin Lab Sci* 42:409–416
- Shah V, Shah S, Barnacle A, Sebire NJ, Brock P, Harper JJ, McHugh K (2011) Mediastinal involvement in lymphangiomas: a previously unreported MRI sign. *Pediatr Radiol* 41:985–992
- Siegel MJ, Ishwaran HI, Fletcher BD, Meyer JS, Hoffer FA, Jaramillo D, Hernandez RJ, Roubal SE, Siegel BA, Caudry DJ, McNeil BJ (2002) Staging of neuroblastoma at imaging: report of the Radiology Diagnostic Oncology Group. *Radiology* 223:168–175
- Siegel MJ, Lee EY, Sweet SC, Hildebolt C (2003) CT of posttransplantation lymphoproliferative disorder in pediatric recipients of lung allografts. *AJR Am J Roentgenol* 181:1125–1131
- Silva CT, Amaral JG, Moineddin R, Doda W, Babyn PS (2010). CT characteristics of lung nodules present at diagnosis of extrapulmonary malignancy in children. *AJR Am J Roentgenol* 194:772–8
- Siminovich M, Galluzzo L, Lopez J, Lubieniecki F, de Davila MT (2012) Inflammatory myofibroblastic tumor of the lung in children: anaplastic lymphoma kinase (ALK) expression and clinico-pathological correlation. *Pediatr Dev Pathol* 15:179–186
- Slade I, Bacchelli C, Davies H, Murray A, Abbaszadeh F, Hanks S, Barfoot R, Burke A, Chisholm J, Hewitt M, Jenkinson H, King D, Morland B, Pizer B, Prescott K, Sagar A, Side L, Trautnecker H, Vaidya S, Ward P, Futreal PA, Vujanec G, Nicholson AG, Sebire N, Turnbull C, Priest JR, Pritchard-Jones K, Houlston R, Stiller C, Stratton MR, Douglas J, Rahman N (2010) DICER1 syndrome: clarifying the diagnosis, clinical features and management implications of a pleiotropic tumour predisposition syndrome. *J Med Genet* 48:273–278
- Smets AM, van Tinteren H, Bergeron C, De Camargo B, Graf N, Pritchard-Jones K, de Kraker J (2012) The contribution of chest CT-scan at diagnosis in children with unilateral Wilms' tumour. Results of the SIOP 2001 study. *Eur J Cancer* 48:1060–1065
- Soldatski I, Onufrieva E, Steklov A, Schepin NV (2005) Tracheal, bronchial and pulmonary papillomatosis in children. *Laryngoscope* 115:1848–1854
- Stratakis CA, Carney JA (2009) The triad of paragangliomas, gastric stromal tumours and pulmonary chondromas (Carney triad), and the dyad of paragangliomas and gastric stromal sarcomas (Carney-Stratakis syndrome): molecular genetics and clinical implications. *J Intern Med* 266:43–52
- Strollo DC, Rosado de Christenson ML, Jett JR (1997) Primary mediastinal tumors. Part 1: tumors of the anterior mediastinum. *Chest* 112:511–522
- Swenson SJ, Hartman TE, Mayo JR, Colby TV, Tazelaar HD, Muller NL (1995) Diffuse pulmonary lymphangiomatosis: CT findings. *J Comput Assist Tomogr* 19:348–352
- Takayama Y, Yabuuchi H, Matsuo Y, Soeda H, Okafuji T, Kamitani T, Kinoshita Y, Kubokura N, Sakai S, Oda Y, Hatakenaka M, Honda H (2008) Computed tomographic and magnetic resonance features of inflammatory myofibroblastic tumor of the lung in children. *Radiat Med* 26:613–617
- Tanaka M, Kato K, Gomi K, Yoshida M, Niwa T, Aida N, Kigasawa H, Ohama Y, Tanaka Y (2012) NUT midline carcinoma: report of 2 cases suggestive of pulmonary origin. *Am J Surg Path* 36:381–388
- Travis WD, Dehner LP, Manabe T, Tazelaar HD (2004) Congenital peribronchial myofibroblastic tumor. In: Travis WD, Brambilla E, Muller-Hermelink HK, Harris CC (eds) World Health Organization classification of tumours: pathology and genetics of tumors of the lung, pleura, thymus, and heart. IARC Press, Lyon, pp 102–103
- Tronc F, Conter C, Perrine MB, Bossard N, Remontet L, Orsini A, Gamondes JP, Louis D (2008) Prognostic factors and long-term results of pulmonary metastasectomy for pediatric histologies. *Eur J Cardiothorac Surg* 34:1240–1246
- Verbeke JIM, Verbeke AAPH, den Hollander JC, Robben SGF (1999) Inflammatory myofibroblastic tumour of the lung manifesting as progressive atelectasis. *Pediatr Radiol* 29:816–819
- Verschuur A, Van Tinteren H, Graf N, Bergeron C, Sandstedt B, de Kraker J (2012) Treatment of pulmonary metastases in children with stage IV neuroblastoma with risk-based use of pulmonary radiotherapy. *J Clin Oncol* 30:3533–3539
- Wang CW, Teng YH, Huang CC, Wu YC, Chao YK, Wu CT (2013) Intrapulmonary lymph nodes: computed tomography findings with histopathologic correlations. *Clin Imaging* 37:487–492
- Wang LT, Wilkins EW Jr, Bode HH (1993) Bronchial carcinoid tumors in pediatric patients. *Chest* 103:1426–1428
- Warmann SW, Nourkani N, Fruhwald M, Leuschner I, Schenk JP, Fuchs J, Graf N (2012) Primary lung metastases in pediatric malignant non-Wilms renal tumors: data from SIOP 93–01/GPOH and SIOP 2011/GPOH. *Klin Padiatr* 224:148–152
- Wilde GE, Moore DJ, Bellah RD (2005) Posttransplantation lymphoproliferative disorder in pediatric recipients of solid organ transplants: timing and location of disease. *AJR Am J Roentgenol* 185:1335–1341
- Williams SD, Jamieson DH, Prescott CA (1994) Clinical and radiological features in three cases of pulmonary involvement from recurrent respiratory papillomatosis. *Int J Pediatr Otorhinolaryngol* 30:71–77
- Wu M, Wang Q, Xu XF, Xiang JJ (2011) Bronchial mucoepidermoid carcinoma in children. *Thorac Cardiovasc Surg* 59:443–445
- Wunderbaldinger P, Paya P, Partik B, Turetschek K, Hormann M, Horcher E, Bankier AA (2000) CT and MR imaging of generalized cystic lymphangiomatosis in pediatric patients. *AJR Am J Roentgenol* 174:827–832
- Xi JJ, Jiang W, Lu SH, Zhang CY, Fan H, Wang Q (2012) Primary pulmonary mucoepidermoid carcinoma: an analysis of 21 cases. *World J Surg Oncol* 10:232



Yalcin B, Demir HA, Tanyel FC, Akcoren Z, Varan A, Akyuz C, Kutluk T, Buyukpamukcu M (2012) Mediastinal germ cell tumors in childhood. *Pediatr Hematol Oncol* 29:633–642

Yousem SA, Tazelaar HD, Manabe T, Dehner LP (2004) Inflammatory myofibroblastic tumor. In: Travis WD, Brambilla E, Muller-

Hermelink HK, Harris CC (eds) World Health Organization classification of tumours: pathology and genetics of tumors of the lung, pleura, thymus, and heart. IARC Press, Lyon, pp 105–106

---

# Diffuse Lung Disease

R. Paul Guillerman

## Contents

<b>1</b>	<b>Introduction.....</b>	<b>373</b>
<b>2</b>	<b>Clinical Presentations and Classification.....</b>	<b>374</b>
<b>3</b>	<b>Categories of Disorders.....</b>	<b>375</b>
3.1	Diffuse Developmental Disorders.....	375
3.2	Growth Abnormalities.....	376
3.3	Specific Disorders of Unknown Etiology.....	377
3.4	Surfactant Dysfunction Disorders.....	380
3.5	Disorders Related to Systemic Disease Processes.....	383
3.6	Disorders of the Normal Immunocompetent Host.....	383
3.7	Vascular Disorders Masquerading as Diffuse Lung Disease.....	388
3.8	Conclusion.....	390
	<b>References.....</b>	<b>391</b>

---

## Abstract

Diffuse lung disease (DLD) comprises a diverse group of disorders characterized by widespread pulmonary parenchymal pathology and impaired gas exchange. While many of these disorders are categorized under the rubric of interstitial lung disease (ILD), some of these disorders involve the airspaces or peripheral airways in addition to, or rather than, the interstitium. Some of these disorders are present primarily in infancy or early childhood, while others that are prevalent in adulthood rarely occur in childhood. This chapter will review the classification of pediatric DLD and the characteristic imaging findings of specific disorders to facilitate accurate diagnosis and guide appropriate treatment of children with these disorders.

---

## 1 Introduction

Diffuse lung disease (DLD) comprises a diverse group of disorders characterized by widespread pulmonary parenchymal pathology and impaired gas exchange. While many of these disorders in children are categorized under the rubric of interstitial lung disease (ILD), some of these disorders involve the airspaces or peripheral airways in addition to, or rather than, the interstitium, so that DLD is a less specific, but more inclusive term. The American Thoracic Society (ATS) /European Respiratory Society (ERS) international multidisciplinary classification of the idiopathic interstitial pneumonias (Travis et al. 2013) developed for the adult population is not well suited for children.

Many of the disorders that are most prevalent in adulthood rarely occur in childhood. Usual interstitial pneumonia (UIP), the pathologic correlate of idiopathic pulmonary fibrosis (IPF) and the predominant form of DLD in the adult ATS/ERS classification, is exceedingly rare in children and erroneous diagnoses likely account for reports of better

---

R. P. Guillerman (✉)  
Department of Pediatric Radiology, Texas Children's Hospital,  
Baylor College of Medicine, Houston, TX, USA  
e-mail: rpguille@texaschildrens.org

outcomes of children with UIP compared to adults. Unrecognized mutations in surfactant-related genes likely account for many reported cases of desquamative interstitial pneumonia (DIP) in children diagnosed before the availability of tests for these mutations (Fan et al. 2004; Noguee 2006).

There are several types of DLD that present primarily or exclusively in infancy or early childhood, such as neuroendocrine cell hyperplasia of infancy (NEHI) and pulmonary interstitial glycogenosis (PIG). The stage of lung growth and development affects disease manifestations, and the injury and repair processes in immature lung differ from those in the mature adult lung (Clement and Eber 2008). In recognition of these differences with adult DLD, standardized approaches to the diagnosis and classification of pediatric DLD have been advocated, incorporating insights from diagnostic imaging, infant pulmonary function testing, molecular genetics, immunopathology, and electron microscopy (Deutsch et al. 2007). This chapter will review the classification, clinical features, and imaging findings of pediatric DLD.

## 2 Clinical Presentations and Classification

DLD is less prevalent in children than in adults and more common in infants than in older children. While rare, the true prevalence of pediatric DLD is likely understated in the medical literature as a consequence of more hesitant use of diagnostic lung biopsy in children compared to adults and the lack of familiarity with recently described disorders and appropriate classification.

Pediatric DLD usually presents either with rapid respiratory failure in the neonatal period or with an insidious course of respiratory signs and symptoms, failure to thrive, or exercise intolerance later in infancy, childhood, or adolescence. The signs and symptoms may be misattributed for many months or even years to common disorders, such as pulmonary infection, bronchopulmonary dysplasia (BPD), asthma, congenital heart disease, cystic fibrosis, or immunodeficiency. Once these common disorders have been eliminated as causal, criteria have been devised to assist clinicians in identifying children that warrant further investigation for possible DLD. A neonate or infant is proposed as having “childhood ILD syndrome” or “chILD syndrome” if at least three of the following criteria are present: (1) respiratory symptoms (cough, rapid, and/or difficult breathing, or exercise intolerance), (2) signs (tachypnea, adventitious sounds, retractions, digital clubbing, failure to thrive, or respiratory failure), (3) hypoxemia; and (4) diffuse pulmonary parenchymal abnormality on chest radiograph (CXR) or computed tomography (CT) (Kurland et al. 2013).

Correct diagnosis of a DLD is important due to widely differing prognoses among the disorders and the need for genetic evaluation and counseling for some families. To promote effective communication for clinical care and research, the disorders affecting infants and young children with “chILD syndrome” have been organized by the chILD Research Cooperative into a novel classification scheme (Deutsch et al. 2007) categorized on the basis of the presumed etiology, with overlap of distinct clinical disorders and pathologies among different etiologic categories. For example, pulmonary alveolar proteinosis (PAP), DIP, non-specific interstitial pneumonia (NSIP), and chronic pneumonitis of infancy (CPI) are distinct pathologies that can be associated with genetic surfactant disorders, and NSIP pathology can be observed in genetic disorders of surfactant metabolism, disorders related to systemic disease processes (such as immune-mediated connective tissue disease) or disorders of the normal immunocompetent host (such as hypersensitivity pneumonitis). In such a classification based on etiology, disorders that can be idiopathic or secondary to other conditions are difficult to categorize. Despite its limitations, the chILD classification scheme has been found applicable to over 90 % of cases of DLD encountered in the setting of a children’s hospital, including previously unclassified cases (Soares et al. 2013), and several of the disorders are recognized by diagnosis codes in the latest versions of the International Classification of Diseases by the World Health Organization (Popler et al. 2012). While the chILD classification generally works well for infants and young children (Langston and Dishop 2009), expansion and modification of the classification is necessary for older children and adolescents who may manifest with forms of DLD more prevalent in adults (Rice et al. 2013) (Table 1). Infants are more likely to have developmental, growth, or genetic disorders, while older children and adolescents are more likely to have disorders related to systemic diseases, infections, or environmental exposures.

The imaging technique and diagnostic efficacy of imaging for pediatric DLD have been addressed in previous review articles (Guillerman 2010; Guillerman and Brody 2011; Lee 2013). For some types of pediatric DLD, the imaging findings are highly specific, while for others the imaging findings are nonspecific and laboratory tests or lung biopsy are needed for definitive diagnosis (Kurland et al. 2013). In addition to suggesting or corroborating a specific diagnosis in some cases, imaging can be useful for refining the differential diagnosis, identifying biopsy sites, monitoring disease activity, and assessing response to therapy. The remainder of this chapter will provide an updated summary of the characteristic clinical and imaging features of the disorders categorized under a modified chILD classification scheme of pediatric DLD.



**Table 1** Classification scheme for pediatric diffuse lung disease

Disorders more prevalent in infants and young children
Diffuse developmental disorders
Acinar dysplasia
Congenital alveolar dysplasia
Alveolar capillary dysplasia with misalignment of the pulmonary veins
Growth abnormalities
Pulmonary hypoplasia
Chronic lung disease of infancy
Related to genetic disorders
Related to congenital heart disease
Specific disorders of unknown etiology
Pulmonary interstitial glycogenosis
Neuroendocrine cell hyperplasia of infancy
Surfactant dysfunction disorders
Related to a genetic defect
Related to autoimmune anti-GM-CSF antibody
Consistent histology without a recognized genetic defect
Disorders related to systemic disease processes
Autoimmune and autoinflammatory disorders
Vasculitis
Connective tissue disease
Immunodeficiencies
Primary
Secondary (drug therapy, radiation therapy, bone marrow transplant)
Lymphoid hyperplasia and lymphoproliferative disorders
Granulomatous disorders
Lysosomal storage disorders
Langerhans cell histiocytosis
Disorders of the normal immunocompetent host
Infectious and post-infectious processes
Bronchiolitis obliterans
Eosinophilic pneumonia
Related to exposures
Hypersensitivity pneumonitis
Aspiration pneumonia
Drug reaction
Toxic inhalation
Acute interstitial pneumonia
Cryptogenic organizing pneumonia
Idiopathic nonspecific interstitial pneumonia
Idiopathic pulmonary hemosiderosis
Vascular disorders masquerading as diffuse lung disease
Pulmonary venous congestion or obstruction
Congestive heart failure
Congenital cardiovascular disease
Pulmonary veno-occlusive disease
Lymphangiectasia
Lymphangiomatosis

[adapted from Deutsch et al. (2007) and Rice et al. (2013)]

### 3 Categories of Disorders

#### 3.1 Diffuse Developmental Disorders

Acinar dysplasia is characterized by lung developmental arrest in the pseudoglandular or early canalicular phase, resulting in essentially no alveolar spaces for gas exchange. Congenital alveolar dysplasia is characterized by arrest in the late canalicular/early saccular phase, resulting in incomplete alveolarization. Alveolar capillary dysplasia with misalignment of the pulmonary veins (ACD/MPV) is characterized by malpositioning of the pulmonary vein branches adjacent to the pulmonary artery branches rather than within the interlobular septa, medial hypertrophy of the pulmonary arterioles, reduced alveolar capillary density, and pulmonary lobular maldevelopment. Pulmonary lymphangiectasia is also present in about one-third of cases (Dishop 2011). The misaligned pulmonary veins in ACD/MPV may actually represent anastomotic bronchial veins associated with intra-pulmonary right-to-left shunting. This shunting bypasses the alveolar capillary bed and exacerbates the hypoxemia from right-to-left extrapulmonary shunting associated with persistent pulmonary hypertension of the newborn (PPHN) (Galambos et al. 2014).

The diffuse developmental disorders of the lung are associated with markedly impaired alveolar gas exchange, resulting in respiratory failure and severe PPHN within hours or days of birth in the absence of the usual causative conditions of prematurity, meconium aspiration, congenital heart disease, perinatal asphyxia, or sepsis. Death usually ensues within a few days or weeks, unless the lung involvement is patchy rather than diffuse (Chow et al. 2013), or extracorporeal membrane oxygenation (ECMO) or paracorporeal lung assist devices are available as a bridge to lung transplantation (Sen et al. 2004; Michalsky et al. 2005; Hoganson et al. 2014). Approximately 80 % of cases of ACD/MPV are associated with extrapulmonary malformations, including hypoplastic left heart syndrome, aortic coarctation, alimentary tract atresia, annular pancreas, omphalocele, midgut malrotation, and urinary tract malformation. Sporadic or familial autosomal dominant *FOXF1* gene mutations have been identified as a cause of some cases of ACD/MPV (Stankiewicz et al. 2009; Sen et al. 2013).

Due the severity of the respiratory disease, imaging of patients with diffuse developmental disorders of the lung is usually limited to portable CXRs. Although the initial CXRs may be unimpressive, followup CXRs may demonstrate progressive hazy opacification of the lungs, resembling of the findings of surfactant deficiency of prematurity or genetic surfactant disorders (Fig. 1). Pneumothorax or pneumomediastinum is common and likely attributable to barotrauma (Michalsky et al. 2005; Hugosson et al. 2005; Gillespie et al. 2004; Newman and Yunis 1990).

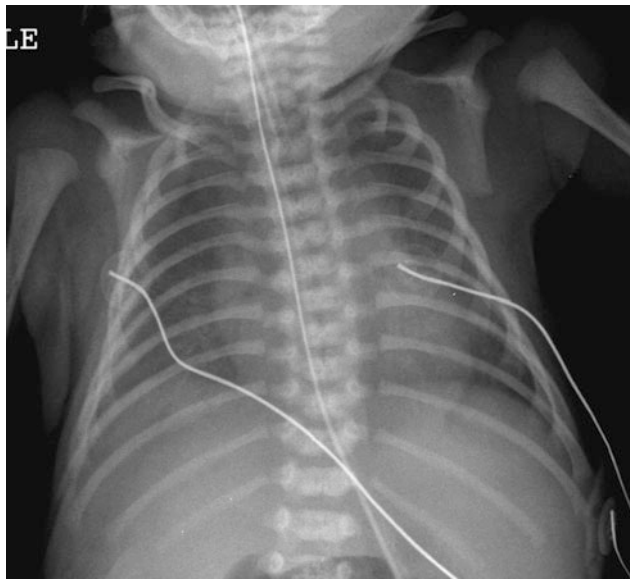


**Fig. 1** Alveolar capillary dysplasia with misalignment of the pulmonary veins (ACD/MPV). A frontal portable CXR of a 33-week gestational age newborn with neonatal RDS shows diffuse, hazy pulmonary opacification indistinguishable from surfactant deficiency of prematurity. The patient rapidly developed hypoxemia and severe PPHN requiring ECMO

### 3.2 Growth Abnormalities

Growth abnormalities constitute the most common cause of chronic DLD in infancy. Lung growth abnormalities are characterized histologically by impaired alveolarization manifesting as lobular simplification with deficient alveolar vascularization and septation, reduced alveolar number, and increased alveolar size resembling emphysema (Dishop 2010). As a consequence, there is diminished total alveolar surface area and reduced pulmonary diffusing capacity relative to alveolar volume (Balinotti et al. 2010). Lung growth abnormalities are often accompanied by patchy PIG or by pulmonary arterial hypertensive changes related to increased vascular resistance from a deficient capillary bed (Dishop 2011).

Lung growth abnormalities can be related to prenatal or postnatal conditions (Deutsch et al. 2007). The most common prenatal form is pulmonary hypoplasia secondary to limited intrathoracic space in utero, such as from a congenital diaphragmatic hernia, oligohydramnios, thoracic mass lesion, or skeletal dysplasia. The most frequently encountered postnatal form is chronic lung disease of infancy (CLDI) related to prematurity. This includes “new” BPD, which is characterized by impaired alveolarization, but less fibrosis and airway obstruction compared to classic BPD (Bhandari and Bhandari 2009), and Wilson-Mikity syndrome, which is characterized by slowly progressive respiratory distress and cyst-like changes of the lungs

developing within the first few weeks of life despite minimal respiratory support at birth (Hoepker et al. 2008; Philip 2009). Growth abnormalities can also be observed in near-term and term infants as an idiopathic disorder or in association with congenital heart disease or certain genetic disorders (Deutsch et al. 2007; Dishop 2010).

Patients with a lung growth abnormality typically present with respiratory difficulty as a neonate, and may either improve or worsen, depending on the extent of catch-up growth of the alveoli over time and whether or not pulmonary hypertension ensues. Most alveolarization occurs by two to three years postnatal age, but recent evidence from hyperpolarized gas magnetic resonance imaging suggests that neo-alveolarization continues to occur throughout childhood and adolescence in normal individuals (Narayanan et al. 2012). Gestational age at birth is an important determinant of subsequent alveolar development (Balinotti et al. 2010), but the capacity for catch-up neo-alveolarization in those with lung growth abnormalities is currently unknown.

The chest imaging findings of infants with BPD and other lung growth abnormalities range from nearly normal to markedly abnormal, with distorted pulmonary lobules of variable shape and attenuation, perilobular reticular opacities, linear subpleural opacities, ground-glass opacities, and foci of decreased lung attenuation, often appearing as cyst-like hyperlucencies (Metwalli et al. 2011) (Fig. 2). The decreased lung attenuation is likely attributable to enlarged alveoli with reduced alveolar septation and vascularization (Mahut et al. 2007). Decreased lung attenuation on CT correlates with the clinical severity of BPD (la Tour et al. 2013). Reproducible quantitative CT scoring systems based on the extent of findings, such as decreased lung attenuation, linear opacities, and architectural distortion at a mean postmenstrual age of 39 weeks show better correlation than do CXR scores with the clinical severity of BPD, and higher CT scores predict a higher risk of rehospitalization for pneumonia (Shin et al. 2013). CT scoring systems are superior to pulmonary function testing for differentiating infants with and without a history of BPD and higher CT scores are associated with a greater number of days on supplemental oxygen (Sarria et al. 2011). Ventilation-perfusion (V/Q) single photon emission computed tomography (SPECT) performed at a mean postmenstrual age of 37 weeks commonly reveals V/Q mismatching, even in clinically mild BPD, and the degree of V/Q mismatching correlates with the duration of mechanical ventilation (Kjellberg et al. 2013). Residual pulmonary abnormalities on CT are very common in adolescent and young adult survivors of classic BPD born in the pre-surfactant era, with the most frequent findings being subpleural, triangular, and linear opacities, air trapping, and emphysema (Aukland et al. 2006; Wong et al. 2008, 2011) (Fig. 3). The imaging findings in adolescent and adult survivors of “new” BPD

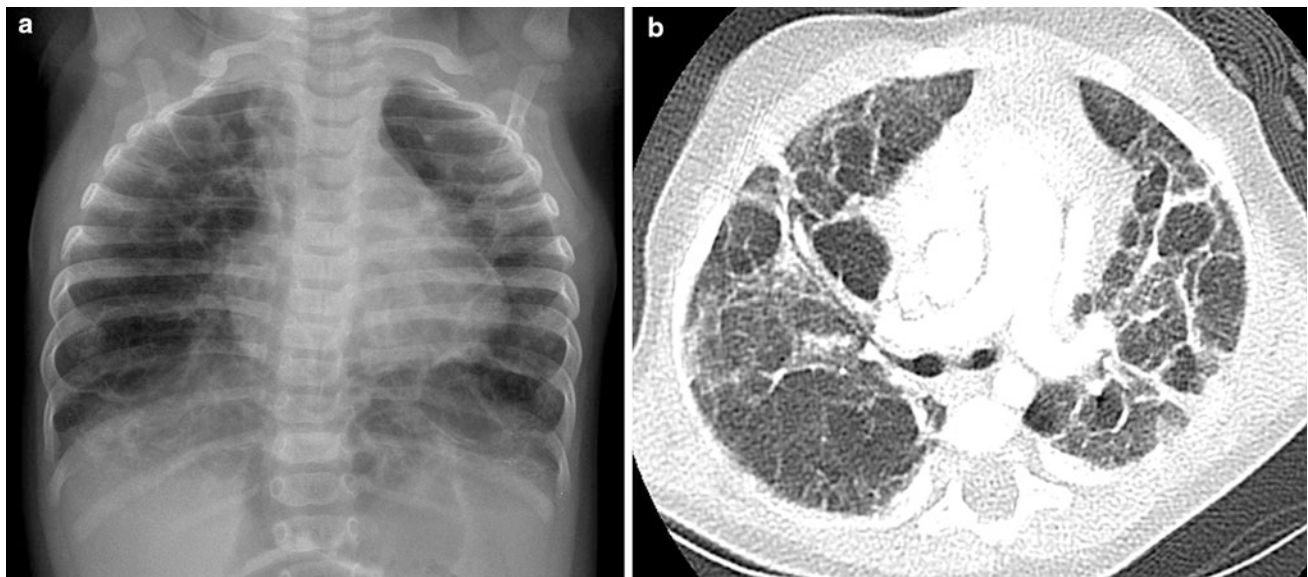


**Fig. 2** Growth abnormality. A frontal CXR (a) of a five-month-old, former 32-week preemie with CLDI and continued supplemental oxygen requirement shows pulmonary hyperinflation, reticular opacities, and cystic changes. An axial chest CT image (b) demonstrates

architectural distortion with ground-glass opacities, thick peribular opacities, and variably-sized pulmonary lobules, some of which exhibit cyst-like hyperlucency related to alveolar simplification

are not yet well described. The imaging findings of BPD are further discussed in the chapter entitled Neonatal Chest Imaging by Crotty in this book.

Down syndrome is associated with a peculiar lung growth abnormality in which the enlargement of the alveoli and alveolar ducts is particularly marked in the subpleural region, resulting in the appearance of subpleural cysts on CT (Biko et al. 2008) (Fig. 4). A lung growth abnormality should be suspected in children with Down syndrome and respiratory difficulties not attributable to congenital heart disease.

A severe progressive lung growth disorder ultimately requiring lung transplantation for survival can develop in infants with X-linked filamin A (*FLNA*) gene mutations. Chest imaging in these patients characteristically shows severe pulmonary hyperinflation and hyperlucency of multiple lobes of the lungs resembling emphysema along with atelectasis and airway malacia. Extrapulmonary manifestations in patients with *FLNA* gene mutations include periventricular nodular gray matter heterotopia, nystagmus, joint hyperextensibility, congenital heart defects, and vascular aneurysms (Guillerman 2010; Masurel-Paulet et al. 2011; de Wit et al. 2011; Guillerman et al. 2013) (Fig. 5).

### 3.3 Specific Disorders of Unknown Etiology

#### 3.3.1 Pulmonary Interstitial Glycogenosis

PIG, previously known as infantile cellular interstitial pneumonitis, is characterized histologically by patchy or diffuse infiltration of the interstitium by vimentin-positive

immature mesenchymal cells containing abundant cytoplasmic glycogen, without prominent inflammation or fibrosis (Smets et al. 2004). PIG has not been observed beyond infancy, suggesting a relationship of PIG to lung development and growth (Deterding 2010; Deutsch and Young 2010). Patchy PIG is often observed concomitantly with a lung growth abnormality (Deutsch et al. 2007), and may contribute to some exacerbations of CLDI (Dishop 2011) or persistent pulmonary hypertension in infants with congenital heart disease (Radman et al. 2013).

Most patients with PIG present in early infancy with tachypnea and a supplemental oxygen requirement. Pulmonary function testing reveals a restrictive lung disease with marked reduction of pulmonary diffusing capacity. The observations that resolution of PIG on histology and improvement in pulmonary diffusion capacity and forced vital capacity coincide with clinical improvement suggest that PIG impairs respiratory function via alveolar septal thickening (Ehsan et al. 2014), although the ultimate clinical outcome primarily depends upon the severity of any underlying lung growth abnormality (King et al. 2011), and no mortality is associated with cases of isolated PIG. Corticosteroid therapy may hasten the resolution of PIG, possibly due to acceleration of lung maturation rather than to suppression of inflammation (Deterding 2010; Deutsch and Young 2010; Canakis et al. 2002; Onland et al. 2005), but should be used judiciously in this self-limited disorder due to the risks of neuro-developmental impairment, immunosuppression, and poor wound healing associated with corticosteroids (Radman et al. 2013).





**Fig. 3** Growth abnormality. A coronal chest CT image from a 15-year-old former preemie with a history of BPD depicts multiple subpleural triangular and linear opacities, and hyperlucent areas resembling emphysema. These findings are commonly observed in adolescent survivors of BPD

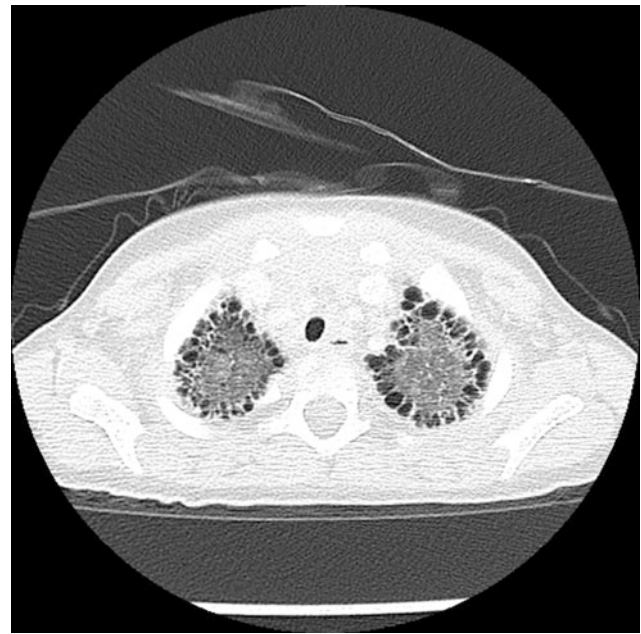


**Fig. 4** Growth abnormality. An axial chest CT image from a two-year-old with Down syndrome shows numerous bilateral subpleural cysts. Enlargement of the alveoli and alveolar ducts is particularly marked in the subpleural region in the lung growth abnormality related to Down syndrome

Reported features of PIG on CXR include hyperinflation and interstitial opacities (Smets et al. 2004; Canakis et al. 2002; Onland et al. 2005; Lanfranchi et al. 2010). Reported features of PIG on CT include pulmonary architectural distortion, interstitial thickening, ground-glass opacities, and hyperlucent areas (Smets et al. 2004; Onland et al. 2005; Lanfranchi et al. 2010; Castillo et al. 2010) (Fig. 6). However, these reports describe findings that are at least in part attributable to coexisting lung growth abnormalities. The imaging appearance of PIG in the absence of a concomitant lung growth abnormality is unknown at present, and lung biopsy is currently required for diagnosis.

### 3.3.2 Neuroendocrine Cell Hyperplasia of Infancy

Neuroendocrine cell hyperplasia of infancy (NEHI), also known as persistent tachypnea of infancy, is characterized histologically by increased numbers of pulmonary neuroendocrine cells (PNECs) and innervated clusters of PNECs called neuroepithelial bodies in the epithelium of the peripheral airways (Deterding et al. 2005). Detection of PNECs on histology is facilitated by special staining for bombesin. PNECs are involved in oxygen sensing and fetal lung development, and rapidly decline in number in normal individuals after the neonatal period. The absence of other significant airway or interstitial disease is an important criterion for the diagnosis of NEHI, since increased numbers of PNECs can also be observed in dissimilar conditions, such

as sudden infant death syndrome, BPD, pulmonary hypertension, cystic fibrosis, mechanical ventilation, and smoke exposure (Dishop 2011). NEHI may be associated with minor patchy inflammation or fibrosis in a small proportion of airways (Young et al. 2010). The existence of familial cases of NEHI suggests a genetic etiology for some cases (Popler et al. 2010). Heterozygous mutations in the NK2 homeobox 1 (*NKX2-1*) gene have been reported in a NEHI case, but are not suspected as the predominant cause of NEHI (Young et al. 2013).

NEHI usually presents by six months of age in full-term infants with persistent tachypnea, hypoxemia, and slow weight gain. There is a male predominance. Auscultation may reveal crackles, but wheezing is unusual. The anteroposterior diameter of the chest is often increased. Symptoms can be precipitated or exacerbated by viral respiratory infections or residence at high altitude (Gomes et al. 2013). Lung function tests show peripheral airway obstruction and profound air trapping with reduced forced expiratory flow (FEV) and markedly elevated functional residual capacity (FRC) and residual volume (RV) (Kerby et al. 2013; Lukkarinen et al. 2013). The severity of air trapping as measured by FRC and RV inversely correlates with room air oxygen saturation at short-term (6–12 months) followup, providing a possible prognostic marker. Compared to BPD patients, NEHI patients have similar degrees of airway obstruction, but greater air trapping (Kerby et al. 2013).



**Fig. 5** Growth abnormality. An axial chest CT inspiratory image (a) from a six-month-old girl with an X-linked filamin A gene mutation demonstrates severe bilateral pulmonary hyperinflation and scattered atelectasis. The corresponding axial chest CT expiratory image (b) reveals narrowing of the trachea related to tracheomalacia. A coronal chest MR angiography image (c) obtained at 2 years of age shows dilation of the ascending aorta and innominate artery

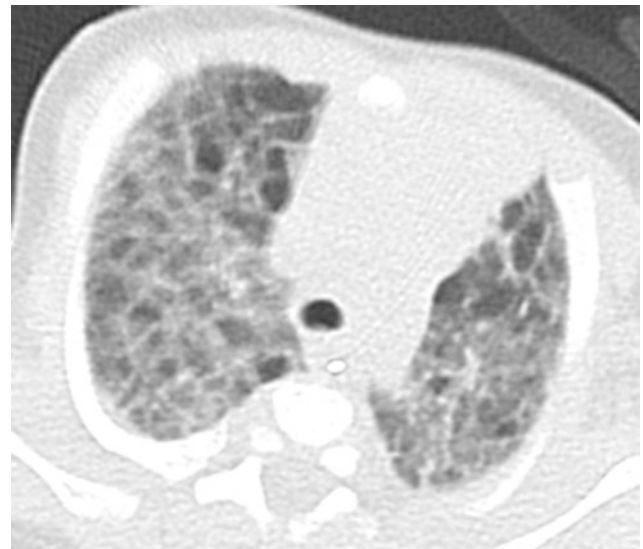


**Fig. 6** Pulmonary interstitial glycogenosis. Axial chest CT image from a 7-week-old, former 29-week preemie with hypoxemia shows both ground-glass opacities and hyperlucent pulmonary lobules. Lung biopsy revealed a growth abnormality with superimposed alveolar wall thickening related to pulmonary interstitial glycogenosis

The severity of airway obstruction correlates with the prominence of PNECs (Young et al. 2010). Treatment is largely supportive and focused on oxygen supplementation and nutritional support. Bronchodilators and corticosteroids have not been shown to be beneficial except for treatment of superimposed viral infections (Kerby et al. 2013; Lukkarinen et al. 2013). NEHI is not a life-threatening condition and most patients show clinical and radiographic improvement, especially after two years of age. However, some patients require supplemental oxygen for months to years, and air trapping and exercise intolerance may persist into adolescence (Deterding 2010; Gomes et al. 2013). The development of nonatopic asthma has also been reported in follow-up (Lukkarinen et al. 2013).

On CXR, NEHI manifests with hyperinflation similar to bronchiolitis or reactive airways disease, but without airway wall thickening. CT findings of diffuse air trapping with mosaic attenuation and geographic ground-glass opacities of the right middle lobe, lingula, parahilar, and paramediastinal lung regions are highly characteristic of NEHI, approaching 100 % specificity in the appropriate clinical setting (Fig. 7). Ground-glass opacities may also be present at the peripheral posterior aspects of the lungs. Consolidation, nodules, septal thickening, cysts, and bronchiectasis are usually absent, and the presence of these findings suggests a superimposed or alternative disorder. NEHI is unable to be excluded by CT, since the sensitivity of CT for NEHI is approximately 80 %, and missed diagnosis may occur when the ground-glass opacities are faint or distributed in an atypical pattern (Brody et al. 2010). Due to variability in the number of PNECs, pathologic confirmation of the diagnosis is not

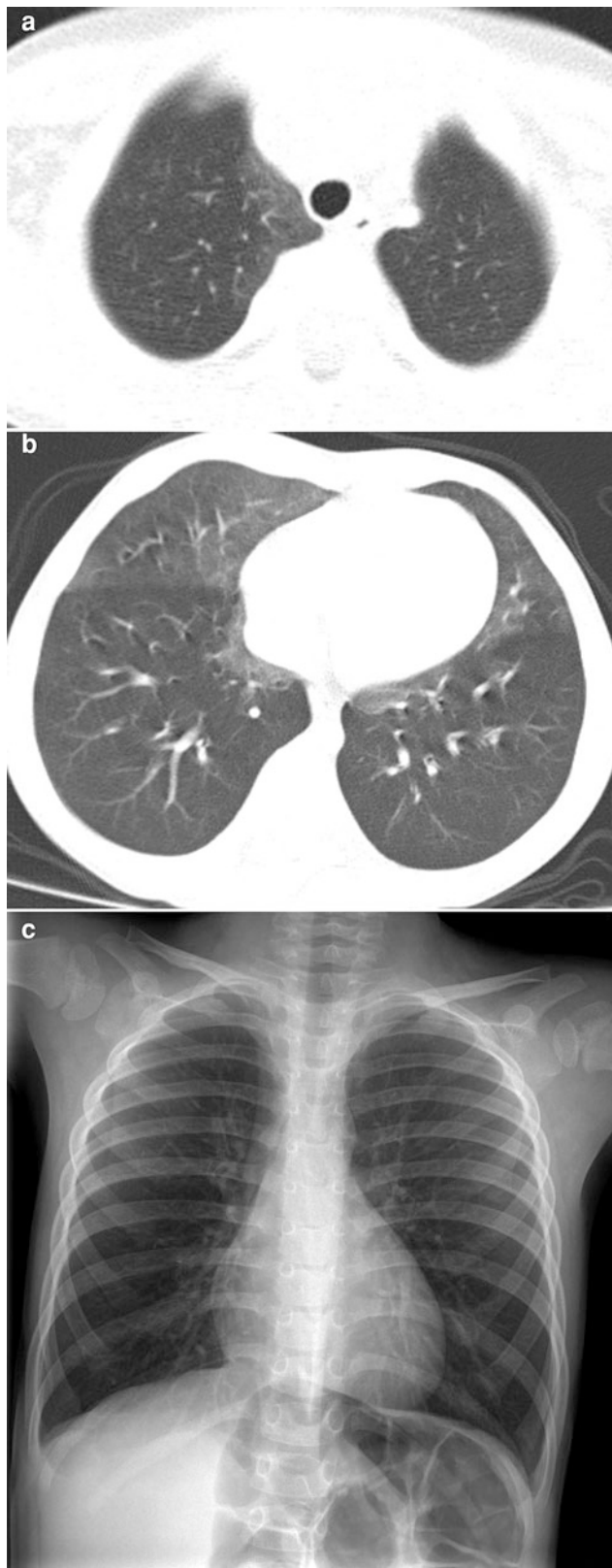


**Fig. 7** Neuroendocrine cell hyperplasia of infancy. Axial chest CT images (**a**, **b**) from a 26-month-old with persistent tachypnea show pulmonary hyperinflation and ground-glass opacities in the right middle lobe, lingula, and paramediastinal regions in a distribution characteristic of neuroendocrine cell hyperplasia of infancy. A frontal CXR (**c**) obtained at 3 years of age shows continued pulmonary hyperinflation

always reliable, especially if airway sampling is limited in the biopsy specimen (Young et al. 2010). A presumptive diagnosis of NEHI can be made without lung biopsy if the clinical presentation and the findings on CT or pulmonary function testing are characteristic (Deterding 2010; Young et al. 2010; Brody et al. 2010; Kerby et al. 2013; Gomes et al. 2013).

### 3.4 Surfactant Dysfunction Disorders

#### 3.4.1 Genetic Disorders of Surfactant Metabolism

Pulmonary surfactant is composed primarily of phospholipids and surfactant proteins secreted by type II alveolar cells. The lowering of intra-alveolar surface tension by surfactant is required for normal respiratory function. Surfactant also plays a role in innate host defense. Surfactant is cleared by uptake into alveolar epithelial cells or alveolar macrophages under stimulation by granulocyte-macrophage colony-stimulating factor (GM-CSF) (Suzuki et al. 2010).

Genetic disorders of surfactant metabolism are a primary cause of unexplained fatal respiratory distress syndrome (RDS) in term neonates, and are increasingly identified as a cause of chronic DLD in older infants, children, and adolescents. The most frequently identified disease-causing mutations involve the genes encoding ATP binding cassette A3 (ABCA3) (Hamvas 2010) and surfactant protein C (SP-C) (Nathan et al. 2012). Other disease-causing mutations may involve the genes encoding surfactant protein B (SP-B), colony-stimulating factor 2 receptor alpha (CSFRA), NK2 homeobox 1 (NKX2-1), and solute carrier family 7 amino acid transporter member 7 (SLC7A7) (Nogee 2010).

In young infants presenting with a genetic disorder of surfactant metabolism, histologic findings usually consist of PAP with diffuse alveolar epithelial hyperplasia and foamy macrophages without hyaline membrane formation. With aging, there tends to be a lesser degree of PAP, and histologic findings of lobular remodeling, cholesterol clefts, variable interstitial fibrosis, and interstitial inflammation develop in a CPI or DIP pattern later in infancy or childhood, or in a NSIP pattern later in childhood or adolescence. Endogenous lipid pneumonia may also be observed. These overlapping histologic patterns limit genotypic-phenotypic correlation, although electron microscopy can be useful for identifying abnormal lamellar bodies that are characteristic of ABCA3 mutations (Dishop 2010).

The typical clinical presentations and imaging findings of the surfactant dysfunction disorders vary with patient's age. Term neonates unable to produce SP-B due to disease-causing biallelic inherited loss-of-function autosomal recessive SP-B gene mutations develop severe RDS within hours of birth. CXRs show diffuse hazy granular pulmonary opacification similar to RDS of prematurity (Fig. 8). However, in contrast to RDS of prematurity, infants with genetic



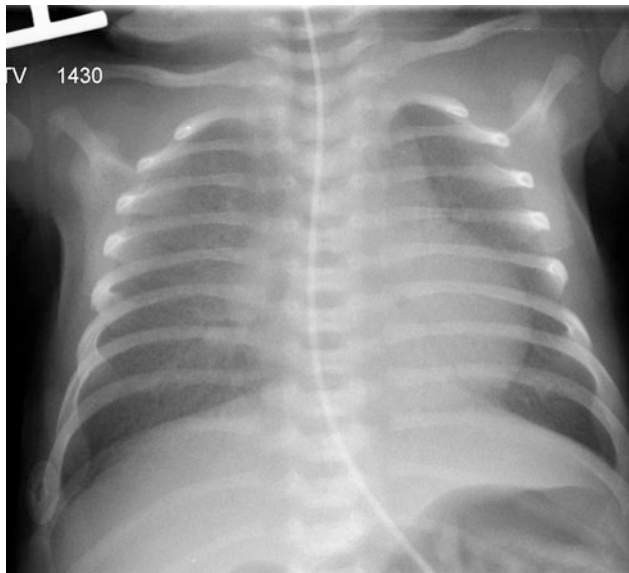
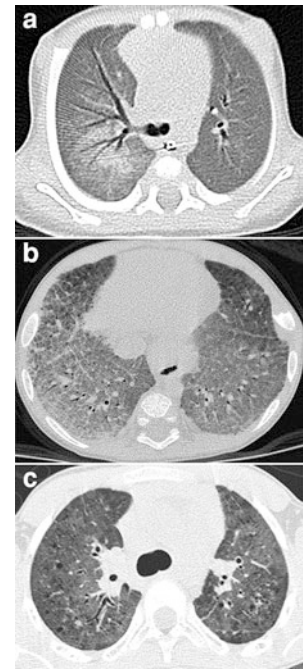


**Fig. 8** Surfactant metabolism disorder related to *SP-B* gene mutation. A frontal CXR of a 12-day-old, full-term infant with respiratory distress demonstrates diffuse hazy granular pulmonary opacities resembling the findings usually associated with surfactant deficiency of prematurity

*SP-B* deficiency progress to respiratory failure that is not ameliorated by exogenous surfactant administration. In the absence of lung transplantation, most die within a few months after birth. In rare cases with mutations that allow some *SP-B* production, longer term survival may be feasible (Nogee 2010; Clement et al. 2010).

Variable phenotypes ranging from acute severe RDS in term neonates to chronic DLD in children and adolescents are associated with spontaneous or inherited autosomal dominant *SP-C* gene mutations (Guillot et al. 2009; Thouvenin et al. 2010) or autosomal recessive *ABCA3* gene mutations (Doan et al. 2008; Flamein et al. 2012). A common clinical presentation of DLD related to *SP-C* or *ABCA3* gene mutations is cough, tachypnea, and hypoxemia beginning in infancy. Alternatively, affected individuals can remain asymptomatic for years despite progressive fibrosis before sudden life-threatening deterioration occurs. Heterozygosity for an *ABCA3* mutation can modify the severity of DLD associated with an *SP-C* mutation (Bullard and Nogee 2007). Interestingly, monoallelic *ABCA3* mutation carriers are overrepresented in infants of >34 weeks gestation age with RDS (Wambach et al. 2012). Treatment with corticosteroids, hydroxychloroquine, or azithromycin may be associated with clinical improvement of patients with genetic disorders of surfactant metabolism, but it is uncertain whether this is entirely due to the therapy or in part to the natural history of the disease, and there are no proven curative therapies except

**Fig. 9** Surfactant metabolism disorder related to *SP-C* gene mutation. An axial chest CT image (a) from a 5-week-old shows diffuse ground-glass opacities and right parahilar consolidation. An axial chest CT image (b) from a five-month-old depicts diffuse ground-glass opacities and septal thickening. An axial chest CT image (c) from a 9-year-old reveals patchy ground-glass opacities and scattered small parenchymal cysts



for lung transplantation in the terminal disease phase (Deterding 2010; Nogee 2010; Thouvenin et al. 2010).

CXRs of young infants with disease-causing *SP-C* or *ABCA3* gene mutations demonstrate diffuse or patchy hazy granular pulmonary opacities, while CT scans show diffuse ground-glass opacities, consolidation, septal thickening, or crazy-paving (Doan et al. 2008; Olsen et al. 2004; Stevens et al. 2005; Prestridge et al. 2006; Soraisham et al. 2006). In older infants and children, the ground-glass opacities tend to decrease and thin-walled cysts develop and increase in number and size with age (Doan et al. 2008; Mechri et al. 2010; Flamein et al. 2012) (Fig. 9). Possibly as an effect of chronic restrictive lung disease on the growing chest wall, pectus excavatum often develops in patients with DLD related to *ABCA3* mutations who survive infancy (Doan et al. 2008). Changes in lung findings on CT do not correlate with lung function or outcome in patients with DLD related to *ABCA3* mutations, and there is no established role for routine chest imaging after the diagnosis has been established (Doan et al. 2008).

Understanding of the spectrum of genetic disorders associated with surfactant dysfunction and pediatric DLD continues to broaden. NK2 homeobox 1 (NKX2-1), also known as thyroid transcription factor-1 (TTF-1), is expressed in the forebrain, thyroid, and lung, and regulates transcription of the genes for surfactant proteins and Clara cell secretory protein. Disease-causing sporadic or inherited autosomal dominant *NKX2-1* gene mutations or deletions



**Fig. 10** Surfactant metabolism disorder related to *NKX2-1* gene mutation. Bilateral patchy ground-glass opacities are shown on an axial chest CT image from a 13-month-old with chorea, hypotonia, hypothyroidism, and chronic pneumonitis of infancy as manifestations of the “brain-lung-thyroid” syndrome

can lead to maldevelopment of the basal ganglia and thyroid and decreased production of surfactant proteins, resulting in “brain-lung-thyroid syndrome” characterized by congenital hypothyroidism, hypotonia, chorea, and lung disease. Only a slight majority of cases manifest with the full syndrome, and there is isolated lung disease in one-fifth of cases at presentation. Mortality related to the lung disease is around 20 % (Carre et al. 2009; Hamvas et al. 2013). Clinical manifestations of the lung disease are varied and illustrate the diverse role *NKX2-1* plays in surfactant function, alveolarization, and innate immunity. The presenting pulmonary phenotype is severe neonatal RDS in about three-fourths of cases and chronic childhood DLD in about one-fifth of cases. Recurrent respiratory infections are also common (Guillot et al. 2010; Hamvas et al. 2013). The histology is heterogeneous, and may include changes of PAP, CPI, DIP, NSIP, or growth abnormality with alveolar simplification. CT findings include diffuse or patchy ground-glass opacities, consolidations, and cysts (Galambos et al. 2010; Hamvas et al. 2013) (Fig. 10). Thyroid ultrasonography or scintigraphy reveals thyroid hypoplasia, hemiagenesis or athyreosis in 45 % of cases (Carre et al. 2009). Intriguingly, a case of NEHI associated with *NKX2-1* mutations has been reported, suggesting that NEHI may result from altered expression of genes regulated by *NKX2-1* other than those in the surfactant system (Young et al. 2013).

Homozygous or compound heterozygous mutations or deletions of the gene encoding colony-stimulating factor 2 receptor alpha (*CSF2RA*), also known as granulocyte-macrophage colony-stimulating factor receptor alpha (*GM-CSFR $\alpha$* ), can severely reduce GM-CSF receptor signaling and impair alveolar macrophage function. This results in PAP

that is characterized by filling of alveoli with surfactant and foamy macrophages and preservation of normal alveolar walls, in contrast to the disorders of surfactant production associated with *SP-B*, *SP-C*, or *ABCA3* mutations, in which alveolar epithelial hyperplasia and lobular remodeling occur. Children with heredity PAP related to *CSF2RA* gene mutations or deletions develop progressive dyspnea, exercise intolerance, or tachypnea at 1–9 years of age, with a mean age of 5 years at symptom onset. The clinical course is often insidious and initial misdiagnosis as asthma or pneumonia is common. Serum and bronchoalveolar (BAL) fluid characteristically show elevated GM-CSF levels. The PAP is typically patchy, leading to patchy pulmonary airspace opacities on CXR and geographic ground opacities and crazy-paving on chest CT (Suzuki et al. 2008; Martinez-Moczygomba et al. 2008; Suzuki et al. 2010). Whole-lung lavage therapy results in clinical and radiographic improvement (Fig. 11), in contrast to patients with disorders of surfactant production who do not respond well to lavage therapy (Suzuki et al. 2010).

Lysinuric protein intolerance (LPI) is a multisystem disease resulting from an inherited defect of cationic amino acid transport attributable to autosomal recessive *SLC7A7* gene mutations. LPI is associated with dietary protein intolerance, failure to thrive, osteoporosis, hepatosplenomegaly, hemophagocytic lymphohistiocytosis, immune dysfunction, nephropathy, and lung involvement (Ogier de Baulny et al. 2012). The lung involvement can occur at any age, including childhood, and is characterized by endogenous lipid pneumonia, PAP, or pulmonary hemorrhage. CT is a sensitive test for diagnosing early lung involvement that manifests as septal thickening, nodules, and subpleural cysts prior to the onset of respiratory symptoms or pulmonary function test abnormalities (Santamaria et al. 1996). Some patients rapidly progress to respiratory failure with widespread pulmonary airspace opacities on CXR and CT related to PAP from alveolar macrophage dysfunction (Parto et al. 1993; Ogier de Baulny et al. 2012). LPI is generally treated with dietary protein restriction and L-citrulline supplementation. The lung involvement can be treated with corticosteroids and whole-lung lavage (Ogier de Baulny et al. 2012).

Recognition of clinical and radiographic findings suggestive of a surfactant dysfunction disorder is important, since the diagnosis may then be confirmed by genetic testing for surfactant gene mutations, avoiding the risk of lung biopsy. Lung biopsy may still be appropriate if genetic testing is nondiagnostic or if awaiting genetic testing results would delay the diagnosis in patients with rapidly progressive disease requiring lung transplantation for continued survival (Doan et al. 2008; Mechri et al. 2010). Occasionally, cases are encountered with imaging and histologic findings suggestive of a surfactant dysfunction disorder, but genetic testing for known disease-causing mutations is negative. Some of these

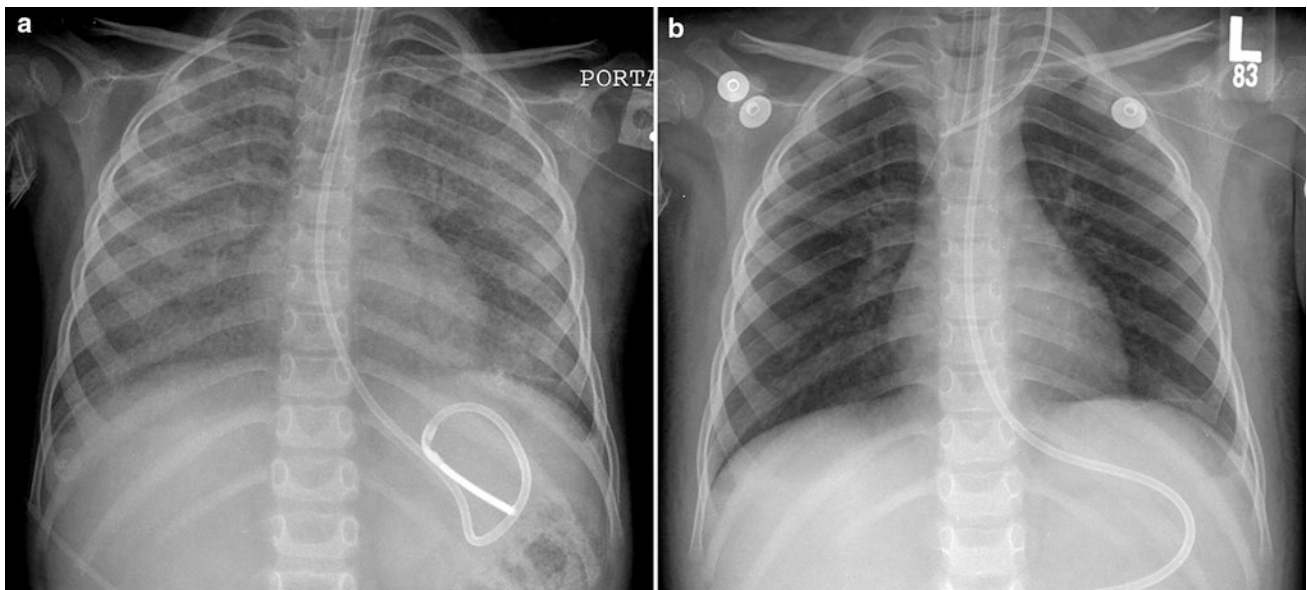


**Fig. 11** Surfactant metabolism disorder related to *CSF2RA* mutation. A frontal CXR (**a**) of a 3-year-old demonstrates diffuse pulmonary airspace opacification. Disrupted GM-CSF receptor signaling in this

genetic disorder results in impaired alveolar macrophage function and pulmonary alveolar proteinosis. Dramatic improvement in lung aeration is shown on a frontal CXR (**b**) following whole-lung lavage

cases are likely related to as yet characterized genetic defects of surfactant metabolism, especially in those with a family history of unexplained childhood-onset DLD.

### 3.4.2 Autoimmune Pulmonary Alveolar Proteinosis

Pediatric PAP is not always attributable to genetic disorders of surfactant metabolism. The catabolism of surfactant by alveolar macrophages can be impaired in multiple acquired conditions, including autoimmune disorders, leukemia, and toxic exposures (Dishop 2010). Autoimmune PAP due to neutralizing autoantibodies to GM-CSF that interfere with alveolar macrophage signaling is the most common cause of sporadic PAP in adults and may present in childhood or adolescence. As with hereditary PAP related to *CSF2RA* genetic defects, the CT findings include ground-glass opacities, septal thickening, and crazy-paving (Fig. 12). CT can be used to monitor the response of autoimmune PAP to therapy with whole-lung lavage and aerosolized GM-CSF (Robinson et al. 2009).

### 3.5 Disorders Related to Systemic Disease Processes

A large, diverse group of systemic disease processes is associated with pediatric DLD. These include vasculitis, connective tissue diseases, granulomatous disorders, lymphoid hyperplasia and lymphoproliferative disorders, primary and secondary immunodeficiencies, lysosomal storage

disorders, and Langerhans cell histiocytosis. The clinical presentations and imaging appearances of these disease processes are covered in the chapter entitled Thoracic Manifestations of Systemic Diseases by Holland, Guillermin, and Brody in this book.

### 3.6 Disorders of the Normal Immunocompetent Host

#### 3.6.1 Bronchiolitis Obliterans

The clinical syndrome of bronchiolitis obliterans (BO) is characterized histologically by constriction or obliteration of the lumens of small airways by a fibroblastic reparative response to injury. The inciting event is typically a respiratory infection (especially adenovirus, influenza virus, or *Mycoplasma pneumoniae*) with extensive airway mucosal necrosis. Other preceding conditions include Stevens-Johnson syndrome, toxic inhalational injury, graft-versus-host disease, and chronic airway rejection in the setting of lung transplantation (Dishop 2010). There is a predominance of male patients. The time interval between infection and symptoms and signs of obstructive lung disease, such as wheezing, tachypnea, and dyspnea is variable and can be as short as a few months, although the diagnosis after onset of symptoms is often delayed for many months (Lino et al. 2013).

CXRs in patients with BO often show hyperinflation, but CXRs are generally nonspecific and insensitive. Characteristic findings of post-infectious pediatric BO on CT include increased lung volume, bronchiectasis, bronchial



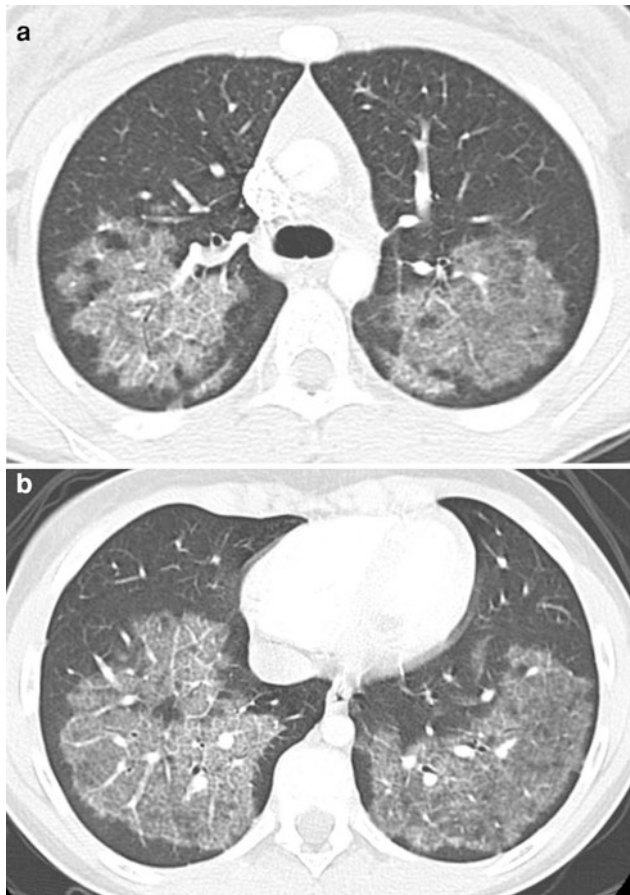
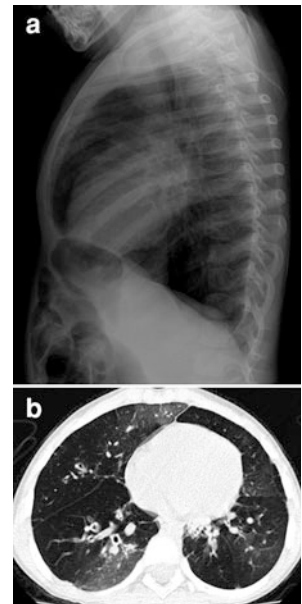


**Fig. 12** Surfactant metabolism disorder related to autoantibodies to GM-CSF. Axial chest CT images (**a**, **b**) from an 11-year-old show geographic ground-glass opacities and crazy-paving. Autoantibodies to GM-CSF in this autoimmune disorder result in impaired alveolar macrophage function and pulmonary alveolar proteinosis

wall thickening, mosaic attenuation, parenchymal hyperlucency, pulmonary vascular attenuation, and expiratory air trapping (Yalcin et al. 2003; Zhang et al. 1999; Bandeira et al. 2011; Lino et al. 2013) (Fig. 13). Hyperlucency, mosaic attenuation, air trapping, and bronchiectasis tend to be more marked in BO than in problematic severe asthma (Bandeira et al. 2011). The combination of a typical clinical history, adenovirus infection, and mosaic attenuation on CT is highly specific for post-infectious BO in young children (Colom and Teper 2009). CT offers the ability to survey the entire lungs, while the heterogeneous distribution of airway involvement in BO poses the risk of a false-negative biopsy from inadequate tissue sampling (Moonnumakal and Fan 2008). A confident diagnosis of BO can be made without the need for lung biopsy in the setting of a child with a suggestive clinical presentation, a fixed obstructive pattern on pulmonary function testing, and characteristic CT findings. The combination of pulmonary vascular attenuation and hyperlucency on CT is highly specific for moderate or

**Fig. 13** Bronchiolitis obliterans. A lateral CXR (**a**) of a 4-year-old with a history of influenza, respiratory syncytial virus, and *Mycoplasma pneumoniae* shows marked pulmonary hyperinflation with diaphragmatic flattening and widening of the retrosternal clear space. A corresponding axial chest CT image (**b**) reveals bronchiectasis, bronchial wall thickening, mosaic attenuation, and pulmonary vascular attenuation in hyperlucent regions



severe nontransplant BO in children (Smith et al. 2011). However, the sensitivity of CT for moderate or severe nontransplant BO in children is only modest, so that CT cannot exclude BO (Smith et al. 2011). CT is valuable as a prognostic tool since severe abnormalities on CT in children under three years of age with post-infectious BO predict poor lung function several years later (Mattiello et al. 2010).

Swyer-James-MacLeod syndrome is a variant of BO that typically presents with a hyperlucent hypovascular lung of small or normal volume on CXR several months or a few years after the inciting infection. In about a half of cases of Swyer-James-MacLeod syndrome, the findings of BO are actually found to be bilateral if CT is performed (Lucaya et al. 1998).

### 3.6.2 Eosinophilic Pneumonia

The eosinophilic lung diseases are a diverse group of disorders that are often, but not always, associated with peripheral eosinophilia. These disorders can be acute or chronic, idiopathic or secondary to parasitic infections or drug reactions, and isolated to the lungs or involve extra-pulmonary tissues. In addition to suggesting the diagnosis of an eosinophilic lung disease, imaging can be useful in assessing the response to therapy (Oermann et al. 2000). The thoracic imaging findings vary with the type of disorder.

Simple eosinophilic pneumonia is often related to drug reaction or parasitic infection, but can be idiopathic. Affected patients can have cough, fever, dyspnea, and hypoxia, although some are asymptomatic. Imaging demonstrates patchy pulmonary ground-glass opacities or consolidations that are often migratory and peripheral (Fig. 14). Clinical and radiographic improvement usually occurs

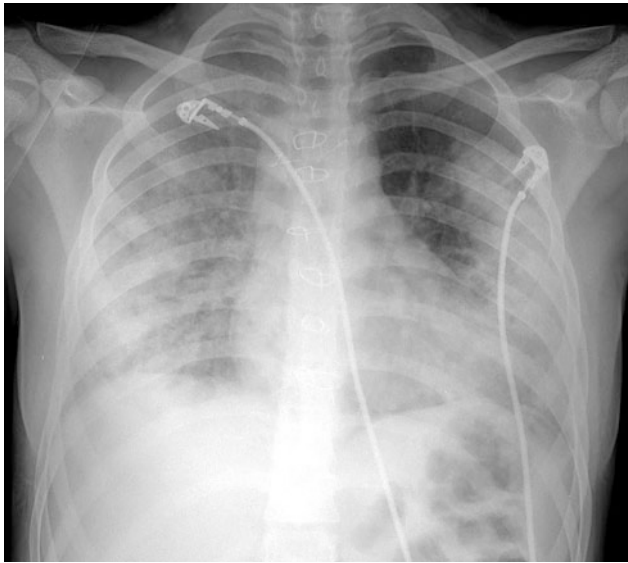


**Fig. 14** Drug-induced eosinophilic pneumonia. A frontal CXR of a 17-year-old with acute hypoxemia and a history of lung transplantation for cystic fibrosis shows extensive bilateral pulmonary airspace opacities that are most pronounced peripherally. BAL lavage demonstrated increased eosinophils. The pneumonia resolved after discontinuation of the inciting drug, doxycycline

promptly after discontinuation of the inciting drug, although corticosteroids may be administered in severe or persistent cases.

The findings of airspace opacities, septal thickening, and pleural effusions typical of idiopathic acute eosinophilic pneumonia (AEP) can be misconstrued as pulmonary edema. A presumptive diagnosis of AEP can be made without biopsy in children with these imaging findings, fever, acute respiratory failure requiring ventilatory support, and marked eosinophilia on BAL (Vece and Fan 2011). Some cases of AEP are thought to be precipitated by exposure to irritants such as smoke. Treatment with corticosteroids usually results in rapid clinical improvement and resolution of radiographic abnormalities.

Idiopathic chronic eosinophilic pneumonia (CEP) is characterized by peripherally-predominant consolidation or ground-glass opacities, marked eosinophilia in BAL fluid or peripheral blood, respiratory symptoms for greater than 4 weeks, and absence of other known causes of eosinophilic lung disease. The diagnosis can also be made with consistent lung biopsy findings in cases without clinical and radiographic improvement after first-line corticosteroid treatment. Many cases of idiopathic CEP are initially misdiagnosed as asthma, and a subset of persistent cases develop reticulonodular interstitial opacities and cysts (Giovannini-Chami et al. 2014).

Idiopathic hypereosinophilic syndrome (IHES) predominantly affects males and is characterized by prolonged



**Fig. 15** Bronchocentric granulomatosis. An axial chest CT image from a 2-year-old depicts multiple, airway-centric, nodular, and short tubular opacities in the right lung related to granulomatous lesions along the airways with endoluminal plugging

eosinophilia and multiorgan damage (especially of the lungs, skin, heart, and nervous system) due to eosinophilic infiltration. Nodules with ground-glass halos are seen in IHES. Allergic bronchopulmonary aspergillosis (ABPA) is characterized by asthma and noninvasive colonization of dilated airways by *Aspergillus*. There may also be patchy peribronchial eosinophilic pneumonia. Imaging shows central bronchiectasis with or without mucoid impaction. Bronchocentric granulomatosis (BCG) develops as an abnormal cell-mediated response to *Aspergillus* and may be part of the spectrum of ABPA or occur as an isolated disorder. BCG is characterized by destructive granulomatous lesions along the bronchi and bronchioles with intraluminal inspissations and surrounding eosinophilic pneumonia, resulting in airway-centric nodular, “sausage-like,” or consolidative opacities on imaging (Jeong et al. 2007; Kradin and Mark 2008) (Fig. 15). Eosinophilic granulomatosis with polyangiitis (EGPA), formerly known as Churg-Strauss syndrome, is a life-threatening systemic necrotizing vasculitis that commonly involves the lungs, upper airway, musculoskeletal system, gastrointestinal system, nervous system, skin, and heart. Subpleural consolidation, centrilobular nodules, bronchial wall thickening, and septal thickening are typical pulmonary imaging manifestations of EGPA (Gendelman et al. 2013).

### 3.6.3 Hypersensitivity Pneumonitis

Hypersensitivity pneumonitis is characterized on histology by lymphocytic infiltration of the bronchioles and adjacent interstitium, with giant cells and poorly formed non-necrotizing granulomas distributed around the bronchioles.

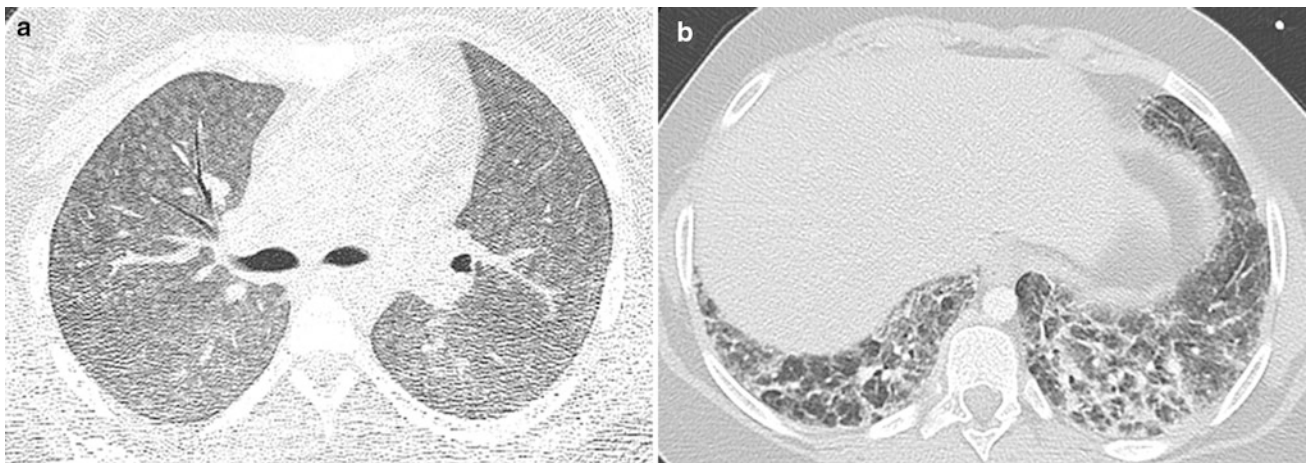


**Fig. 16** Hypersensitivity pneumonitis. An axial chest CT image (a) from a 14-year-old with cough and repetitive bird exposure reveals diffuse centrilobular nodular ground-glass opacities typical of the subacute phase. An axial chest CT image (b) from a 10-year-old with

fatigue and repetitive bird exposure shows coarse reticular opacities and architectural distortion at the lung bases compatible with fibrosis in the chronic phase

A NSIP pattern with interstitial fibrosis and cystic remodeling may be observed in the chronic setting (Dishop 2010). Birds, pets, and molds are the most common precipitating agents in children. Other causes include highly reactive low-molecular-weight compounds in spray paints, epoxy resins, glues, and insecticides, as well as drugs such as methotrexate (Vece and Fan 2010). There is a mean lag time of 11 months from symptom onset to diagnosis, and a meticulous environmental exposure history is a crucial step in the clinical evaluation. The most common symptom is dyspnea with exercise, followed by dyspnea at rest, dry cough, and weight loss. CXRs are limited in sensitivity, being normal in over one-third of cases at initial presentation (Buchvald et al. 2011). The absence of serum-precipitating antibodies does not exclude the diagnosis (Clement et al. 2010; Vece and Fan 2010). A presumptive diagnosis without biopsy can be made in children with an exposure history and positive precipitins, lymphocytosis on BAL, and typical findings on CT (Vece and Fan 2011). Consolidation and ground-glass opacities that can mimic infection or edema are typical on CT in the acute phase. Ill-defined centrilobular nodules, ground-glass opacities, and low attenuation foci of air trapping are characteristic of the subacute phase. Irregular linear or reticular opacities, architectural distortion, and honeycombing indicative of fibrosis can be observed in the chronic phase (Fig. 16). If there is ongoing exposure to the inciting antigen, there can be findings of multiple phases superimposed. The imaging findings associated with the acute and subacute phases usually regress after treatment with corticosteroids and elimination of exposure to the offending antigen, but fibrosis from the chronic phase may persist (Hartman 2003; MacDonald and Müller 2003; Buchvald et al. 2011).

### 3.6.4 Aspiration Pneumonia

While most common in the setting of profound neuromuscular or developmental disorders, silent aspiration can also occur in otherwise healthy children. If unrecognized and untreated, recurrent aspiration can lead to unexplained DLD. The associated clinical signs and symptoms of cough, tachypnea, and fever are nonspecific. The presence of increased lipid-laden macrophages on BAL or lung biopsy is also not specific for aspiration, as this can be observed with other conditions, such as resolving hemorrhage, pneumonia, and surfactant disorders. CT can play an important role in suggesting the correct diagnosis. The findings of bronchiectasis and tree-in-bud centrilobular opacities, especially in dependent lung regions, are suggestive of aspiration. Exogenous lipid pneumonia, most frequently noted in children administered mineral oil for chronic constipation, manifests with consolidation, ground-glass opacities, and crazy-paving on CT (Fig. 17). The finding of fatty attenuation in the lungs as a sign of lipid pneumonia on CT is of limited value since it may be either obscured or simulated by volume averaging of nonfatty inflammatory exudate and air (Zanetti et al. 2007; Marchiori et al. 2010).

### 3.6.5 Acute Interstitial Pneumonia

Diffuse alveolar damage (DAD) is a histopathologic pattern with an exudative phase characterized by edema, hyaline membranes, and interstitial acute inflammation, and an organizing phase characterized by loose organizing fibrosis, alveolar wall thickening, type II pneumocyte hyperplasia, and alveolar collapse. The term diffuse in DAD refers to involvement of all constituents of the alveolar wall, and there are often patchy areas of spared lung (Kligerman et al. 2013). DAD is a nonspecific reaction to variety of insults and can be





**Fig. 17** Aspiration pneumonia. Axial chest CT image from a 17-year-old shows widespread crazy-paving from exogenous lipoid pneumonia related to repetitive aspiration of mineral oil administered for constipation

associated with acute respiratory distress syndrome (ARDS), infection (especially CMV or *Pneumocystis*), toxic inhalation, drug reaction, bone marrow transplantation, primary graft dysfunction in lung transplant recipients, and idiopathic acute interstitial pneumonia (AIP).

AIP has a rapidly progressive course leading to respiratory failure, and can occur in previously healthy children (Liu et al. 2011). The typical CT findings of AIP are patchy or geographic ground-glass opacities and dependent consolidation, followed by architectural distortion and traction bronchiectasis (Bouros et al. 2000). The differential diagnosis includes infectious pneumonia, pulmonary edema, pulmonary hemorrhage, PAP, and AEP (Fan et al. 2004). Although the abnormal pulmonary findings on imaging can resolve, many patients are left with residual fibrosis that is most pronounced in the nondependent portions of the lung (Fig. 18), possibly related to protection of the collapsed dependent lung from oxygen toxicity and barotrauma incurred during treatment (Kligerman et al. 2013).

### 3.6.6 Cryptogenic Organizing Pneumonia

Organizing pneumonia is characterized histologically by fibroblastic tissue in the distal bronchioles, alveolar ducts, and alveoli. Organizing pneumonia in children can be idiopathic or secondary to processes that incite a reparative response in the lung, such as infection, aspiration pneumonia, autoimmune disease, asthma, drug reaction, chemotherapy, and bone marrow transplantation (Fan et al. 2004). When idiopathic, it is termed cryptogenic organizing pneumonia (COP). The typical clinical presentation of COP is a subacute illness with nonproductive cough and dyspnea. The appearance of COP on CT is highly variable, with the most frequent pattern consisting of peripheral or peribronchovascular patchy consolidation with or without surrounding ground-glass

opacities. Air bronchograms and mild bronchial dilation are common within the sites of consolidation, which can be migratory. Other patterns include the “atoll” or “reverse halo” sign (central ground-glass opacity surrounded by a ring of consolidation), peribular thickening, and arciform or band-shaped subpleural opacities (Polverosi et al. 2006) (Fig. 19). A majority of cases of COP recover completely with corticosteroid treatment, but some cases may relapse or undergo progressive fibrosis resulting in reticular opacities and traction bronchiectasis resembling NSIP (Travis et al. 2013; Kligerman et al. 2013).

### 3.6.7 Idiopathic Nonspecific Interstitial Pneumonia

Despite the misleading name, NSIP is a distinct clinical entity characterized histologically by spatially and temporally uniform interstitial thickening with a varying spectrum of cellular to fibrosing patterns (Travis et al. 2008). In children, it can be idiopathic or associated with autoimmune connective tissue disorders, familial pulmonary fibrosis, genetic disorders of surfactant metabolism, or chronic hypersensitivity pneumonitis. The most common symptoms are dyspnea and cough. The most frequently observed findings on CT are peripheral or diffuse ground-glass and fine linear or reticular opacities predominantly involving the lower lung zones. Cysts, traction bronchiectasis, volume loss, and honeycombing may develop over time (Fig. 20). NSIP can resolve, remain stable, or progress (Kligerman et al. 2009).

### 3.6.8 Idiopathic Pulmonary Hemosiderosis

Idiopathic pulmonary hemosiderosis (IPH) is characterized by BAL showing abundant hemosiderin-laden macrophages and lung biopsy showing “bland” pulmonary hemorrhage without vasculitis. The median age at diagnosis is 4 years and the most common clinical manifestations are dyspnea and anemia. Hemoptysis occurs in no more than half of cases, and delay in diagnosis is common (Taytard et al. 2013). Other disorders capable of causing pulmonary hemorrhage, such as respiratory tract infections, airway neoplasms, bronchiectasis, coagulopathies, pulmonary venous hypertension, and pulmonary arteriovenous malformations, should be excluded before a diagnosis of IPH is made. IPH is associated with cow’s milk allergy (Heiner syndrome) (Moissidis et al. 2005), celiac disease (Lane-Hamilton syndrome) (Hendrickx et al. 2011), and Down syndrome (Taytard et al. 2013). Imaging findings can include airspace opacities, nodules, septal thickening, cysts, and honeycombing (Fig. 21). CT is useful for monitoring the response to therapy with corticosteroids or other immunosuppressants. Lung biopsy is advocated for children with anemia and pulmonary opacities, hemoptysis, or hemosiderin-laden macrophages on BAL, even in the absence of anti-neutrophil cytoplasmic antibodies (ANCA),

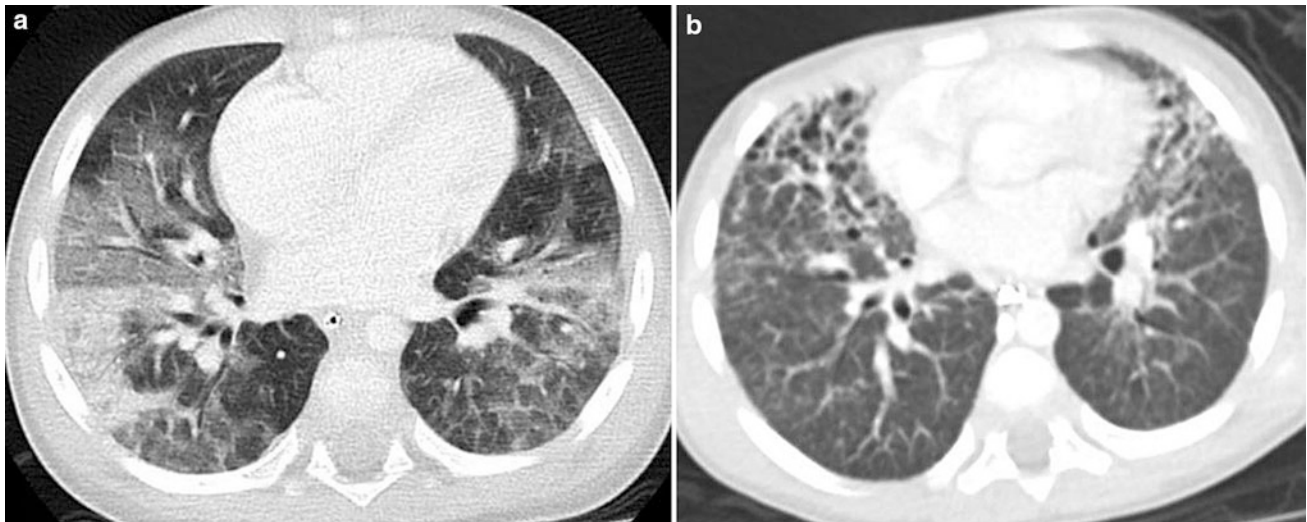
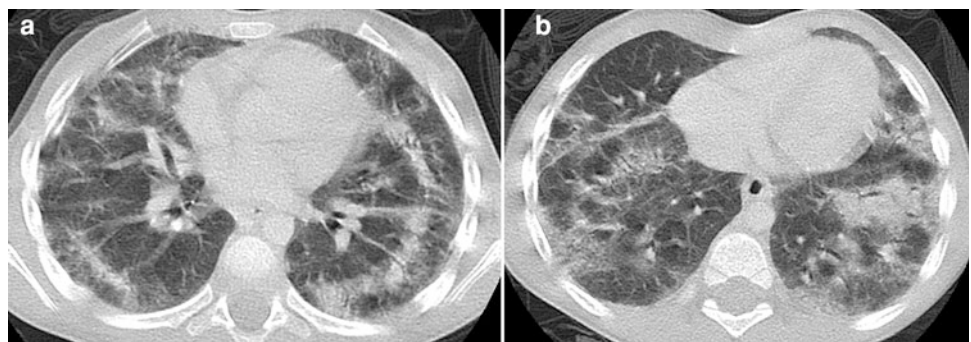


**Fig. 18** Acute interstitial pneumonia. An axial chest CT image (a) from a 2-year-old with fever and acute respiratory failure shows patchy bilateral ground-glass opacities and consolidation related to

diffuse alveolar damage. An axial chest CT image (b) obtained 3 weeks later reveals traction bronchiectasis and architectural distortion of the anterior nondependent lung regions related to fibrosis

**Fig. 19** Cryptogenic organizing pneumonia. Axial chest CT images (a, b) from a 3-year-old with hypoxemia depicts peripheral arciform and patchy peribronchial foci of consolidation



since many of these patients will have capillaritis that confers a worse prognosis than IPH (Vece and Fan 2011). Pulmonary capillaritis is further discussed in the chapter entitled Thoracic Manifestations of Systemic Diseases by Holland, Guillerman, and Brody in this book.

### 3.7 Vascular Disorders Masquerading as Diffuse Lung Disease

The chILD Research Cooperative classification (Deutsch et al. 2007) and expanded chILD classification (Rice et al. 2013) acknowledge the presence of certain vascular disorders with clinical and imaging features that can mimic childhood DLD. These includes disorders such as congestive heart failure, cor triatriatum, congenital mitral stenosis, anomalous pulmonary venous return, pulmonary vein stenosis, pulmonary vein atresia, and pulmonary veno-occlusive disease (PVOD) that are associated with transudative pulmonary

edema from pulmonary venous congestion or obstruction. Also included are disorders such as lymphangiectasia and lymphangiomatosis that are associated with impaired clearance of interstitial lung fluid.

#### 3.7.1 Pulmonary Veno-Occlusive Disease

PVOD is characterized by fibrous obstruction of the post-capillary pulmonary septal veins and pre-septal venules, resulting in pulmonary hypertension, transudative pulmonary edema, and capillary proliferation. PVOD can be idiopathic or associated with connective tissue disease, HIV infection, organ transplantation, chemotherapy, or toxic exposures. Patients with PVOD often present with progressive dyspnea with exertion, and delay in diagnosis is common (Woerner et al. 2014). Typical features of PVOD include normal pulmonary capillary wedge pressure, low pulmonary diffusing capacity, hypoxemia at rest, desaturation with exercise, and occult alveolar hemorrhage on BAL.



**Fig. 20** Nonspecific interstitial pneumonia. An axial CT image from a 13-year-old with cough and a family history of pulmonary fibrosis demonstrates peripheral fine, linear, and ground-glass opacities bilaterally along with scattered tiny cysts and volume loss of the left lung

Characteristic findings of PVOD on CT include smooth septal thickening, lobular ground-glass opacities, pleural effusions, enlargement of mediastinal and hilar lymph nodes, enlargement of the central pulmonary arteries and right heart chambers, and normal appearance of the main pulmonary veins and left heart chambers (Frazier et al. 2007; Montani et al. 2009; Woerner et al. 2014) (Fig. 22). PVOD accounts for 5–10 % of cases initially suspected as idiopathic pulmonary arterial hypertension (PAH) (Montani et al. 2009). It is crucial not to misdiagnose PVOD as idiopathic PAH since the vasodilators used to treat PAH patients can induce fulminant pulmonary edema in patients with PVOD. Pulmonary artery enlargement and mosaic lung attenuation can be seen in either PVOD or PAH, but septal thickening, lobular ground-glass opacities, lymphadenopathy, and pleural effusions are typical of PVOD, but not PAH (Frazier et al. 2007). A presumptive diagnosis of PVOD can be made on the basis of characteristic findings of CT, arterial blood gases, pulmonary function testing, and BAL, thereby avoiding high-risk lung biopsy in these patients. Early recognition is crucial, since PVOD has a poor prognosis with a mean reported survival time of only 14 months after diagnosis, and lung transplantation is the only curative therapy (Montani et al. 2009; Woerner et al. 2014).

### 3.7.2 Pulmonary Lymphangiectasia

Pulmonary lymphangiectasia is characterized histologically by dilation of the lymphatics draining the interstitial and subpleural spaces. Pulmonary lymphangiectasia can be a primary disorder or occur secondary to lymphatic congestion from conditions associated with excessive lung fluid accumulation such as congestive heart failure or obstructed pulmonary veins. Pulmonary lymphangiectasia can also be present as part of the histologic findings in alveolar capillary dysplasia with misalignment of the pulmonary veins

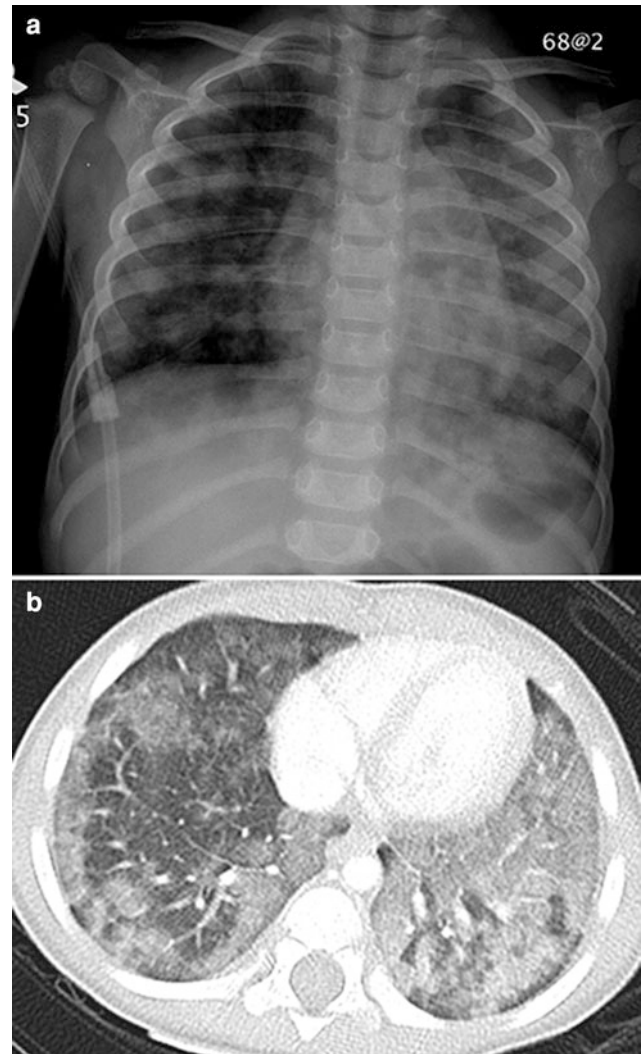


**Fig. 21** Idiopathic pulmonary hemosiderosis. A frontal CXR (a) of a 1-year-old with anemia and a corresponding axial chest CT image (b) show patchy pulmonary airspace opacities, more extensive on the left, related to intra-alveolar pulmonary hemorrhage

(ACD/MPV) (Dishop 2011). Pulmonary lymphangiectasia is most often sporadic, but can be associated with genetic disorders, such as Noonan syndrome, yellow nail syndrome, Knobloch syndrome, Urioste syndrome, and mandibulofacial dysostosis. The primary form is typically congenital and may be accompanied by nonimmune hydrops fetalis, congenital chylothorax, or generalized lymphedema (Bellini et al. 2006). Primary pulmonary lymphangiectasia classically presents in a term neonate with severe respiratory distress, tachypnea, cyanosis, and diffuse hazy opacification of the lungs on CXR resembling the findings of surfactant deficiency of prematurity or a genetic disorder of surfactant metabolism. CT reveals smooth septal thickening, bronchovascular bundle thickening, patchy ground-glass opacities, and pleural effusion (Esther and Barker 2004). The pulmonary opacities and septal



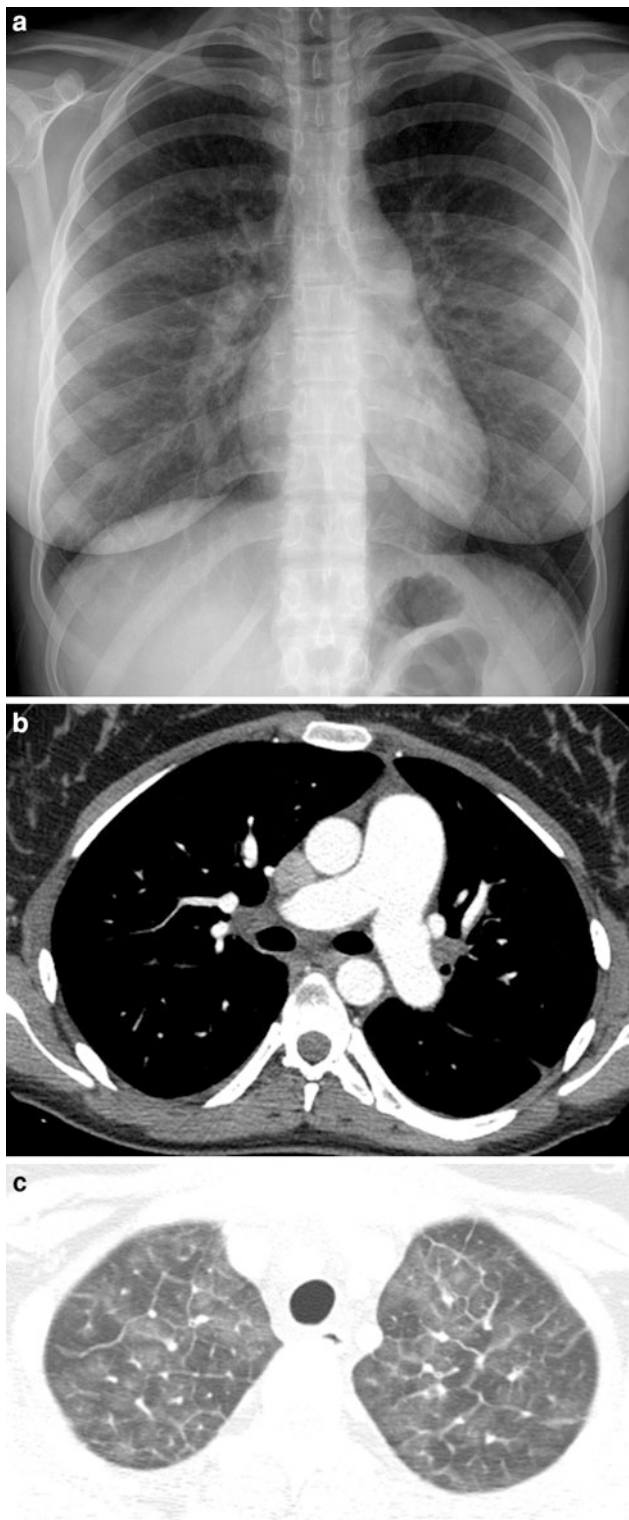


**Fig. 22** Pulmonary veno-occlusive disease. A frontal CXR (a) of an 18-year-old with progressive dyspnea on exertion shows main pulmonary enlargement and subtle Kerley B lines at the lateral lung bases. Axial chest CT images (b, c) confirm the presence of pulmonary artery enlargement and interlobular septal thickening, and reveal mild hilar lymph node enlargement and a tiny pleural effusion

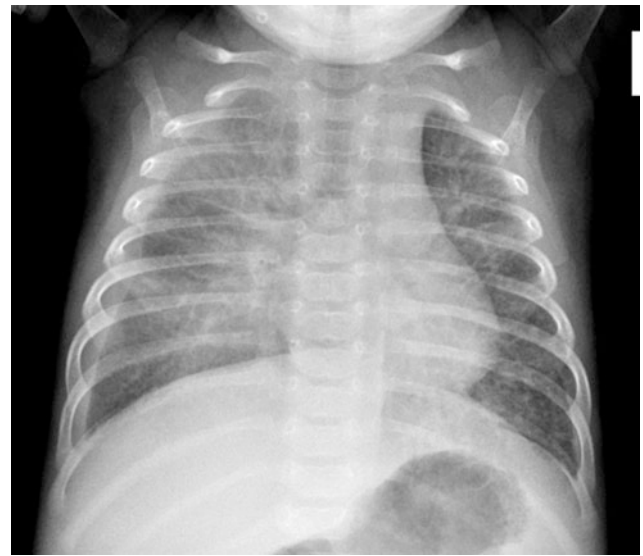


**Fig. 23** Pulmonary lymphangiectasia. A frontal CXR of a 2-month-old with a history of congenital chylothorax demonstrates diffuse pulmonary interstitial thickening, pleural effusion, and a normal-sized heart

thickening become less marked, and hyperinflation develops in those surviving infancy or presenting later in childhood (Barker et al. 2004) (Fig. 23). Treatment of primary pulmonary lymphangiectasia is generally supportive, and the overall prognosis is poor (Mettauer et al. 2009).

Pulmonary lymphangiectasia can be confused for lymphangiomatosis. In lymphangiomatosis, there is proliferation of complex anastomosing lymphatic channels with secondary dilation of the lymphatics. Septal thickening, ground-glass opacities and chylous effusions are observed in both lymphangiomatosis and lymphangiectasia. In contrast to lymphangiectasia, lymphangiomatosis tends to present later in childhood and involve extrapulmonary tissues, with lytic bone lesions and mediastinal soft tissue edema being particularly distinctive (Faul et al. 2000; Swenson et al. 1995; Shah et al. 2011). Lymphangiomatosis is further discussed in the chapter entitled Pulmonary and Extrathymic Mediastinal Tumors by Lyons, Guillerman, and McHugh in this book.

### 3.8 Conclusion

Pediatric DLD comprises a diverse group of disorders with widespread involvement of the pulmonary interstitium, distal airspaces, or peripheral airways resulting in impaired gas exchange and, in some cases, high morbidity and mortality. A novel classification scheme specific for pediatric DLD has been devised, acknowledging the effect of the stage of lung

growth and development on disease manifestations, and incorporating recent insights into the etiology, pathophysiology, genetics, and clinical phenotypes of these disorders, some of which are unique to infants and young children. Familiarity with the classification, clinical presentation, and characteristic imaging features is required for appropriate diagnosis and management of pediatric DLD.

## References

- Aukland SM, Halvorsen T, Fosse KR, Daltveit AK, Rosendahl K (2006) High-resolution CT of the chest in children and young adults who were born prematurely: findings in a population-based study. *AJR Am J Roentgenol* 187:1012–1018
- Balinotti JE, Chakr VC, Tiller C, Kimmel R, Coates C, Kisling J, Yu Z et al (2010) Growth of lung parenchyma in infants and toddlers with chronic lung disease of infancy. *Am J Respir Crit Care Med* 181:1093–1097
- Bandeira T, Negreiro F, Ferreira R, Salguero M, Lobo L, Aguiar P, Trindade JC (2011) Clinical, radiological, and physiological differences between obliterative bronchiolitis and problematic severe asthma in adolescents and young adults: the early origins of the overlap syndrome? *Pediatr Pulmonol* 46:573–580
- Barker PM, Esther CR Jr, Fordham LA, Maygarden SJ, Funkhouser WK (2004) Primary pulmonary lymphangiectasia in infancy and childhood. *Eur Respir J* 24:413–419
- Bellini C, Boccardo F, Campisi C, Bonioli E (2006) Congenital pulmonary lymphangiectasia. *Orphanet J Rare Diseases* 1:43
- Bhandari A, Bhandari V (2009) Pitfalls, problems, and progress in bronchopulmonary dysplasia. *Pediatrics* 123:1562–1573
- Biko DM, Schwartz M, Anupindi SA, Altes TA (2008) Subpleural lung cysts in Down syndrome: prevalence and association with coexisting diagnoses. *Pediatr Radiol* 38:280–284
- Bouros D, Nicholson AC, Polychronopoulos V, du Bois RM (2000) Acute interstitial pneumonia. *Eur Respir J* 15:412–418
- Brody AS, Guilleman RP, Hay TC, Wagner BD, Young LR, Deutsch GH, Fan LL et al (2010) Neuroendocrine cell hyperplasia of infancy: diagnosis with high-resolution CT. *AJR* 194:1–7
- Buchvald F, Petersen BL, Damgaard K, Deterding R, Langston C, Fan LL, Deutsch GH et al (2011) Frequency, treatment, and functional outcome in children with hypersensitivity pneumonitis. *Pediatr Pulmonol* 46:1098–1107
- Bullard JE, Noguee LM (2007) Heterozygosity for ABCA3 mutations modifies the severity of lung disease associated with a surfactant protein C gene (SFTPC) mutation. *Pediatr Res* 62:176–179
- Canakis AM, Kutz E, Manson D, O'Brodovich H (2002) Pulmonary interstitial glycogenosis: a new variant of interstitial neonatal lung disease. *Am J Respir Crit Care Med* 165:1557–1575
- Carre A, Szinnai G, Castanet M, Sura-Trueba S, Tron E, Broutin-L'Hermite I, Barat P et al (2009) Fine new TTF1/NKX2.1 mutations in brain-lung-thyroid syndrome: rescue by PAX8 synergism in one case. *Hum Mol Genet* 18:2266–2276
- Castillo M, Vade A, Lim-Dunham JE, Masuda E, Massarani-Wafai R (2010) Pulmonary interstitial glycogenosis in the setting of lung growth abnormality: radiographic and pathologic correlation. *Pediatr Radiol* 40:1562–1565
- Chow CW, Massie J, Ng J, Mills J, Baker M (2013) Acinar dysplasia of the lungs: variation in the extent of involvement and clinical features. *Pathology* 45:38–43
- Clement A, Eber E (2008) Interstitial lung diseases in infants and children. *Eur Respir J* 31:658–666
- Clement A, Nathan N, Epaud R, Fauroux B, Corvol H (2010) Interstitial lung diseases in children. *Orphanet J Rare Diseases* 5:22
- Colom AJ, Teper AM (2009) Clinical prediction rule to diagnose post-infectious bronchiolitis obliterans in children. *Pediatr Pulmonol* 44:1065–1069
- de Wit MC, Tiddens HA, de Coe IF, Mancini GM (2011) Lung disease in FLNA mutation: confirmatory report. *Eur J Med Genet* 54:299–300
- Deterding RR (2010) Infants and young children with children's interstitial lung disease. *Pediatr Allerg Immunol Pulmonol* 23:25–31
- Deterding RR, Pye C, Fan LL, Langston C (2005) Persistent tachypnea of infancy is associated with neuroendocrine cell hyperplasia. *Pediatr Pulmonol* 40:157–165
- Deutsch GH, Young LR (2010) Pulmonary interstitial glycogenosis: words of caution. *Pediatr Radiol* 40:1471–1475
- Deutsch GH, Young LR, Deterding RR, Fan LL, Dell SD, Bean JA, Brody AS et al (2007) Diffuse lung disease in young children: application of a novel classification scheme. *Am J Respir Crit Care Med* 176:1120–1128
- Dishop MK (2010) Diagnostic pathology of diffuse lung disease in children. *Pediatr Allergy Immunol Pulmonol* 23:69–85
- Dishop MK (2011) Paediatric interstitial lung disease: classification and definitions. *Paediatr Respir Rev* 12:230–237
- Doan ML, Guilleman RP, Dishop MK, Noguee LM, Langston C, Mallory GB, Sockrider MM et al (2008) Clinical, radiological and pathological features of ABCA3 mutations in children. *Thorax* 63:366–373
- Ehsan Z, Montgomery GS, Tiller C, Kisling J, Chang DV, Tepper RS (2014) An infant with pulmonary interstitial glycogenosis: clinical improvement is associated with improvement in the pulmonary diffusion capacity. *Pediatr Pulmonol* 49:E17–E20
- Esther CR Jr, Barker PM (2004) Pulmonary lymphangiectasia: diagnosis and clinical course. *Pediatr Pulmonol* 38:308–313
- Fan LL, Deterding RR, Langston C (2004) Pediatric interstitial lung disease revisited. *Pediatr. Pulmonol* 38:369–378
- Faul JL, Berry GJ, Colby TV, Ruoss SJ, Walter MB, Rosen GD, Raffin TA (2000) Thoracic lymphangiomas, lymphangiectasis, lymphangiomatosis, and lymphatic dysplasia syndrome. *Am J Respir Crit Care Med* 161:1037–10460
- Flamein F, Riffault L, Muselet-Charlier C, Pernelle J, Feldmann D, Jonard L, Durand-Schneider AM et al (2012) Molecular and cellular characteristics of ABCA3 mutations associated with diffuse parenchymal lung diseases in children. *Hum Mol Genet* 21:765–775
- Frazier AA, Franks TJ, Mohammed TL, Ozbudak IH, Galvin JR (2007) From the archives of the AFIP: pulmonary veno-occlusive disease and pulmonary capillary hemangiomatosis. *Radiographics* 27:867–882
- Galambos C, Levy H, Cannon CL, Vargas SO, Reid LM, Cleveland R, Lindeman R et al (2010) Pulmonary pathology in thyroid transcription factor-1 deficiency syndrome. *Am J Respir Crit Care Med* 182:549–554
- Galambos C, Sims-Lucas S, Abman SH (2014) Three-dimensional reconstruction identifies misaligned pulmonary veins as intrapulmonary shunt vessels in alveolar capillary dysplasia. *J Pediatr* 164:192–195
- Gendelman S, Zeff A, Spalding SJ (2013) Childhood-onset eosinophilic granulomatosis with polyangiitis (formerly Churg-Strauss syndrome): a contemporary single-center cohort. *J Rheumatol* 40:929–935
- Gillespie LM, Fenton AC, Wright C (2004) Acinar dysplasia: a rare cause of neonatal respiratory failure. *Acta Paediatr* 93:712–713
- Giovannini-Chami L, Hadchouel A, Nathan N, Bremont F, Dubus J-C, Fayon M, Houdouin V et al (2014) Idiopathic eosinophilic pneumonia in children: the French experience. *Orphanet J Rare Diseases* 9:28

- Gomes VC, Silva MC, Maia JH, Daltro P, Ramos SG, Brody AS, Marchiori E (2013) Diagnostic criteria and follow-up in neuroendocrine cell hyperplasia of infancy: a case series. *J Bras Pneumol* 39:569–578
- Guillerman RP (2010) Imaging of childhood interstitial lung disease. *Pediatr Allerg Immunol Pulmonol* 23:43–68
- Guillerman RP, Brody AS (2011) Contemporary perspectives on pediatric diffuse lung disease. *Radiol Clin N Am* 49:847–868
- Guillerman RP, Metwalli ZA, Burrage LC, Lalani SR, Langston C, Mallory GB (2013) Congenital multilobar pseudo-emphysema: a severe progressive lung growth disorder associated with filamin A gene mutations. *Pediatr Radiol* 43:S304 (Suppl 2)
- Guillot L, Epaul R, Thouvenin G, Jonard L, Mohsni A, Couderc R, Counil F et al (2009) New surfactant protein C gene mutations associated with diffuse lung disease. *J Med Genet* 46:490–494
- Guillot L, Carre A, Szinnai G, Castanet M, Tron E, Jaubert F, Broutin I et al (2010) NKX2-1 mutations leading to surfactant protein promoter dysregulation cause interstitial lung disease in “brain-lung-thyroid” syndrome. *Hum Mutat* 31:E1146–E1162
- Hamvas A (2010) Evaluation and management of inherited disorders of surfactant metabolism. *Chin Med J (Engl)* 123:2943–2947
- Hamvas A, Deterding RR, Wert SE, White FV, Dishop MK, Alfano DN, Halbower AC et al (2013) Heterogeneous pulmonary phenotypes associated with mutations in the thyroid transcription factor gene NKX2-1. *Chest* 144:794–804
- Hartman TE (2003) The HRCT features of extrinsic allergic alveolitis. *Semin Respir Crit Care Med* 24:419–426
- Hendrickx GF, Somers K, Vanderplas Y (2011) Lane-Hamilton syndrome: case report and review of the literature. *Eur J Pediatr* 170:1597–1602
- Hoepker A, Seear M, Petrocheilou A, Hayes D Jr, Nair A, Deodhar J, Kadam S, O’Toole J (2008) Wilson-Mikity syndrome: updated diagnostic criteria based on nine cases and a review of the literature. *Pediatr Pulmonol* 43:1004–1012
- Hoganson DM, Gazit AZ, Boston US, Sweet SC, Grady RM, Huddleston CB, Eghtesady P (2014) Paracorporeal lung assist devices as a bridge to recovery of lung transplantation in neonates and young children. *J Thorac Cardiovasc Surg* 147:420–426
- Hugosson CO, Salama HM, Al-Dayel F, Khoumais N, Kattan AH (2005) Primary alveolar capillary dysplasia (acinar dysplasia) and surfactant protein B deficiency: a clinical, radiological and pathological study. *Pediatr Radiol* 35:311–316
- Jeong YJ, Kim KI, Seo IJ, Lee CH, Lee KN, Kim KN, Kim JS et al (2007) Eosinophilic lung diseases: a clinical, radiologic, and pathologic overview. *Radiographics* 27:617–637
- Kerby GS, Wagner BD, Popler J, Hay TC, Kopecky C, Wilcox SL, Quinones RR et al (2013) Abnormal infant pulmonary function in young children with neuroendocrine cell hyperplasia of infancy. *Pediatric Pulmonol* 48:1008–1015
- King BA, Boyd JT, Kingma PS (2011) Pulmonary maturation arrest and death in a patient with pulmonary interstitial glycogenosis. *Pediatr Pulmonol* 46:1142–1145
- Kjellberg M, Bjorkman K, Rohdin M, Sanchez-Crespo A, Jonsson B (2013) Bronchopulmonary dysplasia: clinical grading in relation to ventilation/perfusion mismatch measured by single photon emission computed tomography. *Pediatr Pulmonol* 48:1206–1213
- Kligerman SJ, Groshong S, Brown KK, Lynch DA (2009) Nonspecific interstitial pneumonia: radiologic, clinical, and pathologic considerations. *Radiographics* 29:73–87
- Kligerman SJ, Franks TJ, Galvin JR (2013) From the radiologic pathology archives: organization and fibrosis as a response to lung injury in diffuse alveolar damage, organizing pneumonia, and acute fibrinous and organizing pneumonia. *Radiographics* 33:1951–1975
- Kradin RL, Mark EJ (2008) The pathology of pulmonary disorders due to *Aspergillus* spp. *Arch Pathol Lab Med* 132:606–614
- Kurland G, Deterding RR, Hagood JS, Young LR, Brody AS, Castile RG, Dell S et al (2013) An official American Thoracic Society clinical practice guideline: classification, evaluation and management of childhood interstitial lung disease in infancy. *Am J Respir Crit Care Med* 188:376–394
- la Tour T, Spadola L, Sayegh Y, Combescure C, Pfister R, Argiroffo CB, Rochat I (2013) Chest CT in bronchopulmonary dysplasia: clinical and radiological correlations. *Pediatr Pulmonol* 48:693–698
- Lanfranchi M, Allbery SM, Wheelock L (2010) Pulmonary interstitial glycogenosis. *Pediatr Radiol* 40:361–365
- Langston C, Dishop MK (2009) Diffuse lung disease in infancy: a proposed classification scheme applied to 259 diagnostic biopsies. *Pediatr Dev Pathol* 12:421–437
- Lee EY (2013) Interstitial lung disease in infants: new classification system, imaging technique, clinical presentation and imaging findings. *Pediatr Radiol* 43:3–13
- Lino CA, Batista AK, Soares MA, de Freitas AE, Gomes LC, M Filho JH, Gomes VC (2013) Bronchiolitis obliterans: clinical and radiological profile of children follow-up in a reference clinic. *Rev Paul Pediatr* 31:10–16
- Liu XY, Jiang ZF, Zhou CJ, Peng Y (2011) Clinical features of 3 cases with acute interstitial pneumonia in children. *Zhonghua Er Ke Za Zhi* 49:98–102
- Lucaya J, Gartner S, García-Peña P, Cobos N, Roca I, Liñan S (1998) Spectrum of manifestations of Swyer-James-MacLeod syndrome. *J Comput Assist Tomogr* 22:592–597
- Lukkarinen K, Pelkonen A, Lohi J, Malmstrom K, Malmberg LK, Kajosaari M, Lindahl H et al (2013) Neuroendocrine cell hyperplasia of infancy: a prospective follow-up of nine children. *Arch Dis Child* 98:141–144
- MacDonald S, Müller NL (2003) Insights from HRCT: how they affect the management of diffuse parenchymal lung disease. *Semin Respir Crit Care Med* 24:357–364
- Mahut B, de Blic J, Emond S, Benoist MR, Jarreau PH, Lacaze-Masmonet T, Magny JF et al (2007) Chest computed tomography findings in bronchopulmonary dysplasia and correlation with lung function. *Arch Dis Child Fetal Neonatal Ed* 92:F459–F464
- Marchiori E, Zanetti G, Mano CM, Irion KL, Daltro PA, Hochegger B (2010) Lipoid pneumonia in 53 patients after aspiration of mineral oil: comparison of high-resolution computed tomography findings in adults and children. *J Comput Assist Tomogr* 34:9–12
- Martinez-Moczygemba M, Doan ML, Elidemir O, Fan LL, Cheung SW, Lei JT, Moore JP et al (2008) Pulmonary alveolar proteinosis caused by deletion of the GM-CSFR $\alpha$  gene in the X chromosome pseudoautosomal region 1. *J Exp Med* 205:2711–2716
- Masurel-Paulet A, Haan E, Thompson EM, Goizet C, Thauvin-Robinet C, Tai A, Kennedy A et al (2011) Lung disease associated with periventricular nodular heterotopia and an FLNA mutation. *Eur J Med Genet* 54:25–28
- Mattiello R, Sarria EE, Mallol J, Fischer GB, Mocelin H, Bello R, Flores JA et al (2010) Post-infectious bronchiolitis obliterans: can CT scan findings at early age anticipate lung function? *Pediatr Pulmonol* 45:315–319
- Mechri M, Epaul R, Emond S, Coulomb A, Jaubert F, Tarrant A, Feldmann D et al (2010) Surfactant protein C gene (SFTPC) mutation-associated lung disease: high-resolution computed tomography (HRCT) findings and its relation to histological analysis. *Pediatr Pulmonol* 45:1021–1029
- Mettauer N, Agrawal S, Pierce C, Ashworth M, Petros A (2009) Outcome of children with pulmonary lymphangiectasis. *Pediatr Pulmonol* 44:351–357



- Metwalli ZA, Guillerman RP, Langston C (2011) Alveolar growth abnormalities: not just BPD. *Pediatr Radiol* 41:S250 (Suppl 1)
- Michalsky MP, Arca MJ, Groenman F, Hammond S, Tibboel D, Caniano DA (2005) Alveolar capillary dysplasia: a logical approach to a fatal disease. *J Pediatr Surg* 40:1100–1105
- Moissidis I, Chaidaroon D, Vichyanond P, Bahna SL (2005) Milk-induced pulmonary disease in infants (Heiner syndrome). *Pediatr Allergy Immunol* 16:545–552
- Montani D, Price LC, Dorfmueller P, Achouh L, Jais X, Yaici A, Sitbon O et al (2009) Pulmonary veno-occlusive disease. *Eur Respir J* 33:189–200
- Moonnumakal SP, Fan LL (2008) Bronchiolitis obliterans in children. *Curr Opin Pediatr* 20:272–278
- Narayanan M, Owers-Bradley J, Beardsmore CS, Mada M, Ball I, Garipov R, Panesar KS et al (2012) Alveolarization continues during childhood and adolescence. New evidence from helium-3 magnetic resonance. *Am J Respir Crit Care Med* 185:186–191
- Nathan N, Taam RA, Epaul R, Delacourt C, Deschildre A, Reix P, Chiron R et al (2012) A national internet-linked based database for pediatric interstitial lung diseases: the French network. *Orphanet J Rare Diseases* 7:40
- Newman B, Yunis E (1990) Primary alveolar capillary dysplasia. *Pediatr Radiol* 21:20–22
- Nogee LM (2006) Genetics of pediatric interstitial lung disease. *Curr Opin Pediatr* 18:287–292
- Nogee LM (2010) Genetic basis of children's interstitial lung disease (chILD). *Pediatr Allerg Immunol Pulmonol* 23:15–24
- Oermann CM, Panesar KS, Langston C, Larsen GL, Menendez AA, Schofield DE, Cosio C et al (2000) Pulmonary infiltrates with eosinophilia syndromes in children. *J Pediatr* 136:351–358
- Ogier de Baulny H, Schiff M, Dionisi-Vici C (2012) Lysinuric protein intolerance (LPI): a multi organ disease by far more complex than a classic urea cycle disorder. *Mol Genet Metab* 106:12–17
- Olsen ØE, Sebire NJ, Jaffe A, Owens CM (2004) Chronic pneumonitis of infancy: high-resolution CT findings. *Pediatr Radiol* 34:86–88
- Onland W, Molenaar JJ, Leguit RJ, van Nierop JC, Noorduyt LA, van Rijn RR, Geukens VG (2005) Pulmonary interstitial glycogenosis in identical twins. *Pediatr Pulmonol* 40:362–366
- Parto K, Svedström E, Majurin ML, Harkonen R, Simell O (1993) Pulmonary manifestations in lysinuric protein intolerance. *Chest* 104:1176–1182
- Phillip AG (2009) Chronic lung disease of prematurity: a short history. *Semin Fetal Neonatal Med* 14:333–338
- Polverosi R, Maffesanti M, Dalpiaz G (2006) Organizing pneumonia: typical and atypical HRCT patterns. *Radiol Med* 111:202–212
- Popler J, Gower WA, Mogayzel PJ Jr, Nogee LM, Langston C, Wilson AC, Hay TC et al (2010) Familial neuroendocrine cell hyperplasia of infancy. *Pediatr Pulmonol* 45:749–755
- Popler J, Lesnick B, Dishop MK, Deterding RR (2012) New coding in the International Classification of Diseases, ninth revision, for children's interstitial lung disease. *Chest* 142:774–780
- Prestridge A, Wooldridge J, Deutsch G, Young LR, Wert SE, Whitsett JA, Nogee L (2006) Persistent tachypnea and hypoxia in a 3-month-old term infant. *J Pediatr* 149:702–706
- Radman MR, Goldhoff P, Jones KD, Azakie A, Datar S, Adatia I, Oishi PE, Fineman JR (2013) Pulmonary interstitial glycogenosis: an unrecognized etiology of persistent pulmonary hypertension of the newborn in congenital heart disease? *Pediatr Cardiol* 34:1254–1257
- Rice A, Tran-Dang M-A, Bush A, Nicholson AG (2013) Diffuse lung disease in infancy and childhood: expanding the chILD classification. *Histopathology* 63:743–755
- Robinson TE, Trapnell BC, Goris ML, Quitell LM, Cornfield DN (2009) Quantitative analysis of longitudinal response to aerosolized granulocyte-macrophage colony-stimulating factor in two adolescents with autoimmune pulmonary alveolar proteinosis. *Chest* 135:842–848
- Santamaria F, Parenti G, Guidi G, Rotondo A, Grillo G, Larocca MR, Celentano L et al (1996) Early detection of lung involvement in lysinuric protein intolerance: role of high-resolution computed tomography and radioisotopic methods. *Am J Respir Crit Care Med* 153:731–735
- Sarria EE, Mattiello R, Rao L, Wanner MR, Raske ME, Tiller C, Kimmel R, Tepper RS (2011) Computed tomography score and pulmonary function in infants with chronic lung disease of infancy. *Eur Respir J* 38:918–923
- Sen P, Thakur N, Stockton DW, Langton C, Bejjani BA (2004) Expanding the phenotype of alveolar capillary dysplasia. *J Pediatr* 145:646–651
- Sen P, Yang Y, Navarro C, Silva I, Szafranski P, Kolodziejska KE, Dharmadhikari AV et al (2013) Novel FOXF1 mutations in sporadic and familial cases of alveolar capillary dysplasia with misaligned pulmonary veins imply a role for its DNA binding domain. *Hum Mutat* 34:801–811
- Shah V, Shah S, Barnacle A, Sebire NJ, Brock P, Harper JJ, McHugh K et al (2011) Mediastinal involvement in lymphangiomatosis: a previously unreported. *Pediatr Radiol* 41:985–992
- Shin S-M, Kim WS, Cheon J-E, Kim HS, Lee W, Jung AY, Kim I-O, Choi JH (2013) Bronchopulmonary dysplasia: new high resolution computed tomography scoring system and correlation between the high resolution computed tomography score and clinical severity. *Korean J Radiol* 14:350–360
- Smets K, Dhaene K, Schelstraete P, Meersschaet V, Vanhaesebrouck P (2004) Neonatal pulmonary interstitial glycogen accumulation disorder. *Eur J Pediatr* 163:408–409
- Smith KJ, Dishop MK, Fan LL, Moonnumakal SP, Smith EO, Bayindir P, Guillerman RP (2011) Diagnosis of bronchiolitis obliterans with computed tomography in children. *Pediatr Allerg Immunol Pulmonol* 23:253–259
- Soares JJ, Deutsch GH, Moore PE, Fazili MF, Austin ED, Brown RF, Sokolow AG et al (2013) Childhood interstitial lung diseases: an 18-year retrospective analysis. *Pediatrics* 132:684
- Soraisham AS, Tierney AJ, Amin HJ (2006) Neonatal respiratory failure associated with mutation in the surfactant protein C gene. *J Perinatol* 26:67–70
- Stankiewicz P, Sen P, Bhatt SS, Storer M, Xia Z, Bejjani BA, Ou Z et al (2009) Genomic and genic deletions of the FOX gene cluster on 16q24.1 and inactivating mutations of FOXF1 cause alveolar capillary dysplasia and other malformations. *Am J Hum Genet* 84:780–791
- Stevens PA, Pettenazzo A, Brasch F, Mulugeta S, Baritussio A, Ochs M, Morrison L et al (2005) Nonspecific interstitial pneumonia, alveolar proteinosis, and abnormal proprotein trafficking resulting from a spontaneous mutation in the surfactant protein C gene. *Pediatr Res* 57:89–98
- Suzuki T, Sakagami T, Rubin BK, Nogee LM, Wood RE, Zimmerman SL, Smolarek T et al (2008) Familial pulmonary alveolar proteinosis caused by mutations in *CSF2RA*. *J Exp Med* 205:2703–2710
- Suzuki T, Sakagami T, Young LR, Carey BC, Wood RE, Luisetti M, Wert SE et al (2010) Hereditary pulmonary alveolar proteinosis: pathogenesis, presentation, diagnosis, and therapy. *Am J Respir Crit Care Med* 182:1292–1304
- Swenson SJ, Hartman TE, Mayo JR, Colby TV, Tazelaar HD, Muller NL (1995) Diffuse pulmonary lymphangiomatosis: CT findings. *J Comput Assist Tomogr* 19:348–352
- Taytard J, Nathan N, de Blic J, Fayon M, Epaul R, Deschildre A, Troussier J et al (2013) New insights into pediatric idiopathic pulmonary hemosiderosis: the French RespiRare Cohort. *Orphanet J Rare Diseases* 8:161
- Thouvenin G, Taam RA, Flamein F, Guillot L, le Bourgeois M, Reix P, Fayon M et al (2010) Characteristics of disorders associated with genetic mutations of surfactant protein C. *Arch Dis Child* 95:449–454

- Travis WD, Hunninghake G, King TE Jr, Lynch DA, Colby TV, Galvin JR, Brown KK et al (2008) Idiopathic nonspecific interstitial pneumonia: report of an American Thoracic Society project. *Am J Respir Crit Care Med* 177:1338–1347
- Travis WD, Costabel U, Hansell DM, King TE Jr, Lynch DA, Nicholson AG, Ryerson CJ et al (2013) An official American Thoracic Society/European Respiratory Society statement: update of the international multidisciplinary classification of the idiopathic interstitial pneumonias. *Am J Respir Crit Care Med* 188:733–748
- Vece TJ, Fan LL (2010) Interstitial lung disease in children older than 2 years. *Pediatr Allerg Immunol Pulmonol* 23:33–41
- Vece TJ, Fan LL (2011) Diagnosis and management of diffuse lung disease in children. *Paediatr Respir Rev* 12:238–242
- Wambach JA, Wegner DJ, Depass K, Heins H, Druley TE, Mitra RD, An P et al (2012) Single ABCA3 mutations increase the risk for neonatal respiratory distress syndrome. *Pediatrics* 130:e1575–e1582
- Woerner C, Cutz E, Yoo S-J, Grasemann H, Humpl T (2014) Pulmonary veno-occlusive disease in childhood. *Chest*. doi: [10.1378/chest.13-0172](https://doi.org/10.1378/chest.13-0172) (Epub ahead of print)
- Wong PM, Lees AN, Louw J, Lee FY, French N, Gain K, Murray CP, Wilson A, Chambers DC (2008) Emphysema in young adult survivors of moderate-to-severe bronchopulmonary dysplasia. *Eur Respir J* 32:321–328
- Wong P, Murray C, Louw J, French N, Chambers D (2011) Adult bronchopulmonary dysplasia: computed tomography findings. *J Med Imaging Radiat Oncol* 55:373–378
- Yalcin E, Dog D, Haliloglu M, Ozcelik U, Kiper N, Gocmen A (2003) Postinfectious bronchiolitis obliterans in children: clinical and radiological profile and prognostic factors. *Respiration* 70:371–375
- Young LR, Brody AS, Inge TH, Acton JD, Bokulic RE, Langston C, Deutsch GH (2010) Neuroendocrine cell distribution and frequency distinguish neuroendocrine cell hyperplasia of infancy from other pulmonary disorders. *Chest* 139:1060–1071
- Young LR, Deutsch GH, Bokulic RE, Brody AS, Nogee LM (2013) A mutation in TTF1/NKX2.1 is associated with familial neuroendocrine cell hyperplasia of infancy. *Chest* 144:1199–1206
- Zanetti G, Marchiori E, Gasparetto TD, Escuissato DL, Soares Souza A Jr (2007) Lipoid pneumonia in children following aspiration of mineral oil used in the treatment of constipation: high-resolution CT findings in 17 patients. *Pediatr Radiol* 37:1135–1139
- Zhang L, Irion K, da Silva Porto N, Abreu e Silva F (1999) High-resolution computed tomography in pediatric patients with post-infectious bronchiolitis obliterans. *J Thorac Imaging* 14:85–89

# Thoracic Manifestations of Systemic Diseases

David V. Holland, R. Paul Guillerman, and Alan S. Brody

## Contents

<b>1</b>	<b>Introduction</b> .....	395
<b>2</b>	<b>Connective Tissue Diseases</b> .....	396
2.1	Juvenile Idiopathic Arthritis.....	396
2.2	Juvenile Systemic Sclerosis.....	396
2.3	Juvenile Dermatomyositis.....	397
2.4	Systemic Lupus Erythematosus.....	397
<b>3</b>	<b>Systemic Granulomatous Disorders</b> .....	398
3.1	Sarcoidosis.....	398
3.2	Crohn Disease.....	399
<b>4</b>	<b>Immunodeficiencies</b> .....	399
4.1	Predominantly Antibody Deficiencies.....	401
4.2	Combined T-Cell and B-Cell Immunodeficiencies.....	404
4.3	Well-defined Syndromes with Immunodeficiency.....	404
4.4	Congenital Defects of Phagocyte Number and/or Function.....	408
4.5	Acquired Immunodeficiency.....	409
<b>5</b>	<b>Vasculitis</b> .....	411
5.1	Granulomatosis with Polyangiitis.....	412
5.2	Microscopic Polyangiitis.....	412
<b>6</b>	<b>Sickle Cell Disease</b> .....	413
<b>7</b>	<b>Cystic Fibrosis</b> .....	414
7.1	Genetics.....	415
7.2	Diagnosis.....	416
7.3	Pulmonary Pathophysiology.....	416
7.4	Lung Care.....	417
7.5	Imaging.....	417
<b>8</b>	<b>Primary Ciliary Dyskinesia</b> .....	419
<b>9</b>	<b>Langerhan Cell Histiocytosis</b> .....	420
<b>10</b>	<b>Tuberous Sclerosis</b> .....	421
<b>11</b>	<b>Lysosomal Storage Diseases</b> .....	422
11.1	Gaucher Disease.....	422
11.2	Niemann–Pick Disease.....	422
11.3	Mucopolysaccharidosis.....	423
	<b>References</b> .....	423

## Abstract

A wide variety of systemic diseases have manifestations in the pediatric chest. Among these systemic diseases are connective tissue diseases, granulomatous diseases, immunodeficiency disorders, vasculitis, sickle cell disease, cystic fibrosis, ciliary dyskinesia, histiocytosis, phakomatoses, and storage disorders. The primary manifestations are diverse, and may include interstitial lung disease, air space disease, pleuritis, lymphadenopathy, and skeletal abnormalities. Secondary effects, such as bronchiectasis from recurrent infection, are also common. Although the underlying systemic disease has often been previously diagnosed, it is not uncommon for pulmonary manifestations to be the first signs of a systemic disease, and knowledge of the pertinent clinical and imaging features may allow the radiologist to be the first to suggest an underlying systemic disease.

## 1 Introduction

A wide variety of systemic diseases have primary or secondary manifestations in the pediatric chest. Although the underlying systemic disease has often been previously diagnosed, it is not uncommon for pulmonary manifestations to be the first signs of a systemic disease. This chapter has two main goals: first, to aid the reader in interpreting imaging findings of known systemic diseases in which lung

D. V. Holland  
Mallinckrodt Institute of Radiology,  
Washington University School of Medicine,  
St. Louis, MO, USA

R. Paul Guillerman (✉)  
Department of Pediatric Radiology,  
Texas Children's Hospital, Baylor College of Medicine,  
6701 Fannin St, Suite 470, Houston, TX 77030, USA  
e-mail: rpguille@texaschildrens.org

A. S. Brody  
Department of Radiology,  
Children's Hospital Medical Center,  
Cincinnati, OH, USA



manifestations are common; second, to provide a guide based on the imaging appearance to allow the reader to suggest the possibility of an undiagnosed systemic disease. In-depth information on the imaging techniques that are used in the evaluation of these and other pediatric thoracic diseases is provided in other chapters of this book, and only pertinent additional comments will be made in this chapter. For each condition or group of conditions, the general features of the condition will be described, followed by a review of the imaging appearance of the thoracic manifestations. Knowledge of the characteristic clinical and imaging features may allow the radiologist to be the first to suggest an underlying systemic disease in these children.

In addition to disease-specific associated thoracic abnormalities, many systemic diseases produce nonspecific secondary effects that can be reflected by thoracic findings on diagnostic imaging. Abnormal host defences frequently result in both an increased incidence of pulmonary infection and a change in the spectrum of infection. Neuromuscular abnormalities can result in aspiration with direct chemical insult to the lungs as well as infection. The likelihood of such effects should be borne in mind, as these abnormalities may be more common in certain clinical settings than the primary pathologies associated with a specific systemic disease.

It is important to note that many of the reports that form the literature in these diseases are more than 10–20-years old. Recent advances in classification, diagnosis, treatment, and complications related to treatment may not be reflected in this literature. Understanding of the spectrum of imaging findings may also be limited by the technology that was available at the time of these reports.

## 2 Connective Tissue Diseases

The connective tissue diseases (CTDs) are a group of diseases characterized by inflammation affecting the connective tissue of various organ systems. Common CTDs in children and adolescents include juvenile idiopathic arthritis (JIA), juvenile-onset systemic sclerosis (JSS), juvenile dermatomyositis (JDM) and systemic lupus erythematosus (SLE). In mixed connective tissue disease (MCTD) or overlap syndrome, patients may present with features of multiple CTDs.

The frequency and pattern of lung involvement vary greatly with the type of CTD (Garcia-Pena et al. 2011). Nonspecific interstitial pneumonitis (NSIP) is the most common histopathologic pattern, but pulmonary lymphoid hyperplasia, organizing pneumonia, vasculopathy and pleuritis may also occur (Dishop 2010). Clinically apparent pulmonary abnormalities are very rare in JIA, rare in JDM, and more common in JSS, SLE, and MCTD. Pulmonary function test (PFT) abnormalities are reported in the

majority of children with active CTD, although abnormalities on chest radiographs (CXR) are uncommon (Cerveri et al. 1992). Due to its superior resolution, computed tomography (CT) is the primary imaging modality used for investigation of lung parenchymal involvement. Echocardiography is the preferred noninvasive method for assessing pulmonary hypertension, which can be a complication of pulmonary involvement by CTDs.

### 2.1 Juvenile Idiopathic Arthritis

Transient pleuritis resulting in pleural effusion is common in juvenile idiopathic arthritis (JIA) patients (Garcia-Pena et al. 2011). Clinically overt pulmonary disease is uncommon in JIA, though, occurring in only 4 % in one study (Athreya et al. 1980). However, when PFTs were performed in 16 children with JIA, 10 had abnormalities (Wagener et al. 1981). Respiratory muscle weakness may be a contributing factor in the lung function abnormalities (Knook et al. 1999). Over the last decade, children with systemic JIA (sJIA) have been reported to have a higher incidence of pulmonary complications including pulmonary hypertension, alveolar proteinosis and interstitial lung disease (ILD). This recent increase is possibly attributable to new medications being used to treat these patients, although no controlled studies are available. Macrophage activation syndrome, common in sJIA, is associated with lipid pneumonia related to deposition of cholesterol granulomas in the interstitium and alveoli (Kimura et al. 2013).

Pleural and pericardial effusions are reported to be the most common abnormalities on chest imaging, occurring in five of 191 children in one report (Athreya et al. 1980) (Fig. 1). Lymphocytic interstitial pneumonitis (LIP) occurred in two children in this group. In two additional reports, LIP preceded other symptoms of JIA by as long as 2 years (Lovell et al. 1984; Uziel et al. 1998). These reports described nonspecific interstitial infiltrates on CXR, but no report of CT findings was given. In a report of LIP on CT, the findings were predominantly ground-glass opacity with associated consolidation, nodules, and cysts (Lynch et al. 1999). A case report describes a patient with onset of JIA at age 5 years who developed cryptogenic organizing pneumonia (COP), also known as bronchiolitis obliterans organizing pneumonia (BOOP), at 25 years of age (Sohn et al. 2007).

### 2.2 Juvenile Systemic Sclerosis

Scleroderma is characterized by fibrotic infiltration of connective tissues. Involvement of the skin and the gastrointestinal tract, particularly the esophagus, is most common. The term systemic sclerosis is used to describe disseminated

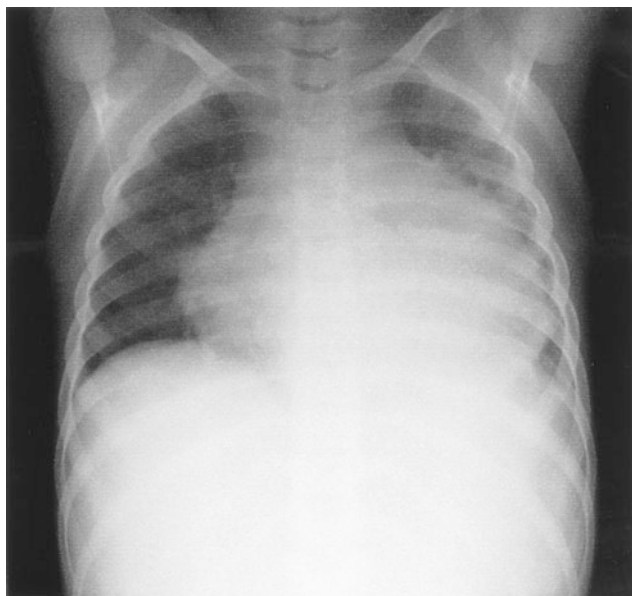


**Fig. 1** Juvenile idiopathic arthritis (JIA). A frontal CXR demonstrates a large pericardial effusion and a small left pleural effusion in an 8-year-old boy with JIA

disease. Systemic sclerosis presents most commonly in adult women, but 10 % of cases present in children as juvenile systemic sclerosis (JSS). Both PFT abnormalities and lung parenchymal abnormalities on imaging are common in JSS. In a study of 11 JSS patients aged 5–19 years, 8 had ILD on CT. The most common abnormalities were peripheral ground-glass opacities in eight, subpleural nodules in seven, peripheral reticular opacities in six, and honeycombing in five (Seely et al. 1998) (Fig. 2). In a more recent and much larger study of 153 JSS patients, the prevalence of ILD on CT was 5 % at diagnosis and 23 % at some point in the overall course. Pulmonary hypertension occurred in 7 % (Martini et al. 2006). The severity of CT abnormalities correlates inversely with FEV<sub>1</sub> (forced expiratory volume in one second), FVC (forced vital capacity), and D<sub>LCO</sub> (lung diffusion capacity for carbon monoxide) values (Panigada et al. 2009). Pulmonary hypertension can develop without lung parenchymal disease, possibly due to direct pulmonary vascular involvement (Cheema and Quismorio 2001).

Although frequently described as honeycombing, the peripheral reticular opacities and cysts that are commonly seen in JSS often do not meet strict diagnostic criteria for honeycombing, and there is poor interobserver agreement for the identification of honeycombing, even among expert thoracic radiologists. In our experience, unlike the case in idiopathic pulmonary fibrosis, these findings may remain stable for long periods of time, which is consistent with reports that there is no correlation between the duration of illness and the severity of the lung disease (Panigada et al.

2009). However, since pulmonary fibrosis is a leading cause of mortality and progression of fibrosis may be clinically silent, measuring serum levels of KL-6 (Vesely et al. 2004) or obtaining serial CT exams (Seely et al. 1998; Panigada et al. 2009) has been suggested to monitor ILD in JSS. Preliminary studies have shown that lung ultrasound findings correlate with CT findings and PFT results in adults with ILD related to systemic sclerosis (Delle Sedie et al. 2012). If validated in children, ultrasound could provide a means to monitor ILD in JSS patients without ionizing radiation exposure. Aspiration and infection must also be considered as potential causes of lung disease in JSS patients given the high rate of esophageal dysmotility and gastroesophageal reflux and the use of immunosuppressive therapy (Christmann et al. 2010).

Scleroderma *sin* scleroderma, a rare form of scleroderma, presents without a skin rash and may be difficult to diagnose. Usually an adult disease, it has been reported in children as young as 6 years of age. Lung involvement is reported in approximately two-thirds of these patients (Toya and Tzelepis 2009).

## 2.3 Juvenile Dermatomyositis

Abnormal PFTs are reported in more than half of patients with juvenile dermatomyositis (JDM) (Takizawa et al. 1987). In a report of five cases, interstitial pneumonia was noted in three and COP in two. All had abnormalities on physical examination or imaging studies at the time of presentation with JDM, although in two cases these abnormalities were initially mild (Kobayashi et al. 2003).

A more recent report of 21 pediatric patients found that respiratory involvement was common, occurring in 76 %, but respiratory symptoms were not the presenting symptoms in any. Respiratory muscle involvement was the most common abnormality followed by interstitial lung disease. Chest CT was abnormal in 12 of the 15 patients in whom CT was performed, with linear opacities, nodules, ground glass opacities, expiratory air trapping, and bronchial wall thickening being the most common findings (Pouessel et al. 2013). Rarely, JDM may be complicated by an acute, rapidly progressive, steroid-refractory, fatal interstitial lung disease (Lin et al. 2002).

## 2.4 Systemic Lupus Erythematosus

Systemic lupus erythematosus (SLE) is a multisystem disease characterized by persistent B-cell activation and overproduction of autoantibodies and immune complexes. Both the activity of the autoantibodies and the deposition of the immune complexes are associated with organ

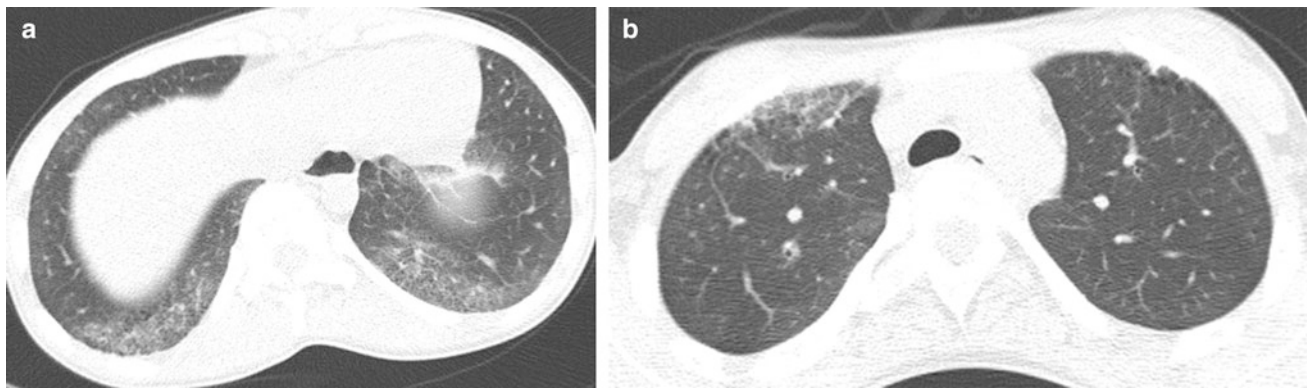


**Fig. 2** Juvenile systemic sclerosis (JSS). Axial chest CT images (a, b) from a 17-year-old girl with JSS show ground-glass opacities, fine reticular opacities, and tiny cysts at the peripheral posterior lower lobes and peripheral anterior upper lobes, as well as esophageal dilation

dysfunction (Lehman 1995). SLE is more common in non-Caucasian than in Caucasian populations, and susceptibility to SLE is thought to be related to multiple genes. The number of SLE susceptibility alleles relates to the likelihood of onset in childhood in African-Americans, but not in populations of Hispanic or European origin (Webb et al. 2011). One-fifth to one-sixth of SLE patients present before the age of 16 years (Arkachaisri and Lehman 1999). A comparison of adult- and pediatric-onset SLE found that children tend to present with more acute illness and have higher mortality rates (Mina and Brunner 2010).

In 37 % of cases of childhood-onset SLE, the pulmonary function is impaired, with a reduction of  $D_{LCO}$  most commonly noted. Pulmonary abnormalities on chest CT are less common, with a prevalence of 8 %, and pulmonary function does not correlate with CT findings (Lilleby et al. 2006). Manifestations of SLE on chest imaging include pleural effusion, pericardial effusion, pneumonitis, obliterative bronchiolitis, vasculitis, pulmonary hemorrhage and pulmonary embolism (Babyn and Doria 2005). Opportunistic infections are a leading cause of death in children with SLE, so infection should be excluded before attributing respiratory signs or symptoms to primary lupus involvement (Wang et al. 2003).

Acute lupus pneumonitis is a rare, life-threatening condition related to diffuse alveolar damage. Acute lupus pneumonitis can be difficult to diagnose due to its nonspecific presentation of shortness of breath and extensive pulmonary opacification that simulates infectious pneumonia or pulmonary edema (Vece and Fan 2010) (Fig. 3).

Alveolar hemorrhage from SLE is more common in children than in adults, and the mortality is higher (Araujo et al. 2012). Patients present with a decrease in hematocrit, but hemoptysis may be absent. This condition can potentially be treated successfully with steroids and cytotoxic agents, so correct identification is important (Schwab et al.

1993). Air space opacities can be seen on CXR and CT. The imaging is not specific, as lupus pneumonitis or infection can produce the same findings. The finding of T2 shortening on magnetic resonance imaging (MRI) has been reported as a means of specifically identifying hemorrhage (Hsu et al. 1992).

“Shrinking lung syndrome” is a term used to describe a progressive decrease in lung volumes seen in some patients with SLE. This is usually identified on CXR as a progressive elevation of the diaphragm despite attempted full inspiration. The etiology is unknown, but may relate to a combination of pleural restriction due to recurrent pleural inflammation, pulmonary restriction due to pulmonary fibrosis, and weakness of the diaphragm and chest wall musculature. African-American patients are most commonly affected (Ferguson and Weinberger 2006).

### 3 Systemic Granulomatous Disorders

#### 3.1 Sarcoidosis

Imaging findings of thoracic sarcoidosis in children are similar to those in adults. The most common thoracic manifestation of sarcoidosis in children is bilateral hilar lymphadenopathy. Pulmonary parenchymal disease occurs in approximately two-thirds of cases, usually in association with lymphadenopathy. Isolated pulmonary parenchymal involvement is found in only 11 % of cases (Keesling et al. 1998). Typical CT findings of pulmonary sarcoidosis in children include nodular beading and thickening of the bronchovascular bundles, interlobular septae, and fissures (Milman et al. 1998) (Fig. 4). Ground-glass opacities are also common, but parenchymal distortion and consolidation are less frequent and cysts or pleural effusions are typically not seen. Decreases in CT finding scores over time are



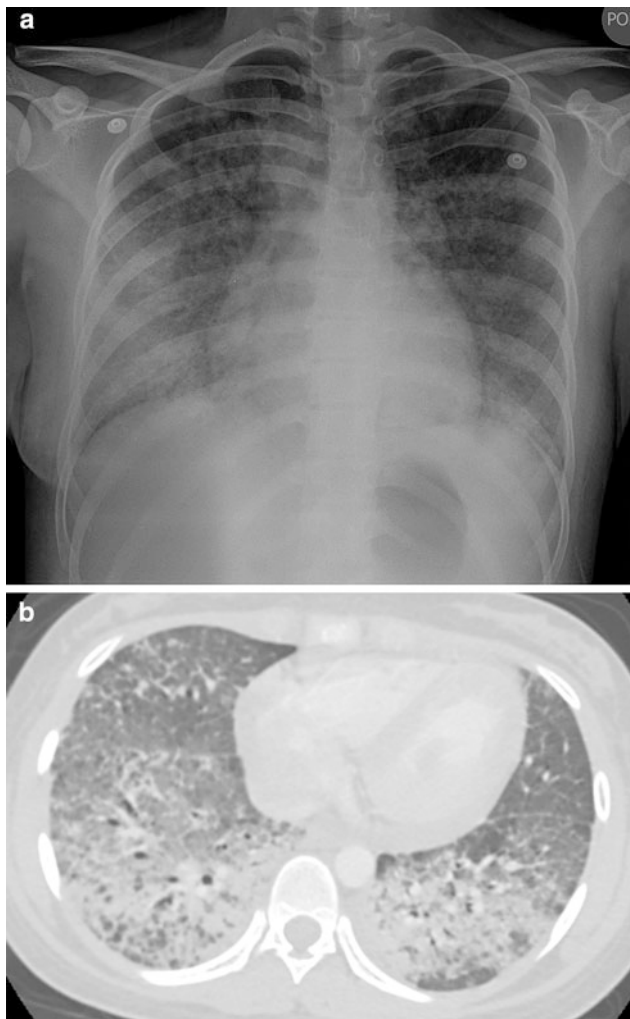


**Fig. 3** Acute lupus pneumonitis. A frontal CXR (a) and an axial chest CT image (b) depict extensive bilateral pulmonary air space opacification in this 13-year-old girl with SLE and acute respiratory symptoms

associated with improvement of pulmonary function measured by  $FEV_1$  and FVC, so that the need for follow-up CT scans may be reduced when PFT results improve over time (Sileo et al. 2013a).

### 3.2 Crohn Disease

Although extraintestinal manifestations of Crohn disease are well known, respiratory tract involvement is uncommon but increasingly recognized, including in children (Al-Binali et al. 2003). Involvement can range from the large central airways (bronchiectasis, chronic bronchitis), to the small airways (bronchiolitis obliterans) and lung parenchyma (eosinophilic pneumonia, organizing pneumonia, granulomatous pneumonitis, interstitial pneumonitis) (Fig. 5).

Drug-induced lung disease should be considered, particularly in the setting of eosinophilic pneumonia in patients on sulfasalazine or mesalamine therapy. Infection, including tuberculosis, should also be considered given the altered immune status of many of these patients. Treatment of pulmonary involvement is usually based on discontinuation of possible inciting drugs and initiation of steroids or other immunosuppressants (Basseri et al. 2010).

## 4 Immunodeficiencies

Defences against infection include physical barriers, B-cells, T-cells, natural killer cells, phagocytes, and complement proteins. Defects in one or more of these components of the immune system result in an increased risk of infection. The lungs are exposed to both inhaled and circulating infectious agents and are frequently the site of infection in immunocompromised children.

Acquired immunodeficiency states are common in children, and can relate to chemotherapy for cancer, solid organ transplantation, hematopoietic stem cell transplantation (HSCT), immunosuppressive therapy for autoimmune disorders, or HIV infection. Although individually rare, the primary immunodeficiency diseases (PIDs) have a collective prevalence of 1/2,000 children in the United States (Boyle and Buckley 2007). Accumulating knowledge of the genetic and molecular basis of the immune system is providing a far more detailed understanding of PID, and specific genetic defects leading to distinct types of PID are increasingly being identified. With this increased understanding has come increased complexity in classifying PID. At least 200 inborn errors of immunity have been genetically defined, and the classification of PID is updated on a biennial basis by an expert committee of the International Union of Immunological Societies (IUIS). Based on disease mechanism, the IUIS classification groups PIDs into eight categories: predominantly antibody deficiencies, combined T-cell and B-cell immunodeficiencies, well-defined syndromes with immunodeficiency, congenital defects of phagocyte number and/or function, diseases of immune dysregulation, defects in innate immunity, auto-inflammatory disorders, and complement deficiencies. There is considerable heterogeneity, as well as overlap, in the phenotypic expression of these disorders (Al-Herz et al. 2011).

The radiologist has several roles when assessing the chest of children with an immunodeficiency. These include suggesting the possibility of an immunodeficiency, noting features characteristic of a specific immunodeficiency, evaluating infections, and detecting malignancies that can occur as a complication of certain immunodeficiencies.

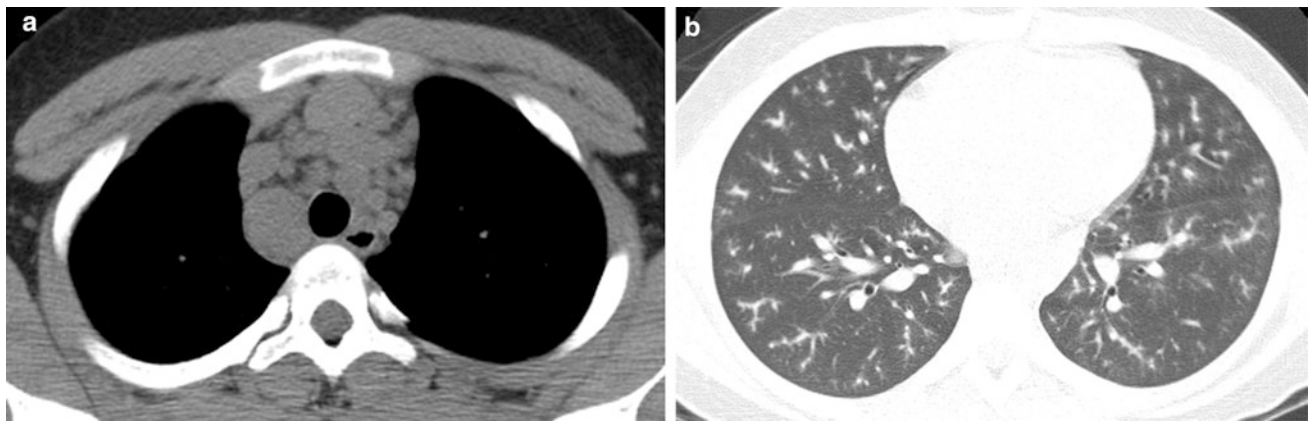


**Fig. 4** Sarcoidosis. An axial chest CT image reconstructed in soft tissue windows (**a**) from a 13-year-old boy with sarcoidosis demonstrates mediastinal lymphadenopathy (**a**). An axial chest image

reconstructed in lung windows (**b**) shows nodular beading of the pulmonary bronchovascular bundles

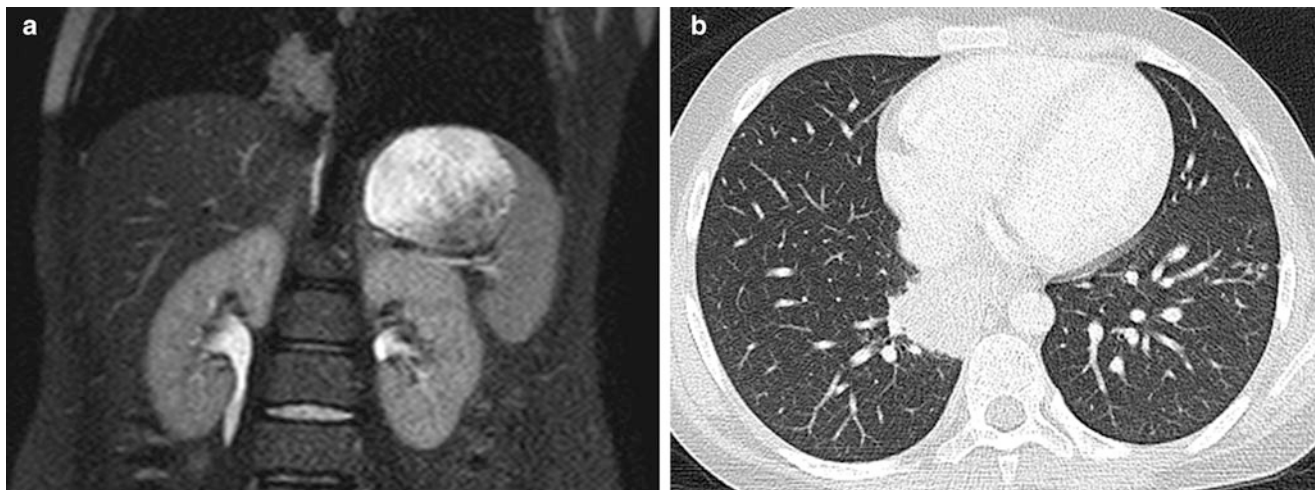


**Fig. 5** Pulmonary Crohn disease. A coronal T2-weighted MR image (**a**) obtained during an MR enterography study on an 11-year-old boy with Crohn disease reveals a mass-like intermediate-to-high signal intensity lesion of the medial basilar right lower lobe. An axial chest

CT image (**b**) shows a mass-like opacity of the medial basilar right lower lobe that was found to represent granulomatous inflammation on subsequent biopsy

By noting repetitive, severe, or refractory infections or recognizing certain patterns of disease, the radiologist may be the first to suggest the possibility of an immunodeficiency. In a recent study, 96 % of children with PIDs were referred to pediatric immunodeficiency centers by hospital clinicians rather than general pediatricians, illustrating the difficulty in making an early diagnosis of PID (Subbarayan et al. 2011). Early recognition of PID is important for several reasons. Bronchiectasis resulting from repeated or inadequately treated respiratory tract infection is irreversible. Outcomes are improved and treatment costs are reduced with institution of appropriate therapy, which can include immunoglobulin replacement therapy, prophylactic antimicrobials, and hematopoietic stem cell reconstitution. Avoidance of live vaccines and nonirradiated cellular blood

products may be needed (Modell et al. 2009). Due to the heritable nature of many of these disorders, genetic testing and counseling may be warranted.

The primary role of thoracic imaging in children with immunodeficiencies is the detection and therapy response assessment of pulmonary infections. CXRs remain the most frequently obtained imaging study. However, CT scanning has long been recognized as both more sensitive and specific than CXR for the evaluation of diffuse infiltrative lung disease (Mathieson et al. 1989). CT is useful in children with antibody deficiency disorders to demonstrate the extent and severity of lung disease (Manson et al. 1997). Aerogenous spread of mycobacterial infection will frequently show a “tree-in-bud” appearance of infectious material filling dilated distal bronchioles (Fig. 6), although this appearance

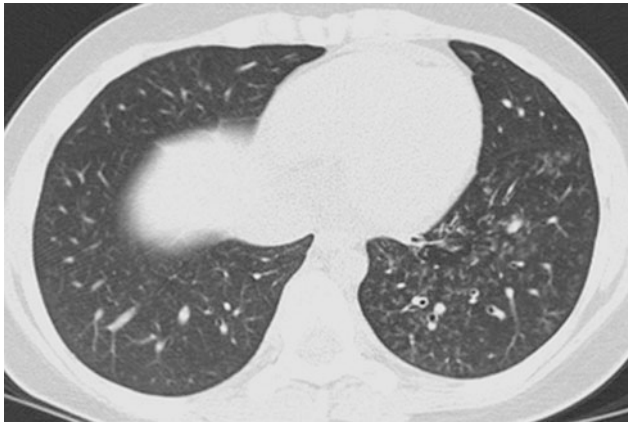


**Fig. 6** Atypical mycobacterial infection. An axial chest CT image in a 14-year old with a history of large cell lymphoma and bone marrow transplantation demonstrates extensive “tree-in-bud” opacities of the left lower lobe

is far less specific than originally reported. Invasive aspergillosis may manifest as pulmonary nodules with a “halo” of ground-glass opacity (Seely et al. 1997) (Fig. 7). *Pneumocystis jirovecii* pneumonia (PCP) has a broad spectrum of findings that can include ground-glass opacities, reticulonodular opacities, septal thickening, and cysts (George et al. 2009) (Fig. 8). When identification of a specific etiology is required, CT can be used to guide bronchoscopy or needle biopsy to increase the yield of these procedures (Spencer et al. 1996).

CT scanning can be overused in children with immunodeficiencies. In one study of children with primary antibody immunodeficiencies and chronic cough, there was little disease progression on CT over 3 years and the authors suggested that annual surveillance may be more than is necessary (Rusconi et al. 2003). While MRI currently lags CT in spatial resolution, MRI has been shown to reliably identify pneumonia in immunocompromised patients when compared to CT, and is more sensitive for necrotizing pneumonia than CT (Leutner et al. 2000).

Due to the large number of types and varied phenotypic expressions of PID, only the disorders that are the most common or have the most characteristic imaging manifestations will be further discussed in this chapter.

## 4.1 Predominantly Antibody Deficiencies

The predominantly antibody deficiencies result from a decreased ability to produce immunoglobulins from B-cells and, in aggregate, account for more than half of all cases of PID (Buckley 2004). Genetic defects resulting in impaired immunoglobulin formation have been identified in multiple discrete steps in B-cell development (Cunningham-Rundles

and Ponda 2005). Antibody deficiencies predispose to recurrent respiratory tract infection with encapsulated bacteria such as *Streptococcus* and *Haemophilus influenzae*, leading to bronchiectasis (Buckley 2004). Despite the presence of chronic respiratory symptoms, delay in diagnosis is common and can result in progressive lung damage with development of respiratory insufficiency and cor pulmonale (Wood et al. 2007).

### 4.1.1 IgA Deficiency

IgA deficiency is the most common PID and is noted in as many as 1 in 333 blood donors (Cunningham-Rundles 2001). IgA is secreted onto epithelial surfaces, and is present in smaller amounts in serum as well. Most individuals with IgA deficiency are asymptomatic. However, an increased propensity for infections of the respiratory, gastrointestinal, and genitourinary tracts is seen in some affected individuals. Pyogenic sinopulmonary infections are the most common (Cunningham-Rundles 2001), and the presence of IgA and IgG subclass antibody deficiencies is associated with greater pulmonary damage in children with recurrent respiratory tract infections (Ozkan et al. 2005).

### 4.1.2 X-Linked Agammaglobulinemia

X-linked agammaglobulinemia (XLA) is responsible for approximately 85 % of cases of childhood agammaglobulinemia (Plebani et al. 2002). There may be a family history of an affected brother, uncle, or male cousin. XLA most often results from a mutation in the X-linked gene encoding the Bruton tyrosine kinase. Deficiency of this kinase prevents precursor cells from maturing into circulating B-cells and plasma cells, resulting in impaired production of immunoglobulins of all isotypes (Buckley 2004). Infants with XLA typically present after the first several months of life coinciding the waning of maternally transmitted IgG (Fried and Bonilla 2009). Without IgG therapy, recurrent bacterial infections occur (Fig. 9). Bronchiectasis due to recurring infections usually affects the lower lungs. Similar involvement of both the right and left lungs may help differentiate these patients from those with bronchiectasis related to aspiration (Curtin et al. 1991). Pulmonary insufficiency is a common cause of death. *Streptococcus*, *H. influenzae* and *Mycoplasma* are the most typical cause of infections. There is an increased rate of hepatitis and enterovirus infections, but other viral infections are usually handled normally (Winkelstein et al. 2006). *Pneumocystis* and other fungal infections are rare. The adenoids, tonsils, and lymph nodes are typically small, while the thymus is usually normal in size. A lateral airway radiograph demonstrating diminutive adenoid tissue is the absence of a history of adenoidectomy can be very helpful in suggesting this diagnosis (Buckley 2004) (Fig. 9).



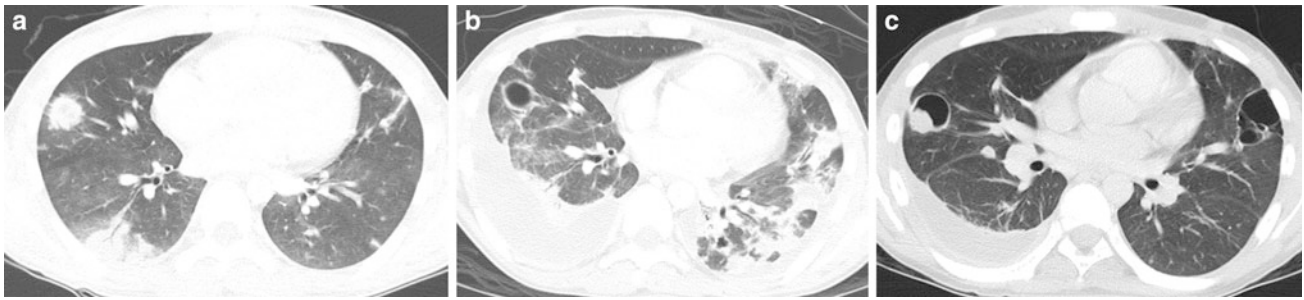


**Fig. 7** Invasive aspergillosis. An axial chest CT image (a) in a febrile neutropenic 12-year old with acute lymphoblastic leukemia undergoing induction chemotherapy shows multiple pulmonary nodules with a ground-glass “halo” in the right lung. An axial chest CT image

(b) obtained 19 days later after neutrophil recovery shows cavitation of the anterior right lung lesion. An axial CT chest image (c) obtained a further 2 weeks later reveals development of a mural nodule in the cavitary lesion that was due to cytomegalovirus superinfection

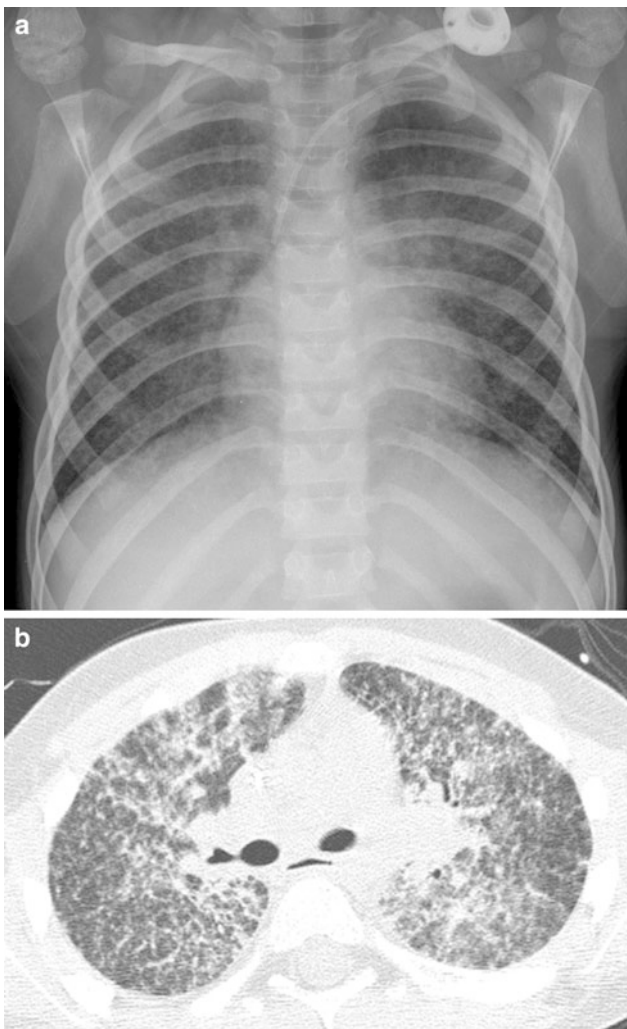


**Fig. 8** *Pneumocystis jiroveci* pneumonia (PCP). A frontal CXR (a) and an axial chest CT image (b) from a 5-year old with acute lymphoblastic leukemia undergoing maintenance chemotherapy show diffuse reticulonodular opacities with a central predominance

#### 4.1.3 Common Variable Immunodeficiency Disorder

Common variable immunodeficiency (CVID) is characterized by a failure of terminal differentiation of B-cells to plasma cells, resulting in hypogammaglobulinemia, even though B-cell number may be normal. CVID is usually less severe than agammaglobulinemia and diagnostic delay until the second decade or later is common. The infectious manifestations are otherwise similar to XLA. Unlike the case in XLA, the tonsils, adenoids, and lymph nodes are not small, and may be enlarged. Splenomegaly is seen in about 25 % of cases. Also unlike XLA, CVID is associated with an increased risk for autoimmune cytopenia, lymphoproliferative disease, lymphoma and gastric cancer. The benign lymphoproliferative disease associated with CVID can have a waxing and waning course. The associated lymphadenopathy can be difficult to discern from lymphoma (Cunningham-Rundles 2012) (Fig. 10). The word variable in this disorder refers to the variability of disease severity between patients, and not to temporal variability of disease in a single patient. There are two main phenotypes, one in which infections are characteristic and another in which inflammatory or hematologic complications are prevalent (Cunningham-Rundles 2012).

Approximately three-fourths of CVID patients develop a lung disease with air trapping, bronchiectasis, bronchial wall thickening, and endobronchial mucus plugging closely resembling cystic fibrosis (CF) (Fig. 10). Although this CF-like lung disease is associated with obstructive PFTs, it can be asymptomatic and progress silently. The degree of bronchiectasis at presentation inversely correlates with survival, and the disease can be monitored with a CF-like CT scoring system, although there is no consensus on the optimal surveillance strategy (Touw et al. 2010).

Patients with CVID can also develop granulomatous lymphocytic-interstitial lung disease (GLILD) characterized

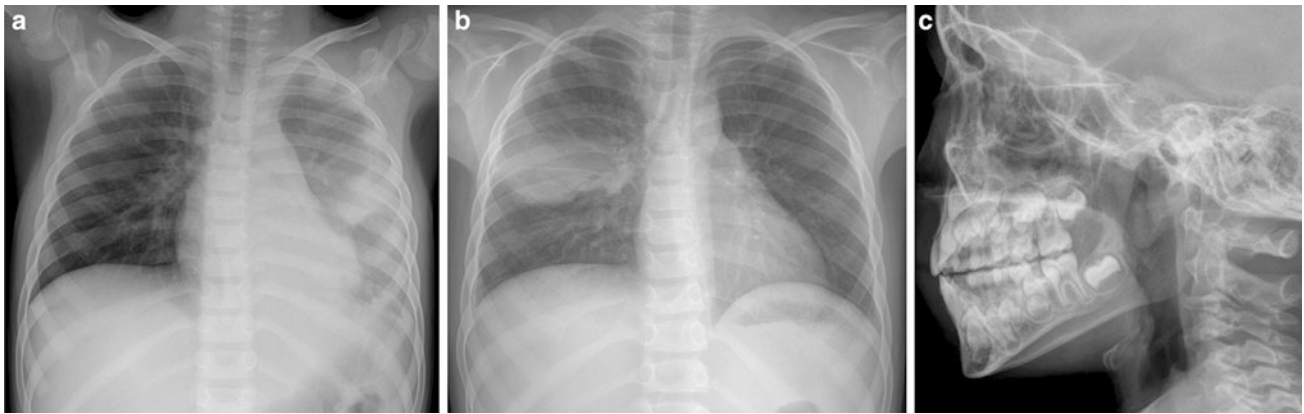


**Fig. 9** X-linked agammaglobulinemia (XLA). A frontal CXR (a) from a 7-year-old boy with XLA depicts patchy air space opacity due to pneumococcal pneumonia. A frontal CXR (b) obtained 3 months later

shows clearance of the previous pneumonia, but a new pneumonia of the right mid lung. A lateral upper airway radiograph (c) demonstrates diminutive adenoidal tissue

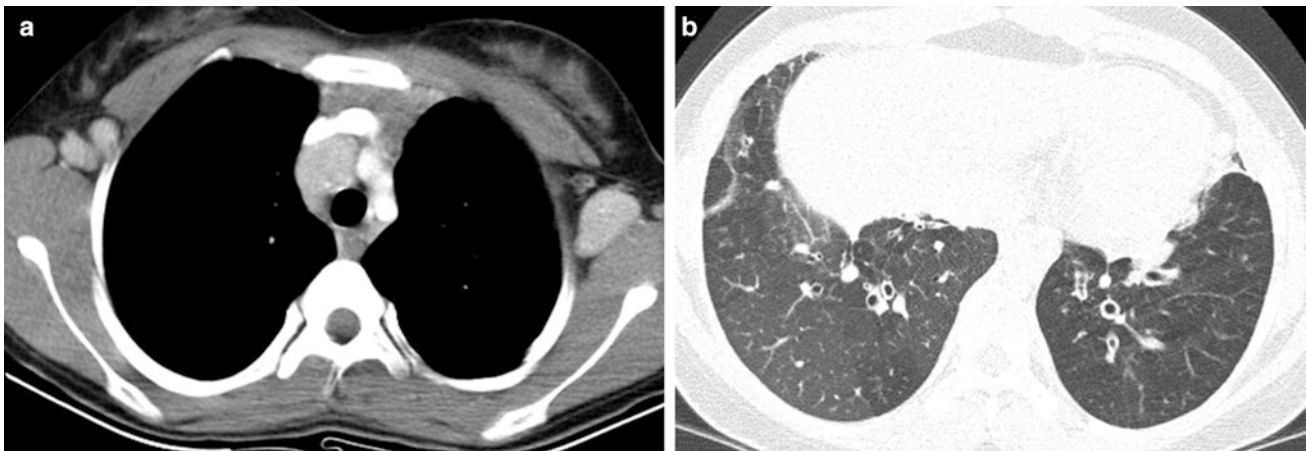


**Fig. 10** Common variable immunodeficiency (CVID). An axial contrast-enhanced chest CT image (a) in a 12-year old demonstrates mediastinal and axillary lymphadenopathy representing CVID-associated benign lymphoproliferative disease that can simulate

lymphoma. An axial chest CT image (b) from the same patient 2 years later shows lower lobe bronchiectasis, bronchial wall thickening, and mosaic lung attenuation from air trapping, resembling changes of cystic fibrosis

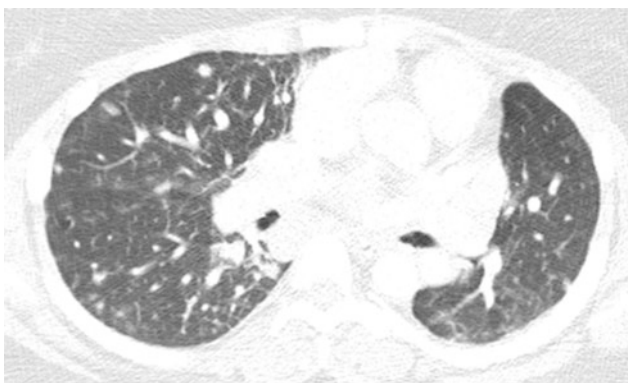


**Fig. 11** Granulomatous lymphocytic-interstitial lung disease (GLILD). An axial chest CT image of a 21-year old with CVID shows multiple pulmonary nodules

by noncaseating granulomatous and lymphoproliferative histologic patterns. Findings on chest imaging can include pulmonary nodules, consolidation, and ground-glass or reticular opacities (Fig. 11). GLILD can precede the diagnosis of CVID and is associated with restrictive PFTs, a high prevalence of autoimmune disorders and decreased survival (Park and Levinson 2010).

#### 4.1.4 Hyper-IgM Syndrome

Children affected by Hyper-IgM syndrome are identified by an elevated or normal IgM level and decreased IgG and IgA levels in serum. There is a normal number of circulating lymphocytes but a defect in signaling between T-cells and B-cells that prevents the switch from producing IgM to IgG or IgA. Most commonly, it is related to an X-linked

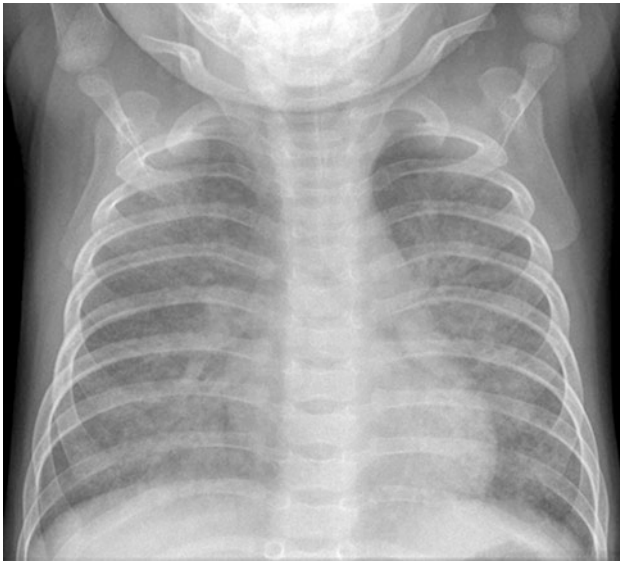


**Fig. 12** X-linked hyper-IgM syndrome. A frontal CXR of a 6-year-old boy with tachypnea and hypoxemia due to *Pneumocystis jirovecii* pneumonia demonstrates diffuse bilateral nodular pulmonary opacities with central confluence of the opacities

mutation of the *CD40L* gene encoding a T-cell surface ligand. Presentation is similar to agammaglobulinemia, with recurrent respiratory and gastrointestinal tract infections by encapsulated bacteria, viruses, fungi and parasites. There is a particular susceptibility for *P. jirovecii* pneumonia (PCP) (Fig. 12). There is also a proclivity for Cryptosporidium-related diarrhea and sclerosing cholangitis, as well as an increased risk of hepatocellular carcinoma (Winkelstein et al. 2003).

## 4.2 Combined T-Cell and B-Cell Immunodeficiencies

T-cells function in the initial response to an antigen and in limiting the potentially harmful immune response. Because antibody production by B-cells is regulated by T-cells, T-cell immunodeficiencies may be accompanied by impaired antibody production. Children with combined T-cell and B-cell immunodeficiencies are susceptible to the same pathogens that afflict those with antibody deficiencies, as well as a variety of opportunistic infections including *Mycobacteria*, viruses, *Pneumocystis* and other fungi (Buckley 2004).

### 4.2.1 Severe Combined Immunodeficiency

Absence of both T-cell and B-cell function results in severe combined immunodeficiency (SCID), the most severe of the primary immunodeficiencies. A number of different genetic defects can cause SCID, including autosomal recessive and X-linked forms (Chan and Puck 2005). Most cases present between 2 and 6 months of age as protection from maternal

antibodies wanes. Recurrent, persistent, severe or opportunistic respiratory infections beginning in early infancy along with thrush, dermatitis, chronic diarrhea or failure to thrive should raise suspicion of SCID. Without HSCT, gene therapy or enzyme replacement therapy, SCID is almost uniformly fatal in the first two years of life, making early diagnosis critical to prevent death from overwhelming infection (Griffith et al. 2009).

The primary role of radiology of the thorax in these children is to evaluate infections that are the main cause of mortality. While SCID patients have a diminutive thymus, physiologic thymic involution in response to stress in normal infants limits the use of this finding for suggesting a diagnosis of SCID (Manson et al. 2000) (Fig. 13). The adenosine deaminase (ADA)-deficient form of SCID is of particular note to radiologists because it is associated with a characteristic chondro-osseous dysplasia that manifests with costochondral junction cupping and splaying, concavity of the lateral margins of the vertebral transverse processes and medial margins of the posterior ribs, and thick growth arrest lines (Chakravarti et al. 1991) (Fig. 13).

### 4.2.2 Combined Immunodeficiency

While the susceptibility to infections may be similar to SCID, there is no lymphopenia in combined immunodeficiency (CID). Some forms of CID have distinctive clinical features. For example, signal transducer and activator of transcription 5B (STAT5b)-deficiency manifest with severe growth hormone-resistant growth failure beginning after birth, recurrent infection, dysmorphic features, atopic disease, autoimmune diatheses, and chronic lung disease beginning in infancy or childhood. The chronic lung disease is typically in the form of LIP (Fig. 14), and can lead to death from respiratory failure (Nadeau et al. 2011).

## 4.3 Well-defined Syndromes with Immunodeficiency

### 4.3.1 DiGeorge Syndrome

DiGeorge syndrome (DGS), also known as velocardiofacial syndrome, is a contiguous gene syndrome due to an inherited autosomal dominant or de novo chromosome 22q11.2 deletion. DGS is characterized by maldevelopment of the third and fourth pharyngeal pouches resulting in distinctive facial features (hypertelorism, saddle nose, short philtrum, low-set ears, cleft palate), conotruncal malformations (including tetralogy of Fallot, interrupted aortic arch, or truncus arteriosus), thymic hypoplasia (leading to immunodeficiency from T-cell lymphopenia and dysfunction) and parathyroid hypoplasia (leading to hypocalcemia from hypoparathyroidism) (Demczuk and Auris 1995). Presentation in the



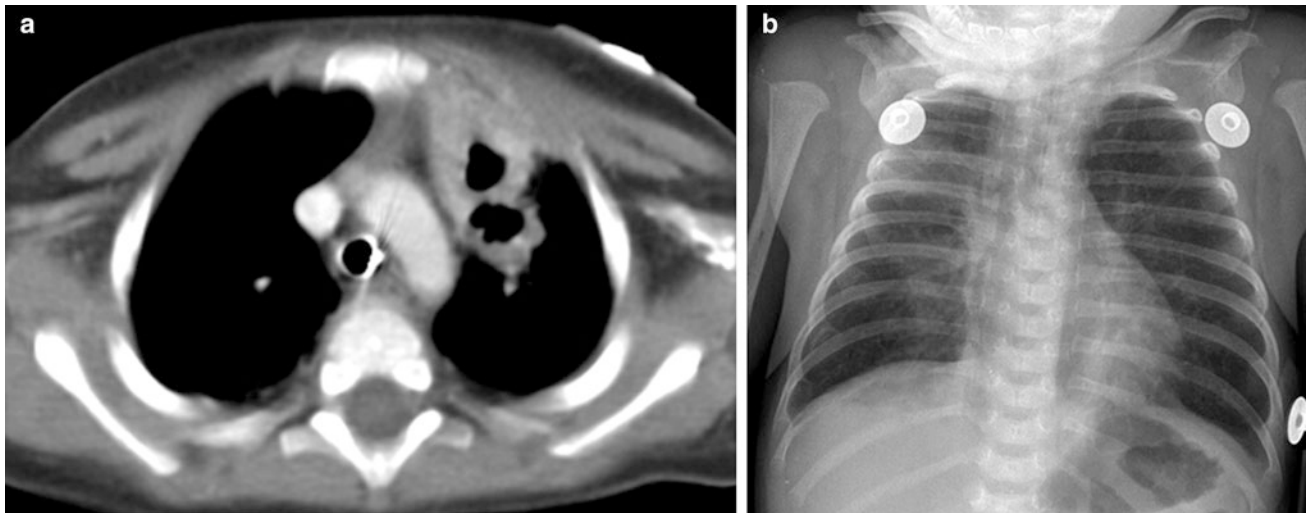


**Fig. 13** Severe combined immunodeficiency (SCID). An axial contrast-enhanced chest CT image (a) in a 6-year old with SCID demonstrates a paucity of thymic tissue in the anterior mediastinum, along with cavitary lesions in the anterior left upper lobe related to

*Nocardia* infection. A frontal CXR (b) in a 2-month old with adenosine deaminase (ADA)-deficient SCID shows cupping and splaying of the anterior rib costochondral junctions, a narrow superior mediastinum related to a diminutive thymus, and patchy bilateral pneumonia



**Fig. 14** Combined immunodeficiency (CID). An axial CT chest image from a 12-year old with *STAT5B* mutation-related CID and chronic respiratory symptoms depicts extensive bilateral ground-glass pulmonary opacities and scattered tiny cysts related to lymphocytic interstitial pneumonitis (LIP)

neonatal period is more often due to hypocalcemia-induced seizures than to immunodeficiency.

DGS may be partial or complete. Partial DGS is associated with mild defects in T-cell numbers and highly variable degrees of immunodeficiency. Patients with partial DGS may experience recurrent sinopulmonary infections. Complete DGS is a form of SCID and is associated with severe T-cell deficiency. Patients with complete DGS are susceptible to opportunistic infections and to graft-versus-host disease from nonirradiated blood products (Jawad et al. 2001).

Thoracic imaging findings of DGS may include an abnormal cardiac silhouette related to a conotruncal malformation, a narrow mediastinum related to a small thymus,

and pneumonia (Fig. 15). Additional findings may include tracheobronchomalacia and anomalies of the ribs or vertebrae (Ryan et al. 1997).

#### 4.3.2 Wiskott-Aldrich Syndrome

X-linked gene mutations resulting in aberrant structure of the Wiskott-Aldrich syndrome (WAS) protein are responsible for this immunodeficiency. In addition to a role in immune defense, the WAS protein functions in a pathway that protects against autoimmune disease (Notarangelo et al. 2008). Clinical manifestations of WAS include recurrent infections, eczema, elevated IgA, autoimmune disease (vasculitis, colitis, glomerulonephritis), malignancy (especially non-Hodgkin lymphoma associated with Epstein-Barr virus), and thrombocytopenia with small platelets. Subtypes exist, with phenotypes ranging from mild intermittent thrombocytopenia to the complete syndrome (Massaad et al. 2013). The association of WAS with abnormal blood clotting that leads to bleeding in the first month of life is unique among the forms of PID. Pulmonary infections with encapsulated *Streptococcus pneumoniae* and *Pneumocystis* are common in affected children. Herpes virus infections also occur (Buckley 2004) (Fig. 16). The only curative treatment is HSCT or gene therapy (Aiuti et al. 2013).

#### 4.3.3 Hyper-IgE syndrome

Hyper-IgE syndrome (HIES) is characterized by a reduction in CD4+ T-cells, eosinophilia and elevated IgE levels. The autosomal dominant form of HIES, also known as Job syndrome, is due to *STAT3* gene mutations (Heimall et al. 2010). Job syndrome is characterized by distinctive facial features

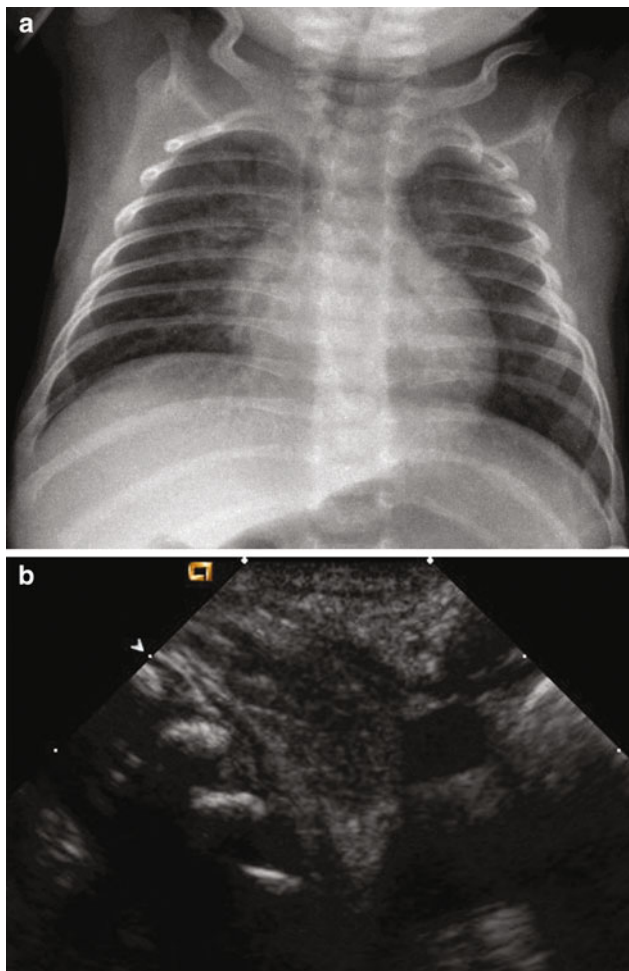


**Fig. 15** DiGeorge syndrome (DGS). The thymic size is unable to be reliably assessed on the frontal CXR (**a**) of a 5-week-old boy with hypocalcemic seizures from parathyroid hypoplasia. A longitudinal chest US image (**b**) reveals a hypoplastic thymus

(broad nasal bridge, high palate, delayed shedding of primary teeth), eczematous dermatitis beginning in infancy, hyper-extensible joints, osteoporosis, fractures, scoliosis, and recurrent *Staphylococcus aureus* and *Candida* infections. Skin infections often begin in infancy and can manifest as “cold” abscesses that lack classical symptoms and signs of inflammation. Sinopulmonary infections are common and can occur in patients who remain afebrile, likely due to the impaired inflammatory response. Thoracic findings include recurrent pneumonia, bronchiectasis, postinfectious pneumatoceles, lymphadenopathy, and esophagitis. Pathologic fractures incurred after mild trauma can mimic child abuse (Woellner et al. 2010; Chandesris et al. 2012) (Fig. 17).



**Fig. 16** Wiskott-Aldrich syndrome (WAS). An axial chest CT image from a 14-year old with a history of eczema and bloody diarrhea in infancy shows septal thickening related to herpes interstitial pneumonitis

#### 4.3.4 Dyskeratosis Congenita

Dyskeratosis congenita (DKC) is a progressive multisystem disorder characterized by the clinical triad of nail dystrophy, lacy reticular skin pigmentation, and oral leukoplakia. Additional features may include developmental delay, short stature, cerebellar hypoplasia, esophageal stenosis, urethral stenosis, osteopenia, liver fibrosis, and pulmonary fibrosis. DKC is most often attributable to mutations in genes involved in telomere maintenance, and inheritance may follow an X-linked, autosomal dominant or autosomal recessive pattern. Patients with DKC are at very high risk of aplastic anemia, myelodysplastic syndrome, leukemia, and squamous cell carcinoma. The bone marrow failure does not respond to immunosuppressive therapy (Savage and Alter 2009). Pulmonary fibrosis is a serious complication and accounts for more than 15 % of deaths in DKC. The pulmonary fibrosis occurs earlier in DKC patients who undergo HSCT and is rapidly progressive with a median survival of less than 2 years after onset of pulmonary symptoms. The presenting features of DKC-related pulmonary fibrosis include persistent dry cough, progressive dyspnea, restrictive PFTs, markedly reduced  $D_{LCO}$ , and patchy or diffuse interstitial pulmonary opacities on CXR or CT (Giri et al. 2011) (Fig. 18).

#### 4.3.5 Ataxia-Telangiectasia

Ataxia-telangiectasia (AT) is attributable to autosomal recessive mutations in the *ATM* gene that encodes a DNA damage response protein. Patients with AT have aberrant T-cells which results in onset of immunodeficiency in infancy. Cerebellar ataxia manifests at toddler age, and is



**Fig. 17** Hyper-IgE syndrome (HIES). An axial chest CT image (a) from an 11-year old with HIES shows pneumatoceles in the right lung related to previous *Staphylococcus* infections. In the same patient, several thoracic vertebral body compression fracture deformities

related to osteoporosis are revealed on a sagittal chest CT image reconstructed with bone windows (b). An esophagram (c) on the same patient demonstrates intramural tracking of contrast related to deep esophageal ulcers from *Candida* esophagitis

often misdiagnosed as cerebral palsy. Oculocutaneous telangiectasias begin to appear at 3–6 years of age, while growth retardation develops later in childhood. An elevated AFP is characteristic and AFP testing in children with persistent ataxia is advised to avoid diagnostic delay (Cabana et al. 1998). Recurrent sinopulmonary bacterial infections and noninfectious granulomatous inflammation of various tissues are typical. In children and adolescents with AT, *S. aureus*, *H. influenzae*, and *S. pneumoniae* are the predominant respiratory infectious agents, while opportunistic infections are not observed (Schroeder and Zielen 2013). There is extreme susceptibility to DNA

damage from ionizing radiation and a high risk of cancer, especially lymphoma, leukemia, and leiomyosarcoma. Life expectancy is only 20–30 years due to the increased mortality from cancer and respiratory disease (Micol et al. 2011).

Thoracic imaging findings can include a small thymus, recurrent pneumonia, bronchiectasis, lymphadenopathy, and a chronic interstitial lung disease unique to ataxia-telangiectasia (AT-ILD). AT-ILD is characterized by lymphocytic infiltrate, bizarre atypical cells, and fibrosis resulting in interstitial and pleural thickening, restrictive PFTs, chronic cough, fever, dyspnea, and an inability to



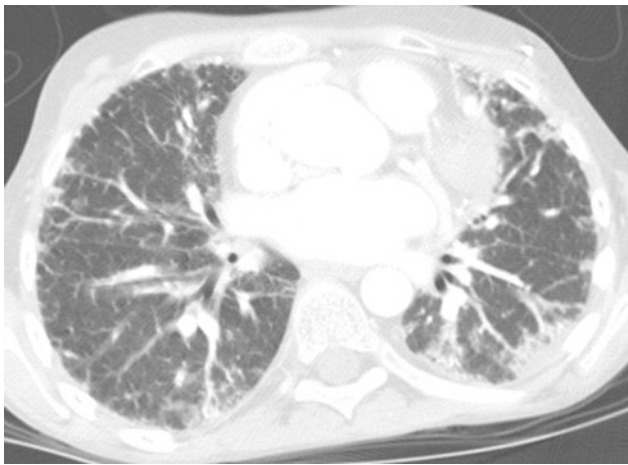


**Fig. 18** Dyskeratosis congenita (DKC). An axial chest CT image of a 12-year old shows diffuse bilateral linear and patchy pulmonary opacities, predominantly in a subpleural distribution, representing DKC-related pulmonary fibrosis

reinflate the lung after pneumothorax (Fig. 19). AT-ILD has a mean age of onset of 17.5 years and a prevalence of at least 25 % in AT patients (Schroeder et al. 2005). Progressive clinical deterioration and death usually ensue within 2 years of diagnosis of AT-ILD, unless steroid therapy is initiated within the first year of onset (McGrath-Morrow et al. 2010).

#### 4.4 Congenital Defects of Phagocyte Number and/or Function

Congenital defects of phagocyte number and/or function manifest with variable susceptibility to infection and exist in neutropenic and nonneutropenic forms. The neutropenic forms can be nonsyndromic or syndromic, as in the case of Shwachman-Diamond syndrome (pancytopenia, exocrine pancreatic insufficiency, and chondrodysplasia). Nonneutropenic forms are subdivided according to the results of a dihydrorhodamine (DHR) assay. A normal DHR assay is seen in pulmonary alveolar proteinosis from alveolar macrophage dysfunction due to *CSF2*-receptor- $\alpha$  (*GM-CSF*-receptor- $\alpha$ ) gene defects, and in Mendelian susceptibility to mycobacteria disease (MSMD) from an abnormal IL12-IFN $\gamma$  axis due to *IFNGR1* gene defects. An abnormal DHR assay is seen in chronic granulomatous disease (CGD) (Bousfiha et al. 2013).

##### 4.4.1 Chronic Granulomatous Disease

Due to a defect in the nicotinamide adenine dinucleotide phosphate-oxidase (NAPDH) complex, the phagocytes in children with chronic granulomatous disease (CGD) are unable to generate the superoxide burst necessary for killing

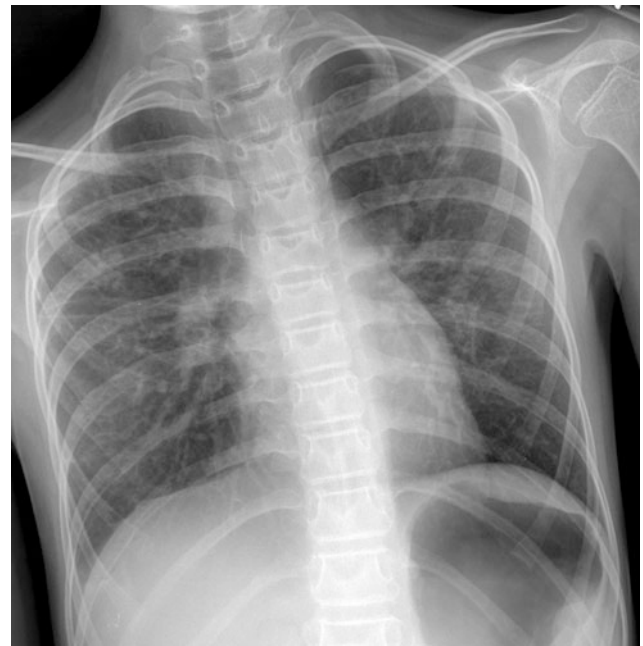


**Fig. 19** Ataxia-telangiectasia (AT). A frontal CXR in a 13-year old with AT and worsening dyspnea demonstrates subtle interstitial opacities, predominantly in the mid and upper lungs, and a small left pneumothorax. These findings are manifestations of a unique interstitial lung disease (AT-ILD) associated with progressive clinical deterioration and high mortality

ingested micro-organisms. CGD occurs in both X-linked and autosomal recessive forms, with the former being more common and severe.

Symptoms or signs of CGD often develop in the first 2 years of life. Presentation and ongoing complications are related to granuloma and abscess formation. These manifestations are likely due to ongoing inflammatory response to viable microorganisms. Histopathologic studies have shown that the granulomas in these patients may contain relatively few organisms and that the predominant portion of the granulomas results from the exuberant inflammatory response (Moskaluk et al. 1994).

Catalase-positive *S. aureus* is the most commonly cultured organism in the granulomas. *Burkholderia* and *Serratia* are also frequently isolated, while *Streptococcus* is relatively rare. Fungi and atypical mycobacteria are other causes of infection. Children with CGD are at high risk for invasive aspergillosis, which is the most common cause of mortality (Tabone 2003).

The lungs are the most common site of involvement, with pneumonia occurring in 80 % of patients (Mahdavian et al. 2013). Lung findings on CT vary depending on the infectious organism and disease chronicity, and may include consolidation, ground-glass opacities, centrilobular opacities, nodules, bronchiectasis, septal thickening, cysts, and parenchymal distortion (Towbin and Chaves 2010). Chronic

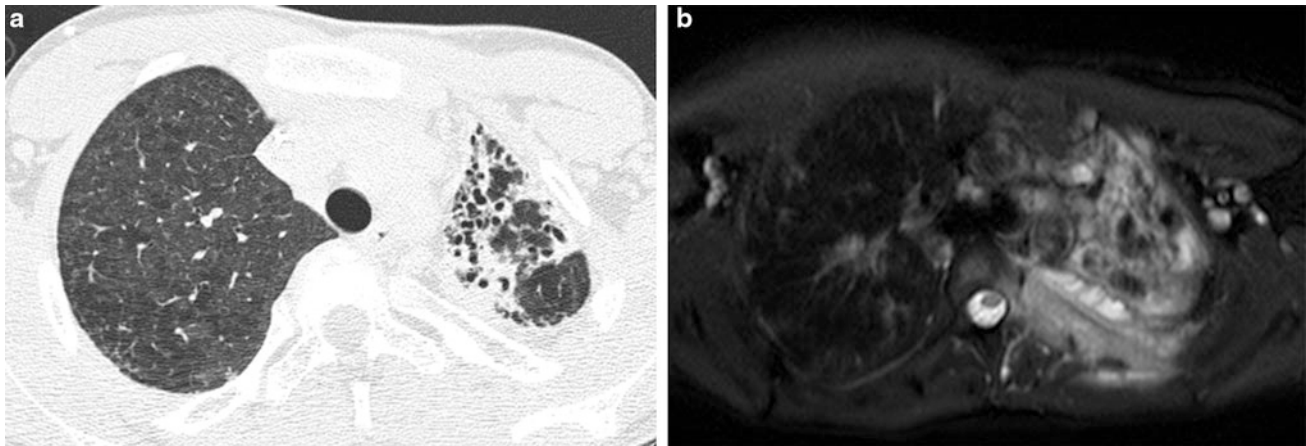


**Fig. 20** Chronic granulomatous disease (CGD). An axial chest CT image (a) from a 13-year old shows left lung volume loss and traction bronchiectasis from fibrosis related to CGD. An axial T2-weighted fat

saturated chest MR image (b) in the same patient at 19 years of age reveals involvement of the left pleura, ribs, and chest wall soft tissues by invasive *Aspergillus*

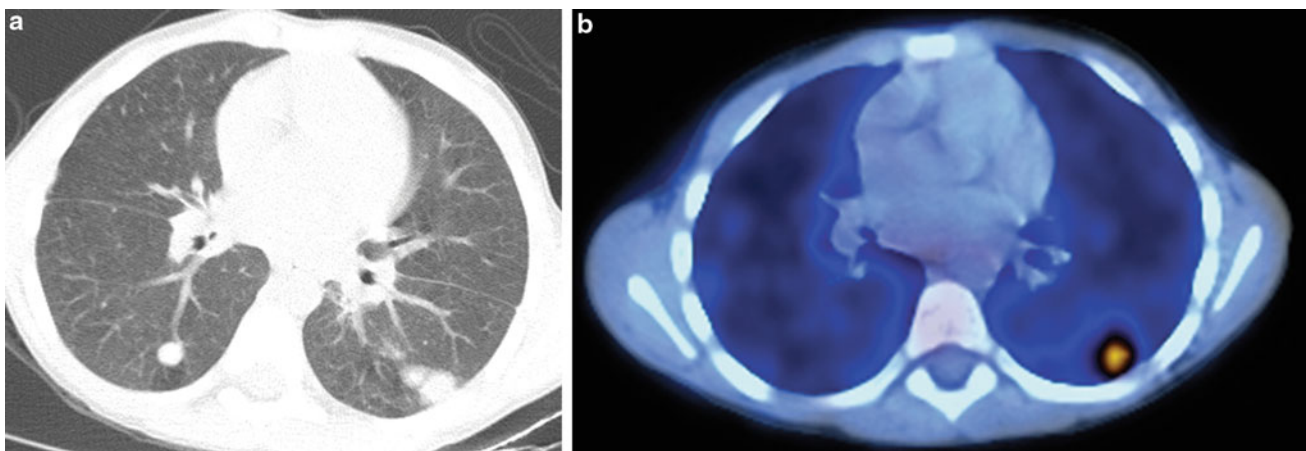


**Fig. 21** Chronic granulomatous disease (CGD). An axial chest CT image (a) in a 6-year old undergoing evaluation for bone marrow transplantation for CGD shows multiple bilateral pulmonary nodules. An axial fused FDG-PET/CT image (b) reveals increased FDG uptake

within only one of the nodules located in the posterior left lung. Subsequent targeted biopsy of the nodule allowed identification of active fungal infection with *Cladophialophora bantiana* that was undiagnosed by other means

lung involvement may lead to pulmonary fibrosis, honeycombing, pulmonary hypertension, and development of systemic blood supply to areas of pulmonary infection (pseudo-sequestration) (Matsuzono et al. 1995). Extrapulmonary thoracic manifestations include suppurative lymphadenopathy, pleuritis, empyema, and rib or vertebral osteomyelitis (Khanna et al. 2005). Infections involving both the lungs and the chest wall are highly suggestive of the diagnosis of CGD (Fig. 20). Fluorodeoxyglucose-positron emission tomography (FDG-PET) is more reliable than CT for distinguishing active disease from quiescent disease or scarring (Fig. 21), an important distinction for evaluating therapy response, identifying sites for biopsy or surgical debridement, and planning for HSCT (Gungor et al. 2001) (Fig. 21).

## 4.5 Acquired Immunodeficiency

### 4.5.1 Acquired Immunodeficiency Syndrome

In the Pediatric Pulmonary and Cardiovascular Complications of Vertically Transmitted HIV (P<sup>2</sup>C<sup>2</sup>) Study from the 1990s, pulmonary infection was the most common cause of death, especially in infants and young children (Langston et al. 2001). Since then, there has been a marked decrease in opportunistic pulmonary infections and deaths related to acquired immunodeficiency syndrome (AIDS) in developed countries as a result of the implementation of highly active antiretroviral therapy (HAART) (Gona et al. 2006). Even in developed countries, though, vigilance for opportunistic infections remains important due to noncompliance and drug resistance.

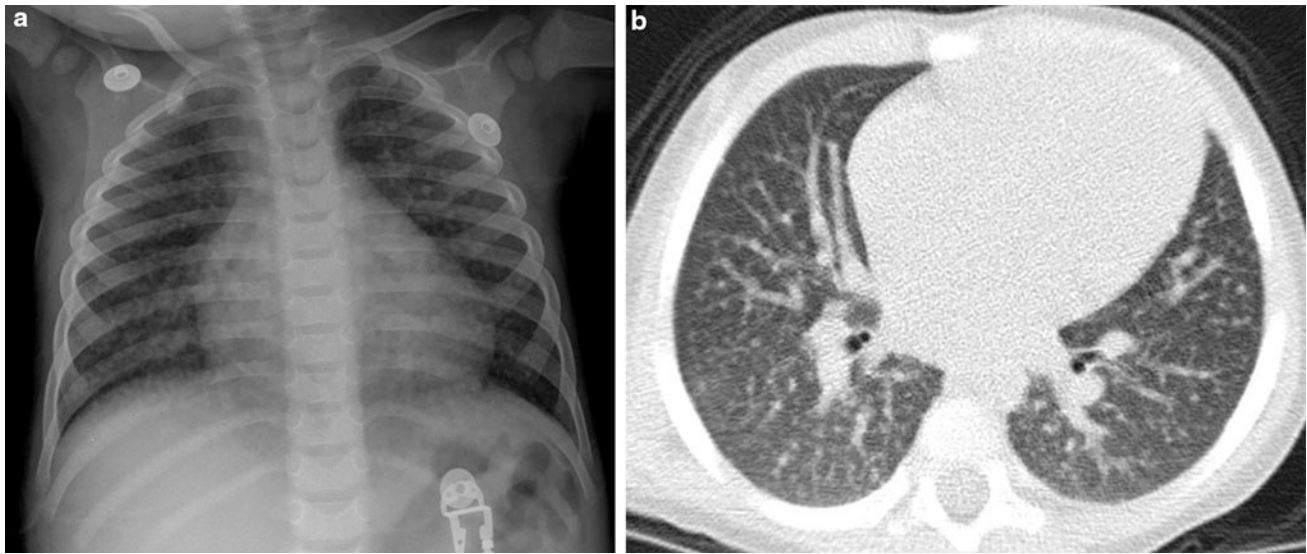


**Fig. 22** Lymphocytic interstitial pneumonitis (LIP). A frontal CXR (a) in a 16-month-old HIV+ patient shows numerous tiny pulmonary nodules. No infectious pathogen was identified, and the nodules persisted

for several months, as demonstrated on a chest CT (b) obtained at 21 months of age

Although HAART has reduced rates of opportunistic infection, bacterial pneumonia still tends to be more severe in HIV-infected children than in HIV-uninfected children related to a higher incidence of abscess and empyema. *Streptococcus* is the most common pathogen, and manifests as lobar or multilobar patchy consolidation. Mycobacterial infection is more likely to be multilobar or miliary, and is associated with necrotic lymphadenopathy. Pneumonias from respiratory syncytial virus (RSV), cytomegalovirus (CMV), parainfluenza, influenza, adenovirus, or human metapneumovirus infections have diverse radiographic appearances that can be indistinguishable from bacterial pneumonias. A patient age of less than 6 months, a respiratory rate  $>59$  breaths/minute, an  $O_2$  saturation  $<93\%$ , and an absence of vomiting are clinical features that suggest *P. jirovecii* pneumonia (PCP), which classically manifests with bilateral diffuse or patchy ground-glass or reticulonodular opacities with perihilar to peripheral progression, although this appearance overlaps with mycobacterial and viral pneumonia. PCP can also be associated with pulmonary cysts that rupture, leading to pneumothorax or pneumomediastinum (George et al. 2009).

Lymphocytic interstitial pneumonitis (LIP) is a form of pulmonary lymphoid hyperplasia characterized by infiltration of the interstitium by lymphocytes and plasma cells and classically presenting in HIV-infected children older than 2 years of age with chronic or recurrent cough and mild hypoxemia (Theron et al. 2009). The 1987 CDC criteria for a presumptive diagnosis stipulate the persistence of diffuse, symmetrical, reticulonodular or nodular pulmonary opacities for at least 2 months without an identifiable pathogen,

or a response to antibiotic therapy (Pitcher et al. 2010). CT reveals nodules in a subpleural, septal, centrilobular, or peribronchial distribution, and ground-glass opacities with or without lymphadenopathy (Becciolini et al. 2001) (Fig. 22). Bronchiectasis and cystic dilated air spaces have also been described (Pitcher et al. 2010). Resolution of LIP in children can be due to response to HAART or corticosteroid therapy, or to immunologic deterioration and progression of HIV disease (Theron et al. 2009).

The immune reconstitution inflammatory syndrome (IRIS) is an exaggerated inflammatory response by the reconstituted immune system occurring 1–6 months after HAART initiation, resulting in apparent clinical worsening. “Unmasking” IRIS occurs in response to a previously unrecognized underlying infection, while “paradoxical” IRIS occurs in response to a previously treated infection. IRIS is most frequently observed in response to mycobacterial, herpes virus, JC virus, PCP, and cryptococcal infections, and can appear as new or worsening lymphadenopathy, pulmonary nodules, or pulmonary consolidation on imaging. IRIS must be distinguished from noncompliance, drug resistance, or newly acquired opportunistic infection, and is treated by NSAIDs, steroids, and discontinuation of HAART (Theron et al. 2009).

A high incidence of swallowing dysfunction and gastroesophageal reflux predisposes to aspiration pneumonia in HIV-infected children. These children may also suffer from odynophagia and dysphagia related to esophagitis caused by *Candida* or CMV infection. HIV-related cardiomyopathy, antiviral therapy cardiotoxicity, accelerated atherosclerosis and chronic anemia can lead to cardiac failure and



pulmonary edema that is misattributed to primary pulmonary infection (Pitcher et al. 2009). In addition, HIV infection is associated with an increased risk of thymic cysts and non-Hodgkin lymphoma, which are covered in the chapter entitled Imaging of the Pediatric Thymus and Thymic Disorders by Sams and Voss, as well as smooth muscle tumors, which are covered in the chapter entitled Pulmonary and Extra-Thymic Mediastinal Tumors by Lyons, Guillerman and McHugh.

#### 4.5.2 Acquired Neutropenia and Invasive Fungal Disease

Neutropenia is common in children undergoing chemotherapy for cancer or allogeneic HSCT, and confers a high risk of invasive fungal disease (IFD) by mold (most frequently *Aspergillus*) or yeast (most frequently *Candida*). The lungs are the most common site of deep organ involvement by IFD. In a neutropenic patient with fever or respiratory symptoms or signs, the traditional approach has been to obtain a CXR, give early empiric broad-spectrum antibacterials, and add empiric antifungals for suspected invasive fungal disease (IFD) if the fever or respiratory symptoms or signs persist >96 h. In the presence of a deficient immune response, findings of infection are often absent or subtle and nonspecific on CXR, so that chest CT is preferred. However, even the yield of chest CT is low in this setting. In a study of 52 pediatric oncology patients with persistent febrile neutropenia, only 18 % of the initial (mean of 5 days of febrile neutropenia) CT scans were positive, and alterations in therapy were made in only 3 % based on the findings of initial CT. Repeat (mean of 17 days of febrile neutropenia) CT had a much higher yield, being positive in 52 % of cases and directing a change in therapy in 20 %. Respiratory symptoms or signs were present in only a minority of cases with a positive chest CT, while all patients with a concern for occult IFD had findings on chest CT, suggesting that initial chest CT should be limited to patients without localized signs or symptoms (Agrawal et al. 2011).

Rather than administering empiric antifungals in all patients at risk with persistent febrile neutropenia, a “pre-emptive” or “diagnostic-driven” approach of administering antifungals only in the setting of either microbiologic (cytology, direct microscopy, culture,  $\beta$ -D-glucan or galactomannan assay of serum, or bronchoalveolar lavage fluid) or chest CT evidence of probable IFD may reduce unnecessary therapy without compromising prognosis (Castagnola et al. 2014). The European Organization for Research and Treatment of Cancer/Mycoses Study Group (EORTC-MSG) chest CT criteria for probable IFD are the presence of well-circumscribed pulmonary lesions (with or without a “halo” sign), an “air-crescent” sign, or a cavity in the appropriate clinical setting (De Pauw et al. 2008).

The “halo” sign consists of a ground-glass halo of alveolar hemorrhage around a nodular or consolidative focus of infarcting lung from fungal vascular invasion and thrombosis that occurs early in IFD. A “reversed halo” sign of focal ground-glass opacity surrounded by a crescent or ring of consolidation may also be observed with early IFD (Georgiadou et al. 2011). An “air-crescent” sign or cavitation is the result of neutrophil recovery with release of proteases that resorb necrotic tissue (McAdams et al. 1995). In the course of IFD, a “halo” sign, nodule, or consolidation is typically visible on chest CT within 5 days of fever onset (Fig. 7). Early initiation of antifungals based on detection of the “halo” sign on chest CT is associated with better response to treatment and improved survival (Greene et al. 2007). Despite effective antifungal therapy, an increase in lesion number and size may be observed for 7–10 days followed by a plateau for a few days, and should not be confused for progressive disease. The “air-crescent” sign and cavitation develop in 2–3 weeks, dependent on the timing of neutrophil recovery (Caillot et al. 2001) (Fig. 7). Refractory IFD is suggested by no decrease in lesion number or size or by lack of development of an “air-crescent” sign or cavitation after 2–3 weeks, but initial or maximal lesion size or number does not impact outcome (Horger et al. 2005). After 2–3 weeks, reappearance of a “halo” sign, development of new lesions, or an increase in wall thickness of a cavitary lesion suggests relapsed or new infection (Fig. 7). Even after clinical remission, there may be fibrotic or thin-walled cavitary remnants visible on chest imaging (Geffer et al. 1985).

The chest imaging findings of IFD are not entirely specific and can also be observed in immunocompromised children with *Mycobacterium*, *Nocardia*, *Pseudomonas*, or herpes virus infections (Gasparetto et al. 2008). Following allogeneic HSCT, children are susceptible not only to opportunistic pulmonary infections, but also to noninfectious pulmonary disorders such as alveolar hemorrhage, pulmonary edema, drug reaction, lymphoproliferative disease, organizing pneumonia, bronchiolitis obliterans, graft-versus-host disease, and idiopathic pneumonia syndrome. These disorders can cause considerable morbidity and mortality in the post-transplant setting, and can be difficult to distinguish on the basis of imaging findings, so that correlation with clinical features, identification of risk factors and institution of preventative measures are paramount in management (Sakaguchi et al. 2012).

---

## 5 Vasculitis

Vasculitis is an inflammatory disease of the blood vessel walls. Apart from invasive aspergillosis, infectious vasculitis is uncommon in childhood. Environmental, autoimmune

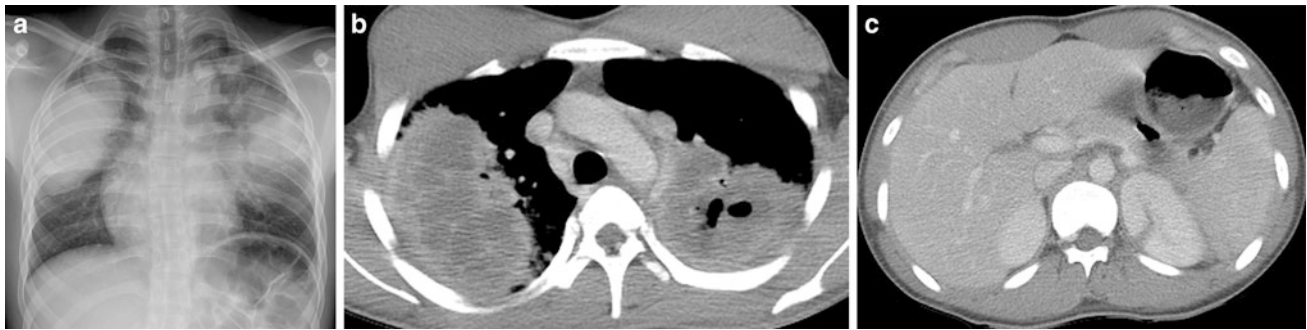


**Fig. 23** Granulomatosis with polyangiitis (GPA). A frontal CXR (a) of a 17-year-old male with hemoptysis, hematuria and elevated anti-PR3 antibodies depicts large mass-like opacities of the mid to upper lungs bilaterally. An axial contrast-enhanced chest CT image

(b) demonstrates low-attenuation necrosis and cavitation within the pulmonary opacities. An axial contrast-enhanced abdominal CT image (c) reveals a wedge-shaped lesion of the posteromedial aspect of the left kidney related to renal vasculitis

and genetic factors play a role in the pathogenesis of non-infectious vasculitis. Vasculitis can be categorized according to the predominant size of the affected vessels. Takayasu arteritis, a large vessel vasculitis, and Kawasaki disease, a medium vessel vasculitis, are covered in the chapters entitled Pediatric Cardiac CT by Sena and Goo and Pediatric Cardiac MRI by Krishnamurthy and Chung. Small vessel vasculitis affecting the pediatric lungs may be associated with a systemic disease (such as SLE), an immune complex deposition disease (such as anti-glomerular basement membrane disease), or diseases with anti-neutrophil cytoplasmic antibodies (ANCA). ANCA-associated vasculitides are characterized by necrotizing inflammation of small vessels (i.e., capillaries, venules, arterioles, small arteries) and encompass overlapping syndromes, including granulomatosis with polyangiitis (GPA) and microscopic polyangiitis (MPA) (Jennette et al. 2013). ANCA directed against proteinase 3 (PR3) are predominantly associated with GPA, and ANCA directed against myeloperoxidase (MPO) are mainly associated with MPA (Millet et al. 2013).

Pediatric vasculitis affecting the lungs is often associated with diffuse pulmonary hemorrhage. This must be distinguished from nonvasculitic causes of pulmonary hemorrhage in childhood, such as idiopathic pulmonary hemosiderosis, cystic fibrosis, coagulopathy, pulmonary venoocclusive disease, and pulmonary arteriovenous malformations (Susarla and Fan 2007).

### 5.1 Granulomatosis with Polyangiitis

Granulomatosis with polyangiitis (GPA), formerly known as Wegener granulomatosis, is characterized by necrotizing vasculitis predominantly affecting small to medium vessels (i.e., capillaries, venules, arterioles, arteries, and veins), usually of the upper and lower respiratory tract. Necrotizing glomerulonephritis is also common. A limited form initially

confined to the lungs may occur. In the acute phase, the predominant pattern of inflammation is purulent rather than granulomatous. In the chronic phase, granulomatous and nongranulomatous extravascular inflammation is common (Jennette et al. 2013). The most common finding at presentation on chest imaging is multiple pulmonary nodules and masses. The lesions may coalesce or cavitate over a period of several days or a few weeks (Fig. 23). Consolidation and ground-glass opacities may also be noted. The airways can be affected, manifesting as tracheobronchial wall thickening, bronchial stenosis or bronchiectasis (Castaner et al. 2010).

### 5.2 Microscopic Polyangiitis

Microscopic polyangiitis (MPA) is characterized by necrotizing vasculitis predominantly affecting small vessels (i.e., capillaries, venules, or arterioles). In distinction to GPA, granulomatous and extravascular inflammation is absent. Renal and lung involvement are common.

In pulmonary capillaritis, there is inflammatory disruption of the alveolar interstitial capillary network, resulting in pulmonary hemorrhage. Although most pediatric patients with pulmonary capillaritis have dyspnea and anemia on presentation, only a minority has hemoptysis, contributing to diagnostic delay (Fullmer et al. 2005). ANCA-associated pulmonary capillaritis is an underappreciated cause of pulmonary hemorrhage and likely accounts for a substantial proportion of pulmonary hemorrhage cases attributed to idiopathic pulmonary hemosiderosis (Taytard et al. 2013).

Acute hemorrhage into the pulmonary airspaces produces ill-defined pulmonary nodules, ground-glass opacities and consolidation on CT (Fig. 24). Aggregates of hemosiderin-laden macrophages from repetitive hemorrhage result in septal thickening and crazy-paving. Parenchymal and subpleural cysts and architectural distortion may be



**Fig. 24** Microscopic polyangiitis (MPA). An axial chest CT image of a 2-year-old girl with anemia, hypoxemia and elevated anti-MPO antibodies show patchy ground-glass opacities of the right lung and consolidative opacities of the left lung. These findings represent alveolar hemorrhage related to pulmonary capillaritis

observed on CT in the chronic setting (Connolly et al. 1996; Ravenel and McAdams 2003).

The finding of ill-defined centrilobular opacities suggest angiocentric inflammation and hemorrhage from small vessel pulmonary vasculitis, but it is not possible to reliably differentiate capillaritis from other causes of diffuse pulmonary hemorrhage on the basis of the imaging features, and lung biopsy is often required for differentiation (Guillerman and Brody 2011). Definitive diagnosis is crucial because successful treatment of pulmonary capillaritis typically requires aggressive and prolonged immunosuppressant therapy. CT can be used to help assess response to therapy (Vece and Fan 2010).

## 6 Sickle Cell Disease

The sickle hemoglobinopathies are autosomal recessive genetic disorders that include the presence of hemoglobin (Hgb) S within red blood cells. A substitution of valine for glutamic acid in the hemoglobin beta chain changes the structure of hemoglobin, allowing the hemoglobin to crystallize under conditions of low oxygen, dehydration, and acidosis. When the hemoglobin crystallizes, the red blood cell becomes less flexible and assumes the namesake sickle shape. These sickle cells have a decreased life span related to hemolysis and resulting in anemia. These nondeformable cells often obstruct small capillaries where slow flow promotes the conditions that encourage further sickling in a cascade effect.

Homozygous Hgb SS produces the most severe disease. Different mutations are associated with different amounts of hemoglobin F, with higher levels of Hgb F being associated with decreased disease severity. Compound heterozygous

conditions occupy a spectrum of disease severity depending on the non-S hemoglobin. The most common are hemoglobin S with hemoglobin C (Hgb SC) and hemoglobin S with  $\beta^0$  or  $\beta^+$  thalassemia. Hgb S $\beta^0$  thalassemia is similar to Hgb SS, while Hgb S $\beta^+$  thalassemia and Hgb SC disease will often have preserved splenic function and less risk of vaso-occlusive crisis and infection. Heterozygous hemoglobin S and hemoglobin A is the asymptomatic carrier state.

Infants with sickle cell disease usually show no abnormalities, and clinical signs and symptoms develop as fetal hemoglobin is replaced by defective adult-type hemoglobin. Hand-foot syndrome, a painful swelling of the hands and feet, may be an early presentation, in which case soft tissue swelling and periosteal new bone formation are seen radiographically (Babhulkar et al. 1995). Anemia and painful crises in other locations then develop. Decreased splenic function causes an increased susceptibility to infection.

The most common cardiovascular imaging findings in children with sickle cell disease are mild cardiomegaly and pulmonary vascular plethora related to chronic anemia. Myocardial perfusion abnormalities in children have been reported (Acar et al. 2000). Bone infarctions are common. CXR may demonstrate biconcave vertebral bodies from impression of the intervertebral discs on the adjacent endplates weakened by microinfarcts.

Lung function can be abnormal from an early age. Evidence of obstructive and restrictive pulmonary disease has been shown on PFTs in infants and young children (Koumbourlis et al. 1997; Arteta et al. 2013). It is increasingly recognized that long-term adverse changes in lung function are a major cause of morbidity and mortality, even in the absence of episodes of acute lung disease (Koumbourlis 2013). Airway hyperreactivity, which is more common in individuals with sickle cell disease, is associated with obstructive physiology (Mekontso Dessap et al. 2013) and may be an additional factor in the development of both acute and chronic lung disease (Leong et al. 1997).

The two most common acute chest complications of sickle cell disease are pneumonia and the acute chest syndrome (ACS). Functional asplenia can occur as young as 6 months of age. Children are then particularly susceptible to infections caused by bacteria with polysaccharide capsules. While *S. pneumoniae* sepsis was once a common cause of death in young children with sickle cell disease, mortality has decreased dramatically in recent years related to the effectiveness of newborn screening, prophylactic penicillin, and vaccination measures (Hamideh and Alvarez 2013).

The acute chest syndrome (ACS) is a major cause of morbidity and mortality in sickle cell disease. ACS a largely descriptive term applied to the clinical situation in which a



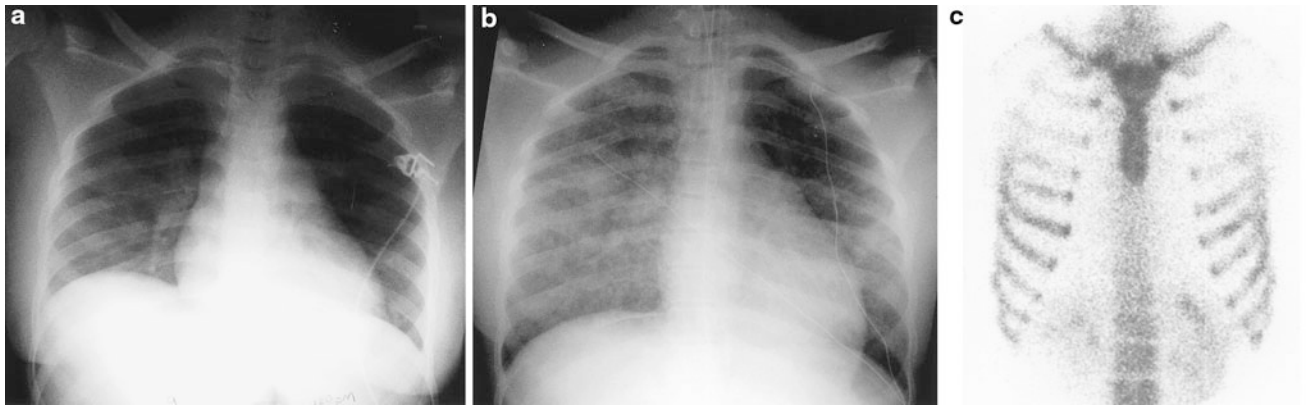


**Fig. 25** Acute chest syndrome. A frontal CXR (a) of a 17-year old with sickle cell/ $\beta$  thalassemia with acute chest pain demonstrates confluent opacity in the left lower lobe and a less well-defined opacity at the right lung base. A frontal CXR (b) obtained 2 days later for

increasing hypoxemia shows diffuse, ill-defined opacities of both lungs. A planar image of the chest from a technetium-99 m methylene diphosphonate bone scan (c) shows increased uptake in multiple ribs representing rib infarcts

patient with sickle cell disease develops a new infiltrate on CXR accompanied by chest pain, fever, and respiratory symptom (Fig. 25). ACS has been reported to account for 30 % of deaths in sickle cell patients under 10 years of age (Martin and Buonomo 1997), but the absolute mortality has decreased in the modern era of hydroxyurea therapy and early aggressive transfusion therapy. In a prospective study of 538 patients admitted for ACS, overall mortality was 3 % (Vichinsky et al. 2000). In adults, ACS-associated mortality is now primarily related to underlying pulmonary hypertension and acute cor pulmonale (Miller and Gladwin 2012). A specific cause can be identified in ACS in 40–70 % of cases. Etiologies include infection, pulmonary infarction, and fat embolism from vasoocclusive crises involving bone marrow (Vichinsky et al. 2000). Rib infarctions have also been identified in ACS (Gelfand et al. 1993) (Fig. 25). Asthma is associated with an increased risk of ACS in children (Boyd et al. 2006), and episodes of ACS predispose children to increased airway resistance (Sylvester et al. 2006). Repetitive episodes of ACS also lead to lung fibrosis, predominantly at the lung bases, contributing to chronic restrictive lung disease (Miller and Gladwin 2012).

By definition, infiltrates of ACS must occupy at least one complete bronchopulmonary segment on CXR without evidence of volume loss. The appearance of the infiltrates alone is not helpful in suggesting an etiology. Longitudinal evaluation may be of benefit. A lack of infiltrate resolution is associated with the presence of an infectious etiology and longer clinical course (Martin and Buonomo 1997). The presence of infiltrates in four or more lobes on the admission CXR is associated with an incidence of complications nine times that of involvement in one lobe (Vichinsky et al.

2000). Increasing infiltrates over the first days of hospitalization are also associated with an increase in complications and prolonged hospitalization.

A study of CT and bedside chest radiographs in 118 adult patients with ACS found that the sensitivity of CXR for consolidation on CT was high, but specificity was low. More than half demonstrated partial, rather than complete opacification of a segment. Presentation and course were more severe in patients with complete opacification. Consolidation was more common than atelectasis or ground glass opacity, and involvement was greatest in the lung bases, decreasing to the apices (Mekontso Dessap et al. 2013). In a 1993 CT study, Bhalla et al. found evidence of decreased peripheral pulmonary vessels in children with ACS (Bhalla et al. 1993). This decrease was not seen in children without sickle cell disease whose CT scans were used as controls. These findings suggest that there is a component of small vessel occlusion in these children.

## 7 Cystic Fibrosis

Within the first few months of postnatal life, the presence of airway inflammation and infection can be identified histologically in children with cystic fibrosis (CF) (Khan et al. 1995). Bronchiectasis is noted in two-thirds of children and air trapping in one-half of children with CF by the age of 5 years (Stick et al. 2009) (Fig. 26). As CF-related lung disease progresses, there is further bronchial dilation and mucous plugging, which become the distinctive features of CF-related lung disease (Fig. 27). Approximately 95 % of people with CF die of respiratory complications. The relative lack of lung disease at birth presents the opportunity to

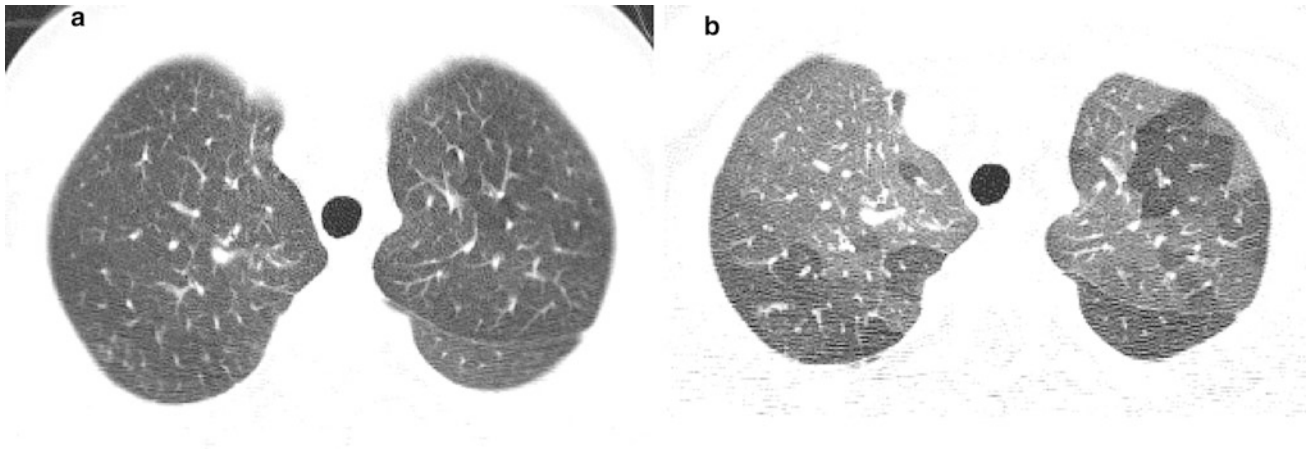


**Fig. 26** Cystic fibrosis (CF). An axial chest CT image acquired at deep inspiration (**a**) in a 12-year old demonstrates no bronchiectasis and only subtle heterogeneity of lung parenchymal attenuation. A

chest CT image acquired at end-expiration at the same axial level (**b**) reveals mosaic attenuation of the lungs bilaterally due to air trapping from CF-related lung disease

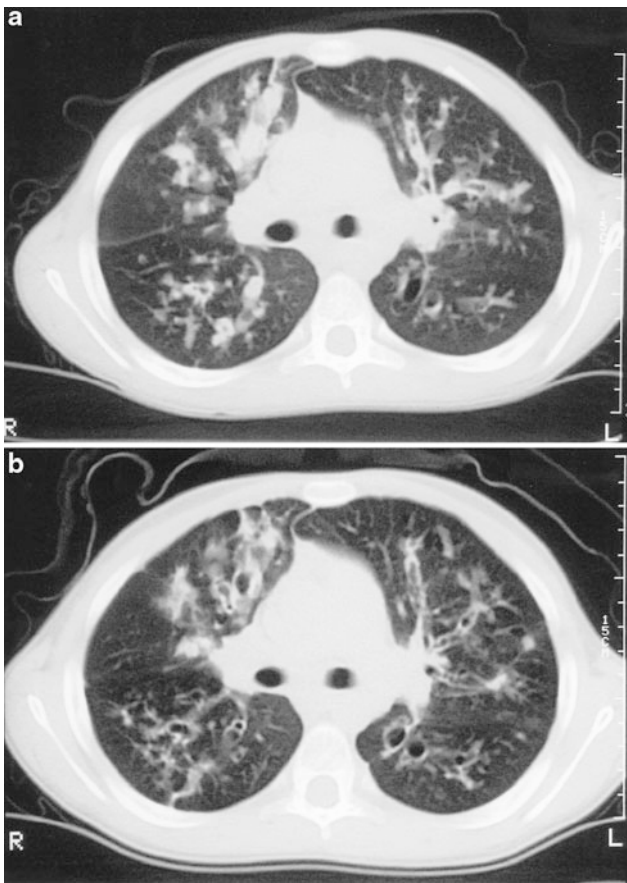


**Fig. 27** Cystic fibrosis (CF). An axial chest CT image (**a**) from an 11-year-old boy with CF shows bronchiectasis, bronchial wall thickening, and multiple sites of endobronchial mucous plugging. An axial chest CT image (**b**) obtained after several months of daily therapy with human recombinant DNase shows clearing of mucous plugs from many of the ectatic bronchi

eliminate these respiratory complications if a treatment can be found. However, any treatment would need to be effective in early infancy to avoid structural lung disease. Even without a cure as yet, the history of CF is one of dramatic advances. This progress is reflected in the fact that the best predictor of life expectancy in CF is the patient's year of birth, and that the rate of improvement of life expectancy in CF patients exceeds that of the general population (Hurley et al. 2014).

Children with CF are a more heterogeneous group than originally described. Pulmonary disease and pancreatic disease are the primary abnormalities in CF, although in 15 % of patients pancreatic function is adequate. The severity of lung disease in CF is also more variable than often appreciated. In patients with homozygous  $\Delta F508$  mutations, disease ranges from the development of bronchiectasis in the first few years of life to a 20-year-old patient with normal PFTs and a normal CXR. Complete bilateral absence of the vas deferens is the mildest expression of the CF spectrum. Genotype predicts phenotype in pancreatic sufficiency, but not the severity or pattern of respiratory disease (Rowntree and Harris 2003).

## 7.1 Genetics

CF is an autosomal recessive disease that affects approximately 1 in 4,000 live births in the United States. CF occurs most commonly in Caucasians, in whom the incidence is 1 in 2,500 live births, with progressively lower frequency in black, Hispanic, and Asian populations. The gene for CF is located on the long arm of chromosome 7 and encodes the CF transmembrane conductance regulator (CFTR). CFTR is

a single chain protein that forms a membrane-bound regulated chloride channel activated by cyclic adenosine monophosphate (cAMP). CFTR functions primarily at the apical cell membrane where it regulates fluid balance across the cell membrane with effects on both chloride and sodium. The most common mutation is a three base pair deletion that causes omission of phenylalanine at position 508 of the protein product. This  $\Delta F508$  mutation is present in almost 90 % of those with CF (CF Foundation 2011). Homozygous  $\Delta F508$  is responsible for about one-half of cases of CF (CF Foundation 2011). More than 1,000 additional mutations of the CF gene have been identified.

## 7.2 Diagnosis

In 1999, 7 % of children diagnosed with CF were identified by neonatal screening (CF Foundation 2000). This has risen to almost 60 % in 2011 (CF Foundation 2011). Newborn screening for CF is now universal in many countries. Neonatal screening is most often performed by measuring the level of immunoreactive trypsinogen in a dried blood spot. Positive screening tests must be confirmed by further tests including meconium lactase, sweat chloride, or genotyping. A controlled trial of neonatal screening in Wisconsin has shown improved growth and nutritional status in children with CF identified by neonatal screening (Farrell et al. 2001). A study in Australia demonstrated improvement in both nutrition and pulmonary function in children identified by neonatal screening (Waters et al. 1999). Other studies have supported the economic benefit of a universal newborn screening program (Sims et al. 2007).

Of the children with CF, 70 % present within the first year, 80 % by the age of 4 years, and 90 % by the age of 12 years. The median age at diagnosis of patients with CF listed in the Cystic Fibrosis Patient Registry in 2004 was 6 months (CF Foundation 2004). In the first year, gastrointestinal findings are more common than respiratory disease. In North America, nearly all Caucasian infants with meconium ileus have CF. In 1999, 19 % of infants diagnosed with CF had meconium ileus (CF Foundation 2000). Gastrointestinal findings after the neonatal period and within the first year include malabsorption and failure to thrive. CF should be suspected in children with these symptoms without regard to the presence or absence of pulmonary disease.

After the first year, respiratory complaints increase, becoming the most common reason to suspect CF. Cystic fibrosis care continues to improve patient outcomes. In 1991, median FEV<sub>1</sub> at 13 years of age was 80 % of predicted. In 2011, median FEV<sub>1</sub> was 95 % of predicted at 13 years of age and did not decline to 80 % until 18 years of age (CF Foundation 2011). In the United States, for the

cohort of individuals with CF born from 1985 to 1994 and surviving infancy, the median predicted life expectancy in years is in the lower 50s for males and lower 40s for females (Jackson et al. 2011).

One of the earliest recognized characteristics of a child with CF was the salty taste of the child's skin. Abnormal sweat chloride was reported in 1953 (Di Sant'Agnese et al. 1953). Sweat chloride determination remains the most common diagnostic test for CF. This test requires careful technique and should only be performed at centers with expertise in sweat chloride determination. Values greater than 60 mEq/ml are generally regarded as positive, 40–60 mEq/ml as indeterminate, and less than 40 mEq/ml as negative. Other methods of making the diagnosis include genotyping and neonatal screening.

Even in a screened population, cases of CF are still detected on clinical grounds. In this group, gastrointestinal symptoms remain more common at presentation than pulmonary symptoms. A sweat test should be requested when the clinical features suggest the diagnosis of CF, even if the child underwent a negative screening (Massie et al. 2000). Of nine children diagnosed with CF after negative neonatal screening in the study of Massie et al., eight presented with failure to thrive or steatorrhea, and one with respiratory symptoms.

## 7.3 Pulmonary Pathophysiology

Abnormal CFTR causes a change in the composition of the fluid lining the airways, which results in numerous alterations in the functioning of the airway epithelium. The mucous becomes abnormal, resulting in airway plugging and decreased mucociliary clearance. Abnormal mucus in CF likely results from both abnormal mucus produced by the mucous glands and the presence of degradation products from white blood cells. Deoxyribonucleic acid is a major component of the degradation products, and is a major contributor to the increased viscosity and tendency of the mucous to form long strands. Both infection and inflammation result in elaboration of proteolytic enzymes that damage the epithelium and the supporting structure of the airways.

Repeated infection and increased inflammatory response cause airway damage that makes the airways more susceptible to infection. Infection then increases in both frequency and severity, inciting greater inflammatory response. This vicious cycle results in progressive respiratory compromise. The hallmarks of CF lung disease are bronchiectasis and air trapping secondary to airway damage and obstruction by the tenacious mucus produced in CF.

Studies using CT to evaluate the onset of CF lung disease have shown that structural lung disease, particularly



bronchiectasis and air trapping, begin in infancy. In a cross-sectional study of infants diagnosed by newborn screening, bronchiectasis was seen by CT in 29 % of 3-month olds and in 62 % of 3-year olds (Sly et al. 2013). A longitudinal study comparing CT scans obtained in children with CF under 7 years of age demonstrated that bronchiectasis persisted once detected in 74 % and progressed in 63 % over a 1-year interval (Mott et al. 2012).

## 7.4 Lung Care

One of the most important factors improving longevity in CF patients in North America is the use of skilled care through a network of CF centers. Two important concepts of care are routine monitoring and early intervention. Pulmonary exacerbations are treated with aggressive pulmonary physiotherapy and parenteral antibiotics.

Regular pulmonary care in CF has traditionally been directed at the clearance of lower airway secretions and the treatment of infection. In the last decade, numerous new techniques have become available. In addition to manual external percussion, airway clearance techniques include airway oscillators and high frequency chest compression with an inflatable vest. The tenacity of secretions can be reduced by the administration of recombinant human deoxyribonuclease (DNase) which breaks up DNA strands (Fig. 27). Inhaled bronchodilators and hypertonic saline can also be administered. Inhaled antibiotics have been shown to improve pulmonary function in initial short term trials (Ramsey et al. 1999). Airway inflammation can also be directly treated. In a 4-year study, Konstan et al. showed that inhaled ibuprofen decreased the decline of pulmonary function in CF, an effect that was most marked in children (Konstan et al. 1995).

Systemically administered drugs such as oral and intravenous antibiotics are also an important part of CF care. Continued advances are leading to the development of new oral and intravenous therapies. In the last decade, high throughput screening has identified new compounds that can directly affect the defect caused by a specific CFTR mutation. The G551D mutation reduces the amount of time that CFTR is “open,” allowing chloride to move from the cell to the airway surface liquid. Ivacaftor is a drug that increases this open time, partially restoring the normal function of the CFTR. A study of children 6–11 years of age treated with ivacaftor showed improvement in lung function by 2 weeks that was sustained over the 48 week study. In addition to pulmonary benefits, subjects taking ivacaftor gained 2.8 kg more weight on average than those taking placebo (Davies et al. 2013).

Despite advances in care, the lung disease in many patients progresses to respiratory insufficiency despite

medical treatment. Lung transplantation is the treatment for end-stage CF lung disease. Both cadaveric transplantation and living donor lobe transplantation can be performed. Since 2001, more than 2,000 people with CF have undergone lung transplantation (CF Foundation 2011).

## 7.5 Imaging

The role of imaging in the care of children with CF is changing. Historically, care has been based on clinical evaluation, with CXR used to confirm clinical impressions and provide an indicator of overall disease severity. CXRs remain the most common imaging study performed in patients with CF. CF center directors report that CTs are frequently obtained, although little has been published on the use of CT in the routine care of patients with CF. Nuclear medicine studies of lung ventilation and perfusion and of aerosol deposition have been reported primarily as a research tool. FDG–PET scanning is currently under investigation as a means of evaluating the degree of inflammation in the CF lung. MRI is an alternative method to follow CF-related lung disease without the use of ionizing radiation.

### 7.5.1 Chest Radiography

CXRs obtained in the first year of life are usually normal. Abnormal CXRs will show changes typical of airways disease, with the appearance being the same as seen with viral or atypical bacterial infections. Features more characteristic of CF, including bronchiectasis and mucous plugging, are typically not seen on CXR in the first several years of life.

Scoring systems for the evaluation of lung disease on CXR include the Brasfield (Brasfield et al. 1979), Chrispin-Norman (Chrispin and Norman 1974) and NIH (Sackrider et al. 1994) scores. One CXR scoring system, the Wisconsin score, was specifically developed for use in young children with CF (Weatherly et al. 1993). Comparison between the different scoring systems shows similar results (Sawyer et al. 1994; Terheggen-Lagro et al. 2003). While these scores correlate with disease severity in older patients, they are insensitive when used in young children (Weatherly et al. 1993). Although early CXRs do not correlate well with clinical changes in young children with mild disease (Koscik et al. 2000), CXRs show a higher correlation with *Pseudomonas* acquisition than with PFTs (Kosorok et al. 2001).

In an adult study, Greene et al. (1994) found that CXRs obtained during an acute exacerbation could not be differentiated from CXRs obtained when the patients were clinically well. No pediatric study has been performed to evaluate the ability of CXRs to reflect changes due to short term treatment, but anecdotal experience suggests that this is very unlikely.

In longitudinal studies of multiple year duration, serial CXRs have been useful. Cleveland et al. developed a database of CXR scores over time to provide reference values for the progression of lung disease (Cleveland et al. 1998). Using this database, a decrease in the lung disease progression as monitored by Brasfield scores has been shown when children were treated with aerosolized tobramycin (Slattery et al. 2004). A study from the Wisconsin Randomized Control Trial of neonatal screening found that the CXR is a very sensitive means to detect the presence of lung disease as measured by CT scanning (Sanders et al. 2012). These investigators have used CXRs to assess risk factors for the development of CF-related lung disease (Sanders et al. 2014), and regional differences in the evolution of lung disease (Li et al. 2012).

### 7.5.2 CT

Currently, high-resolution CT is the most accurate means of evaluating the morphologic changes of CF lung disease. CT can detect and quantify the changes seen in children with CF, including bronchiectasis, peribronchial thickening, mucous plugging, parenchymal air trapping, and lung destruction.

In 1986, Jacobsen et al. compared CXR and CT in 12 adult patients with CF. The authors found that CT was more sensitive for the detection of bronchiectasis, mucous plugging, and hilar lymphadenopathy (Jacobsen et al. 1986). In 1991, Bhalla et al. described a scoring system for CT in CF (Bhalla et al. 1991). This scoring system evaluates the severity of bronchiectasis and peribronchial thickening, and the extent of bronchiectasis, mucous plugging, sacculations or abscesses, bullae, emphysema, and collapse or consolidation. The authors found again that CT was more sensitive than CXR in detecting abnormalities, and that the CT score correlated with the FEV1/FVC ratio. In the same year, Nathanson et al. published a scoring system for CF using electron beam CT in a pediatric population. This scoring system correlated well with PFT and clinical scores (Nathanson et al. 1991). A scoring system devised by Mafessanti et al. (1996) has been adopted and used by several authors.

More recent efforts have examined the ability of CT to evaluate the onset and progression of disease, and response to treatment. An adult study showed that the findings differed when CTs obtained during exacerbations were compared to those obtained when patients were at their baseline health. CT scores were higher during exacerbations. Air-fluid levels in ectatic bronchi during exacerbations resolved on follow-up scans. Centrilobular nodules and mucous plugging improved in about one-third of the cases (Shah et al. 1997).

In a pediatric study, the CT appearance was compared between admission and discharge for treatment of an acute

pulmonary exacerbation (Brody et al. 1999). In this study, the CT appearance improved in 13 of 15 admissions. Peribronchial thickening, mucous plugging, and the overall appearance were all significantly improved on the discharge CT. A second study of 17 children also showed CT improvement following treatment for exacerbation (Robinson et al. 2001). A study that included patients aged between 2 and 32 years evaluated the change in CT appearance over time. The authors found that CT scores increased significantly when the interval between exams was more than 18 months, with no significant change over shorter intervals (Helbich et al. 1999). In a study of children with a mean age of 11 years, de Jong et al. found that CT scans showed progressive disease over 2 years despite stable PFT results (de Jong et al. 2004). CT scanning has been shown to be more sensitive than pulmonary function tests for the presence of lung disease. One study of children 6–10 years old found bronchiectasis in 30 % of children with normal PFTs (Brody et al. 2004). Changes on CT scanning have also been shown to correlate with the number of pulmonary exacerbations (Brody et al. 2005). A follow-up study showed that CT scores correlated with the severity of lung disease 10 years later, and that correlation was higher with CT scores than with PFTs (Sanders et al. 2011). At the time of writing, however, no studies have evaluated the impact of using CT as part of the routine clinical care of the children with CF.

### 7.5.3 Nuclear Medicine

The functional information provided by nuclear medicine imaging has been used to evaluate pulmonary ventilation/perfusion, aerosol deposition, and mucous clearance in patients with CF (Laube et al. 1992; Sirr et al. 1986). Regional pulmonary blood defined by perfusion scintigraphy has been shown to correlate with morphologic findings on CT (Donnelly et al. 1997). The relative sensitivities of the two modalities have not been determined.

FDG-PET scanning can detect and quantify inflammation in the lungs of CF patients. In a study of 28 adults and children with CF, FDG-PET/CT demonstrated multiple focal sites of increased FDG uptake that correlated poorly with the size of bronchiectasis, degree of peribronchial thickening, or location of structural abnormalities (Klein et al. 2009). Seven of these subjects were studied during and after a pulmonary exacerbation, and FDG uptake frequently decreased without a corresponding change in CT appearance. This and other studies suggest that FDG-PET/CT may have a role in the evaluation of interventions directed toward reducing inflammation. However, the quantitation of chronic inflammation has not been well studied, and the relatively high radiation dose of 5–7 mSv may limit the use of FDG-PET in children (Chen et al. 2006).

### 7.5.4 MRI

Initial attempts to use MRI to evaluate CF-related lung disease were disappointing. The relatively small number of protons in aerated lung and magnetic susceptibility artifacts from the air/soft tissue interfaces resulted in very little usable MR signal. One early study demonstrated the ability of MRI to detect hilar lymphadenopathy and bronchiectasis with mucous plugging (Fiel et al. 1987). A subsequent study in 1994 compared conventional axial CT to MRI and found that the limited resolution of MRI did not allow adequate evaluation of the gross features of CF-related lung disease (Carr et al. 1995).

Advances in MRI technology have dramatically improved the ability of MRI to demonstrate pulmonary parenchymal abnormalities. The spatial resolution of conventional proton MRI remains lower than that of CT, but MRI can now provide similar results in demonstrating bronchial wall thickening, mucous plugging, and infiltrates (Puderbach et al. 2007). Early findings of CF lung disease such as air trapping can now be identified on MRI. Currently, MRI is most limited in the detection of peripheral bronchiectasis without wall thickening (Failo et al. 2009). MRI is increasingly being advocated as a way to follow CF-related lung disease without the use of ionizing radiation. In support, a recent study showed a high correlation between MRI and CT scores for CF-related lung disease in children (Sileo et al. 2013b).

MRI using hyperpolarized helium provides very different capabilities. The high signal of the hyperpolarized gas allows single breath-hold evaluation of ventilation. Ventilated portions of the lung show high signal, and unventilated regions are seen as focal defects. The appearance is grossly similar to nuclear medicine ventilation scans, but with much higher resolution.

A preliminary report published in 1999 using hyperpolarized helium and conventional proton MRI in four patients with CF found extensive ventilation defects that were frequently much more striking than the associated morphologic abnormalities (Donnelly et al. 1999). The severity of lung disease shown by hyperpolarized helium MRI correlates with other measure of lung disease severity (van Beek et al. 2007). Other studies have demonstrated ventilation defects in CF patients with normal PFTs, and have shown that these defects improve with treatment (Mentore et al. 2005). A recent trial using hyperpolarized helium demonstrated dramatic improvement in ventilation defects following treatment with a CFTR corrector therapy in children with CF (Altes et al. 2011). This study provides the most convincing data to date on the value of imaging endpoints in CF research trials.

The limited availability of hyperpolarized helium has hampered more widespread adoption of hyperpolarized gas MRI. Hyperpolarized xenon is being studied as an

alternative. Unlike helium, hyperpolarized xenon diffuses across the alveolar walls into the capillaries and allows additional physiologic measurements. The use of hyperpolarized gas MRI in CF and other pediatric pulmonary disorders is discussed more extensively in the chapter entitled Hyperpolarized Gas MRI in Pediatric Lung Disease by Komlosi, Benjamin and Altes. Several additional MR techniques, including phase-contrast (Fleck et al. 2013) and oxygen-enhanced imaging (Stadler et al. 2007), are being used to investigate the pathophysiology of CF-related lung disease.

## 8 Primary Ciliary Dyskinesia

Primary ciliary dyskinesia (PCD) is a genetic disorder characterized by dysfunctional ciliary function resulting in impaired mucociliary clearance. Disease-causing mutations are most often autosomal recessive and may involve genes that encode axonemal motor proteins, regulatory proteins, or cytoplasmic proteins involved in ciliary assembly. To date, at least 19 different genes have been linked to PCD, but known PCD-causing mutations account for only about 60 % of PCD cases (Horani et al. 2013).

Cilia line the respiratory tract from the middle ear to the conducting bronchioles and play an important role in clearing amniotic fluid from the neonatal lungs. Neonatal respiratory distress occurs in up to 70–75 % of patients with PCD, although this is often misattributed to transient tachypnea of the newborn or neonatal pneumonia, and the diagnosis of PCD is frequently delayed until later childhood or even adulthood (Noone et al. 2004). Chronic or recurrent upper and lower respiratory tract infections begin in early childhood, most often caused by *H. influenzae*, *S. aureus*, or *S. pneumoniae*, with *Pseudomonas aeruginosa* and nontuberculous *Mycobacteria* appearing in older patients. This leads to bronchiectasis in a majority of affected children, most commonly of the right middle lobe, lingula and lower lobes, which contrasts with the upper lobe predominance of CF (Fig. 28). The extent and severity of bronchiectasis increase as age progresses. Antibiotics and physiotherapy to improve mucociliary clearance are the mainstays of therapy directed to halting the progression of bronchiectasis. In addition to bronchiectasis, other common pulmonary radiographic findings of PCD include mucus plugging, bronchial wall thickening, peribronchial consolidation, atelectasis and hyperinflation (Kennedy et al. 2007; Santamaria et al. 2008; Magnin et al. 2012).

Although both are chronic suppurative lung disorders, PCD typically shows milder lung damage on CT and a much better prognosis than CF, with many PCD patients living a near normal life span (Santamaria et al. 2008). As with CF, CT is superior to spirometry for detecting



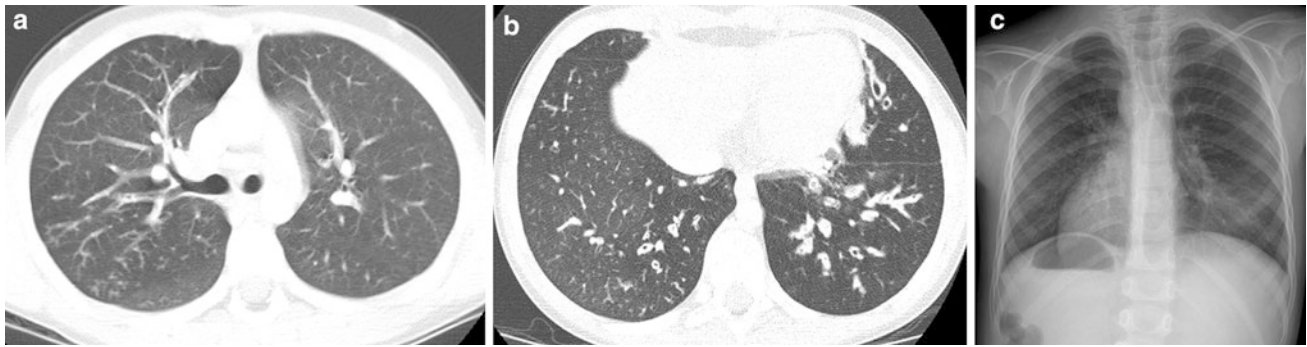


**Fig. 28** Primary ciliary dyskinesia (PCD). Axial chest CT images (a, b) from a 10-year old with a history of chronic sinusitis show bronchiectasis and bronchial wall thickening that resembles CF-related lung disease, but the lower lobe and lingular predominance are more

typical of PCD. A frontal CXR (c) in a 5-year old with a history of recurrent upper and lower respiratory tract infections related to PCD reveals situs inversus totalis and left middle lobe opacity

progression of PCD-related lung disease (Maglione et al. 2012). The degree of lung disease scored by CT in children with PCD significantly increases with age and correlates with declines in functional parameters noted on PFTs. To minimize the burden of ionizing radiation, clinicians could rely on spirometry to monitor disease progression in PCD patients with clinically stable disease, and reserve CT for suspected unstable disease (Magnin et al. 2012). As an alternative to CT, the extent and severity of lung disease in PCD may be scored comparably with MRI (Montella et al. 2009).

Situs inversus or heterotaxy occurs in approximately 50 % of PCD cases (Fig. 28), related to randomization of left-right axis asymmetry from embryonic nodal cilia dysfunction. The classic Kartagener syndrome consists of the combination of bronchiectasis, sinusitis, and situs inversus (Kartagener and Stucki 1962). Pectus excavatum develops in 5–10 % (Kennedy et al. 2007).

Recognition of clinical or imaging features suggestive of PCD should prompt confirmation of diagnosis. Nasal nitric oxide (nNO) measurement has been proposed as a screening test since low nNO is characteristic of PCD, but it is usually not technically feasible in infants or young children. Ultrastructural defects in the cilia detected by transmission electron microscopy were once considered the “gold standard” for diagnosis, but some PCD cases lack these defects and ciliary beat analysis or genetic testing is required for diagnosis (Boon et al. 2013).

## 9 Langerhan Cell Histiocytosis

Langerhan cell histiocytosis (LCH) is characterized by proliferation and infiltration of tissues by Langerhans cells. These cells are histiocytes identifiable by the presence of cytoplasmic Birbeck granules on electron microscopy or by CD-1a positivity on immunohistochemistry. Aggregates of

these histiocytes form granulomas that may later be replaced by fibrosis and cysts. Unlike adult LCH, childhood LCH is clonal and pulmonary involvement is not associated with smoking (Seely et al. 2012).

The previous classification of LCH into eosinophilic granuloma, Letterer-Siwe disease, and Hand-Schüller-Christian disease is no longer in favor. The current classification divides these patients into those with single organ involvement and those with multisystem involvement. Multisystem LCH is more common in children under 2 years of age, and the younger the patient, the worse the prognosis. The presence of multisystem involvement requires more intensive therapy than single system involvement. Pulmonary involvement can be seen either in isolated (primary) pulmonary LCH or in multisystem disease. Isolated pulmonary LCH is uncommon in childhood (Chatkin et al. 1993; Al-Trabolsi et al. 2006). The most common clinical signs and symptoms suggesting pulmonary involvement are tachypnea, cyanosis, chest pain, and chronic or persistent cough.

In a study of 220 children with LCH, 36 (16 %) had pulmonary involvement. Thirty-four (94 %) of these had multisystem LCH and two had primary pulmonary LCH. In 20 (56 %) of the 36, respiratory symptoms or signs were present, and diffuse interstitial involvement was present in all of these. The presence of pulmonary disease without risk organ (liver, spleen, hematopoietic system) involvement was not an adverse prognostic factor (Braier et al. 2004). In a larger, more recent study of 420 children with multisystem LCH, pulmonary involvement was present at diagnosis in 24 %, with a median age at diagnosis of 1.3 years, and strongly correlated with liver and spleen involvement. Pulmonary involvement later developed in an additional 7 % of patients. Pulmonary involvement was not an independent prognostic variable, suggesting that pulmonary involvement should be excluded from the definition of risk organ involvement in LCH (Ronceray et al. 2012).



**Fig. 29** Langerhans cell histiocytosis (LCH). An axial chest CT image in a 7-month old with LCH depicts multiple small pulmonary cysts, as well as an enlarged thymus with calcifications

On CXR, the predominant finding of pulmonary LCH is reticulonodular opacities with or without cysts (Smets et al. 1997). CT depicts small cysts and nodules occult to CXR. Cysts and nodules often coexist and cavitating nodules may be seen during active stages of disease (Odame et al. 2006). The nodules and cysts in children are distributed randomly and usually involve the lung bases. This differs from adults, in whom sparing of the subpleural basilar lung parenchyma is highly characteristic of LCH (Seely et al. 2012). The cysts often have thin or imperceptible walls and may assume bizarre shapes (Fig. 29). Spontaneous pneumothorax can ensue from cyst rupture (Ha et al. 1992). The nodules typically regress, and the appearance of new nodules after cysts are well established suggests disease recurrence or progression (Bano et al. 2014). The cysts usually persist, and extensive cyst formation and surrounding fibrosis can lead to a honeycomb appearance of the lungs. Although pulmonary involvement has no independent effect on survival, it may result in lung parenchymal destruction and fibrosis severe enough to necessitate lung transplantation (Odame et al. 2006; Ronceray et al. 2012).

A recent review of the imaging features of 1,264 LCH patients demonstrated thymic involvement in 18 (14 %). Thymic involvement at presentation was limited to children less than 2-years old with multisystem disease. Patients who presented later all had active disease in at least one additional system at the time thymic involvement was identified. In cases of thymic involvement, thymic calcifications were present in all cases, thymic cysts in 80 %, and thymic enlargement in 67 % (Lakatos et al. 2013) (Fig. 29). Recognition of the characteristic pulmonary or thymic

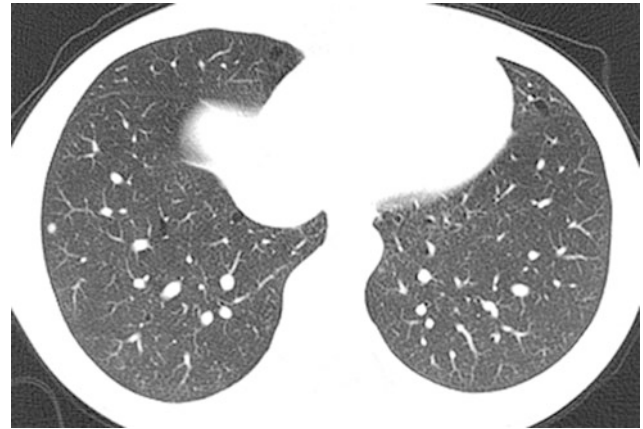


**Fig. 30** Tuberous sclerosis (TS). An axial chest CT image in a 17-year-old female with TS shows several, small, round cysts of the lung bases bilaterally, consistent with lymphangioleiomyomatosis. In addition, there is a small, well-defined nodule of the peripheral lateral right lower lobe, possibly related to micronodular pneumocyte hyperplasia that occurs in the setting of TS

appearances of LCH involvement may allow the diagnosis to be confirmed and lung biopsy avoided by biopsy of an accompanying skin rash or by detection of elevated numbers of CD1a+ cells in bronchoalveolar lavage fluid (Crawley and Guillerman 2010).

## 10 Tuberous Sclerosis

Tuberous sclerosis (TS) is one of a group of genetic neurocutaneous syndromes characterized by involvement of structures that arise from the embryonic ectoderm, although other structures may be involved. TS is attributable to autosomal dominant defects of the *TSC1* or *TSC2* tumor suppressor genes.

The classic clinical triad includes mental retardation, seizures, and adenoma sebaceum. TS, however, affects multiple organ systems. In addition to the central nervous system (CNS) abnormalities of cortical tubers and subependymal nodules, abnormal cellular proliferation results in angiomyolipomas of the kidneys and liver, rhabdomyomas of the heart, and lymphangioleiomyomatosis (LAM) and multifocal micronodular pneumocyte hyperplasia (MMPH) of the lungs. There is a characteristic rash which has been described as a butterfly rash over the cheeks with a narrower affected area on the nose. In women of childbearing age, LAM is the most common thoracic manifestation of TS. In young children, CNS lesions and cardiac rhabdomyomas are by far the most common manifestations (Mettin et al. 2013). Cardiac rhabdomyomas are further discussed in the chapter entitled Pediatric Cardiac MRI by Krishnamurthy and Chung.

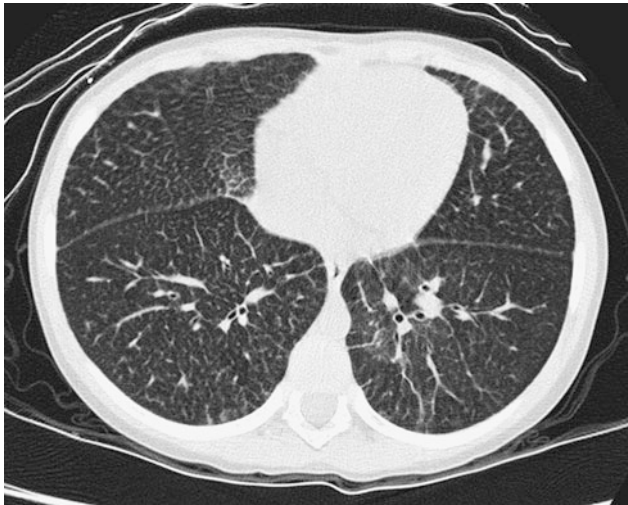


**Fig. 31** Niemann–Pick disease. An axial chest CT image of a 5-year old with type B disease depicts diffuse septal thickening

LAM presents most commonly in the third decade; however, children as young as 11-years old have been diagnosed with LAM. Clinical presentation is usually with dyspnea or spontaneous pneumothorax, and there is typically a slow but inexorable progression to respiratory failure, with a median survival of 8–10 years without lung transplantation. The clinical course may also be complicated by chylous effusions. LAM is difficult to appreciate on CXRs until extensive fibrosis has developed late in the course of the disease. The early appearance of LAM is characterized by the presence of multiple small cysts with thin or imperceptible walls (Fig. 30). These cysts are evenly distributed through the lungs. Unlike the cysts in LCH, the cysts in LAM are round and usually do not coalesce. The presence of normal lung parenchyma between the cysts is useful in differentiating these cysts from other causes of destructive lung disease. In a prospective HRCT screening study of young women with TS, the incidence of lung cysts was 30 % (McCormack et al. 2002). This is much higher than earlier estimates, likely reflecting a high incidence of mild findings that do not present clinically and are not apparent on CXR.

MMPH is characterized by proliferations of enlarged type II pneumocytes that form ill-defined papillae and fill the alveolar spaces. MMPH is very rare before adulthood, and appears as multiple, well-defined pulmonary nodules resembling metastases on CT (Fig. 30). Definitive diagnosis can only be established by lung biopsy (Behnes et al. 2013).

Overactivation of the mammalian target of rapamycin (mTOR) signaling pathway as a result of *TSC1* or *TSC2* gene mutations is thought to be a mechanism of abnormal cellular proliferation in TS. Inhibitors of mTOR may

provide an effective treatment for many of the manifestations of TS. For example, sirolimus has been shown to decrease the size of renal angiomyolipomas, and to improve pulmonary function and decrease chylous effusions in adult patients with LAM (Ando et al. 2013).

## 11 Lysosomal Storage Diseases

Lysosomal storage disorders (LSDs) are genetic diseases characterized by the absence or dysfunction of a lysosomal enzyme, with resulting accumulation of the lipid, glycoprotein or mucopolysaccharide substrate associated with the defective enzyme. The LSDs have a broad phenotypic range depending on the rate, amount and effect of substrate accumulation.

### 11.1 Gaucher Disease

Gaucher disease is the most common LSD and is due to a defect in  $\beta$ -glucocerebrosidase. This results in accumulation of glucocerebroside-laden macrophages (Gaucher cells) in various organs and tissues. The most common clinical manifestations are caused by involvement of the liver, spleen, and bone marrow. Lung involvement at presentation is uncommon, reported in only 2 % in one study (Goitein et al. 2001). Lung abnormalities may be caused by infiltration of Gaucher cells, hepatopulmonary syndrome, or aspiration secondary to neurological compromise (McHugh et al. 2004). Reticulonodular opacities can be seen on CXR, while CT findings include nodules, ground-glass opacities, and septal thickening (Tunaci et al. 1995). Enzyme replacement therapy does not consistently normalize the lung structure or function in these patients (Goitein et al. 2001).

### 11.2 Niemann–Pick Disease

In Niemann–Pick disease, sphingomyelin accumulates in “foamy” macrophages due to deficiency of sphingomyelinase. Pulmonary involvement is a major cause of morbidity and mortality (McGovern et al. 2013). Pulmonary involvement is greatest in Type B disease, which is characterized by lipid-laden macrophages infiltrating the pulmonary interstitium, resulting in the finding of diffuse interstitial thickening on CXR and CT (Guillemot et al. 2007) (Fig. 31). The type C2 form of the disease may present in infants or young children with failure to thrive, hepatosplenomegaly, and respiratory distress from pulmonary alveolar proteinosis



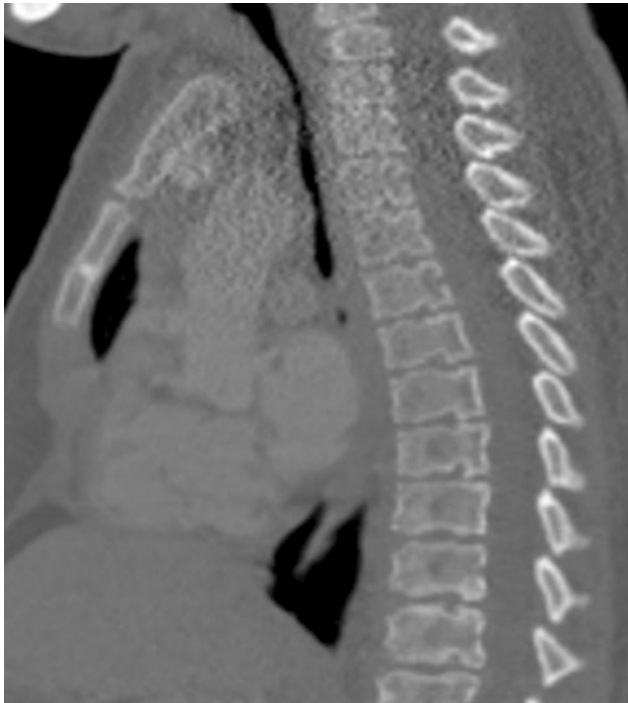


**Fig. 32** Mucopolysaccharidosis (MPS). A sagittal chest CT image reconstructed with bone windows in a 16-year old with Type 2 MPS (Hunter syndrome) shows severe narrowing of the intrathoracic tracheal lumen and spinal dysostosis. Airway obstruction results from a narrowed thoracic inlet and accumulation of glycosaminoglycans in the airway wall

(Griese et al. 2010). Crazy-paving may be observed on chest CT of patients with the type C2 form (Guillerman and Brody 2011).

### 11.3 Mucopolysaccharidosis

The mucopolysaccharidoses (MPS) are characterized by accumulation of glycosaminoglycans in multiple organs and tissues. Eponyms for these diseases include Hurler, Hunter, Sanfilippo, Morquio, Maroteaux-Lamy, and Sly syndromes. Otolaryngological and respiratory problems are very common in patients with MPS. Typical features include upper and lower airway obstruction, restrictive pulmonary disease, and respiratory tract infections. Excess glycosaminoglycan deposition in the airway walls can result in tracheobronchomalacia, airway wall deformity, and airway luminal narrowing and contribute to a high risk of respiratory complications during sedation or anesthesia (Shih et al. 2002) (Fig. 32). Restrictive lung disease is a consequence of skeletal dysplasia limiting chest wall excursion and hepatosplenomegaly limiting diaphragmatic motion (Berger et al. 2013). Pulmonary function generally declines with age, but can be improved with enzyme replacement therapy (Lin et al. 2013).

## References

- Acar P, Sebahoun S, de Pontual L, Maunoury C (2000) Myocardial perfusion in children with sickle cell anaemia. *Pediatr Radiol* 30:352–354
- Agrawal AK, Saini N, Gildengorin G, Feusner JH (2011) Is routine computed tomographic scanning justified in the first week of persistent febrile neutropenia in children with malignancies? *Pediatr Blood Cancer* 57:620–624
- Aiuti A, Biasco L, Scaramuzza S, Ferrua F, Cicalese MP, Baricordi C, Dionisio F et al (2013) Lentiviral hematopoietic stem cell gene therapy in patients with Wiskott-Aldrich syndrome. *Science* 341:1233151. doi:10.1126/science.1233151
- Al-Binali AM, Scott B, Al-Garni A, Montgomery M, Robertson M (2003) Granulomatous pulmonary disease in a child: an unusual presentation of Crohn's disease. *Pediatr Pulmonol* 36:76–80
- Al-Herz W, Bousfiha A, Casanova JL, Chapel H, Conley ME, Cunningham-Rundles C, Etzioni A, Fischer A, Franco JL, Geha RS, Hammarstrom L, Nonoyama S, Notarangelo LD, Ochs HD, Puck JM, Roifman CM, Seger R, Tang ML (2011) Primary immunodeficiency diseases: an update on the classification from the International Union of Immunological Societies Expert Committee for Primary Immunodeficiency. *Front Immunol* 2:54. doi:10.3389/fimmu.2011.00054
- Altes TA, Johnson MA, Miller GW, Mugler JP, Flors L, Mata J, Salinas CL, Tustison N, Lee P, Song T, Yen K, Froh D, Botfield MC (2011) Hyperpolarized helium-3 magnetic resonance imaging of CFTR potentiator therapy in subjects with cystic fibrosis and the G551D mutation. *Pediatr Pulmonol Suppl* 34:284
- Al-Trabolsi HA, Alshehri M, Al-Shomrani A, Shabanah M, Al-Barki AA (2006) "Primary" pulmonary Langerhans cell histiocytosis in a two-year-old child: case report and literature review. *J Pediatr Hematol Oncol* 28:79–81
- Ando K, Kurihara M, Kataoka H, Ueyama M, Togo S, Sato T, Doi T, Iwakami S, Takahashi K, Seyama K, Mikami M (2013) The efficacy and safety of low-dose sirolimus for treatment of lymphangioleiomyomatosis. *Respir Investig* 51:175–183
- Araujo DB, Borba EF, Silva CA, Campos LM, Pereira RM, Bonfa E, Shinjo SK (2012) Alveolar hemorrhage: distinct features of juvenile and adult onset systemic lupus erythematosus. *Lupus* 21:872–877
- Arkachaisri T, Lehman TJ (1999) Systemic lupus erythematosus and related disorders of childhood. *Curr Opin Rheumatol* 11:384–392
- Arteta M, Campbell A, Nouraei A, Rana S, Onyekwere OC, Ensing G, Sable C, Dham N, Darbari D, Luchtman-Jones L, Kato GJ, Gladwin MT, Castro OL, Minniti CP, Gordeuk VR (2013) Abnormal pulmonary function and associated risk factors in children and adolescents with sickle cell anemia. *J Pediatr Hematol Oncol* (Epub ahead of print)
- Athreya BH, Doughty RA, Bookspan M, Schumacher HR, Sewell EM, Chatten J (1980) Pulmonary manifestations of juvenile rheumatoid arthritis. A report of eight cases and review. *Clin Chest Med* 1:361–374
- Babhulkar SS, Pande K, Babhulkar S (1995) The hand-foot syndrome in sickle-cell haemoglobinopathy. *J Bone Joint Surg Br* 77:310–312
- Babyn P, Doria AS (2005) Radiologic investigation of rheumatic diseases. *Pediatr Clin North Am* 52:373–411
- Bano S, Chaudhary V, Narula MK, Anand R, Venkatesan B, Mandal S, Majumdar K (2014) Pulmonary Langerhans cell histiocytosis in children: a spectrum of radiologic findings. *Eur J Radiol* 83:47–56
- Basseri B, Enayati P, Marchevsky A, Papadakis KA (2010) Pulmonary manifestations of inflammatory bowel disease: cases presentations and review. *J Crohns Colitis* 4:390–397

- Becciolini V, Gudinchet F, Cheseaux JJ, Schnyder P (2001) Lymphocytic interstitial pneumonia in children with AIDS: high-resolution CT findings. *Eur Radiol* 11:1015–1020
- Behnes CL, Schutze G, Engelke C, Bremmer F, Gunawan B, Radzun H-J, Schweyer S (2013) 13-year-old tuberous sclerosis patient with renal cell carcinoma associated with multiple renal angiomyolipomas developing multifocal micronodular pneumocyte hyperplasia. *BMC Clin Pathol* 13:4. doi:10.1186/1472-6890-13-4
- Berger KI, Fagondes SC, Giugliani R, Hardy KA, Lee KS, McArdle C, Scarpa M, Tobin MJ, Ward SA, Rapoport DM (2013) Respiratory and sleep disorders in mucopolysaccharidosis. *J Inher Metab Dis* 36:201–210
- Bhalla M, Turcios N, Aponte V, Jenkins M, Leitman BS, McCauley DI, Naidich DP (1991) Cystic fibrosis: scoring system with thin-section CT. *Radiology* 179:783–788
- Bhalla M, Abboud MR, McLoud TC, Shepard JA, Munden MM, Jackson SM, Beaty JR, Laver JH (1993) Acute chest syndrome in sickle cell disease: CT evidence of microvascular occlusion. *Radiology* 187:45–49
- Boon M, Jorissen M, Proesmans M, De Boeck K (2013) Primary ciliary dyskinesia, an orphan disease. *Eur J Pediatr* 172:151–162
- Bousfiha AA, Jeddane L, Ailal F, Al Herz W, Conly ME, Cunningham-Rundles C, Etzioni A, Fischer A, Franco JL, Geha RS, Hammarstrom L, Nonoyama S, Ochs HD, Roifman CM, Seger R, Tang MLK, Puck JM, Chapel H, Notarangelo LD, Casanova J-L (2013) A phenotypic approach for IUIS PID classification and diagnosis: guidelines for clinicians at the bedside. *J Clin Immunol* 33:1078–1087
- Boyd JH, Macklin EA, Strunk RC, DeBaun MR (2006) Asthma is associated with acute chest syndrome and pain in children with sickle cell anemia. *Blood* 108:2923–2927
- Boyle JM, Buckley RH (2007) Population prevalence of diagnosed primary immunodeficiency diseases in the United States. *J Clin Immunol* 27:497–502
- Braier J, Latella A, Balancini B, Castanos C, Rosso D, Chantada G, Ripoli M, Goldberg J (2004) Outcome in children with pulmonary Langerhans cell histiocytosis. *Pediatr Blood Cancer* 43:765–769
- Brasfield D, Hicks G, Soong S, Tiller RE (1979) The chest roentgenogram in cystic fibrosis: a new scoring system. *Pediatrics* 63:24–29
- Brody AS, Molina PL, Klein JS, Rothman BS, Ramagopal M, Swartz DR (1999) High-resolution computed tomography of the chest in children with cystic fibrosis: support for use as an outcome surrogate. *Pediatr Radiol* 29:731–735
- Brody AS, Klein JS, Molina PL, Quan J, Bean JA, Wilmott RW (2004) High-resolution computed tomography in young patients with cystic fibrosis: distribution of abnormalities and correlation with pulmonary function tests. *J Pediatr* 145:32–38
- Brody AS, Sucharew H, Campbell JD, Millard SP, Molina PL, Klein JS, Quan J (2005) Computed tomography correlates with pulmonary exacerbations in children with cystic fibrosis. *Am J Respir Crit Care Med* 172:1128–1132
- Buckley RH (2004) Pulmonary complications of primary immunodeficiencies. *Paediatr Respir Rev* 5(Suppl A):S225–S233
- Cabana MD, Crawford TO, Winkelstein JA, Christensen JR, Lederman HM (1998) Consequences of the delayed diagnosis of ataxia-telangiectasia. *Pediatrics* 102:98–100
- Caillot D, Couaillier JF, Bernard A, Casasnovas O, Denning DW, Mannone L, Lopez J, Couillaud G, Piard F, Vagner O, Guy H (2001) Increasing volume and changing characteristics of invasive pulmonary aspergillosis on sequential thoracic computed tomography scans in patients with neutropenia. *J Clin Oncol* 19:253–259
- Carr DH, Oades P, Trotman-Dickenson B, Mohiaddin R, Wells AU, Bush A (1995) Magnetic resonance scanning in cystic fibrosis: comparison with computed tomography. *Clin Radiol* 50:84–89
- Castagnola E, Bagnasco F, Amoroso L, Caviglia I, Caruso S, Faraci M, Calvillo M, Moroni C, Bandettini R, Cangemi G, Magnanao GM, Buffa P, Moscatell A, Haupt R (2014) Role of management strategies in reducing mortality from invasive fungal disease in children with cancer or receiving hematopoietic stem cell transplant: a single center 30-year experience. *Pediatr Infect Dis J* 33:233–237
- Castaner E, Alguersuari A, Gallardo X, Andreu M, Pallardo Y, Mata JM, Ramirez J (2010) When to suspect pulmonary vasculitis: radiologic and clinical clues. *Radiographics* 30:33–53
- Cerveri I, Bruschi C, Ravelli A, Zoia MC, Fanfulla F, Zonta L, Pellegrini G, Martini A (1992) Pulmonary function in childhood connective tissue diseases. *Eur Respir J* 5:733–738
- Chakravarti VS, Borns P, Lobell J, Douglas SD (1991) Chondroosseous dysplasia in severe combined immunodeficiency due to adenosine deaminase deficiency. *Pediatr Radiol* 21:447–448
- Chan K, Puck JM (2005) Development of population-based newborn screening for severe combined immunodeficiency. *J Allergy Clin Immunol* 115:391–398
- Chandesris MO, Melki I, Natividad A, Puel A, Fieschi C, Yun L, Thumerelle C et al (2012) Autosomal dominant STAT3 deficiency and hyper-IgE syndrome: molecular, cellular, and clinical features from a French National Survey. *Medicine* 91:e1–e19
- Chatkin JM, Bastos JC, Stein RT, Gaiger AM (1993) Sole pulmonary involvement by Langerhans' cell histiocytosis in a child. *Eur Respir J* 6:1226–1228
- Cheema GS, Quismorio FP Jr (2001) Interstitial lung disease in systemic sclerosis. *Curr Opin Pulm Med* 7:283–290
- Chen DL, Ferkol TW, Mintun MA, Pittman JE, Rosenbluth DB, Schuster DP (2006) Quantifying pulmonary inflammation in cystic fibrosis with positron emission tomography. *Am J Respir Crit Care Med* 173:1363–1369
- Chrispin AR, Norman AP (1974) The systematic evaluation of the chest radiograph in cystic fibrosis. *Pediatr Radiol* 2:101–105
- Christmann RB, Wells AU, Capelozzi VL, Silver RM (2010) Gastroesophageal reflux incites interstitial lung disease in systemic sclerosis: clinical, radiologic, histopathologic, and treatment evidence. *Semin Arthritis Rheum* 40:241–249
- Cleveland RH, Neish AS, Zurakowski D, Nichols DP, Wohl ME, Colin AA (1998) Cystic fibrosis: a system for assessing and predicting progression. *Am J Roentgenol* 170:1067–1072
- Connolly B, Manson D, Eberhard A, Laxer RM, Smith C (1996) CT appearance of pulmonary vasculitis in children. *Am J Roentgenol* 167:901–904
- Crawley AJ, Guillermin RP (2010) Langerhans cell histiocytosis with intrathymic calcifications and cavitation. *Pediatr Radiol* 40(Suppl 1):S162
- Cunningham-Rundles C (2001) Physiology of IgA and IgA deficiency. *J Clin Immunol* 21:303–309
- Cunningham-Rundles C (2012) The many faces of common variable immunodeficiency. *Hematology Am Soc Hematol Educ Program* 2012:301–305
- Cunningham-Rundles C, Ponda PP (2005) Molecular defects in T- and B-cell primary immunodeficiency diseases. *Nat Rev Immunol* 5:880–892
- Curtin JJ, Webster AD, Farrant J, Katz D (1991) Bronchiectasis in hypogammaglobulinaemia—a computed tomography assessment. *Clin Radiol* 44:82–84
- Davies JC, Wainwright CE, Canny GJ, Chilvers MA, Howenstine MS, Munck A, Mainz JG, Rodriguez S, Li H, Yen K, Odonez CL, Ahrens R (2013) Efficacy and safety of ivacaftor in patients aged 6 to 11 years with cystic fibrosis with a G551D mutation. *Am J Respir Crit Care Med* 187:1219–1225
- de Jong PA, Nakano Y, Lequin MH, Mayo JR, Woods R, Pare PD, Tiddens HA (2004) Progressive damage on high resolution

- computed tomography despite stable lung function in cystic fibrosis. *Eur Respir J* 23:93–97
- De Pauw B, Walsh TJ, Donnelly JP, Stevens DA, Edwards JE, Calandra T, Pappas PG et al (2008) Revised definitions of invasive fungal disease from the European Organization for Research and Treatment of Cancer/Invasive Fungal Infections Cooperative Group and the National Institute of Allergy and Infectious Diseases Mycoses Study Group (EORTC/MSG) Consensus Group. *Clin Infect Dis* 46:1813–1821
- Delle Sedie A, Carli L, Cioffi E, Bombardieri S, Riente L (2012) The promising role of lung ultrasound in systemic sclerosis. *Clin Rheumatol* 31:1537–1541
- Demczuk S, Aurias A (1995) DiGeorge syndrome and related syndromes associated with 22q11.2 deletions. A review. *Ann Genet* 38:59–76
- Di Sant'Agnese PA, Darling RC, Perera GA, Shea E (1953) Sweat electrolyte disturbances associated with childhood pancreatic disease. *Am J Med* 15:777–784
- Dishop MK (2010) Diagnostic pathology of diffuse lung disease in children. *Pediatr Allergy Immunol Pulmonol* 23:69–85
- Donnelly LF, Gelfand MJ, Brody AS, Wilmott RW (1997) Comparison between morphologic changes seen on high-resolution CT and regional pulmonary perfusion seen on SPECT in patients with cystic fibrosis. *Pediatr Radiol* 27:920–925
- Donnelly LF, MacFall JR, McAdams HP, Majure JM, Smith J, Frush DP, Bogonad P, Charles HC, Ravin CE (1999) Cystic fibrosis: combined hyperpolarized  $^3\text{He}$ -enhanced and conventional proton MR imaging in the lung—preliminary observations. *Radiology* 212:885–889
- Failo R, Wielopolski PA, Tiddens HA, Hop WC, Mucelli RP, Lequin MH (2009) Lung morphology assessment using MRI: a robust ultra-short TR/TE 2D steady state free precession sequence used in cystic fibrosis patients. *Magn Reson Med* 61:299–306
- Farrell PM, Kosorok MR, Rock MJ, Laxova A, Zeng L, Lai HC, Hoffman G, Laessig RH, Splaingard ML (2001) Early diagnosis of cystic fibrosis through neonatal screening prevents severe malnutrition and improves long-term growth. Wisconsin Cystic Fibrosis Neonatal Screening Study Group. *Pediatrics* 107:1–13
- Ferguson PJ, Weinberger M (2006) Shrinking lung syndrome in a 14-year-old boy with systemic lupus erythematosus. *Pediatr Pulmonol* 41:194–197
- Fiel SB, Friedman AC, Caroline DF, Radecki PD, Faerber E, Grumbach K (1987) Magnetic resonance imaging in young adults with cystic fibrosis. *Chest* 91:181–184
- Fleck R, McPhail G, Szczesniak R, Knowlton J, Radhakrishnan R, Clancy J, Amin R (2013) Aortopulmonary collateral flow in cystic fibrosis assessed with phase-contrast MRI. *Pediatr Radiol* 43:1279–1286
- Foundation, CF (2000) Cystic fibrosis foundation patient registry: annual data report 2000. Cystic Fibrosis Foundation, pp 1–22
- Foundation, CF (2004) Cystic fibrosis foundation patient registry: annual data report 2004. Cystic Fibrosis Foundation, pp 1–12
- Foundation, CF (2011). Cystic fibrosis foundation patient registry: annual data report. Cystic Fibrosis Foundation, pp 1–32
- Fried A, Bonilla F (2009) Pathogenesis, diagnosis, and management of primary antibody deficiencies and infections. *Clin Microbiol Rev* 22:396–414
- Fullmer JJ, Langston C, Dishop MK, Fan LL (2005) Pulmonary capillaritis in children: a review of eight cases with comparison to other alveolar hemorrhage syndromes. *J Pediatr* 146:376–381
- Garcia-Pena P, Boixadera H, Barber I, Toran N, Lucaya J, Enriquez G (2011) Thoracic findings of systemic diseases at high-resolution CT in children. *Radiographics* 31:465–482
- Gasparetto TD, Escuissato DL, Marchiori E (2008) Pulmonary infections following bone marrow transplantation: high-resolution CT findings in 35 paediatric patients. *Eur J Radiol* 66:117–121
- Geffer WB, Albelda SM, Talbot GH, Gerson SL, Cassileth PA, Miller WT (1985) Invasive pulmonary aspergillosis and acute leukemia. Limitations in the diagnostic utility of the air crescent sign. *Radiology* 157:605–610
- Gelfand MJ, Daya SA, Rucknagel DL, Kalinyak KA, Paltiel HJ (1993) Simultaneous occurrence of rib infarction and pulmonary infiltrates in sickle cell disease patients with acute chest syndrome. *J Nucl Med* 34:614–618
- George R, Andronikou S, Theron S, Plessis J, Hayes M, Goussard P, Mapukata A, Gie R (2009) Pulmonary infections in HIV-positive children. *Pediatr Radiol* 39:545–554
- Georgiadou SP, Sipsas NV, Marom EM, Kontoyiannis DP (2011) The diagnostic value of halo and reversed halo signs for invasive mold infections in compromised hosts. *Clin Infect Dis* 52:1144–1155
- Giri N, Rees L, Faro A, Huddleston CB, White FV, Alter BP, Savage SA (2011) Lung transplantation for pulmonary fibrosis in dyskeratosis congenita: case report and systematic literature review. *BMC Blood Disorders* 11:3. doi:10.1186/1471-2326-11-3
- Goitein O, Elstein D, Abrahamov A, Hadas-Halpern I, Melzer E, Kerem E, Zimran A (2001) Lung involvement and enzyme replacement therapy in Gaucher's disease. *QJM* 94(8):407–415
- Gona P, Van Dyke RB, Williams PL, Dankner WM, Chernoff MC, Nachman SA, Seage GR 3rd (2006) Incidence of opportunistic and other infections in HIV-infected children in the HAART era. *JAMA* 19:292–300
- Greene KE, Takasugi JE, Godwin JD, Richardson ML, Burke W, Aitken ML (1994) Radiographic changes in acute exacerbations of cystic fibrosis in adults: a pilot study. *Am J Roentgenol* 163:557–562
- Greene RE, Schlamm HT, Oestmann JW, Stark P, Durand C, Lortholary O, Wingard JR, Herbrecht R, Ribaud P, Patterson TF, Troke PF, Denning DW, Bennett JE, de Pauw BE, Rubin RH (2007) Imaging findings in acute invasive aspergillosis: clinical significance of the halo sign. *Clin Infect Dis* 44:373–379
- Griese M, Brasch F, Aldana VR, Cabrera MM, Goelnitz U, Ikonen E, Karam BJ, Liebisch G, Linder MD, Lohse P, Meyer W, Schmitz G, Pamir A, Ripper J, Rolfs A, Schams A, Lezana FJ (2010) Respiratory disease in Niemann-Pick type C2 is caused by pulmonary alveolar proteinosis. *Clin Genet* 77:119–130
- Griffith LM, Cowan MJ, Notarangelo LD, Puck JM, Buckley RH, Candotti F, Conley ME, Fleisher TA, Gaspar HB, Kohn DB, Ochs HD, O'Reilly RJ, Rizzo JD, Roifman CM, Small TN, Shearer WT; Workshop Participants (2009) Improving cellular therapy for primary immune deficiency diseases: recognition, diagnosis, and management. *J Allergy Clin Immunol* 124:1152
- Guillemot N, Troade C, de Villemeur TB, Clement A, Faroux B (2007) Lung disease in Niemann-Pick disease. *Pediatr Pulmonol* 42:1207–1214
- Guillerman RP, Brody AS (2011) Contemporary perspectives on pediatric diffuse lung disease. *Radiol Clin N Am* 49:847–868
- Gungor T, Engel-Bicik I, Eich G, Willi UV, Nadal D, Hossle JP, Seger RA, Steinert HC (2001) Diagnostic and therapeutic impact of whole body positron emission tomography using fluorine-18-fluoro-2-deoxy-D-glucose in children with chronic granulomatous disease. *Arch Dis Child* 85:341–345
- Ha SY, Helms P, Fletcher M, Broadbent V, Pritchard J (1992) Lung involvement in Langerhans' cell histiocytosis: prevalence, clinical features, and outcome. *Pediatrics* 89:466–469
- Hamideh D, Alvarez O (2013) Sickle cell disease related mortality in the United States (1999–2009). *Pediatr Blood Cancer* 60:1482–1486



- Heimall J, Freeman A, Holland SM (2010) Pathogenesis of hyper IgE syndrome. *Clin Rev Allergy Immunol* 38:32–38
- Helbich TH, Heinz-Peer G, Fleischmann D, Wojnarowski C, Wunderbaldinger P, Huber S, Eichler I, Herold CJ (1999) Evolution of CT findings in patients with cystic fibrosis. *Am J Roentgenol* 173:81–88
- Horani A, Brody SL, Ferkol TW (2013) Picking up speed: advances in the genetics of primary ciliary dyskinesia. *Pediatr Res*. doi: [10.1038/pr.2013.200](https://doi.org/10.1038/pr.2013.200) (Epub ahead of print)
- Horger M, Hebart H, Einsele H, Lengerke C, Claussen CD, Vonthein R, Pfannenberger C (2005) Initial CT manifestations of invasive pulmonary aspergillosis in 45 non-HIV immunocompromised patients: association with patient outcome? *Eur J Radiol* 55:434–444
- Hsu BY, Edwards DK 3rd, Trambert MA (1992) Pulmonary hemorrhage complicating systemic lupus erythematosus: role of MR imaging in diagnosis. *Am J Roentgenol* 158:519–520
- Hurley MN, McKeever TM, Prayle AP, Fogarty AW, Smyth AR (2014) Rate of improvement of CF life expectancy exceeds that of general population—observational death registration study. *J Cyst Fibros*. doi: [10.1016/j.cf.2013.12.002](https://doi.org/10.1016/j.cf.2013.12.002) (Epub ahead of print)
- Jackson AD, Daly L, Jackson AL, Kelleher C, Marshall BC, Quinton HB, Fletcher G, Harrington M, Zhou S, McKone EF, Gallagher C, Foley L, Fitzpatrick P (2011) Validation and use of a parametric model for projecting cystic cystic fibrosis survivorship beyond observed data: a birth cohort analysis. *Thorax* 86:674–679
- Jacobsen LE, Houston CS, Habbick BF, Genereux GP, Howie JL (1986) Cystic fibrosis: a comparison of computed tomography and plain chest radiographs. *Can Assoc Radiol J* 37:17–21
- Jawad AF, McDonald-McGinn DM, Zackai E, Sullivan KE (2001) Immunologic features of chromosome 22q11.2 deletion syndrome (DiGeorge syndrome/velocardiofacial syndrome). *J Pediatr* 139:715–723
- Jennette JC, Falk RJ, Bacon PA, Basu N, Cid MC, Ferrario F, Flores-Suarez LF et al (2013) 2012 revised International Chapel Hill Consensus Conference Nomenclature of Vasculitides. *Arthritis Rheum* 65:1–11
- Kartagener M, Stucki P (1962) Bronchiectasis with situs inversus. *Arch Pediatr* 79:193–207
- Keesling CA, Frush DP, O'Hara SM, Fordham LA (1998) Clinical and imaging manifestations of pediatric sarcoidosis. *Acad Radiol* 5:122–132
- Kennedy MP, Noone PG, Leigh MW, Zariwala MA, Minnix SL, Knowles MR, Molina PL (2007) High-resolution CT of patients with primary ciliary dyskinesia. *Am J Roentgenol* 188:1232–1238
- Khan TZ, Wagener JS, Bost T, Martinez J, Accurso FJ, Riches DW (1995) Early pulmonary inflammation in infants with cystic fibrosis. *Am J Respir Crit Care Med* 151:1075–1082
- Khanna G, Kao SC, Kirby P, Sato Y (2005) Imaging of chronic granulomatous disease in children. *Radiographics* 25:1183–1195
- Kimura Y, Weiss E, Haroldson KL, Lee T, Punaro M, Oliveira S, Rabinovich E et al (2013) Pulmonary hypertension and other potentially fatal pulmonary complications in systemic juvenile idiopathic arthritis. *Arthritis Care Res (Hoboken)* 65:745–752
- Klein M, Cohen-Cymberek M, Armoni S, Shoseyov D, Chisin R, Orevi M, Freedman N, Kerem E (2009) 18F-fluorodeoxyglucose-PET/CT imaging of lungs in patients with cystic fibrosis. *Chest* 136:1220–1228
- Knook LM, de Kleer IM, van der Ent CK, van der Net JJ, Prakken BJ, Kuis W (1999) Lung function abnormalities and respiratory muscle weakness in children with juvenile chronic arthritis. *Eur Respir J* 14:529–533
- Kobayashi I, Yamada M, Takahashi Y, Kawamura N, Okano M, Sakiyama Y, Kobayashi K (2003) Interstitial lung disease associated with juvenile dermatomyositis: clinical features and efficacy of cyclosporin A. *Rheumatology (Oxford)* 42:371–374
- Konstan MW, Byard PJ, Hoppel CL, Davis PB (1995) Effect of high-dose ibuprofen in patients with cystic fibrosis. *N Engl J Med* 332:848–854
- Koscik RE, Kosorok MR, Farrell PM, Collins J, Peters ME, Laxova A, Green CG, Zeng L, Rusakow LS, Hardie RC, Campbell PW, Gurney JW (2000) Wisconsin cystic fibrosis chest radiograph scoring system: validation and standardization for application to longitudinal studies. *Pediatr Pulmonol* 29:457–467
- Kosorok MR, Zeng L, West SE, Rock MJ, Splaingard ML, Laxova A, Green CG, Collins J, Farrell PM (2001) Acceleration of lung disease in children with cystic fibrosis after *Pseudomonas aeruginosa* acquisition. *Pediatr Pulmonol* 32:277–287
- Koumbourlis AC (2013) Lung function in sickle cell disease. *Paediatr Respir Rev*. doi: [10.1016/j.prrv.2013.10.002](https://doi.org/10.1016/j.prrv.2013.10.002) (Epub ahead of print)
- Koumbourlis AC, Hurlet-Jensen A, Bye MR (1997) Lung function in infants with sickle cell disease. *Pediatr Pulmonol* 24:277–281
- Lakatos K, Herbruggen H, Potschger U, Prosch H, Minkov M (2013) Radiological features of thymic langerhans cell histiocytosis. *Pediatr Blood Cancer* 60:E143–E145
- Langston C, Cooper ER, Goldfarb J, Easley KA, Husak S, Sunkle S, Starc TJ, Colin AA, P2C2 HIV Study Group (2001) Human immunodeficiency virus-related mortality in infants and children: data from the pediatric pulmonary and cardiovascular complications of vertically transmitted HIV P2C2 Study. *Pediatrics* 107:328–338
- Laube BL, Chang DY, Blask AN, Rosenstein BJ (1992) Radioaerosol assessment of lung improvement in cystic fibrosis patients treated for acute pulmonary exacerbations. *Chest* 101:1302–1308
- Lehman TJ (1995) A practical guide to systemic lupus erythematosus. *Pediatr Clin North Am* 42:1223–1238
- Leong MA, Dampier C, Varlotta L, Allen JL (1997) Airway hyperreactivity in children with sickle cell disease. *J Pediatr* 131:278–283
- Leutner CC, Gieseke J, Lutterbey G, Kuhl CK, Glasmacher A, Wardelmann E, Theisen A, Schild HH (2000) MR imaging of pneumonia in immunocompromised patients: comparison with helical CT. *Am J Roentgenol* 175:391–397
- Li Z, Sanders DB, Rock MJ, Kosorok MR, Collins J, Green CG, Brody AS, Farrell PM (2012) Regional differences in the evolution of lung disease in children with cystic fibrosis. *Pediatr Pulmonol* 47:635–640
- Lilleby V, Aalokken TM, Johansen B, Forre O (2006) Pulmonary involvement in patients with childhood-onset systemic lupus erythematosus. *Clin Exp Rheumatol* 24:203–208
- Lin YC, Yang YH, Lin YT, Chiang BL (2002) Steroid refractory interstitial pneumonitis in a patient with juvenile dermatomyositis. *J Microbiol Immunol Infect* 35:259–261
- Lin SP, Shih SC, Chuang CK, Lee KS, Chen MR, Niu DM, Chiu PC, Lin SJ, Lin HY (2013) Characterization of pulmonary function impairments in patients with mucopolysaccharidoses—changes with age and treatment. *Pediatr Pulmonol*. doi: [10.1002/ppul.22774](https://doi.org/10.1002/ppul.22774) (Epub ahead of print)
- Lovell D, Lindsley C, Langston C (1984) Lymphoid interstitial pneumonia in juvenile rheumatoid arthritis. *J Pediatr* 105:947–950
- Lynch DA, Hay T, Newell JD Jr, Divgi VD, Fan LL (1999) Pediatric diffuse lung disease: diagnosis and classification using high-resolution CT. *Am J Roentgenol* 173:713–718
- Maffessanti M, Candusso M, Brizzi F, Piovesana F (1996) Cystic fibrosis in children: HRCT findings and distribution of disease. *J Thorac Imaging* 11:27–38
- Maglione M, Bush A, Montella S, Mollica C, Manna A, Esposito A, Santamaria F (2012) Progression of lung disease in primary ciliary dyskinesia: is spirometry less accurate than CT? *Pediatr Pulmonol* 47:498–504
- Magnin ML, Cros P, Beydon N, Mahloul M, Tamalet A, Escudier E, Clement A, Le Point HD, Blanchon S (2012) Longitudinal lung

- function and structural changes in children with primary ciliary dyskinesia. *Pediatr Pulmonol* 47:816–825
- Mahdaviani SA, Mohajerani SA, Rezaei N, Casanova JL, Mansouri SD, Velayati AA (2013) Pulmonary manifestations of chronic granulomatous disease. *Expert Rev Clin Immunol* 9:153–160
- Manson D, Reid B, Dalal I, Roifman CM (1997) Clinical utility of high-resolution pulmonary computed tomography in children with antibody deficiency disorders. *Pediatr Radiol* 27:794–798
- Manson DE, Sikka S, Reid B, Roifman C (2000) Primary immunodeficiencies: a pictorial immunology primer for radiologists. *Pediatr Radiol* 30:501–510
- Martin L, Buonomo C (1997) Acute chest syndrome of sickle cell disease: radiographic and clinical analysis of 70 cases. *Pediatr Radiol* 27:637–641
- Martini G, Foeldvari I, Russo R, Cuttica R, Eberhard A, Ravelli A, Lehman TJA et al (2006) Systemic sclerosis in childhood. Clinical and immunologic features of 153 patients in an international database. *Arthritis Rheum* 54:3971–3978
- Massaad MJ, Ramesh N, Geha RS (2013) Wiskott-Aldrich syndrome: a comprehensive review. *Ann N Y Acad Sci* 1285:26–43
- Massie RJ, Olsen M, Glazner J, Robertson CF, Francis I (2000) Newborn screening for cystic fibrosis in Victoria: 10 years' experience (1989–1998). *Med J Aust* 172:584–587
- Mathieson JR, Mayo JR, Staples CA, Muller NL (1989) Chronic diffuse infiltrative lung disease: comparison of diagnostic accuracy of CT and chest radiography. *Radiology* 171:111–116
- Matsuzono Y, Togashi T, Narita M, Taguchi Y, Miura S (1995) Pulmonary aspergillosis and pseudosequestration of the lung in chronic granulomatous disease. *Pediatr Radiol* 25:201–203
- McAdams HP, Rosado-de-Christenson ML, Templeton PA, Lesar M, Moran CA (1995) Thoracic mycoses from opportunistic fungi: radiologic-pathologic correlation. *Radiographics* 15:271–286
- McComack F, Brody A, Meyer C, Leonard J, Chuck G, Dabora S, Sethuraman G, Colby TV, Kwiatkowski DJ, Franz DN (2002) Pulmonary cysts consistent with lymphangioleiomyomatosis are common in women with tuberous sclerosis: genetic and radiographic analysis. *Chest* 121(3 Suppl):61S
- McGovern MM, Lippa N, Bagiella E, Schuchman EH, Desnick RJ, Wasserstein MP (2013) Morbidity and mortality in type B Niemann-Pick disease. *Genet Med* 15:618–623
- McGrath-Morrow SA, Gower WA, Rothblum-Oviatt C, Brody AS, Langston C, Fan LL, Lefton-Greif MA, Crawford TO, Troche M, Sandlund JT, Auwaerter PG, Easley B, Loughlin GM, Carroll JL, Lederman HM (2010) Evaluation and management of pulmonary disease in ataxia-telangiectasia. *Pediatr Pulmonol* 45:847–859
- McHugh K, Olsen EOE, Vellodi A (2004) Gaucher disease in children: radiology of non-central nervous system manifestations. *Clin Radiol* 59:117–123
- Mekontso Dessap A, Deux JF, Habibi A, Abidi N, Godeau B, Adnot S, Brun-Buisson C, Rahmouni A, Galacteros F, Maitre B (2013) Lung imaging during acute chest syndrome in sickle cell disease: computed tomography patterns and diagnostic accuracy of bedside chest radiograph. *Thorax* 69:144–151
- Mentore K, Froh DK, de Lange EE, Brookeman JR, Paget-Brown AO, Altes TA (2005) Hyperpolarized HHe 3 MRI of the lung in cystic fibrosis: assessment at baseline and after bronchodilator and airway clearance treatment. *Acad Radiol* 12:1423–1429
- Mettin RR, Merkschlager A, Bernhard MK, Elix H, Hirsch W, Kiess W, Syrbe S (2013) Wide spectrum of clinical manifestations in children with tuberous sclerosis complex—follow-up of 20 children. *Brain Dev*. doi: [10.1016/j.braindev.2013.05.006](https://doi.org/10.1016/j.braindev.2013.05.006) (Epub ahead of print)
- Micol R, Ben Slama L, Suarez F, Le Mignot L, Beaute J, Mahlaoui N, Dubois d'Enghien C et al (2011) Morbidity and mortality from ataxia-telangiectasia are associated with ATM genotype. *J Allergy Clin Immunol* 128:382–389
- Miller AC, Gladwin MT (2012) Pulmonary complications of sickle cell disease. *Am J Respir Crit Care Med* 185:1154–1165
- Millet A, Pederzoli-Ribeil M, Guillemin L, Witko-Sarsat V, Mouthon L (2013) Antineutrophil cytoplasmic antibody-associated vasculitides: is it time to split up the group. *Ann Rheum Dis* 72:1273–1279
- Milman N, Hoffman AL, Byg KE (1998) Sarcoidosis in children. Epidemiology in Danes, clinical features, diagnosis, treatment and prognosis. *Acta Paediatr* 87:871–878
- Mina R, Brunner HI (2010) Pediatric lupus – are there differences in presentation, genetics, response to therapy, and damage accrual compared with adult lupus? *Rheum Dis Clin North Am* 36:53–80
- Modell F, Puente D, Modell V (2009) From genotype to phenotype. Further studies measuring the impact of a Physician Education and Public Awareness Campaign on early diagnosis and management of Primary Immunodeficiencies. *Immunol Res* 44:132–149
- Montella S, Santamaria F, Salvatore M, Pignata C, Maglione M, Iacotucci P, Mollica C (2009) Assessment of chest high-field magnetic resonance imaging in children and young adults with noncystic fibrosis chronic lung disease: comparison to high-resolution computed tomography and correlation with pulmonary function. *Invest Radiol* 44:532–538
- Moskaluk CA, Pogrebniak HW, Pass HI, Gallin JI, Travis WD (1994) Surgical pathology of the lung in chronic granulomatous disease. *Am J Clin Pathol* 102:684–691
- Mott LS, Park J, Murray CP, Gangell CL, de Klerk NH, Robinson PJ, Robertson CF, Ranganathan SC, Sly PD, Stick SM, AREST CF (2012) Progression of early structural lung disease in young children with cystic fibrosis assessed using CT. *Thorax* 67:509–516
- Nadeau K, Hwa V, Rosenfeld RG (2011) STAT5b deficiency: an unsuspected cause of growth failure, immunodeficiency, and severe pulmonary disease. *J Pediatr* 158:701–708
- Nathanson I, Conboy K, Murphy S, Afshani E, Kuhn JP (1991) Ultrafast computerized tomography of the chest in cystic fibrosis: a new scoring system. *Pediatr Pulmonol* 11:81–86
- Noone PG, Leigh MW, Sannuti A, Minnix SL, Carson JL, Hazucha M, Zariwala MA, Knowles MR (2004) Primary ciliary dyskinesia: diagnostic and phenotypic features. *Am J Respir Crit Care Med* 169:459–467
- Notarangelo LD, Miao CH, Ochs HD (2008) Wiskott-Aldrich syndrome. *Curr Opin Hematol* 15:30–36
- Odame I, Li P, Lau L, Doda W, Noseworthy M, Babyn P, Weitzman S (2006) Pulmonary Langerhans cell histiocytosis: a variable disease in childhood. *Pediatr Blood Cancer* 47:889–893
- Ozkan H, Altihan F, Genel F, Targan S, Gunvar T (2005) IgA and/or IgG subclass deficiency in children with recurrent respiratory infections and its relationship with chronic pulmonary damage. *J Investig Allergol Clin Immunol* 15:69–74
- Panigada S, Ravelli A, Silvestri M, Granata C, Magni-Manzoni S, Cerveri I, Dore R, Toma P, Martini A, Rossi GA, Sacco O (2009) HRCT and pulmonary function tests in monitoring of lung involvement in juvenile systemic sclerosis. *Pediatr Pulmonol* 44:1226–1234
- Park JH, Levinson AI (2010) Granulomatous-lymphocytic interstitial lung disease (GLILD) in common variable immunodeficiency (CVID). *Clin Immunol* 134:97–103
- Pitcher RD, Goddard E, Hendricks M, Lawrenson J (2009) Chest radiographic pulmonary changes reflecting extrapulmonary involvement in paediatric HIV disease. *Pediatr Radiol* 39:565–568
- Pitcher RD, Beningfield SJ, Zar HJ (2010) Chest radiographic features of lymphocytic interstitial pneumonitis in HIV-infected children. *Clin Radiol* 65:150–154
- Plebani A, Soresina A, Rondelli R, Amato GM, Azzari C, Cardinale F, Cazzola G, Consolini R, De Mattia D, Dell'Erba G, Duse M,

- Fiorini M, Martino S, Martire B, Masi M, Monafò V, Moschese V, Notarangelo LD, Orlandi P, Panei P, Pession A, Pietrogrande MC, Pignata C, Quinti I, Ragno V, Rossi P, Sciotto A, Stabile A (2002) Clinical, immunological, and molecular analysis in a large cohort of patients with X-linked agammaglobulinemia: an Italian multicenter study. *Clin Immunol* 104:221–230
- Pouessel G, Deschildre A, Le Bourgeois M, Cuisset JM, Catteau B, Karila C, Neve V, Thumerelle C, Quartier P, Tillie-Leblond I (2013) The lung is involved in juvenile dermatomyositis. *Pediatr Pulmonol* 48:1016–1025
- Puderbach M, Eichinger M, Gahr J, Ley S, Tuengerthal S, Schmahl A, Fink C, Plathow C, Wiebel M, Müller FM, Kauczor HU (2007) Proton MRI appearance of cystic fibrosis: comparison to CT. *Eur Radiol* 17:716–724
- Ramsey BW, Pepe MS, Quan JM, Otto KL, Montgomery AB, Williams-Warren J, Vasiljev KM, Borowitz D, Bowman CM, Marshall BC, Marshall S, Smith AL (1999) Intermittent administration of inhaled tobramycin in patients with cystic fibrosis. Cystic Fibrosis Inhaled Tobramycin Study Group. *N Engl J Med* 340:23–30
- Ravenel JG, McAdams HP (2003) Pulmonary vasculitis: CT features. *Semin Respir Crit Care Med* 24:427–436
- Robinson TE, Leung AN, Northway WH, Blankenberg FG, Bloch DA, Oehlert JW, Al-Dabbagh H, Hubli S, Moss RB (2001) Spirometer-triggered high-resolution computed tomography and pulmonary function measurements during an acute exacerbation in patients with cystic fibrosis. *J Pediatr* 138:553–559
- Roncera L, Potschger U, Janka G, Gadner H, Minkov M; German Society for Pediatric Hematology and Oncology, Langerhans Cell Histiocytosis Study Group (2012) Pulmonary involvement in pediatric-onset multisystem Langerhans cell histiocytosis: effect on course and outcome. *J Pediatr* 161:129–133
- Rowntree RK, Harris A (2003) The phenotypic consequences of CFTR mutations. *Ann Hum Genet* 67(Pt 5):471–485
- Rusconi F, Panisi C, Dellepiane RM, Cardinale F, Chini L, Martire B, Bonelli N, Felisati G, Pietrogrande MC (2003) Pulmonary and sinus diseases in primary humoral immunodeficiencies with chronic productive cough. *Arch Dis Child* 88:1101–1105
- Ryan AK, Goodship JA, Wilson DI, Philip N, Lew A, Seidel H, Schuffenhauer S et al (1997) Spectrum of clinical features associated with interstitial chromosome 22q11 deletions: a European collaborative study. *J Med Genet* 34:798–804
- Sakaguchi H, Takahashi Y, Watanabe N, Doi S, Muramatsu H, Hama A, Shimada A, Yagasaki H, Kudo K, Kojima S (2012) Incidence, clinical features, and risk factors of idiopathic pneumonia syndrome following hematopoietic stem cell transplantation in children. *Pediatr Blood Cancer* 58:780–784
- Sanders DB, Li Z, Brody AS, Farrell PM (2011) Chest computed tomography scores of severity are associated with future lung disease progression in children with cystic fibrosis. *Am J Respir Crit Care Med* 184:816–821
- Sanders DB, Li Z, Rock MJ, Brody AS, Farrell PM (2012) The sensitivity of lung disease surrogates in detecting chest CT abnormalities in children with cystic fibrosis. *Pediatr Pulmonol* 47:567–573
- Sanders DB, Li Z, Laxova A, Rock MJ, Levy H, Collins J, Ferec C, Farrell PM (2014) Risk factors for the progression of cystic fibrosis lung disease throughout childhood. *Ann Am Thorac Soc* 11:63–72
- Santamaria D, Montella S, Tiddens HAWM, Guidi G, Casotti V, Maglione M, de Jong PA (2008) Structural and functional lung disease in primary ciliary dyskinesia. *Chest* 134:351–357
- Savage SA, Alter BP (2009) Dyskeratosis congenita. *Hematol Oncol Clin North Am* 23:215–231
- Sawyer SM, Carlin JB, DeCampo M, Bowes G (1994) Critical evaluation of three chest radiograph scores in cystic fibrosis. *Thorax* 49:863–866
- Schroeder SA, Zielen S (2013) Infections of the respiratory system in patients with ataxia-telangiectasia. *Pediatr Pulmonol*. doi: [10.1002/ppul.22817](https://doi.org/10.1002/ppul.22817) (Epub ahead of print)
- Schroeder SA, Swift M, Sandoval C, Langston C (2005) Interstitial lung disease in patients with ataxia-telangiectasia. *Pediatr Pulmonol* 39:537–543
- Schwab EP, Schumacher HR Jr, Freundlich B, Callegari PE (1993) Pulmonary alveolar hemorrhage in systemic lupus erythematosus. *Semin Arthritis Rheum* 23:8–15
- Seely JM, Effmann EL, Müller NL (1997) High-resolution CT of pediatric lung disease: imaging findings. *Am J Roentgenol* 168:1269–1275
- Seely JM, Jones LT, Wallace C, Sherry D, Effmann EL (1998) Systemic sclerosis: using high-resolution CT to detect lung disease in children. *Am J Roentgenol* 170:691–697
- Seely JM, Salahudeen S Sr, Cadaval-Goncalves AT, Jamieson DH, Dennie CJ, Matzinger FR, Souza CA (2012) Pulmonary Langerhans cell histiocytosis: a comparative study of computed tomography in children and adults. *J Thorac Imaging* 27:65–70
- Shah RM, Sexauer W, Ostrum BJ, Fiel SB, Friedman AC (1997) High-resolution CT in the acute exacerbation of cystic fibrosis: evaluation of acute findings, reversibility of those findings, and clinical correlation. *Am J Roentgenol* 169:375–380
- Shih SL, Lee YJ, Lin SP, Sheu CY, Blickman JG (2002) Airway changes in children with mucopolysaccharidoses. *Acta Radiol* 43:40–43
- Sileo C, Epaud R, Mahloul M, Beydon N, Elia D, Clement A, Pointe HD (2013a) Sarcoidosis in children: HRCT findings and correlation with pulmonary function tests. *Pediatr Pulmonol* Dec 11 (Epub ahead of print)
- Sileo C, Corvol H, Boelle PY, Blondiaux E, Clement A, Ducou Le Pointe H (2013b) HRCT and MRI of the lung in children with cystic fibrosis: comparison of different scoring systems. *J Cyst Fibros*. doi: [10.1016/j.jcf.2013.09.003](https://doi.org/10.1016/j.jcf.2013.09.003) (Epub ahead of print)
- Sims EJ, Mugford M, Clark A, Aitken D, McCormick J, Mehta G, Mehta A, UK Cystic Fibrosis Database Steering Committee (2007) Economic implications of newborn screening for cystic fibrosis: a cost of illness retrospective cohort study. *Lancet* 369:1187–1195
- Sirr SA, Elliott GR, Regelman WE, Juenemann PJ, Morin RL, Boudreau RJ, Warwick WJ, Loken MK (1986) Aerosol penetration ratio: a new index of ventilation. *J Nucl Med* 27:1343–1346
- Slattery DM, Zurkowski D, Colin AA, Cleveland RH (2004) CF: an X-ray database to assess effect of aerosolized tobramycin. *Pediatr Pulmonol* 38:23–30
- Sly PD, Gargell CL, Chen L, Ware RS, Ranganathan S, Mott LS, Murray CP, Stick SM, AREST CF Investigators (2013) Risk factors for bronchiectasis in children with cystic fibrosis. *N Engl J Med* 368:1963–1970
- Smets A, Morteel K, de Praeter G, Francois O, Benoit Y, Kunnen M (1997) Pulmonary and mediastinal lesions in children with Langerhans cell histiocytosis. *Pediatr Radiol* 27:873–876
- Sockrider MM, Swank PR, Seilheimer DK, Schidlow DV (1994) Measuring clinical status in cystic fibrosis: internal validity and reliability of a modified NIH score. *Pediatr Pulmonol* 17:86–96
- Sohn DI, Laborde HA, Bellotti M, Seijo L (2007) Juvenile rheumatoid arthritis and bronchiolitis obliterans organized pneumonia. *Clin Rheumatol* 26:247–250
- Spencer DA, Alton HM, Raafat F, Weller PH (1996) Combined percutaneous lung biopsy and high-resolution computed tomography in the diagnosis and management of lung disease in children. *Pediatr Pulmonol* 22:111–116
- Stadler A, Stiebellehner L, Jakob PM, Arnold JF, Eisenhuber E, von Katzler I, Bankier AA (2007) Quantitative and (2) enhanced MRI of the pathologic lung: findings in emphysema, fibrosis, and cystic fibrosis. *Int J Biomed Imaging* 2007:23624



- Stick SM, Brennan S, Murray C, Douglas T, von Ungern-Sternberg BS, Garratt LW, Gangell CL, De Klerk N, Linnane B, Ranganathan S, Robinson P, Robertson C, Sly PD (2009) Bronchiectasis in infants and preschool children diagnosed with cystic fibrosis after newborn screening. *J Pediatr* 155:623–628
- Subbarayan A, Colarusso G, Hughes SM, Gennery AR, Slatter M, Cant AJ, Arkwright PD (2011) Clinical features that identify children with primary immunodeficiency diseases. *Pediatrics* 127:810–816
- Susarla SC, Fan LL (2007) Diffuse alveolar hemorrhage syndromes in children. *Curr Opin Pediatr* 19:314–320
- Sylvester KP, Patey RA, Milligan P, Rafferty GF, Broughton S, Rees D, Thein SL, Greenough A (2006) Impact of acute chest syndrome on lung function of children with sickle cell disease. *J Pediatr* 149:17–22
- Tabone MD (2003) Invasive pulmonary aspergillosis in immunocompromised children: diagnosis and classification. *Arch Pediatr* 10(Suppl 5):S82s–S87s
- Takizawa H, Shiga J, Moroi Y, Miyachi S, Nishiwaki M, Miyamoto T (1987) Interstitial lung disease in dermatomyositis: clinicopathological study. *J Rheumatol* 14:102–107
- Taytard J, Nathan N, de Blic J, Fayon M, Epaul R, Deschildre A, Troussier F, Lubrano M, Chiron R, Reix P, Cros P, Mahloul M, Michon D, Clement A, Corvol H; French RespiRare® group (2013) New insights into pediatric idiopathic pulmonary hemosiderosis: the French RespiRare® cohort. *Orphanet J Rare Dis* 8:161. doi: [10.1186/1750-1172-8-161](https://doi.org/10.1186/1750-1172-8-161)
- Terheggen-Lagro S, Truijens N, van Poppel N, Gulmans V, van der Laag J, van der Ent C (2003) Correlation of six different cystic fibrosis chest radiograph scoring systems with clinical parameters. *Pediatr Pulmonol* 35:441–445
- Theron S, Andronikou S, George R, du Plessis J, Goussard P, Hayes M, Mapukata A, Gie R (2009) Non-infective pulmonary disease in HIV-positive children. *Pediatr Radiol* 39:555–564
- Touw CML, van de Ven AA, de Jong PA, Terheggen-Lagro S, Beek E, Sanders EA, van Montfrans JM (2010) Detection of pulmonary complications in common variable immunodeficiency. *Pediatr Allergy Immunol* 21:793–805
- Towbin AJ, Chaves I (2010) Chronic granulomatous disease. *Pediatr Radiol* 40:657–668
- Toya SP, Tzelepis GE (2009) The many faces of scleroderma sine scleroderma: a literature review focusing on cardiopulmonary complications. *Rheumatol Int* 29:861–868
- Tunaci A, Berkmen YM, Gokmen E (1995) Pulmonary Gaucher's disease: high-resolution computed tomographic features. *Pediatr Radiol* 25:237–238
- Uziel Y, Hen B, Cordoba M, Wolach B (1998) Lymphocytic interstitial pneumonitis preceding polyarticular juvenile rheumatoid arthritis. *Clin Exp Rheumatol* 16:617–619
- van Beek EJ, Hill C, Woodhouse N, Fischele S, Fleming S, Howe B, Bott S, Wild JM, Taylor CJ (2007) Assessment of lung disease in children with cystic fibrosis using hyperpolarized 3-Helium MRI: comparison with Shwachman score, Chrispin-Norman score and spirometry. *Eur Radiol* 17:1018–1024
- Vecce TJ, Fan LL (2010) Interstitial lung disease in children older than 2 years. *Pediatr Allergy Immunol Pulmonol* 23:33–41
- Vesely R, Vargova V, Ravelli A, Massa M, Oleksak E, D'Alterio R, Martini A, De Benedetti F (2004) Serum level of KL-6 as a marker of interstitial lung disease in patients with juvenile systemic sclerosis. *J Rheumatol* 31:795–800
- Vichinsky EP, Neumayr LD, Earles AN, Williams R, Lennette ET, Dean D, Nickerson B, Orringer E, McKie V, Bellevue R, Daeschner C, Mancini EA (2000) Causes and outcomes of the acute chest syndrome in sickle cell disease. National Acute Chest Syndrome Study Group. *N Engl J Med* 342:1855–1865
- Wagener JS, Taussig LM, DeBenedetti C, Lemen RJ, Loughlin GM (1981) Pulmonary function in juvenile rheumatoid arthritis. *J Pediatr* 99:108–110
- Wang LC, Yang YH, Lu MY, Chiang BL (2003) Retrospective analysis of mortality and morbidity of pediatric systemic lupus erythematosus in the past two decades. *J Microbiol Immunol Infect* 36:203–208
- Waters DL, Wilcken B, Irwing L, Van Asperen P, Mellis C, Simpson JM, Brown J, Gaskin KJ (1999) Clinical outcomes of newborn screening for cystic fibrosis. *Arch Dis Child Fetal Neonatal Ed* 80:F1–F7
- Weatherly MR, Palmer CG, Peters ME, Green CG, Fryback D, Langhough R, Farrell PM (1993) Wisconsin cystic fibrosis chest radiograph scoring system. *Pediatrics* 91:488–495
- Webb R, Kelly JA, Somers EC, Hughes T, Kaufman KM, Sanchez E, Nath SK, Bruner G, Alarcon-Riquelme ME, Gilkeson GS, Kamen DL, Richardson BC, Harley JB, Sawalha AH (2011) Early disease onset is predicted by a higher genetic risk for lupus and is associated with a more severe phenotype in lupus patients. *Ann Rheum Dis* 70:151–156
- Winkelstein JA, Marino MC, Ochs H, Fuleihan R, Scholl PR, Geha R, Stiehm ER, Conley ME (2003) The X-linked hyper-IgM syndrome: clinical and immunological features of 79 patients. *Medicine (Baltimore)* 82:373–384
- Winkelstein JA, Marino MC, Lederman HM, Jones SM, Sullivan K, Burks AW, Conley ME, Cunningham-Rundles C, Ochs HD (2006) X-linked agammaglobulinemia: report on a United States registry of 201 patients. *Medicine (Baltimore)* 85:193–202
- Woellner C, Gertz EM, Schaffer AA, Lagos M, Perro M, Glocker EO, Pietrogrande MC et al (2010) Mutations in STAT3 and diagnostic guidelines for hyper-IgE syndrome. *J Allergy Clin Immunol* 125:424–432
- Wood P, Stanworth S, Burton J, Jones A, Peckham DG, Green T, Hyde C, Chapel H; UK Primary Immunodeficiency Network (2007) Recognition, clinical diagnosis and management of patients with primary antibody deficiencies: a systematic review. *Clin Exp Immunol* 149:410–423

---

# Radiology of the Chest Wall

Georg F. Eich, Christian J. Kellenberger, and Ulrich V. Willi

## Contents

<b>1</b>	<b>Introduction</b> .....	431
<b>2</b>	<b>Normal Variant, Congenital Abnormality, and Deformity</b> .....	432
2.1	Anatomic Variants.....	432
2.2	Malformation and Deformity .....	433
<b>3</b>	<b>Infection</b> .....	439
<b>4</b>	<b>Tumors</b> .....	444
<b>5</b>	<b>Trauma</b> .....	453
5.1	Accidental Trauma .....	453
5.2	Non-accidental Trauma .....	454
	<b>References</b> .....	457

---

## Abstract

Potential abnormalities of the chest wall in a child, including anatomic variants, congenital malformations and deformities, infection, tumors, and trauma will be reviewed. The imaging findings of these entities will be discussed with emphasis on what radiography, ultrasound, computed tomography, or magnetic resonance imaging can contribute to the evaluation of the pediatric chest wall.

---

## 1 Introduction

The chest wall of a child can give rise to a variety of lesions or pseudolesions that can be classified into normal variant, malformation, trauma, infection, and tumor. These lesions pertain to the skin and subcutaneous tissue (superficial layer), muscles and bones of the shoulder girdle and the pectoralis region (intermediate layer), and/or the deep layer, which include the dorsal spine, the ribs and intercostal spaces, the sternum, several fascial layers, and the parietal pleura. Pathology of the breast and the diaphragm is excluded from this review.

This chapter is structured according to the nosological entities mentioned above. We will discuss alterations in the shape of the chest that may be associated with functional or esthetic problems or that may mimic a tumor. The appropriate imaging technique for assessment of a deformity or variant is emphasized. Infections of the chest wall can originate from penetrating wounds or hematogenous spread within bone, joint, or soft tissue. The importance of imaging in defining the exact topography of the focus and its extent is stressed. Chest wall tumors are essentially mesenchymal tumors. Both benign and malignant neoplasms occur. The Ewing sarcoma family of tumors and rhabdomyosarcoma are the most prevalent malignant tumors of the chest wall. The chest may be exposed to trauma (accidental or nonaccidental). The imaging findings of both types of injuries will

---

G. F. Eich  
Pediatric Radiology, Kantonsspital, 5001 Aarau, Switzerland

C. J. Kellenberger (✉)  
Department of Diagnostic Imaging,  
The University Children's Hospital, Steinwiesstrasse 75,  
8032 Zürich, Switzerland  
e-mail: christian.kellenberger@kispi.uzh.ch

U. V. Willi  
Emeritus, Department of Diagnostic Imaging,  
The University Children's Hospital, Steinwiesstrasse 75,  
8032 Zürich, Switzerland

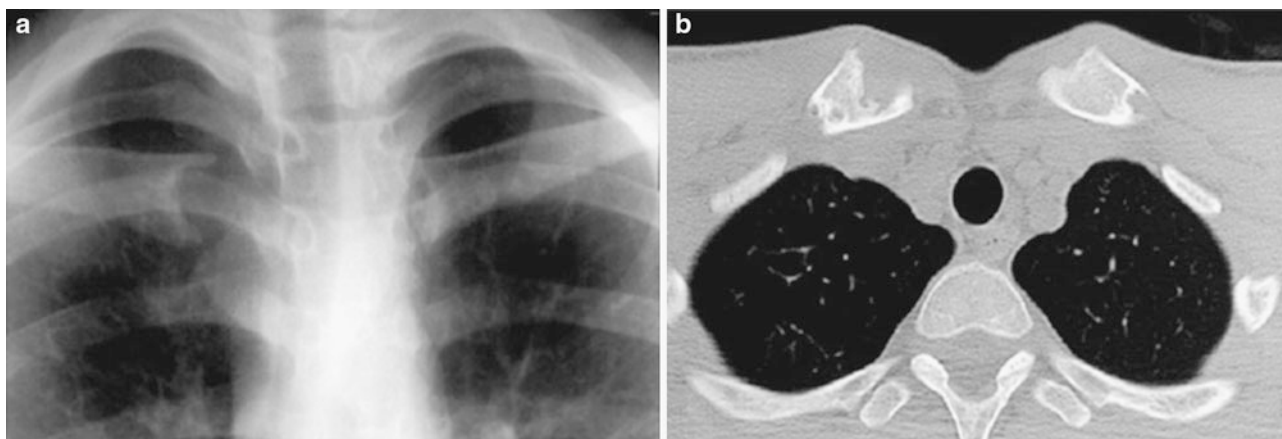


**Fig. 1** Normal variant of clavicles in a 15-year-old boy with fever of unknown origin. **a** Chest radiograph; close-up view of upper median aspect shows irregular sclerosis of right medial clavicular concavity, initially mistaken for osteomyelitis. **b** Axial CT scan through upper

chest area at level of medial clavicular ends shows correlating irregular clavicular contours, especially on the right. No local soft tissue swelling. Subsequently, scintigraphy demonstrated osteomyelitis in the right distal femoral metaphysis

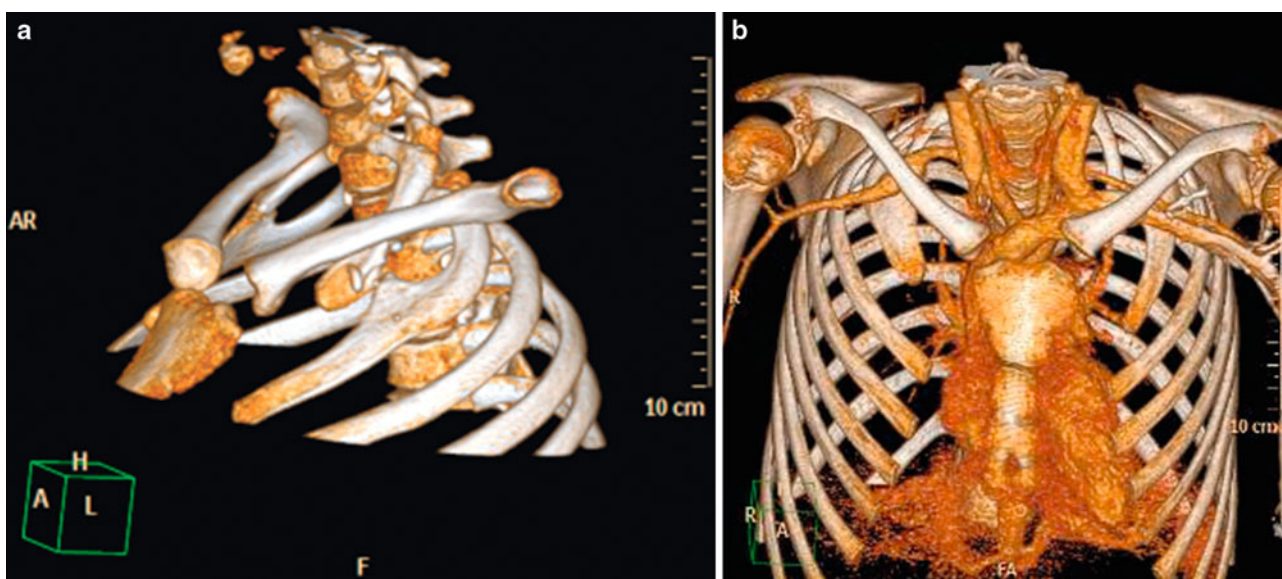


**Fig. 2** Thoracic outlet obstruction in a 13-year-old girl presenting with Raynaud syndrome and decreased pulse pressure in the right arm. Left anterior oblique (**a**) and anterior (**b**) volume rendered views of

contrast-enhanced CT demonstrate bilateral pseudoarticulation of the first and second ribs with compression and aneurysm formation of the right subclavian artery

be discussed, with particular emphasis on sternoclavicular fractures, which are difficult to diagnose both clinically and with conventional radiology.

## 2 Normal Variant, Congenital Abnormality, and Deformity

### 2.1 Anatomic Variants

The normal shape of the chest is fairly symmetrical; the chest is narrower in its upper portion than in the lower

three quarters. Normal infants have a relatively wide anteroposterior diameter of the chest compared to older children. The thoracic index (widest anteroposterior diameter/widest transverse diameter) is about 0.85 in infants compared to 0.72 in older children (Nathanson 1994). The thoracic index is decreased in pectus excavatum and in a child with an idiopathic flat chest. In the latter condition the thorax is flat and wide, the thoracic kyphosis is reduced, the heart is located slightly to the left, but the sternum is normal in position. The thoracic index is increased in pectus carinatum or in a child with a “barrel chest”.



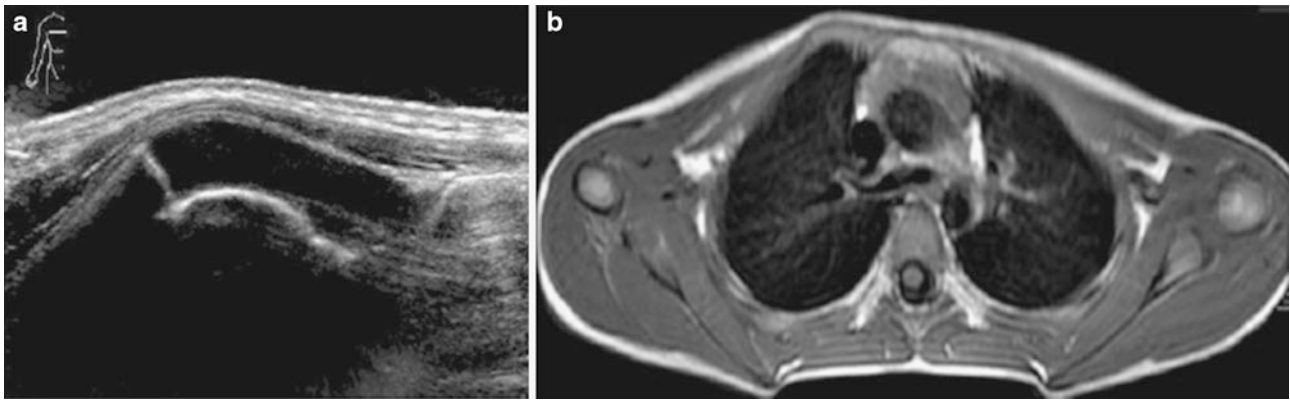


**Fig. 3** Rib deformity in a 6-year-old boy with “chest wall mass”. US scan (a) and axial T1-weighted MR image (b) through right upper thoracic area show redundancy of cartilaginous anterior rib portion (hockey stick shape)

Infants have a prominent double curvature of the *clavicle* which can simulate a fracture on chest radiographs taken with the child in a rotated position. The sternal end of the clavicle may show marked cupping during the second decade, which should not be misinterpreted as osteomyelitis or septic arthritis (Fig. 1).

Isolated *rib anomalies* are common incidental findings, usually of no clinical importance, with an estimated frequency of about 2 % (Coury and Delaporte 1954). Such anomalies include partial aplasia or agenesis of ribs, bridging between two adjacent ribs by synostosis or pseudoarticulation, bifid ribs, and supernumerary ribs. Unilateral or bilateral cervical ribs may arise from the seventh cervical vertebra and, similar to anomalies involving the first and second ribs, can sometimes cause a thoracic outlet syndrome by compression of the brachial plexus or the subclavian artery (Schroeder et al. 2012) (Fig. 2). Intrathoracic rib is a rare anomaly that can be seen on chest radiographs (Kamaruddin et al. 1995). Eleven pairs of ribs occur in isolation or as manifestation of various syndromes like trisomy 18, Down syndrome, and cleidocranial dysplasia (Lachman 2006).

*Anatomic variations of the anterior chest wall* are very common (Donnelly et al. 1999; Wong et al. 2004; Garcia-Peña and Barber 2010). Up to one-third of all children show asymmetry in the shape or size of the rib cartilage or in the position of the sternum. Usually, a palpable anterior chest wall bump is the cause for concern. The underlying anatomical cause may be a tilted sternum, or various anomalies of the rib cartilage such as a prominent anterior convexity, localized thickening, bifid cartilage, or a parachondral nodule. Even a mild degree of pectus excavatum or carinatum can produce a circumscribed protrusion that quite frequently prompts referrals for imaging studies. Of 27 children who underwent computed tomography (CT) or magnetic resonance imaging (MRI) for an asymptomatic,

palpable chest wall bump, all had either benign lesions or normal variants of bone or cartilage formation in the anterior chest wall (Donnelly et al. 1997). Ultrasound (US) is an alternative method that can easily show the underlying anatomic variant and rule out a malignant chest wall mass for anxious parents and referring physicians (Fig. 3).

## 2.2 Malformation and Deformity

Malformation of the chest wall may be a manifestation of a syndrome or *skeletal dysplasia* (Lachman 2006). Of particular interest are the neonatally lethal short rib-polydactyly syndromes, asphyxiating thoracic dystrophy (Jeune Syndrome), thanatophoric dysplasia, achondrogenesis, and other skeletal dysplasias in which maldevelopment of the thoracic cage produces a small and narrow chest due to short, and sometimes deformed ribs (Eich 2007; Glass et al. 2002). Respiratory distress at birth or even intrauterine death is directly related to the severity of the skeletal malformation.

A small thorax with *thin ribs* and small lungs can be a feature of neuromuscular disorders, particularly myasthenia gravis, myotonia, spinal muscular atrophy, and other myopathies. Thin ribs can be a feature of progeria and the trisomies 8, 13, and 18. Preterm infants show gracile ribs with posterior thinning. *Thick ribs* can be a manifestation of thalassemia (Cooley's anemia), mucopolysaccharidosis, and other disorders. Inferior *rib notching* is due to abnormalities of the intercostal neurovascular bundle, such as arterial or venous collaterals (e.g., coarctation of the aorta, superior vena cava syndrome), and to neurogenic tumors (e.g., neurofibromatosis).

*Rib aplasia or hypoplasia*, when isolated, is of little clinical significance. Multiple hypoplastic ribs with or without additional spinal segmentation defects cause

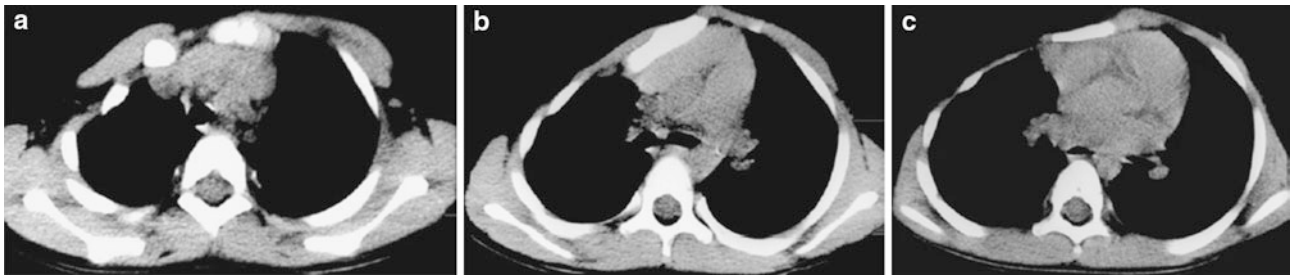


**Fig. 4** Poland syndrome in a 4-year-old boy. Unenhanced axial CT scans at three different levels (a–c) show hypoplasia of major and minor right pectoralis muscles and right hemithorax with asymmetry of rib cage and sternum



**Fig. 5** Congenital pseudoarthrosis of the right clavicle in a 2-year-old girl without history of previous trauma

asymmetric deformity of the chest. Hypoplasia or aplasia of the lung may also cause an asymmetric thoracic cage.

*Kyphoscoliosis* can be idiopathic or congenital (due to vertebral segmentation defects), or it may be a complication of a neuromuscular disorder. The chest shows crowding of ribs on the concave side of the curvature and assessment of the heart and lung and may become difficult. It is not uncommon to find a smaller lung volume and atelectasis on the convex side. CT with three-dimensional (3D) reconstruction may be helpful for delineating vertebral anomalies and chest wall morphology (Bush and Kalen 1999). MRI may be indicated for screening the spinal cord for abnormalities prior to scoliosis surgery, if there is suspicion of spinal cord pathology clinically or in early onset idiopathic scoliosis (Koç et al. 2012).

*Poland syndrome* is characterized by unilateral partial or complete absence of the pectoralis muscles, hypoplasia of subcutaneous or breast tissues, hypoplasia or absence of

ribs, and anomalies of the ipsilateral upper limb. On plain films the affected hemithorax appears hyperlucent. In the preoperative assessment of Poland syndrome, CT or MRI may help in defining the extent of the musculoskeletal and soft tissue anomalies and in showing the available muscles for reconstructive surgery (Wright et al. 1992; Cingel et al. 2013) (Fig. 4).

*Cleidocranial dysplasia*, an autosomal dominant inherited syndrome, is characterized by hypoplasia or absence of one or both clavicles resulting in hypermobile, drooping shoulders. Other features of the chest wall consist of small scapulae, deficient sternal ossification, posterior wedging of thoracic vertebrae, scoliosis, kyphosis, and short ribs with prominent downward slope. Leading features of cleidocranial dysplasia are brachycephaly, wide sutures, persistence of the anterior fontanelle, abnormal dentition, absent or delayed ossification of pubic bones, and wide pubic symphysis (Lachman 2006).

*Congenital pseudoarthrosis of the clavicle* is an isolated anomaly of the clavicle. This rare anomaly presents in infancy with a painless palpable mass. The clavicle shows a smoothly margined defect in the middle third, virtually always on the right side (Fig. 5). There is no history of a prior trauma. Pseudoarthrosis may be caused by the failure of two primary ossification centers to fuse (Cadilhac et al. 2000).

In *Sprengel deformity* the scapula fails to descend from its cervical origin and becomes fixed to the cervical spine by a fibrous band or an omovertebral bone. The scapula is high in position medially and rotated. Additional anomalies of ribs or vertebrae are frequently present (Klippel-Feil syndrome). CT with 3D reconstruction or MRI can be helpful in delineating the deformity and in planning corrective surgery (Cho et al. 2000; Dilli et al. 2011).

*Pectus excavatum*, also known as “funnel chest”, is the most common chest wall deformity. It is usually an isolated lesion that occurs sporadically or it may be inherited with an autosomal dominant trait. It can be associated with Turner syndrome, osteogenesis imperfecta, muscular dystrophy, or with connective tissue disorders like Marfan and Ehlers-

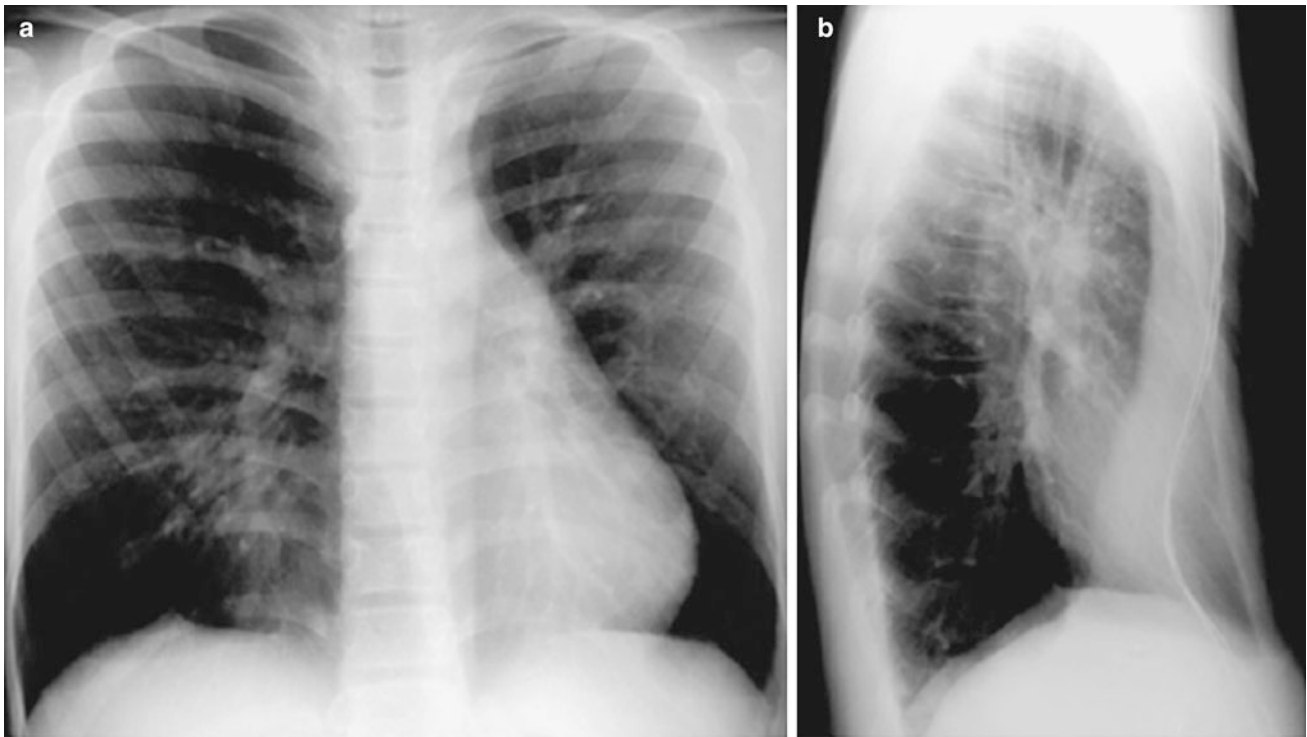


**Fig. 6** Pectus excavatum. Postero-anterior (a) and lateral (b) chest radiographs in a 14-year-old boy show steep course of elongated anterior ribs, cylindric shape of chest and displacement of heart to the

left due to reduced mid-sagittal diameter of chest. The outline of the sternum is enhanced with barium

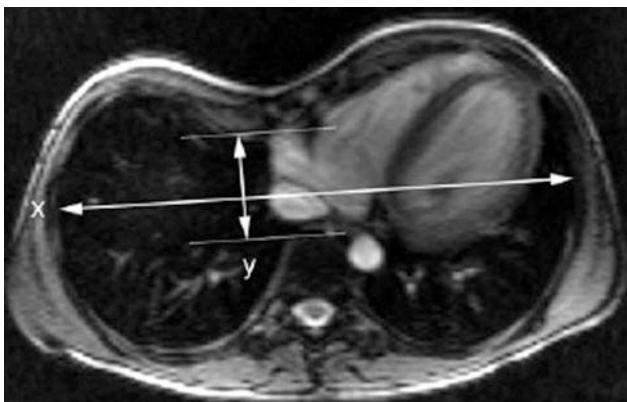


**Fig. 7** Axial steady-state free precession MR image of lower chest region in 11-year-old boy with pectus excavatum shows depression of the sternum and cartilaginous portion of a right rib, and leftward displacement but no compression of the heart. The Haller index is 5.1 and calculated as the maximal internal transverse diameter between rib cortices (x) divided by the minimal anterior-posterior diameter between the deepest point of the chest wall and the anterior cortex of the vertebra (y)



**Fig. 8** Cor pulmonale ("voussure cardiaque") in a 2.5-year-old boy. Axial contrast-enhanced CT scan through lower thoracic region shows (chronic) cardiac enlargement leading to increased sagittal diameter with additional left-sided protuberance of the chest. The child had primary pulmonary hypertension

Danlos syndromes. The lower portion of the sternum shows an inward curvature with a relative protrusion of the attached costal cartilages on each side. The sternum is usually rotated to the right. The characteristic radiographic

findings are easily recognized (Fig. 6). On the antero-posterior view of the chest radiograph, the anterior rib ends have a steep downward course, while the posterior ribs are more horizontally oriented. The heart is shifted to the left



**Fig. 9** Pectus carinatum in a 17-year-old girl. **a** Lateral chest radiograph shows protrusion of upper and mid portions of the sternum. **b** Three-dimensional surface rendered CT reconstruction demonstrates correlating severe sternum deformity

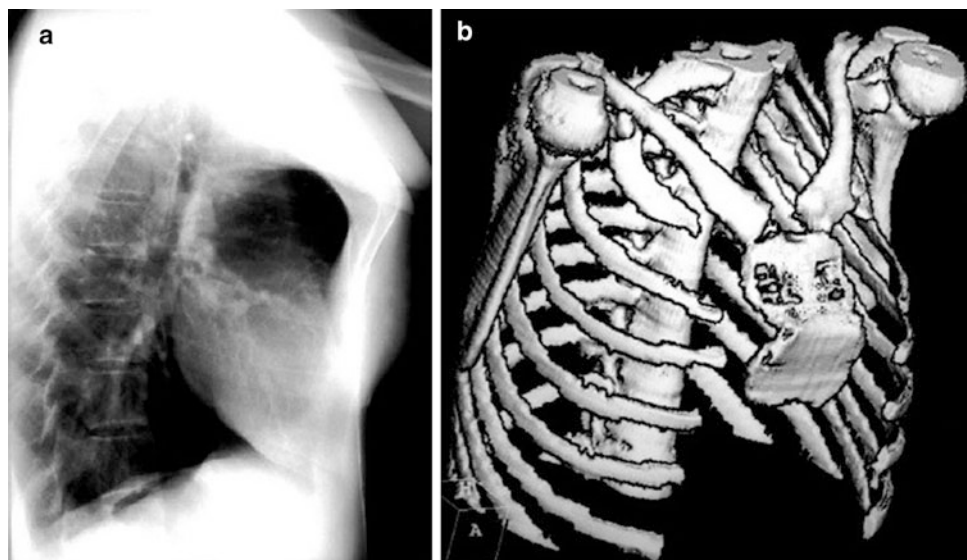
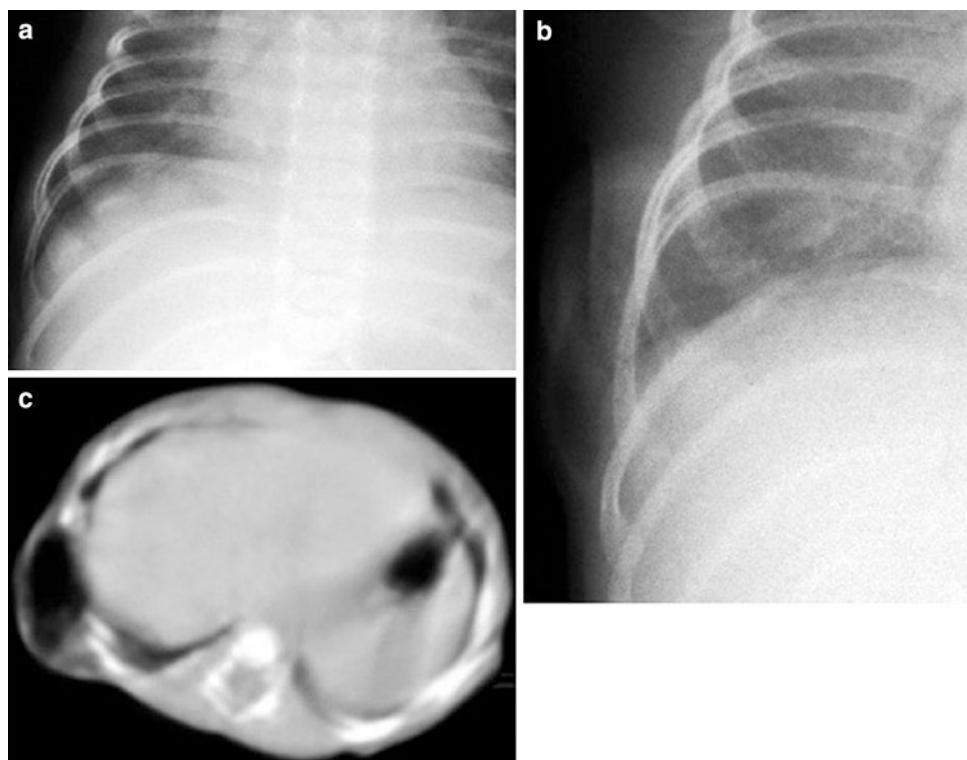


**Fig. 10** Lung herniation in a 4-week-old girl. **a** Chest radiograph at rest shows increased space between right ribs 9 and 10 and no lung prolapse. **b** On repeated chest radiograph while crying, lung herniates between the two ribs. **c** Axial CT while crying shows the herniated lung



and rotated. The right parasternal soft tissues produce a paracardial density and partially obscure the right heart border by a silhouetting effect. This should not be mistaken for middle lobe disease. On the lateral view, the chest is narrow and the degree of the sternal depression is easily seen. Cross-sectional imaging is useful to determine and quantify the severity of the deformity, to assess the degree

of cardiac shift or compression, to identify associated tracheobronchial compression, and to assess the results of surgery (Pretorius et al. 1998; Calloway et al. 2011). Thoracic dimensions in patients with pectus excavatum are quantified by the pectus- or Haller index, which is the ratio of the internal transverse diameter of the chest to the narrowest antero-posterior diameter that commonly is

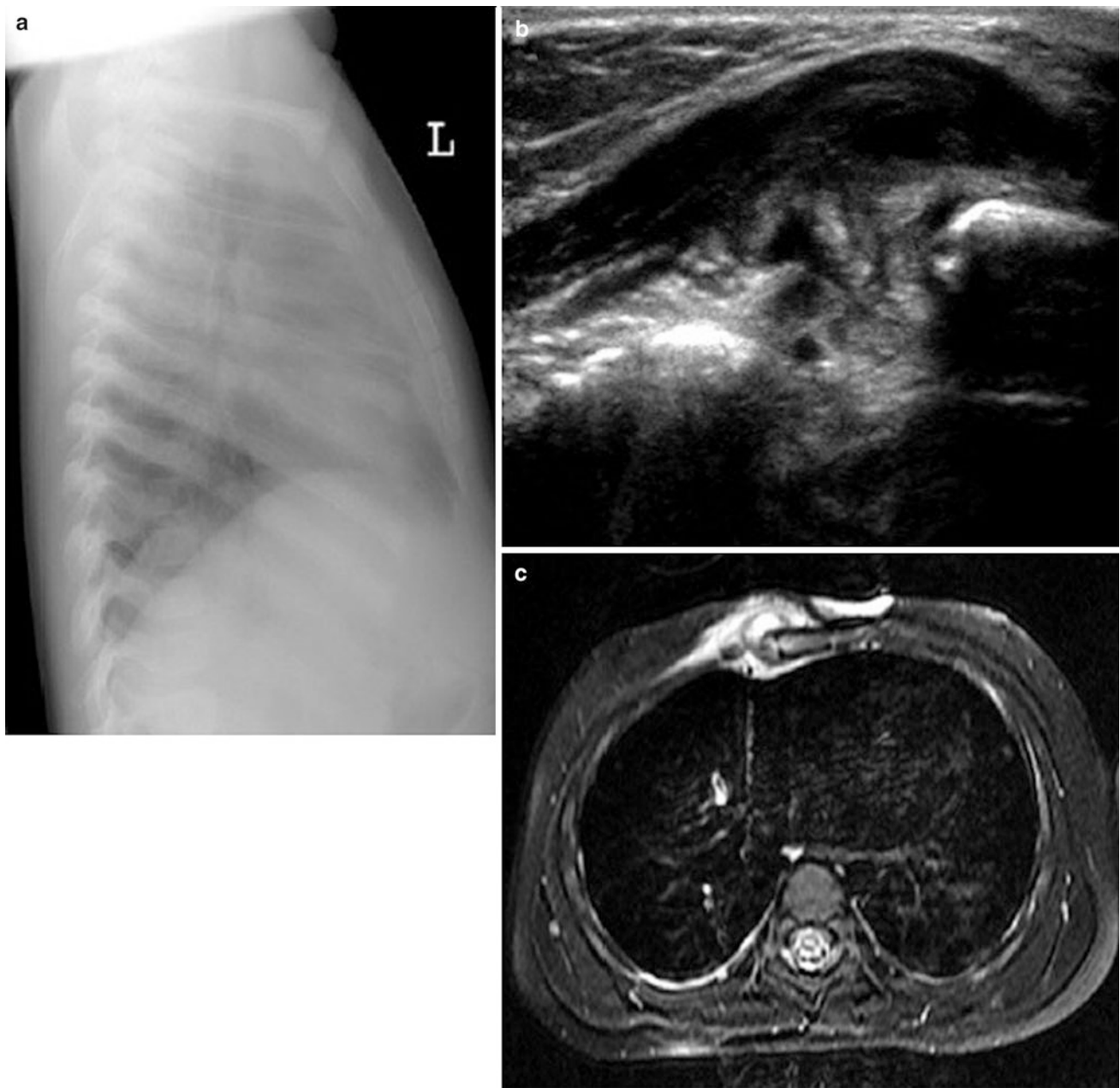


**Fig. 11** Osteomyelitis of the sternum of a 1.5-year-old boy. **a** Lateral chest radiograph shows soft tissue swelling around the lower part of the sternum. **b** Transverse US image confirms the swelling and hypoechoic fluid collections below the pectoralis muscle and in subperiosteal location at the sternum. **c** Axial fat-saturated T2-weighted

MR image shows swollen soft tissue with mildly increased signal around the sternum, a small soft tissue abscess with high signal, and increased bone marrow signal in the sternum, consistent with osteomyelitis

calculated from a single axial scan or a limited CT study (Haller et al. 1987; Chuang and Wan 1995). The same measurements can be obtained without ionizing radiation from an axial MR image (Marcovici et al. 2011; Birkemeier et al. 2011; Lo Piccolo et al. 2012) (Fig. 7). Besides morphologic assessment, MRI also allows dynamic assessment of the chest wall and diaphragm (Raichura et al. 2001; Herrmann et al. 2006).

Patients requiring surgical correction of pectus excavatum usually have a Haller index greater than 3.2, whereas in normal children the Haller index values range from 1.9 to 2.7 due to age-related and sex-related differences in chest wall configuration. The Haller index in normal children under 2 years of age is significantly lower than in older children, and girls between the ages of 0–6 and 12–18 years tend to have higher Haller index values than boys of the

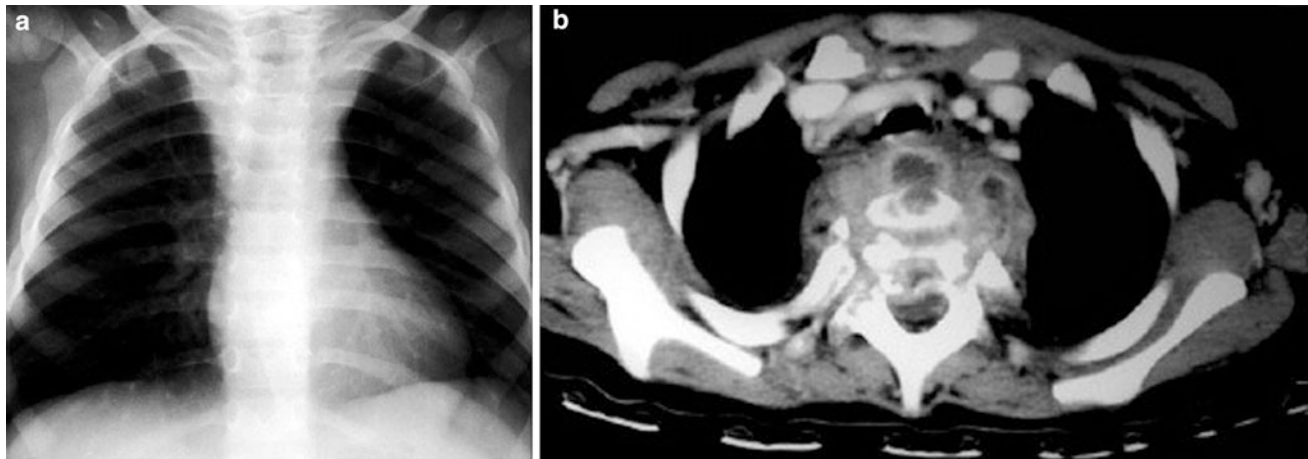


**Fig. 12** TBC abscess with vertebral osteomyelitis in a 2.5-year-old girl. **a** Chest radiograph shows unusual prominent shape of upper mediastinal region. **b** Contrast-enhanced axial CT scan through

upper chest area shows complex paraspinal inflammatory mass with multiple abscesses involving vertebra, spinal arch, and spinal canal

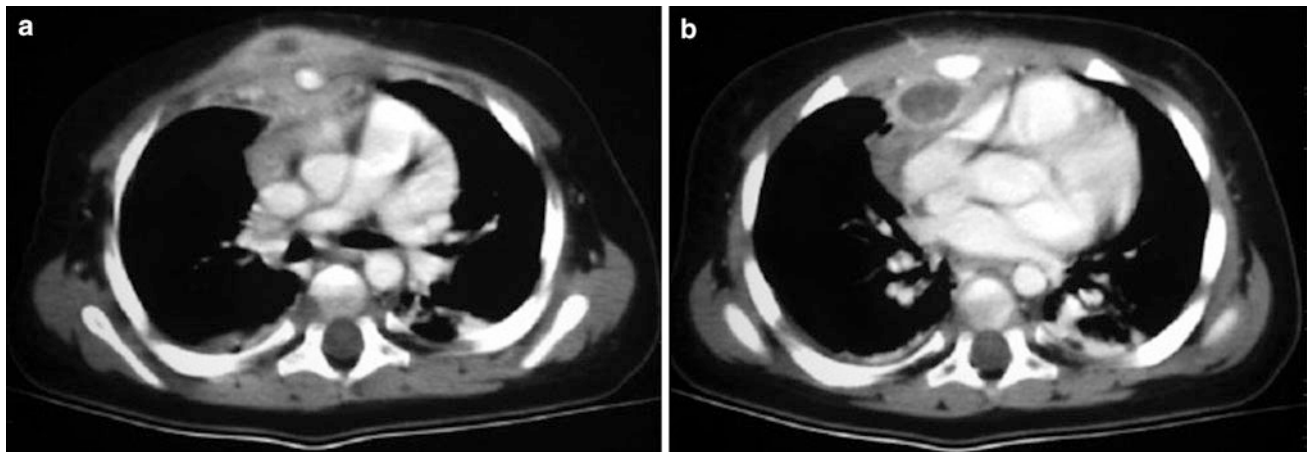


**Fig. 13** **a, b** Osteomyelitis of the sternum due to *Salmonella* sp. following gastroenteritis in a 1-year-old boy. Clinical examination showed presteral swelling. Axial contrast-enhanced CT images show subperiosteal fluid collections of the sternum as well as pre- and retrosternal abscesses

same age (Daunt et al. 2004). In rare cases, respiratory or cardiac symptoms may be present, but most patients with pectus excavatum are asymptomatic and surgical correction is performed for cosmetic reasons. Restrictive lung volumes may not alter following operation, but cardiorespiratory function can increase due to higher cardiac output (Haller and Loughlin 2000).

*Pectus carinatum* or “pigeon breast” is a congenital or acquired deformity that develops with growth and is frequently seen with congenital heart disease (voussure cardiaque) (Shamberger et al. 1988) (Fig. 8). Other causes include long-standing obstructive lung disease, Marfan syndrome, Ehlers-Danlos syndrome, Noonan syndrome, Morquio syndrome, or prune belly syndrome, among others. The deformity seems to be caused by growth disturbance of

both the sternum and costal cartilages with premature sternal fusion (Haje et al. 1999). The short sternum and costal cartilages protrude anteriorly with flattening of the chest laterally (Fig. 9). Most patients with a congenital pectus carinatum are asymptomatic. Surgery can correct the deformity.

Herniation of thoracic contents occurs when there is a defect in bony or soft tissue structures of the chest wall. *Cleft sternum* is a rare congenital lesion caused by partial or complete failure of sternal fusion at an early stage of embryonic development. Depending on the location and degree of the defect, herniation of thymus or the heart can be present (ectopia cordis) (Morales et al. 2000). Association with craniofacial hemangiomas and omphalocele are common associated anomalies (Fokin 2000). *Lung hernia* is



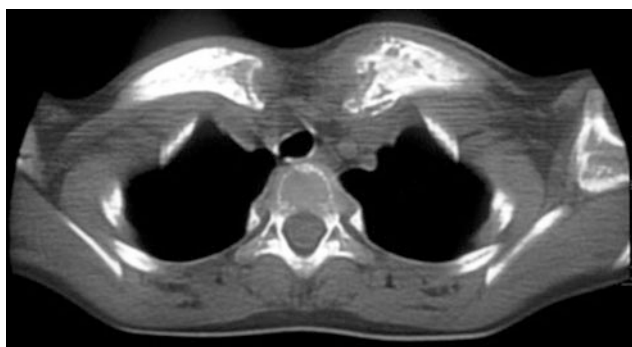


**Fig. 14** Friedrich's disease in a 9-year-old girl. Axial CT scan through upper chest inlet area shows symmetrical changes of clavicles at their medial aspects from chronic inflammatory process

**Table 1** Nosology of chest wall tumors (Shamberger and Grier 1994)

Benign lesions	Malignant lesions
Chondroma	Chondrosarcoma
Osteochondroma	Osteochondrosarcoma
Osteoma	Osteosarcoma
Fibroma	Fibrosarcoma
Lipoma	Mesenchymal sarcoma
Eosinophilic granuloma	Ewing's sarcoma (Askin's tumor)
Hemangioma	Rhabdomyosarcoma
Mesenchymal hamartoma	Leiomyosarcoma
Aneurysmal bone cyst	Lymphoma
Fibrous dysplasia	

a protrusion of pulmonary tissue through a defect of the chest wall. It may be cervical and intercostal in location. The more frequent intercostal hernia is mostly acquired following chest tube placement, surgery, trauma, chest wall neoplasm, or infection, but it can also be due to a congenital chest wall defect (Fig. 10). Cervical or apical hernia is associated with chronic obstructive lung disease in adults. In infants and children it arises spontaneously as a result of a congenital defect in the costovertebral fascia. The main symptom is an intermittent bulging in the supraclavicular or intercostal area that appears with crying, coughing, or straining. Chest radiographs or CT performed during inspiration may fail to show the lung herniation. Fluoroscopy during crying, coughing, or Valsalva maneuver is valuable in diagnosing lung hernias (Thompson 1976).

### 3 Infection

Primary infection of the chest wall is relatively rare in children, but it is potentially fatal since secondary sepsis or spread to the pleural spaces, the mediastinum (Fig. 11), or



**Fig. 15** Langerhans cell histiocytosis in a 14-month-old girl. Chest radiograph shows numerous osteolytic lesions involving almost all ribs, mainly anterior portions, but also scapulae, clavicles, humeri, as well as multiple skeletal parts not shown on this film

pericardium can occur. Chest wall infection originates from hematogenous spread of organisms with sepsis or bacteremia, or from direct extension from a wound after injury or surgery (sternotomy) to the chest. *Staphylococcus aureus* is the most prevalent organism in chest wall infections of patients from Europe or North America (Sharif et al. 1990). *Mycobacterium tuberculosis* (Fig. 12) may be more prevalent in other areas of the world (Wong et al. 2004). Other microorganisms (*Actinomyces*, *Blastomyces*, *Nocardia*, and *Aspergillus* species) and cat-scratch disease can occasionally cause chest wall infections (Golladay et al. 1985; Lew and Waldvogel 1997). Chest wall infections are especially common in immunocompromised patients (Thomas et al. 2003).

Clinical symptoms include fever, pain, and focal signs of inflammation such as edema, erythema, hyperthermia, and occasionally fistulous tracts. Infection can involve the soft tissues and/or bone and cause abscess formation, cellulitis and/or granulation tissue formation. Depending on the structure preferentially affected it is called pyomyositis when muscles are involved, (necrotizing) fasciitis when only subcutaneous fat and fascia are affected, osteomyelitis when there is bone involvement, and pyogenic arthritis where there is joint involvement.

Clinical recognition of a chest wall infection can be difficult, particularly when it is located in the intermediate or deep layers of the chest wall (Garcia-Peña and Barber 2010). The underlying process is often underestimated by physical examination alone. A suspected (or unsuspected)

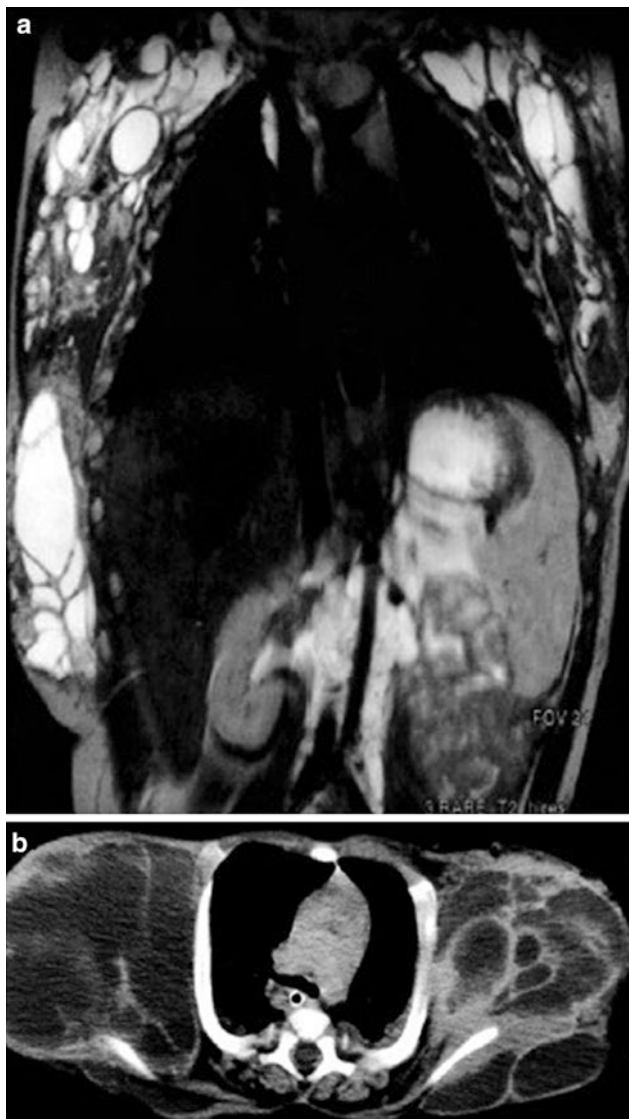


**Fig. 16** Multifocal lymphangioma in a 3-month-old boy. **a** Coronal T2-weighted fat-saturated MRI view of posterior thorax and abdomen demonstrates extensive bilateral involvement of the chest wall and right abdominal wall by complex lymphangioma, as well as involvement of the retroperitoneum with encasement of lower abdominal portions of the inferior vena cava and aorta and extending into the left renal fossa posteriorly. **b** Axial CT view through the chest at carina level shows grotesque expansion of the chest wall by septated lymphangioma

infection of the chest wall is usually first imaged with chest radiographs, which may show a mass lesion within the chest wall or the extrapleural space. Additional signs that may also be present include rib destruction and/or sclerosis, pulmonary infiltrate, pleural effusion, and calcifications, air, or gas within the soft tissues. US, CT, and MRI help to confirm the presence, location, and extent of the single or multiple infectious foci (Figs. 11, 12 and 13). Positron emission tomography (PET) is a very sensitive tool for

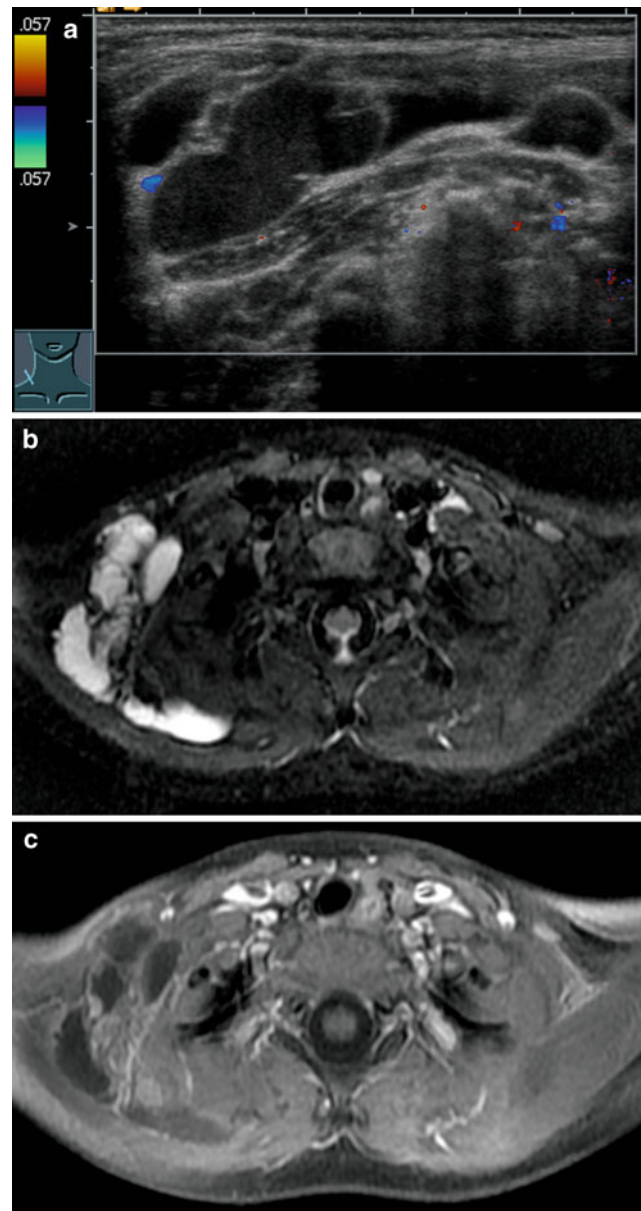


**Fig. 17** Supraclavicular lymphangioma in a 3-year-old boy. **a** Color Doppler US image shows a multicystic mass with slightly echogenic contents indicating hemorrhage or infection. Fat-saturated T2-weighted MR image (**b**) confirms multiple hyperintense cysts of varying sizes, with mild enhancement only of the cyst walls on a contrast-enhanced fat-saturated T1-weighted MR image (**c**)

detecting clinically silent foci of infection in immunocompromised patients. US, CT, and MRI show fluid collections and rib destruction, and can guide percutaneous aspiration or drainage. US is usually sufficient for diagnosing small, superficial and well-delineated lesions, while CT or MRI are the techniques of choice for imaging large, complex, and deep-seated lesions for which surgery is considered. Intraspinal epidural extension may only be visible with CT or MRI (Fig. 12).

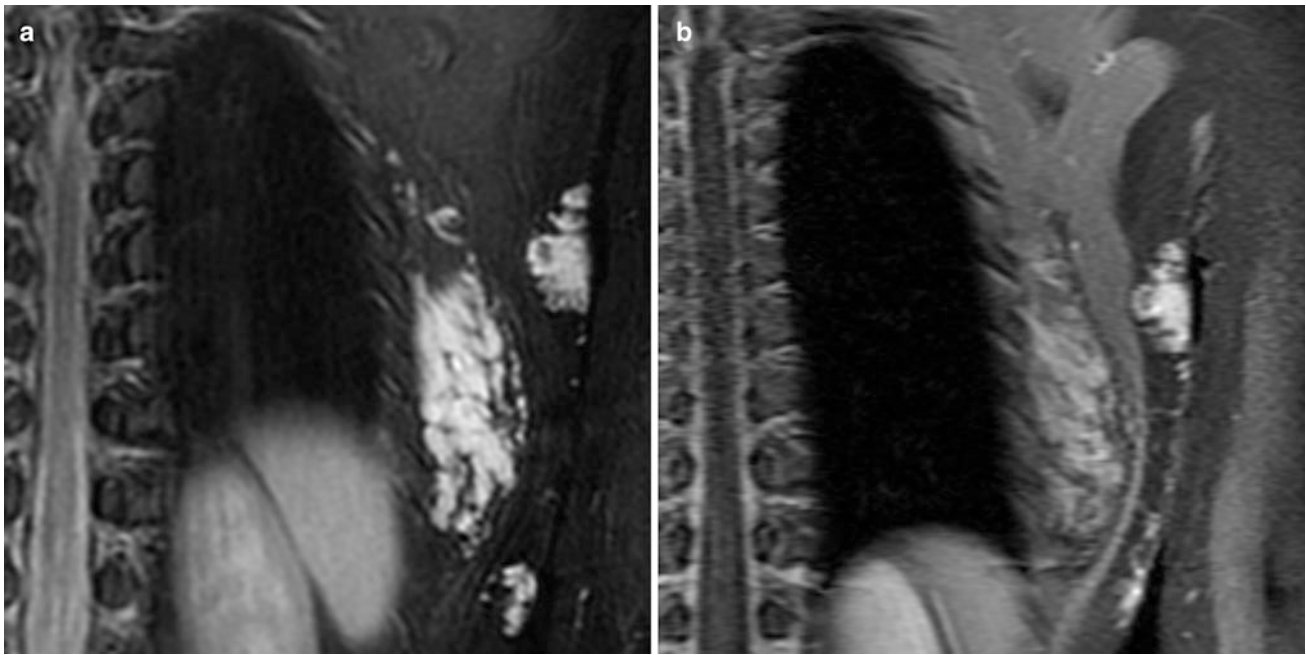


**Fig. 18** Multifocal venous malformation involving subcutaneous and deep soft tissues in a 9-year-old boy. **a** Coronal fat-saturated T2-weighted MR image shows multiple small hyperintense vascular

spaces, some containing hypointense phlebolites. **b** Contrast-enhanced fat-saturated T1-weighted MR image shows varying degrees of enhancement within the lesion

An abscess appears as a sonolucent area on US with increased through transmission and absence of blood flow centrally. Echogenic swirling material within the abscess may occasionally be seen. Contrast-enhanced CT shows an iso- or hypodense, nonenhancing center, and an enhancing rim (Figs. 11, 12, and 13) (Faro et al. 1993), similar to that seen on T1-weighted MRI sequences. T2-weighted and short tau inversion recovery (STIR) sequences show a high signal intensity collection. A moderate increase in signal intensity on T2-weighted sequences may be present in mycotic infection (Sharif et al. 1990). MRI is very sensitive for detecting osteomyelitis and is often more accurate than bone scans for differentiating between soft tissue inflammation and acute osteomyelitis. Chronic osteomyelitis is recognized on radiographs and CT as an area of destruction and reparative sclerosis within and around the affected part of bone. Inflammation of the surrounding soft tissues (cellulitis) appears as thickening in all modalities. In addition to this, US shows increased soft tissue echogenicity and vascularization, while CT and MRI show contrast enhancement. Soft tissue inflammation is best delineated by MRI with fat-suppressed T2-weighted or STIR sequences, or T1-weighted sequences following administration of contrast material, which provide better differentiation from the unaffected subcutaneous fat. In our experience, septic arthritis of the sternoclavicular joint is usually associated with osteomyelitis of the adjacent clavicle or sternum. CT and MRI show the joint effusion and

osteolytic changes of the affected bone more readily than US and they can confirm or exclude posterior extension of the process into the mediastinum (Figs. 11 and 13).

Tuberculous spondylitis is relatively rare in developed countries, but it is the commonest vertebral infection in other parts of the world. The spinal infection mostly stems from primary pulmonary tuberculosis. One or several segments of the spine may be involved, particularly in the thoracic and lumbar region. Usually, the infection is limited to the body of the vertebra, which may become destroyed along with the contiguous intervertebral disk and an adjacent or distant vertebra. Paraspinal abscesses, usually bilateral, are the rule. Calcification within a paraspinal abscess can occur in long-standing cases (Kuhn 2003). Vertebral collapse can lead to kyphosis and/or scoliosis and even to cord compression. The radiographic changes of tuberculous spondylitis are nonspecific, but an indolent presentation is suggestive of tuberculosis. CT and MRI can show the epidural extension of the process and delineate the topography of an abscess (Fig. 12).

Friedrich's disease is a disorder of unknown origin thought to be an aseptic necrosis with clinical and radiologic features that can mimic infection at the sternoclavicular joint (Levy et al. 1981). The lesion is usually unilateral but may be bilateral. Tender swelling at the sternoclavicular region is the typical presenting symptom. The erythrocyte sedimentation rate may be elevated. Radiographs show destruction and repair at the



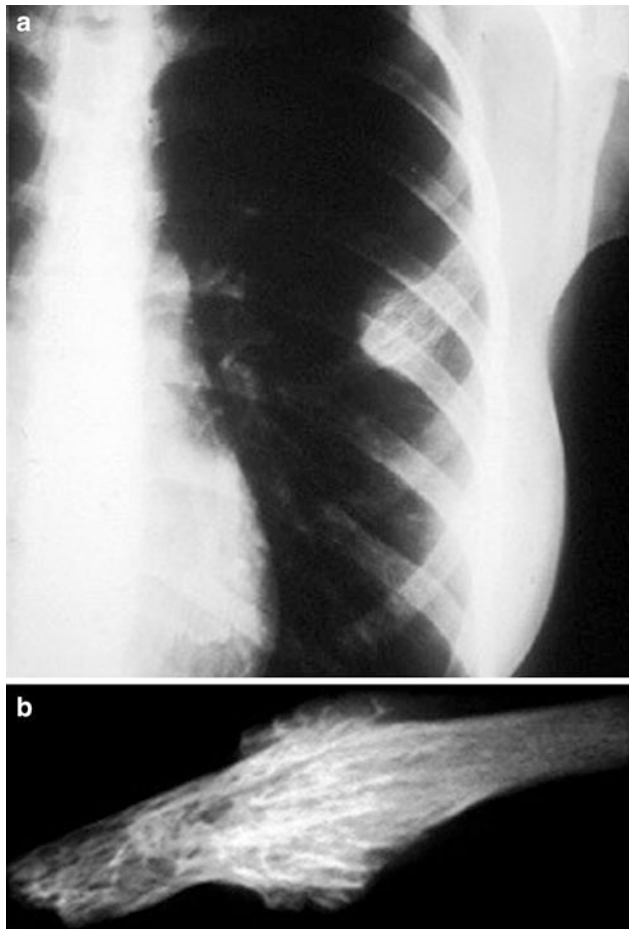


**Fig. 19** Rib hemangioma in a 10-year-old girl. Radiograph of left hemithorax **a** and radiograph of the resected rib specimen **b** show enlarged and sclerotic anterior portion of eighth rib with a radiating lattice-like pattern

**Fig. 20** Gorham disease in a 2.5-year-old girl. Left posterior oblique chest radiograph demonstrating multiple osteolytic and expansive rib lesions and pleural effusion. Several affected dorsal vertebral bodies show a loss of height

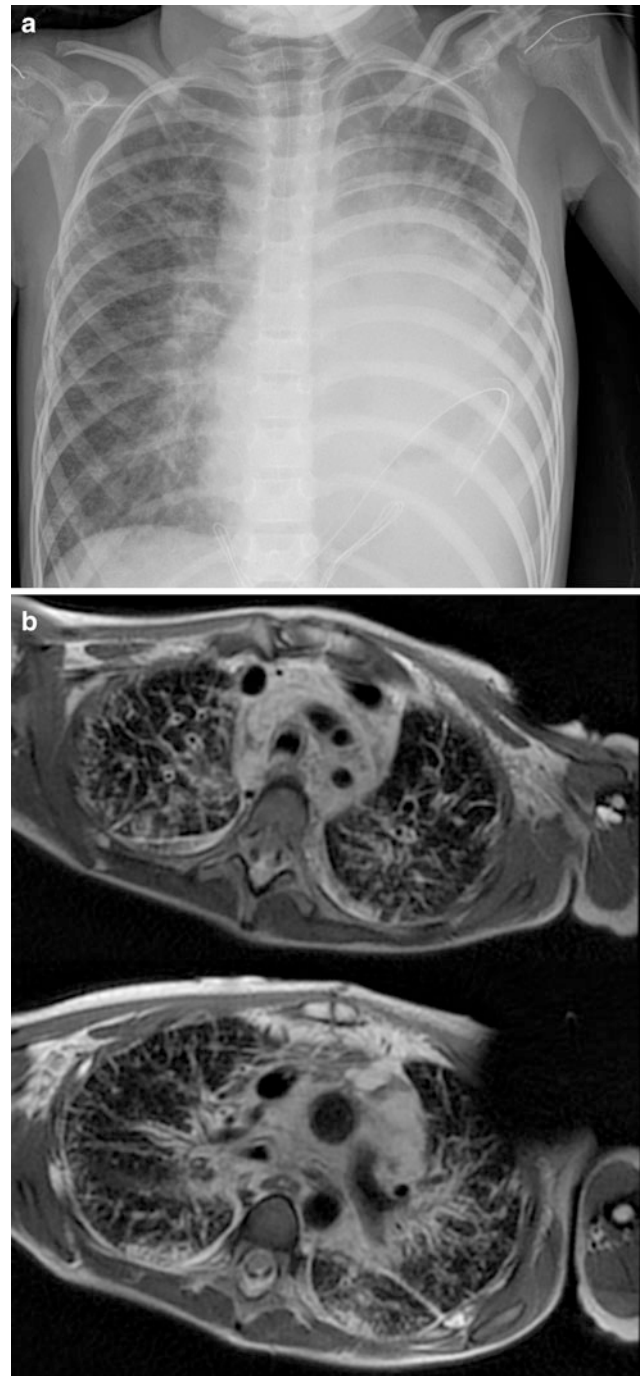


**Fig. 21** Multifocal lymphangiomatosis involving chest wall, mediastinum and lung in a 5-year-old girl that presented with pericardial tamponade. **a** Chest radiograph following pericardial drainage shows multiple slightly expansile well-marginated osteolytic lesions in ribs and left humerus. **b** On axial T2-weighted MR images the bony lesions contain hyperintense fluid that did not enhance (not shown). The mediastinum is diffusely infiltrated by hyperintense not enhancing tissue, the central and peripheral interstitial lung tissues are thickened

medial end of a clavicle (Fig. 14). Histology discloses necrosis of the clavicular epiphyseal region without evidence of infection. Aspiration cultures are negative. The

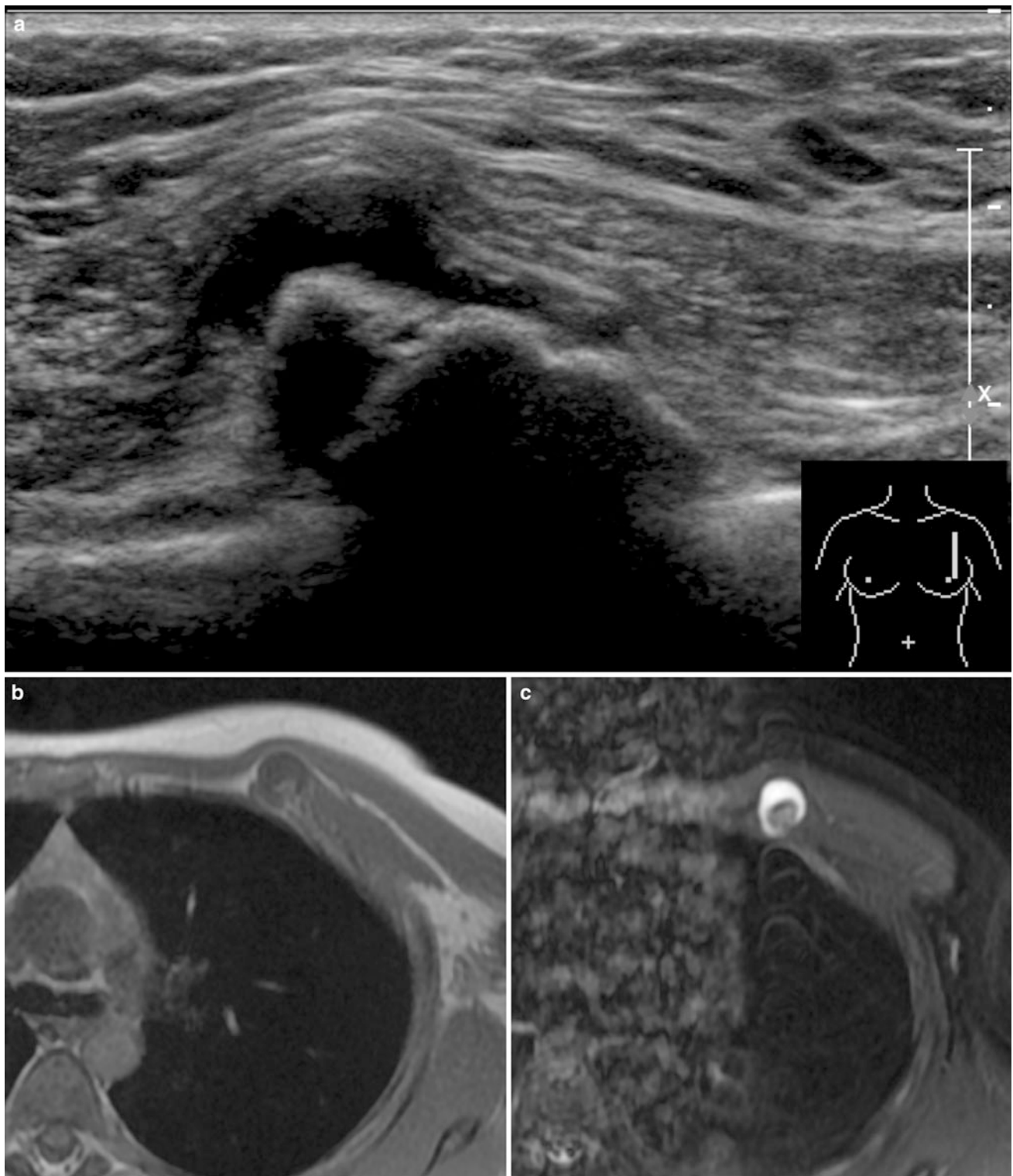


**Fig. 22** Osteochondroma at the costochondral junction in a 14-year-old boy. **a** US image shows a bony protuberance covered by a hypoechoic cartilaginous cap. The cartilaginous cap is hypointense on T1-weighted MR image (**b**) and of high signal intensity on STIR MR image (**c**)

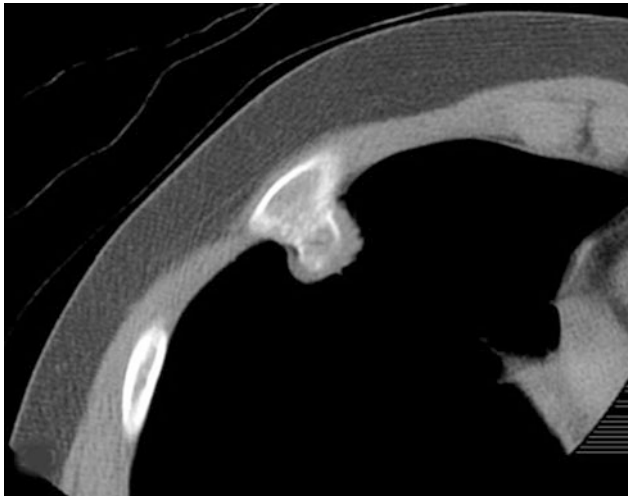


**Fig. 23** Osteochondroma in a school-aged child. Close up section of axial chest CT scan shows ossified chondroma coming off the rib toward the chest inside

symptoms usually subside spontaneously without treatment over several months. Radiological features improve very slowly. Our experience has shown that it may take up to 18 months for the clavicles to become radiologically normal.

There are some similarities between Friedrich's disease and SAPHO syndrome, a disorder characterized by a variable combination of synovitis, acne, pustulosis, hyperostosis, and osteitis. The different aseptic skin abnormalities are associated with chronic recurrent multifocal osteomyelitis (CRMO), a rare, occasionally symmetrical, nonpurulent inflammation of bone. Although it can involve other bones, the inflammation has a predilection for the anterior chest wall where it can cause tenderness, and swelling. Radiographic abnormalities include sclerosis and periostitis with expansion of the affected bone (Letts et al. 1999).

#### 4 Tumors

Imaging is performed to detect a chest wall mass and to determine its location, size, and character (Garcia-Peña and Barber 2010). When a mass that originates in the chest wall expands into the chest cavity, it forms an obtuse angle with the adjacent chest wall. This feature might be recognized on radiographs, CT, or MRI. Masses that produce rib changes are likely to be extrapleural in location. Conventional radiographs are the first tools for imaging a chest wall mass in most places. Radiographs allow an approximate appreciation of the location of the lesion, its extension, rib destruction, and associated intrathoracic component, pleural effusion, or pulmonary metastases. Further imaging may be

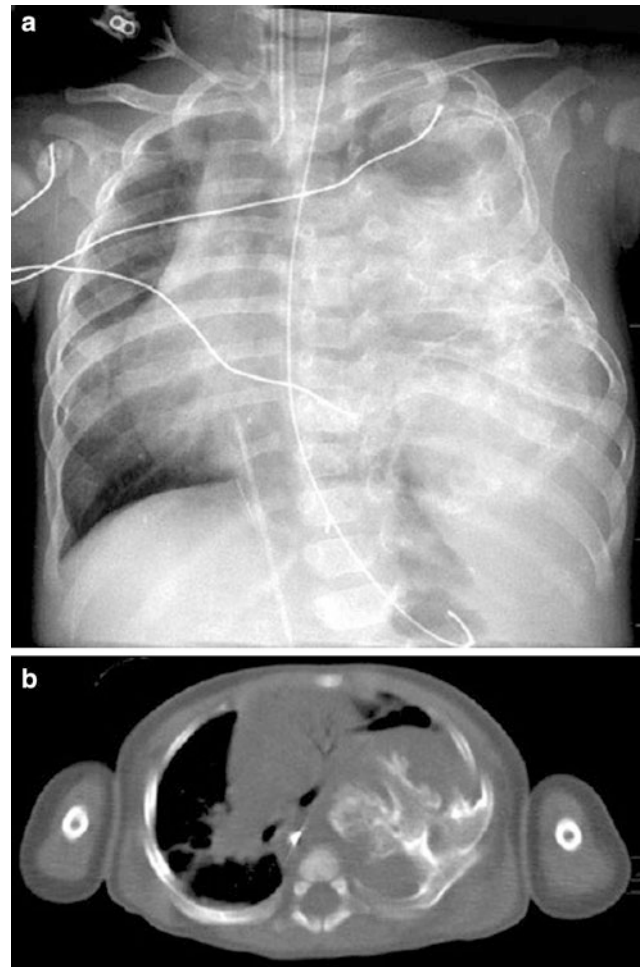


**Fig. 24** On prenatal US, this baby was found to have an intrathoracic mass, confirmed on fetal MRI. At birth he had respiratory distress. Chest radiograph (a) and CT (b) showed marked, complex alterations of the left hemithorax due to bulky expansion of ribs and associated soft tissue changes, confirming the diagnosis of a mesenchymal hamartoma. At the age of 6 months, he was doing well

required in large or aggressive looking lesions for staging purposes. Both CT and MRI are able to delineate the mass, demonstrate osseous changes, and define the margin and internal structure of the lesion, lymphatic spread, and pleural effusion. Currently, CT is better suited than MRI to show metastases to the lungs. Obviously, when faced with a possibly malignant chest wall mass, an interdisciplinary approach should be used, and the choice of the imaging modality may vary with the availability of, and expertise in using, the local imaging tools.

The chest wall can give rise to a wide variety of benign and malignant tumors that are primarily mesenchymal in origin (Laor 2004), in keeping with the predominant tissue components of the chest wall. Tumors of the chest wall are relatively infrequent during infancy and childhood, but a high proportion is malignant (Kumar et al. 1977; Shamberger et al. 1989; Shamberger and Grier 1994). The tumors often present



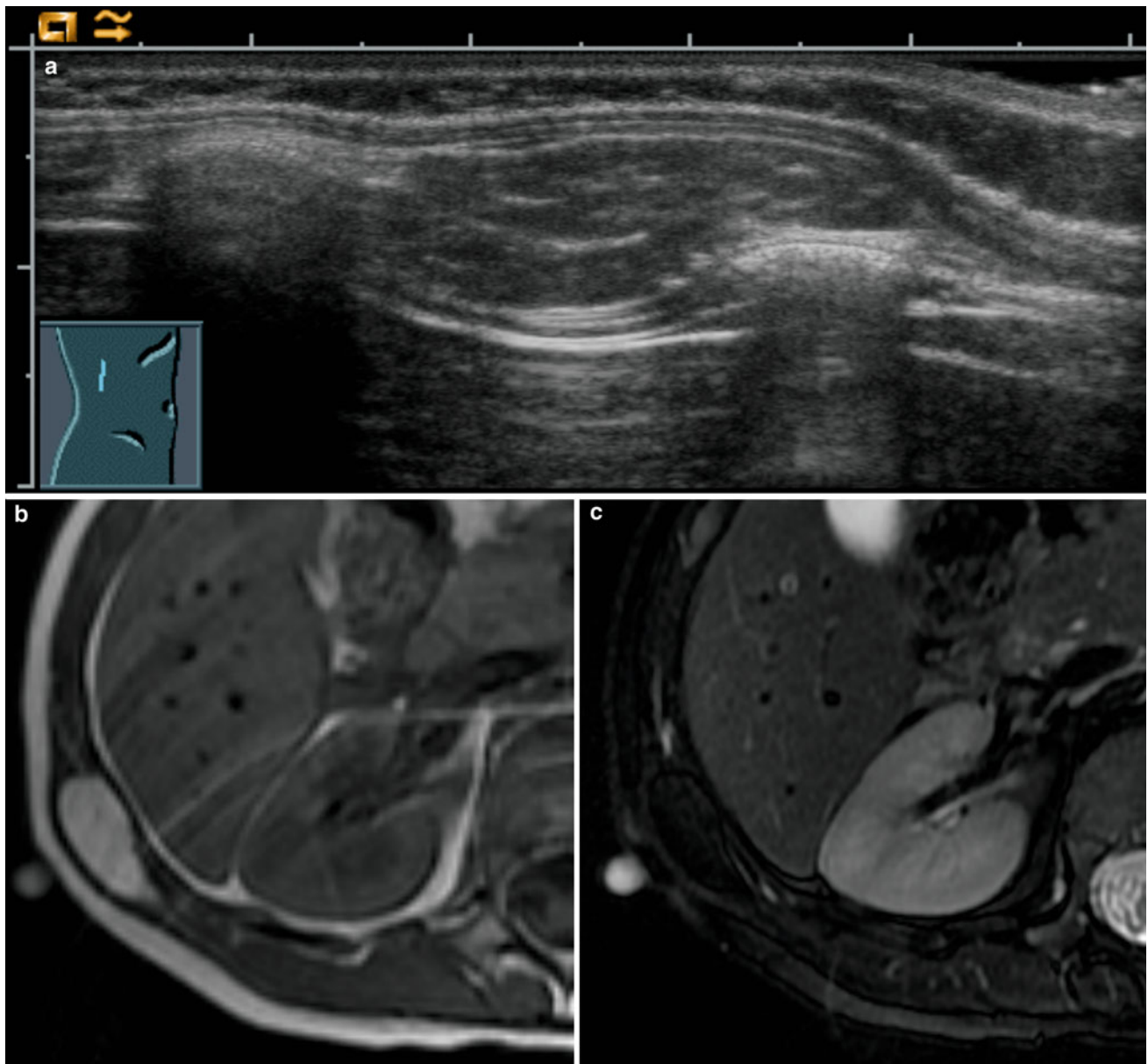


**Fig. 25** Intramuscular lipoma in a 3-year-old boy. **a** Longitudinal US image shows a well-defined mass with similar echogenicity and structure compared to subcutaneous fatty tissue, extending between two adjacent ribs and expanding the intercostal musculature. On MRI,

the lipoma shows isointense signal compared to fatty tissue on T1-weighted (**b**) and fat-saturated T2-weighted (**c**) images. The soft palpable bump is marked with a vitamin D capsule

as a palpable mass, or, less frequently, with pain, cough, or respiratory distress from a large pleural effusion or an extensive intrathoracic component. Secondary involvement of the chest wall from an intrathoracic mass is rare in childhood (Table 1).

The tumor may be located within the bones and/or within the soft tissues of the chest wall. A sharply margined osteolytic lesion usually signifies a slow growing (benign) process; however, differentiation from a malignant lesion is not always possible, and biopsy may be required

(Kozlowski et al. 1989). Multifocal Langerhans cell histiocytosis (eosinophilic granuloma) with typical osteolytic lesions of the skull vault or vertebra plana allow a confident clinical diagnosis (Fig. 15).

Vascular lesions like hemangioma and vascular malformations are amongst the most common soft tissue tumors of childhood that may be found in the chest wall. They are most prevalent in neonates, infants, and young children. According to the Mulliken and Glowacki classification (Mulliken and Glowacki 1982), hemangiomas are benign

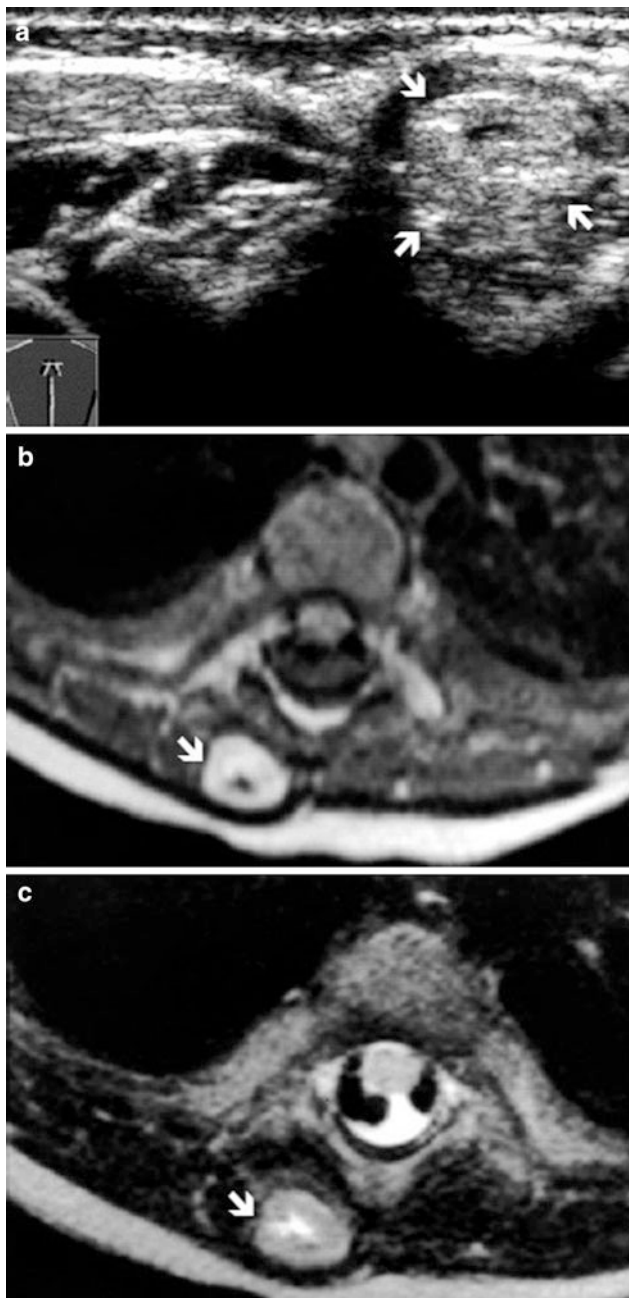


**Fig. 26** Lipoblastoma in a 5-month-old girl. **a** Transverse ultrasound (US) view of upper back region (prone position) shows right paramedian round and mostly hyperechoic structure (*arrows*) with small hypoechoic inner portion. **b, c** Axial T1- and T2-weighted MRI scans show well-defined fatty tumor (*arrows*) correlating with US findings)

proliferating tumors of blood vessels. Infantile hemangiomas typically appear in the first weeks of life, increase rapidly in size during the first year, and subsequently regress gradually until they may disappear completely in early childhood. When located beneath the skin, hemangiomas may exhibit the typical strawberry red color. On US

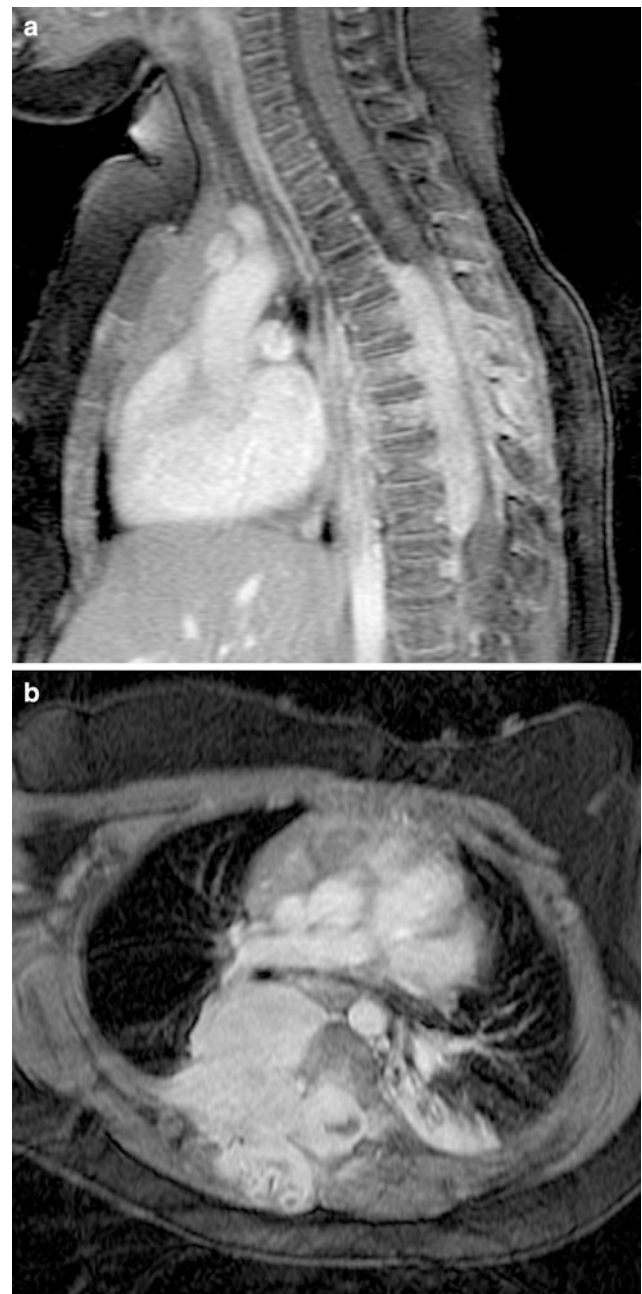


**Fig. 27** Aggressive infantile fibromatosis in a 9-month-old girl. Sagittal (**a**) and axial (**b**) contrast-enhanced fat-saturated T1-weighted MR images show a vividly enhancing paravertebral mass infiltrating erector spinae muscles and vertebrae of the lower thoracic spine, and invading the spinal canal with encasement of the spinal cord

or MRI, hemangiomas are characterized as nonspecific, circumscribed and well-vascularized soft tissue mass with prominent feeding vessels. Vascular malformations are nonneoplastic lesions present at birth and classified based on their vascular composition and amount of blood flow. High-flow malformations include arterial or arterio-venous lesions which can be treated by transcatheter embolization.

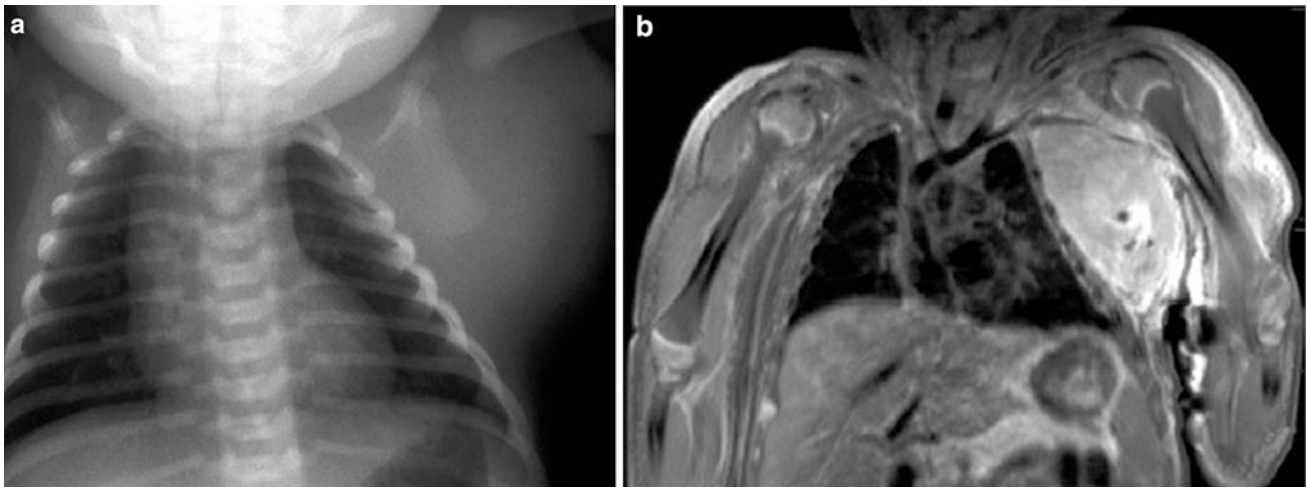
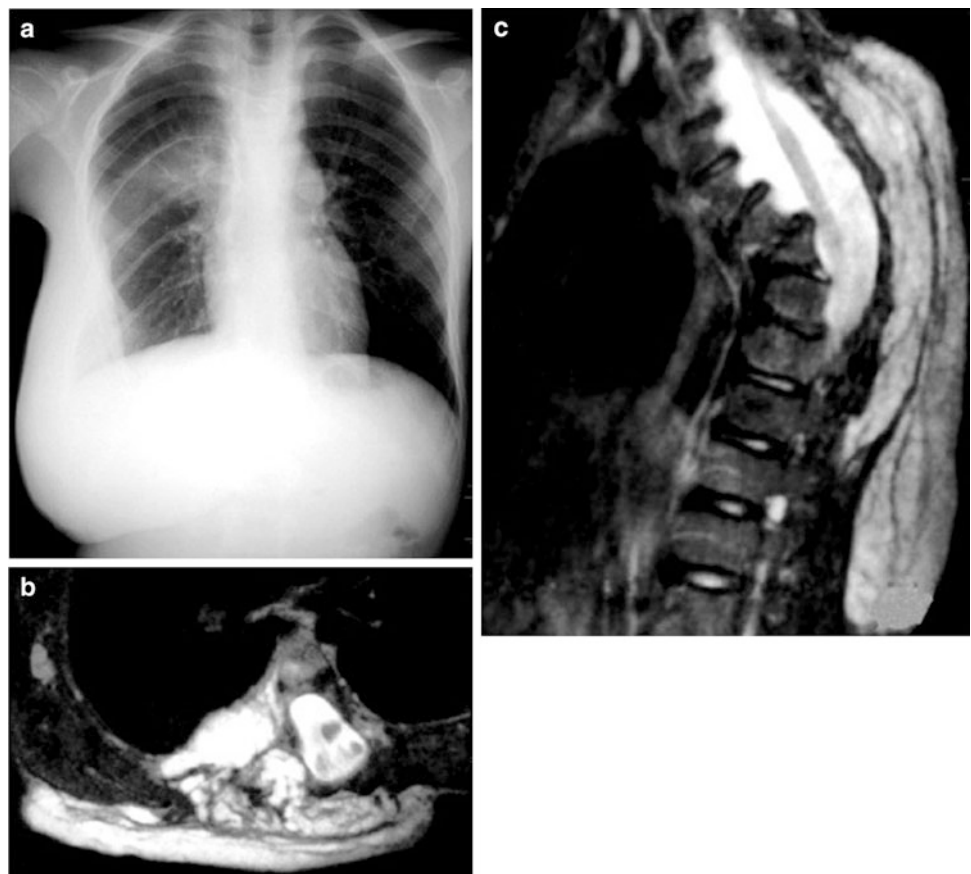


**Fig. 28** Congenital fibrosarcoma in a 3-day-old boy. **a** Chest X-ray shows large left extrathoracic soft tissue mass with severe displacement of ipsilateral scapula and deforming left hemithorax. **b** Coronal

T1-weighted contrast-enhanced MRI view of the thorax with suboptimal fat-saturation demonstrates diffusely enhancing extrathoracic soft tissue mass impinging left lateral chest wall

**Fig. 29** Plexiform neurofibroma (NF1) in an 11-year-old boy.

**a** Chest radiograph demonstrates complex abnormality of right hemithorax with large extrathoracic soft tissue mass invading the pleural space, multiple dysplastic rib changes of varying degree, circumscribed density adjacent to the mediastinum and S-shaped scoliosis. **b** Axial T2-weighted fat-saturated MRI view through the chest at mid-level shows multifocal and complex extra- and intrathoracic portions of neurofibroma with high fat content. Involvement of severely distended spinal canal. **c** Same technique as in **b**; upper mid-sagittal view of the spine shows vertically extended neurofibroma within the soft tissues of upper back region; expansion of upper spinal canal due to dural ectasia with severe hyperkyphosis with local vertebral wedge deformity, also caused by the underlying disease





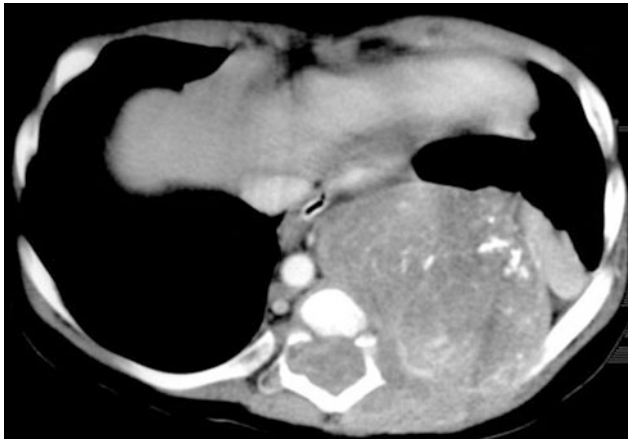


**Fig. 30** Thoraco-abdominal neuroblastoma in a 5-month-old boy. Contrast-enhanced axial CT scan through lower chest area shows huge solid posterior mediastinal mass containing calcifications and extending extrathoracically through posterior chest wall as well as intraspinally. Notice expansive deformity of spinal canal due to long-standing neoplastic process. The child had neurological impairment that persisted after therapy

Low-flow lesions include lymphatic, capillary, venous, or mixed malformations. Lymphatic malformations (Lymphangiomas) are space-occupying, nonneoplastic lesions predominantly composed of lymphatic vessels, and are also called cystic hygromas when dilated lymphatic vessels lead to the formation of large cysts. Lymphangiomas are usually apparent at birth and found in the neck and chest wall. Extension into the mediastinum and axilla can occur (Fig. 16). The growth of lymphangiomas is usually self-limited, but bleeding into the cysts or infection may lead to a sudden increase in size. Venous and capillary malformations have previously also been called cavernous or capillary hemangioma on histopathologic grounds, leading to some confusion in the nomenclature of vascular lesions. As both lymphatic and venous malformations present as mass lesions consisting of multiple fluid-filled spaces, differentiation may only be possible by intravenous contrast administration on CT or MRI. Lymphangiomas will only show contrast enhancement in the walls and septations of macrocysts, or will show diffusely in areas with microcysts (Fig. 17). Venous malformations may contain phlebolites and typically show slow and incomplete enhancement of the vascular spaces on dynamic contrast-enhanced MRI (Fig. 18).

Both lymphangiomas and venous malformations can be multifocal. They can become large and disfiguring or compress blood vessels, the trachea and/or other vital structures (Gorham and Stout 1955; Stout and Lattes 1967). Imaging may be required for staging purposes before surgery or radiologic intervention. Solitary lymphangiomas of bone are rare; radiographically, they are usually single or multiloculated osteolytic lesions. Hemangioma of bone,

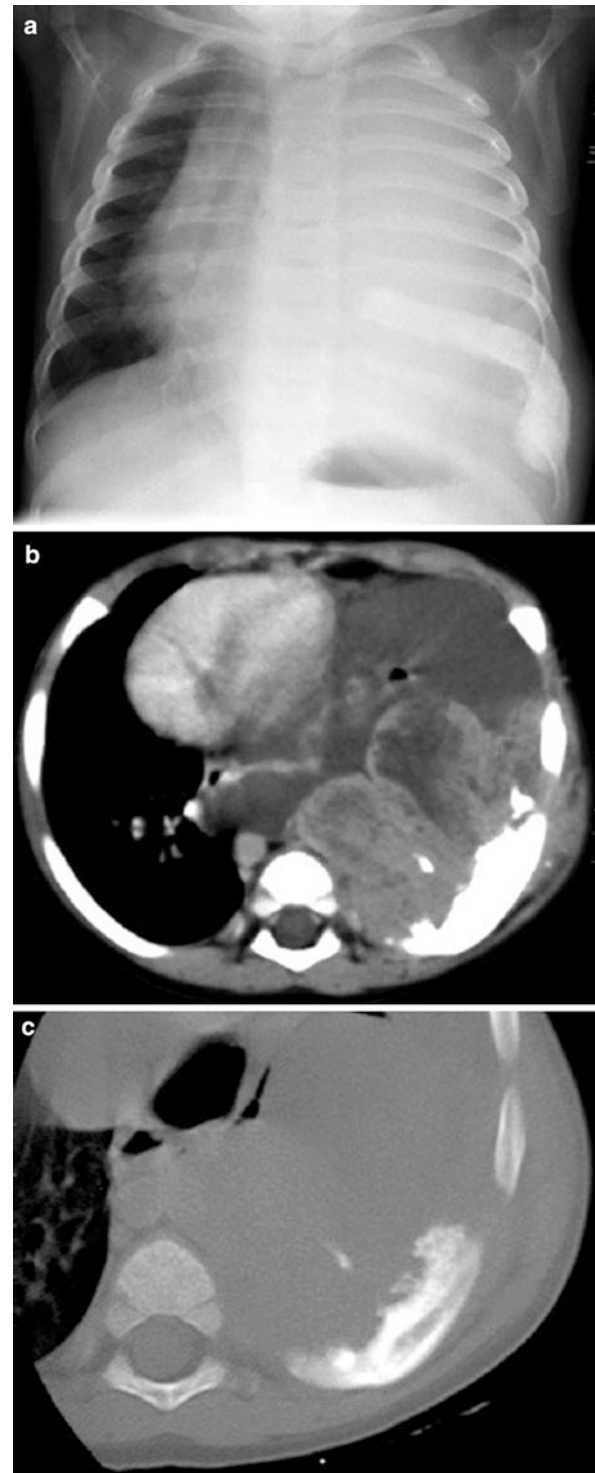


**Fig. 31** Primitive neuroectodermal tumor (PNET) in a 14-month-old boy. **a** Antero-posterior chest radiograph shows mass effect within left hemithorax with displacement of heart and mediastinal structures to the right. Diffusely sclerotic and enlarged eighth left rib. **b** Axial contrast-enhanced CT scan at mid-level of thorax demonstrates irregularly hypertrophic posterior aspect of eighth left rib associated with a huge intrathoracic soft tissue mass. **c** Closeup bone view shows osseous changes in more detail

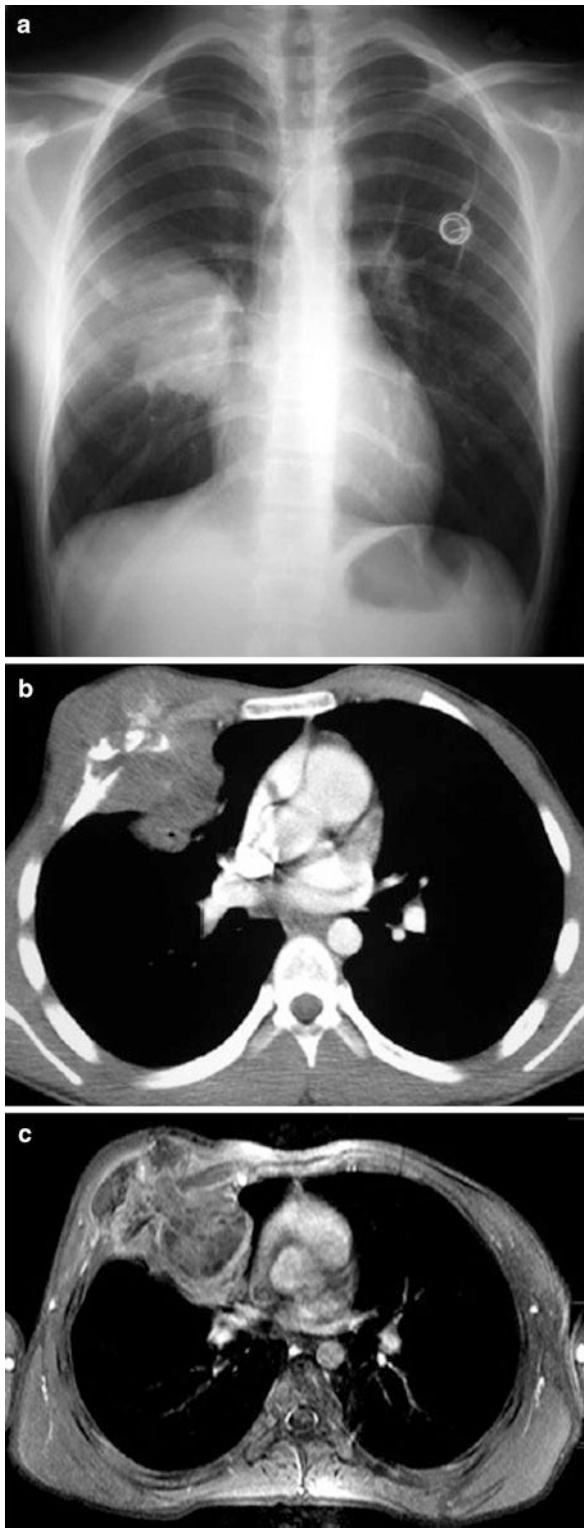


**Fig. 32** A 16-year-old boy with osteosarcoma of third rib on the right. **a** Frontal chest radiograph following insertion of a port-a-cath. **b** Contrast-enhanced axial CT image. **c** Contrast-enhanced fat-saturated T1-weighted axial MR image showing focal destruction of the anterior portion of the rib with an intra- and extrathoracic soft tissue mass with partial calcification



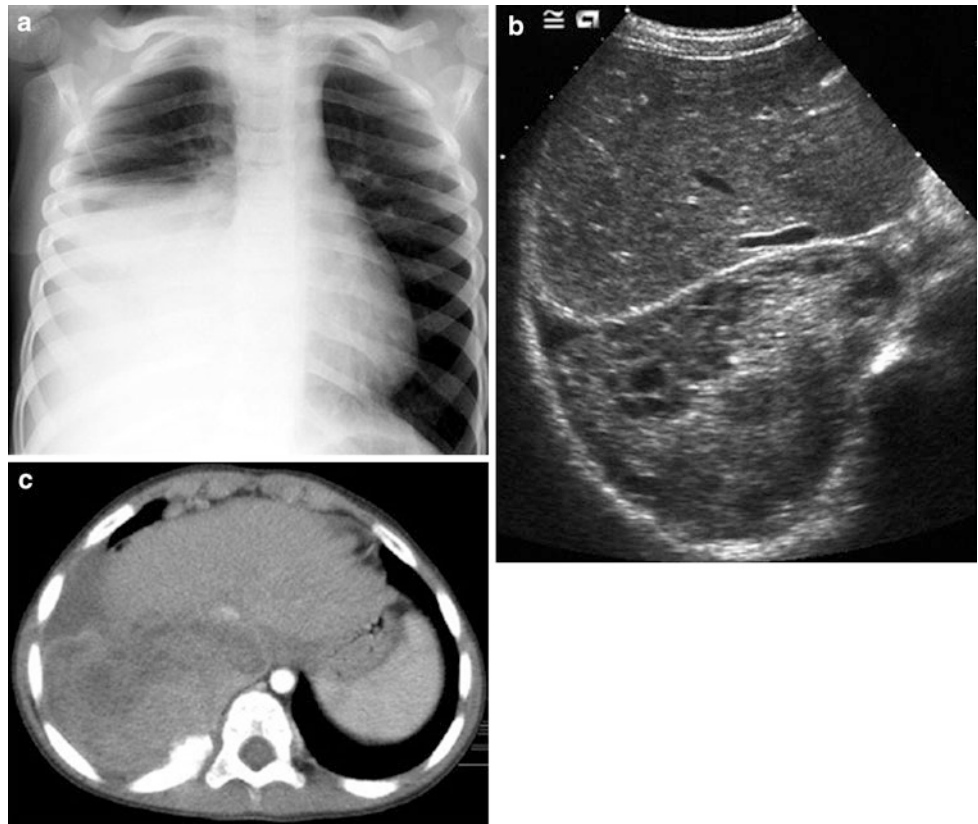
**Fig. 33** Metastatic renal clear cell sarcoma in a 2.5-year-old boy. Contrast-enhanced axial CT scan through lower chest area shows destructive metastatic lesion in the postero-lateral aspect of the ninth right rib extending intra- and extrathoracically. This child had simultaneous vertebral, orbital and cranial vault metastases

which in a biological sense usually is a venous malformation (Bruder et al. 2009), may have a similar radiographic appearance or present as a radiolucent slightly expansile lesion possessing a radiating lattice-like or web-like trabecular pattern (Fig. 19).

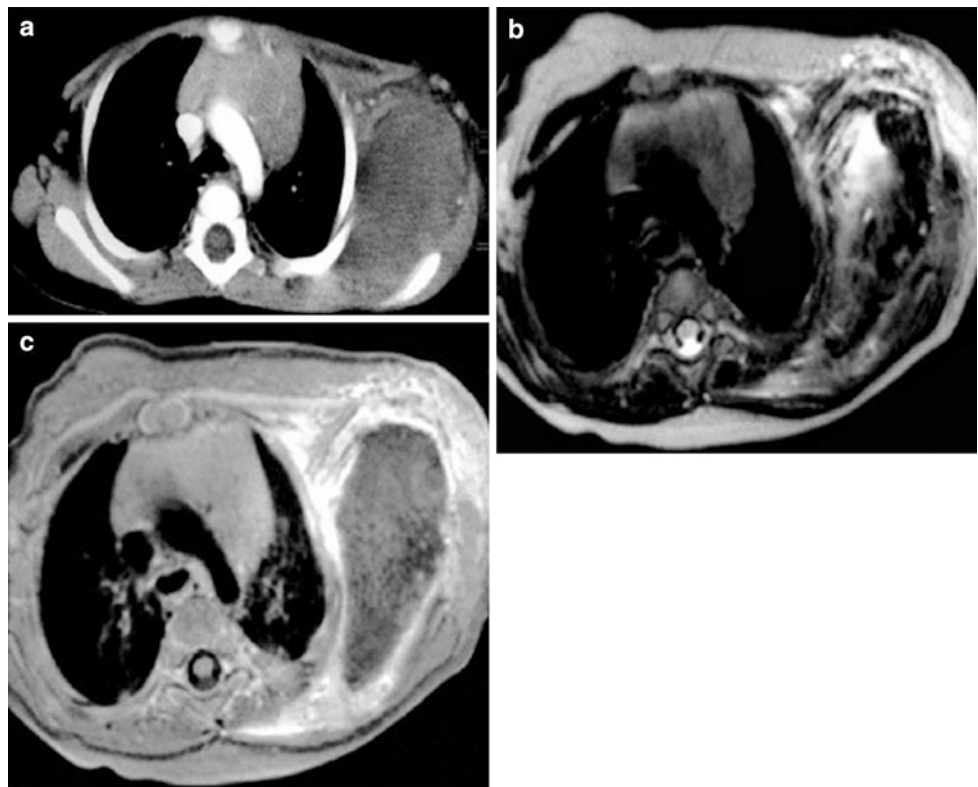
An association between lymphangiomas and hemangiomas with massive osteolysis has been noted in children and young adults particularly in the thoracic and pelvic region. This “vanishing bone disease” or diffuse cystic angiomatosis of bone (Gorham-Stout disease) is a rare condition in which spontaneous, progressive resorption of bone occurs. Autosomal dominant inheritance is recorded. The involved bones show osteoporosis and partial or complete destruction without evidence of reaction. Joints may be crossed, and pleural effusion with thoracic involvement may be present (Fig. 20). MRI can show the underlying vascular tumor (Assoun et al. 1994). Multifocal lymphangiomatosis, which has also been called multifocal lymphangioendotheliomatosis, generalized lymphangiomatosis or cystic angiomatosis, may diffusely infiltrate the mediastinum, pericard, pleura and lung besides involving bone, and superficial soft tissues. It may present as or be complicated by infection, chylothorax, or chylopericardium (Fig. 21).

Osteochondroma is a common benign tumor of the growing skeleton and probably the most common benign bone tumor of the chest wall. It is composed of cortical and medullary bone with a cartilaginous cap and is continuous with the underlying parent bone. It usually projects from the metaphysis of a tubular bone, but a rib, vertebra, clavicle, scapula, and the sternum may also be involved. The rib is most frequently affected near the costochondral junction

**Fig. 34** A 4-year-old boy presenting with raised temperature and right-sided abdominal pain. Initially, appendicitis or pneumonia were suspected. **a** On the chest radiograph a nonspecific, homogeneous density in the right base was noted without evidence for chest wall involvement. **b** Sonography showed a heterogeneous partially cystic mass. A loculated, incompletely organized empyema was considered. **c** Contrast-enhanced CT of the chest confirmed a solid and cystic mass originating from the posterior, locally thickened 10th rib. Histology confirmed a Ewing sarcoma



**Fig. 35** Acute bleeding in B-hemophilia in a 4-month-old boy. **a** Contrast-enhanced axial CT scan through chest at aortic arch level shows huge well-defined “cystic lesion” in the left extrathoracic soft tissues displacing the scapula away from the chest wall and extending into the dorsal musculature. Mass contains contrast material. **b, c** Correlating axial T2-weighted and T1-weighted fat-saturated contrast-enhanced MRI views demonstrate fluid, and respectively blood content of the mass lesion with a peripheral rim of contrast enhancement due to inflammatory response





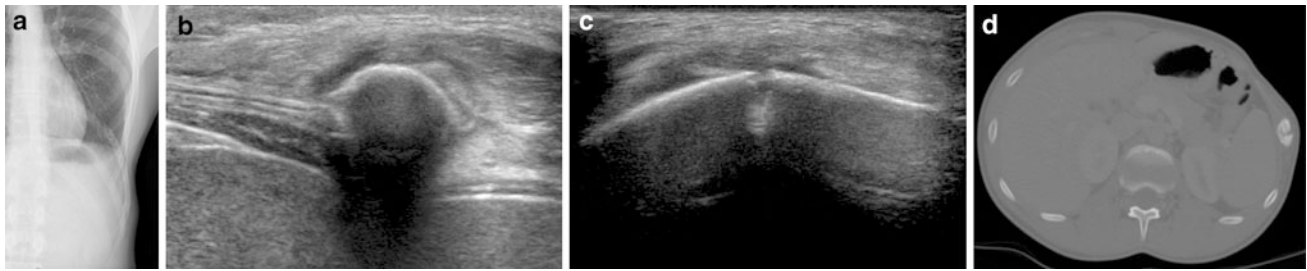


**Fig. 36** Rib fracture in a 16-year-old boy with history of resected Ewing sarcoma of 9th left rib. **a** Chest radiograph shows an irregular margin of the 10th left rib laterally, suspicious for a fracture. Perpendicular (**b**) and parallel (**c**) US images along the 10th rib show

surrounding ill-defined hypoechoic hematoma and demonstrate the fracture as a break in the cortical reflex (**c**). **d** Follow-up CT confirms the now healing fracture with callus formation

**Fig. 37** Rollerblade accident: vertebral fracture in a 10-year-old boy. **a** Partial antero-posterior radiograph of thoracic spine shows left paraspinal soft tissue mass at level of compressed vertebrae 9 and 10 and extending above this level. **b** Axial CT scan (bone window) at T-9 level shows vertebral compression fracture and left paraspinal hemorrhage/edema

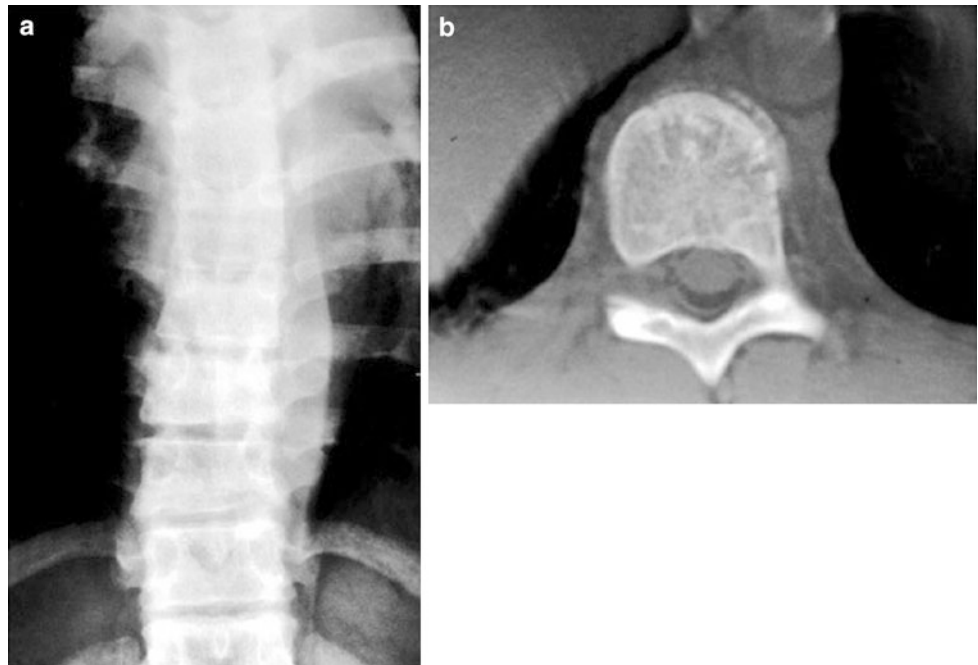


(Fig. 22). Inwardly, projecting osteochondromas of the ribs may produce pleural effusion or hemothorax (Fig. 23). Plain radiographs, US, CT, and MRI are able to depict the exostosis, its origin from the parent bone and potential complications (Lee et al. 2002).

Mesenchymal hamartoma, also known as mesenchymoma, is a rare, benign, nonneoplastic lesion of infants and young children, usually identified at birth. Patients often present with a deforming chest wall mass, but a large intrathoracic mesenchymal hamartoma may cause severe and even fatal respiratory compromise. The lesion always arises in the ribs and is characterized by benign proliferations of skeletal tissues with a prominent cartilaginous component and hemorrhagic cavities (secondary aneurysmal bone cysts). The lesion may be bilateral and multicentric. On radiographs it appears as a partially calcified,

extrapleural mass of the chest wall with involvement of one or more ribs. The rib deformity consists of partial or complete destruction, erosion, and enlargement. The lesion is well delineated, often lobulated, and measures up to 8 cm in diameter. Pathognomonic features recognized on CT and MRI consist of mineralized matrix and hemorrhagic cystic components (aneurysmal bone cysts). The mass may decrease in size without treatment and the prognosis of the patients is excellent. There are no reports of local recurrence following complete excision or metastasis (Ayala et al. 1993; Shamberger and Grier 1994; Groom et al. 2002) (Fig. 24).

Lipoblastoma is a benign soft-tissue tumor composed of fatty tissue, fibrovascular septa, and myxoid stroma. It is encountered in infants and young children, while lipoma is usually found in older individuals (Stout and Lattes 1967)



**Fig. 38** 7-year-old girl with minimal pain after fall on her back. **a** Lateral radiograph shows mild wedging of upper thoracic vertebrae. **b** Sagittal STIR MR image shows increased bone marrow signal in the vertebral bodies 3–6, 8 and 9 implying acute compression fractures and bone bruises

(Fig. 25). The imaging features of a lipoblastoma consist of a fatty tumor containing areas of stroma that may enhance with intravenous contrast (Fig. 26).

Fibrous tumors and tumor-like lesions, a large and diverse group of distinct entities that differ greatly in their clinical behavior, are relatively frequent, particularly in infants and young children, mostly boys. Most fibrous tumors exhibit benign or semimalignant behavior. The chest wall may be affected by extraabdominal fibromatosis (desmoid or aggressive fibromatosis), which can involve the muscle and overlying fascia of the shoulder girdle of adolescents and young adults. The tumor has the potential to grow to a large size, to recur, and to infiltrate neighboring tissues (Fig. 27). The imaging features are usually non-specific, but low signal intensity on T1- and T2-weighted sequences may suggest a fibrous tumor. Other fibrous lesions that can affect the chest wall include fibrous hamartoma of infancy, infantile myofibromatosis, juvenile hyaline fibromatosis, and infantile or adult type fibrosarcoma (Eich et al. 1998) (Fig. 28).

Neurogenic tumors, such as schwannomas and neurofibromas (particularly in patients with neurofibromatosis) or neuroblastoma and its variants (ganglioneuroblastoma and ganglioneuroma), may involve the intercostal nerves or the

sympathetic ganglia. They may lead to erosion, thinning, destruction, and separation of adjacent ribs (Figs. 29 and 30). Patients with neurofibromatosis type I may suffer from extensive involvement of the chest wall by plexiform neurofibromas or malignant neurofibrosarcoma. In addition, such patients may show widening of the ribs (twisted ribbon appearance) and short segment kyphoscoliosis due to dysplastic vertebrae, with widening of the spinal canal and intervertebral foramina, and dorsal scalloping of the vertebral bodies (Kuhn 2003).

The most prevalent malignant tumors of the chest wall belong to the Ewing sarcoma family, including Ewing sarcoma, Askin tumor and peripheral primitive neuroectodermal tumors (PNET) (Fig. 31), and the rhabdomyosarcomas. Of all malignant chest wall tumors in children approximately 50–65 % belong to the Ewing sarcoma group, while up to 33 % are either alveolar or embryonal rhabdomyosarcomas (Shamberger and Grier 1994; Shamberger et al. 1989; Dang et al. 1999). These tumors are dealt with elsewhere in this book. Other malignant tumors, such as osteosarcoma (Fig. 32) are much less common, and metastases to the chest wall are exceedingly rare in children (Fig. 33).

Pediatric chest wall tumors may initially be mistaken for an empyema because of signs and symptoms of inflammation or infection and a pleural mass. Raised white cell count, neutrophilia, elevated C-reactive protein, and moderate to high pyrexia in combination with an opacity on standard chest radiographs may suggest an empyema or a loculated pleural collection rather than a tumor. Ultrasonography of the chest may miss the evidence of the tumor. Even CT without intravenous contrast may fail to show the solid component of the neoplasm (Fig. 34). Therefore, CT or MRI with intravenous contrast is recommended to show the enhancing, solid tumor, its origin, and possible metastases, and to avoid unnecessary thoracocentesis or chest tube insertion (Sharif et al. 2006).

The differential diagnosis of chest wall mass should include pseudotumors of other etiologies than neoplasms. Amongst these, mention should be made of (recurrent) hematomas in a hemophiliac patient, which may present as a mass lesion (Fig. 35). Musculoskeletal hemorrhage of hemophiliac patients most commonly occurs within joints, but hemorrhage within bone and soft tissues can take place and cause local destructive bone changes. Subperiosteal hematomas can induce new bone formation or atrophy, or even complete destruction of the underlying bone. Such hemophiliac pseudotumors are relatively uncommon. They may extend from hemarthrosis under pressure, or develop from intraosseous, subperiosteal, or soft tissue bleeding. They may appear aggressive with a large soft tissue mass with or without bone destruction (Kuhn 2003).

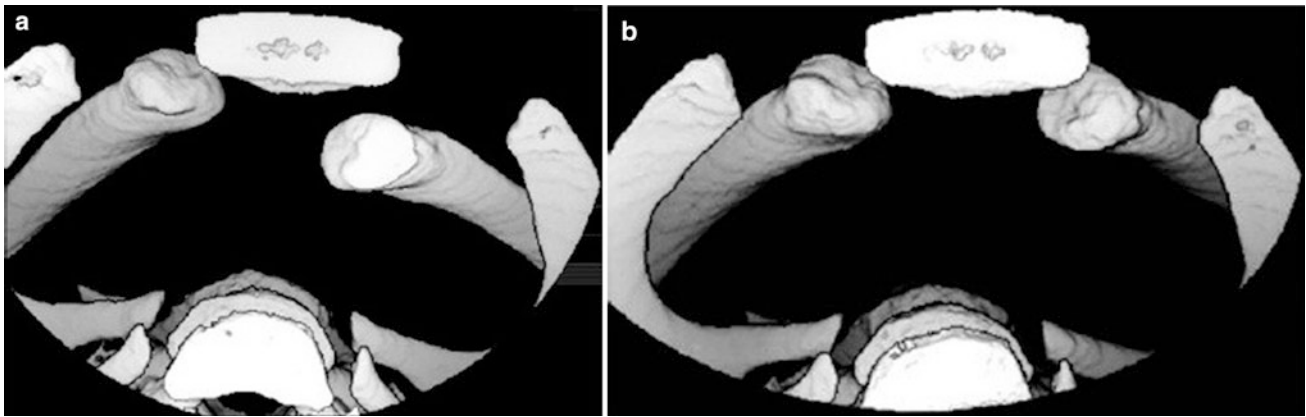


**Fig. 39** Sternoclavicular dislocation (I) in an 8-year-old boy. **a** Three-dimensional CT reconstruction demonstrates posterior dislocation of left clavicle. **b** After closed reduction there is a normal sternoclavicular relationship

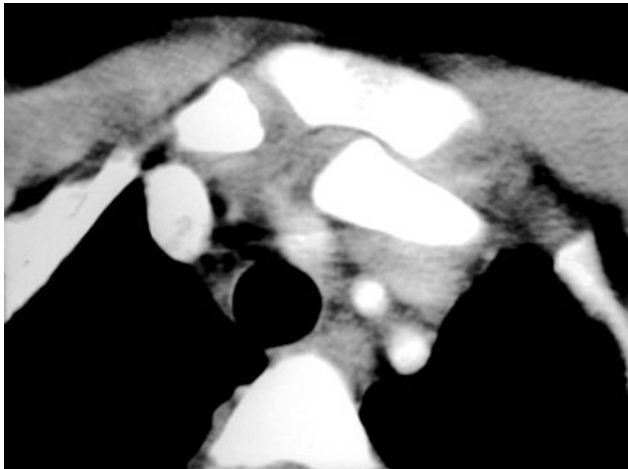


**Fig. 40** Sternoclavicular dislocation (II) in a 15-year-old girl. Axial contrast-enhanced CT scan through sternoclavicular area demonstrates dislocation of left medial clavicular end behind manubrium of sternum and medially, thus space occupying and explaining difficulty in swallowing

## 5 Trauma

### 5.1 Accidental Trauma

With the exception of rib fractures and burns, traumatic lesions of the chest wall are usually part of a more complex injury to the chest (Sartorelli and Vane 2004). They may be caused by direct blunt contusion or compression, axial or bending trauma to the spine, penetrating chest or abdominal trauma, rapid deceleration, and other mechanisms. Severe trauma to the chest or other parts of the body involving the

chest, as in polytrauma, commonly results in damage of multiple thoracic structures, including intrathoracic organs. Referral for imaging usually follows clinical assessment and stabilization of vital conditions. Plain films of the chest and abdomen may reveal life-threatening injuries. CT, however, is the method of choice for evaluation of the chest in a severe or potentially life-threatening posttraumatic emergency situation.

This section focuses on a few traumatic injuries to the child's chest wall that are characteristic of some specific insult or may be difficult to assess and diagnose. Rib fractures are easily overlooked or not evident on an emergency chest film. US may be helpful demonstrating a rib fracture as cause for localized pain (Fig. 36). Adjacent pleural or lung injury may be related to rib fractures and pneumo- and/or hemothorax may coexist. Trauma to the spine due to fall, motor vehicle accident, or various sport activities is not uncommon. The thoracic spine is the most frequently affected segment, although spinal trauma per se accounts for a small percentage of all childhood trauma (Stulik et al. 2006). The injury may consist of one or multiple vertebral compression fractures with paraspinal hemorrhage and edema (Fig. 37). Wedge deformity of multiple compression fractures might be mild and MRI can determine whether it is due to recent trauma or not (Fig. 38). The paraspinal soft tissue mass from local hemorrhage may suggest the presence of associated aortic rupture. However, traumatic rupture of the thoracic or abdominal aorta is rare in the pediatric age group and is excluded or demonstrated by contrast-enhanced CT and transesophageal echocardiography (Lowe et al. 1998; Spouge et al. 1991; Trachiotis et al. 1996). In blunt thoracoabdominal trauma, aortic injury occurs almost exclusively in the thoracic segment (Choit



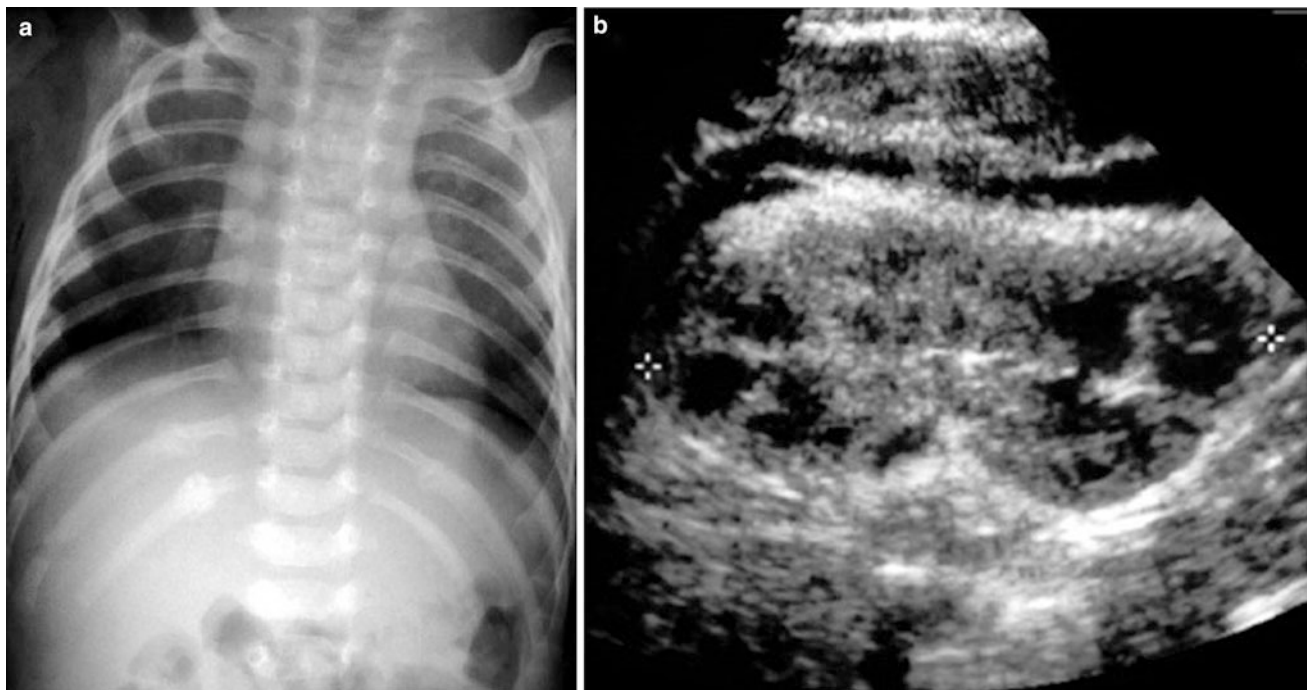


**Fig. 41** Rib fractures from nonaccidental trauma in a 4-week-old boy. **a** Anteroposterior chest radiograph shows healing paraspinal fractures of the 10th and 11th right and the 10th left ribs. **b** On

previous posterior longitudinal ultrasound at 10 days, a fluid collection dorsal to the right kidney was missed

et al. 2006) and angiography might be crucial in such circumstance (Puapong et al. 2006). Involvement of the spinal canal with neurological symptoms is uncommon and is less frequent in children and teenagers than in adults.

In children and adolescents and even in young adults, the so-called sternoclavicular dislocation is, in fact, a Salter type 1 or 2 medial clavicular epiphysiolysis (Cope et al. 1991; Lewonowski and Bassett 1992). It is uncommon and usually missed at the initial clinical examination. A fall on the shoulder, occurring during a bicycle accident or in contact sports, is the typical cause. If a sternoclavicular injury is suspected, contrast-enhanced CT is the diagnostic method of choice (Cope et al. 1991; Yang et al. 1996; Gobet et al. 2004) (Figs. 39 and 40). Intravenous contrast is necessary to demonstrate compromise of the supracardiac vasculature, a complication of retrosternal clavicular dislocation that is less relevant in children than in adults. Dysphagia, however, is common. A radiographic plain film technique using special lateral projections of the sternoclavicular joint, provides specific diagnosis as to posterior or anterior displacement of the clavicle. It needs technical skill and might be used if CT is not available (Heinig 1968; Lee and Gwinn 1974). This projection is, however, difficult to obtain and films often need to be repeated.

## 5.2 Non-accidental Trauma

Child abuse must be considered in any infant and young child with rib fractures (Bulloch et al. 2000; Cadzow and Armstrong 2000). Underlying conditions of skeletal morbidity such as a disorder of bone metabolism, a syndrome, or a dysplasia need to be ruled out. Any apparent accidental trauma, including a motor vehicle accident requires critical consideration in view of its pathogenetic explanation (Spevak et al. 1994).

In child abuse, rib fractures are due to characteristic mechanical factors involved in violence to the child's chest. They are commonly noticed in the posterior rib segments close to the costovertebral joints, but may occur anywhere along the entire rib cage, including the costochondral junctions arc (Kleinman 1992, 1996; Ng and Hall 1998). The rib fractures tend to be multiple and bilateral and somewhat symmetrical (Fig. 41). Ample specific information regarding the mechanism, pathophysiology, anatomic, and histologic findings in skeletal and soft tissue involvement of the entire body in child abuse has been researched and described by Kleinman (1998). If child abuse is suspected, a formal evaluation of the entire skeleton has to be performed and the information transmitted to the clinician(s) responsible for



**Fig. 42** Rib fractures from nonaccidental trauma in a 2-month-old girl. **a** Chest radiograph shows healed fracture of ninth right rib posteriorly and suspected fractures of sixth to eighth left ribs laterally. **b** Coronal STIR MR image shows hyperintense bone marrow edema

and local soft tissue swelling of the involved left ribs correlating with **(a)**. **c** Close-up view of **(a)** and **(b)** comparing to follow-up radiograph 2 weeks later with now visible callus formation (*left to right* sequence)

the child's care (Nimkin and Kleinman 2001). Digital radiography has been introduced successfully in the skeletal evaluation of nonaccidental trauma in infants (Kleinman et al. 2002). Radiography as the primary and main tool to

evaluate the infant's skeleton systematically might be complemented by scintigraphy, CT, and ultrasonography (Nimkin and Kleinman 2001). Whole-body magnetic resonance imaging has a potential for future protocols in the

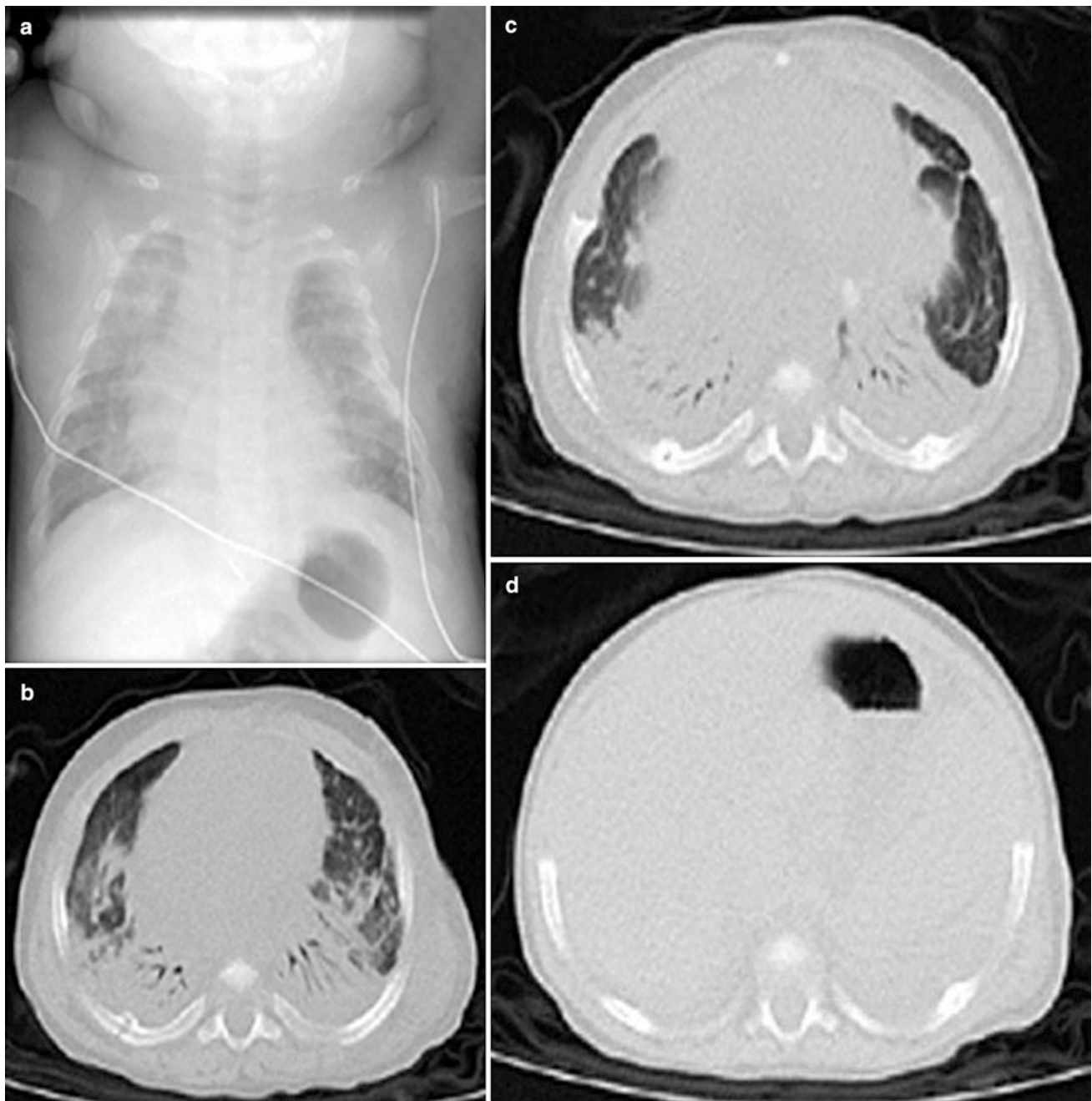


**Fig. 43** Multiple rib fractures from physiotherapy in a 7-month-old former 24 weeks premature boy with severe bronchopulmonary dysplasia. **a** Chest radiograph shows diffuse lung disease with

hyperinflation. Rib lesions were missed. CT on the same day showed fractures of eighth right rib (**b**), both ninth ribs (**c**) and 10th left rib (**d**) and several additional fractures not shown here

differential diagnosis of nonaccidental injuries (Kellenberger et al. 2004; Stranzinger et al. 2007) (Fig. 42).

Premature babies undergoing physiotherapy for chronic lung disease as part of intensive care, may radiographically mimic nonaccidental rib injuries (Fig. 43) (Chalumeau et al. 2002). This may especially become a problem at re-admission if the fractures had remained unrecognized

before primary hospital discharge. In contrast to the effects of physiotherapy, rib fractures from cardiopulmonary resuscitation are unlikely in infants (Spevak et al. 1994).

**Acknowledgments** We would like to acknowledge the contribution of imaging material by Drs. Paul Babyn and David Manson, The Hospital for Sick Children, Toronto, Dr. Javier Lucaya, HMI Vall d'Hebron, Barcelona, and Drs. Miralles and Rasero from Madrid.



## References

- Assoun J, Richardi G, Railhac JJ, Le Guennec P, Caulier M, Dromer C, Sixou L, Fournie B, Mansat M, Durroux D (1994) CT and MRI of massive osteolysis of Gorham. *J Comput Assist Tomogr* 18:981–984
- Ayala AG, Ro JY, Bolio-Solis A, Hernandez-Batres F, Eftekhari F, Edeiken J (1993) Mesenchymal hamartoma of the chest wall in infants and children: a clinicopathological study of five patients. *Skeletal Radiol* 22:569–576
- Birkemeier KL, Podberesky DJ, Salisbury S, Serai S (2011) Breathe in... breathe out... stop breathing: does phase of respiration affect the Haller index in patients with pectus excavatum? *Am J Roentgenol* 197:W934–W939
- Bruder E, Perez-Atayde AR, Jundt G, Alomari AI, Rischewski J, Fishman SJ, Mulliken JB, Kozakewich HP (2009) Vascular lesions of bone in children, adolescents, and young adults. A clinicopathologic reappraisal and application of the ISSVA classification. *Virchows Arch* 454:161–179
- Bulloch B, Schubert CJ, Brophy PD, Johnson N, Reed MH, Shapiro RA (2000) Cause and clinical characteristics of rib fractures in infants. *Pediatrics* 105:E48
- Bush CH, Kalen V (1999) Three-dimensional computed tomography in the assessment of congenital scoliosis. *Skeletal Radiol* 28:632–637
- Cadilhac C, Fenoll B, Peretti A et al (2000) Congenital pseudarthrosis of the clavicle: 25 childhood cases. *Rev Chir Orthop Reparatrice Appar Mot* 86:575–580
- Cadzow SP, Armstrong KL (2000) Rib fractures in infants: red alert! The clinical features, investigations and child protection outcomes. *J Paediatr Child Health* 36:322–326
- Calloway EH, Chhotani AN, Lee YZ, Phillips JD (2011) Three-dimensional computed tomography for evaluation and management of children with complex chest wall anomalies: useful information or just pretty pictures? *J Pediatr Surg* 46:640–647
- Chalumeau M, Foix-L'Helias L, Scheinmann P, Zuani P, Gendrel D, Ducou-le-Pointe H (2002) Rib fractures after chest physiotherapy for bronchiolitis or pneumonia in infants. *Pediatr Radiol* 32:644–647
- Cho TJ, Choi IH, Chung CY et al (2000) The Sprengel deformity. Morphometric analysis using 3D-CT and its clinical relevance. *J Bone Joint Surg Br* 82:711–718
- Choit RL, Tredwell SJ, Leblanc JG, Reilly CW, Mulpuri K (2006) Abdominal aortic injuries with chance fractures in pediatric patients. *J Pediatr Surg* 41:1184–1190
- Chuang JH, Wan YL (1995) Evaluation of pectus excavatum with repeated CT scans. *Pediatr Radiol* 25:654–656
- Cingel V, Bohac M, Mestanova V, Zabojsnikova L, Varga I (2013) Poland syndrome: from embryological basis to plastic surgery. *Surg Radiol Anat* Feb 19 (Epub ahead of print)
- Cope R, Riddervold HO, Shore JL, Siström CL (1991) Dislocations of the sternoclavicular joint: anatomic basis, etiologies, and radiologic diagnosis. *J Orthop Trauma* 5:379–384
- Coury CH, Delaporte J (1954) Les anomalies congenitales des cotes. Formes anatomo-radiologiques et incidences pratiques (a propos de 288 cas). *Sem Hop Paris* 30:2656–2681
- Dang NC, Siegel SE, Phillips JD (1999) Malignant chest wall tumors in children and young adults. *J Pediatr Surg* 34:1773–1778
- Daunt SW, Cohen JH, Miller SF (2004) Age-related normal ranges for the Haller index in children. *Pediatr Radiol* 34:326–330
- Dilli A, Ayaz UY, Damar C, Ersan O, Hekimoglu B (2011) Sprengel deformity: magnetic resonance imaging findings in two pediatric cases. *J Clin Imaging Sci* 1:13
- Donnelly LF, Taylor CN, Emery KH et al (1997) Asymptomatic, palpable, anterior chest wall lesions in children: is cross-sectional imaging necessary? *Radiology* 202:829–831
- Donnelly LF, Frush DP, Foss JN et al (1999) Anterior chest wall: frequency of anatomic variations in children. *Radiology* 212:837–840
- Eich GF (2007) Chest wall abnormalities which cause neonatal respiratory distress. In: Donoghue V (ed) *Radiological imaging of the neonatal chest*. Springer, Berlin (in press)
- Eich GF, Hoeffel JC, Tschappeler H, Gassner I, Willi UV (1998) Fibrous tumours in children: imaging features of a heterogeneous group of disorders. *Pediatr Radiol* 28:500–509
- Faro SH, Mahboubi S, Ortega W (1993) CT diagnosis of rib anomalies, tumors, and infection in children. *Clin Imaging* 17:1–7
- Fokin AA (2000) Cleft sternum and sternal foramen. *Chest Surg Clin North Am* 10:261–276
- Garcia-Peña P, Barber I (2010) Pathology of the thoracic wall: congenital and acquired. *Pediatr Radiol* 40:859–868
- Glass RB, Norton KI, Mitre SA, Kang E (2002) Pediatric ribs: a spectrum of abnormalities. *Radiographics* 22:87–104
- Gobet R, Meuli M, Altermatt S, Jenni V, Willi UV (2004) Medial clavicular epiphysiolysis in children: the so-called sterno-clavicular dislocation. *Emerg Radiol* 10:252–255
- Golladay ES, Hale JA, Mollitt DL, Seibert JJ (1985) Chest wall masses in children. *South Med J* 78:292–295
- Gorham LW, Stout AP (1955) Massive osteolysis (acute spontaneous absorption of bone, phantom bone, disappearing bone): its relation to hemangiomatosis. *J Bone Joint Surg* 37A:985–1004
- Groom KR, Murphey MD, Howard LM, Lonergan GJ, Rosado-De-Christenson ML, Torop AH (2002) Mesenchymal hamartoma of the chest wall: radiologic manifestations with emphasis on cross-sectional imaging and histopathologic comparison. *Radiology* 222:205–211
- Haje SA, Harcke HT, Bowen JR (1999) Growth disturbance of the sternum and pectus deformities: imaging studies and clinical correlation. *Pediatr Radiol* 29:334–341
- Haller JA, Loughlin GM (2000) Cardiorespiratory function is significantly improved following surgery for severe pectus excavatum. Proposed treatment guidelines. *J Cardiovasc Surg (Torino)* 41:125–130
- Haller JA, Kramer SS, Lietman SA (1987) Use of CT scans in selection of patients for pectus excavatum superior: a preliminary report. *J Pediatr Surg* 22:904–906
- Heinig CF (1968) Retrosternal dislocation of the clavicle: early recognition, X-ray diagnosis and management. *J Bone Joint Surg Am* 50:830
- Herrmann K, Zech C, Strauss T, Hatz R, Schoenberg S, Reiser M (2006) Cine-MRI of the thorax in patients with pectus excavatum. *Radiologe* 46:309–316
- Kamaruddin K, Wright NB, Pilling DW (1995) Intrathoracic rib. *Pediatr Radiol* 25:60–61
- Kellenberger CJ, Epelman M, Miller SF, Babyn PS (2004) Fast STIR whole-body MR imaging in children. *Radiographics* 24:1317–1330
- Kleinman PK (1992) Fractures of the rib head in abused infants. *Radiology* 185:119–123
- Kleinman PK (1996) Rib fractures in 31 abused infants: postmortem radiologic-histopathologic study. *Radiology* 200:807–810
- Kleinman PK (1998) *Diagnostic imaging of child abuse*, 2nd edn. Mosby, St Louis
- Kleinman PK, O'Connor B, Nimkin K, Rayder SM, Spevak MR, Belanger PL, Getty DJ, Karellas A (2002) Detection of rib fractures in an abused infant using digital radiography: a laboratory study. *Pediatr Radiol* 32:896–901
- Koç T, Lam KS, Webb JK (2012) Are intraspinal anomalies in early onset idiopathic scoliosis as common as once thought? A two centre United Kingdom study. *Eur Spine J* Dec 6 (Epub ahead of print)
- Kozłowski K, Campbell J, Morris L, Sprague P, Taccone A, Beluffi G, Marcinski A, Porta F, Stevens M (1989) Primary rib tumours in

- children (report of 27 cases with short literature review). *Aust Radiol* 33:210–222
- Kuhn JP (2003) Caffey's pediatric diagnostic imaging, 10th edn. Mosby, Philadelphia
- Kumar AP, Green AL, Smith JW, Pratt CB (1977) Combined therapy for malignant tumors of the chest wall in children. *J Pediatr Surg* 12:991–999
- Lachman RS (2006) Taybi and Lachman's radiology of syndromes, metabolic disorders and skeletal dysplasias, 5th edn. Mosby, St Louis
- Laor T (2004) MR imaging of soft tissue tumors and tumor-like lesions. *Pediatr Radiol* 34:24–37
- Lee FA, Gwinn JL (1974) Retrosternal dislocation of the clavicle. *Radiology* 110:631–634
- Lee KC, Davies AM, Cassar-Pullicino VN (2002) Imaging the complications of osteochondromas. *Clin Radiol* 57:18–28
- Letts M, Davidson D, Birdi N, Joseph M (1999) The SAPHO syndrome in children: a rare cause of hyperostosis and osteitis. *J Pediatr Orthop* 19:297–300
- Levy M, Goldberg I, Fischel RE, Frisch E, Maor P (1981) Friedrich's disease. Aseptic necrosis of the sternal end of the clavicle. *J Bone Joint Surg Br* 63:539–541
- Lew DP, Waldvogel FA (1997) Osteomyelitis. *N Engl J Med* 336:999–1007
- Lewonowski K, Bassett GS (1992) Complete posterior sternoclavicular epiphyseal separation. A case report and review of the literature. *Clin Orthop* 281:84–88
- Lo Piccolo R, Bongini U, Basile M, Savelli S, Morelli C, Cerra C, Spinelli C, Messineo A (2012) Chest fast MRI: an imaging alternative on pre-operative evaluation of Pectus Excavatum. *J Pediatr Surg* 47:485–489
- Lowe LH, Bulas DI, Eichelberger MD, Martin GR (1998) Traumatic aortic injuries in children: radiologic evaluation. *Am J Roentgenol* 170:39–42
- Marcovici PA, LoSasso BE, Kruk P, Dwek JR (2011) MRI for the evaluation of pectus excavatum. *Pediatr Radiol* 41:757–758
- Morales JM, Patel SG, Duff JA, Villareal RL, Simpson JW (2000) Ectopia cordis and other midline defects. *Ann Thorac Surg* 70:111–114
- Mulliken JB, Glowacki J (1982) Hemangiomas and vascular malformations in infants and children: a classification based on endothelial characteristics. *Plast Reconstr Surg* 69:412–420
- Nathanson I (1994) Chest wall abnormalities. In: Loughlin GM, Eigen H (eds) *Respiratory disease in children: diagnosis and management*. Williams and Wilkins, Baltimore, pp 533–541
- Ng CS, Hall CM (1998) Costochondral junction fractures and intra-abdominal trauma in non-accidental injury (child abuse). *Pediatr Radiol* 28:671–676
- Nimkin K, Kleinman PK (2001) Imaging of child abuse. *Radiol Clin North Am* 39:843–864
- Pretorius ES, Haller JA, Fishman EK (1998) Spiral CT with 3D reconstruction in children requiring reoperation for failure of chest wall growth after pectus excavatum surgery. Preliminary observations. *Clin Imaging* 22:108–116
- Puapong D, Brown CV, Katz M, Kasotakis G, Applebaum H, Salim A, Rhee P, Demetriades D (2006) Angiography and the pediatric trauma patient: a 10-year review. *J Pediatr Surg* 41:1859–1863
- Raichura N, Entwisle J, Leverment J, Beardsmore CS (2001) Breath-hold MRI in evaluating patients with pectus excavatum. *Br J Radiol* 74:701–708
- Sartorelli KH, Vane DW (2004) The diagnosis and management of children with blunt injury of the chest. *Semin Pediatr Surg* 13:98–105
- Schroeder S, Cannizzaro E, Kellenberger CJ, Saurenmann RK (2012) A 12-year-old girl with absent radial pulse: arterial thoracic outlet syndrome with subclavian artery aneurysm and thrombosis of the brachial artery. *Eur J Pediatr* 171:1707–1709
- Shamberger RC, Grier HE (1994) Chest wall tumors in infants and children. *Semin Pediatr Surg* 3:267–276
- Shamberger RC, Welch KJ, Castaneda AR, Keane JF, Fyler DC (1988) Anterior chest wall deformities and congenital heart disease. *J Thorac Cardiovasc Surg* 96:427–432
- Shamberger RC, Grier HE, Weinstein HJ, Perez-Atayde AR, Tarbell NJ (1989) Chest wall tumors in infancy and childhood. *Cancer* 63:774–785
- Sharif HS, Clark DC, Aabed MY, Aideyan OA, Haddad MC, Mattsson TA (1990) MR imaging of thoracic and abdominal wall infections: comparison with other imaging procedures. *Am J Roentgenol* 154:989–995
- Sharif K, Alton H, Clarke J, Desai M, Morland B, Parikh D (2006) Paediatric thoracic tumours presenting as empyema. *Pediatr Surg Int* 22:1009–1014
- Spevak MR, Kleinman PK, Belanger PL, Primack C, Richmond JM (1994) Cardiopulmonary resuscitation and rib fractures in infants. A postmortem radiologic-pathologic study. *JAMA* 272:617–618
- Spouge AR, Burrows PE, Armstrong D, Daneman A (1991) Traumatic aortic rupture in the pediatric population. Role of plain film, CT and angiography in the diagnosis. *Pediatr Radiol* 21:324–328
- Stout AP, Lattes R (1967) *Atlas of tumor pathology, second series, fascicle I: tumors of the soft tissues*. Armed Forces Institute of Pathology, Washington DC
- Stranzinger E, Kellenberger CJ, Braunschweig S, Hopper R, Huisman TAGM (2007) Whole body STIR MR imaging in suspected child abuse: an alternative to skeletal survey radiology? *EJR Extra* 63(1):43–47
- Stulik J, Pesi T, Kryl J, Vyskocil T, Sebesta P, Havranek P (2006) Spinal injuries in children and adolescents. *Acta Chir Orthop Traumatol Cech* 73:313–320
- Thomas KE, Owens CM, Veys PA, Novelli V, Costoli V (2003) The radiological spectrum of invasive aspergillosis in children: a 10-year review. *Pediatr Radiol* 33:453–460
- Thompson JS (1976) Cervical herniation of the lung. Report of a case and review of the literature. *Pediatr Radiol* 4:190–192
- Trachiotis GD, Sell JE, Pearson GD, Martin GR, Midgley FM (1996) Traumatic thoracic aortic rupture in the pediatric patient. *Ann Thorac Surg* 62:724–731
- Wong KS, Hung IJ, Wang CR, Lien R (2004) Thoracic wall lesions in children. *Pediatr Pulmonol* 37:257–263
- Wright AR, Milner RH, Bainbridge LC et al (1992) MR and CT in the assessment of Poland syndrome. *J Comput Assist Tomogr* 16:442–444
- Yang J, al-Etani H, Letts M (1996) Diagnosis and treatment of posterior sternoclavicular joint dislocations in children. *Am J Orthop* 25:565–569

---

# Pediatric Cardiac CT

Laureen Sena and Hyun Woo Goo

## Contents

<b>1</b>	<b>Introduction</b> .....	459
<b>2</b>	<b>Technical Considerations</b> .....	460
2.1	Spatial and Temporal Resolution.....	460
2.2	Retrospective ECG Gating and Prospective ECG Triggering .....	460
2.3	Radiation Dose Optimization.....	460
2.4	Planning Scan Technique and Intravenous Contrast Injection .....	461
<b>3</b>	<b>Complementary Role of MDCT and MRI for Cardiac Imaging</b> .....	463
<b>4</b>	<b>Clinical Applications</b> .....	463
4.1	Pulmonary Vasculature .....	463
4.2	Aorta .....	467
4.3	Coronary Artery Anomalies .....	471
4.4	Airway Compromise in Patients with Congenital Heart Disease .....	474
4.5	Cardiac Chamber Morphology and Ventricular Function .....	475
4.6	Postoperative Congenital Heart Disease.....	477
<b>5</b>	<b>Conclusion</b> .....	479
	<b>References</b> .....	479

---

## Abstract

Technological developments have significantly advanced the role of CT for noninvasive imaging of the cardiovascular system in children. This chapter provides an overview of the technical considerations that are essential for performing high quality pediatric cardiac CT using the lowest possible radiation dose. The clinical utility and application of CT compared with MRI is discussed for a wide range of congenital and acquired pediatric cardiovascular diseases involving the systemic and pulmonary vasculature, coronary arteries, heart chamber morphology and function, and thoracic airways. Postoperative considerations following repair of congenital heart disease are also addressed.

---

## 1 Introduction

Recent technical developments in CT imaging have significantly advanced the role of multidetector CT (MDCT) in noninvasive imaging of the cardiovascular system. The number of detector rows has increased from 2 to 320 and the gantry rotation time has decreased down to 270 ms. These two technical improvements result in shorter scan time, longer z-axis coverage, and less motion artifacts on pediatric cardiac CT, and enhance the its diagnostic value in evaluating extracardiac vessels, lungs, and airways in children with congenital heart disease (CHD) (Westra et al. 1999; Kim et al. 2002; Goo et al. 2003, 2005a). Electrocardiography (ECG)-synchronized scan acquisitions are almost always required for evaluating intracardiac structures, ventricular function, and coronary arteries (Goo et al. 2005b, 2010b; Tsai et al. 2007; Goo 2010a, 2011a). New CT applications for children with CHD include dual-energy lung perfusion (Goo 2010b) and four-dimensional (4D) airway (Greenberg 2012) assessments. In this chapter, we will focus on the technical considerations essential for pediatric cardiac CT, discuss the relative merits and demerits of cardiac CT and cardiac MRI,

---

L. Sena (✉)

Department of Radiology, Boston Children's Hospital,  
300 Longview Avenue, Boston, MA 02115, USA  
e-mail: laureen.sena@childrens.harvard.edu

H. W. Goo

Department of Radiology and Research Institute of Radiology,  
University of Ulsan College of Medicine, Asan Medical Center,  
88, Olympic-ro 43-gil, Songpa-gu, Seoul, Korea



and describe clinical applications of pediatric cardiac CT in children with CHD.

## 2 Technical Considerations

### 2.1 Spatial and Temporal Resolution

Thanks to the improved longitudinal (z-axis) spatial resolution (0.5–0.625 mm) of modern MDCT systems, isotropic spatial resolution vastly improving the quality of multiplanar reformatted and three-dimensional (3D) CT images can be achieved (Mahesh 2002). Pediatric cardiac CT particularly demands high temporal resolution because children may not cooperate with a breathing instruction and a child's heart rate is usually high. In this respect, a dual-source scanner is quite helpful to decrease motion artifacts on pediatric cardiac CT by increasing temporal resolution. Only a quarter of gantry rotation (70–83 msec) is necessary for cardiac CT using dual-source scanning and half-scan reconstruction techniques (Petersilka et al. 2008). Recently introduced high-pitch (up to 3.0–3.4) dual-source helical scanning with or without ECG triggering allows substantial reduction of motion artifacts on pediatric cardiac CT (Han et al. 2011; Nie et al. 2012). The benefit of higher temporal resolution of a dual-source CT system has also been proven by improved coronary artery visibility on prospectively ECG-triggered sequential scan (Goo 2010b) and retrospectively ECG-gated helical scan (Ben Saad et al. 2009).

An alternative way to increase temporal resolution of ECG-synchronized scanning includes multi-segment reconstruction. However, multi-segment reconstruction, in which multiple segments with higher temporal resolution acquired over multiple heart beats are used to generate a single image, is not commonly used in clinical practice because it requires much lower pitch lengthening scan time and resulting in degraded image quality caused by increased heart rate variability. On the other hand, beta-blockers may be used to lower heart rates and improve image quality of ECG-synchronized CT by increasing the mid-diastolic cardiac rest period, the so-called “diastasis.” However, satisfactory reduction of heart rates is not always achieved and longer preparation time considerably delays patient throughput. The most effective method to obtain the best image quality of ECG-synchronized CT at higher heart rates (e.g., >75 bpm) is to acquire CT data at the end-systolic phase. Compared with mid-diastolic data acquisition, another benefit of end-systolic data acquisition is that the image quality is less affected by arrhythmia. Scan time and radiation dose of retrospectively ECG-gated CT scanning can be reduced by using heart rate-adapted pitch (e.g., 0.17 for <40 bpm to 0.38 for >100 bpm) (McCollough et al. 2007). However, it should

be kept in mind that gaps in the image data set may occur and result in image degradation if the pitch is too high for a given heart rate.

### 2.2 Retrospective ECG Gating and Prospective ECG Triggering

Retrospective ECG gating and prospective ECG triggering are two methods for ECG-synchronized CT scanning. Retrospective ECG gating is used with helical CT scanning. In this scan mode, helical CT data are continuously acquired with low pitch and images are then retrospectively reconstructed at a desired cardiac phase. The low pitch required for this scan mode, to avoid gaps in the image data, results in high radiation dose and long scan time. Multi-phase image reconstruction (e.g., 10 phases by 10 % of the RR interval) though the entire cardiac cycle allows the assessment of ventricular function and motion of valves. Although adaptive algorithms are incorporated to ameliorate image degradation of retrospectively ECG-gated helical CT images caused by arrhythmia, severe and persistent arrhythmia, such as atrial fibrillation, may result in substantial deterioration of image quality.

In contrast, prospective ECG triggering is used with sequential or step-and-shoot CT scanning. In this scan mode, axial CT data covering beam collimation are acquired at a predefined cardiac phase without table movement. The time for table feeding is mandatory for next axial CT data acquisition. This scan mode delivers a very low radiation dose because there are no data overlapping for image reconstruction. However, total scan time is considerably prolonged and multi-phase image reconstruction usually cannot be obtained. Recently, prospective ECG triggering may be used with high-pitch dual-source helical CT scanning (Han et al. 2011; Nie et al. 2012).

Initially recognized differences between retrospective ECG gating and prospective ECG triggering have become somewhat vague due to further technical developments. As a result, radiation dose of retrospectively ECG-gated helical scanning can be dramatically reduced by means of aggressive ECG-controlled tube current modulation, and multi-phase image reconstruction is also possible for prospectively ECG-triggered sequential scanning by using extended gantry rotation.

### 2.3 Radiation Dose Optimization

It is well known that children are more sensitive to the carcinogenic hazards of ionizing radiation than adults, and have a longer expected lifespan leading to a greater lifetime attributable risk of radiation-induced malignancies. Therefore, the

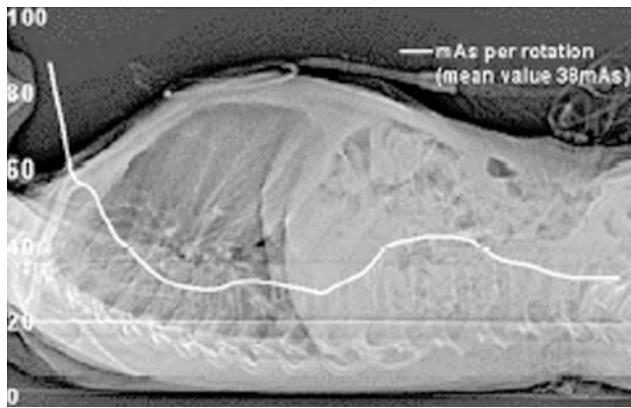


**Fig. 1** Automatic exposure control with MDCT. Lateral topogram (scout view) for thoracoabdominal CT in a 6-year-old child. The curve represents the automatically adapted milliampere-seconds value as a function of z-axis position during scanning with spiral CT. Although the standard adult protocol was used, the average milliampere-seconds value throughout the scan was adjusted to 38 mAs with automatic exposure control (Flohr et al. 2005, used with permission)

radiation dose of pediatric cardiac CT should be minimized while maintaining diagnostic quality. As a first step of the optimization process, we should understand not only important scanning parameters affecting image quality and radiation dose, but also available dose-reducing strategies (Donnelly and Frush 2003; Kalra et al. 2004; Goo 2012). The establishment of body size-adapted CT protocols is particularly important in children. As body size parameters, body weight is most commonly used in our current practice (Yang and Goo 2008) but cross-sectional dimensions, such as diameter, circumference, or area, are better for radiation dose adaptation to body habitus (Menke 2005; Goo 2011b). In addition, all recently manufactured MDCT scanners are now equipped with automatic exposure control using tube current modulation. This dose reduction technique adjusts the tube current along the x-y plane (angular modulation) or along the z-axis (longitudinal modulation) or both (combined modulation) depending on the size, shape, and density of the scanning region (Kalra et al. 2004) (Fig. 1). Algorithms used for tube current modulation are vendor-specific and vary in the image quality reference parameter and in the preferred order of acquisition of the localizer radiographs. For optimal dose reduction, the patient should be positioned in the isocenter of the CT gantry (Lee et al. 2008). When scanning the pediatric thorax for cardiac applications, excluding the arms from the scan range and using optimal tube voltage will allow an even greater tube current reduction by combined tube current modulation (Goo and Suh 2006a, b; Greess et al. 2002).

The benefit of the use of lower tube voltage for pediatric cardiac CT is a higher iodine contrast-to-noise ratio at a

given radiation dose (Yu et al. 2011). When we use low tube voltage with tube current modulation, we should recognize that the tube current may be saturated to its maximum level resulting in excessive image noise and adversely affecting the image quality (Goo and Suh 2006b; Israel et al. 2008). The most practical solution to this problem is to use a lower pitch value. Other important measures to decrease radiation dose of pediatric cardiac CT include confining the study to the anatomical area of interest, avoiding multiphase examinations, and using iterative or other noise-reducing reconstruction algorithms (Goo 2012). In the contemporary MDCT era, a greater contribution of unnecessary over-ranging effect should be seriously considered particularly in CT examinations with a shorter scan range, such as pediatric cardiac CT, (Tzedakis et al. 2007) and volumetric axial scan modes with wide array detector configurations (Kroft et al. 2010) or adaptive section collimation should be used to reduce the over-ranging if applicable (Deak et al. 2009).

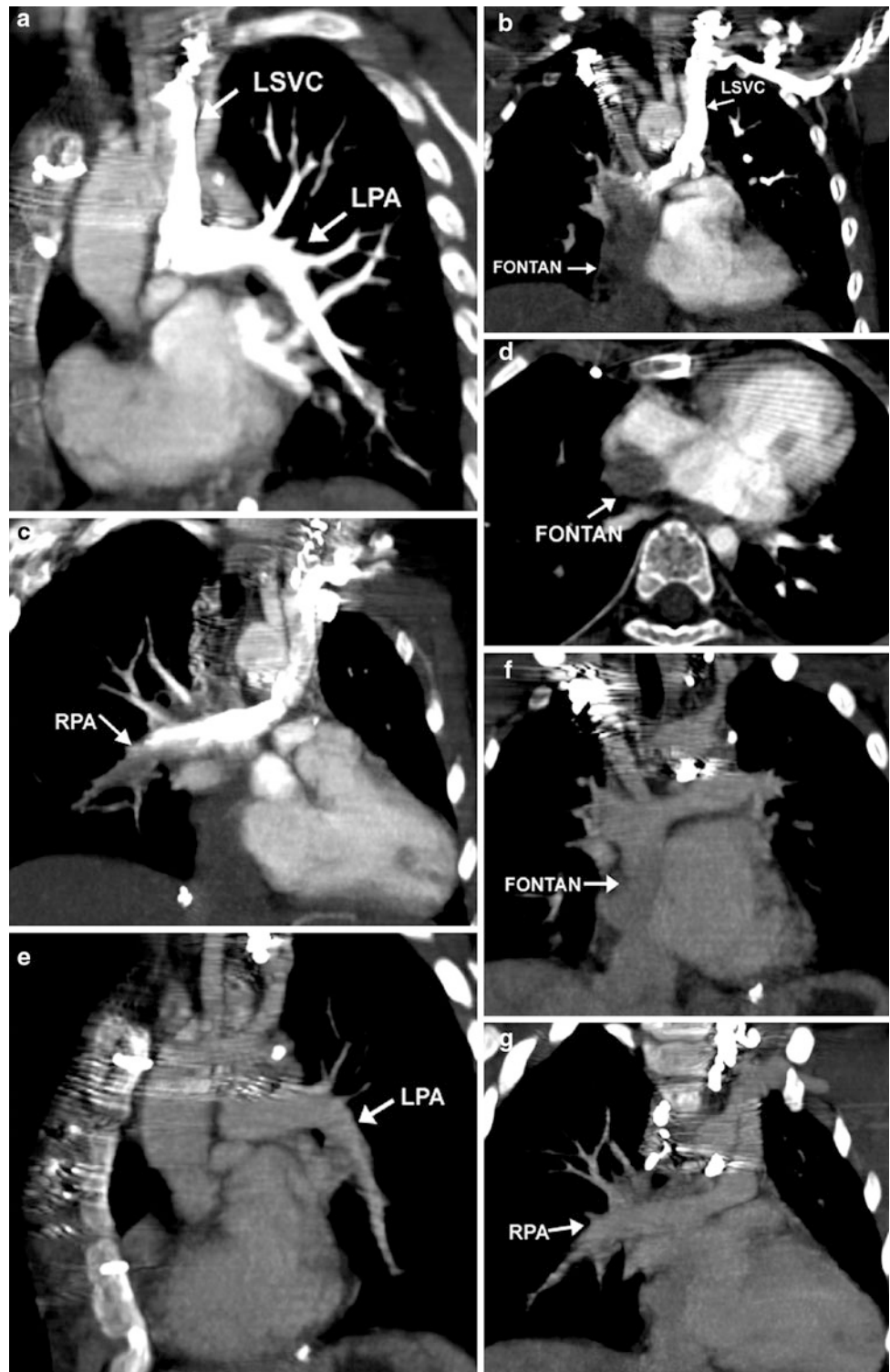
ECG-controlled tube current modulation is a technique available to reduce the radiation dose associated with retrospective gating (Jakobs et al. 2002). In those cardiac phases that are not needed for image reconstruction with high quality, the tube current is reduced to 4–20 % of the initial setting. Cardiac phases demanding the full tube current for high image quality should be appropriately selected according to a patient's heart rate (Weustink et al. 2008).

By using available dose-reduction strategies simultaneously, the radiation dose of pediatric cardiac CT now can often be reduced to less than 1.0 mSv (Goo 2010a, 2011a).

## 2.4 Planning Scan Technique and Intravenous Contrast Injection

It is vital for the radiologist performing and interpreting pediatric cardiac CT to review any information pertaining to the child's form of CHD and surgical repair or palliation prior to scanning. The knowledge helps the radiologist determine scan and intravenous (IV) injection protocols to best visualize anatomic substrates of the child. In addition, the ability of a child to follow breathing instructions is important to determine scan technique. The ultimate goal of IV contrast injection in pediatric cardiac CT is to obtain homogeneous enhancement of cardiovascular structures included in the scan range as much as possible because single-phase scanning should demonstrate all of them clearly to minimize radiation dose. However, homogeneous enhancement on pediatric cardiac CT is not always attainable, particularly in cases with complicated anatomy such as a Fontan pathway (Fig. 2). For optimal enhancement of a Fontan pathway, simultaneous IV injection of 50 % diluted

**Fig. 2** Lack of opacification of the Fontan pathway during arterial phase of scanning. Coronal and axial oblique MIP images demonstrate dense contrast in the LPA via a *left* sided SVC after a *left* arm injection (a). The Fontan pathway from the IVC (b, d) and the distal RPA (c) are incompletely opacified. Coronal oblique images reconstructed from the venous phase demonstrate homogeneous opacification of the LPA (e) Fontan pathway (f), and RPA (g)



or undiluted contrast agent via upper and lower extremities has shown good results (Greenberg and Bhutta 2008; Prabhu et al. 2009; Goo 2011b). Inhomogeneous cardiovascular enhancement may be contradictorily helpful to demonstrate hemodynamic findings, such as collateral vessels and contrast jet through a defect (Goo 2011c).

IV injection rates in children should necessarily be adjusted depending on the size of the IV catheter able to be placed and the amount of contrast to be injected (usually in the range of 1–2 ml/kg). Table 1 provides a guideline for contrast injection rates by size of the IV catheter. The optimal scan delay from the start of IV injection is usually



**Table 1** Maximal intravenous contrast injection rates

Catheter size (g)	Flow rate (cc/s)
18	5–6
20	4–5
22	3–4
24	1–2

determined by using bolus tracking. As compared with a biphasic IV injection protocol, a triphasic protocol, in which undiluted contrast agent is followed by 50–60 % diluted contrast agent and then by a saline chaser, can not only provide improved enhancement of the right heart, but also reduce perivenous contrast artifacts (Litmanovich et al. 2008).

### 3 Complementary Role of MDCT and MRI for Cardiac Imaging

The complementary role of MDCT and MRI for noninvasive cardiac imaging in children with CHD should be clearly recognized. Relative merits and demerits of the two imaging modalities are summarized in Table 2. Recent technical developments in pediatric cardiac CT have changed the complementary role between MDCT and MRI to some extent. Although cardiac MRI techniques have also advanced, major limitations of cardiac MRI particularly in young children are still remained to be overcome: limited accessibility to MRI scanners for pediatric cardiovascular examinations in many hospitals and institutions, longer examination time, more requirement of sedation or anesthesia, and technical expertise to perform routine quality examinations. For the initial evaluation of CHD in infants and young children, echocardiography often provides a complete assessment of intracardiac morphology, flow, and ventricular function. However, echocardiography is limited in evaluating extracardiac structures and may not adequately show intracardiac and coronary artery anatomy. Cardiac CT may be helpful to compensate for these blind spots of echocardiography. Consequently, pediatric cardiac CT is increasingly used as a complementary imaging modality in many institutions before and after surgical correction in young children with CHD. On the other hand, cardiac MRI or invasive cardiac catheter angiography is seldom mandatory for surgical planning in these patients.

As evaluation with echocardiography becomes increasingly more difficult in older and larger patients who have had multiple cardiothoracic surgeries, cardiac MRI is regarded as the noninvasive imaging method of choice for serial follow-up examinations in patients with repaired CHD. Examples include patients with repaired tetralogy of Fallot (TOF), patients with a systemic right ventricle

following the Senning or Mustard operation, and functional single ventricle patients following the Fontan operation. Unfortunately, the image quality of cardiac MRI may be considerably compromised by susceptibility artifact from the previously placed embolization coils, stents, and occlusion devices. In addition, indwelling pacemakers and AICD devices remain contraindications for MRI. On these occasions, cardiac CT may be considered as an alternative imaging method. In fact, cardiac CT is the diagnostic imaging method of choice in assessing vascular stent patency (Eichhorn et al. 2006) (Fig. 3).

## 4 Clinical Applications

### 4.1 Pulmonary Vasculature

#### 4.1.1 Pulmonary Arteries

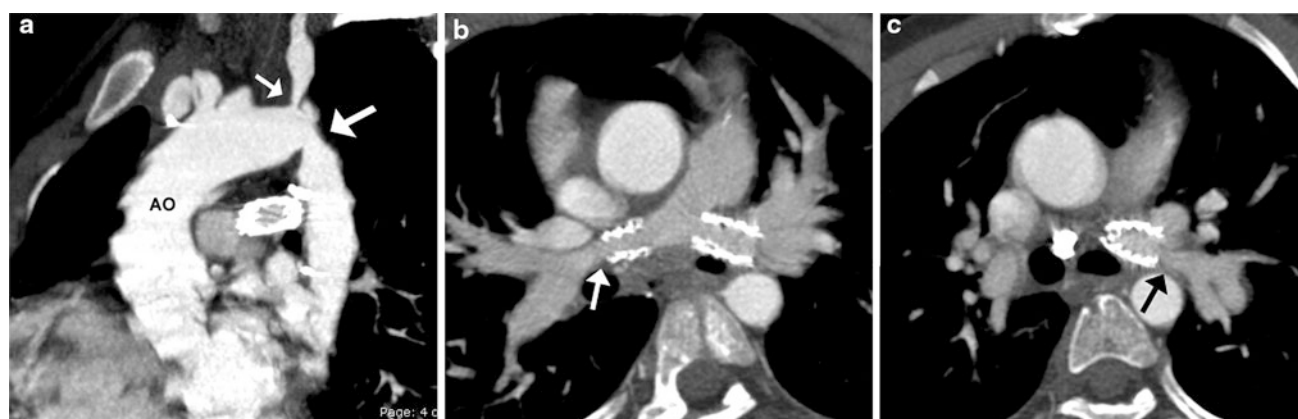
In patients with TOF with pulmonary atresia, precise pre-operative delineation of the presence, size and confluency of the pulmonary arteries, and major aortopulmonary collateral arteries (MAPCAs) is necessary for surgical planning. This diagnostic task can be readily accomplished with cardiac MDCT (Goo et al. 2005a; Greil et al. 2006) (Fig. 4). As a result, the procedure time of catheter angiography and possibility of overlooked MAPCAs can be substantially reduced. Nonetheless, conventional catheter angiography is necessary for identifying communications between pulmonary arterial feeders. Abnormalities of the branch pulmonary arteries that are well depicted on MDCT include an abnormal origin or course such as in truncus arteriosus or pulmonary artery sling (Fig. 5). The branch pulmonary arteries can be atretic, stenotic, or hypoplastic related to decreased blood flow during growth (Fig. 6), extrinsic compression, or as a result of a surgically altered course or anastomosis such as a palliative shunt between the systemic and pulmonary artery circulation (Fig. 7).

#### 4.1.2 Pulmonary Embolism

Pulmonary embolism (PE) is an uncommonly diagnosed condition in children. The clinical presentation is often subtle because symptoms are nonspecific and can be masked by the underlying clinical condition. Delays in diagnosis are frequent because definite signs of associated pulmonary or cardiac dysfunction appear to be less common in children than in adults. Specific risk factors for PE in the pediatric patient include associated deep venous thrombosis, indwelling central venous catheters, cardiac surgery, thrombotic disorders, vascular malformations, and malignancy and multiple factors are often present in the same patient (Babyn et al. 2005). PE may complicate CHD particularly after surgical treatments, such as cavo-pulmonary connections (Fig. 8). Diagnostic strategies for

**Table 2** Complementary role of MDCT and MRI for cardiac imaging

	MDCT	MR
Need for sedation	Sedation required in many patients <4 years	Sedation or GA needed in most patients <7 years
Duration of sedation	Very short	Long
IV contrast	Risk of allergic reaction, renal dysfunction	Risk of nephrogenic systemic fibrosis
Spatial resolution	Better. True isotropic resolution	Good. Near isotropic resolution
Temporal resolution	Good	Better
Dynamics on angiogram	Multiple dynamics possible, but not preferred in children due to radiation risk	Multiple dynamics routinely performed, with separation of right and left-sided and venous structures
Flow quantification	Not currently possible	Many applications: stroke volume, Qp:Qs, regurgitant fraction, gradient measurement through stenosis
Ventricular function	Adequate temporal resolution	Better temporal resolution
Imaging time	Very short (<1 min)	Long (30–60 min)
Contraindications	Acute renal failure	Pacemakers, AICD
Compatibility with coils, stents, and metallic prosthesis	Metal causes artifact, worse with platinum. Best non-invasive means of evaluating stent patency	Unable to assess patency of stents and metallic prostheses due to artifact. Steel coils cause most artifact. Platinum coils cause minimal artifact
Health risks	Radiation	Over-heating of the body
Post processing techniques	3D volume rendering, MIP, MPR	Similar
Ideal indications	Coronary stenosis imaging, anomalous coronaries, emergent studies like aortic dissection or occluded BT shunt, pulmonary embolism, airway evaluation, need to avoid sedation	Conditions requiring serial studies, screening studies, or conditions requiring evaluation of flow, valvular and ventricular function, and chamber morphology

**Fig. 3** TOF and coarctation status post repair. Sagittal oblique MIP image (a) shows recurrent stenosis at the aortic isthmus (*large arrow*) and proximal *left* subclavian artery (*small arrow*) following an end-to-

end anastomosis for coarctation repair. Oblique axial MIP images show patent bilateral proximal branch PA stents with narrowing of the RPA (*arrow* in b) and LPA (*arrow* in c) distal to the stents

detection and treatment of PE in children are mostly extrapolated from evidence that has been compiled in the adult literature.

CT has become the first choice of imaging modalities for detection of PE in symptomatic patients. MDCT has led to improved visualization of peripheral pulmonary arteries for detection of small emboli (Lee et al. 2011), and conventional pulmonary angiography is now rarely performed. Once regarded as the best first noninvasive study for the diagnostic work-up of PE, nuclear medicine

perfusion scintigraphy is also now infrequently requested because as many as 73 % of studies are interpreted as indeterminate (PIOPED 1990) and have poor interobserver correlation (Blachere et al. 2000), and there is limited ability to make alternative diagnoses. Despite excellent diagnostic accuracy of MDCT in detecting PE, thromboembolic risk factors should be used as a first-line triage tool to guide more appropriate use of CT pulmonary angiography in children, with associated reductions in radiation exposure and costs (Lee et al. 2012).

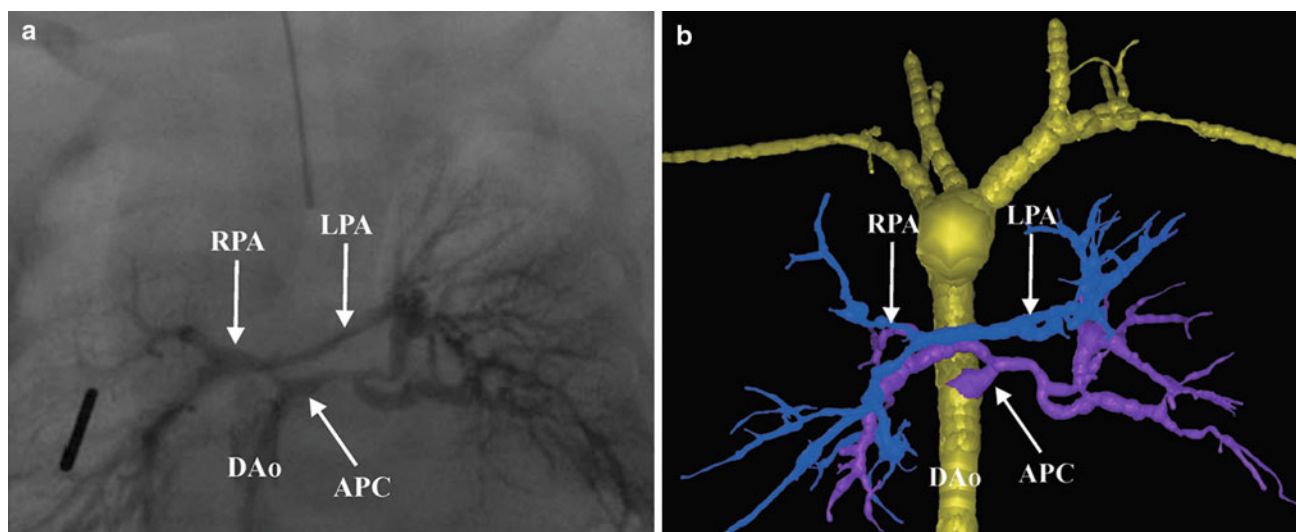


**Fig. 4** Tetralogy with pulmonary atresia and MAPCAs. Segmented 3D surface model from MDCT angiography demonstrates a collateral (APC) from the descending aorta (DAo) to the *left* and *right* lung

connecting to the hypoplastic *left* (LPA) and *right* (RPA) pulmonary arteries (a). Corresponding X-ray angiogram (b) (Greil et al. 2006, used with permission)

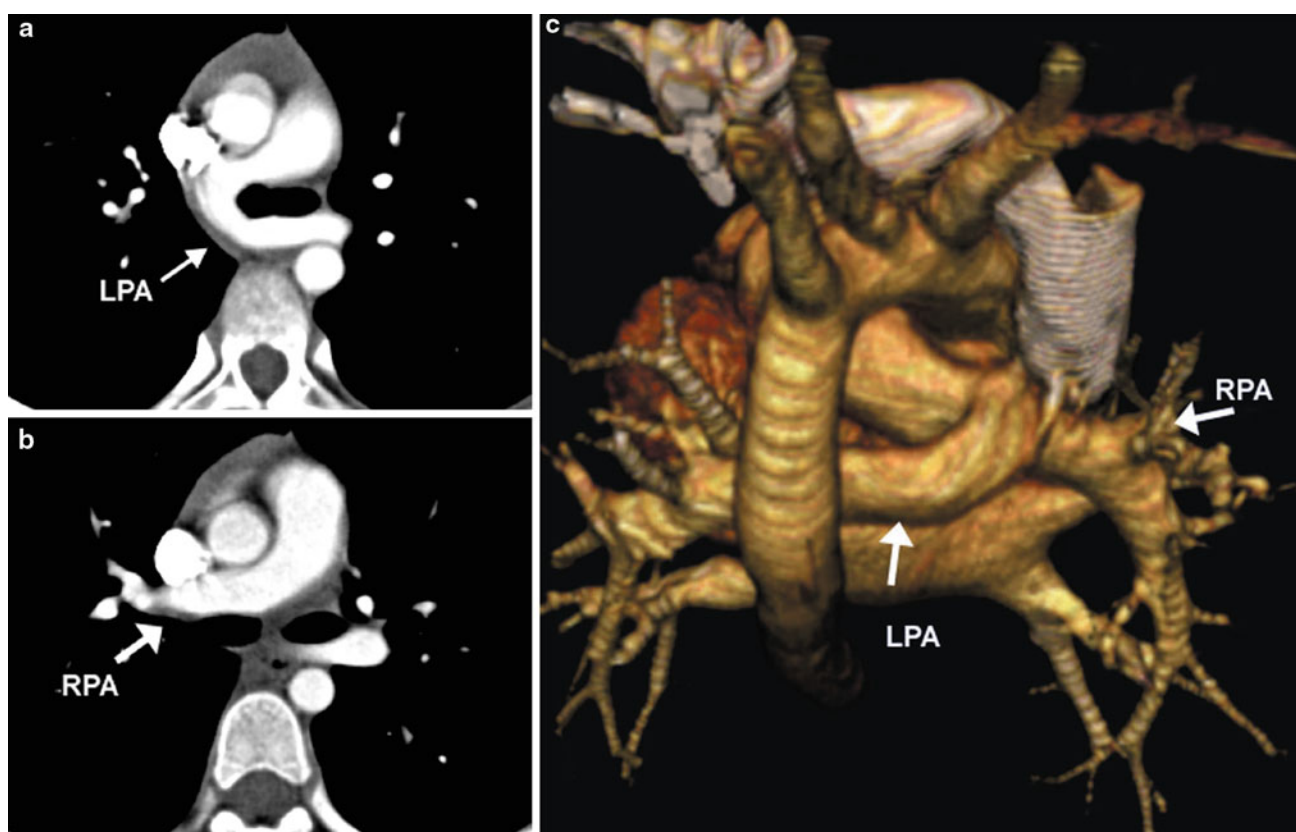


**Fig. 5** Pulmonary artery sling. Axial MDCT images demonstrate the LPA (a) arising from the RPA (b) and passing posterior to the carina. A 3D volume rendered posterior image (c)



**Fig. 6** Branch pulmonary artery stenosis. Axial oblique MIP image (a) and volume rendered image (b) demonstrate a juxta-ductal stenosis (arrow) and kinking of the LPA

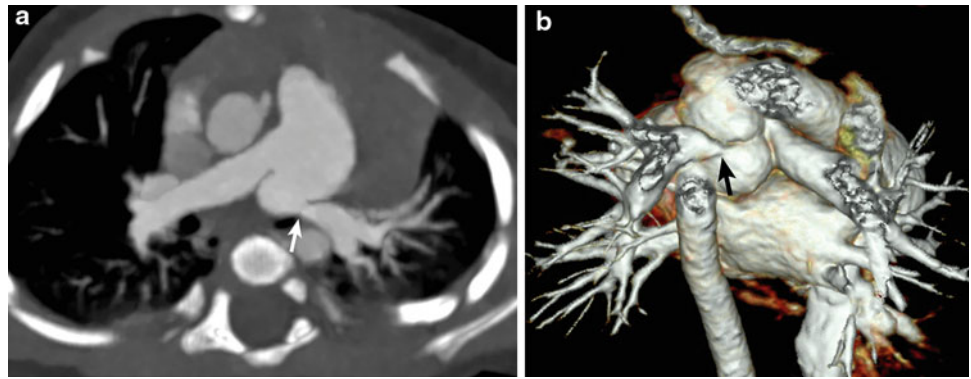
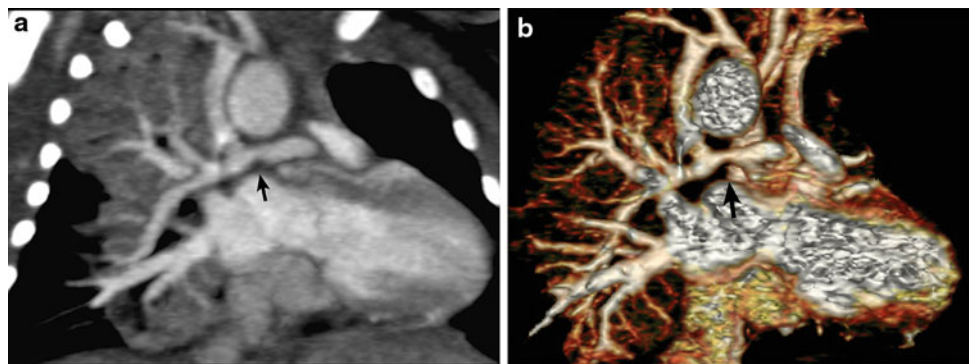


**Fig. 7** Functional single ventricle status post *right* modified BT shunt. Coronal oblique MIP image (a) and volume-rendered image (b) show a stenosis of the RPA (arrow) proximal to the shunt



MDCT angiography findings of acute pulmonary embolism include intraluminal filling defects in the main and branch pulmonary arteries that can partially or completely fill the lumen (Fig. 9). When the embolus completely fills the lumen of a branch pulmonary artery, the artery can enlarge relative to similar-sized arteries in the hilum. Lung parenchymal findings with PE include peripheral wedge-shaped opacities, hyperlucency, and mosaic perfusion. Findings of acute right ventricular failure, such as right ventricular enlargement and septal flattening, may be present in severe cases.

A classic finding of chronic PE is an intraluminal filling defect that makes an obtuse angle with the vessel wall and creates an appearance of asymmetric wall thickening (Fig. 10). Contrast-enhanced peripheral arteries can have irregular wall thickening related to recanalization and the residual thrombus may be calcified. Enlarged bronchiolar and systemic collateral arteries can also be seen in association with chronic PE.

Recently, dual-energy CT scanning enables us to evaluate PE and lung perfusion defects at the same time (Fig. 11). In addition to the accurate diagnosis of PE, pulmonary blood volume assessment using dual-energy CT can predict right heart strain and clinical outcome (Bauer et al. 2011). This emerging CT imaging technique for evaluating PE may also be useful in pediatric patients (Goo 2010b; Zhang et al. 2012).

#### 4.1.3 Pulmonary Veins

MDCT angiography is quite useful and accurate in evaluating anomalous pulmonary venous connections when echocardiography is limited in fully identifying types and obstructions of these total or partial anomalous pulmonary venous connections (Kim et al. 2000). When associated with CHD, pulmonary vein stenosis (PVS) is most often extrinsic due to compression by other vascular structures, or associated with the site of a prior surgical anastomosis (Fig. 12). PVS can rarely be intrinsic and rapidly progressive and refractory to all forms of treatments (Latson and Prieto 2007; Devaney et al. 2006). Progressive PVS can occur in children with or without CHD and MDCT can assess PVS noninvasively and accurately (Ou et al. 2009).

Congenital pulmonary venolobar syndrome or scimitar syndrome is a heterogeneous group of congenital anomalies of the thorax that may occur singly or in combination. The main components of the congenital pulmonary venolobar syndrome are hypogenetic lung (lobar agenesis, aplasia, or hypoplasia), partial anomalous pulmonary venous return, absence of a pulmonary artery, pulmonary sequestration, systemic arterialization of the lung, absence of the inferior vena cava (IVC), and accessory diaphragm (Konen et al. 2003). Horseshoe lung may be rarely associated with this syndrome (Goo et al. 2002). MDCT provides a complete evaluation of all pulmonary and systemic vascular,

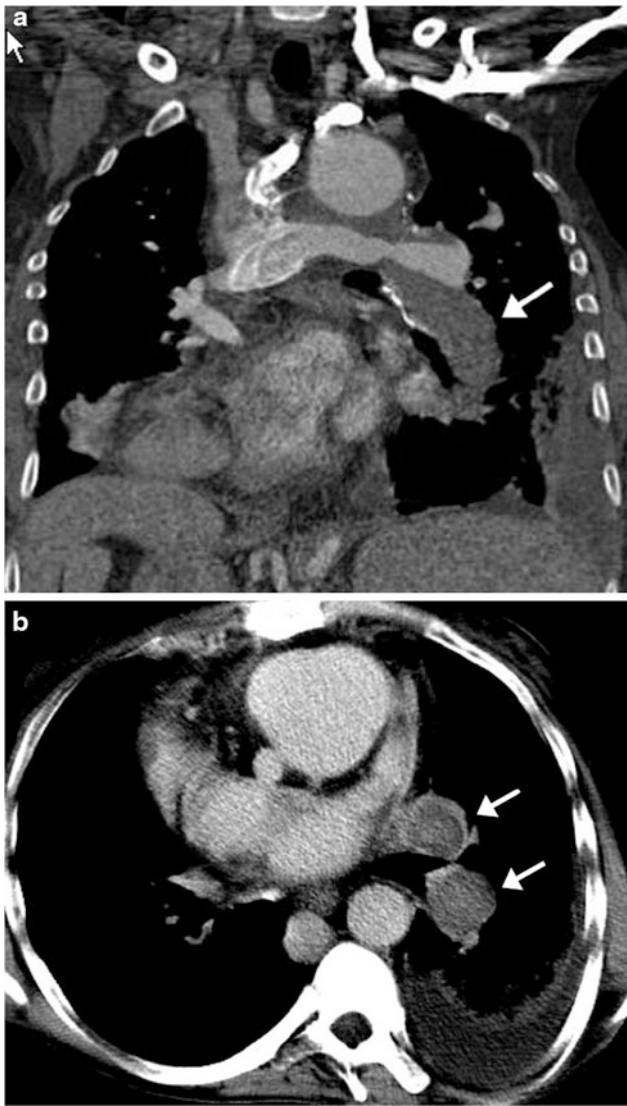


**Fig. 8** Coronal reformatted (a) and axial (b) images of a Fontan patient demonstrate extensive thrombus (arrows) extending from the Fontan pathway into the main and segmental branches of the LPA

tracheobronchial and pulmonary parenchymal anomalies, necessary in patients under consideration for surgical repair (Fig. 13).

## 4.2 Aorta

### 4.2.1 Coarctation of the Aorta

Coarctation of the aorta is a congenital obstructive aortic arch anomaly presenting with arch hypoplasia and focal narrowing of the aortic isthmus at the junction of the ductus arteriosus and the aorta. MDCT can demonstrate anatomic features of the anomaly and collateral arteries, if present (Fig. 14), that are helpful for optimal surgical planning. It should be noted that the anomaly is a dynamic process

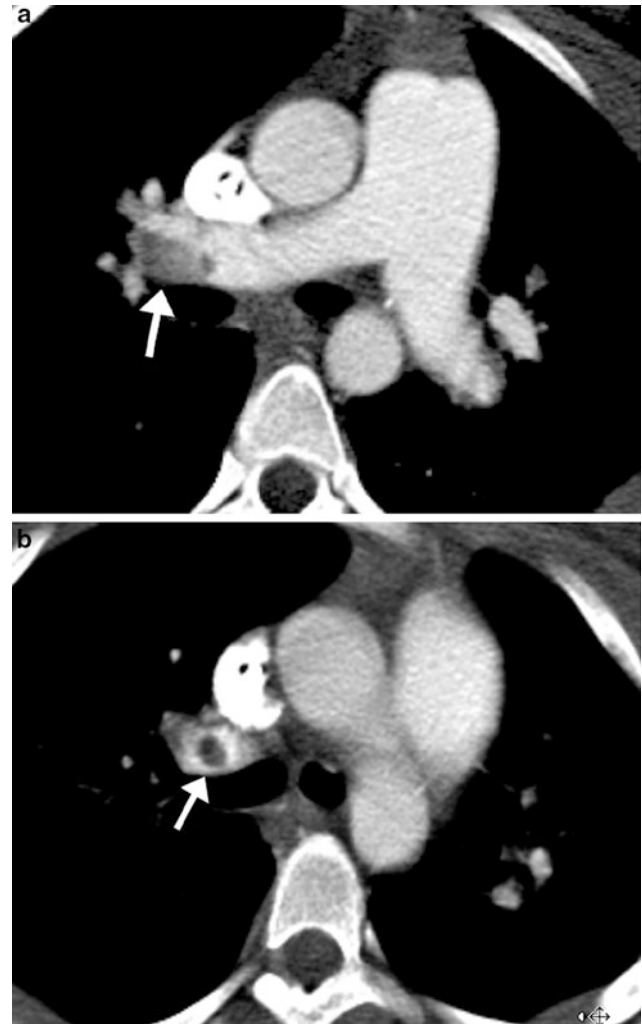


**Fig. 9** Acute pulmonary embolism. Axial images from an MDCT angiogram in a pediatric patient with respiratory distress demonstrate a well-defined filling defect in the distal RPA (arrow in a) extending into the upper lobe pulmonary artery (arrow in b)

showing progressive obstruction in young infants when the patent ductus arteriosus (PDA) is present. Following surgical repair of coarctation, MDCT can be used to detect residual stenosis, recoarctation, or aneurysm formation at the repair site. In order to avoid radiation exposure in children, MRI may be favored for long-term follow-up after surgical repair. MDCT is the imaging method of choice for evaluating associated airway abnormalities and in-stent stenosis after stent placement. In addition, MDCT is also useful for assessing early post-procedural complications, such as pseudoaneurysm formation and dissection (Fig. 15).

### 4.2.2 Interrupted Aortic Arch

Interrupted aortic arch (IAA) is a rare aortic anomaly defined as a complete luminal and anatomic discontinuity of the aortic arch. The anomaly is classified as three types depending on the site of interruption, i.e., distal to the subclavian artery in

**Fig. 10** Repaired tetralogy of Fallot status post pulmonary valve replacement with recurrent bacterial endocarditis. Oblique coronal CT images (**a**, **b**) demonstrate hypodense clot (arrow) making obtuse angle with the vessel wall in the descending branch of the RPA consistent with chronic pulmonary embolism

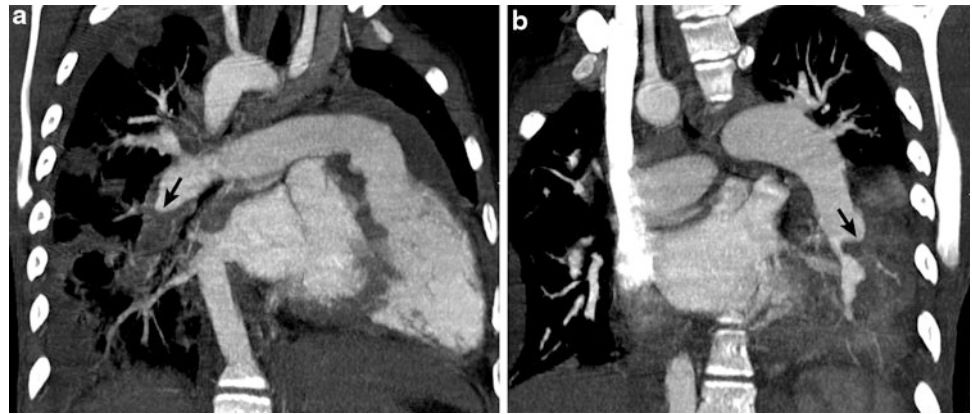


**Fig. 11** Dual-energy lung perfusion CT in a child with leukemia and pulmonary embolism. Coronal weighted-average CT image (**a**) shows an acute embolus (arrow in **a**) in the RPA. Coronal iodine map (**b**) reveals a well-circumscribed perfusion defect (arrows in **b**) in the right lower lung

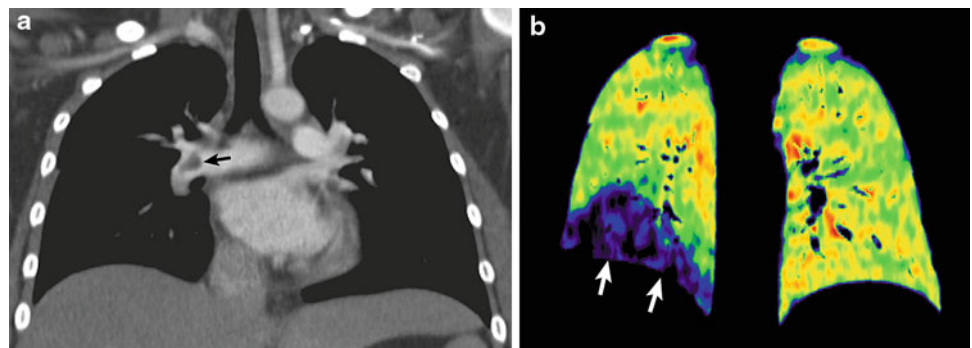
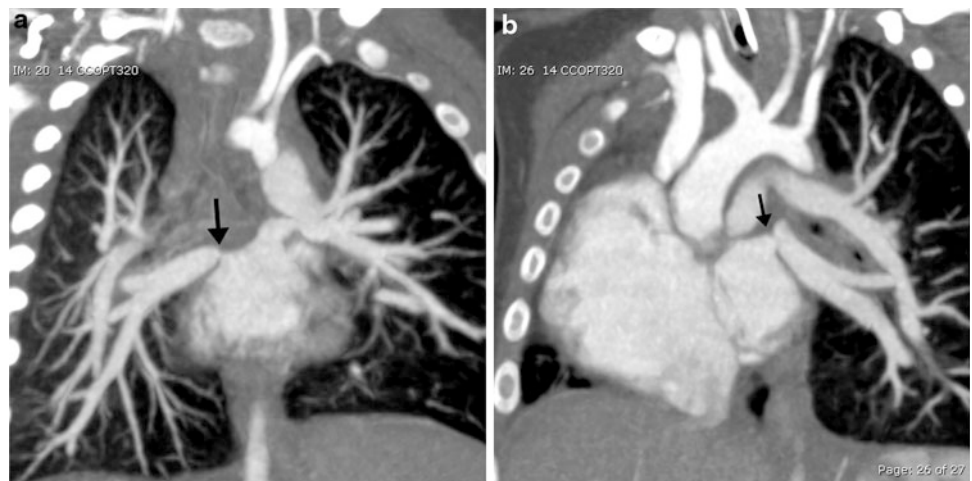


**Fig. 12** Total anomalous pulmonary venous return status post repair with pulmonary venous stenosis. Coronal oblique MIP images demonstrate focal stenosis (arrows) of the right (**a**) and left (**b**) pulmonary veins. (Courtesy of Sjik Westra)

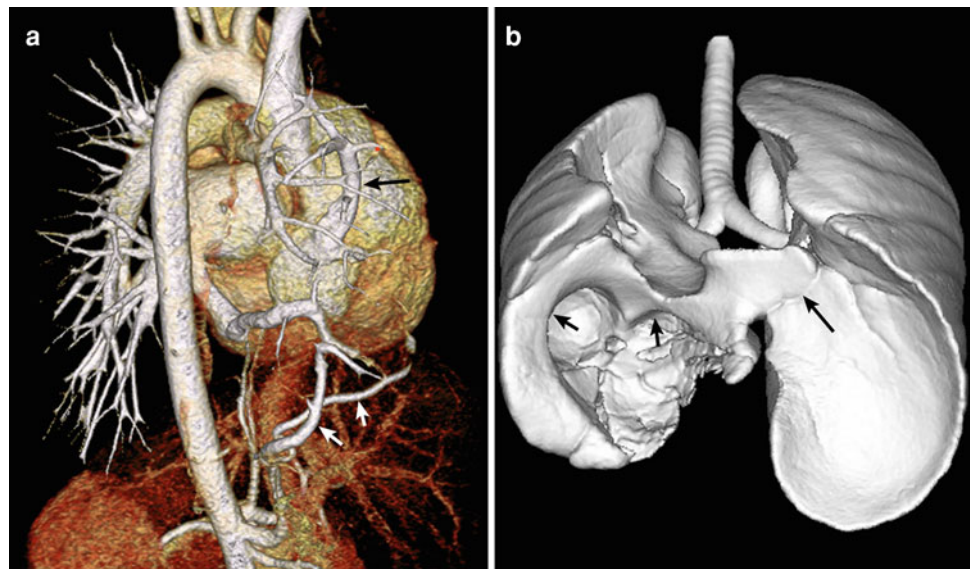


type A, between the second carotid and ipsilateral subclavian arteries in type B, and between two carotid arteries in type C. Type B is most common in the Western population (Fig. 16), while type A is most common in the Asian population (Lee et al. 2006). Each type may be further divided into three subtypes depending on the origin of the subclavian artery, i.e., normal in subtype 1, aberrant in subtype 2, and isolated in subtype 3. In addition to the anatomic types of IAA, cardiac CT may be used to evaluate the distance between the

proximal and distal segments of IAA, the sizes of a PDA, the aorta and the thymus, the presence of subaortic stenosis, and other cardiac defects (Yang et al. 2008). In IAA, a right aortic arch is almost always associated with DiGeorge syndrome and/or chromosome 22q11 deletion (McElhinney et al. 1999b). As in coarctation of the aorta, IAA may be associated with the bicuspid aortic valve and other components of Shone complex including supravalvular mitral membrane, parachute mitral valve, and subaortic stenosis.



**Fig. 13** Scimitar syndrome. Volume-rendered CT image (a) shows partial anomalous pulmonary venous return of the right upper pulmonary vein to the right atrium (long arrow in a). Systemic collateral arteries supplying the right lower lung (short arrows in a) is also depicted. Shaded surface display CT image (b) reveals right lung hypoplasia, horseshoe lung (long arrow in b), and right diaphragmatic hernia (short arrows in b)



#### 4.2.3 Valvular and Supravalvular Aortic Stenosis

Valvular aortic stenosis occurs in approximately 3–6 % of patients with CHD and is often associated with a congenital bicuspid aortic valve. Although the effective valve area can be reduced at birth, the stenosis of a bicuspid valve is progressive and clinical symptoms do not usually develop until young adulthood. MDCT is seldom used for evaluating valvular aortic stenosis because anatomic details of the aortic valve in children are not well-seen on CT and high radiation dose is necessary for the complete assessment of the aortic valve. The surgical approach to aortic valve replacement for severe congenital aortic stenosis in young patients is difficult because placement of a mechanical valve is not a good option because of the risk of long-term anti-coagulation. Other options include placement of homograft or xenograft valves. In the Ross procedure, the stenotic aortic valve is replaced with the patient's pulmonary valve, and a right ventricle to pulmonary artery conduit is placed.

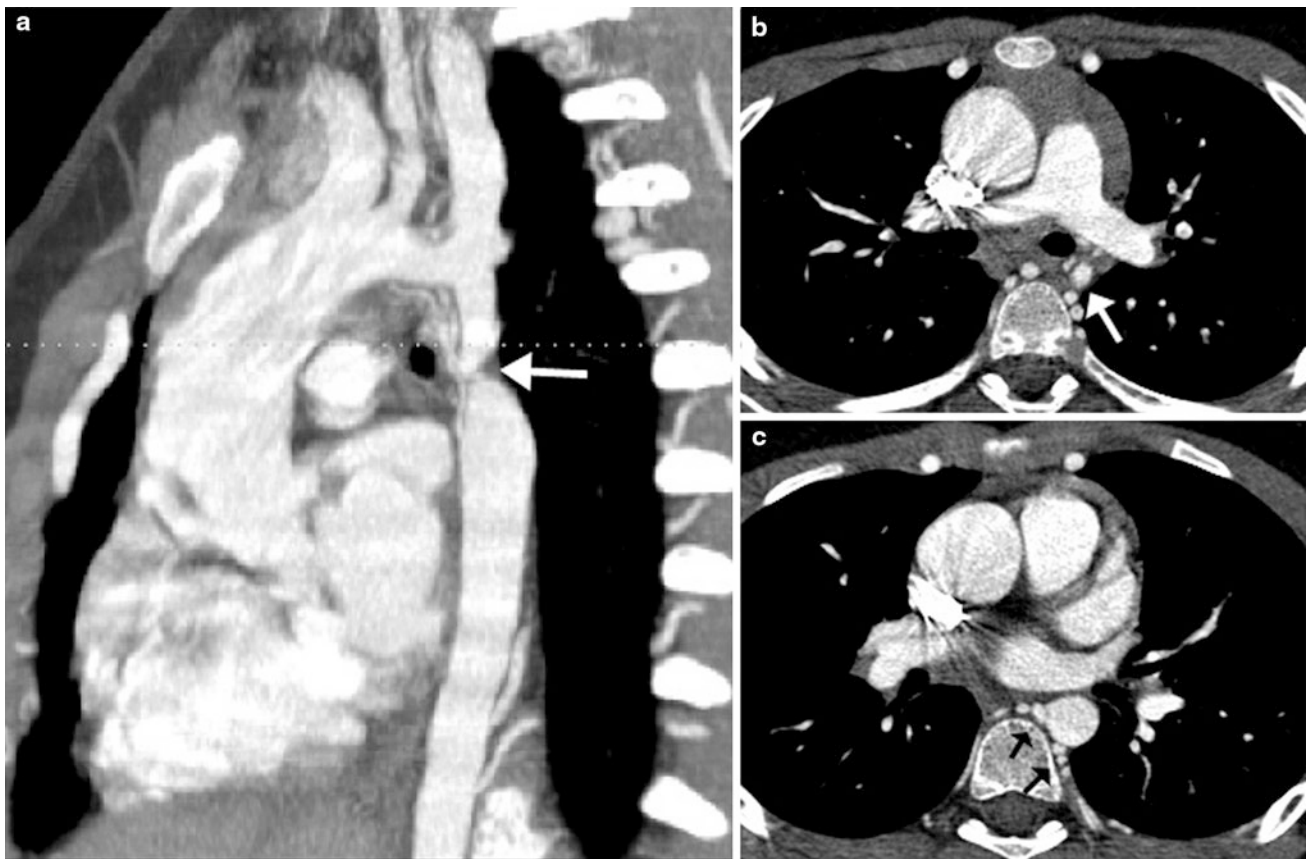
Supravalvular aortic stenosis (SVAS) may be non-syndromic or associated with Williams syndrome. ECG-synchronized cardiac CT can show not only SVAS, but also the bicuspid aortic valve, dilated coronary arteries, coronary ostial stenosis, and left ventricular hypertrophy (Liu et al. 2007). SVAS may be focal (the “hourglass” appearance) (Fig. 17) or diffuse (10–30 % of cases), starting at the sino-tubular junction. Aortoplasty is indicated in symptomatic patients or in those with a transaortic valve gradient greater than or equal to 50 mmHg (Scott et al. 2009).

#### 4.2.4 Connective Tissue Disorders

Marfan syndrome and type IV Ehlers-Danlos syndrome are connective tissue disorders that can have cardiovascular manifestations. Both are associated with cystic medial necrosis of the aortic wall, which adversely affects the ability

of the aortic wall to withstand systemic pressures, leading to dilatation. The characteristic findings of the aorta include dilatation of the aortic root and proximal ascending aorta and effacement of the sino-tubular junction. The dilatation of the aortic root results in suboptimal coaptation of the aortic valve cusps, which can lead to aortic regurgitation that can further weaken the aortic wall as more throughput volume is needed to maintain cardiac output. Both echocardiography and MRI can be used for serial follow-up of ascending aorta size and aortic regurgitation in patients with Marfan syndrome. CT may be used in some patients with severe chest wall deformity limiting echocardiographic evaluation or who cannot tolerate lengthy MRI evaluation (Ha et al. 2007). In general, when the maximum diameter of the ascending aorta is 1.5 times that of the descending thoracic aorta at the level of the diaphragm, an aneurysm is considered to be present. In addition to the maximal diameter of the aortic root, its growth rate should be considered in determining the optimal timing for surgical replacement of the aortic root and/or ascending aorta. Serious complications of Marfan's or type IV Ehlers-Danlos syndrome include dissection and rupture of the ascending aorta (Fig. 18). Although transesophageal echocardiography (TEE) or MRI could be performed urgently if dissection is suspected, MDCT angiography with multiplanar reconstruction is a highly sensitive and specific technique for the detection and characterization of the extent and orientation of the intimal flap, delineation of the true and false lumens, presence of intramural hematoma, and involvement of the major aortic branches and coronary arteries (McMahon and Squirrell 2010).

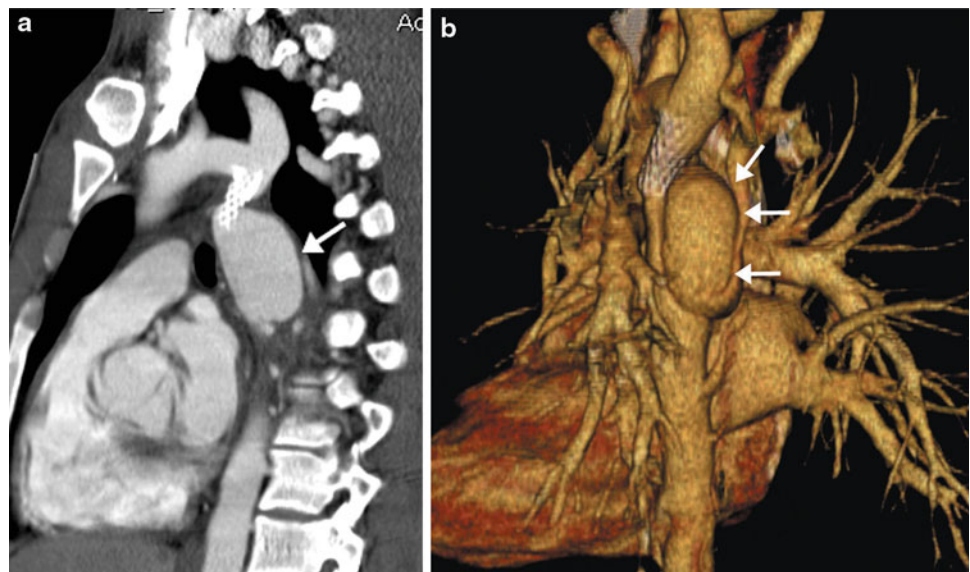
Progressive aneurysmal dilatation of the aorta may also be seen in children with other congenital connective tissue disorders, such as Loeys-Deitz syndrome (Kalra et al. 2011) and arterial tortuosity syndrome (Kalfa et al. 2012).



**Fig. 14** Coarctation with transverse arch hypoplasia. Sagittal oblique MIP image (a) demonstrates a severe discrete narrowing (arrow) of the aortic isthmus. Axial reformatted images show the markedly small

caliber of the isthmus (arrow in b) and numerous dilated intercostal collaterals joining to the proximal descending aorta (arrows in c) (Courtesy of Shi-Joon Yoo)

**Fig. 15** Dissection and pseudoaneurysm of the thoracic aorta following balloon dilatation and stenting of coarctation. Oblique sagittal MIP (a) and volume rendered (b) images demonstrate a stent at the aortic isthmus with a dissection and large pseudoaneurysm (arrow) protruding from the aorta. The patient required an additional covered stent to be placed which closed the entrance of the pseudoaneurysm into the thoracic aorta. The pseudoaneurysm was shown to be thrombosed on subsequent imaging





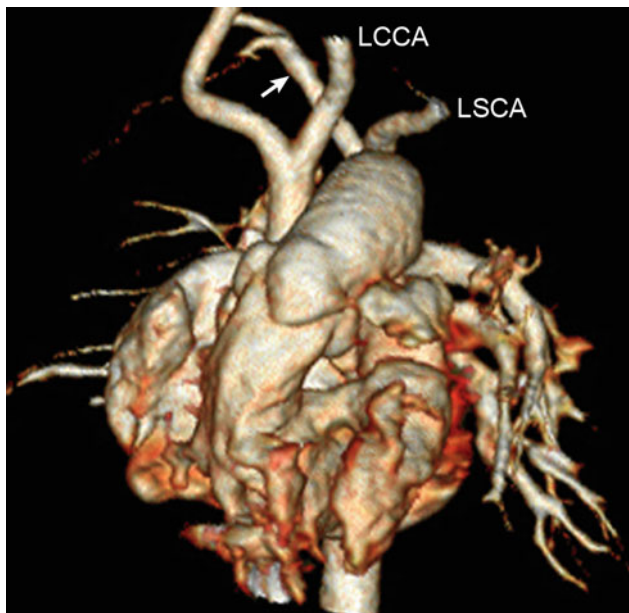


**Fig. 16** Interrupted aortic arch type B2. Volume-rendered CT image shows interruption of aortic arch between the *left* common carotid artery (LCCA) and the *left* subclavian artery (LSCA). Aberrant *right* subclavian artery (arrow) is noted

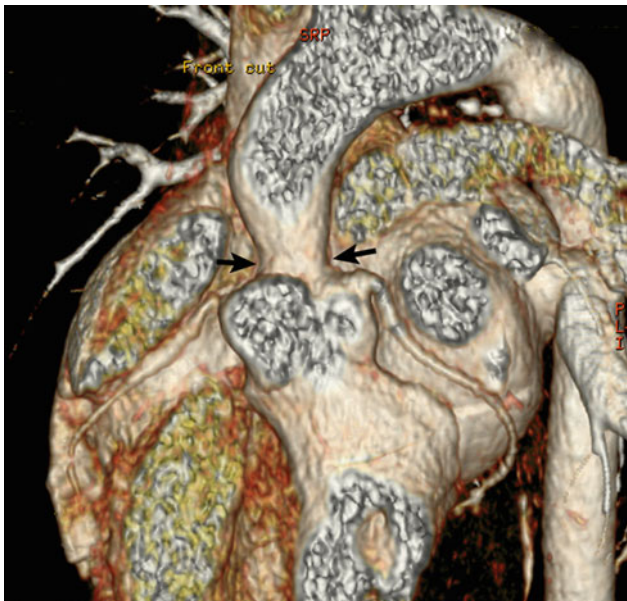


**Fig. 17** Supravalvular aortic stenosis in Williams syndrome. Volume-rendered CT image shows a focal stenosis at the sinotubular junction (arrows). In addition, there is no evidence of coronary ostial stenosis

#### 4.2.5 Takayasu Arteritis

Takayasu arteritis is a progressive large vessel vasculitis that affects the aorta and its major branches as well as the coronary and pulmonary arteries. The accurate diagnosis of the disease depends on imaging studies because the clinical

and laboratory presentation at disease onset is often non-specific. In the early, systemic phase of inflammation, both CT (Zhu et al. 2012) and MRI (Choe et al. 2000) can detect wall thickening and enhancement of the involved vessels and can be used to follow-up response to high-dose steroid therapy. If the disease is not detected and treated early, transmural fibrosis of the vessel wall can lead to the characteristic findings of the late phase, including stenosis, occlusion, mural calcification, intraluminal thrombus, or aneurysmal dilatation of the affected artery (Fig. 19). Both MRA and MDCT angiography can be used for noninvasive detection of the sequelae of chronic disease. Takayasu disease is often recurrent and the timing of progression from early to late phase of disease can be variable, so that early and late findings can be detected concurrently. Children with Takayasu arteritis are more often diagnosed and followed with MRI (Aluquin et al. 2002). CT is more useful for diagnosis of early complications following surgical bypass or transcatheter stenting of vasculitis-induced stenosis, including development of pseudoaneurysms, graft infection, thrombosis, and restenosis.

### 4.3 Coronary Artery Anomalies

Congenital anomalous coronary arteries, although rare, are a well-recognized cause of myocardial ischemia and sudden death in children and young adults, with a much higher prevalence in patients with CHD, especially TOF and transposition of the great arteries (TGA). Hemodynamically significant coronary artery anomalies include anomalous origin from the pulmonary artery, anomalous origin from the opposite sinus of Valsalva with an interarterial course, intramural origin, myocardial bridging, and coronary artery fistula (Goo et al. 2009). Hemodynamically benign anomalies, such as high take-off and multiple ostia, often have clinical significance in patients with CHD (Goo et al. 2009; Tsai et al. 2010). In patients with CHD, certain coronary artery anomalies should be specifically recognized before surgery (Goo et al. 2009).

Echocardiography with color Doppler has replaced cardiac catheterization as the standard method of visualizing the proximal coronary arteries in infants and children (Satomi et al. 1984), but further evaluation with CT or MRI is often necessary to increase diagnostic confidence. Albeit useful in assessing coronary artery anomalies, MRI is still limited in assessing coronary arteries in young infants and distal segments in children mainly due to low spatial resolution (Tangcharoen et al. 2011). In addition, MRI evaluation of coronary arteries is relatively time-consuming. In contrast, MDCT considerably increases coronary artery visibility even without ECG synchronization (Goo et al. 2005b). Nevertheless, ECG-synchronized CT scanning



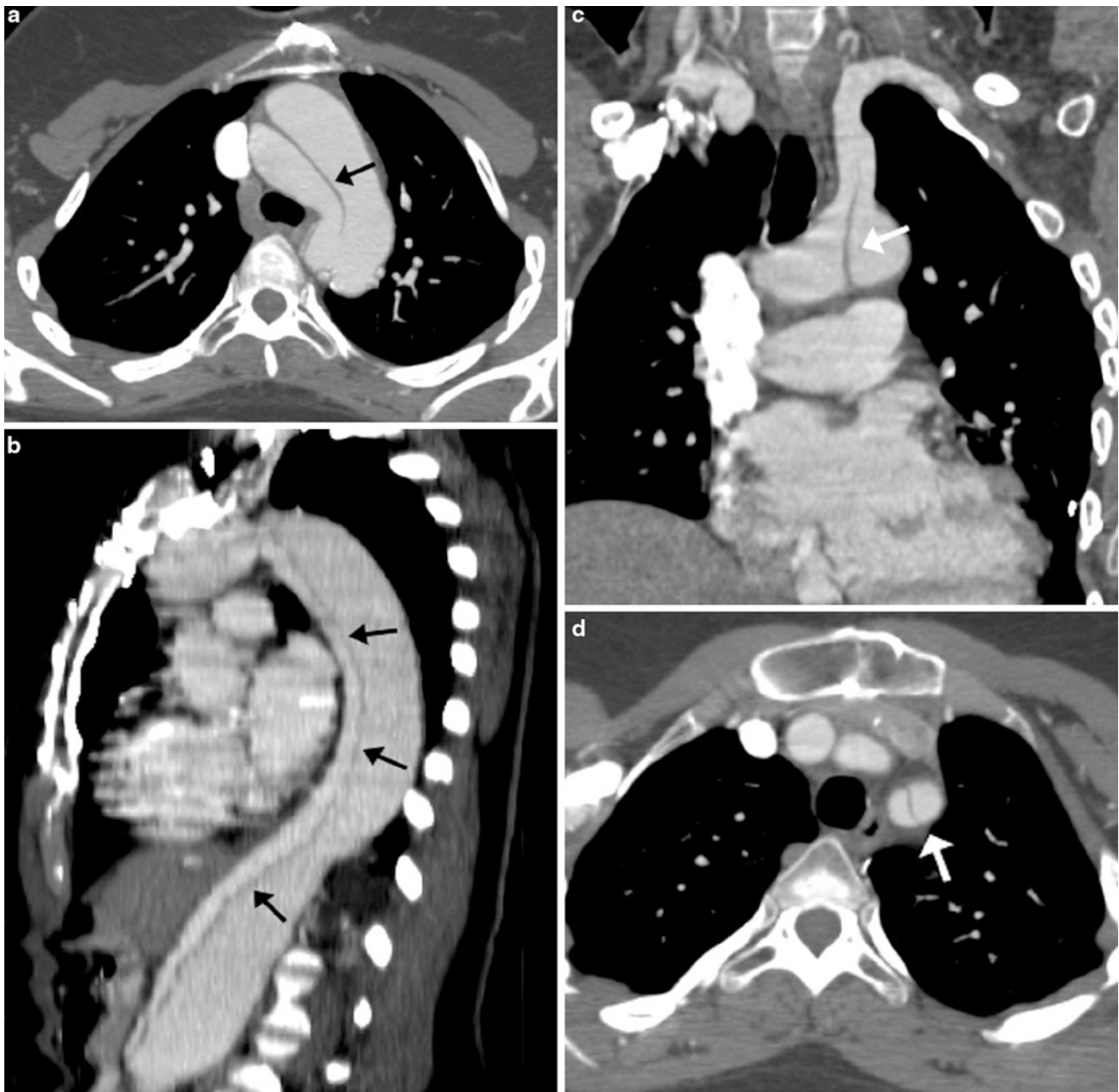


**Fig. 18** Aortic dissection in Marfan syndrome. Extensive dissection of the thoracic aorta in a teenager who subsequently had the ascending and descending thoracic and abdominal aorta replaced. Oblique MIP

images demonstrate the dissection involving the transverse arch (arrow in **a**), extending into the thoracic and abdominal aorta (**b**), and also extending into the *left* subclavian artery (arrows in **c**, **d**)

should be used for evaluating coronary artery anomalies (Tsai et al. 2007; Ben Saad et al. 2009; Goo and Yang 2010). MDCT is particularly advantageous in patients presenting with acute symptoms including palpitations, dizziness, atypical or typical exertional chest pain, and dyspnea on exertion, especially in young athletes (Deibler et al. 2004). These coronary artery anomalies can be reliably detected on ECG-synchronized cardiac CT (Figs. 20 and 21).

#### 4.3.1 Kawasaki Disease

Kawasaki disease is a vasculitis of unknown origin that occurs most often in young children. It begins as a pancarditis with vasculitis of small vessels (stage 1), progresses to vasculitis of the epicardial coronary arteries (stage 2), followed by resolution of vascular inflammation with decrease in size of the aneurysms (stage 3), and scarring of the coronary arteries with stenoses (stage 4) (Fujiwara and Hamashima



**Fig. 19** Takayasu arteritis and coarctation status post balloon dilatation and stenting. Sagittal oblique MIP image demonstrates a stent at the aortic isthmus and diffuse calcification (*large arrows*) of the aortic wall consistent with chronic arteritis. The proximal *left* common carotid and subclavian arteries are moderately stenotic and ectatic (*small arrows*)

1978). Coronary artery aneurysms can develop in up to 15–25 % of untreated cases and can be associated with thrombotic events leading to myocardial ischemia and infarction later in their life (Kato et al. 1996). In addition to the standard initial therapy with intravenous gamma-globulin and high dose aspirin, infliximab and steroids are promising new therapies potentially further reducing incidence of coronary artery abnormalities (Dominquez and Anderson 2013). Now we have an increasing chance to see adult patients with cardiovascular sequelae from Kawasaki disease because only recently have these patients reached adulthood (Daniels et al. 2012). Serial follow-up of patients with Kawasaki disease is essential because the size of aneurysms and severity of coronary artery stenosis can change over time. Transthoracic echocardiography is usually used to follow small children for the development of aneurysms, but adequate visualization of the proximal coronaries tends to diminish with increasing age and size of the patients. Coronary artery aneurysms and wall thickenings can be assessed with coronary MR angiography (Greil et al. 2007), but current MRI techniques have limited spatial resolution for reliable detection of obstructive coronary artery lesions, and abnormalities of the distal coronary arteries, compared with coronary CT angiography (Goo et al. 2006).

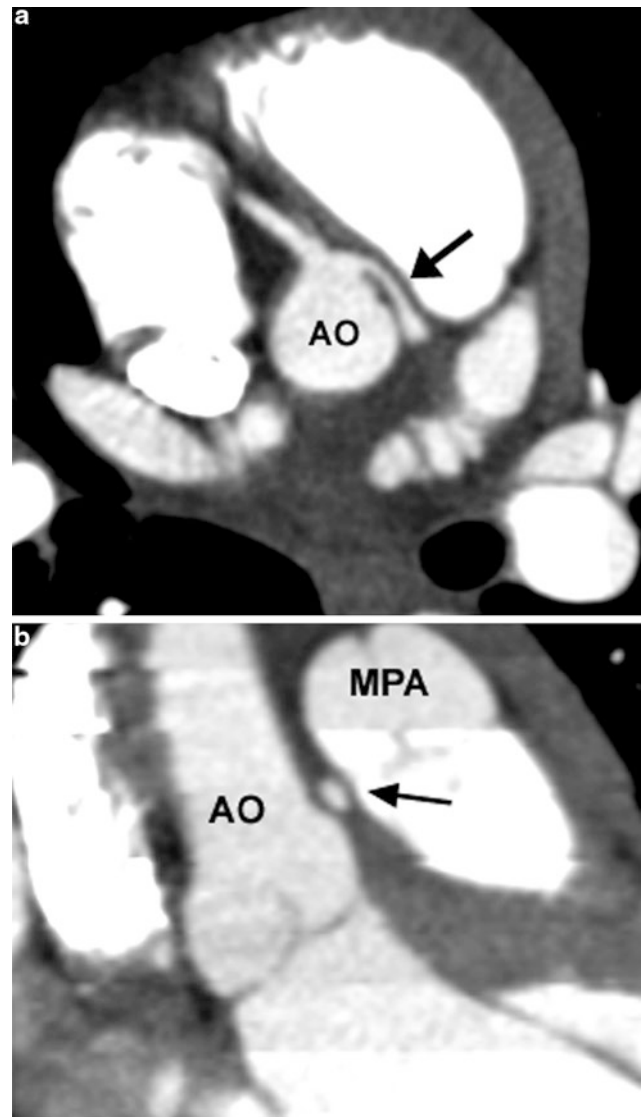


**Fig. 20** Anomalous *left* coronary artery. Axial (a) and coronal (b) MIP images obtained from a retrospectively gated coronary CTA demonstrate an anomalous *left* coronary artery (*large arrow*) arising from the *right* coronary sinus and passing between the ascending aorta (Ao) and main pulmonary artery (MPA)

In a study of adolescents with Kawasaki disease, ECG-gated coronary CT angiography accurately demonstrated not only aneurysms, but also complete occlusions and stenoses (Sato et al. 2003). Recent technical developments in ECG-synchronized cardiac CT have considerably improved diagnostic performance in assessing coronary artery abnormalities in Kawasaki disease, even in small children with higher heart rates (Duan et al. 2012) (Fig. 22). However, it should be kept in mind that coronary CT angiography is limited in assessing heavily calcified lesions and myocardial perfusion state. On these occasions, MRI can show better luminal assessment of heavily calcified lesions,

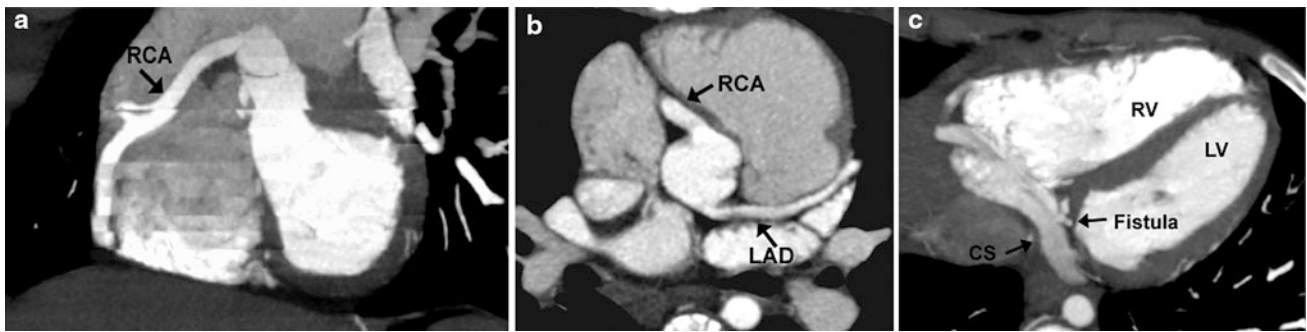
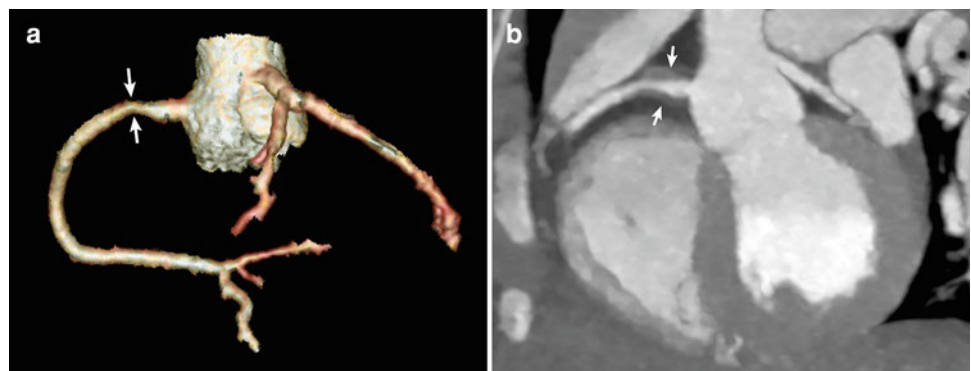


**Fig. 21** Coronary artery fistula in a 9-year-old girl with Noonan syndrome. Oblique coronal (a) and oblique axial (b, c) images from a retrospectively gated coronary CTA demonstrate diffuse enlargement of the right coronary artery (RCA) with a tortuous distal branch that

enters a dilated coronary sinus (CS). Flow through the fistulous connection was coil occluded to prevent coronary steal. (LAD) left anterior descending coronary artery

**Fig. 22** Kawasaki disease with mild coronary artery stenosis in a 3-year-old boy. Volume-rendered CT image (a) and reformatted CT image demonstrate a newly developed mild narrowing (arrows in a) and wall thickening (arrows in b) of the proximal right coronary artery



and a study (Tacke et al. 2011) demonstrated that MRI could provide the comprehensive evaluation of myocardial perfusion and viability in patients with Kawasaki disease.

#### 4.4 Airway Compromise in Patients with Congenital Heart Disease

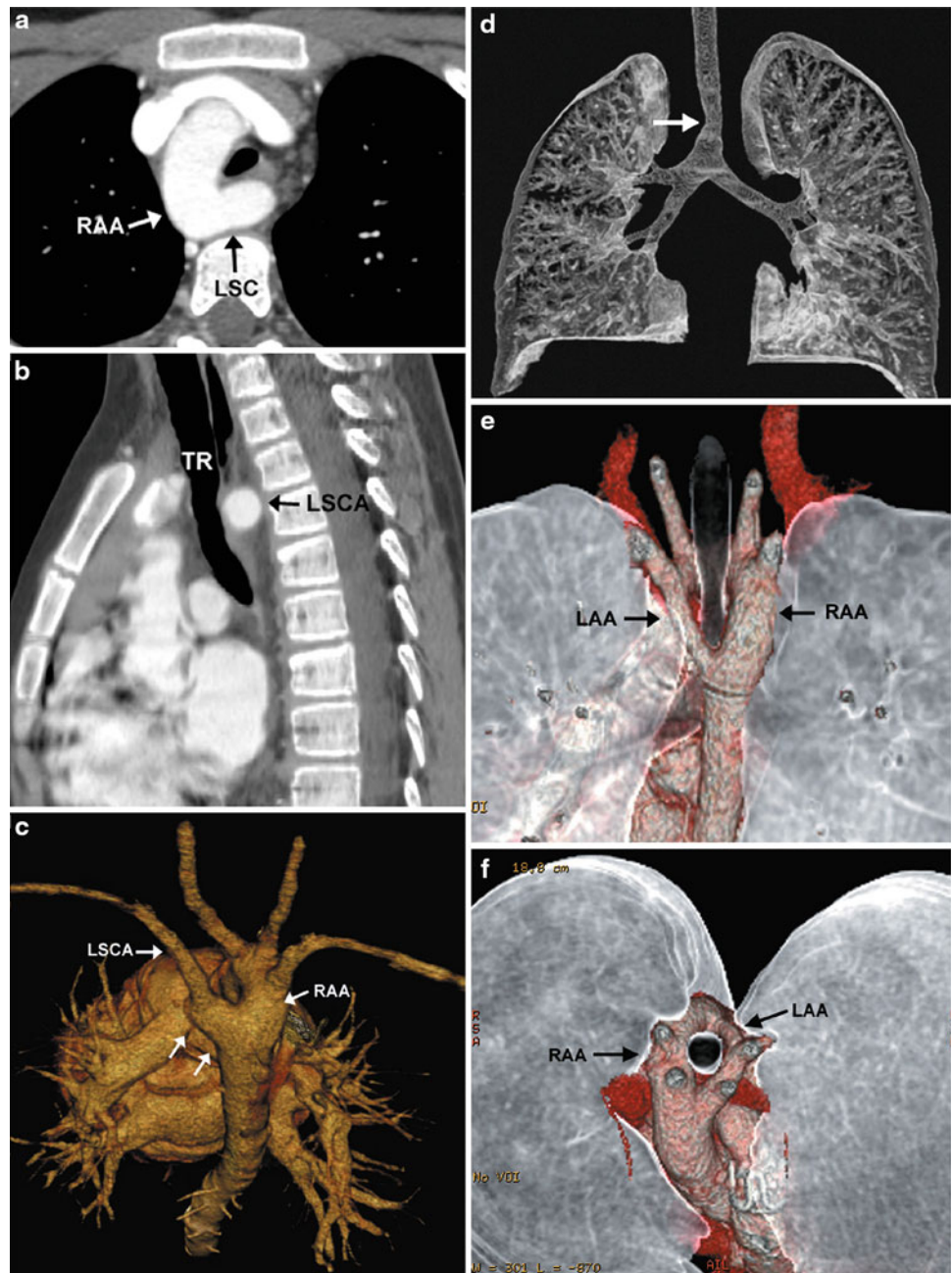
The most common types of vascular anomalies to cause symptomatic tracheal and esophageal compression are the right aortic arch with an aberrant left subclavian artery and the double aortic arch (Fig. 23). In infants and children with these anomalies, symptoms can vary from wheezing to frank respiratory failure, related in part to the direct effect of vascular compression as well as secondary tracheobronchomalacia that can result from prolonged compression. If the vascular ring exhibits less compression, it may be diagnosed in the older child with symptoms primarily of esophageal compression. The double aortic arch is less common than right arch with an aberrant left subclavian artery, but it more often results in a tight ring necessitating earlier surgical intervention for airway obstruction. With the double aortic arch, the right arch is more often dominant and cephalic in location compared

with the left arch. However, the left arch is occasionally dominant and one of the arches may be atretic or have an associated coarctation.

MDCT provides imaging in multiple planes to completely characterize the anomalous vasculature and the extent of airway compression. The current trend of performing minimally invasive surgery for repair of vascular ring using video-assisted thoracoscopic or robotic endoscopic techniques has advantages over lateral thoracotomy including a smaller incision, improved visualization inside the chest cavity, reduced postoperative pain, and risk of chest wall deformity. These less invasive techniques require more precise 3D delineation of cardiovascular structures and airways on preoperative CT (Lambert et al. 2005). In addition to the vascular anomalies described above, there are more rare conditions that can result in symptomatic airway and/or esophageal compression, including pulmonary artery sling (Fig. 5), anomalous innominate artery, circumflex aorta, and cervical aortic arch. Patients with TOF and absent pulmonary valve syndrome can have severe pulmonary regurgitation, which can lead to markedly enlarged pulsatile pulmonary arteries that can cause severe bronchial compression associated with bronchomalacia (Taragin et al. 2006) (Fig. 24).



**Fig. 23** Common vascular rings. Axial (a) and sagittal (b) MIP images demonstrate a right aortic arch (RAA) and aberrant left subclavian artery (LSCA) extending posterior to the trachea and causing narrowing and anterior bowing of the trachea (TR). Posterior volume rendered image (c) shows the dilated proximal left subclavian artery consistent with a diverticulum of Kommerell (arrows) related to ductal flow into the subclavian artery in utero. A 3D bronchographic image (d) demonstrates mild narrowing of the distal trachea (arrow). Posterior and superior volume rendered views (e, f) of a double aortic arch with lungs and trachea included demonstrate tracheal narrowing at the level of the left (LAA) and right (RAA) arches passing to either side of the trachea. The left aortic arch is smaller than the right arch, as is typical (Courtesy of Hyun Woo Goo)



MDCT not only provides a rapid assessment of the ICU patient for potential causes of failed extubation in the early postoperative period in patients with CHD, but also helps surgical planning to prevent postoperative airway compression (Kim et al. 2002; Goo 2004). The airway compression may be related to the patient's intrinsic anatomy, such as ascending aorta dilatation (McElhinney et al. 1999a) (Fig. 25), or due to surgically reconstructed vessels, such as with arterial switch operation and aortic arch reconstruction (Jhang et al. 2008). MDCT is also helpful in evaluating small airway abnormalities, such as air trapping (Goo and Kim 2006), mosaic lung attenuation,

and plastic bronchitis (Goo et al. 2008), in children with CHD. Furthermore, dynamic airway CT can differentiate tracheobronchomalacia from fixed vascular airway compression (Greenberg 2012).

#### 4.5 Cardiac Chamber Morphology and Ventricular Function

The current ECG-synchronized cardiac CT imaging techniques with excellent spatial and temporal resolutions allow accurate assessment of cardiac chamber morphology and

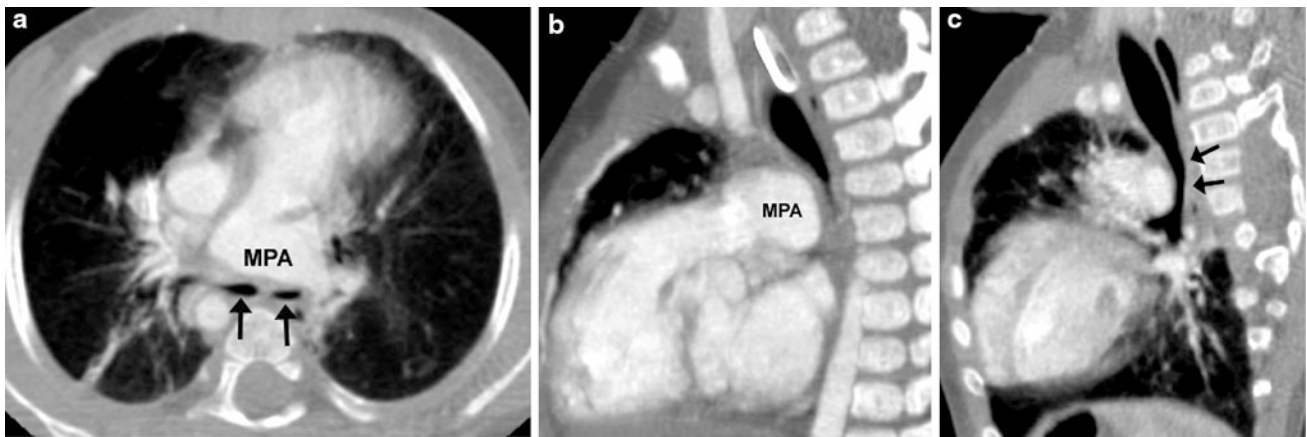
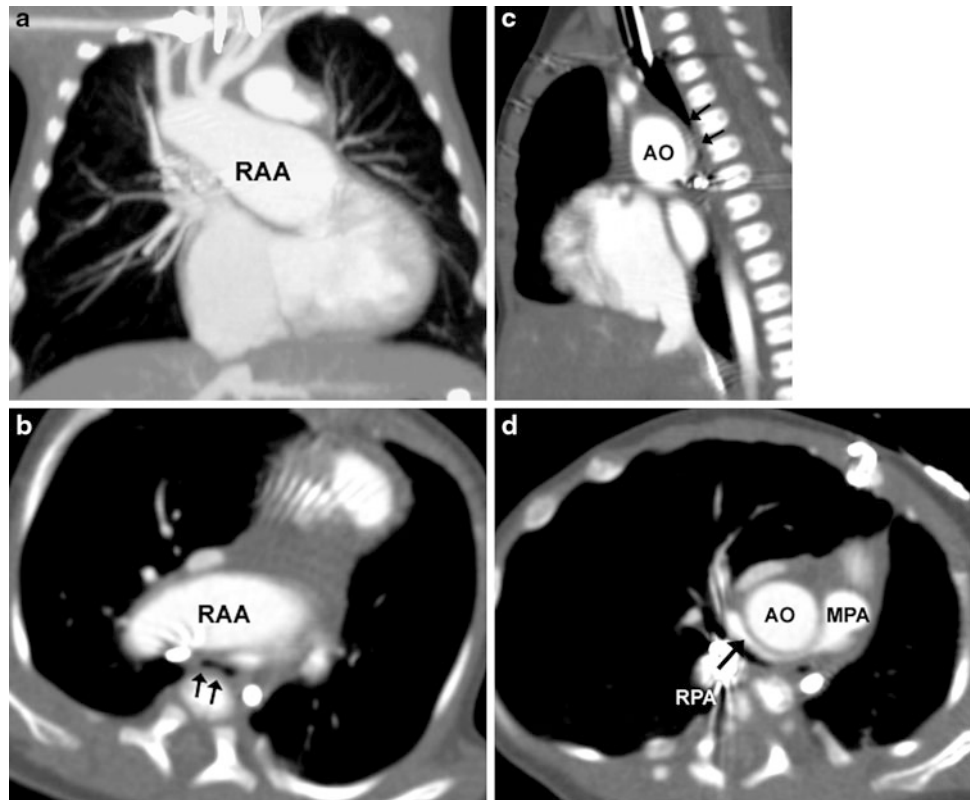


**Fig. 24** Tetralogy of Fallot with absent pulmonary valve syndrome status post repair. Axial (a) and sagittal oblique (b, c) MIP images from an MDCTA demonstrate severe dilatation of the main pulmonary

artery (MPA) and proximal branch PAs causing severe compression of the distal trachea and proximal main stem bronchi (arrows)

**Fig. 25** Malposition of the aortic arch causing severe airway and branch pulmonary artery narrowing in an infant with severe respiratory compromise following repair of tetralogy of Fallot and pulmonary atresia. Coronal (a), axial (b, d) and sagittal (c) oblique MIP images demonstrate a markedly dilated right aortic arch (RAA) positioned posteriorly within the chest, resulting in severe compression of the distal trachea and carina (small arrows), as well as the right pulmonary artery (arrow in d)



ventricular function in children with CHD (Goo 2010a, 2011b). With retrospective ECG gating or prospective ECG triggering, multi-phase cardiac imaging can be obtained for quantitative assessment of ventricular volumes, mass and global function at the expense of higher radiation dose (Fig. 26).

Recently, cardiac CT was found more accurate than biplane cineventriculography and both 2D and 3D echocardiography in assessing left ventricular function with MRI as the reference standard (Greupner et al. 2012), and cardiac CT

was accurate as MRI for left ventricular and right ventricular volume measurement (Maffei et al. 2012). Ventricular volumes measured by cardiac CT may be used for the enlarged right ventricle in repaired TOF to determine the optimal timing of pulmonary valve replacement and for the marginally small ventricle to decide the feasibility of biventricular repair (Kim et al. 2013). In addition, cardiac CT has great potential as a complementary imaging modality in characterizing cardiac chamber morphology in patients with CHD. CT has been shown to depict fatty tissue within the

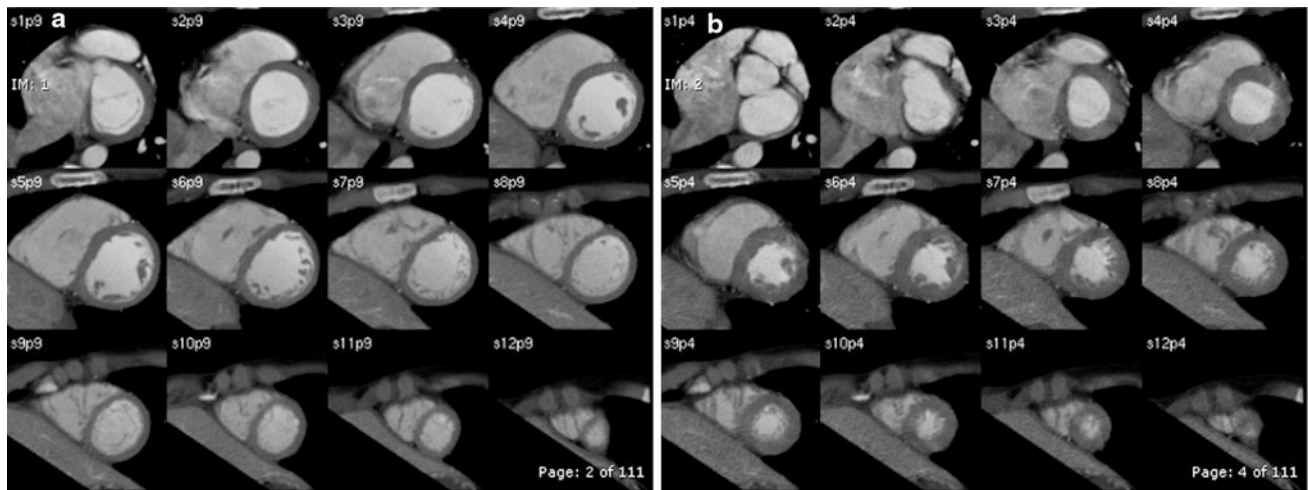


**Fig. 26** Short-axis reconstructed images through the heart in diastole (a) and systole (b) for quantification of ventricular function

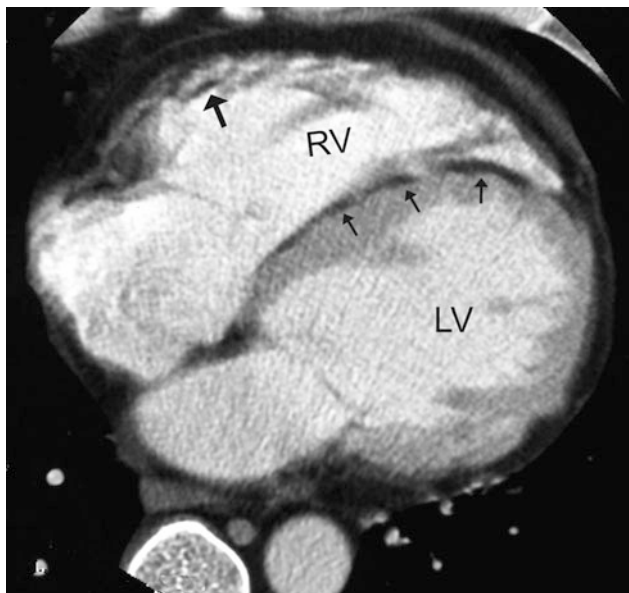


**Fig. 27** MDCT of ARVD. Axial ECG-gated MDCT image demonstrates fatty tissue in the trabeculae of the RV (*large arrow*) and along the RV side of the interventricular septum (*small arrows*). (Used with permission from Kimura et al. 2002)

ventricular wall in patients with arrhythmogenic right ventricular dysplasia (ARVD) (Kimura et al 2002; Tandri et al. 2004) (Fig. 27).

#### 4.6 Postoperative Congenital Heart Disease

The evaluation of surgical results and possible complications involving palliative shunts, conduits, and intracardiac baffles and the patency of the pulmonary arteries has become a major application of noninvasive imaging of postoperative

CHD. CT is most often utilized if a full evaluation of the postoperative vascular morphology is limited on MRI due to artifacts from indwelling ferromagnetic materials such as stents, coils, and occlusion devices, or when a patient has claustrophobia, which tends to be more of an issue with older patients.

Extracardiac conduits are prosthetic or homograft tubes used to create venoarterial, ventriculoarterial, and arterioarterial connections when the structures to be connected are too far away from each other to allow a direct anastomosis. There are three different mechanisms of conduit obstruction: formation of a thick endothelial peel, scarring at sites of anastomosis, and relative narrowing of the conduit associated with growth of structures at either end. Both cardiac CT and MRI allow a more complete visualization of conduits in their entirety than echocardiography or angiography due to a wide field of view and 3D imaging capability.

There are two main types of intracardiac baffles used to redirect venous blood flow through the heart: the atrial inversion procedure (Mustard or Senning operations) for TGA and the Fontan procedure for functionally univentricular hearts. In the Mustard or Senning operation, the native intra-atrial septum is excised and a baffle is inserted to direct superior vena cava (SVC) and IVC blood flow toward the mitral valve. The pulmonary venous blood passes around the baffle and is directed toward the tricuspid valve. Both systemic and pulmonary venous pathways have the potential for obstruction, which can be assessed by CT (Fig. 28). In the Fontan operation, a surgically created pathway reroutes the systemic venous return from the IVC and SVC directly to the pulmonary arteries. Possible complications include pulmonary arteriovenous malformations (Fig. 29), pulmonary venous obstruction due to extrinsic compression by an intracardiac or extracardiac baffle, or an



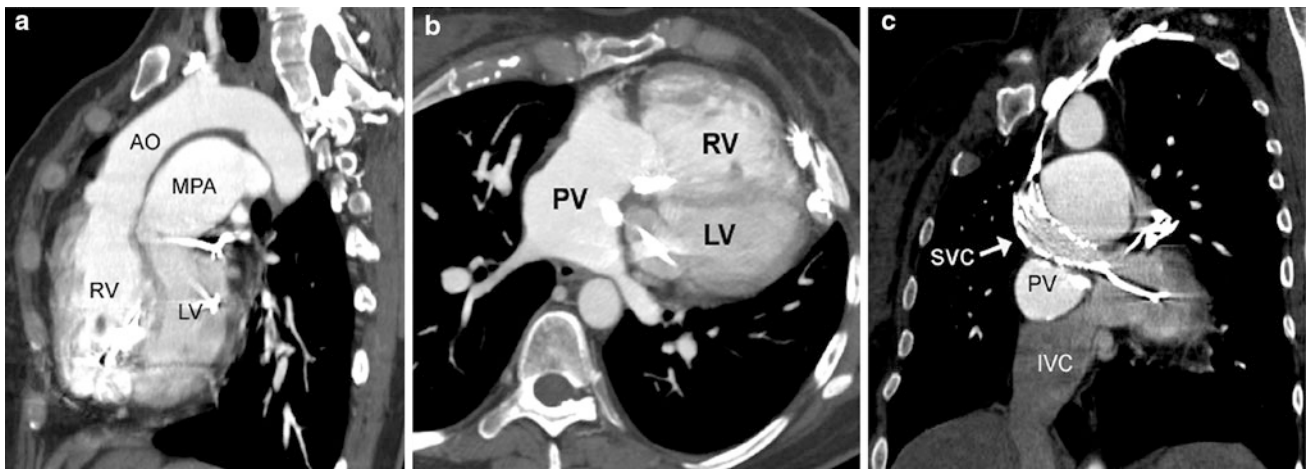
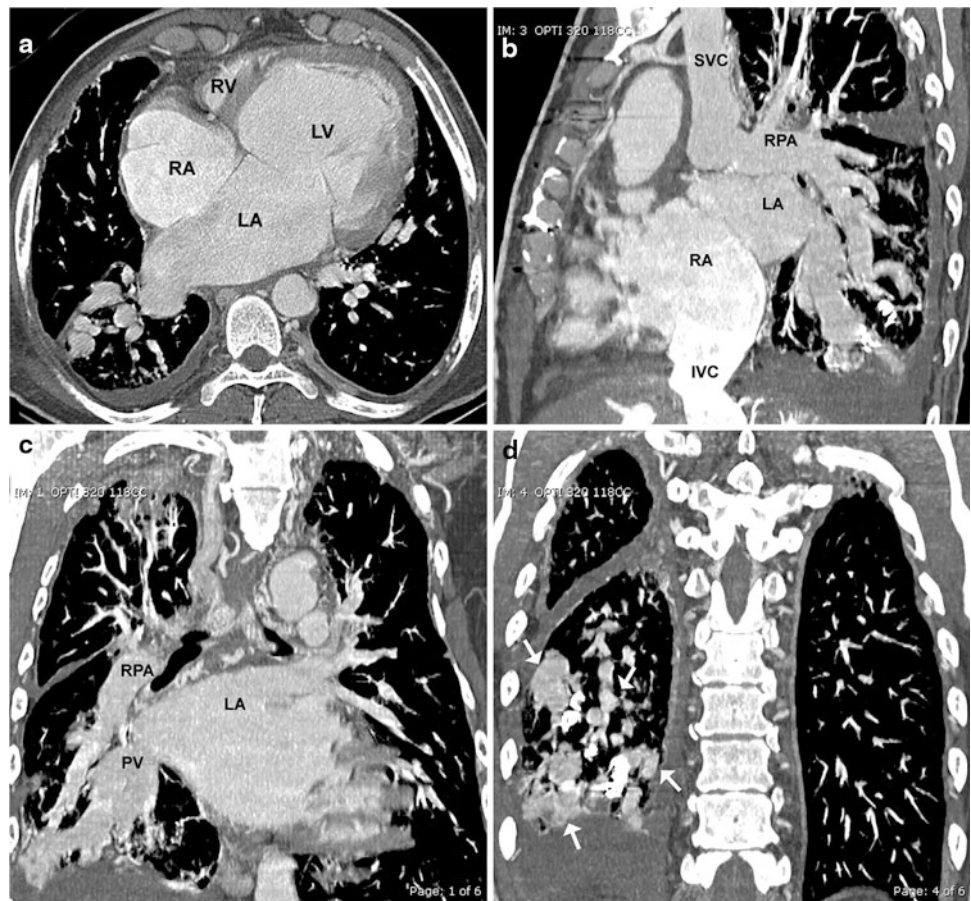


**Fig. 28** Complete-TGA status post Senning. Sagittal oblique (a) MIP image demonstrates the characteristic morphology of complete TGA with the anterior aorta arising from the RV and posterior main pulmonary artery arising from the LV. Axial MIP image (b) demonstrates the pulmonary venous (PV) pathway that directs oxygenated

blood to the systemic RV positioned anteriorly. Coronal reformatted image (c) demonstrates the typical “pant leg” configuration of the IVC and SVC (with stent) pathway directed to the left ventricle separated by an intra-atrial baffle from the PV pathway

**Fig. 29** Pulmonary arteriovenous malformations (AVMs) in a patient with tricuspid atresia status post Glenn shunt to the RPA. Oblique axial image in a four-chamber projection (a) demonstrates a dilated right atrium and hypoplastic RV with fatty tissue completely separating them. Sagittal oblique image (b) demonstrates the patent cavopulmonary anastomosis between the SVC and RPA. Coronal images of the chest (c, d) show marked dilatation of the distal branches of the RPA and pulmonary veins (PV) draining the right lower lobe related to multiple small AVMs, some of which have been occluded by embolization coils. The right lung has become hypoplastic due to steal of blood supply through the AVMs



enlarged cardiac structure used for Fontan pathway. Pulmonary artery obstruction at the level of cavopulmonary anastomosis or due to distortion from a prior Blalock-Taussig (BT) shunt or prior surgical pulmonary artery

reconstruction can also develop. Imaging evaluation is directed to establish the overall patency of the Fontan operation. In the early versions of the Fontan operation, the right atrium is incorporated into the systemic venous to

pulmonary artery connection, and not infrequently, patients can develop thrombus in the pathway due to relative stasis of slow flowing blood (Fig. 8).

## 5 Conclusion

In summary, pediatric cardiac CT provides a number of important advantages for morphologic and functional assessment of the cardiovascular system, airways, and lungs. MDCT is now a major diagnostic tool increasingly used in children with CHD, and when performed for appropriate indications with optimized techniques, the benefits far exceed the very small individual risks.

## References

- Aluquin VP, Albano SA, Chan F et al (2002) Magnetic resonance imaging in the diagnosis and follow up of Takayasu's arteritis in children. *Ann Rheum Dis* 61:526–529
- Babyn PS, Gahunia Hk, Massicotte P (2005) Pulmonary thromboembolism in children. *Pediatr Radiol* 35:258–274
- Bauer RW, Frellesen C, Renker M et al (2011) Dual energy CT pulmonary blood volume assessment in acute pulmonary embolism—correlation with D-dimer level, right heart strain and clinical outcome. *Eur Radiol* 21:1914–1921
- Ben Saad M, Rohnean A, Sigal-Cinqualbre A et al (2009) Evaluation of image quality and radiation dose of thoracic and coronary dual-source CT in 110 infants with congenital heart disease. *Pediatr Radiol* 39:668–676
- Blachere H, Latrabe V, Montaudon M et al (2000) Pulmonary embolism revealed on helical CT angiography: comparison with ventilation-perfusion radionuclide lung scanning. *AJR Am J Roentgenol* 174:1041–1047
- Choe YH, Han BK, Koh EM et al (2000) Takayasu's arteritis: assessment of disease activity with contrast-enhanced MR imaging. *AJR Am J Roentgenol* 175:505–511
- Daniels LB, Gordon JB, Burns JC (2012) Kawasaki disease: late cardiovascular sequelae. *Curr Opin Cardiol* 27:572–577
- Deak PD, Langner O, Leil M et al (2009) Effects of adaptive section collimation on patient radiation dose in multisection spiral CT. *Radiology* 252:140–147
- Deibler AR, Kuzo RS, Vohringer M et al (2004) Imaging of congenital coronary anomalies with multislice computed tomography. *Mayo Clin Proc* 79:1017–1023
- Devaney EJ, Chang AC, Ohye RG et al (2006) Management of congenital and acquired pulmonary vein stenosis. *Ann Thorac Surg* 81:992–995
- Dominquez SR, Anderson MS (2013) Advances in the treatment of Kawasaki disease. *Curr Opin Pediatr* 25:103–109
- Donnelly LF, Frush DP (2003) Pediatric multidetector body CT. *Radiol Clin North Am* 41:637–655
- Duan Y, Wang X, Cheng Z et al (2012) Application of prospective ECG-triggered dual-source CT coronary angiography for infants and children with coronary artery aneurysms due to Kawasaki disease. *Br J Radiol* 85:e1190–e1197
- Eichhorn JG, Long FR, Hill SL et al (2006) Assessment of in-stent stenosis in small children with congenital heart disease using multidetector computed tomography: a validation study. *Catheter Cardiovasc Interv* 68:11–20
- Fujiwara H, Hamashima Y (1978) Pathology of the heart in Kawasaki disease. *Pediatrics* 61:100–107
- Goo HW, Kim YH, Ko JK et al (2002) Horseshoe lung: useful angiographic and bronchographic images using multidetector-row spiral CT in two infants. *Pediatr Radiol* 32:529–532
- Goo HW, Park IS, Ko JK et al (2003) CT of congenital heart disease: normal anatomy and typical pathologic conditions. *Radiographics* 23(spec no):S147–S165
- Goo HW (2004) Evaluation of the airways in patients with congenital heart disease using multislice CT. *J Korean Pediatr Cardiol Soc* 8:37–43
- Goo HW, Park IS, Ko JK et al (2005a) Computed tomography for the diagnosis of congenital heart disease in pediatric and adult patients. *Int J Cardiovasc Imaging* 21:347–365
- Goo HW, Park IS, Ko JK et al (2005b) Visibility of the origin and proximal course of coronary arteries on non-ECG-gated heart CT in patients with congenital heart disease. *Pediatr Radiol* 35:792–798
- Goo HW, Kim HJ (2006) Detection of air trapping on inspiratory and expiratory phase images obtained by 0.3 s cine CT in the lungs of free-breathing young children. *AJR Am J Roentgenol* 187:1019–1023
- Goo HW, Park I, Ko JK et al (2006) Coronary CT angiography and MR angiography of Kawasaki disease. *Pediatr Radiol* 36:699–700
- Goo HW, Suh DS (2006a) Tube current reduction in pediatric non-ECG-gated heart CT by combined tube current modulation. *Pediatr Radiol* 36:344–351
- Goo HW, Suh DS (2006b) The influences of tube voltage and scan direction on combined tube current modulation; a phantom study. *Pediatr Radiol* 36:833–840
- Goo HW, Jhang WK, Kim YH et al (2008) CT findings of plastic bronchitis in children after Fontan operation. *Pediatr Radiol* 38:989–993
- Goo HW, Seo DM, Yun TJ et al (2009) Coronary artery anomalies and clinically important anatomy in patients with congenital heart disease: multislice CT findings. *Pediatr Radiol* 39:265–273
- Goo HW (2010a) State-of-the-art CT imaging techniques for congenital heart disease. *Korean J Radiol* 11:4–18
- Goo HW (2010b) Initial experience of dual-energy lung perfusion CT using a dual-source CT system in children. *Pediatr Radiol* 40:1536–1544
- Goo HW, Yang DH (2010) Coronary artery visibility in free-breathing young children with congenital heart disease on cardiac 64-slice CT: dual-source ECG-triggered sequential scan versus single-source non-ECG-synchronized spiral scan. *Pediatr Radiol* 40:1670–1680
- Goo HW (2011a) Cardiac MDCT in children: CT technology overview and interpretation. *Radiol Clin N Am* 49:997–1010
- Goo HW (2011b) Individualized volume CT dose index determined by cross-sectional area and mean density of the body to achieve uniform image noise of contrast-enhanced pediatric chest CT obtained at variable kV levels and with combined tube current modulation. *Pediatr Radiol* 41:839–847
- Goo HW (2011c) Haemodynamic findings on cardiac CT in children with congenital heart disease. *Pediatr Radiol* 41:250–261
- Goo HW (2012) CT radiation dose optimization and estimation: an update for radiologists. *Korean J Radiol* 13:1–11
- Greenberg SB, Bhutta ST (2008) A dual contrast injection technique for multidetector computed tomography angiography of Fontan procedures. *Int J Cardiovasc Imaging* 24:345–348
- Greenberg SB (2012) Dynamic pulmonary CT in children. *AJR Am J Roentgenol* 199:435–440
- Greess H, Nomayr A, Wolf H et al (2002) Dose reduction in CT examination of children by an attenuation-based online modulation of tube current (CARE Dose). *Eur Radiol* 12:1571–1576
- Greil GF, Schoebinger M, Kuettner A et al (2006) Imaging of aortopulmonary collateral arteries with high-resolution multidetector CT. *Pediatr Radiol* 36:502–509

- Greil GF, Seeger A, Miller S et al (2007) Coronary magnetic resonance angiography and vessel wall imaging in children with Kawasaki disease. *Pediatr Radiol* 37:666–673
- Greupner J, Zimmermann E, Grohmann A et al (2012) Head-to-head comparison of left ventricular function assessment with 64-row computed tomography, biplane left cineventriculography, and both 2- and 3-dimensional transthoracic echocardiography: comparison with magnetic resonance imaging at the reference standard. *J Am Coll Cardiol* 59:1897–1907
- Ha HI, Seo JB, Lee SH et al (2007) Imaging of Marfan syndrome: multisystemic manifestations. *Radiographics* 27:989–1004
- Han BK, Lindberg J, Grant K et al (2011) Accuracy and safety of high pitch computed tomography imaging in young children with complex congenital heart disease. *Am J Cardiol* 107:1541–1546
- Israel GM, Herlihy S, Rubinowitz AN et al (2008) Does a combination of dose modulation with fast gantry rotation time limit CT image quality? *AJR Am J Roentgenol* 191:140–144
- Jakobs TF, Becker CR, Ohnesorge B et al (2002) Multislice helical CT of the heart with retrospective ECG gating: reduction of radiation exposure by ECG-controlled tube current modulation. *Eur Radiol* 12:1081–1086
- Jhang WK, Park JJ, Seo DM et al (2008) Perioperative evaluation of airways in patients with arch obstruction and intracardiac defects. *Ann Thorac Surg* 85:1753–1758
- Kalfa D, Gronier C, Ly M et al (2012) Giant aortic aneurysm in an infant with arterial tortuosity syndrome. *Ann Thorac Surg* 94:e51
- Kalra MK, Maher MM, Toth TL et al (2004) Strategies for CT radiation dose optimization. *Radiology* 230:619–628
- Kalra VB, Gilbert JW, Malhotra A (2011) Loeys-Dietz syndrome: cardiovascular, neuroradiological and musculoskeletal imaging findings. *Pediatr Radiol* 41:1495–1504
- Kato H, Sugimura T, Akagi T et al (1996) Long-term consequences of Kawasaki disease. A 10- to 21-year follow-up study of 594 patients. *Circulation* 94:1379–1385
- Kim HJ, Goo HW, Park SH et al (2013) Left ventricle volume measured by cardiac CT in an infant with a small left ventricle: a new and accurate method in determining uni- or biventricular repair. *Pediatr Radiol* 42:243–246
- Kim TH, Kim YM, Suh CH et al (2000) Helical CT angiography and three-dimensional reconstruction of total anomalous pulmonary venous connections in neonates and infants. *AJR Am J Roentgenol* 175:1381–1386
- Kim YM, Yoo SJ, Kim TH et al (2002) Three-dimensional computed tomography in children with compression of the central airways complicating congenital heart disease. *Cardiol Young* 12:44–50
- Kimura F, Sakai F, Sakomura Y et al (2002) Helical CT features of arrhythmogenic right ventricular cardiomyopathy. *Radiographics* 22:1111–1124
- Konen E, Raviv-Zilka L, Cohen RA et al (2003) Congenital pulmonary venolobar syndrome: spectrum of helical CT findings with emphasis on computerized reformatting. *Radiographics* 23:1175–1184
- Kroft LJ, Roelofs JJ, Geleijns J (2010) Scan time and patient dose for thoracic imaging in neonates and small children using axial volumetric 320-detector row CT compared to helical 64-, 32-, and 16-detector row CT acquisitions. *Pediatr Radiol* 40:294–300
- Lambert V, Sigal-Cinqualbre A, Belli E et al (2005) Preoperative and postoperative evaluation of airways compression in pediatric patients with 3-dimensional multislice computed tomographic scanning: effect on surgical management. *J Thorac Cardiovasc Surg* 129:1111–1118
- Latson LA, Prieto LR (2007) Congenital and acquired pulmonary vein stenosis. *Circulation* 115:103–108
- Lee CH, Goo JM, Ye HJ et al (2008) Radiation dose modulation techniques in the multidetector CT era: from basics to practice. *Radiographics* 28:1451–1459
- Lee EY, Zucker EJ, Tsai J et al (2011) Pulmonary MDCT angiography: value of multiplanar reformatted images in detecting pulmonary embolism in children. *AJR Am J Roentgenol* 197:1460–1465
- Lee EY, Tse SK, Zurakowski D et al (2012) Children suspected of having pulmonary embolism: multidetector CT pulmonary angiography-thromboembolic risk factors and implications for appropriate use. *Radiology* 262:242–251
- Lee JR, Kwak JG, Ban JE et al (2006) Analysis of the causes of and risk factors for mortality in the surgical repair of interrupted aortic arch. *Korean J Thorac Cardiovasc Surg* 39:99–105
- Litmanovich D, Zamboni GA, Hauser TH et al (2008) ECG-gated chest CT angiography with 64-MDCT and tri-phasic IV contrast administration regimen in patients with acute non-specific chest pain. *Eur Radiol* 18:308–317
- Liu PS, St John Sutton MG, Litt HI (2007) Diffuse supra-aortic stenosis: comprehensive imaging with ECG-gated CT angiography. *Int J Cardiovasc Imaging* 23:269–272
- Maffei E, Messalli G, Martini C et al (2012) Left and right ventricle assessment with cardiac CT: validation study versus cardiac MR. *Eur Radiol* 22:1041–1049
- Mahesh M (2002) Search for isotropic resolution in CT from conventional through multiple-row detector. *Radiographics* 22:949–962
- McCollough CH, Primak AN, Saba O et al (2007) Dose performance of a 64-channel dual-source CT scanner. *Radiology* 243:775–784
- McElhinney DB, Reddy VM, Pian MS et al. (1999a) Compression of the central airways by a dilated aorta in infants and children with congenital heart disease. *Ann Thorac Surg* 67:1130–1136
- McElhinney DB, Tworetzky W, Hanley FL et al (1999b) Congenital obstructive lesions of the right aortic arch. *Ann Thorac Surg* 67:1194–1202
- McMahon MA, Squirrell CA (2010) Multidetector CT of aortic dissection: a pictorial review. *Radiographics* 30:445–460
- Menke J (2005) Comparison of different body size parameters for individual dose adaptation in body CT of adults. *Radiology* 236:565–571
- Nie P, Wang X, Cheng Z et al (2012) Accuracy, image quality and radiation dose comparison of high-pitch spiral and sequential acquisition on 128-slice dual-source CT angiography in children with congenital heart disease. *Eur Radiol* 22:2057–2066
- Ou P, Marini D, Celermajer DS et al (2009) Non-invasive assessment of congenital pulmonary vein stenosis in children using cardiac-non-gated CT with 64-slice technology. *Eur J Radiol* 70:595–599
- Petersilka M, Bruder H, Krauss B et al (2008) Technical principles of dual source CT. *Eur J Radiol* 68:362–368
- PIOPED Investigators (1990) Value of the ventilation/perfusion scan in acute pulmonary embolism. Results of the prospective investigation of pulmonary embolism diagnosis (PIOPED). *Jama* 263:2753–2759
- Prabhu SP, Mahmood S, Sena L et al (2009) MDCT evaluation of pulmonary embolism in children and young adults following a lateral tunnel Fontan procedure: optimizing contrast-enhancement techniques. *Pediatr Radiol* 39:938–944
- Sato Y, Kato M, Inoue F et al (2003) Detection of coronary artery aneurysms, stenoses and occlusions by multislice spiral computed tomography in adolescents with Kawasaki disease. *Circ J* 67:427–430
- Satomi G, Nakamura K, Narai S et al (1984) Systematic visualization of coronary arteries by two-dimensional echocardiography in children and infants: evaluation in Kawasaki's disease and coronary arteriovenous fistulas. *Am Heart J* 107:497–505
- Scott DJ, Campbell DN, Clarke DR et al (2009) Twenty-year surgical experience with congenital supra-aortic stenosis. *Ann Thorac Surg* 87:1501–1507
- Tacke CE, Kuipers IM, Groenink M et al (2011) Cardiac magnetic resonance imaging for noninvasive assessment of cardiovascular disease during the follow-up of patients with Kawasaki disease. *Circ Cardiovasc Imaging* 4:712–720



- Tandri H, Bomma C, Calkins H et al (2004) Magnetic resonance and computed tomography imaging of arrhythmogenic right ventricular dysplasia. *J Magn Reson Imaging* 19:848–858
- Tangcharoen T, Bell A, Hegde S et al (2011) Detection of coronary artery anomalies in infants and young children with congenital heart disease by using MR imaging. *Radiology* 259:240–247
- Taragin BH, Berdon WE, Printz B (2006) MRI assessment of bronchial compression in absent pulmonary valve syndrome and review of the syndrome. *Pediatr Radiol* 36:71–75
- Tsai IC, Lee T, Chen MC et al (2007) Visualization of neonatal coronary arteries on multidetector row CT: ECG-gated versus non-ECG-gated technique. *Pediatr Radiol* 37:818–825
- Tsai WL, Wei HJ, Tsai IC (2010) High-take-off coronary artery: a haemodynamically minor, but surgically important coronary anomaly. *Pediatr Radiol* 40:232–233
- Tzedakis A, Damilakis J, Perisinakis K et al (2007) Influence of z overscanning on normalized effective doses calculated for pediatric patients undergoing multidetector CT examinations. *Med Phys* 34:1163–1175
- Westra SJ, Hill JA, Alejos JC et al (1999) Three-dimensional helical CT of pulmonary arteries in infants and children with congenital heart disease. *AJR Am J Roentgenol* 173:109–115
- Weustink AC, Mollet NR, Pugliese F et al (2008) Optimal electrocardiographic pulsing windows and heart rate: effect on image quality and radiation exposure at dual-source coronary CT angiography. *Radiology* 248:792–798
- Yang DH, Goo HW (2008) Pediatric 16-slice CT protocols: radiation dose and image quality. *J Korean Radiol Soc* 59:333–347
- Yang DH, Goo HW, Seo DM et al (2008) Multislice CT angiography of interrupted aortic arch. *Pediatr Radiol* 38:89–100
- Yu L, Bruesewitz MR, Thomas KB et al (2011) Optimal tube potential for radiation dose reduction in pediatric CT: principles, clinical implementations, and pitfalls. *Radiographics* 31:835–848
- Zhang LJ, Wang ZJ, Zhou CS et al (2012) Evaluation of pulmonary embolism in pediatric patients with nephrotic syndrome with dual energy CT pulmonary angiography. *Acad Radiol* 19:341–348
- Zhu FP, Luo S, Wang ZJ et al (2012) Takayasu arteritis: imaging spectrum at multidetector CT angiography. *Br J Radiol* 85:e1282–e1292

---

# Pediatric Cardiac MRI

Rajesh Krishnamurthy and Taylor Chung

## Contents

<b>1</b>	<b>Introduction.....</b>	<b>483</b>
<b>2</b>	<b>Pediatric Cardiovascular MRI Techniques.....</b>	<b>484</b>
2.1	Setting Up a Pediatric Cardiac MRI Study.....	484
2.2	ECG-Triggering.....	484
2.3	Coil Selection, Parameters, and Planes.....	484
2.4	Pulse Sequences.....	485
<b>3</b>	<b>Evaluation of Extra-Cardiac Vasculature.....</b>	<b>491</b>
3.1	Aorta.....	491
3.2	Pulmonary Artery.....	492
3.3	Pulmonary Veins.....	493
3.4	Systemic Veins.....	493
<b>4</b>	<b>Evaluation of Cardiac Morphology.....</b>	<b>493</b>
4.1	Clarifying Complex Segmental Cardiac Anatomy.....	494
4.2	Atrial Pathology.....	494
4.3	Atrioventricular Connections.....	496
4.4	Ventricular and Outflow Tract Pathology.....	496
4.5	Valvular Pathology.....	497
4.6	Miscellaneous Cardiac Pathology.....	497
<b>5</b>	<b>Postoperative Evaluation of Congenital Heart Disease ..</b>	<b>499</b>
<b>6</b>	<b>Limitations of Cardiac MRI in Children.....</b>	<b>500</b>
<b>7</b>	<b>Conclusion.....</b>	<b>501</b>
	<b>References.....</b>	<b>501</b>

---

## Abstract

MRI plays an important complementary role to echocardiography in the evaluation of cardiac morphology and function in children with cardiovascular disease in the pre-operative and post-operative period. Recent technological advancements including free breathing capabilities, improved image resolution, ultra-short imaging time, and real-time imaging, a spurt in clinical validation studies, and the lack of ionizing radiation have all combined to significantly expand the indications for MRI in pediatric cardiovascular disease over the last several years. This chapter provides an overview of relevant technical parameters in children, critical imaging findings and role of imaging in management of common congenital and acquired cardiovascular diseases in children.

---

## 1 Introduction

Accurate anatomical and physiological diagnosis of pediatric cardiac disease allows appropriate selection of therapeutic options: medical, surgical, or both. Echocardiography (echo) plays a central role in the noninvasive delineation of congenital heart disease at all ages. The failure rate with echo increases in the postoperative setting, and in older children, when acoustic windows diminish. There are numerous examples involving the *extra-cardiac vasculature*, in which the lack of optimal acoustic windows results in inadequate characterization of pathology by echo. These include aortic coarctation, anomalous pulmonary veins, scimitar syndrome, systemic venous anomalies, branch pulmonary artery stenosis, anomalous coronaries, etc. The role of MRI and CT in characterizing the extra-cardiac vasculature in such patients is well established. On the other hand, echo is quite successful in the vast majority of cases, in delineating the *intra-cardiac pathology*, including atrial, ventricular and great arterial situs, the segmental connections, ventricular function, the status of the atrial and ventricular septum and the cardiac

---

R. Krishnamurthy (✉)  
Department of Pediatric Radiology, Texas Children's Hospital,  
Associate Professor of Radiology and Pediatrics,  
Baylor College of Medicine, 6701 Fannin St,  
Suite 1280, Houston, TX 77030, USA  
e-mail: rxkrishn@texaschildrens.org

T. Chung  
Body and Cardiovascular Imaging,  
Department of Diagnostic Imaging,  
Children's Hospital and Research Center Oakland,  
747 52nd Street, Oakland, CA 94609, USA

valves. But, even in expert hands, some intracardiac defects remain difficult to diagnose by echo. There are only a few papers in the literature addressing the role of MRI as a troubleshooting modality in such situations. A good example is decision-making regarding single- versus two-ventricle repair in patients with borderline hypoplasia of the left ventricle, in which ventricular volumetry using MRI complements the assessment of intracardiac anatomy by echo. In the *post-operative period*, the complementary role of MRI to echo in the evaluation of cardiovascular morphology and function is well established. Examples include tetralogy of Fallot, complex two-ventricle repair, and single ventricle repair. This chapter will provide an overview of the technique and clinical role of MRI in the diagnosis of cardiac morphology and extra-cardiac vascular pathology in congenital heart disease in the preoperative and postoperative period.

## 2 Pediatric Cardiovascular MRI Techniques

### 2.1 Setting Up a Pediatric Cardiac MRI Study

“The child is not a small adult” is an oft-repeated cliché that resonates throughout the field of pediatric cardiac MRI. The differences between the adult and pediatric cardiac MRI studies are not restricted to clinical indications, but include study preparation, technical parameters, and the prescribed imaging planes. Most patients under the age of 8 years who undergo a cardiac MRI study will need either intravenous sedation or general anesthesia with endotracheal intubation. Endotracheal intubation with pharmacologically-induced paralysis is needed, if breath-holding is desirable. Intravenous sedation is a preferred alternative to intubation among parents and many anesthesiologists, but has two important requirements: anesthesiologists experienced in administering intravenous sedation in patients with congenital heart disease, and the ability to modify the MRI sequences for free-breathing acquisition.

With recent availability of 3T MRI scanners with multi-transmit technology, adult and pediatric cardiac MRI clinical examinations are increasingly being performed using 3T, resulting in diagnostic studies without traditional compromises related to image artifacts or image contrast (Mueller et al. 2012; Chung 2012). However, there is an increase in susceptibility artifacts on 3T, especially in postoperative patients with implanted MRI compatible devices such as valves, conduits, stents, coils, and closure devices. Depending on the goal of the cardiac MRI exam, these patients may benefit from being imaged in a 1.5T scanner, with the decision being made on a case-by-case basis.

The clinical indication for the MRI study varies depending on the natural history and treatment status of the patient, as

well as information from previous imaging studies. For instance, the primary indication for MRI in a patient with tetralogy of Fallot may be any of the following: RV size and function, pulmonary regurgitation, atrioventricular valve regurgitation, RV outflow tract anatomy, branch pulmonary artery stenosis, aortic root dilatation, or the location of aortopulmonary collaterals. Being familiar with the clinical data prior to the study is essential to target the MRI study, so that the relevant data may be obtained in a timely fashion.

### 2.2 ECG-Triggering

With the advent of vectorcardiogram (VCG) triggering system (Chia et al. 2000; Fischer et al. 1999), the technical difficulties associated with obtaining accurate cardiac triggering and gating for cardiac MRI examinations were essentially eliminated in 1.5T scanners. Coupled with fiber-optic hardware, the VCG system provides reliable ECG-triggering for all patients. Initial clinical experience with the VCG system in 3T MRI scanners is limited but generally seems favorable, although the 3T environment produces a higher level of noise.

### 2.3 Coil Selection, Parameters, and Planes

Phased arrays coils are used universally for cardiac imaging, since they provide optimal signal-to-noise ratio (SNR) and the ability to utilize parallel imaging techniques. Parallel imaging was introduced in the late 1990s as Simultaneous Acquisition of Spatial Harmonics (SMASH) (Sodickson and Manning 1997) and SENSitivity Encoding (SENSE) (Pruessmann et al. 1999), and is now available commercially as SENSE from Philips Healthcare (Best, Netherlands), iPAT (mSENSE, GRAPPA) from Siemens Medical Solutions (Erlangen, Germany), or ASSET and ARC from General Electric Medical Systems (Milwaukee, Wisconsin, USA). The choice of size of coil is dictated by the desired field of view (FOV). For example, in suspected anomalous origin of the coronaries in a small infant, a two-element phased array all-purpose coil or phased array neonatal body coil can be used to get the desired FOV of 140 to 180 mm to demonstrate the small coronary arteries (Fig. 1a, d). On the other hand, in a larger patient with Kawasaki disease or anomalous coronaries, or to screen the branches of the aorta for evidence of systemic vasculitis, one would use either an adult cardiac or body phased array coil with a large field of view (Fig. 1b). The choice of in-plane and through-plane spatial resolution, and temporal resolution for a given sequence will vary depending on the size of the patient, the heart rate, as well as the clinical indication. Commonly used imaging planes include standard axial, sagittal, and coronal



**Fig. 1** **a** Large aneurysms (arrows) involving the proximal right and left coronary arteries in a 3 month old patient with Kawasaki disease obtained using a small field of view high resolution 3D cine TFE sequence with a two-element phased array coil. **b** In the same patient, a large field of view MR angiogram was performed with a cardiac phased array coil to demonstrate systemic involvement. Arrows point to aneurysms involving the right axillary and left iliac arteries. **c** Follow-up study 5 years later demonstrates complete resolution of aneurysmal changes in the right coronary artery. **d** High resolution imaging of the anomalous right coronary artery using a cardiac phased array coil on a 3T magnet, demonstrating the proximal intramural course (arrows)



planes for an overview of extra-cardiac vascular anatomy of the chest using rapidly acquired single-shot sequences with steady state free precession (SSFP) or turbo spin echo (TSE); conventional vertical long axis, three chamber, four chamber, and short axis planes for cardiac anatomy and functional analysis, and customized double-oblique planes for evaluation of baffles and conduits, coronaries, or unusual topography of the cardiac chambers.

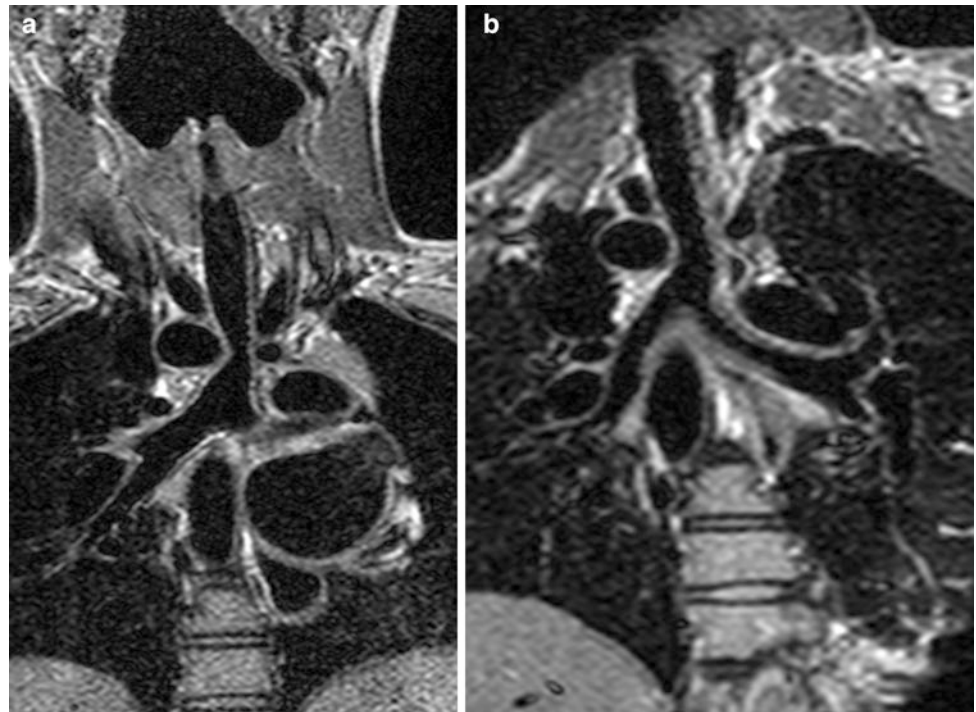
## 2.4 Pulse Sequences

### 2.4.1 Black Blood Sequences

Conventional spin echo (CSE) T1-weighted sequence with ECG-triggering and respiratory compensation (Bailes et al. 1985) has traditionally been the mainstay for black blood imaging since the early days of cardiac MRI (Herfkens et al. 1983). This CSE sequence is no longer used primarily due to

the long scan time. Acquisition time for spin echo sequences can be shortened by using segmented  $k$ -space technique as in TSE or fast spin echo (FSE), by using echo planar imaging (EPI) readout, and by using parallel imaging techniques in combination. Parallel imaging allows for the use of higher number of signal averages (NSA) to compensate for respiratory motion (Chung and Muthupillai 2004) without significant increases in scan time. Respiratory triggering as a means of respiratory compensation can be used to reduce the number of signal averages needed, and in combination with thin sections of 2 mm or less, can be used to evaluate coarctation, vascular rings, vessel wall thickness, and airway compromise (Fig. 2). The general disadvantage with spin echo imaging is an incomplete “black blood” appearance with slow flow artifacts. Double or triple inversion recovery TSE sequence has been shown to produce excellent quality black blood images (Simonetti et al. 1996). However, breath-holding is necessary, which limits its utility in the

**Fig. 2** Coronal black blood T1 echo planar images before (a) and after (b) surgery in a patient with double aortic arch with partial atresia of the left arch, demonstrating relief of airway compression after surgery



pediatric population. This sequence can be used on freely-breathing patients with either multiple NSAs or with respiratory triggering, although the scan duration is longer. Clinically, this sequence is used when better nulling of the blood signal is needed, to minimize metallic artifacts from endovascular stents, and for myocardial tissue characterization to improve conspicuity of lesions such as cardiac tumors. A triple inversion recovery sequence provides additional fat suppression and can be used in edema imaging with T2-weighted sequences in acute myocarditis (Friedrich et al. 2009). With some modifications of this sequence, and in combination with respiratory navigator gating, black blood coronary artery imaging can be accomplished (Stuber et al. 2001). The dielectric shading artifacts on 3T MRI scanner has been minimized by multi-transmit radiofrequency (RF) technology such that reproducible diagnostic quality double inversion recovery black blood images can be produced routinely on 3T MRI scanners. (Mueller et al. 2012).

## 2.4.2 Bright Blood Sequences

### 2.4.2.1 Contrast-Enhanced MRI Angiography

For bright blood imaging, 3D contrast-enhanced magnetic resonance angiography (CE-MRA), initially introduced in the early 1990s (Prince et al. 1993), is the most efficient sequence for the evaluation of extra-cardiac vascular anatomy in the chest. The current implementation of this sequence is in the form of a 3D acquisition of T1-weighted fast gradient echo or turbo field echo (TFE) using a flip angle of 40–45°, and the shortest repetition time (TR) and

echo time (TE) available on the scanner. This sequence is typically run with acquisition of multiple dynamic phases using gadolinium-based contrast agents injected intravenously. The early phases provide information about the pulmonary arterial tree, pulmonary veins, and the aorta and its branches, while the later phases provide information on systemic venous return. There is always a trade-off between spatial resolution and temporal resolution. In general, for the highest spatial resolution, respiration must be suspended and the arrival of contrast must be precisely timed to the vasculature of interest. But, by sacrificing some spatial resolution and using parallel imaging techniques, short dynamic scan times of 4–8 s can be achieved (Muthupillai et al. 2003; Chung and Krishnamurthy 2005). Therefore, in a young patient with high heart rates, who is sedated or cannot breath-hold, CE-MRA with parallel imaging offers an accurate and reproducible means of evaluating the extra-cardiac vasculature, with the rapid dynamics providing unsubtracted separation of the right heart, left heart, and systemic venous phases (Fig. 1b). The 3D volume rendered images provide an excellent overview of cardiovascular morphology (Fig. 3a) in cases with complex spatial relationships of the chambers. By combining with other rapid imaging strategies such as TRICKS (Grist and Thornton 2005) or CENTRA-keyhole-SENSE techniques (Beerbaum et al. 2006; Goo et al. 2007), CE-MRA can be achieved with temporal resolution of less than 2 s without compromise of spatial resolution. When the temporal resolution matches the respiratory cycle duration, the respiratory motion artifacts can be minimized during free-breathing

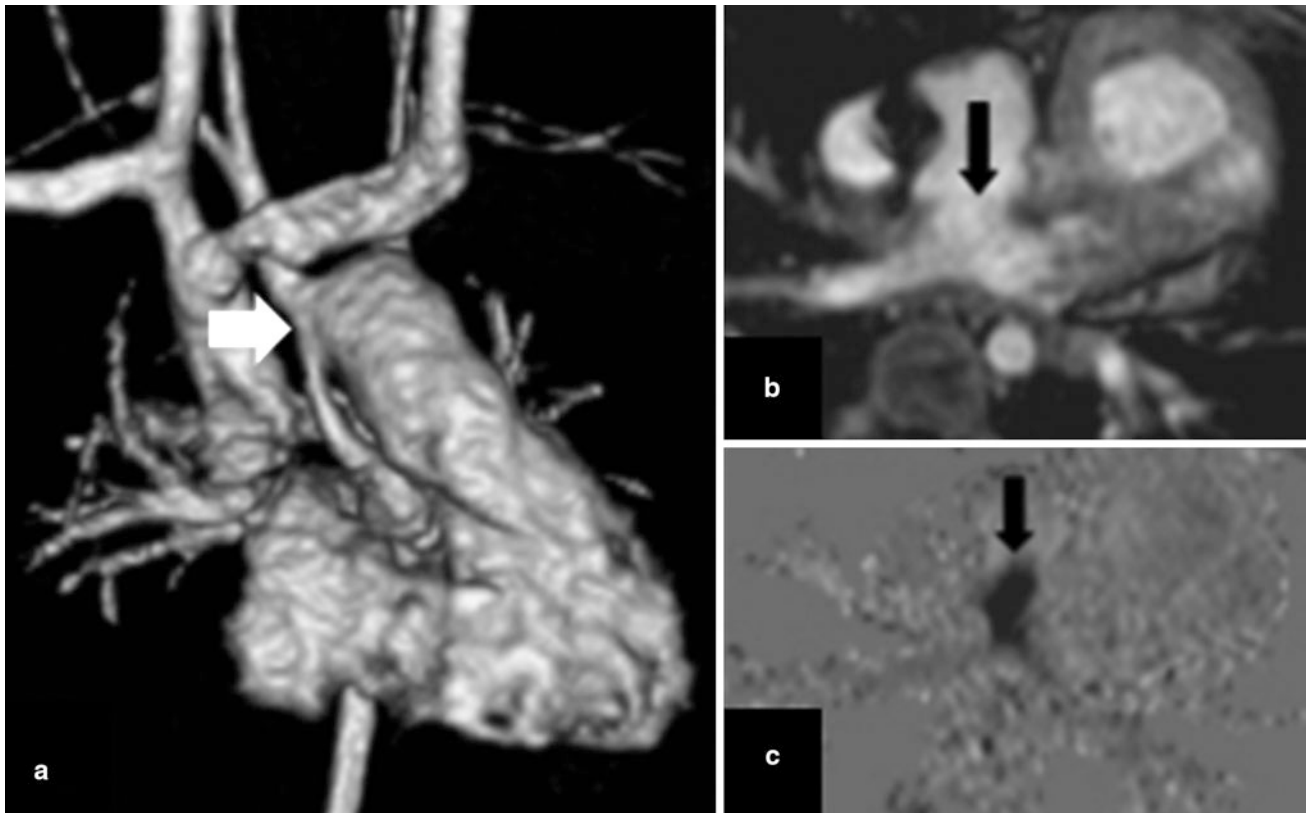


**Fig. 3** Phase contrast imaging revealing restrictive atrial communication after a Norwood procedure for hypoplastic left heart syndrome. **a** 3D volume rendered image from an MRA shows changes of a Damus-Kaye-Stansel anastomosis between the main pulmonary artery

and the hypoplastic ascending aorta (*arrow*). **b** Apparently patent atrial septostomy on the magnitude image (*arrow*). **c** Turbulent flow across septostomy demonstrated on the phase image, consistent with obstruction (*arrow*)



**Fig. 4** Axial cine TFE image demonstrating high-grade stenosis of the origin of the right pulmonary artery (*arrow*)

acquisition (Krishnamurthy et al. 2010). Such high temporal and spatial resolution MRA techniques provide dynamic information on blood flow, parenchymal perfusion, shunting, and collateral pathways typically not available on CT angiography, and demonstrate diagnostic utility in a variety of pediatric conditions, including pulmonary artery stenosis,

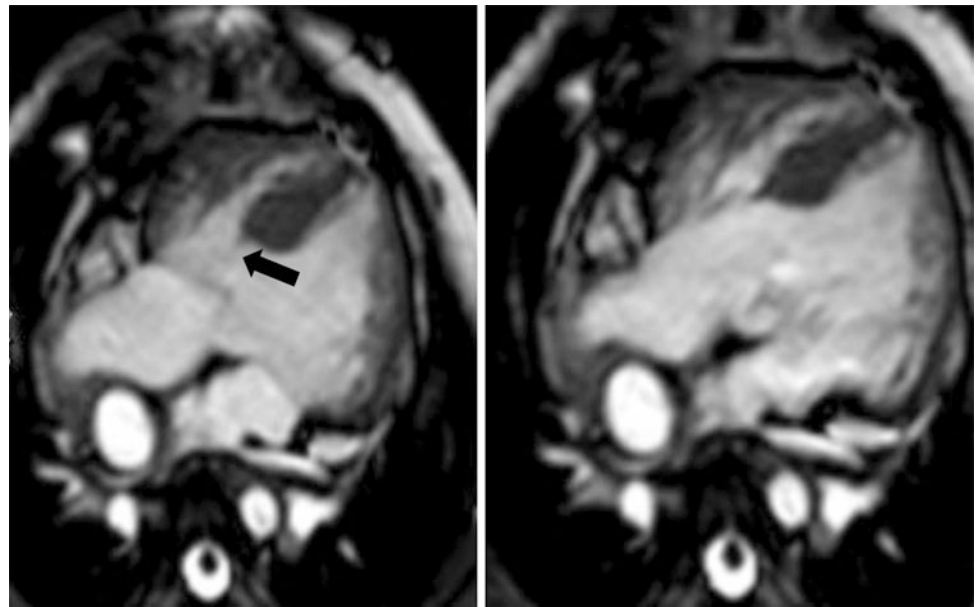
pulmonary vein stenosis, systemic vein obstruction, and arteriovenous malformations.

#### 2.4.2.2 Cine Bright Blood Imaging

For cine bright blood imaging, ECG-triggered cine fast gradient echo or cine TFE with segmented k-space filling (Hernandez et al. 1993) and cine steady state free precession (SSFP) sequences are available. Despite the inherent flow related artifacts of the cine TFE sequence, this sequence is still preferred over SSFP for morphologic evaluation of extra-cardiac vascular pathology (Fig. 4), especially in smaller patients (Wood 2006). Higher spatial resolution can be achieved with cine TFE than with cine SSFP. Typically, 3 NSA with a SENSE reduction factor of 2 can yield adequate SNR on a cine TFE sequence. A saturation band placed over the anterior chest wall fat decreases ghosting artifacts related to breathing. Scan time will depend on the desired number of phases per cardiac cycle. In contrast, the cine SSFP sequence, known as true FISP (Free Induction Steady state Precession), bTFE (balanced Turbo Field Echo), or FIESTA (Fast Imaging Employing Steady state Acquisition) depending on the



**Fig. 5** Cine SSFP images in a patient with over-riding (valvular orifice over-riding the crest of the muscular ventricular septum) and straddling (arrow) (tension apparatus of the atrioventricular valve is attached in both ventricles) of the tricuspid valve in systole (left) and diastole (right)



manufacturer, is acquired with breath-holding, and yields excellent quality images for intracardiac morphology and ventricular function (Fig. 5). When this sequence was first conceived in 1986 (Oppelt et al. 1986), the MRI hardware could not produce the short TR ( $<4$  ms) and TE ( $<2$  ms) necessary for the sequence to be clinically useful. Now, with advances in gradient strength, this is the sequence of choice for ventricular function evaluation due to its high temporal resolution, and excellent myocardial blood pool contrast (Carr et al. 2001). While using the cine SSFP sequence for ventricular function and intracardiac morphology evaluation, the aim is for a temporal resolution of 30–40 ms or approximately 20–25 phases per cardiac cycle with in-plane spatial resolution of 1.5–2.5 mm, depending on the strength and speed of the gradients of the MRI scanner. Parallel imaging is used with acceleration factor up to 2, whenever possible, to decrease the duration of breath-holding. Significant artifacts related to flow acceleration or pulsatile flow can be present in SSFP sequence despite careful shimming (Markl and Pelc 2004). To minimize artifacts, the lowest TR/TE is desirable, and there is a trade-off with spatial resolution. Cine TFE with segmented k-space filling may be a better choice for dynamic bright blood imaging in the setting of turbulent flow when higher spatial resolution is needed.

For non-breath-hold cine SSFP scanning, multiple NSA can be used, but results are variable depending on the regularity of respiratory motion. The quality of the non-breath-hold scans in the short axis plane tends to be quite acceptable in the majority of patients, especially when they are sedated. Limited clinical experience has been reported with respiratory-triggered or navigator respiratory-gated free-breathing ventricular functional assessment using cine

SSFP (Krishnamurthy et al. 2012; Atweh et al. 2013). Whether these new techniques can replicate or improve the excellent image quality associated with breath-held cine SSFP remains to be proven clinically, but they do offer the potential of free-breathing three-dimensional dynamic imaging of morphology and function of the entire chest in a single sequence. With the advent of multi-transmit radio-frequency technology in 3T MRI scanners, adequate diagnostic quality cine SSFP can be achieved routinely (Mueller et al. 2012; Chung 2012).

#### 2.4.2.3 Coronary Imaging

Techniques of white-blood coronary artery imaging with respiratory navigator gating and fast gradient echo sequences (Kim et al. 2001; Flamm and Muthupillai 2004) are well developed for the evaluation of ischemic heart disease in adults. An isotropic whole-heart MRI examination with respiratory navigator gating and 3D SSFP has been used in adults to evaluate the coronary arteries (Weber et al. 2003; Sakuma et al. 2005), and has been applied to patients with congenital heart disease for global assessment of cardiac and extra-cardiac vascular anatomy (Sorensen et al. 2004). These techniques have also been used in the pediatric population in postoperative evaluation after coronary artery reimplantation, in patients with Kawasaki disease (Fig. 1), and in suspected coronary artery anomalies (Greil et al. 2002a, b; Su et al. 2004, 2005, 2007; Taylor et al. 2005a, b). Successful imaging with the higher heart rates encountered in children can be achieved with triggering to end-systole and shortening the data acquisition duration for every R–R interval (Beerbaum et al. 2009). With increasing availability of 3T clinical MRI scanners, high resolution (sub-mm in-plane resolution) coronary

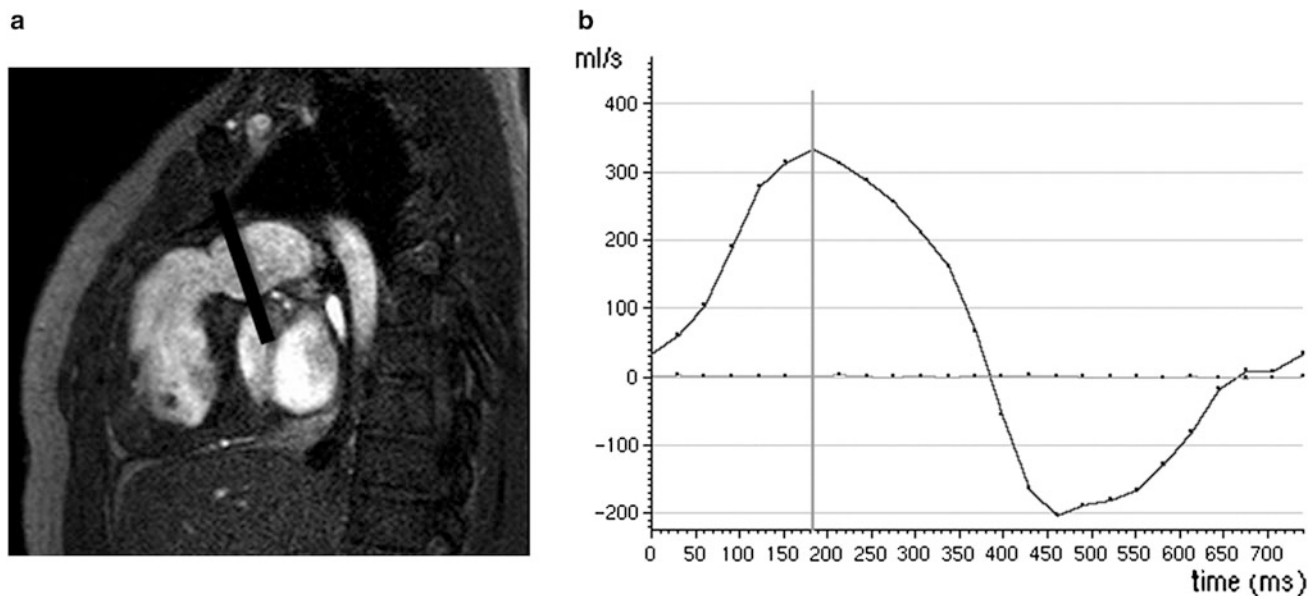


**Fig. 6** **a** Cine TFE image in a 12-year-old patient with treated tetralogy of Fallot, showing a dilated right ventricular outflow tract due to severe pulmonary regurgitation, which can be quantified using a

phase contrast sequence with a plane perpendicular to the RVOT (*black line*). **b** Quantitative flow volume curve across the RVOT reveals a stroke volume of 44 cc, and a regurgitant fraction of 45 %

MRA can be achieved in selective applications such as demonstration of the intramural segment of anomalous coronary arteries (Fig. 1d). The whole-heart MRI examination has been recently enhanced by the use of the intravascular contrast agent, gadofosveset trisodium, in combination with an inversion recovery prepped SSFP or TFE sequence with inversion time of 260–280 ms (Makowski et al. 2011).

### 2.4.3 Flow Quantification

Noninvasive quantitative blood flow analysis is yet another powerful tool that MRI adds to the diagnostic armamentarium. The most widely used pulse sequence is a retrospective ECG-triggered cine phase contrast (PC), also known as velocity-encoded cine MRI (Brenner et al. 1992; Caputo et al. 1991; Helbing et al. 1996; Hundley et al. 1995; Powell and Geva 2000; Rebergen et al. 1993a, b, 1995; Sieverding et al. 1992; Steffens et al. 1994). The accuracy of this technique has been validated both in vitro and in vivo (Bogren et al. 1989; Evans et al. 1993; Firmin et al. 1987; Frayne et al. 1995; Kondo et al. 1991a, b; Powell et al. 2000; Greil et al. 2002a, b). Scan time can be shortened using segmented k-space technique, with the penalty of decreased temporal resolution (Kellenberger et al. 2005), and by combining parallel imaging techniques (Beerbaum et al. 2003; Prakash et al. 2006). Real-time phase contrast has also been applied clinically (Korperich et al. 2004). The main clinical applications include estimation of regurgitant fraction (Fig. 6) in patients with

pulmonary regurgitation after repair of right ventricular outflow obstructive lesions such as tetralogy of Fallot (Helbing and de Roos 2000; Oosterhof et al. 2006), differential pulmonary flow to the right and left lungs (Roman et al. 2005; Sridharan et al. 2006), and systemic-to-pulmonary shunts (Powell and Geva 2000). Phase contrast techniques have also been used as a sensitive means of detecting flow dephasing to locate the presence of atrial and ventricular septal defects, to detect flow restrictive conditions (Fig. 3), and also for quantification of the gradient across a stenosis (Oshinski et al. 1996). The  $Q_P:Q_S$  is calculated by phase contrast imaging across the main pulmonary artery and ascending aorta, and provides an important decision-making tool in the presence of an atrial septal defect (ASD), ventricular septal defect (VSD), or anomalous pulmonary veins. 3D whole-heart volume acquisition of phase contrast data (4D flow) has been reported widely, although there are compromises related to decreased temporal resolution (Markl et al. 2011; Sorensen et al. 2005). More recently, exciting research work has been presented that combines compressed sensing on the acquisition side to speed up scan time and sophisticated post-processing tools to allow for simultaneous flow quantification, 3D flow visualization, and ventricular functional evaluation using the same 4D flow dataset (Hsiao et al. 2012). This has great potential to allow for operator-independent acquisition of volumetric data for congenital heart disease evaluation, and possibly even improve on flow quantification accuracy (Nordmeyer et al. 2013).

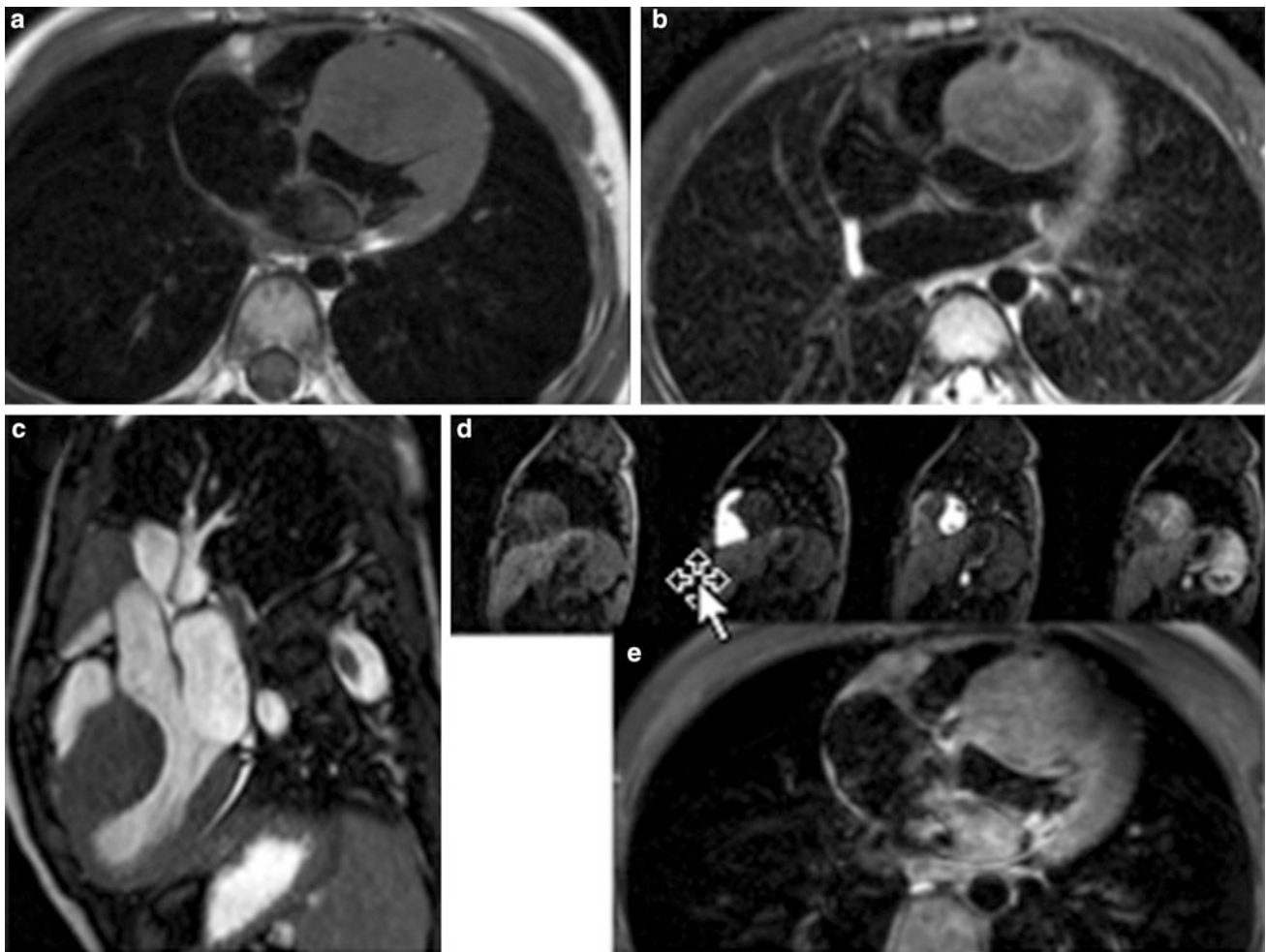


**Fig. 7** Fibroma of the interventricular septum appearing isointense to myocardium on T1-weighted (a), and on T2-weighted (b) images, causing mild obstruction to LV outflow on cine SSFP (c), with

perfusion (d) and enhancement (e) characteristics similar to myocardium after administration of gadolinium

#### 2.4.4 Myocardial Function, Perfusion, Viability, and Tissue Characterization

Besides using cine SSFP, as previously described, for evaluation of global and regional myocardial function and wall motion, techniques for perfusion imaging (Schwitter 2006) with fast gradient echo (fGRE) or hybrid EPI-FGRE pulse sequences, (Jahnke et al. 2006), and viability imaging with an inversion recovery T1-weighted FGRE sequence (Kim et al. 2000) have been well established in adults for evaluation of ischemic heart disease. These techniques have also been applied to the pediatric population in the setting of treated congenital heart disease, especially after coronary reimplantation (Buechel et al. 2009a, b; Fratz et al. 2011), prolonged bypass procedures, tumors (Fig. 7), thrombus, right ventricular dysfunction, systemic right ventricle (Babu-Narayan et al. 2005; Fratz et al. 2006), single left ventricle (Rathod et al. 2010; Robinson et al. 2010), cardiomyopathy, myocarditis, and vasculitis (Prakash et al. 2004; Taylor et al. 2005a, b). With the widespread

availability of phase-sensitive inversion recovery viability imaging (Kellman et al. 2002), robust viability imaging can be acquired in combination with respiratory navigator for sedated freely-breathing infants and young children. The acquisition can be performed either in end-systole or end-diastole. The right ventricular free wall can be more easily assessed in end-systole as the myocardium is thicker. An extension of this technique is quantitative T1-mapping of the myocardium, which may have potential for diagnosis of microscopic fibrosis in cardiomyopathy or myocarditis (Messroghli et al. 2007).

Another technique of myocardial tissue characterization is T2\* mapping. T2\* mapping for iron quantification is a well-established clinical cardiac MRI examination in patients with thalassemia and sickle cell disease (Anderson et al. 2001; Westwood et al. 2005a, b; Wood 2009). Typically, a multi-echo fast gradient echo sequence with multiple TE's is used and the T2\* decay is measured in the septal wall after background noise correction (Westwood et al. 2003).



Myocardial tissue tagging was first applied clinically in the late 1980s (Zerhouni et al. 1988; Axel and Dougherty 1989). The basic principle is to “tag” the myocardium with either one-dimensional RF saturation lines or two-dimensional RF saturation grid at the beginning of a cardiac cycle. As the myocardium contracts, the “tag lines or grids” will deform. By analyzing the deformation of these tags, the mechanical properties of the myocardium such as stress and strain can be estimated. With the introduction of harmonic phase (HARP) MRI that allows for a faster and automated method of tagging analysis, there is more widespread application of tagging clinically (Castillo et al. 2005). On the hardware side, with 3T MRI, the tags persist much longer throughout the cardiac cycle compared to that on 1.5T, thereby improving the results of myocardial tagging (Valeti et al. 2006). It has been successfully applied in congenital heart disease (Fogel et al. 1998; Menteer et al. 2005), as well as in pediatric cardiology for the evaluation of cardiomyopathy due to Duchenne muscular dystrophy (Hor et al. 2009, 2011).

### 3 Evaluation of Extra-Cardiac Vasculature

MRI plays an important role in evaluation of the extra-cardiac vasculature in the preoperative and postoperative period. Evaluation of the systemic and pulmonary veins, branch pulmonary arteries, and the aorta by echocardiography is frequently limited by the lack of acoustic windows in older children, and in the postoperative setting. MRI provides various advantages over echo or CT in this situation, including a large field of view, arbitrary planes of evaluation, 3D imaging with high spatial resolution, excellent contrast resolution, excellent temporal resolution, freedom from artifacts related to surgical patch prostheses and calcification, the use of intravenous contrast with low nephrotoxic potential, and lack of ionizing radiation.

#### 3.1 Aorta

##### 3.1.1 Coarctation

MRI is a useful adjunct to echocardiography in the preoperative evaluation of coarctation, especially in the setting of suboptimal acoustic windows, or in atypical coarctation. In infancy and early childhood, echocardiography provides adequate information prior to surgery or balloon dilatation in discrete coarctation. But, if there is associated tubular hypoplasia of the aortic arch or atypical thoracic coarctation, then MRA or CTA help to define the extent of narrowing, the status of the head and neck arteries, as well as the collateral arterial supply, all of which are essential

for surgical planning. In the postoperative period, echo windows diminished considerably, and MRA is preferred to CTA for serial follow-up due to the lack of ionizing radiation. The MRI protocol for recurrent coarctation comprises dynamic sequences for ventricular function, left ventricular outflow tract, as well as the aortic arch. The severity of the coarctation is determined by measuring the luminal caliber of the aorta, measuring the pressure gradient across the stenosis by flow velocity mapping of the aortic arch (Oshinski et al. 1996) (Fig. 8a), and by quantifying the amount of collateral arterial supply to the descending thoracic aorta by flow velocity mapping across the proximal and distal descending thoracic aorta (Steffens et al. 1994). Gadolinium-enhanced MRA demonstrates the location and extent of stenosis, the presence of pseudoaneurysms, the status of the head and neck arteries, as well as collateral arterial supply to the descending thoracic aorta (Fig. 8b).

##### 3.1.2 Aortic Root Dilatation

Patients with Marfan syndrome, Ehlers-Danlos syndrome, bicuspid aortic valve, or a history of a Ross procedure (replacing a dysplastic aortic valve with the native pulmonary valve) have a tendency to develop progressive aortic root dilatation (Grotenhuis et al. 2006). MRI provides an accurate, reproducible, and safe means of assessing aortic root caliber over time, which is essential to track stability or progression, and for decision-making regarding surgery. It overcomes the limitations of echocardiography, which is error-prone in the setting of eccentric aortic root dilatation. Ungated CT angiography is also limited in this location due to pulsation artifacts. The most helpful information is obtained from a stack of thin-section dynamic bright blood images performed perpendicular to the long axis of the aortic root and proximal ascending aorta, which allows calculation of maximal luminal caliber in systole and diastole, as well as extent of involvement (Fig. 9).

Flow velocity mapping across the ascending aorta is essential to calculate the aortic regurgitant fraction. In some cases, 3D coronary angiography is helpful to determine the status of the coronary origins prior to surgery, or in the postoperative setting.

##### 3.1.3 Vascular Rings and Aortic Arch Anomalies

MRA provides an accurate and rapid means of determining the presence and nature of a vascular ring. Sequences include thin-section axial dynamic bright blood images through the upper thorax, and gadolinium-enhanced 3D MRA. High resolution black blood imaging is also performed to determine the status of the airway (Fig. 2). While the diagnoses of right arch with an aberrant left subclavian artery or double aortic arch are fairly straightforward, variations such as double aortic arch with partial atresia of

**Fig. 8** **a** Flow velocity mapping of the aortic arch in a patient with coarctation showing a dephasing jet (*arrow*) distal to the stenosis with a peak velocity of 450 m/s. **b** Volume rendered image of a gadolinium-enhanced 3D MRA in the same patient showing the severity of stenosis, as well as the extent of collateral flow to the descending aorta

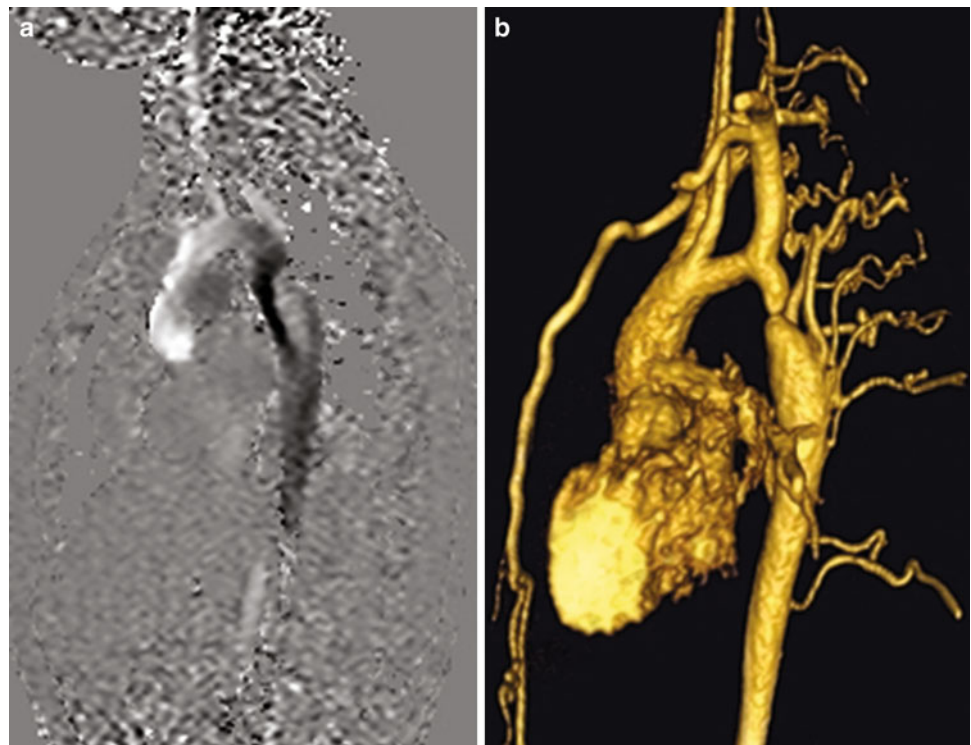


**Fig. 9** Cine TFE image perpendicular to the aortic root in systole demonstrates severe aortic root dilatation in a 12 year old patient, who underwent a Ross procedure for sub-aortic stenosis

the left arch may benefit from the dynamic nature of the MRI data when compared to CT angiography (Schlesinger et al. 2005). MRA is also accurate in diagnosing a number of other aortic arch anomalies including persistent fifth arch, interrupted aortic arch, and cervical aortic arch.

## 3.2 Pulmonary Artery

### 3.2.1 Pulmonary Sling

In a pulmonary sling, the left pulmonary artery arises anomalously from the right pulmonary artery, and travels between the trachea and esophagus to supply the left lung. There is associated compromise of the airway resulting from mass effect or coexisting tracheomalacia and bronchomalacia. Tracheal branching anomalies, including a T-shaped trachea, or complete cartilaginous tracheal rings, may also be present. The anomalous left pulmonary artery is frequently hypoplastic or has focal stenosis (Fig. 10). Using bright blood and black blood sequences as well as MRA, the entire spectrum of vascular and airway anomalies may be accurately depicted by MRI (Lee et al. 2001). Differential blood flow to the lungs may also be calculated using flow velocity mapping sequences.

### 3.2.2 Branch Pulmonary Artery Stenosis

Branch pulmonary artery stenosis may be present as an isolated entity (Fig. 4), but is more commonly seen in the setting of Alagille syndrome, Williams syndrome, treated pulmonary atresia, tetralogy of Fallot, an arterial switch procedure for transposition of great arteries, or any condition involving RVOT conduit placement. The use of thin-section dynamic bright blood sequences, flow velocity mapping, and time-resolved contrast MRA successfully provides all clinically relevant information, including the severity and extent of stenosis, the pressure gradient across

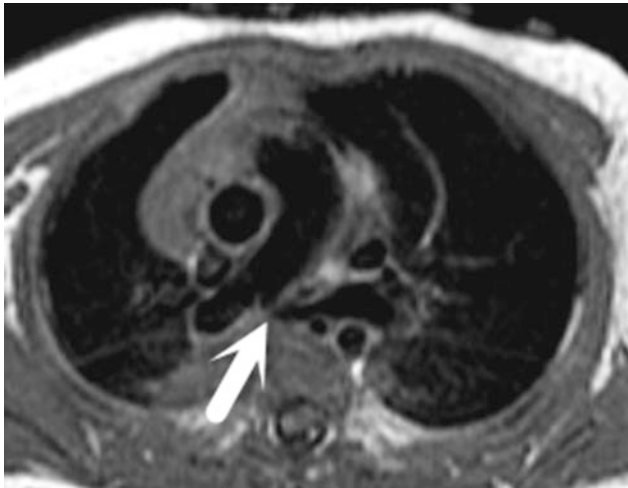


**Fig. 10** Axial black blood fast spin echo double inversion recovery image demonstrating a pulmonary sling with high-grade stenosis of the proximal left pulmonary artery as it courses between the trachea and esophagus (arrow)

the stenosis, the status of the peripheral pulmonary vasculature, the differential pulmonary flow to both lungs, as well as the presence and location of aortopulmonary collaterals. The presence of associated pulmonary regurgitation or RV dysfunction may also be ascertained simultaneously using MRI. This is one of the more common indications for cardiac MRI in most pediatric practices.

### 3.3 Pulmonary Veins

#### 3.3.1 Anomalous Pulmonary Veins

MRI is commonly used in the preoperative and postoperative setting for partial or total anomalous pulmonary venous return (Festa et al. 2006). In partial anomalous pulmonary venous return, which is associated with conditions like scimitar syndrome or sinus venosus defects, MRI is helpful in determining the presence and location of the pulmonary vein, the drainage area, the presence of associated obstruction, the degree of left to right shunting ( $Q_p:Q_s$ ), and the presence of associated anomalies like pulmonary artery hypoplasia, aortopulmonary collaterals, and pulmonary airway malformations. MRI provides the most objective and reproducible data for surgical decision-making in partial anomalous pulmonary venous return. Most cases of total anomalous pulmonary venous return are successfully diagnosed by echocardiography in the newborn, with the use of MRI restricted to cases with complex anatomy like heterotaxy (Fig. 11), or in the setting of suboptimal echo windows. MRI has been successfully used to diagnose an unusual course of the aberrant pulmonary vein, as well as the presence of associated stenosis, both in infradiaphragmatic and supradiaphragmatic TAPVR.

#### 3.3.2 Pulmonary Vein Stenosis

Pulmonary vein stenosis may occur as an isolated entity, or after repair of anomalous pulmonary venous return or other types of congenital heart surgery (Fig. 12), and is usually difficult to manage with a poor prognosis. MRI determines the presence, severity, and extent of stenosis, as well as its impact on pulmonary arterial supply, differential pulmonary blood flow, and ventricular function (Valsangiocomo et al. 2003). One major limitation of MRI in this setting is its inability to determine pulmonary vascular resistance and right ventricular chamber pressures, although estimates may be obtained from pulmonary artery caliber and interventricular septal motion.

### 3.4 Systemic Veins

Systemic venous anomalies frequently coexist with congenital heart disease, especially in the setting of heterotaxy (Fig. 11). The most common anomaly is a persistent left superior vena cava, which drains into the coronary sinus. A connecting vein between the two superior vena cavae is typically absent in this setting. Interruption of the IVC with azygos continuation, and/or aberrant hepatic venous drainage is frequently present in heterotaxy. These anomalies significantly alter surgical management in single ventricle repair, in which the cavopulmonary connections have to be modified to accommodate the aberrant venous drainage.

Systemic venous obstruction is common after congenital heart surgery or prolonged central vascular catheter usage, and MR venography (MRV) offers an accurate means of diagnosing the extent of thrombosis, the acuity of the process, and the degree and adequacy of collateral venous flow. Simultaneous imaging of the brain should be considered in the setting of SVC or bilateral jugular vein thrombosis to assess for elevated intracranial pressure, which may manifest with ventriculomegaly or intracranial hemorrhage.

## 4 Evaluation of Cardiac Morphology

The **segmental approach** to the diagnosis of congenital heart disease (Van Praagh 1984) includes the following analyses:

1. *What is the anatomic type of the three major cardiac segments: the viscero-atrial situs, the ventricles, and the great arteries?* Consider the example of a patient with complete transposition of the great arteries (d-TGA) with VSD and pulmonary stenosis. The cardiac segments are: situs solitus of the atria and viscera, D-looping of the ventricles (morphologic right ventricle lies to the right of the morphologic left ventricle), and D-malposition of the great arteries (aortic valve annulus lies anterior and to the right of the pulmonary annulus).



**Fig. 11** MIP (a) and volume rendered (b) images of an MRA in a newborn with heterotaxy and right isomerism, showing total anomalous pulmonary venous return below the diaphragm to a hepatic vein (*large white arrow*), a left sided IVC (*small black arrow*), a transverse liver with asplenia, and a right-sided stomach

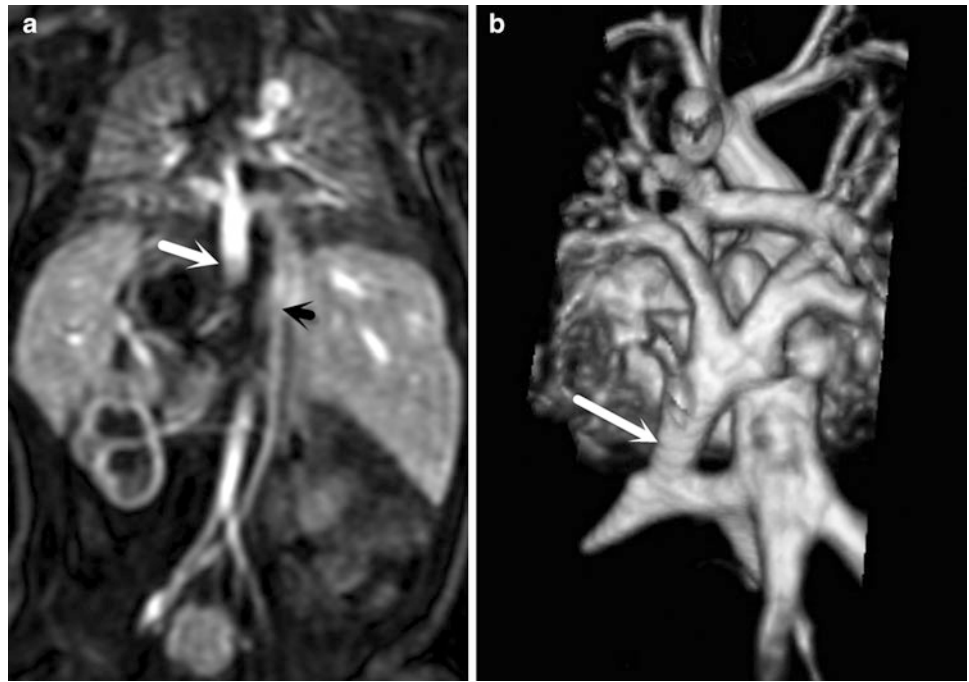


**Fig. 12** Recurrent severe pulmonary vein stenosis (*arrow*) after repair of total anomalous pulmonary venous return

2. *How is each segment connected to the adjacent segment?* In the example of d-TGA described above, there is atrioventricular concordance and ventriculoarterial discordance.

3. *What are the associated malformations?* In the example described above, the patient also has a conoventricular VSD and pulmonary valve stenosis associated with d-TGA.

4. *How do the segmental combinations and connections, along with the associated malformations, function?* The patient with the morphology described above will have cyanosis and reduced pulmonary blood flow.

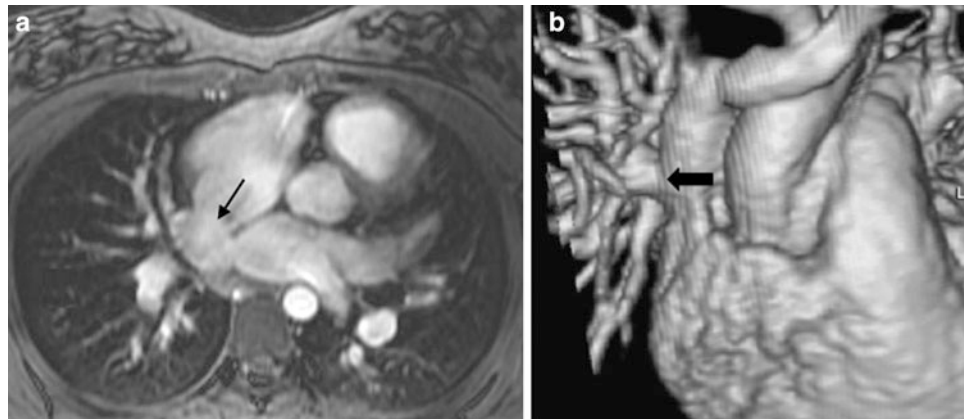
#### 4.1 Clarifying Complex Segmental Cardiac Anatomy

Viscero-atrial situs abnormalities and cardiac malpositions are usually easily identified by echo. However, in the presence of situs ambiguous, atrioventricular or ventriculoarterial discordance, or anomalous pulmonary or systemic venous connections (Fig. 11), difficulties may arise in defining the topographic relation of the major cardiac segments (Araoz et al. 2002). MRI is an excellent technique for defining the morphologic features of each atrium and ventricle. MRI depicts anatomical details that are easily related to the surrounding structures of the body, and thus provides reliable diagnoses in heterotaxy (Sorensen et al. 2004; Kersting-Sommerhoff et al. 1990a, b). In patients with complex anomalies, especially in older patients, MRI may be the primary imaging technique so as to maximize non-invasive information prior to catheterization.

#### 4.2 Atrial Pathology

The sensitivity of echo for diagnosing secundum-type ASD is close to 100 % in infancy, but drops to 85–90 % in older children and adults. Transesophageal echocardiography

**Fig. 13** Superior sinus venosus defect demonstrating the extra-septal communication (arrow) between the posterior wall of the SVC/RA junction and the left atrium (a), with associated partial anomalous venous return of right upper lobe pulmonary vein to the SVC (arrow) (b)



(TEE) is a trusted method of sizing an ASD prior to surgery or percutaneous device closure, but is invasive, uncomfortable, and may carry a small risk of morbidity and mortality. MRI may be a useful noninvasive alternative in patients who refuse or are unable to tolerate TEE and may provide additional information on the shape and location of the ASD. ASD sizing by MRI using bFFE and phase contrast (PC) protocols correlates well with TEE estimations, and PC-MRI provides additional information on ASD shape and proximity to adjacent structures (Piaw et al. 2006). MRI guidance has also been used to navigate endovascular catheters and deliver ASD closure devices (Henk et al. 2005).

The superior sinus venosus defect is the most difficult form of atrial septal defect to detect echocardiographically due to the extreme rightward and superior position of this type of defect. The inferior type is also difficult to depict by transthoracic echocardiography because of its infero-posterior location relative to the fossa ovalis. MRI has become the gold standard for depiction of sinus venosus defects (Fig. 13). The coronary sinus septal defect involves partial absence of the atrial septum between the coronary sinus and the left atrium due to incomplete development of the left atrio-venous fold. It may be associated with left SVC to coronary sinus, unroofing of the coronary sinus, and other complex congenital heart defects, and its evaluation by MRI can overcome the limitations of echocardiography. MRI may also identify ASD or partial anomalous pulmonary venous connection in adults with right-sided chamber enlargement, hypertrophy, or dysfunction of unknown etiology. In all forms of septal defects, quantification of shunt size (pulmonary to systemic flow ratio, otherwise known as the Qp:Qs) by flow velocity mapping compares favorably to other imaging techniques, and enables decision-making regarding conservative therapy versus surgery (Hundley et al. 1995).

The common pulmonary vein is usually largely incorporated into the left atrium and forms the part of the left atrial posterior wall between the entrances of the pulmonary veins.

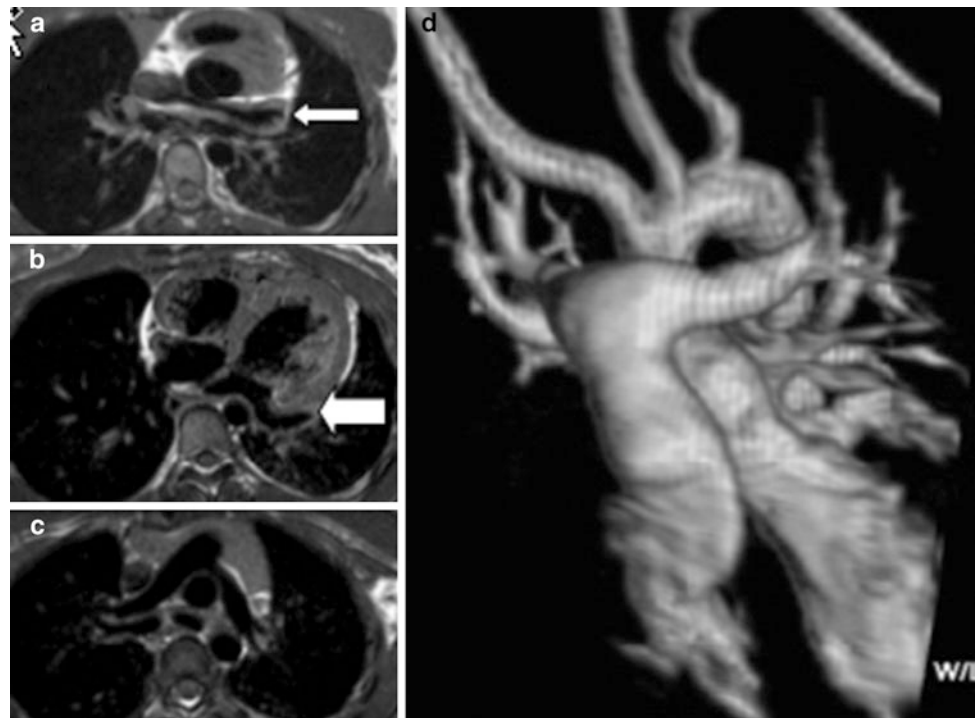


**Fig. 14** Malposition of the septum primum to the left (arrow), resulting in partial anomalous venous return of the right-sided pulmonary veins to the right atrium, which is severely dilated

If the point of junction of the common pulmonary vein and the left atrium is stenotic, a membrane develops between the common pulmonary vein and the left atrium, resulting in an anomaly known as cor triatriatum. The membrane lies between the entrance of the pulmonary veins posteriorly and the foramen ovale and the left atrial appendage anteriorly, in contrast to the supramitral ring that attaches between the foramen ovale and the left atrial appendage posteriorly and the mitral annulus anteriorly. The distinction between these two entities can occasionally be difficult on echocardiography, but is easily accomplished by MRI.

Malposition of the septum primum towards the left atrium can result in anomalous pulmonary venous drainage into the right atrium. In severe cases, the entire venous system of both lungs will be connected with the right atrium. This condition must be differentiated from partial or total anomalous pulmonary venous return to the right atrium

**Fig. 15** Left juxtaposition of the atrial appendages in d-transposition of the great arteries, s/p arterial switch procedure. The right appendage (a) (*small arrow*) and the left appendage (b) (*large arrow*) are on the same side. The typical orientation of the pulmonary artery and aorta (c, d) after an arterial switch



by demonstrating that the pulmonary veins have a normal relationship with each other and to the posterior wall of the atrium, and the anomalous venous return occurs due to malposition of the atrial septum (Fig. 14). MRI can make the diagnosis more reliable than echo. Recognition of this condition leads to appropriate therapy, which is surgically restoring the correct position of the atrial septum.

MRI has also been used to demonstrate a broad range of pathologies involving the atrial appendages. These include abnormal appendage symmetry in heterotaxy, juxtaposition of the atrial appendages in association with other complex malformations (Fig. 15), and thrombi within the appendages.

### 4.3 Atrioventricular Connections

MRI can demonstrate discordant atrioventricular connections and crisscross atrioventricular connections. MRI has also been used for demonstrating double inlet ventricle (Yoo et al. 1999), straddling atrioventricular valve (Fig. 5), tricuspid atresia, and mitral atresia. Echo is usually employed initially for these abnormalities and MRI is used to supplement the information from echo. MRI is superior to echo for quantifying ventricular volumes in these abnormalities, which may be critical for surgical decisions regarding biventricular repair versus the Fontan procedure.

### 4.4 Ventricular and Outflow Tract Pathology

MRI adds little, if any, anatomical information in isolated VSD when the diagnosis is already established by echocardiography, except that MRI can readily quantify shunt volume. MRI is highly sensitive and specific for the quantification and detection of VSDs (Didier and Higgins 1986; Mirowitz et al. 1989) and detection and localization of jets is helpful (Sechtem et al. 1987). Certain types of VSD that are difficult to evaluate by echo are well suited to imaging by MRI, including conal septal defects and apical muscular defects. MRI can readily depict ventricular anatomy in complex cases of tetralogy of Fallot, pulmonary atresia, tricuspid atresia, and univentricular hearts (Razavi et al. 2003; Kersting-Sommerhoff et al. 1990a, b). In functional or morphologic single ventricle, the differentiation of a single right ventricle from a single left ventricle can be made with a high degree of confidence in most cases. MRI has been used to help surgical decision-making regarding univentricular repair (Fontan), one and a half ventricle repair, or biventricular repair in patients who have two functioning ventricles but factors preventing biventricular repair like straddling atrioventricular valves, unfavorable location of the VSD or suboptimal ventricular morphology, or function (Fig. 16). MRI can precisely depict the location of the VSD in relation to the great arteries in double outlet ventricles (Mayo et al. 1990). MRI is the most accurate



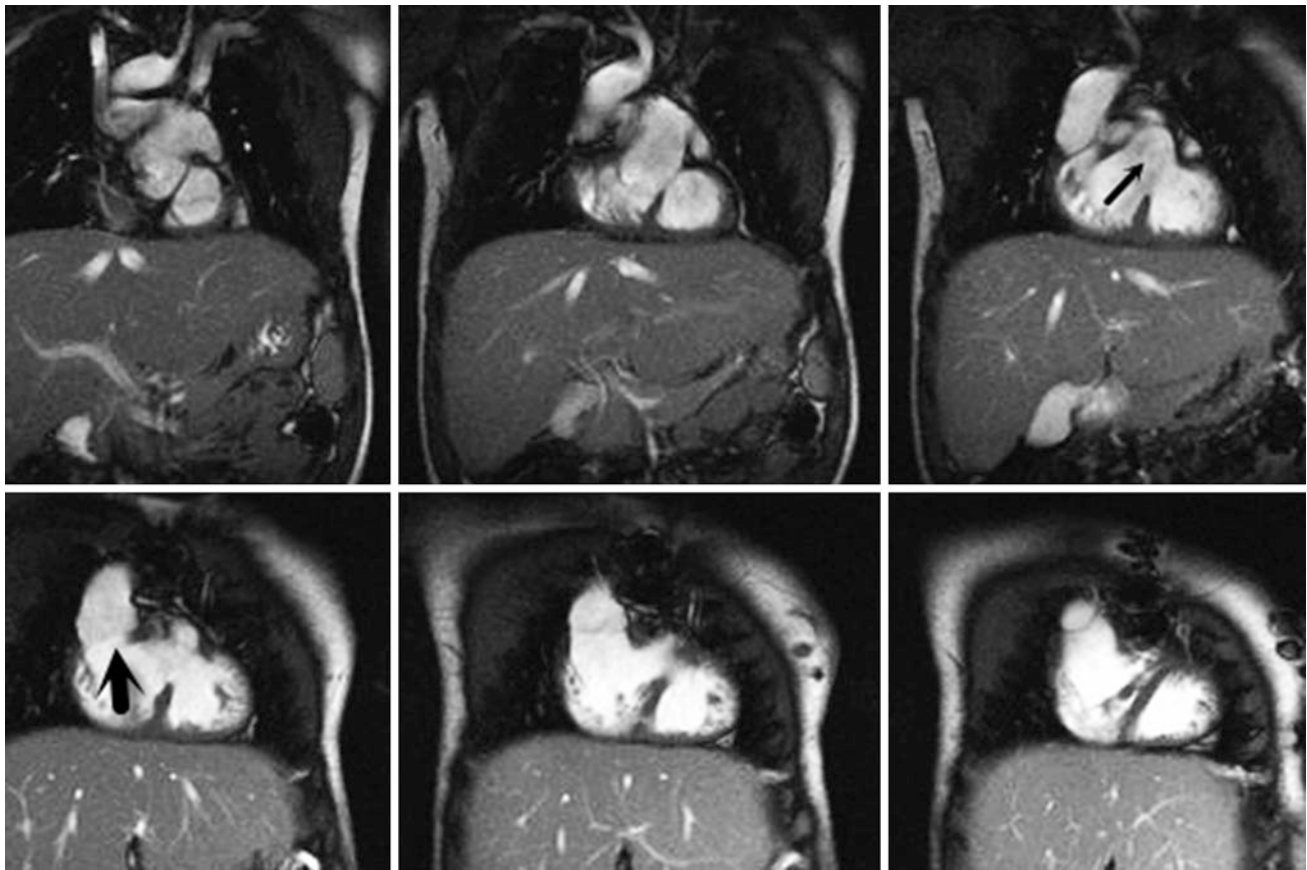


**Fig. 16** Coronal bright blood images oriented posterior to anterior in a patient with double outlet right ventricle and a sub-pulmonary VSD. Since the aorta (*large arrow*) is located far to the right, away from the VSD and the LV, this patient would likely not be a candidate for a two-ventricle repair in which a baffle must be created from the left

ventricle to the aorta across the VSD. In this case, the baffle would have obstructed the right ventricular outflow tract (*small arrow*) and the tricuspid inflow. Hence, this patient went on to have a single ventricle repair in spite of having two well-formed ventricles

technique for quantifying left and right ventricular masses and volumes. The quantitative capabilities of cardiac MRI allow decision-making regarding single versus two-ventricle repair in neonates with borderline hypoplasia of the left ventricle (Grosse-Wortmann et al. 2008).

#### 4.5 Valvular Pathology

The high temporal resolution, spatial resolution, and interactive real-time nature of echo makes it the primary imaging modality for defining valve morphology, including the number of leaflets, the valve thickness, and the presence of vegetations, as well as valve function, and estimation of valvular stenosis and regurgitation. However, MRI flow velocity mapping is a more accurate and reproducible means of quantifying the severity of regurgitation (Fig. 6). This is valuable for sequential monitoring of the severity of valvular regurgitation and determining

the optimal timing for valve replacement. Common MRI applications include monitoring of pulmonary regurgitation after outflow patch surgery for tetralogy of Fallot, and after placement of right ventricle to pulmonary artery conduits as well as monitoring idiopathic aortic root dilation and aortic regurgitation in patients with Marfan syndrome, tetralogy of Fallot, or history of a Ross procedure (Fig. 9). MRI is also effective for the morphologic depiction of tricuspid atresia, Shone syndrome, and Ebstein anomaly (Link et al. 1988). Moreover, it can provide precise ventricular volumetric and functional assessment in these disorders (Choi et al. 1994).

#### 4.6 Miscellaneous Cardiac Pathology

MRI is proving increasingly valuable in the identification and management of cardiac thrombus and of various forms of cardiomyopathy and cardiac tumors.

#### 4.6.1 Cardiac Thrombus

The Fontan procedure is associated with a high incidence of thromboembolic complications (Casolo et al. 2004). Intracavitary thrombi are also frequently found in patients with impaired ventricular function, or within the atrium in atrial fibrillation. MRI is a sensitive tool in the detection of intracardiac thrombi, and overcomes some of the near-field limitations of 2D echo. Bright blood cine, black blood, and post gadolinium delayed enhancement sequences are the most helpful. However, both the bright blood and black blood sequences are prone to artifact from stasis and slow flow. In the future, fibrin-specific MRI contrast agents may offer selective visualization of acute cardiac and vascular thrombi (Spuentrup et al. 2005).

#### 4.6.2 Cardiac Tumors

Primary heart tumors in childhood are rare and mostly benign. Surgical treatment is advocated when symptoms or hemodynamic impairment are present. Rhabdomyoma is the most common cardiac tumor diagnosed in children. Rhabdomyomas are usually multiple, most often involve the ventricular myocardium, and project into the cavity or move freely as a pedunculated mass. Tuberous sclerosis is present in about one-third of patients with rhabdomyomas. Fibromas (Fig. 7) usually appear within a ventricular wall (i.e., intramural). Calcific deposits may be present within the neoplasm. Sudden death occurs in about a third of the patients, presumably the result of an arrhythmia or an obstruction to outflow from a ventricle. Treatment strategy varies according to tumor type. For example, rhabdomyomas are treated conservatively due to a high rate of spontaneous regression. Total or partial resection of a fibroma may relieve obstruction with an excellent probability of long-term survival. A Purkinje cell tumor associated with high-grade ventricular ectopy may require surgical resection, whereas a cardiac hemangioma may be treated with high-dose steroids or interferon. Malignant cardiac tumors are rare, but must always be considered in the differential diagnosis. MRI has only limited specificity for identifying the likely tissue type of the tumor in children (Kiaffas et al. 2002), but is ideally suited for the noninvasive evaluation of tumor size, location, number, and relationship to adjacent structures (Hoffmann et al. 2003). MRI also helps in distinguishing cardiac tumors from tumor-like conditions, including pericardial cysts, lipomatous hypertrophy of the atrial septum, thrombi, and sarcoidosis.

#### 4.6.3 Cardiomyopathy

##### 4.6.3.1 Hypertrophic Obstructive Cardiomyopathy

Cardiac MRI has been used to define the distribution of hypertrophy and its functional consequences. This is especially true for apical and anterolateral wall involvement,

which is difficult to diagnose by echo (Rickers et al. 2005). Delayed enhancement gadolinium MRI has also been used in hypertrophic cardiomyopathy to demonstrate areas of fibrosis (Teraoka 2005), and the extent of this abnormal uptake is linked to the risk of sudden death and development of left ventricular dilation and heart failure. MRI has also been used to identify the functional and anatomical consequences of septal resection. In addition, MRI is ideal for screening of relatives of probands because of its phenotypic accuracy.

##### 4.6.3.2 Left Ventricular Noncompaction

Noncompaction of the ventricular myocardium is a rare congenital cardiomyopathy characterized by numerous excessively prominent trabeculations and deep intertrabecular recesses. Noncompaction of the ventricular myocardium is most often an isolated cardiac malformation presenting as a sporadic disease. Associated cardiac anomalies are present in some patients. The following criteria have been proposed for diagnosis of isolated LV noncompaction by echo: (1) absence of coexisting cardiac abnormalities, (2) a 2-layered structure of the left ventricular wall, with the end systolic ratio of noncompacted to compacted layer  $>2$ , (3) finding this structure predominantly in the apical and mid-ventricular areas, and (4) blood flow directly from the ventricular cavity into the deep intertrabecular recesses as assessed by Doppler echocardiography (van der Loo and Jenni 2003). MRI appears ideal for identification of this condition, and may provide the ability to detect a broader spectrum and more subtle variants of noncompaction (Fig. 17). Trabecular mass of greater than 20 % of total myocardial mass may be a useful index to suggest the diagnosis of isolated left ventricular noncompaction (Korcyk et al. 2004). A ratio of noncompacted to compacted myocardium of  $>2.3$  in diastole distinguishes pathological noncompaction with a sensitivity, specificity, and positive and negative predictive value of 86, 99, 75, and 99 %, respectively (Petersen et al. 2005). A diagnosis of noncompaction has important implications because of the need for familial screening and the possible association with other cardiac anomalies and/or muscle disorders, progressive left ventricular dysfunction, risk of systemic embolism, and life-threatening arrhythmias.

##### 4.6.3.3 Arrhythmogenic Right Ventricular Cardiomyopathy

Arrhythmogenic right ventricular cardiomyopathy (ARVC) has been reported as the etiology of up to 42 % of cases of sudden death in young adults secondary to arrhythmia (Cho et al. 2003). It is characterized histologically by fatty or fibro-fatty infiltration of the right ventricular myocardium. The imaging protocol includes cine MRI sequences for evaluation of segmental and global right ventricular

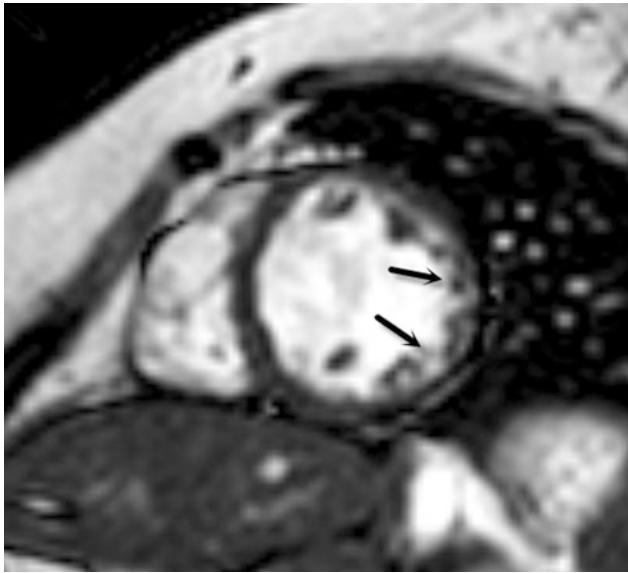


**Fig. 17** LV noncompaction in an 18-year-old male with Duchenne's muscular dystrophy. On this diastolic short axis image, note the prominent trabeculations, the deep intertrabecular recesses (*arrow*), and a noncompacted/compacted myocardial ratio of  $>3$

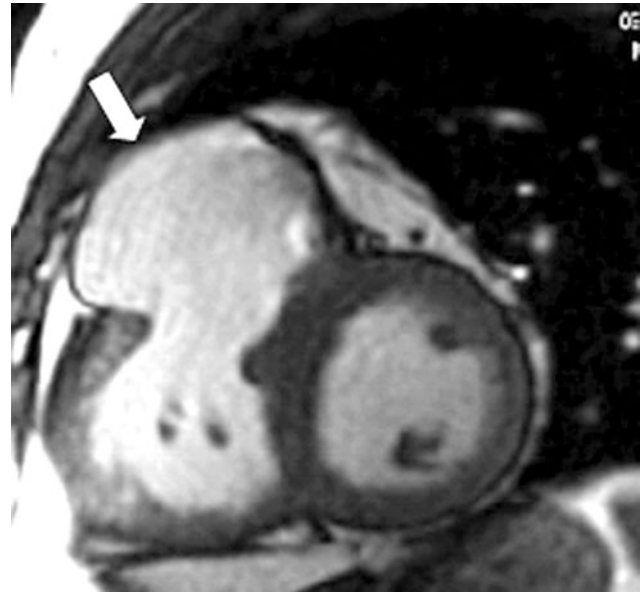


**Fig. 18** Cine SSFP image showing right ventricular outflow tract patch aneurysm (*arrow*) in corrected tetralogy of Fallot

function and wall motion, and anatomic sequences to detect fatty or fibro-fatty infiltration of the right ventricular myocardium. Delayed enhancement techniques appear to have a high sensitivity for fibro-fatty infiltration of the right ventricular wall, and should be considered an important part of the MRI protocol (Tandri et al. 2005). The diagnostic criteria of ARVC include regional wall motion abnormalities, increased right ventricular volumes, morphological abnormalities (aneurysms, trabecular disarray), and increased myocardial signal suggesting fatty infiltration. Isolated findings of right ventricular wall thinning or focal intramyocardial fat must be interpreted with caution (Bomma et al. 2004). Focal wall motion abnormalities, especially focal dyskinesia, are generally felt to be a more reliable indicator of ARVD on MRI than intramyocardial fat.

#### 4.6.3.4 Iron Overload Cardiomyopathy

Iron overload cardiomyopathy remains the leading cause of death in patients with hemochromatosis or the inherited severe anemias, which require regular blood transfusions from infancy. MRI is ideally suited for monitoring thalassemia patients because it can detect cardiac and liver iron burdens as well as accurately measure left ventricular dimensions and function (Westwood et al. 2005a, b). Repeated assessment of myocardial iron using biopsy is difficult because of safety issues, sampling error, and patchy iron distribution.

Measurement of T2\* using MRI has been shown to reflect tissue iron, and has good reproducibility (Westwood et al. 2005a, b). There is a clear relation between reduced

myocardial T2\* ( $<20$  ms) indicating iron overload, and LV dysfunction (Westwood et al. 2005a, b). Myocardial T2\* increases in concert with left ventricular function recovery in thalassemia patients with heart failure. MRI has been used to evaluate the effectiveness of different chelation regimes on the myocardium.

## 5 Postoperative Evaluation of Congenital Heart Disease

MRI provides more precise and reproducible quantification of ventricular volumes, mass, and function than 2D echo (Helbing et al. 1995). This is especially the case for the right ventricle (Grothues et al. 2004; Helbing et al. 1996) which is usually the chamber implicated in congenital heart disease. Sequential measurements of right ventricular volumes, mass, and function, and pulmonary regurgitant fraction are important for postoperative management after repair of tetralogy of Fallot (Figs. 6, 18) (Niezen et al. 1996), and intra-atrial repair of d-transposition of great arteries (Fig. 19). This information may have prognostic and therapeutic implications for the management of postoperative patients. MRI parameters are the best predictors of adverse clinical outcome in patients with treated tetralogy of Fallot. The timing of pulmonary valve replacement for corrected tetralogy of Fallot is still evolving, and is increasingly being shaped by measures of right ventricular size and function determined by MRI. The typical cardiac MRI protocol in the setting of postoperative tetralogy of Fallot, or after a



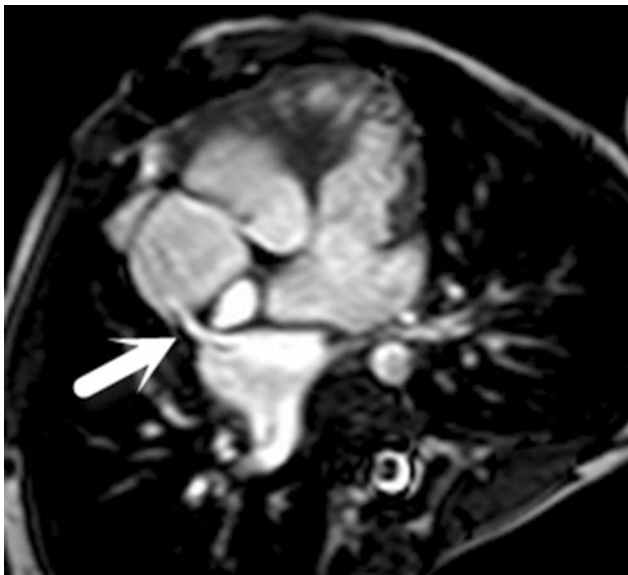


**Fig. 19** Severe stenosis of the pulmonary venous baffle (arrow) after an atrial switch procedure for d-transposition of great arteries

complex two-ventricle repair, is comprised of the following sequences: dynamic bright blood imaging of ventricular function; thin-section bright blood imaging of the branch pulmonary arteries, right ventricular and left ventricular outflow tracts, and the aortic arch; flow velocity mapping of the pulmonary artery, ascending aorta, atrioventricular valves and the branch pulmonary arteries to determine  $Q_P:Q_S$ , the degree of pulmonary, aortic and atrioventricular valve regurgitation, and the differential pulmonary flow to both lungs respectively; and gadolinium-enhanced 3D MRA to determine the status of the extra-cardiac vasculature.

MRI is also indicated for evaluation of cardiovascular morphology and function both during and after the various stages of surgical repair for hypoplastic left heart syndrome (Kondo et al. 1991a, b) (Fig. 3) or a single ventricle (Fogel et al. 1996). MRI can replace cardiac catheterization for routine evaluation of cardiovascular morphology and function prior to superior cavopulmonary connection in the majority of patients undergoing single ventricle repair (Brown et al. 2007).

MRI is effective for demonstrating stenoses of intra-atrial baffles (Fig. 19) after repair of transposition of the great arteries (Chung et al. 1988). Following a single ventricle repair, or following an intra-atrial repair for transposition of great arteries, additional bright blood sequences are performed of the atrial baffle (Fig. 20) or the Fontan circuit, as necessary. Following a Fontan procedure, the performance of the MRA may be modified with simultaneous upper and lower extremity intravenous contrast injections to accommodate the slow venous return, and to reduce artifacts from unopacified venous blood.

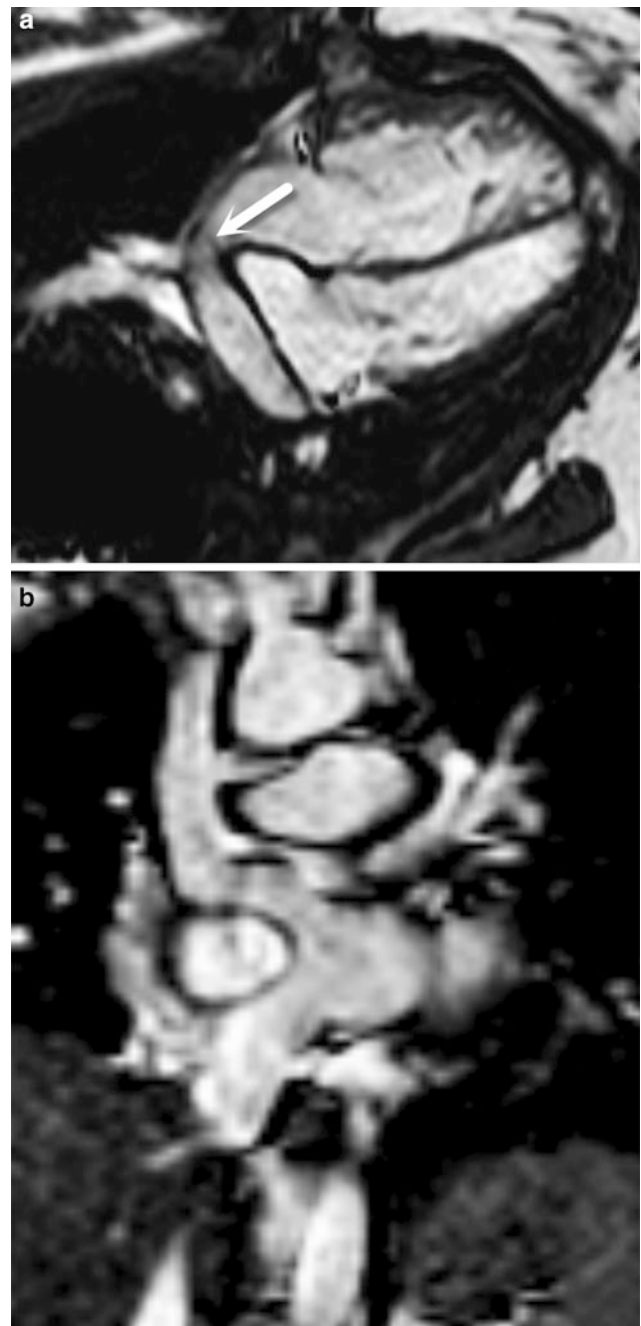


**Fig. 20** **a** Cine TFE image showing mildly hypertrophied right ventricle in a patient with d-transposition of great arteries after an atrial switch procedure. Arrow points to the pulmonary venous baffle directed towards the RV. **b** Characteristic 'trouser-like' appearance of the SVC and IVC entering the systemic venous baffle in the same patient

## 6 Limitations of Cardiac MRI in Children

MRI does have a number of limitations in the evaluation of the pediatric heart. Sedation or anesthesia is required for most patients less than 8 years of age. Artifacts caused by stainless steel coils, stents, and clips may limit the information gained

in the vicinity of the metallic object, or occasionally, may negate the utility of the entire study. Pacemakers, defibrillators, and epicardial wires are relative contra-indications for performance of an MRI, but protocols for performance of MRI in patients with permanent pacemakers and defibrillators have been devised (Nazarian et al. 2006).

Some MRI techniques like coronary MRA, perfusion, and viability imaging are technically challenging in the setting of very small patient sizes or high heart rates. Conventional MRI cannot measure pressure gradients, pulmonary vascular resistance, or oxygen saturation, and therefore cannot obviate the need for a diagnostic cardiac catheterization in a number of cases. The spatial resolution of conventional MRI sequences is usually inadequate to assess thin and mobile valvular structures like chordae, cusps, or commissures.

Finally, there is a paucity of standardized MRI data giving normal reference values for pediatric patients. Normal values for ventricular volumes, function, and some other structural measurements have been published (Kaiser et al. 2008; Buechel et al. 2009a, b) and multicenter data is now being accumulated. It is crucial that these data incorporate, or at least attempt to unify, the multitude of different imaging and post-processing conventions that have evolved in the international centers performing pediatric cardiac MRI (Ntsinjana et al. 2011).

## 7 Conclusion

MRI plays an important complementary role to echocardiography in the evaluation of cardiac morphology and function in children with congenital heart disease in the preoperative and postoperative periods. Recent technological advancements including free-breathing capabilities, improved image resolution, ultrashort imaging time, and real-time imaging, along with a burgeoning trained user-base, increasing accessibility to MRI scanners, a steady stream of clinical validation studies, and the lack of ionizing radiation have all combined to significantly expand the indications for MRI in pediatric cardiovascular disease over the last several years.

## References

- Anderson LJ, Holden S, Davis B et al (2001) Cardiovascular T2-star (T2\*) magnetic resonance for the early diagnosis of myocardial iron overload. *Eur Heart J* 22:2171–2179
- Araoz PA, Reddy GP, Thomson PD, Higgins CB (2002) Images in cardiovascular medicine. Magnetic resonance angiography of crisscross heart. *Circulation* 105:537–538
- Atweh LA, Jadhav S, Vogelius E, Pednekar A, Muthupillai R, Krishnamurthy R (2013) Clinical validation of free-breathing navigator triggered retrospectively cardiac gated cine steady state free precession (NAV-SSFP) imaging in sedated children. In: Radiological Society of North America 99th scientific assembly and annual meeting, Chicago IL, December 3, 2013 (abstract)
- Axel L, Dougherty L (1989) Heart wall motion: improved method of spatial modulation of magnetization for MR imaging. *Radiology* 172:349–350
- Babu-Narayan SV, Goktekin O, Moon JC et al (2005) Late gadolinium enhancement cardiovascular magnetic resonance of the systemic right ventricle in adults with previous atrial redirection surgery for transposition of the great arteries. *Circulation* 111:2091–2098
- Bailes DR, Gilerdale DJ, Bydder GM et al (1985) Respiratory ordered phase encoding (ROPE): a method for reducing respiratory motion artifacts in MR imaging. *J Comput Assist Tomogr* 9:835–838
- Beerbaum P, Korperich H, Gieseke J et al (2003) Rapid left to-right shunt quantification in children by phase contrast magnetic resonance imaging combined with sensitivity encoding. *Circulation* 108:1355–1361
- Beerbaum P, Koerperich H, Sarikouch S et al (2006) Time resolved “Cine” 3D contrast-enhanced MR angiography using Centra-Keyhole-SENSE in congenital heart diseases with pulmonary artery pathology. *J Cardiovasc MR* 8:26 (abstract)
- Beerbaum P, Sarikouch S, Laser KT, Greil G, Burchert W, Körperich H (2009) Coronary anomalies assessed by whole-heart isotropic 3D magnetic resonance imaging for cardiac morphology in congenital heart disease. *J Magn Reson Imaging* 29:320–327
- Bogren HG, Klipstein RH, Firmin DN et al (1989) Quantitation of antegrade and retrograde blood flow in the human aorta by magnetic resonance velocity mapping. *Am Heart J* 117:1214–1222
- Bomma C, Rutberg J, Tandri H et al (2004) Misdiagnosis of arrhythmogenic right ventricular dysplasia/cardiomyopathy. *J Cardiovasc Electrophysiol* 15:300–306
- Brenner LD, Caputo GR, Mostbeck G et al (1992) Quantification of antegrade and retrograde blood flow in the human aorta by magnetic resonance imaging. *J Am Coll Cardiol* 20:1246–1250
- Brown DW, Gauvreau K, Powell AJ et al (2007) Cardiac magnetic resonance versus routine cardiac catheterization before bidirectional glenn anastomosis in infants with functional single ventricle: a prospective randomized trial. *Circulation* 116:2718–2725
- Buechel ER, Balmer C, Bauersfeld U, Kellenberger CJ, Schwitter J (2009a) Feasibility of perfusion cardiovascular magnetic resonance in pediatric patients. *J Cardiovasc Magn Reson* 11:51–58
- Buechel E, Kaiser T, Jackson C, Schmitz A, Kellenberger C (2009b) Normal right- and left ventricular volumes and myocardial mass in children measured by steady state free precession cardiovascular magnetic resonance. *J Cardiovasc Magn Reson* 11:19
- Caputo GR, Kondo C, Masui T et al (1991) Right and left lung perfusion: in vitro and in vivo validation with oblique angle, velocity-encoded cine MR imaging. *Radiology* 180:693–698
- Carr JC, Simonetti O, Bundy J et al (2001) Cine MR angiography of the heart with segmented true fast imaging with steady state precession. *Radiology* 219:828–834
- Casolo G, Rega L, Gensini GF (2004) Detection of right atrial and pulmonary artery thrombosis after the Fontan procedure by magnetic resonance imaging. *Heart* 90:825
- Castillo E, Osman NF, Reson BD et al (2005) Quantitative assessment of regional myocardial function with MR-tagging in a multi-center study: interobserver and intraobserver agreement of fast strain analysis with Harmonic Phase (HARP) MRI. *J Cardiovasc Magn Reson* 7:783–791
- Chia JM, Fischer SE, Wickline SA et al (2000) Performance of QRS detection for cardiac magnetic resonance imaging with a novel vectorcardiographic triggering method. *J Magn Reson Imaging* 12:678–688
- Cho Y, Park T, Yang DH et al (2003) Arrhythmogenic right ventricular cardiomyopathy and sudden cardiac death in young Koreans. *Circ J* 67:925–928

- Choi YH, Park JH, Choe YH et al (1994) MR imaging of Ebstein's anomaly of the tricuspid valve. *AJR Am J Roentgenol* 163:539–543
- Chung KJ, Simpson IA, Glass RF et al (1988) Cine magnetic resonance imaging after surgical repair in patients with transposition of the great arteries. *Circulation* 77:104–109
- Chung T (2012) Initial clinical experience in congenital heart disease MR examinations with multi-transmit radiofrequency (RF) technology on 3T. *Pediatr Rad* 42(S2):S254
- Chung T, Muthupillai R (2004) Application of SENSE in clinical pediatric body MR imaging. *Top Magn Reson Imaging* 15:187–196
- Chung T, Krishnamurthy R (2005) Contrast-enhanced MR angiography in infants and children. *Magn Reson Imaging Clin N Am* 13:161–170
- Didier D, Higgins CB (1986) Identification and localization of ventricular septal defect by gated magnetic resonance imaging. *Am J Cardiol* 57:1363–1368
- Evans AJ, Iwai F, Grist TA et al (1993) Magnetic resonance imaging of blood flow with a phase subtraction technique. In vitro and in vivo validation. *Invest Radiol* 28:109–115
- Festa P, Ait-Ali L, Cerillo AG et al (2006) Magnetic resonance imaging is the diagnostic tool of choice in the preoperative evaluation of patients with partial anomalous pulmonary venous return. *Int J Cardiovasc Imaging* 22:685–693
- Firmin DN, Naylor GL, Klipstein RH et al (1987) In vivo validation of MR velocity imaging. *J Comput Assis Tomogr* 11:751–756
- Fischer SE, Wickline SA, Lorenz CH (1999) Novel real-time R-wave detection algorithm based on the vectorcardiogram for accurate gated magnetic resonance acquisitions. *Magn Reson Med* 42:361–370
- Flamm SD, Muthupillai R (2004) Coronary artery magnetic resonance angiography. *J Magn Reson Imaging* 19:686–709
- Fogel MA, Weinberg PM, Chin AJ et al (1996) Late ventricular geometry and performance changes of functional single ventricle throughout staged Fontan reconstruction assessed by magnetic resonance imaging. *J Am Coll Cardiol* 28:212–221
- Fogel MA, Weinberg PM, Gupta KB et al (1998) Mechanics of the single left ventricle: a study in ventricular–ventricular interaction II. *Circulation* 98:330–338
- Fogel MA (2000) Assessment of cardiac function by magnetic resonance imaging. *Pediatr Cardiol* 21:59–69
- Fratz S, Hager A, Schreiber C, Schwaiger M, Hess J, Stern HC (2011) Long-term myocardial scarring after operation for anomalous left coronary artery from the pulmonary artery. *Ann Thorac Surg* 92:1761–1766
- Fratz S, Hauser M, Bengel FM et al (2006) Myocardial scars determined by delayed-enhancement magnetic resonance imaging and positron emission tomography are not common in right ventricles with systemic function in long-term follow up. *Heart* 92:1673–1677
- Frayne R, Steinman DA, Ethier CR et al (1995) Accuracy of MR phase contrast velocity measurements for unsteady flow. *J Magn Reson Imaging* 5:428–431
- Friedrich MG, Sechtem U, Schulz-Menger J, et al (2009) Cardiovascular magnetic resonance in myocarditis: A JACC white paper. *J Am Coll Cardiol* 53:1475–1487
- Goo HW, Yang DH, Park IS et al (2007) Time-resolved three dimensional contrast-enhanced magnetic resonance angiography in patients with Fontan operation or bidirectional cavopulmonary connection: initial experience. *J Magn Reson Imaging* 25:727–736
- Greil GF, Geva T, Maier SE et al (2002a) Effect of acquisition parameters on the accuracy of velocity encoded cine magnetic resonance imaging blood flow measurements. *J Magn Reson Imaging* 15:47–54
- Greil GF, Stuber M, Botnar RM et al (2002b) Coronary magnetic resonance angiography in adolescents and young adults with Kawasaki disease. *Circulation* 105:908–911
- Grist TM, Thornton FJ (2005) Magnetic resonance angiography in children: technique, indications, and imaging findings. *Pediatr Radiol* 35:26–39
- Grotenhuis HB, Westenberg JJ, Doornbos J et al (2006) Aortic root dysfunctioning and its effect on left ventricular function in Ross procedure patients assessed with magnetic resonance imaging. *Am Heart J* 152(975):e1–e8
- Grosse-Wortmann L, Yun TJ, Al-Radi O et al (2008) Borderline hypoplasia of the left ventricle in neonates: insights for decision-making from functional assessment with magnetic resonance imaging. *J Thorac Cardiovasc Surg* 136:1429–1436
- Grothues F, Moon JC, Bellenger NG et al (2004) Interstudy reproducibility of right ventricular volumes, function and mass with cardiovascular magnetic resonance. *Am Heart J* 147:218–223
- Helbing WA, Bosch HG, Maliopaard C et al (1995) Comparison of echocardiographic methods with magnetic resonance imaging for assessment of right ventricular function in children. *Am J Cardiol* 76:589–594
- Helbing WA, Niezen RA, Cessie SL et al (1996) Right ventricular diastolic function in children with pulmonary regurgitation after repair of tetralogy of Fallot: volumetric evaluation by magnetic resonance velocity mapping. *J Am Coll Cardiol* 28:1827–1835
- Helbing WA, de Roos A (2000) Clinical applications of cardiac magnetic resonance imaging after repair of tetralogy of Fallot. *Pediatr Cardiol* 21:70–79
- Henk CB, Higgins CB, Saeed M (2005) Endovascular interventional MRI. *J Magn Reson Imaging* 22:451–460
- Herkens RJ, Higgins CB, Hricak H et al (1983) Nuclear magnetic resonance imaging of the cardiovascular system: normal and pathologic findings. *Radiology* 147:749–759
- Hernandez RJ, Aisen AM, Foo TKF et al (1993) Thoracic cardiovascular anomalies in children: evaluation with a fast gradient-recalled-echo sequence with cardiac-triggered segmented acquisition. *Radiology* 188:755–780
- Hoffmann U, Globits S, Schima W et al (2003) Usefulness of magnetic resonance imaging of cardiac and paracardiac masses. *Am J Cardiol* 92:890–895
- Hor KN, Wansapura J, Markham LW et al (2009) Circumferential strain analysis identifies strata of cardiomyopathy in Duchenne muscular dystrophy: a cardiac magnetic resonance tagging study. *J Am Coll Cardiol* 53:1204–1210
- Hor KN, Mazur W, Taylor MD et al (2011) Effects of steroids and angiotensin converting enzyme inhibition on circumferential strain in boys with Duchenne muscular dystrophy: a cross-sectional and longitudinal study utilizing cardiovascular magnetic resonance. *J Cardiovasc Magn Reson* 13:60
- Hsiao A, Lustig M, Alley MT et al (2012) Rapid pediatric cardiac assessment of flow and ventricular volume with compressed sensing parallel imaging volumetric cine phase contrast MRI. *AJR Am J Roentgenol* 198:W250–W259
- Hundley WG, Li HF, Lange RA et al (1995) Assessment of left-to-right intracardiac shunting by velocity-encoded, phase-difference magnetic resonance imaging. A comparison with oximetric and indicator dilution techniques. *Circulation* 91:2955–2960
- Jahnke C, Paetsch I, Gebker R et al (2006) Accelerated 4D dobutamine stress MR imaging with k-t BLAST: feasibility and diagnostic performance. *Radiology* 241:718–728
- Kaiser T, Kellenberger C, Albisetti M, Bergstrasser E, Valsangiacomo Buechel E (2008) Normal values for aortic diameters in children and adolescents—assessment in vivo by contrast-enhanced CMR-angiography. *J Cardiovasc Magn Reson* 10:56
- Kellenberger CJ, Macgowan CK, Roman KS et al (2005) Hemodynamic evaluation for the peripheral pulmonary circulation by cine phase contrast magnetic resonance imaging. *J Magn Reson Imaging* 22:780–787



- Kellman P, Arai AE, McVeigh ER, Aletras AH (2002) Phase sensitive inversion recovery for detecting myocardial infarction using gadolinium delayed hyperenhancement. *Magn Reson Med* 47:372–383
- Kersting-Sommerhoff BA, Diethelm L, Stanger P et al (1990a) Evaluation of complex congenital ventricular anomalies with magnetic resonance imaging. *Am Heart J* 120:133–142
- Kersting-Sommerhoff B, Seelos KC, Hardy C et al (1990b) Evaluation of surgical procedures for cyanotic congenital heart disease by using MR imaging. *AJR Am J Roentgenol* 155:259–266
- Kiaffas MG, Powell AJ, Geva T (2002) Magnetic resonance imaging evaluation of cardiac tumor characteristics in infants and children. *Am J Cardiol* 89:1229–1233
- Kim RJ, Wu E, Rafael A et al (2000) The use of contrast-enhanced magnetic resonance imaging to identify reversible myocardial dysfunction. *N Engl J Med* 343:1445–1453
- Kim WY, Danias PG, Stuber M et al (2001) Coronary magnetic resonance angiography for the detection of coronary stenoses. *N Engl J Med* 345:1445–1453
- Kondo C, Caputo GR, Semelka R et al (1991a) Right and left ventricular stroke volume measurements with velocity encoded cine MR imaging: in vitro and in vivo validation. *AJR Am J Roentgenol* 157:9–16
- Kondo C, Hardy C, Higgins SS et al (1991b) Nuclear magnetic resonance imaging of the palliative operation for hypoplastic left heart syndrome. *J Am Coll Cardiol* 18:817–823
- Korcyk D, Edwards CC, Armstrong G et al (2004) Contrast-enhanced cardiac magnetic resonance in a patient with familial isolated ventricular noncompaction. *J Cardiovasc Magn Reson* 6:569–576
- Korperich H, Gieseke J, Barth P et al (2004) Flow volume and shunt quantification in pediatric congenital heart disease by real-time magnetic resonance velocity mapping. *Circulation* 109:1987–1993
- Krishnamurthy R, Slesnick T, Browne L, Taylor MD, Nutting A, Muthupillai R (2010) Free-breathing high temporal resolution time resolved contrast-enhanced MRA (4D MRA) at high heart rates using keyhole SENSE CENTRA in congenital heart disease. *J Cardiovasc Magn Reson* 12(Suppl 1):O31
- Krishnamurthy R, Pednekar A, Vogelius E et al (2012) Clinical validation of free-breathing respiratory triggered retrospectively cardiac gated cine steady state free precession (RT-SSFP) imaging in sedated children. *J Cardiovasc Magn Reson* 15 (Suppl 1):O98
- Lee KH, Yoon CS, Chow KO et al (2001) Use of imaging for assessing anatomical relationships of tracheobronchial anomalies associated with left pulmonary artery sling. *Pediatr Radiol* 31:269–278
- Link KM, Herrera MA, D'Souza VJ et al (1988) MR imaging of Ebstein anomaly: results in four cases. *AJR Am J Roentgenol* 150:363–367
- Makowski MR, Wiethoff AJ, Uribe S et al (2011) Congenital heart disease: cardiovascular MR imaging by using an intravascular blood pool contrast agent. *Radiology* 260:681–688
- Markl M, Pelc NJ (2004) On flow effects in balanced steady state free precession imaging: pictorial description, parameter dependence and clinical implications. *J Magn Reson Imaging* 20:697–705
- Markl M, Kilner P, Ebbers T (2011) Comprehensive 4D velocity mapping of the heart and great vessels by cardiovascular magnetic resonance. *J Cardiovasc Magn Reson* 13:7
- Mayo JR, Roberson D, Sommerhoff B et al (1990) MR imaging of double outlet right ventricle. *J Comput Assist Tomogr* 14:336–339
- Menteer J, Weinberg PM, Fogel MA (2005) Quantifying regional right ventricular function in tetralogy of Fallot. *J Cardiovasc Magn Reson* 7:753–761
- Messroghli DR, Greiser A, Fröhlich M, Dietz R, Schulz-Menger J (2007) Optimization and validation of a fully-integrated pulse sequence for modified Look-Locker inversion-recovery (MOLLI) T1 mapping of the heart. *J Magn Reson Imaging* 24:1081–1086
- Mirowitz SA, Gutierrez FR, Canter CE et al (1989) Tetralogy of Fallot: MR findings. *Radiology* 171:207–212
- Mueller A, Kouwenhoven M, Naehle CP et al (2012) Dual-Source radiofrequency transmission with patient-adaptive local radiofrequency shimming for 3.0T cardiac MR. *Radiology* 263:77–85
- Muthupillai R, Vick GW, Flamm SD et al (2003) Time-resolved contrast-enhanced magnetic resonance angiography in pediatric patients using sensitivity encoding. *J Magn Reson Imaging* 17:559–564
- Nazarian S, Roguin A, Zviman MM et al (2006) Clinical utility and safety of a protocol for noncardiac and cardiac magnetic resonance imaging of patients with permanent pacemakers and implantable-cardioverter defibrillators at 1.5 tesla. *Circulation* 114:1277–1284
- Niezen RA, Helbing WA, van der Wall EE et al (1996) Biventricular systolic function and mass studied with MR imaging in children with pulmonary regurgitation after repair for tetralogy of Fallot. *Radiology* 201:135–140
- Nordmeyer S, Riesenkauff E, Messroghli D et al (2013) Four-dimensional velocity-encoded magnetic resonance imaging improves blood flow quantification in patients with complex accelerated flow. *J Magn Reson Imaging* 37:208–216
- Ntsinjana HN, Hughes ML, Taylor AM (2011) The role of cardiovascular magnetic resonance in pediatric congenital heart disease. *J Cardiovasc Magn Reson* 13:51
- Oosterhof T, Mulder BJM, Hubert WV et al (2006) Cardiovascular magnetic resonance in the follow-up of patients with corrected tetralogy of Fallot: a review. *Am Heart J* 151:265–272
- Oppelt A, Graumann R, Barfuss H (1986) Fisp—a new fast MRI sequence. *Electromedica* 54:15–18
- Oshinski JN, Parks WJ, Markou CP et al (1996) Improved measurement of pressure gradients in aortic coarctation by magnetic resonance imaging. *J Am Coll Cardiol* 28:1818–1826
- Petersen SE, Selvanayagam JB, Wiesmann F et al (2005) Left ventricular noncompaction: insights from cardiovascular magnetic resonance imaging. *J Am Coll Cardiol* 46:101–105
- Piaw CS, Kiam OT, Rapae A et al (2006) Use of noninvasive phase contrast magnetic resonance imaging for estimation of atrial septal defect size and morphology: a comparison with transesophageal echo. *Cardiovasc Intervent Radiol* 29:230–234
- Powell AJ, Geva T (2000) Blood flow measurement by magnetic resonance imaging in congenital heart disease. *Pediatr Cardiol* 21:47–58
- Powell AJ, Maier SE, Chung T et al (2000) Phase-velocity cine magnetic resonance imaging measurement of pulsatile blood flow in children and young adults: in vitro and in vivo validation. *Pediatr Cardiol* 21:104–110
- Prakash A, Garg R, Marcus EN et al (2006) Faster flow quantification using sensitivity encoding for velocity-encoded cine magnetic resonance imaging: in vitro and in vivo validation. *J Magn Reson Imaging* 24:676–682
- Prakash A, Powell AJ, Krishnamurthy R et al (2004) Magnetic resonance imaging evaluation of myocardial perfusion and viability in congenital and acquired pediatric heart disease. *Am J Cardiol* 93:657–661
- Prince MR, Yucel E, Kaufman J et al (1993) Dynamic gadolinium-enhanced three-dimensional abdominal MR arteriography. *J Magn Reson Imaging* 3:877–881
- Pruessmann KP, Weiger M, Schiedegger MB et al (1999) SENSE: sensitivity encoding for fast MRI. *Magn Reson Med* 42:952–962
- Rathod RH, Prakash A, Powell AJ, Geva T (2010) Myocardial fibrosis identified by cardiac magnetic resonance late gadolinium enhancement is associated with adverse ventricular mechanics and ventricular tachycardia late after Fontan operation. *J Am Coll Cardiol* 55:1721–1728

- Razavi R, Hill DL, Keevil SF et al (2003) Cardiac catheterization guided by MRI in children and adults with congenital heart disease. *Lancet* 362:1877–1882
- Rebergen SA, Chin J, Ottenkamp J et al (1993a) Pulmonary regurgitation in the late postoperative follow-up of tetralogy of Fallot. Volumetric quantitation by nuclear magnetic resonance velocity mapping. *Circulation* 88:2257–2266
- Rebergen SA, Ottenkamp J, Doornbos J et al (1993b) Postoperative pulmonary flow dynamics after Fontan surgery: assessment with nuclear magnetic resonance velocity mapping. *J Am Coll Cardiol* 21:123–131
- Rebergen SA, Helbing WA, van der Wall EE et al (1995) MR velocity mapping of tricuspid flow in healthy children and in patients who have undergone Mustard or Senning repair. *Radiology* 194:505–512
- Rickers C, Wilke NM, Jerosch-Herold M et al (2005) Utility of cardiac magnetic resonance imaging in the diagnosis of hypertrophic cardiomyopathy. *Circulation* 112:855–861
- Robinson JD, Del Nido PJ, Geggel RL, Perez-Atayde AR, Lock JE, Powell AJ (2010) Left ventricular diastolic heart failure in teenagers who underwent balloon aortic valvuloplasty in early infancy. *Am J Cardiol* 106:426–429
- Roman KS, Kellenberger CJ, Farooq S et al (2005) Comparative imaging of differential pulmonary blood flow in patients with congenital heart disease: magnetic resonance imaging versus lung perfusion scintigraphy. *Pediatr Radiol* 25:295–301
- Sakuma H, Yasutaka I, Suzawa N et al (2005) Assessment of coronary arteries with total study time of less than 30 min by using whole-heart coronary MR angiography. *Radiology* 237:316–321
- Schlesinger AE, Krishnamurthy R, Sena LM, Guillerman RP, Chung T et al (2005) Incomplete double aortic arch with atresia of the distal left arch: distinctive imaging appearance. *AJR Am J Roentgenol* 184:1634–1639
- Schwitt J (2006) Myocardial perfusion. *J Magn Reson Imaging* 24:953–963
- Sechtem U, Pfleger P, Cassidy MC et al (1987) Ventricular septal defect: visualization of shunt flow and determination of shunt size by cine MR imaging. *AJR Am J Roentgenol* 149:689–692
- Sieverding L, Jung WJ, Klose U et al (1992) Noninvasive blood flow measurement and quantification of shunt volume by cine magnetic resonance in congenital heart disease. Preliminary results. *Pediatr Radiol* 22:48–54
- Simonetti OP, Finn JP, White RD et al (1996) “Black blood” T2-weighted inversion-recovery MR imaging of the heart. *Radiology* 199:45–57
- Sodickson DK, Manning WJ (1997) Simultaneous acquisition of spatial harmonics (SMASH): ultra-fast imaging with radiofrequency coil arrays. *Magn Reson Med* 38:591–603
- Sorensen TS, Korperich H, Greil GF et al (2004) Operator-independent isotropic three-dimensional magnetic resonance imaging for morphology in congenital heart disease. *Circulation* 110:163–169
- Sorensen TS, Beerbaum P, Korperich H et al (2005) Three dimensional, isotropic MRI: a unified approach to quantification and visualization in congenital heart disease. *Int J Cardiovasc Imag* 21:283–292
- Spuentrup E, Fausten B, Kinzel S et al (2005) Molecular magnetic resonance imaging of atrial clots in a swine model. *Circulation* 112:396–399
- Sridharan S, Derrick G, Deanfield J et al (2006) Assessment of differential branch pulmonary blood flow: a comparative study of phase contrast magnetic resonance imaging and radionuclide lung perfusion imaging. *Heart* 92:963–968
- Steffens JC, Bourne MW, Sakuma H et al (1994) Quantification of collateral blood flow in coarctation of the aorta by velocity encoded cine magnetic resonance imaging. *Circulation* 90:937–943
- Stuber M, Botnar RM, Kissinger KV et al (2001) Free-breathing black blood coronary MR angiography: initial results. *Radiology* 219:278–283
- Su JT, Chung T, Muthupillai R et al (2005) Usefulness of real-time navigator magnetic resonance imaging for evaluating coronary artery origins in pediatric patients. *Am J Cardiol* 95:679–682
- Su JT, Chung T, Kovalchin JP (2004) Magnetic resonance imaging of coronary and systemic aneurysms in Kawasaki disease. *Cardiol Young* 14:198–199
- Su JT, Krishnamurthy R, Chung T et al (2007) Anomalous right coronary artery from the pulmonary artery: noninvasive diagnosis and serial evaluation. *J Cardiovasc Magn Reson* 9:57–61
- Tandri H, Saranathan M, Rodriguez ER et al (2005) Noninvasive detection of myocardial fibrosis in arrhythmogenic right ventricular cardiomyopathy using delayed-enhancement magnetic resonance imaging. *J Am Coll Cardiol* 45:98–103
- Taylor AM, Dymarkowski S, Meerleer K De et al (2005a) Validation and application of single breath-hold cine cardiac MR for ventricular function assessment in children with congenital heart disease at rest and during adenosine stress. *J Cardiovasc Magn Reson* 7:743–751
- Taylor AM, Dymarkowski S, Hamaekers P et al (2005b) MR coronary angiography and late-enhancement myocardial MR in children who underwent arterial switch surgery for transposition of great arteries. *Radiology* 234:542–547
- Teraoka K (2005) Delayed contrast enhancement of MRI in hypertrophic cardiomyopathy. *Magn Reson Imaging* 23:701
- Valeti VU, Chun W, Potter DD et al (2006) Myocardial tagging and strain analysis at 3 Tesla: comparison with 1.5 Tesla imaging. *J Magn Reson Imaging* 23:477–480
- van der Loo B, Jenni R (2003) Isolated noncompaction of the myocardium. *Circulation* 107:e50
- Van Praagh R (1984) The segmental approach clarified. *Cardiovasc Intervent Radiol* 7:320–325
- Valsangiacomo ER, Barrea C, MacGowan CK et al (2003) Phase contrast MR assessment of pulmonary venous blood flow in children with surgically repaired pulmonary veins. *Pediatr Radiol* 33:607–613
- Weber OM, Martin AJ, Higgins CB (2003) Whole-heart steady state free precession coronary artery magnetic resonance angiography. *Magn Reson Med* 50:1223–1228
- Westwood MA, Firmin DN, Gildo M et al (2005a) Intercenter reproducibility of magnetic resonance T2\* measurements of myocardial iron in thalassaemia. *Int J Cardiovasc Imaging* 21:531–538
- Westwood MA, Wonke B, Maceira AM et al (2005b) Left ventricular diastolic function compared with T2\* cardiovascular magnetic resonance for early detection of myocardial iron overload in thalassemia major. *J Magn Reson Imaging* 22:229–233
- Westwood M, Anderson LJ, Firmin DN et al (2003) A single breath-hold multiecho T2\* cardiovascular magnetic resonance technique for diagnosis of myocardial iron overload. *J Magn Reson Imaging* 18:33–39
- Wood JC (2006) Anatomical assessment of congenital heart disease. *J Cardiovasc Magn Reson* 8:595–606
- Wood JC (2009) History and current impact of cardiac magnetic resonance imaging on the management of iron overload. *Circulation* 120:1937–1939
- Yoo SJ, Kim YM, Choe YH (1999) Magnetic resonance imaging of complex congenital heart disease. *Int J Card Imaging* 15:151–160
- Zerhouni EA, Parish DM, Rogers WJ et al (1988) Human heart: tagging with MR imaging—a method of noninvasive assessment of myocardial motion. *Radiology* 169:59–63

---

# MRI of Lung Morphology and Perfusion

Sebastian Ley and Julia Ley-Zaporozhan

## Contents

<b>1</b>	<b>Introduction</b> .....	505
<b>2</b>	<b>Morphology</b> .....	506
2.1	Airways .....	506
2.2	Pneumonia.....	507
2.3	Cystic Fibrosis .....	508
2.4	Pulmonary Tumors .....	509
2.5	Thoracic Deformities.....	509
<b>3</b>	<b>Perfusion</b> .....	509
<b>4</b>	<b>Summary</b> .....	511

---

## Abstract

The use of magnetic resonance imaging (MRI) of the chest is becoming more frequent and standard examination protocols are now available for various diseases. Given the lack of ionizing radiation exposure, this technique is especially well suited for examinations of children. MRI provides good visualization of the lung parenchyma, especially in the setting of diseases associated with air space filling, like pneumonia, or severe airway abnormalities, like cystic fibrosis. Functional information regarding chest wall, diaphragmatic, and airway motion during free breathing can be acquired with MRI. Furthermore, lung perfusion can be assessed with good spatial and temporal resolution. Lung perfusion determined by MRI is a promising functional biomarker for assessing disease severity and monitoring treatment response. This chapter will provide examination protocols, clinical indications, and imaging findings for typical applications of MRI for investigating lung morphology and perfusion.

---

## 1 Introduction

Magnetic resonance imaging (MRI) is becoming a viable option for evaluating the lung parenchyma in the pediatric community. It has major advantages over the established techniques like CT and scintigraphy as it combines morphological and functional imaging without the use of ionizing radiation. There is increasing evidence that MR morphological images of the lungs are similar in quality to those of CT and superior to chest radiography. The major drawback of MRI is that the acquisition time is longer than in CT or radiography. A standard MR examination protocol however, can be accomplished within 25 min (Table 1). As parents usually can stay with their children inside the scanning room, patients usually tolerate the examination without sedation down to the age of 8 years. Below this age, sedation is usually required, although general anesthesia is

---

S. Ley (✉)  
Department of Diagnostic and Interventional Radiology,  
Chirurgische Klinik Dr. Rinecker, Am Isarkanal 30,  
81379 Munich, Germany  
e-mail: ley@gmx.net

S. Ley · J. Ley-Zaporozhan  
Division of Pediatric Radiology,  
Diagnostic and Interventional Radiology,  
Im Neuenheimer Feld 430, 69120 Heidelberg, Germany

J. Ley-Zaporozhan  
Division of Pediatric Radiology,  
Institute of Clinical Radiology, University Hospital Munich,  
Lindwurmstr. 4, 80337 Munich, Germany



**Table 1** Example MR protocol for sedated (non breath-hold compliant) patients

Basic protocol (without contrast media)	Advanced protocol (contrast media)
Localizer	
TrueFISP transverse and coronal and sagittal, overlapping (2 mm slice thickness, effective)	
T2 HASTE coronal and transverse (PACE)	
T2 TSE (BLADE) FS transverse and coronal (PACE)	
T1 VIBE transverse, no FS (3 averages)	
T1 VIBE coronal, FS (3 averages)	
	Contrast media
	T1 flash 3D (TWIST), 30 consecutive dynamic acquisition
	Start of contrast media application parallel to image acquisition
	T1 VIBE transverse and coronal, 3 averages, fat sat
TrueFISP coronal, dynamic (angulated between lung apex and diaphragmatic dome), temporal resolution 3 images/s	

MRI protocol for sedated (nonbreath-hold compliant) patients

The “basic” protocol is without application of contrast media and uses the inherent soft tissue contrast. If contrast media is needed, it should be administered at the given position. The protocol can be performed in approximately 25 min and is therefore suitable for routine clinical application

*FS* fat sat; *FISP* fast imaging with steady state precession; *HASTE* half Fourier acquisition single shot turbo spin echo; *VIBE* 3D volumetric interpolated breath-hold examination; *PACE* respiratory navigator gating; *BLADE* periodically rotated overlapping parallel lines with enhanced reconstruction; *TWIST* time-resolved angiography with interleaved stochastic trajectories

*Sequence acronyms* (Siemens/GE/Philips), trueFISP/FIESTA/Balanced FFE, HASTE/Single-Shot FSE/Single-Shot TSE, VIBE/Lava-XV/THRIVE, TSE/FSE/TSE, BLADE/PROPELLER/MultiVane, TWIST/TRICKS XV/Keyhole (4D TRAK)

typically not needed. MRI sequences can compensate for respiratory and cardiac motion, so that a quietly breathing patient can be easily examined.

MRI scanners are available with different magnetic field strengths ranging from 0.2 to 3 Tesla for routine clinical use (even 7 Tesla are being used for human research applications). The lung consists of many air/tissue interfaces. These interfaces generate local field inhomogeneity leading to decreased signal. This so-called susceptibility artifact increases with increasing magnetic field strength. Therefore, a low field strength of 0.2 Tesla can be advantageous for

lung parenchymal imaging; however, in the clinical setting 1.5 Tesla scanners are the most common and thus, most studies are done using these scanners.

## 2 Morphology

Morphological imaging is done using single shot or turbo spin echo (TSE) T2-weighted and gradient echo (GRE) T1-weighted images (Table 1) and can be accomplished within 25 min. Images should be acquired in at least two plane orientations as sometimes subtle pulsation or respiratory artifacts can hamper clear perception of the pathology. Especially, well-visualized pathologies are those with an increase in soft tissue or fluid relative to air, like inflammation. The inherent soft tissue contrast allows good differentiation between consolidations, effusions, and abscess formations without the use of contrast media. Even hilar and mediastinal lymph nodes are visualized well. Contrast media is only used in cases with suspected pulmonary perfusion abnormalities or in tumors.

Proton MRI is limited by the short transverse relaxation times of the lung parenchyma (T2 around 80 ms). Therefore, conventional T2 images are hampered by T2 blurring limiting assessment of fine-scale structures. Recently, 3D sequences facilitating ultrashort TE times were developed and combined with respiratory gating (Johnson et al. 2013). The spatial resolution can be as high as 1.25 mm isotropic. The initial results in healthy volunteers showed high quality visualization of the lung parenchyma. This approach yields great opportunities for future use of lung MRI, especially in the pediatric population.

### 2.1 Airways

Pathologies of the tracheobronchial tree in children are usually either due to a cartilaginous instability or an extrinsic compression. In children, the primary diagnostic tool for assessment of tracheomalacia is bronchoscopy or CT. However, if an external compression due to aberrant vasculature is suspected, MRI can be used, although the functional degree of stenosis is difficult to assess. MRI comes routinely into play after the trachea has reached a sufficient calibre to be visualized, in our experience at an age of 8 years. After surgery, MRI is capable of visualizing the tracheal lumen and assess for residual instability. Visualization in axial and coronal orientation should be accomplished (Fig. 1). T1-weighted sequences, like VIBE (volume-interpolated breath-hold examination) provide a spatial resolution of approximately  $1.4 \times 1.4 \times 4 \text{ mm}^3$  in a breath-hold of 18 s. T2-weighted TSE sequences have a spatial resolution of  $0.9 \times 0.7 \times 3 \text{ mm}^3$  and image

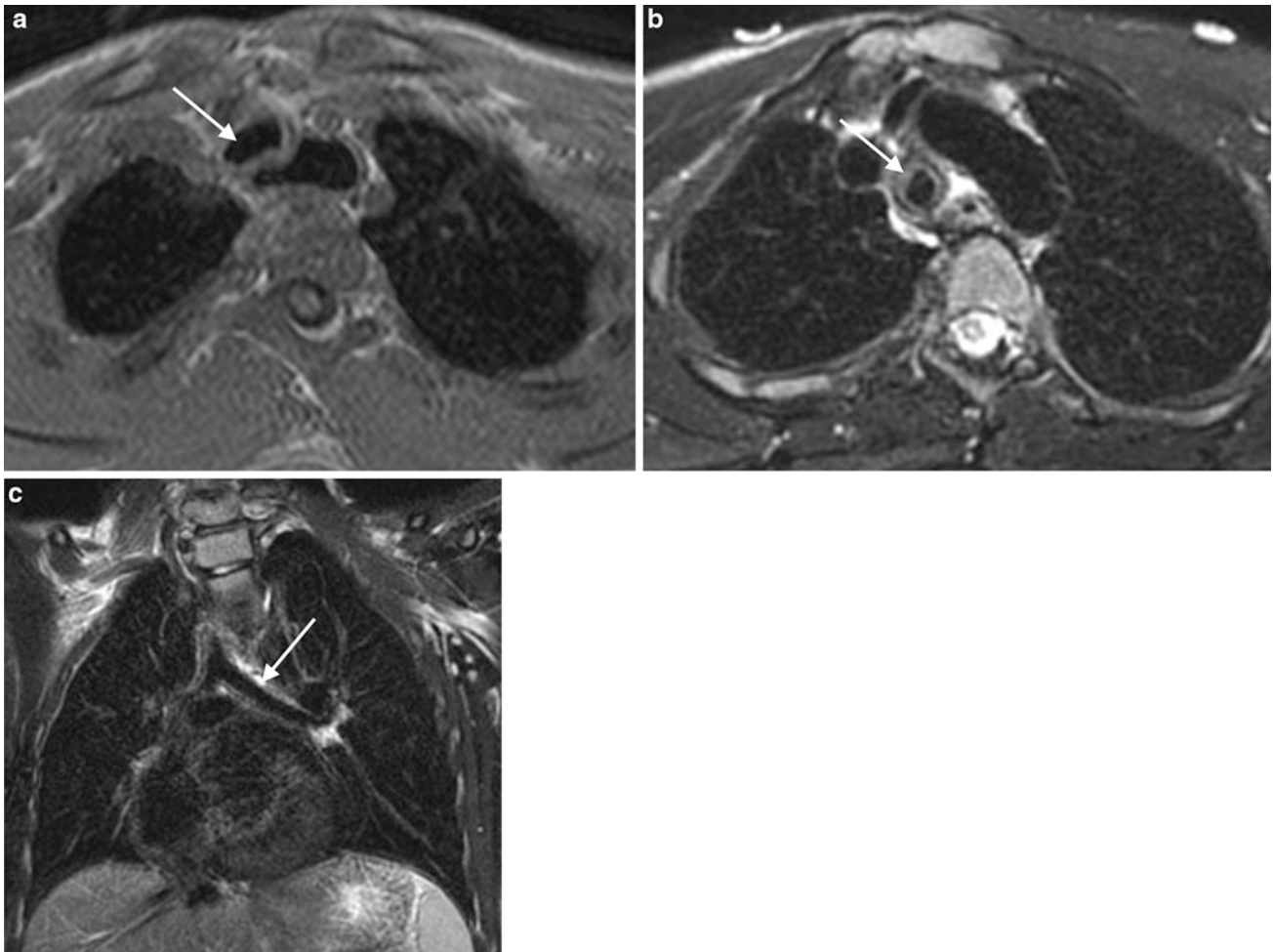


**Fig. 1** Nine-year-old boy after tracheal stabilization surgery. **a** T1-weighted VIBE axial image. The *arrow* points to the trachea. **b** T2-weighted BLADE axial image. The trachea is designated by the *arrow*.

**c** T2-weighted BLADE coronal image. The *arrow* points to the left mainstem bronchus. Even in free breathing, MRI is capable of depicting the trachea and proximal bronchi

acquisition is done during free respiration (Ley et al. 2010). After stent implantation, MRI is less useful as the metal leads to strong signal artifacts and loss of signal.

For assessment of tracheal and diaphragmatic motion during free or forced respiration, dynamic, time-resolved techniques can be applied. Usually, a steady-state free precession sequence (spatial resolution  $3 \times 2 \times 6 \text{ mm}^3$ , temporal resolution 3 images/s) is used. This allows easy visualization of diaphragmatic paresis after cardiothoracic surgery or lack of expiration in obstructive disease, as in patients with Swyer–James syndrome.

## 2.2 Pneumonia

As pointed out above, pathologies with an increase in soft tissue or fluid are easier to visualize on MRI than diseases

with a deficiency of parenchymal structures (like alveolar simplification in patients with bronchopulmonary dysplasia). Therefore, the majority of publications on lung MRI are on the topic of pneumonia or cystic fibrosis.

MRI had a high agreement with CT (95 %) in the diagnosis of pneumonia in a study of adults (Eibel et al. 2006). In neutropenic patients, MRI showed the same findings as CT in 91 % of cases (Rieger et al. 2008). These positive reports about the capability of MRI are confirmed in our own experience (Fig. 2). However, although pediatric patients are radiosensitive subjects the use of MRI for pneumonia detection is rare. Usually, it is used in cases with a prolonged history or persistence despite antibiotic therapy (Fig. 3). In these cases, evaluation for a pulmonary abscess is needed and can be easily done by MRI. Also, characterization of pleural effusions is possible by MRI without contrast media, as well as planning of drainage placement.

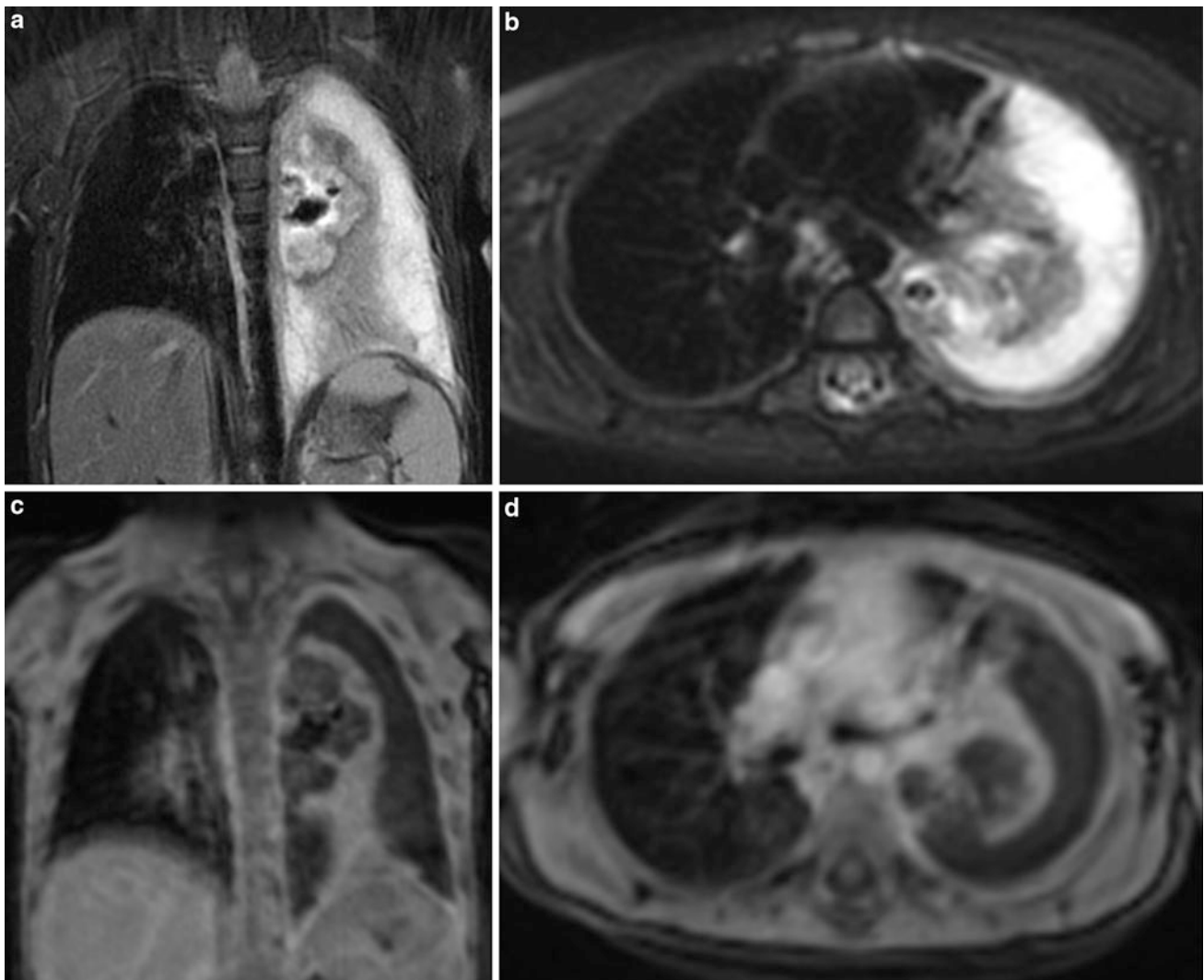


**Fig. 2** Two-year-old girl with complicated pneumonia. There is a large left pleural effusion with septations. A large abscess is noted in the collapsed left lung. This abscess was not seen by ultrasound.

T2-weighted BLADE coronal (a) and axial (b) images. Post-contrast T1-weighted VIBE coronal (c) and axial (d) images

### 2.3 Cystic Fibrosis

Cystic fibrosis leads to chronic lung infection, airway obstruction, and progressive destruction of the lung parenchyma. These pulmonary pathologies are the main reason for hospitalization and reduced quality of life in cystic fibrosis patients. Frequent imaging studies, usually chest radiographs, are performed beginning in early childhood. This is a group of patients who could greatly benefit from MRI examinations of the lung as it allows morphological and functional assessment of disease activity without radiation.

Typical findings in cystic fibrosis are bronchial wall thickening, bronchiectasis, mucus plugging, and consolidations (Puderbach et al. 2007a; Wielputz et al. 2013) (Fig. 4). As cystic fibrosis patients are most often short-of-breath, less motion-sensitive rapid single shot techniques

like HASTE (half Fourier acquisition single shot TSE) are valuable. To even better visualize the mucus-filled airways and the edematous enlarged bronchial walls more heavily T2-weighted techniques with respiratory gating are recommended (Fig. 5). For cystic fibrosis patients, good agreement between thin-section CT and MRI has been found: median concordance on a lobar basis of 80 % for bronchiectasis, 77 % for mucus plugging, 93 %, for sacculation/abscesses, and 100 % for collapse/consolidation (Puderbach et al. 2007b). For noncystic fibrosis patients, compared to CT, MRI has shown a high sensitivity for detection of bronchiectasis (97 %), mucus plugging (100 %), peribronchial wall thickening (100 %), collapse or consolidation (100 %), and sacculations or abscesses (100 %). Bullae (sensitivity 60 %) and emphysema (75 %) were less well detected by MRI (Montella et al. 2012).



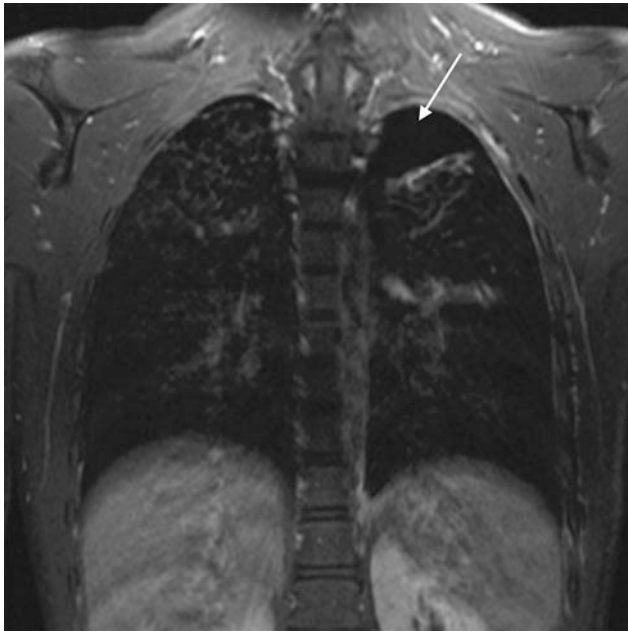


**Fig. 3** Sixteen-year-old male patient with Langerhans cell histiocytosis and a history of recurrent pneumothoraces. The T2-weighted TSE image shows a left pneumothorax (arrow). In the right lung apex, typical cystic lung lesions are demonstrated

## 2.4 Pulmonary Tumors

Primary pulmonary tumors in children are rare. The majority of pediatric pulmonary tumors are metastatic (e.g., Wilms tumor, osteosarcoma, Ewing sarcoma, hepatoblastoma). Most children with a primary or secondary pulmonary malignancy will present co-incidentally while seeking attention for another medical problem, or with nonspecific abnormalities such as cough with collapse or consolidation on the chest radiograph (McCahon 2006). The usual work-up starts therefore with a chest radiograph followed by a CT of the chest. However, it has been shown that T1-weighted GRE (e.g., VIBE) and T2-weighted TSE techniques allow for visualization of pulmonary nodules larger than 5 mm with a sensitivity close to 100 % (Biederer et al. 2008). Furthermore, MRI is a reliable method to estimate chest wall or mediastinal adhesion and invasion by tumor by use of dynamic spoiled GRE, e.g., FLASH (fast low angle shot) or true coherent GRE, e.g., trueFISP (fast imaging with steady state precession) sequences. Due to the high soft tissue contrast, MRI is useful for assessment of pleural disease, and has been shown to be superior to CT for differentiation between malignant and benign pleural lesions in adults (Hirsholzer et al. 2000). Beside the morphological characterization of a lesion, dynamic contrast-enhanced MRI may be helpful in differentiating benign from malignant pulmonary nodules. Absence of significant enhancement is a strong predictor that a solitary pulmonary nodule is benign in adults (Zou et al. 2008), but this has not been validated in children.

## 2.5 Thoracic Deformities

Pectus excavatum is a frequent congenital thoracic deformity (incidence 1:300 births), and is characterized by a sternal retraction due to anomalies of the cartilaginous rib/sternum junction. It can be present at birth or develop during growth, usually in teenagers. To measure the severity, Haller and colleagues developed the pectus index. The pectus index is derived by dividing the internal transverse distance of the thorax by the vertebral–sternal distance at the most depressed portion of the deformity using axial images from a CT scan (Haller et al. 1987). The pectus index correlates with the level of physical impairment during exercise (normal value = 2.5, mild impairment if 2.5–4, severe impairment if >4) (Malek et al. 2003). As these juvenile patients are usually otherwise healthy, the use of CT is not necessary if MRI is available as an alternative. The pectus index and chest wall movement patterns can easily be determined from thoracic cine MRI using HASTE sequences that can be performed in approximately 5 min (Herrmann et al. 2006).

## 3 Perfusion

Visualization of pulmonary perfusion can easily be accomplished with MRI. However, quantification of perfusion is a more difficult task using MRI (Ley and Ley-Zaporozhan 2012). Perfusion can be assessed by different techniques, either with or without intravenous injection of contrast media. In clinical practice, techniques using contrast media are more often used.

In principle, a 3D T1-weighted sequence is acquired multiple times (e.g., 30 times), optimized for a high temporal resolution (each 3D dataset should be acquired within 1–3 s). The contrast media injection is done after the first dataset, providing a baseline dataset. The baseline dataset is then subtracted from the dataset with the peak enhancement of the lung parenchyma to eliminate signal from static tissue (like the chest wall) and to generate a perfusion dataset. Given the fast acquisition of the datasets, this technique can even be used in patients who cannot hold their breath, such as sedated patients (especially since sedated patients do show a regular breathing pattern without deep inspiration).

Another technique, called arterial spin labeling (ASL), marks the inflowing blood to the lungs by a special pulse design. While this technique does not require intravenous contrast media, image acquisition takes several minutes. Also, the signal intensity is inferior to the contrast-enhanced techniques. Therefore, there are only a few reports describing the use of the ASL technique in clinical practice (Schraml et al. 2012).

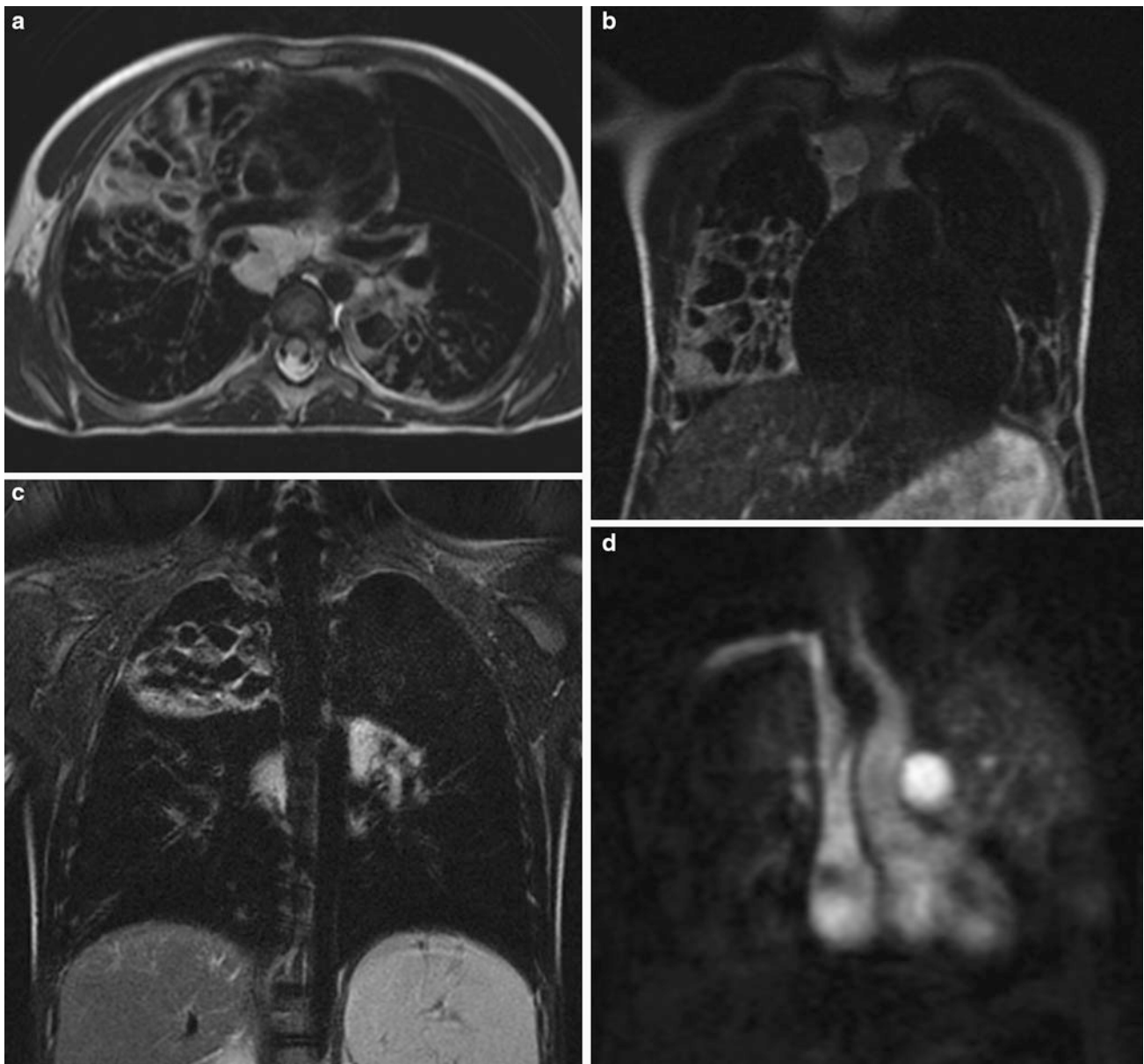


**Fig. 4** Eight-year-old patient with cystic fibrosis. **a** T2-weighted TSE axial image demonstrating the typical findings in cystic fibrosis of bronchiectasis, bronchial wall thickening, mucus plugging, and peribronchial consolidation in the right upper lobe. Similar findings are seen within the right middle lobe and the lingula on a T2-weighted TSE coronal image. **b** The same can be seen within the right middle

lobe and the lingula on a T2-weighted TSE coronal image. **c** T2-weighted BLADE coronal image demonstrating pulmonary changes within the right upper lobe and perihilar lymphadenopathy. **d** A perfusion-weighted dataset shows preserved perfusion in the left upper lobe and large perfusion defects within the right lung and left paracardial area

Morphological changes in lung disease do not necessarily correspond to the functional impairment resulting from these changes. Based on the Euler–Liljestrand mechanism, pulmonary perfusion is reduced where oxygenation is impaired. Therefore, perfusion measurements may constitute a valuable tool for functional assessment of disease severity and for treatment monitoring.

Most MRI perfusion studies have been done in patients with cystic fibrosis (Figs. 4, 5). In children with cystic fibrosis, normal lung parenchyma shows homogeneous perfusion, while severe morphological changes are associated with perfusion defects. Segments with moderate morphological changes show normal perfusion in 53 % and impaired perfusion in 47 % (Eichinger et al. 2006). Recently, excellent

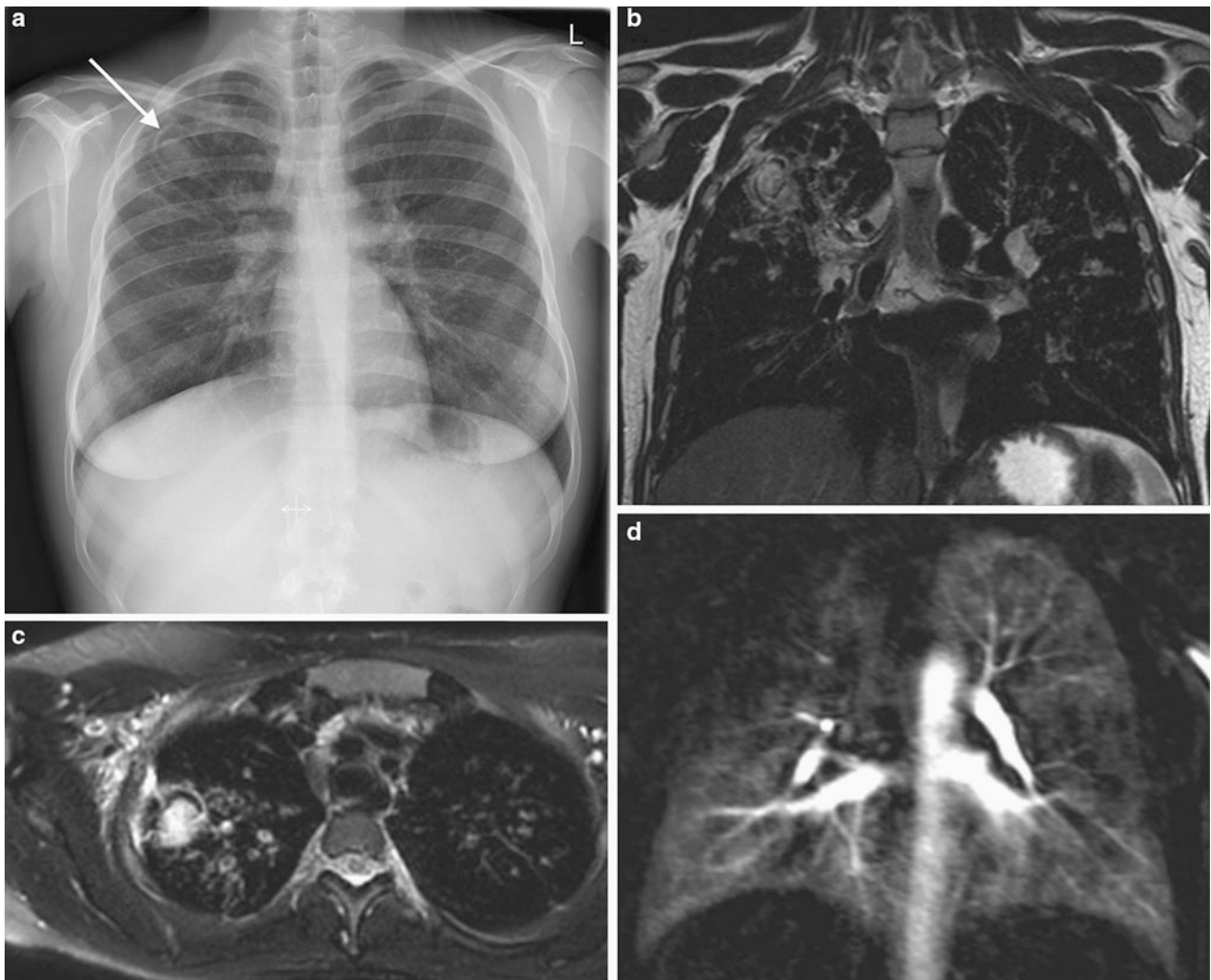


**Fig. 5** Twenty five-year-old patient with cystic fibrosis presenting with an air-crescent sign (arrow) on chest radiography. **a** A T2-weighted TSE coronal image, **b** and a T2-weighted BLADE axial image, **c** demonstrate the same finding, as well as the typical changes

of cystic fibrosis. A perfusion-weighted dataset, **d** shows gross perfusion loss in the right upper lobe and focal areas of loss of perfusion in the left lung, corresponding to areas of mucus plugging and consolidations in (**b**)

inter-reader agreement and reproducibility were found for scoring of MRI perfusion defects in cystic fibrosis lung disease, supporting the use of MRI for assessing disease severity in clinical trials (Eichinger et al. 2012). The value of MRI in patients with cystic fibrosis is not limited to assessment of lung morphology and perfusion. Investigation of pulmonary ventilation with MRI is discussed in this book in the chapter entitled Hyperpolarized Gas MRI in Pediatric Lung Disease by Komlosi, Benjamin and Altes.

#### 4 Summary

MRI of the chest can be routinely used in the pediatric population. It provides good visualization of the lung parenchyma, especially in the setting of common diseases

with air space filling or severe airway abnormalities. In addition to providing static morphological information, MRI can be used to dynamically assess chest wall, diaphragmatic, and airway motion during free breathing. Lung perfusion can also be assessed by MRI as a biomarker of disease severity and for treatment monitoring.

#### References

- Biederer J, Hintze C, Fabel M (2008) MRI of pulmonary nodules: technique and diagnostic value. *Cancer Imaging* 8:125–130
- Eibel R, Herzog P, Dietrich O, Rieger CT, Ostermann H, Reiser MF, Schoenberg SO (2006) Pulmonary abnormalities in immunocompromised patients: comparative detection with parallel acquisition MR imaging and thin-section helical CT. *Radiology* 241:880–891



- Eichinger M, Puderbach M, Fink C, Gahr J, Ley S, Plathow C, Tuengerthal S, Zuna I, Muller FM, Kauczor HU (2006) Contrast-enhanced 3D MRI of lung perfusion in children with cystic fibrosis-initial results. *Eur Radiol* 16:2147–2152
- Eichinger M, Optazaite DE, Kopp-Schneider A, Hintze C, Biederer J, Niemann A, Mall MA, Wielputz MO, Kauczor HU, Puderbach M (2012) Morphologic and functional scoring of cystic fibrosis lung disease using MRI. *Eur J Radiol* 81:1321–1329
- Haller HA Jr, Kramer SS, Lietman SA (1987) Use of CT scans in selection of patients for pectus excavatum surgery: a preliminary report. *J Pediatr Surg* 22:904–906
- Herrmann KA, Zech C, Strauss T, Hatz R, Schoenberg S, Reiser M (2006) Cine MRI of the thorax in patients with pectus excavatum. *Radiologe* 46:309–316
- Hierholzer J, Luo L, Bittner RC, Stroszczyński C, Schroder RJ, Schoenfeld N, Dorow P, Loddenkemper R, Grassot A (2000) MRI and CT in the differential diagnosis of pleural disease. *Chest* 118:604–609
- Johnson KM, Fain SB, Schiebler ML, Nagle S (2013) Optimized 3D ultrashort echo time pulmonary MRI. *Magn Reson Med* 70:1241–1250
- Ley S, Ley-Zaporozhan J (2012) Pulmonary perfusion imaging using MRI: clinical application. *Insights Imaging* 3:61–71
- Ley S, Loukanov T, Ley-Zaporozhan J, Springer W, Sebening C, Sommerburg O, Hagl S, Gorenflo M (2010) Long-term outcome after external tracheal stabilization due to congenital tracheal instability. *Ann Thorac Surg* 89:918–925
- Malek MH, Fonkalsrud EW, Cooper CB (2003) Ventilatory and cardiovascular responses to exercise in patients with pectus excavatum. *Chest* 124:870–882
- McCahon E (2006) Lung tumours in children. *Paediatr Respir Rev* 7:191–196
- Montella S, Maglione M, Bruzzese D, Mollica C, Pignata C, Aloj G, Manna A, Esposito A, Mirra V, Santamaria F (2012) Magnetic resonance imaging is an accurate and reliable method to evaluate non-cystic fibrosis paediatric lung disease. *Respirology* 17:87–91
- Puderbach M, Eichinger M, Gahr J, Ley S, Tuengerthal S, Schmahl A, Fink C, Plathow C, Wiebel M, Muller FM, Kauczor HU (2007a) Proton MRI appearance of cystic fibrosis: comparison to CT. *Eur Radiol* 17:716–724
- Puderbach M, Eichinger M, Haeselbarth J, Ley S, Kopp-Schneider A, Tuengerthal S, Schmaehl A, Fink C, Plathow C, Wiebel M, Demirakca S, Muller FM, Kauczor HU (2007b) Assessment of morphological MRI for pulmonary changes in cystic fibrosis (CF) patients: comparison to thin-section CT and chest x-ray. *Invest Radiol* 42:715–725
- Rieger C, Herzog P, Eibel R, Fiegl M, Ostermann H (2008) Pulmonary MRI—a new approach for the evaluation of febrile neutropenic patients with malignancies. *Support Care Cancer* 16:599–606
- Schraml C, Schwenzer NF, Martirosian P, Boss A, Schick F, Schafer S, Stern M, Claussen CD, Schafer JF (2012) Non-invasive pulmonary perfusion assessment in young patients with cystic fibrosis using an arterial spin labeling MR technique at 1.5 T. *MAGMA* 25:155–162
- Wielputz MO, Eichinger M, Puderbach M (2013) Magnetic resonance imaging of cystic fibrosis lung disease. *J Thorac Imaging* 28:151–159
- Zou Y, Zhang M, Wang Q, Shang D, Wang L, Yu G (2008) Quantitative investigation of solitary pulmonary nodules: dynamic contrast-enhanced MRI and histopathologic analysis. *AJR Am J Roentgenol* 191:252–259

---

# Hyperpolarized Gas MRI in Pediatric Lung Disease

Peter Komlosi, Jennifer L. Benjamin, and Talissa A. Altes

## Contents

<b>1</b>	<b>Introduction</b> .....	513
<b>2</b>	<b>Technique</b> .....	514
2.1	Differences Between He-3 and Xe-129.....	514
2.2	MR Sequences.....	514
<b>3</b>	<b>Applications in Pediatric Lung Disease</b> .....	515
3.1	Healthy.....	515
3.2	Asthma.....	517
3.3	Cystic Fibrosis.....	518
3.4	Bronchopulmonary Dysplasia (Chronic Lung Disease of Prematurity).....	519
3.5	Infants.....	519
<b>4</b>	<b>Summary</b> .....	520
	<b>References</b> .....	520

---

## Abstract

Hyperpolarized gas magnetic resonance imaging (HG-MRI) of the lung provides high temporal and spatial resolution images of the air spaces of the lung and can be used to elucidate both lung function and morphology. Because no ionizing radiation is involved, HG-MRI is a promising technique for the evaluation of pediatric lung diseases. In this chapter, we describe briefly the basic principles of HG-MRI, review the literature of HG-MRI in three pediatric lung diseases (asthma, cystic fibrosis, and bronchopulmonary dysplasia), and discuss possible future clinical applications of hyperpolarized gas imaging in pediatric lung disease.

---

## 1 Introduction

As covered in previous chapters, chest radiography and computed tomography (CT) are currently the most commonly used lung imaging techniques. CT provides superior image quality and has the ability to depict small anatomic structures. However, CT imaging provides only indirect information regarding pulmonary function. CT also has risk associated with exposure to ionizing radiation. Hyperpolarized inhaled gaseous MRI contrast agents [Helium-3 (He-3) and Xenon-129 (Xe-129)] provide high temporal and spatial resolution images of lung structure and function without the use of ionizing radiation. Currently, hyperpolarized He-3 and Xe-129 gases are classified as investigational new drugs awaiting FDA approval for general clinical use. Using specialized equipment, the He-3 or Xe-129 gases are polarized prior to administration to the patients. The high level of polarization provides a high MRI signal despite the low physical density of gas. These gases function well as contrast agents because they fill the airspaces of the lung, thereby permitting visualization and detailed measurement of the ventilated airspaces of the lung. Magnetic resonance imaging with He-3 and Xe-129 lung

---

P. Komlosi (✉) · J. L. Benjamin · T. A. Altes  
Department of Radiology and Medical Imaging,  
University of Virginia, 1215 Lee Street,  
Charlottesville, VA, USA  
e-mail: pk9h@virginia.edu

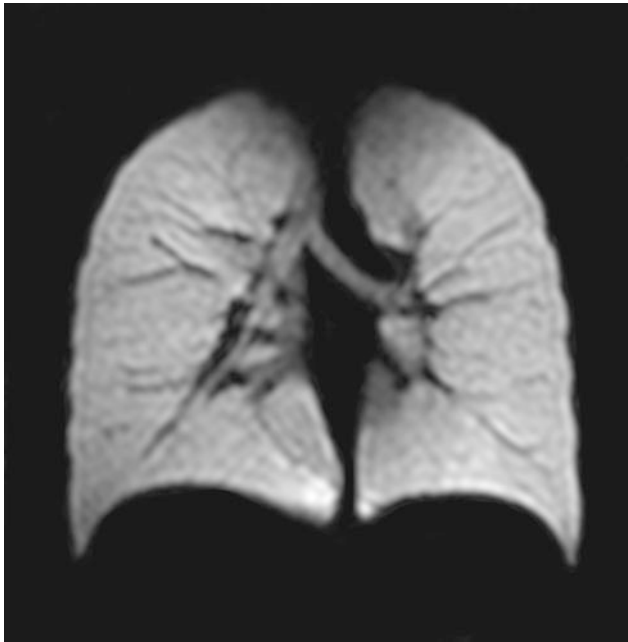


**Fig. 1** Coronal He-3 MR ventilation image of the lungs of a healthy subject. Uniformly high signal is obtained from the lung airspaces and there are no ventilation defects

contrast agents has the benefit of reducing the risk of exposure to ionizing radiation for the pediatric population as well as providing functional lung data not available with CT imaging.

## 2 Technique

Conventional proton MR uses magnetization induced in hydrogen nuclei by the strong magnetic field of the MR scanner. Due to the low proton density of the lungs, the lung parenchyma produces a weak MR signal. Furthermore, there are numerous air-tissue interfaces within the lung that introduce susceptibility effects that cause rapid decay of what little signal is generated by the lung. Thus, conventional proton MRI of the lung is challenging and until recently has been limited to the denser soft tissue structures within the thorax. With the development of techniques to hyperpolarize He-3 and Xe-129 in sufficient quantities for medical imaging, MRI of the lung airspaces is now possible (Albert et al. 1994; Middleton et al. 1995). Hyperpolarization of He-3 and Xe-129 is achieved using an optical pumping method that renders a high degree of polarization (10–60 %) to unpaired nuclear protons in the He-3 and Xe-129 atoms. With current polarizers, it is possible to achieve 100,000 times the polarization of hydrogen nuclei in a 1.5 T magnetic field (Hersman et al. 2008). This large net polarization permits visualization of the lung airspaces with MRI despite the low physical density of the gas.

### 2.1 Differences Between He-3 and Xe-129

There are important differences between He-3 and Xe-129 as MRI contrast agents. Specifically:

He-3	Xe-129
Essentially insoluble in biological tissue	Weakly soluble in biological tissue
Cannot provide gas exchange information	Provides gas exchange information
No known side effects	CNS (euphoric and anesthetic) side effects
Low molecular weight	High molecular weight
Large diffusion coefficient	Small diffusion coefficient
Higher percentage of atomic polarization <sup>a</sup>	Lower percentage of atomic polarization <sup>a</sup>
Shortage of supply	Readily available
>\$500/L	<\$200/L

<sup>a</sup> Historically higher polarization values could be achieved with He-3 than Xe-129, but recent advances in Xe-129 polarization technology have closed the gap (Hersman et al. 2008)

He-3 is relatively insoluble in biological tissue and, therefore, is not taken up by the body through the alveolar-capillary interface. Xe-129 is weakly soluble in biological tissues and demonstrates a relatively large chemical shift between Xe-129 in the gas phase and Xe-129 dissolved in tissue or blood. By exploiting this property, regional information about pulmonary gas exchange can be obtained. The biological solubility of Xe-129 also results in side effects. At the doses used in medical imaging, some patients experience transient CNS effects including euphoria, altered sensations, and drowsiness. At doses higher than typically used in imaging, xenon has anesthetic effects. He-3 has few, if any, side effects. Historically, higher polarizations could be achieved with He-3 than Xe-129. Thus, much of the initial human research with HG-MRI was done with He-3. However, recent technical advances have greatly increased the polarizations achievable with Xe-129 (Hersman et al. 2008). He-3, as a low molecular weight atom, has a much larger diffusion coefficient than Xe-129 which has implications for diffusion imaging. A current shortage of He-3 has resulted in increased costs, making Xe-129 more attractive as a contrast agent for MRI (Shea and Morgan 2010).

### 2.2 MR Sequences

Five basic MRI techniques using hyperpolarized gas contrast imaging have been developed. The first four techniques below can be performed with either He-3 or Xe-129, but the fifth, Dissolved Phase Imaging, is limited to Xe-129.



1. Static Spin Density (Ventilation Imaging)—used to assess pulmonary ventilation.
2. Dynamic Spin Density Imaging—used to assess the temporal kinetics of gas flow in the lung.
3. Diffusion Imaging—used to assess lung microstructure by measuring the restriction to diffusion of the He-3 or Xe-129 atoms.
4. Oxygen Sensitive Imaging—used to quantify the alveolar partial pressure of oxygen.
5. Dissolved Phase Imaging—used to measure the movement of Xe-129 atoms from the lung airspace into the tissue and blood, that is, gas exchange.

### 2.2.1 Static Spin Density Imaging

With static spin density imaging, the patient inhales the hyperpolarized gas and spin density imaging is performed during a short breath hold. Assuming a homogenous B1 field, the signal received from any area of the lung is proportional to the number of polarized gas atoms within that area. Assuming that the rate of depolarization of the gas is similar throughout the lung over the course of the breath hold, the signal is approximately proportional to the ventilation in that region of the lung. Well-ventilated regions will contain a large number of polarized gas atoms and thus produce a strong signal (appearing white on the images). Areas of the lung that are poorly ventilated will contain fewer polarized gas atoms and appear grey or black on the ventilation images, so-called ventilation defects. Ventilation defects have been found in patients with obstructive lung diseases including asthma, cystic fibrosis (CF), COPD, and bronchiolitis obliterans (Altes et al. 2001; Donnelly et al. 1999; Kauczor et al. 1996; McAdams et al. 1999, 2000).

### 2.2.2 Dynamic Spin Density Imaging

With dynamic spin density imaging very rapid spin density acquisitions are performed while the patient inhales or exhales the hyperpolarized gas. The resulting images depict the dynamics of gas flow/distribution within the lungs (Saam et al. 1999; Salerno et al. 2001).

### 2.2.3 Diffusion Imaging

Similar to proton-based diffusion imaging, hyperpolarized gas diffusion imaging assesses the degree to which the hyperpolarized gas atoms are restricted in movement. A typically derived measure of the degree of restriction is the apparent diffusion coefficient (ADC). Within the lungs, the gas atom movement is restricted by the airway and alveolar walls. Thus, the ADC reflects the size and connectedness of the lung airspaces. In patients with COPD, the hyperpolarized gas ADC is elevated relative to age-matched healthy subjects, a finding which is thought to reflect the known alveolar enlargement in this disease (Kirby et al. 2012; Saam et al. 2000; Salerno et al. 2002). Histology studies in animal

models of emphysema and in explanted human lungs have confirmed the correlation between ADC and alveolar size (Chen et al. 2000; Mata et al. 2007; Woods et al. 2006).

### 2.2.4 Oxygen Sensitive Imaging

The rate of decay of the polarization of both He-3 and Xe-129 depends upon the local environment and is hastened by molecular oxygen. Thus, by measuring the T1 of the He-3 or Xe-129 gas in the lungs, it is possible to estimate the partial pressure of oxygen regionally within the lungs (Deninger et al. 1999; Fischer et al. 2004; Kadlecsek et al. 2013). Little work has been done with oxygen sensitive imaging in children so this technique will not be discussed further here.

### 2.2.5 Dissolved Phase Imaging

Because Xe-129 is weakly soluble in biological tissues and there is a relatively large chemical shift between gas phase and dissolved phase Xe-129, it is possible to image the regional gas transfer within the lung (Kaushik et al. 2013; Qing et al. 2013; Ruppert et al. 2000). This technique in concert with ventilation imaging permits a comprehensive evaluation of lung physiology and the relative contribution of airway and vascular processes to lung disease. For example, ventilation imaging shows the airway component of asthma, but there may be a vascular component that could be elucidated with dissolved phase imaging. Little work has been done with dissolved phase imaging to date in the pediatric population.

## 3 Applications in Pediatric Lung Disease

### 3.1 Healthy

The lung in disease-free children and young adults characteristically demonstrates a homogenous, high signal on hyperpolarized gas MR spin density (ventilation) imaging (Fig. 1) (Altes et al. 2001; Lee et al. 2009). Small peripheral ventilation defects occur in healthy individuals, with increased prevalence in older adults (Parraga et al. 2007). It is possible that ventilation defects occur with normal aging, but these defects could be related to prior environmental or infectious insults.

Enlargement of alveoli during childhood can be detected using diffusion-weighted He-3 MRI (Fig. 2) (Altes et al. 2006b). Prior to He-3 MRI, it was thought that alveolar development ceased in early childhood (age 2–5 years) and that further lung growth was simply due to expansion in size of the existing lung structures. A recent study found that the He-3 MR ADC in the lungs increased with increasing age during childhood, but the rate of increase was less than expected if lung growth occurred only by expansion of

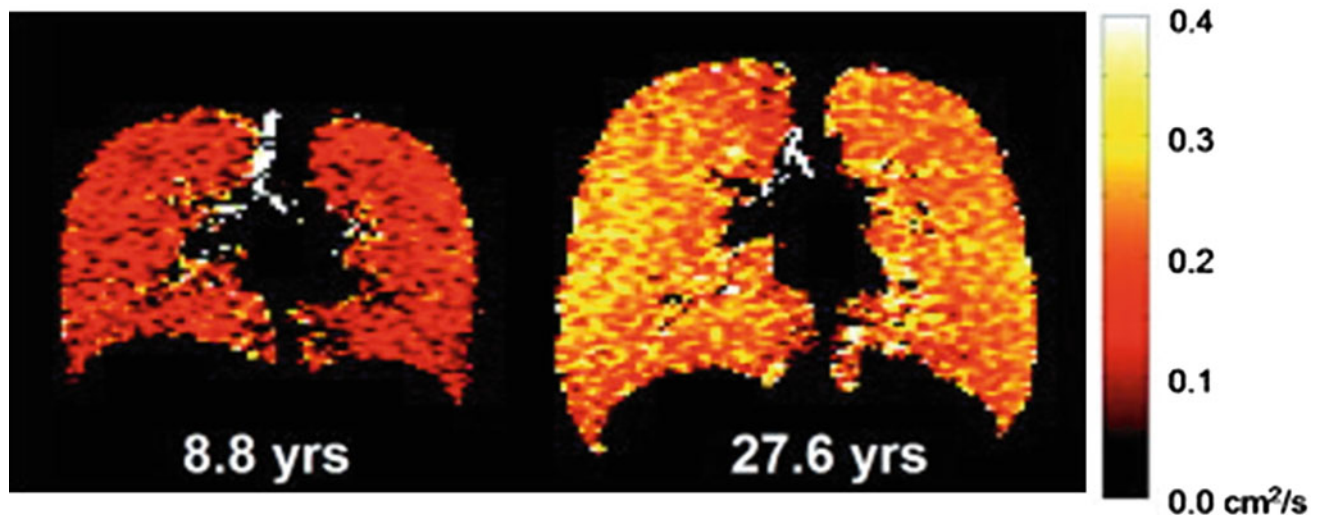


**Fig. 2** Coronal He-3 ADC maps of two healthy subjects age 8.8 and 27.6 years. Very high ADC values are present in the trachea and main bronchi where the diffusion of the gas is less restricted. The ADC values in the young adult are much higher than in the child, indicating

less restriction of diffusion of He-3 atoms within the airspaces of the lungs. This is thought to relate to the known enlargement of alveoli from lung growth in childhood. Reprinted with permission from Altes et al. (2006b)

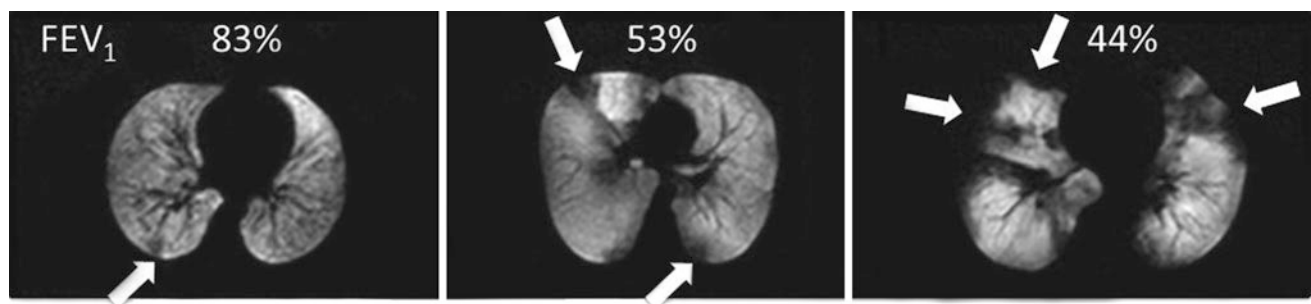


**Fig. 3** Axial He-3 MR ventilation images in three patients with asthma. There are increasing numbers of ventilation defects (arrows denoting black and grey areas) with increasing asthma severity and decreasing FEV<sub>1</sub> % predicted

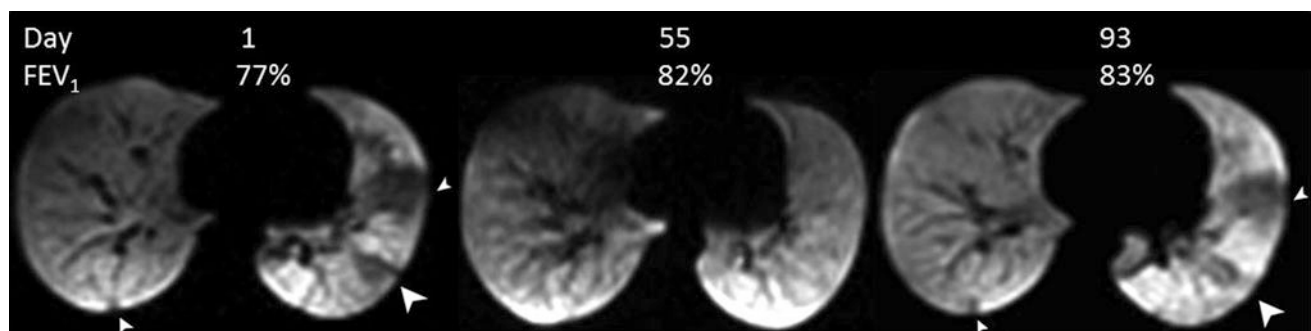


**Fig. 4** Axial He-3 MR ventilation images from a single subject imaged on three different days. The three ventilation defects present on Day 1 resolve on Day 55 but recur on Day 93. There is striking

similarity in the appearance of the defects on Day 1 and Day 93. Modified and reprinted with permission from de Lange et al. (2009)

the preexisting alveoli. This finding suggests that there is both enlargement of the individual alveoli and growth of new alveoli (neoeolization) occurring simultaneously throughout childhood and adolescence (Narayanan et al. 2012). Diffusion-weighted HG-MRI provides the

opportunity to noninvasively assess alveolar development in childhood, both in healthy children and in children with disorders that perturb alveolar development such as bronchopulmonary dysplasia (BPD) and congenital diaphragmatic hernia.

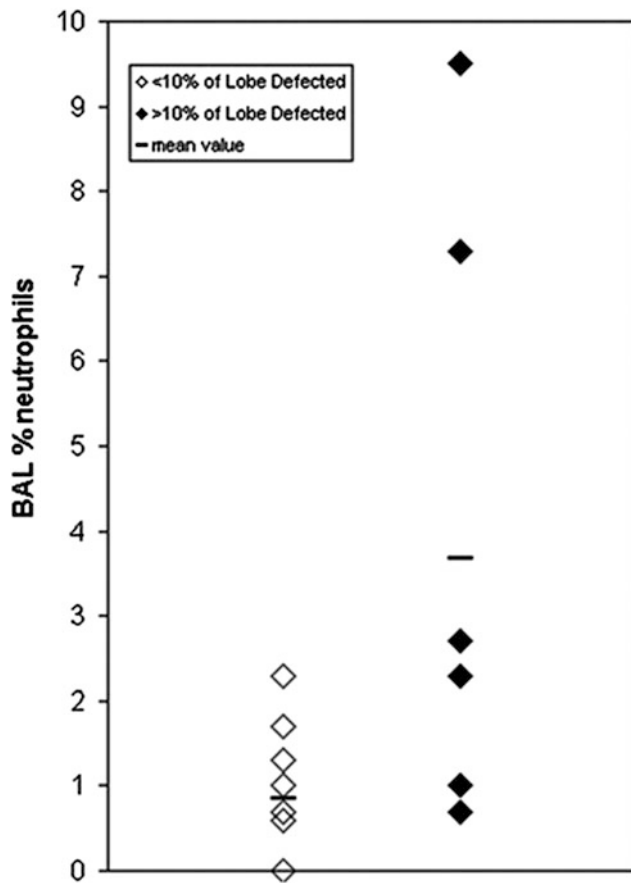


**Fig. 5** Scatterplot of high and low defected lobes showing increased percentage of neutrophils ( $P = 0.03$ ) in lobes sampled with bronchoalveolar lavage and greater than 10 % defect volume compared with lobes with less than 10 % defect volume. Reprinted with permission from Fain et al. (2008)

### 3.2 Asthma

Asthma is the most common chronic disease of childhood, affecting as many as 20 % of children at some time during childhood. The disease predominantly involves the small and medium-sized airways with symptoms usually associated with variable airflow obstruction, caused by bronchoconstriction, airway wall edema, mucous plug formation, and airway remodeling (Campana et al. 2009; Hogg 2002). There is a growing concept that the severity of the disease in adulthood may be significantly reduced through early childhood diagnosis and control. The majority of HG-MRI studies in asthmatics have been performed in young adults, with a few studies conducted on children. The majority of the studies in asthma employed ventilation imaging.

In patients with asthma, ventilation defects are common and increase with disease severity as assessed by spirometry and symptomatology, Fig. 3 (Altes et al. 2001; de Lange et al. 2006). Ventilation defects in asthmatics could be caused by focal airway narrowing, mucus plugging, and/or

airway closure. Ventilation defects are found in asthmatics with normal spirometry, indicating that hyperpolarized gas MRI detects ventilation abnormalities in the lungs with greater sensitivity than does spirometry.

Hyperpolarized gas MR is capable of detecting regional patterns of airway closure. HG-MRI can be repeated to assess changes in the regional patterns of airway closure in response to treatment or over time without the risk of ionizing radiation exposure to the patient. de Lange et al. (2009) found that ventilation defects in individual asthmatics tend to persist or recur in the same locations in the lung over time periods of weeks to months (Fig. 4). This suggests that asthma may not affect all regions of the lung equally but may instead have a regional predisposition in individual patients, analogous to the regional heterogeneity of other autoimmune diseases such as Crohn disease.

Administration of inhaled bronchodilator medications in asthmatic patients generally results in improved ventilation on hyperpolarized gas MRI. This is demonstrated by a decrease in size and number of ventilation defects (Altes et al. 2001). Conversely, ventilation defects develop or worsen when a bronchoconstrictor such as methacholine is given and then subsequently improve or resolve with administration of a bronchodilator such as albuterol (Altes and de Lange 2003; Costella et al. 2012). The amount of air trapping as assessed with diffusion imaging also rises following administration of a bronchoconstrictor and improves following a bronchodilator (Costella et al. 2012). Moreover, bronchial constriction and subsequent heterogeneity on hyperpolarized gas MR is not a characteristic unique to the asthmatic airway but rather a behavior intrinsic to all airway trees when provoked with a large enough dose of methacholine. Ventilation defects recur in the same location on different days following sequential challenges with a bronchoconstrictor or exercise, again demonstrating the persistent regional heterogeneity of bronchial reactivity within the lung (de Lange et al. 2007; Kruger et al. 2013). Further supporting a regional association between inflammation and ventilation defects on MRI, a retrospective study found increased number and percentage of neutrophil leukocytes in bronchoalveolar lavage fluid specimens sampled at locations of ventilation defects (Fig. 5) (Fain et al. 2008). In an analysis of Severe Asthma Research Program (SARP) participants, there was an association between the ventilation defect volume and plasma markers of vascular endothelial cell perturbation (Johansson et al. 2013). The potential importance of angiogenesis and vascular remodeling in asthma is an active area of research and is primarily being investigated with bronchoscopic studies. Dissolved phase hyperpolarized Xe-129 MRI could have a role in helping to elucidate the role of the vasculature in asthma by providing regional information about gas uptake by red blood cells.



**Fig. 6** Coronal ventilation images from three different patients with CF each imaged with both He-3 (*top row*) and Xe-129 (*bottom row*) on the same day. More ventilation defects are present in patients with more severe pulmonary CF. The He-3 and Xe-129 ventilation images are similar but in some subjects more or larger ventilation defects are seen with Xe-129

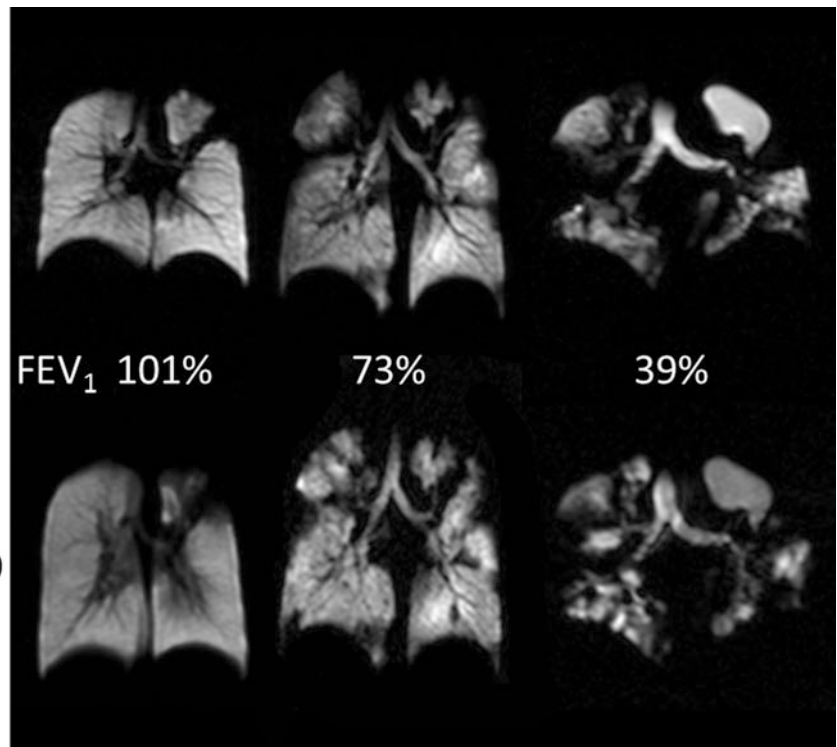
He-3

FEV<sub>1</sub> 101%

73%

39%

Xe-129



### 3.3 Cystic Fibrosis

Cystic fibrosis (CF) is the most frequent lethal single-gene, genetic pediatric disease in the Caucasian population, affecting approximately 30,000 individuals in the United States. Several treatment options have been developed, approaching the disease from a variety of different functional directions, including bronchodilators, anti-inflammatory agents, mucolytics, and antibiotics. Recently, a new class of medications has become available that aim to correct the basic defect of chloride channel dysfunction in certain genetic subtypes of the disease. Unfortunately, assessment of the functional efficacy of therapeutics for CF has been constrained by limitations in existing tests of lung function. Spirometry is used in clinical practice to monitor lung function and evaluate therapeutic interventions but only yields global results, which are not overly sensitive in the detection of early lung damage. However, hyperpolarized gas MR allows direct, high-resolution MRI of the central airways and periphery, providing a complete picture of functional lung ventilation, region by region, with great detail (Fig. 6).

Initial studies in patients with CF using a combination of proton and hyperpolarized helium MRI showed both morphologic abnormalities and, often more extensive, ventilation abnormalities (Donnelly et al. 1999). Further studies confirmed reproducibility of the technique, providing support for hyperpolarized MRI as a promising outcome measure (Woodhouse et al. 2009). Kirby et al. (2011) found that

the high sensitivity and reproducibility of He-3 MRI functional imaging permits the use of relatively small sample sizes in CF interventional studies, much smaller than those required if spirometry is used as the outcome measure.

Disease severity in CF patients is well demonstrated by hyperpolarized He-3 and Xe-129 MR. Ventilation defects correlate with spirometry, change with treatment, and are elevated in number in patients with CF (Mentore et al. 2005). The He-3 MR images provided detailed information on precisely where in the lungs gas was reaching and showed that hyperpolarized gas MR has high sensitivity to regional ventilation heterogeneity related to CF, which may have clinical significance because it may detect specific aspects of disease that are not well assessed by spirometry (Sun et al. 2011). Even a single chest physiotherapy session induces changes in the distribution and extent of ventilation defects (Bannier et al. 2010). Other studies show that He-3 MR correlates strongly with structural abnormalities found on high-resolution CT images and is a stronger correlate of spirometry than high-resolution CT (McMahon et al. 2006). Similar to the finding in asthma, the ventilation defects in patients with CF show remarkable regional stability over a time course of 5 weeks (Couch et al. 2012). Because hyperpolarized He-3 MRI demonstrates ventilation defects that correlate with spirometry, change with treatment, and are elevated in number in patients with CF (even those patients with normal spirometry values), hyperpolarized He-3 MR appears to possess many of the characteristics

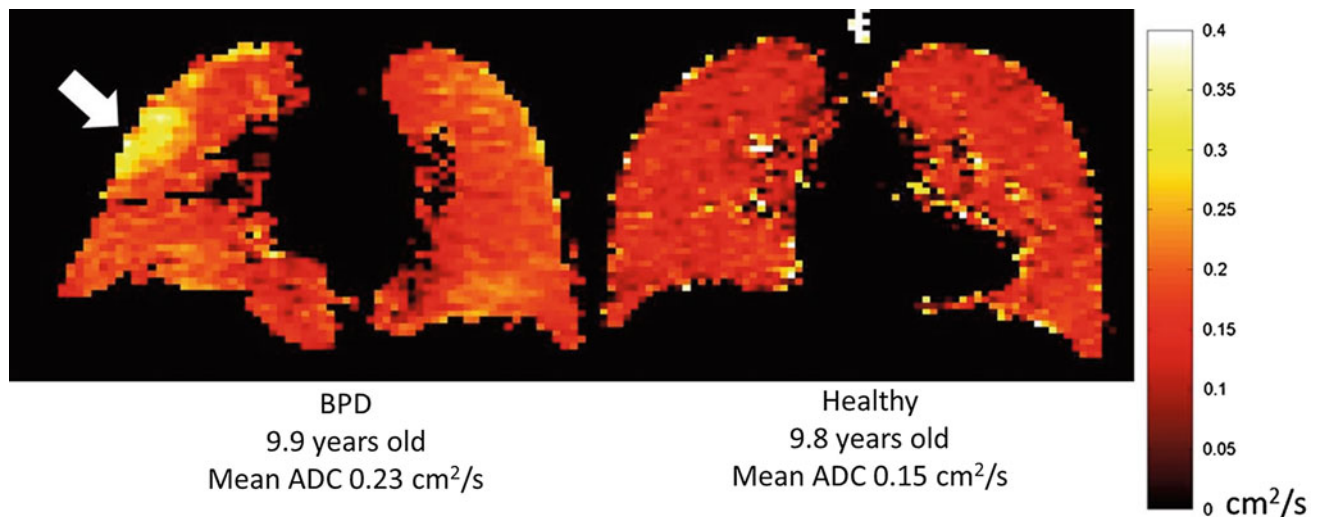


**Fig. 7** Coronal He-3 diffusion (ADC) images of two 9-year-old children: one with BPD and the other healthy. The mean ADC is elevated in the patient with BPD indicating diffusely large alveoli. In

addition a focal area of very elevated ADC values is present in the *right upper lobe* (arrow) of the patient with BPD which may be an area of scarring or partial tissue destruction

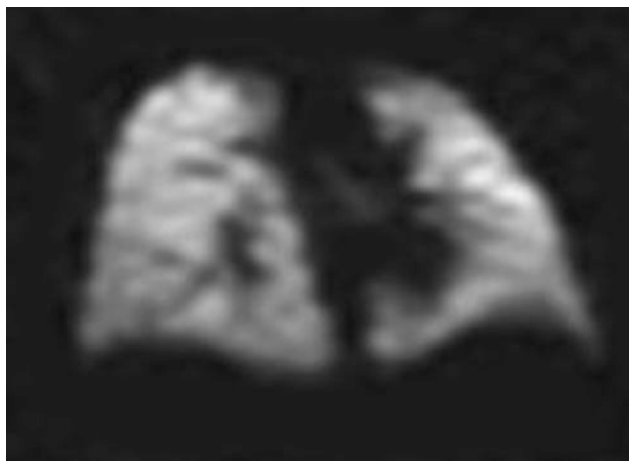


**Fig. 8** Coronal He-3 MR ventilation image of a healthy 1-year-old subject. The subject was not sedated for the examination. A fast imaging sequence (spiral) was used to, in essence, freeze motion. The acquisition time for the slice shown was 0.12 s

required of a biomarker for pulmonary CF and may be useful in the evaluation of CF pulmonary disease severity or progression (Mentore et al. 2005).

### 3.4 Bronchopulmonary Dysplasia (Chronic Lung Disease of Prematurity)

Bronchopulmonary dysplasia (BPD) is a chronic lung disease that begins when an infant is born prematurely and the lungs are forced to function as a gas exchange organ during a stage of lung development when alveoli are just beginning

to form and are immature for the task. Inflammation and injury to the lung at this time are thought to affect subsequent lung development and result in alveoli that are abnormally large in size and reduced in number. However, our understanding of the morphological alterations of lung structure in children with BPD is limited due to the difficulty of obtaining lung tissue from the living child and the small number of studies investigating lung autopsy specimens from patients with BPD.

Preliminary studies using hyperpolarized He-3 have demonstrated that children with a history of preterm birth and BPD have elevated lung ADC values and the same or slightly lower lung volumes as compared with age-matched healthy control subjects, Fig. 7 (Altes et al. 2006a). These findings are consistent with the histological data demonstrating that children with BPD have enlarged alveoli that are reduced in number. Currently, there are no noninvasive methods for assessing alterations in lung structural development so it is difficult to monitor the effectiveness of treatment in infants or children with BPD. Diffusion He-3 MR has the potential to provide this much needed information.

### 3.5 Infants

One promising area of ongoing research is adapting hyperpolarized gas MR techniques for use in non-sedated infants. Improvements in CT technology decreased CT scanning time and the need for sedation in infants and young children. Similarly, by imaging very rapidly using non-Cartesian k-space sampling and parallel imaging, it is possible to image non-sedated infants and young children

with HG-MRI (Fig. 8) (Altes et al. 2012). Further, since the gas is polarized outside of the scanner, it is possible to image hyperpolarized gases with very low magnetic field strength scanners that could easily be sited in an NICU.

## 4 Summary

Hyperpolarized gas MRI has already provided new information about pediatric lung diseases. Using HG-MRI, the propensity for airway closure has been found to be heterogeneously distributed within the lungs of individual asthmatics in a pattern that persists or recurs over time. Similar regional patterns of ventilation abnormalities are seen in CF. In both asthma and CF, hyperpolarized gas MR ventilation imaging is very sensitive to abnormalities in lung ventilation, routinely showing ventilation defects in patients with normal spirometry. Early results in BPD suggest that hyperpolarized gas diffusion-weighted MRI can detect the abnormal alveolar development characteristic of this disease. The absence of ionizing radiation is a significant advantage compared with CT and allows HG-MRI to be performed repeatedly in the same patient. Thus, hyperpolarized gas MRI of the lung can safely provide new information about the pathophysiology of pediatric lung diseases and may ultimately have a role in clinical trials and in the clinical management of children with lung disease.

## References

- Albert MS, Cates GD, Driehuys B, Happer W, Saam B, Springer CS Jr et al (1994) Biological magnetic resonance imaging using laser-polarized  $^{129}\text{Xe}$ . *Nature* 370(6486):199–201
- Altes TA, de Lange EE (2003) Applications of hyperpolarized helium-3 gas magnetic resonance imaging in pediatric lung disease. *Top Magn Reson Imaging* 14(3):231–236
- Altes TA, Powers PL, Knight-Scott J, Rakes G, Platts-Mills TA, de Lange EE et al (2001) Hyperpolarized  $^3\text{He}$  MR lung ventilation imaging in asthmatics: preliminary findings. *J Magn Reson Imaging* 13(3):378–384
- Altes TA, Mata J, Froh DK (2006a) Abnormalities of lung structure in children with bronchopulmonary dysplasia as assessed by diffusion hyperpolarized helium-3 MRI. *Proc Intl Soc Magn Reson Med* 14:86
- Altes TA, Mata J, de Lange EE, Brookeman JR, Mugler JP III (2006b) Assessment of lung development using hyperpolarized helium-3 diffusion MR imaging. *J Magn Reson Imaging* 24(6):1277–1283
- Altes TA, Meyer CH, Mata J, Froh DK, Paget-Brown AO, Fain S et al (2012) Hyperpolarized helium-3 MR imaging of a non-sedated infant: a proof-of-concept study. *Proc Intl Soc Magn Reson Med* 20:1355
- Bannier E, Cieslar K, Mosbah K, Aubert F, Duboeuf F, Salhi Z et al (2010) Hyperpolarized  $^3\text{He}$  MR for sensitive imaging of ventilation function and treatment efficiency in young cystic fibrosis patients with normal lung function. *Radiology* 255(1):225–232
- Campana L, Kenyon J, Zhalchdoust-Sani S, Tzeng YS, Sun Y, Albert M et al (2009) Probing airway conditions governing ventilation defects in asthma via hyperpolarized MRI image functional modeling. *J Appl Physiol: Respir Environ Exerc Physiol* 106(4):1293–1300
- Chen XJ, Hedlund LW, Moller HE, Chawla MS, Maronpot RR, Johnson GA (2000) Detection of emphysema in rat lungs by using magnetic resonance measurements of  $^3\text{He}$  diffusion. *Proc Natl Acad Sci U S A* 97(21):11478–11481
- Costella S, Kirby M, Maksym GN, McCormack DG, Paterson NA, Parraga G (2012) Regional pulmonary response to a methacholine challenge using hyperpolarized ( $^3\text{He}$ ) magnetic resonance imaging. *Respirology* 17(8):1237–1246
- Couch MJ, O'Sullivan B, Roche J, Walvick R, Zheng S, Albert M et al (2012) Assessment of Repeatability of Hyperpolarized Gas MR Ventilation Imaging in Cystic Fibrosis Patients *Proc Intl Soc Magn Reson Med* 20:4001
- de Lange EE, Altes TA, Patrie JT, Gaare JD, Knake JJ, Mugler JP III et al (2006) Evaluation of asthma with hyperpolarized helium-3 MRI: correlation with clinical severity and spirometry. *Chest* 130(4):1055–1062
- de Lange EE, Altes TA, Patrie JT, Parmar J, Brookeman JR, Mugler JP III et al (2007) The variability of regional airflow obstruction within the lungs of patients with asthma: assessment with hyperpolarized helium-3 magnetic resonance imaging. *J Allergy Clin Immunol* 119(5):1072–1078
- de Lange EE, Altes TA, Patrie JT, Battiston JJ, Juersivich AP, Mugler JP III et al (2009) Changes in regional airflow obstruction over time in the lungs of patients with asthma: evaluation with  $^3\text{He}$  MR imaging. *Radiology* 250(2):567–575
- Deninger AJ, Eberle B, Ebert M, Grossmann T, Heil W, Kauczor H et al (1999) Quantification of regional intrapulmonary oxygen partial pressure evolution during apnea by ( $^3\text{He}$ ) MRI. *J Magn Reson (San Diego, Calif.: 1997)* 141(2):207–216
- Donnelly LF, MacFall JR, McAdams HP, Majure JM, Smith J, Frush DP et al (1999) Cystic fibrosis: combined hyperpolarized  $^3\text{He}$ -enhanced and conventional proton MR imaging in the lung—preliminary observations. *Radiology* 212(3):885–889
- Fain SB, Gonzalez-Fernandez G, Peterson ET, Evans MD, Sorkness RL, Jarjour NN et al (2008) Evaluation of structure-function relationships in asthma using multidetector CT and hyperpolarized  $^3\text{He}$  MRI. *Acad Radiol* 15(6):753–762
- Fischer MC, Spector ZZ, Ishii M, Yu J, Emami K, Itkin M et al (2004) Single-acquisition sequence for the measurement of oxygen partial pressure by hyperpolarized gas MRI. *Magn Reson Med* 52(4):766–773
- Hersman FW, Ruset IC, Ketel S, Muradian I, Covrig SD, Distelbrink J et al (2008) Large production system for hyperpolarized  $^{129}\text{Xe}$  for human lung imaging studies. *Acad Radiol* 15(6):683–692
- Hogg JC (2002) Airway pathology. In: Barnes P, Drazen J, Rennard S, Thomson N (eds) *Asthma and COPD: basic mechanisms and clinical management*. Academic Press, London, pp 57–66
- Johansson MW, Kruger SJ, Schiebler ML, Evans MD, Sorkness RL, Denlinger LC et al (2013) Markers of vascular perturbation correlate with airway structural change in asthma. *Am J Respir Crit Care Med* 188(2):167–178
- Kadlecek S, Hamedani H, Xu Y, Emami K, Xin Y, Ishii M et al (2013) Regional alveolar partial pressure of oxygen measurement with parallel accelerated hyperpolarized gas MRI. *Acad Radiol* 20(10):1224–1233
- Kauczor HU, Hofmann D, Kreitner KF, Nilgens H, Surkau R, Heil W et al (1996) Normal and abnormal pulmonary ventilation: visualization at hyperpolarized  $^3\text{He}$  MR imaging. *Radiology* 201(2):564–568
- Kaushik SS, Freeman MS, Cleveland ZI, Davies J, Stiles J, Virgincar RS et al (2013) Probing the regional distribution of pulmonary gas exchange through single-breath gas- and dissolved-phase  $^{129}\text{Xe}$  MR imaging. *J Appl Physiol (Bethesda, Md.: 1985)* 115(6):850–860



- Kirby M, Svenningsen S, Ahmed H, Wheatley A, Etemad-Rezai R, Paterson NA et al (2011) Quantitative evaluation of hyperpolarized helium-3 magnetic resonance imaging of lung function variability in cystic fibrosis. *Acad Radiol* 18(8):1006–1013
- Kirby M, Svenningsen S, Owringi A, Wheatley A, Farag A, Ouriadov A et al (2012) Hyperpolarized  $^3\text{He}$  and  $^{129}\text{Xe}$  MR imaging in healthy volunteers and patients with chronic obstructive pulmonary disease. *Radiology* 265(2):600–610
- Kruger SJ, Niles DJ, Dardzinski B, Harman A, Jarjour NN, Ruddy M et al (2013) Hyperpolarized Helium-3 MRI of exercise-induced bronchoconstriction during challenge and therapy. *J Magn Reson Imaging* (In Press)
- Lee EY, Sun Y, Zurakowski D, Hatabu H, Khatwa U, Albert MS (2009) Hyperpolarized  $^3\text{He}$  MR imaging of the lung: normal range of ventilation defects and PFT correlation in young adults. *J Thorac Imaging* 24(2):110–114
- Mata JF, Altes TA, Cai J, Ruppert K, Mitzner W, Hagspiel KD et al (2007) Evaluation of emphysema severity and progression in a rabbit model: comparison of hyperpolarized  $^3\text{He}$  and  $^{129}\text{Xe}$  diffusion MRI with lung morphometry. *J Appl Physiol* (Bethesda, Md.: 1985) 102(3):1273–1280
- McAdams HP, Palmer SM, Donnelly LF, Charles HC, Tapson VF, MacFall JR (1999) Hyperpolarized  $^3\text{He}$ -enhanced MR imaging of lung transplant recipients: preliminary results. *Am J Roentgenol* 173(4):955–959
- McAdams HP, Hatabu H, Donnelly LF, Chen Q, Tadamura E, MacFall JR (2000) Novel techniques for MR imaging of pulmonary airspaces. *Magn Reson Imaging Clin N Am* 8(1):205–219
- McMahon CJ, Dodd JD, Hill C, Woodhouse N, Wild JM, Fischele S et al (2006) Hyperpolarized  $^3\text{He}$  magnetic resonance ventilation imaging of the lung in cystic fibrosis: comparison with high resolution CT and spirometry. *Eur Radiol* 16(11):2483–2490
- Mentore K, Froh DK, de Lange EE, Brookeman JR, Paget-Brown AO, Altes TA (2005) Hyperpolarized  $^3\text{He}$  MRI of the lung in cystic fibrosis: assessment at baseline and after bronchodilator and airway clearance treatment. *Acad Radiol* 12(11):1423–1429
- Middleton H, Black RD, Saam B, Cates GD, Cofer GP, Guenther R et al (1995) MR imaging with hyperpolarized  $^3\text{He}$  gas. *Magn Reson Med* 33(2):271–275
- Narayanan M, Owers-Bradley J, Beardsmore CS, Mada M, Ball I, Garipov R et al (2012) Alveolarization continues during childhood and adolescence: new evidence from helium-3 magnetic resonance. *Am J Respir Crit Care Med* 185(2):186–191
- Parraga G, Ouriadov A, Evans A, McKay S, Lam WW, Fenster A et al (2007) Hyperpolarized  $^3\text{He}$  ventilation defects and apparent diffusion coefficients in chronic obstructive pulmonary disease: preliminary results at 3.0 Tesla. *Invest Radiol* 42(6):384–391
- Qing K, Ruppert K, Jiang Y, Mata JF, Miller GW, Shim YM et al (2013) Regional mapping of gas uptake by blood and tissue in the human lung using hyperpolarized xenon-129 MRI. *J Magn Reson Imaging* (In Press)
- Ruppert K, Brookeman JR, Hagspiel KD and Mugler JP 3rd (2000) Probing lung physiology with xenon polarization transfer contrast (XTC). *Magn Reson Med* 44(3):349–357
- Saam B, Yablonskiy DA, Gierada DS, Conradi MS (1999) Rapid imaging of hyperpolarized gas using EPI. *Magn Reson Med* 42(3):507–514
- Saam BT, Yablonskiy DA, Kodibagkar VD, Leawoods JC, Gierada DS, Cooper JD et al (2000) MR imaging of diffusion of  $(^3\text{He})$  gas in healthy and diseased lungs. *Magn Reson Med* 44(2):174–179
- Salerno M, Altes TA, Brookeman JR, de Lange EE and Mugler JP, 3rd (2001) Dynamic spiral MRI of pulmonary gas flow using hyperpolarized  $(^3\text{He})$ : preliminary studies in healthy and diseased lungs. *Magn Reson Med* 46(4):667–677
- Salerno M, de Lange EE, Altes TA, Truwit JD, Brookeman JR, Mugler JP 3rd (2002) Emphysema: hyperpolarized helium 3 diffusion MR imaging of the lungs compared with spirometric indexes—initial experience. *Radiology* 222(1):252–260
- Shea DA, Morgan D (2010) The helium-3 shortage: supply, demand, and options for congress. Congressional Research Service Technical Report: R41419
- Sun Y, O'Sullivan BP, Roche JP, Walvick R, Reno A, Baker D et al (2011) Using hyperpolarized  $^3\text{He}$  MRI to evaluate treatment efficacy in cystic fibrosis patients. *J Magn Reson Imaging* 34(5):1206–1211
- Woodhouse N, Wild JM, van Beek EJ, Hoggard N, Barker N, Taylor CJ (2009) Assessment of hyperpolarized  $^3\text{He}$  lung MRI for regional evaluation of interventional therapy: a pilot study in pediatric cystic fibrosis. *J Magn Reson Imaging* 30(5):981–988
- Woods JC, Choong CK, Yablonskiy DA, Bentley J, Wong J, Pierce JA et al (2006) Hyperpolarized  $^3\text{He}$  diffusion MRI and histology in pulmonary emphysema. *Magn Reson Med* 56(6):1293–1300

---

# Interventional Radiology Management of Pediatric Chest Disorders

William E. Shiels II

## Contents

<b>1</b>	<b>Introduction.....</b>	<b>523</b>
<b>2</b>	<b>Patient Care and Sedation Concepts .....</b>	<b>523</b>
<b>3</b>	<b>Interventional Radiology Procedures in the Pediatric Chest.....</b>	<b>524</b>
3.1	Foreign Body Removal.....	524
3.2	Esophageal Stricture Balloon Dilation .....	525
3.3	Percutaneous Drainage of Parapneumonic Effusion and Treatment of Empyema.....	525
3.4	Lung Abscess Drainage.....	527
3.5	Mediastinal Abscess Drainage .....	527
3.6	Percutaneous Biopsy.....	527
3.7	Thermal Ablation of Thoracic Malignancy.....	529
3.8	Chest Arteriography .....	530
3.9	Sclerotherapy of Vascular Malformations.....	532
3.10	Percutaneous Treatment of Aneurysmal Bone Cysts.....	534
3.11	Thoracic Duct Lymphangiography and Embolization.....	535
	<b>References .....</b>	<b>535</b>

---

## Abstract

This chapter will focus on diagnostic and therapeutic applications of interventional radiology in the pediatric chest. Diagnostic interventional radiologic topics discussed include patient care and sedation concepts, CT- and US-guided intrathoracic biopsy, thoracic angiography for aortic trauma and other causes of thoracic hemorrhage, and percutaneous intrathoracic lymphangiography. Therapeutic interventional radiologic topics discussed include balloon dilation of esophageal strictures, transesophageal and percutaneous foreign body removal, transarterial embolization treatment for hemoptysis thoracic duct embolization, thermal ablation of treatment of benign and malignant thoracic masses, percutaneous drainage of pulmonary and mediastinal abscesses, transcatheter fibrinolytic therapy for empyema, percutaneous sclerotherapy of vascular malformations, and definitive percutaneous treatment of thoracic aneurysmal bone cysts.

---

## 1 Introduction

Interventional radiological of the pediatric patient has evolved over recent years such that pediatric interventional radiological procedures are safe and effective as primary management options, or following failed medical or surgical management of various disorders in the pediatric chest. This chapter will provide a practical focus on effective management and for a broad spectrum of common pediatric disorders in the chest treatable with interventional radiologic techniques. The primary for pediatric thoracic radiologic intervention center around management of sepsis, life-threatening hemorrhage, percutaneous and treatment of thoracic neoplasia, percutaneous of vascular malformations, and thoracic foreign body removal.

---

W. E. Shiels II (✉)  
Department of Radiology, Children's Hospital,  
Children's Radiological Institute, 700 Children's Drive,  
Columbus, OH 43205, USA  
e-mail: william.shiels@nationwidechildrens.org

## 2 Patient Care and Sedation Concepts

In the radiological care process of the pediatric patient, support and frequent monitoring of physiologic parameters is essential, and is best provided by a dedicated team that includes radiologists (or pediatric sedation specialists/anesthesiologists) and nurses specifically trained in pediatric sedation care and techniques. Intraprocedural care of the child begins with support of temperature balance by means of warm blankets and appropriate body covering, heating lamps, and expedited procedures to minimize unnecessary heat loss and temperature instability.

Sedation or anesthesia of the pediatric patient is often required in order to efficiently and successfully complete complex procedures. Sedation protocols vary by institution and with physician preference. In children, intravenous sedation is frequently provided using a combination of intravenous pentobarbital (Nembutal, Abbott Laboratories, Chicago, IL) and fentanyl (Sublimaze, Janssen Pharmaceutica, Titusville, NJ). This drug combination is administered in a tailored and titrated fashion, beginning with pentobarbital 2–3 mg/kg and fentanyl 1 µg/kg. The total titrated doses do not exceed pentobarbital 8 mg/kg and fentanyl 3 µg/kg, all administered in the radiology department. Depending on physician preference, midazolam (0.1 mg/kg) may be substituted for pentobarbital. Patient sedation is provided with continuous monitoring of heart rate and oximetry. Further physiologic monitoring of respiratory, ECG, and blood pressure parameters are monitored as needed. When patients have failed prior attempts of intravenous sedation or require lengthy and complex procedures, patients are referred for general anesthesia in the interventional radiology suite.

---

## 3 Interventional Radiology Procedures in the Pediatric Chest

### 3.1 Foreign Body Removal

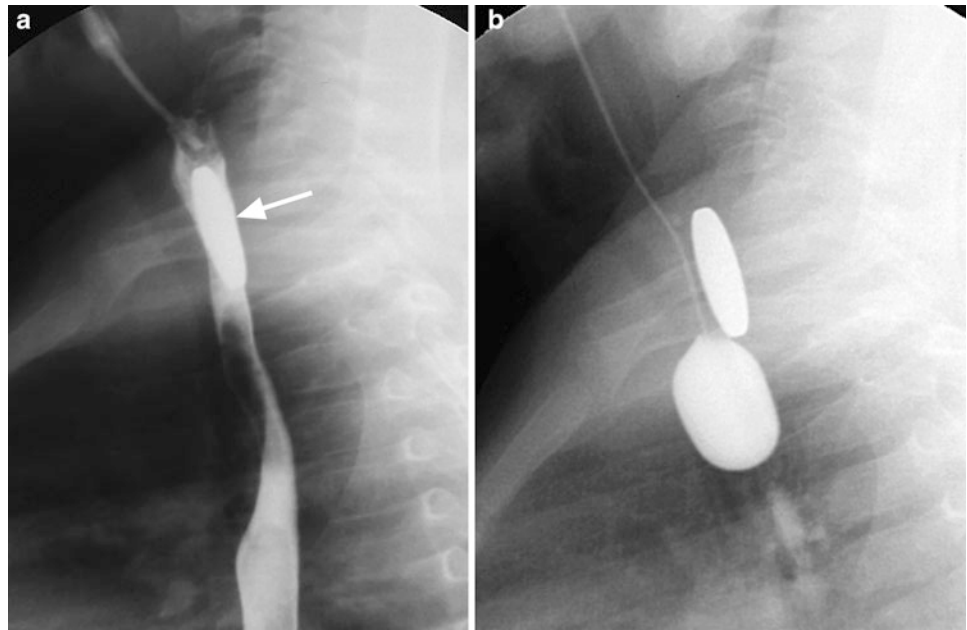
Image-guided foreign body removal is focused on three indications in children: ingested esophageal foreign bodies; transcatheter retrieval of vascular catheter fragments, and percutaneous ultrasound-guided removal of soft-tissue foreign bodies. Ingested foreign bodies often are retained in the esophagus and children present for emergent management due to either feeding intolerance or respiratory difficulty. In most settings, sharp or pointed foreign bodies are operatively managed with endoscopic or surgical removal. Coins are the most frequently encountered smooth esophageal foreign body in children. Less frequently, food/meat

impaction may be the presenting complaint associated with the diagnosis of achalasia or esophageal stricture. Based on the site of retention, ingested coins are divided into two main groups: lower esophageal and upper esophageal. In our experience, lower esophageal coins are most frequently managed without the need for image-guided extraction or operative management. Patients with uncomplicated lower esophageal coins are instructed to drink a carbonated beverage (or take effervescent crystals) in the upright position and ambulate for 1 h. A follow-up radiograph of the abdomen most often reveals successful passage of the coin into the stomach for later intestinal passage. If the coin does not pass into the stomach after this maneuver, the coin can be pushed into the stomach using a 14-French (14F) Foley nasoesophageal catheter with the balloon inflated with contrast. Coins embedded in the esophageal wall, or associated with esophageal perforation are operatively removed.

Ingested coins in the upper esophagus may be successfully removed using a transnasal or transoral Foley balloon extraction technique with fluoroscopic guidance (Campbell and Davis 1973; Little et al. 2006). The most common location for esophageal coins to lodge is at the thoracic inlet. Patient selection for Foley balloon foreign body extraction is essential, as contraindications to Foley balloon extraction include patients with respiratory distress and evidence of tracheoesophageal stripe thickening or airway compromise on lateral neck and/or chest radiographs. If there are no contraindications to fluoroscopically guided removal, the patient is prepared with intranasal anesthesia. Nasal anesthesia is most comfortably administered with viscous Lidocaine HCl 2 %, administered via syringe in the bilateral nares. Following nasal anesthesia, the patient is immobilized in either a body wrap, or preferably on an octagon immobilization board (Enterprises Octostop, Quebec, Canada). A 14-French Foley balloon catheter is passed either transnasally or transorally into the upper esophagus. During the extraction procedure the patient is positioned in the right lateral decubitus position, preferably with the table in mild Trendelenburg position. Due to the potential for impaction of a nonradiopaque food bolus resting on top of the coin or unsuspected esophageal erosion, the author recommends injection of a small amount of barium suspension (or water-soluble, nonionic contrast medium) above the coin prior to attempted coin removal. If no retained food particles or other esophageal complications are detected, the Foley catheter is advanced under fluoroscopic guidance past the coin, and the balloon is inflated with contrast. With the balloon inflated, the catheter is then withdrawn slowly (Fig. 1), drawing the coin into the cervical esophagus and eventually into the oropharynx. Resistance is occasionally met at the level of the cricopharyngeus muscle, usually



**Fig. 1** Esophageal coin removal in a 2-year-old girl. **a** Barium esophagram with 14-French Foley catheter demonstrating the esophageal coin (*arrow*) at the thoracic inlet without complicating food bolus. **b** Foley catheter balloon inflated, withdrawing the coin into the hypopharynx and mouth for expectoration



overcome with mild balloon tension. Once the coin is located within the oral cavity, the child is instructed to spit the coin out. If this instruction is not successful, the coin may be removed manually with a controlled finger sweep. When using a transnasal approach, it is important to remember to deflate the balloon prior to removal of the catheter beyond the oropharynx. A post-procedural esophogram is performed to evaluate for esophageal abnormalities.

Soft-tissue foreign bodies are a common clinical problem in both children and adults (Shiels et al. 1990; Shiels 2007; Close et al. 2009; Young et al. 2010). Most soft-tissue foreign bodies are impaled during domestic activity, involve the superficial soft tissues as a result of low velocity trauma and the majority can be removed without the need for image guidance. High velocity objects embedded in deep soft tissues are usually seen in as a result of weapons, blast injuries, or motorized tool-related accidents.

The primary indications for soft-tissue foreign body removal are recurrent pain or the development of infectious complications (Shiels 2007; Close et al. 2009; Young et al. 2010). With the advent of meticulous sonographic techniques, high-resolution sonography is the main imaging tool used for detection and localization of nonradiopaque soft-tissue foreign bodies, as well as for precise guided removal of radiopaque and nonradiopaque foreign bodies. Sonography is effectively used to guide the administration of percutaneous operative field local anesthesia, hydrodissect soft tissues surrounding the foreign body, blunt dissection, and forceps removal of foreign bodies (Fig. 2). In cases when granulation or fibrotic tissue encases a chronic embedded

foreign body, sonography is used to guide sharp dissection (scalpel or large gauge needle [e.g., 12 G angiocatheter needle]) of the foreign body prior to forceps removal (Shiels 2007; Close et al. 2009; Young et al. 2010).

### 3.2 Esophageal Stricture Balloon Dilation

In children, the most common indications for esophageal stricture balloon dilation are feeding intolerance following surgical repair of esophageal atresia, congenital dystrophic epidermolysis bullosa, and stricture from caustic ingestion (Ball et al. 1984; Spiliopoulos et al. 2012; Ko et al. 2006). The barium esophagram in such patients classically demonstrates food pooling in the upper esophageal pouch, a variable-sized anastomotic stricture, and poor motility in the distal esophageal segment. Fluoroscopically guided low-profile angioplasty balloon stricture dilation is most often performed carefully over a series of weeks, progressively dilating the stricture to 10 mm (30F) in young infants (Fig. 3) and 12 mm (36F) in older infants and toddlers (author recommendation, unpublished). Adjunctive topical administration of mitomycin-C during stricture dilation is a promising technique for reducing the rate of stricture recurrence (Chung et al. 2010; Heran et al. 2008).

Radiological intervention following surgical treatment of achalasia centers on balloon dilation of post-myotomy strictures. Balloon dilation of a distal esophageal stricture associated with achalasia with fluoroscopic guidance is safe to a diameter of 30 mm.

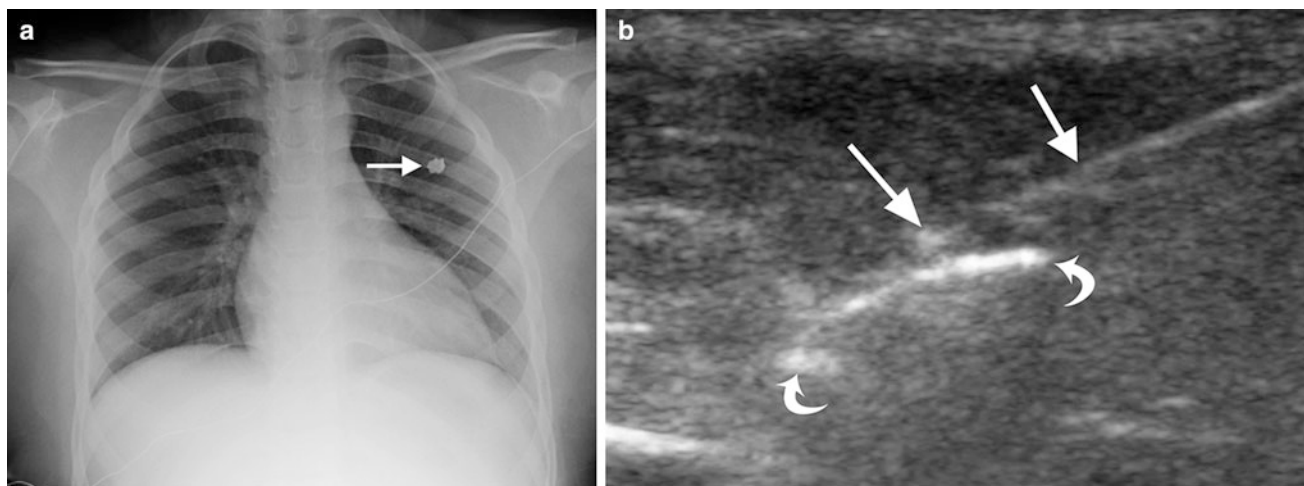
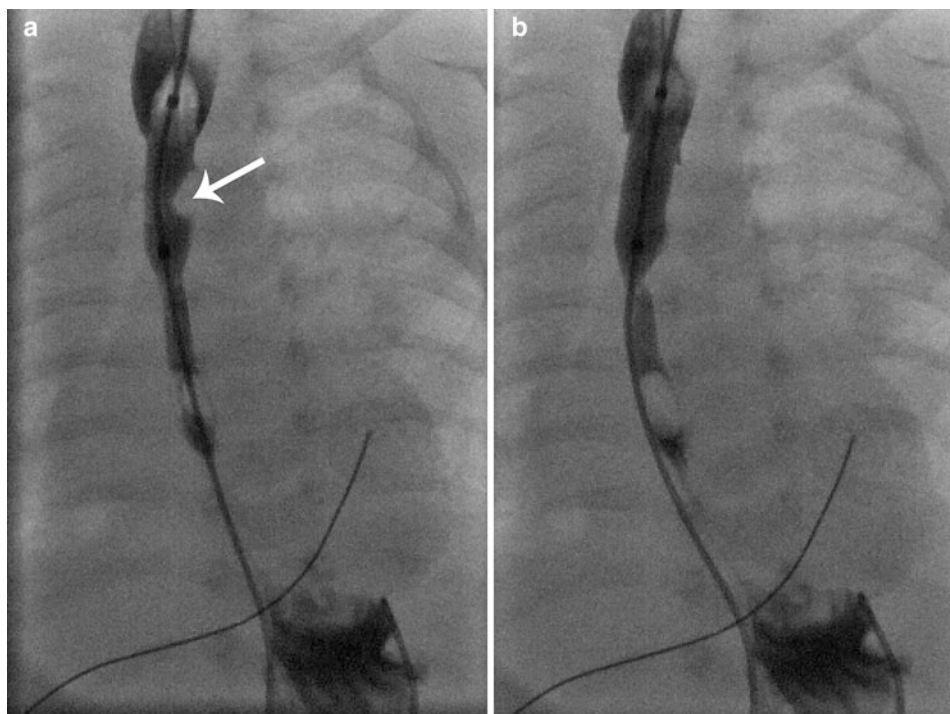


**Fig. 2** Percutaneous removal of a chest wall foreign body from a gunshot injury in a 12-year-old male. **a** Supine AP chest radiograph demonstrating metallic bullet shell fragment (*arrow*) in the anterior

chest wall soft tissues. **b** Ultrasound showing the metallic shell casing (*curved arrows*) and forceps (*straight arrows*) prior to grasping of the foreign body during ultrasound-guided removal

**Fig. 3** Balloon dilation of anastomotic stricture in a 1-month-old boy following repair of esophageal atresia.

**a** Fluoroscopic image showing a waist-like impression by the stricture on the 10 mm balloon (*arrow*) during dilation. **b** Image following full 10 mm balloon inflation with elimination of the stricture without esophageal rupture



### 3.3 Percutaneous Drainage of Parapneumonic Effusion and Treatment of Empyema

Thoracentesis is occasionally performed as an adjunctive procedure in the diagnostic management of children with pneumonia, as a means of isolating organisms, treating associated respiratory distress from a large parapneumonic effusion, or treating pleural empyema. Simple thoracentesis

is most safely and efficiently performed using sonographic guidance. Angiocatheter needles of 20–22 gauge provide excellent access systems with polyethylene sheaths that can be used for fluid aspiration without risk of pleural laceration. If a parapneumonic effusion is causing respiratory distress, catheter drainage is preferred over simple thoracentesis followed by immediate removal of the aspiration sheath. Mitri and colleagues demonstrated that simple thoracentesis followed by immediate removal of the aspiration

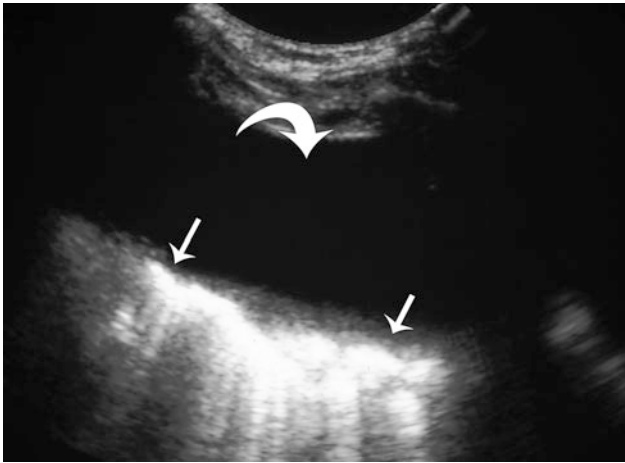


**Fig. 4** Ultrasound of simple parapneumonic effusion (*curved arrow*) in a 3-year-old girl prior to percutaneous catheter drainage over 3 days. Note the lack of fibrinous organization or septations. Adjacent consolidated lung (*straight arrows*) is displaced medially by the effusion

sheath is associated with a 27 % rate of recurrence of the parapneumonic effusion, necessitating a second sedation/anesthesia and drainage catheter placement (Mitri et al. 2002). For this reason, after initial catheter drainage of the parapneumonic effusion, the author and his colleagues routinely maintain the drainage catheter in place for a few days, until pleural drainage ceases during medical treatment of the associated pneumonia (Fig. 4).

Empyema drainage is usually performed with sonographic rather than CT guidance. Diagnostic chest sonography complements CT in the evaluation of pleural fluid collections, often revealing fibrinous organization, septations, and loculations not revealed by chest CT (Fig. 5). Real-time sonography provides excellent guidance for controlled needle, guidewire, dilator, and catheter placement in the pleural empyema cavity. Sonography is effectively coupled with fluoroscopy for final catheter placement, manipulation, and fluid drainage. A 4-French or 5-French Yueh Centesis needle (Cook Inc, Bloomington, IN) is an excellent pleural access needle and sheath system, which immediately accepts a 0.035 inch guidewire for dilator and catheter placement. Empyemas with fibrinous septations are safely and effectively treated with percutaneous catheter drainage and intracavitary tissue plasminogen activator (tPA) with efficacy of 80–84 % (16–20 % of patients require surgical decortication) (Gates et al. 2004; Gasior et al. 2013). Intracavitary tPA in children is safely and effectively administered as 2 units tPA in 20 ml of saline. The tPA is injected into the catheter, and the catheter is closed for 60 min prior to resumption of drainage. This technique is repeated every 12 h until clearance of residual fibrinous empyema fluid.

### 3.4 Lung Abscess Drainage

Lung abscesses that have not responded to initial treatment with intravenous antibiotics may be successfully drained with percutaneous catheter drainage techniques. Lung abscesses that abut the pleural surface can be drained safely with little risk of pneumothorax, using techniques and catheters as described for empyema and drainage of other abscesses. As a general rule, abscesses require 8-French or larger catheter systems for effective drainage. Lung abscesses smaller than 3 cm may be effectively drained with a 5F catheter, saline lavage, and a few days of drainage catheter suction (Fig. 6). Lung abscesses that abut the pleural surface are excellent candidates for sonographically guided drainage. In the author's experience, lung abscesses with persistent bronchial connection following drainage have represented infected congenital bronchopulmonary foregut malformations such as congenital pulmonary airway malformation (CPAM). In these patients, preoperative percutaneous drainage has been used by the author, allowing controlled surgical removal of the CPAM, reducing the risk of intraoperative cyst fluid decompression into the tracheobronchial tree of the dependent lung.

### 3.5 Mediastinal Abscess Drainage

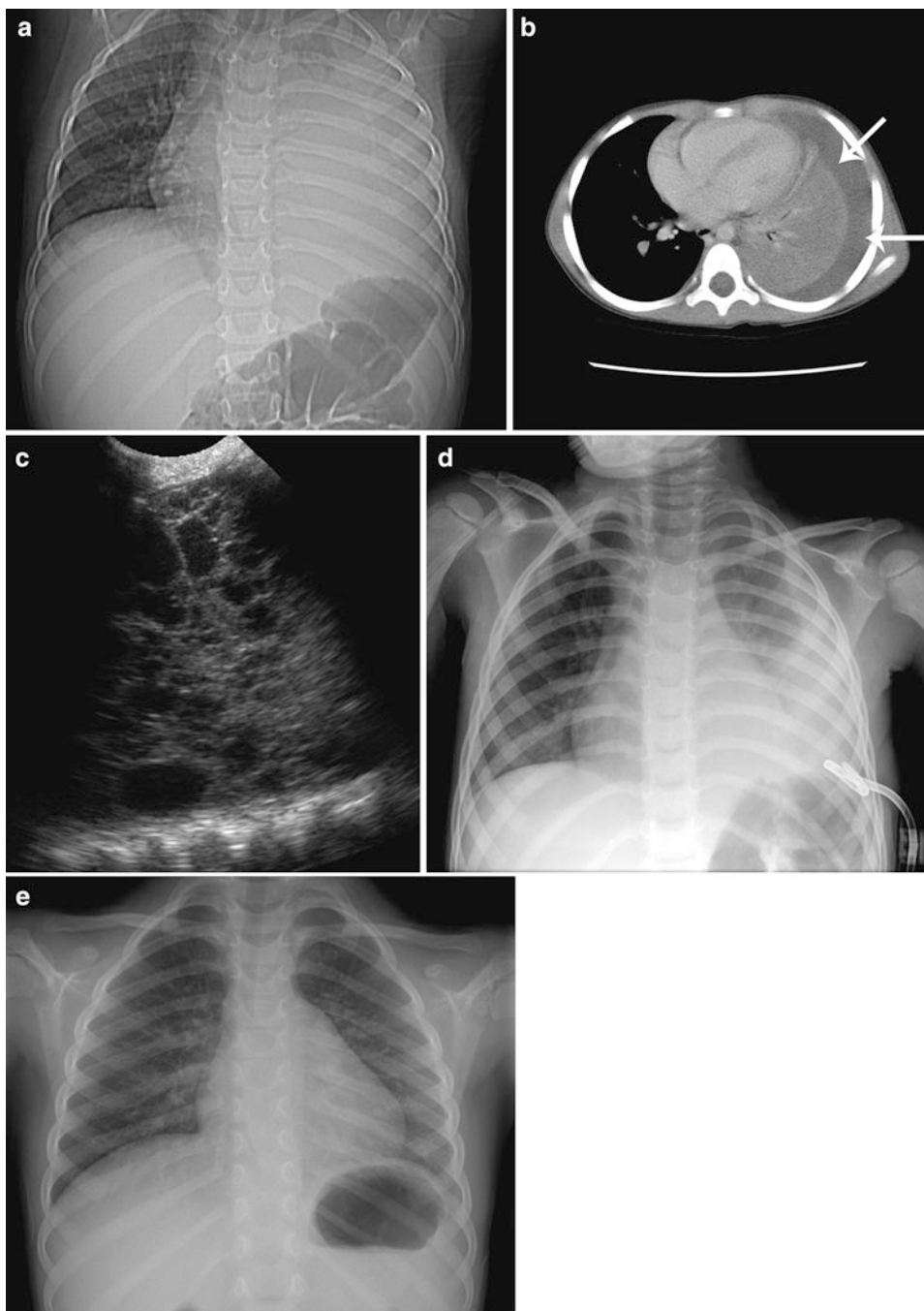
Anterior mediastinal, pericardial, and subpleural abscesses may occur as an extension of complicated deep neck infections. Real-time, high-resolution ultrasound guidance allows millimeter accuracy and control, allowing interventional radiologists the ability to avoid critical structures in the neck and chest during abscess drainage. In the author's clinical experience, the unossified sternum of infants and children provides for unique and excellent retrosternal visualization and guidance for safe drainage of both pericardial and anterior mediastinal abscesses, as well as vascular malformation treatment access. During anterior mediastinal abscess drainage, sonography is used to guide parasternal needle, guidewire, and drainage catheter placement (Fig. 7). It is important to remember that many mediastinal and subpleural infections that complicate deep neck infections may be limited to a phlegmon, with no drainable fluid, and may respond well to appropriate antibiotic therapy.

### 3.6 Percutaneous Biopsy

Children presenting with large chest or mediastinal neoplasms (especially anterior mediastinal) may not be candidates for open surgical biopsy, due to the risk of anesthesia associated with airway and/or central vascular compression



**Fig. 5** Left lower lobe pneumonia with empyema in an 8-year-old girl drained with ultrasound guidance. **a** Supine chest CT localizer radiograph showing dense opacification of the left hemithorax. **b** Axial chest CT image revealing a left pleural effusion (arrows) without appreciable septations or loculations. **c** Left hemithorax intercostal ultrasound image obtained during US-guided drainage catheter placement demonstrating the multilocular nature of the empyema with fibrinous organization not revealed by CT. **d** AP chest radiograph showing a 12F drainage catheter used for tPA fibrinolytic infusion therapy to facilitate empyema drainage. **e** Upright PA chest radiograph, 1 month following therapy, demonstrating resolution of both the left lower lobe pneumonia and the empyema



by the mass (Sola et al. 2013). When consulted by surgeons or oncologists to perform initial diagnostic biopsies in these patients, 14–18 G core biopsy techniques are safely utilized, with either sonographic or CT guidance (Roebuck et al. 2011; Hoffer et al. 1996). Particularly in the chest and mediastinum, freehand sonographic guidance allows real-time control of the procedure, specifically avoiding intrathoracic blood vessels and the lung. Core biopsy procedures are performed using the above described intravenous sedation protocol, supplemented with deep local anesthesia. Deep local anesthesia (Lidocaine 1 %) is most effectively

administered under direct sonographic guidance to the level of the tumor or pleural surface. Due to the need for multiple samples of adequate volume for histologic diagnosis, automated core needle biopsy systems are used, placed in a coaxial fashion through a guiding canula. This canula technique allows a single entry site into the tumor, obtaining 3–5 large core samples. Sonography allows precise placement of hemostatic gelatin sponge in the tract as the guiding canula is removed. Large core biopsies have proven sufficient for diagnosis of small cell pediatric tumors (Roebuck et al. 2011; Hoffer et al. 1996).

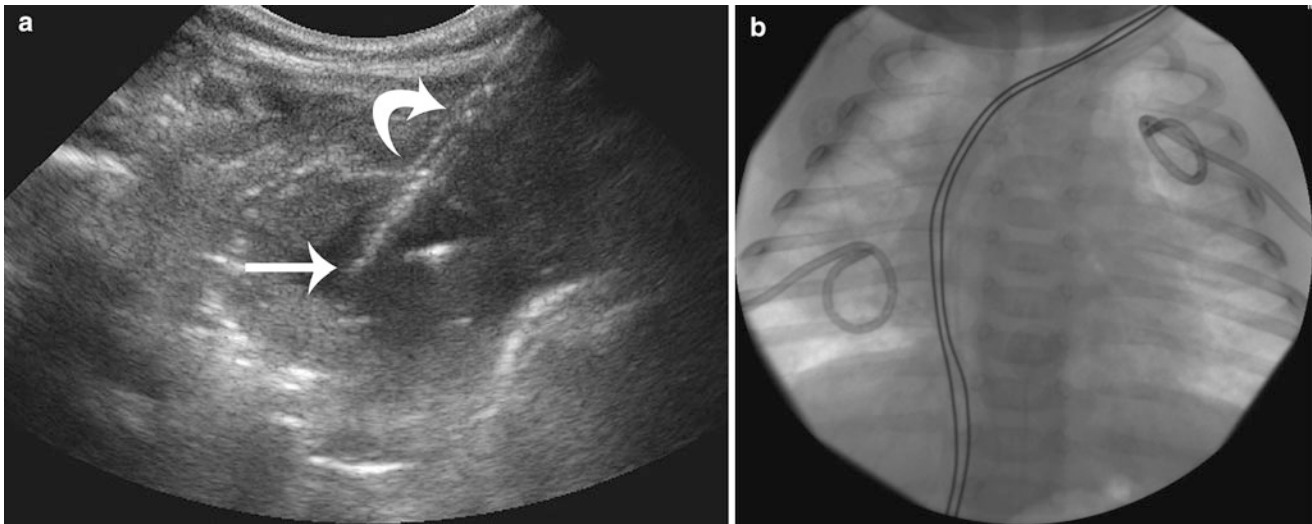


**Fig. 6** Ultrasound-guided bilateral lung streptococcal abscess drainages in a 6-month-old boy. **a** Ultrasound image of the left upper lobe abscess during coaxial placement of a 5F drainage catheter. The 5F pigtail drainage catheter (*straight arrow*) is seen exiting the coaxial

15G peel-away sheath (*curved arrow*). **b** AP chest radiograph showing bilateral 5F drainage catheters that were in place for 3 days prior to cessation of drainage and fever defervescence

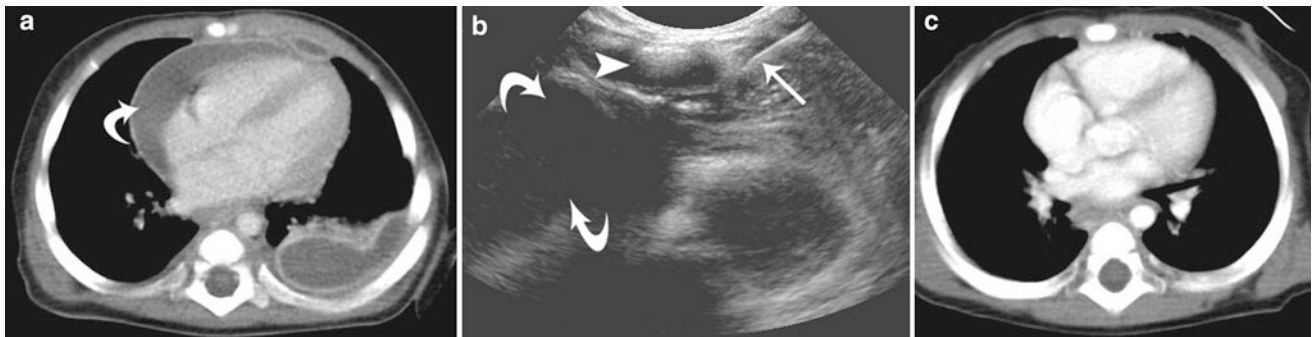


**Fig. 7** Ultrasound and fluoroscopic guidance for anterior mediastinal staphylococcal (MRSA) abscess catheter drainage in a 6-month-old girl. **a** Axial chest CT image demonstrating a pericardial abscess (*curved arrow*). **b** Ultrasound image demonstrating a 21G needle (*straight arrow*) being placed under the unossified sternum

(*arrowhead*) into the pericardial abscess (*curved arrows*), prior to placement of a 6F drainage catheter over a guidewire. **c** Axial chest CT image 1 month following abscess drainage, demonstrating complete resolution of the pericardial abscess

Fine needle aspirates have not proven adequate for the required battery of diagnostic oncologic tests in most pediatric tumors. However, ultrasound is effective for guiding fine needle aspiration of pneumonia for culture, in cases of indeterminate infectious etiology, as well as guiding biopsy of peripheral and subpleural lung nodules (Fig. 8). Surgical resection (open or thorascopic) of small lung nodules is greatly facilitated by immediate preoperative CT or ultrasound-guided needle and guidewire localization (Partrick et al. 2002). A parasternal or anterior intercostal approach is safely used for ultrasound or CT-guided percutaneous anterior mediastinal tumor biopsy (Fig. 9). Middle mediastinal mass biopsy is safely performed by prospective pleural catheter placement and

creation of a controlled pneumothorax, allowing the ipsilateral lung to collapse, thus being displaced and allowing an unobstructed path for percutaneous CT-guided biopsy (Lin and Li 2009) (Fig. 10).

### 3.7 Thermal Ablation of Thoracic Malignancy

Radiofrequency ablation (RFA), microwave ablation, and cryoablation techniques continue to expand providing minimally invasive options for treatment of lung malignancies in children and adults (Shiels and Brown 2005). Unlike adults, children rarely present with primary malignancies of the lung. In the author's clinical experience,

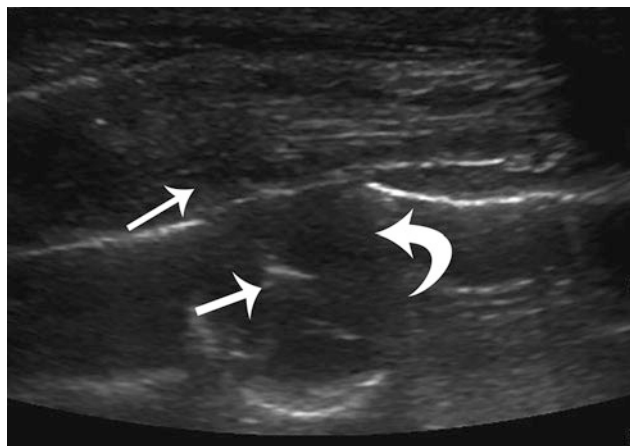


**Fig. 8** Ultrasound-guided 16G core biopsy of a subpleural lung nodule in a 16-year-old male. Ultrasound image demonstrating a 16G core biopsy needle (*straight arrows*) within the subpleural nodule (*curved arrow*). Histological diagnosis of the nodule was Ewing sarcoma metastasis

palliative RFA of metastases is currently, and will likely continue to be the most frequent indication for lung tumor thermal ablation in children. In the lung, the author's experience is focused primarily on the treatment of metastatic osteogenic sarcoma patients who are not operative candidates (Fig. 11). With RFA and microwave ablation, a minimum target temperature of 60 °C over 12 min is required for effective ablation. Ultrasound and CT guidance may be used for lung tumor ablation cases, with CT proving to be most useful when the location of the tumor in the lung precludes an effective sonographic window. The author has safely provided palliative RFA treatment for metastatic lesions as large as 8 cm. The insulating effect of lung limits the extension of necrosis into adjacent tissue. In palliative treatment of metastatic lung lesions, the tissue most resistant to ablation is adjacent to the heart and chest wall, likely due to heat sink effects in these two areas. CT scans demonstrate significant cavitation without pneumothoraces. In the large bilateral tumor ablations, core body temperature elevations are maintained at 38–39 °C or below with the use of a hypothermic blanket system (Medi-Therm II; Gaymar, Orchard Park, NY), with blanket cooling temperatures as low as 20 °C. Following thoracic thermal ablation, it is critical to manage post-procedural pleuritic pain and post-ablation syndrome issues, to include aggressive analgesic and fluid hydration protocols.

## 3.8 Chest Arteriography

### 3.8.1 Aortic Trauma

Aortic injury in the pediatric patient is thankfully rare (Trachiotis et al. 1996; Peclet et al. 1990; Cooper et al. 1994; Eddy et al. 1990; Vignon et al. 1996). Children with

traumatic aortic injury are usually pedestrians struck by automobiles and passengers in motor vehicle accidents (Fisher et al. 1997). While mortality for isolated chest trauma in the pediatric population is only 5 %, this increases to 75 % with aortic injury (Peclet et al. 1990; Cooper et al. 1994). Thoracic aortic injury typically involves the arch at the level of the ligamentum arteriosum, although occasionally it may involve the aortic root (Trachiotis et al. 1996; Peclet et al. 1990; Cooper et al. 1994; Eddy et al. 1990; Vignon et al. 1996; Fisher et al. 1997; Pabon-Ramos et al. 2010). Although this injury is uncommon, a high level of suspicion is warranted due to the devastating effects (Eddy et al. 1990). The initial evaluation is typically accomplished with a portable supine radiograph. Signs of mediastinal hematoma, such as a widened mediastinum, indistinctness of the aortic arch, or tracheal deviation may be present, as well as accessory signs such as first rib fracture or apical capping. These findings may be difficult to evaluate in a child who has a disproportionately large thymus and the absence of these findings does not exclude aortic or great vessel injury. Thoracic computed tomography (with CT angiography) and transesophageal echocardiography have been advocated in the adult literature to demonstrate the mediastinal hematoma (Vignon et al. 1996). Improved technology and accuracy of thoracic CT and CT angiography have been associated with reduction in the need to perform diagnostic catheter-based aortography in children (Pabon-Ramos et al. 2010). In cases where there is questionable traumatic aortic injury, catheter-based aortography is indicated. Transfemoral aortography is performed through a vascular sheath. The appropriate size flush catheter (3–5 French) is directed into the supra-avalvular aortic arch. Small aortas may require the placement of a straight flush catheter. Either digital subtraction or cut film arteriography is performed in two planes, typically left anterior oblique (LAO) and AP. The proximal carotid, brachiocephalic, and subclavian arteries should be included in the imaging field. Injection volume should be 1–1.5 cc/kg over 1–2 s. Rapid filming (3 images/s) should be performed, initially followed by delayed images (1 image/s) to evaluate for areas of focal flow stasis. Care must be taken in the evaluation of the images since ductal diverticula and infundibula of the brachiocephalic arteries can mimic aortic injury (Fisher et al. 1997).

### 3.8.2 Transcatheter Embolization Treatment of Hemoptysis

Life-threatening hemoptysis in the pediatric population is most commonly a complication of cystic fibrosis (Fellows et al. 1979; Sweezey and Fellows 1990; Cohen et al. 1990; Porter et al. 1983; Cipolli et al. 1995). Traditional therapy had included transfusions, antibiotic therapy, and cessation of percussion and postural drainage (PPD). Percutaneous arteriography with embolization has become an accepted



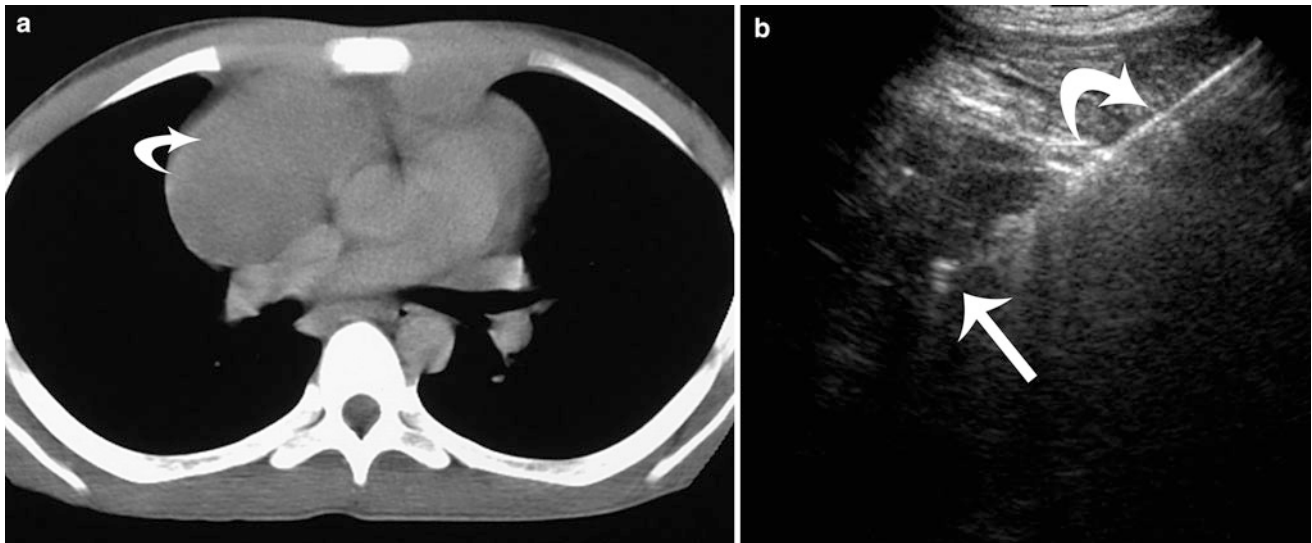


**Fig. 9** Anterior mediastinal lymphoma with central vascular compression in a 6-year-old boy. **a** Axial chest CT image demonstrates superior vena caval compression from the anterior mediastinal mass

(curved arrow). **b** Ultrasound image demonstrates the 13G guiding cannula (curved arrow) and the 14 G biopsy needle (straight arrow) during retrieval of five core biopsies for definitive histologic diagnosis



**Fig. 10** CT-guided middle mediastinal biopsy with artificial pneumothorax access in a 13-year-old girl. Axial chest CT image with the patient in prone position demonstrates an artificial pneumothorax in the right hemithorax with a 16G core biopsy needle in the mass. Histologic diagnosis was histoplasmosis

and often preferred method of treatment in these patients. Indications for embolization include severe hemoptysis (> 300 cc in 24 h), recurrent or persistent hemoptysis, or hemoptysis that interferes with the patient's therapy or lifestyle (Cipolli et al. 1995). Prior to performing this procedure, it is important to explain all complications possible, including the risk of damage to the spinal cord with



**Fig. 11** Radiofrequency ablation (RFA) of bilateral metastatic osteosarcoma in a 16-year-old male. CT-guided RFA procedure with three RFA needles in a left lung mass with air cavitation (arrows) in other bilateral metastatic masses post-ablation

subsequent neurological compromise (Fellows et al. 1979; Sweezey and Fellows 1990; Cohen et al. 1990; Porter et al. 1983; Cipolli et al. 1995; Barben et al. 2002). While bronchoscopy has been advocated to determine the side of bleeding, the patient often can tell due to either a “funny feeling” or “gurgling” isolated to one side. In the setting of acute life-threatening hemoptysis, bronchoscopy serves little useful purpose and delays appropriate intervention. Hemoptysis is usually from hypertrophied bronchial arteries, usually arising at or near the level of the carina. Multiple collaterals often exist, however, and multiple anastomoses can exist distally in the lung. A vascular sheath is placed in

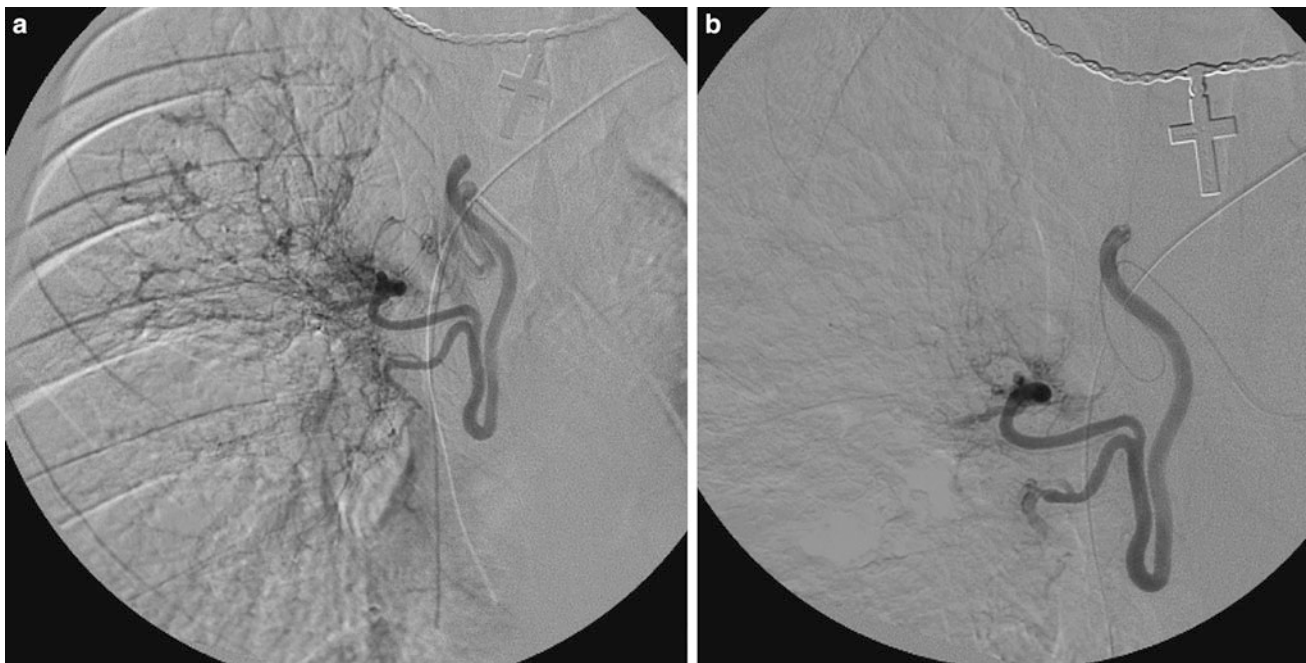


**Fig. 12** Bronchial artery embolization in 23-year-old female cystic fibrosis patient with recurrent hemoptysis. **a** Diagnostic digital subtraction arteriography with microcatheter selection of a hypertrophied right bronchial artery corresponding to the side of patient

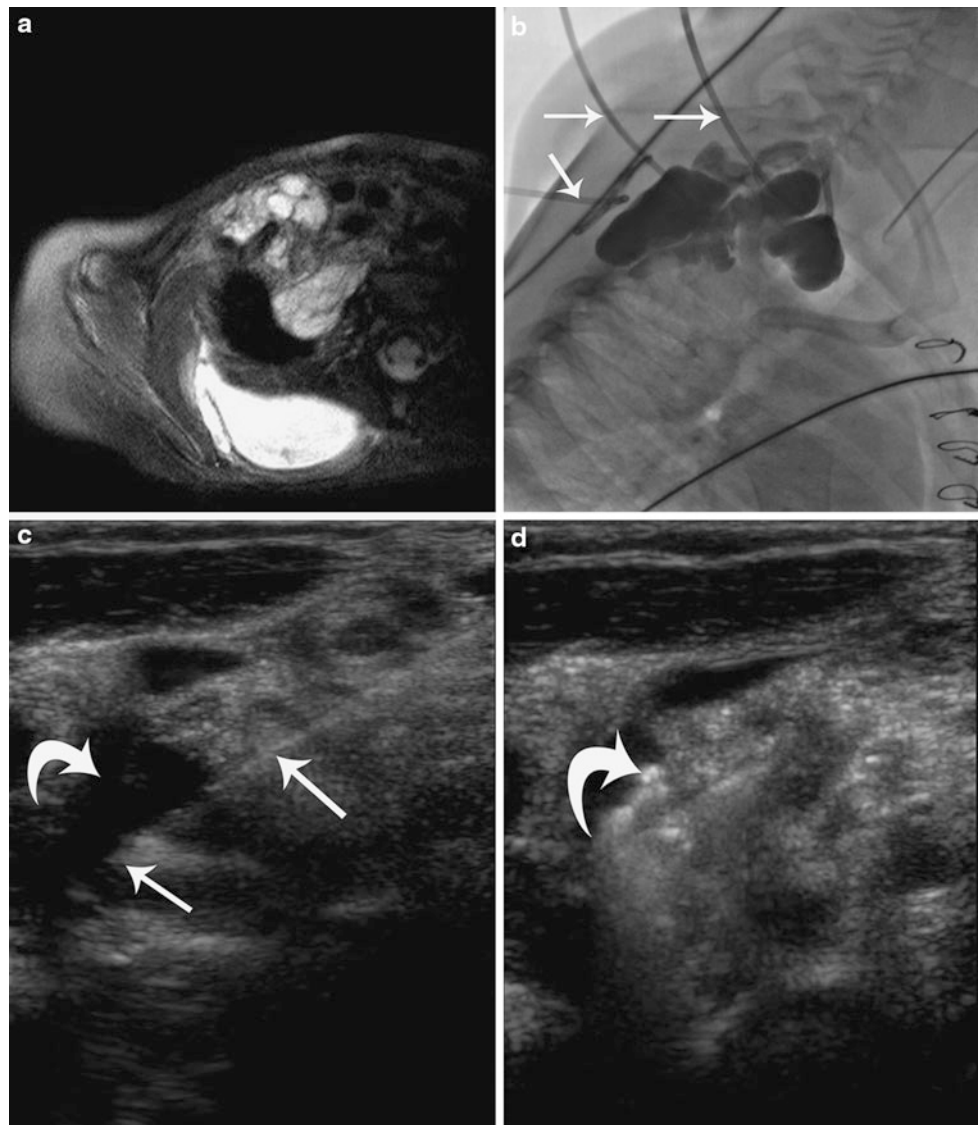
symptoms. **b** Digital subtraction arteriogram following bronchial artery embolization with polyvinyl alcohol particles demonstrates distal embolization and proximal flow stasis in the selected bronchial artery

the femoral artery, and 4- to 5-French catheters are advanced into the thoracic aorta near the carina. The bronchial arteries are cannulated and arteriography performed. The images are carefully evaluated to identify the anterior spinal artery. Either the diagnostic catheter or a microcatheter in a coaxial technique is then advanced into the vessel to a point safe for embolization. If a spinal artery is identified, embolization can only be performed if the catheter can be safely advanced distal to its origin. Distal embolization, with either gelatin sponge particles or polyvinyl alcohol particles, is performed to the point of flow stasis (Fig. 12). Supra-distal agents, such as gelatin sponge powder, alcohol, or liquid tissue adhesives should be avoided due to the high risk of bronchial necrosis. Proximal coil embolization, if performed, should only take place after distal embolization. Anastomoses with other collaterals may keep the distal inflammatory bed open, while cutting off access proximally. After embolizing all identified bronchial arteries, we evaluate the subclavian and brachiocephalic arteries to exclude and/or treat other contributing arteries. We perform aortography only if there is difficulty in identifying or cannulating the bronchial arteries, or at completion of embolization to document that all contributors have been treated. The patient may experience chest pain after the procedure and should be treated with narcotics if necessary. PPD may be restarted after 48 h. Reembolization will be needed in 21–45 % of patients within 1 year (Cipolli et al. 1995; Barben et al. 2002).

### 3.9 Sclerotherapy of Vascular Malformations

Lymphatic malformation (LM) is the most common indication for sclerotherapy in the pediatric chest, and accounts for about 5 % of benign tumors in children (Shiels et al. 2008). Pathologically, LM components are defined as macrocystic (cyst size larger than 10 mm), microcystic (1–10 mm), and solid (solid LM) tissue with no discernible cysts by sonography or MRI (Shiels et al. 2008, 2009). Sclerotherapy of macrocystic LM can be performed with one of two techniques: Needle access of cysts with infusion and long-term dwell of liquid sclerosant, or indwelling catheter placement with time-limited sclerosant contact followed by suction drainage. Sclerotherapy of macrocystic LM is most commonly performed with either doxycycline, bleomycin, OK-432, or sequential injection of sodium tetradecyl sulfate (STS) (followed by aspiration) and ethanol (ETOH) (Shiels et al. 2008, 2009; Hill et al. 2012; Burrows et al. 2008; Okazaki et al. 2007; Giguere et al. 2002a, b; Dubois et al. 1997; Alomari et al. 2006; Lee et al. 2005; Molitch et al. 1995; Kim et al. 2004; Ogita et al. 1994; Giguere et al. 2002a, b). Ethanol as a sole agent, in the author's experience, has extremely unpredictable efficacy in the treatment of LM. Microcystic LM is treated with small gauge (25G) needle access, aspiration, and subsequent injection of Doxycycline microfoam (Shiels et al. 2008, 2009; Hill et al. 2012). Doxycycline is the author's

**Fig. 13** Mediastinal lymphatic malformation treatment in a 3-year-old girl. **a** T2-weighted axial MRI image demonstrating a multifocal macrocystic and microcystic lymphatic malformation involving the neck, mediastinum, and chest wall. **b** Fluoroscopic image following ultrasound-guided placement of three 5F drainage catheters for dual-drug (STS and ETOH) short-term dwell sclerotherapy. **c** Ultrasound image showing cyst (curved arrow) puncture with a 25G needle (straight arrows) prior to aspiration. **d** Ultrasound image showing the cyst injected with echogenic doxycycline microfoam (curved arrow)



preferred sclerosant for long-term dwell liquid sclerotherapy, given predictable results and limited pain that can be managed with deep sedation. Doxycycline is mixed to a concentration of 10 mg/ml with saline and water-soluble contrast material (320 mgI/cc). Sonography is used for needle guidance and aspiration, followed by fluoroscopic cystography. Authors vary in the volume of sclerosant used, ranging from 30 to 100 % of original cyst volume (Burrows et al. 2008; Okazaki et al. 2007; Giguere et al. 2002a, b; Dubois et al. 1997; Alomari et al. 2006; Lee et al. 2005; Molitch et al. 1995; Kim et al. 2004). With long-term dwell doxycycline sclerotherapy, the sclerosant is injected and the needle is removed. Long-term dwell doxycycline treatment results compare with OK-432, with reported excellent response in 20–64 % of patients and complications in 22–46 % of patients to include neuropathy, myoglobinuria, and pain (Burrows et al. 2008; Ogita et al. 1994; Giguere et al. 2002a, b).

A catheter-based, short-term dwell, infusion/aspiration protocol for macrocyst ablation is reported to have an efficacy greater than 95 %, without complications of pain, neuropathy, or myoglobinuria (Shiels et al. 2008, 2009; Hill et al. 2012). In this regimen, using a 5–8F catheter access system, liquid STS 3 % is maintained for 2 min, with aspiration, followed by ETOH for 15 min (Fig. 13). Following aspiration of the ETOH, the catheter is then connected to a suction bulb system for 3 days.

Microcystic LM is effectively treated with precise injection of doxycycline foam (5–10 mg/ml). Doxycycline foam is formulated in the interventional radiology suite with a 1:1 mixture of doxycycline and human serum albumin 25 % (HSA) (Pipitone et al. 2010; Shiels and Mayerson 2013). Air is agitated 30 times with the doxycycline/albumin mixture in a double syringe and stopcock system to make a microfoam (medical meringue) that is echogenic and allows for sustained release of doxycycline from the protein bound albumin



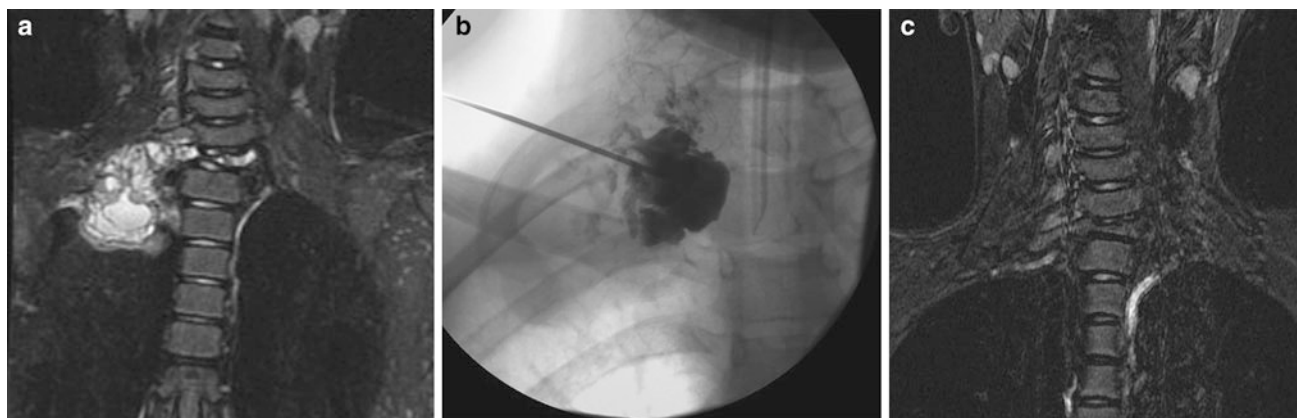


**Fig. 14** Percutaneous treatment of an exophytic intrathoracic aneurysmal bone cyst (ABC) arising from the C7 vertebra in an 8-year-old girl. **a** T2-weighted coronal MRI image demonstrating the exophytic intrathoracic component of the ABC, with collapse of the involved C7 vertebra. **b** Fluoroscopic image following contrast injection in the

ABC demonstrating vascular channels prior to doxycycline foam injection treatment. **c** T2-weighted coronal MRI image following ABC treatment with complete resolution of the intrathoracic component, and healing of the collapsed C7 vertebra

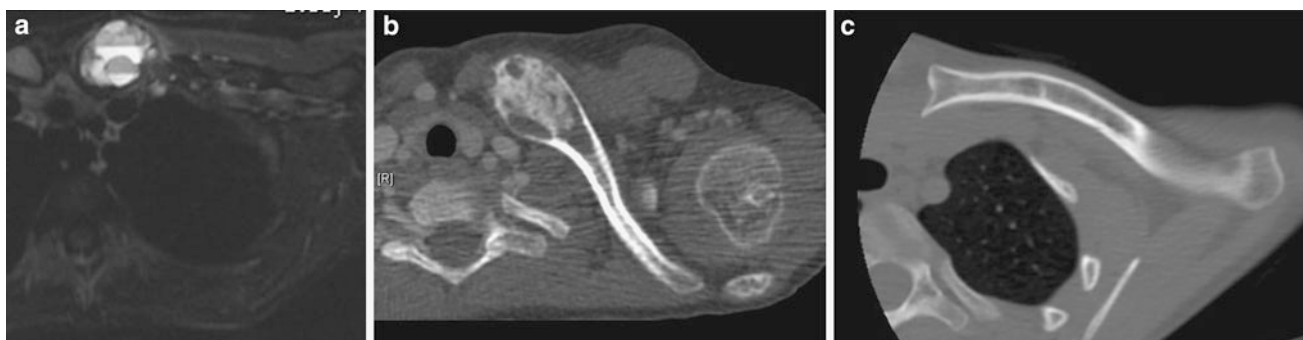


**Fig. 15** Percutaneous treatment of a medial left clavicle ABC in a 13-year-old male. **a** T2-weighted axial MRI image demonstrating an expansile, multilocular cystic lesion of the medial left clavicle. **b** Axial CT image demonstrates interval sclerotic healing of the ABC during

the 4-session treatment protocol. **c** Axial CT image shows excellent healing and remodeling of the left clavicle 1 year following percutaneous treatment of the ABC

carrier. Sonography allows precise targeting of individual microcysts (1–10 mm), with accurate cyst aspiration and intracystic doxycycline injection (Fig. 13).

Venous malformation sclerotherapy is most commonly performed with either STS foam, polidocanol, ethanol, or bleomycin (Gulsen et al. 2011; Kok et al. 2012; Lee et al. 2009; O'Donovan et al. 1997; Zhang et al. 2013). Bleomycin is carefully used in selective cases due to the potential for pulmonary fibrosis with high-dose bleomycin administration. STS and ETOH have similar reported clinical benefit (84–86 %), with STS having a greater safety profile, without the complication of cardiovascular collapse reported with ETOH injection (Kok et al. 2012; Lee et al. 2009; O'Donovan et al. 1997; Zhang et al. 2013). STS, as a detergent, is rapidly agitated into a foam for injection into the venous lakes with either digital subtraction venography or with sonographic guidance. The addition of Lipiodol

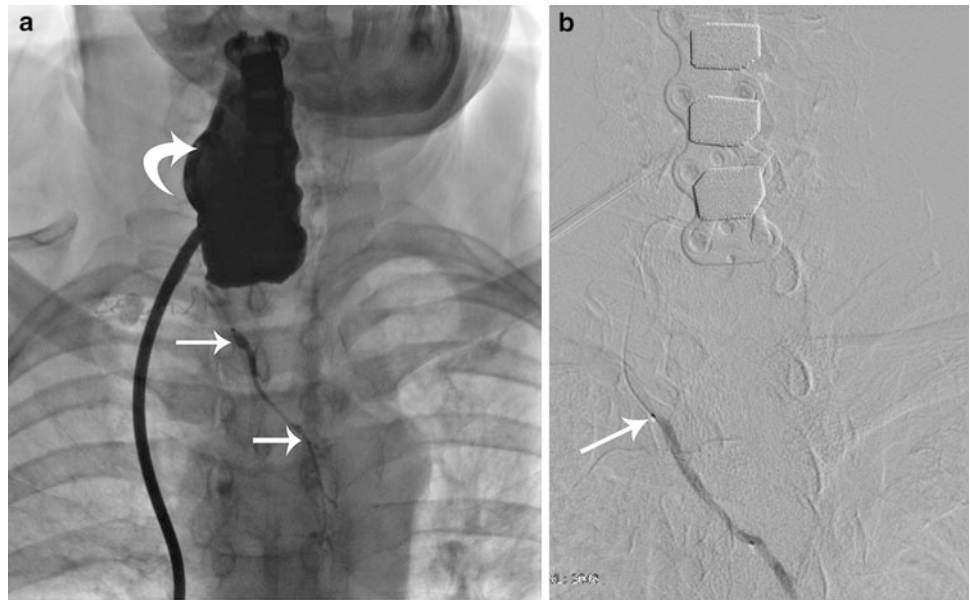
(Guerbet, Cedex, France) oily contrast with the STS creates a radiopaque foam for positive contrast visualization during venography.

### 3.10 Percutaneous Treatment of Aneurysmal Bone Cysts

Aneurysmal bone cyst (ABC) is a highly destructive lesion in bone, representing 1–6 % of all solid bone tumors (Shiels and Mayerson 2013). Approximately 70 % of ABCs are primary lesions, with the remaining 30 % occurring coincidentally with other bone lesions such as giant cell tumor, osteoblastoma, chondroblastoma, fibrous dysplasia, and telangiectatic osteosarcoma (Shiels and Mayerson 2013). ABC may involve any bone in the thorax, most commonly the clavicle, scapula, or thoracic spine, or C7 cervical spine

**Fig. 16** Transcervical approach for thoracic duct embolization.

**a** Fluoroscopic image demonstrating a large cervical lymphocele (*curved arrow*) following anterior spinal fusion, with the right cervical lymphatic duct (*straight arrows*) communicating with the thoracic duct. **b** Digital subtraction lymphangiogram demonstrating intraductal placement of a microcatheter (*straight arrow*) prior to thoracic duct embolization with n-butyl cyanoacrylate glue



involvement with exophytic extension into the thoracic cavity (Fig. 14). Previously considered to be an idiopathic bone cyst consisting of multiple honeycomb blood-filled locules, primary ABC is now known to represent a clonal benign neoplastic tumor of bone associated with translocations of the 16 and 17 chromosomes and rearrangements of the ubiquitin-specific protease 6 (USP6/TRE17) oncogene in spindle cells, resulting in the development of destructive solid fibroproliferative stroma, giant cell-like osteoclasts, and vascular spaces (Panoutsakopoulos et al. 1999; Dal Cin et al. 2000; Sciort et al. 2000; Althof et al. 2004; Baruffi et al. 2001; Oliveira et al. 2004). In addition, overexpression of the oncogene upregulates production of matrix metalloproteinase (MMP) that attacks and destroys the underlying collagenous matrix of bone (Kumta et al. 2003; Ye et al. 2010), as well as the production of vascular endothelial growth factor (VEGF) (Kumta et al. 2003).

Aneurysmal bone cyst in children has reported surgical treatment success of 25–50 %, with the highest recurrence rate of 75 % in juxtaphyseal ABC (Shiels and Mayerson 2013; Dormans et al. 2004; Freiberg et al. 1994; Lin et al. 2008; Dubois et al. 2003). When ABC was considered to be an idiopathic cyst, or a form of bone venous malformation, alternatives to surgical treatment involved percutaneous sclerotherapy of ABC attempted with alcohol solution of zein and polidocanol, with success rates ranging from 58 to 94 %, and complications including pulmonary embolism, skin necrosis, pain, swelling, and fever (Dubois et al. 2003; George et al. 2009; Topouchian et al. 2004; Shisha et al. 2007; Rastogi et al. 2006). Recent research reports document percutaneous ABC treatment in long bones and the spine with greater than 95 % efficacy using doxycycline foam with excellent bone healing and remodeling (Fig. 15)

(Shiels and Mayerson 2013). Doxycycline has chemotherapeutic properties that specifically target and cause necrosis of the fibroproliferative ABC stromal cells. In addition, doxycycline causes apoptosis (programmed cell death) of the giant cell-like osteoclasts in ABC, inhibits both MMP and VEGF, and stimulates osteoblastic bone healing (Shiels and Mayerson 2013).

### 3.11 Thoracic Duct Lymphangiography and Embolization

Disruption of the thoracic duct is a significant clinical challenge and presents most often as a chyloous effusion or cervical lymphocele. The role of the pediatric interventional radiologist in these settings is twofold: (1) define the site of thoracic duct leak with thoracic duct lymphangiography; and, if possible (2) perform percutaneous thoracic duct ligation embolization for definitive treatment of the leak. Thoracic duct lymphangiography is most often performed after access of the lymphatic ductal system via direct intranodal puncture with subsequent lymphangiography (Nadolski and Itkin 2012). Following delineation of the abdominal and thoracic lymphatic ductal network, the thoracic duct is most often accessed via a percutaneous transabdominal approach (Cope et al. 1999; Itkin and Chen 2011). If the thoracic duct leak presents as a lymphocele in the neck soft tissues, access for thoracic duct lymphangiography and thoracic duct embolization (Fig. 16) can be performed via a cervical trans-lymphocele approach (Warren et al. 2013). Once secure access is accomplished, definitive percutaneous thoracic duct embolization (PTDE) is performed with microcatheter-directed coil and/or n-butyl cyanoacrylate glue embolization (Fig. 16).

## References

- Alomari AI, Karian VE, Lord DJ, Padua HM, Burrows PE (2006) Percutaneous sclerotherapy for lymphatic malformations: a retrospective analysis of patient-evaluated improvement. *J Vasc Interv Radiol* 17:1639–1648
- Althof PA, Ohmori K, Zhou M et al (2004) Cytogenetic and molecular cytogenetic findings in 43 aneurysmal bone cysts: aberrations of 17p mapped to 17p13.2 by fluorescence in situ hybridization. *Mod Pathol* 17:518–525
- Ball WS, Strife JL, Rosenkrantz J et al (1984) Esophageal strictures in children treatment with balloon dilation. *Radiology* 150:263–264
- Barben J, Robertson D, Olinsky A, Ditchfield M (2002) Bronchial artery embolization for hemoptysis in young patients with cystic fibrosis. *Radiology* 224:124–130
- Baruffi MR, Barbieri Neto JB, Barbieri CH, Casartelli C (2001) Aneurysmal bone cyst with chromosomal changes involving 7q and 16p. *Cancer Genet Cytogenet* 129:177–180
- Burrows PE, Mitri RK, Alomari A et al (2008) Percutaneous sclerotherapy of lymphatic malformations with doxycycline. *Lymphatic Res Biol* 6:209–216
- Campbell JB, Davis WS (1973) Catheter technique for extraction of blunt esophageal foreign bodies. *Radiology* 108:438–440
- Chung J, Connolly B, Langer J, Marcon M, Temple M, Amaral JG (2010) Fluoroscopy-guided topical application of mitomycin-C in a case of refractory esophageal stricture. *J Vasc Interv Radiol* 21:152–155
- Cipolli M, Perini S, Valletta EA, Mastella G (1995) Bronchial artery embolization in the management of hemoptysis in cystic fibrosis. *Pediatr Pulmonol* 19:344–347
- Close JK, Shiels WE, Foster JA, Powell DA (2009) Percutaneous ultrasound-guided intraorbital foreign body removal. *Ophthalmic Plast Reconstr Surg* 25:335–337
- Cohen AM, Doershuk CF, Stern RC (1990) Bronchial artery embolization to control hemoptysis in cystic fibrosis. *Radiology* 175:401–405
- Cooper A, Barlow B, DiScala C, String D (1994) Mortality and truncal injury: the pediatric perspective. *J Pediatr Surg* 29:33–38
- Cope C, Salem R, Kaiser LR (1999) Management of chylothorax by percutaneous catheterization and embolization of the thoracic duct: prospective trial. *J Vasc Interv Radiol* 10:1248–1254
- Dal Cin P, Kozakewich HP, Goumnerova L et al (2000) Variant translocations involving 16q22 and 17p13 in solid variant and extraosseous forms of aneurysmal bone cyst. *Genes Chromosom Cancer* 28:233–234
- Dormans JP, Hanna BG, Johnston DR, Khurana JS (2004) Surgical treatment and recurrence rate of aneurysmal bone cysts in children. *Clin Orthop Relat Res* 421:205–211
- Dubois J, Chigot V, Grimard G, Isler M, Garel L (2003) Sclerotherapy in aneurysmal bone cysts in children: a review of 17 cases. *Pediatr Radiol* 33:365–372
- Dubois J, Garel L, Abela A, Laberge L, Yazbeck S (1997) Lymphangiomas in children: percutaneous sclerotherapy with an alcoholic solution of Zein. *Radiology* 204:651–654
- Eddy AC, Rusch VW, Fligner CL, Reay DT, Rice CL (1990) The epidemiology of traumatic rupture of the thoracic aorta in children: a 13-year review. *J Trauma* 30:989–991
- Fellows KE, Khaw KT, Schuster S, Shwachman H (1979) Bronchial artery embolization in cystic fibrosis: technique and long-term results. *J Pediatr* 95:959–963
- Fisher RG, Sanchez-Torres M, Whighan CJ, Thomas JW (1997) “Lumps” and “bumps” that mimic acute aortic and brachiocephalic vessel injury. *Radiographics* 17:825–834
- Freiberg AA, Loder RT, Heidelberger KP, Hensinger RN (1994) Aneurysmal bone cysts in young children. *J Pediatr Orthop* 14:86–91
- Gasior AC, Knott EM, Sharp SW et al (2013) Experience with an evidence-based protocol using fibrinolysis as first line treatment for empyema in children. *J Pediatr Surg* 48:1312–1315
- Gates RI, Hogan M, Weinstein S et al (2004) Drainage, fibrinolytics, or surgery: A comparison of treatment options in pediatric empyema. *J Pediatr Surg* 39:1638–1642
- George HL, Unnikrishnan PN, Garg NK, Sampath JS, Bass A, Bruce CE (2009) Long-term follow-up of Ethibloc injection in aneurysmal bone cysts. *J Pediatr Orthop* 18:375–380
- Giguere CM, Bauman NM, Sato Y et al (2002a) Treatment of lymphangiomas with OK-432 (Picibanil) sclerotherapy: a prospective multi-institutional trial. *Arch Otolaryngol Head Neck Surg* 128:1137–1144
- Giguere CM, Bauman NM, Smith RJ (2002b) New treatment options for lymphangioma in infants and children. *Ann Otol Rhinol Laryngol* 111:1066–1075
- Gulsen F, Cantasdemir M, Solak S, Gulsen G, Ozluk E, Numan F (2011) Percutaneous sclerotherapy of peripheral venous malformations in pediatric patients. *Pediatr Surg Int* 27:1283–1287
- Heran MK, Baird R, Blair GK et al (2008) Topical mitomycin-C for recalcitrant esophageal strictures: a novel endoscopic/fluoroscopic technique for safe endoluminal delivery. *J Pediatr Surg* 43:815–818
- Hill RH 3rd, Shiels WE 2nd, Foster JA et al (2012) Percutaneous drainage and ablation as first line therapy for macrocystic and microcystic orbital lymphatic malformations. *Ophthalmic Plast Reconstr Surg* 28:119–125
- Hoffer FA, Chung T, Diller L, Kozakewich H, Fletcher JA, Shamberger RC (1996) Percutaneous biopsy for prognostic testing of neuroblastoma. *Radiology* 200:213–216
- Itkin M, Chen E (2011) Thoracic duct embolization. *Semin Intervent Radiol* 29:261–266
- Kim KH, Sung MW, Roh JL, Han MH (2004) Sclerotherapy for congenital lesions in the head and neck. *Otolaryngol Head Neck Surg* 131:307–316
- Ko HK, Shin JH, Song HY, Kim YJ, Ko GY, Yoon HK, Sung KB (2006) Balloon dilation of anastomotic strictures secondary to surgical repair of esophageal atresia in a pediatric population: long-term results. *J Vasc Interv Radiol* 17:1327–1333
- Kok K, McCafferty I, Monaghan A, Nishikawa H (2012) Percutaneous sclerotherapy of vascular malformations in children using sodium tetradecyl sulphate: the Birmingham experience. *J Plast Reconstr Aesthetic Surg* 65:1451–1460
- Kumta SM, Huang L, Cheng YY et al (2003) Expression of VEGF and MMP-9 in giant cell tumor of bone and other osteolytic lesions. *Life Sci* 73:1427–1436
- Lee BB, Kim YW, Seo JM et al (2005) Current concepts in lymphatic malformation. *Vasc Endovasc Surg* 39:67–81
- Lee IH, Kim KH, Jeon P (2009) Ethanol sclerotherapy for the management of craniofacial venous malformations: the interim results. *Korean J Radiol* 10:269–276
- Lin PP, Brown C, Raymond AK, Deavers MT, Yasko AW (2008) Aneurysmal bone cysts recur at Juxtaphyseal locations in skeletally immature patients. *Clin Orthop Relat Res* 466:722–728
- Lin ZY, Li YG (2009) Artificial pneumothorax with position adjustment for computed tomography-guided percutaneous core biopsy of mediastinum lesions. *Ann Thorac Surg* 87:920–924
- Little DC, Shah SS, St Peter SD et al (2006) Esophageal foreign bodies in the pediatric population: our first 500 cases. *J Pediatr Surg* 41:914–918
- Mitri RK, Brown SD, Zurakowski D, Chung KY, Konez O, Burrows PE, Colin AA (2002) Outcomes of primary image-guided drainage of parapneumonic effusions in children. *Pediatrics* 100:e37



- Molitch HI, Unger EC, Witte CL et al (1995) Percutaneous sclerotherapy of lymphangiomas. *Radiology* 194:343–347
- Nadolski G, Itkin M (2012) Feasibility of ultrasound-guided intranodal lymphangiogram for thoracic duct embolization. *J Vasc Interv Radiol* 23:613–616
- O'Donovan JC, Donaldson JS, Morello FP et al (1997) Symptomatic hemangiomas and venous malformations in infants, children, and young adults: treatment with percutaneous injection of sodium tetradecyl sulfate. *Am J Roentgenol* 169:723–729
- Ogita S, Tsuto T, Nakamura K et al (1994) OK-432 therapy in 64 patients with lymphangioma. *J Pediatr Surg* 29:784–785
- Okazaki T, Iwatani S, Yanai T et al (2007) Treatment of lymphangioma in children: our experience of 128 cases. *J Pediatr Surg* 42:386–389
- Oliveira AM, Perez-Atayde AR, Inwards CY et al (2004) USP6 and CDH11 oncogenes identify the neoplastic cell in primary aneurysmal bone cysts and are absent in so-called secondary aneurysmal bone cysts. *Am J Pathol* 165:1773–1780
- Pabon-Ramos WM, Williams DM, Strouse PJ (2010) Radiologic evaluation of blunt thoracic aortic injury in pediatric patients. *Am J Roentgenol* 194:1197–1203
- Panoutsakopoulos G, Pandis N, Kyriazoglou I et al (1999) Recurrent (16;17) (q22;p13) in aneurysmal bone cysts. *Genes Chromosomes Cancer* 26:265–266
- Partrick DA, Bensard DD, Teitelbaum DH, Geiger JD, Strouse P, Harned RK (2002) Successful thoracoscopic lung biopsy in children utilizing preoperative CT-guided localization. *J Pediatr Surg* 37:970–973
- Peclat MH, Newman KD, Eichelberger MR, Gotschall CS, Garcia VF, Bowman M (1990) Thoracic trauma in children: an indicator of increased mortality. *J Pediatr Surg* 25:961–966
- Pipitone BD, McCrate ME, Shiels WE (2010) In vitro assessment of a protein foam drug delivery system. *JVIR* 21(2S):51
- Porter DK, Van Every MJ, Anthracite RF, Mack JW (1983) Massive hemoptysis in cystic fibrosis. *Arch Intern Med* 143:287–290
- Rastogi S, Varshney MK, Trikha V, Khan SA, Choudhury B, Safaya R (2006) Treatment of aneurysmal bone cysts with percutaneous sclerotherapy using polidocanol. A review of 72 cases with long-term follow-up. *J Bone Joint Surg Br* 88:1212–1216
- Roebuck DJ, Hogan MJ, Connolly B, McLaren CA (2011) Interventions in the chest in children. *Tech Vasc Interv Radiol* 14:8–15
- Sola C, Choquet O, Prodhomme O, Capdevila X, Dadure C (2013) Management of mediastinal syndromes in pediatrics: a new challenge of ultrasound guidance to avoid high-risk general anesthesia. *Pediatr Anaesth* doi: [10.1111/pan.12300](https://doi.org/10.1111/pan.12300) [Epub ahead of print]
- Sciot R, Dorfman H, Brys P, Dal Cin P, De Wever I et al (2000) Cytogenetic-morphologic correlations in aneurysmal bone cyst, giant cell tumor of bone and combined lesions. A report from the CHAMP study group. *Mod Pathol* 13:1206–1210
- Shiels WE (2007) Soft tissue foreign bodies: sonographic diagnosis and therapeutic management. *Ultrasound Clin* 2:669–681
- Shiels WE, Babcock DS, Wilson JL, Burch RA (1990) Localization and guided removal of soft-tissue foreign bodies with sonography. *Am J Roentgenol* 155:1277–1281
- Shiels WE II, Brown SD (2005) Radiofrequency tumor ablation in children. In: van Sonnenberg E, McMullen WN, Solbiati L (eds) *Tumor ablation: principles and practice*. Springer, New York
- Shiels WE, Kang D, Murakami J, Hogan M, Wiet G (2009) Percutaneous treatment of lymphatic malformations. *Otolaryngol Head Neck Surg* 141:219–224
- Shiels WE, Kenney B, Caniano D, Besner G (2008) Definitive percutaneous treatment of lymphatic malformations of the trunk and extremities. *J Pediatr Surg* 43:136–140
- Shiels WE II, Mayerson JL (2013) Percutaneous doxycycline treatment of aneurysmal bone cysts with low recurrence rate: a preliminary report. *Clin Orthop Relat Res* 47:2675–2683
- Shisha T, Marton-Szucs G, Dunay M et al (2007) The dangers of intraosseous fibrosing agent injection in the treatment of bone cysts. The origin of major complications shown in rabbit model. *Int Orthop* 31:359–362
- Spiliopoulos S, Sabharwal T, Krokidis M et al (2012) Fluoroscopically guided dilation of esophageal strictures in patients with dystrophic epidermolysis bullosa: long-term results. *Am J Roentgenol* 199:208–212
- Sweezey NB, Fellows KE (1990) Bronchial artery embolization for severe hemoptysis in cystic fibrosis. *Chest* 97:1322–1326
- Trachiotis GD, Sell JE, Pearson GD, Martin GR, Midgley FM (1996) Traumatic thoracic aortic rupture in the pediatric patient. *Ann Thorac Surg* 62:724–731
- Topouchian V, Mazda K, Hamze B, Laredo JD, Pennecot GF (2004) Aneurysmal bone cysts in children; complications of fibrosing agent injection. *Radiology* 232:522–526
- Vignon P, Lagrange P, Boncoeur MP, Francois B, Gastinne H, Lang RM (1996) Routine transesophageal echocardiography for the diagnosis of aortic disruption in trauma patients without enlarged mediastinum. *J Trauma* 40:422–427
- Warren PS, Hogan MJ, Shiels WE (2013) Percutaneous transcervical thoracic duct embolization for treatment of a cervical lymphocele following anterior spinal fusion: a case report. *J Vasc Interv Radiol* 24:1901–1905
- Ye Y, Pringle LM, Lau AW et al (2010) TRE17/USP6 oncogene translocated in aneurysmal bone cyst induces matrix metalloproteinase production via activation of NF- $\kappa$ B. *Oncogene* 29:3619–3629
- Young AS, Shiels WE, Murakami JW, Coley BD, Hogan MJ (2010) Self-embedded behavior: radiological management of self-inflicted soft tissue foreign bodies. *Radiology* 257:233–239
- Zhang J, Li HB, Zhou SY (2013) Comparison between absolute ethanol and bleomycin for the treatment of venous malformation in children. *Exp Ther Med* 6:305–309

---

# Index

## A

Acquired, 220, 227, 228, 232–235, 237  
Agenesis-hypoplasia complex, 208, 225  
Air leaks, 183, 187  
Air-space diseases, 150  
Airways, 135, 219, 474  
Airways disorders, 104, 124, 135, 219–238  
    technique, 220  
    congenital, 222–228  
    acquired, 228–237  
    neoplasm, 231  
    trauma, 234  
Airways compromised in CHD (congenital heart disease), 474  
Airways, mimic lesions, 237  
Allergic bronchopulmonary aspergillosis, 138  
Alveolar development, 515  
Alveolar microlithiasis, 147  
Alveolar proteinosis, 143, 383  
Aneurism, 259  
Angel wing sign, 199  
Aorta, 101, 243, 467  
Aorta, MRI, 491  
    aortic arch anomalies, 491  
    aortic root dilatation, 491  
    coarctation, 491  
    vascular rings, 491  
Aortic arch, 226, 243, 491  
    double aortic arch, 226  
    right aortic arch, 226  
Apparent diffusion coefficient (ADC), 515  
Arterious malformation, 162, 448  
Aspergillosis, 150  
    invasive pulmonary aspergillosis, 150  
Aspiration pneumonia, 386  
Atypical pneumonia, 272  
Atresia, 168, 198  
Asplenia, 174  
Asthma, 138, 517  
Ataxia-Telangiectasis, 406–408

## B

Bacterial pneumonia, 273  
Beckwith-Weideman syndrome, 335  
Bronchial anomalies, 222  
Bronchial atresia, 198

Bronchial tumors, 105, 360  
Bronchiectasis, 136  
    conditions, 137  
    types, 136  
Bronchiolitis obliterans, 24, 139, 383  
Bronchiolitis obliterans organizing pneumonia (BOOP), 140  
Bronchogenic cyst, 36, 98, 162, 200  
Bronchopulmonary dysplasia (BPD), 149, 180, 516, 519

## C

Carcinoid tumor, 360  
Carcinoma, 361  
Cardiac CT, 459–479  
    dose optimization, 460  
    Fontan pathway, 461  
    intravenous contrast injection, 461–463  
    multidetector CT (MDCT), 459  
    prospective ECG triggering, 460  
    radiation, 460  
    retrospective ECG gating, 460  
    role of MDCT and MRI, 463  
    scan technique, 461–463  
    spatial-temporal resolution, 460  
    techniques, 460–463  
Cardiac CT, clinical applications  
    airway compromise in CHD, 474  
    aorta, 467–471  
    cardiac chamber morphology, 475–477  
    coarctation of the aorta, 467  
    connective tissue disorders, 469  
    coronary arteries, 471  
    dual-energy CT, 466  
    interrupted aortic arch, 467  
    Kawasaki disease, 472–474  
    mayor aortopulmonary collateral arteries (MAPCAs), 463  
    postoperative evaluation, 477–479  
    pulmonary arteries, 463  
    pulmonary embolism, 463–464  
    pulmonary vasculature, 463–467  
    pulmonary veins, 466–467  
    Takayasu arteritis, 260, 471  
Cardiac malformations, 168, 475, 493–498  
Cardiac morphology, MRI, 493–499  
    atrial pathology, 494  
    atrioventricular connections, 496

- complex segmental anatomy, 494
  - evaluation, 493
  - miscellaneous pathology, 497
  - outflow tract pathology, 496
  - segmental approach, 493
  - valvular pathology, 497
  - ventricular pathology, 496
  - Cardiac MRI, 483–501
    - indications, 484
  - Cardiac MRI, limitations, 500
  - Cardiac postoperative evaluation, 499, 477
    - congenital heart disease, 499
    - Fontan procedure, 500
  - Cardiac thrombus, 498
  - Cardiac tumors, 498
    - fibromas, 498
    - hemangioma, 498
    - malignant tumors, 498
    - Purkinje cell tumor, 498
    - rhabdomyoma, 498
    - tumor-like conditions, 498
  - Cardiac vasculature, MRI, 491–493
    - extra-cardiac vasculature, 491
      - aorta, 491
      - pulmonary artery, 492
      - pulmonary veins, 493
      - systemic veins, 493
  - Cardiomyopathy, 498
    - arrhythmogenic right ventricular cardiomyopathy, 498
    - hypertrophic obstructive cardiomyopathy, 498
    - iron overload cardiomyopathy, 499
    - left ventricular noncompaction, 498
  - Cardiovascular MRI, 484–501
    - black blood sequences, 485
    - bright blood sequences, 486
    - cine bright blood imaging, 487
    - contrast-enhanced MRI Angiography, 486
    - coil selection, 484
    - coronary imaging, 488
    - ECG-triggering, 484
    - flow quantification, 489
    - myocardial function, 490
    - parameters, 484
    - perfusion, 490
    - planes, 484
    - pulse sequences, 485
    - setting up a MRI study, 484
    - sedation, 484
    - techniques, 484
    - tissue characterization, 490
    - viability, 490
  - Chest Radiography, 1, 13–29
    - pitfalls, 15
    - technical pitfalls, 19
    - radiological density, 19
    - systematic approach, 13
    - techniques, 1–11
  - Chest Wall, 21, 431–456
    - congenital abnormalities, 432
    - infection, 439
    - lung herniation, 438
    - malformations and deformities, 433
    - normal variants, 432
    - Poland syndrome, 21
  - Chest wall, tumors, 444–453
    - Ewing sarcoma family, 452
    - fibrous tumor, 452
    - hemangioma, 445
    - lipoblastoma, 451
    - lymphangiomas, 448
    - mesenchymal hamartoma, 451
    - neurogenic tumors, 452
    - osteochondroma, 449
    - pseudotumors, 452
    - rhabdomyosarcoma, 452
    - vascular, 445
  - Chlamydia trachomatis pneumonia, 185
  - Ciliary dyskinesia, 419
  - Computed radiography, 4
  - Collagen-vascular disease, 145
  - Congenital, 220, 222, 224, 225, 227, 237
  - Congenital pulmonary airways malformation (CPAM), 159, 201
  - Connective tissue diseases, 396–398
    - juvenile dermatomyositis, 397
    - juvenile idiopathic arthritis, 396
    - juvenile systemic sclerosis, 396–397
    - systemic lupus erythematosus, 397–398
  - Constrictive bronchiolitis, 139, 140
  - Constrictive bronchiolitis after transplantation, 140
  - Continuous diaphragm sign, 199
  - Croup, 228
  - Cryptogenic organizing pneumonia, 387
  - Cushing syndrome, 339
  - Cystic fibrosis (CF), 137, 414, 518
    - diagnosis, 416
    - genetics, 415
    - imaging
      - chest radiograph, 417
      - CT, 418
      - MRI, 419
      - nuclear medicine, 418
      - lung care, 417
      - pulmonary pathophysiology, 416
      - scoring systems, 137
  - Cysts, 36, 102, 131, 162, 182, 200, 325
- ## D
- Dermatomyositis, 397
  - Diaphragm, accessory, 215
  - Diaphragmatic hernia, 48, 106, 164
  - Diaphragmatic rupture, 279
  - Deep sulcus sign, 199
  - Diffuse infiltrative lung disease, 141
    - chronic diffuse infiltrative disease, 141
    - classification, 141
  - Diffuse lung disease, 373–391
    - classification, 374
    - diffuse developmental disorders, 375
    - disorders of the normal immunocompetent host, 383
    - growth abnormalities, 376
    - specific disorders of unknown etiology, 377
    - systemic diseases, 383
    - vascular disorders, 388
  - Diffusion imaging, 515
  - DiGeorge syndrome, 334
  - Digital radiography, 3, 6
  - Digital flat-panel radiography, 5
  - Dissolved phase imaging, 515
  - Dose exposure, 8–11



Dynamic spin density imaging, 515  
 Dyskeratosis congenital, 406  
 Dysmorphic lung, 208

## E

Embryology, 328  
 Eosinophilic pneumonia, 384  
 Epiglottitis, 230  
 Escherichia coli, 185  
 ETT, 193  
 Extracorporeal membrane oxygenation, 183  
 Extrinsic allergic alveolitis, 142  
   Farmer's lung, 142

## F

Fetal MR, 157–170  
   cardiac malformations, 168  
   congenital malformations, 159  
   diaphragmatic hernia, 164  
   hydrothorax, 162  
   indications, 159  
   laryngeal atresia, 168  
   normal anatomy, 158  
   pulmonary lesions, 159  
   technique, 158  
   tumors, 170  
 Foreign body aspiration, 235, 305–321  
   clinical findings, 312  
   complications, 318  
   differential diagnosis, 312  
   imaging findings, 317  
   imaging techniques, 313  
   mechanisms airway obstruction, 310  
   types, 306  
 Function, 329, 418, 473, 475, 490, 505, 513

## G

Gaucher's disease, 148, 422  
 Germ cell tumors, 363  
 Glycogenosis, 149  
 Gorham's disease, 147  
 Granulomatous disorders, 398  
 Group B beta hemolytic streptococcus (GBS), 185  
 Growth abnormalities, 376

## H

Hamartoma, 355  
 Heart, 15, 459, 483  
 Helical multidetector CT, 75–106  
   CT angiography, 101  
   central airways, 104  
   dual-energy dual-source CT, 96  
   dual-source CT, 95  
   image postprocessing, 89  
   indications, 98–106  
   intravenous contrast, 83  
   parameters and protocols, 86  
   pitfalls, 79  
   sedation, 80  
   320-slice MDCT, 95  
   technique, 76  
 Helium-3 (He-3), 513

Hemangiomas, 170, 449  
 Hemosiderosis, 387  
 Heterotaxy, 174, 223  
 High-Resolution CT (HRCT), 111–132

  air-trapping, 127  
   emphysema, 132  
   expiratory slices, 121  
   G-G opacity, 124  
   halo sign, 132  
   honeycombing, 130  
   HRCT features, 124–132  
   lateral decubitus technique, 121  
   mosaic pattern, 130  
   parenchymal bands, 128  
   prone views, 121  
   pulmonary nodules, 125  
   sedation, 116  
   septal thickening, 128  
   signet ring sign, 132  
   special techniques, 119  
   technique, 112

High-Resolution CT, clinical applications, 135–151

High-Resolution CT findings in specific diseases, 141–151

Histology, 328

Histoplasmosis, 230

Horseshoe lung, 214

Hyaline membrane disease, 180

Hyaline membranes, 177

Hydrothorax, 162

Hyperpolarized gas magnetic resonance imaging (HG-MRI), 513–520

  indications, 515–520

  MR sequences, 328

  technique, 514

Hypersensitivity pneumonitis, 385

Hypogammaglobulinemia, 338

Hypogenetic lung syndrome, 211

## I

Imaging evaluation, 220, 237

Immotile cilia, 138

Immunodeficiencies, 399–411

  combined immunodeficiency, 404

  combined T-cell and B-cell immunodeficiencies, 404

  common variable immunodeficiency, 402

  hyper-IgM syndrome, 403

  Ig A deficiency, 401

  predominantly antibody deficiencies, 401–404

  severe combined immunodeficiency, 404

  X-linked agammaglobulinemia, 401

Immunodeficiencies, acquired, 409–411

  acquired immunodeficiency syndrome, 409

  acquired neutropenia invasive fungal disease, 411

Immunodeficiencies, defects of phagocyte, 408

  congenital defects of phagocyte number and/or function, 408

  chronic granulomatous disease, 408

Immunodeficiencies, syndromes, 404–407

  DiGeorge syndrome, 404–405

  Dyskeratosis congenita, 406

  hyper-IgE syndrome, 405–406

  Wiskott-Aldrich syndrome, 405

  ataxia-telangiectasia, 406

Infection, thorax, 268–277

  acute thoracic infection, 268

  atypical pneumonias, 272

  bacterial pneumonias, 273

- bronchiectasis, 277
- cavity necrosis, 277
- complications of pneumonia, 276
- differential diagnosis, 271
- evaluation of pneumonia, 270
- follow-up controls, 275
- fungal pneumonias, 274
- imaging techniques, 268
  - computed tomography, 268
  - fluoroscopy, 269
  - magnetic resonance imaging, 269
  - radiology, 268
  - ultrasound, 268
- lung abscess, 277
- parapneumonic effusions, 276
- parasitic lung infection, 275
- physiological considerations, 269
- pulmonary infiltrates, 269
- Swyer-James syndrome, 277
- viral pneumonias, 271
- Interstitial disease, 40, 373, 395
- Interstitial glycogenosis, 149, 377
- Interstitial emphysema, 187
- Interstitial pneumonias, 143, 386
  - acute interstitial pneumonia (AIP), 144, 386
  - desquamative interstitial pneumonitis (DIP), 144
  - idiopathic interstitial pneumonia, 144, 387
  - nonspecific interstitial pneumonia and fibrosis (NIPF), 144, 387
  - usual interstitial pneumonitis (UIP), 144
- Interventional radiology, 523–535
  - diagnosis, 523
  - indications, 523
  - management, 523
  - patient care, 524
  - protocols, 523
  - sedation, 524
  - techniques, 523
  - treatment, 523
- Interventional radiology procedures, 524–535
  - chest arteriography, 530
  - aortic trauma, 530
  - hemoptysis treatment, 530
  - transcatheter embolization, 530
  - empyema drainage, 527
  - esophageal stricture balloon dilatation, 525
  - foreign body removal, 524
  - lung abscess drainage, 527
  - mediastinal abscess drainage, 527
  - parapneumonic effusion, 526
  - percutaneous biopsy, 527
  - percutaneous drainage, 526
  - percutaneous treatment of aneurysmal bone, 534
  - thoracic duct embolization, 535
  - thoracic duct ligation, 535
  - thoracic duct lymphangiography, 535
  - sclerotherapy of vascular malformations, 532
  - lymphatic malformation, 532
  - venous malformation, 534
  - thermal ablation of thoracic malignancy, 529
    - cryoablation, 529
    - radiofrequency ablation, 529
    - microwave ablation, 529
  - thoracocentesis, 526
- Isomerism, 223
- J**
  - Juvenile idiopathic arthritis, 396
- K**
  - Kawasaki disease, 260
- L**
  - Langerhans' cell histiocytosis, 141, 420–421
  - Large airway, 219–222, 225–229, 231–234, 237, 238
  - Large airway disorders, 219–238
    - acquired, 228–237
    - congenital, 222–228
    - technique, 220–222
  - Large airway, mimic lesions, 237
  - Large airway, neoplasm, 231–234
    - carcinoid, 232
    - hemangiomas, 231
    - metastasis, 234
    - mucocystic, 233
    - papillomatosis, 232
  - Large airway, trauma, 234
  - Laryngeal atresia, 168
  - Leiomyoma, 363
  - Leiomyomatosis, 367
  - Leiomyosarcoma, 363
  - Leukemia, 340
  - Lobar agenesis-aplasia complex, 209, 211, 212
  - Lobar emphysema, 35, 198
  - Lobar malformations, 209
  - Lung, 21, 32, 66, 99, 111, 135, 176
    - decreased lung density, 21
    - horseshoe lung, 35
    - hypogenetic lung, 214
    - increased lung density, 25
    - increased volume, decreased vascularity, 23
    - increased volume, normal vasculature, 21
    - normal volume, decreased vascularity, 21
    - unilateral hyperlucent lungs, 24
  - Lung function, 513
  - Lung malformations, 197–215
  - Lung MRI, 505–511
    - lung morphology, 506
    - lung pathologies, 506
    - lung perfusion, 509
  - Lupus erythematosus, 397
  - Lymphangiectasia, 146, 162, 389
  - Lymphangiomas, 147, 365
  - Lymphangitic carcinomatosis, 145
  - Lymphocytic interstitial pneumonia, 145
  - Lymphoma, 341–347, 354
    - Hodgkin Lymphoma, 341
      - Ann Arbor staging, 341
      - Bulky disease, 342
      - non-Hodgkin Lymphoma, 342
    - anaplastic large cell lymphoma (ALCL), 342
    - Burkitt lymphoma (BL), 342
    - diffuse large B-cell lymphoma (DLBCL), 342
    - Jude staging, 342
    - primary mediastinal B-cell lymphoma (PMBL), 343
    - T-cell neoplasm lymphoblastic lymphoma (T-LBL), 342
    - staging, 345
    - International Harmonization Criteria, 346

surveillance, 346  
Lymphoproliferative disorders, 354  
Lysosomal store disease, 422

## M

Meconium aspiration syndrome (MAS), 182  
Mediastinal masses, 335–463, 363–367  
    benign thymic masses, 335  
    esophageal leiomyomatosis, 335  
    germ cell tumors, 363  
    lymphangiomatosis, 365  
    malignant thymic masses, 367  
    neuroblastic tumors, 364  
Mediastinal vascular disorders, 241  
    acquired, 258  
    congenital, 243  
    technique, 242  
Mediastinum, 14, 55, 241, 349  
Mucopolysaccharidosis, 423  
Myasthenia gravis, 338  
Myofibroblastic tumor, 357  
Myofibromatosis, 356

## N

Neoalveolarization, 516  
Neonatal chest, 173–194  
Neonatal chest diseases, 176–189  
Neonatal pneumonia, 183  
Neuroblastic tumors, 364  
Neuroendocrine cell hyperplasia, 149, 378  
Neuroenteric cyst, 162  
Niemann-Pick disease, 422  
Nuclear medicine, 65–72  
    clinical interpretation, 67, 72  
    PET, 70  
    PET/CT, 70  
    SPECT, 67  
    technique, 66

## O

Organizing pneumonia, 140  
Oxygen sensitive imaging, 515

## P

Papillomas, 362  
Pediatric patients, 225, 227, 228, 233–236  
Persistent pulmonary hypertension of the newborn (PPHN), 183  
PET imaging, 70, 332, 345  
Pleura, 26  
    pleural effusion, 26  
    pneumothorax, 28  
Pleuropulmonary blastoma, 359  
Pneumocystic Carinii pneumonia, 150  
Pneumomediastinum, 187  
Pneumonia, 183, 270, 384  
Pneumopericardium, 189  
Pneumothorax, 188  
Polysplenia, 174  
Primary ciliary dyskinesia, 419  
Pulmonary agenesis, 225  
Pulmonary artery, 248, 492, 463  
Pulmonary artery, MRI, 492

    pulmonary artery stenosis, 492  
    pulmonary sling, 492  
Pulmonary fibrosis, 143  
Pulmonary hamartoma, 355  
Pulmonary hemorrhage, 147  
Pulmonary hemosiderosis, 387  
Pulmonary hypoplasia, 208, 225  
Pulmonary interstitial emphysema (PIE), 187  
Pulmonary lymphangiectasia, 146, 162, 389  
Pulmonary lymphangitic carcinomatosis, 145  
Pulmonary malformations, 36, 197  
Pulmonary sling, 226  
Pulmonary tumors, 349, 351–363  
    blastoma, 359  
    carcinoids, 360  
    chondroma, 355  
    fetal lung interstitial tumor, 355  
    hamartoma, 355  
    leiomyoma, 363  
    leiomyosarcoma, 363  
    lymphoma, 354  
    metastases, 352  
    mucoepidermoid carcinoma, 361  
    myofibroblastic tumors, 357  
    myofibromatosis, 356  
    NUT middle carcinoma, 361  
    papillomas, 362  
    squamous cell carcinoma, 362  
Pulmonary veins, 212, 255, 266, 493  
Pulmonary veins, MRI, 493  
    anomalous pulmonary veins, 493  
    pulmonary vein stenosis, 493  
    systemic veins, 493  
Pulmonary veno-occlusive disease, 388

## R

Rebound thymic hyperplasia, 336  
Red cell aplasia, 338  
Respiratory distress syndrome (RDS), 174, 176

## S

Sarcoidosis, 142, 398  
Sedation, 80, 116  
Sequestration, 36, 102, 159, 204  
Severe Combined immunodeficiency (SCID), 334  
Scimitar syndrome, 212  
Sickle cell disease, 413  
Static spin density imaging, 515  
Storage disease, 422  
    Gaucher disease, 422  
    lysosomal storage disease, 422  
    mucopolysaccharidosis, 423  
    Niemann-Pick disease, 422–423  
Subpleural cysts, 182  
Surfactant, 177  
Surfactant deficiency, 176  
Surfactant deficiency disease, 180  
Surfactant dysfunction diseases, 149, 380  
    abnormalities of TTF1, 149  
    autosomal dominant surfactant protein C (Sp-C), 149  
    autosomal-recessive protein A3 (ABCA3), 149  
    autosomal-recessive surfactant protein B (Sp-B), 149  
    genetic disorders, 380  
    others, 149



SVC syndrome, 343  
 Swyer-James-MacLeod's syndrome, 139, 277  
 Systemic diseases, 395–423, 383  
 Systemic granulomatous disorders, 398  
 Systemic sclerosis, 396  
 Systemic supply to normal lung, 207  
 Systemic veins, 493, 463

## T

Techniques, 1–11  
 Thymic disorders, 327–347  
 Thymic masses, 335–347  
   carcinoids, 339  
   carcinoma, 338  
   cysts, 335  
   other masses, 339–347  
   thymic hyperplasia, 336  
   thymolipoma, 336  
   thymoma, 337  
 Thymus, 14, 55, 327–347  
   accessory cervical thymic tissue, 333  
   anatomy, 329  
   cardiothymic incisures, 14  
   congenital and developmental anomalies, 333  
   congenital thymic hyperplasia, 335  
   imaging appearance, 329  
   involution, 329  
   normal thymus, 14  
   retrocaval, 333  
   sail sign, 14, 330  
   suprasternal extension, 333  
   thymic rebound, 14  
   wave sign, 14  
 Tomosynthesis, 10  
 Trachea, 15, 219, 222, 227, 228, 234  
   abnormalities, 15, 222  
   pitfalls, 15  
   subglottic trachea, 15  
 Tracheal stenosis, 224  
 Tracheitis, 229  
 Tracheomalacia, 15, 17, 227  
 Transient tachypnea of the newborn (TTN), 176  
 Trauma, thorax, 258, 277–282, 453  
   chest wall injuries, 279, 453  
   diaphragmatic rupture, 279  
   esophageal rupture, 281  
   imaging techniques, 278  
   lung laceration, 281  
   mediastinal injuries, 281  
   pneumothorax, 280  
   pulmonary contusion, 280  
   tracheobronchial injuries, 280  
   traumatic lung cyst, 281  
   traumatic vascular lesions, 258  
 Trauma, non-accidental, 454  
 Tuberculosis, 230, 285–300  
   clinical aspects, 288  
   complications, 299  
   congenital TB, 297  
   disease, 288  
   epidemiology, 286  
   Ghon focus, 291  
   imaging techniques, 290  
   infection, 287, 290  
   lymph nodes disease, 288

  military disease, 295  
   pathogenesis, 287  
   pericardial disease, 297  
   pleural disease, 295  
   primary complex, 290  
   unusual presentation, 299  
 Tuberculosis, adult type disease, 297  
 Tuberculosis, HIV infection, 299  
 Tuberculous sclerosis, 421–422  
 Tumors, 42, 231, 335, 349, 351–367, 444, 498

## U

Ultrasound, 31–60  
   chest wall, 46  
   congenital malformations, 32  
   diaphragm, 47  
   interstitial disease, 32  
   lung consolidation, 37  
   lung parenchyma, 32  
   lung tumors, 42  
   management of congenital malformations, 32  
   mediastinum, 49–60  
   opaque hemithorax, 45  
   pitfalls, 51  
   pleura, 42  
   technique, 32  
 Umbilical recess, 192  
 Ureaplasma urealyticum, 185  
 UVC and UAC, 199

## V

VACTERL, 174  
 Valvular-supravalvular aortic stenosis, 469  
 Vascular anatomy, 101  
 Vascular disorders, 241–262, 388  
   technique, 242  
 Vascular disorders, acquired, 258–262  
   infectious lesions, 259  
   mycotic lesions, 259  
   traumatic lesions, 258  
   thrombotic lesions, 261  
   vasculitis, 259  
 Vascular disorders affecting large airways, 225–227  
 Vascular disorders, congenital, 243–358  
   aortic arch hypoplasia, 252  
   aortopulmonary collaterals, 255  
   coarctation of the aorta, 250  
   double aortic arch, 243  
   interruption of the aortic arch, 252  
   left aortic arch anomalies, 248  
   patent ductus arteriosus, 254  
   pulmonary artery sling, 248  
   right aortic arch anomalies, 245  
   venous lesions, 255–258  
 Vascular rings, 101, 243  
 Vasculitis, 145, 259, 411  
   Chug-Strauss angitis, 145  
   granulomatosis with polyangiitis, 412  
   Kawasaki disease, 260  
   lupus erythematosus, 146  
   microscopic polyangiitis, 145, 412–413  
   systemic connective tissue disease, 146  
   systemic sclerosis, 146  
   Takayasu arteritis, 260

Wegener 's granulomatosis, [145](#)  
Venolobar syndrome, [212](#)  
Veno-occlusive disease, [388](#)  
Venous lesions, [255–258](#)  
    anomalous systemic venous connection, [257](#)  
    pulmonary varix, [257](#)  
    pulmonary vein atresia/hypoplasia, [255](#)  
    pulmonary vein stenosis, [256](#)

    pulmonary veins anomalies, [255](#)  
Ventricular finction, [473](#)  
Viral pneumonia, [271](#)

## **X**

Xenon-129 (Xe-129), [98](#), [513](#)